european society for precision engineering and nanotechnology

Conference Proceedings

26th International Conference & Exhibition

Monday 8th to Friday 12th June 2026

Premier Hotel,
Kraków, Poland

RENISHAW
apply innovation™

euspen

Proceedings of the 26th international conference of the **eu**ropean **s**ociety for **p**recision **e**ngineering and **n**anotechnology

8th – 12th June 2026
Kraków, PL

Editors:
O. Riemer

Internal Review Committee:
A. Archenti
L. Blunt
D. Reynaerts
O. Riemer
J. A. Yagüe-Fabra

Proceedings Compilation:
N. Birsan
S. Moxom
D. Phillips
R. Phillips

euspen

Proceedings of the 26th international conference of the **eu**ropean **s**ociety for **p**recision **e**ngineering and **n**anotechnology

International Scientific Committee:

Assoc. Prof. J.A. Albajez, *University of Zaragoza, Spain*

Prof. A. Archenti, *KTH Royal Institute of Technology, Sweden*

Dr F. Balzer, *Hexagon Metrology, Germany*

Dr C. Bermudez, *Sensofar Metrology, Spain*

Dr F. Blateyron, *Digital Surf, France*

N. Blondiaux, *CSEM SA, Switzerland*

Prof. L. Blunt, *University of Huddersfield, UK*

Dr H. Bosse, *PTB, Germany*

Dr E. Buice, *Lawrence Berkeley National Laboratory, USA*

B. Bulla, *son-x GmbH, Germany*

S. Catalucci, *University of Padua, Italy*

Prof. K. Cheng, *Brunel University, UK*

Dr. C.L.F. de Assis, *Federal Institute of São Paulo, Brazil*

Dr P. de Groot, *Zygo, USA*

Prof. F. Ducobu, *Université de Mons, Belgium*

Dr J. Edelmann, *Fraunhofer IWU, Germany*

Prof. M. Galetto, *Politecnico di Torino, Italy*

Prof. A. Gąska, *Cracow University of Technology, Poland*

Dr. S. Gasparin, *LEGO Systems A/S, Denmark*

Prof. R. Goulart Jasinevicius, *University of São Paulo, Brazil*

Dr. R. Grejda, *Corning Tropel, USA*

Prof. J. Guo, *Dalian University of Technology, China*

Prof. H. Haitjema, *KU Leuven, Belgium*

Prof. H. Hansen, *Technical University of Denmark, Denmark*

Dr O. Horejs, *Czech Technical University in Prague, Czech Republic*

Dr A. Islam, *Technical University of Denmark, Denmark*

Prof. K-N. Joo, *Chosun University, South Korea*

Assist. Prof. E. Kamenar, *University of Rijeka, Croatia*

Prof. T. Kissinger, *Technical University of Ilmenau, Germany*

Dr B. Knapp, *Professional Instruments Company, USA*

Dr. W. Knapp, *Engineering Office, Schleitheim, Switzerland*

Dr S. Kühne, *Technical University of Berlin, Germany*

Y. J. Lee, *National University of Singapore, Singapore*

Y. Li, *Fine Optical Engineering Research Center, China*

Dr T. Liebrich, *Rhysearch, Switzerland*

G. Liotto, *Laser Metrology S.R.L, Italy*

Dr S. Lou, *University of Huddersfield, UK*

Dr S. Ludwick, *Aerotech Inc., USA*

Prof. X. Luo, *University of Strathclyde, UK*

Dr H. Mainaud Durand, *CERN, Switzerland*

Dr M. Mareš, *Czech Technical University in Prague, Czech Republic*

Dr P. Martin, *AWE, UK*

Prof. Dr. Ing. M. Marxer, *NTB, PWO, Switzerland*

Dr J. Mayr, *IWF, ETH Zurich, Zurich*

Prof. G. McFarland, *Renishaw plc, UK*

Dr. R. Meeß, *PTB, Germany*

Dr C. Mehdi-Souzani, *ENS, France*

Dr U. Mutilba, *Tekniker, Spain*

Prof. W. Natsu, *Tokyo University of Agriculture and Technology, Japan*

Dr. H. Nouira, *LNE, France*

Prof. Dr D. Oberschmidt, *TU Berlin, Germany*

Dr G. Olea, *HUBER GmbH Co.KG, Germany*

Asst. Prof. T. Österlind, *KTH Royal Institute of Technology, Sweden*

Dr M. Percic, *University of Rijeka, Croatia*

Prof. G. Percoco, *Politecnico di Bari, Italy*

Dr J. Qian, *KU Leuven, Belgium*

Prof. D. Reynaerts, *KU Leuven, Belgium*

Dr O. Riemer, *University of Bremen (LFM), Germany*

Prof. M. Rucki, *Kazimierz Pulaski University of Technology and Humanities in Radom, Poland*

Prof. E. Savio, *University of Padova, Italy*

Prof. S. Skoczypiec, *Cracow University of Technology, Poland*

Dr H. Spaan, *IBS Precision Engineering, Netherlands*

Dr J. Stammers, *AMRC, UK*

Dr N. Y. J. Tan, *Advanced Remanufacturing and Technology Centre, Singapore*

Dr J. S. Taylor, *University of North Carolina at Charlotte, USA*

Dr R. Tomkowski, *KTH Royal Institute of Technology, Sweden*

Prof. Z. Tong, *Shanghai Jiao Tong University, China*

Assoc. Prof. G. Tosello, *Technical University of Denmark (DTU), Denmark*

Dr H. Urreta, *IDEKO, Spain*

Prof. H. Van Brussel, *KU Leuven, Belgium*

Dr P. Vavruska, *Czech University, Czech Republic*

Asst. Prof. R. Viitala, *Aalto University School of Engineering, Finland*

Dr C. Wang, *The Hong Kong Polytechnic University, Hong Kong*

Asst. Prof. H. Wang, *National University of Singapore, Singapore*

Prof. J. Yague-Fabra, *University of Zaragoza, Spain*

Asst. Prof. Dr N. Yu, *University of Edinburgh, UK*

Dr F. Zanini, *University of Padua, Italy*

Prof. S. Zelenika, *University of Rijeka, Croatia*

Asst. Prof. J. Zhang, *National University of Singapore, Singapore*

Published by eu**spen**
ISBN: 978-1-9989991-9-4

Printed in the UK, June 2026
twenty10
33 Rothersthorpe Crescent Mews
Northampton, NN4 8JD, UK

© eu**spen** Headquarters
Cranfield University Campus
Building 90, College Road
Bedford MK43 0AL, UK
Tel: +44 (0) 1234 754023
Website: www.euspen.eu

Information correct at time of print and may become subject to change

SPONSORING CORPORATE MEMBERS

eu**spen** is grateful for the generous sponsorship of these leading companies who set the standard for developments in precision engineering and nanotechnology.

AEROTECH	ASML	BOSCH
fives Cranfield Precision	HEIDENHAIN	MI Partners PARTNERS IN MECHATRONIC INNOVATION
MICRO-EPSILON	NPL National Physical Laboratory	precitech
	RENISHAW apply innovation™	

RENISHAW
apply innovation™

The future of metrology is here

Renishaw continues to innovate with powerful solutions for process automation, closed-loop process control, and rapid part verification.

We've been shaping the future of industry for over 50 years. Our latest innovations include the Equator-X™ 500 dual-method gauge and revolutionary, MODUS™ IM Equator intelligent metrology software.

The future of metrology is not just on the horizon – it's here, now.

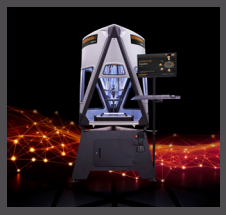

www.renishaw.com

Renishaw plc, New Mills, Wotton-under-Edge, Gloucestershire, UK, GL12 8JR +44 (0)1453 524524 uk@renishaw.com
© 2026 Renishaw plc. All rights reserved.

Foreword

The 26th eu**spen** conference and exhibition will be held at the Cracow University of Technology in Poland, from June 8th – 12th, 2026. The organising committee is formed by Cracow University of Technology, Rzeszow University of Technology and eu**spen** HQ.

Economic development in Poland in recent decades has been marked by a clear shift toward high-technology sectors, including precision engineering, the automotive and aerospace industries, and advanced manufacturing methods. A key role has been played by integration with the European market, access to EU funds, and the development of research and development infrastructure. This is particularly evident in the Lesser Poland region, which thanks to a strong academic center in Krakow and well-developed innovation infrastructure has become an important technological hub. In this region, companies specializing in precision engineering are developing dynamically, including the production of high-accuracy components for the medical, electronics, and aerospace industries. The automotive sector includes numerous supplier companies and service centers supporting production. The aerospace industry, in turn, benefits from proximity to the Podkarpackie region (the so-called "Aviation Valley"), which fosters cooperation and knowledge transfer. An important driver of growth is also the adoption of modern manufacturing methods such as automation, robotics, and additive manufacturing, which increase the competitiveness of enterprises.

Cracow University of Technology (CUT) is a leading public university with 80 years of tradition in educating engineers and advancing Polish science and technology. Established in 1945 and named after national hero and engineer Tadeusz Kościuszko, CUT combines respect for tradition with openness to innovation. With a vibrant community of approximately 12,000 students and more than 1,100 academic teachers, CUT has educated more than 115,000 alumni who have pursued successful careers in business, government, academia, and research worldwide.

The three keynotes for this conference originate from Warsaw University of Technology, Eastern Switzerland University of Applied Sciences (OST) and from Fraunhofer IPK. **Prof. Adam Woźniak** will speak about on-machine in-process coordinate measurement, **Prof. Michael Marxer** will report on aperture calibration at 0 °C and metrological challenges related with this process and **Prof. Julian Polte** will present on empowering global health by precision engineering.

Prof. Adam Woźniak is a Professor of technical sciences and academic lecturer at Warsaw University of technology (Poland). He is the author of two monographs and nearly 200 scientific papers. He has led over a dozen research projects and participated in international research teams under NSERC, Canada Collaborative Research and Development Grants.

Prof. Woźniak will in his presentation analyse sources of errors in measurements performed on CNC machine tools related to probe errors, he will also present patented system designed to directly test the metrological characteristics of measuring probes used in CNC machine tools. The results of modelling and error correction of measuring probes used in CNC machine tools will also be presented. Topics will be discussed regarding changes in the metrological properties and reliability of probes during operation, taking into account load levels and failure limits.

Prof. Michael Marxer is currently a Professor in the Institute for Microtechnology and Photonics, Eastern Switzerland University of Applied Sciences (Buchs, Switzerland). His professional interests include production metrology, multi-sensor coordinate metrology, sensor development, calibration and traceability, roughness metrology, and industrial measurement processes. He is President of CMTrain e.V., an association dedicated to education and training in coordinate metrology using blended learning concepts, and a member of the guideline committee VDI 2617 in Germany.

Prof Marxer will give a keynote presentation on aperture calibration at 0 °C and metrological challenges beyond established standards. This keynote will reflect on practical experience gained from the manufacturing and calibration of high-precision apertures at the OST – Eastern Switzerland University of Applied Sciences, in close collaboration with RhySearch. A particular focus will be placed on the calibration of apertures at 0 °C, rather than the conventional reference temperature of 20 °C. This shift introduces fundamental challenges related to thermal behaviour, measurement uncertainty, traceability, and the validity of established metrological concepts.

Prof. Julian Polte serves as Managing Director of the Institute for Machine Tools and Factory Management IWF at Technical University Berlin and Head of Chair as Professor while concurrently holding the position of Deputy Director of Fraunhofer IPK. Prof. Polte's expertise encompasses the entire spectrum of production technology, ranging from ultra-precision and high-precision cutting to non-conventional processes such as EDM and additive manufacturing. A central pillar of his research involves manufacturing technologies, process development, and machine tool development for advanced production systems.

Prof. Polte in his keynote will speak about empowering global health by precision engineering. The keynote discusses how precision engineering is driving the transformation of global healthcare, particularly in response to the growing burden of chronic diseases and the need for more resilient medical systems. It highlights real-world innovations such as ultra-miniaturized heart pumps and advanced manufacturing technologies that enable both life-saving interventions and the shift toward personalized medicine. Overall, the talk will emphasize the integration of engineering, digitalization, and human–AI collaboration as key to making advanced, scalable, and accessible healthcare solutions worldwide.

This conference and exhibition will provide a leading forum for industrialists and academics alike to review the best of world-wide industrial innovation, progressive research and technology development, with relevant examples and cases from Poland and other parts of the world. The conference will provide ample scope for strategic networking among attendees from industry and academia and the academic contributions will be supplemented by industrial presentation and a comprehensive technical exhibition show-casing leading technologies in the precision engineering sector.

We cordially invite you to Cracow University of Technology and to visit the wonderful host City, and we are looking forward to meeting you there.

Andreas Archenti

eu**spen** President

Adam Gąska

on behalf of the Organising committee

Keynotes

K1 **On-machine in-process coordinate measurement** **34**
Prof. Adam Woźniak
Warsaw University of Technology, Poland

K2 **Aperture Calibration at 0 °C: Metrological Challenges Beyond Established Standards** **35**
Prof. Dr.-Ing Michael Marxer
Eastern Switzerland University of Applied Sciences, Institute for Microtechnology and Photonics, Competence Centre for Production Metrology

K3 **Empowering Global Health by Precision Engineering** **36**
Prof. Julian Polte
TU Berlin; Deputy Director Fraunhofer IPK, Head of Business Unit Production Systems at IPK; Managing Director Institute for Machine Tools and Factory Management (IWF); Head of Chair Machines and Technologies for Additive Precision Manufacturing of Metal Components at IWF

Session 1: Metrology

O1.01 **Development of a compact gear measuring machine based on modified line-of-action scanning for high-precision tooth profile measurement** **40**
Yohan Kondo[1], Yuta Miyakawa[2], Yukihiro Kato[2], Kazuya Matsuzaki[1], Osamu Sato[1]
[1]National Metrology Institute of Japan(NMIJ), National Institute of Advanced Industrial Science and Technology (AIST)
[2]Tokyo Technical Instruments Inc.

O1.02 **Investigating filter end-effects on profiles having form, in the context of ISO 21920** **44**
Faivre A[1], Blateyron F[1]
[1]Digital Surf, Besançon, France

O1.03 **Enhanced In-Situ Focus Variation Surface Metrology via Pattern-Projected Illumination for Highly Polished Electrochemical Surfaces** **48**
Hussam Muhamedsalih, Aalim M. Mustafa, Prashant Kumar, Xiangqian (Jane) Jiang, Liam Blunt
University of Huddersfield Queensgate, Huddersfield, HD1 3DH

O1.04 **Ultra-compact metalens-based phase shifting interferometry for surface metrology** **52**
Dawei Tang[1], Hangyu Li[1], James Williamson[1], Daniel Townend[1], Jun-Yu Ou[2], Haydn Martin[1], Andrew Henning[1], Xiangqian (Jane) Jiang[1]
[1]Centre for Precision Technologies, University of Huddersfield, Huddersfield, HD1 3DH, UK,
[2]School of Physics and Astronomy, University of Southampton, Southampton, SO17 1BJ, UK

O1.05 **Modeling of coordinate measurement uncertainty using an expert system with machine learning elements** **54**
Danuta Owczarek[1], Łukasz Wilk[1], Wiktor Harmatys[1], Michał Jedynak[1], Piotr Gąska[2], Maciej Gruza[1], Konrad Kobiela[1], Karol Stroński[1], Katarzyna Składanowska[1], Izabela Sanetra[1], Marek Markiewicz[1]
[1]Laboratory of Coordinate Metrology, Faculty of Mechanical Engineering, Cracow University of Technology, al. Jana Pawła II 37, Krakow, Poland
[2]Faculty of Mechanical Engineering and Robotics, AGH University of Krakow, al. Mickiewicza 30, Krakow, Poland

P1.01 **Analysis of measurement uncertainty contributions of optical sensors for the development of digital-metrological twins in coordinate metrology** **56**
Daniel Heißelmann[1], Lea-Jean Frömel[1], Katharina Janzen[1], Wiktor Harmatys[2], Adam Gąska[2], Ulrich Neuschaefer-Rube[1]
[1]Physikalisch-Technische Bundesanstalt (PTB), Coordinate Metrology Department, Braunschweig, Germany
[2]Cracow University of Technology, Mechanical Dep. Laboratory of Coordinate Metrology M10, Krakow, Poland

P1.02 **Wafer warpage measurements by stitching lateral shearing interferometry** **60**
Seongwook Jang[1] and Ki-Nam Joo[1]
[1]Department of Photonic Engineering, Chosun University, 309 Pilmun-daero, Dong-gu, Gwangju 61452, South Korea

P1.03 **Lateral resolution enhancement of white light scanning interferometer** **62**
Min Seo Cho[1] and Ki-Nam Joo[1]
[1]Department of Photonic engineering, Chosun University, Gwangju, Republic of Korea

P1.04 **Assembly and evaluation of a spectrometer by using a spectral interferometer** **66**
Seoyoon Lee[1] and Ki-Nam Joo[1]
[1]Department of Photonic Engineering, Chosun University, 309 Pilmun-daero, Dong-gu, Gwangju 61452, South Korea

P1.06 **Thermal behavior analysis of a novel measurement system for precise displacement sensors calibration** **68**
Luka Čas, Bojan Ačko and Rok Klobučar
University of Maribor, Faculty of Mechanical Engineering, Laboratory for Production Measurement

P1.07 **Multisensory and multiscale characterization of selected technological surfaces using optical methods** **72**
Michał Jakubowicz[1], Karol Grochalski[1], Tomasz Bartkowiak[1], Bartosz Gapiński[1], Michał Wieczorowski[1]
[1]Poznan University of Technology, Jacka Rychlewskiego Street 1, 61-131 Poznan

P1.08 **Glossary of terms and definitions of digital metrological twins for freeform metrology** **76**

Ivana Linkeová[1], Jan Soukal[1], Daniel Heißelmann[2], Katharina Janzen[2], Ulrich Neuschaefer-Rube[2], Lea-Jean Frömel[2], Adam Wojtowicz[3,11], Dariusz Czulek[3], Hichem Nouira[4], Ermes Xhafa[4], Sten Bergstrand[5], Andreas Thore[5], Carl-Henrik Hanquist[5], Walter Knulst[6], Marcel van Dijk[6], Devrim Nalbantoglu[6], Gertjan Kok[6], Björn Hemming[7], Ville Heikkinen[7], Antti Lassila[7], Guido Tossello[8], Nabil Anwer[9], Pablo Puerto[10], Asier Garcia Berdote[10], Adam Gaska[11], Wiktor Harmatys[11], Giacomo Maculotti[12], Maurizio Galetto[12], Elisa Verna[12], Gianfranco Genta[12], Matthias Bodenbenner[13], Yixiang Dang[13], Robert H. Schmitt[13], Gorka Kortaberria[14], Eneko Gomez-Acedo[14], Unai Mutilba[14], Enrico Savio[15], Sofia Catalucci[15], Lorenzo Didonè[15], Hageney Hageney[16], Andreas Pierro[16], Florian Paul[16], Thomas Maresch[17], Makoto Abe[18], Dietrich Imkamp[19], Osamu Sato[20]

[1]Czech Metrology Institut (CMI), Czechia
[2]Physikalisch-Technische Bundesanstalt (PTB), Germany
[3]Central Office of Measures (GUM), Poland
[4]Laboratoire national de métrologie et d'essais (LNE), France
[5]RISE Research Institutes of Sweden AB, Sweden
[6]VSL B.V., Netherlands
[7]Teknologian tutkimuskeskus VTT Oy, Finland
[8]Danmarks Tekniske Universitet (DTU), Denmark
[9]Ecole Normale Supérieure Paris-Saclay, France
[10]IDEKO, Basque Research and Technology Alliance (BRTA), Spain
[11]Cracow University of Technology, Faculty of Mechanical Engineering, Poland
[12]Dept. of Management and Production Engineering, Politecnico di Torino, Italy
[13]WZL-IQS | RWTH Aachen University, Germany
[14]Fundacion Tekniker, Spain
[15]Università degli Studi di Padova, Italy
[16]Eumetron GmbH, Germany
[17]Hexagon Metrology GmbH, Germany
[18]Mitutoyo CTL Germany GmbH, Germany
[19]Carl Zeiss Industrielle Messtechnik GmbH, Germany
[20]National Institute of Advanced Industrial Science and Technology (AIST), Japan

P1.09 **Mathematical softgauges: a new method for validating metrology algorithms** **80**

Blateyron F[1]

[1]Digital Surf, Besançon, France

P1.10 **Automated Geometric Segmentation of Additively Manufactured Strut-Based Lattices for Geometric Characterization: Node – based Analysis** **82**

Y. Zekalmi [1a], D. Gallardo[2], L.C. Díaz-Pérez[2], J.A. Albajez[2], J.A. Yagüe-Fabra[2]
[1]University of Zaragoza, Zaragoza, Spain
[2]I3A, Universidad de Zaragoza, Zaragoza, Spain

P1.11 **Deep learning-based removal of phase shift errors in phase-shifting interferometry for high-accuracy surface metrology** **86**

Young-Sik Ghim[1, 2], Manh The Nguyen[1], Hyug-Gyo Rhee[1, 2]

[1]Length and Dimensional Metrology Group, Division of Physical Metrology, Korea Research Institute of Standards and Science (KRISS), Science Town, Daejeon 34113, South Korea,
[2]Department of Science and Measurement, University of Science and Technology (UST), Science Town, Daejeon 34113, South Korea

P1.12 **Generalization of area-scale analysis for complex additively manufactured freeform surfaces** **88**
Tomasz Bartkowiak[1], Antoni Milecki[1], Michał Jakubowicz[1], Patryk Mietiński[1], Michał Wieczorowski[1], Christopher A. Brown[2]
[1]Institute of Mechanical Technology, Poznan University of Technology, Poland
[2]Surface Metrology Laboratory, Worcester Polytechnic Instutute, Worcester, MA, USA

P1.13 **Assessment of Geometric Errors in Coordinate Measuring Machines with Ring Gages** **92**
Sousa, Andre[1]
[1]Federal Institute of Science and Technology of Santa Catarina, Brazil

P1.15 **Digital metrological twins for stereovision systems - A literature review** **96**
Katarina Josic[1,2,3], Ladji Fofana[1,2,3], Louis-Ferdinand Lafon[1], Charyar Mehdi-Souzani[2], Romain Brault[3], Nabil Anwer[2], Olivier Bruneau[2], Hichem Nouira[1]
[1]Laboratoire national de métrologie et d'essais/Conservatoire national des arts et métiers, 1 Rue Gaston Boissier, 75015 Paris, France,
[2]Université Paris-Saclay, ENS Paris-Saclay, LURPA, 91190 Gif-sur-Yvette, France,
[3]Centre technique des industries mécaniques, 52 Avenue Félix Louat, 60300 Senlis, France

P1.16 **Non-contact calibration of resin gauge for assessing measurement errors of X-ray CT** **100**
Mari Watanabe[1,2], Osamu Sato[1], Mariko Kajima[1], Youichi Bitou[1], Masaki Michihata[2], Satoru Takahashi[2]
[1]Dimensional Standards Group, Research Institute for Engineering Measurement, NMIJ, AIST,
[2]Department of Precision Engineering, School of Engineering, The University of Tokyo

P1.17 **Probe head errors module for digital-metrological twin of five-axis CMM based on use of neural networks** **102**
Piotr Gąska[1], Wiktor Harmatys[2], Maciej Gruza[2], Adam Gąska[2]
[1]AGH University of Krakow, Faculty of Mechanical Engineering and Robotics,
[2]Cracow University of Technology, Faculty of Mechanical Engineering

P1.20 **Evaluation of radii in machined components** **106**
Adam Szczepański[1], Marek Magdziak[2]
[1]Pratt & Whitney Rzeszów, Poland,
[2]Faculty of Mechanical Engineering and Aeronautics, Rzeszów University of Technology, Rzeszów, Poland

P1.21 **Surface Analysis and Evaluation of Corrosion-Induced and Pore-Like Textures** **110**
Aleksandra Mirowska[1,2], Robert Tomkowski[2], Michał Dobrzyński[1], Amir Rashid[2], Sasan Dadbakhsh[2]
[1]Faculty of Mechanical Engineering and Ship Technology, Gdansk University of Technology, Narutowicza 11/12,80-233 Gdansk, Poland,
[2]Department of Production Engineering, KTH Royal Institute of Technology, Brinellvägen 68, 114 28 Stockholm, Sweden

P1.22 **Deep learning-driven visual inspection methodology for automated defect detection and dimensional assessment in die-cast parts** **114**
Sofia Catalucci and Enrico Savio
University of Padua, Department of Industrial Engineering (DII), Italy

P1.25 **Complex coordinate measurement models for GUM uncertainty framework** **116**
Wojciech Płowucha[1], Mirosław Wojtyła[1], Izabela Hura[1], Alessandro Balsamo[2]
[1]University of Bielsko-Biała, Laboratory of Metrology, Willowa 2, PL43-309 Bielsko-Biała
[2]INRIM (National Institute of Research in Metrology), Str. delle Cacce, 91, 10135 Torino TO, Italy

P1.26 **Surface roughness influence on chromatic confocal dimensional measurements** **120**
Lorenzo Didonè, Sofia Catalucci, Enrico Savio
Dept. of Industrial Eng. University of Padua, UNIPD, Via Venezia 1, Padova, Italy

P1.27 **Systematic error correction for thickness measurements with optical distance sensors** **122**
Dario Pasin, Sofia Catalucci, Enrico Savio
Università degli Studi di Padova, Department of Industrial Engineering, Padova, Italy

P1.28 **Digital twin of a reference rotary table for traceable angular metrology** **124**
Rim Bennoune[1, 2], Nabil Anwer[2], Mohamed Damak[3], Hichem Nouira[1]
[1]Laboratoire national de métrologie et d'essais (LNE), France,
[2]Université Paris-Saclay, ENS Paris-Saclay, LURPA, 91190, Gif-sur-Yvette, France,
[3]GEOMNIA - École Nationale Supérieure des Arts et Métiers (LISPEN), France

P1.29 **Multi-Material Empirical Artifact Correction (MEAK): Efficient Algorithm for Correcting Beam Hardening Artifacts in Multi-Material CT** **126**
Philip Trapp[1,2], Frederic Ballach[2], Tobias Müller[2], Michael Hammer[2], Raoul Christoph[2], Ralf Christoph[2], and Marc Kachelrieß[1]
[1]German Cancer Research Center (DKFZ), Im Neuenheimer Feld 280, 69120 Heidelberg, Germany,
[2]Werth Messtechnik GmbH, Siemensstraße 19, 35394 Giessen, Germany

P1.30 **Device for roundness measurement of continuously changing diameter objects** **128**
Sampo Haikonen[1], Nhat Huy Nguyen[1], Elmo Laine[1], Raine Viitala[1]
[1]Aalto University, Department of Energy and Mechanical Engineering

P1.31 **An ultra-compact chromatic confocal sensing probe enabled by metasurfaces and micron resolution 3D printing** **132**
J. Williamson[1], D.J. Townend[1], D. Tang[1], R. Owen[2], W. Zhong [1], A.J. Henning[1], H. Martin[1], V.R. Konnanath Puthanveetil[1], X. Jiang[1]
[1]Centre for Precision Technologies, University of Huddersfield, Queensgate, Huddersfield, HD1 3DH,
[2]School of Pharmacy, University of Nottingham Biodiscovery Institute, University of Nottingham, University Park, Nottingham, UK

P1.32 **Investigating non-uniformity of spatial resolution in X-ray computed tomography** **134**
Shiran Shan[1], Wenjuan Sun[1,2], Xiao Chen[3], Shan Lou[3]
[1]Department of Mechanical Engineering, Celestijnenlaan 300, KU Leuven, 3001 Leuven, Belgium,
[2]Flanders Make @KU Leuven, 3001 Leuven, Belgium,
[3]EPSRC Future Metrology Hub, University of Huddersfield, Queensgate, Huddersfield, UK

P1.33 **European Metrology Network (EMN) for Advanced Manufacturing: Understanding the challenges and requirements for metrology for advanced materials** **136**

Fernando A. Castro[1], Luca Boarino[2], Alexander Evans[3], Anita Przyklenk[4], Harald Bosse[4], Walter Knulst[5], Daniel O'Connor[1], Antti Lassila[6], Virpi Korpelainen[6] and Dishi Phillips[7]

[1] National Physical Laboratory (NPL), Teddington, United Kingdom.

[2]Istituto Nazionale di Ricerca Metrologica (INRIM), Torino, Italy.

[3]Bundesanstalt für Materialforschung und -prüfung (BAM), Berlin, Germany.

[4]Physikalisch-Technische Bundesanstalt (PTB), Braunschweig, Germany.

[5]VSL National Metrology Institute (VSL), Delft, Netherland.

[6] VTT Technical Research Centre of Finland Ltd, Centre for Metrology MIKES (MIKES), Espoo, Finland.

[7]European Society for Precision Engineering and Nanotechnology (euspen), Cranfield, UK.

Session 2: Measuring Instruments and Machine Tools: Design and Performance

O2.01 **Aerostatic journal bearing as a capacitive sensor for in-situ radial rotor position measurement** **140**
Petteri Haverinen[1], Mikael Miettinen[1], Raine Viitala[1]
[1]Aalto University

O2.02 **Error propagation in two-axis feed drives using physical error injection and multibody simulation** **144**
Pu Sun[1, 2], Tim Wendel[1], Andreas Archenti[1]
[1]Department of Production Engineering, KTH Royal Institute of Technology, Brinellvägen 68, 11428 Stockholm, Sweden
[2] AstraZeneca Sweden Operations, Storgatan 51, 15136 Södertälje, Sweden

O2.03 **Telecentric Under-Surface Imaging System for In-situ Observation of Polishing Pad Glass Contact** **146**
Adam Wilczek[1], Nico Zettler[1], Prof. Dr. Rainer Börret[1]
[1]Aalen University, Center for Optical Technologies (ZOT), Beethovenstr. 1, 73430 Aalen, Germany

O2.04 **Autocollimation and Reflected-Power Optimization in High-Refractive-Index Glass Retroreflectors for Robust, Cost-Effective Systems** **150**
Mateusz Sosin[1], Martin Dušek[1,2], Jean-Christophe Gayde[1], Kryštof Polák[1,2], Miroslav Šulc[2,3], Leonard Watrelot[1]
[1]CERN – European Organization for Nuclear Research, Geneva, Switzerland
[2]Technical University of Liberec, Liberec, Czech Republic
[3]Institute of Plasma Physics of the Czech Academy of Sciences, Prague, Czech Republic

O2.05 **Development of a Critical Assembly Quality Analysis Method for Machine Tools Based on the Jacobian-Torsor Model** **154**
Lin Tsao[1], Sheng-Hsiang Hung[1]
[1]Center for Measurement Standards, Industrial Technology Research Institute, Hsinchu, Taiwan

P2.01 **On-machine optical tool characterisation using dictionary-based sub-pixel edge detection** **158**
Moritz Genzwürker[1], Matthias Geiselhart[1], Giuliano Bissacco[1]
[1]Technical University of Denmark, Department of Mechanical Engineering, 2800 Kgs. Lyngby, Denmark

P2.02 **Modeling and Quantification of Parameter-Induced Thermal Errors in a Hydrostatic Turntable System** **162**
Jun Zha[1,2], Changhui Ke[3], Lipu Song[1,2], Chengwei Kang[1,2]
[1]School of Mechanical Engineering, Xi'an Jiaotong University, Xi'an 710049, China
[2]Xi'an Jiaotong University-Genertec Joint Research Institute, Xi'an 710049, China
[3]School of Mechanical and Precision Instrument Engineering, Xi'an University of Technology, Xi'an 710048, China

P2.03 **Simulation study on viscous friction reduction effect of textured oil-lubricated hydrostatic bearings** **166**
Dmytro Fedorynenko[1], Naofumi Ohnishi[1], and Yohichi Nakao[2]
[1]Department of Aerospace Engineering, Tohoku University, Sendai, Japan
[2]Department of Mechanical Engineering, Kanagawa University, Yokohama, Japan

P2.04 **A new backlight imaging method for in-machine measurement of flank wear** **170**
Lukas Jansen[1], Knut Sørby[1]
[1]Department of Mechanical and Industrial Engineering, NTNU Norwegian University of Science and Technology, Trondheim, Norway

P2.05 **Measurement and improvement of bit error rate in 16QAM using laser hydrophones** **174**
Rin Furuya[1], Norio Tsuda[1], and Daisuke Mizushima[1]
[1]Aichi Institute of Technology

P2.08 **Investigation of a novel motorised milling spindle with thermoelectric temperature control system based on a tubular Peltier module** **176**
Eckart Uhlmann[1,2], Mitchel Polte[1,2], Florian Triebel[1], Alphin Judy[1], Roland Binninger[3], Andreas Moll[4], Jörn Sieberg[4]
[1]Technische Universität Berlin, Institute for Machine Tools and Factory Management IWF, Pascalstr. 8-9, 10587 Berlin, Germany,
[2]Fraunhofer Institute for Production Systems and Design Technology IPK, Pascalstr. 8-9, 10587 Berlin, Germany,
[3]Fraunhofer Institute for Physical Measurement Techniques IPM, Georges-Köhler-Allee 301, 79110 Freiburg, Germany,
[4]FISCHER Deutschland GmbH, Marie-Curie-Strasse 2, 40764 Langenfeld, Germany

P2.09 **Evaluation of the temperature influence in the measurement uncertainty of a telescopic simultaneous ball-bar for manufacturing systems verification** **180**
Francisco Javier Brosed[1,2,3], Juan José Aguilar[1,2], Sergio Aguado[1,2], Marcos Pueo[1,2], Ana Cristina Majarena[1,2], Jesús Velázquez[1,2]
[1]Department of Design and Manufacturing Engineering, University of Zaragoza, María de Luna 3, 50018 Zaragoza, Spain.
[2]Instituto de Investigación en Ingeniería de Aragón (I3A), 50018 Zaragoza, Spain

P2.10 **A compact cube-shaped parallel kinematic machine for dynamic and high-precision positioning in six degrees of freedom** **184**
Tillmann Volz [1], Stefan Schulz[1], Stephanie Streit[1]
[1]Physik Instrumente (PI) SE & Co. KG

P2.11 **Design and calibration of a single-camera near-field photometric stereo head with tiltable illumination** **186**
Seunghun Oh[1], Jinsung Son[1], Kihyun Kim[2], Hyo-Young Kim[2], Moon-Gu Lee[3] and Jaehong Shim[2]
[1]Department of IT and Semiconductor Convergence Engineering, Graduate School, Tech University of Korea (TU Korea),
[2]Department of Mechatronics Engineering, Tech University of Korea (TU Korea),
[3]School of Mechanical Engineering, Ajou University, Korea

P2.13 **A novel approach for a coordinate measuring machine probing head with a levitating probe integrating the Kibble-balance principle and a Maxwell-clamp-like mounting concept** **190**
Yujie Zhong[1], Tino Hausotte[1], Georg Hein[2], Julien Schinn[1], Norbert Rogge[2] and Thomas Fröhlich[2]
[1]Chair of Manufacturing Metrology, Friedrich-Alexander-Universität Erlangen-Nürnberg (FAU), Faculty of Engineering, Department of Mechanical Engineering, [2]Institute of Process Measurement and Sensor Technology, Technische Universität Ilmenau, Department of Mechanical Engineering

P2.14 **A Reduced-Order Modelling Framework for the Receptance Coupling Method** **192**
Özgür Taylan Kenanoğlu[1,2], Yiğit Özcan[1,2], Shashwat Kuswaha[1,2], Dominiek Reynaerts[1,2]
[1]Department of Mechanical Engineering, Manufacturing Processes and Systems, KU Leuven, Leuven 3001, Belgium
[2]Member Flanders Make, Belgium

P2.15 **Metrological constraints in predicting tool deflection for error compensation** **196**
Paweł Majda[1], Paweł Dunaj[1], Bartosz Powałka[1] and Andreas Archenti[2]
[1]West Pomeranian University of Technology, Szczecin, Poland,
[2]KTH Royal Institute of Technology, Stockholm, Sweden

P2.18 **Capability Modelling of Robotic Machining System based on Digital Twin** **200**
Abdullah All Mamun Anik[1], Andrew Longstaff[1], Simon Fletcher[1], Xianzhi Zhang[1]
[1]School of Computing and Engineering, University of Huddersfield, Huddersfield, Queensgate, United Kingdom

P2.20 **Axial spindle deformation due to Poisson's effect under centrifugal loading** **204**
Byron R. Knapp, Dave Arneson, and Dan Oss
Professional Instruments Company, Hopkins, Minnesota, USA

P2.21 **Investigation of spindle thermal displacement and cooling unit energy consumption characteristics under various operating conditions** **208**
Gyungho Khim[1], Sungchuel Lee[1], and Jeong Seok Oh[1]
[1]Department of Ultra Precision Machines & Systems, Research Institute of Autonomous Manufacturing, Korea Institute of Machinery and Materials

P2.22 **Robust Parameter Estimation for Optical Surface Roughness Measurement Using a Physics-Based Model** **210**
Sungcheul Lee[1], Hyun-soo Kim[1], Seong-Kook Ro[1]
[1]Ultra Precision Machines and Systems, Korea Institute of Machinery and Materials, 156, Gajeongbuk-ro, Yuseong-gu, Deajeon, Republic of Korea

P2.23 **Design and experimental analysis of a thermoelectrically temperature controlled bearing shield for motorised spindles** **212**
Leon Naatz[1,2], Florian Triebel[1], Katrin Schmitt[3,4], Jürgen Wöllenstein[3,4], Roland Binninger[3]
[1]Technische Universität Berlin, Institute for Machine Tools and Factory Management IWF, Pascalstr. 8-9 10587 Berlin, Germany,
[2]Technical University of Applied Sciences Wildau, Hochschulring 1, 15745 Wildau, Germany,
[3]Fraunhofer Institute for Physical Measurement Techniques IPM, Georges-Köhler-Allee 301 79110 Freiburg, Germany,
[4]University of Freiburg, Department of Microsystems Engineering – IMTEK, Laboratory for Gas Sensors, Georges-Köhler-Allee 102, 79110 Freiburg, Germany

P2.24 **Automatic Text Analysis for Machine Maintenance in Float-Zone Crystal Growth Production** **216**
Eugenia Freggia[1], Marta Barbieri[2], Irene Spada[1], Gualtiero Fantoni[1], Matteo Calaon[2]
[1]University of Pisa, 56122 Pisa, Italy
[2]Technical University of Denmark, 2800 Kgs. Lyngby, Denmark

P2.25 **A multiphysics finite element model for hydrostatic guideway systems** **218**
Markel Alaña[1], Julen Bastardo[1], Gorka Aguirre[1], Harkaitz Urreta[1]
[1]Design and Precision Engineering, IDEKO, Elgoibar, Gipuzkoa, Spain

Session 3: Precision Manufacturing Processes

O3.01 **Monocular Vision for Online Feedback Control in Volumetric 3D Printing** **222**
Shuai Peng[1, 2,] Boyang Cai[1,2,] Geming Chen[1, 2] & Yu Liu[1, 2, *]
[1]School of Mechanical Engineering, Jiangnan University
[2]Jiangsu Key Laboratory of Advanced Food Manufacturing Equipment &Technology, Jiangnan University

O3.02 **Microstructuring of Cutting Punches for Tribological Optimization of Stamping Processes** **224**
Torsten Schmidt[1], Karsten Richter[1], Jan Edelmann[1], Verena Kräusel[1]
[1]Fraunhofer Institute for Machine Tools and Forming Technology IWU, Chemnitz, Germany

O3.03 **Recycled Walnut Shell Abrasives as a Sustainable Feedstock for Binder Jetting** **228**
Luwen Zhang[1], Rezo Aliyev[1] and Henning Zeidler[1]
[1]Institute for Machine Elements, Engineering Design and Manufacturing, Chair of Additive Manufacturing, TU Bergakademie Freiberg, 09599 Freiberg, Germany

O3.04 **Automated Algorithm for the Evaluating of Burr Formation in Micro Milling** **230**
Maximilian Vierling[1], Jan C. Aurich[1]
[1]University of Kaiserslautern-Landau, Institute for Manufacturing Technology and Production Systems

O3.05 **Development of an Innovative Process Chain to Enhance the Durability of Functionalized Polymer Surfaces for Real-World Applications** **234**
G. Baruffa[1]; G. Lucchetta[1]; M. Sorgato[1]
[1]Dept of Industrial Eng., University of Padova, via Venezia [1], Padova, 35131, Italy

P3.01 **Ultrafast laser fabrication of transparent superhydrophobic silica glass for optical window applications** **238**
Kai Liao[1], Chi Fai Cheung[1], Chunjin Wang[1]
[1]State Key Laboratory of Ultra-precision Machining Technology, Department of Industrial and Systems Engineering, The Hong Kong Polytechnic University, Hung Hom, Kowloon, Hong Kong, China

P3.02 **Porous metal aerostatic bearing restrictors manufactured with laser-based powder bed fusion** **242**
Onni Leutonen[1], Mikael Miettinen[1], Valtteri Vainio[1], Roy Björkstrand[1], Mika Salmi[1], Raine Viitala[1]
[1]Aalto University, School of Engineering, Department of Energy and Mechanical Engineering, Espoo, Finland

P3.05 **Investigation of the transferability of pulsed electrochemical machining process parameters from simple substitute models to complex manufacturing applications** **246**
Falko Böttcher[1], Sepideh Ghorbanalipour[2], Jan Edelmann[1]
[1]Fraunhofer IWU, Institute for Machine Tools and Forming Technology, Reichenhainer Straße 88, 09126 Chemnitz, Germany
[2]Chemnitz University of Technology, Reichenhainer Straße 70, 09126 Chemnitz, Germany

P3.06 **Study on effect of tool edge geometry on residual stress in metal cutting** **250**
Hiroyuki Sasahara [1] and Tatsuya Tanaka [1]
[1]Tokyo University of Agriculture and Technology

P3.07 **Dimensional accuracy and IT7 fits in FDM-printed PLA elements: statistical evaluation and correction guidelines** **254**
Bartłomiej Byczuk[1], Mirosław Rucki[1], Marcin Wikło[2], Arturas Kilikevicius[1], Patryk Osuch[3]
[1]Vilnius Gediminas Technical University, Vilnius, Lithuania
[2]Casimir Pulaski Radom University, Radom, Poland
[3]Precision Machine Parts Poland sp. z o.o., Radom, Poland

P3.09 **Sustainable manufacturing of metallic wires through solid-state processes with continuous Al6061 chips** **256**
Zichen WANG[1,2], Vincent Beng Chye TAN[1], Dennis Wee Keong NEO[2], and Nicholas Yew Jin TAN[2,3]
[1]Department of Mechanical Engineering, National University of Singapore, 9 Engineering Drive 1, Singapore 117575, Republic of Singapore
*[2]Singapore Institute of Manufacturing Technology (SIMTech), Agency for Science, Technology and Research (A*STAR), 5 Cleantech Loop, Singapore 636732, Republic of Singapore*
*[3]Advanced Remanufacturing and Technology Centre (ARTC), Agency for Science, Technology and Research (A*STAR), 3 Cleantech Loop, Singapore 637143, Republic of Singapore*

P3.10 **Robust design of diffractive optical elements for anticounterfeiting mould texturing** **260**
Marco Sorgato[1]; Giacomo Baruffa[1]; Giovanni Lucchetta[1]; Enrico Savio[1]
[1]Department of Industrial Engineering, University of Padova, via Gradenigo 6/A, 35131 Padova, Italy

P3.11 **Influence of Cutting Temperature on Affected Layer in Cutting of Aluminum Alloy Castings with PCD tool** **264**
Hiroo Shizuka[1,] Katsuhiko Sakai[1,] Koki Tokai[1]
[1] Shizuoka University,3-5-1 Johoku Naka-ku Hamamatsu Shizuoka 432-8561 Japan

P3.13 **Electrochemical Machining of Pre-Defined Kinematic Surface Roughness on Nickel 201 with Continuous Electrolyte Jet** **266**
André Martin[1];Tehreem Javed[1], Sepideh Ghorbanalipour[1], Andreas Schubert[1]
[1]Chemnitz University of Technology, Professorship Micromanufacturing Technology, Reichenhainer Str. 70, 09126 Chemnitz, Germany

P3.14 **Surface Alloying of Stainless-Steel Parts with Tungsten During Electrical Discharge Machining for Increased Hardness** **270**
Viet D. Bui[1*], André Martin[1], Andreas Schubert[1,2]
[1]Chemnitz University of Technology, Professorship Micromanufacturing Technology, Reichenhainer Str. 70, 09126 Chemnitz, Germany
[2]Fraunhofer Institute for Machine Tools and Forming Technology, Reichenhainer Str. 88, 09126 Chemnitz, Germany

P3.15 **Pore-aware dwell map construction from in-situ pad-glass contact imaging in optical polishing** **274**
Nico Zettler[1], Adam Wilczek[1], Prof. Dr. Rainer Börret[1]
[1]Aalen University, Center for Optical Technologies (ZOT), Beethovenstr. 1, 73430 Aalen, Germany

P3.16 **Residual stress modification and surface enhancement of PBF-LB/M components via particle blasting and plasma electrolytic polishing** **278**
Neel Kamal Gupta[1]*, Toni Böttger[1], Christian Schimpf[2], Henning Zeidler[1]
[1]Institute for Machine Elements, Engineering Design and Manufacturing (IMKF), Technische Universität Bergakademie Freiberg, Freiberg, Germany
[2]Faculty for Materials Science and Materials Technology, Technische Universität Bergakademie Freiberg, Freiberg, Germany

P3.17 **Voxel-Scale Misalignment Detection for Orthogonal Metasurface-Produced Holograms via error-compensated Volumetric Imaging** **280**
Gavin Stafford[1], Timothy Yap[2], Michael Cullinan [1]
[1,2]The University of Texas at Austin, Walker Department of Mechanical Engineering

P3.18 **Novel niobium carbide cermet and manufacturing techniques for moulds; improving durability and flowability in ceramic injection moulding** **284**
Muhammad Hazak Arshad[1,5], Victor Laermans[2], Mian Monib Ur Rehman[3,5,] Tim Evens[2], Shuigen Huang[4,] Krishna Kumar Saxena[1,5], Sylvie Castagne[3,5,] Albert Van Bael[2], Jozef Vleugels[4], Dominiek Reynaerts[1,5,*]
[1]Department of Mechanical Engineering, Manufacturing Processes and Systems, Micro- & Precision Engineering Group, KU Leuven, Leuven, Belgium.
[2]Department of Materials Engineering, Structural Composites and Alloys, Integrity and Nondestructive Testing, Polymer Processing & Engineering Group, KU Leuven, Diepenbeek, Belgium.
[3]Department of Mechanical Engineering, Manufacturing Processes and Systems, Laser Micromanufacturing Group, KU Leuven, Leuven, Belgium.
[4]Department of Materials Engineering, Surface and Interface Engineered Materials, KU Leuven, Leuven, Belgium.
[5]Member Flanders Make, Leuven, Belgium.

P3.19 **Fused Filament Fabrication System for continuous fibre reinforcement** **288**
J. Polte[1, 2,] E. Uhlmann[1, 2], S. Bode[1], L.-A. Edinger[1]
[1]Institute for Machine Tools and Factory Management IWF, Technische Universität Berlin, Germany
[2]Fraunhofer Institute for Production Systems and Design Technology IPK, Germany

P3.22 **Electrochemical deposition of active materials towards integrated sensing on mechanical components** **290**
Zhaozhi Lyu[1, 2,] Muhammad Hazak Arshad[1, 2,] Krishna Kumar Saxena[1, 2, *,] Dominiek Reynaerts[1], [2, *]
[1]KU Leuven, Department of Mechanical Engineering, Manufacturing Processes and Systems, Micro- & Precision Engineering Group, Leuven, Belgium.
[2]Member Flanders Make, Leuven, Belgium.

P3.23 **Metrological Characterization of Shrinkage in Precision Injection Moulded Polypropylene Plates through Experimental Measurements and Process Simulation** **292**
Juan J. Ortiz-Vazquez[1,2,] Hallgrimur Kjartansson[1], Renan Melhado Mazza[3], J. Israel Martínez-López[2], Alireza Mollaei Ardestani[1], Yang Zhang[1] and Guido Tosello[1]
[1]Department of Civil and Mechanical Engineering, Technical University of Denmark, DK-2800 Kgs. Lyngby, Denmark
[2]School of Engineering and Science, Tecnologico de Monterrey, MX-64700 Monterrey, México
[3]AB Tetra Pak, SE-223 55 Lund, Sweden

P3.25 **Mechanical properties of additive manufactured components with combined short and continuous fiber reinforcement** **296**
J. Polte[1, 2,] S. Bode[1], S.Yazgan[1]
[1]Institute for Machine Tools and Factory Management IWF, Technische Universität Berlin, Germany
[2]Fraunhofer Institute for Production Systems and Design Technology IPK, Germany

P3.26 **Development of Lattice Structures of pure Tungsten for Applications in Fusion Energy** **298**
Miguel Zavala-Arredondo[1], Ahmed Tawfik[2], Liam Blunt[2], Jeong-Ha You[3]
[1]UKAEA, 2A Lanchester Way, Advanced Manufacturing Park, Rotherham, UK.
[2]The Future Advanced Metrology Hub fr Sustainably Manufacturing, University of Huddersfield, UK
[3]IPP (Max Planck Institute for Plasma Physics), Garching, Germany

P3.27 **Productivity enhancement and burr reduction in Ti6Al4V single lip microdrilling using ultrasonic vibration assistance** **300**
Bernie Cheruiyot[*,] Richard Börner, Andreas Nestler, Andreas Schubert
Professorship Micromanufacturing Technology, Chemnitz University of Technology, Reichenhainer Str. 70 09126 Chemnitz, Germany

P3.28 **Elucidating the effect of wobble frequency on the fluid flow and keyhole dynamics in the laser lap welding of electric vehicles battery packs** **304**
Akash Meena[1], Guido Tosello[1]
[1]Dept of Civil and Mechanical Engineering, Technical University of Denmark, 2800 Kgs. Lyngby, Denmark

P3.29 **Determination of packing parameters influence on the accuracy of precision moulded components by coordinate metrology** **308**
Guido Tosello[1], Giacomo Pietrobon[1,2], Alireza Mollaei Ardestani[1], Klaus Litorp[1], Carsten Lund[3], Lorenzo Didonè[2], Enrico Savio[2]
[1]Dept.of Civil and Mechanical Eng. Technical University of Denmark, 2800 Kgs. Lyngby, Denmark
[2]Università degli Studi di Padova, Dipartimento di Ingegneria Industriale, 35131 Padova, Italy
[3]Epsilonplus, 4295 Stenlille, Denmark

P3.31 **Electrochemical accretion of high entropy alloy traces from aqueous electrolytes towards modular moulds, tools and integrated sensing applications** **312**

Krishna Kumar Saxena[1,2], Adnan Al Farisi[1,2], Muhammad Hazak Arshad[1,2], Dominiek Reynaerts[1,2]

[1]*KU Leuven, Dept of Mechanical Eng. Micro-&Precision Engineering Group, Belgium.*

[2]*Member Flanders Make, Belgium*

Session 4: Advances in Precision Engineering

O4.01 **Design of Test Setup for Measurement of Microslip in Clamped Interfaces using a Balanced Heterodyne Interferometer with Picometer-Resolution** **316**
Walter Knulst[1], Pablo Ruiz Beltri[2], Joris Looman[3], Kees Verbaan[2]
[1]VSL, National Metrology Institute, Thijsseweg 11, 2629 JA, Delft, The Netherlands
[2]Mechanical Engineering (DPE-group), Eindhoven University of Technology, Groene Loper 3, 5612 AE, Eindhoven, The Netherlands
[3]ASML B.V., De Run, Veldhoven, The Netherlands

O4.02 **Challenges in the design of force sensors based on the structure of high-precision weighing cells** **320**
Lennart Frentzel[1], Martin Wittke[1], Matthias Wolf[1], René Theska[1], Hannes Scheibe[1]
Technische Universität Ilmenau, Department of Mechanical Engineering,
[1]Institute for Design and Precision Engineering, Precision Engineering Group

O4.03 **Data-Driven Framework for Machine Learning-Based Uncertainty Evaluation in Coordinate Measuring Machines** **322**
Alireza Mollaei Ardestani[1*,] Gianfranco Genta[2], Giacomo Maculotti[2], Emanuele Barini[3], Maurizio Galetto[2], Guido Tosello[1]
[1]Department of Civil and Mechanical Engineering, Technical University of Denmark, 2800 Kgs. Lyngby, Denmark
[2]Department of Management and Production Engineering, Politecnico di Torino, 10129 Torino, Italy
[3]Hexagon Metrology S.p.A., 10090 Grugliasco, Italy

O4.04 **The Satisloh Plasma Polisher: the science, technology development, and commercialisation of atmospheric pressure surface figuring for ultra-precision optics** **326**
Dr. Adam Bennett[1,2,] Dr. Katherine Gobey[1], Steffen Moos[3], Paul Sauer[3], Hans-Joerg Schlemper[3], Dr. Jürgen Bode[3]
[1]Cranfield Plasma Solutions Limited, College Road, Wharley End, Cranfield, MK43 0AL, England.
[2]Cranfield University, College Road, Wharley End, Cranfield, MK43 0AL, England;
[3]Satisloh GmbH, Wilhelm-Loh-Straße 2-4, 35578 Wetzlar, Germany.

O4.05 **Flexure-based inverted pendulum mechanical inclinometer** **330**
Loïc Tissot-Daguette[1], Salah Hasnaoui[1], Florent Cosandier[1], Charles Baur[1] and Simon Henein[1]
[1]Instant-Lab, EPFL, Switzerland

P4.02 **Magnetically driven internal finishing of stainless-steel tubes by a novel electrostatic flocking and drum-shaped polishing tool** **334**
Zhanjie Zhang[1], Chongrui Wang[1] and Jiong Zhang[1*]
[1] Department of Mechanical Engineering, City University of Hong Kong, 83 Tat Chee Avenue, Kowloon Tong, Kowloon, Hong Kong SAR

P4.03 **Thermal modulation of the water-induced surface ordering effect for tunable machining performance in copper micro-cutting** **338**
Zhenyu Liu [1], Jiuxing Tang [2], Wai Sze Yip [2], Jiong Zhang [1, *]
[1]Department of Mechanical Engineering, College of Engineering, City University of Hong Kong, Hong Kong SAR, China
[2]State Key Laboratory of Ultra-precision Machining Technology, Department of Industrial and Systems Engineering, The Hong Kong Polytechnic University, Hong Kong SAR, China

P4.04 **Design and testing of an advanced honeybee waste heat-powered energy harvester** **342**
Petar Gljušćić[1, 2] Saša Zelenika[1, 2] and Priyesh Pappinisseri Puluckul[3]
[1]University of Rijeka, Faculty of Engineering, Precision Engineering Laboratory, Vukovarska 58, 51000 Rijeka, Croatia
[2]University of Rijeka, Centre for Micro- and Nanosciences and Technologies, Radmile Matejčić 2, 51000 Rijeka, Croatia [3]IDLab, Faculty of Applied Engineering, University of Antwerp - imec, Sint-Pietersvliet 7, 2000 Antwerp, Belgium

P4.08 **Oxidation Behaviour of OVPE-GaN Substrates for Slurry-less Photoelectrochemical Mechanical Polishing** **346**
Yuya Ohnishi[1], Sun Rongyan[1], Shigeyoshi Usami[2], Yuji Ohkubo[1], Masayuki Imanishi[2], Yusuke Mori[2], Kazuya Yamamura[1]
[1]Research Center for Precision Engineering, Graduate School of Engineering, The University of Osaka, Osaka, Japan
[2]Division of Electric, Electronic and Information Engineering, Graduate School of Engineering, The University of Osaka, Osaka, Japan

P4.11 **Experimental characterization of a force sensor for orientation-independent SI traceable measurements** **348**
Martin Wittke[1], Lennart Frentzel[1], Matthias Wolf[1], Hannes Scheibe[1], Thomas Fröhlich[2], René Theska[1]
Technische Universität Ilmenau, Department of Mechanical Engineering,
[1]Institute for Design and Precision Engineering, Precision Engineering Group
[2]Institute of Process Measurement & Sensor Technology, Process Metrology Group

P4.13 **Design principles for ultimate mechanical stability** **350**
Robin Trines[1], Martijn Denissen[1], Niels Bouman[1]
[1] JPE

P4.14 **Modelling of 3D Surface Topography in Micromilling Process with Material Accumulation Effect** **354**
Marcin Gołaszewski[1] Bartosz Powałka[1]
[1]West Pomeranian University of Technology in Szczecin, Poland

P4.18 **Investigation of a positioning mechanism for adjustments with minimal side effects** **358**
Mario André Torres Melgarejo, René Theska, Hannes Scheibe
Technische Universität Ilmenau, Department of Mechanical Engineering
Institute for Design and Precision Engineering, Precision Engineering Group

Session 5: Large Scale Precision Engineering and Metrology

O5.01 **Development of high pressure and high temperature injection modules for 4D µCT in synchrotron environment** **362**

Antonio Neto[1], Cassiano Bueno[1], Débora Jesus[1], Everton Oliveira[1], Felipe Varga[1], Gabriel Baldon[1], Gabriel Caron[1], Gabriel Moreno[1], Gabriel Schubert[1], Guilherme Pimentel[1], Gustavo Pozza[1], Jair Neyra[1], João Pereira[1], João Matoso[1], João Silva[1], Ketlen Brito[1],Lucca Campoi[1], Nathaly Archilha[1], Mailson Souza[1], Paloma Zanella[1], Pedro Coutinho[1], Rafael Maluf[1], Stefano Coluccini[1], Talisson Borges[1], Victor Santos[1], Vitor Amaral[1], Arend Aerts[2], Bart Van Dijck[2], Bram Witteman[2], Corne Van Haren[2], Maryn Wijnhoven[2], Martijn Princen[2], Robin Franssen[2], Theo Ruijl[2]

[1]Brazilian Center for Research in Energy and Materials (CNPEM),
[2]MI-Partners BV

O5.02 **Dense Data Fusion and Uncertainty Quantification in Optical Metrology: The Duster++ Framework** **366**

Ladji Fofana[1,2], Katarina Josic[1,2], Louis-Ferdinand Lafon[1], Charyar Mehdi-Souzani[3], Nabil Anwer[2], Hichem Nouira[1]

[1]Laboratoire national de métrologie et d'essais/Conservatoire national des arts et métiers, 1 Rue Gaston Boissier, 75015 Paris, France,
[2]Université Paris-Saclay, ENS Paris-Saclay, LURPA, 91190, Gif-sur-Yvette, France,
[3]Université Paris-Saclay, ENS Paris-Saclay, LURPA, Université Sorbonne Paris Nord, 91190, Gif-sur-Yvette, France

O5.03 **Internal Quality Optimisation of Material Extrusion Additive Manufacturing via Computer Vision-Enhanced Layerwise Surface Topography Measurement** **370**

Kexin Yin[1], Yuchu Qin[1], Shan Lou[1], Paul Scott[1], Xiangqian Jiang[1]

[1]EPSRC Future Advanced Metrology Hub for Sustainable Manufacturing, University of Huddersfield, Huddersfield, United Kingdom, HD1 3DH

O5.04 **Verification of a Next Generation γ-Ray Spectrometer Mechanical Requirements: Gamma-Ray Energy Tracking Array** **374**

Eric S. Buice, Collin Anderson, Heather L. Crawford, and Paul Fallon

Lawrence Berkeley National Laboratory, Berkeley, California 94720 USA

O5.05 **Nanomotion for ALBA II: laboratory, metrology and control for precision engineering** **378**

Juan Luis Frieiro[1], Nilson Bernardo Pereira[1], Nahikari González[1], Carles Colldelram[1], Josep Nicolás[1]

[1]ALBA synchrotron, Cerdanyola del Vallés, Barcelona, Spain

P5.01 **Basics of preparing a digital twin for a cooperative robot (cobot) with an attached rigid-contact head** **382**

Przemysław Jędrzejak[1], Sebastian Kąkol[1], Karol Stroński[1], Łukasz Giza[1], Konrad Kobiela[1], Ksenia Ostrowska[1]

[1]Cracow University of Technology

P5.02 **Preload and alignment mechanism for large scale aerostatic bearing** **386**

Jesper Riihola[1], Onni Leutonen[1], Mikael Miettinen[1], Raine Viitala[1]

[1]Aalto University

P5.03 **Control system modeling for a micro machining spindle with an active magnetic bearing actuator** **388**
Felix Zell[1], Maximilian Vierling[1], Jan C. Aurich[1]
[1]University of Kaiserslautern-Landau, Institute for Manufacturing Technology and Production Systems

P5.06 **Parametric influence of gear surface and geometric features on dynamic performance** **392**
Himanshu Singh Maurya[1], Robert Tomkowski[1], Andreas Archenti[1]
[1]Department of Production Engineering, KTH Royal Institute of Technology, Brinellvägen 68, 114 28 Stockholm, Sweden

P5.07 **FEA-Informed Compensation of Thermal Volumetric Effects on Machine Structure** **394**
Daniel Divíšek[1], Martin Mareš[1], Otakar Horejš[1], Matěj Sulitka[1]
[1]Czech Technical University in Prague, Faculty of Mechanical Engineering, Department of Production Machines and Equipment, RCMT, Horská 3, 128 00 Prague, Czech Republic

Session 6: Applications of Precision Engineering in Bio-Tech Devices

O6.01 **Ultra-precision machining of superhydrophobic surfaces with re-entrant microstructures** **400**

Douwei Liu, Wenbin Zhong*, Wenhan Zeng, Xiangqian Jiang

EPSRC Future Metrology Hub, Centre for Precision Technologies, School of Computing and Engineering, University of Huddersfield, Huddersfield, HD1 3DH, UK

O6.02 **Automated Multi-Balloon Drug-Coating System with Configurable Process Parameters** **404**

Yixue Wang[1], Michal Szczepanski[1], Nicolas Kayser[1], Gregor Dürre[2], Robby Simon[3], Frank Wasmuth[3], André Hutsky[3], Annika Brehmer[1], Julian Polte[1]

[1]Fraunhofer Institute for Production Systems and Design Technology IPK, Germany

[2] InnoRa GmbH, Germany

[3] Organical CAD/CAM GmbH, Germany

O6.03 **Modular child lower limb phantom with seven degrees of freedom simulating micrometric bone growth** **408**

Krzysztof Popielski[1],[2], J.R.R. Mayer [1], Adam Woźniak[2]

[1]Department of Mechanical Engineering, École Polytechnique de Montréal, 2500, chemin de Polytechnique, Montréal (Québec), H3T 1J4, Canada

[2]Warsaw University of Technology, Department of Mechatronics, sw. Andrzeja Boboli 8, 02-525 Warsaw, Poland

O6.04 **Functional tools micro-texturing for controlled chip formation in precision dry machining of PEEK** **412**

Anna Bottin, Rachele Bertolini, Enrico Savio, Stefania Bruschi

University of Padua, Department of Industrial Engineering (DII), Italy

P6.01 **Functionalization of tantalum oxide coatings on commercially pure titanium by PEO** **414**

Pedro Paulo da Graça de Morais[1], Mizael Rodrigues[2], Eduardo Guy Perpétuo Bock[3], Natallie Zillio de Souza Teixeira[1], Nilson da Cruz[2]

[1]Instituto Federal de São Paulo (IFSP), Campus Boituva, Brazil

[2]Universidade Estadual Paulista (UNESP), Campus Sorocaba, Brazil

[3]Instituto Federal de São Paulo (IFSP), Campus São Paulo, Brazil

P6.02 **Fundamental Investigation of Cutting Mechanisms in Ultra-Precision Machining of KTP Crystals for Quantum Communication** **418**

E. Uhlmann[1,2], M. Polte[1,2], T. Hocke[1,2], T. D. Le[1]

[1]Institute for Machine Tools and Factory Management IWF, Technische Universität Berlin, Germany

[2]Fraunhofer Institute for Production Systems and Design Technology IPK, Germany

P6.04 **Green-EDM approaches for biocompatible processing of rolled and 3D printed titanium alloys** **422**

Agnieszka Żyra[1], Sebastian Skoczypiec[1]

[1]Cracow University of Technology, Faculty of Mechanical Engineering, al. Jana Pawła II 37, 31-864, Krakow, Poland

Session 7: Mechatronics and Control

O7.01 **A dynamics toolbox for modelling and prediction of interconnected systems** **426**
Wouter Jutte[1], Nard Strijbosch[1], Max Bolderman[1], Teunis van Dam[1], Arjan van der Wel[1], Ruben Merks[1], Theresa Spaan-Burke[1], Henny Spaan[1]
[1]IBS Precision Engineering BV

O7.02 **Investigation of Motor Characteristic Analysis under Low Magnetic Field Conditions in Planar Maglev Stages** **430**
Takanori Kato[1] and Motohiro Takahashi[1]
[1]Research and Development Group, Hitachi, Ltd.

O7.03 **Performance of an X-Y-Theta actuator using piezoelectric elements and electropermanent magnets** **432**
Akihiro Torii[1], Yuto Takayama[1], Takato Sakai[1], Suguru Mototani[1], Kae Doki[1]
[1]Aichi Institute of Technology, Japan

O7.04 **Measuring the future - Nanometrology for advanced manufacturing of miniaturized devices** **434**
Agnieszka Maria Jastrzębska[1], Madhurya Chandel[1], Andreas Rosenkranz[2], Daniel Moraru[3], Adam Woźniak[1]
[1] Warsaw University of Technology, Faculty of Mechatronics, św. Andrzeja Boboli 8, 02-525 Warsaw, Poland.
[2] Department of Chemical Engineering, Biotechnology and Materials, University of Chile, Avenida Beauchef 851, Santiago, Chile
[3] Research Institute of Electronics, Shizuoka University, 3-5-1 Johoku, Chūō-ku, Hamamatsu, 432-8011 Japan

P7.01 **Levitation characteristics and vibration behavior in ultrasonic levitation actuators** **436**
Shota Aoki [1,] Akihiro Torii [1], Suguru Mototani [1,] Kae Doki [1]
[1]Aichi Institute of Technology, Aichi, Japan

Keynotes

euspen's 26th International Conference & Exhibition, Krakow, PL, June 2026
www.euspen.eu

On-machine in-process coordinate measurement

Adam Woźniak[1]
[1] *Warsaw University of Technology, Faculty of Mechatronics, św. Andrzeja Boboli 8, 02-525 Warsaw, Poland.*

adam.wozniak@pw.edu.pl

Abstract
Currently, the manufacturing process of machine parts and devices on CNC machine tools is almost entirely automated. This has been made possible by the use of measuring probes. Equipping CNC machine tools with measuring probes has also made them coordinate measuring systems capable of performing geometric measurements during or after machining (on-machine measurement). This potentially eliminates the need for external measuring devices, such as coordinate measuring machines (CMMs) or other single-purpose devices for measuring geometric quantities. This also translates into a significant reduction in production time and costs, which is of paramount importance for this dynamically developing industry.

Sources of errors in measurements performed on CNC machine tools related to probe errors will be presented and analysed. The Warsaw University of Technology has developed a globally unique patented system designed to directly test the metrological characteristics of measuring probes used in CNC machine tools. This system enables testing to be conducted both in laboratory and industrial settings – directly on CNC machine tools. The results of modelling and error correction of measuring probes used in CNC machine tools will be presented. Topics will be discussed regarding changes in the metrological properties and reliability of probes during operation, taking into account load levels and failure limits.

on-machine measurement, in-process measurement, CNC machine tool, coordinate metrology, probe

Biography

Adam Woźniak is a full professor of technical sciences and academic lecturer. He specializes in geometric metrology, mainly in the development of algorithms, modeling, and accuracy testing of broadly defined measurement systems for the automotive, aerospace, energy, and precision industries.

He is the author of two monographs and nearly 200 scientific papers. He has led over a dozen research projects and participated in international research teams under NSERC, Canada Collaborative Research and Development Grants. He has supervised 8 Ph.D. students including 3 under the thesis co-supervision international program.

From 2012 to 2020, he served as Director of the Institute of Metrology and Biomedical Engineering, then Dean of the Faculty of Mechatronics, and is currently Vice-Rector for Development at the Warsaw University of Technology. Previously, from 2005 to 2006, he worked as a visiting professor at the Polytechnique de Montréal in Canada. From 2008 to 2011, he was a member of the Standardization Council for the second term, in 2017, he joined the Metrology Council for the first term (2017-2022) and is currently the Chairman of the Metrology Council for the second term (2022-2027). He is a member of the presidium of the Science Evaluation Commission for the 2023-2027 term, the American Society for Precision Engineering, and the Warsaw Scientific Society.

euspen's 26th International Conference & Exhibition, Krakow, PL, June 2026
www.euspen.eu

Aperture Calibration at 0 °C: Metrological Challenges Beyond Established Standards

Prof. Dr.-Ing. Michael Marxer[1]

[1] *Eastern Switzerland University of Applied Sciences, Institute for Microtechnology and Photonics, Competence Centre for Production Metrology*

Abstract
High-precision apertures are a key enabling element for radiometric measurements on Earth and in space, for example for determining the radiative power density of celestial bodies such as the Sun. Their calibration directly affects the reliability of climate monitoring, long-term solar observation, and space-based measurement systems. Despite their importance, aperture calibration is often treated as a well-established task—an assumption that quickly breaks down when moving beyond standard laboratory conditions.

This keynote reflects on practical experience gained from the manufacturing and calibration of high-precision apertures at the OST – Eastern Switzerland University of Applied Sciences, in close collaboration with RhySearch. A particular focus is placed on the calibration of apertures at 0 °C, rather than the conventional reference temperature of 20 °C. This shift introduces fundamental challenges related to thermal behavior, measurement uncertainty, traceability, and the validity of established metrological concepts. Dedicated calibration procedures based on multisensor coordinate measuring systems were developed to achieve the lowest possible measurement uncertainty under these non-standard conditions. Different measurement strategies and sensor concepts are critically discussed, highlighting their strengths, limitations, and practical applicability. Special attention is given to the question of traceability at 0 °C, which proved to be one of the central challenges of the work.

Rather than presenting a single solution, this keynote aims to share lessons learned at the interface of ultra-precision manufacturing and production metrology. It highlights how metrological challenges evolve when measurement conditions deviate from established standards, and discusses the implications for future high-accuracy measurements in space instrumentation, radiometry, and climate observation.

metrology, mechanical manufacturing processes

Biography

Michael Marxer is Professor of Production Metrology at the OST – Eastern Switzerland University of Applied Sciences, where he leads the Production Metrology Group and serves as Head of the Production Metrology Measurement Laboratory in Buchs, Switzerland.
He studied Precision Engineering at the NTB Buchs (University of Applied Sciences Buchs) from 1993 to 1996. He received his doctorate from Friedrich-Alexander University Erlangen-Nuremberg under the supervision of Prof. Albert Weckenmann, with his research focusing on coordinate metrology, with particular emphasis on multisensor coordinate measuring systems and sensor development.

Following the merger of several universities into OST, Prof. Marxer took on responsibility for the SCS calibration laboratory (Swiss Calibration Service) and the STS testing laboratory (Swiss Testing Service) at OST, ensuring traceability and quality assurance for industrial metrology applications, including roughness metrology, which is offered as a dedicated calibration service.
He is President of CMTrain e.V., an association dedicated to education and training in coordinate metrology using blended learning concepts, and a member of the guideline committee VDI 2617 in Germany.

His professional interests include production metrology, multisensor coordinate metrology, sensor development, calibration and traceability, roughness metrology, and industrial measurement processes, with a strong focus on bridging academic research and industrial application.

euspen's 26th International Conference & Exhibition, Krakow, PL, June 2026
www.euspen.eu

Empowering Global Health by Precision Engineering

Prof. Dr.-Ing. Julian Polte[1]

Deputy Director Fraunhofer IPK, Head of Business Unit Production Systems at IPK, Managing Director Institute for Machine Tools and Factory Management (IWF), Head of Chair Machines and Technologies for Additive Precision Manufacturing of Metal Components at IWF

Abstract

Evolving global health landscapes are characterized by an expanding prevalence of chronic diseases and a pressing socio-economic imperative for enhanced medical resilience. In this context, precision engineering serves as a powerful enabler, providing the technical sophistication necessary to realize next-generation medical interventions. This keynote explores the strategic alignment of precision engineering and clinical excellence, illustrating how advanced engineering empowers the next wave of global healthcare solutions.

The profound impact of precision engineering-driven innovation is exemplified in the management of cardiovascular diseases, the leading cause of global mortality. The Impella® heart pump family by Johnson & Johnson MedTech represents a benchmark of this development. As the world's smallest heart pumps, they integrate complex micro-axial fluid dynamics with high-reliability manufacturing. With over 400,000 clinical applications, the Impella® platform provides empirical evidence for how extreme miniaturization and ultra-precision tolerances directly translate into enhanced patient survival and sustained healthcare efficiency.
Extending beyond device engineering, this presentation delineates the technological trajectory toward personalized medicine. The shift from standardized therapeutics to patient-specific interventions presents a pivotal engineering challenge, requiring a seamless translation from nanoscale development to high-volume, individualized production. Fraunhofer FDMix dynamic mixing technology addresses this critical scalability gap, enabling high-precision, industrial-scale manufacturing of complex formulations required for tailor-made pharmaceuticals.

The effective scaling of such systems necessitates an evolution of production and manufacturing paradigms, spanning specialized, craft-like processes to fully digitally integrated environments. Central to this transition is Human-AI-Machine-Teaming, which provides the operational agility required to master evolving clinical demands and establishes precision-driven workflows as the foundational driver for accessible global health solutions.

Consequently, the future of global health is closely linked to these advancements in precision engineering. Through the integration of engineering excellence and the life sciences, traditional scalability barriers are effectively addressed, ensuring that sophisticated medical innovations become more accessible, reliable, and sustainable worldwide.

Biography

Prof. Dr.-Ing. Julian Polte studied Mechanical Engineering at Brandenburg University of Applied Sciences, where he received his Dipl.-Ing. (FH) degree in 2010. He subsequently completed his Master of Science in Production Technology at the Technical University Berlin in 2012 and received awards from the Association of German Engineers (VDI) for his academic achievements at both institutions. Following these achievements, he pursued his doctoral studies at Technical University Berlin, earning his Dr.-Ing. degree in 2017 with a specialization in ultra-precision cutting.

Since 2012, he has held various leadership positions, consistently expanding his scope of managerial responsibility. Currently, he serves as Managing Director of the Institute for Machine Tools and Factory Management IWF at Technical University Berlin and Head of Chair as Professor while concurrently holding the position of Deputy Director of Fraunhofer IPK. In this dual capacity, he has spearheaded and continues to lead two business units with multiple departments of the Fraunhofer IPK at the same time. Professor Polte`s experience includes the leadership of over 100 bilateral projects successfully conducted in collaboration with industry partners. Furthermore, he contributes to industrial development as Co-Chair of the Additive Manufacturing Working Group at the Association of German Tool and Moldmakers (VDWF e.V.) and as the elected Vice Chairman of the Advisory Board for the Automotive Transformation Network Berlin-Brandenburg (ReTraNetz-BB). His professional profile is further complemented by his roles as Project Manager of the Fraunhofer Lighthouse Project EMOTION and as a member of the Board of Directors of the High-Performance Center for Digital Networking (LZDV).

He is actively involved in academic teaching and supervision, particularly in the fields of additive manufacturing and precision engineering. His extensive contributions to the scientific community include editorial, reviewing, and committee activities. These responsibilities involve evaluating research proposals and scientific journals, notably for the German Research Foundation (DFG) and

the International Academy for Production Engineering (CIRP), as well as international conferences in the field of manufacturing and materials engineering. Between 2018 and 2020, he held the status of Research Affiliate at CIRP, completing the maximum duration possible for this affiliation. Since 2024, he is a member of the editorial board of Progress in Additive Manufacturing. His academic profile is further distinguished by contributions to international standardization and scientific bodies, encompassing active roles within ASTM and DIN, alongside his involvement in the young researchers' initiative of the German Academic Society for Production Engineering (WGP).

Prof. Polte's expertise encompasses the entire spectrum of production technology, ranging from ultra-precision and high-precision cutting to non-conventional processes such as EDM and additive manufacturing. A central pillar of his research involves manufacturing technologies, process development, and machine tool development for advanced production systems. By integrating Artificial Intelligence and human-AI-machine teaming, he continues to orchestrate complex industrial ecosystems at the intersection of teaching, research, and large-scale industrial application. His scientific impact is substantiated by a prolific record of over 250 publications, including peer-reviewed journal articles and conference papers, as well as patents and keynote presentations at leading international conferences and forums.

Committed to fostering an inclusive academic environment, he actively establishes and supports initiatives aimed at increasing the representation of women in Engineering. Since 2024, he has been involved in dedicated teaching and workshop formats for women in additive manufacturing at the Technical University of Berlin, alongside mentoring and advocacy in cooperation with national and international programs such as Fraunhofer TALENTA and IGSTC. His activities also include the organization of workshops in cooperation with the Girls Gearing Up International Leadership Academy and hosting events as part of Girls' Day initiatives, contributing to the promotion of young female talents in engineering.

Session 1: Metrology

euspen's 26th International Conference & Exhibition, Krakow, PL, June 2026
www.euspen.eu

Development of a compact gear measuring machine based on modified line-of-action scanning for high-precision tooth profile measurement

Yohan Kondo [1)], Yuta Miyakawa [2)], Yukihiro Kato [2)], Kazuya Matsuzaki [1)] and Osamu Sato[1)]

[1)] *National Metrology Institute of Japan(NMIJ), National Institute of Advanced Industrial Science and Technology (AIST)*
[2)] *Tokyo Technical Instruments Inc.*

kondou.y@aist.go.jp

Abstract
The accuracy of the tooth profile in cylindrical involute gears is crucial for ensuring reliable performance in many industrial applications, and dedicated gear measuring machines (GMMs) are widely used for this purpose. Conventional GMMs are based on the principle of involute generation, in which the probe scans along the line of action tangential to the base circle. To measure both the left and right flanks, however, the probe must be laterally offset along the line of action. This offset enlarges the overall machine size, while the increased movement of the Z-axis column reduces structural rigidity and can significantly degrade measurement accuracy. In this study, a measurement principle that adapts conventional line-of-action scanning based on the theory of involute generation is proposed to reduce the required lateral offset. While the scanning approach along the line of action is retained, the angle of the line of action is individually adjusted for the left and right flanks. This modification allows the measurement regions for both flanks to be substantially coincident, thereby reducing the required XY measuring range of the machine. The downsizing of the gear measuring machine provides significant benefits, including enhanced stage rigidity and reduced manufacturing cost. However, the proposed approach changes the orientation of the line of action, so that the normal direction of the tooth surface does not necessarily coincide with the sensitivity direction of the probe. In this paper, the probe characteristics with respect to the sensitivity direction were experimentally evaluated to clarify their influence on tooth profile measurement. To validate the modified line-of-action scanning, we developed a GMM. The measurement accuracy was evaluated using a master gear calibrated by a coordinate measuring machine operated as Japan's national standard. Experimental results showed that the tooth profile deviations measured by the proposed GMM agree with those obtained by a national standard CMM within ±1 µm, demonstrating its potential as a practical and high-precision solution for industrial gear inspection.

Gear measuring machine, involute gear tooth, line of action, probe characteristics, calibration, master gear

1. Introduction

Gears are essential mechanical components used for power transmission in automobiles, power generators, aircraft, marine vessels, medical equipment such as CT scanners, and construction machinery. To improve transmission efficiency, enhance durability, and reduce noise, the geometric deviations of gear teeth must be minimized. Large gears additionally require high structural rigidity because they cannot be easily replaced or repaired. For such gears, the surface profile of tooth flanks must be manufactured with micrometer-level accuracy.

Advancing the geometric accuracy of gears requires reliable methods for measuring the tooth-flank geometry. In industry, dedicated gear measuring machines—configured as a polar-coordinate system consisting of three orthogonal linear axes (X, Y, Z), a rotary table (θ), and a probing system—are commonly employed for this purpose [1-2]. Figure 1(a) illustrates the basic measurement principle for an involute cylindrical gear. The workpiece is rotated while the probe is translated along the tangent to the base circle (the line of action) in synchronization with the gear rotation. This motion reflects the involute generation theory. The tooth profile deviation is detected as the probe displacement from its theoretical position.

To measure both the left and right flanks of the gear, the probe must travel a long distance along the line of action. However, this long travel can lead to motion errors in the Z-column. To suppress these errors, the measuring machine must be designed with high structural rigidity, which is a major factor contributing to the high cost of large-gear measuring systems.

M. Yuzaki proposed a measurement approach in which the rolling angle of the base point A on the involute profile is shifted by $\pm\alpha_t$—where the positive sign corresponds to the right flank and the negative sign to the left flank—to define different lines of action for the two flank measurements [3]. Here, α_t denotes the transverse pressure angle of the gear under test. In this method, the probe is controlled in the orthogonal X- and Y-directions in synchronization with the gear rolling angle ε, as illustrated in Figure 1(b). Similar to conventional gear metrology, the probe scans along the line of action. In the conventional measurement principle, the line of action is parallel to the X-axis of the machine coordinate system. In the proposed method, the orientation of the line of action is modified by adjusting the transverse pressure angle $+\alpha_t$ and $-\alpha_t$ for the left and right flanks.

Because a smaller probe-travel range is sufficient for large gears, reducing the required probe travel makes it possible to design a more compact measuring system, which contributes to lower manufacturing cost. In addition, the smaller travel range facilitates a high-rigidity structure, an advantage that is particularly important for large-gear measuring machines.

Furthermore, conventional methods sometimes fail to evaluate small internal gears—such internal gears are used in

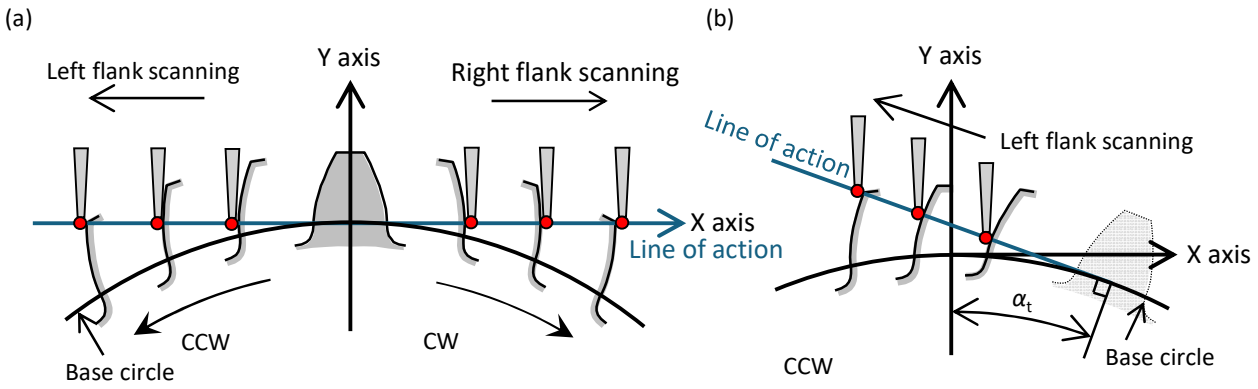

Figure 1. Schematic of involute gear profile measurement:(a) Traditional measurement principle, requiring a large probe travel due to different measurement regions on the left and right flanks. (b) Measurement principle based on modified line-of-action scanning for the left flank.

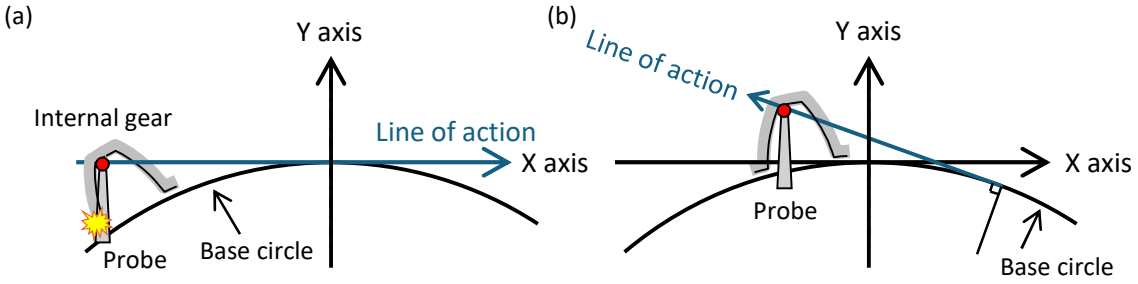

Figure 2. Schematic of internal gear profile measurement: (a) Traditional measurement principle, where probe interference is an issue and a special probe is required. (b) Modified line-of-action scanning, in which probe interference is avoided.

micro-actuator components for electric vehicles, medical evaluate small internal gears—such internal gears are used in micro-actuator components for electric vehicles, medical equipment, and communication devices—because of probe interference. The proposed method overcomes this limitation, making it possible to measure these internal gears without probe collisions, as shown in Figure 2.

However, in the modified line-of-action scanning approach—a compact gear measuring method—the line of action is not aligned with the surface normal of the tooth flank. When a probe with unidirectional sensitivity is used, the probe characteristics influence the measurement accuracy of tooth form deviation and thus become a source of measurement error. A similar mismatch between the surface normal and the line of action also exists for helical gears in conventional measurement systems.

In this study, a probe calibration device was developed, and the relationship between the tooth-flank contact angle and the probe characteristics was evaluated. A compact gear measuring machine equipped with a probe calibrated using the developed system was constructed, and the validity of the proposed approach was confirmed through comparative measurements against a master gear calibrated with a coordinate measuring machine operated as Japan's national standard.

2. Evaluation of probe characteristics

A probe calibration system was developed to evaluate the characteristics of GMM probes. In this study, two commercially available probes (1. TD-1R/Zero, Tokyo technical and 2. SP80H, Renishaw) were selected as representative probes, and their characteristics were evaluated using the developed system. Figure 3 shows the configuration of the system. It consists of a laser interferometer (Renishaw, XL-80), a piezoelectric stage (THK Precision, PS1L80-700U), a spherical measurement target (ruby sphere, ϕ8 mm), and the probe under test. The measurement beam of the interferometer is aligned with the motion axis of the piezo stage within five arcminutes. The measurement beam of the interferometer is adjusted so that its central axis passes through the center of the target sphere. The sensitivity direction of the probe under test is aligned with the motion axis of the piezo stage. The target sphere is moved in steps over a range of ±100 µm in 10 µm increments. By comparing the outputs of the probe and the laser interferometer, the sensitivity (gain) of the probe is calibrated. Because the probe is used to measure both the left and right flanks of a gear, the calibration is performed for both directions by changing the probe contact direction accordingly. The calibration system satisfies Abbe's principle, and the stage displacement is measured in real time using a laser interferometer. The alignment between the interferometer beam and the motion axis was adjusted within five arcminutes, resulting in a cosine error below 1 nm. In addition, the probe contacts the same point on the spherical target during calibration, the influence of the probe tip form is negligible.

In actual gear-tooth measurements, the surface normal of the tooth flank does not coincide with the probe's sensitivity axis.

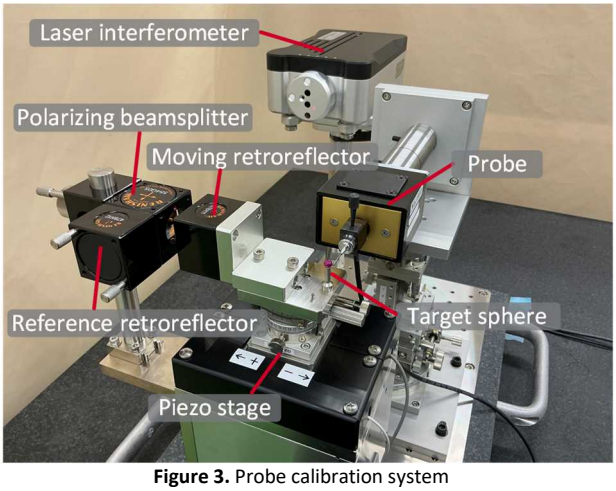

Figure 3. Probe calibration system

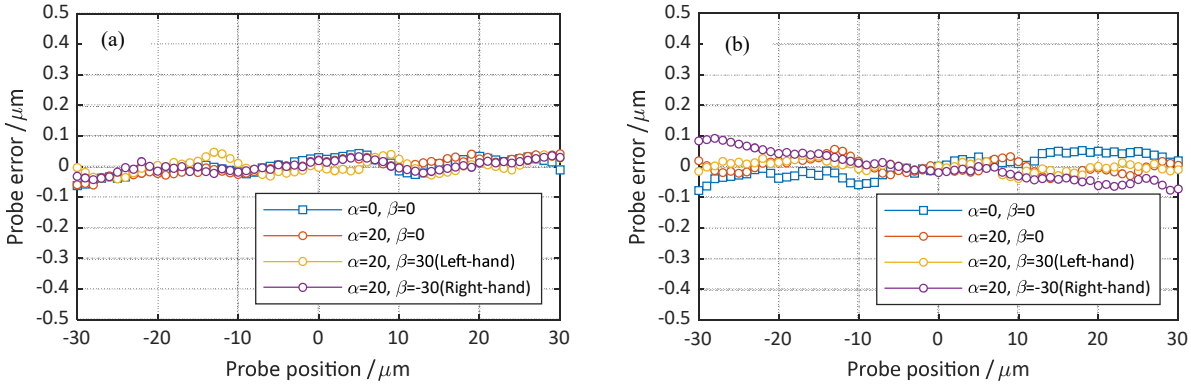

Figure 4. Evaluation results of the probe (TD-1R/Zero, Tokyo Technical): (a) left tooth flank and (b) right tooth flank

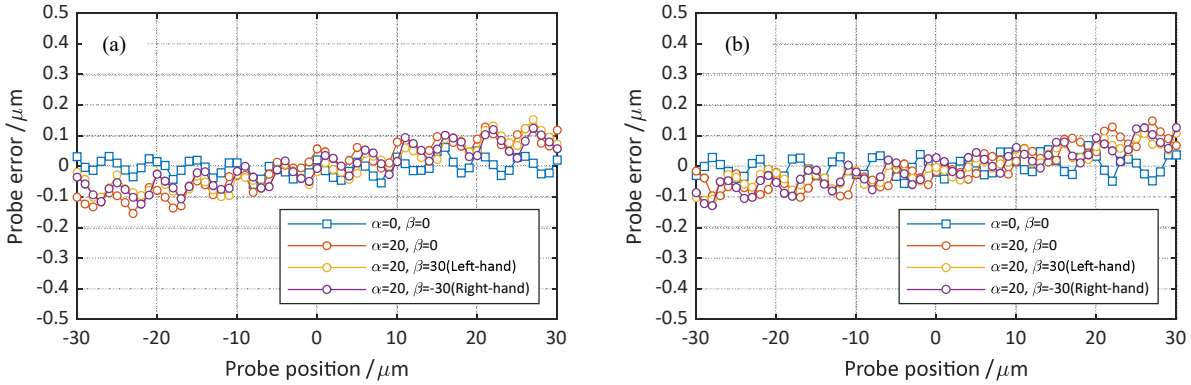

Figure 5. Evaluation results of the probe (SP80H, Renishaw): (a) left tooth flank and (b) right tooth flank

Therefore, probe characteristics were evaluated for spur and helical gears with a pressure angle of α = 20°, helix angles β = 0°, ±15°, and ±30°. The probe was brought into contact with the target sphere at positions corresponding to the expected surface-normal directions, starting from the equator of the sphere as a reference position. The probe characteristics were evaluated by scanning over ±30 μm in 1 μm increments and comparing the probe output with that of the laser interferometer. Figures 4 and 5 shows the evaluation results.

The evaluation results for the TD-1R/Zero and the SP80H are shown in Figs. 4 and 5. In each figure, (a) corresponds to the left tooth flank and (b) to the right tooth flank. The combination $(\alpha, \beta) = (0,0)$represents the condition in which the motion axis of the piezo stage (the sphere normal) is aligned with the probe sensitivity axis, i.e., the state used for probe calibration. The results clearly show that the probe characteristics vary depending on the pressure angle and the helix angle. Nevertheless, within the evaluation range of ±30 μm, the probe error remains within ±0.2 μm for both probes.

The probe characteristics are influenced by the difference between the tooth-surface normal direction, which changes with the pressure angle and the helix angle of the gear, and the fixed probe sensitivity axis. For high-accuracy measurements, it is therefore meaningful to apply different probe sensitivity coefficients depending on the target gear. The probe sensitivity calibrated under the condition (α, β) = (20°, 0°) was applied in the subsequent GMM measurements. The influence of the probe gain error on the evaluated tooth profile deviation depends on the amount of tooth profile modification and becomes larger for gears with larger profile modifications.

3. Experimental validation of the proposed scanning method

To validate the modified line-of-action scanning method, a general-purpose gear measuring machine (GMM) was developed. Figure 6 shows the developed GMM. The machine is

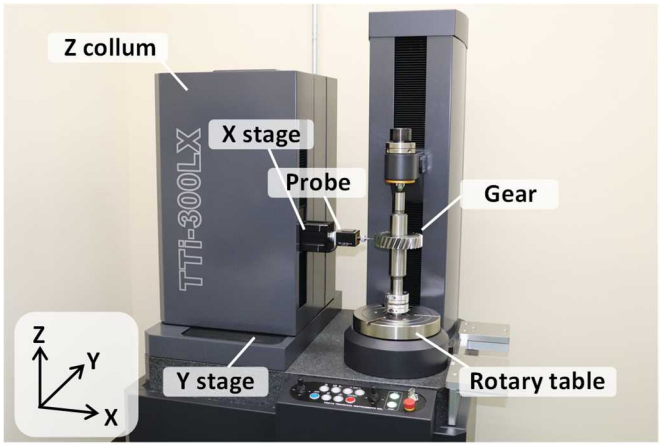

Figure 6. General-purpose gear measuring machine (GMM) developed for the modified line-of-action scanning method

Table 1 Master gear specifications

Gear type	Helical gear (right-hand)
Module	4 mm
Number of teeth	30
Normal pressure angle	20°
Helix angle on reference cylinder	20°
Face width	30 mm
Base circle diameter	119.0809 mm

equipped with three orthogonal linear axes with travel ranges of of 180 mm (X), 130 mm (Y), and 370 mm (Z). The Z-axis column is mounted on the Y-axis stage, and the X-axis is installed on the developed. Figure 6 shows the developed GMM. The machine is equipped with three orthogonal linear axes with travel ranges of 180 mm (X), 130 mm (Y), and 370 mm (Z). The Z-axis column is mounted on the Y-axis stage, and the X-axis is installed on the Z-axis column. The X-, Y-, and Z-axes are constructed using commercially available linear motion guides, linear motors, and linear scales. The rotary θ-axis is also composed of commercially

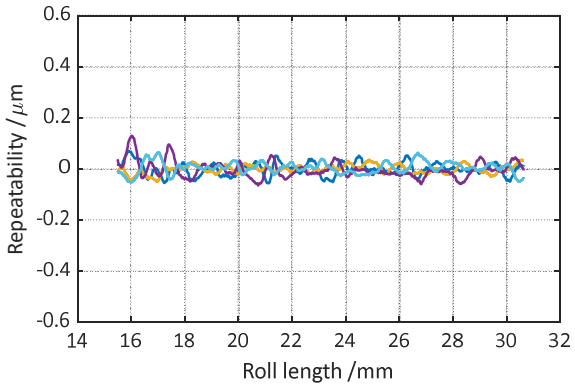

Figure 7. Repeatability of tooth No.1 at orientation 1

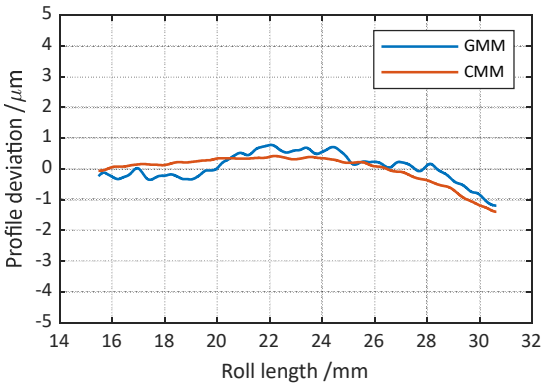

Figure 9. Comparison between GMM and CMM for tooth No. 1

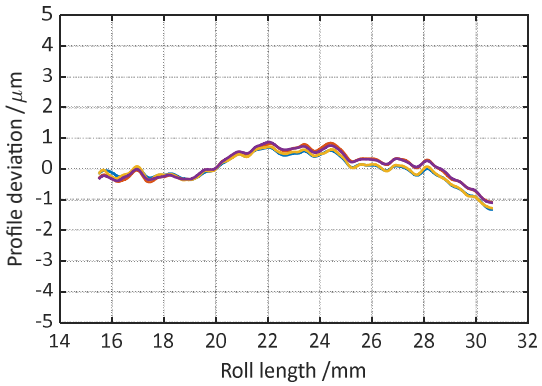

Figure 8. Reproducibility among four orientations for tooth No.1

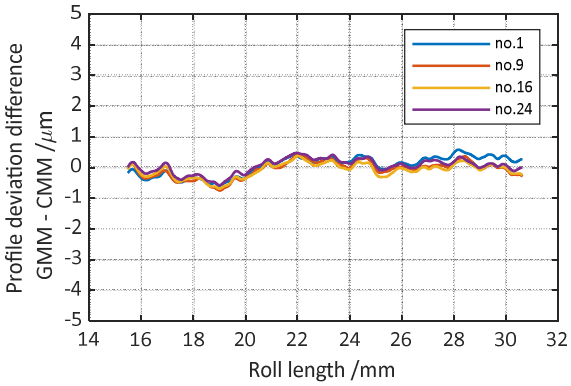

Figure 10. Difference curves between the GMM and the CMM for teeth Nos. 1, 9, 16, and 24

available rolling bearing and a direct-drive motor. As the probing system, the TD-1R/Zero probe evaluated in Section 2 was mounted on the machine. The measurements were conducted under laboratory conditions with the temperature controlled at 20 °C ± 0.5 °C, a probing force of approximately 0.05 N, and 480 points along each profile.

Table 1 shows the specifications of the master gear used for the evaluation. The master gear was mounted on the rotary axis of the GMM in four orientations, equally spaced at 90°. The averaging over four orientations was performed to reduce the influence of mounting eccentricity. Since the mounting error affects both the traditional and the proposed methods but is not related to the modification of the line of action, the mean profile over the four orientations was used for the comparison. Other error sources, such as probe errors and stage motion errors, are not cancelled by this averaging and remain in the results. For each orientation, six repeated measurements of the gear tooth profile were performed. The obtained tooth profile was then determined as the average profile over all orientations.

The measurement results for selected teeth (Nos. 1, 9, 16, and 24), which are approximately evenly spaced on the 30-tooth gear, on the left flank of the master gear are presented. Figure 7 shows the repeated measurement results for tooth No.1 at orientation 1. The standard deviation of the residuals from the mean curve was 0.025 µm, indicating high repeatability. Figure 8 shows the dispersion of the mean curves obtained from the four orientations for the same flank. The standard deviation among the orientations was 0.081 µm, demonstrating high reproducibility. These results confirm that sub-micrometer repeatability and reproducibility can be achieved even without employing an ultra-precision stage or applying error compensation techniques.

Next, to evaluate the validity of the obtained tooth profile deviation curves, the same tooth flank was measured using a coordinate measuring machine (CMM) operated as Japan's national standard. The expanded uncertainty of the CMM for tooth profile measurement is 0.4 µm (k = 2). Figure 9 compares the tooth profile deviation curves for tooth no.1 measured by the developed GMM and the CMM, and Fig. 10 shows the corresponding differences between the four selected teeth (Nos. 1, 9, 16, and 24). The maximum root-mean-square (RMS) value among the difference curves was 0.42 µm, and all difference curves were within ±1 µm. These results indicate that the tooth profile deviations measured by the proposed GMM agree with the CMM measurement within ±1 µm, even without using high-precision stages or advanced compensation methods.

By adopting higher-precision stages, such as air slides and air spindles, and by applying various compensation techniques for scale errors, motion errors, and workpiece mounting eccentricity, further improvement in measurement accuracy is expected.

4. Conclusion

A general-purpose gear measuring machine (GMM) based on the modified line-of-action scanning method was developed and experimentally evaluated. The probe characteristics were investigated, showing that the probe response depends on the pressure angle and the helix angle through variations in the tooth-surface normal relative to the fixed probe sensitivity axis. Comparisons of the master gear measurements with a coordinate measuring machine (CMM) showed good agreement. The proposed GMM can measure tooth profile deviations with an accuracy better than 1 µm using a simple and practical system.

References

[1] Goch G 2003 Gear metrology *CIRP Ann.* **52** 659–95
[2] Goch G, Guenther A, Peng Y and Ni K 2023 Gear metrology – an update *CIRP Ann.* **72** 725–51
[3] Yuzaki M 2011 Gear measuring machine by "NDG method" for gears ranging from miniature to super-large metrology *Gear Technol.* **March/April** 55–60

euspen's 26th International Conference & Exhibition, Krakow, PL, June 2026
www.euspen.eu

Investigating filter end-effects on profiles having form, in the context of ISO 21920

Faivre A[1], Blateyron F[1]
[1] Digital Surf, Besançon, France
Corresponding author: fblateyron@digitalsurf.fr

Abstract

ISO 21920-2 introduced a change in the order of operations required to obtain the Primary profile. Now, the microroughness S-Filter (with *Nis* nesting index, equivalent to λs) is applied first, before the F-Operation (levelling or form removal), contrary to what was done earlier with ISO 3274. This change implies that a profile with form can be smoothed by a Gaussian filter (the default filter type) which is notoriously not robust against form, leading to end-effects that may affect parameter calculations. This paper compares different methods for managing end-effects, as described in ISO 16610-28, discusses their respective advantages and drawbacks, and introduces a possible alternative way to minimize biases on parameter results.

Keywords: Filtration, end-effects, ISO 21920, S-Filter, F-Operation

1. Introduction

ISO 21920-2 [1] changed the order between S-Filter and F-Operation, so it is now possible to smooth a profile, using a small-scales S-Filter, while the form is present (slope or geometrical form). The problem is that the Gaussian filter does not cope well with form, therefore, the smoothed profile exhibits end-effects when applied on a profile with form, sometimes leading to huge differences, for example in peak-to-valley parameters. This drawback could be a huge obstacle for users wishing to move from ISO 3274 [2] to the new ISO 21920 standard.

Literature on the subject of filter end-effects (also called edge effects) is quite rare. ISO standards describe end-effects management methods (EEM method), but without explaining their advantages or drawbacks. Moreover, users are left with inconsistencies between different documents, such as ISO 16610-21 [3] which recommends the "moment retainment" method for the Gaussian filter, and ISO 16610-22 [4] which includes the "line extension" method in the Spline filter, while ISO 16610-28 [5] proposes a collection of possible methods. Besides, Part 28 does not have an equivalent document for surfaces (that should be Part 68), yet surfaces are also impacted by the same end-effects.

Several authors though have investigated end-effects and have proposed filter variants, sometimes by exploring other types of filters [6, 7, 8, 9]. However, a complete characterization of all the proposed EEM methods does not seem to exist.

This is why, we propose in this paper to explore the impact of each EEM method on a selection of test profiles, in order to recommend good practices. We also propose an alternative method, suitable for surface texture, that minimizes end-effects, in particular of the small scales S-Filter with a *Nis* nesting index.

2. Methodology

In order to characterize the impact of each EEM method, a specific experimental workflow is used in the Mountains® software and applied on test profiles.

2.1 Test profiles

This experimental workflow is applied on a bank of profiles, composed of 4 different base texture profiles (see Table 1) superimposed on 7 different form components, 6 of them given in Table 2 plus No Form, which makes a total of 28 test profiles.

Table 1: *texture bases of the test profiles*

Honing1	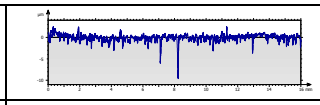
Noise	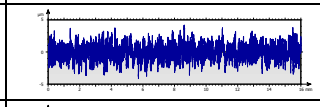
Sym Noise	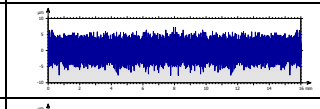
Square	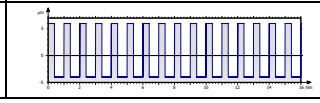

Honing1 is a stratified profile measured on a cylinder bore; Noise was created with a random generator using a Gaussian distribution, but where several instances of the same value are possible (which may influence the mean line position), Symmetrical noise has only one instance per value to ensure that the mean line is centred; Square is a rectangular shape periodical profile with a non-symmetrical duty cycle.

Regarding the Form components, there are two inclined line segments, to compare the impact of the amplitude of form, two different arcs, one almost centred and the other taken on the side, each with a different radius, and two polynomial profiles, a parabola and a 3rd-order polynomial.

The resulting test profiles are obtained by summing a texture with a Form component.

Table 2: *Form components*

10° slope	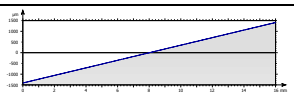
30° slope	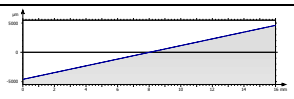
Arc 10mm	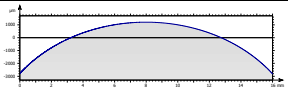
Arc 20mm	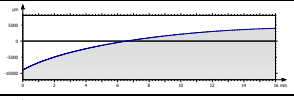
Parabola	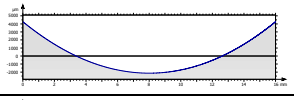
3rd-order polynomial	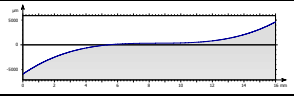

2.2 Workflow

The workflow presented in Figure 1 is designed to allow the assessment of an EEM method by comparing a particular filtered profile with an end-effects management method with the filtered profile without end-effects.

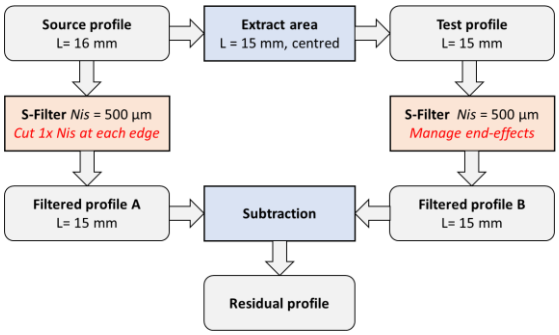

Figure 1: *workflow used to characterize end-effects*

The left side of the workflow produces the *Filtered profile A* where the S-Filter cuts one cut-off at each end. Profile A acts as a reference (that has no end-effects). The right side of the workflow uses one of the EEM method under test, and the residual profile is characterized in amplitude and/or in lateral span. Figure 2 shows an example of residual profile.

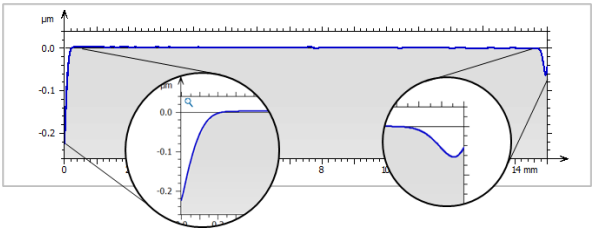

Figure 2: *Example of residual profile showing end-effects*

2.3 End-effect management methods

The study applied the above workflow to various EEM methods, defined in ISO 16610-28, plus the additional suggested method, defined in section 4. Some of the methods extend each end of the profile by a length equal to one cut-off length and others modify the filter equation within the end-effect zone (EEZ).

The tested methods were:

- Zero padding (ZP)
  Extends the profile by adding zeros on both ends.
- Copy last point (LP)
  Extends the profile by copying the first or last point.
- Simple mirror (SM)
  Copies the points of the EEZ by horizontal symmetry.
- Double mirror (DM)
  Copies the points of the EEZ by horizontal and vertical symmetry.
- Slope extension (SE)
  Extends the profile with a LS line calculated in the EEZ.
- Retain moments (RM)
  Modifies the filter equation in the EEZ.

3. Alternative EEM method

Considering that the inversion between the S-Filter and F-Operation is the main cause of troubles, a simple solution is proposed, as shown in Figure 3.

1. A first F-Operation is applied before the S-Filter in order to allow the filtration without end-effects
2. Then the form is put back after the S-Filter to obtain a smoothed profile with the original form
3. Then the specified F-Operation is done

This method minimizes end-effects due to the S-Filter, as it is applied on a profile without form, as before with ISO 3274. However, it stays compatible with the aim of ISO 21920-2 as the final F-Operation is applied on a smoothed profile.

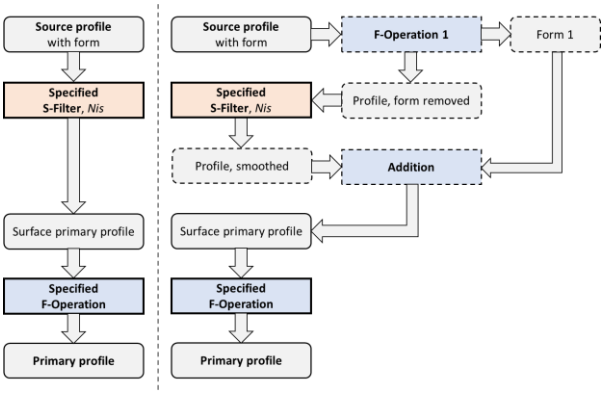

Figure 3: standard workflow to obtain the primary profile (left) and *proposed alternative workflow (right)*

In Figure 3, the alternative EEM method is shown with dotted boxes. It might look trivial but it simply separates the texture and the form, to filter the texture without end-effects, and produce a smoothed version of the source profile. The second F-Operation is applied on the smoothed profile, so the removed form it is slightly different from the first form calculated on the source profile. In this paper, we suggest to call this method *Preliminary Form Removal* (FR).

4. Test results

Test profiles have been characterized using a document that implements the workflow described above, in MountainsMap® version 11.1, using a special function that enables to change the EEM method in the S-Filter. The 28 test profiles have been filtered using one of the 7 EEM methods, to produce 196 results.

In the tables below, the best and worst EEM methods are given for each type of texture, using the 2-letter code provided in 2.3, and the deviation in percentage of the texture amplitude is given.

Table 3: *results on No Form*

Texture	Best EEM method	Worst EEM method
Honing1	**FR** (0,006%)	ZP (5,9%)
Noise	**ZP** (4,1%)	DM (31%)
Sym Noise	**SM** (0,34%)	DM (24%)
Square	**FR** (8%)	RM (35%)

Table 4: *results on 10° slope*

Texture	Best EEM method	Worst EEM method
Honing1	**ES** (1,6%)	ZP (49%)
Noise	**ES** (0,03%)	ZP (49%)
Sym Noise	**ES** (0,002%)	ZP (50%)
Square	**DM** (0,2%)	ZP (49%)

Table 5: *results on 30° slope*

Texture	Best EEM method	Worst EEM method
Honing1	**FR** (0,01%)	ZP (49%)
Noise	**ES** (0,01%)	ZP (48%)
Sym Noise	**ES** (< 0,001%)	ZP (49%)
Square	**FR** (0,05%)	ZP (49%)

Table 6: *results on Arc 10mm*

Texture	Best EEM method	Worst EEM method
Honing1	**FR** (0,04%)	ZP (35%)
Noise	**DM** (0,07%)	ZP (35%)
Sym Noise	**FR** (0,003%)	ZP (35%)
Square	**DM** (0,005%)	ZP (35%)

Table 7: *results on Arc 20mm*

Texture	Best EEM method	Worst EEM method
Honing1	**FR** (0,01%)	ZP (40%)
Noise	**DM** (0,02%)	ZP (49%)
Sym Noise	**FR** (0,001%)	ZP (49%)
Square	**DM** (0,02%)	ZP (49%)

Table 8: *results on Parabola*

Texture	Best EEM method	Worst EEM method
Honing1	**FR** (0,02%)	ZP (92%)
Noise	**RM** (0,04%)	ZP (34%)
Sym Noise	**FR** (0,001%)	ZP (22%)
Square	**DM** (0,04%)	ZP (34%)

Table 9: *results on 3rd order polynomial*

Texture	Best EEM method	Worst EEM method
Honing1	**FR** (0,01%)	ZP (22%)
Noise	**DM** (0,03%)	ZP (47%)
Sym Noise	**FR** (0,001%)	ZP (47%)
Square	**DM** (0,06%)	ZP (46%)

5. Discussion

In order to classify the methods, we calculate a score based on the number of cases where the method is the best minus the number of cases where the method is the worst.

Using this score, we obtain:

1. FR (Form removal): 12 – 0 = 12 points
2. DM (double mirror): 8 – 3 = 5 points
3. ES (Extend slope): 5 – 0 = 5 points

But in some cases, two or three methods provide good results with close percentages. So, in order to take them into account, even though they are not the very best, we also calculated the number of times where the deviation is lower than 1% (so where the EEM method is good) minus the number of times where the deviation is larger than 10% (the method is not very good). Deviations are calculated with respect to the test profile that contains form.

With this second score, we obtain:

1. FR (Form removal): 25 – 1 = 24 points
2. ES (Extend slope): 25 – 2 = 23 points
3. RM (Retain moments): 24 – 2 = 22 points
4. DM (double mirror): 24 – 3 = 21 points

The other methods are clearly behind in terms of score, i.e. of performance (CP: 10 pts; SM: 6 pts; ZP: -25 pts).

However, it is more realistic to calculate deviations with respect to the texture profile without form.

In that case, we obtain the following podium:

1. FR (Form removal)
2. RM (Retain moments)
3. DM (double mirror)
4. ES (Extend slope)

The deviations calculated using this method are always quite high, demonstrating that any EEM method, applied on a profile that has form, introduces errors and that the only harmless solution is to cut ends.

Choosing the Retain moments (RM) method as the default EEM method for the Gaussian filter is sound, as it provides the second lowest deviations. The Extend slope method (ES) implemented by default in the Spline filter is acceptable, but it may not be adequate in case of small cut-offs, as the slope is calculated on a too small EEZ. The Double mirror (DM) is the default method implemented in MountainsMap®, except for the small scales S-Filter which implements the Retain moments. The Double mirror is a good solution for stochastic profiles but less adequate for structured profiles.

The Form removal method (FR) is always the best solution, for any texture and any form. It is an artificial way to come back to the previous workflow where the F-Operation was done prior to the S-Filter. It may be a kind of trick but it confirms that for surface texture applications, it should be the preferred workflow.

6. Conclusion

The change in the order of operations in ISO 21920 created some confusion amongst users. The initial idea was to allow the use of filters and parameters in form deviation applications (such as Contour analysis), but effects on roughness profiles is sometimes significant, especially in presence of slope or form. It is therefore important to either use a small scales filter type that is robust against form, such as a Robust Gaussian filter [11] or to use a proper end-effects management method, or to cut the profile ends to remove the end-effects.

This paper provided hints to understand the properties of each EEM method.

The proposed alternative method (FR) provides a better solution for surface texture applications and is also simple to understand and simple to implement. It solves the problems due to the inversion in the order of operations.

This inversion was not necessarily a good idea for surface texture users, although it opens the scope of filtration to a broader range of applications such as evaluation of form deviation.

It is important to remember that applying a EEM method always introduces a deviation compared to the solution of cutting edges. It was already the case even when the F-Operation was done first, but it is even more true with the new workflow.

The solution could be to separate applications, and recommend to keep the previous workflow (F-Operation then S-Filter) for surface texture applications and have the inverted workflow (S-Filter then F-Operation) for form deviation analysis.

7. Future work

As explained, different EEM methods are included in the Gaussian and Spline filters, in the ISO 16610 series, and in addition, other methods are proposed is Part 28 that could be used and specified. All of these methods are not equivalent and some of them should be avoided. ISO TC213 WG16 should revise these documents in the future to clarify this point and if possible, homogenize a single method for all filters.

Our study focused on profile filters but it would be important to carry on the same study on surfaces to check if the conclusions are consistent or not.

Note on the implementation in Mountains®

All the EEM methods discussed in this paper have been implemented within Mountains® for the purpose of this investigation. However, users do not have access to the selection of the EEM method when applying a filter. The only choice is whether to cut ends or manage end-effects. By default, the Double mirror (DM) is used. Since version 11.1, the Retain moments (RM) is used for the small scales S-Filter when calculating parameters from ISO 21920-2 or when using the S-Filter operator, in order to minimize end-effects discussed in this paper. For other parameters or other filters, the manage end-effects still applies the Double mirror.

References

[1] ISO 21920-2:2021 Geometrical product specifications (GPS) — Surface texture: Profile Part 2: *Terms, definitions and surface texture parameters*

[2] ISO 3274:1996 Geometrical Product Specifications (GPS) — Surface texture: Profile method — *Nominal characteristics of contact (stylus) instruments*

[3] ISO 16610-21:2025 Geometrical product specifications (GPS) — Filtration Part 21: *Linear profile filters: Gaussian filters*

[4] ISO 16610-22:2015 Geometrical product specifications (GPS) — Filtration Part 22: *Linear profile filters: Spline filters*

[5] ISO 16610-28:2016 Geometrical product specifications (GPS) — Filtration Part 28: *Profile filters: End effects*

[6] Janecki D 2012 *Edge effect elimination in the recursive implementation of Gaussian filters*, Prec. Eng. **36**(1) 128-136

[7] Kondo Y et al. 2017 *Low-pass filter without the end effect for estimating transmission characteristics—Simultaneous attaining of the end effect problem and guarantee of the transmission characteristics*, Prec. Eng. **48**(4) 243-253

[8] Podulka P 2021 *Reduction of the end-effect in surface texture analysis*, J. Phys.: Conf. Ser. **1736** 012013

[9] Guo P et al. 2022 *Surface texture characterisation with reduced boundary effect for diamond- turned micro-structured surfaces*, Prec. Eng. **79**(1) 236-244

[10] MountainsMap®, surface texture analysis software by Digital Surf, France. https://www.digitalsurf.com/software-solutions/profilometry/

[11] ISO 16610-31:2016 Geometrical product specifications (GPS) — Filtration Part 31: *Robust Profile filters: Gaussian regression filters*

euspen's 26th International Conference & Exhibition, Krakow, PL, June 2026
www.euspen.eu

Enhanced In-Situ Focus Variation Surface Metrology via Pattern-Projected Illumination for Highly Polished Additive Manufacturing Surfaces

Hussam Muhamedsalih, Aalim M. Mustafa, Prashant Kumar, Xiangqian (Jane) Jiang, Liam Blunt

University of Huddersfield Queensgate, Huddersfield, HD1 3DH

h.muhamedsalih@hud.ac.uk

Abstract
Electrochemical polishing (ECP) is widely adopted to improve the surface finish of additive-manufactured (AM) metal components. Focus variation (FV) optical metrology has demonstrated strong capability for measuring rough AM surfaces; however, as ECP progressively reduces surface roughness to sub-micron levels, conventional FV systems fail to measure them due to a lack of contrast. This work presents an enhanced in-situ Focus Variation (FV) system designed to extend the measurable roughness range toward smooth surfaces. The enhancement is achieved by integrating a pixelated phase mask into the optical path, introducing artificial contrast that enables stable focus detection independent of intrinsic surface texture. Experimental validation was conducted on Additive manufactured (AM) metal components subjected to Electrochemical polishing (ECP). Comparative measurements acquired with and without the phase mask demonstrate that the enhanced system reliably captures surface topography for roughness values below 0.5 µm, where conventional FV systems typically fail. The proposed approach significantly broadens the operational range of focus variation metrology, enabling continuous and reliable in-situ surface assessment throughout the entire electrochemical polishing process.

Keywords: Enhanced Focus Variation, Additive Manufacturing (AM), Electrochemical Polishing (ECP).

1. Introduction

Additive manufacturing (AM) is increasingly embedded across modern manufacturing because it offers design freedom and customisation that are difficult to achieve with conventional processes [1]. By building parts layer-by-layer, AM enables the fabrication of lightweight components with complex internal features, often without the tooling constraints of conventional machining methods [2,3]. Despite these advantages, metal AM parts typically exhibit relatively high surface roughness arising from partially fused particles and layer fabrication, which can degrade functional performance in many applications [4]. As a result, post-processing is frequently required to achieve application-ready surfaces.

Among the available finishing methods, electrochemical polishing (ECP) is widely adopted for metal AM components due to its non-contact nature and its ability to smooth surfaces while accessing complex or inaccessible geometries [5]. In ECP, material is removed by anodic dissolution in an electrolyte under an applied electric current, enabling controllable surface finishing that can be applied locally or globally, depending on process configuration [5]. However, as ECP progresses and surfaces transition from rough to highly polished, it becomes essential to verify (preferably in situ) whether the surface has reached the required quality level.

Robust in-situ metrology is therefore a key enabler for integrating ECP into automated manufacturing workflows, allowing quantitative tracking of surface evolution and reliable determination of process end-points. Previous work by the authors [6] demonstrated the implementation of a Focus Variation (FV) system for in-situ surface metrology of ECP post-processed parts. However, the study measured unpolished surfaces and medium-polished surfaces, where texture remains sufficiently rough for robust focus detection, a main parameter for using the proposed focus variation instrument.

However, FV performance degrades on smooth or specular surfaces, because such surfaces provide low contrast between neighbouring pixels. FV relies on local intensity variations within a neighbourhood window to construct a focus-measure curve as the focal plane is scanned. When the surface lacks sufficient texture, the focus-measure response becomes weak or ambiguous, leading to missing points, outliers, and unreliable reconstruction.

Several approaches have been explored to address FV limitations on smooth surfaces by introducing artificial contrast through projected patterns. Noguchi and Nayar [7] demonstrated chessboard illumination using an optical filter, but the achievable pattern pitch limited lateral resolution. Digital micromirror devices (DMDs) have been used to project high-frequency, programmable patterns [8-10]. While DMD systems provide flexibility and can operate over a wide spectral range, they typically require additional alignment, control electronics, and power at the measurement head, which complicates in-situ integration. Microdisplay-based active illumination FV has also been proposed [11], offering smaller pitch patterns than early passive approaches, but similarly requiring controllers and powered components.

Building on our previous demonstration of pixelated pattern illumination for chromatic focus variation (CFV) to enable specular surface measurement [12], this paper targets the manufacturing critical case of ECP, where surfaces evolve from rough AM textures to highly polished, low-contrast finishes that are unsuitable for conventional FV instruments. We integrate the mask-assisted illumination concept into the in-situ FV metrology configuration used from the ECP platform. Therefore, enabling the quantitative performance across all polishing

stages. In addition, we address the periodic mask pattern imprint that appears in the reconstructed height map by applying wavelet-based extraction, enabling corrected topography.

2. In-situ FV integration in the ECP platform

In a previous publication [6], the authors reported the development of an in-laboratory focus variation (FV) system to measure surface topography of additively manufactured and polished metal samples using the Holdson ECP machine. The system was integrated into the machine to enable on-machine metrology, see Figure 1.

Figure 1. FV integrated into Holdson ECP machine. (a) unpolished sample, (b) medium polished sample, (c) highly polished sample

The machine can produce different levels of polishing from low to high polishing, with surface roughness that can be less than 1 micron. Figure 2 shows medium and high polishing with respect to the unpolished sample. It can be seen that the unpolished and medium polished samples provide better contrast between neighbouring pixels compared to the highly polished surface, a condition required to satisfy the operating principle of the focus variation system for extracting surface topography. As such, measurement of highly polished surfaces with FV can produce surface topographies with missing data, see Figure 3.

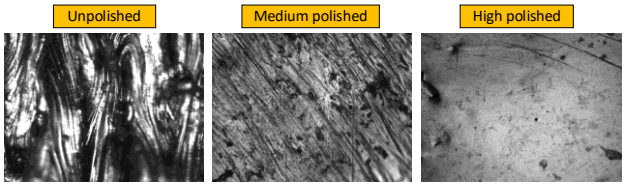

Figure 2. Additive-manufactured samples at different levels of polishing

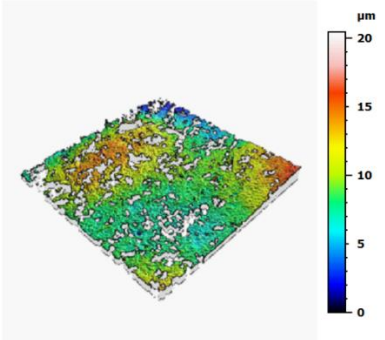

Figure 3. Surface measurement of a highly polished surface using FV system.

3. Mask-assisted FV modification

The experimental FV setup comprised a broadband light source (LS-WL1, Laser Components Ltd) collimated into a 10× Mitutoyo objective lens, which is mounted on a piezoelectric actuator (PIFOC-P-721), see Figure 4. The actuator facilitated vertical scanning of the focal plane across the sample surface. Light reflected from the sample was collected through the objective lens and focused on a CCD camera (Imperx ICLB0620M-KC000) via a 200 mm tube lens. During focal plane scanning, 128 images were acquired and subsequently analysed to generate a focus measure profile for each pixel, from which the surface topography was reconstructed.

Exemplar additively manufactured stainless steel samples were measured using this conventional setup before and after polishing. Medium polishing resulted in a reduction of surface roughness from 11.30 µm to 6.25 µm.

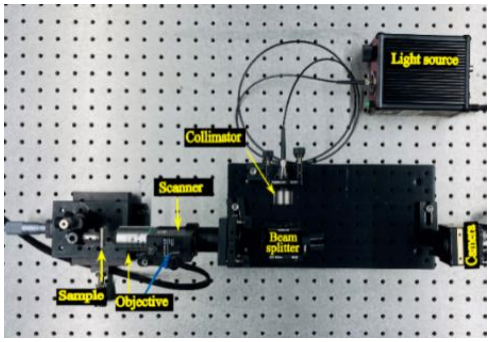

Figure 4. Original experimental setup of the FV system [6]

In the present study [6], Ultra-polished surfaces with roughness below 1 µm were investigated using the conventional FV system. The high degree of surface smoothness resulted in insufficient contrast between neighbouring pixels, leading to missing or unreliable data.

To overcome this limitation, the setup was modified to project an artificial pattern onto the sample surface through the objective lens using a pixelated phase mask, see Figure 5.

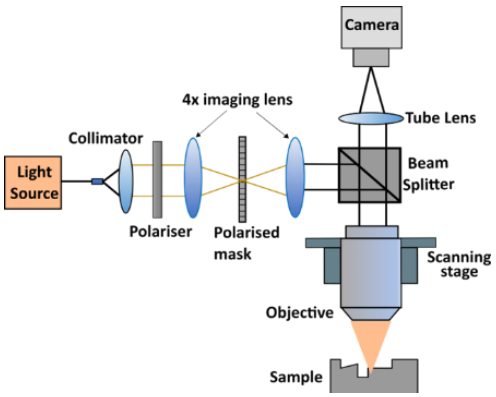

Figure 5. Enhanced FV with pixelated mask projection element

4. Results and discussion

Polarised light was focused onto the mask and subsequently collimated into the optical path. The resulting chessboard-like pattern was projected onto the sample and scanned synchronously with the focal plane, see **Figure 6**.

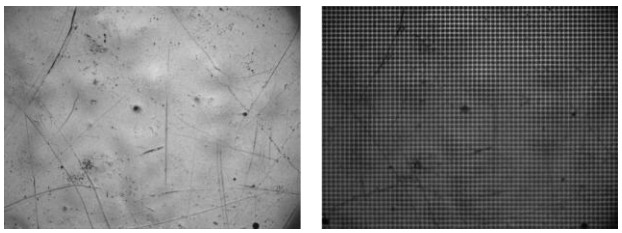

Figure 6. Highly polished surface with and without projected pattern

The piezoelectric actuator was scanned over a vertical range of 100 µm, with and without projection of the virtual pattern for comparison. As shown in Figure 7(a), the measurement without pattern projection exhibited significant missing data and outliers due to the high surface smoothness, which resulted in an insufficiently defined focus measure profile, see Figure 8 (red profile).

In contrast, when the projected pattern was applied, the missing data were eliminated, and the outliers were completely suppressed without the need for threshold-based filtering, as illustrated in Figure 7 (b). The Focus measure has been significantly enhanced, as shown in Figure 8 (green profile).

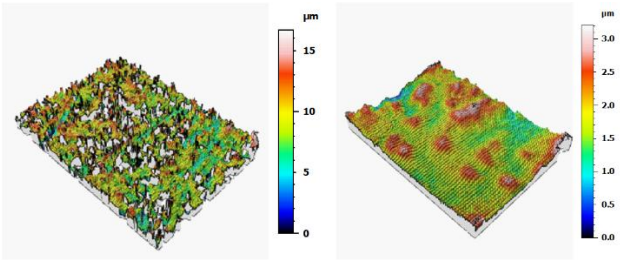

Figure 7. Surface measurement of a highly polished surface with and without projected pattern.

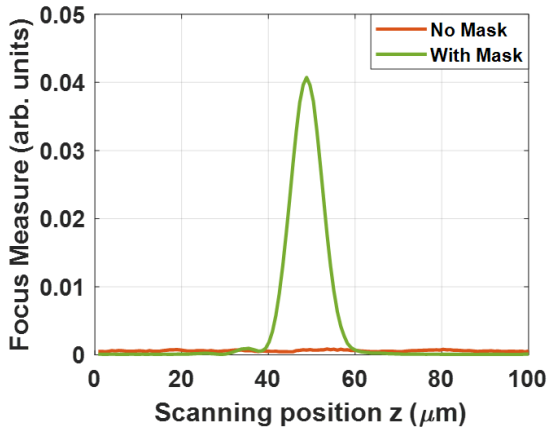

Figure 8. highly polished surface measured by the lab setup FV system: a FM profile area with and without mask.

A periodic artefact associated with the projected pattern was observed across the reconstructed surface. This artefact was effectively removed by applying a Coiflet wavelet filter (family 5, decomposition level 3), as shown in Figure 9. Following filtering, the measured surface roughness was 0.325 µm.

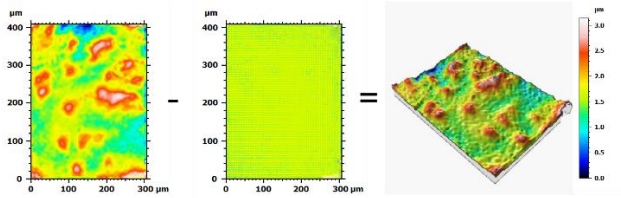

Figure 9. Filtered surface after subtracting the extracted artefact from the original measurement

This enhancement renders the FV system independent of surface-induced contrast and enables reliable acquisition of surface topography on smooth samples, thereby extending the measurable range to include submicron roughness levels.

5. Conclusion and remarks

This work presented an enhanced focus variation (FV) approach for reliable in-situ surface measurement of additively manufactured (AM) metal components undergoing electrochemical polishing (ECP). Conventional FV systems struggle to measure highly polished surfaces due to insufficient contrast, leading to missing data and unreliable reconstruction. To overcome this challenge, a pixelated phase mask was integrated into the optical path of the FV system to introduce an illumination pattern and provide the necessary local contrast required for robust focus detection.

The proposed mask-assisted approach effectively improved measurement reliability for highly polished surfaces and eliminated missing data when measuring highly polished surfaces with roughness values below 0.5 µm. The proposed enhancement extends the measurable range of FV systems and enables continuous monitoring of surface evolution throughout the ECP process.

References

[1] L. Zhou *et al.*, 2024 "Additive Manufacturing: A Comprehensive Review," *Sensors*, **24**(9), p. 2668.

[2] G. Sossou, F. Demoly, G. Montavon, and S. Gomes, 2018 "An additive manufacturing oriented design approach to mechanical assemblies," *J. Comput. Des. Eng.*, **5**(1), pp. 3–18.

[3] S. A. M. Tofail, E. P. Koumoulos, A. Bandyopadhyay, S. Bose, L. O'Donoghue, and C. Charitidis, 2018 "Additive manufacturing: scientific and technological challenges, market uptake and opportunities," *Materials Today*, **21**(1), pp. 22–37.

[4] S. Pourrahimi and L. A. Hof, 2024 "On the Post-Processing of Complex Additive Manufactured Metallic Parts: A Review," *Adv. Eng. Mater.*, **26**(10), p. 2301511.

[5] Z. Chaghazardi and R. Wüthrich, 2022 "Electropolishing of Additive Manufactured Metal Parts," *J. Electrochem. Soc.*,**169**(4), p. 043510.

[6] P. Kumar, H. Muhamedsalih, Z. Jamil, A. Mustafa, and L. Blunt, 2025 "The use of in-situ surface metrology for advanced electrochemical polishing applications," in *25th International Conference & Exhibition for European Society for Precision Engineering and Nanotechnology*, euspen.

[7] M. Noguchi and S. K. Nayar, 1994 "Microscopic Shape from Focus Using Active Illumination," in *Proceedings of 12th International Conference on Pattern Recognition*, IEEE, pp. 147–152.

[8] D. Dan *et al.*, 2013 “DMD-based LED-illumination super-resolution and optical sectioning microscopy,” *Sci. Rep.*, **3**(1), p. 1116.
[9] N. Chakrova, B. Rieger, and S. Stallinga, 2015 “Development of a DMD-based fluorescence microscope,” in *Three-Dimensional and Multidimensional Microscopy: Image Acquisition and Processing XXII*, SPIE, pp. 23–33.
[10] L. Yuan and T. Guo, 2025 “Active illumination mode with checkerboard pattern in focus variation microscopy: Analysis and application,” *Opt. Lasers Eng.*, **184**, p. 108584.
[11] C. Bermudez, P. Martínez, C. Cadevall, and R. Artigas, 2019 “Active illumination focus variation,” in *Optical Measurement Systems for Industrial Inspection XI*, SPIE, pp. 213–223.
[12] Muhamedsalih, H., Mustafa, A., Tang, D., Kumar, P., & Jiang, J. euspen’s 25th International Conference & Exhibition, Zaragoza, ES, June 2025.

euspen's 26th International Conference & Exhibition, Krakow, PL, June 2026
www.euspen.eu

Ultra-compact metalens-based phase shifting interferometry for surface metrology

Dawei Tang[1*], Hangyu Li[1], James Williamson[1], Daniel Townend[1], Jun-Yu Ou[2], Haydn Martin[1], Andrew Henning[1], Xianqian Jiang[1]

[1]*Centre for Precision Technologies, University of Huddersfield, Huddersfield, HD1 3DH, UK*
[2]*School of Physics and Astronomy, University of Southampton, Southampton, SO17 1BJ, UK*

**d.tang@hud.ac.uk*

Abstract

The transition toward Industry 4.0 has created a significant demand for compact, integration-ready optical sensors capable of enabling on-machine measurement and closed-loop process control. Conventional optical metrology systems remain limited by bulky and heavy refractive components, which restrict their deployment in space-constrained manufacturing platforms. This paper reports on the design, fabrication, and experimental validation of a high-performance GaN-based metalens doublet and its implementation in an ultra-compact phase shifting interferometry system. The metalens doublet was designed with a 2 mm field of view within a total axial length of 11.5 mm. Phase modulation is achieved through a truncated optical waveguide mechanism, where nanopillars (750 nm height, 70–180 nm radius) are etched into a GaN layer on an Al_2O_3 substrate and arranged in a 450 nm square lattice. By tailoring pillar dimensions, full 2π phase coverage is realised at a design wavelength of 660 nm. Optical simulations and experimental characterisation confirm high-quality imaging performance suitable for objective lens applications. The metalens doublet is integrated into a phase-shifting interferometric module with a total optical footprint of 6.25 mm × 9.5 mm × 5 mm. Surface measurements of a calibrated 43.7 nm step-height standard show strong agreement with results obtained from a commercial white-light interferometer, demonstrating nanometre-scale measurement capability. These results establish metasurface-based optics as a viable platform for compact, robust, and integration-ready metrology systems for advanced manufacturing environments.

Keywords: metasurfaces, optical metrology, on-machine measurement, phase-shifting interferometer

1. Introduction

The rapid evolution toward smart, interconnected manufacturing under the Industry 4.0 paradigm has increased the demand for compact, integration-ready metrology systems capable of operating directly within production platforms [1]. In-process and on-machine measurement enable closed-loop control, reduced downtime, and enhanced product quality. However, conventional optical metrology instruments remain constrained by bulky refractive components and complex assemblies. These limitations hinder seamless integration into confined manufacturing platforms and restrict their deployment in distributed sensing architectures.

In recent years, metasurfaces have emerged as a viable technology for achieving the functionality of conventional refractive optics without the associated size and weight. Composed of arrays of nanostructures, often referred as meta-atoms, metasurfaces provide precise control over the phase, polarisation, and amplitude of incident light [2]. By spatially arranging these elements, desired optical functions equivalent to the combined effect of multiple traditional components can be realised within a single planar device. This capability enables substantial reductions in system size and weight, opening the path toward ultra-compact, lightweight optical sensors suitable for smart factories.

In this work, we present the design, fabrication, and experimental validation of a high-performance metalens doublet and its implementation in an ultra-compact phase shifting interferometry system. The metalens doublet was designed with a 2 mm field of view (FOV) within a total axial length of only 11.5 mm. To verify practical utility, the doublet is integrated into an ultra-compact phase-shifting interferometric module with a total optical footprint of 6.25 mm × 9.5 mm × 5 mm. Phase shifting was implemented using a simple mechanical translation of the tested sample as a proof-of-concept demonstration. Surface measurements of a calibrated step-height standard (VLSI Standards) show strong agreement with those obtained using a commercial white-light interferometer, confirming the viability of metasurface-enabled optical sensors for high-resolution surface metrology.

2. Metalens doublet design

One of the key elements for microscopy based optical sensors is the objective lens, which provides high resolution imaging across the field of view (FoV). While a single metalens can achieve compact focusing, off-axis aberrations often limit usable field of view. To address this, we designed a metalens doublet configuration. The first metasurface performs the primary wavefront shaping required for focusing, while the second metasurface compensates for residual aberrations, thereby extending the field of view to 2 mm. To facilitate subsequent integration in a metrology system, a glass plate with a thickness of 5 mm serving as a beamsplitter was incorporated into the optical design to optimise imaging performance.

As shown in Figure 1, the complete optical system has a total axial length of 11.5 mm. Ray-tracing simulations performed in Zemax OpticStudio confirm near diffraction-limited performance across the full FoV. The spot diagrams indicate a root mean square (RMS) spot radius ranging from 1.3 to 2.6 µm, which is suitable for surface imaging and metrology applications.

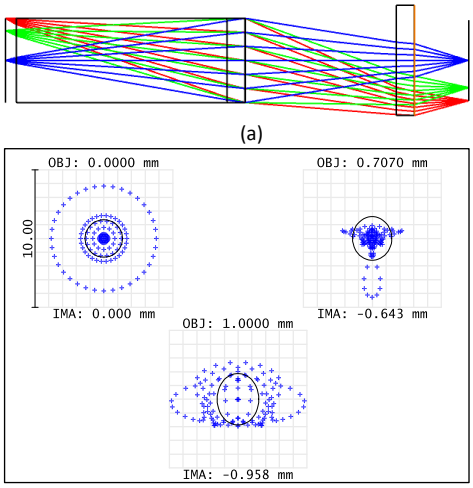

Figure 1. Metalens doublet design: (a) optical layout, (b) spot diagram.

3. Fabrication and Characterisation

The metalenses were fabricated using electron-beam lithography and dry etching. The nanopillars were etched to a depth of 750 nm into a 4.5 µm-thick GaN layer grown on an Al_2O_3 substrate with a thickness of 430 ± 25 µm. For ease of manufacture the pillars are restricted to a set with radii ranging from 70 nm to 180 nm in 10 nm increments [3].

A 50× microscopy setup was constructed to characterise the focal spots of the metalens doublet by scanning along the optical axis. Figure 2 shows the cross-section beam profiles in the x–z and y–z planes for point sources positioned at different field locations (0 mm and 1 mm). The measured maximum full width at half maximum (FWHM) is less than 4 µm, demonstrating the good focusing performance of the metalens doublet.

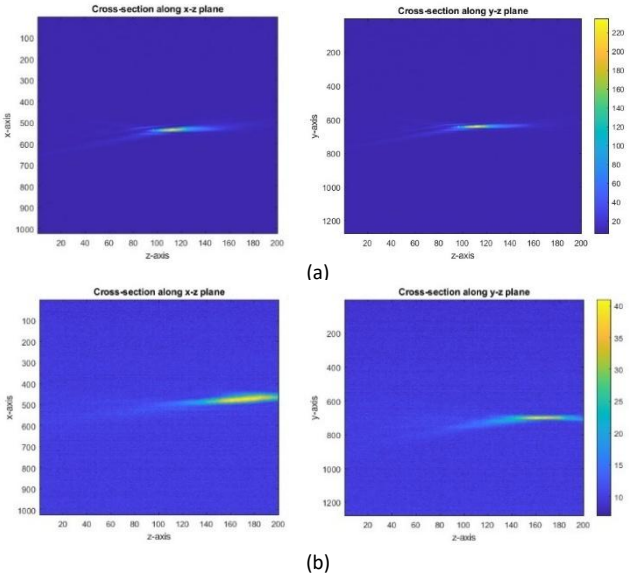

Figure 2. Cross-section beam profiles: (a) on-axis field position (0 mm); (b) off-axis field position (1 mm).

4. Metalens-based phase shifting interferometer and results

A compact metasurface-based phase-shifting interferometric module was constructed using the fabricated metalens doublet, together with a reference mirror bonded to a 5 mm beamsplitter using optical adhesive. The resulting interferometer module has an optical footprint of just 6.25 mm × 9.5 mm × 5 mm. An experimental setup was constructed in which the module was illuminated with a 660 nm light source (Figure 3(a)). Phase shifting was achieved by translating the sample in four discrete steps, each corresponding to λ/8 [4]. A calibrated standard sample with a 43.7 nm step height was measured, and the resulting interference fringes were captured using a 10× microscope system to magnify the surface features. The measured mean step height of 43.11 nm (Figure 3(b)) closely matched those obtained using a commercial white-light interferometer.

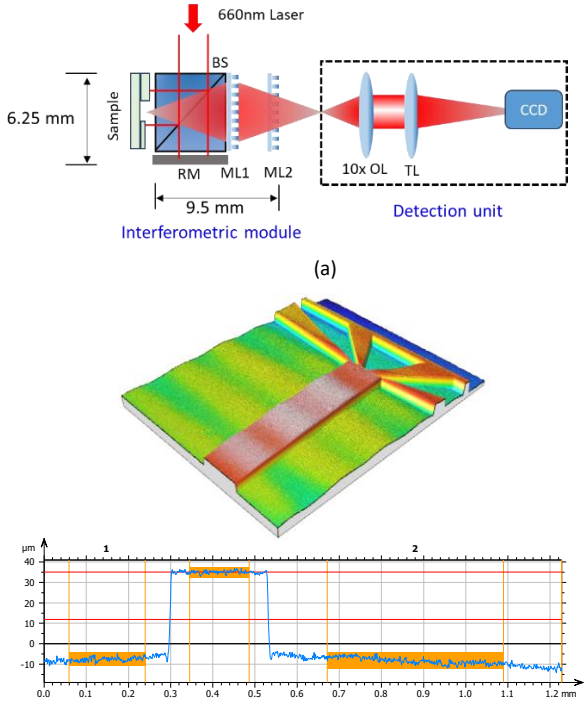

Figure 3. Demonstration of Metalens-based phase shifting interferometer: (a) schematic of the experimental setup; (b) reconstructed surface topography and extracted line profile.

5. Conclusion and future work

This work demonstrates the design, fabrication, and experimental validation of a GaN-based metalens doublet and its implementation for ultra-compact interferometric surface metrology, establishing metasurface optics as a viable platform for compact, mechanically robust, and integration-ready metrology systems. Future work will focus on the development of mechanically free phase-shifting approaches for metalens-based interferometry, as well as long-term stability testing under manufacturing environments.

Acknowledgements

The authors gratefully acknowledge the UK's Engineering and Physical Sciences Research Council (EPSRC) funded programme EP/T02643X/1, EPSRC Future Advanced Metrology Hub for Sustainable Manufacturing EP/Z53285X/1, and the UK's Royal Academy of Engineering and Renishaw PLC who sponsor Xiangqian Jiang's REng/Renishaw Research Chair.

References

[1] Barbosa C R H, Sousa M C, Almeida M F L, and Calili R F 2022 *Sensors* **22** 6114

[2] Kuznetsov A I, et al. 2024 *ACS photonics* **11** 816-865

[3] Chan J H T, Tang D, Williamson J, Martin H, Henning A J, and Jiang X 2023 *CIRP Annals* **72** 465-468

[4] Quan C, Wang S H, and Tay C J 2006 *Precis. Eng.* **30** 23-31

euspen's 26th International Conference & Exhibition, Krakow, PL, June 2026
www.euspen.eu

Modeling of coordinate measurement uncertainty using an expert system with machine learning elements

Danuta Owczarek[1], Łukasz Wilk[1], Wiktor Harmatys[1], Michał Jedynak[1], Piotr Gąska[2], Maciej Gruza[1], Konrad Kobiela[1], Karol Stroński[1], Katarzyna Składanowska[1], Izabela Sanetra[1], Marek Markiewicz[1]

[1]*Laboratory od Coordinate Metrology, Faculty of Mechanical Engineering, Cracow University of Technology, al. Jana Pawła II 37, Krakow, Poland*
[2]*Faculty of Mechanical Engineering and Robotics, AGH University of Krakow, al. Mickiewicza 30, Krakow, Poland*

danuta.owczarek@pk.edu.pl

Abstract
The estimation of coordinate measurement uncertainty is a fundamental and necessary task when assessing product conformity with specifications using coordinate metrology. Existing methods for uncertainty estimation in industrial environments are widely regarded as complex and time-consuming. This paper presents a novel tool currently under development at the Laboratory of Coordinate Metrology at Cracow University of Technology, aimed at rapid estimation of coordinate measurement uncertainty based on prior knowledge of the measurement task—without the need for conducting a real measurement.
For the first time, the conventional sequence of uncertainty estimation is reversed. Instead of estimating uncertainty during or after measurement, this approach enables users to predict measurement uncertainty beforehand. This capability is particularly valuable in scenarios where traditional uncertainty estimation is infeasible—for example, due to limited access to measuring machines or when the object exists only in the design phase.
Predicting uncertainty during the measurement task design phase shortens procurement processes for coordinate measuring machines (CMMs), supports simulation of measurement strategies for hard-to-access parts, facilitates efficient production line design, and enables optimal selection of measurement equipment for specific applications.
The paper includes metrological investigations carried out with modern multisensor CMMs, statistical analyses, and programming efforts focused on developing an expert system-based application enhanced with machine learning techniques. A key component of the application is a valuable computational module that utilizes information on the quality of fit of measurement tasks. The study also includes method testing, validation, and verification. The study concludes with a set of findings and outlines future research directions aimed at improving product safety. By making uncertainty estimation more accessible and applicable in practice, the presented method can help reduce the risk of incorrect conformity declarations.

Uncertainty estimation, Coordinate Measuring Machine (CMM), expert system, machine learning, multisensor system

1. Introduction

Uncertainty estimation is a key issue in assessing product conformity with specifications; however, the methods currently used in industrial practice are widely regarded as time-consuming and complex. As a result, machine operators may incorrectly adopt the machine's Maximum Permissible Error (MPE) as the measurement uncertainty, which may lead to unsafe decisions and erroneous conformity assessments. Consequently, the development of fast and simple methods for measurement uncertainty estimation has become a significant challenge. In practice, laboratories mainly use standardized methods for uncertainty estimation. The most commonly used approach is the comparative method described in ISO 15530-3:2011 [1], which is based on repeated measurements of a calibrated standard similar in size and shape to the measured object, or the multi-position method [2], which involves measuring the object in different locations and orientations. Although these methods provide a high level of accuracy, they are time-consuming and require complex measurement procedures as well as a wide range of reference standards.

Trends driven by Industry 4.0 and 5.0 have led to growing interest in simulation-based methods [3]. Numerous studies have focused on the development of virtual machines [4,5], which significantly accelerate the process of measurement accuracy assessment. A widely adopted approach is the Monte Carlo simulation method [6,7], which enables uncertainty estimation through statistical analysis of simulation results.

However, existing approaches are mainly focused on simulating errors in the machine space, whereas the concept presented in this paper adopts a more parametric approach, based on information about the measurement task and dedicated databases. This paper presents the concept of a new tool for fast and simple estimation of coordinate measurement uncertainty. The work is discussed with particular emphasis on the data acquisition stage, and includes results from both an exemplary measurement and the developed model, followed by a summary and an outline of future development directions for the proposed tool.

2. Methods and equipment

The key component of the developed tool is a model based on machine learning methods and archival data, which enables the prediction of measurement uncertainty for measurement tasks prior to performing the actual measurement. The process of data collection for training the model is an important and time-consuming stage of the work (Fig. 1). The data must be acquired in accordance with the standards of an accredited laboratory

and following good metrological practice. Data are obtained from multi-sensor coordinate machines, such as the Zeiss O-Inspect or the Romer Absolute Arm 7320RI. Measurements are performed under varying conditions of the measurement task, by changing individual elements of the task, e.g., the object, the measured feature, the method of uncertainty estimation, or the standard (input data – **x**), so that the influence of each component on the measurement uncertainty (output data – **y**) can be examined. The databases are supplemented with data from archival tests, with reduced weighting applied to account for potential discrepancies arising over time, even when ostensibly identical measurement strategies were used.

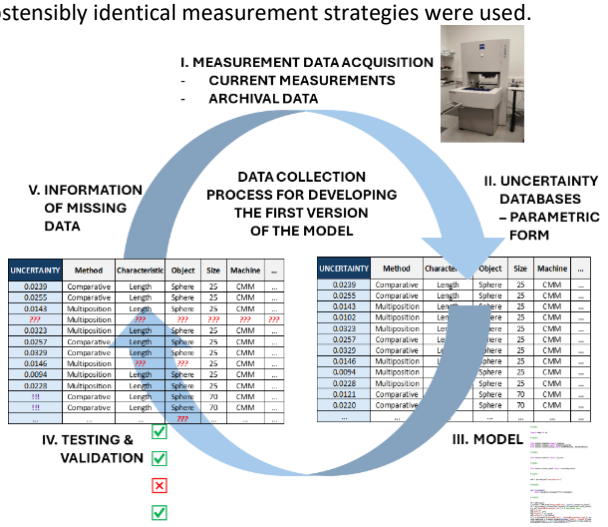

Figure 1. Data acquisition process scheme

The application code was developed in Python. The Pandas library was used for data loading, processing, and analysis, while regression models were implemented using the Scikit-Learn library. Regression for the current dataset provides satisfactory results; however, in cases where a decrease in prediction quality is observed, modifications to the model are allowed. Records corresponding to the same measurement tasks are considered collectively during model building and training. When different uncertainty values occur under identical measurement conditions, their root mean square is taken as the representative value. This approach helps to minimize the impact of random deviations and increases the reliability of the predicted uncertainty.

3. Results

As an example of the acquired data, the results of ring measurements performed on the ZEISS O-Inspect multisensor measuring system are presented. The Maximum Permissible Error MPE(E0) = 0.0019 + 0.004 · L/1000 mm for tactile and 0.0022 + 0.004 · L/1000 mm for optical measurements.

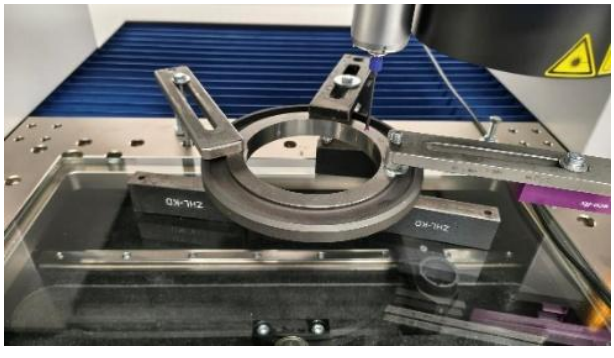

Figure 2. Ring measurement on the Zeiss O-Inspect system

Table 1 Corrected calibration results with expanded uncertainty U for ring measurement, mm

Tactile	Diameter_Circle			Diameter _Cylinder
	_Bottom	_Middle	_Top	
Result	99.99689	99.99710	99.99706	99.99699
U	0.00028	0.00121	0.00371	0.00092
Optical	Diameter_CIR_OPT_8		Diameter_CIR_OPT_3x8	
Result	99.99769		99.99757	
U	0.00030		0.00037	

Uncertainty prediction is performed using linear regression. The data are transformed according to the following scheme: categorical data are encoded using one-hot encoding, while for columns with numerical data, additional columns containing nonlinear transformations of the original features are added to capture potential nonlinear relationships. Based on the first data sample, a coefficient of determination R^2 of 0.92154 was obtained, which is considered a high-quality fit in practice. This allows the project to proceed with the inclusion of additional rows representing various data combinations, the addition of columns with new parameters, and further work on model refinement.

4. Summary

The initial version of the developed tool has been successfully validated, as described in [8]; however, a full evaluation of the model will be conducted after the database is expanded with additional measurement records. Model testing will include an assessment of the recommendation rankings from both practical and technical perspectives. The system will then be enhanced with expert-based recommendations regarding task similarities – this is crucial for predicting uncertainty for tasks lacking training data. Users will be informed when recommendations are based on partially mismatched tasks, with several scenarios planned, including the option to calculate a weighted average from the best results. A key challenge is not only developing a model with high predictive performance but also ensuring its proper adaptation to market realities and the actual needs of potential users, for example in terms of minimizing measurement uncertainty or supporting the selection of optimal measurement conditions and strategies.

Acknowledgements

This study was supported by the National Center for Research and Development, Poland, under the LIDER program (grant no. LIDER15/0306/2024).

References

[1] ISO 15530-3:2011 GPS CMM Use of calibrated workpieces or measurement standards

[2] ISO/TS 15530-2 (draft) GPS CMM Use of multiple workpiece orientations and calibrated simple standards

[3] Gąska A, Sładek J and Gąska P 2020 In: Proceedings of 5th International Conference on the Industry 4.0 Wang L, Majstorovic V, Mourtzis D, Carpanzano E, Moroni G and Galantucci L (eds) Springer, Cham, 92–104

[4] Rost K Wendt K and Härtig F 2016 *Precis. Eng.* **44** 220-230

[5] Stojadinovic S M, Majstorovic V M, Durakbasa N M and Stanic D 2022 *Meas.: Sens.* **22** 100372

[6] Xia H, Ding Y, Chen W, Zhang J, Li H, Zhao H and Song R 2026 *Meas.* **258A** 119031

[7] Garg N, Yadav S and Aswal D K 2019 *Mapan - J. Metrol. Soc. I.* **34** 299–304

[8] Owczarek D 2017 Uncertainty Model in Optical Coordinate Measurement, *Monograph Cracow University of Technology*

euspen's 26th International Conference & Exhibition, Krakow, PL, June 2026
www.euspen.eu

Analysis of measurement uncertainty contributions of optical sensors for the development of digital-metrological twins in coordinate metrology

Daniel Heißelmann[1], Lea-Jean Frömel[1], Katharina Janzen[1], Wiktor Harmatys[2], Adam Gąska[2], Ulrich Neuschaefer-Rube[1]

[1]*Physikalisch-Technische Bundesanstalt (PTB), Coordinate Metrology Department, Braunschweig, Germany*
[2]*Cracow University of Technology, Mechanical Dep. Laboratory of Coordinate Metrology M10, Krakow, Poland*

daniel.heisselmann@ptb.de

Abstract
To assess the measurement uncertainty of coordinate measuring machine (CMM) measurements, simulation techniques following e. g GUM Supplement 1, such as the Virtual Coordinate Measuring Machine (VCMM) are increasingly important. Particularly for measurement tasks in advanced manufacturing employing optical probing systems on prismatic parts and freeform geometries, measurement uncertainty evaluation by Digital-Metrological Twins (D-MTs) provide great benefits. However, mathematical-physical models are neither widely available nor economically usable, yet. We will present a strategy to systematically study the uncertainty contributions of different optical point sensors systems commonly used on CMM. Furthermore, results of the investigation of influencing parameters, such as the distance to the probed surface, the light incident angles, the point density, and the measuring speed conducted on measurement standards of different surface properties are presented. The reported results are suited to derive D-MT models for the determination of task-specific measurement uncertainty in industrial quality control for the selected sensor's measurement principles

Digital-Metrological Twins, Virtual Coordinate Measuring Machine, Optical Sensor Systems, Coordinate Metrology, Measurement Uncertainty, Advanced Manufacturing

1. Introduction

Modern production of industrial parts spans a wide variety of designs tailored to the need of specific applications, such as automotive engineering, aerospace, healthcare, or energy generation. Therefore, a variety of geometrical shapes, materials and advanced manufacturing techniques are incorporated. This paradigm shift in manufacturing poses a challenge to the quality assurance processes in production metrology and demands metrological methods for the measurements of complex workpieces comprising freeform geometries, such as blades, blisks, medical implants or aspheric moulds [1].

Coordinate measuring systems are a crucial pillar of industrial quality control. They are versatile instruments to measure three-dimensional geometries enabling users to assess the outcome of the production process of almost any part in a wide size range. Particularly, coordinate measuring machines (CMM) allow for high accuracy measurements as required for the evaluation of very tight design tolerances. While tactile measurement techniques have been used for a long time, recent advances in sensor technology and the availability of different commercial optical probing system as part of modern multi-sensor coordinate measuring machines allow for fast, contactless and holistic capturing of the outer geometries of complex parts [2]. The determination of the task-specific measurement uncertainty is crucial in all use cases, and as a consequence of increasing level of complexity of the measurement tasks, the available methods need to be expanded to provide trustworthy and reliable measurement results.

While the Guide to the expression of uncertainty in measurement [3] focusses on measurement uncertainty determination by either statistical analysis of repeated measurements (Type A) or analytical calculations (Type B), its Supplement 1 [4] describes the measurement uncertatinty evaluation by use of Monte Carlo simulations (MCS). In the past decades the latter method has gained more and more importance and is applied to tactile measurements of prismatic geometries by the so-called virtual coordinate measuring machine (VCMM) [5, 6]. The VCMM is a digital-metrological twin (D-MT) of the CMM, including the measurement device, the measurement process and the influeces of environment and workpiece [7, 8]. It can be used for metrological purposes and calibrations, since all model parameters are determined in a traceable manner, models have been validated, and fulfill the conditions of ISO 15530-4 [9].

There are only a few approaches for applying the MCS to the use of optical probe systems [10, 11], and thus, the existing models of VCMM need to be expanded to cover, e.g., the uncertatinty contribution of the probing systems and the surface-light interaction with the workpiece.

Section 2 gives an overview of commonly used optical probing systems and details the relevant uncertainty contributions. Section 3 outlines the methodology to test the influences of different parameters related to the uncertainty contributors, while section 4 provides exemplary results and the implications for a strategy to model the uncertatinty contributions to be included in MCS. Section 5 summarises the work and gives an outlook to future work.

2. Optical probing systems

While modern coordinate measuring machines can be equipped with a large variety of different optical probing systems, interferometric point sensors, line scanning sensors and chromatic confocal white-light sensors (CCS) are among the most common types. Although all of the above are currently investigated within the European Partnership on Metrology's project 23IND12 ADAM [12], this work exemplarily focusses on the characterisation of CCS. Four different CCS probing systems of two manufacturers were investigated. They were mounted on four different CMMs with different measurement volumes and different kinematic configurations.

2.1. Identification of uncertatinty contributors

Besides typical uncertatinty contributions of the geometric construction and the kinematics of the CMM, the thermal properties of the measured part and the environmental conditions, the probing process is an important contributor to the overall measurement uncertainty.

For coordinate measurements incorporating CCS, five possible uncertainty contributors (see fig. 1) tied to the optical probing system where identified:

(1) the step width S of sampled points,
(2) the measurement speed v,
(3) the surface slope angle α with respect to the incoming light,
(4) the measurement frequency f, and
(5) the vertical distance d to the measured object.

The identified parameters are typically selected and modified depending on the measured feature and can (in many cases) be defined by the user/operator of the CMM using the manufacturer's software. It should be noted, that although all optical probing systems of the CCS type share the same measurement principle, the specific build constrains the specifications for each model individually.

2.2. Parameter selection

The goal of the investigation was to retrieve information about possible uncertainty contributions depending on sensor parameters either constraint by the measurement task or set by the software/the operator of the CMM. To determine the range of values for each parameter, the rated operating conditions provided by the sensor manufacturer were considered. In case no specifications were available, the range of possible settings has been tested experimentally by repeated measurement using different parameters. Consequently, for the latter, the limits were set by the lowest and highest parameter values that still allowed capturing of coordinates by the standard operating software provided by the CMM manufacturer.

3. Test strategy

Using the information gathered about the limits of the available sensors, a common test procedure was derived. The goal of the procedure was to conduct the same investigation for each of the different sensors on different CMMs, laying groundwork for comparison and interpretation of commonalities to enable future modelling.

Once the ranges for all contributors of each of the studied CCS probing systems had been retrieved, parameters for the tests were fixed. Therefore, five levels , labeled *low* (L), *medium low* (ML), *medium* (M), *medium high* (MH), and *high* (H), were chosen and calculated for each of the parameters.

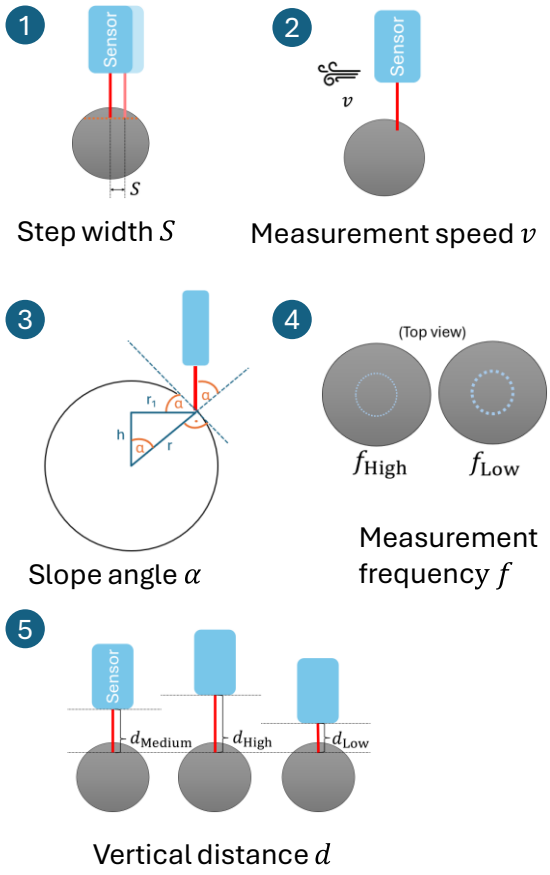

Figure 1. Five measurement uncertainty contributors were identified for investigation.

The selected values were distributed at the fractions of 0.1, 0.3, 0.5, 0.7, and 0.9 of the range specified or determined in experimental studies. For the example of a surface slope angle specified between $\alpha = 0°$ and $\alpha = 40°$ the values for all five levels can be found in table 1. A similar calculation was carried out for each contributor yielding a full set of parameters for the investigation of each CCS.

Table 1 Selected levels for the test of the uncertainty contribution by the slope angle α for a specified range of $\alpha = 0°$ to $\alpha = 40°$.

Level	**Slope angle α**
Low (L)	4°
Medium low (ML)	12°
Medium (M)	20°
Medium high (MH)	28°
High (H)	36°

Using the determined levels, five measurement runs were performed for each of the contributors. In these runs, the other four parameters were kept constant at their medium level, while each level of the tested parameter was set, thus neglecting correlations between the parameters as a first step. Within each of the measurement runs, ten repeated measurements with identical settings were performed.

The selected test strategy was chosen to be generically applicable to other sensors than the CCS as well. It resulted in five sets of five parameter variations each, with five of them being identical, so a total of 21 combination of parameter levels were tested in the study of each CCS probing system available.

In order to separate the general beahviour of the investigated CCS systems from the contribution of the surface properties of

the measured part, all measurements were conducted on four calibrated reference spheres (cf. fig. 2). They were made of ceramics and metal, respectively, and covered a wide range of surface roughness levels.

It should be noted that for the comparability and interpretability of any results obtainted during the measurements, it is of utmost importance to minimise any additional measurement deviations resulting from the probe qualification process and the determination of the workpiece coordinate system (WCS). Thus great care was taken, that the procedures used for these purposes were aligned.

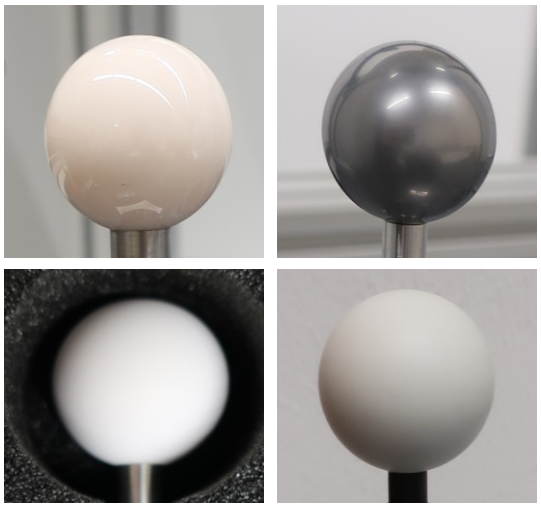

Figure 2. Four different reference spheres were used to test the dependency of parameters on workpiece properties, such as roughness, material, and colour.

4. Results

4.1. Measurement results

By analysis of measurements following the test strategy described in section 3 and using the reference spheres depicted in fig. 2, some commonalities and trends can be extracted.

From the measurement of circle paths on the surface of the reference spheres, the respective deviation to the spheres' calibrated radii were computed.

In a first step, a comparison to tactile measurements of a reference sphere with a polished surface has been carried out. For this purpose, measurement data has been gathered in single point measurement mode and scanning measurement mode for both of the sensor types, i.e., tactile and optical sensors, respectively. An example of the observation can be seen in fig. 3.

The results show both, an offset of the measured radius with respect to the calibrated radius, as well in comparison of the optical measurements to the tactile measurements. In contrast, no signifiact discrepancy between single point measurements and scanning measurements could be observed for any of the two sensors. However, a characteristic directional behaviour of the optical sensor is present for the single point mesasurements and the scanning measurements alike. The curve depicted in fig. 3 is representative for this particular sensor, but may differ in shape amplitude, as well as position of peaks and dips for different sensors.

In addition to the comparison of tactile and optical measurements, the systematic variation of the parameters provides valuable information on the trends in the measurement behaviour of the CCS probing systems.

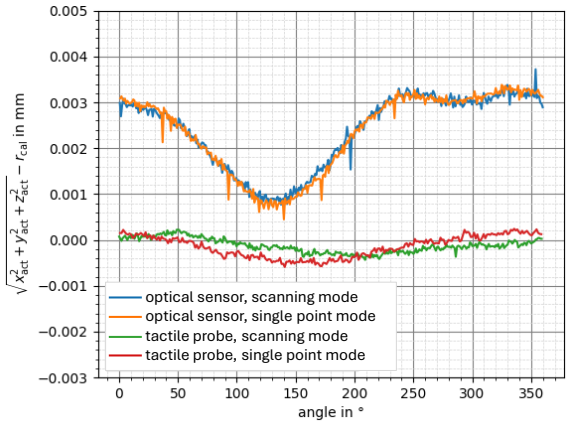

Figure 3. The comparison of the results from tactile and optical measurements show a characteristic directional devitation of the measurement of the optical sensor as well as an overall offset with respect to the calibrated radius.

An example of the results for the parameter *measurement velocity* that has been evaluated for one of the CCS probing systems using all four reference spheres, is displayed in fig. 4.

In this case, for each of the measurements using the same reference sphere (i.e., the same panel of fig. 4) it is clearly visible that the velocity dependence is very weak, if not negligible. Furthermore, an increase in scattering of the deviations can be observed with rising surface roughness of the measured objects (top to bottom panels in fig. 4). Both findings are plausible, while particularly the latter can be expected as a results of local surface variation with respect to the spot sizes of the CCS probing systems, which are typically a few micrometers in diameter.

While some of the parameter variations show clear trends or indicate that they do not influence the measurement results, for other influences this is not the immeditate case. These need more detailed investigations to create a solid base for modelling of the sensor behaviour.

In general, neither an influence of the selected step width nor of the measurement frequency could be observed in the study. For some of the CCS, a variation of the measurement speed showed slight shifts in the characteristic deviation curve of the respective sensor, while maintaining the overall shape of the curve. The attribution of this finding to the sensor or the CMM kinematics is further scrutinized in future work. A clear dependency of the observed radial deviations was visible for the vertical distance of the sensor to the probed surface and the local surface slope angle.

4.2. Implications for modelling

For the modelling of uncertainty contributions it is of great importance that the behaviour of the sensor can either be described by a model equation or by an empirical look-up table characterising the influence on the measured 3D coordinates. In case a model equation can be set up, this is favorable.

Since the metrological conditions of the measurement system may change depending on the measurement settings and strategy, parameters of the model equations have to be determined to enable reliable results. Thus, they have to be described by statistical properties of the realistic parameters, such as their mean value and their probability distribution function.

To enable a wide-spread usability of the D-MT models for the analysis of measurement uncertatinty, traceability to the international system of units (SI) has to be established and users

of D-MTs including the models have to be assisted by suitable strategies to derive parameters and their distribution functions. This can be achieved by measurement plans and evaluation routines tailored to the CCS probing system that are carried out on calibrated measurement standards.

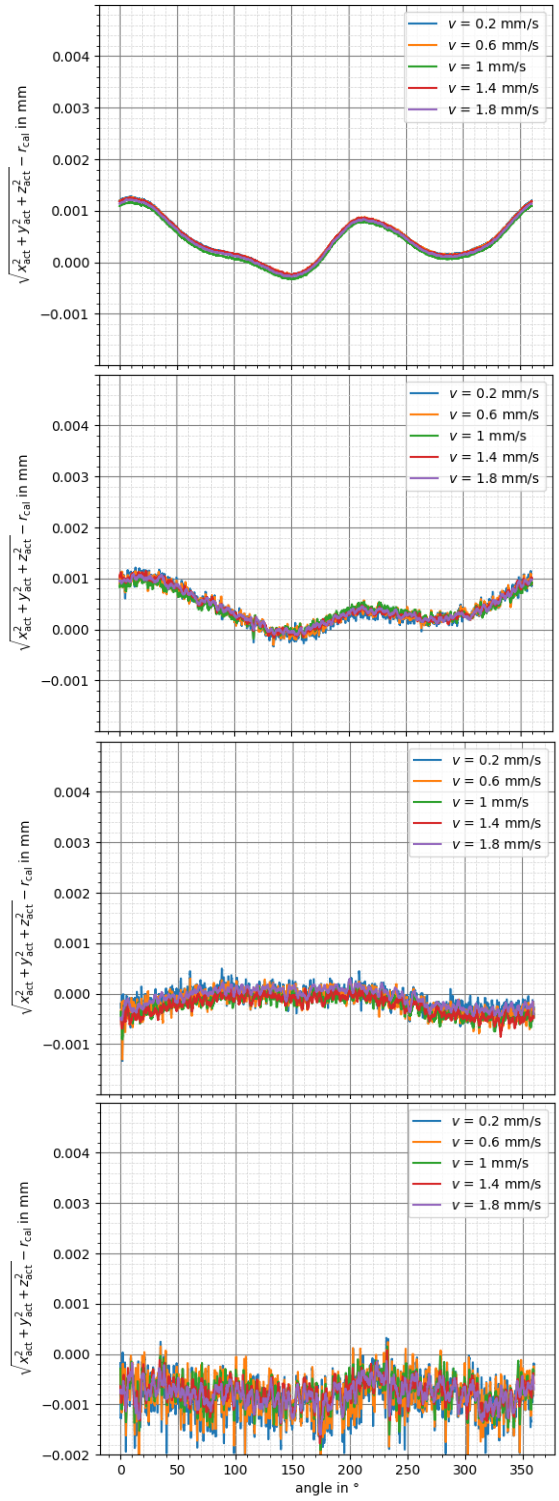

Figure 4. Four different reference spheres have been measurend with settings of five different levels of each parameter. The example of the velocity dependence shows a characteristic deviation behaviour for each object and a clear increase in scatted with increasing surface roughness from top to bottom.

5. Conclusions

In this work, a method has been presented to assess parameters contributing to the measurement uncertatiny of coordinate measurements using chromatic confocal sensors on CMM (cf. section 3). The parameters have been tested within the specified or evaluated limits of their respective parameter range enabling judgements on their respective importance and providing evidence for strategies to derive models to include in D-MTs (see section 3).

While for some parameters, no influence of their variation on the outcomes of the measurements could be observed, in particular, a clear dependency of the observed radial deviations was visible for the vertical distance of the sensor to the probed surface and the local surface slope angle. As presented in section 4, in general, increased scatter of coordinate measurements was present with increased surface roughness of the workpiece. Since not all of the tested parameters showed a clear trend that could be described by a model equation, further investigations will focus on these. Furthermore, it should be noted, that the possible correlations between different uncertainty contributors have to be investigated in future work

The identified influences will be modelled based on the experimental results and are expected to be included in D-MTs such as the VCMM.

Acknowledgments

The project 23IND12 ADAM has received funding from the European Partnership on Metrology, co-financed from the European Union's Horizon Europe Research and Innovation Programme and by the Participating States.

References

[1] European Network for Advanced Manufacturing 2024 Strategic Research Agenda Braunschweig, (EURAMET e.V) ISBN 978-3-942992-85-5

[2] Imkamp D, Berthold J, Heizmann M, Kniel K, Manske E, Peterek M, Schmitt R, Seidler J and Sommer K-D 2016 Challenges and trends in manufacturing measurement technology – the "Industrie 4.0" concept *J. Sens. Sens. Syst.* **5** 325-335

[3] JCGM 100 2008 Evaluation of Measurement Data—Guide to the Expression of Uncertainty in Measurement (International Bureau of Weights and Measures (BIPM))

[4] JCGM 101 2008 Evaluation of Measurement Data—Supplement 1 to the "Guide to the Expression of Uncertainty in Measurement"—Propagation of Distributions Using a Monte Carlo Method (International Bureau of Weights and Measures)

[5] Balsamo A, Di Ciommo M, Mugno R, Rebaglia B, Ricci E and Grella R 1999 Evaluation of CMM Uncertainty Through Monte Carlo Simulations *CIRP Ann.* **48** 425-428

[6] Heißelmann D, Franke M, Rost K, Wendt K, Kistner T and Schwehn C 2018 Determination of measurement uncertainty by Monte Carlo simulation. *In: Advanced Mathematical and Computational Tools in Metrology and Testing XI* (World Scientific, Singapore) 192-202.

[7] Härtig F, Kniel K and Heißelmann D 2023 Das Virtuelle Koordinatenmessgerät—Ein Digitaler Metrologischer Zwilling. *Tm-Tech. Mess.* **90** 548-556

[8] Schmelter S, Fortmeier I and Heißelmann D 2025 Metrology for Virtual Measuring Instruments Illustrated by Three Applications *Metrology* **5** 54

[9] ISO/TS 15530-4:2008 Geometrical Product Specifications (GPS)—Coordinate Measuring Machines (CMM): Technique for Determining the Uncertainty of Measurement—Part 4: Evaluating Task-Specific Measurement Uncertainty Using Simulation

[10] Gąska A, Harmatys W, Gąska P, Gruza M, Gromczak K and Ostrowska K 2017 Virtual CMM-based model for uncertainty estimation of coordinate measurements performed in industrial conditions *Measurement* **98** 361-371

[11] Vlaeyen M, Haitjema H and Dewulf W 2021 Digital twin of an optical measurement system *Sensors* **21** 6638

[12] https://adam.ptb.de 2026 (last accessed 2026-01-12)

euspen's 26th International Conference & Exhibition, Krakow, PL, June 2026
www.euspen.eu

Wafer warpage measurements by stitching lateral shearing interferometry

Seongwook Jang[1] and Ki-Nam Joo[1]

[1]*Department of Photonic Engineering, Chosun University, 309 Pilmun-daero, Dong-gu, Gwangju 61452, South Korea*

knjoo@chosun.ac.kr

Abstract

In this investigation, we describe a wafer warpage measurement system by using a lateral shearing interferometer. The proposed system uses a beam expander to enlarge the beam size and employs two polarization gratings, rotated at 0° and 90° to generate two laterally sheared beams along x- and y- directions. A polarization CMOS camera is used to obtain four phase-shifted interferograms to obtain the wavefront gradient in a single measurement. Then, the wafer warpage is reconstructed using an accumulation-based method. To extend the field of measurement, the stitching technique is adopted, and the proposed system was verified by comparison with measurement results obtained from a Fizeau interferometry.

Wafer warpage measurement, Stitching interferometer, Lateral shearing interferometer

1. Introduction

The wafer size in the semiconductor industry has been increasing for high throughput and productivity. Moreover, 3D stacking technologies have been introduced to confirm multi-functional performance, leading to the fabrication of thinner wafers. However, these structural changes cause the wafer warpage, which induces the alignment errors during semiconductor integration. Subsequently, the wafer warpage alleviates both yield and performance of the devices, and can even result in significant thermal issues. Accordingly, wafer warpage in the entire large surface should be precisely measured. In the conventional large-area surface metrology systems, deflectometry based on the fringe projection [1] and optical interferometry [2] have been used. For the precise measurements, Fizeau interferometry, which offers high stability and reliability, is primarily used, but it is still sensitive to environmental disturbances such as floor vibrations and requires a well-defined reference surface corresponding to the size of the measurement area. On the other hand, shearing interferometry is very attractive to precisely measure the surface figure of a specimen because it does not need a reference mirror. Instead of using the well-defined reference surface, it uses the self-interference by using two spatially sheared wavefronts from the measurement wavefront. Among several shearing interferometers, a lateral shearing interferometer is relatively appropriate for free-form surface measurements because it measures x- and y-gradient maps opposed to other shearing interferometers.

In this investigation, we describe a wafer warpage measurement system by using a lateral shearing interferometer. By using a polarization grating, a very simple lateral shearing unit is configured, and its common path characteristic avoids the use of a spatial coherent light source [3]. Two laterally-shifted beams are parallel to each other, which makes the interference fringes null in the polarization pixelated camera to instantaneously obtain the surface gradient maps. Based on x- and y-directional surface gradient maps, the surface figures of wafers are reconstructed. To reduce the system size and cost, the stitching interferometric principle is adopted.

2. Lateral shearing interferometric module

Figure 1(a) shows the lateral shearing interferometric module, which consists of a polarization grating (PG), a flat mirror (M) and a polarization CMOS camera (PCMOS), with the polarization multiplexing technique [3]. As one of a variety of geometric phase components, the PG enables a circular polarization-dependent diffraction grating, and the beam incident to the PG is diffracted, which is dependent on the polarization status of the incident beam. When a beam with a linear polarization, which can be decomposed into the sum of a right-handed circular polarization and a left-handed circular polarization, is incident to the PG, two diffracted beams are generated of $\pm 1^{st}$ order and propagated with an angle of $\pm\theta$, respectively. In addition, the PG generates phase retardation as a half-wave plate.

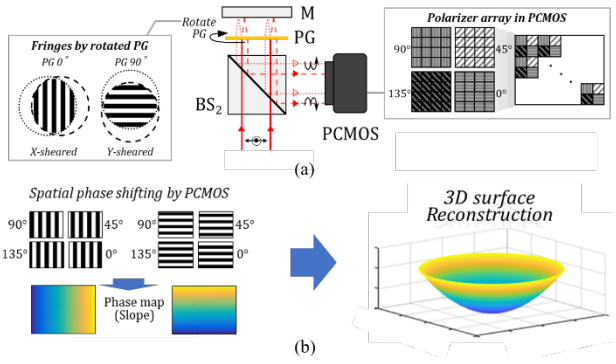

Figure 1. (a) Lateral shearing interferometric module using a polarization grating and (b) wavefront reconstruction; PG, polarization grating; BS, beam splitter; M, flat mirror; PCMOS, polarization CMOS camera.

In the module, therefore, the incident beam is split into two beams by the PG, and the returning beams are laterally shifted after reflecting off the M and passing through the PG again. These two beams are not only laterally shifted, but also their

polarization states are orthogonal to each other as circular polarizations. Then, the PCMOS, where a polarizer array with 0°, 45°, 90° and 135° transmission axes is put on the imaging sensor, can obtain four phase-shifted interferograms at once to calculate the phase map based on the spatial phase shifting technique. With a single image obtained by the PCMOS, the proposed module can obtain the phase map corresponding to the x-sheared interferogram, and the other phase map can be calculated from the other single image obtained by the 90° rotation of the PG. These two phase maps indicate the slopes or gradients of the wavefront along x- and y-directions. Then, the original wavefront corresponding to the surface of the specimen can be reconstructed via the wavefront reconstruction algorithms as shown in Fig. 1(b).

3. Wafer warpage measurements by using a lateral shearing interferometer

Figure 2 shows the optical configuration for wafer warpage measurements. As light source, a LED is used, and the beam size is expanded by using a beam expander (BE). The reflected beam from a wafer is incident to lateral shearing interferometric module to obtain x- and y-directional gradient map. In the interferometer, two beam shutters are used for the acquisition of x- and y-sheared interferograms individually.

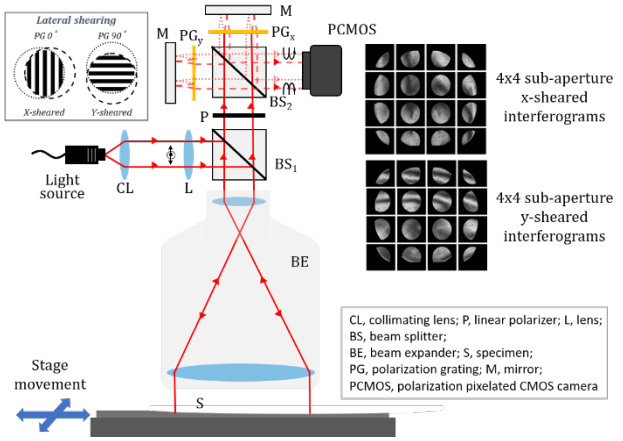

Figure 2. Wafer warpage measurements by using a lateral shearing interferometer.

After obtaining x- and y-directional gradient maps, an accumulative integration technique is used for efficient and rapid calculation of the surface reconstruction. It is based on zonal method proposed by Saunders [4], but it is an expanded version for 2D wavefront reconstruction without minimizing least-squares. Even though the lateral resolution of the surface reconstructed by the accumulative integration technique is relatively low, it is sufficient to evaluate the warpage of a wafer. Furthermore, for the entire surface measurement of a silicon wafer, a stitching method of the sub-aperture measurement results is introduced to the measurement system by using a motorized stage as shown in Fig. 2, and 6 DOF parameters including the lateral positioning errors and the rotational error are considered in the stitching process based the XY stage position measurement results.

To validate the feasibility of the proposed lateral shearing interferometer, we preliminary measured a concave mirror surface, and it was confirmed that the radius of curvature of the reconstructed surface agreed with the designed value within a 2% error margin. By incorporating a beam expander and replacing an imaging telecentric lens, then, we enlarged the effective aperture size as 140 mm such that the system can measure the full area of silicon wafers by using the stitching technique. Figure 3(c) shows the entire wafer warpage measurements results by using 4x4 sub-aperture x- and y-directional gradient maps as shown in Figs. 3(a) and 3(b). As shown in Fig. 3(c), the wafer was bent as 13.2 µm as a peak-and-valley (PV) value, and the validity of the measurement was confirmed by comparing the reconstructed wafer warpages after rotating the wafer by 90° as shown in Fig. 3(d). The measurement repeatability as defined by the mean value of the standard deviation for 10 consecutive surface measurement results was calculated to be on the order of 10 nm. For more rigorous verification of measurement capability, comparative measurements with a 3-inch flat mirror were implemented with a commercialized Fizeau interferometer from Zygo Corp. As a result, the deviation was less than 0.4 µm, attributed to the difference between two measurement procedures and experimental conditions although both of the reconstructed surface profiles were similar to each other.

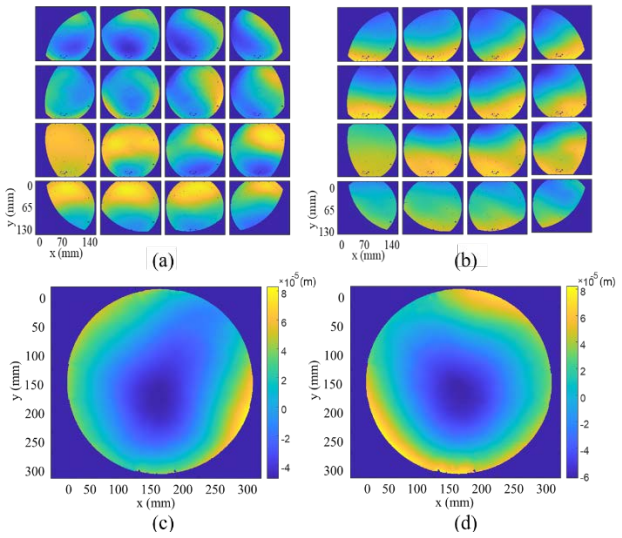

Figure 3. 4x4 sub-aperture measurement results of (a) x-sheared and (b) y-sheared gradient maps, (c) reconstructed wafer warpage measurement result and (d) reconstructed wafer warpage measurement when the specimen was rotated with 90°.

4. Conclusion

To summarize, we proposed and experimentally verified a stitching lateral shearing interferometer based on a polarization grating in this investigation. By the polarization nature of the system, a polarization CMOS camera can directly obtain the surface gradient map with two orthogonally polarized wavefronts. In the experiments, silicon wafers with 300 nm diameter was measured, and the errors of the proposed interferometer were discussed. It is expected that the proposed interferometer can be a good alternative to measure the wafer warpage for the large area when the remaining system errors are minimized..

References

[1] Huang L, Idir M, Zuo C and Asundi A 2018 Review of phase measuring deflectometry *Opt. Lasers Eng.* **107** 247-257

[2] Ma Z, Chen L, Ma J, Zheng D, Zhang Z and Liu Y 2024 Absolute tests of three flats for interferometer with 800 mm aperture *Opt. Express* **32** 3779-92

[3] Jeong H B, Park H M, Ghim Y S and Joo, K -N 2022 Flexible lateral shearing interferometry based on polarization gratings for surface figure metrology *Opt. Lasers Eng.* **154** 107020

[4] Saunders J B 1961 Wavefront reconstruction for interferometry *J. Opt. Soc. Am.* **51** 210-213

euspen's 26th International Conference & Exhibition, Krakow, PL, June 2026
www.euspen.eu

Lateral resolution enhancement of white light scanning interferometer

Min Seo Cho[1] and Ki-Nam Joo[1]

[1]*Department of Photonic engineering, Chosun University, Gwangju, Republic of Korea*

Corresponding Author: Knjoo@chosun.ac.kr

Abstract
Recently, semiconductor manufacturing technologies have been developed to achieve high integration in semiconductor processes. Various 3D surface measurement optical instruments are currently used in the industry, and structured illumination microscopy can reconstruct high resolution 2D surface of the specimen through the phase shifting of the pattern. Also, white light scanning interferometry can reconstruct the 3D surface of the specimen through scanning of the specimen by interference signal. In this investigation, we propose high resolution white light scanning interferometry which merges structured illumination microscopy and white light scanning interferometry.

Structured illumination microscopy, White light scanning interferometry, Structured illumination white-light scanning interferometry

1. Introduction

Recently, various semiconductor manufacturing technologies such as miniaturization and multi-chip package (MCP) have been developed to achieve high integration in semiconductor processes. In the miniaturization and MCP process of these semiconductors, 3D measurement and inspection technologies are essential elements for improving product performance and process stability. For the purpose, confocal scanning microscopes and interferometric microscopes [1-4] are currently applied to meet the demands required by industries. However, the conventional microscopes have fundamental limitations in obtaining high-resolution images due to the lateral resolution limit by the numerical aperture (NA) of the objective lens, which causes problems in obtaining accurate height values of 3D reconstruction results. In 3D surface profilers, furthermore, the lateral resolution limit is propagated to height measurement capability of the system, and the height measurement precision and accuracy can be significantly alleviated.

Meanwhile, structured illumination microscopy widely used in the biomedical fields can obtain the extended spatial frequency content from the image by applying multiple rotating phase-shifted sinusoidal patterns, and restores a high-resolution image that overcomes the diffraction limit through the entire spatial frequency domain obtained computationally from all images.

In this investigation, we propose high resolution white light scanning interferometry (HR-WLSI) that is a combination of white light scanning interferometry (WLSI) and structured illumination microscopy (SIM), which can overcome the lateral resolution limit through various angle rotation and phase shifting of sinusoidal illumination pattern [5-7]. A digital micromirror device (DMD) is used to generate sinusoidal illumination patterns of various rotation angles, and a Mirau type objective lens is used to acquire interference signals. To experimentally verify the system performance, various step height standard specimens were measured.

2. The principle of lateral resolution enhancement of white light scanning interferometry

2.1 HR-WLSI

Figure 1 shows an optical configuration of HR-WLSI, which is a combination of WLSI and SIM. In HR-WLSI, a DMD was used for generating the sinusoidal pattern for the illumination, of which the pattern was rotated and phase shifted. The illumination pattern generated by DMD passes through the focal lens and objective lens, and it is imaged on the specimen. At this time, the objective lens is a Mirau type objective lens, and an interference fringe is generated through an internal reference mirror and plate beam splitter. After, an image is acquired from a camera through a tube lens.

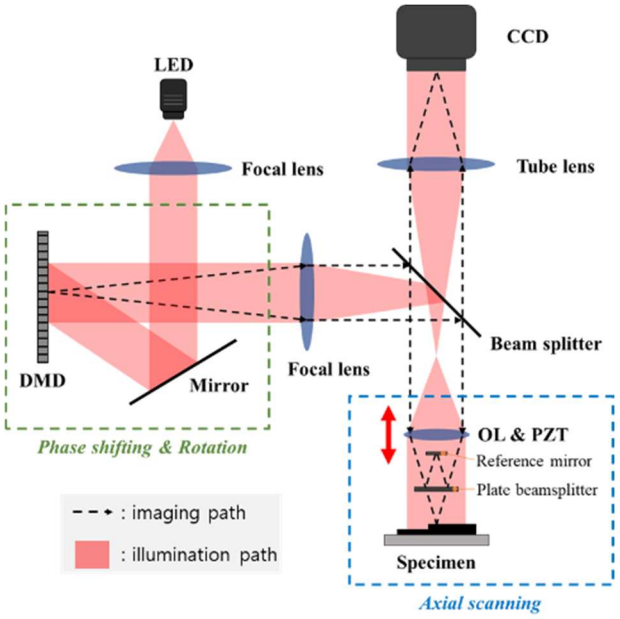

Figure 1. Optical configuration of HR-WLSI

At each axial position, high-resolution image of the generated various angle illumination pattern is obtained using 2D Fourier transform, and an interference signal graph (I) according to the scanning of the specimen is obtained as

$$I = [I_0(1 + Vcos\phi)] \quad (1)$$

where I_0 is the light intensity, V is the envelope of the interference signal, and ϕ is the phase of the interference fringe. A high-resolution 3D image of the specimen is reconstructed by analyzing the interference signal graph (I) obtained through a white light scanning interferometry algorithm [8].

2.2 Lateral resolution enhancement principle

As shown in Fig. 2, lateral resolution can be improved through frequency synthesis of pattern images with phase shifted at various angles. Using phase shifted pattern images at three different rotation angles, three images are obtained for each rotation angle according to the phase shift. Representing these in the spatial frequency domain regions the following

$$\begin{aligned} D_{\theta,\phi_n}(k) = \frac{I_0}{2}[&S(k) \times H(k) \\ &+ \frac{1}{2}e^{-i\phi_n}S(k - k_\theta) \times H(k) \\ &+ \frac{1}{2}e^{i\phi_n}S(k + k_\theta) \times H(k)] \end{aligned} \quad (2)$$

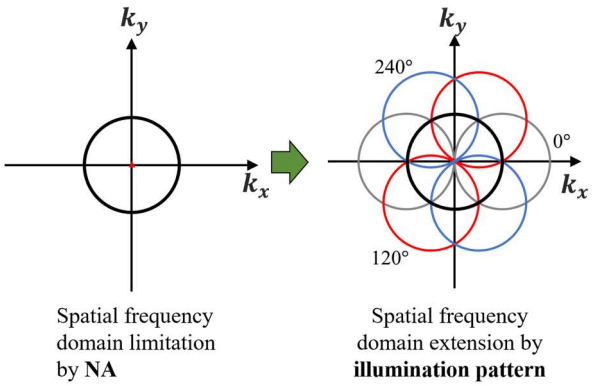

Figure 2. Extended spatial frequency region by SR-SIM

In Eq. (2), D_{θ,ϕ_n} represents the spatial frequency distribution of the phase shifted image at the rotation angle θ of the pattern, and $H(k)$ is the optical transfer function. Additionally, $S(k) \times H(k)$, $S(k - k_\theta) \times H(k)$, $S(k + k_\theta) \times H(k)$ denote the background noise and the spatial frequency distribution of the sample caused by the pattern in the spatial frequency domain. When the illumination pattern is phase-shifted with $\phi_{1,2,3}$=0, 2π/3 and 4π/3, these three components can be separately obtained with the following matrix operation.

$$\begin{bmatrix} S(k) \times H(k) \\ S(k - k_\theta) \times H(k) \\ S(k + k_\theta) \times H(k) \end{bmatrix} = \frac{2}{A}\begin{bmatrix} 2 & e^{-i0} & e^{i0} \\ 2 & e^{-i2\pi/3} & e^{i2\pi/3} \\ 2 & e^{-i4\pi/3} & e^{i4\pi/3} \end{bmatrix}^{-1}\begin{bmatrix} D_{\theta,0}(k) \\ D_{\theta,2\pi/3}(k) \\ D_{\theta,\pi/3}(k) \end{bmatrix} \quad (3)$$

As known in Eq. (3), there are three unknown parameters ($S(k) \times H(k)$, $S(k - k_\theta) \times H(k)$ and $S(k + k_\theta) \times H(k)$) with three phase-shifted measurement results at each rotation angle (ϕ_n) of the sinusoidal pattern, and then they can be calculated. In case of θ=0°, 120° and 240°, therefore, each set of $S(k) \times H(k)$, $S(k - k_\theta) \times H(k)$ and $S(k + k_\theta) \times H(k)$ is also obtained by using Eq. (3), and the extended whole spatial frequency content can be synthesized by the summation of all results with the aid of the Wiener filter to temper the discontinuity in the overlapped region. Subsequently, the synthesized spatial frequency region is broader than the original one limited by the NA of the objective lens as shown in Fig. 2, and the image reconstructed by the spatial frequency synthesis has higher lateral resolution than the original image [9].

3. Simulation results

Before the experiments, we performed simulations using a mosaic-patterned height sample. To replicate real experimental conditions, we generated 300 images containing interference signals and added angle-dependent phase-shifted pattern effects. Additionally, blur effects caused by scanning along the optical axis were incorporated into each image. The interference signals were analyzed using both the proposed method and the conventional WLSI algorithm [8,10] to perform a comparative verification.

The simulation parameters were set to central wavelength of 550 nm, NA of 0.1, magnification of 20x, and scanning step size of 50 nm. Figure 3 presents the reconstruction results and spatial frequency contents obtained using the proposed method compared to conventional WLSI. The expansion of the spatial frequency bandwidth enabled the retrieval of high-frequency components that were previously limited by the NA. Consequently, as demonstrated by the cross-sectional profile in Fig. 4, we confirmed that the period and height of the generated sample were precisely reconstructed.

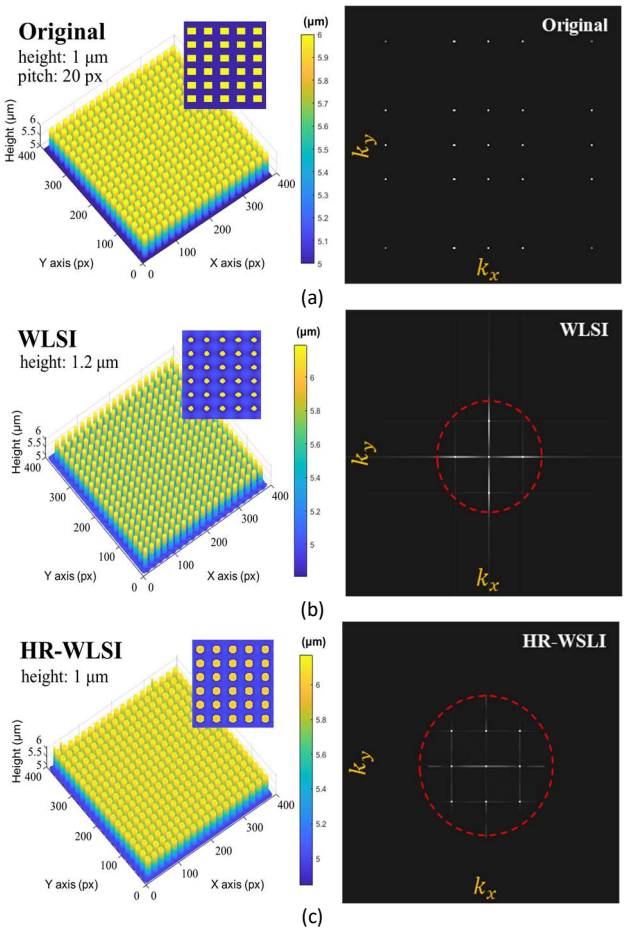

Figure 3. 3D surface profile and its spatial frequency content of (a) original specimen, (b) typical WLSI result and (c) HR-WLSI result

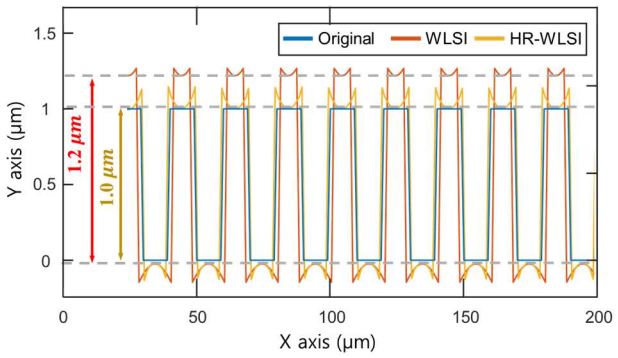

Figure 4. Cross-sectional spatial frequency content of resolution enhanced graph from the simulation of mosaic pattern

4. Experimental results

Based on the simulation results, specimen measurements were implemented. Figure 5 illustrates the measurement results of a defected plane mirror, confirming that scratches clearly appear using the proposed method compared to those by the conventional WLSI because of its better lateral resolution. In this setup, we observed that the spatial frequency region was expanded by a factor of approximately 1.44 as shown in Fig. 6.

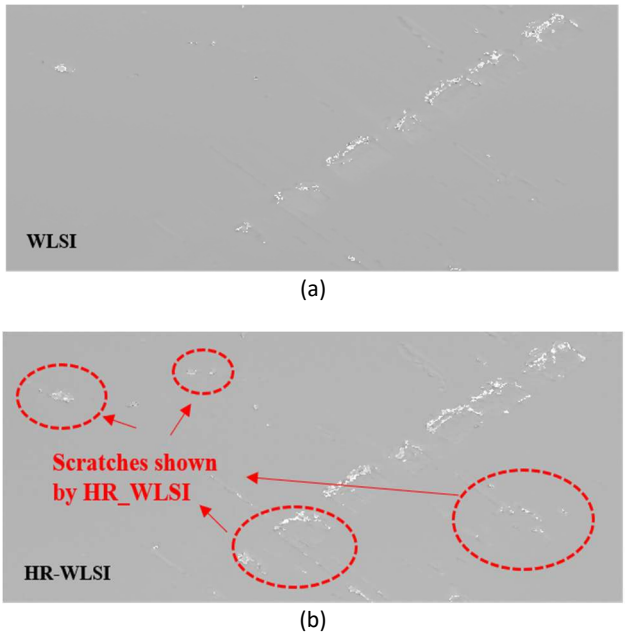

Figure 5. Mirror scratches obtained by (a) typical WLSI and (b) HR-WLSI

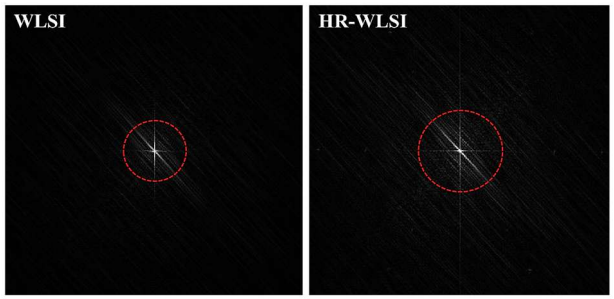

Figure 6. Spatial frequency content of defected plane mirror

Furthermore, as shown in Fig. 7 and Fig. 8, the measurement of a grating sample with a 3 μm pitch and 1 μm height yielded a height of 1.04 μm using the proposed method, whereas the WLSI method resulted in 1.48 μm. This confirms that the specimen height is reconstructed with greater precision due to the enhancement in lateral resolution.

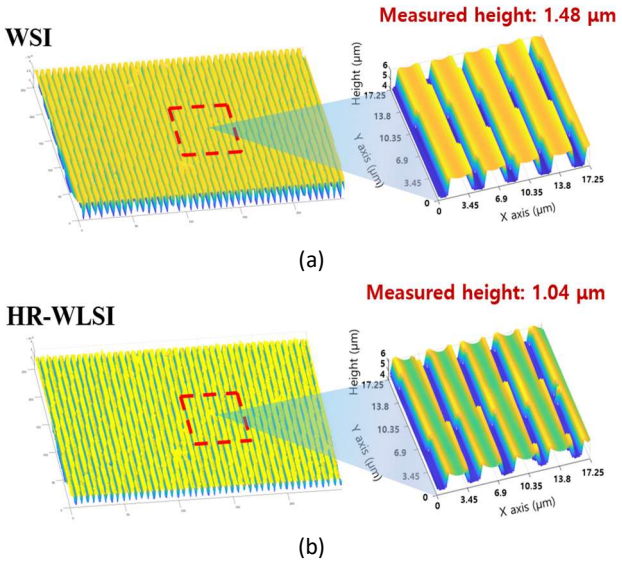

Figure 7. Reconstruction results of grating sample by (a) typical WLSI and (b) HR-WLSI

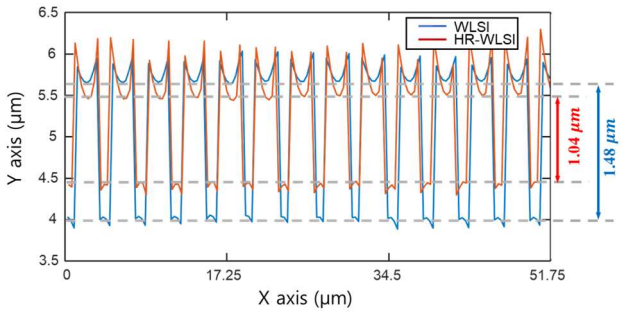

Figure 8. Cross-sectional result of grating sample

5. Conclusion

We demonstrated high resolution white light scanning interferometry by combining the operating principles of SIM and WLSI. In the experiments, the grating specimen was used to confirm the lateral resolution enhancement and 3D measurement capability, respectively. Additionally, we plan to conduct experiments to assess the uncertainty and precision of the results. We believe this combined system can be successfully applied in semiconductor and display industries.

References

[1] Kewei E, Li D, Yang L, Guo G, Li M, Wang X and Xiong Z 2017 Novel method for high accuracy figure measurement of optical flat Opt. Lasers Eng. **88** 162–166
[2] Schwider J and Falkenstoerfer O R 1995 Twyman-Green interferometer for testing microspheres Opt. Eng. **34** 2972-2975
[3] Nicolaus R A 1993 Precise method of determining systematic errors in phase-shifting interferometry on Fizeau interferences Appl. Opt. **32** 6380-6386
[4] Tay C J, Quan C and Shang H M 1998 Shape identification using phase shifting interferometry and liquid-crystal phase modulator Opt. Laser Technol. **30** 545–550
[5] Chen X, Zhong S, Hou Y, Cao R, Wang W, Li D, Dai Q, Kim D and Xi P 2023 Superresolution structured illumination microscopy reconstruction algorithms: a review Light Sci. Appl. **12** 172
[6] Gustafsson M G L 2005 Nonlinear structured-illumination microscopy: wide-field fluorescence imaging with theoretically unlimited resolution Proc. Natl. Acad. Sci. USA **102** 13081-13086

[7] Gustafsson M G L 2000 Surpassing the lateral resolution limit by a factor of two using structured illumination microscopy J. Microsc. **198** 82-87
[8] De Groot P and Deck L 1995 Surface profiling by analysis of white-light interferograms in the spatial frequency domain J. Mod. Opt. **42** 389-401
[9] Shroff S A, Fienup J R and Williams D R 2008 OTF compensation in structured illumination superresolution images Proc. SPIE **7094** 7-17
[10] De Groot P 2015 Principles of interference microscopy for the measurement of surface topography Adv. Opt. Photonics **7** 1-65

euspen's 26th International Conference & Exhibition, Krakow, PL, June 2026
www.euspen.eu

Assembly and evaluation of a spectrometer by using a spectral interferometer

Seoyoon Lee[1] and Ki-Nam Joo[1,#]

[1]*Department of Photonic Engineering, Chosun University, 309 Pilmun-daero, Dong-gu, Gwangju 61452, South Korea*

[#]*Corresponding author: knjoo@chosun.ac.kr*

Abstract
Optical spectrometers require precise optical alignment for reliable performance evaluation. Conventional calibration techniques using emission lamps are limited by discrete spectral lines and low optical power. In this investigation, spectral interferometry is introduced as an optical source for assembling and evaluating an optical spectrometer. The fringe contrast is used for the alignment of optical components, and spectral resolution is determined by the maximum measurable distance of the spectral interferometer. The proposed method provides an efficient tool for both the calibration and performance evaluation of spectrometers.

spectral interferometer, optical spectrometer, alignment tool, performance evaluation

1. Introduction

An optical spectrometer, which typically consists of a slit, a collimating mirror, a diffraction grating, and a focusing mirror, has been essential for material inspection in various fields because of its capability to measure spectral intensity [1]. To achieve the intended spectral range and resolution, most important task is to align and assemble all optical components. Conventional techniques use spectral lines from lamps such as Hg, Ar, and Ne [2], but they provide limited wavelength coverage and low optical power, increasing calibration effort. In this investigation, spectral interferometry is introduced as an alternative light source for spectrometer construction and calibration. Interferometric fringes provide broadband alignment information, and the maximum measurable distance can estimate the spectral resolution of a spectrometer.

2. Method

2.1. Spectral Interferometer

A spectral interferometer uses a broadband light source to generate a spectral interferogram corresponding to the optical path difference (OPD) between a reference arm and a measurement arm. Because the spectral interferogram is generated over a wide spectral range, its contrast can be used for the assembly of a spectrometer. On the other hand, the spectral interferogram becomes denser as the OPD increases and the maximum measurable distance (ΔL_{max}) of the spectral interferometer, which defines the spectral resolution (Δv) as [3]

$$\Delta L_{max} = \frac{c}{4\Delta v} \quad (1)$$

where c is the speed of light. As known in Eq.(1), the resolution of a spectrometer can be determined by ΔL_{max}.

2.2. Assembly and evaluation of an optical spectrometer

When a spectral interferometer is used as a light source for assembling a spectrometer as shown in Fig. 1, it assists spectrometer assembly in two ways. First, the spectral interferometer generates interference fringes across the full bandwidth of the source, enabling alignment without relying on discrete emission lines. The assembly can be optimized by monitoring fringe contrast, where maximum and uniform contrast indicate proper positioning and tilt of optical elements. Unlike conventional calibration using standard lamps, this alignment can be performed across the entire spectrum.

Second, the spectral resolution of the spectrometer can be estimated from the ΔL_{max}. In this case, a well-calibrated spectrometer with higher resolution is used as a reference. As OPD increases, the interferogram is observed simultaneously in both spectrometers until the fringes disappear in the spectrometer under construction. At that point, the resolution can be derived by using Eq.(1) obtained from the reference spectrometer [4].

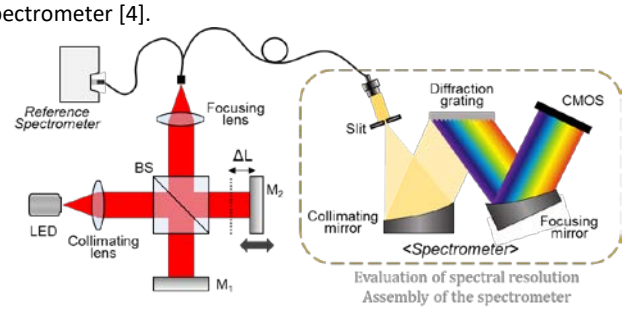

Fig. 1. Assembly and spectral resolution evaluation of the spectrometer using a spectral interferometer.

3. Experimental results

3.1. Alignment of a spectrometer by using a spectral interferometer

Figure 2(a) shows the spectral interferometer configured in this investigation. The light from the LED was delivered by a multi-mode fiber and split by a beam splitter. In the Michelson-type interferometric configuration, one of the mirrors was mounted on a manually translated stage to adjust the OPD. The two reflected beams were recombined, and the spectral interferogram was simultaneously detected by the reference spectrometer and the CMOS camera of the spectrometer under construction. As the reference spectrometer, a commercial high-resolution spectrometer with 0.12 nm resolution in the wavelength range from 350 nm to 800 nm was used, and the spectral interferogram was detected as shown in Fig. 2(b).

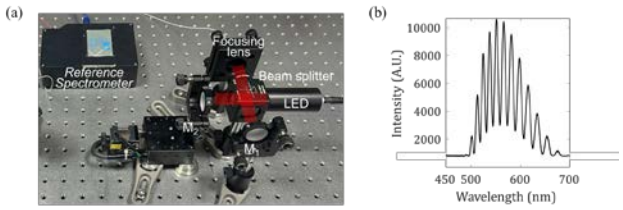

Fig. 2. (a) Photograph of the spectral interferometer setup and (b) its spectral interferogram obtained by the reference spectrometer.

Using the spectral interferogram from the spectral interferometer, the tilt of the CMOS camera of the spectrometer was adjusted using the contrast uniformity of the spectral interferogram. When the CMOS camera was tilted, the spectral interferogram on the camera was changed, and its contrast was also varied. In particular, the contrast uniformity of the spectral interferogram was strongly affected by the angle-deviation from the expected posture. In the experiment, the contrast uniformity of the spectral interferogram was monitored while the CMOS camera was tilted, and the best alignment status was determined as the contrast uniformity of the spectral interferogram was less than 0.07 for the peak-to-valley value as shown in Fig. 3(a).

Then, the position of the CMOS camera was adjusted to detect the spectral interferogram obtained by the reference spectrometer. As shown in Fig. 3(b), the spectral interferogram obtained by the reference spectrometer was clearly observed, and its contrast was approximately 0.6. The contrast of the interferogram obtained by the CMOS camera was varied with detector positions, and the best position was identified as shown in Fig. 3(c) as the contrast was maximum. In this case, the contrast was similar to that of the reference. It is noted that the fringe contrast was calculated from the signal magnitude after removing the upper and the lower envelopes of the spectral interferogram.

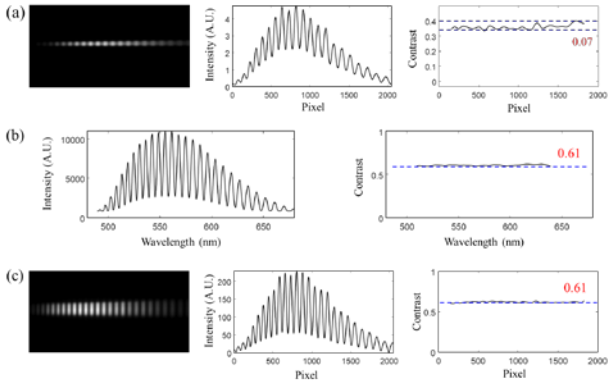

Fig. 3. (a) Spectral interferogram and its contrast with the angle-deviation of 0˚ and (b) Spectral interferogram and its contrast obtained using the reference spectrometer and (c) Spectral interferogram and its contrast with the position deviation of 0 mm.

3.2. Spectral resolution evaluation and wavelength calibration

After the alignment of the spectrometer was completed, its spectral resolution was evaluated using the maximum measurable distance of the spectral interferometer. As the OPD of the spectral interferometer increased, the spectral interferogram became denser in the reference spectrometer as shown in Fig. 4(a), and eventually disappeared in the spectrometer under construction as shown in Fig. 4(b), when the OPD was 52.97 μm. Using Eq.(1), the corresponding spectral width Δν was calculated from the reference spectrometer result and converted into the wavelength.

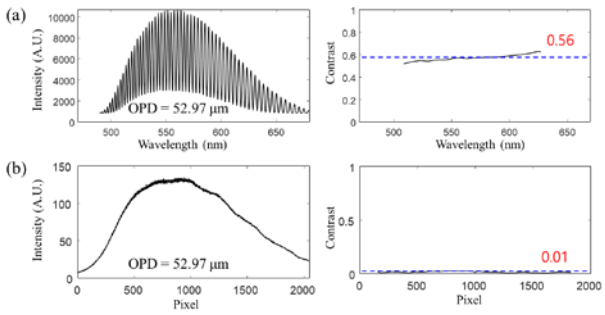

Fig. 4. Spectral interferogram and its contrast obtained by (a) the reference spectrometer and (b) CMOS camera at OPD = 52.97 μm.

The spectral interferometer was also used for the wavelength calibration of the constructed spectrometer. Using the reference spectrometer as a calibration reference, the wavelengths corresponding to the constructive interference peaks in the interferogram were identified. Figures 5(a) and (b) show the spectral interferograms measured by the reference spectrometer and the constructed spectrometer, respectively. Based on the similarity between the two interferograms, peak positions were paired to match pixel indices of the CMOS detector with reference wavelengths. After assigning wavelength values to each constructive interference peak, the full spectrum was calibrated using third-order polynomial curve fitting, as commonly employed in spectrometer calibration. As the result, the fitting residual was 0.3 nm RMSE over the spectral range of 480–650 nm, confirming accurate wavelength reconstruction.

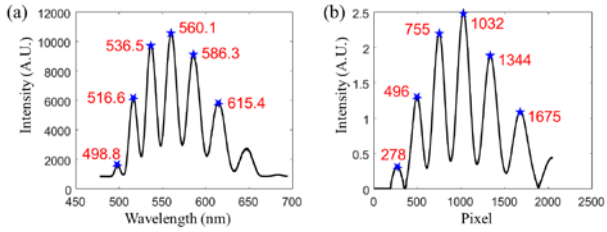

Fig. 5. Spectral interferograms with peak locations obtained by (a) the reference spectrometer and (b) the constructed spectrometer.

4. Conclusion

In this investigation, a spectral interferometer was used as a broadband source to assemble and evaluate an optical spectrometer. Interferometric fringes enabled full-spectrum alignment without standard lamps, while fringe contrast was used to optimize the spectrometer assembly. A spectral interferometry offers a compact and efficient method for spectrometer alignment, calibration, and performance evaluation.

Acknowledgements

It is noted that this conference proceeding is written and modified based on the journal paper [4].

References

[1] Naeem M, Fatima N-u-a, Hussain M, Imran T and Bhatti A S 2022 *Optics* **3** 1–7

[2] Sun Y C, Huang C, Xia G, Jin S Q and Lu H B 2017 *J. Opt. Soc. Am. A* **34** 498–505

[3] Yun Y H, Seo Y B and Joo K N 2016 *Measurement Science and Technology* **27** 035004

[4] Lee S, Seo S I and Joo K N 2025 *Measurement* **256** 118366

euspen's 26th International Conference & Exhibition, Krakow, PL, June 2026
www.euspen.eu

Thermal behavior analysis of a novel measurement system for precise displacement sensors calibration

Luka Čas, Bojan Ačko and Rok Klobučar

University of Maribor, Faculty of Mechanical Engineering, Laboratory for Production Measurement

luka.cas@um.si

Abstract
High-precision displacement sensors, typically inductive, capacitive or incremental, are widely used in dimensional metrology due to their sub-micrometer accuracy. Their increasing use in industrial and laboratory applications has created a clear need for traceable calibration methods. As the national holder of the length standard in Slovenia, the Laboratory for Production Measurement (MIRS/UM-FS/LTM) is responsible for ensuring traceability of length measurements in this field. To meet this need, we have initiated the development of a custom measurement system for calibration of precise displacement sensors up to 150 mm. As part of this development, we investigated the influence of thermal effects on structural deformations and their impact on calibration uncertainty especially, their contribution to geometric errors. Although environmental conditions in precise length measurement are typically controlled using climate chambers, even minor air temperature variations can cause micrometer-level deformations in calibration setups. Due to the lack of direct measurement methods to determine thermal deformations, this study focuses on evaluating their impact using finite element simulations. A CAD model of the mechanical structure was developed and analysed in ANSYS. The structure was exposed to thermal boundary conditions derived from real temperature measurements performed on the actual measurement system setup placed inside a controlled climate chamber. The TEMP 14 sensor system was used to acquire temperature data, using two air sensors and eight material sensors distributed on the structure. Measured air temperature fluctuations were approximated by mathematical functions using the least squares method, which served as boundary inputs in the simulations. Both static and transient thermal simulations were conducted, followed by structural analyses to determine resulting displacements. Results show that thermal stabilization of the structure in simulation occurred after approximately 4 hours, closely matching experimental measurements. The maximum thermal deformation occurred at the tip of the sensor mount and slightly exceeded 17 µm. The resulting displacement field was used to evaluate the change in the sensor's geometric alignment. Although the sensor was assumed to be perfectly aligned initially, thermal expansion introduced a cosine error on the order of $e_{cosT} = 2.5 \cdot 10^{-10} \cdot L$ and caused a maximum axis displacement of approximately 10 µm. These findings form an important part of the ongoing development of a precision calibration system for displacement sensors.

Thermal deformation, Finite element analysis, Calibration, Precise displacement sensors, Length measurement

1. Introduction

High-precision displacement sensors, also known as transducers, are widely used in dimensional metrology due to their ability to measure very small displacements with sub-micrometer accuracy [1]. These sensors, typically contact-type, are commonly employed in advanced manufacturing, precise positioning, laboratory measurements and calibration systems (e.g. gauge block comparators) [2-4].

In recent years, the Slovenian National Laboratory for Length has observed an increasing demand for calibrations of high-precision displacement sensors. To meet this demand and fulfill our responsibility for traceable length measurements in the country, we started developing a novel measurement system for calibrating these sensors.

While the calibration of displacement sensors is relatively straightforward, the main challenge lies in achieving sufficiently low measurement uncertainty. This requires a clear identification and quantification of all error sources that may influence the measurement result, including thermally induced structural deformations.

Temperature variations can have a significant effect on length measurements, as even small changes can induce micrometer-level deformations in the measurement setup. To reduce these effects, most laboratories rely on climate-controlled environments [5, 6] and temperature monitoring using sensors, combined with compensation techniques to correct for thermal expansion. Because such temperature controlled chambers with very high stability can be very expensive, metrology laboratories have increasingly explored alternative approaches for compensating temperature induced measurement errors.

With recent advances in simulation software, finite element analysis (FEA) is increasingly used to predict structural responses to applied loads, particularly in mechanical engineering. Most studies, where FEA were used to assess thermal errors in production engineering have been performed on CNC machines tools [7, 8] and hydraulic presses [9].

Despite its growing adoption, applications in high-precision dimensional metrology remain relatively rare. However, studies that have applied FEA in this field [10, 11] demonstrate its potential to accurately predict thermally and mechanically induced deformations, supporting its use in evaluating calibration uncertainties.

In this study, we investigated how our new system, constructed from commercially available components, behaves under controlled temperature conditions in our climatic chamber. We studied the influence of temperature on structural expansions and the resulting geometric errors of the calibrated sensor. Due to the lack of direct measurement methods to determine these thermal deformations, we focused on evaluating their impact using finite element simulations.

2. Methods

The following methods detail the measurement setup, temperature monitoring and FEA used to assess thermal and structural effects.

2.1. Measurement system setup

The measurement system developed for calibrating high-precision displacement sensors consists of commercially available components assembled into a modular mechanical structure. At its core, the system consists of a displacement-generating mechanism and a modular set of elements forming the platform on which the sensor under calibration is mounted

The entire system is placed within a controlled laboratory chamber, providing active temperature regulation with ±0.1 °C stability and continuous humidity monitoring. Once fully developed, all calibrations will be conducted within this chamber to maintain consistent environmental conditions.

For the analysis, we focused exclusively on the portion of the structure that forms the mount for the sensor under calibration. The displacement-generating mechanism was not included in the simulations, as our primary interest lies in evaluating how thermal effects influence the geometric errors of the sensor itself.

To support the thermal analysis a CAD model of the measurement system was created in SolidWorks. Figure 1 shows the full prototype, with the outlined portion indicating the part of the system included in the analysis.

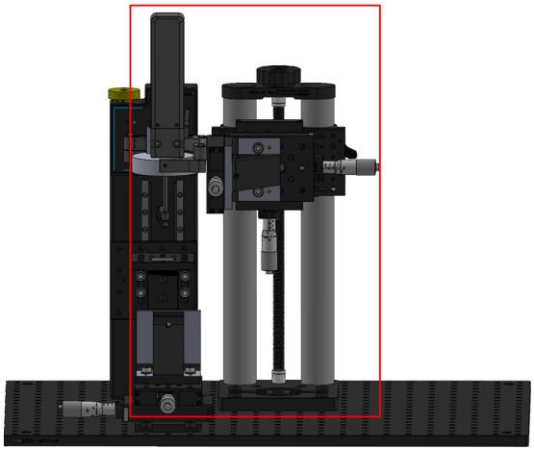

Figure 1. CAD model of the measurement system, showing the section included in simulations

The initial model, composed of six main components, was simplified to optimize meshing and solver efficiency while preserving the key stiffness, mass distribution, and thermal load paths. Components were positioned in their extreme operational configurations to define boundary conditions and ensure relevance for evaluating thermal effects on the sensor. The sensor itself was modelled at its maximum calibration length of 150 mm to capture the worst-case thermal deformation scenario.

2.2. Temperature Monitoring of the Measurement System

To determine the environmental conditions within the chamber, both air and material temperatures of the measurement system were continuously monitored using the TEMP 14 sensor system (JENAer Meßtechnik), which offers high precision with expanded calibration uncertainties of 15 mK for material sensors and 50 mK for air probes. The calibration of the system is traceable to the national temperature standard in Slovenia.

Eight material sensors were distributed across the structure, while two air sensors were placed at opposite ends of the base plate, separated by 0.6 m, to capture the overall temperature field, as shown in Figure 2. These measurements were used to define the boundary conditions for subsequent finite element simulations.

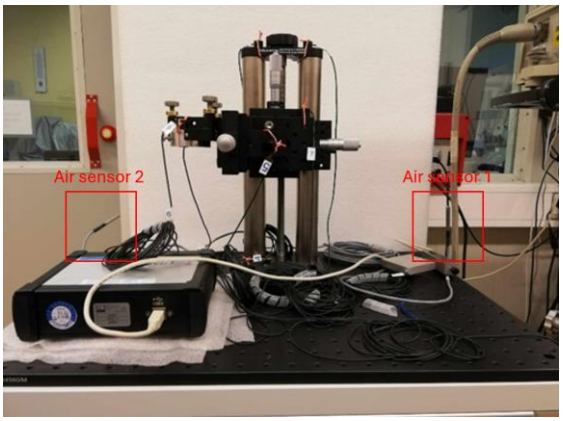

Figure 2. Placement of air and material sensors on the measurement system and monitoring under real chamber conditions.

Measurements began immediately after placing the system in the climatic chamber and continued for almost an entire day.

2.3. Temperature Approximation

To define the boundary conditions for the thermal analysis, the measured air temperature fluctuations in the chamber were approximated using a mathematical model. The measurements at the two air sensor positions along the base plate (T_1 at x = 0 m and T_2 at x = 0.6 m) were fitted to sinusoidal functions using the least squares method. For simplicity, the fluctuations were assumed to be in phase and to share the same frequency.

The general form of the fitted function was:

$$T(t) = A \cdot \sin(\omega t + \Phi) + T_0 \quad (1)$$

where:

- A – amplitude of the sinusoidal variation,
- ω – frequency of the sinusoidal variation,
- ϕ – phase shift of the sinusoidal variation,
- T_0 – mean temperature.

The fitted functions for the two measurement locations were:

$$T_1(t) = 0{,}03673 \cdot \sin(-0{,}005383 \cdot t + 1{,}865) + 19{,}593 \quad (2)$$

$$T_2(t) = 0{,}02935 \cdot \sin(-0{,}005008 \cdot t + 1{,}869) + 19{,}729 \quad (3)$$

Because both measured signals varied in phase and exhibited nearly identical frequency, the expressions were simplified by assuming a common frequency:

$$T_1(t) = 0{,}03673 \cdot \sin(-0{,}005 \cdot t) + 19{,}593 \quad (4)$$

$$T_2(t) = 0{,}02935 \cdot \sin(-0{,}005 \cdot t) + 19{,}729 \quad (5)$$

For the thermal analysis, the air temperature distribution along the length of the system was assumed to vary only in the x-direction, consistent with the sensor placement, while remaining constant in the y-direction due to the limited number of air sensors.

The temperature at any position x along the base plate was obtained by linear interpolation between $T_1(t)$ and $T_2(t)$:

$$T(x,t) = T_1 + (T_2 - T_1) \cdot \left(\frac{x - x_1}{x_2 - x_1}\right) \quad (6)$$

Substituting the simplified expressions yields the final spatial- and time-dependent boundary condition:

$$T(x,t) = 19.593 + 0.03673 \cdot \sin(-0.005 \cdot t) + 0.2275 \cdot x - 0.01231 \cdot x \cdot \sin(-0.005 \cdot t) \quad (7)$$

The resulting spatial and time dependent function was then used as the boundary condition for the subsequent thermal deformation analysis of the sensor, capturing the measured environmental fluctuations in the chamber.

2.4. Simulation setup: materials and meshing

The finite element simulations were carried out in ANSYS using the simplified CAD model described earlier. The structure consists of four materials, with aluminium 6061-T6 as the primary one. Additional components are made from aluminium 7075-T6, AISI 1026 DOM steel and ferritic stainless steel. The model was discretized using ANSYS automatic mesh settings. A medium density mesh was selected after preliminary convergence checks, resulting in approximately 1.5 million nodes.

2.5. Thermal and Structural Analysis

A steady-state thermal analysis was first performed to determine the temperature field within the structure. The analysis assumes time-independent conditions, i.e., the system is in thermal equilibrium. The ambient temperature distribution was defined using a linear approximation obtained from the average readings of two air probes:

$$T(x) = 19.59 + 0.233\,x \quad (8)$$

Convective boundary conditions were applied to all exposed surfaces, while the bottom surface of the base plate was constrained to the measured granite temperature. The initial temperature of the model was set to 20 °C.

Based on the resulting temperature field, a static structural analysis was carried out to evaluate the thermally induced deformations. The temperature distribution from the thermal analysis was imported into the structural model. Gravity was applied as an additional load, and the base plate was fixed at its interface with the granite support.

A time-dependent thermal analysis was performed to evaluate the transient temperature evolution of the structure. The initial temperature of the entire model was set to 24 °C, representing the room temperature prior to cooling. Boundary conditions included the granite base temperature and convection applied to all exposed surfaces. In contrast to the steady-state analysis, the convection boundary was defined using the full temperature function from equation (7), which depends on both position and time. The duration of the simulation was set to 6 hours. This value was chosen based on experimental observations indicating that the system reaches thermal equilibrium after approximately 6 hours inside the climatic chamber, while still keeping the computational effort reasonable.

3. Results

This section presents thermal and structural analysis results, including their impact on sensor alignment, cosine, and Abbe errors.

3.1. Experimental results

The thermal behaviour of the system was evaluated through continuous temperature monitoring inside the climatic chamber. Measurements started immediately after the system was placed in the chamber and were recorded for nearly 24 hours. The structure reached thermal stabilization after approximately 6 hours, with the material sensors recording an average temperature of 19.9 °C and a maximum difference of 0.05 °C. Air temperature measurements showed periodic fluctuations at both ends of the base plate, which varied in phase, with maximum differences of 0.15 °C and 0.12 °C, respectively. The complete time evolution of both material and air temperatures is shown in Figure 3, illustrating the stabilization period and the characteristic behaviour of the air temperature fluctuations.

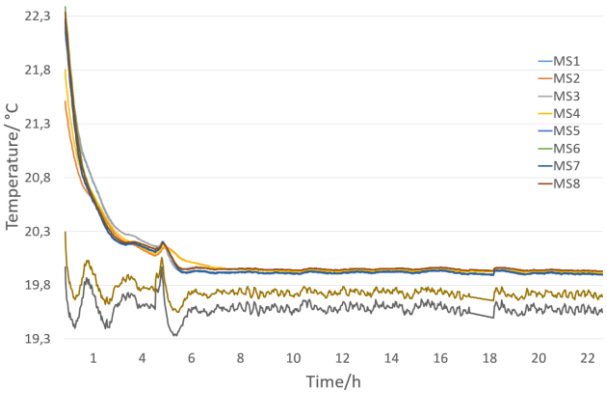

Figure 3. Temperature measurements of air and material sensors over time

3.2. Thermal and Structural Analysis Results

The steady-state thermal simulation provided the equilibrium temperature distribution along the structure. The maximum temperature (19.91 °C) occurred at the base plate in contact with the granite support, while temperatures decreased along the length, reaching a minimum of 19.65 °C at the top. Based on the resulting temperature field, static structural analysis showed maximum displacements of 17 µm at the sensor tip and rotational handle.

Time-dependent thermal simulations captured the evolution of the structure's temperature over 6 hours. The maximum temperature decreased from 24 °C and stabilized after approximately 4 hours, oscillating between 19.64 °C and 19.66 °C, while the minimum temperature remained near 19.91 °C. A summary of the simulation results, together with measured data from the real system, is presented in Table 1.

Table 1 Summary of ANSYS simulation results and measured data

Analysis Type	ANSYS min	ANSYS max	Measured on real system
Steady-state thermal	19.65 °C	19.91 °C	/
Steady-state structural	/	17.3 µm	/
Transient-thermal	19.64 °C	19.66 °C	/
Temp. stabilization	4 h		6 h

3.3. Geometric Errors Analysis

The resulting displacement field was used to evaluate the change in the sensor's geometric alignment. To evaluate the influence of structural deformations on the cosine error of the sensor stylus caused by temperature fluctuations, the ANSYS tip displacement data were post-processed in MATLAB. Two points at the ends of the 150 mm tip were tracked, and their displacements along the x and y axes were used to compute the resulting angular deviations from the initial alignment. The sensor was assumed to be initially perfectly aligned, with the cosine error set to zero.

The analysis, shown in Figure 4, indicates that the maximum angular deviations correspond to a cosine error of the sensor tip:

- x axis: $e_{\mathrm{cosTx}} = 2 \cdot 10^{-10} \cdot L$
- y axis: $e_{\mathrm{cosTy}} = 4 \cdot 10^{-11} \cdot L$

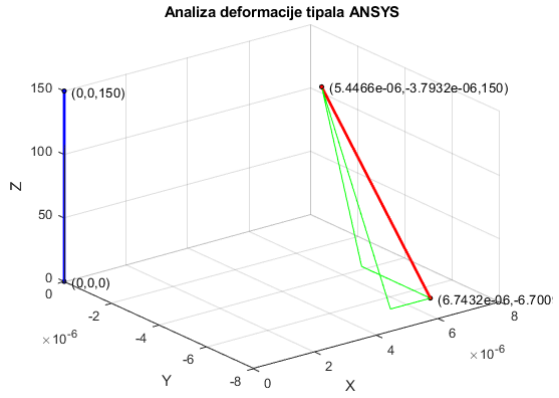

Figure 4. MATLAB analysis of sensor stylus angular deviations

The resulting combined cosine error along both axes (x and y) is approximately $e_{\mathrm{cosT}} = 2.5 \cdot 10^{-10} \cdot L$. For comparison, the current laboratory capability allows aligning a 10 mm sensor stylus within an interval of approximately 3 µm, corresponding to a cosine error of $e_{\mathrm{cosT}} = 10^{-7} \cdot L$.

To determine the Abbe error, between the sensor axis and the measurement axis of the reference laser beam positioned on the opposite side of the sensor, we performed an experiment measuring of pitch and yaw of the vertical stage. The largest measured angle was 8 µm/m, which corresponds to an Abbe error of 4 nm at the 0.5 mm offset of the axes. Thermal analysis indicated a maximum axis displacement of approximately 10 µm, which is negligible relative to the achievable 0.5 mm alignment.

Overall, the analysis demonstrates that temperature-induced deformations have a negligible impact on the sensor's geometric errors, including both cosine and Abbe errors.

4. Conclusion

A detailed investigation of the thermal and structural behaviour of the newly developed displacement sensor calibration system was performed using experimental measurements and finite element simulations. The results indicate that, under the tested temperature conditions, thermally induced deformations of the system have a negligible effect on the geometric accuracy of the sensor. Both the cosine and Abbe errors remain well below the laboratory's alignment capability. The analysis also confirms that the commercially available components and the overall modular assembly provide a mechanically and thermally stable structure. These findings support the use of the system for reliable and traceable sensor calibrations, without significant influence from temperature variations.

The ongoing work focuses on finalizing the automated calibration procedure, including the development and validation of calibration algorithms. Through further system optimization, additional reductions in measurement uncertainty are expected. The ultimate goal is to achieve an expanded uncertainty of 100 nm (k =2) over a 150 mm range, providing a fully automated, high-precision calibration capability for displacement sensors, thereby ensuring traceability for Slovenian accredited metrology laboratories and supporting the national industry.

5. Acknowledgement

The authors acknowledge the financial support from the Slovenian Research Agency (Research Core Funding No. P2-0190, Grant numbers 1000-20-0552, 6316-3/2018-255, 603-1/2018-16), as well as from the Metrology Institute of the Republic of Slovenia (funding of national standard of length; Contract No. C3212-10-000072). Furthermore, the authors would like to acknowledge the use of research equipment for processing and monitoring the machining and forming processes: Laser measuring systems for machine tools and coordinate measuring machines, procured within the project "Upgrading national research infrastructures - RIUM", which was co-financed by the Republic of Slovenia, the Ministry of Education. This specific research was also a part of the national project No. V2-24074 within the framework of the Targeted Research Program "CRP 2024" and the European project 23IND08-Di-Vision within the framework of the European Partnership on Metrology. Therefore, we would also like to acknowledge the support of the Slovenian Research Agency, Ministry of the Economy, Tourism and Sport, and the European Commission.

References

[1] Hermann G and Rudas I, Calibration system for tactile measuring probes, *SISY 2015 – IEEE, 13th Int. Symp. Intell. Syst. Informatics, Proc.*, pp. **145–148**, 2015

[2] Peingbangyang S and Wongsaroj J, Characteristics of Linear Variable Differential Transformer(LVDT) Probe for Gauge Blocks Calibration, *J. Phys. Conf.Ser.*, vol. **901**, 2017

[3] C Lipus L, Acko B, and Tompa J, Experimental determination of influences on a gauge block's stack length, *Adv. Prod. Eng. Manag.*, vol. **17**, 2022

[4] Ma Z, Choi J, and Sohn H, Structural displacement sensing techniques for civil infrastructure: A review, *J. Infrastruct. Intell. Resil.*, vol. **2**, 2023

[5] Byman V, Jaakkola T, Palosuo I, and Lassila A, High accuracy step gauge interferometer, Meas. Sci. Technol., vol. **29**, 2018

[6] Stoup J and Faust B, Measuring Step Gauges Using the NIST M48 CMM, *NCSLI Meas.*, vol. **6**, 2011

[7] Zhang L, Li J, Wu Y, Zhang K, Wang Y, Prediction model and experimental validation for the thermal deformation of motorized spindle, *Heat Mass Transf Und Stoffuebertragung*, **54**, 2018

[8] Naumann A, Ruprecht D, Wensch J, Toward transient finite element simulation of thermal deformation of machine tools in real-time *Comput Mech*, **62**, 2018

[9] Zheng E, Yang Y, Peng Z, Zhu Y, Zhao X, Lin X and Kang M, Thermal characteristics analysis and error prediction for lubricated multi-link high-speed precision presses, *J Mech Sci Technol*, **33**, 2019

[10] Šafarič J, Dolšak B, Klobučar R, Ačko B, Analysis of thermal contribution to the measurement uncertainty in step gauge calibration, *Precision Engineering*, **66**, 2022

[11] Chenyang Z, Cheng C and Hang Z, Study on nonlinear thermal error of the measurement machine, *IEEE 2011 10th International Conference on Electronic Measurement & Instruments*, Chengdu, China, 2011

euspen's 26th International Conference & Exhibition, Krakow, PL, June 2026
www.euspen.eu

Multisensory and multiscale characterization of selected technological surfaces using optical methods

Michał Jakubowicz[1], Karol Grochalski[1], Tomasz Bartkowiak[1], Bartosz Gapiński[1], Michał Wieczorowski[1]

[1] *Poznan University of Technology, Jacka Rychlewskiego Street 1, 61-131 Poznan*

michal.jakubowicz@put.poznan.pl

Abstract

Contemporary industry, regardless of sector, places increasingly high demands on the precision and quality of manufactured components. One of the key aspects of quality control is the measurement of surface roughness and topography, which provides essential information about the functional properties and durability of products. Traditional measurement methods, based mainly on contact profilometry, although still widely used, have limitations related to time consumption, potential interference with the surface of the tested component, and restricted spatial analysis capabilities. The dynamic development of optical technologies enables the application of modern, non-contact measurement methods, which not only ensure high accuracy but also allow three-dimensional analysis of the geometric structure of surfaces. This paper presents a methodology for investigating the topography of selected technological surfaces using multisensory and multiscale optical techniques. The analysis covers measurement data obtained from various manufacturing and processing methods, acquired with tools such as focus variation microscopy, white light interferometry, and confocal profilometry. The research included both quantitative and qualitative assessments, considering different measurement parameters and data filtering procedures. The implementation also addresses the complex issue of how the type and degree of data filtering influence the metrological parameters measured with different techniques. The results obtained were compared with those from classical contact profilometry, allowing a comparative evaluation of the effectiveness and applicability of the analysed methods. The collected data constitute a valuable source of information that supports a comprehensive assessment of the geometric structure of the examined surfaces. The use of optical methods paves the way for fast, precise, and non-destructive quality evaluation, which is crucial for the further development of production processes across various industries

multisensors measurement systems; optical metrology; roughness; surfaces topography

1. Introduction

Contemporary industry, regardless of the area of application, is characterized by a systematic increase in requirements for the precision and quality of manufactured components. One of the key aspects of quality assessment is the measurement of surface roughness and topography, which provides essential information on the functional properties and service life of products across various fields [1-5]. Traditional measurement methods, based primarily on contact profilometry techniques [6], despite their widespread use, exhibit certain limitations, including high time consumption [7], the risk of affecting the measured surface, and restricted spatial analysis capabilities [8-10]. The dynamic development of optical technologies enables the implementation of modern non-contact measurement methods that ensure high accuracy and allow for three-dimensional analysis of surface geometric structures [11].

Non-contact methods, such as optical profilometry, offer several advantages over contact techniques. They are generally faster, non-destructive, and capable of providing detailed spatial analysis without the risk of surface damage [12, 13]. These methods involve interferometry, structured light, and digital holography to capture surface profiles accurately and efficiently [14-16]. The most popular non-contact methods for measuring the geometric structure of a surface include coherence scanning interferometry [17], imaging confocal microscopy [18] and focus variation microscopy [19]. Non-contact techniques are particularly beneficial in applications requiring high precision and minimal interference with the surface, such as in medical, aerospace, and advanced manufacturing fields [20, 21]. In conclusion, while contact profilometry techniques are widely used, their limitations in terms of time consumption, risk of surface impact, and spatial analysis capabilities make non-contact methods a preferable alternative in many advanced applications.

Advanced surface characterization increasingly relies on multisensory and multiscale approaches to capture the full geometric complexity of engineering surfaces [22]. Surface features occur across a wide range of spatial scales, from nanometric roughness to macroscopic form, and no single measurement technique can provide a complete and reliable description of topography. Multisensory strategies, which combine contact and non-contact techniques, exploit the complementary strengths of individual sensors to improve measurement accuracy, robustness, and reliability [23]. Simultaneously, multiscale analysis enables surface features to be evaluated according to their spatial extent and functional relevance, allowing the separation of roughness, waviness, and form. By integrating multisensory data acquisition with multiscale analytical methods and advanced mathematical and statistical tools, a comprehensive framework for surface assessment is established. Such approaches are essential for understanding, quantifying, and optimizing surface properties across diverse engineering applications, from precision manufacturing [24] to heritage science [25], and for enhancing the correlation between measured topography and functional performance.

Despite the dynamic development of optical methods for surface topography measurement, the literature still lacks clear and systematic comparisons of different optical techniques. The influence of applied data filtering methods on the values of metrological parameters remains insufficiently understood, which hinders their unambiguous interpretation. In addition, there is a need to relate results obtained using optical methods to classical measurement techniques in order to ensure consistency and reliability in surface evaluation.

2. Methodology

2.1. Materials

The investigated specimens were isotropic, textured surfaces produced by sandblasting at working pressures of 2 (2-BAR), 4 (4-BAR, and 6 bar (6-BAR). The parts were made of 7075 aluminium alloy. Each specimen was marked by micromachining a 4.0 mm × 4.0 mm outline, with the analyzed texture located at its centre. This step was essential to ensure unambiguous orientation and identification of the measurement area for the surface texture measurement techniques and instruments considered. Figure 1 shows the overview of analyzed surfaces.

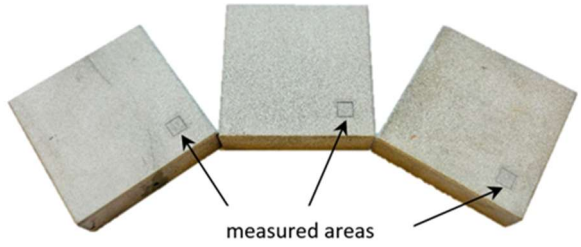

Figure 1. View of samples made of 7075 aluminum alloy

The measured area for each part was 4.0 mm × 4.0 mm. The measurement data were levelled to remove form error, filtered using an S–L Gaussian filter, truncated at a maximum material ratio of 0.5%, and completed by filling unmeasured points. The processed areas were then subjected to qualitative (non-parametric) and quantitative (parametric) analyses

Analysis of surface topography involved comparing areal parameters, specifically Sa (arithmetic mean height), Sq (root mean square height), Sku (kurtosis of surface height distribution), Sk (core roughness depth), Spk (reduced peak height), and Svk (reduced valley depth), which together describe the average roughness, peak and valley characteristics, and the sharpness or flatness of the surface.

The relative error δ_{Rel} was adopted as a measure of measurement convergence and was defined as the quotient of the difference between the measurement result obtained using one of the optical methods and that obtained using the reference (stylus) device, divided by the value obtained using the reference device:

$$\delta_{Rel} = \frac{A - B}{B} \cdot 100\% \quad (1)$$

where:

A – value of the selected surface topography parameter obtained by one of the optical methods (confocal profilometry, focus variation, and white-light interferometry).

B – value of the selected surface topography parameter using the Hommel-Etamic Roundscan T8000 device (reference device).

This allowed for comparison of the tested surfaces and their evaluation in terms of various measurement techniques.

2.2. Methods for analyzing the structure

The approach here was focused on analyzing the similarity of selected areal surface parameters across the applied measurement techniques. The following methods were considered: contact (stylus) technique as the reference method, confocal profilometry, focus variation (FV), and white-light interferometry (WLI).

Contact (stylus) profilometry was adopted as the reference. The Hommel-Etamic T8000 (Jenoptik Industrial Metrology Germany GmbH) is a system for measuring surface topography using a profile-based approach; when combined with a motorised traversing stage, it also enables three-dimensional (3D) topography measurements. The instrument was equipped with a TKU300 measuring head. A diamond stylus tip with a 90° apex angle and a 2 µm tip radius was used for the measurements. The profilometer operated within a measurement range of ±80 µm.

Another technique used in this study was the non-contact AltiSurf 520 profilometer (Altimet). It is a non-contact system for 3D topography measurement, in which surface height is determined optically based on the confocality condition—typically implemented in a chromatic configuration. The operating principle relies on the fact that different wavelengths are brought to focus at different heights, and the surface position along the Z-axis is estimated from the spectrum of light returning to the detector [26]. In this study, a CL1 objective with a measurement range of 130 µm was used.

Surface topography measurements were also performed using an Alicona µCMM optical micro-measuring machine (Alicona Imaging GmbH). This device enables precise measurement of dimensions, positional and shape deviations, as well as surface topography. This system is based on the principle of focus variation microscopy, which involves analyzing the sharpness of an optical image to assess changes in surface features [27].

Another instrument employed in this study is a multisensor system based on an optical machine. Additional measurement heads were incorporated, enabling observations at both micro- and nanoscale levels. The Optiv Reference 763 Dual Z (Hexagon AB) features a granite portal-type construction with a fixed portal and two independent vertical spindles, which support a vision sensor, a scanning contact sensor, and a white light interferometer (WLI). The WLI functions as a coherent scanning interferometer (CSI), as defined by ISO 25178-604 [28]. In interferometric systems of this type, white light interferometers are used instead of a single-wavelength light source. The entire system is controlled using PC-DMIS CAD++ software, which, in addition to providing numerous measurement options, allows data acquisition from multiple sensors within a common coordinate system.

For clarity in the following sections of the article, the measurement methods used in the study are represented using a simplified notation, as presented in Table 1.

Table 1 Symbols used for devices used in research

Device	Symbol
Hommel-Etamic T8000	I-90N
AltiSurf 520	CL-1
Alicona µCMM	A20×
Optiv Reference 763 Dual Z	WLI20×

For the optical methods (Alicona µCMM and Optiv Reference 763 Dual Z), the same 20× magnification was applied. In both techniques, stitching was used. For both the Alicona microscope and the Optiv device, the overlap between adjacent measurement fields was set to 30%.

An important factor affecting the comparability of the techniques is the resolution, or equivalently the signal sampling

density. For Focus Variation (FV) microscopy, the lateral resolution was 500 nm and the vertical (Z-axis) resolution was 70 nm. Analogous parameters were applied for the WLI technique. For the profile-based methods, the spacing (step) between consecutive points along a single profile was 0.7 µm for both the contact profilometer (T8000) and the confocal profilometer (AltiSurf 520), while the signal was sampled at 10,000 points per measurement trace. The obtained datasets underwent parametric analysis using MountainsMap software, facilitating the extraction of information regarding various parameters of the geometric structure for each of the tested surfaces.

3. Results and discussion

Surface measurements performed using the considered measurement techniques enabled their graphical visualisation. This allows for rapid comparison and the identification of similarities. A selected example of a three-dimensional surface (6-BAR – Alicona µCMM) is shown in figure 2.

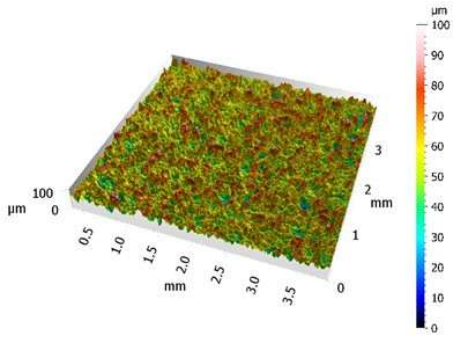

Figure 2. View of 3D representative sample texture (6-BAR)

The recorded data also enabled a parametric assessment of the surface structure for selected parameters depending on the applied measurement technique. Figure 3 presents selected areal parameters (from the full set of surface parameters), which are described later in the text.

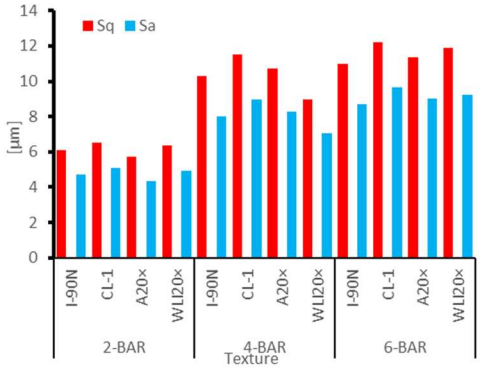

Figure 3. Selected surface parameters for the tested measurement techniques

Figure 3 presents the values of the areal surface texture parameters Sa and Sq obtained for three isotropic surfaces measured using four measurement techniques. Regardless of the structure and the technique, Sq takes higher values than Sa, which is typical because Sq is more sensitive to larger height deviations than Sa (which is based on averaged values). Within each structure, differences resulting from the applied measurement technique are also observed. For all three structures, confocal profilometry (CL-1) yields the highest Sa and Sq values, suggesting that it captures a greater contribution of components with large deviations (i.e., higher sensitivity to peaks and valleys) compared to the other methods. At the same time, the spread of the reported parameters across the measurement techniques is not constant: the greatest differentiation of Sa and Sq is observed for the 4-BAR surface, whereas for 2-BAR the differences are smaller. Overall, the results indicate that the structure/forming level (2/4/6-BAR) is the primary factor affecting Sa and Sq, while the measurement technique influences the obtained values in a systematic manner, with CL-1 consistently providing the highest readings for both parameters.

The relative error values for different surface texture parameters measured on isotropic sandblasted 7075 aluminium specimens at working pressures of 2, 4, and 6 bar are summarised in Table 2.

Table 2 Relative error δ_{Rel} values of selected surface topography parameters

	Symbol	Sq	Sa	Sku	Sk	Spk	Svk
		[%]	[%]	[%]	[%]	[%]	[%]
2-BAR	CL-1	6.8	6.9	-0.1	4.8	-18.5	18.9
	A20×	-6.2	-7.9	10.7	-9.4	-11.7	8.4
	WLI20×	4.1	4.2	-1.9	3.3	-18.5	11.2
4-BAR	CL-1	12.2	11.9	2.5	11.4	8.9	20.3
	A20×	4.1	3.4	6.3	2.6	2.4	12.0
	WLI20×	-13.1	-11.9	-11.3	-10.5	-23.3	-13.4
6-BAR	CL-1	11.2	10.6	0.8	9.2	6.9	19.8
	A20×	3.3	3.2	-0.5	2.4	0.9	5.5
	WLI20×	8.2	5.6	15.6	-1.8	7.5	32.5

For the 2-BAR specimens, measurements performed with the AltiSurf 520 profilometer (CL-1) show moderate relative errors for height parameters, with 6.8% for Sq and 6.9% for Sa, while peak and valley parameters exhibit larger deviations, particularly Spk (-18.5%) and Svk (18.9%). The focus variation microscopy device (A20x) tends to underestimate height parameters (Sq -6.2%, Sa -7.9%) but shows a positive relative error for Sku (10.7%). White-light interferometry results are closer to the reference for height parameters (Sq 4.1%, Sa 4.2%) but display significant deviations for Spk (-18.5%) and Svk (11.2%).

For the 4-BAR specimens, relative errors generally increase for CL-1, with Sq and Sa exceeding 12% (Sq = 12.2%, Sq = 11.9%), indicating higher sensitivity to surface roughness variations at increased sandblasting pressure. The Alicona µCMM provides smaller deviations, with Sq and Sa below 5%, and moderate overestimation of Sku (6.3%). WLI20x shows considerable underestimation across most parameters, particularly Sq (-13.1%), Sa (-11.9%), and Spk (-23.3%), suggesting challenges in accurately capturing surfaces with more pronounced textures.

For the 6-BAR specimens, the AltiSurf 520 profilometer continues to show high relative errors for height and valley parameters (Sq 11.2%, Svk 19.8%), while Alicona µCMM optical micro-measuring machine (A20x) again demonstrates better agreement with the reference, with Sq 3.3% and Svk 5.5%. The Optiv Reference 763 Dual Z (WLI20x) exhibits mixed performance, overestimating Sku (15.6%) and Svk (32.5%) while showing moderate errors for height parameters (Sq 8.2%, Sa 5.6%).

Overall, the analysis indicates that relative errors tend to increase with sandblasting pressure for all devices, reflecting the more complex surface textures at higher pressures. The non-contact AltiSurf 520 profilometer shows moderate errors for height parameters but larger deviations for peak and valley parameters. In comparison, the Alicona µCMM provides the

most consistent results across all surface pressures, with generally low relative errors for Sq, Sa, and Svk. The white light interferometer, on the other hand, exhibits larger deviations, particularly for Spk and Svk, indicating potential limitations in capturing sharp peaks and deep valleys on strongly textured surfaces. These findings highlight the importance of careful device selection and the potential limitations of optical measurement methods when analyzing complex, sandblasted aluminium surfaces.

4. Conclusion

The conducted study enabled the evaluation of the accuracy of various non-contact surface topography measurement methods. The obtained results allow for the identification of the limitations of individual techniques and the determination of optimal methods for the analysis of complex surface structures. Based on the conducted research and analyses, the following conclusions were drawn:

- Optical methods reduce the influence of the profilometer tip, eliminating the need for morphological filtering.
- Relative measurement errors are primarily governed by the surface texturing process rather than the measurement technique.
- Proper selection of measurement parameters is essential to minimize non-measured points in non-contact measurements.
- Optical methods effectively capture general height parameters but may underrepresent sharp peaks and deep valleys on highly rough surfaces.

Future work will focus on:

- Quantifying the effect of filtering on selected topography parameters.
- Assessing the impact of measurement parameters on the occurrence of non-measured points.

References

[1] Salazar F, Barrientos A, 2013 Surface Roughness Measurement on a Wing Aircraft by Speckle Correlation *Sensors* **13**, 11772-11781

[2] Ramesh S, Karunamoorthy L, Palanikumar K, 2012 Measurement and analysis of surface roughness in turning of aerospace titanium alloy (gr5), *Measurement* **45**(5), 1266-1276

[3] Jakubowicz M, Gapiński B, Marciniak-Podsadna L, Mendak M, Mietliński P, Wieczorowski M 2023 Multiscale Evaluation of Jaw Geometry Reproduction Obtained Via the Use of Selected Orthodontic Materials in Dental Implants and Orthodontics—In Vitro Case Study *Appl. Sci.* **13**, 6932,

[4] Bartkowiak T, Peta K, Królczyk JB, Niesłony P, Bogdan-Chudy M, Przeszłowski Ł, Trych-Wildner A, Wojciechowska N, Królczyk GM, Wieczorowski M, 2025 Wetting properties of polymer additively manufactured surfaces – Multiscale and multi-technique study into the surface-measurement-function interactions, *Tribology International* **202**, 110394

[5] Nieslony P, Krolczyk GM, Krolczyk JB, Gupta MK, Bogdan-Chudy M, Grochalski K, Wojciechowski S, Wieczorowski M, Maruda RW, 2025 A novel use of non-contact methods in analyzing the physical and technical surface characteristics of different materials using electromagnetic measurement techniques *Measurement* **241**, 115672

[6] Grochalski, K, Mendak M, Jakubowicz M, Gapiński, B, Swojak N, Wieczorowski M, Krawczyk A 2021 Differences in Roughness Parameter Values from Skid and Skidless Contact Stylus Profilometers. *Advances in Science and Technology Research Journal* **15**(1), 58-70

[7] Koblar V, Filipič B, 2021 Evolutionary design of a system for online surface roughness measurements *Mathematics* **9**(16), 1904

[8] Rojewski M, Nowinka B, Czyżewski P 2024 3D Optical and Mechanical Roughness Measurements of Complex and Irregular Structures on the Basis of Polypropylene Moldings. *Advances in Science and Technology Research Journal* **18**(5), 245-257

[9] Duboust N, Ghadbeigi H, Pinna C, Ayvar-Soberanis S, Collis A, Scaife R, Kerrigan K 2016 An optical method for measuring surface roughness of machined carbon fibre-reinforced plastic composites. *Journal of Composite Materials* **51**(3), 289-302

[10] Pawlus, P.; Wieczorowski, M.; Mathia, T. *The Errors of Stylus Methods in Surface Topography Measurements*; Zapol: Szczecin, Poland, 2014.

[11] Leach, R. (Ed.). Optical Measurement of Surface Topography. Springer, 2013.

[12] Kiran MB 2021 A novel on-line surface roughness measuring method, Proceedings of the International Conference on Industrial Engineering and Operations Management, 2907 – 2916

[13] Joyce AM, Kane DM, Chater RJ 2006 Optical surface profilometry of low reflectance materials - Evaluation as a laser processing diagnostic, PICALO 2006 - 2nd Pacific International Conference on Applications of Laser and Optics - Conference Proceedings, 406-410

[14] Forgács I, Antal Á 2025 Comparison of Structured Light Projection-based Surface Reconstruction Methods, *Periodica Polytechnica Mechanical Engineering*, **69**(2), 151-163

[15] Zhao F, Tang H, Zou X, Li X 2025 A Review of Optical Metrology Techniques for Advanced Manufacturing Applications, *Micromachines* **16**(11), 1224

[16] Idicula MS, Mitura P, Józwik M, Choo H-G, Martinez-Carranza J, Wen K, Kozacki T 2022 Multi-incident holography profilometry for low and high gradient object Proceedings of SPIE - The International Society for Optical Engineering, 12138

[17] Petzing J, Coupland JM, Leach R 2010 The measurement of rough surface topography using coherence scanning interferometry. Measurement Good Practice Guide No. 116, National Physical Laboratory

[18] Newton L, Thanki A, Bermudez C, Artigas R, Thompson A, Haitjema H, Leach R. 2023 Optimisation of Imaging Confocal Microscopy for Topography Measurements of Metal Additive Surfaces. *Metrology* **3**(2) 186-221

[19] Mustafa A M, Muhamedsalih H, Tang D, Kumar P, Jiang J 2024 Chromatic focus variation microscopy for surface metrology *Opt. Express* **32**, 35527-35541

[20] Zhao F, Tang H, Zou X, Li X. 2025 A Review of Optical Metrology Techniques for Advanced Manufacturing Applications. *Micromachines* **16**(11), 1224

[21] Ma YD, Xiao YC, Wang QQ , Yao K, Wang XR, Zhou YP, Liu YC, Sun Y, Duan J 2025 Applications of Chromatic Confocal Technology in Precision Geometric Measurement of Workpieces Journal of Physics: Conference Series, 2460, International Symposium on Advanced Launch Technologies 2460 012077

[22] Gogolewski D, Kozior T, Zmarzły P. 2024 Multiscale Analysis of Surface Topography for Engineering Applications in the Casting Industry. *Materials* **17**(21):5272

[23] Weckenmann A, Jiang X, Sommer K-D, Neuschaefer-Rube U, Seewig J, Shaw L, Estler T, 2009 Multisensor data fusion in dimensional metrology, *CIRP Annals* **58**(2), 701-721

[24] Le Goïc G, Bigerelle M, Samper S, Favrelière H, Pillet M. 2016 Multiscale roughness analysis of engineering surfaces: A comparison of methods for the investigation of functional correlations *Mechanical Systems and Signal Processing* **66-67**, 437-457

[25] Macdonald DA, Martisius NL, Stemp WJ, Brown CA, Guthrie L, Gleason MA 2025 Quantification of microwear on experimental shell tools: First results using focus variation microscopy, surface roughness, and multiscale geometric analyses. *J Archaeol Sci Rep.* **62**,104986

[26] Wang A, Xie, B, Liu Z, 2017 Design of measurement system of 3D surface profile based on chromatic confocal technology," Proc. SPIE 10616, International Conference on Optical Instruments and Technology: Optical Systems and Modern Optoelectronic Instruments, 1061618

[27] Danzl R, Helmli F, Scherer S. 2011 Focus Variation – a Robust Technology for High Resolution Optical 3D Surface Metrology. *Strojniški vestnik - Journal of Mechanical Engineering*, **57**(3), 245-256

[28] ISO 25178-604:2025 Geometrical product specifications (GPS) — Surface texture: ArealPart 604: Design and characteristics of non-contact (coherence scanning interferometry) instruments

euspen's 26th International Conference & Exhibition, Krakow, PL, June 2026
www.euspen.eu

Glossary of terms and definitions of digital metrological twins for freeform metrology

Ivana Linkeová[1], Jan Soukal[1], Daniel Heißelmann[2], Katharina Janzen[2], Ulrich Neuschaefer-Rube[2], Lea-Jean Frömel[2], Adam Wojtowicz[3,11], Dariusz Czulek[3], Hichem Nouira[4], Ermes Xhafa[4], Sten Bergstrand[5], Andreas Thore[5], Carl-Henrik Hanquist[5], Walter Knulst[6], Marcel van Dijk[6], Devrim Nalbantoglu[6], Gertjan Kok[6], Björn Hemming[7], Ville Heikkinen[7], Antti Lassila[7], Guido Tossello[8], Nabil Anwer[9], Pablo Puerto[10], Asier Garcia Berdote[10], Adam Gaska[11], Wiktor Harmatys[11], Giacomo Maculotti[12], Maurizio Galetto[12], Elisa Verna[12], Gianfranco Genta[12], Matthias Bodenbenner[13], Yixiang Dang[13], Robert H. Schmitt[13], Gorka Kortaberria[14], Eneko Gomez-Acedo[14], Unai Mutilba[14], Enrico Savio[15], Sofia Catalucci[15], Lorenzo Didonè[15], Hageney Hageney[16], Andreas Pierro[16], Florian Paul[16], Thomas Maresch[17], Makoto Abe[18], Dietrich Imkamp[19], Osamu Sato[20]

[1] *Czech Metrology Institut (CMI), Czechia*
[2] *Physikalisch-Technische Bundesanstalt (PTB), Germany*
[3] *Central Office of Measures (GUM), Poland*
[4] *Laboratoire national de métrologie et d'essais (LNE), France*
[5] *RISE Research Institutes of Sweden AB, Sweden*
[6] *VSL B.V., Netherlands*
[7] *Teknologian tutkimuskeskus VTT Oy, Finland*
[8] *Danmarks Tekniske Universitet (DTU), Denmark*
[9] *Ecole Normale Supérieure Paris-Saclay, France*
[10] *IDEKO, Basque Research and Technology Alliance (BRTA), Spain*
[11] *Cracow University of Technology, Faculty of Mechanical Engineering, Poland*
[12] *Department of Management and Production Engineering, Politecnico di Torino, Italy*
[13] *WZL-IQS | RWTH Aachen University, Germany*
[14] *Fundacion Tekniker, Spain*
[15] *Università degli Studi di Padova, Italy*
[16] *eumetron GmbH, Germany*
[17] *Hexagon Metrology GmbH, Germany*
[18] *Mitutoyo CTL Germany GmbH, Germany*
[19] *Carl Zeiss Industrielle Messtechnik GmbH, Germany*
[20] *National Institute of Advanced Industrial Science and Technology (AIST), Japan*

ivana.linkeova@cmi.gov.cz

Abstract

This paper aims to introduce the "Glossary of terms and definitions of Digital-Metrological Twins (D-MTs) for freeform metrology" (Glossary) compiled for the purposes of the 23IND12 ADAM: Application of Digital-Metrological Twins for emerging measurement technology in advanced manufacturing, a Joint Research Project (JRP) within the European Partnership on Metrology (EPM). The main objective of the Glossary is to unify technical terminology and enable precise and unambiguous communication between partner institutions. A number of ISO standards and scientific papers have been studied in order to select clear and consistent definitions of key terms and concepts that are essential for the correct understanding and implementation of advanced models, methods and technologies used in the field of D-MT freeform metrology. The terms and definitions in the Glossary are accompanied by a number of original images for better understanding, hyperlinks and an alphabetical index for easy navigation. In September 2026, the Glossary will be published on the 23IND12 ADAM project website https://www.adam.ptb.de.

Digital metrological twin, freeform metrology, advanced manufacturing, coordinate measuring, freeform surface

1. Introduction

The project 23IND12 ADAM: Application of Digital-Metrological Twins for emerging measurement technology in advanced manufacturing (ADAM) aims to develop reliable mathematical models and traceable parameterisable methods for evaluating the measurement uncertainty applicable in Digital Metrological Twins (D-MTs), with an emphasis on industrial products with complex freeform geometries [1]. This paper presents the "Glossary of Terms and Definitions for D-MTs for Freeform Metrology" (Glossary), compiled within the ADAM project, which collects established and defines new terms in the field of D-MT for freeform metrology. The Glossary enables unification of terminology and definitions, which is crucial for accurate communication and understanding among all involved

experts as well as less experienced users in the field of advanced manufacturing engineering, metrology and digital twin development. The Glossary provides a basis for standardising D-MTs terminology, thereby increasing the scientific accuracy and practical applicability of D-MTs across industries.

The paper is organized as follows: Section 2 describes the structure of the Glossary. Section 3 provides some examples of the most important terms used in the interdisciplinary field focused on the mathematical-geometric theory of freeform surfaces design and inspection with the application of D-MTs. Section 4 concludes the paper and discusses the possible impact of the Glossary on the metrological and scientific community, as well as on relevant standards.

2. The Glossary structure

The Glossary is represented by a pdf document where the terms and definitions are listed together with important textual and visual information as well as with the references to the relevant ISO standards or scientific papers where the original description can be found, see example in Fig. 1. Where necessary or appropriate for better understanding, the original description is expanded with broader explanations, notes, examples, formulas, images, etc.

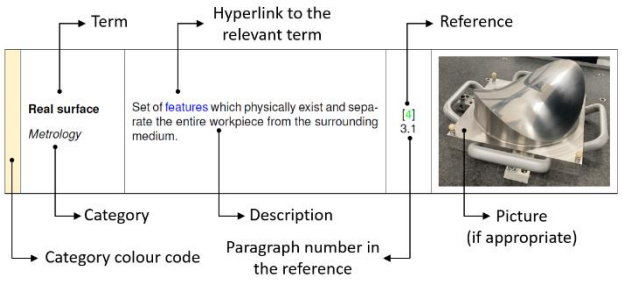

Figure 1. Information structure used to present terms and definitions

All terms in the Glossary are divided into the following five categories (distinguished by colour codes for better orientation):

- *General* (green) for terms or expressions used in scientific and technical disciplines for precise and unambiguous communication between experts,
- *Metrology* (yellow) for specific terms or expressions used in the field of coordinate metrology to ensure the accuracy and reliability of measurements,
- *Virtual geometry* (pink) representing Computer Aided Design (CAD) models of physical or non-physical 3D objects or abstract mathematical representations of 3D objects,
- *Numerical simulations* (orange) involving processes, algorithms and computational methods to analyse and model various systems and phenomena that would be difficult or impossible to analyse analytically, and
- *Advanced technology* (blue) for tools, equipment and systems designed to improve manufacturing processes.

All the main terms are listed in an Alphabetical index and a number of hyperlinks ensure easy navigation.

3. Examples of terms and definitions important for D-MTs

This section provides examples of several Glossary terms that are important for D-MTs developed for advanced industrial applications of complex freeform geometries.

3.1. Digital twin, digital metrological twin

The terms *Digital twin* (DT) and *Digital metrological twin* (D-MT) undoubtedly represent the most important terms in the ADAM project. While the concept of digital twin as a virtual model of a real object or system enabling its monitoring, analysis and optimisation in real time is introduced in ISO standards and currently widely used in various areas of technical practice, the definition of D-MT is not defined in ISO standards yet. Therefore, in the Glossary, the definition of DT is taken from the ISO/IEC 30173 [2] and formulation published in [3] is used as the definition of D-MT:

Digital twin is a digital representation of a target entity with data connections that enable convergence between the physical and digital states at an appropriate rate of synchronisation [2]. DT has some or all of the capabilities of connection, integration, analysis, simulation, visualisation, optimisation, collaboration, etc. DT can provide an integrated view throughout the life.

Digital Metrological Twin [3] is a numerical model that depicts a specific measurement process and indicates an associated measurement uncertainty for a specific measured value, which is traceable to the units of the International System of Units (SI). Moreover, it complies with the requirements that

- the measurement uncertainty is calculated according to recognised standards and guidelines,
- all input parameters are traceably determined and are stated with the corresponding measurement uncertainty,
- the calculated measurement uncertainty is validated by traceable measurements.

3.2. Freeform, invariance class and surface classification

Many papers refer to ISO 17450-1 [4] when defining a freeform geometry (curve, surface), but the definitions of the terms freeform shape or freeform surface are not given in this standard. However, using the invariance class concept [4] as a useful approach to surface classification [5], it is clear that the common term "freeform surface" means complex surface.

According to [4], the *invariance class* concept expresses the set of objects that share the same invariant under some symmetry or transformation. It means that all ideal geometrical features belong to one of the seven invariance classes characterised by the number and type of degrees of freedom.

In the Glossary, the invariance classes are described as shown in Tab. 1.

Using the invariance class concept, each surface class is defined by the rigid motions (translations and rotations) that leave the geometrical surface unchanged (invariant), see the red arrows in the pictures in Tab. 1 (to keep the pictures clear, the rotation arrows are oriented in only one direction, rotation in the opposite direction is also possible). Thus, the following classes of surfaces can be distinguished: complex, prismatic, revolute, helical, cylindrical, planar or spherical.

Complex surfaces are often called freeform surfaces in industry. True *freeform* surface falls into the complex invariance class where the surface shape has no continuous translational or rotational symmetry around any axes. Example of true freeform surface is shown in the Complex (Freeform) row in Tab. 1. Many types of surfaces are also defined as freeform by industry, e.g. off-centred rotational optics and toroidal surfaces. These are mathematically not true freeform surfaces as they do have an axis, but this axis does not pass through the functional surface. In [5], these surfaces are called “quasi-freeform surfaces”.

Surface of revolute, helical and prismatic class can be generated by motion of generating curve g with respect to directing curve d. If at least one of these curves is freeform, the surface in the Glossary is classified as freeform and it is called a freeform revolute surface, freeform rail-revolute surface, freeform helical surface and freeform prismatic surface. Examples of these freeform surfaces together with the description of the generating principle are given in Tab. 2.

Table 1. Invariance classes

Invariance class	Unconstrained degrees of freedom	Example
Complex (Freeform)	none or none of the below	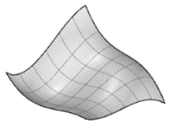
Prismatic	1 translation along a straight line	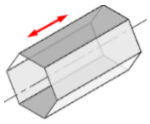
Revolute	1 rotation around a straight line	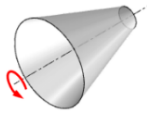
Helical	1 translation along and 1 rotation combined around a straight line	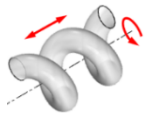
Cylindrical	1 translation along and 1 rotation around a straight line	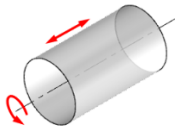
Planar	1 rotation around a straight line and 2 translation in a plane perpendicular to the straight line	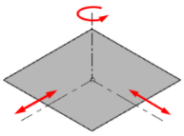
Spherical	3 rotations around a point	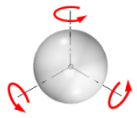

Table 2. Freeform surfaces

Surface	Generating principle	Example
Freeform revolute	Revolution of freeform generating curve g along axis a of revolution. Directing curve d is a circle with centre on axis a lying in plane perpendicular to axis a.	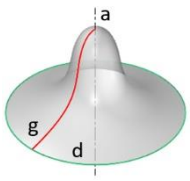
Freeform rail-revolute	Revolution of generating curve g that defines the surface shape around axis a of revolution with respect to the rail (directing) curve d that defines the surface edge.	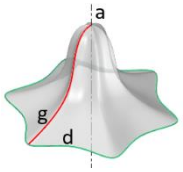
Freeform helical	Combination of revolution of generating curve g around axis a of helical motion and translation of generating curve g along axis a. The directing curve d is a helix.	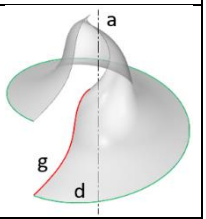
Freeform prismatic	Translation of generating curve g along directing straight line d.	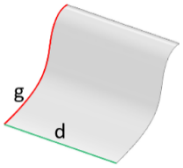

3.3. Nominal model, non-ideal surface model, freeform digital twin

A *nominal model* represents the ideal, theoretical shape of a surface or object intended by the designer [4], which does not take into account any physical deviations or deformations. Usually, the nominal model of freeform geometry is virtually represented by a CAD model. However, manufacturing technologies have their limitations in accuracy, and therefore the machined surface deviates from the nominal CAD model.

In order to include machined deviations in the virtual CAD representation of the workpiece, a *non-ideal surface model* (*skin model*) is defined in ISO 17450-1 [4] as a virtual model of the physical interface of the workpiece with its environment. The non-ideal surface model is developed based on numerical simulation of the physical interface of the workpiece by a smooth [4] or discrete [6] surface. The numerical simulations used to create a non-ideal surface model are supposed to cover geometric deviations that are expected, predicted or already observed in real manufacturing processes [6].

A novel approach to develop a non-ideal surface model called *Calibrated CAD model* (CCAD) was firstly introduced in [7] where the physical machined surface was mathematically modelled based on calibration data obtained by high precision tactile point-to-point measurement. In [8], this method has been updated and the shape information contained in the calibration data obtained by high-precision tactile scanning has been fully utilised. Thus, the non-ideal surface model called *FreeForm Digital Twin* (FFDT) was introduced based on calibration data as B-spline continuous surface that compensates for the residual manufacturing errors of the freeform functional surface with associated uncertainty. The novelty of the FFDT approach lies in the fact that measurement results with FFDT as a reference CAD model does not indicate the manufacturing errors of the machined surface (as is the case when using a reference nominal CAD model), but an error of the measuring system with a known uncertainty.

The definition of FFDT is included in the Glossary in the following way: FFDT is a mathematical (B-spline) or virtual (CAD) representation of the physical interface of the functional freeform surface with its environment throughout the life cycle of the material standard. Both mathematical (B-spline) and virtual (CAD) representations of the real surface are based on calibration data and indicate a continuous associated measurement uncertainty for the surface profile measurand, which is traceable to SI units. Continuous means that FFDT is represented by a smooth surface and not e.g. by a polygonal mesh or a set of points only. In the context of freeform metrology, the life cycle is a period of validity until the time of damage/wear or until the expiration date of the freeform standard calibration.

To compare the above-mentioned variants of CAD models, the functional freeform surface (hyperbolic paraboloid) of the CMI freeform standard Hyperbolic Paraboloid HP 300 [8] shown in Fig. 1 was chosen as an example. The nominal CAD model of the whole standard is depicted in Fig. 2(a), FFDT CAD model developed in [8] is shown in (b) and examples of smooth and discrete non-ideal surface models based on numerical simulations are drawn in (c) and (d).

It is clear from Fig. 2 that the shape information contained in the FFDT faithfully documents the actual shape of the physical functional surface. In the case of the HP 300, both the manufacturing and measurement strategies can even be revealed from the course of the continuous surface of FFDT. Non-ideal surface models obtained by numerical simulation cannot have such informative power.

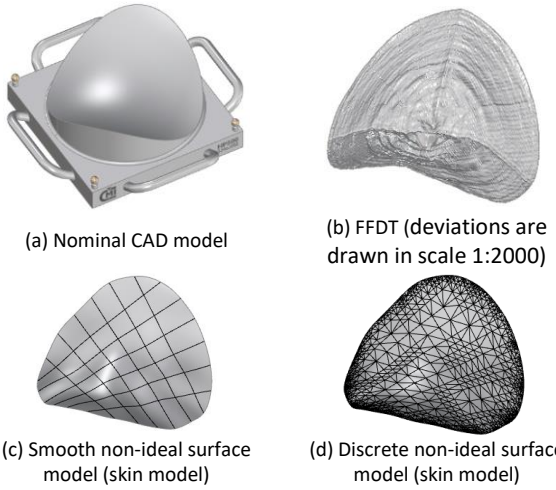

(a) Nominal CAD model

(b) FFDT (deviations are drawn in scale 1:2000)

(c) Smooth non-ideal surface model (skin model)

(d) Discrete non-ideal surface model (skin model)

Figure 2. Comparison of nominal a non-ideal CAD models of HP 300

3.4. Line and surface profile measurand

In case of freeform surfaces inspection, the deviations (normal distances) of a set of measured points from the reference CAD model of the inspected surface are evaluated. Usually, the best fit transformation with respect to the nominal CAD model of the freeform surface is applied to minimise the surface profile deviation in the sense of ISO 1101 [9]. According to [9], the *surface profile* is defined by the condition that all measured points must lie between two equidistant surfaces surrounding a set of spheres of diameter T, the centers of which lie on the surface with theoretically accurate geometric shape, see the schematic representation in Fig. 3. Here, the theoretically accurate geometric surface is drawn in green, the measured points in black and the two equidistant surfaces in grey.

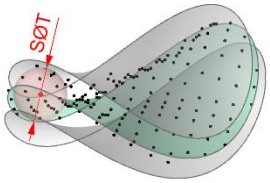

Figure 3. Definition of surface profile (example of HP 300 surface)

The *line profile* definition in ISO 1101 [9] used to assess curve measurement is defined similarly – in each cross-section parallel to the base plane the extracted profile line must lie between two equidistant curves enclosing a set of circles of diameter T whose centers lie on the curve with the theoretically exact geometric shape, see the schematic representation in Fig. 4(a). Here, the theoretically exact geometric shape is drawn in green, the black measured points lie on the extracted profile line and their normal deviations from the theoretical line are shown in blue. Surprisingly, this definition assumes only planar surface sections and therefore it would be possible to evaluate the line profile only when measuring 2D curves.

Therefore, in addition to the 2D line profile, the Glossary also includes an extension of the *3D line profile* recommended for measuring 3D curves in the following way: the 3D line profile is determined by the double value (in the case of oriented deviations by the double absolute value) T of maximum deviation of the measured point from the theoretically accurate 3D curve measured in the normal direction to the theoretical curve. The geometrical consequence of this definition is that the extracted 3D curve must lie in the canal surface surrounding the system of spheres of diameter T with the centers on the curve with theoretically accurate geometric shape, see Fig. 4(b).

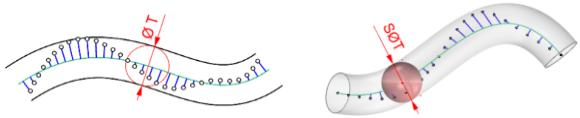

(a) 2D curve

(b) 3D curve

Figure 4. Definition of line profile

4. Conclusion

The document “Glossary of terms and definitions of digital metrological twins for freeform metrology” compiled within the 23IND12 ADAM: Application of Digital-Metrological Twins for emerging measurement technology in advanced manufacturing project will help to establish consistency across the metrology and scientific communities. The glossary will be disseminated to the metrological and scientific communities together with the project’s good practice guidelines via the project website https://www.adam.ptb.de and an open access repository. This should support an increase in the use and understanding of digital metrological twins by calibration laboratories and less experienced users in the scientific community.

Introducing new terms into the Glossary can provide input to international and national standards bodies dealing with freeform coordinate metrology for future extensions of the ISO 10360 and ISO 1101 series and support more consistent terminology for digital twin concepts in advanced manufacturing.

Acknowledgement

The project “Application of Digital-Metrological Twins for emerging measurement technology in advanced manufacturing” (ADAM, grant number 23IND12) has received funding from the European Partnership on Metrology, co-financed from the European Union’s Horizon Europe Research and Innovation Programme and by the Participating States.

References

[1] 23IND12 ADAM: Application of Digital-Metrological Twins for emerging measurement technology in advanced manufacturing. https://www.adam.ptb.de/home. 2024 – 2027 [Accessed 05-01-2026]

[2] ISO/IEC 30173:2023 Digital twin — Concepts and terminology

[3] Härtig F, Kniel K and Heißelmann D 2023 Das Virtuelle Koordinatenmessgerät – ein Digitaler Metrologischer Zwilling *tm – Technisches Messen* **90.9** pp. 548–556 doi.org/10.1515/teme-2023-0066

[4] ISO 17450-1:2011 Geometrical product specifications (GPS) — General concepts Part 1: Model for geometrical specification and verification

[5] Jiang J X and Scott J P 2020 Advanced Metrology Chapter 1 – Introduction, Academic Press pp. 1–9. ISBN: 978-0-12-821815-0 doi.org/10.1016/B978-0-12-821815-0.00001-0

[6] Anwer N, Ballu A and Mathieu L 2013 The skin model, a comprehensive geometric model for engineering design *CIRP Annals* **62.1** pp. 143–146. ISSN: 0007-8506 doi.org/10.1016/j.cirp.2013.03.078

[7] Zelený V, Linkeová I and Skalník P 2015 Calibration of freeform standard, Proceedings of the 15th International Conference of the European Society for Precision Engineering and Nanotechnology, EUSPEN, 2015, pp. 147–148.

[8] Sýkora J, Linkeová I and Skalník P 2023 Freeform digital twin approach to develop the HP 300 freeform verification standard *Measurement* **218** p. 113227 ISSN: 0263-2241 doi.org/10.1016/j.measurement.2023.113227

[9] ISO 1101:2017 Geometrical Product Specifications (GPS) – Geometrical Tolerancing – Tolerances of Form, Orientation, Location and Run-Out

euspen's 26th International Conference & Exhibition, Krakow, PL, June 2026
www.euspen.eu

Mathematical softgauges: a new method for validating metrology algorithms

Blateyron F[1]
[1] Digital Surf, Besançon, France
Corresponding author: fblateyron@digitalsurf.fr

Abstract
Surface texture parameters, filters and association methods are defined by ISO standards in the continuous world (ISO 21920-2 [1], ISO 25178-2 [2]…). However, their implementations in software packages are always done in the discrete world and applied on digital data. Metrology software editors need to be able to check their implementations against references, the same way instrument manufacturers use material measures to calibrate their instruments and calculate uncertainties. For several years, NMIs have issued so-called *reference software* or algorithms, in an effort to standardize implementations, but these reference software packages have never been close to a reference, with even different reference software giving different results! [3]. This is why, in the recent years, a new concept was introduced, based on mathematics, and with a framework allowing editors to check any implementation and assess the deviation from true values. This method is currently described in a draft standard within the ISO 25178 series (part 74). This paper provides a short overview of the benefits of this method and its applications.

Keywords: material measure, mathematical softgauge, ISO 5436-2, reference software

1. Introduction

The purpose of the proposed method is to provide an absolute reference that is independent from any implementation, based on mathematics. The input data (profile or surface) is defined by an equation (called a *mathematical softgauge*), then is inserted in the definition equation of a surface texture parameter and the combined equation is then solved formally to obtain the parameter result value as an equation (called *mathematical true value*).

The pair [*mathematical softgauge*, *mathematical true value]* can be considered as a software material measure, with a similar use as a hardware material measure and its calibrated value. This method is quite new to surface texture as the concept of reference software (type F2 software measurement standard) was previously preferred. A few authors have applied similar methods but without explaining clearly the global framework [3, 4].

2. Methodology

In order to test an implementation, it is necessary to create a discrete version of the *mathematical softgauge*, called the *realised softgauge*. On the other hand, a *realised true value* is calculated with any number of decimal places.

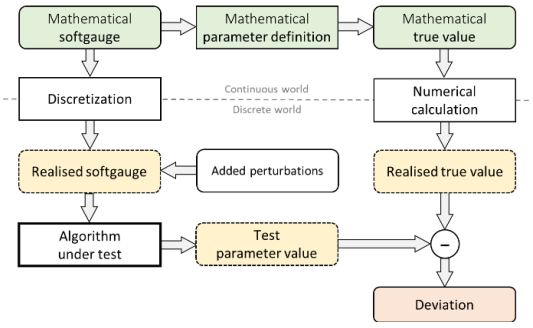

Figure 1: *workflow for testing a parameter algorithm*

ISO/WD 25178-74, under development, defines new terms:

- Mathematical softgauge: input data described by an equation $z = f(x)$ for a profile or $z = f(x, y)$ for a surface. These equations may depend on design parameters (amplitude, wavelength, …)
- Mathematical true value: equation obtained by combining the equation of the mathematical softgauge and the equation of the parameter (or filter).
- Realised softgauge: data file obtained by sampling the mathematical softgauge with a given lateral resolution and with a given discretization step in Z. This file is used as an input to the algorithm under test.
- Realised true value: numerical value obtained by assigning values to the design parameters of the mathematical true value, and calculated to a given number of decimal places.

The method for testing an algorithm consists in loading the *realised softgauge* into the software, calculate the *test parameter value*, and compare it to the *realised true value*. The deviation allows the editor to identify potential causes of inaccuracies.

This method also makes it possible to assess the stability of a parameter definition by adding perturbations in the realised softgauge, such as noise, outliers, slope, etc. Unstable algorithms (or parameter definitions) can be identified when the output value shows large deviations for a small input perturbation.

The method is also compatible with the test of filters (Gaussian, Spline…) [5] and association methods (levelling, form removal…) [6].

Finally, the mathematical softgauge can represent other types of curves such as the Abbott or autocorrelation curve, in order to test material ratio or volume parameters [7].

An example can be given with a sinusoidal profile defined by:

$$z(x) = A \sin\left(\frac{2\pi x}{\lambda}\right)$$

By combining this equation with parameter equations, we can deduce their respective *mathematical true values*, and by assigning values to the amplitude *A*, we can calculate the numerical approximation (*realised true value*).

Mathematical true value	Realised true value
$P_a = \frac{2A}{\pi}$	$P_a = 3{,}183\ 098\ 861\ 838\ \mu m$
$P_q = \frac{A}{\sqrt{2}}$	$P_q = 3{,}535\ 533\ 905\ 933\ \mu m$
$P_{sk} = 0$	$P_{sk} = 0{,}000\ 000\ 000\ 000\ \mu m$
$P_{ku} = \frac{3}{2}$	$P_{ku} = 1{,}500\ 000\ 000\ 000\ \mu m$

3. Towards a new standard

The working group WG16 of ISO TC 213 has started in 2024 the drafting a new standard describing this method with the intention to complement existing standards related to material measures and softgauge file format. This standard will replace ISO 5436-2 [9] that defines reference data (type F1) and reference software (type F2). Together with the replacement of ISO 5436-1 [8] by ISO 25178-70 [10], it will be possible to withdraw both parts of ISO 5436 that are more than 25 years old.

Mathematical softgauges are introduced as a type F3 software measurement standard, and the two other ones are renamed:

- *reference data* is now called *traceable softgauge*
- *reference software* is now called *traceable software*

The three software measurement standards are organized in a hierarchical way, similar to the chain of traceable references used in accreditation tasks.

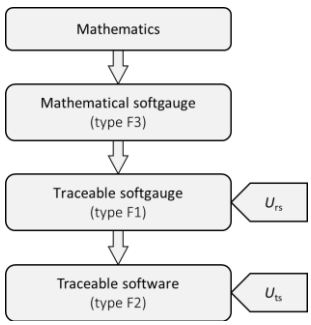

Figure 2: *hierarchy chain for software measurement standards*

The type F3 standard remains in the mathematical domain but the *traceable softgauge* is a discrete data file that is affected by an uncertainty U_{rs} that represents errors due to the sampling and discretisation.

The *traceable software* is an algorithm that implements a parameter calculation or a filter. It is affected by an uncertainty U_{ts} that represents errors due to implementation choices such as the type of integration (simple summation, linear interpolation, spline interpolation…) or the type of gradient (simple difference, 3-term approximation, 5-term approximation…) A traceable software needs to be validated for a set of parameters using mathematical softgauges. Once it is validated, it can verify real data files that are measured by instruments or generated by an algorithm.

4. Conclusion

Mathematical softgauges allow software developers to implement their algorithms as they wish but provide them a mean of calibrating the results produced by their implementations.

This new concept is independent from any implementation and is based upon mathematics. It can therefore be considered as a genuine reference, contrary to the old concept of reference software that could not be considered as references despite their name [3].

Unfortunately, not all parameters can be validated that way because either the calculation of the mathematical true value is too complex, or because the parameter is not defined using an equation but rather by an algorithm, such as the R&W parameters of ISO 12085 [11].

The majority of profile and areal parameters implemented in the Mountains® analysis software [12] have been successfully tested with this method. This method has revealed its potential for detecting small numerical inaccuracies in algorithm implementations [6], which are normally undetectable on real data and are often indicative of sub-optimal implementation.

References

[1] ISO 21920-2:2021 Geometrical product specifications (GPS) — Surface texture: Profile Part 2: *Terms, definitions and surface texture parameters*

[2] ISO 25178-2:2021 Geometrical product specifications (GPS) — Surface texture: Areal Part 2: *Terms, definitions and surface texture parameters*

[3] Todhunter L, Leach R K, Lawes S D A, Blateyron F, 2017, *An Analysis of Type F2 Software Measurement Standards for Profile Surface Texture Parameters*, Measurement Science and Technology, DOI: 10.1088/1361-6501/aa6924

[3] Todhunter L, Leach RK, Lawes SDA, Harris P, Blateyron F, 2019, *Mathematical approach to the validation of functional surface texture parameter software*, Surf. Topogr.: Metrol. Prop.

[4] Todhunter L, Leach RK, Lawes SDA, Harris P, Blateyron F , 2020, *Mathematical approach to the validation of field surface texture parameter software*, Surf. Topogr.: Metrol. Prop.

[5] Todhunter L, Leach RK, Blateyron F, 2020, *Mathematical approach to the validation of surface texture filtration software*, Surf. Topogr.: Metrol. Prop.

[6] Todhunter L, Leach RK, Blateyron F, 2020, *Mathematical approach to the validation of surface texture form removal software*, Surf. Topogr.: Metrol. Prop.

[7] Blateyron F, Breton S, 2024, *Mathematical softgauges for material ratio parameters*, Surf. Topogr.: Metrol. Prop.

[8] ISO 5436-1:2000 Geometrical product specifications (GPS) — Profile method: Measurement standards, Part 1: material measures

[9] ISO 5436-2:2000 Geometrical product specifications (GPS) — Profile method: Measurement standards, Part 2: Software measurement standards

[10] ISO 25178-70:2014 Geometrical product specifications (GPS) — Surface texture: Areal, Part 70: Material measures

[11] ISO 12085:1996 Geometrical product specifications (GPS) — Profile method: Motif parameters

[12] MountainsMap®, surface texture analysis software by Digital Surf, France. https://www.digitalsurf.com/software-solutions/profilometry/

euspen's 26th International Conference & Exhibition, Krakow, PL, June 2026
www.euspen.eu

Automated Geometric Segmentation of Additively Manufactured Strut-Based Lattices for Geometric Characterization: Node – based Analysis

Y. Zekalmi [1a], D. Gallardo[2], L.C. Díaz-Pérez[2], J.A. Albajez[2], J.A. Yagüe-Fabra[2]

[1] *University of Zaragoza, Zaragoza, Spain*
[2] *I3A, Universidad de Zaragoza, Zaragoza, Spain*

[1a] *yzekalmi@unizar.es*

Abstract

The metrological characterization of strut-based lattices manufactured through additive processes is a crucial step for quality assurance and bridge the gap between nominal designs and the actual fabricated geometries. Understanding this discrepancy is particularly relevant for predicting performance, since deviations in shape, surface quality, or internal structure may significantly affect the mechanical response. In this work, we present a first approach to a general automated framework for lattice evaluation through a node – based segmentation of the structure, combining digital design models with data acquired from high-resolution X-ray computed tomography (XCT) measurements. The workflow incorporates robust geometric operations to segment and analyse individual features of the lattice, ensuring scalability and reproducibility across different unit cells and fabrication routes. Comparisons between reference models and manufactured parts allow systematic quantification of deviations, highlighting the role of process-induced imperfections on lattice morphology. This initial stage lays the foundation for a methodology that offers a flexible and reliable approach for the assessment of strut-based architectures, providing valuable insights to support optimization and performance prediction in a wide range of engineering applications.

Keywords: lattice structures, additive manufacturing, x-ray computed tomography, geometric analysis

1. Introduction

Additive manufacturing (AM) enables lattice architectures that combine low mass with tailored stiffness, energy absorption, and functional performance, making them attractive for aerospace, biomedical and lightweight engineering applications [1]. However, the as-built geometry of strut-based lattices often departs from the nominal CAD definition because the process locally alters strut cross-sections, junction morphology and surface texture, which in turn changes load paths and amplifies stress concentrations. For this reason, robust geometric verification is a prerequisite for trustworthy performance prediction and for closing the design–manufacture loop.

X-ray computed tomography (XCT) is particularly suited to lattice metrology because it provides non-destructive 3D access to internal and external geometry, but it also raises the practical challenge of making CAD-XCT comparisons repeatable at scale. Recent studies have advanced traceable XCT workflows for lattice dimensional verification using calibrated artefacts [2], and have proposed experimental strategies to determine measurement uncertainty specifically for lattice geometries [3]. Hybrid approaches that combine tactile probing with XCT have been used to strengthen dimensional metrology of complex lattices [4], while holistic XCT-based evaluation strategies have been proposed to quantify strut-level geometric characteristics across the structure [5]. In parallel, dedicated geometry-processing tools have been released to extract surface and geometric descriptors from lattice data in a more automated manner [6]. These contributions confirm the maturity of XCT for lattice inspection, yet they also highlight that most reported metrics remain global or strut-averaged, which can mask highly localized defects.

At the feature scale, node morphology is increasingly recognized as critical because junction overgrowth, under-melting, and local defects strongly influence stiffness and failure initiation. Node-focused work has included non-destructive, simulation-driven studies of node defects extracted from lattice reconstructions [7], and image-based methodologies to characterize node geometry in additively manufactured lattices [8]. More recent efforts have combined XCT with surface metrology to quantify lattice surface characteristics beyond simple dimensional error [9], and have studied how strut shape affects as-built quality and mechanical response [10]. Related investigations have examined how node size impacts lattice behaviour [11] and how geometric defects propagate in lattice-filled thin-walled structures [12]. Progress on XCT accuracy/traceability for polymer AM has been done; wall-thickness/through-hole evaluation in thin hollow lattices [13], and XCT-based porosity assessment further reinforces the need for feature-consistent, traceable characterization pipelines [14].

In this paper, we address one of the remaining gaps: XCT inspection provides high amount of metrological data; however, CAD-XCT comparison is still not consistent feature-by-feature across many repeated nodes. We exploit the known CAD topology by using CAD node centres, obtained after a proper registration. Using these positions, the XCT mesh is automatically partitioned to recover the as-manufactured node locations. This nominal–real correspondence enables consistent node-wise deviation and lattice-graph deviation analyses. The

final objective is to provide a robust, automated basis for quantifying manufacturing-induced geometric variability in strut-based lattices.

2. Methodology

This section outlines the workflow to compare a designed lattice (CAD) with its manufactured geometry (obtained by XCT) in a simple, repeatable way. The method has five stages: (1) align the XCT mesh to the CAD model with a rigid best-fit, so both are in the same position and orientation; (2) read the nominal lattice layout from CAD and extract the node centers (the junction points where struts meet); (3) define a small "neighborhood" around each node (a region of influence) to look for that junction in CT; (4) assign the XCT surface points to their nearest node neighborhood, creating one small XCT sub-mesh per node; and (5) compute easy node-level descriptors (such as node offset and a graph-based deviation view along strut connections) to compare CAD vs XCT, highlight spatial trends, and flag outlier nodes for inspection.

3. Proposed node segmentation workflow

This section introduces the node-seeded workflow that converts dense XCT surfaces into topology-consistent, per-node descriptors.

Fig. 1 summarizes the nominal lattice and its graph: nodes represent junction centers and edges represent strut connectivity between nodes. This graph view is later used to define node-centered search regions so that CAD–XCT comparisons are performed feature-by-feature, not only as a global distance map.

In this work, the workflow is demonstrated and validated using a simple cubic unit cell (SC). However, the procedure is fully automated and formulated independently of the unit-cell definition, allowing node-region segmentation to be applied to lattices based on arbitrary strut-based unit-cell topologies.The graph is written as $G = (V, E)$:

• V (nodes): the junction points where struts meet (black dots in Fig. 1).

• E (edges): links between pairs of nodes. In a lattice, each edge corresponds to one strut segment between two junctions.

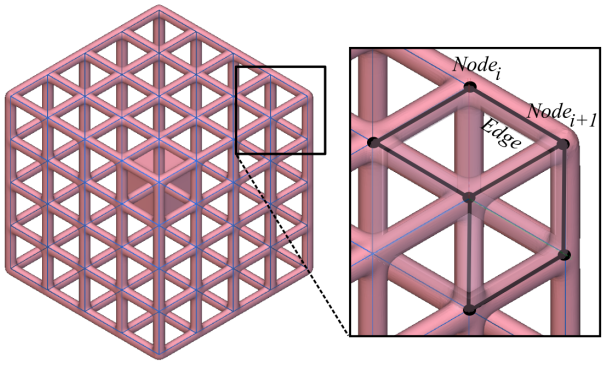

Figure 1. Lattice graph of a simple cubic unit cell. Nodes and edges.

3.1. XCT to CAD allignement and registration

Reliable CAD–XCT comparison requires aligning the XCT-derived (as-manufactured) surface with the nominal CAD lattice in a common frame. For periodic lattices, global registration can be ambiguous due to geometric symmetry, as multiple orientations may yield similar residuals. To ensure a unique and reliable initial alignment, a small reference cube is added at a known external corner of the CAD lattice. XCT mesh is then rigidly refined to the CAD using iterative closest point (ICP) algorithm with ZEISS Inspect. Fig. 2 shows the CAD–XCT deviation map and histogram: positive values mean XCT lies outside CAD, negative inside. Vertical struts (+Z) show mostly negative deviation (reduced diameter), while horizontal struts show positive deviation on top/bottom faces (expansion along Z).

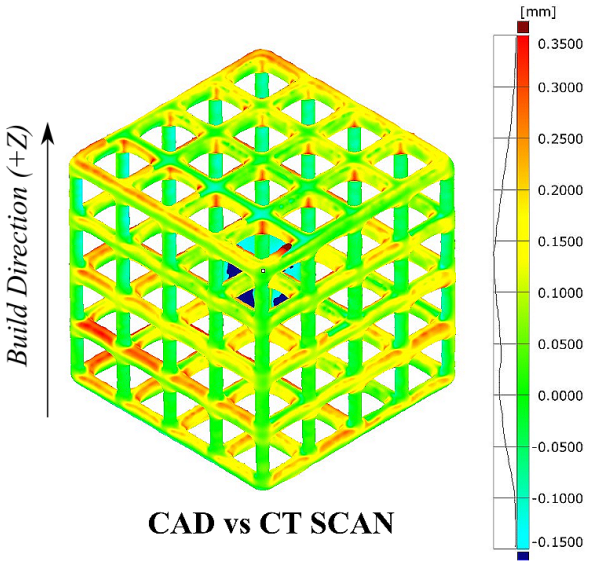

Figure 2. CAD and XCT scan surfaces comparison; Deviation (mm).

This comparison is informative; however, additional validation is needed to assess how node junctions deviate during the manufacturing process. In particular, node-level deviations should be quantified consistently, since local effects may not be fully captured by a global surface comparison.

3.2 Automated node finding and computation

The global alignment reduces the overall deviation between the designed geometry (CAD) and the manufactured part (XCT scan), but it does not enable a node-wise, local comparison of the two surfaces. Therefore, an automated procedure is required to identify and match corresponding nodes on the XCT geometry, so that local deviations can be quantified consistently.

After rigid CAD–XCT registration, the as-manufactured node locations are automatically recovered using the nominal CAD nodes as seeds. Fig. 3 summarizes the workflow: each designed node center c_i defines a Sphere of Interest (SOI) intended to enclose the local junction geometry (the node and the adjacent strut roots). The SOI provides a local search window, preventing ambiguity caused by the periodic repetition of lattice unit cells. The SOI radius r_{SOI} is chosen to fully capture node swelling while minimizing overlap with neighboring nodes. For every XCT surface vertex x we evaluate the signed distance function (SDF) of the SOI sphere $\varphi_i(x)$. Vertices with $\varphi_i(x) < 0$ lie inside the sphere and are kept; vertices with $\varphi_i(x) \geq 0$ are discarded, Eq. 1. Then, the retained vertex subset for node i is V_i, Eq. 2.

$$\varphi_i(x) = \|x - c_i\| - r_{SOI} \qquad (1)$$

$$\mathcal{V}_i = x_k \, (\varphi_i(x_k) < 0) \qquad (2)$$

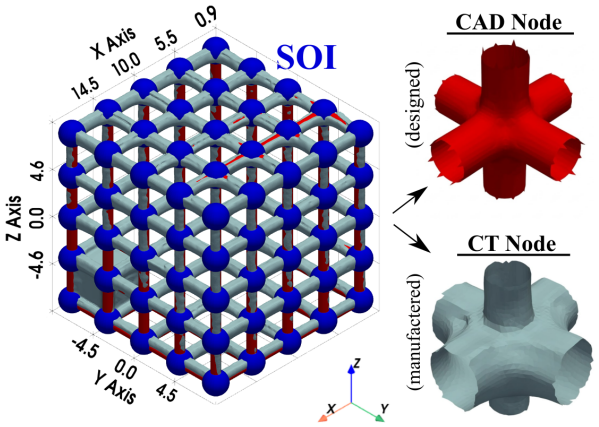

Figure 3. Node segmentation of XCT surfaces using Spheres of Interest (SOI) seeded from nominal CAD node centers.

This filtering step is computationally efficient because it only requires Euclidean distance evaluations and can be applied in a vectorized manner over all XCT vertices. The retained vertices define a local XCT surface patch around the node region. However, XCT meshes often exhibit non-uniform triangle sizes and vertex densities (for example, higher sampling in high-curvature areas), which can bias a simple mean or centroid estimate. For this reason, the extracted patch is uniformly remeshed to obtain a more even (approximately area-uniform) sampling of the surface, so that all parts of the node contribute more equally to the estimated center. After remeshing, the node location is estimated as a robust "center" of the patch; the geometric mean, described in Eq. 3, where N_v is the number of vertices inside the SOI.

$$p_i^{CT} = \frac{1}{Nv}\sum x_k \qquad (3)$$

In practice, for speed, we use the centroid of the uniformly remeshed vertices, which becomes the recovered XCT node center. Finally, the node deviation between ideal and manufactured is computed with Eq. 4. This provides per-node displacement components that can be plotted across the lattice to reveal spatial trends and identify outliers for deeper inspection. This algorithm has been developed in Python, including data analysis and visualization.

$$\Delta p_i = p_i^{CT} - c_i = [d_{x,i}, d_{y,i}, d_{z,i}]^{\mathrm{T}} \qquad (4)$$

4. Experiments and results

This section presents the validation of the proposed workflow evaluated on an SLS strut lattice. After rigid CAD–XCT alignment, each CAD node seeds extraction of a XCT node patch, which is uniformly remeshed to recover XCT node centers. Node deviations are computed and visualized per node and across the node–edge graph to obtain a readable graph deviation field.

Table 1 summarizes the specimen and measurement settings. The lattice has external dimensions of 16 × 16 × 16 mm and a unit cell size of 4 × 4 × 4 mm, resulting in a regular array of repeated node–edge patterns. This controlled geometry is useful because it separates two effects: (i) deviations caused by registration or reconstruction noise and (ii) systematic manufacturing effects that vary with position (interior vs boundary) and height (bottom vs top, along the build direction +Z).

Fig. 4 reports node-level results. Fig. 4(a) plots d_x, d_y and d_z for all nodes (ordered by index), showing that displacement is not uniform and that peaks occur at specific node locations. This plot is informative because it separates directional effects: for example, a systematic bias in d_z would indicate build-direction drift, whereas larger variations in d_x or d_y can indicate lateral distortion or residual alignment error.

***Table 1**. Specimen and XCT measurement summary*

Item	Value
Lattice type	Simple cubic strut-based lattice; node–edge graph representation
External dimensions	16 × 16 × 16 mm
Unit cell dimensions	4 × 4 × 4 mm
Strut diameter	1 mm
Manufacturing process	SLS, material: (PA12)
Build direction	+Z
XCT scanner / settings	Zeiss Metrotom 800/225 HR, 120 kV, 220 µA, Al 2.0 mm filter, exposure time 1000 ms, 1500 projections.
Voxel size / resolution	24.59 µm
Reconstruction/surface extraction	Adaptative local gradient

Fig. 4(b) shows a representative node (Node 50) with minimal deviation, where the manufactured node surface remains close to the designed CAD junction after alignment. Fig. 4(c) shows a node with maximal deviation (Node 120), where the XCT node surface visibly deviates from the designed junction shape. Importantly, the node-wise framework makes such outliers traceable: the node index identifies which junction to inspect in the XCT volume, while the deviation components provide a quantitative trigger for automated flagging.

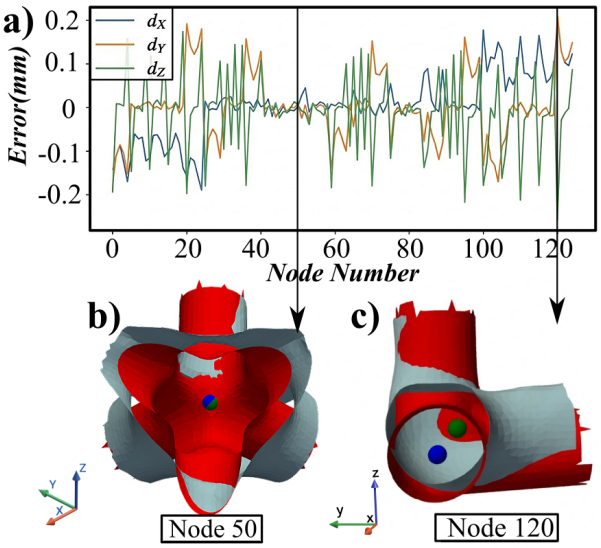

Figure 4. (a) Node difference between CAD and XCT scanned (Δp_i), designed vs manufactered. (b) Node 50 with minimal difference, and (c) Node 120 with maximum deviation.

Fig. 5 complements the node plots by visualizing deviations on the lattice graph. In Fig. 5(a) (isometric view), the deviation field highlights a spatial gradient from the interior (lower deviation) toward the boundary (higher deviation). The YZ view in Fig. 5(b) emphasizes height-dependent behavior along the build direction: lower planes near Z=-8 mm show reduced deviations compared with the upper planes near Z=+8 mm. Presenting results in graph form is helpful because it ties deviations directly to topology (nodes and their connections), which is the natural description used in downstream models such as homogenization or graph-based learning. Deviations are smaller near the lattice center and larger at the boundaries, likely because interior nodes have higher connectivity and are more constrained.

Deviations also increase with build height: nodes near the build plate show less deviation than those near the top, consistent with stronger support and heat sinking at lower layers and greater accumulated distortion above. Overall, these results demonstrate that the proposed segmentation provides a consistent CAD to XCT correspondence at the feature level and enables both local (node) and global (graph) deviation interpretation in a way that remains readable even for large lattices.

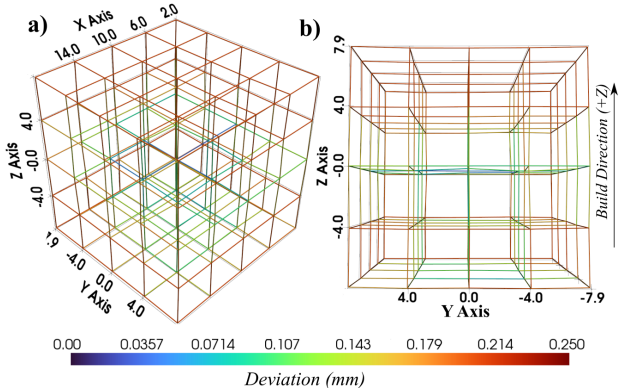

Figure 5. CAD-to-XCT Edge Deviation Field on the Lattice Graph. (a) Isometric view, and (b) YZ view.

5. Conclusions and future work.

An automated node-based workflow was used to compare a nominal CAD lattice with an as-manufactured XCT mesh. After rigid alignment, each CAD node was used as a seed to isolate a local XCT node region using a sphere-of-interest distance filter, and node centers were recovered from the filtered surface. Deviations are not uniform: they are typically smaller near the lattice core and larger near external boundaries, consistent with interior nodes being more constrained by higher connectivity while boundary nodes are more sensitive to free-surface process effects. The main effect is due to the best-fit allignement o the software. A build-direction trend is also observed: nodes closer to the build plate show lower deviations than nodes near the top.

The method enables repeatable node-by-node inspection and automated outlier detection. Future work will implement local best-fit alignment within each segmented zone, extend segmentation to strut-only regions for strut-level metrics, and link geometric deviations to mechanical response via simulation or homogenization with repeatability studies across builds and XCT settings.

Acknowledgments

This work was supported by grant PID2024-157236OB-I00 funded by MICIU/AEI/10.13039/501100011033 and, “ERDF A way of making Europe”, by “ERDF/EU”. The authors also thank the Gobierno de Aragón for its support within the framework of grants for research activity of recognized groups (T56_23R: GIFMA). Additionally, the authors acknowledge the use of Servicio General de Apoyo a la Investigación-SAI, Universidad de Zaragoza.

References

[1] F. Zanini, M. Sorgato, E. Savio, and S. Carmignato, “Dimensional verification of metal additively manufactured lattice structures by X-ray computed tomography: Use of a newly developed calibrated artefact to achieve metrological traceability,” Additive Manufacturing, 2021. DOI 10.1016/j.addma.2021.102229

[2] F. Zanini, S. Carmignato, and E. Savio, “Two different experimental approaches for the uncertainty determination of X-ray computed tomography dimensional measurements on lattice structures,” CIRP Journal of Manufacturing Science and Technology, 2024. DOI 10.1016/j.cirpj.2023.10.004

[3] A. du Plessis, A. Townsend, P. J. Scott, and R. K. Leach, “Dimensional metrology of additively manufactured lattice structures by combined tactile probe and X-ray tomography,” Materials Design & Processing Communications, 2021. DOI 10.1002/mdp2.216

[4] D. Rathore, P. A. Williams, and K. S. Rao, “A Methodology for Computed Tomography-Based Non-Destructive Geometrical Evaluations of Lattice Structures by Holistic Strut Measurements Approach,” Journal of Manufacturing Science and Engineering, 2021. DOI 10.1115/1.4049492

[5] B. Lozanovski, C. Downing, and A. T. Clare, “Non-destructive simulation of node defects in additively manufactured lattice structures,” Additive Manufacturing, 2020. DOI 10.1016/j.addma.2020.101593

[6] B. Lozanovski, A. T. Clare, and R. S. Trask, “Image-Based Geometrical Characterization of Nodes in Additively Manufactured Lattice Structures,” 3D Printing and Additive Manufacturing, 2021. DOI 10.1089/3dp.2020.0091

[7] L. Jiang, Y. Li, M. Dong, J. Zhao, and Y. Du, “Micro-CT-based strut shape analysis reveals manufacturing and post-processing effects in additively manufactured lattice structures,” Additive Manufacturing Letters, 2025. DOI 10.1016/j.addlet.2025.100346

[8] J. E. Oosterbeek and J. R. Jeffers, “StrutSurf: A geometry and surface analysis tool for additively manufactured lattice structures,” StrutSurf, 2022. DOI 10.1016/j.softx.2022.101043

[9] Q. Zheng, Y. Huang, H. Huang, L. Wang, L. Zhang, and S. Xu, “Quantitative surface characterisation and stress concentration factors of additively manufactured lattice struts,” The International Journal of Advanced Manufacturing Technology, 2024. DOI 10.1007/s00170-024-13024-w

[10] L. Liu, B. Zhang, and B. Wang, “Dimensional effect and mechanical performance of additively manufactured lattice structures based on different node sizes,” Virtual and Physical Prototyping, 2023. DOI 10.1080/17452759.2023.2240306

[11] H. Li, S. Huang, Y. Zhou, Z. Zhou, M. Gao, and C. Chen, “Effect of geometric defects on mechanical properties of lattice-filled thin-walled structures fabricated by additive manufacturing,” Thin-Walled Structures, 2024. DOI 10.1016/j.tws.2024.112497

[12] D. Gallardo, L. C. Díaz-Pérez, J. A. Albajez, and J. A. Yagüe-Fabra, “Progress toward the Definition of Accuracy and Traceability of X-ray Computed Tomography Measurements for Polymer Additive Manufacturing,” Polymers, 2024. DOI 10.3390/polym16101419

[13] M. Holgado, H. Villarraga-Gómez, M. Martínez, J. A. Yagüe-Fabra, and D. Gallardo, “Towards the Metrological Evaluation and Accuracy Improvement of Wall Thickness Estimations and Through-Hole Measurements in Industrial X-Ray Computed Tomography,” Journal of Nondestructive Evaluation, 2025. DOI 10.1007/s10921-025-01269-8

[14] A. Chahid, L. M. Enquist, M. A. Gomaa, S. M. Wald, H. M. ElSawy, and N. M. Wereley, “Parametrically Designed Surface Topography on CAD Models of Additively Manufactured Lattice Structures for Improved Design Validation,” Additive Manufacturing, 2021. DOI 10.1016/j.addma.2020.101731

euspen's 26th International Conference & Exhibition, Krakow, PL, June 2026
www.euspen.eu

Deep learning-based removal of phase shift errors in phase-shifting interferometry for high-accuracy surface metrology

Young-Sik Ghim[1, 2,*], Manh The Nguyen[1], Hyug-Gyo Rhee[1, 2]

[1]*Length and Dimensional Metrology Group, Division of Physical Metrology, Korea Research Institute of Standards and Science (KRISS), Science Town, Daejeon 34113, South Korea*
[2]*Department of Science and Measurement, University of Science and Technology (UST), Science Town, Daejeon 34113, South Korea*

**young.ghim@kriss.re.kr*

Abstract
Accurate 3D surface metrology is indispensable in high-technology sectors such as semiconductor and aerospace industries. Phase-shifting interferometry is a well-established optical technique, renowned for its exceptional precision and speed, making it suitable for industrial inspection and measurement. However, phase-shift inaccuracies between interferograms can result in fringe-print-through errors, effecting the precision of surface measurements. In this paper, we present a novel deep learning-based method to mitigate these errors in phase-shifting interferometry. Our proposed approach utilizes a UNet++ deep learning model that processes an error-embedded surface phase map as input to directly predict the corresponding phase-shifting errors. Trained exclusively on simulated datasets, the model learns to isolate and quantify these specific inaccuracies. Both simulation and experimental results confirm that our deep-learning approach effectively eliminates phase-shifting errors with high versatility, rapid processing, and robustness. This advancement results in a significant improvement in the measurement accuracy of phase-shifting interferometry, enhancing its reliability for demanding metrological applications.

Phase-shifting interferometry, Fringe-print-through error, Deep learning

1. Introduction

Optical interferometry plays a crucial role in measuring the flatness, surface roughness, and film thickness of semiconductor wafers with high precision. The phase-shifting technique [1, 2] provides 3D surface profiles with sub-nanometer resolution, making it a key metrology solution in the semiconductor industry. However, in phase-shifting interferometry, measurement errors typically arise from inaccurate phase shift amounts and environmental factors such as temperature, vibration, and air turbulence [3, 4].

Dynamic interferometry using polarization-based retrieval [5-8] offers real-time single-shot measurements, but is highly susceptible to errors from optical components. The fringe-print-through (FPT) phenomenon [9, 10], caused by inaccurate phase retardation, misaligned polarization angles, and nonuniform transmittance, introduces ripple-like phase errors that significantly compromise measurement accuracy. While various approaches have been proposed to address these errors, model-based algorithms struggle to fully adapt to varying conditions. This paper proposes a novel deep learning-based measurement algorithm using Unet++ architecture to effectively remove FPT errors while maintaining the real-time advantage of dynamic interferometry [11].

2. Fringe-print-through error removal using deep learning

2.1. Network architecture and training strategy

The proposed FPT error removal method uses Unet++ deep learning architecture. The input is the phase map with FPT error after removing 64 Zernike terms, and the output is the corresponding FPT error. The network learns to predict FPT error directly from the input phase map through proper training. The encoder path consists of convolution blocks with filter size of 32, kernel size of 3, ReLU activation, and MaxPooling layers. The input size is defined as (None, None) to accept different image sizes during inference

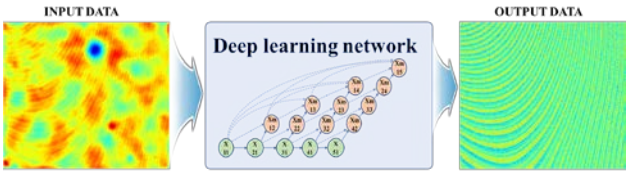

Figure 1. General diagram of proposed method. Our general idea is by training a deep learning network with the input is phase map with nonlinearity error from polarized camera and output is the corresponding nonlinearity error, the model can learn how to predict error from new phase map

2.2. Training data generation

An interferometry system with polarized camera and a piezoelectric deformable mirror (Thorlab DMH40/M-P01) was used to generate training data. By randomly changing Zernike coefficients, different mirror shapes were generated. For each shape, 10 phase-shift patterns were captured with 50nm steps. The ground truth phase (without FPT error) was obtained by averaging 10 unwrapped phases. The phase from a single interferogram contains FPT error and is used as input. The output training data is the difference between the input phase and the ground truth phase. After Zernike polynomial fitting up to 64 terms to remove the free-form shape, the FPT error becomes clearly visible. A total of 1,000 training data (1024×1224 pixels) were generated and cropped into 16,000 images (256×256 pixels), divided into 13,000 training and 3,000 validation set.

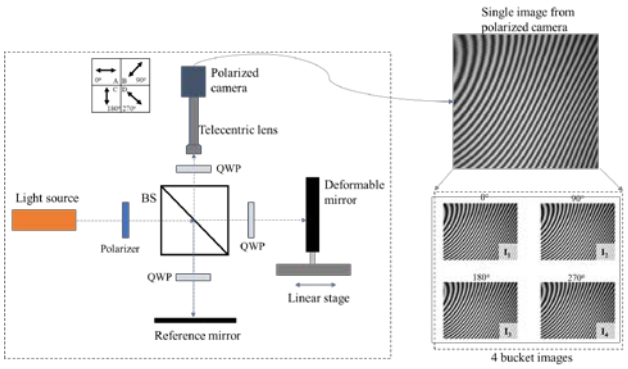

Figure 2. System setup for generating training data. Polarized camera captured the single interferogram images which contain 4 phase-shift images

3. Results

In real application, after getting the new input phase from single image using polarized camera, we remove the first 64 Zernike terms to get the phase with FPT error presented as input data. Then, DL network will be used to predict the FPT error from input data and the final error-free phase is obtained by subtracting the input data to predicted phase error as described in Fig. 3.

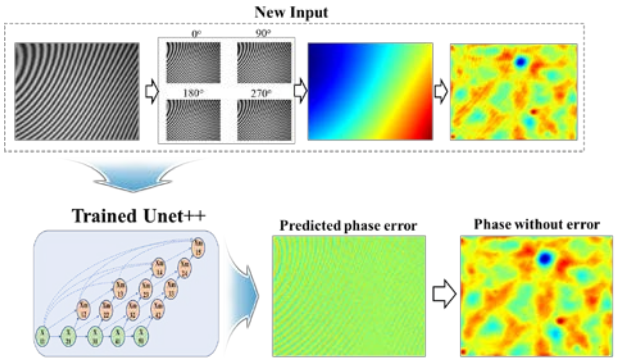

Figure 3. General FPT error removal process from a single polarized camera image with trained deep learning network

In order to evaluate the effectiveness of proposed method, we performed an experiment by measuring a concave mirror. The concave mirror sample is Thorlabs CM508-200-G01. As we can see in Fig. 3 (c), the FPT error is greatly reduced compare to original one even though it is still not completely removed. There are still small amount of FPT error presented in the phase map. This could be improved by using more phase-shifting images to improve the ground-truth in the training and increasing the number of training data.

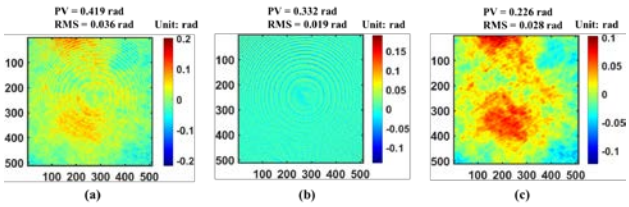

Figure 4. FPT error removal in free-form surface measurement using interferometer. (a) Phase of concave mirror with FPT error, (b) Predicted FPT error, and (c) Phase after subtracting the FPT error.

4. Conclusion

In conclusion, we demonstrated a deep learning based- FPT error removal method for polarized camera. By using deformable mirror to obtain training data and averaging technique to obtain error-free ground truth, trained deep learning network could effectively help to reduce the FPT error on the phase map by half as demonstrated in the experimental section. The performance of deep learning network could be improved more if we can obtain better error-free ground truth by increasing the number of phase-shift and increasing the number of data in the averaging step with the trade-off of increasing the time for preparing training data. However, once model is trained, we can removed the FPT error on the phase map obtained from polarized camera very quickly and efficiently which help perform one-shot or real-time measurement with higher accuracy. The performance of deep-learning based FPT error removal could also be improved if we can optimize and apply state-of-the-art deep learning networks. In general, this deep-learning based FPT method open up a new robust, high-speed method in improving the measurement accuracy of dynamic interferometry.

5. Funding

This work was supported by the Technology Innovation Program (or Industrial Strategic Technology Development Program) ("RS-2023-00237714", Development of Dynamic Metrology Tool for CMP Process Stabilization) funded By the Ministry of Trade, Industry & Energy (MOTIE, Korea) (1415187786)

References

[1] J. H. Bruning, D. R. Herriott, J. E. Gallagher, D. P. Rosenfeld, A. D. White, and D. J. Brangaccio, "Digital Wavefront Measuring Interferometer for Testing Optical Surfaces and Lenses," Appl. Opt. 13, 2693-2703, 1974.

[2] J. C. Wyant, “Interferometric optical metrology: basic system and principles,” Laser Focus 65–71, 1982

[3] K. Kinnstaetter, Adolf W. Lohmann, Johannes Schwider, and Norbert Streibl, "Accuracy of phase shifting interferometry," Appl. Opt. 27, 5082-5089, 1988.

[4] J. Schmit and K. Creath, "Extended averaging technique for derivation of error-compensating algorithms in phase-shifting interferometry," Appl. Opt. 34, 3610-3619, 1995.

[5] J. Millerd, N. Brock, J. Hayes, M. North-Morris, M. Novak and J. C. Wyant, “Pixelated phase-mask dynamic interferometer,” Fringe 2005: The 5th International Workshop on Automatic Processing of Fringe Patterns. Springer Berlin Heidelberg, 2006

[6] N. Brock, J. Hayes, B. Kimbrough, J. Millerd, M. North-Morris, M. Novak and J. C. Wyant, "Dynamic interferometry." Novel optical systems design and optimization VIII. Vol. 5875. SPIE, 2005.

[7] D. M. Sykora, and Peter de Groot. "Instantaneous measurement Fizeau interferometer with high spatial resolution." Optical manufacturing and testing IX. Vol. 8126. SPIE, 2011.

[8] Y.-S. Ghim, Y. B. Seo, K.-N. Joo, and H.-G. Rhee, "Single-shot spectrally resolved interferometry for the simultaneous measurement of the thickness and surface profile of multilayer films," Opt. Express 29, 25524-25534, 2021.

[9] B. Kimbrough, "Correction of errors in polarization based dynamic phase shifting interferometers." Int. J. Optomechatronics 8(4), 304-312, 2014

[10] C. T. Farrell and M. A. Player. "Phase step measurement and variable step algorithms in phase-shifting interferometry." Meas. Sci. Technol. 3(10) 953, 1992.

[11] M. Th. Nguyen, I. K. Park, H. -G. Rhee, and Y.-S. Ghim, , "Deep learning based fringe-print-through error and noise removal for dynamic phase-shifting interferometry," Opt. Laser Technol. 191, 113313, 2025.

euspen's 26th International Conference & Exhibition, Krakow, PL, June 2026
www.euspen.eu

Generalization of area-scale analysis for complex additively manufactured freeform surfaces

Tomasz Bartkowiak[1], Antoni Milecki[1], Michał Jakubowicz[1], Patryk Mietiński[1], Michał Wieczorowski[1], Christopher A. Brown[2]

[1]*Institute of Mechanical Technology, Poznan University of Technology, Poland*
[2]*Surface Metrology Laboratory, Worcester Polytechnic Instutute, Worcester, MA, USA*

tomasz.bartkowiak@put.poznan.pl

Abstract

Additively manufactured metal surfaces often exhibit complex freeform morphologies with re-entrant features that cannot be represented as single-valued height maps, limiting the applicability of conventional surface texture analysis. This work presents a generalized area-scale analysis framework that extends the classical area-scale concept to three-dimensional surface meshes derived from X-ray micro-computed tomography. The method enables robust multiscale characterization of surfaces containing undercuts, overhangs, and partially fused particles. The approach was applied to selectively laser melted Ti-6Al-4V parts produced using varied laser power and scanning speed. Strong, scale-dependent correlations were identified between process parameters and surface morphology. Relative surface area showed strong dependence on laser power ($R^2 > 0.6$ for scales ≥ 4,050 µm²), while surface complexity, quantified by the fractal dimension D_{as}, was primarily governed by scanning speed ($R^2 = 0.817$). These results demonstrate that the proposed method captures both surface development and hierarchical organization in a physically interpretable manner. The generalized area-scale framework provides quantitative insights not accessible through conventional roughness parameters or height-map-based analyses and offers a unified basis for linking additive manufacturing process conditions with multiscale surface geometry, supporting process optimization and functional surface design.

Multiscale analysis, X-ray micro-computed tomography, additive manufacturing, area-scale analysis

1. Introduction

Area-scale analysis, standardized in ISO 25178-2 [1] and ASME B46.1 [2], is a powerful and well-established tool for multiscale characterization of surface topographies. By evaluating the relative surface area as a function of scale, it enables quantitative assessment of surface development and geometric complexity across multiple length scales [3]. However, its conventional formulation fundamentally relies on a single-valued surface representation, where each in-plane location (x, y) corresponds to exactly one height value z [4].

This assumption significantly limits the applicability of area-scale analysis to a wide class of surfaces encountered in modern manufacturing. In particular, additive manufacturing (AM) processes such as selective laser melting (SLM) produce surfaces with highly complex morphologies that cannot be described as single-valued height maps [5]. These surfaces are best described as freeform geometries, containing a multitude of re-entrant features, including overhangs, undercuts, partially fused powder particles, and enclosed cavities [6–8]. Such features violate the $z = z(x, y)$ condition and are therefore incompatible with standard area-scale implementations [9].

At the same time, these re-entrant surface morphologies are not merely geometric artefacts but play a critical role in functional performance. They influence wettability [10], adhesion [11], heat transfer, fatigue behavior [12,13], and biological response [14], particularly in applications such as heat exchangers and biomedical implants [15]. Accurate and scale-sensitive characterization of these freeform surfaces is therefore essential for understanding and controlling AM process–structure relationships.

In this work, we propose a generalization of area-scale analysis for freeform surfaces that explicitly accommodates geometries with re-entrant features where there can be more than one height at each location. The proposed approach operates directly on three-dimensional surface representations obtained from high-resolution X-ray micro-computed tomography, bypassing the limitations of height-map-based methods. By extending the area-scale concept to mesh-based surface descriptions, the method enables the quantification of surface development and fractal complexity for additively manufactured freeform surfaces across a wide range of scales. Consistent with Brown [16], who argues that meaningful surface metrology depends on identifying strong functional correlations through scale-sensitive analyses and the use of geometric characterizations that are directly pertinent to the underlying physical interactions, this study adopts a multiscale, geometry-driven perspective on surface texture.

2. Materials and methods

2.1. Test surface and manufacturing parameters

The study was conducted on twenty additively manufactured parts produced using the laser powder-bed fusion process. All parts were fabricated from Ti-6Al-4V titanium alloy powder with

a particle size distribution of 15–45 µm, a material widely used in aerospace and biomedical applications due to its high strength-to-weight ratio and biocompatibility.

Each specimen had identical nominal geometry in the form of a quarter-cylinder with a height of 25 mm and a radius of 5 mm, ensuring that observed differences in surface morphology were solely attributable to process parameters. The parts were manufactured on an EOS M290 system using twenty distinct combinations of laser power and scanning speed. Laser power was varied from 107 W to 267 W in incremental steps of 40 W, while scanning speed ranged from 250 mm/s to 1000 mm/s in steps of 250 mm/s. This parameter matrix enabled systematic investigation of the individual and combined effects of energy input and scan dynamics on surface morphology.

2.2. Surface acquisition using X-ray micro-computed tomography

Due to the presence of re-entrant and multi-valued surface features, conventional optical or tactile surface measurement techniques were unsuitable for accurate surface acquisition. Therefore, all parts were measured using metrological X-ray micro-computed tomography (µCT). The scanner used here was Baker Hughes/General Electric v|tome|x s240. The voxel size was 5.5 µm.

The µCT measurements provided full volumetric reconstructions of each specimen, capturing undercuts, overhangs, and enclosed features that are inaccessible to line-of-sight methods. The reconstructed data were exported as STL surface meshes, preserving the true three-dimensional geometry of the surfaces. To ensure computational tractability, each surface mesh, originally consisting of several million triangles, was subdivided into smaller regions prior to analysis.

2.3. Generalized area-scale analysis

A generalized area-scale analysis framework was developed to enable multiscale characterization of freeform surfaces with re-entrant geometries. Unlike the conventional area-scale method defined for height-map representations, the proposed approach operates directly on three-dimensional surface meshes.

The surface was partitioned into a set of triangular patches of constant area across a range of predefined scales. For each scale, cross-sectional slicing of the surface mesh was performed, followed by triangulation and mesh-based approximation of the local surface geometry. The distance *d* between two adjacent cross-sectional profiles was associated with scale *s* so that $s=0.5\times d^2$. The computations were performed for *d* between 5 and 150 µm with an increment of 5 µm (*s* ranging between 12.5 11,250 µm²). The patchwork algorithm was performed for all pairs of adjacent profiles following the original algorithm by Brown et al. [4]. The relative surface area was then calculated as the ratio of the true surface area represented by the triangular patches to the projected or nominal reference area. Reference area was considered flat.

By repeating this procedure over multiple scales, an area-scale relationship was obtained and represented in log–log space. The fractal dimension D_{as} was determined from the slope of the linear region of the log–log plot, in accordance with the principles of ISO 25178-2[1]. All data processing and analysis steps were implemented in a custom algorithm developed in Python, ensuring repeatability and consistency across all samples.

The calculated parameter Srel was regressed linearly with laser power and scanning speed independently. The strengths of correlations, denoted as R^2, were plotted as a function of scale to reveal the scale-dependent interactions between formation parameters and resulted surface texture. Fractal dimensions were also regressed linearly. Non-linear quadratic model was used to associate both technological parameters with D_{as} and S_{rel} at a particular scales of observations.

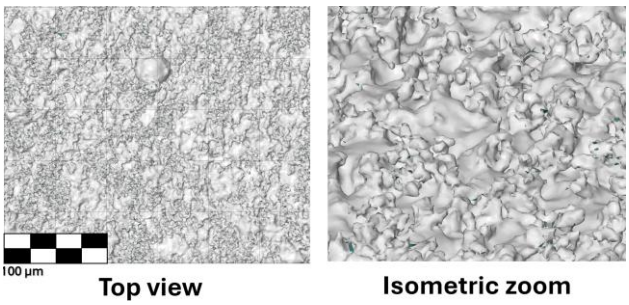

Figure 1. Exemplary surface views of studied parts with evident re-entrant features

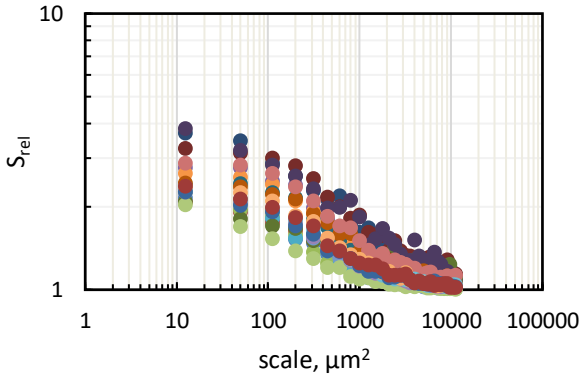

Figure 2. Evolution of relative area S_{rel} as a function of scale for 20 studied surfaces

3. Results

3.1. Relative surface area

The presence of re-entrant features in studied surfaces is strong and evident (Figure 1). The shape and size of re-entrant formations appear to differ depending on the particular part. The exemplary relation of relative area S_{rel} as function of scale calculated for all 20 studied surfaces is shown in Figure 2. It can be noted that the values tend to converge to 1.0 as the scale gets larger but the trends are different depending on the particular surface. It should be noted that for the finest scales relative area exceed 2.0. This is due to the presence of re-entrant geometries which add additional area to the calculation of total area.

The relative surface area S_{rel} showed a strong and systematic dependence on laser power. This effect was evident for scales greater than or equal to 4,050 µm² (R^2>0.6) as seen in Figure 3. Increasing laser power led to higher values of S_{rel} across all analyzed scales and scanning speeds. This behavior indicates enhanced surface development at higher energy input, consistent with increased melt pool size and intensified adhesion of partially melted powder particles.

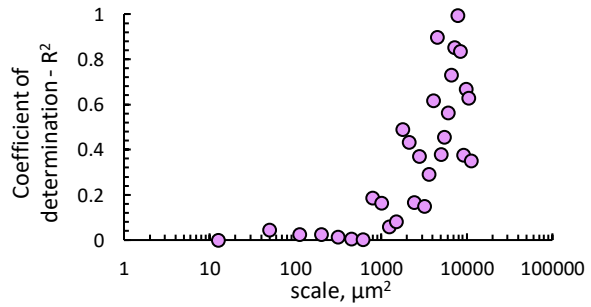

Figure 3. Strengths of linear correlation between relative area S_{rel} and laser power as a function of scale

The effect of scanning speed on S_{rel} was comparatively weaker but still moderately strong. It was noted that changes in scanning speed produced decreasing relation across the full parameter range. This was observed also for the larger scales starting from 4,050 µm² (R^2>0.6) as depicted in Figure 4. These results indicate that surface development, as quantified by area-scale analysis, is also governed by scanning speed.

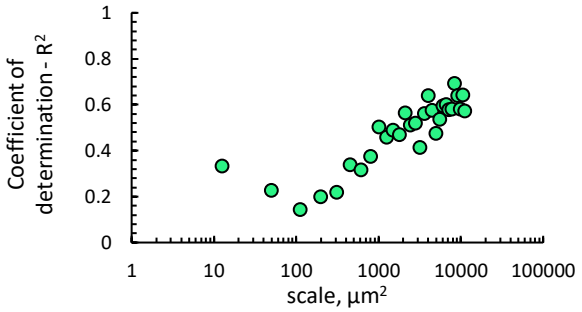

Figure 4. Strengths of linear correlation between relative area S_{rel} and scanning speed as a function of scale

3.2. Fractal dimension

The fractal complexity parameter D_{as}, obtained from the slope of the area-scale curves in log–log space, exhibited a strong dependence on scanning speed (R^2=0.817). As demonstrated in Figure 5, increasing scanning speed resulted in a systematic increase in D_{as}, indicating a prevalence in geometric complexity at higher scan velocities. This means that the surface becomes more self-affine as the scanning speed increases, resulting in less intense local heat transfer.

The influence of laser power on D_{as} was also strong (R^2=0.719). As shown in Figure 6, higher laser power produced only moderate changes in complexity, suggesting that power affects the magnitude of surface growth rather than the hierarchical, self-similar organization of surface features.

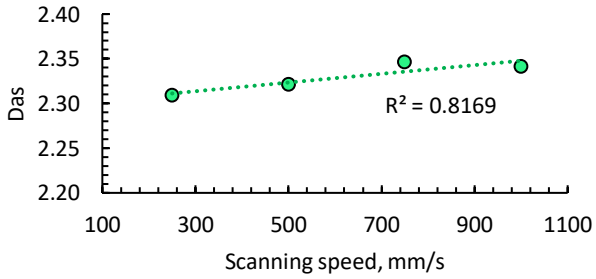

Figure 5. Fractal dimension as a function of scanning speed

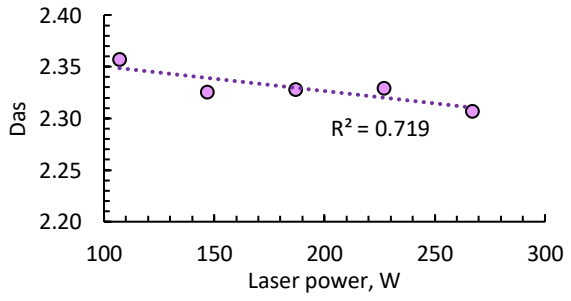

Figure 6. Fractal dimension as a function of laser power

4.3. Combined effects of process parameters

The combined influence of laser power and scanning speed on surface fractal dimensions is visualized in Figure 7. These results reveal a clear separation of parameter roles, low laser power and high scanning speed lead to the greater fractal dimension. At this manufacturing conditions the powder is fused at the lowest heat intensity, meaning that the resulting surface morphology is the product of the metal powder geometry. Manufacturing at the slowest scanning speed and highest laser power ends with intense powder melting and the formation of less self-affine structures.

The strengths of correlation between combined technological parameters and relative area is dependent on the scale of observation. Strongest correlations were observed starting from the scale of 4,050 µm² , as shown in Figure 8 (left). The effect of laser power is the most noticeable at the slowest and the fastest scanning speeds. No correlations were found at the finest range of scales as depicted in Figure 8 (right).

Overall, the results demonstrate that the generalized area-scale analysis is sensitive to both surface growth and multiscale structural organization, enabling quantitative differentiation of the effects of key powder-bed fusion process parameters on freeform, re-entrant surface morphologies.

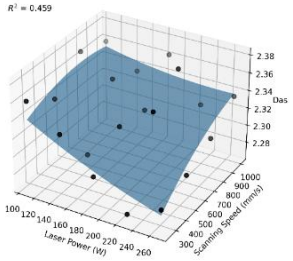

Figure 7. Fractal dimension as a function of laser power and scanning speed.

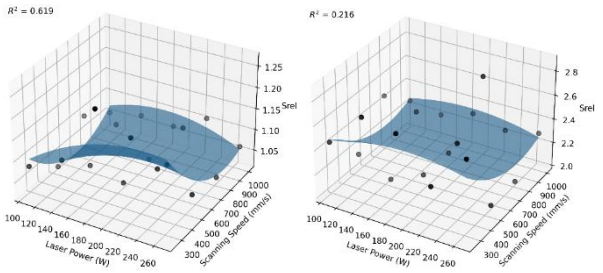

Figure 8. Relative area as a function of laser power and scanning speed calculated at scale equal to 4,050 µm² (left figure) and 12.5 µm² (right)

4. Discussion

This study shows that area-scale analysis can be successfully generalized to freeform, re-entrant surfaces measured by µCT, enabling multiscale characterization beyond the limitations of single-valued height maps. The stability of the area–scale relationships confirms that relative surface area remains meaningful when extended to freeform geometries with evident re-entrant features.

The observed effects of process parameters are consistent with earlier work on the same parts using multiscale curvature analysis [5]. In both studies, correlations with processing conditions are strongest at larger scales, while fine scales associated with powder particle size show little sensitivity. Laser power primarily governs surface development, reflected here by changes in relative area, whereas scanning speed more strongly affects geometric complexity, captured by fractal dimension. This agrees with the curvature-based finding that scanning speed controls shape complexity while laser power mainly influences the magnitude of surface formation. Thus, both methods converge on a common physical interpretation of the L-PBF process.

Compared with curvature analysis, the generalized area-scale approach provides complementary information. Curvature

describes local shape without requiring a datum [17], whereas area-scale analysis quantifies global surface development, explicitly capturing the contribution of re-entrant features to total surface area. This makes the method particularly relevant for functional properties linked to surface enlargement, such as wettability, adhesion, and biological response.

The main strengths of the proposed method are: (i) its direct applicability to re-entrant geometries, (ii) its ability to distinguish between surface development and hierarchical self-similar organization within a single framework, and (iii) its clear physical interpretability in terms of melt pool dynamics and energy input. However, the approach is computationally more demanding than profile-based methods, depends on mesh quality and segmentation of µCT data, and shows limited sensitivity at the finest scales where substrate powder geometry dominates. It also requires fine resolution scanning which limits the application to small-size objects. In addition, relative area provides a global measure of surface development but does not describe local feature morphology in detail.

The fact that the strongest correlations were observed starting at a scale of 4,050 µm², corresponding to the spacing distance *d* equal to 90 µm, is particularly significant from a process–physics perspective. This characteristic scale is very close to the effective laser spot radius used during manufacturing (approx. 100 µm), suggesting that the generalized area-scale analysis becomes most sensitive when the observation scale matches the dominant length scale of energy input in the L-PBF process. At this scale, surface morphology is no longer governed primarily by individual powder particles or voxel-level measurement noise, but by melt pool geometry, resolidification behavior, and material redistribution induced directly by the laser beam. Strong correlations of similar nature were also found by Lemoine et al. who studied Inconel alloy 718 and the effect of linear energy density on relative area and fractal complexity [18]. They used optical microscopy which cannot capture re-entrant geometries but they found that process parameters correlated strongly starting also at large scales (>7,000 µm²).

Overall, the results demonstrate that generalized area-scale analysis complements existing multiscale methods for freeform AM surfaces. Together with curvature-based approaches, it offers a robust framework for linking additive manufacturing process parameters with multiscale surface geometry and supports more informed surface engineering.

5. Conclusion

This work introduces a generalized area-scale analysis framework for the characterization of complex freeform surfaces produced by additive manufacturing. By extending the conventional area-scale concept beyond single-valued height representations and applying it directly to three-dimensional surface meshes obtained from X-ray micro-computed tomography, the proposed method enables consistent multiscale analysis of surfaces containing re-entrant geometries. Application of the method to selectively laser melted Ti-6Al-4V parts revealed clear and physically interpretable relationships between process parameters and surface morphology. Laser power was identified as the primary factor controlling surface development, reflected in strong linear correlations with relative surface area ($R^2 > 0.6$) for scales above 4,050 µm², while scanning speed predominantly governed surface complexity and hierarchical organization, as captured by the fractal dimension D_{as} ($R^2 = 0.817$). The influence of laser power on D_{as} was also significant ($R^2 = 0.719$), confirming distinct but complementary roles of both parameters.

These results demonstrate that the generalized area-scale approach yields quantitative insights that are inaccessible to conventional roughness parameters and height-map-based analyses. The method provides a unified framework for linking additive manufacturing process conditions with multiscale surface geometry and shows strong potential for process optimization and the design of functionally tailored surfaces in advanced manufacturing.

References

[1] ISO 25178-2:2021 Geometrical product specifications (GPS) — Surface texture: Areal — Part 2: Terms, definitions and surface texture parameters.

[2] 2009 ASME Standard, B46.1 Surface Texture, Surface Roughness, Waviness and Lay

[3] Brown C A, Hansen H N, Jiang X J, Blateyron F, Berglund J, Senin N, Bartkowiak T, Dixon B, Le Goïc G, Quinsat Y, Stemp W J, Thompson M K, Ungar P S and Zahouani E H 2018 Multiscale analyses and characterizations of surface topographies *CIRP Annals* **67** 839–62

[4] Brown C A, Charles P D, Johnsen W A and Chesters S 1993 Fractal analysis of topographic data by the patchwork method *Wear* **161** 61–7

[5] Bartkowiak T, Gapiński B, Wieczorowski M, Mietliński P and Brown C A 2023 Capturing and characterizing geometric complexities of metal additively manufactured parts using x-ray micro-computed tomography and multiscale curvature analyses *Surf Topogr* **11** 014002

[6] Zanini F, Pagani L, Savio E and Carmignato S 2019 Characterisation of additively manufactured metal surfaces by means of X-ray computed tomography and generalised surface texture parameters *CIRP Annals* **68** 515–8

[7] Scott P J and Jiang X 2014 Freeform surface characterisation: theory and practice *J Phys Conf Ser* **483** 012005

[8] Pagani L, Qi Q, Jiang X and Scott P J 2017 Towards a new definition of areal surface texture parameters on freeform surface *Measurement* **109** 281–91

[9] Macdonald D A, Bartkowiak T, Mendak M, Stemp W J, Key A, de la Torre I and Wieczorowski M 2022 Revisiting lithic edge characterization with microCT: multiscale study of edge curvature, re-entrant features, and profile geometry on Olduvai Gorge quartzite flakes *Archaeol Anthropol Sci* **14** 33

[10] Vu H H, Nguyen N-K, Singha P, Walker G, Nguyen N-T and Kashaninejad N 2024 Exploring Wettability of Re-Entrant Microstructures: Effects of Geometry and Material Composition *Adv Mater Interfaces* **11**

[11] Petersen D S, Kleinteich T, Gorb S N and Heepe L 2018 Competing with barnacle cement: Wetting resistance of a re-entrant surface reduces underwater adhesion of barnacles *J R Soc Interface* **15**

[12] Nečemer B, Kramberger J and Glodež S 2021 Fatigue crack growth in the re-entrant auxetic structure *Procedia Structural Integrity* vol **39** pp 34–40

[13] Nečemer B, Vuherer T, Glodež S and Kramberger J 2022 Fatigue behaviour of re-entrant auxetic structures made of the aluminium alloy AA7075-T651 *Thin Walled Structures* **180**

[14] Dong Z, Schumann M F, Hokkanen M J, Chang B, Welle A, Zhou Q, Ras R H A, Xu Z, Wegener M and Levkin P A 2018 Superoleophobic Slippery Lubricant-Infused Surfaces: Combining Two Extremes in the Same Surface *Advanced Materials* **30**

[15] Peta K, Bartkowiak T, Rybicki M, Galek P, Mendak M, Wieczorowski M and Brown C A 2024 Scale-dependent wetting behavior of bioinspired lubricants on electrical discharge machined Ti6Al4V surfaces *Tribol Int* **194** 109562

[16] Brown C A 2021 Surface Metrology Principles for Snow and Ice Friction Studies *Front Mech Eng* **7**

[17] Bartkowiak T and Brown C A 2019 Multiscale 3D curvature analysis of processed surface textures of aluminum alloy 6061 T6 *Materials* **12** 257

[18] Lemoine A C ., Mancini M P, Velez J A and Brown C A 2016 On the metrology of surface produced by laser melting of powders *Proceedings of ASPE Summer Topical on Dimensional Accuracy and Surface Finish in Additive Manufacturing* (Raleigh, NC, USA) pp 174–9

euspen's 26th International Conference & Exhibition, Krakow, PL, June 2026
www.euspen.eu

Assessment of Geometric Errors in Coordinate Measuring Machines with Ring Gages

Sousa, Andre[1]

[1, 2]*Federal Institute of Science and Technology of Santa Catarina, Brazil.*

asousa@ifsc.edu.br

Abstract

Coordinate Measuring Machines (CMMs) are affected to 21 geometric errors, including linear, angular, and squareness deviations, which may significantly affect measurement accuracy. To ensure robust metrological reliability, it is essential to perform interim checks capable of monitoring the machine's stability between calibrations. A wide range of methods and instruments is available to assess CMM performance. Some of these are highly sophisticated, enabling the simultaneous identification of multiple geometric errors with high precision; others are simpler and lower cost, but typically limited to detecting only one or a few error types. This paper presents and discusses an experimental approach employing ring gages as a practical means of evaluating linear positioning errors (XPX, YPY, ZPZ) and squareness errors (XWY, XWZ, YWZ). Ring gages are low-cost precision artefacts widely available in industrial and research metrology laboratories. Their ease of handling, high dimensional stability, and broad availability make them an attractive alternative for implementing efficient, low-cost interim checks of their measuring equipment. The proposed methodology and its mathematical principles are presented, along with the results from experiments compared with more sophisticated and commercially available testing techniques, highlighting its strengths and limitations.

Keywords: Coordinate Measuring Machines; Dimensional Metrology; Calibration; Interim checks.

1. Assessment of Geometric Errors in CMMs

Coordinate Measuring Machines (CMMs) are among the most important measurement systems used in dimensional control of products and processes in industry, and the accuracy of their results is essential to achieve high standards of quality and productivity.

Measurement accuracy depends on several factors, including the geometric conformity of the CMM. Three-axis Cartesian CMMs exhibit 21 geometric errors arising from imperfections in their mechanical structure and measurement scales [1]. Each Cartesian axis exhibits six geometric errors, and an additional three squareness errors exist between the axes. Figure 1 illustrates these errors.

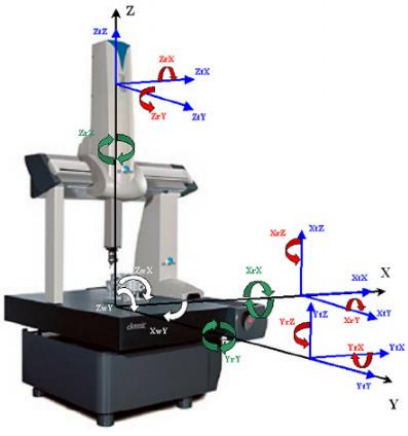

Figure 1. Geometric errors of a CMM [1]

According to ISO 230, the 21 geometric error components of a three-axis machine are designated as follows:

- 3 linear positioning errors: XPX, YPY, ZPZ
- 6 straightness errors: XTY, XTZ, YTX, YTZ, ZTX, ZTY
- 9 angular errors: XRX, XRY, XRZ, YRX, YRY, YRZ, ZRX, ZRY, ZRZ
- 3 squareness errors: XWY, XWZ, YWZ

These geometric errors, acting in combination, introduce deviations when measuring different features and tolerances on workpieces. Some errors mainly affect size measurements, while others have a stronger influence on location, form, and orientation characteristics.

To ensure adequate metrological accuracy, CMMs undergo periodic calibration and adjustment, typically at one-year intervals. In addition, periodic tests carried out at shorter intervals are essential to verify that the machine remains within acceptable error limits.

Although calibration and adjustment are necessary, periodic testing is indispensable to assess machine accuracy between calibrations. Such tests can identify potential problems in the CMM and provide valuable information to optimize calibration and adjustment intervals.

Several test systems and methods are available for evaluating CMMs, ranging from simple dimensional artefacts to sophisticated systems such as laser interferometers. While all are useful, some methods are limited to assessing only a subset of geometric errors, whereas others are capable of separately measuring all 21 parametric errors.

2. Methodology of CMM evaluation with ring gages

Different testing methods exhibit varying capabilities for measuring the 21 geometric errors. Some methods, such as ball plates [2] and laser interferometers [3], are capable of separately quantifying all parametric error components. Other methods focus on the most significant errors for CMM performance, namely linear positioning errors and squareness errors between the Cartesian axes. Ring gage testing falls into this latter category.

The proposed methodology using a ring gage considers a circle with a calibrated diameter and roundness error small compared to the measurement accuracy of the CMM. The circle is automatically probed at eight points equally spaced by 45°, and four diametral distances between opposite points are calculated, designated as D1, D2, D3, and D4, in mm.

Figure 2 illustrates this concept in the XY plane of the CMM; the same approach applies to the XZ and YZ planes.

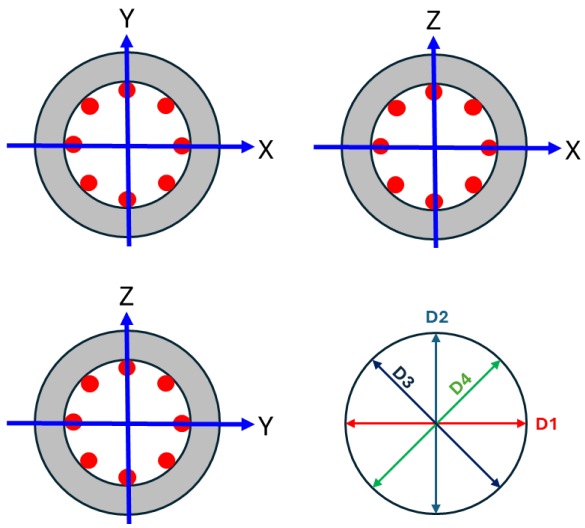

Figure 2. Probing strategy and distances extracted

In practice, any measurement result obtained with a CMM is influenced by the combined effect of the 21 geometric error components of the machine. However, for the purpose of estimating specific parametric errors using a simple artefact-based test, a simplified model is adopted.

The equations presented in this work assume that the measured distances are predominantly influenced by the geometric error under investigation (linear positioning or squareness), while the remaining error components are considered to have a secondary influence within the test configuration. This simplification is commonly adopted in practical interim tests, where the objective is not the complete identification of all parametric errors but rather the detection of variations in the dominant error components affecting the measurement result.

Under this assumption, the distances obtained from the probing strategy allow the estimation of the following geometric errors:

- **3 linear positioning errors:** XPX, YPY, ZPZ
- **3 squareness errors:** XWY, XWZ, YWZ

The linear positioning errors (scale errors, in µm/m) are determined by comparing the distances along the Cartesian axes (DX and DY) with the calibrated diameter of the ring gage, as shown in Equations (1) and (2) for the XY plane:

$$XPX = (D1 / \text{Calibrated Diameter} - 1) \times 1000 \quad (1)$$

$$YPY = (D2 / \text{Calibrated Diameter} - 1) \times 1000 \quad (2)$$

The squareness error, expressed in µm/m, is determined from the difference between the two diagonal distances D3 and D4, according to Equation (3):

$$XWY = (2.10^6 \times |D3 - D4|) / (D3 + D4) \quad (3)$$

For testing in the XZ plane, the errors are calculated as:

$$ZPZ = (D2 / \text{Calibrated Diameter} - 1) \times 1000 \quad (4)$$

$$XWZ = (2.10^6 * |D3 - D4|) / (D3 + D4) \quad (5)$$

In the YZ plane, the squareness error, in µm/m, is given by:

$$YWZ = (2.10^6 \times |D3 - D4|) / (D3 + D4) \quad (6)$$

As an accuracy criterion for practical implementation, the uncertainty of the calibrated diameter and the roundness error of the ring gage must be less than 20% of the CMM measurement uncertainty for size measurements. This condition is necessary to ensure the validity of the experimental results.

3. Experimental evaluation of a CMM using a ring gage

The tests were carried out on a CNC CMM with a maximum permissible error MPE = (2 + L / 500) µm, in accordance with ISO 10360-2 [4]. A 200 mm diameter ring gage was used, as this was the largest available artefact in the metrology laboratory at the time of testing.

The roundness of the ring gage was measured to verify that the form error was compatible with the accuracy requirements of the CMM. Measurements were performed using a Mitutoyo RA1600 form measuring machine, resulting in a roundness deviation of 0,27 ± 0,05 µm (Figure 3), after applying a 50 UPR low-pass filter and calculating the reference circle using the minimum zone (Chebyshev) method, in accordance with ISO 12181 [5].

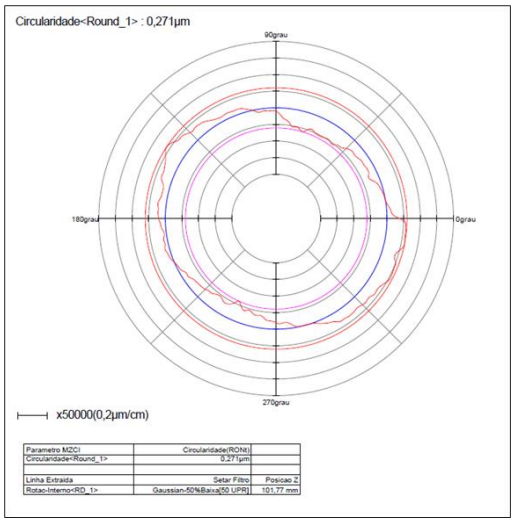

Figure 3. Ring gage roundness error

The diameter of the ring gage was calibrated using the comparison method with thermal expansion correction. The calibrated diameter obtained under these conditions was 199,997 ± 0,001 mm.

After calibration in terms of size and form, the ring gage was used to evaluate the geometric errors of the CMM. The ring gage was positioned in each Cartesian plane, aligned as closely as possible with the machine coordinate system. A mathematical leveling and centering procedure was then performed, using the top plane of the ring for leveling and the fitted circle for coordinate system localization. Both plane and circle were fitted using the least-squares method. Figure 4 illustrates the alignment and measurement procedure in the three Cartesian planes.

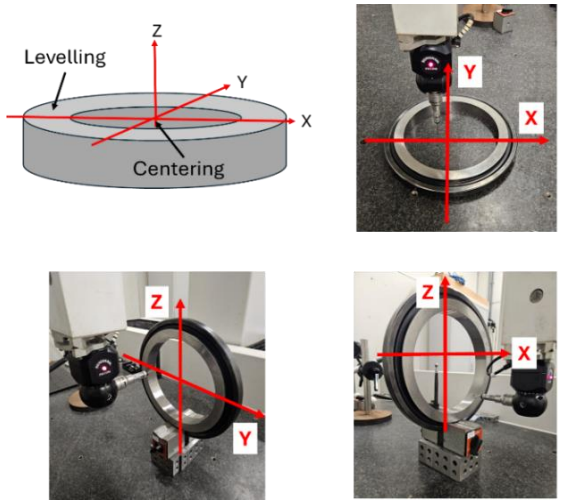

Figure 4. Alignment and measurement procedure

Eight probing points were measured as described in Section 2, and the data were processed using a dedicated spreadsheet developed to estimate linear positioning and squareness errors (Figure 5).

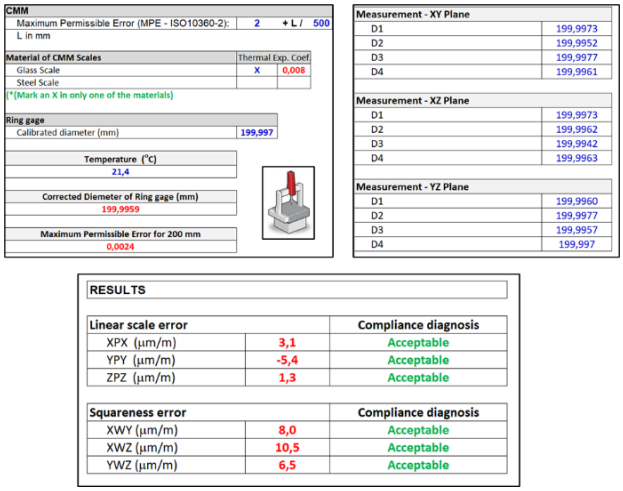

CMM			
Maximum Permissible Error (MPE - ISO10360-2):		2	+ L / 500
L in mm			
Material of CMM Scales	Thermal Exp. Coef.		
Glass Scale	X	0,008	
Steel Scale			
(*(Mark an X in only one of the materials)			
Ring gage			
Calibrated diameter (mm)	199,997		
Temperature (°C)	21,4		
Corrected Diemeter of Ring gage (mm)	199,9959		
Maximum Permissible Error for 200 mm	0,0024		

Measurement - XY Plane	
D1	199,9973
D2	199,9952
D3	199,9977
D4	199,9961

Measurement - XZ Plane	
D1	199,9973
D2	199,9962
D3	199,9942
D4	199,9963

Measurement - YZ Plane	
D1	199,9960
D2	199,9977
D3	199,9957
D4	199,997

RESULTS		
Linear scale error		**Compliance diagnosis**
XPX (µm/m)	3,1	Acceptable
YPY (µm/m)	-5,4	Acceptable
ZPZ (µm/m)	1,3	Acceptable
Squareness error		**Compliance diagnosis**
XWY (µm/m)	8,0	Acceptable
XWZ (µm/m)	10,5	Acceptable
YWZ (µm/m)	6,5	Acceptable

Figure 5. Test management spreadsheet and error calculation

In addition to calculating geometric errors, the spreadsheet evaluates whether these errors are significant based on the CMM accuracy specification, using the MPE equation for the ring gage size (approximately 200 mm):

$$MPE = \pm (2{,}0 + L/500)\ [mm] \quad (12)$$

$$MPE = \pm (2{,}0 + 200/500) = \pm 0{,}0024\ mm$$

Thus, for a linear positioning error to be acceptable, it must be below the MPE value of 2,4 µm for the ring gage size. For squareness errors, the difference between the diagonal measurements must also be less than 2,4 µm.

Five repetitions were performed in each Cartesian plane, producing the average results shown in Table 1. The measurement repeatability observed in the tests was better than 1,2 µm/m.

Table 1 – Geometric errors measured with the ring gage

Geometric Error	Result (µm/m)
XPX	3,1
YPY	-5,4
ZPZ	1,3
XWY	8,0
XWZ	10,5
YWZ	6,5

After the tests performed with the ring gage, the same CMM was evaluated using two different methods. One of them was the orbital testing system Machine Checking Gage (MCG) from Renishaw (Figure 6), which is widely used in industry, with the objective of comparing the errors obtained by different methods and validating the previous results.

The MCG consists of a fixed-length carbon fiber bar, supported by a spherical joint at one end and by the CMM probe at the other, allowing the machine to perform orbital movements in different spatial orientations. Using the MCG, it is possible to identify scale errors, volumetric errors, and squareness deviations between the machine axes.

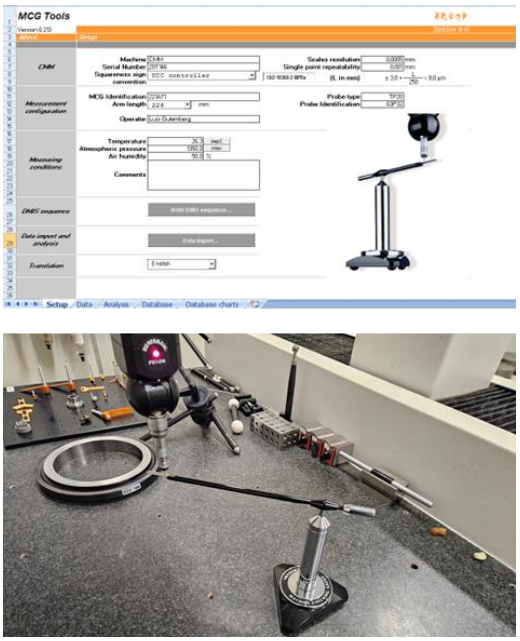

Figure 6. CMM tested with machine checking gage

In addition to the MCG, the CMM was evaluated using a dimensional artefact in the form of a tetrahedron (Figure 7). The system, developed by the company Trapet Precision Engineering, consists of a carbon fiber tetrahedron with four spheres at its vertices, with the distances between the vertices being calibrated.

The CMM under test measures the distances between each pair of spheres in six different directions, compares these measurements with the calibrated values, and, based on the resulting differences, calculates scale errors along the three Cartesian axes as well as squareness errors between the axes.

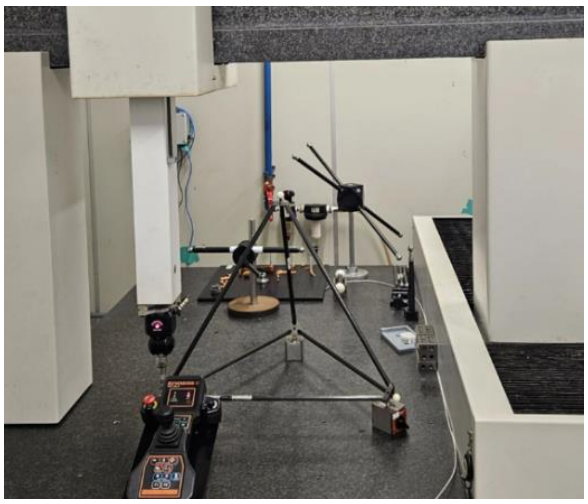

Figure 7. CMM tested using tetrahedron

The errors provided by both the MCG and the tetrahedron systems are the linear positioning errors (scale errors XPX, YPY, and ZPZ) and the squareness errors between the Cartesian axes (XWY, XWZ, and YWZ). Table 2 presents the results obtained using these systems. The repeatability observed in the tests performed with the MCG system was better than 3,0 µm/m, while the tests performed with the tetrahedron artefact showed a repeatability better than 1,8 µm/m.

Table 2 – Errors measured with the MCG System

Geometric Error	Result (µm/m)	
	MCG	Tetrahedron
XPX	6,0	4,7
YPY	-5,3	-5,9
ZPZ	-1,2	2,1
XWY	6,9	5,3
XWZ	11,3	8,7
YWZ	4,8	5,7

Based on these values, a comparison between the methods was established, as shown in Figure 8. Although the procedures are different and involve different measurement volumes, the results exhibited similar values, with differences compatible with the uncertainty of the CMM, indicating that the ring gage testing method proved capable of revealing the geometric condition of the measuring machine. Maximum deviations between methods were below 3 µm/m.

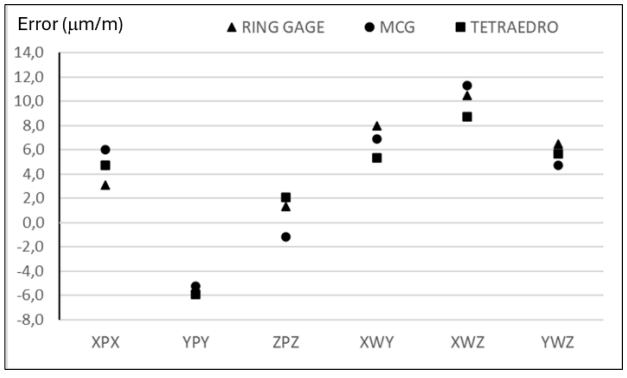

Figure 8. Comparison of results between the evaluated systems

4. Conclusions

This study evaluated the use of a ring gage to assess linear scale errors and squareness errors in a Coordinate Measuring Machine, with the primary objective of investigating the potential of a practical and low-cost method for periodic CMM testing.

The results indicate that the method is promising when compared with well-established industrial testing techniques. The values obtained were similar, even for a CMM in good metrological condition. For machines with larger errors, an even better agreement between methods is expected.

The test proved to be practical and fast, although an important limitation is the size of the ring gage relative to the measurement volume of the CMM. In the present study, a 200 mm ring gage was used, but a diameter of at least 300 mm would be recommended.

The method provides an approximate estimation of dominant geometric errors, but its main purpose is the detection of variations in machine behaviour during periodic stability checks. For this purpose, the method demonstrated a good capability to reveal errors in the measuring machine, with a very short testing time, using a dimensional artefact that is widely available in industry.

Future work will focus on evaluating the reliability of angular error assessment using the ring gage method, based on a procedure similar to that described in this work, as well as on a detailed estimation of the measurement uncertainty associated with the test results.

In this study, the test was performed near the centre of the CMM measuring volume. Evaluating the method at different locations within the measuring volume is also a relevant topic for future work.

References

[1] Sładek J., Gawlik K. Looking for uncertainty of measurement. Virtual Machines based on the Matrix Method using artificial neural networks. IV International Congress on Precision Machining, Sandomierz-Kielce 2007.

[2] E. Trapet., F. Wäldele.: A reference object based method to determine the parametric error components of coordinate measuring machines and machine tools. *Measurement* Vol 9, No 1, Jan- Mar 1991, p.17-22.

[3] GĄSKA, Adam; GRUZA, Maciej; GĄSKA, Piotr; KARPIUK, Michał; SŁADEK, Jerzy. *Identification and correction of coordinate measuring machine geometrical errors using LaserTracer systems*. Advances in Science and Technology – Research Journal, 2013, vol. 7, no. 20, p. 17–22. DOI 10.5604/20804075.1073047.

[4] INTERNATIONAL ORGANIZATION FOR STANDARDIZATION. *ISO 10360-2:2010 — Geometrical product specifications (GPS) — Acceptance and reverification tests for coordinate measuring machines (CMM) — Part 2: CMMs used for measuring linear dimensions*. Geneva: ISO, 2010.

[5] INTERNATIONAL ORGANIZATION FOR STANDARDIZATION. *ISO 12181-3:2011 — Geometrical product specifications (GPS) — Roundness — Part 3: Measurement methods*. Geneva: ISO, 2011.

euspen's 26th International Conference & Exhibition, Krakow, PL, June 2026
www.euspen.eu

Digital metrological twins for stereovision systems - A literature review

Katarina Josic[1,2,3], Ladji Fofana[1,2,3], Louis-Ferdinand Lafon[1], Charyar Mehdi-Souzani[2], Romain Brault[3], Nabil Anwer[2], Olivier Bruneau[2], Hichem Nouira[1]

[1] *Laboratoire national de métrologie et d'essais/Conservatoire national des arts et métiers, 1 Rue Gaston Boissier, 75015 Paris, France*
[2] *Université Paris-Saclay, ENS Paris-Saclay, LURPA, 91190 Gif-sur-Yvette, France*
[3] *Centre technique des industries mécaniques, 52 Avenue Félix Louat, 60300 Senlis, France*

katarina.josic@lne.fr

Abstract

Stereovision can be defined as a measurement process reliant on multiple images taken from different perspectives to estimate three-dimensional dense informations and parameters, thereby enabling the metrological evaluation of form errors and surface texture parameters. Digital Metrological Twin is defined as a numerical model that depicts a specific measurement process and indicates an associated measurement uncertainty for a specific measurement value, which is traceable to the units of the international system of units. A comprehensive literature review on the integration of stereovision systems and digital metrological twins has been conducted using a PRISMA methodology, exploring different applications, frameworks and challenges. Digital twins of stereovision systems could be useful tools for developing, modeling, testing, and optimizing the usage of stereovision in many industrial contexts. By bridging the gap between the digital and physical domains, they enable virtual testing and validation and pave the way for the more accurate, effective and efficient implementation of stereovision technologies in the real world. This review reveals a major barrier to the integration of digital twins and stereovision systems for industrial applications in terms of availability of standards among hardware, software, and data layers. Achieving high accuracy in intelligent industrial settings is limited due to increased complexity, expenses and lack of calibration standards for stereovision systems. Future efforts to resolve these gaps will aid in promoting widespread adoption. This research is beneficial for the creation of a digital twin for a stereovision 3D scanning system being developed at LNE in the scope of the 23IND08 Di-Vision project.

Systematic literature review, stereovision, digital twins, metrology

1. Introduction

Stereovision allows visual feedback of spatial connections and distances, and comprehension of complex object geometry by recreating three-dimensional information from two-dimensional images using the principle of triangulation. This feature, which provides rich 3D information with basic and affordable sensor technology, has become a fundamental component in disciplines including autonomous navigation, collaborative robots, and intelligent manufacturing. Stereovision has become even more relevant in recent years due to its integration with digital twin technologies. Digital twins are digital representations of real-world entities constantly fed by dynamic, bidirectional communication and updates throughout the lifecycle of these sophisticated paired systems [1]. Since digital twins depend on accurate, real-time representations of observable entities, stereovision provides an effective method of 3D reconstruction of these entities. The development of a digital twin for a structured light stereovision 3D scanning system at the French National Metrology Laboratory (LNE) as part of the 23IND08 Di-Vision [2] European project benefits from this study.

2. Methodology

This literature review was conducted using the PRISMA methodology [3] and the scientific database Google Scholar. Publications from 2018 to 2025 were included in a thorough preliminary search for literature on the integration of digital twins and stereovision systems, as a rapid growth in the number of publications was noted beginning from 2018. The assessment focused on keywords "digital twin," "stereovision," "industry," and "production" .

Out of the 200 materials that were found, 63 were eliminated because they lacked citations, as to ensure the review's credibility. After the 137 remaining records were screened, 124 resources were eliminated because they did not fall inside the review's scope for a variety of reasons, mostly because they addressed digital twins and stereovision systems in unrelated contexts. Finally, 13 materials were selected and reviewed. The selection process is illustrated in **Figure 1**.

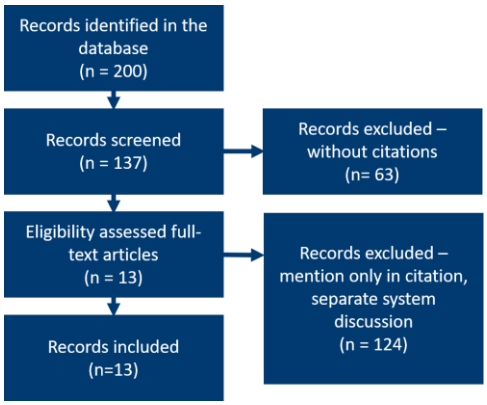

Figure 1: Resource selection

3.Stereovision

Stereovision is a measurement technology used for 3D reconstruction and depth perception, applicable in many industrial fields [4]. It is based on stereo correspondence, which is the method of creating a 3D representation of an item from two or more images of the same scene. According to the literature [4, 5, 6], this technology is divided into two types: passive stereovision, which uses ambient light and features to find correspondences, and active stereovision, which projects structured light (such as grids or coded patterns) onto objects to aid in the matching process, particularly for featureless or smooth surfaces. Passive stereovision scanners use two cameras [4], whereas active stereovision systems combine cameras and projectors [7], as illustrated in **Figure *2***. The difference between modeling these two systems is that the projector is treated as an inverted camera, transmitting rather than receiving light. A single camera is limited in terms of depth information, as many 3D points might correspond to the same pixel point on the image [8]. While active techniques are more robust in poor visibility conditions [6] and provide easier height measurement through laser triangulation [9], they can sometimes be burdened by outlier points caused by interreflection, whereas passive systems may provide denser and cleaner point clouds if a scene is naturally rich in detail [6, 10]. Complementary and integrated use of both passive and active stereovision systems as a strategy to overcome the constraints of each individual approach is explored [4, 6, 9]. A common issue with passive stereo vision is the "false boundary problem" [4]. When a stereovision sensor's two cameras see a smooth and curved surface, each camera's inspection of the surface's border may differ from the surface's real boundary. Consequently, the surface boundary that is retrieved by comparing these two artificial borders in the two cameras will be inaccurate. A combined technique employs passive stereovision to identify rough surface borders and active stereovision to detect interior curvatures and surface features [4]. This problem is effectively resolved by calibrating structured light in active stereovision and dynamically positioning the cameras in passive stereovision. Moreover, systems can benefit from the consistent surface coverage and texture independence offered by active techniques in low visibility situations while taking use of the high point density frequently observed in passive techniques by combining a point cloud collected by both passive and active approaches.

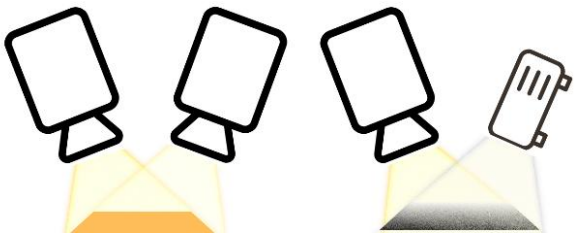

Figure 2: Passive stereovision (left) and active stereovision (right)

4. Digital twins

The digital twin was first presented by NASA as a *"an integrated multiphysics, multiscale, probabilistic simulation of an as-built vehicle or system that uses the best available physical models, sensor updates, fleet history, etc., to mirror the life of its corresponding flying twin*" [11]. Michael Grieves expanded this idea beyond aerospace by defining the digital twin as the "*a set of virtual information constructs that fully describes a potential or actual physical manufactured product from the micro-atomic level to the macro-geometrical level*" [12]. The digital twin was formalized specifically for manufacturing by the ISO 23247 as a "*fit for purpose digital representation of an observable manufacturing element with synchronization between the element and its digital representation*" [13]. This standard provided a reference architecture for digital twins widely used today, displayed in **Figure *3***.

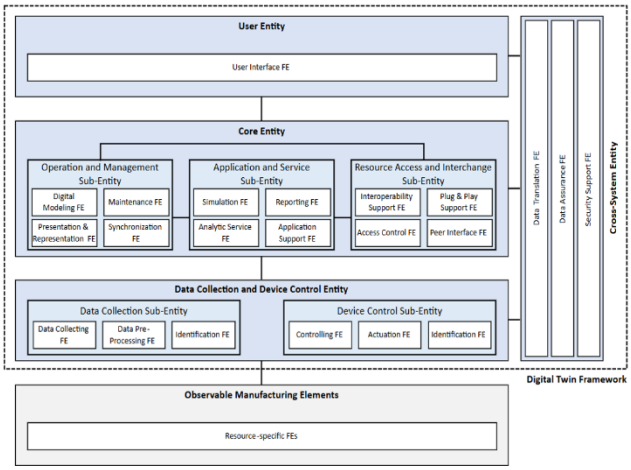

Figure 3: Reference architecture [12]

This term was formalized again when ISO/IEC 30173 provided a domain-agnostic definition of a digital twin as a "*a digital representation of a target entity with data connections that enable convergence between the physical and digital states at an appropriate rate of synchronization*" [14]. In a metrological context, a Digital Metrological Twin is defined as "*a numerical model that depicts a specific measurement process and indicates an associated measurement uncertainty for a specific measurement value, which is traceable to the units of the international system of units*" [15]. It is possible to expand these concepts to suggest a digital twin in metrology as "*a digital model of a measurement process connected to the physical system by a closed loop, then providing the associated measurement uncertainty for a given measured value traceable to the meter unit definition*".

5. Integration of digital twins and stereovision systems

The integration of digital twins with stereovision systems provides significant value by offering a high-fidelity simulation environment that enables for the safe testing and validation of complicated navigation and safety algorithms without endangering actual hardware or human lives [16]. Before any software is installed on the actual machine, digital twins enable the validation of navigation algorithms and safety features in a risk-free virtual environment [17]. Virtual stereoscopic cameras and environmental factors are simulated by engines such as Gazebo [10, 17]. Researchers can test localization and navigation algorithms in a virtual operating environment when the environment is not available for testing by replicating the system's operational environment as part of the digital twin using this tool. The digital twin is becoming more and more used in the digitization and automation of production processes [18]. Digital twins can be used for virtual simulation and testing of vision-based systems with an infinite number of design options [19]. The system can look for ideal topologies and parameters that meet certain job requirements using different deep-learning methods for various metrological purposes[19]. To increase inference speed and matching accuracy, digital twins can be programmed to tune the underlying neural networks of stereovision systems, such as those used for stereo matching or depth estimation [19].

In mixed reality (MR) contexts, digital twins can enable real-time distance measurement and collision detection between virtual components and unknown real-world objects [20]. The virtual world mesh and the scene mesh captured by the stereovision system can be intersected to accomplish this [20]. Digital twins also assist to reduce the load of streaming high-resolution 3D point clouds. In order to minimize interruptions to crucial control links, engineers can detect network bottlenecks and split visual data to different networks by modeling sensor data flows [17]. Through the integration of MR goggles and stereovision concepts, the digital twin can allow operators to use natural human motions to operate a physical robot. These systems make use of imitation-based motion mapping, which tracks the user's hand motions and translates these into orders for the robot's tool center point's spatial velocity. The digital twin makes it easier for novel users to use this technology [20]. Digital twins facilitate the generation of precise virtual coordinates for camera frames by visualizing hand-eye calibration data, thus enabling system traceability. This allows virtual sensors to be calibrated with identical distortion coefficients and focal lengths as their physical counterparts, ensuring accurate visual feedback [16]. Moreover, by allowing the user to interact with the system's replica in MR while concurrently viewing real-time sensor data from the remote site, the digital twin helps address problems with virtual transparency [20]. Virtual transparency is the degree to which the MR interface allows the user to "see through" the virtual layer in order to fully understand the actual or simulated system underlying it, rather than the interface limiting that insight.

6. Industrial applications

Stereovision combined with digital metrological twins provides precise three-dimensional information about objects, processes, and surroundings, reflecting real-world situations more realistically and responsively. In industrial settings, where accurate spatial awareness and real-time updates are crucial for various processes, this combination is especially beneficial. Stereovision systems integrated with digital metrological twins offer a diverse range of high-precision industrial applications.

6.1. Autonomous navigation

In the field of mobile robotics and logistics, these integration enables autonomous navigation and "virtual docking" by providing a Digital World Model that allows robots to plan collision-free paths and adjust their behavior to dynamic shopfloor changes without disrupting active production [16]. "Virtual docking" is a localization method where the mobile robot uses fiducial markers (like AprilTags) to precisely locate itself in front of a workstation. This increases shopfloor flexibility by eliminating the requirement for physical clamping devices. Although the stereo camera used for these tasks had 3D capabilities, only 2D data was used for the localization, achieving good results with a smaller amount of data to create a real-time map for collision-free trajectory planning.

6.2. Manufacturing systems

Stereovision systems have been shown to contribute to the efficiency and precision of weld route recognition [9], particularly for complex welds during production [21]. Active stereovision (projecting structured light, such as dot matrices or laser lines) is used for weld seam tracking and bead inspection because the regular patterns make it easier to retrieve height and contour information independent of the metal's surface roughness [9]. For weld pool monitoring, passive stereovision is used since it offers trustworthy geometric characteristics like width, length, and convexity to forecast penetration states. Digital twins serve as visual monitors for robotic arc welding, using multi-sensor fusion to estimate weld pool penetration and track seams in real time [21].

Robotic manipulators rely on stereovision systems for accurate identifying, grasping, and placing objects, which is essential for robust manufacturing [16]. To guarantee safe handling, systems employ CAD matching and 3D point-cloud matching to determine the posture of complex objects. Stereovision was utilized for the localization and grasping of dampers in an automobile vehicle front-axle assembly, illustrating its potential to improve assembly line reconfigurability. Integrated digital twins provide real-time distance assessment between virtual robot components and unknown real-world barriers using MR goggles [20]. Moreover, automation of sorting tasks can be performed using cognitive cells which feature stereovision technology [22]. A cognitive cell is made up of two components: a cooperative robot acting as an actuator and a passive stereovision system carrying out sensor operations. The cognitive cell could determine the height where the object is placed via computer vision triangulation to determine depth using two cameras in full high definition. A monochrome cube served as the object in this piece. Furthermore, the cameras recognized each object's color individually and compared the results to improve accuracy. The cell's cognitive abilities were improved by this stereovision system [22]. Digital twins for these systems enable task flexibility, allowing for adaptation to changes in the environment or production, as well as rapid task planning [10].

6.3. Harsh environments

Stereovision is a useful technique in marine biology and archaeology for digitizing items that cannot be transported [6]. Active stereovision produces more stable 3D coordinates in unclear water than passive stereovision, which is limited by poor contrast and scattering. However, in clear water, passive stereovision can generate denser point clouds. A combination of 3D point clouds obtained using both stereovision methods results in higher point density from the passive technique and more coverage of the object surface from the active technique [6]. In hazardous situations like deep-sea research, space repair, nuclear rehabilitation, and remote robotic surgery, stereoscopic vision combined with a digital twin provides critical depth signals for operators operating robots remotely [21]. These signals eliminate the uncertainty present in standard 2D displays, where operators struggle to estimate the distance between a robotic gripper and a target.

7. Challenges

The literature points to certain research gaps that impact the integration of digital twins with stereovision systems. One of the main issues is a lack of consistent standards, design patterns, and universal IT tools [1, 17], [18]. These limits make it difficult to apply digital twins in real-world industrial environments. Every digital twin implementation in industry needs to be handled differently due to the low degree of universalism and the absence of approved design patterns. Design teams have to develop their own programming libraries and IT tools from scratch. This increases the time it takes to popularize such solutions in the commercial environment and raises the cost of implementing digital twins. Moreover, current systems have poor generalization in unforeseen circumstances [1], as certain frameworks based on neural networks created for one environment frequently fail when presented with various lighting or textures in the field [19]. Furthermore, certain resources highlight that communication latency and real-time synchronization problems make it challenging to maintain a

zero-delay link. Broadcasting high-resolution 3D point clouds also puts a significant demand on industrial network capacity, frequently mandating the separation of vision data to prevent control system failures [16]. Time is an important factor in measurement processes and improving the communication between the virtual and physical systems is critical for the reduction of measurement uncertainty of stereovision systems.

8. Conclusion

The convergence of stereovision and digital metrological twins systems is a big step toward safer, more reliable, adaptable and accurat physical assets and processes. Without endangering actual hardware or interfering with ongoing manufacturing lines, digital twins offer a high-fidelity simulation and decision-making environment for the secure testing and validation of algorithms. They provide more accurate measurement, monitoring, process optimization, and automation in industry. However, research findings suggest that in order to proceed, important gaps including the absence of uniform standards, communication latency problems, and the severe network load associated with streaming high-resolution 3D point clouds need to be tackled.

Acknowledgment

This work is part of the project 23IND08 DI-Vision, which has received funding from the European Partnership on Metrology, co-financed from the European Union's Horizon Europe Research and Innovation Programme and by the Participating States.

References

[1] N. Anwer, R. Stark, F. Tao, and J. A. Erkoyuncu, 'Developing and leveraging digital twins in engineering design', *CIRP Ann.*, vol. **74**, no. 2, pp. 843–868, Jan. 2025, doi: 10.1016/j.cirp.2025.05.002.

[2] 'DI-VISION'. Accessed: Jan. 04, 2026. [Online]. Available: https://projects.lne.eu/jrp-di-vision/

[3] M. J. Page *et al.*, 'The PRISMA 2020 statement: an updated guideline for reporting systematic reviews', *BMJ*, vol. **372**, p. n71, Mar. 2021, doi: 10.1136/bmj.n71.

[4] C. Chen and Y. F. Zheng, 'Passive and active stereo vision for smooth surface detection of deformed plates', *IEEE Trans. Ind. Electron.*, vol. **42**, no. 3, pp. 300–306, Jun. 1995, doi: 10.1109/41.382141.

[5] D. Beltran and L. Basañez, 'A Comparison between Active and Passive 3D Vision Sensors: BumblebeeXB3 and Microsoft Kinect', in *ROBOT2013: First Iberian Robotics Conference: Advances in Robotics, Vol. 1*, M. A. Armada, A. Sanfeliu, and M. Ferre, Eds, Cham: Springer International Publishing, 2014, pp. 725–734. doi: 10.1007/978-3-319-03413-3_54.

[6] G. Bianco, A. Gallo, F. Bruno, and M. Muzzupappa, 'A Comparative Analysis between Active and Passive Techniques for Underwater 3D Reconstruction of Close-Range Objects', *Sensors*, vol. **13**, no. 8, Art. no. 8, Aug. 2013, doi: 10.3390/s130811007.

[7] I. Martynov, J.-K. Kamarainen, and L. Lensu, 'Projector Calibration by "Inverse Camera Calibration"', in *Image Analysis*, A. Heyden and F. Kahl, Eds, Berlin, Heidelberg: Springer, 2011, pp. 536–544. doi: 10.1007/978-3-642-21227-7_50.

[8] R. Hartley, 'Triangulation, Computer Vision and Image Understanding', *Comput. Vis. Image Underst.*, 1997, Accessed: Apr. 12, 2025. [Online]. Available: https://www.semanticscholar.org/paper/Triangulation%2C-Computer-Vision-and-Image-Hartley/77f0fc6beb53d96c1f9e38a57ba6fc74f939982b

[9] F. Xu, Y. Xu, H. Zhang, and S. Chen, 'Application of sensing technology in intelligent robotic arc welding: A review', *J. Manuf. Process.*, vol. **79**, pp. 854–880, Jul. 2022, doi: 10.1016/j.jmapro.2022.05.029.

[10] X. Yang, Z. Zhou, J. H. Sørensen, C. B. Christensen, M. Ünalan, and X. Zhang, 'Automation of SME production with a Cobot system powered by learning-based vision', *Robot. Comput.-Integr. Manuf.*, vol. **83**, p. 102564, Oct. 2023, doi: 10.1016/j.rcim.2023.102564.

[11] E. Glaessgen and D. Stargel, 'The Digital Twin Paradigm for Future NASA and U.S. Air Force Vehicles', in *53rd AIAA/ASME/ASCE/AHS/ASC Structures, Structural Dynamics and Materials Conference*, American Institute of Aeronautics and Astronautics. doi: 10.2514/6.2012-1818.

[12] M. Grieves and J. Vickers, 'Digital Twin: Mitigating Unpredictable, Undesirable Emergent Behavior in Complex Systems', in *Transdisciplinary Perspectives on Complex Systems*, F.-J. Kahlen, S. Flumerfelt, and A. Alves, Eds, Cham: Springer International Publishing, 2017, pp. 85–113. doi: 10.1007/978-3-319-38756-7_4.

[13] 'ISO 23247-1:2021', ISO. Accessed: Dec. 26, 2025. [Online]. Available: https://www.iso.org/standard/75066.html

[14] 'ISO/IEC 30173:2023(en), Digital twin — Concepts and terminology'. Accessed: May 22, 2025. [Online]. Available: https://www.iso.org/obp/ui/en/#iso:std:iso-iec:30173:ed-1:v1:en

[15] O. Baer *et al.*, 'Digital Twin concept of a force measuring device based on the finite element method', *Acta IMEKO*, vol. **12**, pp. 1–5, Mar. 2023, doi: 10.21014/actaimeko.v12i1.1404.

[16] A. C. Bavelos *et al.*, 'Enabling Flexibility in Manufacturing by Integrating Shopfloor and Process Perception for Mobile Robot Workers', *Appl. Sci.*, vol. **11**, no. 9, p. 3985, Apr. 2021, doi: 10.3390/app11093985.

[17] P. Stączek, J. Pizoń, W. Danilczuk, and A. Gola, 'A Digital Twin Approach for the Improvement of an Autonomous Mobile Robots (AMR's) Operating Environment—A Case Study', *Sensors*, vol. **21**, no. 23, p. 7830, Nov. 2021, doi: 10.3390/s21237830.

[18] L. Zhou, L. Zhang, and N. Konz, 'Computer Vision Techniques in Manufacturing', *IEEE Trans. Syst. Man Cybern. Syst.*, vol. **53**, no. 1, pp. 105–117, Jan. 2023, doi: 10.1109/TSMC.2022.3166397.

[19] W. Li *et al.*, 'Modular design automation of the morphologies, controllers, and vision systems for intelligent robots: a survey', *Vis. Intell.*, vol. **1**, no. 1, p. 2, May 2023, doi: 10.1007/s44267-023-00006-x.

[20] K. Lalik and S. Flaga, 'A Real-Time Distance Measurement System for a Digital Twin Using Mixed Reality Goggles', *Sensors*, vol. **21**, no. 23, p. 7870, Nov. 2021, doi: 10.3390/s21237870.

[21] Y.-P. Su, X.-Q. Chen, C. Zhou, L. H. Pearson, C. G. Pretty, and J. G. Chase, 'Integrating Virtual, Mixed, and Augmented Reality into Remote Robotic Applications: A Brief Review of Extended Reality-Enhanced Robotic Systems for Intuitive Telemanipulation and Telemanufacturing Tasks in Hazardous Conditions', *Appl. Sci.*, vol. **13**, no. 22, p. 12129, Nov. 2023, doi: 10.3390/app132212129.

[22] W. A. A. Cotta, S. I. Lopes, and R. F. Vassallo, 'Towards the Cognitive Factory in Industry 5.0: From Concept to Implementation', *Smart Cities*, vol. **6**, no. 4, pp. 1901–1921, Aug. 2023, doi: 10.3390/smartcities6040088.

euspen's 26th International Conference & Exhibition, Krakow, PL, June 2026
www.euspen.eu

Non-contact calibration of resin gauge for assessing measurement errors of X-ray CT

Mari Watanabe[1,2], Osamu Sato[1], Mariko Kajima[1], Youichi Bitou[1], Masaki Michihata[2], Satoru Takahashi[2]

[1]) Dimensional Standards Group, Research Institute for Engineering Measurement, NMIJ, AIST
[2]) Department of Precision Engineering, School of Engineering, The University of Tokyo

marie.watanabe@aist.go.jp

Abstract
X-ray computed tomography (X-ray CT) is widely used for non-destructive three-dimensional inspection of industrial parts. For measurement applications, the accuracy of X-ray CT must be validated using reference gauges calibrated with traceability to the SI unit. We have developed a resin gauge with embedded spheres, whose center-to-center distances are calibrated using X-ray CT with an uncertainty of 3 µm. To improve the calibration uncertainty of the resin gauge to less than 1 µm, an optical non-contact calibration system is being developed. This study reports verification results for the measurement repeatability of the optical calibration system.

Dimensional, Measurement, X-ray, Calibration

1. Introduction

X-ray computed tomography (X-ray CT) is a powerful tool for measuring the external and internal geometrical features of industrial parts without destruction. To ensure accurate three-dimensional (3D) measurements, it is necessary to evaluate the length measurement accuracy of X-ray CT at various positions and in various directions within the measurement volume using a reference gauge [1]. We have proposed a new gauge with spheres embedded in resin, as shown in Fig. 1 [2], and are developing an optical non-contact measurement system for this gauge. The target calibration uncertainty using this system is less than 1 µm. In this study, the optical calibration system under development is introduced, and its measurement repeatability is evaluated.

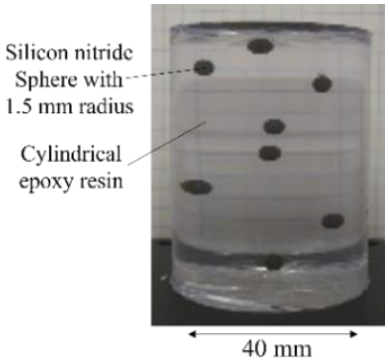

Figure 1. Resin gauge for assessing measurement errors of X-ray CT

2. Overview of the optical calibration system for a resin gauge

The center-to-center distances between the embedded spheres of the resin gauge are calibrated using the optical calibration system shown in Fig. 2. The resin gauge is placed on the X and Z stages of the system, and the center positions (x_c, z_c) of the spheres embedded in the resin gauge are measured. To acquire images of the spheres within the field of view of the telecentric microscope, the resin gauge is moved by the X and Z stages. The positions of the X and Z stages are measured by laser interferometers. The microscope is focused on the sphere by moving the Y stage. The gauge is then rotated by 90° around the Z axis, and the center positions ($x_{c(90°)}$, $z_{c(90°)}$) of the spheres are measured. From the center positions (x_c, z_c) and ($x_{c(90°)}$, $z_{c(90°)}$) of the spheres, the distances between them are calculated. By improving the structure of the optical calibration system reported in [3], Abbe errors are reduced in the current system.

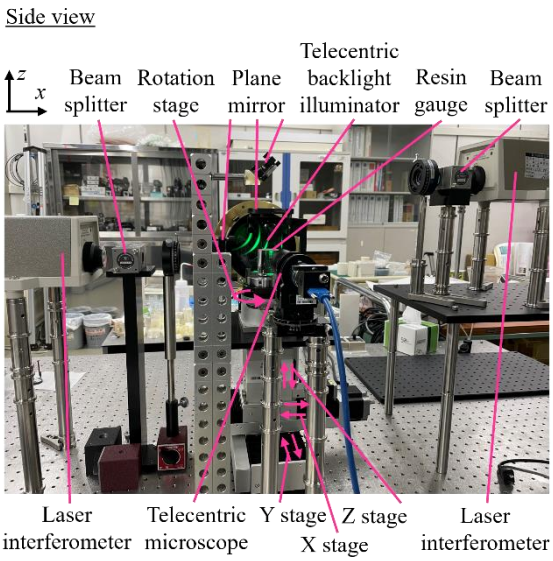

Figure 2. Optical calibration system for a resin gauge

To calibrate the resin gauge, it is necessary to evaluate the calibration uncertainties. The dominant calibration uncertainties of the resin gauge using the current system under development include repeatability, uncertainty due to the calculation method of the sphere center position, uncertainty due to thermal expansion of the resin gauge, geometric errors of the optical calibration system, and uncertainty due to refraction within the resin gauge.

3. Verification

To verify the repeatability of measurements of the sphere center positions using the optical calibration system, the sphere center positions of a 30 mm gauge, shown in Fig. 3, were measured repeatedly. In this gauge, ruby spheres with a diameter of 3 mm are fixed to carbon fiber–reinforced polymer (CFRP) support rods. The center positions of the spheres were measured 10 times at the original position and at the position after rotation, respectively.

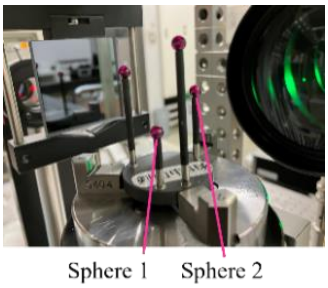

Figure 3. Gauge for the measurement repeatability verification 4of the optical calibration system

4. Results and discussion

Figures 4 and 5 show the deviations of the measured values from the average values of x_c, $x_{c(90°)}$, z_c, and $z_{c(90°)}$ for sphere 1 and sphere 2. Table 1 summarizes the measurement repeatability, expressed as standard deviation (SD) and peak-to-valley (PV), of the center positions of sphere 1 and sphere 2. The measurement repeatability (SD) of x_c and $x_{c(90°)}$ was within 1.0 µm, and that of z_c and $z_{c(90°)}$ was within 2.1 µm.

Through the verification experiment, it was confirmed that reducing Abbe errors in the measurement system improves the repeatability of the system. Before improvement of the instrument structure, the measurement repeatability (SD) of x_c and $x_{c(90°)}$ was within 1.7 µm, and that of z_c and $z_{c(90°)}$ was within 2.8 µm. Because the spheres of the gauge used for the verification are supported by CFRP rods, fluctuations due to thermal expansion of the gauge can be smaller than sub-micrometer.

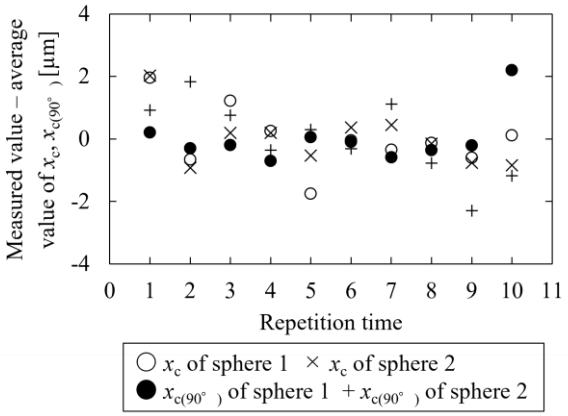

Figure 4. Deviations of the measured value from the average value of x_c, $x_{c(90°)}$

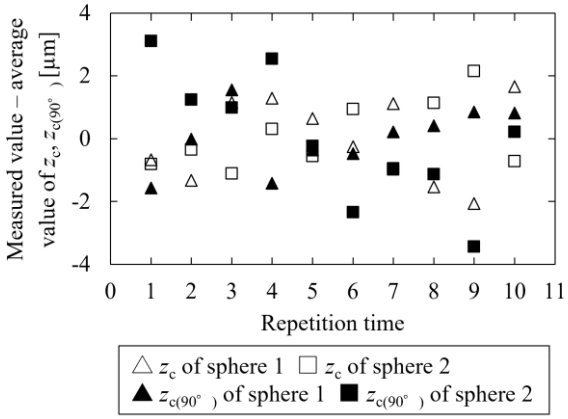

Figure 5. Deviations of the measured value from the average value of z_c, $z_{c(90°)}$

Table 1 Measurement repeatability of sphere 1 and 2's center positions

	Measurement repeatability [µm]
x_c	SD: 1.0 µm (Sphere 1), 0.8 µm (Sphere 2)
	PV: 3.7 µm (Sphere 1), 2.9 µm (Sphere 2)
z_c	SD: 1.3 µm (Sphere 1), 1.1 µm (Sphere 2)
	PV: 3.7 µm (Sphere 1), 3.3 µm (Sphere 2)
$x_{c(90°)}$	SD: 0.8 µm (Sphere 1), 0.8 µm (Sphere 2)
	PV: 2.5 µm (Sphere 1), 2.4 µm (Sphere 2)
$z_{c(90°)}$	SD: 1.0 µm (Sphere 1), 2.1 µm (Sphere 2)
	PV: 3.1 µm (Sphere 1), 6.5 µm (Sphere 2)

To achieve the target calibration uncertainty in this study, further improvement is required. The lasers fluctuated with an SD of 0.2 µm due to air turbulence and temperature drift. In addition, the measured values may vary because the rigidity of the laser mounts in the current system is still low. The measurement repeatability of z_c and $z_{c(90°)}$ was lower than that of x_c and $x_{c(90°)}$. This may be because the position of the mirror used to measure the position of the Z stage fluctuates in accordance with the stage movement during measurement. Therefore, it is necessary to reduce fluctuations due to instability of the laser units and the mirror setting.

5. Summary

The measurement repeatability of the optical calibration system under development for the resin gauge was verified. The measurement repeatability was within an SD of 2.1 µm. To achieve the target calibration uncertainty, it is necessary to further improve the measurement repeatability by stabilizing the laser units and the mirror setting and by reducing other contributions to uncertainty.

References

[1] Obaton A, Klinga CG, Rivet C, Mohaghegh K, Baier S, Andreasen J, Carli L, Chiffre L 2020 Reference standards for XCT measurements of additively manufactured parts 10th Conference on Industrial Computed Tomography

[2] Watanabe M, Sato O, Matsuzaki K, Telada S, Watanabe T, Bitou Y, Takatsuji T 2023 A resin gauge for performance testing of X-ray CT and its calibration by multiple orientation measurements Precis. Eng. **84** 15-20

[3] Watanabe M, Matsuzaki K, Sato O, Kajima M, Watanabe T 2024 Optical calibration system for resin gauges used in X-ray CT The 20th International Conference on Precision Engineering 1-4

euspen's 26th International Conference & Exhibition, Krakow, PL, June 2026
www.euspen.eu

Probe head errors module for digital-metrological twin of five-axis CMM based on use of neural networks

Piotr Gąska[1], Wiktor Harmatys[2], Maciej Gruza[2], Adam Gąska[2]

[1]AGH University of Krakow, Faculty of Mechanical Engineering and Robotics
[2]Cracow University of Technology, Faculty of Mechanical Engineering

adam.gaska@pk.edu.pl

Abstract
Currently, in the era of Industry 4.0, smart factories, and digital manufacturing also in the field of metrological solutions, which form the basis of quality control systems in production, many new concepts are emerging that aim to minimize human intervention in the measurement process, its evaluation, and the assessment of measurement accuracy. Example of such solutions are digital-metrological twins, which are used to synchronize the digital representation of a measurement system or process with the actual state of real system or process. Digital metrological twins of coordinate measuring systems typically consist of several modules that replicate and simulate the errors of individual CMM subsystems (e.g., a module simulating kinematic errors of the CMM or errors of the measuring probe) or factors that affect the accuracy of measurements performed on a CMM (e.g., a module simulating the influence of temperature or vibrations). This article presents the concept of a new module that simulates probe head errors, based on the application of neural networks, for use in a digital metrological twin of a five-axis CMM. The article presents experiments based on measuring standard rings in different orientations, that aim at determining error distributions of probe heads used in five-axis CMMs. A method is also presented for simulating measurement errors in arbitrary probe head orientations, using data obtained in the aforementioned phase together with neural networks. The correctness of the developed module is verified by comparing its results with experimentally obtained error values, for points different from those used in the process of identification of the probe head error distributions. The verification results proved that the errors simulated by the developed module faithfully represent the actual probe head error values, which means that the module can be successfully implemented in the digital metrological twin model of a five-axis CMM.

CMM, digital twin, accuracy, five-axis, uncertainty

1. Introduction

In recent years, a rapid development of solutions in the field of artificial intelligence has been observed, resulting in numerous applications also within the domain of geometric metrology [1]. Potential areas of application of this technology include, among others, the identification of errors in coordinate measuring machines [2], support of surface roughness evaluation processes [3], errors correction of optical measuring systems [4] and measurement uncertainty estimation [5]. In the latter area, methods based on various forms of machine learning align with the ongoing trend toward the development of simulation-based approaches for assessing measurement accuracy.

These methods, offering a number of undeniable advantages such as high computational efficiency and usability by operators without extensive expertise in measurement uncertainty, constitute a highly desirable alternative to classical approaches, such as the calibrated-workpiece method [6] or the guidelines described in the GUM [7]. Although the well-known methods of uncertainty estimation are supported by numerous application examples and well-defined computational frameworks, they still pose a significant challenge in practice, as evidenced by the ambiguity of results obtained by different institutions [8].

This article presents a description and the results of an experimental study focused on the use of artificial neural networks for modelling the errors of a measurement probe employed in a five-axis coordinate measuring system. The importance of this system component requires no further justification [9], while in five-axis systems the probe plays a critical role by fundamentally influencing the measurement process and enabling improvements in both accuracy and repeatability [10]. The subsequent sections describe the development of the AI-based model for probe errors and its comparison with experimental results as well as with an existing error model for this type of probe.

2. Methodology and Experiments

The described investigations were carried out on a five-axis coordinate measuring system consisting of a Zeiss WMM 850S coordinate measuring machine and a Renishaw PH20 probe head mounted on its quill, operating in conjunction with a TP20 SF touch-trigger probe (Fig.1). The system working volume is 800 × 1000 × 600 mm, and its accuracy can be described as (1):

$$E_{E0,MPE} = 2{,}5 + 2{,}5 * L/1000 \quad (1)$$

where: L is measured length given in mm

Figure 1. Five-axis coordinate system utilized during experiments consisting of Zeiss WMM 850S with installed probing system Renishaw PH20.

Accuracy of probing system can be characterized with a PForm.Sph.1x25:SS:Tact value of 0.0021 mm. The PH20 probe head constitutes a key component of the five-axis system, as it enables measurements to be performed using the rotational motions of the probe head rather than, as in conventional CMMs with a fixed declared probe orientation, relying on the linear movements of the measuring machine itself.

The probe head features two rotary axes whose theoretical point of intersection lies on the quill axis responsible for motion along the vertical direction. The vertical rotation angle is denoted by the letter B and can vary within the range from −180° to 180°, while the horizontal rotation angle is denoted by A and can vary from −100° to 100°. The probe stylus is aligned parallel to the quill axis when the angular positions are set to A = 0° and B = 0°.

The data required for the model (treated as input data) were obtained through repeated measurements of a reference ring with a diameter of 20 mm and a small form deviation (approximately 0.2 µm), performed in various orientations relative to the working range of the probing system. Each ring orientation was defined by the A and B angle values, which represent the angular positions of the probing system when it is oriented parallel to the main axis of the reference ring. Measurements were carried out with the B angle varying in increments of 20° from −160° to 180°, and the A angle varying in increments of 15° from 0° to 90°. For each ring orientation, the ring was measured at 64 evenly distributed points located at the mid-height of the ring (Fig. 2).

Figure 2. Five-axis coordinate system utilized during experiments consisting of Zeiss WMM 850S with installed probing system Renishaw PH20.

A local coordinate system was established using the inner cylindrical surface of the ring gauge (as the main spatial axis), the ring plane (to define the datum origin), and measurements of one side of the block to which the ring was attached (to define the second direction of the coordinate system). During the circle measurements, only the movements of the probing system were employed. The radial error at each measured point was determined relative to a least-squares fitted circle. Such errors due to small size of reference ring (diameter of 20 mm) and its small form deviation (about 0,2 µm) can be treated as a representation of probing system errors [11]. For each orientation, the measurements were repeated ten times.

The results obtained for approximately 120 orientations were used as input data for the AI model, comprising about 76,000 measured points and corresponding deviations. Some of the orientations measured during the experiment were deliberately excluded from the input dataset to allow their subsequent use for verification of the model's performance.

The AI model architecture consists of three main dense blocks. The first two hidden layers each had 256 neurons, and the third layer had 128 neurons. Layer Normalization (LN) and GELU nonlinearity were applied after each of the first two layers, followed by a 0.10 dropout to reduce overfitting and improve generalization for unseen pairs (A, B). After the third layer, normalization and GELU activation without dropout were applied to preserve the model's ability to accurately estimate small values. The output layer was linear and returned a vector of 1+2K Fourier coefficients; for the example configuration K=8, this means 17 output parameters. Additionally, L2 regularization (of the order of 10^{-4}) was applied to the dense layers, acting as a mild constraint on model complexity, especially important when the number of unique configurations (A, B) is small. The coefficients predicted by the network were transformed to d̂(n) values at each training iteration by matrix multiplication with a Fourier basis matrix corresponding to a 64 number of measured points n. The d'(n) waveform was then compared to the reference d(n), minimizing the weighted Huber loss. The mean absolute error (MAE) and RMSE, also calculated at the full curve level in µm, were used as diagnostic metrics.

Optimization was performed using the AdamW method, an Adam variant with explicit weight decay, with an initial training step of 10^{-3} and a weight decay of 10^{-4}. The training process was supported by a ReduceLROnPlateau learning step reduction schedule that monitored the MAE validation metric of the curve, with the minimum learning step limited to 10^{-6}, and a patient Early Stopping mechanism, which allowed for a stable approach to the optimum without the risk of quality degradation in the validation set. A key element of the validation protocol was the division of the data into training, validation, and test sets, implemented at the group level (A,B), so that the probe head configurations in the test set were not visible during training.

After the AI model was created, it was used in the next step to predict error values at individual measurement points for the selected orientations that had been measured but were not included in the model input dataset. The model predictions were compared with the results obtained from direct measurements and with those simulated using an error model based on trilinear interpolation combined with the Monte Carlo method, as described in [12]. For each point, the simulation error ε_s was determined according to the following equation (2):

$$\varepsilon_s = \delta_{AI} - \delta_m \quad (2)$$

where: δ_{AI} – deviation given by AI model; : δ_m – deviation obtained through measuremnts

3. Results and discussion

In the following figures, the results obtained from measurements of the ring, as well as those given by the AI model and the trilinear interpolation model, are presented. The verification was performed at the following positions: A 15, B -20 (Fig. 3), A 75, B 40 (Fig. 4), and A 45, B -20 (Fig. 5). Additionally, measurements were conducted at an extra position located between the orientations considered in the model: A 43, B 91 (Fig. 6).

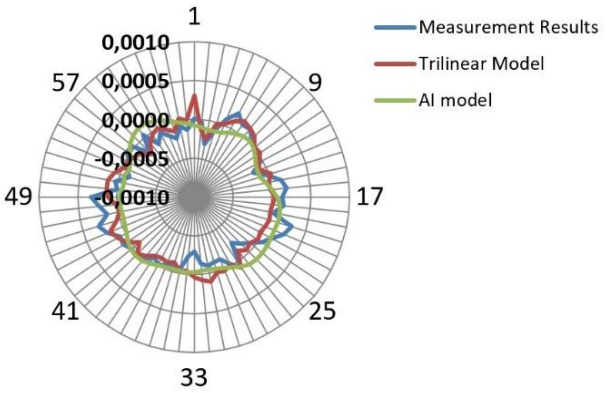

Figure 3. Ring orientation **A 15 B -20**. Results of verification of developed AI model and its comparision with probing system errors model based on usage of trilinear interpolation and Monte Carlo method. The error values are represented along the radial axis expressed in mm. The values indicated along the circumference represent the measurement points numbers.

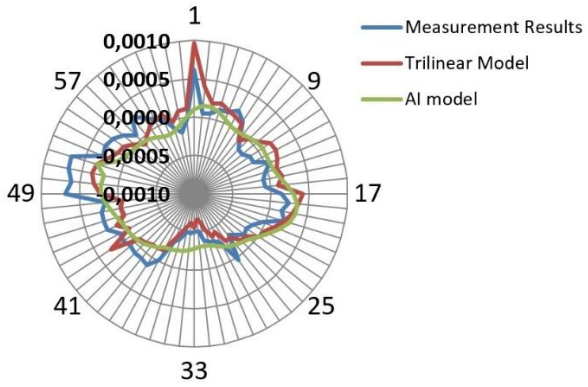

Figure 4. Ring orientation **A 75 B 40**. Results of verification of developed AI model and its comparision with probing system errors model based on usage of trilinear interpolation and Monte Carlo method. The error values are represented along the radial axis expressed in mm. The values indicated along the circumference represent the measurement points numbers.

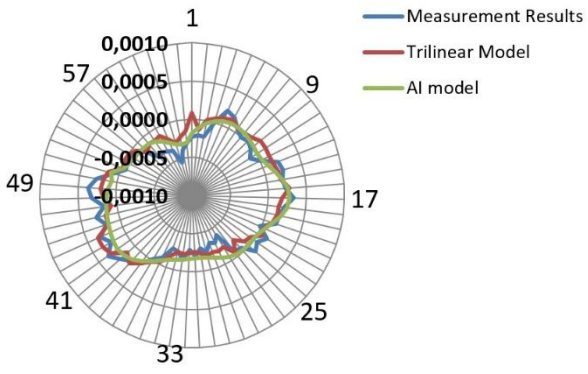

Figure 5. Ring orientation **A 45 B -20**. Results of verification of developed AI model and its comparision with probing system errors model based on usage of trilinear interpolation and Monte Carlo method. The error values are represented along the radial axis expressed in mm. The values indicated along the circumference represent the measurement points numbers.

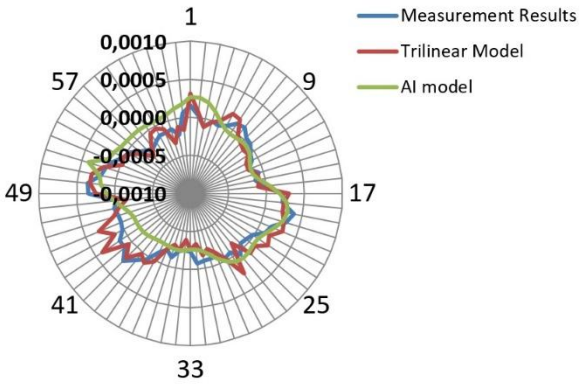

Figure 6. Ring orientation **A 43 B90**. Results of verification of developed AI model and its comparision with probing system errors model based on usage of trilinear interpolation and Monte Carlo method. The error values are represented along the radial axis expressed in mm. The values indicated along the circumference represent the measurement points numbers.

A characteristic feature of the PH20 probe head is the change in the error distribution obtained when measuring the same ring using different orientations [12]. The AI model was able to reproduce this variation. When analyzing the presented plots, it should be noted that both error models considered in the experiment yielded overall error characteristics that are similar in shape to those obtained from the measurements. However, it is evident that the AI model performed less effectively in reproducing sudden irregularities in the error characteristics, tending instead to smooth the probe head error values.

Below, Tables 1–3 present a ranges of probe errors obtained from measurements and modelled using considered models, the maximum absolute probe head error and the mean absolute simulation error.

Table 1 Range calculated from probe errors obtained for different orientations of reference ring from measurements and via simulation using AI model and trilinear interpolation model. Range values given in µm.

Ring orientation	Range / µm		
	Measurement	AI model	Trilinear model
A 15 B -20	0,60	0,70	0,60
A 75 B 40	1,20	0,80	0,80
A 45 B -20	0,90	0,60	0,50
A 43 B 90	0,60	0,80	0,60

Table 2 . Maximum absolute value of of probe error obtained for different orientations of reference ring from measurements and via simulation using AI model and trilinear interpolation model. Error values given in µm.

Ring orientation	Maximum absolute probe error / µm		
	Measurement	AI model	Trilinear model
A 15 B -20	0,30	0,40	0,30
A 75 B 40	0,70	0,50	0,97
A 45 B -20	0,60	0,33	0,31
A 43 B 90	0,40	0,50	0,40

Table 3 Mean absolute simulation error in relation to experimentaly obtained data for AI model and trilinear interpolation model. Error values given in µm.

Ring orientation	Mean absolute simulation error / µm	
	AI model	Trilinear model
A 15 B -20	0,12	0,11
A 75 B 40	0,18	0,17
A 45 B -20	0,11	0,13
A 43 B 90	0,14	0,10

An analysis of the obtained error results indicates that both models generated very similar values. It is difficult to unequivocally determine which model is closer to the reference values obtained from the measurements, as in nearly every considered case, for two of the ring orientations the AI model produced results that were more accurate or more consistent with the measured values, while for the remaining two orientations better agreement was achieved by the model based on trilinear interpolation combined with the Monte Carlo method.

What deserves particular attention and emphasis is the fact that the observed discrepancies with respect to the measurement-derived errors are on the order of a few tenths of a micrometer. Moreover, for none of the considered ring orientations does the mean absolute simulation error exceed 0.2 µm. Taking into account that the manufacturer of the TP20 probe, which is mounted on the PH20 probe head, specifies a pre-travel variation of ±0.8 µm for the standard trigger force version and a unidirectional repeatability of ±0.35 µm, as well as that PForm.Sph.1x25:SS:Tact of the utilized five-axis system is about of 2 µm the observed results should be regarded as highly satisfactory.

Considering only the results presented in Tables 1–3, it can be concluded that the AI-based model could perform sufficiently well as a component of a digital twin for measurement uncertainty estimation in the context of probe head error modeling in a five-axis coordinate measuring system.

At the same time, it is important to acknowledge a limitation of the proposed solution. As noted in the Materials & Methods section, the training of the model required probe head error information obtained at nearly 75,000 measurement points. This is a large dataset, implying the need for extensive and time-consuming experimental campaigns. By comparison, the model based on trilinear interpolation and the Monte Carlo method relies on error information observed at approximately 15,000 points. Although this still represents a substantial amount of measurement data, it nonetheless requires roughly five times less experimental effort

4. Conclusions

The presented AI-based model for generating probe head errors in five-axis coordinate measuring systems achieved satisfactory agreement with experimentally obtained data. The error characteristics produced by the AI model are slightly smoothed compared to the measurement data, which may suggest that, in its current form, the model would be difficult to apply directly for probe head error compensation. At the same time, as demonstrated by the verification experiments conducted for different orientations of the reference ring, the model was able to capture changes in the error distribution across different regions of the probe head working volume so it seems that it could be useful in estimation of measurement uncertainty.

The observed simulation errors, determined with respect to experimentally acquired values, were significantly lower than the probe head repeatability declared by the manufacturer. However, the most significant limitation of the current model is the requirement for a large amount of input data, which raises concerns regarding its practical applicability. When comparing the AI-based approach with another model reported in the literature [12], no clear advantages of the AI model can be identified. Considering a substantially larger number of preliminary measurements required for the AI model than for the one based on trilinear interpolation combined with the Monte Carlo method, the use of AI in this specific case does not appear to be the most effective available option. This finding may serve as an argument against the prevailing tendency to apply AI indiscriminately to all possible applications and problem domains.

References

[1] Wieczorowski M, Kucharski D, Sniatala P, Pawlus P, Krolczyk G and Gapinski B 2023 *Meas.* **217** 113051
[2] Chen G, Mehdi-Souzani C, Anwer N 2026 *Adv. Eng. Inform.* **70** 104142
[3] Yang H, Zheng H and Zhang T 2024 *Tribol. Int.* **199** 109935
[4] Harmatys W, Gąska A, Gąska P and Gruza M 2026 *Meas.* **260** 119863
[5] Samadi H, Ahsan M and Raman S 2025 *Next Research* **2** 100299
[6] ISO 15530-3:2011 GPS CMM Use of calibrated workpieces or measurement standards
[7] JCGM 100, Evaluation of measurement data. Guide to the expression of uncertainty in measurement, 2008
[8] Hansen H N and De Chiffre L 1999 *Prec. Eng*. **23** 3 185-195
[9] Weckenmann A, Estler T, Peggs G and McMurtry 2004 CIRP Ann. Manuf. Technol. 53 2 657-684
[10] Gruza M, Gąska A, Gąska P, Harmatys W and Sładek J 2016 Mechanik 11 1708-1709
[11] Sładek J 2016 Coordinate Metrology Accuracy of Systems and Measurements Springer: Berlin, Germany
[12] Gąska A, Gąska P and Gruza M 2016 Appl. Sci.6 144

euspen's 26th International Conference & Exhibition, Krakow, PL, June 2026
www.euspen.eu

Evaluation of radii in machined components

Adam Szczepański[1], Marek Magdziak[2]

[1]*Pratt & Whitney Rzeszów, Poland*
[2]*Faculty of Mechanical Engineering and Aeronautics, Rzeszów University of Technology, Rzeszów, Poland*

adam.szczepanski@prattwhitney.com

Abstract

The paper addresses the requirements specified in the ASME Y14.5-2018 standard concerning the radii of machined parts, with particular emphasis on the controlled radius specification. The controlled radius differs from a regular radius requirement in that it defines not only the nominal size of a radius but also constrains its form and smoothness, excluding flats, reversals, and local irregularities. This type of specification is commonly applied to aerodynamic and rotating components, where geometric continuity and smooth surface transitions are critical. This paper investigates the influence of profile deviations in a radius curve on the measured radius value obtained using CMM scanning. A reference object containing several radii with intentionally simulated defects in the form of flattened areas was scanned under various measurement strategies. The scanning velocities were varied to evaluate their influence on the radii evaluated in accordance with the selected requirement specified in ASME Y14.5-2018.

Keywords: controlled radius, CMM, scanning

1. Introduction

The aerospace industry faces a growing challenge in maintaining the highest levels of operational safety while continuously pursuing weight reduction, increased energy efficiency, and extended engine lifetime. One of the key factors influencing the reliability of rotating assemblies is the dimensional and geometric accuracy of their mechanical components, particularly in surface regions that are critical to fluid flow, stress distribution, and fatigue resistance. Even minor deviations in curvature transitions can result in stress concentrations, which may subsequently initiate cracks and lead to component failure during engine operation [1].

Within this context, the proper definition and control of transitional radii become essential. According to ASME Y14.5–2018 [2], the Controlled Radius (CR) measurement characteristic may be used for such a task. The CR is defined as a smoothly blended transition between two surfaces, free from reversals of curvature or local discontinuities, while maintaining the radius value within specified tolerance limits throughout the entire feature.

The subsequent sections of the paper present:

- a comparison of various methods used to define radius requirements,
- the experiments carried out using a coordinate measuring machine (CMM), with measurements performed on a specially designed object containing different curvatures and intentional defects,
- final conclusions regarding the conducted investigations.

2. Radius requirements discussion

In geometric dimensioning and tolerancing (GD&T), as specified in [2], there are three primary methods used to define a radius. The first and most traditional method, applied for many years, is the standard radius, which allows a profile to assume essentially any shape as long as it lies within a crescent-shaped tolerance zone (in cases where the center of the radius is not specified). The interpretation of this type of requirement is shown in Figure 1. However, this approach does not guarantee the continuity or smoothness of a profile and is therefore inadequate for sufficiently constraining local variations in curvature.

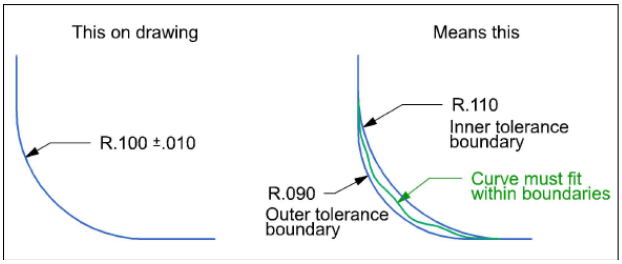

Figure 1. Definition of the standard radius [2]

Another possibility is the application of profile of a line tolerance to control the radius. The tolerance zone is created by offsetting the basic radius-shaped curve by a value equal to half of the specified profile tolerance on both sides. This method is often preferred from a metrological point of view, as it guarantees repeatable and consistent inspection results, unlike the standard method, where the results may vary significantly due to changes in the curvature. However, this approach is less suitable when the objective is to limit distortions in the shape of a curve. The interpretation of this characteristic is shown in Figure 2.

The CR was introduced to limit distortions of the radius of a curve and to ensure uniform stress distribution along the transition. The standard [2] defines the CR requirements but does not provide any detailed guidelines for inspection methods. The key question is to what extent an imperfection constitutes a violation of the CR specification. Therefore, it is recommended that such limits should be defined in company

standards or equivalent internal documents. The interpretation of the CR characteristic is illustrated in Figure 3. A method for assessing this characteristic was proposed in [3].

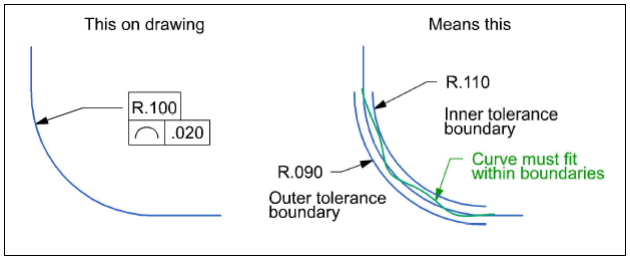

Figure 2. Profile of a line controlling a radius [2]

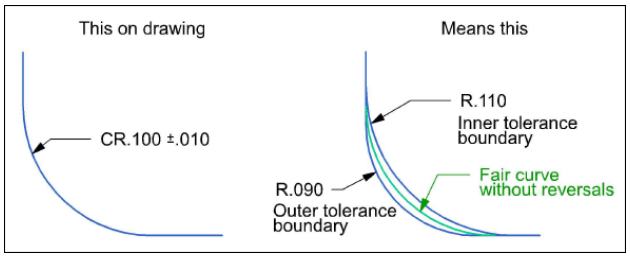

Figure 3. Interpretation of the controlled radius [2]

The evaluation path may be composed of the stages presented in Figure 4. It should be noted that the same method can be used to determine the actual radius value for both R and CR, however, CR requires radius defects evaluation, which is not required for an ordinary radius.

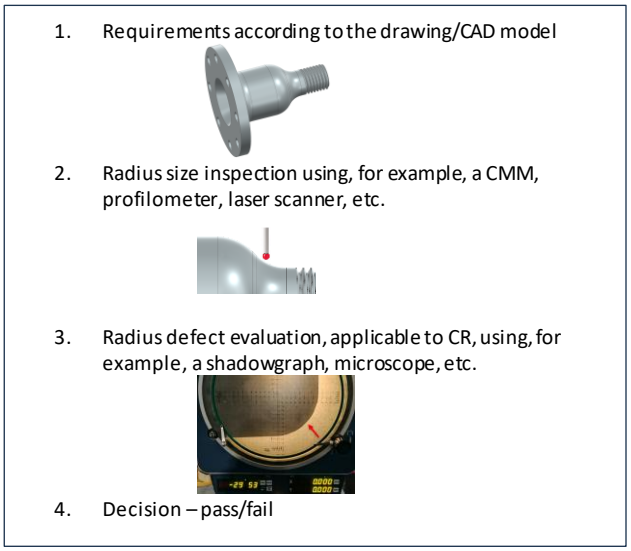

Figure 4. Radius evaluation steps for the CR characteristic

In another study, the authors investigated the standardization of CR evaluation by involving three professional quality inspectors to assess the consistency of their judgments and to develop an acceptance matrix. A shadowgraph equipped with a 20× magnification lens was used for the examination, enabling the inspectors to identify very small defects. The detection threshold was established using the same artifact presented in this paper. In addition, the use of a coordinate measuring machine for the evaluation of defects of the inspected radius was also investigated.

3. Experimental investigation

The purpose of the experiment described herein is to determine how defects located on a radius curve affect the repeatability of inspection results at various scanning speeds when using a coordinate measuring machine. The inspection was carried out on an artifact specifically designed for this purpose.

3.1. Examined object

The reference object containing curves with radii ranging from R=2 mm to R=20 mm was designed, see Figure 5. The radii were intentionally distorted to introduce controlled defects in the form of flattened regions, with depths ranging from 0.005 mm to 0.08 mm. The artifact was manufactured as a sheet metal component using wire electrical discharge machining (wire EDM) to ensure high dimensional accuracy.

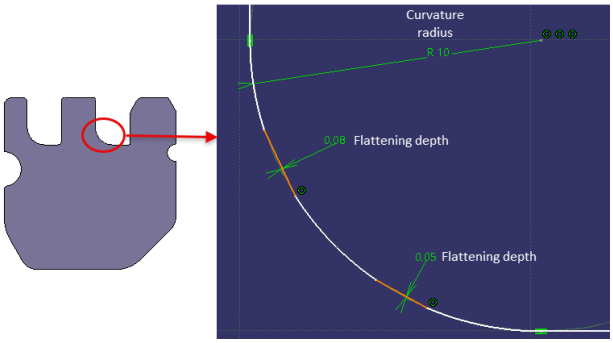

Figure 5. Reference object and an example of a simulated radius defect

Table 1 summarizes the defects. It should be noted that the radii were located at corners with different angles as presented in Figure 6, and in many cases more than one defect was present on a single curve.

Table 1. Summary of radii and defect sizes

Radius index	Radius size [mm]	Defect size [mm]	R at corner angle [deg]
B4	2	0.01	120
B10	2	0.015; 0.02	90
B11	2	0.05	90
B17	2	0	115
B5	5	0.005; 0.01; 0.015	120
B6	5	0	150
B14	5	0.02; 0.025; 0.03	90
B1	5	0	not in corner, groove radius
B8	10	0.005; 0.01; 0.015; 0.02; 0.03	90
B12	10	0.05; 0.08	90
B16	10	0	not in corner, groove radius
B19	10	0.05	120
B21	10	0.08	135

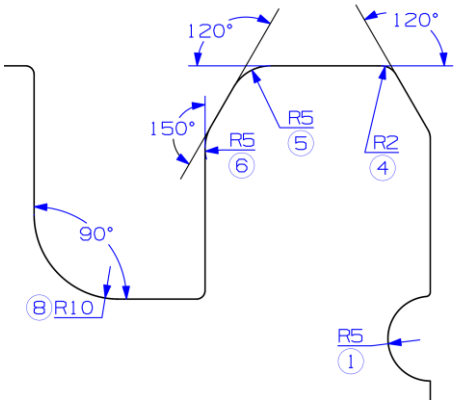

Figure 6. Fragment of the artifact with marked corner angles

3.2. CMM inspection

The contour of the reference object was scanned using a CMM equipped with a VAST Gold active scanning head, controlled by Calypso software. The scanning path was based on the CAD model of the artifact, with a point resolution of 0.02 mm. A ruby stylus with a diameter of 0.5 mm was used, and no software filtering was applied. In order to calculate the values of actual radii the Gaussian fitting algorithm was selected. Three scanning speeds: 10 mm/s, 5 mm/s, and 1 mm/s were applied, and ten repeated measurements were carried out for each speed in order to evaluate repeatability. The resulting scans were then used to measure two types of radius characteristics: R and CR as well as a line profile. R and CR were identical in terms of radius size evaluation. Figure 7 shows the artifact during the CMM scanning process.

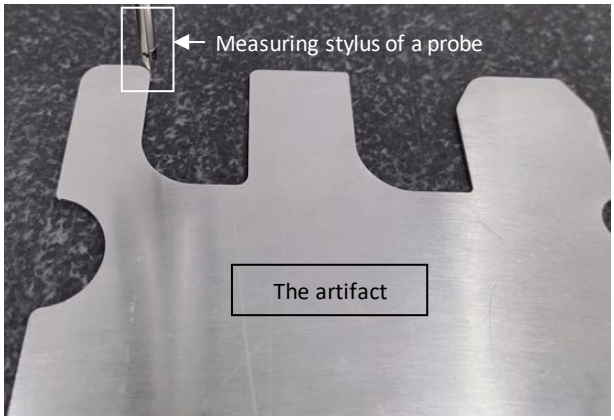

Figure 7. CMM Inspection

4. Results of investigations

Figure 8 presents the results of the radius value inspection, illustrating the influence of the applied scanning speed and simulated defects on the variation of the measured radius values. Since the evaluation method is identical for both R and CR, the obtained results are also identical. However, within a standard quality inspection process, CR requires additional assessment of profile defects (like presented in Figure 4).

The experiment reveals that the scanning speed within the assumed range has a limited influence on the observed variation. Although it could be expected that the stability at 1 mm/s would be better than at 10 mm/s, the measured values do not confirm such an assumption in all cases. There are examples in which the scanning speed has only a negligible effect on the variation, as observed for radii B10, B17, B8, and B16.

In some cases, the differences in variation between individual scanning speeds were clearly noticeable, however, there is no consistent trend supporting the claim that the variation increases with increasing speed. There are even examples in which a lower scanning speed resulted in greater variation, as can be seen for B11 and B5.

The variation observed for B1 at 10 mm/s and for B12 at 5 mm/s appears to be random, as it is significantly different from the values obtained at the two remaining scanning speeds. Nevertheless, B12 contains two significant defects (0.05 mm and 0.08 mm), which makes this radius more susceptible to increased variation. This leads to the conclusion that the highest variation is generally associated with larger defect sizes. A similar relationship can also be observed for other radii, such as B11 (defect of 0.05 mm), B19 (defect of 0.05 mm), and B21 (defect of 0.08 mm).

This effect is additionally strengthened by the fact that these curves are located at corners with obtuse angles. This is a well-known phenomenon affecting coordinate-based inspection methods, including CMMs, profilometers, laser scanners, and similar systems. In general, the wider the included angle, the poorer the repeatability of the inspection results.

The results of the line profile evaluation are presented in Figure 9. The same data points that were used for the actual radius calculation were also applied for the profile computation. The profile of each curve was best fitted to the nominal curve using Gaussian method.

It is immediately visible that, compared with the actual radius value evaluation, the line profile results are more stable across the entire range of radii and scanning speeds. There is one case for B10 in which the variation at 1 mm/s significantly differs from the values obtained for the other two scanning speeds, therefore, it can be regarded as an exceptional result.

The most interesting portion of the data is related to the radii with a nominal size of 10 mm. Although B8 contains numerous defects and B12 includes the largest individual defects, the variation remains at a very low level for both radii. These two features are located at corners with a right angle.

A reduction in the repeatability of the profile results can be observed for B16, B19, and B21. The radius indexed as B16 is not located at a corner but represents a groove radius. It contains the highest number of inspection points, which is generally considered beneficial in coordinate metrology. On the other hand, a larger number of points also increases the likelihood that random deviations may influence the result. Unlike the calculation of the actual radius using the Gaussian fitting method, where the result is effectively averaged, profile evaluation is more sensitive because each individual point contributes directly to the final value.

For B19 and B21, which are located at corners with obtuse angles, the variation occurs at a level comparable to that observed for B16, and it also correlates with the variation of the R value inspection results. For B19, in both evaluation methods, the highest variation is visible at 5 mm/s, whereas for B21 the highest variation occurs at 10 mm/s. This leads to the conclusion that, for both methods, the quality of the scanned data has a greater influence on the results than the applied evaluation method.

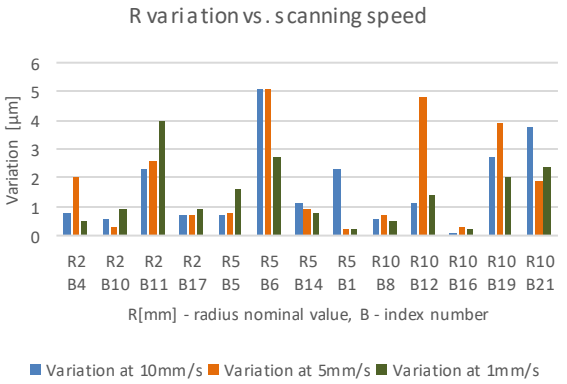

Figure 8. Radius actual value variation for different scanning speeds and radii sizes

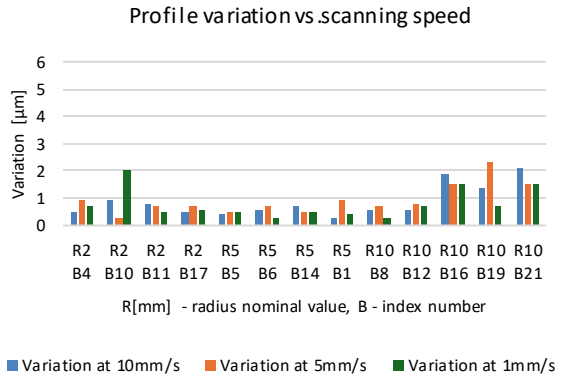

Figure 9. Radius profile variation for different scanning speeds and radii sizes

5. Conclusions

The conducted experiments revealed that the measurement results depend on the applied scanning speed only to a limited extent. Although scanning speed may have an influence on the measured values, the measuring system and software used in the study appear to minimize this effect, thereby limiting the dispersion of the obtained data. When scanning with the active VAST Gold probe, the system automatically adjusts the actual scanning speed to the local curvature of the measured feature, even if a higher nominal scanning speed has been defined in the software. As a result, the probe slows down in regions with smaller radii or more complex geometry, which improves contact stability and reduces the influence of the programmed scanning speed on the final measurement results. The most significant variation in radius values (for the standard radius characteristic) was observed for curves containing the largest simulated manufacturing defects.

The comparison between the two evaluation methods (actual radius value computation and line profile assessment), shows that the second one provides less variable results. The repeatability of the profile results, typically below one micrometer and only in a few cases between one and two micrometers, supports this conclusion.

Further investigations will focus on the analysis of defect detection levels, including other typical defects such as mismatch, double R, cusp, and similar irregularities. Additional research will address the development of advanced algorithms for automated CR evaluation within coordinate inspection systems. The authors plan to continue this work in collaboration with an aviation industry company producing safety-critical rotating components.

References

[1] National Transportation Safety Board (NTSB), 2023, Aviation Investigation Final Report: Accident Number WPR22LA019,
[2] The American Society of Mechanical Engineers (ASME), 2018, ASME Y14.5-2018: Dimensioning and Tolerancing Engineering Product Definition and Related Document Practices
[3] Magdziak M. 2024, Application of Coordinate Measuring Machines for Analysis of a Controlled Radius Based on Linear Regression, Adv. Sci. Technol. Res. J. **18(2)** 11-25

euspen's 26th International Conference & Exhibition, Krakow, PL, June 2026
www.euspen.eu

Surface Analysis and Evaluation of Corrosion-Induced and Pore-Like Textures

Aleksandra Mirowska[1,2], Robert Tomkowski[2], Michał Dobrzyński[1], Amir Rashid[2], Sasan Dadbakhsh[2]

[1]*Faculty of Mechanical Engineering and Ship Technology, Gdansk University of Technology, Narutowicza 11/12,80-233 Gdansk, Poland*
[2]*Department of Production Engineering, KTH Royal Institute of Technology, Brinellvägen 68, 114 28 Stockholm, Sweden*

aleksandra.mirowska@pg.edu.pl

Abstract
Surfaces exhibiting corrosion degradation effects and similar pore structures present complex topographical features that significantly influence material performance and durability. This study develops and evaluates comprehensive measurement methodologies for characterising surfaces displaying both corrosion-induced degradation patterns and analogous pore-like structural features. Using integrated optical profilometry, scanning electron microscopy (SEM) and three-dimensional (3D) surface reconstruction techniques, surfaces were systematically analysed for their morphological characteristics. Key parameters including pore/pit size distribution, surface roughness metrics, texture similarity indices, and topographical complexity were quantitatively assessed across multiple sample conditions. The analysis reveals that corrosion-damaged surfaces and engineered pore structures exhibit comparable textural signatures with distinguishable differences in feature organisation and spacing patterns. A standardised evaluation protocol was developed to objectively measure and classify these corrosion-like surface textures based on morphological parameters and spatial characteristics. The proposed framework enables reliable differentiation and quantitative assessment of corroded versus artificially created pore-textured surfaces. The results demonstrate practical applications for surface quality control and corrosion monitoring. This work provides essential methodology for consistent reproducible evaluation of complex corrosion and pore-structured surfaces in materials science and industrial applications.

Surface porosity measurement, corrosion-like surfaces, 3D topography characterization, surface roughness evaluation

1. Introduction

Material surfaces exhibiting corrosion and porous structures are a key focus of modern materials science due to their complex topography, which has a significant impact on the properties and durability of the material. Both natural processes, such as corrosion degradation, and manufacturing technologies generate an irregular distribution of pits, pores and peaks with a multi-dimensional distribution characterised by high spatial variability [1]. Corrosion processes result in deep, localized pits (pitting corrosion) with highly irregular morphology, ranging from a few to tens of micrometers in diameter, with depths often exceeding 10 µm [2]. The distribution of pits on the surface is subject to statistical fluctuations, and in long-term potentiodynamic tests, it takes the form of irregular, branching structures. This topography symptomatically contains bimodal height distributions: pit bottoms (local depths of several micrometers) and the core of the surface between pits, which is reflected in the roughness parameters. Surfaces produced using laser powder bed fusion (LPBF), due to the high temperatures involved in the process, are characterised by a topography consisting of regularly spaced peaks and valleys, and also contain surface and subsurface pores comparable in size to corrosion pits [3]. Such topography has a significant impact on the functional properties of the materials [4]. In the case of highly complex surfaces, traditional two-dimensional roughness parameters (Ra, Rz) are insufficient [5,6]. In the last two decades, with the development of optical profilometry methods and the standardisation of three-dimensional surface texture parameters in ISO 25178, there has been a transformation in the approach to characterising topography [7]. The methodological challenge is to develop reliable, repeatable characterisation procedures that would enable objective characterisation of such complex surfaces [8–10].

Focus Variation (FV) is a non-contact method of 3D optical profilometry based on sequential image acquisition at different focus distances and identification of the maximum contrast corresponding to the surface topography. The choice of lens magnification is a fundamental metrological challenge due to the interrelationships between depth of field (DOF), lateral resolution, field of view and measurement reliability. Rojewski [11] in his work on non-alloy steel surface stated that the microscope magnification plays a critical role in the accuracy of the surface topography representation. Depth of field is inversely proportional to the square of the numerical aperture ($DOF \propto \lambda/NA^2$), which means that at low magnification (5×) it is several tens of micrometres, while at high magnification (50×) it is only a few micrometres [12]. A wide DOF at low magnification generates flat, multimodal contrast functions, preventing the algorithm from accurately determining the topography, especially in low-contrast areas, resulting in higher fraction of non-measured points (NMPs). Narrow DOF at high magnification produces sharp, single-peak contrast features, enabling reliable topography identification and reducing NPMs. The pixel size varies from 3–5 µm at 5× to 0.3–0.5 µm at 50×, which radically affects the representation of topography: at low magnification, pores are underrepresented, reducing their amplitude, while at high magnification they occupy hundreds of pixels. However, the use of low-magnification objective lenses allows for imaging of a larger area, which can provide a better view of the textures being investigated. Some studies show that the amplitude parameters decrease significantly when switching objective lenses from 5× to 50× [13]. The field of view decreases proportionally to the magnification, limiting the sampling area, while the resolution in the Z direction improves from low

magnification to high magnification. Surface texture contrast also plays a key role – at low magnification, the number of pixels representing the structure is small, reducing the possibility of signal averaging, while at high magnification, hundreds of pixels allow for better integration and noise resistance. Choosing the optimal magnification therefore requires a careful compromise between reducing NMPs, improving resolution, narrowing the field of view, and possible inaccuracies in the amplitude of roughness parameters.

The aim of this study is to systematically evaluate the impact of lens magnification (5×, 10×, 20×, 50×) on surface roughness parameters and the percentage of non-measured points (NMPs) for corroded 316L steel samples and laser powder bed fusion Osprey® HWTS 50 tool steel samples, in order to develop a standardised protocol for reliable and repeatable characterisation of complex topographies in materials science and industrial applications.

2. Methodology

2.1. Samples preparation

In this study, two types of porous surfaces were prepared: 316L steel subjected to potentiodynamic tests and laser powder bed fusion (LPBF) tool steel samples.

For the corrosion tests, the disc-shaped samples with an exposure area of 1 cm² were wet-ground to a final gradation of #2000. The samples were cleaned and degreased using isopropanol with 99.7% purity (POCH, Poland). Electrochemical tests were performed using potentiostat/galvanostat (Atlas 0531, Atlas Sollich, Poland) in NaCl (99.8% purity, Warchem, Poland) solutions of 3.5, 10 and 20 wt(%) to obtain low, medium and high porosity surfaces, respectively (CORR_LOW, CORR_MEDIUM, CORR_HIGH samples). A three-electrode setup was employed, consisting of a platinum electrode as the counter electrode, a saturated calomel electrode as the reference electrode, and aluminum samples as the working electrode. The measurements began with determining the open circuit potential (OCP) over 30 min. Corrosion process were obtained using the potentiodynamic tests over a potential range of -2 V to + 1 V, with a scanning rate of 1 mV/s. After testing, salt deposits were removed from the tested surfaces by cleaning in an ultrasonic cleaner (MKD-6, MKD ULTRASONIC, Poland).

For manufacturing the LPBF samples, a mixture of metal powder and a binder was provided to create a more emphasized surface roughness in the form of a semi-fluid paste. In the paste mixture, the metal powder were spherical in a size range between (15-45microns) from tool steel Osprey® HWTS 50. Then, 40g of the tool steel powder was mixed with 1.1g of corn starch dissolving in 5ml of water (mixing was done when water was boiled). This formulation allowed adequate binding strength to maintain layer cohesion while ensuring the paste could be applied uniformly across the base plate. Afterwards, a layer of paste is applied manually on a still base plate and then the applied layer was moved into a EOS M270 laser powder bed fusion additive manufacturing machine. In the laser powder bed fusion machine, the applied layer was scanned as 10mm*10mm squares with a fibre laser using a laser power of 100W, a scanning velocity of 75-800 mm/s and a hatch spacing of 0.1 mm. This procedure was manually repeated layer-by-layer until 1-2 mm tool still parts were made. This procedure allowed to obtain LPBF_LOW, LPBF_MEDIUM and LPBF_HIGH samples.

2.2. Scanning Electron Microscopy observations

All of the obtained surfaces were observed using scanning electron microscopy (SEM) operating at an accelerating voltage of 10 kV (Tescan Vega G4, Czech Republic). A magnification of 100x was applied.

2.3. Surface measurements

The topography of the resulting surfaces was characterized using a 3D optical profilometer based on FV microscopy (Sensofar S Neox, Sensofar Metrology, Terrassa, Spain). Nikon EPI objectives with magnifications of 5×, 10×, 20×, and 50× were employed, and the data were initially processed using SensoSCAN S Neox 7.7 software. The technical specifications of the lenses are summarized in Table 1. For each sample, three randomly selected areas were analyzed. Fig. 1 presents a schematic representation of the analyzed regions and their dimensions for the different objective magnifications applied in the study. Surface analysis was subsequently carried out using SensoMAP Premium 9.1 software. The procedure used to determine the required parameters was in accordance with the ISO 25178 and ISO 21920 standards.

Table 1. Objective lenses properties on Sensofar S Neox 7 optical profilometer.

Magnification	5x	10x	20x	50x
NA	0.15	0.30	0.45	0.8
WD [mm]	23.50	17.50	4.50	1.00
FOV [µm x µm]	3378 x 2826	1689 x 1413	845 x 707	338 x 283
Spatial sampling [µm]	1.38	0.69	0.34	0.13
Optical resolution [µm]	1.08	0.54	0.36	0.20

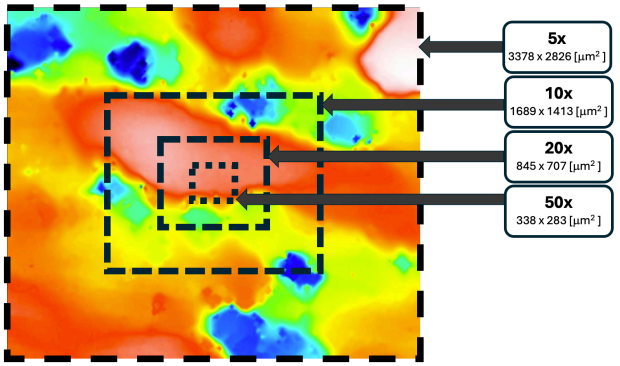

Figure 1. Schematic representation of the selection of measurement areas and locations. Based on the example of LPBF_HIGH surface.

3. Results and Discussion

Fig. 2 shows images of samples obtained with a scanning electron microscope. It can be observed that both surfaces subjected to corrosion processes and those produced by the LPBF method exhibit a complex structure with numerous pores and pits. The degree of surface complexity increases from the CORR_LOW (a) and LPBF_LOW (b) samples, through CORR_MEDIUM (c) and LPBF _MEDIUM (d), to the most complex surfaces for CORR_HIGH (e) and LPBF _HIGH (f).

Fig. 3 shows the percentage of NMPs for all tested samples depending on the lens magnification used. It should be noted that at higher lens magnifications, the number of NMPs decreases. NMPs are considered a good indicator of the ability of the measuring system used to correctly reflect the surface. At low magnifications (5×), the depth of field is significantly higher. The measurement algorithm has difficulty in precisely finding a single peak contrast height when multiple heights produce a similar focus signal. As a result, many pixels are dismissed as unmeasured because the focus signal is unclear and multimodal. At higher magnifications (20×, 50×), the DOF is significantly

narrower. This means that very clear, single-peak focus signals are obtained during the measurement process, resulting in a reduction in the number of NMPs. For the LPBF _HIGH sample, it was impossible to perform the measurement using a 50x lens due to the very small WD range of this lens. As expected, surfaces with higher complexity (CORR_HIGH, LPBF _HIGH) are more challenging to characterize accurately and therefore exhibit the highest number of NMPs. In contrast, smoother surfaces show a markedly lower proportion of NMPs, both for corroded samples and for those manufactured using the LPBF process.

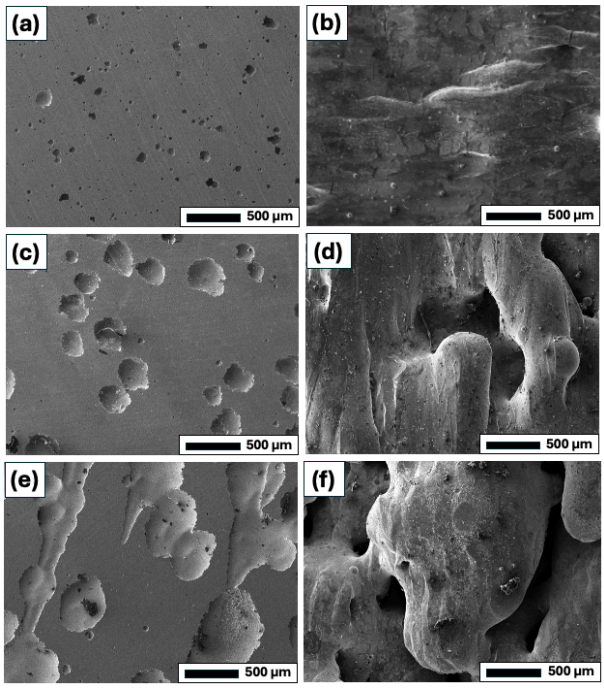

Figure 2. SEM images of the investigated surfaces – corroded samples (a, c, e) and LPBF samples (b, d, f) with low (a, b), medium (c, d) and high (e, f) porosity.

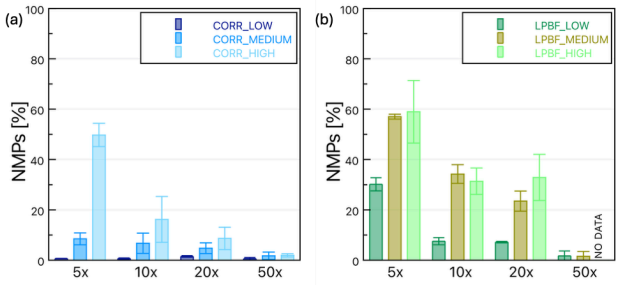

Figure 3. NMPs values for the corrosion-affected samples (a) and LPBF samples (b) for different objective lenses employed.

Fig. 4 and Fig. 5 show a summary of the basic roughness parameters - Sa and Sz, respectively. Tables (a) and (c) refer to samples subjected to corrosion degradation, while (b) and (d) refer to samples produced using the LPBF method. Tables (a) and (b) show the average value of the measurements performed, while (c) and (d) indicate the standard deviations obtained. It can be observed that as the magnification of the lens increases, the standard deviation values also increase, which is particularly evident for samples after corrosion degradation. This means that at high magnifications and the associated small imaging areas, the topographic data is very local and does not reflect the overall topography of the sample surfaces.

(a)

Sa [µm]			
MAGNIFICATION	CORR_LOW	CORR_MEDIUM	CORR_HIGH
5x	2,13	14,69	15,23
10x	1,81	11,92	29,72
20x	2,78	14,38	33,27
50x	0,98	14,92	18,40

(b)

Sa [µm]			
MAGNIFICATION	LPBF_LOW	LPBF_MEDIUM	LPBF_HIGH
5x	48,75	91,76	262,29
10x	33,54	69,85	198,81
20x	12,46	29,37	140,90
50x	6,63	24,27	NO DATA

(c)

Sa deviation [µm]			
MAGNIFICATION	CORR_LOW	CORR_MEDIUM	CORR_HIGH
5x	0,12	1,55	5,41
10x	0,34	7,79	5,42
20x	0,97	6,56	10,65
50x	1,25	12,65	12,52

(d)

Sa deviation [µm]			
MAGNIFICATION	LPBF_LOW	LPBF_MEDIUM	LPBF_HIGH
5x	4,43	7,87	56,33
10x	7,54	21,44	39,72
20x	7,60	15,33	58,43
50x	8,13	22,20	NO DATA

Figure 4. Average Sa parameter (a, b) and Sa standard deviations (c, d) heatmaps for the corrosion affected (a, c) and LPBF (b, d) samples.

(a)

Sz [µm]			
MAGNIFICATION	CORR_LOW	CORR_MEDIUM	CORR_HIGH
5x	100,20	131,56	144,33
10x	82,08	116,33	149,49
20x	88,25	105,76	132,85
50x	24,04	77,71	86,63

(b)

Sz [µm]			
MAGNIFICATION	LPBF_LOW	LPBF_MEDIUM	LPBF_HIGH
5x	560,08	781,69	1789,14
10x	264,56	489,49	1805,61
20x	105,00	313,61	1388,86
50x	43,69	53,05	NO DATA

(c)

Sz deviation [µm]			
MAGNIFICATION	CORR_LOW	CORR_MEDIUM	CORR_HIGH
5x	8,59	9,00	8,51
10x	5,36	9,77	18,68
20x	12,79	22,03	21,41
50x	8,45	47,12	52,71

(d)

Sz deviation [µm]			
MAGNIFICATION	LPBF_LOW	LPBF_MEDIUM	LPBF_HIGH
5x	23,21	46,98	235,95
10x	131,60	39,97	225,14
20x	47,08	100,00	210,60
50x	27,07	28,94	NO DATA

Figure 5. Average Sz parameter (a, b) and Sz standard deviations (c, d) heatmaps for the corrosion affected (a, c) and LPBF (b, d) samples.

When analyzing extensive surfaces, including those affected by degradation processes, it is important to quantitatively determine the ratio of pits to undamaged material. Standard height parameters such as Sa and Sz do not provide sufficient information about the distribution, quantity, and proportion of pits in the total topography under investigation. Fig. 6 shows a visual interpretation of the peak-hole analysis for a selected sample.

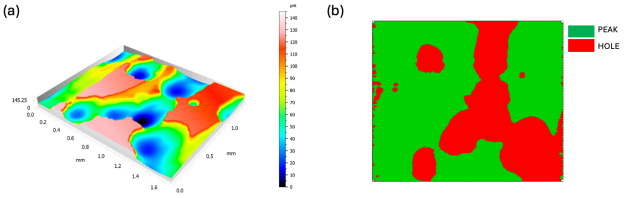

Figure 6. 3D surface topography visualisation for a CORR_HIGH sample with the 10x magnification objective (a) and peak-hole analysis for this surface (b).

A quantitative analysis of these observations is presented in Fig. 7 as a percentage indicator of the area of holes. Naturally, an increase in the percentage of holes was observed in samples from LOW to HIGH, both after the corrosion process and LPBF. For the 50x lens, the values obtained differ slightly from those for lenses with lower magnifications, and the standard deviations are large. These observations are consistent with the analysis of the height parameters Sa and Sz.

Considering the above observations, it is recommended to use lenses with magnifications of 10x and 20x for this type of measurement. They are the optimal choice in terms of the number of NMPs and the image size representing the topography under examination.

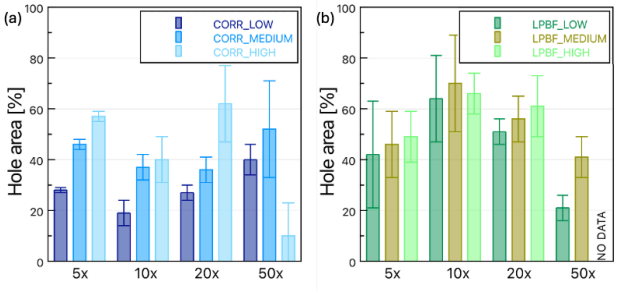

Figure 7. Hole area calculations for the corrosion-affected samples (a) and LPBF samples (b) for different objective lenses employed.

The parameters Vvc (core void volume) and Vvv (dale void volume) from ISO 25178 are particularly useful for surfaces with extensive pits, such as after pitting corrosion or LPBF printing, as they quantify the volume of voids rather than just height characteristics. Height parameters such as Sa or Sz ignore the number, size, and total capacity of the pits, for instance many small pits can result in a low Sa but a high Vvv. These parameters may indicate the functional properties of surfaces, such as their retention, liquid load-bearing capacity, and corrosion prediction. In the case of samples after corrosion degradation, lower Vvc and Vvv parameters were observed than for the samples produced using the LPBF method. It can be concluded that for samples subjected to corrosion processes, 10x and 20x lenses give comparable volume parameter values and similar standard deviation values. For LPBF samples, the use of a higher magnification lens gives slightly lower Vvv and Vvc parameter values. This may be a result of the smaller size of the observed area.

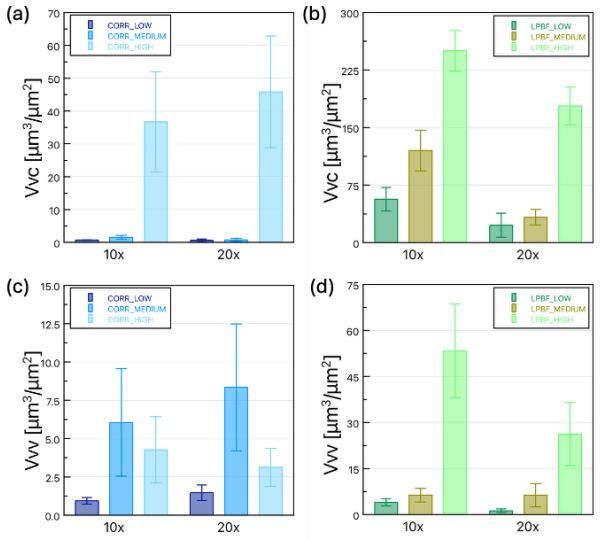

Figure 8. Vvc (a and b) and Vvv (c and d) values for the corrosion-affected samples (a and c) and LPBF samples (b and d) for two different objective lenses employed.

4. Conslusions

This paper presents a methodology for measuring and analyzing complex surfaces with a high degree of porosity, based on the example of surfaces after corrosion degradation processes and surfaces of samples produced using the LPBF method.

The influence of lens magnification in the FV method on the measurement results obtained was analyzed. At higher lens magnifications (20×, 50×), the number of non-measured points (NMPs) decreases significantly. This is due to a narrower depth of field (DOF), which provides clear, single-modal focus signals, eliminating the ambiguity that occurs at low magnifications (5×). More complex surfaces (CORR_HIGH, LPBF _HIGH) have the highest percentage of NMPs, indicating difficulties in accurately mapping highly developed topography. Smoother surfaces show a significantly lower proportion of NMPs for both corroded and LPBF -produced samples. The NMPs value is a reliable indicator of the measuring system's ability to accurately map surface topography. Minimizing NMPs by using the appropriate magnification is crucial for obtaining representative data on surfaces with complex pore and pit structures. Special attention should also be paid to the size of the imaged area. For high-magnification lenses, the size of the imaged area may be insufficient and may not represent the surface of the sample. Taking the above factors into account, magnifications of 10x and 20x are recommended for porous surfaces.

Selected height and volume parameters were analyzed. It was found that height parameters do not clearly reflect the degree of surface complexity, as they ignore the size, dimensions, and distribution of pores. Volume parameters such as Vvv and Vvc are more reliable indicators of surface quality. They can be supported by additional analyses, such as peak-hole surface analysis.

Acknowledgements

Financial support of these studies from Gdańsk University of Technology by the DEC-10/1/2025/IDUB/II.1b/Am grant under the Americium International Career Development - 'Excellence Initiative - Research University' program is gratefully acknowledged.

References

[1] Coelho L B, Kossman S, Mejias A, Noirfalise X, Montagne A, Van Gorp A, Poorteman M and Olivier M-G 2020 Mechanical and corrosion characterization of industrially treated 316L stainless steel surfaces *Surf. Coat. Technol.* **382** 125175

[2] Nugroho F A, Garhuom W, Andresen-Paulsen G and Ehlers S 2022 Numerical analysis of the correlation between the pitting severity and surface roughness of corroded specimens *Ships Offshore Struct.* **17** 2699–714

[3] Galati M, Minetola P and Rizza G 2019 Surface Roughness Characterisation and Analysis of the Electron Beam Melting (EBM) Process *Materials* **12** 2211

[4] Agrawal A K and Thoma D J 2022 High-throughput surface characterization to identify porosity defects in additively manufactured 316L stainless steel *Addit. Manuf. Lett.* **3** 100093

[5] Mirabal A, Loza-Hernandez I, Clark C, Hooks D E, McBride M and Stull J A 2023 Roughness measurements across topographically varied additively manufactured metal surfaces *Addit. Manuf.* **69** 103540

[6] Mendieta-Echevarría L, Sáenz-Nuño M A and Rubio E M 2025 Comparing the Effectiveness of R and S Roughness Parameters on Surfaces Lubricated with Standardized Nominal Particle Size Lubricants *Lubricants* **13** 148

[7] Anon ISO 25178-2: Geometrical Product Specifications (GPS) – Surface texture: Areal – Part 2: Terms, definitions and surface texture parameters.

[8] Walid A and Eifler M 2025 Common Practices and Methodologies in Scientific Functional Characterization of Surface Topography *Metrology* **5** 33

[9] Alar V, Razumić A, Runje B, Stojanović I, Kurtela M and Štrbac B 2025 Application of Areal Topography Parameters in Surface Characterization *Appl. Sci.* **15** 6573

[10] Tomkowski R, Xiaoyu Z, Leiro A and Archenti A 2022 Areal topography evaluation of a Ni-based alloy printed by electron beam melting (EBM) process European Society for Precision Engineering and Nanotechnology, Conference Proceedings: 22nd International Conference and Exhibition, EUSPEN 2022 (Geneva: euspen) pp 433–6

[11] Rojewski M 2026 Influence of digital optical microscope configuration and illumination conditions on the accuracy of surface roughness evaluation *Adv. Sci. Technol. Res. J.* **20** 406–22

[12] Mustafa A M, Muhamedsalih H, Tang D, Kumar P, Blunt L and Jiang J 2025 Investigation of focus variation microscopy immunity to vibrations *Precis. Eng.* **93** 87–98

[13] Rosentritt M, Schmutzler A, Hahnel S and Kurzendorfer-Brose L 2024 The Influence of CLSM Magnification on the Measured Roughness of Differently Prepared Dental Materials *Materials* **17** 5954

euspen's 26th International Conference & Exhibition, Krakow, PL, June 2026
www.euspen.eu

Deep learning-driven visual inspection methodology for automated defect detection and dimensional assessment in die-cast parts

Sofia Catalucci and Enrico Savio

University of Padua, Department of Industrial Engineering (DII), Italy

sofia.catalucci@unipd.it

Abstract
Defect detection is critical across industrial manufacturing processes such as casting, moulding, machining, and additive manufacturing, as imperfections (e.g., burrs, porosities, surface discontinuities) can compromise assembly, performance, and structural reliability. When defects exhibit a three-dimensional morphology, conventional image-based inspection becomes less effective and human visual inspection struggles to deliver consistent, objective decisions. This work presents a metrologically validated pipeline that employs optical acquisition of 3D point clouds from a machine vision system by means of laser triangulation, compares them with a reference point cloud acquired from a conforming part, and converts the resulting deviation maps into images for automated deep learning-driven defect localisation, followed by skeletonization-based dimensional assessment. Validation is performed against reference measurements acquired with a multisensor coordinate measuring machine. Automotive die-cast aluminium components are used as a case study to demonstrate robust burr detection and dimensional quantification under industrial constraints, supporting integration into in-line quality control workflows.

Defect detection; deep learning; dimensional measurement; metrological validation; die-casting

1. Introduction

In modern manufacturing, surface defect detection is pivotal to ensuring the functionality and reliability of industrial components, particularly in high-volume production, where even small surface imperfections can lead to assembly issues, failures, or downstream rework [1]. In this context, three-dimensional (3D) surface defects (i.e., geometrical imperfections such as protrusions, discontinuities, or burrs) are particularly critical because their detectability depends strongly on scale, morphology, and local surface conditions. Traditionally, detection of surface defects relies on human visual inspection (HVI) supported by simple tools. While HVI remains widespread, it is inherently affected by operator subjectivity and fatigue, which limit repeatability and robustness. To mitigate these issues, automated machine vision systems (MVS) are increasingly deployed in-line; however, their effectiveness still depends critically on illumination setup and on the complexity of part geometry and surface characteristics. Changes in lighting, surface reflectivity, and viewing angle can significantly alter defect visibility and detection reliability.

Recently, deep learning (DL) approaches have improved defect detection performance; however, many solutions provide qualitative outputs and rarely include metrological validation. This work introduces a DL-based inspection pipeline that couples 3D surface defect localisation with dimensional assessment via skeletonization [2]. The approach is demonstrated on burr detection and quantification on automotive die-cast aluminium components under industrially representative conditions.

2. Materials and Methods

The proposed pipeline adopts supervised transfer learning, using a convolutional detector initialised from pre-trained weights and fine-tuned on pre-labelled data to localise surface defects. The detector operates on two-dimensional (2D) deviation maps obtained by comparing 3D point clouds acquired via laser triangulation on die-cast parts against a high-density scan of a conforming part. After registration in a common reference frame, the resulting deviation maps are converted into images, augmented to mimic industrial variability, and used as input to the network. For each detected region, defect dimensions are estimated through a skeletonization-based step that extracts the defect medial axis and related geometric descriptors. The methodology is validated against reference measurements acquired using a multisensor coordinate measuring machine (CMM). The workflow is shown in Figure 1.

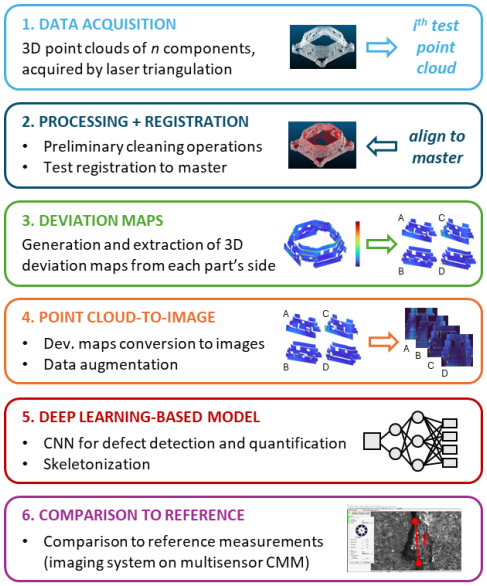

Figure 1. Workflow for defect detection and quantification.

2.1. Case study and data acquisition

The present work focuses on detecting burrs (i.e., raised sharp edges) on aluminium alloy AlSi12(Fe) housings for automotive long-range radar sensors [2]. On these components, residual burr size typically ranges from 0.4 to 2 mm, originating from both the moulding stage and the subsequent shearing operations used to remove the sprue and casting attachments. Parts were measured using a laser triangulation system Nikon MCAx, generating point clouds with an average point sampling of 100 µm. This sampling supports reliable visualisation of defects ≥ 1 mm and provides sufficient detail for imperfections of approx. 0.6 mm. Each scan was registered to a reference point cloud acquired from a conforming part with higher density (10 µm average point sampling). Registration was performed by means of best-fit algorithm in the software CloudCompare. Table 1 reports both instruments' specifications.

Table 1. Instruments specifications

	Technology	Sampling	Accuracy*	Point count
Reference optical setup	Laser-based	10 µm	±0.2 µm	approx. 1,100,000
AACMM Nikon MCAx	Laser-based	100 µm	±10 µm	approx. 800,000

*stated by the manufacturer (term not used in the strict VIM sense)

2.2. Image preparation and deep learning model

After alignment, 3D deviation maps representing local surface height differences with respect to the master geometry were obtained. The four lateral faces of each component were segmented (Sides A–D), and the resulting deviation maps were projected onto reference planes and exported as 2D colour-encoded images. These images were independently normalised for input to the detector, while missing-data regions were handled via masking. From 92 parts, 368 images were generated and a balanced subset (85 defective, 75 non-defective) was selected to reduce class bias. Data preparation and augmentation were performed in Roboflow (online tool for computer vision tasks) to simulate realistic in-line inspection variability (exposure ±10%, brightness and saturation ±15%, rotation ±5°), producing a working dataset of 400 images. A bounding box annotation operation was performed on a subset of defect cases. All images were resized to 640 × 640 pixels (without padding), and the dataset was split into train/validation/test (70/20/10), keeping validation/test restricted to non-augmented images to ensure unbiased evaluation. The network adopted in this work was YOLOv8 (Ultralytics, Python API).

2.3. Defect detection, dimensional inspection and validation

After training, the DL model in its best configuration (based on the metrics defined in [3]) was applied to the unlabelled images. For each image predicted as defective, defect localisation was obtained from a) the predicted bounding box, providing position and an initial estimate of the defect extent; b) dimensional assessment was then refined by applying a skeletonization algorithm to the detected region. The total length L_{sk} of each detected defect was computed as the sum of the lengths l_{sk_i} of the n skeleton segments that compose it, as in equation (1).

$$L_{sk} = \sum_{i=1}^{n} l_{sk_i} \quad (1)$$

All pixel-based measurements were converted to metric units using a conversion factor equal to 0.046 mm/pixel, derived from the part height (29.4 mm) and the image resolution (640 pixels).

Reference measurements were acquired using a multisensor CMM ZEISS O-Inspect equipped with an imaging probing system (MPE = 1.9 + L/150 µm for 2D length measurements), using a repeatable clamping fixture and two alignments to inspect all four lateral faces of the part. A dimensional tolerance of 0.6 mm was set as the limit beyond which any detected protrusion is deemed non-conforming, and the part should be rejected. For validation, burr size was quantified by averaging five measurements of the distance $\bar{l}$ between two points selected by the user at the burr endpoints. Examples are shown in Figure 2.

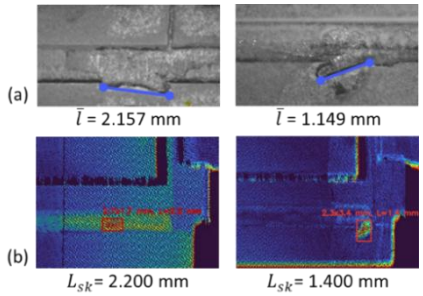

Figure 2. (a) Imaging lengths, and (b) DL-driven skeletonization.

3. Results and discussion

The YOLOv8 detector was trained across five configurations (5, 10, 20, 50, and 100 epochs). Model selection was based on the best validation epoch, rather than the final epoch, to capture peak generalisation and limit late-stage overfitting. Performance improved from 5 to 50 epochs, with the 50-epoch configuration achieving the best overall results, as 100 epochs indicated increased selectivity and potential overfitting. Bounding box initial estimate of the defect extent showed an average deviation of 0.30 mm from the imaging sensor reference for burrs of 1.5-2 mm and above, but it systematically overestimated defects below 1.5 mm. For this reason, estimates were complemented with skeletonization. Compared to the imaging reference, the skeleton-based length showed a mean deviation of 0.29 mm. Missed detections were attributed to insufficient point density, which affected the deviation maps. Skeletonization tended to slightly overestimate sub-millimetre defects, while being more conservative for larger ones.

4. Conclusions and outlook

This work proposes a metrologically validated pipeline for automated burr detection and dimensional assessment on die-cast parts. YOLOv8 was applied to deviation maps converted into images derived from registered 3D scans, and defect length was estimated via bounding box and skeletonization. Dimensional results were validated against reference measurements. From an industrial perspective, the method can support HVI within quality control systems. Current limitations mainly relate to point cloud quality and reduced robustness for sub-millimetre defects. Future work will focus on extending to additional defect types/processes, and exploring in-line data collection and active learning to improve generalisation and scalability.

Acknowledgements

The project (23IND08 DI-Vision) has received funding from the European Partnership on Metrology, co-financed from the European Union's Horizon Europe Research and Innovation Programme and by the Participating States.

References

[1] Catalucci S, Thompson A, Piano S, Branson DT and Leach R 2022 Optical metrology for digital manufacturing: a review *Int. J. Adv. Manuf. Technol.* **120** 4271-4290

[2] Catalucci S and Savio E 2026 Metrological validation of a deep learning pipeline for in-line detection and dimensional quantification of three-dimensional surface defects *CIRP J. Manuf. Sci. Technol.* **64** 107-119

[3] Mullany B, Savio E, Haitjema H and Leach R 2022 The implication and evaluation of geometrical imperfections on manufactured surfaces *CIRP Ann.* **71** 717-739

euspen's 26th International Conference & Exhibition, Krakow, PL, June 2026
www.euspen.eu

Complex coordinate measurement models for GUM uncertainty framework

Wojciech Płowucha[1], Mirosław Wojtyła[1], Izabela Hura[1], Alessandro Balsamo[2]

[1]*University of Bielsko-Biała, Laboratory of Metrology, Willowa 2, PL43-309 Bielsko-Biała*
[2]*INRIM (National Institute of Research in Metrology), Str. delle Cacce, 91, 10135 Torino TO, Italy*

wplowucha@ubb.edu.pl

Abstract

The aim of the research is to develop a method for estimating coordinate measurement uncertainty that is understandable and easy to use in industrial conditions. It was decided to develop a method which, according to the classification given in ISO/TS 15530-1, belongs to the "sensitivity analysis" group. This method requires the development of separate models for each measured characteristic. The term "characteristic" includes dimensions, but above all, various geometrical deviations. In many cases, it is necessary to develop several models for a single type of geometrical deviation (e.g. parallelism deviations), such as parallelism of axes, parallelism of planes, etc. In the article, models with uncertainty evaluation for geometric deviations are presented: parallelism and perpendicularity, position of a point, axis and plane with respect to different datum systems.

Keywords: task specific uncertainty, coordinate measurement models, type B evaluation, sensitivity analysis

1. Introduction

The search for a simple, industrially applicable method of estimating the uncertainty of coordinate measurements is in progress. The basic problem is that numerous different characteristics (dimensions, geometric deviations) are measured in a single measurement run, and each characteristic is measured with a different measurement uncertainty.

According to the ISO 15530-3 standard [1], measurement uncertainty can be assessed experimentally. However, this requires the use of a calibrated workpiece [2–5]. Mutilba [2] notes that due to the requirement of similarity between the manufactured part and the reference part, this approach is only useful in mass production. In contrast, Strbac [3] considers the method presented in [1] as a reference method, but too expensive for everyday use. Furthermore, he is aware that MPE directly concerns only point-to-point distances. Therefore, he attempts to apply the GUM methodology and use information about CMM MPE to determine the uncertainty of flatness measurements. Cheng [4] highlights the diverse geometric characteristics encountered in machine part measurements. While acknowledging the strengths of the method described in [1], he also identifies the necessity for more straightforward approaches. To address this, Cheng suggests a simplified methodology that incorporates MPE data along with repeatability test outcomes, even though it may result in overestimated findings. Kortaberria [5] points out the expenses associated with storing and maintaining reference parts when employing the technique outlined in [1]. Considerable expectations were placed on simulation techniques [6-10]. Heisselmann [6] observes the substantial information requirements for implementing such methods. Forbes [7] elaborates on the model utilized in VCMM software, whereas Baldwin [8] discusses the approach adopted in Pundit software. Aggogeri [9] introduces a streamlined simulation method from Politecnico di Torino based on the bootstrap technique. Sładek [10] presents a method developed at CUT that leverages laser tracker test results to assess CMM accuracy. Currently, only VCMM and Pundit software are available commercially, with VCMM being employed in some calibration laboratories.

Between June 2019 and November 2021, the EURAMET project 17NRM03 EUCoM, titled "Standards for the Evaluation of the Uncertainty of Coordinate Measurements in Industry," was conducted. The project coordinator was A. Balsamo from the Italian Metrology Institute (INRIM). The project partners were national metrology institutes: PTB (Germany), NPL (Great Britain), CMI (Czech Republic), GUM (Poland), DTI (Denmark), TUBITAK (Turkey) and AIST (Japan), research institutes IK4-TEKNIKER (Spain) and Metrosert (Estonia) and universities: University of Padua, University of Bielsko-Biała, Cracow University of Technology joined the partnership. As part of the project, several studies were conducted on three approaches to estimating the uncertainty in coordinate measurements:

- multi-position method, which was the subject of draft standard ISO 15530-2,
- method based on a simplified CMM kinematic model and
- sensitivity analysis method (named after classification from ISO/TS 15530-1).

The paper presents results concerning the last method.

The possibility of evaluation of coordinate measurement uncertainty for significant number of geometrical deviations (straightness, flatness, coaxiality, concentricity, position of axis, runout and position of a point, axis and plane related to a datum plane) based on the $E_{L,MPE}$ formula and possibly the CMM verification test results was presented in works [17, 18]. Appropriate measurement models directly used formulae for the point-straight line distance [17, 19] or point-plane distance [18, 19]. All combined standard uncertainty components are calculated by type B evaluation.

The general formula for distance l between point S and straight-line p defined by point P and unit vector v is (the analysed distance is equal to the length of the vector which is the vector product of two vectors):

$$l(S,p) = |(\boldsymbol{P} - \boldsymbol{S}) \times \boldsymbol{v}| = |\boldsymbol{SP} \times \boldsymbol{v}| \quad (1)$$

The general formula for distance *l* between point *S* and plane *p* defined by point *P* and unit normal vector *v* is (the analysed distance is equal to the absolute value of the dot product of two vectors):

$$l(S,p) = |(\boldsymbol{P} - \boldsymbol{S}) \cdot \boldsymbol{v}| = |\boldsymbol{SP} \cdot \boldsymbol{v}| \quad (2)$$

The important assumption of the presented methodology is that the models used express the measured quantities as a function of distance, and more precisely as a function of the coordinate differences of pairs of points. Another element of the methodology is the ISO 14253-2 guideline [20] which states how „MPE values can be used to derive the related uncertainty components".

In the equations (1) and (2) the vectors' coordinates are the differences of the coordinates of the characteristic points, which means that the output quantity *l* is a function of six inputs and thus the uncertainty budget will consist of six components. In individual uncertainty budget rows there will be following sensitivity coefficients $\frac{\partial l}{\partial sp_1}, \frac{\partial l}{\partial sp_2}, \frac{\partial l}{\partial sp_3}, \frac{\partial l}{\partial v_1}, \frac{\partial l}{\partial v_2}, \frac{\partial l}{\partial v_3}$.

Thus, the combined standard uncertainty of the distance *l*

$$u_l = \sqrt{\sum_{i=1}^{n} \left(\frac{\partial l}{\partial x_i} u_{xi}\right)^2} \quad (3)$$

in which

$$u_{xi} = b \cdot E_{L,MPE}(x_i) \quad (4)$$

According to the classification of techniques for uncertainty estimation given in [21], the presented technique belongs to the "sensitivity analysis" approach. According to the classification given in [22], the developed technique belongs to the "GUM uncertainty framework". The assumption which was crucial for development of measurement models is that the coordinate measurement is treated as an indirect measurement, relying on the smallest possible number of points mathematically. The differences between the coordinates of these points serve as the input values for the measurement model. These points can be points of integral feature (surface points) as well as derived feature (points of axes and planes of symmetry, centre of the sphere) and are called "characteristic points". In actual measurements, the number of sampling points is much greater than the minimum mathematical number. Substituting the probing points with characteristic points makes a lot easier developing the measurement models which become clear to understand even for a regular CMM user. Earlier publications [17, 18] showed that the calculated measurement uncertainty does not depend on the position and orientation of the object in the CMM space. This allows to perform calculations in the coordinate system of the workpiece.

It is worth recalling that in many measurement models, a vector normal to the plane defined by ABC points can be determined using the vector product in three ways as: $AB \times AC$, $BA \times BC$ or $CA \times CB$. Then it is necessary to consider all three options and use the one that gives the lowest uncertainty value.

2. Models

2.1. Distance between the point and the straight line defined by given point and parallel to the straight line defined by two points

The straight line *p* in the formula (1) is defined by the point *K* and is parallel to the straight line defined by points *A* and *B* (Figure 1).

The measurement model is

$$l(AB, KS) = \left|\boldsymbol{KS} \times \frac{\boldsymbol{AB}}{|\boldsymbol{AB}|}\right| \quad (5)$$

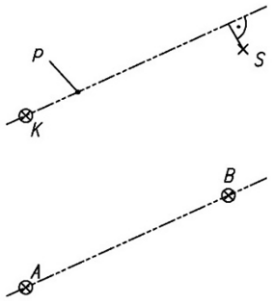

Figure 1. Distance between the point *S* and the straight-line *p* defined by point *K* and parallel to the straight line defined by points *A* and *B*

It should be understood as follows: parallelism is a function of two vectors i.e. six coordinates of these vectors

$$l(ab_1, ab_2, ab_3, ks_1, ks_2, ks_3) = \left|\boldsymbol{KS} \times \frac{\boldsymbol{AB}}{|\boldsymbol{AB}|}\right| \quad (6)$$

The vector coordinate is the difference of the coordinates of the characteristic points, which means that the output quantity *l* is a function of six inputs and thus the uncertainty budget will consist of six components. In individual uncertainty budget rows there will be following sensitivity coefficients $\frac{\partial l}{\partial ab_1}, \frac{\partial l}{\partial ab_2}, \frac{\partial l}{\partial ab_3}, \frac{\partial l}{\partial ks_1}, \frac{\partial l}{\partial ks_2}, \frac{\partial l}{\partial ks_3}$.

Example. The parallelism of axes with cylindrical tolerance zone *PRLAX* equals the distance *l* between point *S* (nominally laying on the toleranced axis) and straight line passing through the point *K* and parallel to the datum axis *AB* (*PRLAX* = *l*) (Figure 2).

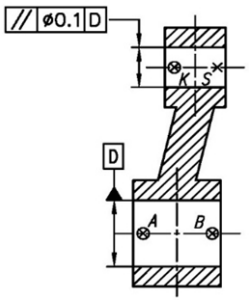

Figure 2. Example of specification with characteristic points of parallelism of axes with cylindrical tolerance zone

The uncertainty of measurement of the parallelism of axes u_{PRLAX} equals the uncertainty u_l of measurement of the distance *l* ($u_{PRLAX} = u_l$).

The table presents the uncertainty budget for following input data (coordinates of four characteristic points): *A*(50, 50, 10), *B*(350, 50, 10), *C*(200, 350, 10), *S*(200, 150, 10.1). The CMM used for measurement has maximum permissible error $E_{0,MPE} = 2 + L/250$. Because a rectangular distribution of errors was assumed, the coefficient *b* was set to 0.58 (see formula 4).

Table 1 Example uncertainty budget for parallelism of axes

Name	x_i	$\partial l/\partial x_i$	$E_{0,MPE}(x_i)$	u_{xi}	$\partial l/\partial x_i \cdot u_{xi}$
xAB	20	0	2.1	1.21	0
yAB	0	0	2	1.16	0
zAB	0	-1	2	1.16	-1.16
xKS	20	0	2.1	1.21	0
yKS	0	0	2	1.16	0
zKS	0,01	1	2	1.16	1.16
				u_{PRLAX}	1.64

If the length of the element and the length of the datum are the same the uncertainty does not depend on the distances of the lines or on the distances between the points defining the lines (i.e. on the lengths of the lines). Therefore, only the constant component (*A*) from the $E_{0,\mathrm{MPE}}$ formula is important. There are two identical, non-zero components in the budget, both with a weight of 1. Therefore, the measurement uncertainty of the straight-line parallelism deviation can be calculated according to the formula

$$u = \sqrt{2} \cdot A \cdot b \tag{7}$$

2.2. Distance between the point and the plane defined by the given point and parallel to the plane defined by three points

In case the plane *p* is represented by point *K* and is parallel to the plane defined by points *A*, *B* and *C* (Figure 3) the unit normal vector $\boldsymbol{\nu}$ can be defined in three ways and as the point *P* in the formula (2) the point *K* is assumed. Thus, there are three variants of the model:

$$l_1(AB, AC, KS) = \left| \boldsymbol{KS} \cdot \frac{\boldsymbol{AB} \times \boldsymbol{AC}}{|\boldsymbol{AB} \times \boldsymbol{AC}|} \right| \tag{8}$$

$$l_2(BA, BC, KS) = \left| \boldsymbol{KS} \cdot \frac{\boldsymbol{BA} \times \boldsymbol{BC}}{|\boldsymbol{BA} \times \boldsymbol{BC}|} \right| \tag{9}$$

$$l_3(CA, CB, KS) = \left| \boldsymbol{KS} \cdot \frac{\boldsymbol{CA} \times \boldsymbol{CB}}{|\boldsymbol{CA} \times \boldsymbol{CB}|} \right| \tag{10}$$

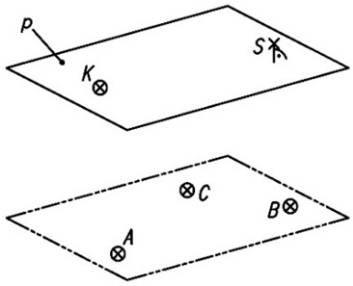

Figure 3. Distance between the point S and the plane p defined by the point K and parallel to the plane defined by points A, B and C.

The uncertainty of measurement of the distance *l* equals the minimum of uncertainties u_{li} of measurement of the distance l_i ($u_l = \min\{u_{li}\}$).

Example. The parallelism of planes *PRLPL* (Figure 4a) as well as parallelism of straight line in regard to plane *PRLSTRL* (Figure 4b) equals the distance *l* between point *S* (laying on the toleranced element) and plane passing through the point *K* and parallel to the plane *ABC* (*PRLSTRL* = *PRLPL* = *l*).

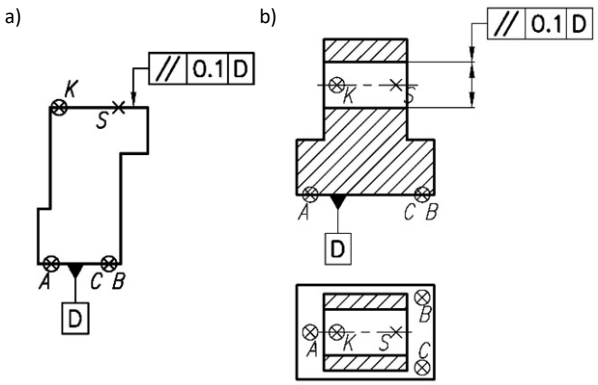

Figure 4. Example of specification with characteristic points: a) parallelism of planes b) parallelism of axis in regard to plane

Thus, the uncertainty of measurement of the parallelism u_{PRLPL} and $u_{PRLSTRL}$ equals the uncertainty u_l of measurement of the distance *l* ($u_{PRLPL} = u_{PRLSTRL} = u_l$).

2.2. Distance between the point and the plane defined by two points and perpendicular to the plane defined by three points

In case the plane is represented by two points *D* and *E* and is perpendicular to plane defined by points *A*, *B* and *C* (Figure 5) as the point *P* in the formula (**2**) the point *D* or *E* can be assumed and the unit normal vector $\boldsymbol{\nu}$ can be defined as a cross product of the normal vector of the plane *ABC* and vector *DE*.

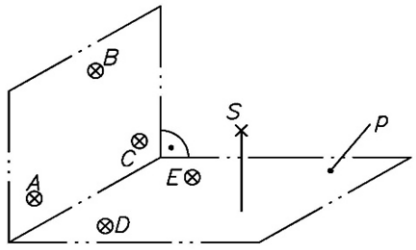

Figure 5. Distance between the point *S* and the plane *p* defined by points *D, E* and perpendicular to the plane *ABC*

Since the normal vector of plane ABC can be determined by three distinct methods (for example, using different combinations of points or vector products), and for each method, either point D or E can be chosen as point P in formula (2), this results in a total of six possible measurement model variants:

$$l_1(AB, AC, DE, DS) = \left| \boldsymbol{DS} \cdot \frac{(\boldsymbol{AB} \times \boldsymbol{AC}) \times \boldsymbol{DE}}{|(\boldsymbol{AB} \times \boldsymbol{AC}) \times \boldsymbol{DE}|} \right| \tag{11}$$

$$l_2(BA, BC, DE, DS) = \left| \boldsymbol{DS} \cdot \frac{(\boldsymbol{BA} \times \boldsymbol{BC}) \times \boldsymbol{DE}}{|(\boldsymbol{BA} \times \boldsymbol{BC}) \times \boldsymbol{DE}|} \right| \tag{12}$$

$$l_3(CA, CB, DE, DS) = \left| \boldsymbol{DS} \cdot \frac{(\boldsymbol{CA} \times \boldsymbol{CB}) \times \boldsymbol{DE}}{|(\boldsymbol{CA} \times \boldsymbol{CB}) \times \boldsymbol{DE}|} \right| \tag{13}$$

$$l_4(AB, AC, DE, ES) = \left| \boldsymbol{ES} \cdot \frac{(\boldsymbol{AB} \times \boldsymbol{AC}) \times \boldsymbol{DE}}{|(\boldsymbol{AB} \times \boldsymbol{AC}) \times \boldsymbol{DE}|} \right| \tag{14}$$

$$l_5(BA, BC, DE, ES) = \left| \boldsymbol{ES} \cdot \frac{(\boldsymbol{BA} \times \boldsymbol{BC}) \times \boldsymbol{DE}}{|(\boldsymbol{BA} \times \boldsymbol{BC}) \times \boldsymbol{DE}|} \right| \tag{15}$$

$$l_6(CA, CB, DE, ES) = \left| \boldsymbol{ES} \cdot \frac{(\boldsymbol{CA} \times \boldsymbol{CB}) \times \boldsymbol{DE}}{|(\boldsymbol{CA} \times \boldsymbol{CB}) \times \boldsymbol{DE}|} \right| \tag{16}$$

The uncertainty of measurement of the distance *l* equals the minimum of uncertainties u_{li} of measurement of the distance l_i ($u_l = \min\{u_{li}\}$).

Example. The position of the point (centre of the ball) *POS* relative to secondary datum of the datum system (Figure 6) is a doubled value of the distance *l* of the point *S* from the plane positioned at the theoretically exact position defined by *TED* (*POS* = 2 (*l* – *TED*)).

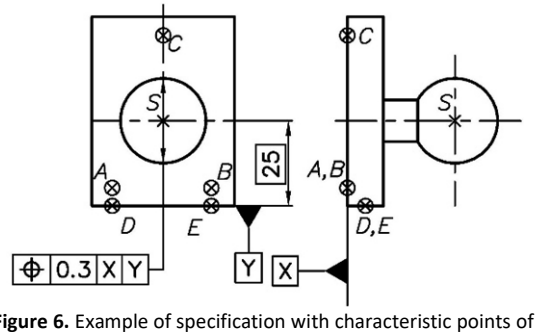

Figure 6. Example of specification with characteristic points of position of the point (centre of the ball) in regard to the secondary datum of datum system defined by two perpendicular planes

Therefore, the uncertainty of measurement of the position u_{POS} equals twice the uncertainty u_l of the distance of the point from the plane being the secondary datum (*TED* =25) ($u_{POS} = 2u_l$).

Example. The position of the axis of a hole *POS* relative to secondary datum of the datum system (Figure 7) is a doubled value of the distance *l* of the point *S* from the plane positioned at the theoretically exact position defined by *TED* (*POS* = 2 (*l* – *TED*)).

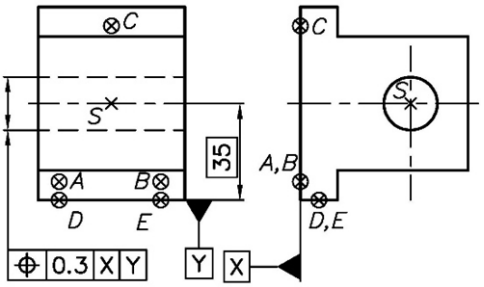

Figure 7. Example of specification with characteristic points of position of the axis of a hole related to the datum system

Therefore, the uncertainty of measurement of the position u_{POS} equals twice the uncertainty u_l of the distance of the point from the plane being the secondary datum (*TED*=35) ($u_{POS} = 2u_l$). The mid-point of the axis can be considered as point *S* in the calculation.

Example. The perpendicularity *PER* of the plane in regard to datum plane (Figure 8) is a value of the distance *l* of the point *S* from the plane defined by points *K* and *L* and perpendicular to plane defined by point *A*, *B* and *C* (*PER* = *l*).

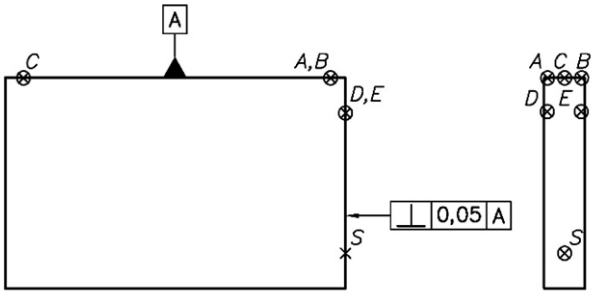

Figure 8. Example of specification with characteristic points of perpendicularity of two planes

Therefore, the uncertainty of measurement of the perpendicularity u_{PER} equals the uncertainty u_l of the distance of the point from the plane ($u_{PER} = u_l$).

2. Conclusions

Individual models have the form of distance of a point from a straight line or a plane, for particular geometrical deviations equal to this distance or twice the value of this distance. The second case concerns particularly position deviations.

Developed method allows for the estimation of the measurement uncertainty of all geometrical deviations.

Models for several cases of parallelism, perpendicularity and position were described. In the examples, there are tolerance zones defined by a pair of planes and a cylinder.

Performing the necessary calculations requires the use of software that performs operations on vectors (e.g. Maple, Matlab).

Described method may take the form of a standard and be applicable in industrial conditions.

Acknowledgements

The presented work is part of the EMPIR EURAMET-founded joint research project no. 17NRM03 "Standards for the evaluation of the uncertainty of coordinate measurements in industry EUCoM" coordinated by Alessandro Balsamo, INRIM.

References

[1] ISO 15530-3:2011 Geometrical product specifications (GPS). Coordinate measuring machines (CMM): Technique for determining the uncertainty of measurement. Part 3: Use of calibrated workpieces or measurement standards
[2] Mutilba U et al. Traceability of on-machine tool measurement: Uncertainty budget assessment on shop floor conditions *Measurement* **135** (2019) 180–188
[3] Štrbac B et al. The difference between GUM and ISO/TC 15530-3 method to evaluate the measurement uncertainty of flatness by a CMM *MAPAN* **32** (4) (2017) 251–257
[4] Cheng Y et al. Evaluation and optimization of task-oriented measurement uncertainty for coordinate measuring machines based on geometrical product specifications *Applied Sciences* **9** (1) (2019) 1-22
[5] Kortaberria G. et al. Three-dimensional point cloud task-specific uncertainty assessment based on ISO 15530-3 and ISO 15530-4 technical specifications and model-based definition strategy, Metrology 2022, 2, 394–413. https://doi.org/10.3390/metrology2040024
[6] Heisselmann D et al. Determination of measurement uncertainty by simulation *Proceedings of Advanced Mathematical and Computational Tools in Metrology and Testing* **XI**, 2017
[7] Forbes A et al. Simulated instruments and uncertainty estimation *NPL Report CMSC* **01/00**, Teddington, 2000
[8] Baldwin J Application of simulation software to coordinate measurement uncertainty evaluations *Measure* **2** (2007) 40–52
[9] Aggogeri F et al. Measurement uncertainty assessment of Coordinate Measuring Machines by simulation and planned experimentation *CIRP Journal of Manufacturing Science and Technology* **4** (2011) 51–56
[10] Sładek J. et al. Virtual coordinate measuring machine built using lasertracer system and spherical standard, Metrol. Meas. Syst., Vol. XX (2013), No. 1, pp. 77–86
[11] ISO 1101:2017 Geometrical product specifications (GPS). Geometrical tolerancing. Tolerances of form, orientation, location and run-out
[12] ISO 5459:2011 Geometrical product specifications (GPS). Geometrical tolerancing. Datums and datum systems
[13] Humienny Z State of art in standardization in the geometrical product specification area a decade later *CIRP Journal of Manufacturing Science and Technology* **33** (2021) 42–51
[14] Wojtyła M et al. Verification of sensitivity analysis method of measurement uncertainty evaluation *Measurement: Sensors* **18** (2021) 100274
[15] Rosner P et al. Uncertainty evaluation for complex GPS characteristics *Measurement: Sensors* **18** (2021) 100323
[16] Płowucha W et al. Proposal for changes in the ISO 15530 series of standards *Calitatea* **13** (5) (2012) 237–240
[17] Płowucha W Point-straight line distance as model for uncertainty evaluation of coordinate measurement *Measurement* **135** (2019) 83–95
[18] Płowucha W Point-plane distance as model for uncertainty evaluation of coordinate measurement *Metrol. Meas. Syst.* **27** (2020) 625–639
[19] ISO 17450-1:2011 Geometrical product specifications (GPS). General concepts. Part 1: Model for geometrical specification and verification
[20] ISO 14253-2:2011 Geometrical product specifications (GPS). Inspection by measurement of workpieces and measuring equipment. Part 2: Guidance for the estimation of uncertainty in GPS measurement, in calibration of measuring equipment and in product verification
[21] ISO/TS 15530-1:2013 Geometrical product specifications (GPS). Coordinate measuring machines (CMM): Technique for determining the uncertainty of measurement. Part 1: Overview and metrological characteristics
[22] JCGM 104:2009 Evaluation of measurement data. An introduction to the "Guide to the Expression of Uncertainty in Measurement" and related documents

euspen's 26th International Conference & Exhibition, Krakow, PL, June 2026
www.euspen.eu

Surface roughness influence on chromatic confocal dimensional measurements

Lorenzo Didonè*, Sofia Catalucci, Enrico Savio

Department of Industrial Engineering, University of Padua, UNIPD, Via Venezia 1, Padova, Italy

**Corresponding author: lorenzo.didone@phd.unipd.it*

Abstract

Over the last decades, optical metrology has gained increasing relevance in the industrial scenario, due to the growing demand for high-speed, high-precision, and non-invasive measurements. In this context, chromatic confocal sensors (CCSs) have emerged as a valuable solution offering nanometric resolution and sub-micrometric accuracy, making them suitable for use in metrological applications. On the other hand, their performance can be significantly affected when dealing with non-cooperative surfaces, i.e., surfaces that pose challenges to optical systems due to their inherent characteristics (e.g., complex geometry, reflectivity-related effects, etc.), such as rough surfaces. This contribution focuses on the systematic offset observed on rough surfaces when CCS-based dimensional measurements are compared with tactile ones. An extensive experimental campaign was conducted on stainless-steel specimens produced by different processes and surface roughness *Ra* in the range 0.01-50 µm. Results reveal that for fine finishes, the deviation between the CCS and tactile probe remains within the probing-size error limits, whereas on rougher surfaces, CCS measurements exhibit systematic deviations exceeding the optical distance probe specifications. Based on the experimental results, a simple and straightforward correction model based on surface roughness parameters is proposed.

Dimensional metrology; Chromatic confocal distance sensor; Surface roughness; Optical-tactile deviation; Error compensation.

1. Introduction

The increasing demand for high-throughput and high-precision inspection in advanced manufacturing has favoured the adoption of optical sensors in dimensional metrology [1]. Compared with contact probing systems, optical technologies offer higher acquisition rates and avoid surface deformation, making them attractive for inspecting fragile or complex components [2]. Among optical distance sensors, chromatic confocal sensors (CCSs) have emerged as they provide nanometric resolution and sub-micrometric accuracy [3]. Despite these advantages, the interaction between optical sensors and industrial surfaces remains a critical issue. Unlike calibrated artefacts, manufactured components often exhibit non-cooperative surface conditions, such as high roughness, which can significantly affect optical measurements [4]. In practice, this may lead to discrepancies when optical and tactile measurements are compared. Previous studies have investigated the influence of surface properties on CCS performance, often focusing on a limited range of roughness values. However, a quantitative understanding of how roughness affects CCS-based dimensional measurements across a wide, industrially relevant range of surface roughness values remains incomplete.

This contribution focuses on the effect of surface roughness on CCS-based dimensional measurements, with two main objectives: (i) identifying the surface roughness regime in which CCS measurements remain consistent with tactile probing, and (ii) proposing a simple and straightforward compensation strategy to reduce systematic optical-tactile deviations on rough surfaces.

2. Materials and methods

The experimental campaign was designed to assess the influence of surface roughness on dimensional measurements using a CCS (also referred to as optical distance sensor) mounted on a multisensor CMM. The analysis was carried out assuming that the optical probe axis is normal to the test surface selected in this study. The measured distance d provided by the CCS can be expressed as:

$$d = d_m + \Delta d \quad (1)$$

where d_m is the distance measured and Δd is the systematic optical-tactile deviation, defined as the difference between CCS and tactile measurements acquired in the same measuring volume. The aim of this study is to characterise Δd as a function of surface roughness and to identify conditions under which a correction is required. The analysis focuses on the high-roughness range, where CCS deviations are expected to be most significant.

2.1. Experimental setup

Measurements were carried out in a temperature-controlled laboratory (20 ± 0.5 °C) using a multisensor CMM ZEISS O-Inspect 322 equipped with a 2 mm stylus tip. The maximum permissible error of length measurement is $E_{0,MPE}$ = (1.6 + L / 200) µm (L in mm), and the repeatability limit is $R_{0,MPL}$ = 1.2 µm. The CCS features a micrometric optical spot and a maximum permissible probing size error (PS-MPE) of 5 µm.

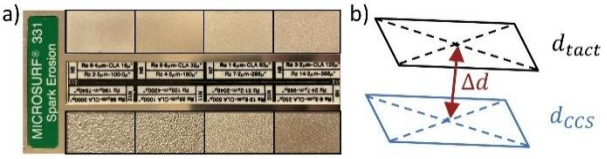

Figure 1. a) spark erosion roughness specimen; b) schematic definition of the optical-tactile deviation Δd.

Four stainless-steel roughness specimens, produced by polishing, grinding, end milling and spark erosion were selected to span typical industrial surface textures (*Ra* ≈ 0.01 - 50 µm), for a total of 29 test surfaces. Figure 1a) shows an example roughness specimen. For each surface, a 5 × 5 mm region was acquired using both probes along 10 parallel scan lines, resulting in approximately 1000 measured points per dataset. A least-squares plane was fitted to each point cloud. The optical-tactile deviation Δd, defined in Equation (1), was evaluated as the difference along the z-direction between d_{CCS} and d_{tact}, corresponding to the coordinates of the centres of the planes fitted to the optical and tactile datasets, respectively. A schematic representation of the definition of the optical-tactile deviation Δd is shown in Figure 1b).

Surface texture characterisation was carried out using an optical profiler (Sensofar S Neox) operating in confocal microscopy mode with a 20× objective. Roughness parameters were evaluated in accordance with the ISO 21920 series.

3. Results and discussion

In Figure 2, the mean of the optical-tactile deviation Δd and the standard deviation of ten repetitions are summarized as a function of the surface roughness parameter *Ra* for all 29 test surfaces. For fine surfaces, corresponding to *Ra* values below approximately 3 µm, the deviation remains within the probing size limits specified for the CCS. In this roughness regime, CCS-based dimensional measurements can therefore be considered consistent with tactile probing, and no systematic correction is required.

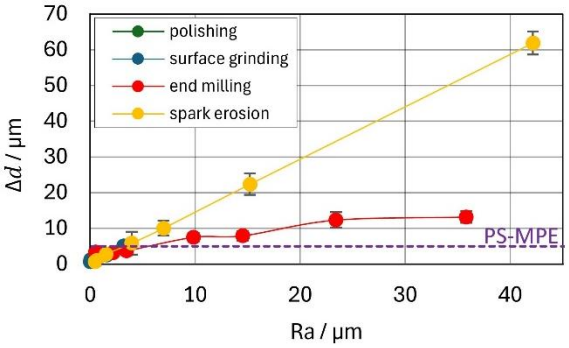

Figure 2. Optical-tactile deviation Δd as a function of *Ra*

As surface roughness increases, a clear systematic deviation emerges. For rougher surfaces, particularly those produced by end milling and spark erosion, Δd exceeds the nominal probing-size error of the optical sensor.

Although *Ra* provides a first indication of this trend, it does not fully describe the observed deviations across different manufacturing processes. A stronger correlation was found with the mean peak height parameter *Rp*. When Δd is plotted against *Rp*, as reported in Figure 3, the data tends to stabilise onto a constant value, regardless of the machining process.

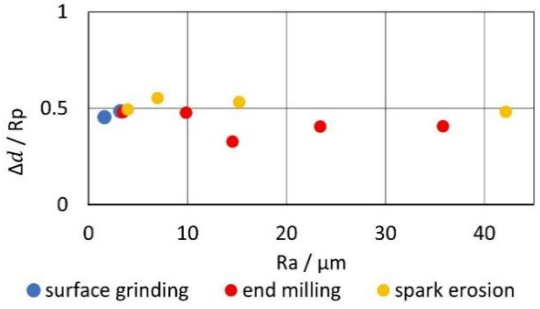

Figure 3. Ratio $\Delta d/Rp$ in relation to *Ra*

Based on the experimental evidence, a simple empirical compensation model was formulated by expressing the optical-tactile deviation as a proportional function of *Rp*:

$$\Delta d \approx k \cdot R_p \qquad (2)$$

where k is an experimentally determined coefficient. For the investigated conditions, k was found to be approximately 0.5. This behaviour can be explained by the fundamentally different interaction mechanisms of optical and tactile probes. The CCS, characterised by a micrometric optical spot, samples both peaks and valleys of the surface, whereas the tactile probe predominantly interacts with surface asperities due to its finite tip size. As the height of the surface peaks increases, this difference in interaction leads to an increasing offset between the two measurement principles.

By compensating for the roughness-induced bias, CCSs can be reliably employed beyond their typical operating domain, enabling their application to rough, non-cooperative surfaces.

5. Conclusions and outlook

This paper investigated the influence of surface roughness on dimensional measurements obtained using a CCS mounted on a multisensor CMM, with tactile probing from the same measuring volume used as reference. An extensive experimental campaign was conducted on stainless-steel surfaces produced by different manufacturing processes and spanning a wide surface roughness range (*Ra* ≈ 0.01 - 50 µm).

The results demonstrate that for fine surfaces (*Ra* < 3 µm), CCS-based measurements are consistent with tactile probing within the sensor specifications. For rougher surfaces, however, a systematic optical-tactile deviation emerges and increases with surface roughness, exceeding the nominal probing-size limits of the optical sensor.

A correlation between the deviation and the mean peak height parameter *Rp* was identified. This enabled the formulation of a simple roughness-based compensation model that reduces the mismatch between optical and tactile measurements on rough surfaces. The proposed approach extends the reliable applicability of CCSs in dimensional metrology under non-ideal surface conditions. Future work will address the influence of probe size, surface tilting, and complex geometries on the proposed compensation strategy. ~~, as well as~~ It will also investigate the use of areal parameters to further refine the model, and integrate ~~the integration of~~ roughness-based correction models into uncertainty evaluation frameworks for multisensor dimensional measurements.

Acknowledgements

The project (23IND12 ADAM) has received funding from the European Partnership on Metrology, co-financed from the European Union's Horizon Europe Research and Innovation Programme and by the Participating States.

References

[1] Archenti A, Gao W, Donmez A, Savio E, Irino N. Integrated metrology for advanced manufacturing. CIRP Ann 2024;**73**:639-65

[2] Catalucci S, Thompson A, Piano S, Branson DT, Leach R. Optical metrology for digital manufacturing: a review. Int J Adv Manuf Technol 2022;**120**:4271-90.

[3] Ye L, Qian J, Haitjema H, Reynaerts D. On-machine chromatic confocal measurement for micro-EDM drilling and milling. Precis Eng 2022;**76**:110-23.

[4] Carmignato S, Voltan A, Savio E. Metrological performance of optical coordinate measuring machines under industrial conditions. CIRP Ann 2010;**59**:497-500.

euspen's 26th International Conference & Exhibition, Krakow, PL, June 2026
www.euspen.eu

Systematic error correction for thickness measurements with optical distance sensors

Dario Pasin, Sofia Catalucci, Enrico Savio

Università degli Studi di Padova, Department of Industrial Engineering, Padova, Italy

dario.pasin@phd.unipd.it

Abstract

Confocal chromatic optical distance sensors enable rapid, non-contact thickness measurements of transparent materials. This technology is particularly promising for applications in which the inner surface of components made of translucent glass or polymer is not accessible. The refractive index of the transparent material is an important input quantity and can be the dominant error source. This work proposes an opto-tactile error correction approach, implemented on a multi-sensor coordinate measuring machine, in which both confocal chromatic and contact probing measurement points are acquired. Two glass carpules and two glass syringes were measured using repeated acquisitions across multiple axial sections, collecting paired inner/outer surface data to compute thickness. A correction factor is identified via least-squares minimization to best match confocal and contact-derived thickness values; the resulting factor is then used to scale optical measurements. Preliminary results show that unknown materials exhibit a larger, yet repeatable, mismatch. The proposed correction reduces the systematic error in thickness measurements and yields an accurate estimate for the specific measurement condition, thereby supporting optical thickness inspection of transparent components.

Thickness Measurement; Confocal Chromatic Sensor; Optical Probe; Error Correction

1. Introduction

Confocal chromatic distance sensors have seen increased adoption as non-contact probes for dimensional metrology. Interestingly, the chromatic aberration principle enables measuring thicknesses for transparent materials by detecting the two wavelengths having maximum intensity, in focus on the two surfaces of the part [1] (Figure 1).

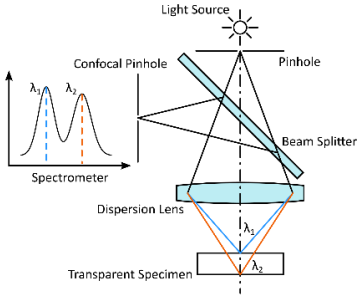

Figure 1. Thickness measurement with a confocal chromatic probe.

Representative applications of optical thickness measurements include automotive glass and polymeric parts (e.g. windshields, lighting covers, etc.), glass tube production, liquid crystal display adhesives and optical lenses [2].

Accurate thickness evaluation with confocal chromatic probes requires knowledge of the refractive index of the workpiece material, to account for light refraction [3]. The basic formula used to account for optical properties is:

$$d = \frac{d'n'}{n} \quad (1)$$

where d is the measured material thickness, taking into account the optical properties; d' is the material thickness obtained by the confocal chromatic probe, without considering the material influence; n is the refractive index outside of the material (typically air); n' is the specimen material refractive index.

In typical industrial conditions, however, the refractive index of the specific transparent materials is unknown, and a generic value n_s is used. This leads to inaccuracies in measurements, and an error e is introduced:

$$e = \frac{d'(n' - n_s)}{n} \quad (2)$$

This error can be considered systematic for a given material and measurement configuration and can therefore be corrected. The present work investigates a correction approach using a multi-sensor coordinate measuring machine (CMM) to acquire both contact reference data and confocal chromatic measurements.

2. Methodology

The experimental part of this research comprises a series of thickness measurements performed on different glass products. Specifically, two syringes and two carpules (i.e., pharmaceutical cartridges with a puncturable cap).

All samples are measured using both tactile probing and the confocal chromatic probe, both mounted in a Zeiss O-Inspect 3-2-2 multi-sensor CMM, which has MPE figures for 3D length measurements of 2.4 µm + L/150 for contact probing and 3.2 µm + L/150 for confocal chromatic probing. Each container is placed in the measuring volume using Mitutoyo "eco-fix" fixtures, oriented with its axis along the CMM x-axis.

Alignment is performed by fitting the outer cylindrical surface of the container to define an axis, and by setting the origin at the intersection between this axis and the plane fitted to the syringe flange or the carpule cap. Contact measurements are performed with both vertical and horizontal styli to access both the outer and inner surfaces. The acquired data consists of a series of points at multiple axial positions (Figure 2), enabling both contact and confocal-based thickness evaluations at several cross sections of the container.

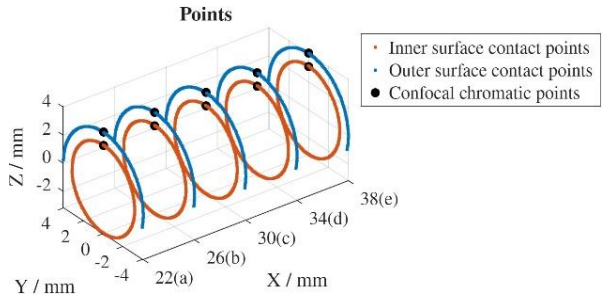

Figure 2. Data acquired on the glass container geometry.

Three measurement cycles are repeated for each sample, highlighting two different conditions: for the carpules, made of known material (fused silica), the opto-tactile thickness difference is limited to at most 10 µm; in contrast, for the syringes, whose material is unknown, the observed difference is significant, on the order of a tenth of a millimetre.

2.1 Correction factor

The opto-tactile difference observed is considered a systematic effect caused by using approximate refractive indexes. A correction factor c_f is defined as a scale factor that best matches the optical thickness values to the contact reference values, utilizing a least-squares approach:

$$c_f = \arg\min_c \left\| t_{cont} - c t_{conf} \right\|^2 \quad (3)$$

where t_{cont} is the vector of thickness values acquired by contact probing at different locations along the container axis, and t_{conf} represents a vector of thickness values acquired by the confocal chromatic probe at the corresponding locations. With the correction factor applied, the measured material thickness expressed in equation (1) becomes:

$$d_{corrected} = c_f d = c_f \frac{d' n'}{n} = \frac{d'(n' c_f)}{n} \quad (4)$$

Accordingly, $n' c_f$ can be interpreted as an estimate of the unknown refractive index for the specific measurement condition, based on contact and chromatic confocal data.

3. Results

Table 1 gives an overview of the differences between carpules and syringes, showing that the confocal chromatic principle is accurate when the material is known. The average results of three measurement cycles per each specimen are shown; each cycle considers multiple sections.

Table 1. Mean thickness **(d)** and standard deviation **(std)** figures

	Carpule 1	Carpule 2	Syringe 1	Syringe 2
$d_{contact}$/mm	0.9515	0.9579	0.9080	0.8954
$std_{contact}$/mm	0.0016	0.0044	0.0010	0.0026
$d_{confocal}$/mm	0.9607	0.9550	0.9327	0.9166
$std_{confocal}$/mm	0.0007	0.0031	0.0010	0.0023

As expected, confocal chromatic thickness measurements are most accurate for the two fused silica carpules, which have a known refractive index. The proposed approach for systematic error correction shows accurate results that are consistent with the reference data provided by contact probing.

The correction factor c_f is calculated for both syringes; to prevent self-correction, the factor obtained from one syringe is used to correct the results of the other. The results in Table 2 show that this approach returns corrected thickness values that are consistent with the contact measured ones.

Table 2. Cross-applied correction factors **(c_f)** on syringes

	Syringe 1	Syringe 2
$d_{contact}$/mm	0.9080	0.8954
$d_{confocal}$/mm	0.9327	0.9166
c_f	0.9735	0.9768
$d_{corrected}$/mm	0.9111	0.8923
$d_{contact}$-$d_{corrected}$/mm	-0.0031	0.0031

The same approach is tested on the carpules, intentionally selecting an incorrect material (e.g., D236T glass) and performing the correction. Table 3 shows promising results and agreement between the uncorrected results with the correct fused silica setting and the corrected results obtained using the incorrect D236T material setting.

Table 3. Carpules: correcting D236T glass measurements

	Carpule 1	Carpule 2
$d_{contact}$/mm	0.9515	0.9579
$d_{confocal_FS}$/mm	0.9607	0.9550
$d_{confocal_D236T}$/mm	1.0016	0.9996
c_f	0.9502	0.9584
$d_{corrected}$/mm	0.9599	0.9499
$d_{contact}$-$d_{corrected}$/mm	-0.0084	0.0080
$n'c_f$	1.4473	1.4597

Moreover, the $n' c_f$ estimate of the refractive index starting from the D236T refractive index of 1.5231 returns values close to the correct refractive index of the fused silica glass, 1.4585.

4. Conclusions and future work

This work presents an effective error correction approach for thickness measurements with optical distance sensors in dimensional metrology. The approach consists in the correction of the refractive index influence by applying a correction factor, calculated from contact reference data. Experimental results show that the corrected opto-tactile difference is reduced to at most a few micrometres.

Applying a correction factor identified on one specimen to another specimen indicates that the method has potential for batch inspections, provided stable measurement conditions. This is particularly interesting for large production lots, where the opportunity to measure one sample contact-wise and correct all the other optical measurements can enable fast and accurate in-line inspection.

Future work will include the identification of an uncertainty contribution for the error correction and more extensive tests on larger sample sets.

Acknowledgements

The project (23IND08 DI-Vision) has received funding from the European Partnership on Metrology, co-financed from the European Union's Horizon Europe Research and Innovation Programme and by the Participating States. The authors would like to thank Brevetti CEA, involved in the definition of the case study.

References

[1] Liu C, Lu G, Liu C, Li D 2023 Compact chromatic confocal sensor for displacement and thickness measurements, *Measurement Science and Technology* **34**, 5 055104

[2] Ma Y D, Xiao Y C, Wang Q Q, Yao K, Wang X R, Zhou Y P, Liu Y C, Sun Y and Duan J 2023 Applications of chromatic confocal technology in precision geometric measurement of workpieces *J. Phys.: Conf. Ser.* **2460** 012077

[3] Leach R 2011 *Optical Measurement of Surface Topography* Heidelberg (Springer)

euspen's 26th International Conference & Exhibition, Krakow, PL, June 2026
www.euspen.eu

Digital twin of a reference rotary table for traceable angular metrology

Rim Bennoune[1, 2], Nabil Anwer[2], Mohamed Damak[3], Hichem Nouira[1]

[1]*Laboratoire national de métrologie et d'essais (LNE), France*

[2]*Université Paris-Saclay, ENS Paris-Saclay, LURPA, 91190, Gif-sur-Yvette, France*

[3]*GEOMNIA - École Nationale Supérieure des Arts et Métiers (LISPEN), France*

rim.bennoune@lne.fr
Hichem.Nouira@lne.fr

Abstract
This work presents a digital twin framework for angular error compensation in a high-precision rotary table. The approach exploits continuous interaction between the physical rotary table and its virtual counterpart, where the physical system provides real-time measurements from a dual encoder, thermal probes, and capacitive sensors representative of the actual operating state. These measurements are fused in a particle-filter-based data assimilation module. The virtual rotary table is continuously updated and incorporates three complementary models: a geometrical error model, a thermal drift model, and sensor error models. By synchronizing the virtual entity with the physical system, the framework estimates the true angular position and delivers a corrected angle in real time. This corrected angle is used for metrological evaluation or fed back into the control loop.

Digital twin, particle filter, rotary table, angular metrology, uncertainty evaluation

1. Introduction

The physical system (Figure 1) is the primary angular calibration standard developed at LNE [1], its performance is affected by encoder microinterpolation errors, geometric errors and thermal instabilities, leading to expanded uncertainties of about ±0.01". The proposed digital twin exploits continuous interaction between the physical rotary table and its virtual entity, integrating geometrical and thermal models with multisensor observations from a dual encoder, an autocollimator, capacitive probes, and thermal sensors to represent the actual operating state.

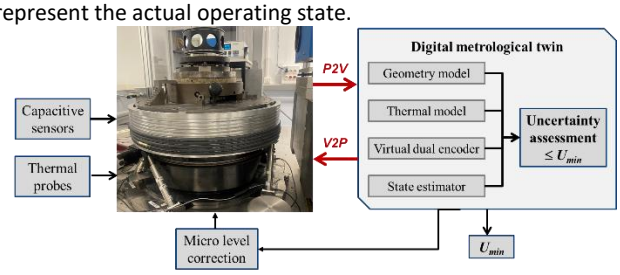

Figure 1: Reference rotary table digital twin framework

The framework is structured in three main phases: a virtual experiment that models the measurement process, an uncertainty assessment, and a control phase for real-time correction using a 6-DoF hexapod.

2. Geometrical error model

2.1. Projection process of SDT (Small Displacement Torsor)

For each of the eight operational capacitive sensors (Figure 2), the sensor position and measuring direction are defined within the configuration matrix H. The measured displacement d_i for the i-th sensor is modelled as:

$$d_i = \mathrm{h}_i \cdot \mathrm{u} \quad (1)$$

where h_i denotes the i-th row of the configuration matrix $\mathrm{H} \in \mathbb{R}^{8\times6}$, and $\mathrm{u} = [T_x, T_y, T_z, R_x, R_y, R_z]^T$ represents the parasitic translations and rotations to be estimated at the measured position angle θ.

Extending Equation (1) to all eight sensors yields the overdetermined linear system:

$$\mathrm{d} = \mathrm{Hu} \quad (2)$$

with solution $\hat{\mathrm{u}} = (\mathrm{H}^T\mathrm{H})^{-1}\mathrm{H}^T\mathrm{d}$.

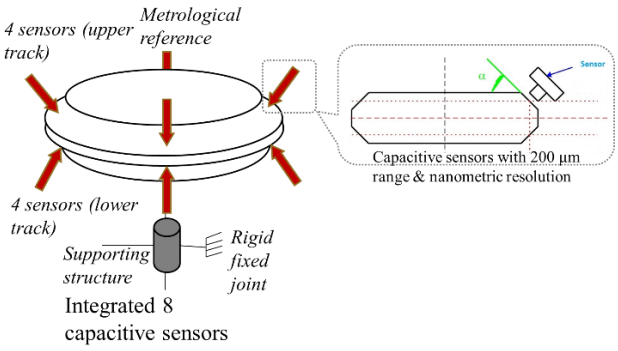

Figure 2: Capacitive sensing principle of the metrological reference

2.2. Geometrical error effect on angle measurement

The geometric error model is expressed as:

$$e_g(\theta) = \sum_{k=1}^{N} [a_k \cos(k\theta) + b_k \sin(k\theta)] \quad (3)$$

This model characterises the angular signature of geometric errors as a function of the nominal angular position θ. It decomposes the error into harmonic contributions primarily associated with radial runout, tilt, and axial motion of the rotary table [2].

3. Thermal drift model

the thermally induced angular error is expressed as a function of temperature proxies and sensitivity coefficients [3].

$e_{\text{th}} = k_0 + k_U \cdot U + k_{G1} \cdot G_1 + k_{G2} \cdot G_2$ (4)

where:

k_0 = constant angular offset (µrad)

$U = T - T_{\text{ref}}$ = uniform thermal expansion proxy (difference from reference temperature, °C)

$G_1 = \frac{dT}{dt}$ = rate of temperature change (°C/s) captures transient gradient effects

$G_2 = H(T)$ = thermal imbalance function

k_U, k_{G1}, k_{G2} = identified sensitivities (µrad/°C, µrad/(°C/s), µrad/°C respectively)

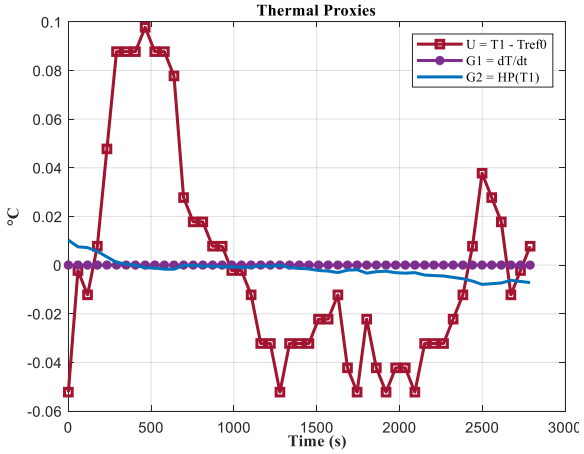

Figure 3: Thermal proxies

Figure 3 illustrates the thermal proxies, showing quasi-static behavior with limited dynamic variations.

4. Virtual dual encoder

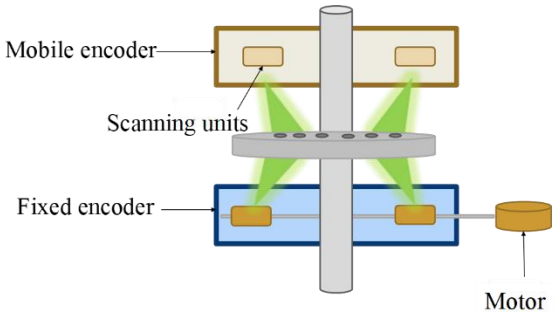

Figure 4: Dual encoder

The virtual dual encoder (Figure 4) reproduces the measurement sequence of the reference rotary table [1], including continuous shaft rotation, independent encoder readings, error superposition, and differential signal integration over one revolution.

Each encoder output includes:

- Graduation errors: $e_g(\theta) = A\sin(2\pi f\theta + \phi)$ (where A is the amplitude, f the frequency, and ϕ the phase shift)
- Eccentricity: first-harmonic $e_e \approx e/r$ (for small eccentricity e, radius r).
- Interpolation: high-frequency

The Fixed encoder measured angle is θ_f the mobile one is θ_m (offset α_0). Differential signal: $\delta\theta = \theta_m - \theta_f = \alpha_0 + e_d$, where $e_d = e_m - e_f$ is periodic.

➔ $\hat{\alpha}_0 = \frac{1}{2\pi}\int_0^{2\pi} \delta\,\theta(\phi)d\phi$.

Table 1 below shows the results of the virtual dual encoder.

Table 1 Virtual dual encoder simulation results

Nominal angle (°)	Virtual measured angle (°)
0	0.0098
15	14.9973
30	29.9888
45	44.9302

5. Results and discussion

A simulation and an experiment were conducted on a 24-face polygon (Figure 5). Table 2 compares estimated and measured angles.

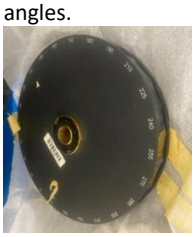

Figure 5: 24 faces polygon

The particle filter operates on a state vector that combines the true angle with key model parameters [4]. At discrete time step k, this is defined as:

$$\mathrm{x}_k = [\theta_k, \mathrm{u}_k^{\mathsf{T}}, \beta^{\mathsf{T}}, \mathrm{p}^{\mathsf{T}}]^{\mathsf{T}}$$

where θ_k is the rotary table angle, u_k represents the small-displacement torsor (SDT), β contains the thermal sensitivities of the proxy-based drift model, and p groups the dual encoder parameters.

Table 2 Particle filter estimation of the corrected angle

Estimated angle (°)	Measured angle (°)	Filter error(″)
359.998831576929	359.999700000000	3.126
345.000800000000	344.998589418415	7.958
330.000100000000	329.998687987665	5.083
315.000100000000	314.998755776230	4.839

6. Conclusions and future work

This paper presents a digital twin framework for real-time angular error compensation of a reference rotary table. By combining geometrical, thermal, and sensor error models with particle-filter-based data fusion, the proposed approach enables improved estimation of the true angular position.

Preliminary results demonstrate the relevance of the framework for reducing angular measurement errors. However, remaining discrepancies highlight the influence of simplified thermal modeling and unmodeled dynamic effects.

Future work will focus on enhancing the thermal model using physics-based approaches. These developments aim to improve uncertainty evaluation and ensure traceability in high-precision angular metrology.

References

[1] Leleu S 2000 Contribution à l'évaluation des angles: conception, réalisation et validation d'un plateau pivotant de très haute précision.

[2] ISO 230-1 2012 Test code for machine tools — Part 1: Geometric accuracy of machines operating under no-load or quasi-static conditions (Geneva: ISO).

[3] Gao W et al. 2023 Machine tool calibration: Measurement, modeling, and compensation of machine tool errors, Int. J. Mach. Tools Manuf. 187, 104017.

[4] Ward R et al. 2020 Continuous calibration of a digital twin: a particle filter approach, NeurIPS Workshop.

euspen's 26th International Conference & Exhibition, Krakow, PL, June 2026
www.euspen.eu

Multi-Material Empirical Artifact Correction (MEAK): Efficient Algorithm for Correcting Beam Hardening Artifacts in Multi-Material CT

Philip Trapp[1,2] , Frederic Ballach[2] , Tobias Müller[2] , Michael Hammer[2] , Raoul Christoph[2] , Ralf Christoph[2] , and Marc Kachelrieß[1]

[1] *German Cancer Research Center (DKFZ), Im Neuenheimer Feld 280, 69120 Heidelberg, Germany*
[2] *Werth Messtechnik GmbH, Siemensstraße 19, 35394 Giessen, Germany*

Corresponding author: frederic.ballach@werth.de

Abstract
Industrial X-ray computed tomography (CT) has become a well-established method for the fast, complete, and non-destructive measurement of workpieces. However, in multi-material components containing highly absorbing materials, beam hardening artifacts result in systematic measurement errors [1]. Existing approaches to artifact reduction, such as the use of hard prefilters and multi-spectral CT (MSP-CT) methods [2], require additional measurement time and reduce the contrast-to-noise ratio (CNR) [3]. This contribution introduces the Multi-Material Empirical Artifact Correction (MEAK), a novel correction method that reduces beam hardening artifacts without increasing measurement time and can be seamlessly integrated into existing processes. Comparative measurements demonstrate that MEAK reduces both linear and non-linear artifacts, preserves the CNR, and halves the measurement time compared to MSP-CT.

artifact reduction, measurement time reduction, multi-material, metrology

1. Introduction

CT has become a well-established method for the fast, complete, and non-destructive measurement of workpieces. However, multi-material components containing highly absorbing materials, such as metals, are subject to beam hardening artifacts. These artifacts cause systematic measurement errors and limit the applicability of CT for dimensional metrology [1]. A common method for reducing beam hardening artifacts is the use of strong pre-filters to harden the X-ray spectrum. However, attenuating lowenergy photons reduce the contrast-to-noise ratio (CNR), leading to increased measurement uncertainty. MSP-CT methods combine measurements acquired with different spectra to correct artifacts, but the additional measurements result in longer measurement times and often lead to a reduced CNR [2]. The MEAK method, presented in the following, extends the empirical beam hardening correction (EBHC) introduced by Kyriakou et al. [3]. MEAK reduces both linear and non-linear beam hardening artifacts without requiring additional measurements or prior knowledge of the CT system or the workpiece.

2. Materials and methods

2.1. Method

The approach is based on EBHC and has been further developed to meet industrial requirements. It accounts for both linear and non-linear artifacts. Artifact reduction is achieved using base volumes, which are calculated from the measured data and represent the artifacts in the reconstructed volume. The measured volume is corrected by applying a weighted linear combination of these base volumes.

2.2. Method validation

To validate the method, a measurement of an industrial connector made of several materials was performed. The scan was carried out at 270 kV, 80 W, using a 1-mm-thick tin prefilter. The measurement time was 10 minutes. The results were compared with those of the MSP-CT and high-resolution MSP-CT (MSP-CT HR) methods, among others, for which a second measurement was performed at 160 kV, 50 W, and with a 1-mm-copper prefilter, with the same measurement time. This doubled the total measurement time for the MSP-CT methods to 20 minutes, compared to 10 minutes for MEAK. All other parameters were kept constant.

3. Results

Figure 1 shows the results of MEAK in comparison to the correction methods EBHC, MSP-CT, and MSP-CT HR. EBHC is unable to correct non-linear partial volume artifacts, and high-frequency striping artifacts remain visible. MSP-CT significantly reduces artifacts but fails to preserve the CNR, as evident in the resulting point clouds. MSP-CT HR delivers the best performance in terms of artifact reduction and CNR preservation. However, it requires a second scan, thereby doubling the total measurement time (see Section 2.1). MEAK effectively reduces both linear and non-linear artifacts in a single scan while maintaining CNR.
It therefore provides a time-efficient alternative to multispectral methods, particularly in industrial applications requiring high image quality and throughput.

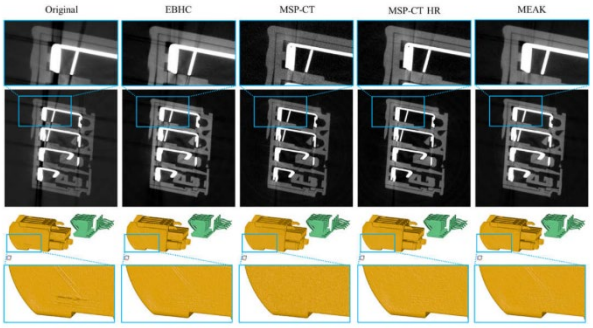

Figure 1 Example volume sections of the uncorrected initial volume of the connector measurement (left), as well as the resultant volumes after corrections using EBHC, MSP-CT, MSP-CT HR, and MEAK. The lower row shows point clouds in STL-format generated from the volume data for both materials present in the object (plastic: gold; metal: green).

4. Summary and outlook

MEAK has been presented as a practical algorithm for reducing beam hardening and partial volume artifacts in CT measurements of multi-material components. Compared to multi-spectral methods, MEAK achieves a well-balanced combination of image quality and measurement time: linear and non-linear artifacts are significantly reduced, the contrast-to-noise ratio is preserved, and the measurement time is halved relative to MSP-CT HR. The method has been experimentally validated on representative multi-material workpieces and integrated into the WinWerth® measurement software.

Acknowledgments

This study was supported by the German Federal Ministry of Education and Research (BMBF) via the funding program Photonics Research Germany under grant number 13N14804. Parts of the reconstruction software were provided by RayConStruct® GmbH.

References

[1] R. Christoph, M. Kachelrieß, Computertomografie in der Koordinatenmesstechnik, in: R.H. Schmitt, E. Dietrich (Eds.), *Handbuch Messtechnik in der industriellen Produktion: Valide Messergebnisse planen, erhalten, auswerten und verteilen,* Carl Hanser Verlag, München, 2023, pp. 459–495.

[2] P. Trapp, F. Ballach, R. Christoph, and M. Kachelrieß. Spatial resolution-optimized artifact reduction by combining dual energy X-ray CT data using a frequency split. In: *Proc. 13th Conference on Industrial Computed Tomography (iCT 2024)*, Wels, Austria, 2024.

[3] Y. Kyriakou, E. Meyer, D. Prell, and M. Kachelrieß. Empirical beam hardening correction (EBHC) for CT. *Med. Phys.* 37 (2010) 5179–5187.

euspen's 26th International Conference & Exhibition, Krakow, PL, June 2026
www.euspen.eu

Device for roundness measurement of continuously changing diameter objects

Sampo Haikonen[1], Nhat Huy Nguyen[1], Elmo Laine[1], Raine Viitala[1]

[1]*Aalto University, Department of Energy and Mechanical Engineering*
sampo.haikonen@aalto.fi

Abstract
This paper presents a device designed to measure the roundness of objects whose diameters change continuously, such as rolls of paper, plastic film, or thin metal sheets. The device is equipped with four probes to implement a redundant multi-point roundness method. This approach is necessary to accommodate the object's changing conditions, specifically the motion of the center point caused by variations in mass. The device can measure objects with diameters ranging from 100 mm to 750 mm. Validation was conducted using a steel reference disk, which was measured with both the presented device and a Mitutoyo RA-2200 roundness tester. Additionally, measurements of a paper roll with approximately 2500 layers are presented to demonstrate the capability to detect roundness changes during reeling. The device was found to be able to measure the test steel roundness profile within micrometer accuracy which is adequate for the intended application of the device.

Roundness measurement, Multi-probe method, Changing diameter

1. Introduction

Measuring roundness is one of the routine operations in precision metrology. Current devices face significant limitations when applied to large-scale objects or those with variable diameters. Objects such as paper rolls, thin-film plastic rolls, and metal strip coils cannot be accommodated by standard instruments due to their size and dynamic geometry. Consequently, accurate in-process roundness measurement for these materials remains a partially unresolved challenge in the industry.

Previous methods and devices for measuring large objects, such as paper machine rolls employ the multi-probe roundness measurement method. The use of more than one measurement probe is necessary when the object cannot be assumed rigid and rotate around a fixed center point [1]. To separate the center point motion from the object surface at least three probes are needed [2]. Alternative methods exist, which include rearranging the object and/or measurement probe to different angles to achieve the same outcome [3,4].

Typical large scale roundness measurement devices widely used in roll servicing industries use an arch with one, two, three or four radially spaced probes [5]. These applications typically employ sensors such as contacting length gauges, eddy current sensors or lasers. On the other hand, smaller work pieces in laboratory conditions can be measured with roundness testers which often only use single probe but are equipped with a precision spindle to eliminate center point motion. Also, coordinate measurement machines can be used to measure roundness to a certain extent.

This paper describes a device and method to measure objects such as paper roll during reeling which have a constantly increasing diameter. The presented device uses the multi-probe roundness measurement scheme.

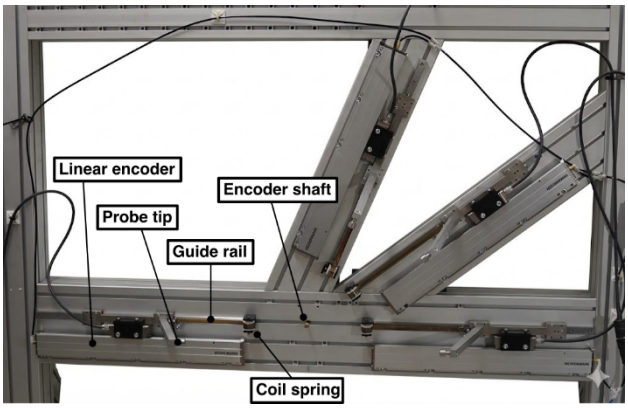

Figure 1. Image of the presented roundness measuring device. The device consists of the four measurement probes attached to linear encoders via linear guide rails. The probes are constantly tensioned against the work piece using constant force springs.

2. Methods

The structure of the device is shown in Figure 1. The device is assembled on aluminum frame with four radially placed guide rails (Hiwin MGNR). Each guide rail has a probe tip riding on a block, which is also attached to linear encoder (Heidenhain LF185C) to detect the block position. A rotary encoder (Heidenhain ROD 480-5000) is used to capture the angular position of the work piece. The blocks are additionally spring loaded with small 20N brass constant force coil springs. The encoder data was captured using Heidenhain EIB741 data acquisition device.

Four measurement probes are used, each attached to the linear guide rail with an angled beam. The four probes are arranged radially around the work piece with nominal angles [0, 38, 67, 180]. These angles provide were adoped as they are a known reliable configuration suggested by Kato [7]. Movement of the probes is recorded by the linear encoders, and the rotary encoder is used to trigger the measurement at equally spaced intervals 5000 times per revolution. Thus, the angular sampling interval between measurement points was 0.072 degrees. Schematic indicating the probe angles and movement of the linear encoders is shown in Figure 2. The device is designed to measure the roundness of objects with diameters ranging from 100 mm to 750 mm.

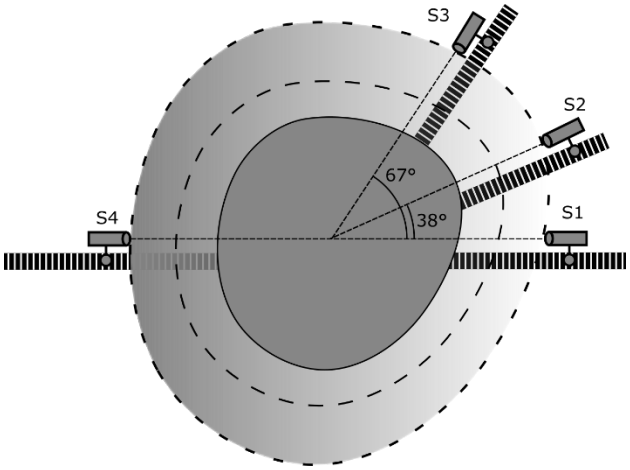

Figure 2. Schematic of the probe arrangement. The probes have maximum moving distance 340mm radially with respect to the measured object. This movement allows the object diameter to increase while the measurement is being conducted, useful for example if the object is a paper roll being reeled.

The regular and hybrid multi-probe measurement processes are relatively straightforward for an object with constant geometry, and the theory has been well-documented in previous studies. Let the displacement of the rotational center in the x- and y-axis and the roundness deviation be denoted by $x(\phi)$, $y(\phi)$, and $r(\phi)$, respectively. The measurement signals can be modelled as:

$$s_{k(\phi)}(\phi) = x(\phi)\cos(\phi_k) + y(\phi)\sin(\phi_k) + r(\phi - \phi_k), \quad (1)$$

where ϕ is the rotated angle of the object, k is the probe index, and ϕ_k is the position of the probe. Jansen et. al. [6] showed that the nth complex Fourier coefficients S_{kn}, x_n , y_n , and r_n of the parameters are related:

$$S_{kn} = x_n \cos(\phi_k) + y_n \sin(\phi_k) + r_n \exp(-in\phi_k), \quad (2)$$

With all the probes, a matrix form equation can be constructed:

$$\mathbf{S}_n = \mathbf{H}_n \mathbf{x}_n \quad (3)$$

$$\begin{bmatrix} S_{1n} \\ S_{2n} \\ \vdots \end{bmatrix} = \begin{bmatrix} \cos(\phi_1) & \sin(\phi_1) & \exp(in\phi_2) \\ \cos(\phi_2) & \sin(\phi_2) & \exp(in\phi_2) \\ \vdots & \vdots & \vdots \end{bmatrix} \quad (4)$$

To solve for $\mathbf{x}_n$, at least three probes are needed. For more probes, $\mathbf{x}_n$ can be solved with the least square method:

$$\hat{\mathbf{x}}_n = (\mathbf{H}_n^T \mathbf{H}_n)^{-1} \mathbf{H}_n^T \mathbf{S}_n \quad (5)$$

For $\hat{\boldsymbol{x}}_n$ to not be sensitive to relatively small changes in $\mathbf{H}_n$ and for reducing harmonic suppression, $\mathbf{H}_\mathrm{n}$ should be well-conditioned [6]. This depends on the angles ϕ_k. These can be chosen so that suppression is reduced for harmonics of interest. For example, [7] suggested a reliable combination of angles for four-probe method being [0, 38, 67, 180], which is used in our device.

The zeroth and first coefficients of r can be set to 0, since they are the average offset and the eccentricity, respectively. These properties are not of interest in roundness measurement.

An alternative approach to extract roundness measurement from the probe signals is the hybrid method, where subsets of the harmonics are solved from different combinations of the probes, before the individual harmonics are assembled to obtain the full range [8]. For example, from four probes with the angle combination above, the even harmonics can be calculated from two opposing probes, and the odd harmonics can be calculated from three non-opposing probes.

For an object with increasing diameter, e.g., a winding paper roll, the probe signals are the sum of the roundness profile for each revolution and the change in radius (or diameter). For the case of the winding paper roll, this change in radius is approximately linear as layers of paper are approximately the same thickness. This linear increase in radius seen in the probe signals is then easily removed by detrending the signals for example by subtracting a least-squares fitted line function.

A precision-manufactured steel disk (240mm diameter, 10mm thick) was used to validate the accuracy of the measurement device. The setup of the disk in the roundness measuring device is depicted in Figure 3. The disk was mounted on the evaluated roundness tester in an overhung-rotor configuration, supported by two ball bearings on one side. Measurements were taken while slowly rotating the disk using a small DC motor and a belt-pulley drive. To minimize friction and suppress chatter, the disk surface was lightly coated with synthetic lubricant. The same disk was then mounted, centered, and measured on a Mitutoyo RA-2200 roundness tester to give comparison. Measurement repeatability of the proposed device was evaluated by calculating the standard deviations over all angular positions over 40 rotation cycles.

Figure 3. Reference steel disk mounted on the presented roundness measuring device. The disk was rotated with small electric motor and supported by two ball bearings. Encoder is directly attached to the steel disk.

A small paper-roll sample was used to demonstrate the variable-diameter operation of the roundness-measuring device. The paper was wound onto a cardboard core with an initial diameter of approximately 100 mm using a Tapio laboratory paper analyzer. Winding was performed at a slow speed. The measurement probes tracked the paper surface and moved radially outward from the center as the roll diameter increased. Final diameter of the paper roll was around 600 mm.

3. Results

Figure 4 illustrates the displacement signals obtained via TSA. To characterize measurement repeatability, uncertainty intervals are included, representing the standard deviation over 40 cycles for each angular position. The actual standard deviations are also shown as function of rotation angle below each displacement figure in Figure 4. The average and maximum values of these standard deviations are shown in Table 1.

The roundness profile of the steel disk is presented in Figure 5. The depicted profiles were calculated with the filter level set to 1024 undulations per revolution. The profile measured with the presented device is overlaid with a profile measured with the Mitutoyo RA-2200. The first 50 harmonics of both the RA-2200 and presented device are shown in Figure 6.

The roundness profile for different layers of the sample paper roll measured with the device is depicted in Figure 7 as a heatmap for each layer separately.

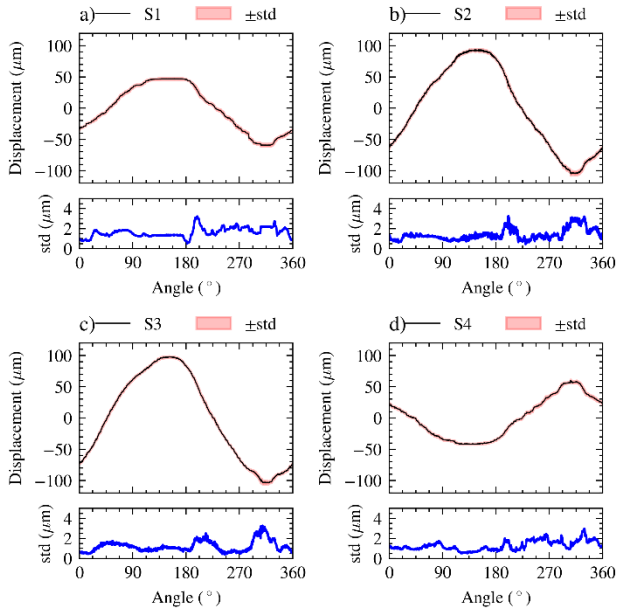

Figure 4. Displacement readings for the four probes averaged over 40 revolutions. Red highlight depicts the standard deviation limits around the mean and small figures below each figure indicates the exact standard deviation as function of rotation angle.

Table 1 Average and maximum values for standard deviation of displacement measurements from the steel disk over 40 revolutions.

Probe	Average std (μm)	Max std (μm)
1	1.6	3.2
2	1.4	3.3
3	1.2	3.3
4	1.3	3.0

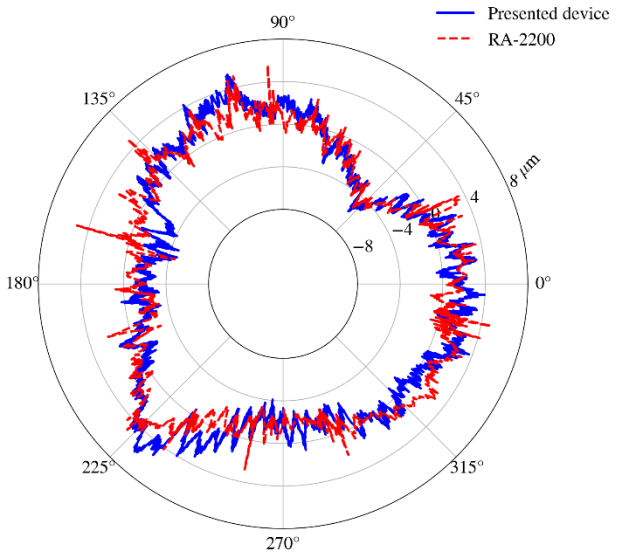

Figure 5. Roundness profiles of the test disk measured with the presented device and the RA-2200 roundness tester.

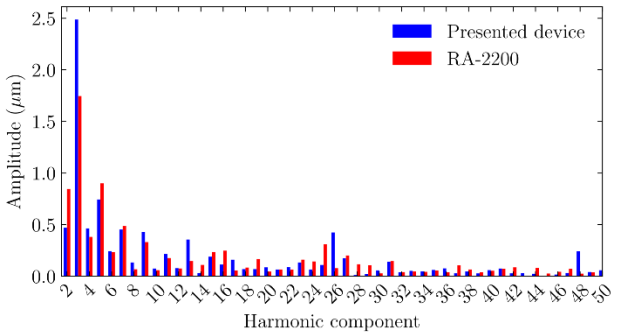

Figure 6. Amplitudes for different harmonics of the roundness profiles measured from the steel disk with the presented device and the RA-2200. Only the first 50 harmonics are depicted in this figure.

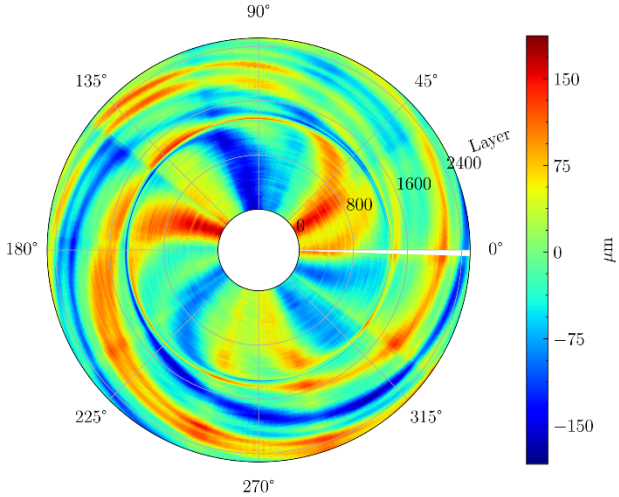

Figure 7. Heatmap of roundness profiles for a reeled small paper roll. The radial axis is the layers of paper, and the color illustrates the roundness profile of each layer. The first harmonic component has been filtered out.

4. Discussion

A device for measuring roundness of variable diameter objects was shown in this paper. The applicability of the device concept was studied and a preliminary validations and tests are presented.

The device showed good repeatability with the test disk. The maximum standard deviation among all probes was only 3.3 µm, with the best being 3.0 µm. Figure 4 shows that the test disk had eccentricity, most likely due to lack of alignment. The eccentricity was well compensated away using the multiprobe method. Some variability in the measurement standard deviation at different angles was detected. All sensors showed increased variability at around 200° and 330°. These angles appear to have some slope in runout, which could lead to a change in contact force and affecting friction. A change in friction force due to probe kinematics might explain the increased uncertainty. Nevertheless, the standard deviations are quite small. Validation measurement performed on a steel disk showed good agreement between commercial RA-2200 instrument and the presented device. Deviations in the roundness profile presented in Figure 5 are minor and within few micrometers from each other. The manufacturer indicated that the accuracy of the linear encoders is 2 µm, which can explain at least some of the deviation to the reference profile. Other error source in the measurement device can be attributed to Abbe error which is result from bending of the probe supporting beam and slack between linear rails and the sliding blocks. Additionally, the test disk was likely measured from slightly different axial position leading to small surface imperfections being different thus causing differences in the roundness profiles.

Observing the harmonic components of the roundness profiles in Figure 6, a deviation between reference measurement can be noticed at components 3, 13, 26 and 48. Possible reasons for the differences can be error in probe angles, radial alignment of lack of stiffness of the probe beams [9], or any of the above detailed error sources. Most of the harmonic components are relatively similar, establishing that the presented device is indeed capable of estimating the roundness harmonics with good accuracy.

A key contribution of this paper is handling the continuous change in diameter without interrupting the measurement. By using a rotary encoder for angular synchronization and four probes for center-motion separation, the device isolates roundness from center displacement and monotonic radius growth. Advantage of the design presented is that it allows harmonic content of true roundness to be tracked across successive layers.

The paper roll experiment captured roundness profile across approximately 2500 layers of paper shown in Figure 7. Unlike the steel test disk, the roll exhibits significantly larger geometric variation, which relaxes the need for sub-micrometer accuracy in this application while still requiring robust separation of center motion.

Each layer could be measured only once, causing more noisy estimates for the roundness as synchronous averaging could not be used. Since paper is compressible, local compaction under probe contact can possibly affect the measurement readings. Surface slip or slight creep during reeling can change the phase of the roundness features between layers.

Overall, the device produced stable, interpretable roundness profiles over thousands of layers, allowing visualization of how the geometry of the roll changes as it is reeled. This capability is directly relevant for diagnosing winding errors, such as out-of-roundness build-up.

5. Conclusions

A four-probe, encoder-synchronized roundness device was developed for large objects with continuously changing diameters (100–750 mm). By applying multi-probe roundness algorithms and suppressing mean radius drift, the system separates roundness from center-point motion during reeling.

Validation on a steel disk confirming the device's capability to recover roundness harmonics accurately. Observed deviations at specific harmonic orders are consistent with prototype mechanical and alignment limitations and can be reduced by improved calibration and stiffness. Measurements over ~2500 paper layers demonstrated the device's ability to track roundness evolution. Despite material compressibility and occasional phase changes due to surface slip, the system revealed meaningful harmonic trends and layer-wise deviations that are substantially larger than those of the test disk. The device is suitable for analyzing paper roll winding errors, providing a practical pathway to correlate harmonic content with process conditions. Future work will focus on improving probe stiffness, reducing rail friction and investigation roundness of paper rolls. More thorough investigation of the measurement device errors should still be done to quantify device limitations.

References

[1] Tiainen T 2020 Multi-probe roundness measurement of large rotors

[2] Ozono S 1974 On a new method of roundness measurement based on the three points method *Proceedings of 1st Int. Conf. on Production Engineering, Tokyo*

[3] Donaldson R R 1972 A simple method for separating spindle error from test ball roundness error *Annals of the CIRP* **21** 125

[4] Marsh E R, Arneson D A and Martin D L 2010 A comparison of reversal and multiprobe error separation *Precision engineering* **34** 85–91

[5] Widmaier T 2012 Optimisation of the roll geometry for production conditions

[6] Jansen M, Schellekens P and De Veer B 2001 Advanced spindle runout-roundness separation method *Advanced Mathematical and Computational Tools in Metrology V* (World Scientific) 212–219

[7] Kato H, Sone R and Nomura Y 1991 In-situ measuring system of circularity using an industrial robot and a piezoactuator *International journal of the Japan society for precision engineering* **25** 130–135

[8] Shi S, Lin J, Wang X and Zhao M 2016 A hybrid three-probe method for measuring the roundness error and the spindle error *Precision Engineering* **45** 403–413

[9] Viitala R, Widmaier T, Hemming B, Tammi K and Kuosmanen P 2018 Uncertainty analysis of phase and amplitude of harmonic components of bearing inner ring four-point roundness measurement *Precision Engineering* **54** 118–130

euspen's 26th International Conference & Exhibition, Krakow, PL, June 2026

www.euspen.eu

An ultra-compact chromatic confocal sensing probe enabled by metasurfaces and micron resolution 3D printing

J. Williamson[1*], D.J. Townend[1], D. Tang[1], R. Owen[2], W. Zhong [1], A.J. Henning[1], H. Martin[1], V.R. Konnanath Puthanveetil[1], X. Jiang[1]

[1]*Centre for Precision Technologies, University of Huddersfield, Queensgate, Huddersfield, HD1 3DH*
[2]*School of Pharmacy, University of Nottingham Biodiscovery Institute, University of Nottingham, University Park, Nottingham, NG7 2RD*

*james.f.williamson@hud.ac.uk

Abstract

The ever-increasing demand for on-machine and in-situ metrology has driven substantial recent progress towards the reduction in size and weight of surface metrology instrumentation. Use of integrated metrology is vital to improve process performance in ultra-precision manufacturing, with chromatic confocal sensing (CCS) a popular choice for single-point surface topography and thickness measurement in volume restricted applications. These applications include, but are not limited to, single-point diamond turning and roll-to-roll manufacturing where early detection of non-conformant processes leads to significant improvements in productivity and energy efficiency.

Here we demonstrate a novel fibre-linked CCS sensor approaching the size of a grain of rice (8 mm long, 3 mm diameter), with a weight of less than 0.1 g while maintaining an axial measurement range of over 150 µm. We discuss metasurface design and assembly of high tolerance two-photon polymerisation (2PP) printed parts to ensure precise positioning of a single mode fibre behind a 2.6 mm diameter metasurface substrate. We establish the relationship between returned wavelength and the location of the measurand and then present an initial 2.5D surface topography measurement of a step height sample.

Keywords: Metasurface, Optical Sensors, Metrology, Confocal

1. Introduction

A significant effort is currently underway to change the way optical metrology is deployed in manufacturing to realise the vision of 'Industry 4.0'[1,2]. Measurements are trending towards on-machine and in-situ providing rapid feedback which unlocks real-time process correction and monitoring of manufacturing processes. To achieve this there is a requirement to produce sensors in an ultra-compact form suitable to deliver in-line, in-process measurements.

Optical sensors are ideal for this task due to their ability to provide non-contact, high speed, and high-resolution measurements of surfaces, however the large size and weight of current optical components limits their deployment in some cases. While efforts have been made to reduce the size of optical instrumentation, progress is incremental[3]. Optical metasurfaces, nanostructured surfaces that allow the precise manipulation of light and are capable of replicating and combining the function of conventional optical elements without the associated size and weight, offer a solution to provide a step-change in the development of ultra-compact optical instrumentation[4].

In the following we present our work on the development of an ultra-compact chromatic confocal sensing (CCS) probe constructed from a single metasurface lens and high precision two-photon polymerisation (2PP) 3D printed probe body. This development builds upon our previous proof-of-principle work showing how we have transitioned from a table top demonstrator using large kinematic mounts[5,6], into a 8 x 3 mm probe ready for deployment for on-machine measurements. The metasurface design is described, followed by the probe design and assembly. The range of the probe is evaluated, and measurement of a step height artefact is performed to demonstrate the functionality of the sensor.

2. Metasurface design

The metasurface presented here simply functions as a lens which takes light from an on-axis point source before the metasurface and focusses it to an on-axis point after, a set distance away at the design wavelength. Changes in the wavelength, and the wavelength dependence of the phase delay that the pillars impart, mean that the light is focussed to a different point in space along the optical axis for each wavelength. The metasurface design uses the truncated

waveguide approach to control the phase delay of the incident light[7], and cylindrical nanopillars are chosen due to their polarisation insensitivity. The metasurface is constructed of gallium nitride (GaN) nanopillars etched from the surface of a 4.5 µm layer of GaN on a 430 µm thick sapphire (Al_2O_3) wafer. The nanopillars have a height of 750 nm and are arranged in a square lattice with a period of 450 nm. To achieve the required 2π phase delay needed to convert an arbitrary incoming wavefront into an arbitrary outgoing wavefront, modulo 2π, the nanopillar radii are varied from 70 nm to 180 nm in 10 nm steps, at an incident wavelength of 660 nm.

3. Probe design and assembly

Figure 1 shows the CCS probe body, manufactured using a 2-photon polymerisation printer (UpNano Nano One), which acts as a custom ferrule to precisely position a single mode fibre behind the metasurface substrate. The substrate is glued to the front of the body resulting in a probe which measures just 8 mm long and 3 mm diameter, as shown in figure 2.

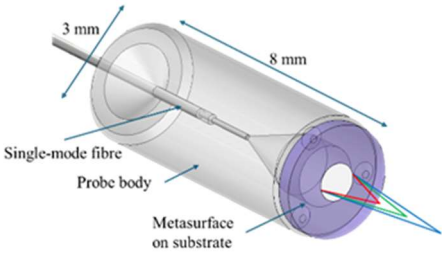

Figure 1. *Schematic showing how the fibre, probe body and substrate are located.*

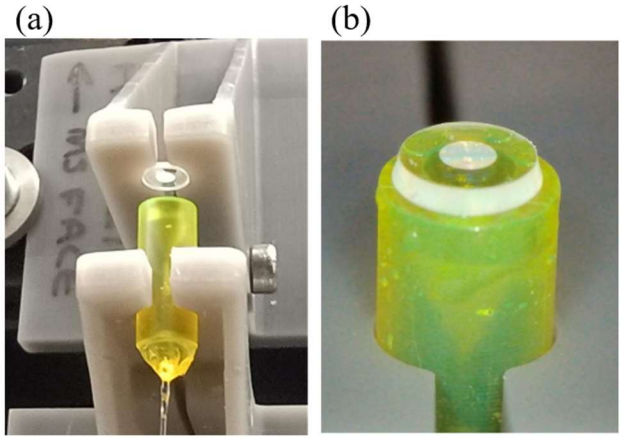

Figure 2 *(a) Left: Assembly of the metasurface probe. (b) Right: a completed probe with metasurface substrate glued to the probe body.*

5. Probe performance evaluation

To use the probe as a distance sensor, light from a broadband source is coupled to the probe with a 2x2 fibre optic coupler (FOC). The light returning from the probe then couples back though the FOC into a spectrometer.

Initial assessment of the CCS probe was carried out to determine the chromatic confocal response of the system by scanning a mirror along the optical axis and recording the measured signal over a range of 300 µm, as shown in figure 3.

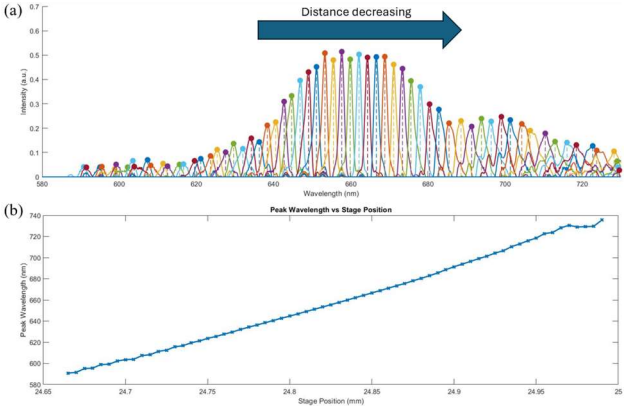

Figure 3. *(a) Intensity of the measured signal as a mirror is scanned along the optical axis. (b) Resulting measurement positions.*

A 2.5D surface topography measurement of a 30 µm step height artefact was carried out by scanning the probe with a motorised XY translation stage. The result of this surface topography measurement is shown in figure 4.

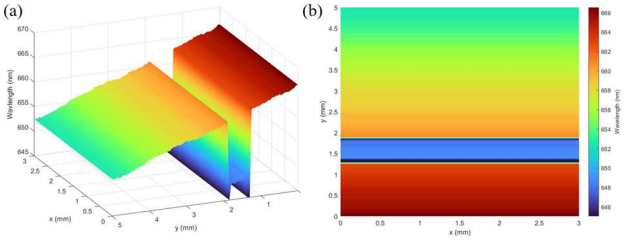

Figure 4. *A 2.5D surface topography measurement of a 30 µm step height artefact. (a) shows a 3D plot of the measurement result. (b) shows a top view.*

6. Summary and further work

We have developed an ultra-compact, robust, monolithic metasurface CCS probe suitable for deployment for on-machine measurements. We have characterised the chromatic confocal behaviour of the probe to determine its range and demonstrated 2.5D surface topography measurement of a 30 µm step height artefact.

Acknowledgements

The authors gratefully acknowledge the UK's Engineering and Physical Sciences Research Council (EPSRC) funded programmes EP/T02643X/1, EP/Z53285X/1 and EP/W017032/1 along with the UK's Royal Academy of Engineering and Renishaw PLC who sponsor Xiangqian Jiang's REng/Renishaw Research Chair.

References

[1] M. Hermann, T. Pentek, B. Otto, in *Proc. Annu. Hawaii Int. Conf. Syst. Sci.*, IEEE Computer Society, **2016**, pp. 3928–3937.

[2] A. Schütze, N. Helwig, T. Schneider, *J. Sensors Sens. Syst.* **2018**, *7*, 359.

[3] T. Santoso, W. P. Syam, S. Darukumalli, R. Leach, *Measurement* **2022**, *187*, 110311.

[4] X. Jiang, A. Henning, *Contemp. Phys.* **2021**, *62*, 199.

[5] P. Falak, J. H.-T. Chan, J. Williamson, A. Henning, T. Lee, S. Zahertar, C. Holmes, M. Beresna, H. Martin, G. Brambilla, X. Jiang, *IEEE Trans. Instrum. Meas.* **2024**, *73*, 1.

[6] J. H. T. Chan, D. Tang, J. Williamson, H. Martin, A. J. Henning, X. Jiang, *CIRP Ann.* **2023**, *72*, 465.

[7] M. Khorasaninejad, A. Y. Zhu, C. Roques-Carmes, W. T. Chen, J. Oh, I. Mishra, R. C. Devlin, F. Capasso, *Nano Lett.* **2016**, *16*, 7229.

euspen's 26th International Conference & Exhibition, Krakow, PL, June 2026
www.euspen.eu

Investigating non-uniformity of spatial resolution in X-ray computed tomography

Shiran Shan[1], Wenjuan Sun[1,2], Xiao Chen[3], Shan Lou[3]

[1]*Department of Mechanical Engineering, Celestijnenlaan 300, KU Leuven, 3001 Leuven, Belgium*
[2]*Flanders Make @KU Leuven, 3001 Leuven, Belgium*
[3]*EPSRC Future Metrology Hub, University of Huddersfield, Queensgate, Huddersfield HD1 3DH, United Kingdom*

shiran.shan@kuleuven.be

Abstract
An experimental study was conducted to evaluate how spatial resolution varies within the measurement volume of X-ray computed tomography (XCT). Because central position is typically associated with higher sampling, edge-positioned samples are expected to be more affected by lower sampling rates. Two Nitinol tubes from the same production batch were scanned simultaneously in both XCT simulation and physical scans, with one positioned at the centre of the manipulator and the other near the edge to study this spatial-resolution effect. Subsequently, modulation transfer function was applied to the reconstructed XCT cross-sectional images to evaluate the spatial resolution, enabling a direct comparison between the measurement results of spatial resolution at the centre and edge positions under matched scanning conditions. The results show that the edge-positioned sample consistently exhibits lower spatial resolution. The study highlights the non-uniformity of spatial resolution in XCT.

X-ray computed tomography, dimensional metrology, spatial resolution, modulation transfer function

1. Introduction

X-ray computed tomography (XCT) is being increasingly adopted in industrial applications, among which dimensional metrology is one of the most promising fields [1,2]. Compared with conventional tactile and optical coordinate measurement methods, XCT provides several distinct advantages, including non-destructive evaluation of internal features, full-volume measurements of workpieces, acquisition of dense volumetric data, support for dimensional quality assurance, and detailed visualization of internal and external object structures [3]. Nevertheless, differences in product position within the scan volume may cause non-uniformity in the reconstructed spatial resolution. As illustrated in Fig 1, products positioned near the centre of the sample stage tend to have more sampling during data acquisition than those located near the edge, resulting in higher spatial resolution in the central position. However, there is no study concerning the variance of spatial resolution in the measurement volume.

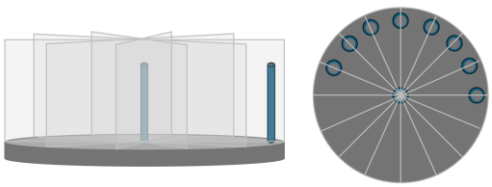

Figure 1. Scheme of the signal acquisition for samples at different location.

To systematically investigate and quantify spatial resolution inhomogeneity in X-ray computed tomography (XCT), two Nitinol tubes from the same production batch were used in this study. The tubes were scanned simultaneously, with one positioned at the centre of the sample stage and the other at the edge. Data were acquired from both simulation and physical XCT scans to enable comparison and cross-validation. The reconstructed slices were then evaluated using the modulation transfer function, allowing direct comparison of the spatial resolution differences between the centre and edge positions under matched conditions. The results show that the edge resolution of samples at the centre position is better than that of samples at the edge position. The importance of non-uniformity of spatial resolution has not been considered or evaluated in the context of XCT for dimensional metrology. By analysing the resolution of tubes at different locations, we conducted preliminary work to quantitatively evaluating the non-uniformity of spatial resolution.

2. Materials and Methods

2.1. Samples

Two high precision Nitinol (55 % nickel and 45 % titanium) tubes from the same production batch were selected as the samples for this study. The tubes have an inner diameter of 3.4 mm, an outer diameter of 4.0 mm, and a length of 50 mm, as shown in Fig 2 (left) and (middle).

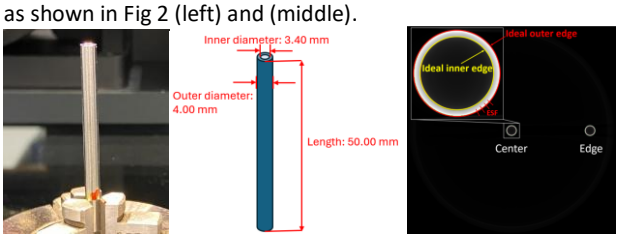

Figure 2. Sample and experimental setup. (left). A Nitinol tube. (middle). its fabrication parameters. (right). Position of tubes in simulation and physical scans. Note: ideal edges are defined by the nominal values.

2.2. Experimental Design

In both simulation and physical scans, the distance between the centres of the two tubes was approximately 30 mm. One tube was placed at the centre of the rotation, and the other was located at the edge position.

Simulation data were obtained using aRTist 2.12.6. The physical scan data were obtained from a Nikon XT H 450. Data reconstruction and analysis was performed using Feldkamp-

Davis-Kress (FDK) algorithm using Python 3.13. Slices were processed and exported using VG Studio 2025.1.

At the present stage of this research, the physical XCT scan and simulation configurations are limited to the positional arrangement of the tubes and the configurations specified in Table 1. There is also no noise and scatter considered in the simulation to evaluate the impact of space variation. The spatial resolution at the outer edge of the tubes was evaluated using the modulation transfer function (MTF).

Table 1 Configurations of XCT physical scans and simulation.

Parameters	Simulation	Physical scans
Voltage	200 kV	200 kV
Current	133 µA	133 µA
Detector size	2000 × 2000	2000 × 2000
Voxel size	40 µm	40 µm
Magnification	×5	×5
Exposure	300 ms	300 ms
Projection numbers	3142	3142

3. Results and Discussion

Fig 2(right) illustrates the slices at central height of 3D volume after reconstruction using the FDK algorithm, which shows the position of tubes in slices. The size of images was upsampled to 4000 × 4000 with linear interpolation for higher resolution. To further investigate the influence of location on resolution, the intensity profile of the tube outer edges were extracted along the normal direction, yielding the edge spread function (ESF), ESF maps were obtained for each ring along the radial direction at all angles, as shown in Fig 3(a)–(d). Taking the ideal outer-edge position as 0, the mean ESF of each ring was calculated, and its first derivative was then used to derive the mean line spread function (LSF), shown in Fig 3(e).

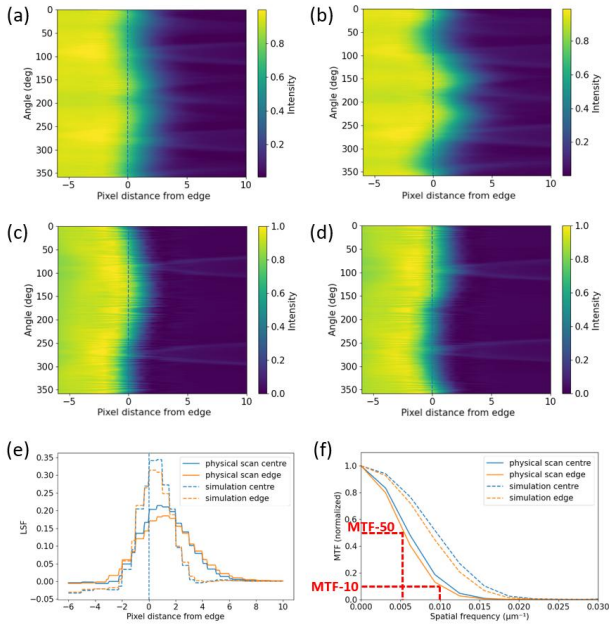

Figure 3. ESF maps of outer edge for (a) centre position in physical scan, (b) edge position in physical scan, (c) centre position in simulation, and (d) edge position in simulation. (e) Mean LSF curves. (f) Mean MTF curves.

In both the physical scanned and simulated slices, the outer edge of the tube located at the centre exhibited smaller full width at half maximum (FWHM) than that of the tube located at edge, representing a more rapid transition of intensity. This result confirms that spatial position, particularly the difference between the centre and the edge, affects sample slice quality in XCT scanning.

The mean LSF was subsequently transformed into the mean MTF through Fourier transform [4], as shown in Fig 3(f), to further evaluate differences in spatial resolution. In both the measured and simulated results, the MTF curve corresponding to the tube located near the centre shows higher spatial frequencies overall than that corresponding to the tube located near the edge. This indicates that, at the same level of contrast retention, the central tubes preserve higher spatial frequencies and are therefore capable of resolving finer structural details, indicating superior resolution. We further quantified the resolution differences between the central and edge tubes using MTF-10 and MTF-50, which represent the spatial frequencies at which the MTF falls to 10% and 50% of its zero-frequency value[5], respectively. The corresponding spatial wavelengths of MTF-10 and MTF-50 were extracted and are summarized in Table 2. Both the simulation and physical scan results showed consistently lower values at the centre than at the edges, which further confirms that image resolution is superior in the central region compared with the edges. These consistent results from both simulation and physical scans demonstrate that different position in XCT measurements leads to non-uniformity of spatial resolution, with higher spatial resolution at the centre.

Table 2 Spatial resolution characterized by MTF-10 and MTF-50.

MTF	Spatial resolution converted from MTF-10 (µm)	Spatial resolution converted from MTF-50 (µm)
simulated centre	63.7	104
simulated edge	67.3	114
physical centre	88.5	165
physical edge	97.3	183

4. Conclusion

The spatial resolution difference of tubes located at centre and edge positions within the XCT scan volume was investigated in this study. The results show that image sharpness and spatial resolution are higher at the centre position than at the edge position, indicating the non-uniformity of spatial resolution across different positions. This developed method enables the quantitative determination of spatial resolution across 3D measurement volume, providing the examination of measurement quality for XCT measurement tasks. Future work will aim to quantify the uncertainty introduced by this effect in XCT metrology and to further extend the present study.

References

[1] Kruth J P, Bartscher M, Carmignato S, et al. *CIRP Ann*, **60**/2:821-842

[2] Sun W, Symes D R, Brenner C M, et al. *Rep Prog Phys*. 2022 Feb 7;**85**(1).

[3] Dewulf W, Bosse H, Carmignato S, et al. *CIRP Ann*, Volume **71**, Issue 2, 2022

[4] Sun W, Konstantinidis A, Billas I, et al. *euspen's 16th International Conference & Exhibition* Nottingham, United Kingdom

[5] Anam C, Naufal A, Lubis A E, et al. *Physica Medica*, Volume **129**, 2025, 104876, ISSN 1120-1797.

euspen's 26th International Conference & Exhibition, Krakow, PL, June 2026
www.euspen.eu

European Metrology Network (EMN) for Advanced Manufacturing: Understanding the challenges and requirements for metrology for advanced materials

Fernando A. Castro[1*], Luca Boarino[2], Alexander Evans[3], Anita Przyklenk[4], Harald Bosse[4], Walter Knulst[5], Daniel O'Connor[1], Antti Lassila[6], Virpi Korpelainen[6] and Dishi Phillips[7]

[1] *National Physical Laboratory (NPL), Teddington, United Kingdom*
[2] *Istituto Nazionale di Ricerca Metrologica (INRIM), Torino, Italy*
[3] *Bundesanstalt für Materialforschung und -prüfung (BAM), Berlin, Germany*
[4] *Physikalisch-Technische Bundesanstalt (PTB), Braunschweig, Germany*
[5] *VSL National Metrology Institute (VSL), Delft, Netherlands*
[6] *VTT Technical Research Centre of Finland Ltd, Centre for Metrology MIKES (MIKES), Espoo, Finland*
[7] *European Society for Precision Engineering and Nanotechnology (euspen), Cranfield, UK*

**fernando.castro@npl.co.uk*

Abstract

EURAMET's European Metrology Network (EMN) for Advanced Manufacturing supported by European National Metrology Instititutes (NMI's) and Designated Institutes (DIs), along with our partners and stakeholder Council continues to advocate for the metrology community supporting the progress in advanced manufacturing. Over the past year the EMN has placed a particular focus on Advanced Materials, recognising that innovation in this area is progressing faster than the availability of robust, standardised measurement and evaluation methods. This gap affects confidence, scale-up, investment and global trade. To address this, the EMN organised two large stakeholder workshops on Metrology for Advanced Materials to better understand future needs. This paper summarises key findings, and highlights developments of the EMN for Advanced Manufacturing.

Metrology, Advanced Manufacturing, Advanced Materials, European Metrology Network, open consultation

1. European Metrology Network for Advanced Manufacturing

The EMN for Advanced Manufacturing coordinates European metrology efforts on advanced manufacturing and advanced materials. Building on the Strategic Research Agenda (SRA) [1], the EMN has focused this year on advanced materials, an area where stakeholders consistently cite the need for reliable, comparable and traceable metrics, and one of the eight Cross-cutting Topics of the EMN (Fig. 1). This article reviews the progress made in understanding the challenges faced by stakeholders and the gaps in European capabilities, which aim to be addressed through future research topics.

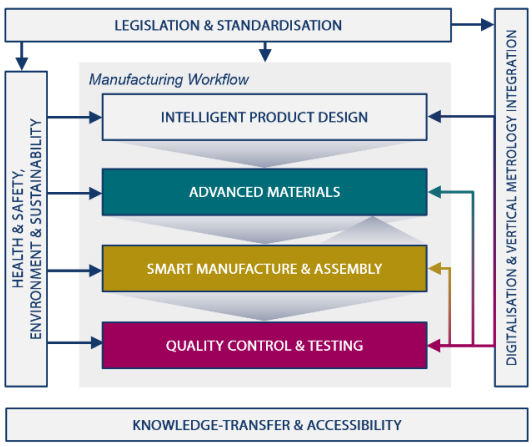

Figure 1. Cross-Cutting Topics of the EMN and their interrelationships. The three highlighted topics correspond to the EMN sections [1].

2. Annual General Meeting of the EMN

The annual general meeting of the EMN was held in hybrid mode and hosted at GUM, Kielce, Poland on 15th October 2025, including open and closed sessions.

2.1. Open stakeholder meeting

The open session, with over 40 participants, emphasised the need for integrated metrology approaches across emerging digital and manufacturing technologies, covering the following:

- Digitalisation in dimensional metrology
- Digital metrological twins in advanced manufacture
- Metrology for Industry 5.0
- European perspective on advanced manufacturing

2.2. Nanometrology for emerging national metrology institutes

An associated workshop addressed nanometrology capacity-building for emerging NMIs, covering:

- Introduction to nanometrology
- Metrology needs of stakeholders
- Towards traceable surface texture measurements using optical microscopes – EURAMET project 1242 and EMPIR TracOptic
- Nanoscopic technologies for nanometrology
- Perspectives from multiple European NMIs
- Traceability challenges in emerging NMIs

The outcome of the event was improved cooperation and support of European NMIs on the topic of Nanometrology.

3. Stakeholder consultation: Metrology for Advanced Materials

The EMN held two large stakeholder workshops in 2025 [2] with more than 300 participants to identify needs and priorities to support the Advanced Materials sector. The consultations covered Critical Materials, and Advanced Materials for Clean Energy, for Future Electronics, and for a Digital World.

Figure 2. One of the large stakeholder workshops organised by the EMN in 2025 (follow the QR code for further information)

The events included keynote contributions from the European Commission, IAM4EU, EURAMET, the EMN as well as from EU industry and leading academics to set the scene by highlighting the importance of advanced materials in the European commission strategy and how metrology is a key enabler for the advanced materials.

Open discussion sessions highlighted the need for reliable, comparable and traceable metrics for novel advanced materials and for accelerating the metrology standardisation process. The event reinforced that metrology is essential for confidence in novel advanced materials—from research to industrialisation—and that Europe needs faster development of standardised, traceable measurement methods.

3.1. Advanced Materials for Clean Energy

Focusing on photovoltaics, batteries and hydrogen technologies, the session highlighted:

- The need for reliable and comparable metrics
- Importance of operando and dynamic measurements
- Need for reproducibility and harmonised testing
- Need for benchmarks and traceability

3.2. Advanced Materials for Future Electronics

Focusing on complexity and scaling of semiconductor manufacturing, the session highlighted:

- Integration of multiple measurement techniques
- Introduction of new and complex materials
- Contamination analysis in semicond. manufacturing
- Scaling limits, especially for 2D and ultrathin layers
- Need to anticipate metrology requirements early to avoid industrialisation delays

3.3. Advanced Materials for a Digital World

Focusing on the requirements for Integrated Computational Materials Engineering (ICME) and Material Digitalization, the session highlighted:

- Data management based on FAIR principles
- Standardised uncertainty handling
- Material benchmarks for model validation
- AI and Machine Learling to fill data gaps
- Metrology to feed ICME and digital-twin dataflows

3.4. Critical Materials

Focused on emerging measurement and standardisation needs for Critical Materials, the event covered applications areas ranging from materials and composites to semiconductor and hydrogen technologies and explored how metrology supports innovation, circularity and resilience. The session highlighted:

- Substitution and recycling strategies
- Need for harmonised standards and digital traceability
- Challenges in reuse and end-of-life recovery

Breakout discussion sessions helped to identify and prioritise:

- Emerging measurement challenges (e.g. impurities, in-line metrology, data traceability)
- Areas for joint research (e.g. harmonised standards, lifecycle analysis, recycling protocols)
- Standardisation needs (e.g. reference materials, digital passports, design-for-recycling)

3.5. Outlook and perspective

Participants emphasised the need for early alignment of metrology with R&D roadmaps, ensuring measurement infrastructure keeps pace with materials innovation.

4. EU projects on metrology for advanced manufacturing

Running and recently completed research projects related to metrology for Advanced Manufacturing and Advanced Materials, funded by the European Partnership for Metrology can be found here [4], including:

- Traceability for industrial 3D digitalisation by advanced scanning systems – ScanClouDT
- Traceable machine vision systems for digital industrial application – DI-Vision
- Application of Digital Metrological Twins for emerging measurement technology in advanced manufacturing – ADAM
- Memristive devices as quantum standard for nanometrology – MEMQuD
- Standardised measurements of surface functionalities on nanoparticles – SMURFnano [3]

5. Conclusions

This article aimed to review the recent activities of the EMN for Advanced Manufacturing, in particular on the topic of Metrology for Advanced Materials.

Ongoing European Partnership on Metrology projects are already addressing key advanced-materials challenges, particularly the need for reliable, comparable and traceable metrics and accelerated standardisation.

Gaps identified in the SRA for Metrology for Advanced Manufacturing are being reassessed following the open consultation, and these insights will inform future updates.

References

[1]https://www.euramet.org/european-metrology-networks/advanced-manufacturing/strategy/strategic-research-agenda
[2]https://www.euramet.org/european-metrology-networks/advanced-manufacturing/events
[3]https://www.euramet.org/european-metrology-networks/advanced-manufacturing/research/projects/details/project/standardised-measurements-of-surface-functionalities-on-nanoparticles.
[4]https://www.euramet.org/european-metrology-networks/advanced-manufacturing/research/projects

Session 2: Measuring Instruments & Machine Tools: Design and Performance

euspen's 26th International Conference & Exhibition, Krakow, PL, June 2026
www.euspen.eu

Aerostatic journal bearing as a capacitive sensor for in-situ radial rotor position measurement

Petteri Haverinen[1], Mikael Miettinen[1], Raine Viitala[1]

[1]*Aalto University*

Petteri.haverinen@aalto.fi

Abstract
Aerostatic journal bearings are low friction bearings, like plain bearings or bushings, which have a high-pressure gas film between a shaft and the bearing. In cases, where the restrictor of the bearing is electrically conductive material, such as porous graphite, it is possible to measure the average thickness of the air film using capacitive sensing. To measure runout and angular velocity of the shaft, the bearing can be split into multiple sections, where the thickness of the air film is measured between each of the sections and the shaft.
Previous methods have utilized external sensors in conjunction with journal bearings to characterize the parameters of the bearing, such as runout. However, little work has been done to utilize the bearing as a sensor.
In the present study, a porous journal bearing with four electrically insulated rigid bearing pads was developed and characterized. The bearing used graphite restrictors, which were also used as electrodes for the capacitive displacement sensor. Adjacent external capacitive sensors were used to verify the accuracy of the proposed method. A rigid rotor supported by the investigated bearing was rotated with an unbalanced mass mounted to the rotor to induce runout. The shaft position was measured with the integrated sensors and adjacent external reference sensors. Results show that the accuracy of the proposed method is 326 nm, highlighting the feasibility of integrated capacitive sensing in aerostatic bearing systems.

Gas bearings, Journal bearings, capacitive sensing, runout

1. Introduction

Porous aerostatic bearings are externally pressurized cylindrical bearings, sharing similarities with plain bearings [1]. However, instead of an oil film, the pressurized gas produces a thin air gap between the rotating shaft and the bearing. This gap allows for low-friction motion, ideal for high speed or high accuracy applications [2].

One of such use cases is in high-speed precision spindles, where the rotating toolholder is supported by a journal bearing in conjunction with two thrust bearings, forming an H-spindle. As the tool contacts the workpiece, the spindle experiences load which may induce motion to the spindle itself [3]. Furthermore, the spindle shaft tolerances in cylindricity and roundness has been observed to cause unbalanced force produced by the air gap causing instability in the spindle [4].

To monitor and account in real time for the radial motion of the shaft, a measurement system is required to measure the shaft position in real time. Previous works have utilized external sensors to measure the spindle motion [4, 5]. However, previous developments in utilizing aerostatic bearings as sensors [6] have pointed to developing a journal bearing, which can measure the air gap thickness at sections to measure the shaft position.

The present work investigates a novel aerostatic journal bearing with split restrictor to measure the air gap and the shaft position. A journal bearing with a sensor functionality was developed in conjunction with measurement electronics and the performance was experimentally validated with unbalanced mass to induce runout in the bearing.

2. Methods

The present work developed a porous journal bearing with a split restrictor. The radial position of the shaft was measured with the electrodes using capacitive sensing. The measurement electronics were developed and verified against reference sensors.

The shaft was rotated at different angular velocities and with an eccentric shaft. The radial position of the shaft was measured with the bearing and reference sensors. The output of the developed sensor was fitted with the data from the reference sensors.

2.1. Investigated bearing

The bearing was constructed in two halves with alignment pins and bolt connection. This allowed for the aerostatic pads to be adhered to the body and turned into the final geometry at a later stage. The bearing body was manufactured from hard-anodized aluminium to prevent electrical contact from the bearing pads to the body. The journal bearing pads were manufactured from porous graphite and adhered to the bearing body with epoxy. After the epoxy had cured, the bearing was mounted on a lathe, and the inside was bored to 39.995 mm and lapped with a 40 mm hydraulic cylinder rod for final tolerance.

Each bearing pad had an electrical feedthrough and a port for pressure supply. The electrical feedthroughs consisted of a nylon bolt with a 1 mm hole to accommodate a 1 mm tig welding rod, which was fixed in place with cyanoacrylate adhesive.

The bearing consumed air at 4 l/min at 0.4 MPa operating pressure with the shaft installed. The short circuit flow of the bearing was 6.4 l/min.

The main dimensions and construction of the bearing are presented in figure 1.

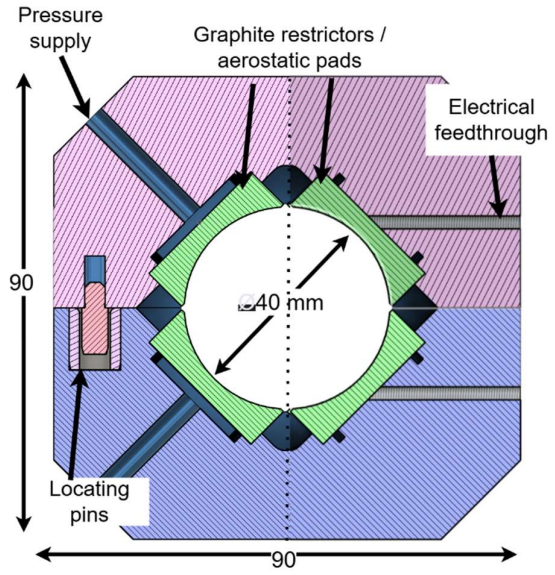

Figure 1. Diagram of the investigated bearing. Each corner had a pressure supply port with M5 thread. The picture is a section from front with two section depths at the dotted line. The locating pins were mounted to ensure alignment with one side having a cylinder pin and the other a diamond shaped pin. The electrical feedthroughs were 2.5 mm in diameter piercing to the graphite off to the side from the pressure supply.

2.2. Measurement electronics

For the electrodes to measure the position of the shaft, measurement electronics are required. While multiple methods to measure capacitance exist [7], the present work utilized a capacitance-to-voltage converter circuit.

Each electrode had a capacitance in respect to measurement ground through the rotating shaft due to the air gap [8]. As the air gap decreases, the capacitance of the adjacent electrode increases. The change in capacitance was measured by measuring current through the capacitor. A sine wave excitation signal with 10 MHz frequency and 10 V amplitude was supplied to each electrode through a resistor. The voltage drop over the capacitor was rectified with a diode and a low-pass filter set to 16 kHz. The potential difference over opposing capacitors (electrodes) was amplified with a difference amplifier. The position in each axis was therefore represented by the output voltage of the amplifier ranging from -5 to +5 V in respect to the measurement ground. The circuit diagram is presented in figure 2.

The circuit response in relation to the distance is linear. Assuming, that the time constant is large, the voltage drop over opposing capacitors (Figure 2. C1 & C2, C3 & C4) can be approximated as:

$$U_c \approx \frac{U_s}{j\omega RC}$$

Where U_s is the amplitude of the excitation signal, R is the resistor in series with the capacitor and ω is angular velocity of the excitation signal. The output in the circuit is the difference between the voltage drops over the opposing capacitors as:

$$U_{out} = U_{C1} - U_{C2}$$

The capacitances are inversely proportional to each other. As the distance between the shaft and the electrode of C1 decreases its capacitance increases, while simultaneously the distance between the shaft and electrode of C2 increases, its capacitance decreases. This relationship can be expressed as:

$$d_{C1} = d_0 - \Delta d$$
$$d_{C2} = d_0 + \Delta d$$

The capacitance relating to the distances is:

$$C = \varepsilon_0 \varepsilon_r \frac{A}{d}$$

Where d is the distance d_{C1}or d_{C2}, A is the surface area of the electrode, ε_0 is the permittivity of free space and ε_r is the relative permittivity of air, which is approximately 1 [9].

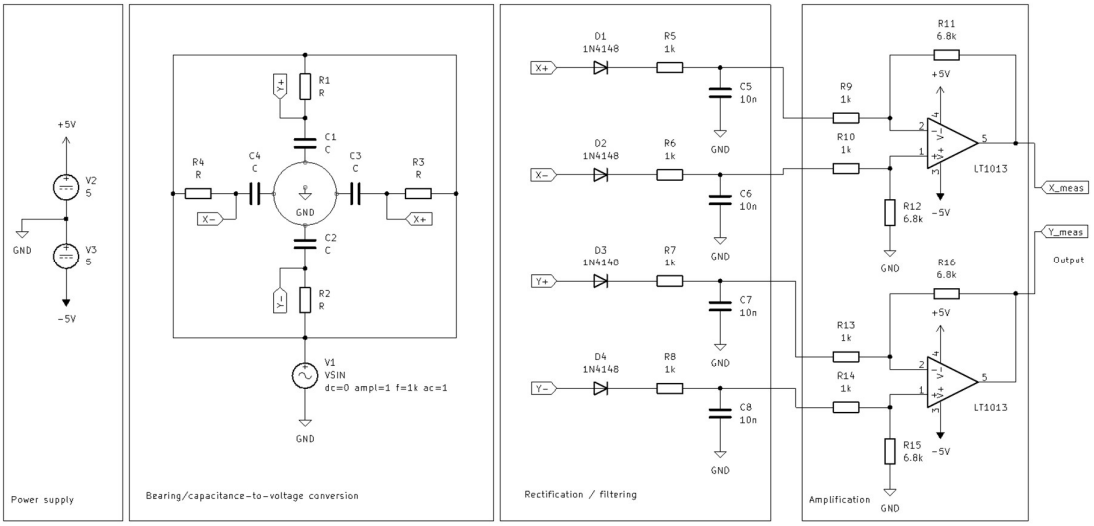

Figure 2. Schematic of the measurement circuit. The capacitance formed between the air gap and each electrode was converted to voltage using an RC circuit with a sinusoidal excitation at 10 MHz and 10 V peak-to-peak amplitude. The voltage drop across each capacitor was rectified and filtered with a low pass filter. The voltage output (X_meas & Y_meas) was the difference across the opposing capacitors amplified by gain of 3.3.

By combining these equations, the response of the circuit before the amplifier is:

$$U_{out} = \frac{2U_s \Delta d}{\omega R \varepsilon_0 \varepsilon_r A}$$

From the equation, it is evident that the output increases linearly to the change in distance:

$$U_{out} \propto \Delta d$$

2.3. Experiments

The bearing was mounted on a testbench with a 40 mm diameter shaft. The shaft was loaded against a sphere on one end with a magnetic preload on the opposing end. The spherical contact allowed for electrical grounding the shaft while keeping the contact friction relatively low. The bearing was pressurized at 0.4 MPa. External reference sensors were used at 45 degrees from the bearing electrodes to calibrate the integrated sensor and to verify the results.

The shaft was rotated with pressurized air, and its radial position was measured with the external reference sensor in conjunction with the output voltage from the measurement circuit. The experiment was repeated with an unbalanced mass produced by attaching magnets to the shaft. The mass of each magnet was 30 grams. The radius of the masses was 14 mm, producing an unbalance of $U = 840g \cdot mm$.

To measure the output of the reference sensors and the voltage form the measurement circuit, a NI-USB6001 was used. Each measurement lasted 20 seconds at 10 ks/s sampling rate. The test setup is presented in figure 3.

Due to the axial offset between the reference sensors and the geometric deviations in the shaft, only the low frequency components relating to the mean displacement of the shaft were analysed from the measurement data. The measured data was passed through at a 20 Hz low pass filter.

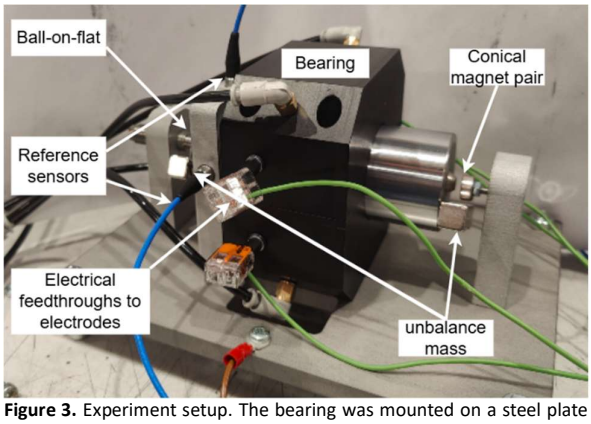

Figure 3. Experiment setup. The bearing was mounted on a steel plate with bolts, supported by a spherical ball-on-flat contact on one end and by opposing conical magnets on one end. The unbalance masses were mounted on same radial location on opposing ends of the shaft.

3. Results and Discussion

The shaft had an average rotational speed of 1165 RPM. The rotational speed varied since the shaft was accelerated by compressed air. The rotational speed was derived from the output of the reference sensor signal. The rotational speed measurement is presented in figure 4. The results are presented in the window of 8-10 second, where the rotational speed had lowest amount of variation.

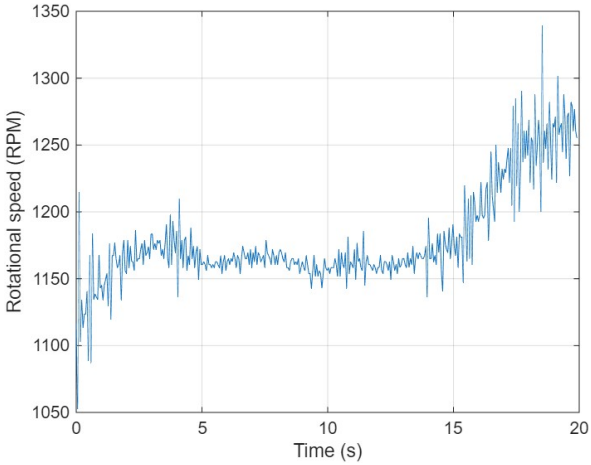

Figure 4. Rotational speed of the shaft. The variation in the rotational speed was a result of using compressed air to accelerate the shaft.

The sensor output was linear in respect to the displacement measured by the reference sensors. The phase of the reference sensor signal was rotated to match the phase of the measurement electronics signal, since the reference sensors were offset by 45 degrees. The sensor output in respect to the reference sensor and the used fit for scaling the output are presented in figure 5.

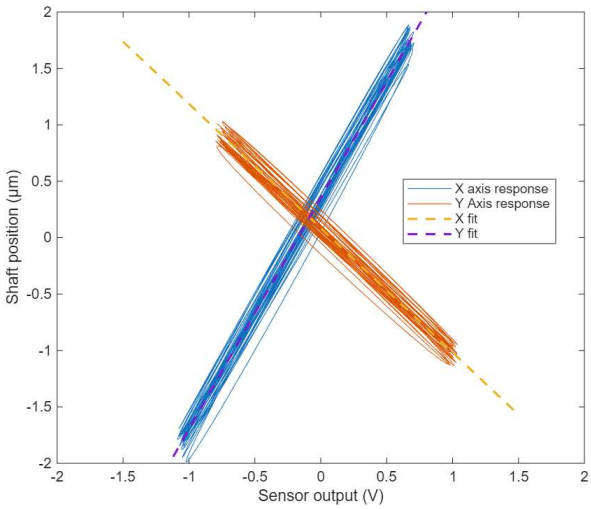

Figure 5. Output of the measurement electronics vs the shaft position measured by the reference sensors. Blue is the X axis output, red is the Y axis, yellow dotted line is the X axis fit and purple is the Y axis fit. The fitted lines were:
$f_x(U_x) = -1.102\ U_x + 0.084$ and $f_y(U_y) = 2.051\ U_y + 0.355$

The trajectory of the shaft during the measurement is presented in figure 6, where A) presents the trajectory as seen by the measurement electronics, B) presents the measurement electronics output scaled to micrometres with the reference measurements overlayed on top.

The sensor output varied from -1.087 V to 0.707 V on Y axis and from -0.797 V to 1.037 V on X axis. The maximum deviation on Y axis after fitting the sensor data to the reference sensor data was 326 nm and on X axis 229 nm, corresponding to 8.4% and 10.6% relative error.

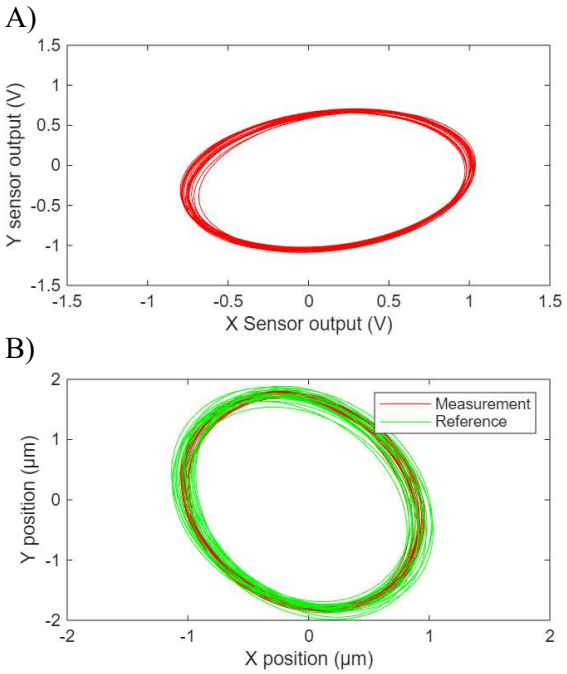

Figure 6. A) Orbit as a voltage from the measurement electronics, B) orbit from the reference sensor and the developed sensor. The shaft had a displacement of 2.167 µm on X axis and 3.873 µm on Y axis.

The reference sensor measurement had more variation, than the developed sensor. A major factor impacting the result is that the reference sensor does not measure directly from inside of the bearing. The sensors were mounted 10 mm away from the bearing, thus being further away from the support. Moreover, future work will incorporate the measurement electronics in a shielded enclosure to reduce the effect of electromagnetic noise on the measurements.

While the present work acts a as a solid proof-of-concept, the accuracy reported is not suitable for high precision spindles. The measurement accuracy must be in nanometre scale as the error motion in these spindles can be in tens of nanometres [10].

Future work must address the higher frequency components on the measured signal. The present work provides a solid foundation for calibrating and characterising a porous aerostatic journal bearing with capacitive displacement sensor capability but has yet to address the dynamic range due to low-pass filtering used. The high frequency components due to surface geometry remains unvalidated and must be further researched.

5. Conclusions

The present work developed and experimentally investigated a novel porous aerostatic journal bearing acting as a capacitive displacement sensor for shaft radial position measurement. The shaft was unbalanced with an unbalance of $U = 840g \cdot mm$ and rotated at 1165 RPM. The resulting orbit was measured with external capacitive reference sensors and with the bearing using developed measurement electronics.

The sensor had a maximum deviation of 326 nm on Y axis, which was 8.4% relative error and 229 nm deviation on the X axis with 10.6% relative error respectively.

References

[1] Farid Al-Bender. Air bearings : theory, design and applications. Hoboken, Nj, Usa: Wiley; 2020.

[2] Gao Q, Chen W, Lu L, Huo D, Cheng K. Aerostatic bearings design and analysis with the application to precision engineering: State-of-the-art and future perspectives. Tribology International [Internet]. 2019 Jul 1 [cited 2023 Mar 30];135:1–17. Available from: https://www.sciencedirect.com/science/article/pii/S0301679X19300830

[3] Kim JH, Chang HK, Han DC, Jang DY, Oh SI. Cutting Force Estimation by Measuring Spindle Displacement in Milling Process. CIRP Annals. 2005;54(1):67–70.

[4] Zhang, Guoqing, et al. "Rotation Accuracy Analysis of Aerostatic Spindle Considering Shaft's Roundness and Cylindricity." Applied Sciences, vol. 11, no. 17, 27 Aug. 2021, p. 7912, https://doi.org/10.3390/app11177912. Accessed 19 Feb. 2023.

[5] Miao H, Li C, Wang C, Xu M, Zhang Y. The vibration analysis of the CNC vertical milling machine spindle system considering nonlinear and nonsmooth bearing restoring force. Mechanical Systems and Signal Processing. 2021 Dec;161:107970.

[6] Haverinen P, Miettinen M, Viitala R. Porous aerostatic bearing with integrated air gap height measurement. Measurement [Internet]. 2025 Jun 27;256:118128. Available from: https://www.sciencedirect.com/science/article/pii/S0263224125014873#b1

[7] Kanoun O, Kallel AY, Fendri A. Measurement Methods for Capacitances in the Range of 1 pF–1 nF: A review. Measurement. 2022 May;195:111067.

[8] Haverinen P, Miettinen M, Harding L, Vainio V, Leutonen O, Theska R, et al. Integrated capacitive measurement of air gap height in aerostatic bearings [Internet]. 2024 [cited 2026 Feb 2]. Available from: https://www.euspen.eu/knowledge-base/ICE24211.pdf

[9] Hector LG, Schultz HL. The Dielectric Constant of Air at Radiofrequencies. Physics. 1936 Apr;7(4):133–6.

[10] Knapp B, Arneson D. Dynamic Characterization of a Micro-machining Spindle. Wiscedu [Internet]. 2026 [cited 2026 Feb 2]; Available from: http://digital.library.wisc.edu/1793/68586

euspen's 26th International Conference & Exhibition, Krakow, PL, June 2026
www.euspen.eu

Error propagation in two-axis feed drives using physical error injection and multibody simulation

Pu Sun[1, 2], Tim Wendel[1], Andreas Archenti[1]

[1]*Department of Production Engineering, KTH Royal Institute of Technology, Brinellvägen 68, 11428 Stockholm, Sweden*
[2]*AstraZeneca Sweden Operations, Storgatan 51, 15136 Södertälje, Sweden*

pus@kth.se

Abstract
Linear and rotational motions in machine tools are generated by feed-drive systems, which are critical subsystems of precision machinery. Small geometric errors within these systems can propagate through the structural loop and result in table-positioning deviations. This study investigates error propagation in a redundantly constrained, dual-rail feed drive system integrated in a testbed. Controlled guideway rail deformation was introduced via pusher bolts, and linear positioning tests were performed using laser interferometer. A physics-based multibody simulation model was used to replicate the same positioning tests and evaluate the positioning deviation induced by the injected guideway straightness error. The results demonstrate that the simulation replicates the spatial characteristics of the guideway straightness error and its corresponding scaling effect on positioning accuracy, validating the physics-based mapping between rail deformation and table displacement. The observed deviation profile confirms that localized guideway geometry directly influences the structural-loop response in overconstrained configurations. Thus, this study establishes a validated multibody modelling approach for analyzing geometric error propagation in overconstrained feed-drive systems.

Feed-drive system, Geometric error propagation, Multibody simulation, Validation, Accuracy

1. Introduction

Linear feed drive systems in machine tools convert rotary motor motion into translational table movement and directly determine positioning accuracy [1,2]. The motion transmission path comprises the motor, ball screw-nut assembly, carriage supported table and linear guideways, which together define the structural loop of the axis. The axial and torsional stiffness of these elements determine the static deformation of the loop under load and influence positioning performance [3]. Beyond elastic deformation, linear axes exhibit geometric component errors, including positioning, straightness and angular deviations, which propagate through the machine kinematic chain and affect overall volumetric positioning accuracy [4].

While geometric errors of linear axes can be characterized individually [5], their propagation depends on the guideway constraint topology. In dual-rail configurations employing multiple carriages, the guideway assembly becomes overconstrained. Small geometric inconsistencies between parallel rails can induce internal load redistribution among carriages, altering the effective stiffness distribution of the structural loop and introducing nonlinear sensitivity to localized rail straightness error.

Despite extensive stiffness and dynamic modelling of feed drive systems [3], experimental validation of geometric error propagation in overconstrained guideway configurations remains limited. In particular, the capability of physics-based simulation to reproduce positioning deviations induced by controlled geometric error injection has not been systematically assessed. This study addresses this gap by introducing controlled rail deformation into a dual-rail feed drive testbed and evaluating a multibody simulation model against interferometric measurements.

2. Methodology

2.1. Multibody model of the feed-drive testbed

The physical two-axis feed-drive testbed and its corresponding virtual model are shown in Figure 1. The model was implemented in MATLAB®/Simulink® R2024b using Simscape™ Multibody toolbox, with the top-level modeling architecture illustrated in Figure 2. The modeling implementation follows the detailed formulation reported in [6].

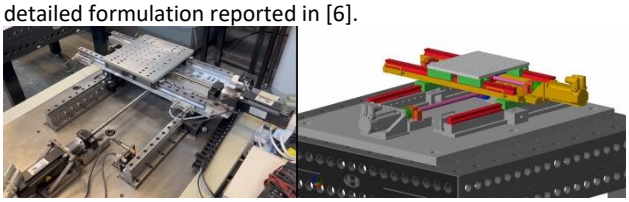

Figure 1. Physical two-axis feed-drive testbed in a stacked-axis configuration (left) and its corresponding virtual model (right).

The model represents the structural loop of the testbed from motor torque input to translational displacement at the center reference point. The structure comprises an X-axis stage and a stacked Y-axis stage, each featuring dual linear guides and a screw-nut transmission. Guideway geometry is represented by a spline-based profile, allowing rail deformation to be introduced as a geometric disturbance input. Shaft rotation is converted into linear displacement through a lead screw joint in parallel with linear guides, reflecting the overconstrained configuration.

Friction at the carriage-rail interface is modelled using externally applied Coulomb and viscous components based on carriage velocity. The mechanical model is coupled with cascaded P-PI control loops to generate torque inputs. In the X axis stage block, rails are fixed to the base using weld joints, and carriage-to-plate connections are represented by 6-DoF joints to allow limited compliance under rail deformation.

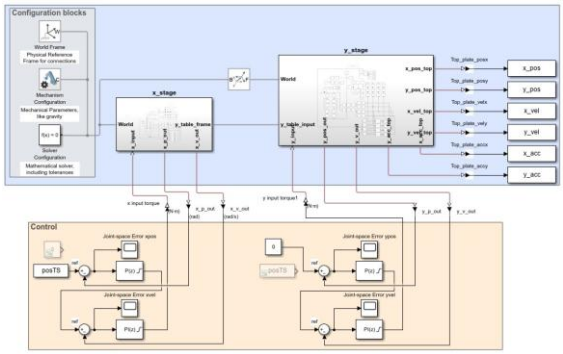

Figure 2. Top-level architecture of the two-axis feed-drive testbed model implemented in MATLAB®/Simulink® R2024b using Simscape™ Multibody toolbox.

2.2. Error injection and validation procedure

Controlled rail deformation was introduced via pusher bolts tightened to defined torque levels (Figure 3), generating vertical rail displacement in the physical testbed. The measured deformation profile was reconstructed as a continuous rail curve and implemented in the simulation by modifying the spline used in the point-on-curve constraints, enabling direct injection into the structural loop without altering other model parameters.

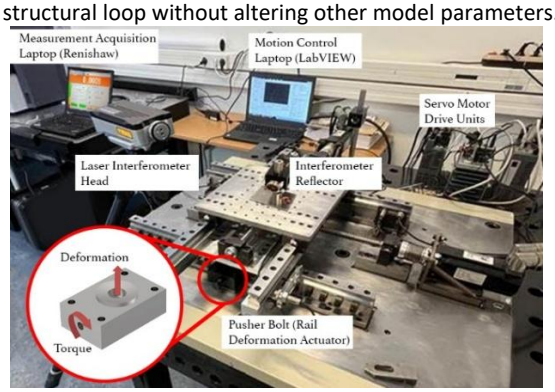

Figure 3. Experimental setup for interferometric linear positioning measurement with controlled rail deformation.

Linear positioning tests were conducted along the X axis from 30 mm to 240 mm and back in 30 mm increments. At each target position, stationary samples were extracted to eliminate dynamic transients. A laser interferometer reflector was mounted at the center of the moving table, corresponding to the defined measurement reference point.

Positioning deviation was calculated as the difference between the stationary displacement and the commanded reference position issued by motion controller to the servo drives. Simulation results were compared with interferometer measurements along the stationary line at $y = 0$ mm.

3. Results

Linear positioning tests were performed under undeformed and two controlled deformation levels (τ = 10 Nm，15 Nm). Under the undeformed condition, physical measurements exhibited a systematic position-dependent deviation (Figure 4(a)), while the simulation predicted negligible deviation under ideal alignment (Figure 4(b)).

With deformation applied, measurements followed the baseline trend but increased in magnitude, scaling with the torque level. By defining the deformation-induced deviation as the difference between deformed and undeformed conditions, both experiment and simulation revealed a localized mid-travel feature. The spatial profile of this feature reflected the injected guideway straightness error, and its magnitude scaled consistently with the applied deformation level.

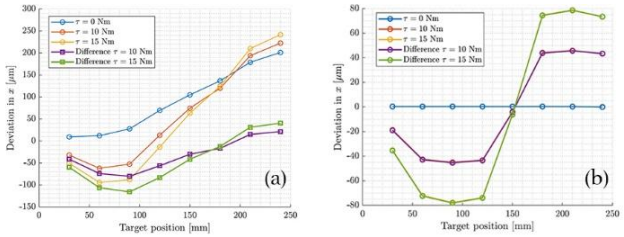

Figure 4. Positioning deviation along the x-axis under controlled rail deformation: (a) interferometer measurements, (b) simulation. Curves show undeformed (τ = 0), deformed (τ = 10 Nm, τ = 15 Nm), and deformation-induced deviation (deformed − undeformed).

The simulation captures the spatial characteristics and scaling of the deformation-induced deviation. Quantitative agreement is assessed via Mean Absolute Error (MAE) and Root Mean Square Error (RMSE) (Table 1), reflecting average residuals and sensitivity to larger deviations, respectively. The slight decrease in agreement at higher deformation may reflect increased sensitivity to unmodeled carriage–rail contact and assembly effects.

Table 1 Simulated MAE and RMSE metrics for deformation-induced positioning deviation.

Deformation torque τ (Nm)	MAE (μm)	RMSE (μm)
10	9.9	13.1
15	15.9	22.1

4. Discussion and Conclusions

The experimental results indicate that localized guideway deformation is a dominant contributor to the positioning deviation at the structural-loop output. A mid-travel deviation feature was observed near the location of maximum rail deformation point, consistent with error propagation through the overconstrained structural loop. With the measured rail deformation profile as input, the multibody model predicts the positioning-deviation profile and its scaling with deformation level, supporting its use for error-propagation analysis in such systems.

Future work will incorporate experimentally identified assembly parameters and improve carriage-rail contact compliance to enhance accuracy. The approach will further be extended to synchronized X–Y axis motion to analyze error propagation and positioning deviation under coupled multi-axis operation, accompanied by a comprehensive uncertainty budget.

References

[1] Vogl G W, Donmez M A and Archenti A 2016 Diagnostics for geometric performance of machine tool linear axes *CIRP Ann. - Manuf. Technol.* **65** 377-80

[2] Szipka K, Archenti A, Vogl G W and Donmez M A 2019 Identification of machine tool squareness errors via inertial measurements *CIRP Ann. - Manuf. Technol.* **68** 547-50

[3] Altintas Y, Verl A, Brecher C, Uriarte L and Pritschow G 2011 Machine tool feed drives *CIRP Ann. - Manuf. Technol.* **60** 779–796

[4] Schwenke H, Knapp W, Haitjema H, Weckenmann A, Schmitt R and Delbressine F L M 2008 Geometric error measurement and compensation of machines: an update *CIRP Ann. - Manuf. Technol.* **57** 660–675

[5] Xing K, Achiche S, Esmaeili S and Mayer J R R 2018 Comparison of direct and indirect methods for five-axis machine tools geometric error measurement *Procedia CIRP* **78** 231–236

[6] Wendel T A M 2025 Modeling and Experimental Validation of a Two-Axis Feed Drive Testbed for Precision Motion Systems Internship Report DC 2025.072, Department of Mechanical Engineering, Eindhoven University of Technology

euspen's 26th International Conference & Exhibition, Krakow, PL, June 2026
www.euspen.eu

Telecentric Under-Surface Imaging System for In-situ Observation of Polishing Pad–Glass Contact

Adam Wilczek[1], Nico Zettler[1], Prof. Dr. Rainer Börret[1]

[1]*Aalen University, Center for Optical Technologies (ZOT), Beethovenstr. 1, 73430 Aalen, Germany*

adam.wilczek@hs-aalen.de

Abstract
In computer-controlled optical polishing, direct observation of pad–surface contact is hindered by slurry, refractive interfaces, and motion. We present a telecentric under-surface imaging system that records pad–glass contact through the workpiece during force-controlled polishing of N-BK7 (10 N, ~830 rpm). A 5 MP camera with a telecentric objective acquires images at ~12 fps while a coaxial LED module provides uniform illumination. We report quantitative characterization of the imaging system: spatial resolution of approximately 50 µm (sufficient to resolve individual pad pores), illumination uniformity within ±5 % across the aperture, motion blur of ~180 µm at 350 µs exposure, and frame-to-frame intensity variation below 1.1 %. The pulsed illumination mode enables short exposures despite surface speeds exceeding 0.5 m/s. In-situ imaging reveals the heterogeneous contact distribution created by the porous pad microstructure and captures previously undocumented phenomena including progressive contact intensity changes and slurry sedimentation patterns. Comparison of accumulated contact maps with white-light interferometry measurements confirms qualitative correspondence with material removal profiles.

telecentric imaging, in-situ metrology, illumination uniformity, high-speed vision, optical polishing instrumentation

1. Introduction

Computer-controlled optical polishing relies on precise control of the pad–workpiece interaction to achieve deterministic material removal [1]. According to the Preston equation, removal rate depends on contact pressure and relative velocity [2]. Finite element simulations have been employed to model elastic pad deformation and predict material removal based on calculated pressure distributions [3], and dwell time algorithms optimize tool paths to correct surface figure errors through controlled local removal [4]. However, these models typically assume a time-invariant, spatially uniform tool influence function (TIF) derived from Gaussian or Hertzian contact mechanics.

Recent work has shown that the TIF during sub-aperture polishing is influenced by numerous factors including pad porosity, slurry transport, and spatially varying friction coefficients [5]. Comprehensive reviews of dwell time optimization highlight that TIF stability remains a key challenge for achieving sub-nanometer surface accuracy [6]. While analytical TIF models have been developed for curved surfaces [7] and microscale contact mechanics have been studied for porous pads [8], experimental validation of the actual contact distribution, particularly the heterogeneous contact created by porous pad microstructures, remains limited.

Various in-situ monitoring approaches have been developed for chemical mechanical polishing (CMP). Evanescent-wave microscopy enables nanoscale observation of slurry particle behavior near the contact interface [9], while dual-emission laser-induced fluorescence (DELIF) provides high-resolution maps of slurry film thickness beneath transparent substrates [10]. Interferometric methods have been applied for in-situ pad surface characterization [11], and sensor-based approaches using accelerometers or force transducers monitor process stability [12]. However, these techniques either require specialized optical setups incompatible with rotating tools, operate at microscopic scales unsuitable for full-pad observation, or provide indirect measurements rather than direct contact imaging.

For sub-aperture polishing with small rotating pads, direct imaging of the pad–glass contact presents specific challenges: the imaging system must capture the entire pad area (~12 mm diameter) at sufficient resolution to resolve pore structures (~50–200 µm), maintain sharp images despite surface speeds exceeding 0.5 m/s, and provide uniform illumination without introducing reflections from the slurry-filled interface.

In this work, we present the design and characterization of a telecentric under-surface imaging system for in-situ observation of pad–glass contact during optical polishing. The system employs a telecentric objective with coaxial illumination to image through transparent N-BK7 substrates at approximately

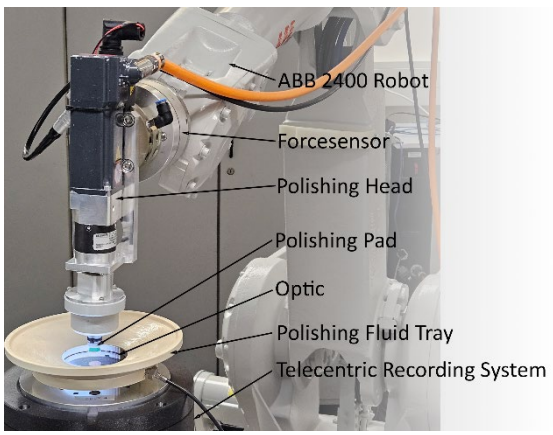

Figure 1. Experimental setup showing all components of the polishing system.

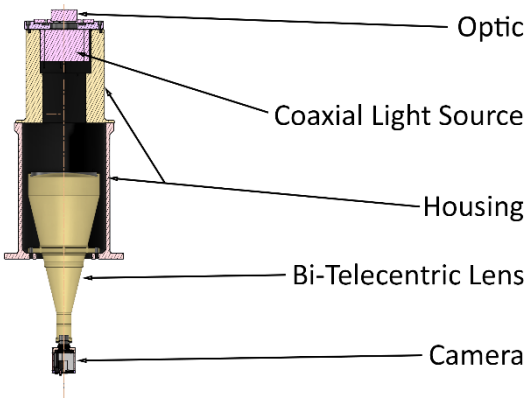

Figure 2. Schematic of the telecentric imaging system with individual components.

12 frames per second. We report quantitative characterization of resolution, illumination uniformity, and motion blur, and demonstrate pore-resolved contact imaging under process conditions. A companion submission to this conference addresses the use of these image sequences for constructing pore-aware dwell maps.

2. Experimental Setup

The experimental setup comprises three main subsystems (figure 1): a robotic positioning system, a rotating polishing head, and a telecentric imaging unit mounted beneath the workpiece.

2.1. Polishing system

An ABB IRB 2400 industrial robot (ABB Ltd., Switzerland) positions the polishing head across the workpiece surface. A force sensor mounted between the robot flange and the polishing head enables force-controlled operation in the vertical direction. The polishing head carries a porous polyurethane pad (12 mm diameter) driven by a pneumatic spindle at approximately 830 rpm. Motor control is implemented using a Beckhoff automation system. Trajectory planning is performed using in-house developed software (Zaphod, Pandora).

All experiments were conducted on plane-parallel N-BK7 glass substrates (65 mm diameter) with surface form deviation below 3 µm. The substrates were mounted in a retaining ring that holds a stationary slurry bath, ensuring the glass surface remains submerged approximately 1–2 mm below the slurry level throughout polishing. Cerium oxide slurry was prepared at a 10:1 ratio of deionized water to abrasive. No slurry circulation was employed.

The polishing trajectory follows a meander pattern with 14 mm path spacing at a constant normal force of 10 N. This spacing exceeds the pad diameter, resulting in non-overlapping passes—a deliberate choice to isolate individual track signatures for validation purposes.

2.2 Telecentric imaging system

The imaging system is positioned beneath the transparent substrate to capture the pad–glass contact zone during polishing (figure 2). The optical path comprises four main components: substrate holder, coaxial illumination module, telecentric objective, and camera.

The N-BK7 substrate is bonded at its periphery using optical wax, leaving a central aperture clear for imaging. Both substrate surfaces were polished to better than 10 nm RMS roughness prior to mounting, ensuring high optical transmission in the visible range (380–780 nm).

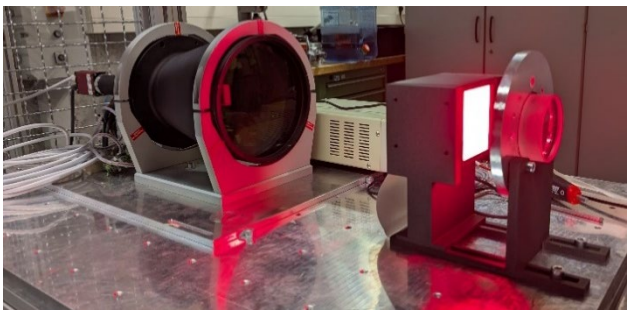

Figure 3. Experimental setup showing camera with telecentric objective (left), coaxial illumination module (red), and test substrate (right).

Illumination is provided by a coaxial LED module (FLFV-Si70N2-IP65-W, Falcon Illumination) with a 70 mm × 70 mm field of view. Coaxial geometry was selected over ring illumination to eliminate specular reflections from the LED array and camera objective that had caused artifacts in earlier setups. The LED module is synchronized with the camera exposure, enabling pulsed operation at approximately three times the continuous power rating. This increased intensity permits exposure times of 350 µs, which is critical for minimizing motion blur at the pad's peripheral velocity (~0.5 m/s).

The imaging optics consist of a telecentric objective (TC23110, Opto Engineering) coupled to a 5-megapixel monochrome camera (Manta G-504B, Allied Vision). The telecentric design maintains constant magnification regardless of object distance within the depth of field, eliminating perspective distortion that would otherwise affect contact area measurements. The complete optical assembly is enclosed in a 3D-printed housing (black PLA) to exclude ambient light. Figure 3 shows the individual components prior to integration.

Table 1 summarizes the key specifications of the imaging system.

Table 1. Specifications of the telecentric imaging system.

Parameter	Value
Camera	Allied Vision Manta G-504B
Resolution	5 MP (2452 × 2056 pixels)
Frame rate	~12 fps
Objective	Opto Engineering TC23110
Field of view	70 mm × 70 mm (limited by substrate: 65 mm)
Spatial resolution	~43 µm/pixel
Exposure time	350 µs
Illumination	Coaxial LED, pulsed

3. Image Quality Characterization

To validate the imaging system for quantitative contact analysis, we characterized its optical performance in terms of spatial resolution, illumination uniformity, and motion blur.

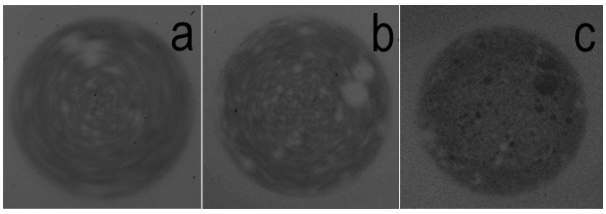

Figure 5. Pad images at different exposure times: (a) 3172 µs, (b) 1500 µs, and (c) 350 µs, demonstrating reduced motion blur with shorter exposure.

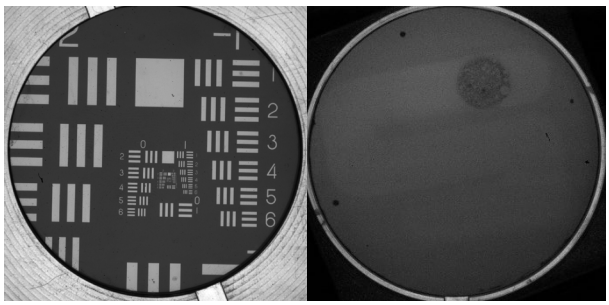

Figure 4. Left: USAF 1951 resolution target imaged through the telecentric optical system with N-BK7 substrate in place. Right: Representative in-situ image during polishing showing the 12 mm diameter pad in the slurry bath at approximately 830 rpm.

3.1 Spatial resolution

Spatial resolution was assessed using a United States Airforce (USAF) 1951 resolution target (figure 4). Under static conditions with the target positioned at the nominal working distance, line pairs in Group 3, Element 3 (approximately 50 µm feature size) were clearly resolved. This resolution is sufficient to distinguish individual pad pores, which typically range from 100 to 500 µm in diameter for the polyurethane pads used in this study.

The telecentric objective provides an extended depth of field exceeding 5 mm, ensuring that the pad–glass contact remains in focus despite minor axial displacement during polishing.

3.2 Illumination uniformity

Illumination uniformity was evaluated from flat-field images acquired through the substrate without the polishing pad present. The coaxial illumination geometry produced highly uniform intensity across the 65 mm aperture, with pixel intensity varying by less than ±5 % from the mean value (excluding the peripheral region outside the substrate).

Compared to earlier setups using ring illumination, the coaxial configuration eliminated three critical artifacts: (i) specular reflections of individual LEDs visible in the image, (ii) intensity gradients caused by non-uniform illumination angles, and (iii) thermal drift due to LED heating during extended acquisition. The enclosed housing further improved stability by excluding ambient light.

3.3 Motion blur

At a spindle speed of 830 rpm, the pad periphery moves at approximately 0.53 m/s. Motion blur was evaluated by imaging edge transitions at various exposure times (figure 5). At exposure times exceeding 500 µs, edges appeared visibly blurred. Reducing the exposure to 350 µs decreased the transition width to approximately 180 µm (corresponding to ~4 pixels), which is acceptable given the target pore sizes.

Further reduction of exposure time improved edge sharpness but increased image noise due to reduced photon count. The pulsed illumination mode, which delivers approximately three times the continuous LED power, was essential to maintain adequate signal-to-noise ratio at 350 µs exposure. This exposure time represents an optimized trade-off between motion blur and image noise for the current hardware configuration.

3.4 Temporal stability

Frame-to-frame intensity stability was assessed by acquiring 1000 consecutive frames under constant illumination without the polishing pad. The mean intensity varied by less than 1.1 % (standard deviation) across the sequence, confirming stable illumination and sensor response over the typical duration of a polishing experiment (~90 s, ~1000 frames).

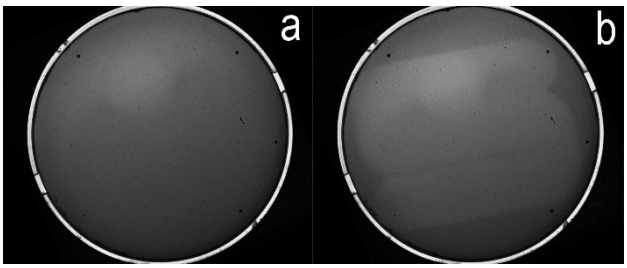

Figure 6. Substrate (a) before and (b) after polishing, showing slurry sedimentation patterns.

Table 2 summarizes the measured imaging performance parameters.

Table 2. Measured imaging performance.

Parameter	Value
Spatial resolution	~50 µm (USAF Gr. 3-3)
Illumination uniformity	±5 % (radial)
Motion blur at 350 µs	~180 µm (~4 pixels)
Frame-to-frame intensity variation	< 1.1 % (std)

4. Results

4.1 In-situ imaging during polishing

All polishing experiments were conducted in a climate-controlled environment at 21 °C ± 1 K. Figure 4 right shows a representative in-situ image acquired during polishing at 10 N normal force and approximately 830 rpm spindle speed.

The porous pad microstructure is clearly visible in the contact zone. Dark regions correspond to pad material in contact with the glass surface, while bright regions indicate pores where no contact occurs. The pad boundary is well-defined, enabling automated detection of the pad position and diameter in each frame.

Three reference holes drilled into the substrate periphery (visible in figure 4 right) serve as fiducial markers for registering the camera images to subsequent white-light interferometry (WLI) measurements. Minor contamination particles on the optical surfaces are visible as stationary spots in the image; these were not removed during the current experiments but affect only a small fraction of the field of view.

4.2 Observed contact phenomena

The in-situ image sequences revealed several phenomena relevant to polishing process understanding:

Slurry sedimentation. In the stationary slurry bath configuration, sedimentation of abrasive particles was observed over time. Figure 6 compares images acquired before and after a polishing run. The polished track appears brighter than the surrounding area, indicating that slurry particles have settled preferentially in regions where no pad contact occurred. The magnitude of this sedimentation effect has not yet been quantified.

Progressive contact intensity change. During each polishing run, the pad contact regions became progressively darker over three to four meander passes. This observation suggests that the imaging contrast evolves as the pad conditions into the slurry, possibly due to slurry absorption into the pad pores, removal of a surface layer from the pad, or smoothing of the glass surface increasing optical contact.

Pad wear signatures. Repeated imaging of the same pad across multiple experiments revealed gradual changes in the pore pattern consistent with pad wear and glazing. While not systematically quantified in this work, these observations

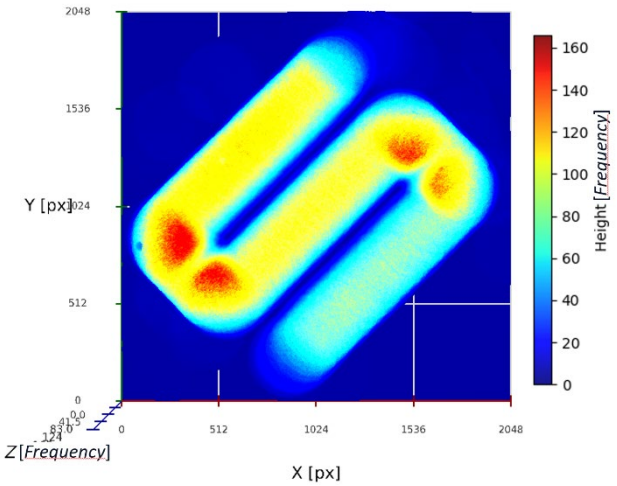

Figure 7. Accumulated contact intensity map from in-situ image sequence.

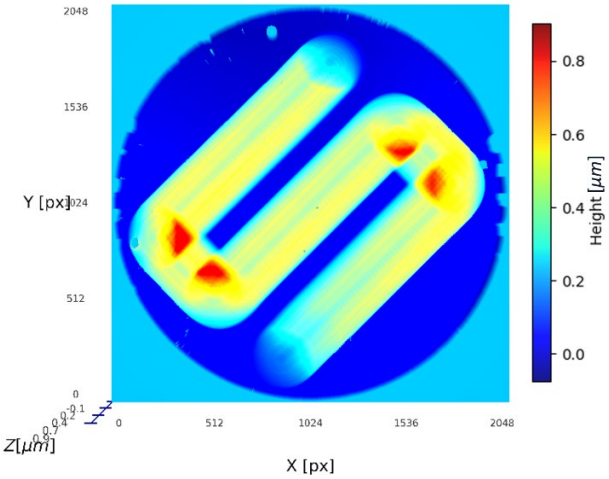

Figure 8. Material removal profile measured by white-light interferometry (Zygo NewView 8300).

demonstrate the system's potential for in-situ pad condition monitoring.

4.3 Comparison with interferometric measurements

To validate that the in-situ contact images correlate with actual material removal, we compared temporally accumulated contact maps with WLI-measured removal profiles. Figure 7 shows a contact accumulation map generated by summing the contact intensity across all frames of a polishing experiment. Figure 8 shows the corresponding material removal measured by WLI (Zygo NewView 8300).

The two maps exhibit clear qualitative correspondence: the meander trajectory pattern is visible in both, and regions of higher accumulated contact generally correspond to regions of greater material removal. However, several systematic differences are apparent:

(i) The accumulated contact map does not capture the characteristic removal depression along the track centerline visible in the WLI data.

(ii) Start and end positions of the polishing path show spatial offsets between camera and WLI data.

(iii) The 90° turns in the meander pattern appear more pronounced in the contact accumulation than in the measured removal.

These discrepancies indicate that raw contact accumulation alone does not fully predict material removal. A companion submission to this conference addresses these limitations through radial velocity correction, drift compensation, and edge weighting.

5. Conclusion and Outlook

We have presented the design and characterization of a telecentric under-surface imaging system for in-situ observation of pad–glass contact during optical polishing. The system achieves a spatial resolution of approximately 50 µm, sufficient to resolve individual pad pores, while operating at ~12 fps with 350 µs exposure to minimize motion blur at typical polishing speeds. Coaxial illumination provides uniform lighting across the 65 mm substrate aperture and eliminates reflection artifacts that affected earlier configurations.

The imaging system successfully captures the heterogeneous contact distribution created by the porous pad microstructure. In-situ observations revealed previously undocumented phenomena including progressive contact intensity changes during polishing and slurry sedimentation patterns in stationary bath configurations. Comparison with interferometric removal measurements confirmed qualitative correspondence between accumulated contact and material removal, while also identifying systematic deviations that require model-based correction.

Future development includes synchronizing the camera trigger with the spindle encoder for phase-locked acquisition, enabling analysis of pad deformation during rotation. Upgrading to a camera with higher frame rate, resolution, and quantum efficiency would improve temporal sampling, resolve smaller pore structures, and permit shorter exposure times with reduced noise.

The current visible-spectrum operation (380–780 nm) is constrained by N-BK7 transmission. Infrared-transmitting substrates (e.g., calcium fluoride) could enable thermal imaging of frictional heating at the pad–glass interface.

Beyond fundamental research, the telecentric imaging approach offers potential for industrial process monitoring, where real-time detection of pad wear, slurry starvation, or contamination could enable closed-loop control.

In summary, the telecentric under-surface imaging system provides a validated platform for pore-resolved observation of pad–glass contact, enabling both fundamental process understanding and quantitative data acquisition for predictive removal models.

Acknowledgement

This research is part of the “MoKI-pro” project (Grant No. 13FH114KA1), funded by Bundesministerium für Bildung und Forschung, and conducted at Aalen University.

References

[1] Li H et al. 2022 Light: Adv. Manuf. 3 28
[2] Preston F W 1927 J. Soc. Glass Technol. 11 214–56
[3] Almeida R et al. 2016 J. Eur. Opt. Soc.-Rapid Publ. 11 16012
[4] Jones R A 1977 Appl. Opt. 16 218–24
[5] Suratwala T et al. 2021 Appl. Opt. 60 201–14
[6] Wang T et al. 2024 Light: Adv. Manuf. 5 21
[7] Wan S et al. 2018 Precis. Eng. 52 332–42
[8] Fu G et al. 2022 Int. J. Mech. Sci. 227 107420
[9] Takahashi Y et al. 2023 Precis. Eng. 82 1–12
[10] Gray C et al. 2004 MRS Proc. 816 K5.8
[11] Park J et al. 2021 Appl. Sci. 11 6839
[12] Schneckenburger M et al. 2022 SN Appl. Sci. 4 21

euspen's 26th International Conference & Exhibition, Krakow, PL, June 2026
www.euspen.eu

Autocollimation and Reflected-Power Optimization in High-Refractive-Index Glass Retroreflectors for Robust, Cost-Effective Systems

Mateusz Sosin[1], Martin Dušek[1,2], Jean-Christophe Gayde[1], Kryštof Polák[1,2], Miroslav Šulc[2,3], Leonard Watrelot[1]

[1]*CERN – European Organization for Nuclear Research, Geneva, Switzerland*
[2]*Technical University of Liberec, Liberec, Czech Republic*
[3]*Institute of Plasma Physics of the Czech Academy of Sciences, Prague, Czech Republic*

Mateusz.sosin@cern.ch

Abstract

Spherical ball lenses with a refractive index of about 2 have, for several years, been recognized as a cost-effective alternative to classical mirror retroreflectors, owing to their ability to reflect incident light back toward its source with near-perfect fidelity. Their functionality, however, extends beyond basic retroreflection. When a substantial part of the ball is illuminated with coherent input, such as Gaussian beams, the reflected light forms so-called Structured Laser Beams (SLBs)—pseudo-non-diffractive optical beams. These beams arise from the interference of reflected light, with specific phase delays imposed on the coherent input by optical aberrations within the high-refractive-index glass sphere. This mechanism generates beams with a bright central core surrounded by concentric rings, capable of maintaining their spatial structure over theoretically unlimited propagation distances. SLBs exhibit an exceptionally low divergence of the inner core (down to approximately 10 µrad). When produced using glass-balls placed in the path of a divergent Gaussian beam with a spherical wavefront, the part of the light that enters the ball is reflected as an SLB, demonstrating excellent autocollimation, making such a reflector highly attractive for simple, cost-effective metrological systems. This paper outlines the operational principles, describes a qualitative measurement campaign using CERN's FSI systems while demonstrating reflected intensity optimization via ball diameter selection for robust autocollimation.

Keywords: metrology, interferometry, optical, high-refractive-index glass ball retroreflector

1. Introduction

High–refractive–index glass spheres (with n ≈ 2) have recently emerged as an attractive, low–cost alternative to classical mirror-based retroreflectors in optical metrology. Their usefulness was initially attributed to the simple geometric mechanism of refraction and internal reflection inside a homogeneous sphere [1-4], which enables light to return close to its incident direction over exceptionally large acceptance angles -up to 360° in principle - as demonstrated for S-LAH79 glass spheres with n = 1.996 at 633 nm [1]. Such "ball retroreflectors" have already been implemented in alignment and interferometric systems where compact, robust, and omnidirectional optical targets are required [1-3, 5].

However, the optical behaviour of these elements extends far beyond basic retroreflection. Due to the perfect rotational symmetry of the sphere and the large refractive volume traversed by the incoming radiation, ray optics is not sufficient for the description of the emerging field. When a coherent Gaussian beam illuminates a sufficiently large fraction of the spherical surface, rays travelling through different radial zones acquire different optical path lengths. This introduces controlled phase delays that are rotationally symmetric, dominated by spherical aberrations and by the defocus aberration. As shown in [6, 7], the resulting interference field forms a structured output beam with transverse intensity resembling a Bessel-type distribution (cf. Fig.1a).

This beam, referred to as a Structured Laser Beam (SLB), exhibits a bright, narrow central core surrounded by concentric rings [7]. SLBs belong to the class of pseudo–non-diffractive beams: their inner core maintains low divergence, typically of order 10 µrad, over propagation distances reaching hundreds of meters. Experimental results have shown SLB propagation over 140 m with a preserved millimetre-scale core diameter [7], and successful propagation has been demonstrated up to 900 m [8]. This behaviour distinguishes SLBs from Gaussian beams, which diverge significantly under comparable conditions.

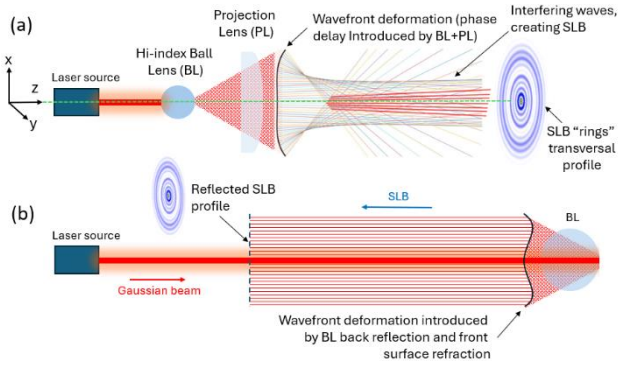

Figure 1. Schematic of two SLB generation methods: (a) wavefront shaping via projection through a high-index ball lens (BL) and a projection lens (PL); (b) wavefront shaping via back-surface reflection and front-surface refraction in the high-index BL.

A particularly relevant configuration for interferometric measurements arises when a high-index glass ball is used not as a forward generator of SLBs (cf. Fig.1a), but as a *retro-reflector*

that sends a structured beam back toward the source. This special case is explicitly described in [6], where the spherical ball lens both returns the beam and imposes the aberration-driven phase structure responsible for SLB formation (cf. Fig.1b). When a Gaussian beam is reflected by the glass reflector, the portion of light entering the ball is returned, forming a back-reflected SLB. Such a configuration produces a stable, autocollimating return beam, with a high-intensity SLB central core, without requiring complex optical assemblies.

This makes high-index glass balls particularly appealing for robust, cost-effective implementations of these reflectors within interferometric systems.

The objective of this initial study is to qualitatively validate SLB formation and power integration in high-index glass retroreflectors via lab experiments, comparing trends to wave optical models without full quantitative calibration.

2. Enhancing optical system performance through high-index glass ball reflector properties

Two properties of high-refractive-index glass ball reflectors (with n ≈ 2) are particularly relevant for interferometric distance measurement architectures: (1) their ability to generate an autocollimated, high-intensity Structured Laser Beam (SLB) core upon reflection, and (2) the possibility of optimizing the reflected SLB core power by appropriately selecting the reflector diameter. Together, these properties enable simple, alignment-tolerant, and power-scalable optical layouts that are especially attractive for fibre-based measurement systems.

The autocollimation effect greatly simplifies the optical head design in interferometric systems (eg. using bare fibre simplified optics). When the measurement beam is launched directly from a bare optical fibre, the emitted wavefront is approximately spherical, and the beam acquires a conical shape determined by the fibre's Numerical Aperture (NA). Upon interacting with the high-index spherical reflector, the SLB-forming mechanism causes the bright central core of the reflected field to propagate back along the axis of the incoming spherical wavefront—effectively steering the main energy concentration back toward the fibre tip (cf. Fig. 2).

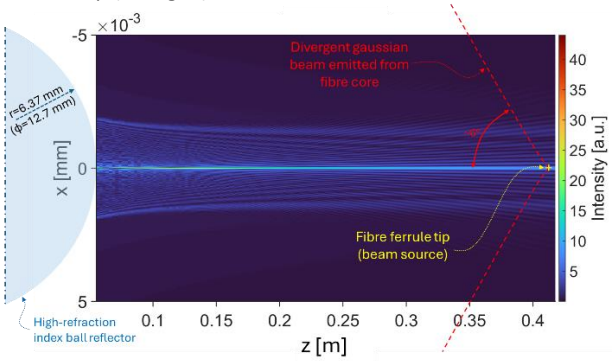

Figure 2. Longitudinal profile of the SLB field amplitude, created as back reflection from ϕ12.7 mm TAFD 55 glass ball reflector (at incident Gaussian beam of λ = 1550 nm), obtained from numerical simulations.

As a result, even with minimal or no collimating optics, a significant portion of the reflected SLB core is efficiently coupled back into the small fibre aperture. Simulations (as illustrated in Fig. 2) demonstrate that the bright central core remains narrow and well confined, enabling stable and robust power return even under relaxed alignment conditions. This geometry is therefore highly advantageous for compact interferometric distance sensors, where optical simplicity, coupling robustness, and compactness are essential.

In addition to its autocollimation capability, the high-index glass ball reflector enables direct control over the SLB core power by tailoring its diameter. In the considered configuration, the ball is illuminated by a Gaussian beam, and the reflected field assumes an SLB-like transverse structure. This transverse intensity distribution can be approximated by:

$$I_{SLB(x,y)} \approx I_0 (J_0 (k_T \cdot r))^2, \quad r = \sqrt{(x - x^0)^2 + (y - y^0)^2}, \tag{1}$$

were, J_0 is the zeroth-order Bessel function of the first kind, I_0 is the peak on-axis intensity of the SLB core, and k_T is the transverse wave-vector determined by the SLB generator [9], x-y coordinates as on Fig. 1. For a fixed SLB configuration, the radius of the SLB core (defined by the first dark ring of the Bessel pattern) is essentially independent of the diameter D of the high-index glass ball.

When the ball is illuminated by a Gaussian beam with $1/e^2$ radius w (for simplicity we assume the axis of the Gaussian beam concentric with ball lens centre), the optical power intercepted by the ball aperture (diameter D) is:

$$P_{in}(D) = \left(\frac{\pi I_{G0} w^2}{2}\right) \cdot \left[1 - \exp\left(-\frac{D^2}{2w^2}\right)\right], \tag{2}$$

where I_{G0} is the peak intensity of the incident Gaussian beam. A fixed fraction η_{core} of this power forms the SLB-like central core after reflection. Thus:

$$P_{core}(D) \approx \eta_{core} \cdot P_{in}(D), \tag{3}$$

and the core intensity:

$$I_{core}(D) \approx \frac{P_{core}(D)}{\pi \cdot r_{core}^2}. \tag{4}$$

For ball diameters considerably smaller than the incident Gaussian beam width ($D \ll w$), the intercepted power—and therefore both $P_{core}(D)$ and $I_{core}(D)$ —scales approximately with D^2. In this regime, increasing the reflector diameter effectively integrates a larger portion of the Gaussian beam power, which is subsequently funneled into the same narrow SLB core. Consequently, the SLB core intensity grows with the illuminated area of the reflector. For large diameters ($D \gg w$), the intercepted power saturates as the reflector already captures nearly all of the Gaussian beam energy; further increases in D no longer raise the SLB core intensity.

This behaviour provides a simple and effective optimization parameter: by selecting the reflector diameter, the designer can scale the SLB core power. Such power-scaling capability offers additional flexibility for adapting the returned optical signal level to detector sensitivity, interferometer dynamic range, or long-distance propagation requirements.

High–refractive–index glass ball reflectors have been widely investigated to be used within CERN's Frequency-Sweeping Interferometry (FSI) systems since almost a decade [3], primarily as compact, omnidirectional retroreflectors enabling robust position monitoring with minimal optical hardware [5]. In their earliest implementations, these elements were treated as simple reflective targets: the design philosophy intentionally favoured cost-effective instrumentation composed only of a fibre-ferrule launch and a spherical reflector. Nevertheless, operational experience accumulated across large-scale installations consistently revealed two favourable characteristics: (i) a high return power, and (ii) a clean and stable interferometric signal response.

These empirical observations, together with the parallel development of SLB theory and experiments [6–9], triggered an investigation into the power-integration behaviour and autocollimation properties of high-index ball reflectors, described hereafter.

3. Qualitative measurements campaign

The aim of the measurement campaign presented in this section is to provide an initial qualitative study, establishing visual and trend agreement between experiment and wave optical SLB models. Two complementary investigations were performed: (i) a quantitative assessment of reflected signal magnitude as a function of reflector diameter, and (ii) a direct visualisation of the generated SLB core to confirm its spatial structure.

3.1. Diameter-dependent reflected power measurements

To assess the influence of reflector diameter on the returned signal level, six commercial high-index glass ball reflectors (Hoya TAFD-55 and Schott P-SF68, uncoated, nominal refractive index $n \approx 2$; see Fig. 3) with diameters of 4 mm, 6 mm, 10 mm, 12.6 mm, 12.7 mm, and 30 mm were examined. Each reflector was mounted on the same conical support and tested at two axial distances from a bare-fibre Gaussian-beam launch: 0.42 m and 1.1 m.

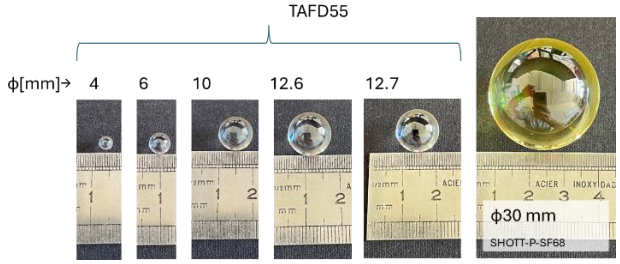

Figure 3. Measured glass ball reflectors.

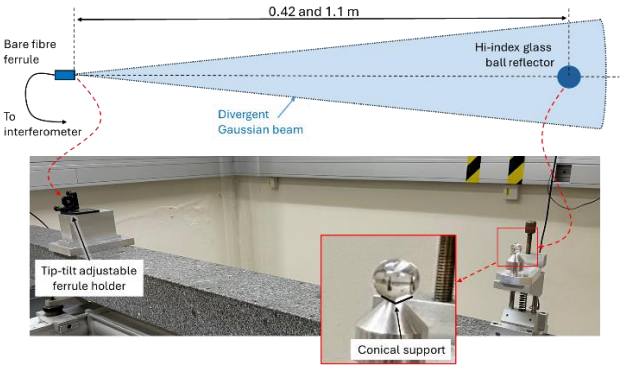

Figure 4. Measurement setup - bare fibre–ferrule installed in the tip–tilt mount to align the output Gaussian beam axis concentrically with the reflector.

The input beam was coarsely aligned so that the maximum-intensity region of the spherical Gaussian beam was positioned approximately 1 cm above the conical support—placing it close to the geometric centre of the reflectors (see Fig. 4). No additional collimation optics were employed, in order to replicate the simple, minimal-hardware configurations typical of FSI installations, with Gaussian beam encompassing the reflector.

For each ball diameter and distance, 21 independent measurements were acquired using CERN's FSI interferometer [5]. The system simultaneously recorded the reconstructed optical distance and the magnitude of the interferometric response, received through the aperture of the fibre. Although the measured magnitude does not represent an absolute optical power—because the FSI amplitude is not calibrated to physical intensity—it provides a consistent and reliable relative indicator of the returned power under fixed operating conditions. Throughout all tests, the optical power emitted from the fibre-ferrule launch (sweeping over the C-band, ~1530–1565 nm) was kept constant at approximately 5 mW. The resulting signal magnitudes as a function of ball diameter are summarised in Fig. 5.

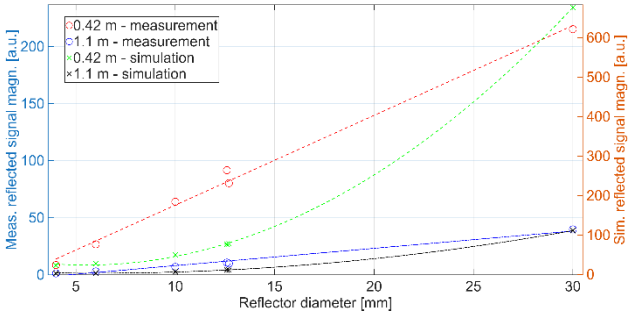

Figure 5. Comparison of measured and simulated (reflected) power for different ball reflectors.

In parallel, numerical simulations were carried out using an SLB propagation model based on the framework presented in [9]. For each reflector diameter, the model computed the expected SLB core intensity—under equivalent Gaussian illumination—and the fraction re-coupled back into the fibre ferrule (see Fig. 2). The resulting simulated trend is plotted alongside the measurements in Fig. 5 for comparison.

The experimental data show that the measured interferometric magnitude increases approximately linearly with reflector diameter, in contrast to the quadratic (D^2) dependence predicted by the simulation. In the theoretical model, the D^2 scaling arises because larger spheres intercept a proportionally greater fraction of the Gaussian beam, while the resulting SLB core maintains an approximately diameter-independent width. The observed linear trend can be explained by several practical factors. First, residual alignment errors: maintaining perfect coaxiality between the Gaussian beam and each sphere was challenging due to the single-reflector mounting approach. Even small lateral misalignments, introduced when swapping reflectors, modify the fraction of Gaussian power incident on the effective aperture of the sphere, thereby altering the returned SLB core power. Second, diameter-dependent variations in coupling efficiency may also play a role; SLB cores produced by spheres of different sizes might couple into the detection optics with slightly different efficiencies, though quantifying this effect lies beyond the scope of the present study. Third, the largest sphere tested (ϕ30 mm, SCHOTT P-SF68) was fabricated from a different glass than the smaller ones (HOYA TAFD55). The corresponding differences in refractive index and material properties could influence internal attenuation and Fresnel losses, contributing to the deviation from the idealised D^2 trend.

Despite these limitations, the overall increase in returned power with reflector diameter is clearly evident, qualitatively confirming the expected power-integration behaviour of high-index spheres. This monotonic trend validates diameter as an optimization parameter for practical FSI systems.

3.2. Direct visualisation of the SLB core

To confirm the formation of SLB with high intensity core under reflective illumination, a second experiment was conducted. In this setup, illustrated in Fig. 6, a fibre-ferrule emitter launched a divergent Gaussian beam toward a partially reflective mirror, which redirected a portion of the light toward a ϕ12.7 mm glass ball reflector. The reflector generated a retroreflected SLB that subsequently passed back through the semi-reflective mirror and a beam expander—used to scale the SLB to the size of the camera's CCD—and was finally imaged onto a near-infrared-sensitive camera (Gentec BEAMAGE-4M-IR series). This configuration enabled direct observation of both the intensity distribution and spatial structure of the resulting SLB.

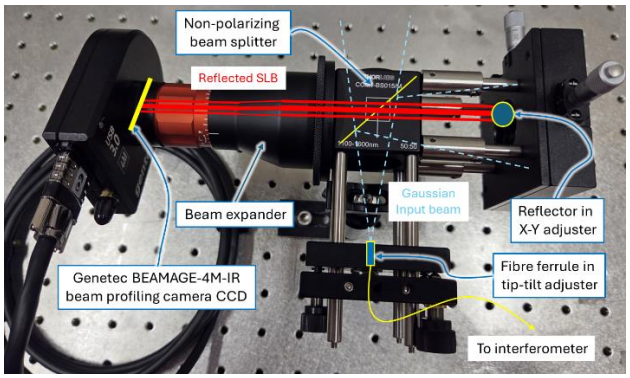

Figure 6. Measurement setup to visualize the reflected SLB and intensity of the core.

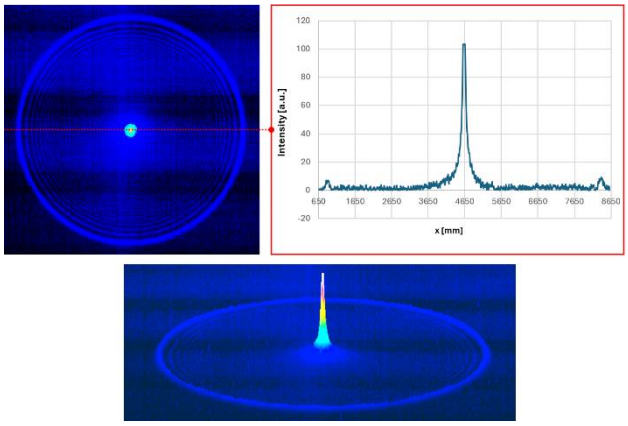

Figure 7. Visualization of the measurement of the SLB pattern with a clearly defined high-intensity core.

The recorded intensity distribution is shown in Fig. 7. The image reveals the characteristic SLB morphology [7,8]: a bright, narrow central core—with a width far below that of the incident Gaussian beam—surrounded by well-defined concentric rings of decreasing intensity. The clear separation between the high-intensity core and its surrounding rings confirms the expected quasi-Bessel, pseudo-non-diffractive structure. Most importantly for optimization of optical applications, the central core is smooth, symmetric, and sharply confined, indicating that a substantial fraction of the power is concentrated into a spatial mode that can be efficiently coupled back into the small acceptance aperture of a fibre or compact photodetector.

This observation provides direct, visual confirmation of the SLB-based retroreflection mechanism responsible for the strong and stable return signals seen in operational FSI systems.

4. Conclusions

The measurement campaign provides qualitative confirmation that high-index glass ball retroreflectors are capable of integrating a substantial fraction of the incident optical power and returning it as a structured, autocollimated beam. Crucially, the paper demonstrates that this behaviour cannot be fully understood using ray optics alone. By incorporating the wave nature of light into the analysis, we are able to model the formation and propagation of the SLB, including features such as the intensity structure, core narrowing, and coupling efficiency—effects that arise beyond purely geometric descriptions.

Although the expected D^2 scaling of the SLB core power was not fully reproduced experimentally—most likely due to coupling-efficiency limits, alignment imperfections and biggest reflector material difference—the monotonic increase of the returned signal with reflector diameter reinforces the underlying power-integration principle predicted by wave-optical model.

Direct imaging of the reflected field further confirms the emergence of a narrow, high-intensity SLB core, well suited for coupling into compact optical launches such as bare fibre ferrules. This provides experimental validation that ball-based retroreflectors can serve as efficient, alignment-tolerant elements in interferometric systems when both ray- and wave-optical effects are properly accounted for.

The results presented here represent an initial exploration aimed at establishing qualitative agreement between experiment and wave-enhanced modelling of SLB behaviour. A more comprehensive quantitative study—including calibrated power measurements, angular-tolerance characterisation, detailed wavefront analysis, and long-distance propagation tests—will be reported in future work.

References

[1] M. Sulc, "High index glass spherical targets for laser interferometry," ser. 1-st PACMAN Workshop. Geneva, Switzerland: CERN, February 2015. [Online]. Available: https://indico.cern.ch/event/332431/contributions/775845.

[2] G. Kautzmann, J.-C. Gayde, F. Klumb, Y. Kadi, J. Bensinger, K. Hashemi, and M. Sulc, "HIE Isolde – General Presentation of MATHILDE," CERN, Geneva, Tech. Rep., 2014. [Online]. Available: https://cds.cern.ch/record/2040166.

[3] S. W. Kamugasa, "Development and validation of a Frequency Scanning Interferometry Network for Compact Linear Collider component fiducialization," Ph.D. dissertation, ETH Zurich, 2018. [Online]. Available: https://doi.org/10.3929/ethz-b-000317637.

[4] Egidi, A.; Balsamo, A.; Pisani, M. High-Index Glass Ball Retroreflectors for Measuring Lateral Positions. Sensors 2019, 19, 1082. https://doi.org/10.3390/s19051082

[5] M. Sosin; J.D. Gonzalez Cobas; M. Isa; R. Leach; M. Lipiński; V. Rude; J. Rutkowski; L. Watrelot. An Interferometric Multi-Sensor Absolute Distance Measurement System for Use in Harsh Environments. Sensors 2025, 25, 5487. Available: https://doi.org/10.3390/s25175487

[6] M. Sulc and J.-C. Gayde, "An optical system for producing a Structured Beam," Patent EP3564734, 2019. [Online]. Available: https://data.epo.org/publication-server/rest/v1.2/patents/EP3564734NWA1/document.html.

[7] J.-C. Gayde, M. Sulc, and K. Polak, "Introduction to structured laser beam for alignment and status of the r&d," in 16th International Workshop on Accelerator Alignment (IWAA 2022). Ferney Voltaire (France). CERN Document Server, https://cds.cern.ch/record/2849065/, October 2022.

[8] Gayde, J.-C., et.al. The potential contribution of a structured laser beam to accelerator alignment technology. In Proceedings of the 14th International Particle Accelerator Conference (IPAC'23) (pp. 4044–4046). Venice, Italy: JACoW Publishing. https://doi.org/10.18429/JACoW-IPAC2023-THPA041.

[9] K. Polak, M. Sulc, and J.-C. Gayde, "Structured laser beam in non-homogeneous environment," in 16th International Workshop on Accelerator Alignment (IWAA 2022). Ferney Voltaire (France): CERN Document Server, https://cds.cern.ch/record/2849070, October 2022.

euspen's 26th International Conference & Exhibition, Krakow, PL, June 2026
www.euspen.eu

Development of a Critical Assembly Quality Analysis Method for Machine Tools Based on the Jacobian-Torsor Model

Lin Tsao[1], Sheng-Hsiang Hung[2]

[1,2] Center for Measurement Standards, Industrial Technology Research Institute, Hsinchu, Taiwan

Abstract
To enhance the precision and reliability of machine tools, assembly quality has become a critical concern in high-precision manufacturing. This study proposes a systematic assembly quality analysis method based on the Jacobian–Torsor model. By integrating geometric specifications, tolerance information, and the kinematic chain of mechanical components, an error propagation model is established to evaluate positioning accuracy across six degrees of freedom. Monte Carlo simulation is employed to statistically quantify tolerance contributions and identify critical assembly parameters. The results demonstrate that dominant tolerances can be clearly ranked using contribution and sensitivity indices, enabling targeted optimization during design and assembly stages. The proposed framework provides a digital foundation for intelligent tolerance allocation and precision enhancement in advanced machine tool manufacturing.

Jacobian-Torsor model, Small displacement torsor, Geometric error

1. Introduction

Assembly quality analysis and precision compensation techniques for machine tools are currently developed independently by individual manufacturers, lacking a unified analytical framework. Consequently, improvements in machining accuracy often rely on repeated trial-and-error processes on physical machines, resulting in extended occupation time, reduced productivity, and increased resource consumption.

Under the digital twin paradigm, the integration of virtual modeling and data-driven analysis provides new opportunities for systematic precision optimization. However, a structured method to model assembly error propagation and quantitatively evaluate tolerance contributions remains insufficiently developed.

This study proposes a digital modeling approach for analyzing critical assembly parameters of linear axis systems in multi-axis machine tools. Based on the Jacobian–Torsor framework, dimensional and assembly errors are propagated through the kinematic chain according to the assembly sequence. The model takes key assembly tolerances as inputs and outputs six geometric error components (three translational and three rotational). By ranking tolerance contributions, the method enables precise identification of dominant assembly parameters and supports targeted quality improvement.

Tolerance analysis methodologies based on the Jacobian–Torsor model have been widely studied [1–3], while geometric error compensation in machine tools has been extensively addressed in precision engineering research [6–8].

2. Jabonian-Torsor model

The Jacobian–Torsor Model [1,2] is a theoretical framework that integrates the Small Displacement Torsor (SDT) with the Jacobian matrix, and is widely applied in tolerance analysis and geometric error propagation modeling of assemblies. In this approach, SDTs are used to represent small deviations between actual geometric features and their nominal ideal positions. The Jacobian matrix then maps these local geometric errors to the global assembly system, enabling the propagation and accumulation of errors across multiple components. Owing to its capability to simultaneously evaluate geometric sensitivity and support statistical analysis, the Jacobian–Torsor Model is particularly well suited for comprehensive assembly error assessment and process tolerance optimization in complex mechanical systems. It provides an effective and systematic analytical tool for quality control and predictive modeling in precision mechanical assembly.[2,5]

2.1. Small displacement torsor

The Small Displacement Torsor (SDT) is used to represent the infinitesimal motion of a rigid body in space. It consists of six motion components, including three translational components (u, v, w) and three rotational components (α, β, γ), as shown in **Equation (1)**.

$$\mathbf{T}_i = \{u_i \ v_i \ w_i \ \alpha_i \ \beta_i \ \gamma_i\}^T \quad (1)$$

This six-dimensional vector provides a complete description of the small deviations of a geometric feature from its nominal ideal position. In practical engineering applications, most geometric features of mechanical components can be classified into seven basic geometric types, such as planes, lines, and cylinders. Different geometric features correspond to different tolerance requirements, including flatness, straightness, and cylindricity, which in turn lead to different forms of SDT representations.

Taking a planar feature as an example, the SDT modeling and constraint formulation are illustrated. In theory, a plane possesses six degrees of freedom. However, under practical geometric tolerances and functional constraints, its degrees of freedom are restricted by positioning and assembly conditions. As shown in Fig. 1, only the translational displacement along the z-axis and the rotational motions about the x and y axes are permitted. Consequently, the SDT representation of the planar feature can be expressed as $(0, 0, w, \alpha, \beta, 0)$.

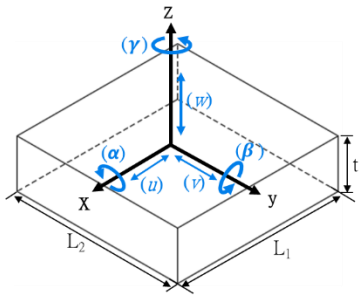

Figure 1. Fundamental geometric characteristics of flatness.

2.2. Jacobian matrix

In the Jacobian–Torsor model, the Jacobian matrix is used to describe how the Small Displacement Torsors (SDTs) of individual Functional Elements (FEs) are propagated to the Functional Requirement (FR). The Jacobian matrix is derived from the coordinate transformations between the local coordinate systems of the FEs and the global coordinate system associated with the functional requirement. Each functional element corresponds to a 6×6 submatrix, which represents its contribution and influence on the FR.

$$[J]_{FE_i} = \begin{bmatrix} [R_0^i]_{3\times3} & [W_i^n]_{3\times3} \cdot [R_0^i]_{3\times3} \\ 0 & [R_0^i]_{3\times3} \end{bmatrix}_{6\times6} \quad (2)$$

where $\mathbf{W}_i^n \in \mathbb{R}^{3\times3}$ is the skew-symmetric matrix of the position vector, representing the effect of rotational motion on translational displacement. $\mathbf{R}_0^i \in \mathbb{R}^{3\times3}$ is the rotation matrix of the functional element with respect to the global coordinate system.

The skew-symmetric matrix $\mathbf{W}_i^n$ is defined as:

$$\mathbf{W}_i^n = \begin{bmatrix} 0 & -z_i & y_i \\ z_i & 0 & -x_i \\ -y_i & x_i & 0 \end{bmatrix} \quad (3)$$

where $(x_i,\ y_i,\ z_i)$ denotes the position vector of the functional element. The block structure of Eq. (2) reflects the rigid-body kinematic mapping between the rotational and translational components of the SDT.

2.3. Calculation Method and Steps

The primary sources of the final precision target error stem from manufacturing and assembly deviations in individual components, represented by torsor $T_1, T_2, \ldots, T_n$ and corresponding Jacobian matrices $J_1, J_2, \ldots, J_n$. The total error $[J]_{FR}$ can be expressed as:

$$[J]_{FR} = \sum_{i=1}^{n} [J]_{FE_i} \cdot T_{FE_i} \quad (4)$$

Since it is known that dimensional/assembly errors in mass production generally follow specific probability distributions (e.g., normal distribution, rectangular distribution), statistical Monte Carlo simulation is applied to this model to accurately reflect the impact of error sources on overall precision. By randomly sampling error sources under this specific probability distribution and generating large datasets through iterative methods for simulation analysis.

3. Linear Axis Structural Assembly Analysis

In linear-axis-dominated error propagation paths, the geometric characteristics of individual components are closely associated with their assembly relationships. The guide system considered in this study—including the base, linear guide rails, slide blocks, and workbench—was characterized in terms of nominal dimensions, permissible tolerance ranges, and potential geometric deviation types (e.g., flatness, straightness, and parallelism). These specifications are summarized in Table 1.

Based on the assembly hierarchy, a small-displacement torsor (SDT) model was established to represent infinitesimal geometric deviations. The corresponding Jacobian matrix was constructed according to the error propagation sequence (base → guide → slider → workbench), as illustrated in Fig. 2. [3]

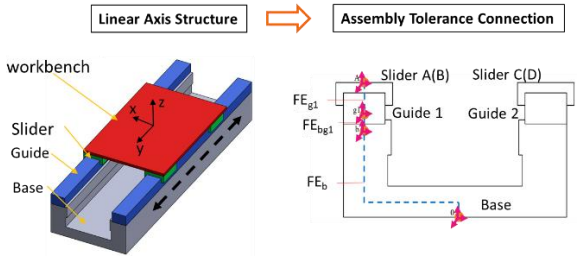

Figure 2. Configuration of the linear axis workbench and corresponding geometric error chain based on the Jacobian–Torsor model.

Furthermore, Monte Carlo simulation was employed to generate random samples representing stochastic geometric deviations that may occur during the actual assembly process. Six-degree-of-freedom geometric errors were simulated for each functional component according to the specified tolerance distributions.

The assembly errors of individual linear axes were first evaluated independently. These errors were then superimposed according to the structural configuration of the machine tool to obtain the overall system-level geometric deviation.

Subsequently, statistical sensitivity analysis and tolerance contribution evaluation were conducted using the control variable method to quantify the influence of each assembly quality parameter on the total geometric error. The dimensional specifications and tolerance ranges of all components used in the simulation are summarized in Table 1.

Table 1 . Geometric parameters and tolerance ranges used in the simulation.

Component	dimension(mm)	Tolerance Items	Tolerance
Base	1200×800×50 $(L_b \times W_b \times H_b)$	Flatness f_b	0.01 mm
Guide 1	800×45×38 $(L_{g1} \times W_{g1} \times H_{g1})$	Flatness f_{g1}	0.01 mm
		straightness S_{M1}	0.01 mm/m
		Installation straightness in the x-direction S_{1x}	0.01 mm/m
		Installation straightness in the z-direction S_{1z}	0.01 mm/m
Guide 2	800×45×38 $(L_{g2} \times W_{g1} \times H_{g2})$	Flatness f_{g2}	0.01 mm
		Straightness S_{M2}	0.01 mm/m
		Installation straightness in the x-direction S_{2x}	0.01 mm/m
		Installation straightness in the z-direction S_{2z}	0.01 mm/m

3.1. Analysis of Assembly Quality Control Parameters

Applying the Jacobian-Torsor model, the six geometric errors of a slider A in the calculation are expressed as:

$$\begin{bmatrix} u \\ v \\ w \\ \alpha \\ \beta \\ \gamma \end{bmatrix}_{FR_A} = \boldsymbol{J} \times \boldsymbol{D} = [\boldsymbol{J_b} \quad \boldsymbol{J_{bg1}} \quad \boldsymbol{J_{g1}}] \begin{bmatrix} \boldsymbol{T_b} \\ \boldsymbol{T_{bg1}} \\ \boldsymbol{T_{g1}} \end{bmatrix} \quad (5)$$

The workbench is supported by four sliders (A, B, C, and D) and a lead screw. Each individual error chain is propagated through the assembly process and integrated into a total system-level error chain. The overall translational error of the workbench—resulting from the superposition of errors in the same direction across the four sliders—can be expressed as:

$$\begin{bmatrix} u_o \\ v_o \\ w_o \end{bmatrix} = \frac{1}{4}\left\{ \begin{bmatrix} u_A \\ v_A \\ w_A \end{bmatrix} + \begin{bmatrix} u_B \\ v_B \\ w_B \end{bmatrix} + \begin{bmatrix} u_C \\ v_C \\ w_C \end{bmatrix} + \begin{bmatrix} u_D \\ v_D \\ w_D \end{bmatrix} \right\} \quad (6)$$

The rotational deviations of the workbench around the X, Y, and Z axes (pitch, yaw, and roll) are determined by the relative

vertical and lateral displacements of the four sliders. These relationships can be expressed as:

$$\begin{bmatrix}\alpha_o\\ \beta_o\\ \gamma_o\end{bmatrix}=\begin{bmatrix}\frac{\frac{w_B+w_D}{2}-\frac{w_A+w_C}{2}}{D_y}\\ \frac{\frac{w_C+w_D}{2}-\frac{w_A+w_B}{2}}{D_x}\\ \frac{1}{4}\left(\frac{u_A-u_B}{D_y}+\frac{v_C-v_A}{D_x}+\frac{u_C-u_D}{D_y}+\frac{v_D-v_B}{D_x}\right)\end{bmatrix} \quad (7)$$

Where D_x and D_y denote the distances between sliders along the X and Y direction respectively.

Using the Monte Carlo simulation approach to statistically analyze six-degree-of-freedom geometric errors. The error propagation mechanism is established based on the Jacobian–Torsor model, incorporating the statistical distributions of typical geometric error sources from individual components through random sampling.

Analysis points are defined at 5 mm intervals along the entire travel range of the linear axis. At each position, 10,000 random samples are generated to perform numerical simulations and evaluate the resulting error distributions. Finally, the variation range of the six geometric errors is quantified using the 3σ confidence interval to characterize the statistical behavior of the system's spatial accuracy.

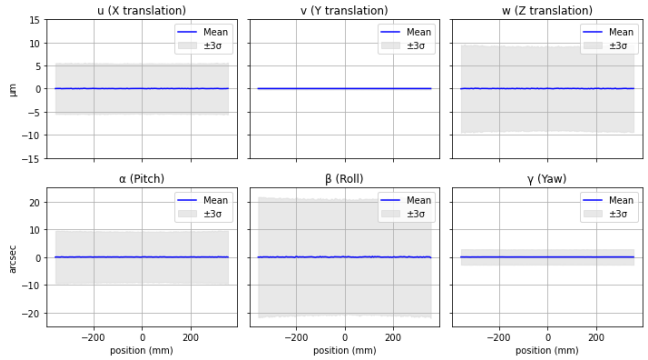

Figure 3. Distribution of six-degree-of-freedom geometric errors along the linear axis travel range.

3.2. Critical Tolerance Analysis of Assembly Tolerances

Critical tolerance identification was performed based on two quantitative metrics:

(1) percentage contribution of each tolerance source and

(2) tolerance sensitivity.

Assuming that all geometric error sources are statistically independent and follow random distributions (e.g., normal distributions), the standard deviation of the overall platform error can be obtained by variance superposition:

$$\sigma_{total}=\sqrt{\sum_i \sigma_i^2} \quad (8)$$

where σ_i denotes the standard deviation of the error induced by the i-th tolerance source. The influence of each error source on the final error can be expressed as $FE_i = J_i \times T_i$, where FE_i represents the impact of the i^{th} error term on the output error, J_i denotes the corresponding Jacobian matrix, and T_i is the small displacement vector of that error source. The contribution percentage of each error source to the total variation is further calculated, where σ is the standard deviation.

Tolerance sensitivity quantifies the extent to which variation in an individual tolerance source affects the overall assembly error.Sensitivity was evaluated using the one-at-a-time (OAT) method, in which:

- only one tolerance source is randomly varied
- all other tolerances are set to zero

Monte Carlo simulations are then performed to observe the resulting variation in the six-degree-of-freedom output. The standard deviation (or variance) of the response is used as the sensitivity index, $S_{i,j}$, representing the sensitivity of tolerance i to degree of freedom j.

To jointly evaluate both statistical contribution and sensitivity, a critical tolerance index is defined as:

$$k_{i,j} = (\%PC)_{i,j} \times S_{i,j} \quad (8)$$

This index reflects both:

- how much a tolerance contributes to overall variation
- how strongly the system responds to that tolerance

For each degree of freedom j, tolerance sources are ranked in descending order of $k_{i,j}$ to identify the dominant contributors to assembly error. This ranking provides a quantitative basis for targeted tolerance optimization, enabling precision improvement without uniformly tightening all tolerances.

4. Results

Monte Carlo simulation indicates that the maximum 3σ translational deviation in the u-direction reaches approximately 5 μm at the center of the linear axis travel. As shown in Fig. 4, contribution analysis shows that tolerances S_{1x} and S_{2x} are the dominant contributors in this direction, jointly accounting for more than 80% of the total error variance.

For the v- and w-directions, base plate flatness is identified as the primary influencing factor. It exhibits both the highest percentage contribution (Fig. 4) and the largest sensitivity index (Fig. 5). The remaining tolerance parameters each contribute less than 10% individually, indicating relatively minor influence on overall geometric deviation.

Furthermore, the dominance of tolerance sources varies across different degrees of freedom. As illustrated in Fig. 6, the critical tolerance ranking differs for each directional error component, confirming that geometric error behavior is direction-dependent rather than uniformly distributed.

These results demonstrate that volumetric accuracy is governed by a limited subset of assembly tolerances. Therefore, targeted optimization of dominant tolerances can significantly improve positioning performance without uniformly tightening all tolerance specifications. The results quantitatively confirm that geometric error propagation in linear axis assemblies is anisotropic and governed by structurally coupled tolerance parameters.

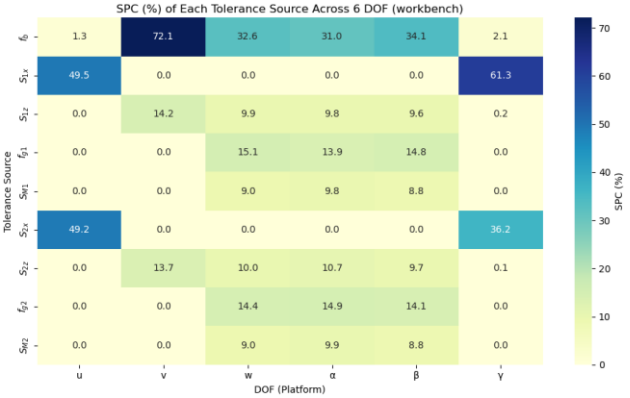

Figure 4. Percentage contribution of individual tolerance sources to the geometric error of the linear axis workbench.

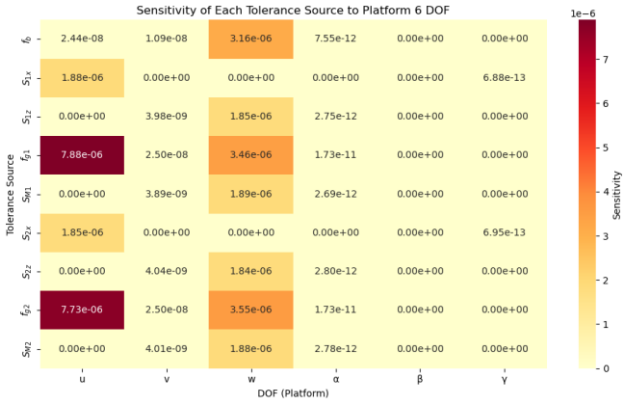

Figure 5. Sensitivity analysis of tolerance parameters affecting workbench geometric deviations.

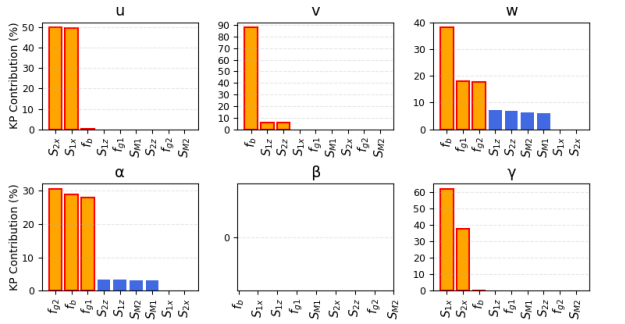

Figure 6. Identified critical tolerances for each degree of freedom at the center position of the linear axis workbench.

5. Summary

This study developed a Jacobian–Torsor-based tolerance analysis framework to quantitatively identify critical assembly parameters in linear axis systems. The results demonstrate that volumetric error is predominantly governed by a limited subset of tolerance sources, with the top three parameters accounting for more than 80% of total error variance. These findings indicate that uniformly tightening all tolerances is neither necessary nor efficient.

Instead, targeted optimization of dominant tolerances can significantly enhance positioning accuracy while reducing assembly cost and complexity. The proposed framework provides a systematic and computationally efficient foundation for precision-oriented assembly design, enabling the transition from empirical adjustment to data-driven tolerance allocation.

References

[1] Ghie W., Laperrière L., Desrochers A., “A unified Jacobian-torsor model for analysis in computer aided tolerancing,” Springer Netherlands, 2003.

[2] Ghie, W., Laperrière, L., & Desrochers, A., “Statistical tolerance analysis using the unified Jacobian–Torsor model,” *International Journal of Production Research*, **48**(15), 4609-4630, 2010.

[3] Du, Z., Wu, J., & Yang, J., “Geometric error modeling and sensitivity analysis of single-axis assembly in three-axis vertical machine center based on jacobian-torsor model,” *ASCE-ASME Journal of Risk and Uncertainty in Engineering Systems, Part B: Mechanical Engineering*, **4**(3), 031004, 2017.

[4] Chen H., Li X., Jin S., “A statistical method of distinguishing and quantifying tolerances in assemblies,” *Computers & Industrial Engineering*, **156**, 10725, 2021.

[5] Tian, A., Liu, S., Chen, K. et al. “Spatial Expression of Assembly Geometric Errors for Multi-axis Machine Tool Based on Kinematic Jacobian-Torsor Model,” *Chinese Journal of Mechanical Engineering*, **36**, 44, 2023.

[6] Schwenke H., Knapp W., Haitjema H., Weckenmann A., Schmitt R., Delbressine F., “Geometric error measurement and compensation of machines—An update,” *CIRP Annals – Manufacturing Technology*, **57**(2), 660–675, 2008.

[7] Bringmann B., Küng A., Knapp W., “Model-based ‘chase-the-ball’ calibration of a 5-axis machining center,” *CIRP Annals – Manufacturing Technology*, **57**(1), 531–534, 2008.

[8] Mayr J., Jedrzejewski J., Uhlmann E., Donmez A., Knapp W., Hartig F., Wendt K., Moriwaki T., Shore P., Schmitt R., et al., “Thermal issues in machine tools,” *CIRP Annals – Manufacturing Technology*, **61**(2), 771–791, 2012.

euspen's 26th International Conference & Exhibition, Krakow, PL, June 2026
www.euspen.eu

On-machine optical tool characterisation using dictionary-based sub-pixel edge detection

Moritz Genzwürker[1], Matthias Geiselhart[1], Giuliano Bissacco[1]

[1] *Technical University of Denmark, Department of Mechanical Engineering, 2800 Kgs. Lyngby, Denmark*

morge@dtu.dk

Abstract

An on-machine optical measurement system is developed for 3D reconstruction of spindle-mounted rotating cutting tools, addressing the need for near real-time cutting-edge geometry data to support surface generation prediction in precision machining. The system is calibrated on the machine and achieves sub-pixel resolution in the direction perpendicular to the edge profile. A novel on-machine camera alignment process based on a spherical artefact facilitates the measurement process. Performance evaluation following ISO 15530-3 is carried out, yielding an expanded uncertainty of 9.8 µm (k=2) and a repeatability of 0.074 µm for radius measurements. The system is shown capable of reconstructing cutting-edge profiles and quantifying radius and runout. The primary error source is a systematic bias of 4.8 µm, which, if corrected, could significantly improve system performance.

Machining, Measuring instrument, Precision, Tool

1. Introduction

In precision manufacturing, the quality of machined surfaces directly determines component functionality, service life and production cost. With industries pushing towards tighter tolerances and higher requirements regarding surface integrity, the ability to predict and control surface topography has become a critical competitive factor.

High-fidelity surface generation prediction for finishing milling operations requires high-resolution information on the morphology of the cutting edges engaging the workpiece surface. High-resolution cutting-edge characterisation is possible using off-machine instruments such as optical profilometers [1]. However, the cutting-edge morphology changes during machining operations, and so does the topography of the generated surfaces [2-3]. Thus, in order to exploit surface generation models in production, it is vital to provide them with real-time information on the cutting edges' morphology in their current condition. Automated on-machine tool measurement systems exist in the form of laser beam interruption systems, laser scan micrometres and camera systems [4]; however, these are either incapable of characterising the full profile of the cutting edges or do not currently deliver sufficient resolution to facilitate high-fidelity wear monitoring and edge morphology characterisation.

This paper presents the initial steps in the development of an optical on-machine tool measurement system capable of reconstructing the 3D cutting-edge geometry of endmills of generic profile geometries. A novel variant of dictionary-based sub-pixel edge detection is introduced, where the reference profiles are generated from CNC-controlled motion of an uncalibrated artefact. Section 2 details the system design, including an on-machine camera alignment strategy, calibration and post-processing methodology. Section 3 presents a metrological evaluation of the prototype system in accordance with ISO 15530-3. Section 4 concludes the paper and outlines directions for future work.

2. System Design and Methodology

2.1 Setup

Figure 1 shows the experimental setup inside the working envelope of a FANUC ROBODRILL α-D21LiB5adv. A Basler a2A1920-160umBAS greyscale global shutter camera with a VS-TCH1.5-65 telecentric lens is mounted opposite a collimated light source (green LED) in a shadowgraph-like setup. The camera pulses the LED for 10 µs per exposure using an EU-38-TTL LED driver to reduce the effective shutter speed and observed motion blur. The setup is connected to a power supply and PC outside the machine.

Spindle-mounted cutting tools smaller than the camera's field of view of 4.5 x 2.8 mm are moved to their measurement position (determined as described in Section 2.2) using the machine's linear drives. The camera captures silhouette images of the cutting tool at a sampling frequency determined using Equation 1. This is to compensate for the spindle speed, ω, being many times faster than the camera's maximum sampling frequency, $\mathrm{fps}_{\max}$, of 160 Hz. Images of the tool are captured over multiple rotations with a known angular step and appear in order of orientation. Here, ω is the spindle speed and k the number of revolutions between images to enable the desired angular resolution, α.

$$\mathrm{fps(k)} = \frac{\omega \cdot 2\pi}{\alpha + 2\pi \cdot k} < \mathrm{fps}_{\max}, \quad k = 0,1,2,.. \tag{1}$$

Figure 2 shows images of two spindle-mounted artefacts captured at 6000 rpm using the setup (a flat endmill and a square bar). The chosen camera/lens combination gives the system an image scale of 2.3 µm px^{-1}. This is far too coarse for high-accuracy edge profile characterisation. Section 2.4, therefore, introduces a novel approach to on-machine camera calibration and sub-pixel interpolation.

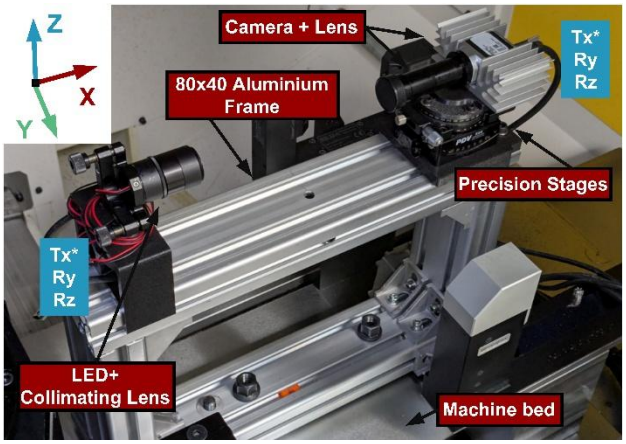

Figure 1. Experimental setup inside the CNC machine. The camera and backlight are mounted on precision manual stages, facilitating rotation around the Y and Z axes. Both components can be moved along the X-axis to tune the illumination distance.

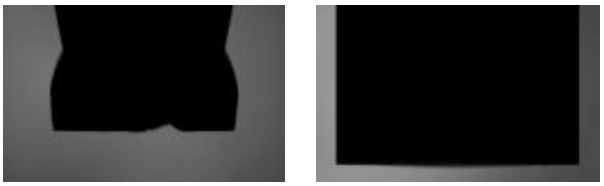

a) b)

Figure 2. Silhouette images captured by the system of a) a 3 mm, four-fluted flat endmill and b) a square bar at 6000 rpm.

2.2 Locating the focal plane

Extraction of accurate, repeatable data from the acquired images requires that the tool be in optimal focus. This occurs when the spindle axis lies on the lenses' focal plane. Here, due to the geometry of cutting tools, the outermost segments of the cutting edges appear maximally sharp (as seen in Figure 2a).

The focal point of the optical system is located within the machine tool working volume using a tube-mounted Ø 12 mm uncalibrated steel sphere fixed in a tool holder and clamped to the spindle. The exact geometry of the sphere is not critical since no dimensional information from it will be used to inform the measurement process. The layout is shown in Figure ***3***.

From the camera's perspective, the sphere appears as a circular silhouette regardless of alignment. The silhouette's perimeter is most in focus when the spindle axis intersects the focal plane. The focal point (ideal measurement position along the optical axis) can hence be determined using a Sobel Gradient-based focus measure, along the perimeter of the sphere projection, computed according to Equation 2.

$$\mathrm{F_{edge}} = \frac{1}{N} \sum_{(i,j) \in \mathrm{edge}} (G_i(i,j)^2 + G_j(i,j)^2) \qquad (2)$$

Where (i, j) are pixel coordinates, I the local intensity and $G_i \approx \frac{\partial I}{\partial i}$ and $G_j \approx \frac{\partial I}{\partial j}$ are the derivatives of intensity in two orthogonal directions. The sphere is then swept along the X axis of the machine until a peak in $\mathrm{F_{edge}}$ is detected. The X position of the spindle is recorded and used to position the cutting tools during subsequent measurements. To compensate for runout, the sphere is rotated at low rpm during this process.

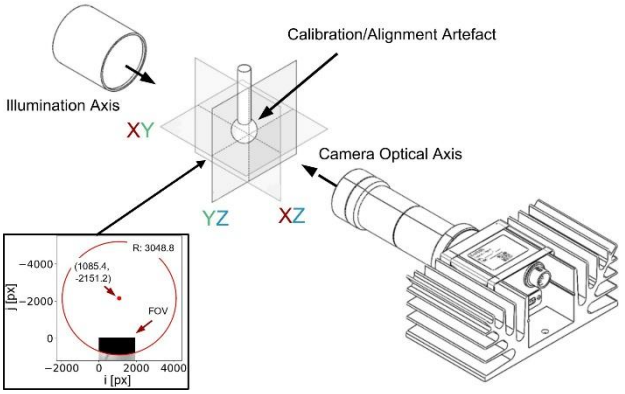

Figure 3. Setup for focusing, alignment and calibration of the optical system using a Ø 12 mm spindle-mounted sphere.

2.3 Focal plane alignment with machine axes

To facilitate on-machine calibration, the camera's focal plane must be aligned with the CNC machine's YZ plane. This is achieved via a live post-processing script that fits a circle to the visible parts of the sphere's silhouette (see Figure 3). The centre position of the sphere is then easily traceable at sub-pixel resolution. When the camera is correctly aligned (i.e. the X axis is parallel with the optical axis), sweeping the sphere along the machine's X axis should not change its centre position (beyond minor fluctuations due to vibrations). Drift of the tracked centre caused by motion of the sphere along the X axis can be corrected using the set precision stages (see Figure ***1***). This enables fine-tuning of the camera's alignment to within approximately 0.12 deg. The main limitation in this process is currently the backlash in the stages. This will be mitigated with a better mechanical alignment solution in the future.

2.4 Calibration and edge detection

During initial testing, a pixel-level attempt was made to reconstruct the 3D cutting-edge geometry of a cutting tool from images acquired by the system. A series of 400 silhouette images of the endmill shown in Figure 2a, rotating at 6000 rpm were captured using the system. One point per cutting edge per frame was extracted (in pixel coordinates), where the cutting edge was most in focus. This point was identified as the pixel with the maximum magnitude of the intensity gradient in the direction normal to the edge. Since the rotation of the tool between images is known (angular resolution, α), these points can be used to generate a point cloud representing the cutting tool. The result is shown in Figure 4.

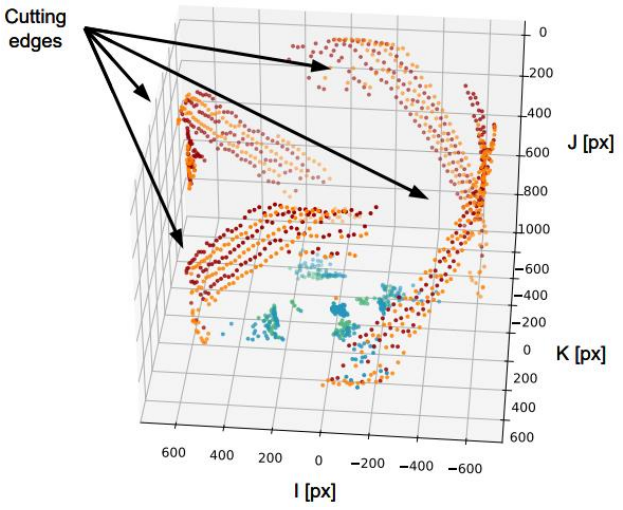

Figure 4. Preliminary 3D reconstruction of the flat endmill shown in Figure 2a at pixel-level.

However, to facilitate tool presetting and surface prediction, geometric data finer than the image scale is needed. This requires calibration of the camera and the implementation of an edge detection algorithm and a sub-pixel interpolation method. A multitude of techniques exist in this field, with different sensitivities and accuracies.

A common method is dictionary-based sub-pixel edge detection, where local image neighbourhoods are matched against preexisting edge profiles with known sub-pixel offsets. This method is often used in high-precision vision applications with computationally generated reference edge profiles. The main pitfall of this method is that the reference profiles are created based on assumptions regarding the optics and generally do not capture, e.g. non-uniformities in the illumination or lens imperfections.

To circumvent these limitations, the prototype system exploits the CNC machine's high-precision movements to generate a set of true reference profiles that represent the unique characteristics of the optical components.

With the camera aligned with the machine axes, the sphere is initially swept in the positive Y direction across the field of view at a constant feed (0.9 mm min^{-1}). The camera captures this motion at 150 Hz, creating a dataset of the sensor's response to right-facing edges (dark→light, left→right as seen by the camera) in 100 nm steps. This process is illustrated in Figure 5. Repeating the above by sweeping the sphere in the negative Y direction, as well as the negative Z direction, builds a full dictionary of the system's response to all edges around the perimeter of spindle-mounted objects. The proposed method encodes lens aberrations, illumination gradients, and scattering directly into the dictionary, eliminating model-dependent errors.

During post-processing of the tool data, the edge profiles are compared with the profile dictionary generated from the sphere's motion. The comparison is performed according to Equation 3 (cosine similarity). Where $V_{I.tool}$ is a 1D vector containing the intensity across the edge profile of the measured tool in a given pixel row or column, and $V_{I.reference}$ is the library of edge profiles for that row or column.

Figure 6 shows the edge profile over the left-facing edge of a cutting tool (black) overlaid with the most similar edge profile acquired during the passing of the sphere (blue). The index of the most similar profile, together with the known spacing of the reference profiles (100 nm), is then used to back-calculate the edge position. The conversion assumes constant feed during the generation of the reference profiles.

$$\text{Similarity} = \frac{V_{I.tool} \cdot V_{I.reference}}{\|V_{I.tool}\| \|V_{I.reference}\|} \quad (3)$$

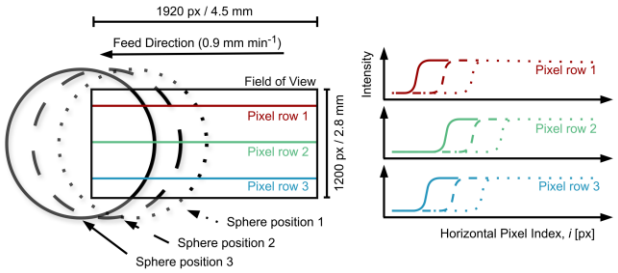

Figure 5. Illustration of the on-machine camera calibration process during creation of the right-facing edge dictionary. The horizontal intensity profiles, shown here for three arbitrary rows at three time steps, are extracted and used as reference profiles. (The size of the sphere is not to scale)

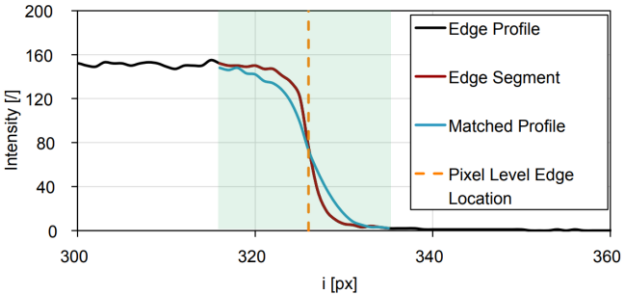

Figure 6. Intensity profile across the left edge of a cutting tool overlaid with the most similar profile (determined according to Equation 3) from the calibration process.

This method improves the system's edge localisation precision, yielding finer measurements in the radial direction of the tool and of tool length. However, on its own, the proposed approach cannot improve the measurement point density along the cutting edges, which remains constrained to the image scale of 2.3 µm px^{-1}. The development of a method to increase axial measurement resolution is left for future work.

2.5 Artefact measurement

Figure 7 shows the edge detection process applied to 400 images captured of a calibrated artefact with a square cross-section (Figure 2b) rotating at 6000 rpm. The left-facing edge profiles, 0.261 mm from the bottom surface in each image, were compared to the dictionary and converted to distances from the spindle axis in millimetres.

As Figure 7 shows, two full revolutions of the square bar were captured. The runout of the rotating artefact is clearly visible, as the difference between the longest and the shortest edge. The plot is overlaid with the cosine similarity (Equation 3), whose peaks coincide with those in the distance from the spindle axis. This should be the case because the edges will be most in focus (i.e., better agreement between the dictionary data and the instantaneous edge profile) when one of the diagonals of the square is aligned with the focal plane.

Applying this edge detection process to all pixel rows and columns, and assuming a constant spindle speed during the measurement, will enable the generation of a 3D point cloud visualising the edge geometry. The reconstruction will have a measurement resolution determined by the 100 nm dictionary spacing and an axial resolution constrained by the image scale, appearing similar to Figure 4.

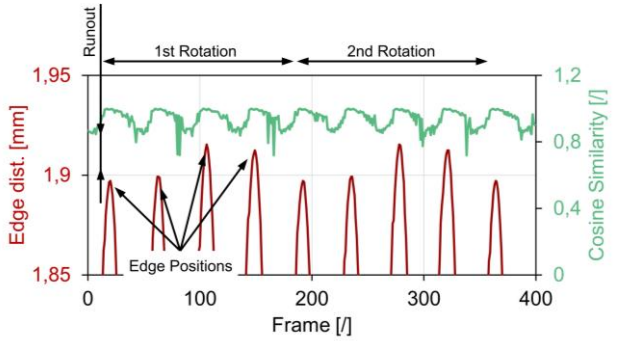

Figure 7. Post-processing of the left-facing edges from images of the square bar from Figure 2b.

3. System Evaluation

The metrological performance of the prototype system was assessed by characterising the edge position and runout of the square bar shown in Figure 2b at an axial position 0.261 mm from its bottom face. Reference values were obtained from prior

artefact calibration [5], though it should be noted that the artefact was calibrated off-machine, meaning that clamping errors during mounting in the spindle will have affected the accuracy of the reference data.

All measurements were performed after a 30-minute thermal stabilisation period with the spindle running at the measurement speed (6000 rpm). In accordance with ISO 15530 part-3 [6], twenty repeated measurements were used to establish the system's repeatability. Between measurements, the spindle was moved to the top of its Z-axis range and returned to the measurement position.

Table 1 summarises the results. The largest edge radial distance was recorded at 1.9151 mm, with a repeatability of 0.074 µm. The runout, calculated as the difference between the largest and smallest edge radii, came to a mean of 24.081 µm, with a repeatability of 0.178 µm.

Figure 8 shows the average of the measured distances of the four edges from the spindle axis as measured by the system over the 20 trials, compared to the reference measurements from [5].

Following ISO 15530 part-3 [6] and the method proposed in [5], the expanded measurement uncertainty was evaluated as U_M = 9.8 µm (k=2, 95.45 % confidence interval). This value is obtained by calculating the uncertainty for each individual artefact edge and taking the largest one. As per the standard, the uncertainty accounts for the random and systematic errors summarised in Equation 4.

$$U_M = k\sqrt{{u_{cal}}^2 + {u_b}^2 + {u_p}^2 + {u_w}^2} \quad (4)$$

Here, u_{cal} is the standard uncertainty of the square artefact of 0.74 µm [5], u_b is the systematic error obtained as the difference between the average measurement and the reference value, $u_p = s/\sqrt{n}$ (where s is the standard deviation across repeated measurements and n the number of samples) and u_w the workpiece variation during use. Because the measurements were carried out in immediate succession, it is assumed that there is no variation. The contribution of u_p is calculated to 0.04 µm. Systematic bias contributes 4.8 µm to the uncertainty and could, if corrected, drastically improve the system's performance. The main contributors to the bias are likely residual camera misalignment and rotation blur mismatch, since the dictionary is built from a non-rotating object with minimal motion blur, but the artefact is measured at high rpm.

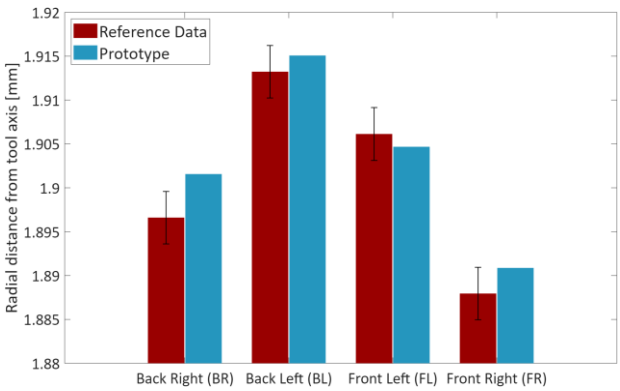

Figure 8. Cutting-edge radii measured by the prototype system (purple) compared to reference data from [5].

Table 1. Data from 20 repeated measurements of the square artefact, 0.261 mm from its bottom face.

Largest Radius		Runout	
Average	Repeatability	Average	Repeatability
1.9151 mm	0.074 µm	24.081 µm	0.178 µm

4. Conclusions and Future Work

This work demonstrates that generating an edge-response dictionary in situ from CNC-controlled motion of a geometrically undefined artefact offers a viable path towards high-resolution on-machine tool characterisation. The prototype system achieved an expanded measurement uncertainty of 9.8 µm for edge position measurements on a calibrated square bar, which could be reduced significantly upon correction of the 4.8 µm systematic bias. The system's repeatability is 0.074 µm over a set of twenty measurements.

The system would be suitable for industrial pre-setting applications, but will be expanded in the future to improve its performance in edge-profile characterisation for wear measurement in fine-finishing operations.

References

[1] F. G. Biondani and G. Bissacco, "Effect of cutting edge micro geometry on surface generation in ball end milling," *CIRP Annals*, vol. 68, no. 1, pp. 571–574, Jan. 2019, doi: 10.1016/j.cirp.2019.04.017.

[2] A. Shaheen, Ø. Svinning, I. Nedrehagen, and G. Bissacco, "On-machine high accuracy radial wear characterization of rotating milling tools using a camera-based system," *J Manuf Process*, vol. 157, pp. 62–77, Jan. 2026, doi: 10.1016/j.jmapro.2025.11.064.

[3] B. Denkena and D. Biermann, "Cutting edge geometries", doi: 10.1016/j.cirp.2014.05.009.

[4] W. Wang, W. Liu, Y. Zhang, Y. Liu, P. Zhang, and Z. Jia, "Precise measurement of geometric and physical quantities in cutting tools inspection and condition monitoring: A review," 2023, doi: 10.1016/j.cja.2023.08.011.

[5] A. Shaheen and G. Bissacco, "Metrological characterisation of tool pre-setting optical systems based on 2D imaging," *Measurement (Lond)*, vol. 228, Mar. 2024, doi: 10.1016/j.measurement.2024.114327.

[6] "ISO 15530-3:2011 - Geometrical product specifications (GPS) — Coordinate measuring machines (CMM): Technique for determining the uncertainty of measurement — Part 3: Use of calibrated workpieces or measurement standards." Accessed: Jan. 10, 2026. [Online]. Available: https://www.iso.org/standard/53627.html

euspen's 26th International Conference & Exhibition, Krakow, PL, June 2026
www.euspen.eu

Modeling and Quantification of Parameter-Induced Thermal Errors in a Hydrostatic Turntable System

Jun Zha[1,2], Changhui Ke[3], Lipu Song[1,2], Chengwei Kang[1,2]

[1]*School of Mechanical Engineering, Xi'an Jiaotong University, Xi'an 710049, China*
[2]*Xi'an Jiaotong University-Genertec Joint Research Institute, Xi'an 710049, China*
[3]*School of Mechanical and Precision Instrument Engineering, Xi'an University of Technology, Xi'an 710048, China*

jun_zha@xjtu.edu.cn, chengwei.kang@xjtu.edu.cn

Abstract

Thermal errors in hydrostatic turntable systems are a primary impediment to achieving sub-micron accuracy in ultra-precision machine tools, directly impacting workpiece dimensional stability. These errors are predominantly caused by heat generated from the oil pump and viscous friction within the bearing's oil film during operation. This research aims to systematically model and quantify the influence of key operating parameters, specifically oil supply pressure and oil film gap, on the system's thermo-mechanical behavior.

The methodology is centered on a thermo-mechanical coupling model developed to simulate the system's response. The process began by establishing a detailed temperature field model through a thermal balance calculation, which quantified the heat generated by system components against heat dissipated. This thermal analysis was then coupled with a structural model, using the calculated temperature distribution as a thermal load to accurately predict the resulting deformation and strain. A parametric study was performed using this model to analyze the turntable's behavior under a range of different service conditions.

The results effectively map the internal temperature and total deformation fields during turntable operation, establishing a direct monotonic correlation between rotation speed, oil supply pressure, oil film gap, and the resulting thermal error. Analysis of the internal temperature confirmed a pronounced thermal stratification: the highest temperature occurs at the oil sealing surface, followed by the mandrel, and the frame. The temperature exhibits a clear gradient distribution, decreasing from the axis end outward. Total deformation is maximized at the motor, minimized at the base, and generally increases toward the mandrel end. The study identified that while elevated rotation speed leads to a greater temperature rise, a larger oil film gap is beneficial for decelerating this rise. Significantly, oil supply pressure was determined to be the more dominant factor governing both temperature increase and thermal deformation compared to the oil film gap and the rotation speed. This work provides a quantitative framework for optimizing operational parameters to minimize thermal errors, thereby contributing valuable theoretical insights for the design and control of high-precision hydrostatic turntable systems.

Hydrostatic Turntable; Thermal Error; Thermo-mechanical Coupling Model; Parametric Analysis

1. Introduction

Thermal error represents the primary obstacle preventing hydrostatic rotary table systems from achieving sub-micron accuracy in ultra-precision machine tools, directly impacting workpiece dimensional stability[1]. The thermal error of hydrostatic rotary table refers to that the heat energy generated by bearing friction and oil pump operation during the working process of the rotary table will increase the temperature of lubricating oil, spindle and bearing seat in the bearing clearance through heat transfer, resulting in thermal error issues such as intensified thermal deformation and reduced viscosity of lubricating medium, which seriously affects the machining accuracy of machine tools[2][3]. Research indicates that thermal error accounts for 40% to 70% of the total error in precision machining, representing the single largest and most challenging error source to suppress [4]. Consequently, analyzing and investigating the thermal error of hydrostatic turntables is of considerable significance for developing effective thermal error suppression methods and enhancing the machining accuracy of machine tools. Thermal error analysis of hydrostatic rotary table operation continues to be a central research hotspot[5], with existing work, such as the mathematical model for fan-shaped oil pads by Bao et al, providing foundational insights[6].

Despite these efforts, current research predominantly relies on mathematical modeling and simulation to explore the effects of single parameters (e.g., oil film pressure or clearance). Comprehensive, comparative studies that analyze the combined influence of multiple operational parameters across various working conditions are still insufficient. This study aims to bridge this gap by systematically modeling and quantifying the integrated impact of essential operating variables, specifically oil supply pressure, oil film clearance, and rotation speed, on the system's thermal error. We achieve this by establishing a refined thermal error model for the hydrostatic turntable, investigating the internal thermal error distribution, and quantifying the influence of different working condition parameters on the turntable's thermal performance.

2. Thermal error analysis of the hydrostatic turntable

2.1. Hydrostatic turntable structure

The hydrostatic turntable system examined in this paper is illustrated in Figure 1, and primarily comprises the table, the hydrostatic bearing, and the frame. The hydrostatic bearing itself is composed of an inner radial bearing and a thrust bearing, which are symmetrically distributed along the axial direction. In operation, an external oil supply system pressurizes the bearing recess to establish a lubricating oil film. This film allows the mandrel to float and maintain a small, controlled gap, thereby achieving a state of complete liquid friction. Subsequently, the built-in motor housed within the frame drives the bearing and the workbench to rotate axially.

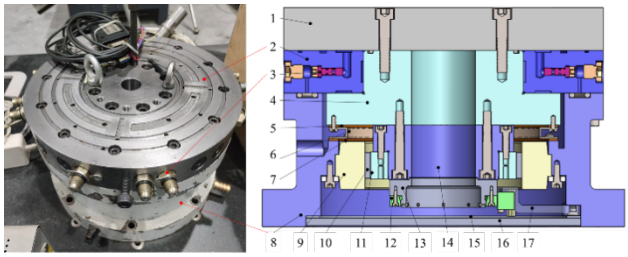

1-Tabletop; 2-Hydrostatic bearing; 3-Annular slit restrictors; 4-Bearing rotor; 5-Upper seal ring; 6-Oil blocking plate; 7-Lower seal ring; 8-Base; 9-Motor stator; 10-Motor armature; 11-Motor rotor; 12-Reading head; 13-Fixed shaft; 14-Mandrel; 15-Rubber pad; 16-Bottom plate; 17-Reading headstock

Figure 1. Hydrostatic turntable structure diagram

2.2. Thermal error model of hydrostatic turntable

Under the service conditions of the hydrostatic turntable, the temperature rise primarily arises from bearing friction and other external environmental heat sources. Among these, because the heat generated by external environmental sources and other secondary sources is much smaller than the heat generated by the bearing, it can be reasonably neglected. This simplifies the mixed temperature field model, which is typically affected by multiple variables and complex fields, into a single temperature field model dominated by bearing friction. The temperature field of the turntable is then modeled by calculating the heat generation of the radial bearing and the thrust bearing.

When lubricating oil flows inside the hydrostatic bearing, it may exhibit laminar flow, turbulent flow, or a transitional state between the two. The flow field characteristics vary with the flow state, and accordingly, different calculation methods are required. Therefore, to establish a temperature field model, it is necessary to first determine the fluid flow state using the Reynolds number formula shown in Eq. (1). If the calculated Reynolds number is less than 2000, the fluid is considered to be in laminar flow. If it exceeds 4000, the fluid is considered turbulent. When the Reynolds number lies between 2000 and 4000, the fluid is assumed to be in the transitional regime. In this study, the flow velocity is assumed to be 20 m/s, yielding a Reynolds number of 12.5, which is far below 2000. Therefore, the fluid inside the bearing is considered to be in laminar flow, and static performance calculations are applicable.

$$\mathrm{Re}=\rho v_l l/\mu \tag{1}$$

Where ρ is the density of the hydraulic oil, v_l is the fluid velocity, l is the equivalent radius through the interface, and μ is the dynamic viscosity of the hydraulic oil.

After determining the flow state of the lubricating oil inside the bearing, to establish the temperature field model of the bearing, the following isothermal assumptions need to be made :

Both the pump power and friction power are converted into thermal energy, while other less influential heat sources are neglected. It is assumed that all resulting heat is absorbed entirely by the lubricating oil within the hydrostatic bearing system.

Thermodynamic properties, such as the convective heat transfer coefficients of the lubricating medium and the surrounding air, are assumed to remain constant and independent of temperature. The temperature rise of the hydraulic oil due to internal friction power adheres to the law of conservation of energy.

The temperature rise of the bearing is primarily attributed to the liquid friction power N_f and the oil pump power N_p. N_f represents the power loss due to liquid friction during the relative sliding motion of the mandrel and is dependent on the rotational speed. N_p represents the power consumption caused by the laminar flow of the lubricating oil film driven by the oil supply system. Since the radial velocity of the bearing bush and the linear velocity of the thrust recess vary with position, N_f must be calculated separately for each component. N_p denotes the power consumption of the oil supply system. The detailed calculation is presented in Eq. (2) and Eq. (3).

$$\begin{cases} N_{fj} = n \cdot \mu \cdot v^2 \left(\dfrac{A_1}{h_0} + \dfrac{A_2}{h_0 + z_1} \right) \\ N_p = p_s \cdot n \cdot q \\ \Delta T = \dfrac{N_f + N_p}{c \rho q} \end{cases} \tag{2}$$

$$\begin{cases} N_{fz} = n \sum_{i=1}^{5} P_{zi} \\ P_{z1} = P_{z2} = \int_{R_1}^{R_4} \mu \left(\dfrac{2\pi n R}{60} \right)^2 \dfrac{R\alpha_1}{h_0} dR \\ P_{z3} = \int_{R_3}^{R_4} \mu \left(\dfrac{2\pi n R}{60} \right)^2 \dfrac{R\alpha_2}{h_0} dR \\ P_{z4} = \int_{R_2}^{R_3} \mu \left(\dfrac{2\pi n R}{60} \right)^2 \dfrac{R\alpha_2}{h_0 + z_1} dR \\ P_{z5} = \int_{R_1}^{R_2} \mu \left(\dfrac{2\pi n R}{60} \right)^2 \dfrac{R\alpha_2}{h_0} dR \end{cases} \tag{3}$$

Where N_{fj} is the liquid friction power of the radial bearing, n is the number of oil recesses, v is the rotational speed, A_1 and A_2 represent the areas of the hydraulic support surface and the recess of a single recess, respectively. h_0 is the oil film thickness, z_1 is the recess depth, p_s is the oil supply pressure, q is the flow rate of a single oil recess, ΔT is the temperature rise of the bearing bush, and c is the specific heat capacity of the lubricating oil at constant pressure, N_{fz} is the thrust bearing liquid friction power, P_{zi} is the liquid friction power of each region of thrust bearing recess.

Once the temperature rise of the bearing is obtained, the corresponding thermal deformation can be calculated based on the theory of thermal expansion using Eq. (4):

$$\Delta L = \alpha L_0 \Delta T \tag{4}$$

where ΔL is the linear thermal deformation of the object, α is the coefficient of thermal expansion, and L_0 is the initial length.

3. Thermal error finite element analysis of the hydrostatic turntable

To investigate the temperature and deformation distributions of the hydrostatic turntable under various operating conditions, a steady-state thermal-structural coupling simulation was performed using ANSYS. The meshed model is presented in Figure 2. Different components of the turntable were meshed using separate techniques, specifically sweeping, multi-region, and automatic methods, to ensure mesh quality. Furthermore, four layers of surface meshing were applied to individual thin-walled parts. The global element size was set to 5 mm, with key regions such as the bearing oil sealing surfaces and the oil cavities refined to 2 mm. This strategy resulted in a final mesh comprising approximately 1.5 million elements, with an element quality metric (such as element mass or orthogonal quality) of 0.8, which fully satisfies the established simulation requirements.

Figure 2. The turntable model after meshing

The steady-state thermal boundary conditions were defined as summarized in Table 1. The thermal power values, N_f and N_p, are subsequently applied as thermal loads in the form of heat flux to the oil seal surfaces of the radial bearing and thrust bearing, respectively. Concurrently, the appropriate material properties were assigned to the various components of the turntable. Thermal convection was incorporated at all interfaces between the turntable and the ambient, while the influence of thermal radiation was deemed negligible and therefore ignored. To ensure the accuracy and reliability of the numerical results, the automatic solution mode was selected for the solver.

Table 1. Steady-state thermal boundary conditions

Boundary conditions	**Values**
Oil inlet pressure/MPa	2
Recess pressure/MPa	1
Oil outlet pressure/MPa	0
Heat flow of Radial bearing/W	10.21
Heat flow of thrust bearing/W	19.95
Ambient temperature/℃	22

The simulated distributions of the temperature field and total deformation under varied operating conditions are illustrated in Figure 3. Analysis of the results yields the following:

Obvious thermal stratification was observed. Taking working condition (b) as an example, the highest temperature of 24.26 °C was recorded on the recess sealing surface, followed by the mandrel, while the base registered the lowest temperature at 20.47 °C. The internal temperature also follows a clear gradient, escalating along the circumferential path from the turntable's periphery towards the axis end.

Total deformation exhibits a monotonic increase from the outer edge towards the mandrel end. The turntable base displays the minimum deformation, with the maximum deformation concentrated around the motor bearing assembly. Taking mode (b) as an example, the minimum deformation of 0.62 μm occurs at the base, while the maximum deformation is observed at the motor bearing assembly, reaching 5.58 μm.

Quantitative comparison of the four working conditions shows that a 1 °C rise in temperature requires either a 13 rpm increase in speed or a 0.32 MPa increase in supply pressure. Likewise, a 1 μm increase in total bearing deformation necessitates a 10 rpm higher speed, or a 0.23 MPa higher supply pressure. It is evident that temperature rise and total deformation are positively correlated with rotational speed and supply pressure, but negatively correlated with oil film gap.

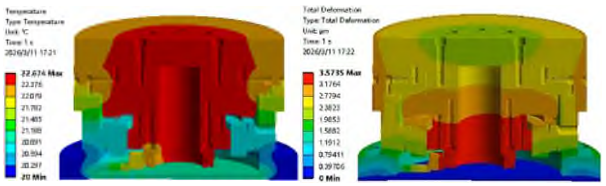

a) Mode 1(v=30rpm, h=20μm, p_s=2Mpa)

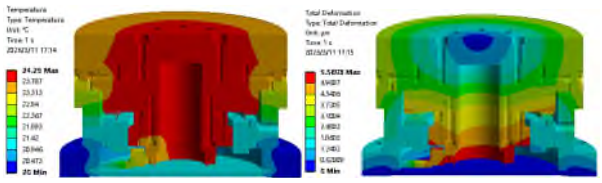

b) Mode 2(v=50rpm, h=20μm, p_s=2Mpa)

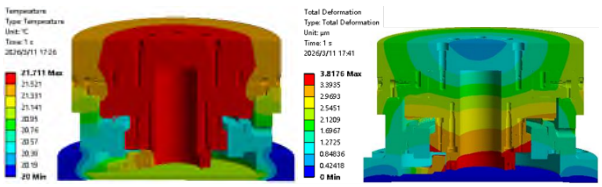

c) Mode 3(v=30rpm, h=40μm, p_s=2Mpa)

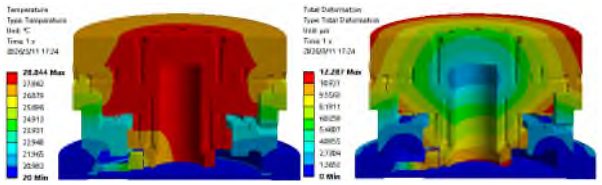

d) Mode 3(v=30rpm, h=20μm, p_s=4Mpa)

Figure 3. The temperature field and total deformation distribution of the turntable under different working conditions

4. Conclusion

To realize a quantitative improvement in the accuracy of hydrostatic turntable systems, this study successfully conducted a detailed thermal error calculation and thermo-solid coupling analysis on the system's key components. This systematic approach effectively modeled and quantified the impact of key operating parameters on the thermal error. The following main results were obtained:

A clear internal temperature stratification was identified (oil seal surface > mandrel > base) alongside a distinct axial temperature gradient.

The total deformation profile reveals a significant increase from the periphery towards the mandrel end, with the minimum

deformation located at the base and the maximum at the motor bearing.

The thermal performance is influenced differently by rotational speed, oil supply pressure, and oil film gap, with oil supply pressure having a markedly stronger effect on temperature rise and total deformation than speed and oil film gap. Overall, the quantitative results presented in this paper provide a valuable new framework for the thermal error study of hydrostatic turntables, paving the way for targeted design and control strategies to enhance the system's stability and overall reliability.

Fundings

The authors gratefully acknowledge financial support from National Science and Technology Major Project (2026ZD0719001), National Natural Science Foundation of China (52575597), Genertec Group Science and Technology Innovation Project (G2025040-XA)

References

[1]Zha J, Cheng K, Xue F, Wu D X, and Liu X 2024. *Tribol*. Int. **200** 110060.
[2]Lang S, Zorzini M, Scholze S, Mayr J, and Bambach M 2025 *J. Manuf. Sys.* **80** 243-257.
[3]Wang J L, Ke C H, Hu K Y, and Zha J 2025. *Machines*, **13**(7), 598-598.
[4]Zha J, Cheng K, Wu D X, Zhang H J, and Xue F 2026. *Precis. Eng*. **97** 1060-1086.
[5]Liu T, Bei Z, Wang H, Duan R, Chen F and Zhang J 2025 *Appl. Therm. Eng.* **266** 125618-125618.
[6]Bao J, Liu X, Jiao J, Liu Z, Zhang C, Wang M, and Lin Z 2026 *Int. J. Heat. Mass. Tran.* **256** 128062-128062.

euspen's 26th International Conference & Exhibition, Krakow, PL, June 2026
www.euspen.eu

Simulation study on viscous friction reduction effect of textured oil-lubricated hydrostatic bearings

Dmytro Fedorynenko[1], Naofumi Ohnishi[1], and Yohichi Nakao[2]

[1] *Department of Aerospace Engineering, Tohoku University, Sendai, Japan*

[2] *Department of Mechanical Engineering, Kanagawa University, Yokohama, Japan* [1]

Correspondence: fedorynenko.dmytro.b3@tohoku.ac.jp

Abstract

In this study, the efficiency of a grinding spindle with textured oil-lubricated journal hydrostatic bearings was investigated via simulation. The bearing lubrication properties were defined using CFD simulations in ANSYS Fluent. A new approach for CFD analysis of textured hydrostatic bearings has been proposed, which simplifies the bearing fluid domain by dividing it into several subdomains with predefined boundary conditions. Then, the influence of rectangular-shaped micro-geometric patterns on oil velocity, pressure distribution, and power losses in the bearing-flowing parts was investigated for both streamwise and transverse groove orientations. The physical mechanism of friction reduction is identified as lid-driven cavity vortex formation within the grooves, which partially decouples the moving wall shear from the bulk lubricant flow. Transverse grooves on the moving wall achieve up to 48% wall shear stress reduction on circumferential lands, significantly outperforming streamwise grooves (~33%). The impact on bearing stiffness is assessed and shown to be minimal and can be fully recovered by restrictor re-optimization. It is demonstrated that applying specific texturing to bearing surfaces results in a decrease (approximately 30-48%) in the average wall shear stress and viscous friction losses without compromising bearing performance.

Keywords: textured bearing, hydrostatic bearing, grinding spindle, friction reduction, power consumption, CFD simulation, vortex

1. Introduction

Green tribology is a new research field that aims to achieve carbon neutrality. One constantly evolving direction in green tribology is improving bearing performance by reducing friction and achieving lower power consumption.

Hydrostatic bearings are precision mechanical components that utilize externally pressurized fluid films to support loads without metal-to-metal contacts. However, viscous shear in the lubricant film results in power losses that can significantly impact the overall efficiency of the system [1].

In recent years, micro-texturing has attracted considerable attention as an effective method for improving tribological performance [2-3]. By introducing controlled micro-scale features on bearing surfaces, it is possible to modify local fluid dynamics and reduce friction while maintaining, or even enhancing, load-carrying capacity (LCC).

However, there is currently no general explanation of how surface texturing affects spindle bearing performance in precision machining, where shaft eccentricity is small or close to zero. In this paper, the effects of micro-texturing of bearing surfaces on reducing viscous friction are considered for simplified flat regions that model the lands of a hydrostatic journal bearing. This study identifies the dominant friction reduction mechanism as lid-driven cavity vortex formation within the grooves, evaluates both streamwise and transverse groove orientations, and assesses the impact of texturing on bearing stiffness and load-carrying capacity to ensure that friction reduction does not compromise bearing performance.

2. Methodology

2.1. Computational Domain and Boundary Conditions

A typical hydrostatic bearing land surface can be divided into two areas as depicted in Fig. 1(a). The journal bearing has four recesses arranged symmetrically on the casing surface, separated by narrow lands. Figure 1(c) shows a 3D view of the journal surface; Figure 1(a) presents the corresponding developed (unfolded) view, where the cylindrical surface is mapped onto a plane with the circumferential direction running horizontally and the axial direction running vertically. Accordingly, the bearing computation domain representing the sliding part was modelled using two fluid subdomains, one for the circumferential land (fluid domain 1) and one for the axial land (fluid domain 2), shown in Fig. 1. In the simulations, flat squared regions are considered as bearing surfaces, as presented by colored parts in Fig. 1(a).

The value of recess pressure p_r was used as the pressure inlet and outlet conditions for the fluid domain 1 as shown in Fig. 1(b). For fluid domain 2, the inlet pressure was defined as p_r, and the pressure outlet value was set to 0 as boundary conditions.

2.2 Texture Configurations

Four micro-texturing configurations were analysed in this study, as detailed in Table 1, for the streamwise and transverse directions of texture as shown in Fig. 2. In the streamwise orientation (0°), grooves are aligned parallel to the shaft sliding direction; in the transverse orientation (90°), grooves are perpendicular to it. 16 possible combinations of the four configurations were analysed for the fluid domains 1 and 2 in the

streamwise direction. The same approach was then applied to the transverse direction, yielding 32 structural combinations.

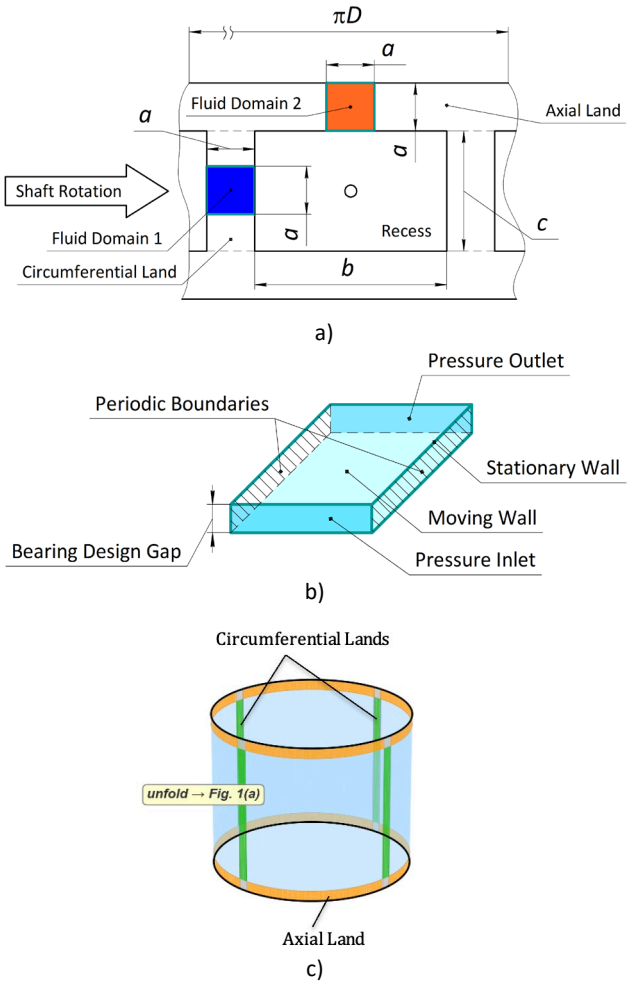

Figure 1. Bearing computation domains (a), boundary conditions (b), and (c) is 3D view of the journal bearing surface with four pockets (blue), circumferential lands (green), and axial lands (orange)

Table 1. Bearing surface configurations

Configuration	Stationary wall	Moving wall	Groove orientation
Smooth	smooth	smooth	-
Texture 1	textured	smooth	0°/90°
Texture 2	textured	textured	0°/90°
Texture 3	smooth	textured	0°/90°

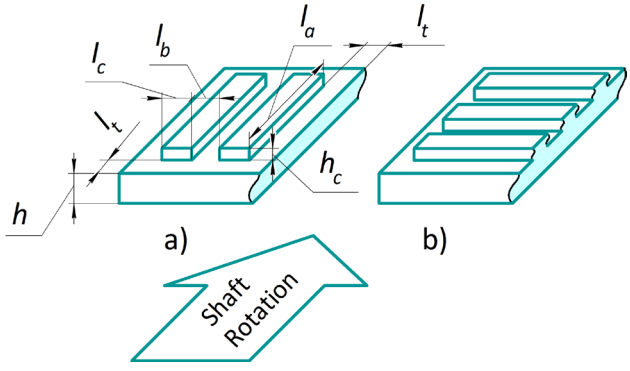

Figure 2. Fluid domain for streamwise (a) and transverse (b) directions of texture

The geometry of the transverse texture is identical to that of the streamwise texture, but rotated by 90°. In this study, the shaft rotation is aligned with the direction of the moving wall translational motion.

2.3 CFD Simulation Setup

Numerical simulations were performed using ANSYS Fluent with the following settings: steady-state, incompressible flow, no-slip boundary conditions at solid surfaces, and an isothermal assumption.

The thickness h of the bearing design gap was covered by 10 cells. The mesh resolution was refined near texture features using five boundary layers with a thickness of 0.5 μm each to capture flow gradients accurately. Grid independence was verified through mesh sensitivity studies.

The Reynolds number based on gap height is $Re = \rho U h/\eta$ = 51.5, confirming that the flow is well within the laminar regime ($Re \ll 2000$) and the steady-state assumption is valid. In the above formula ρ and η are the density and dynamic viscosity of fluid, respectively; U – journal sliding velocity. The groove-scale Reynolds number $Re_groove = \rho U h_c/\eta$ = 20.6 is even smaller, ensuring that the cavity vortex remains laminar and steady. h_c denotes the groove depth (h_c =0.01 mm).

2.4 Performance Metrics

Total losses L in a journal hydrostatic bearing were defined as

$$L = \frac{p_s Q_m}{\rho} + U\left(\tau_{av} A_{sl} + n_r \frac{\eta A_r U}{h+h_r}\right), \quad (1)$$

where p_s – supply pressure; Q_m – mass flow rate through bearing axial lands; τ_{av} – area-averaged shear stress on the bearing circumferential and axial lands; A_{sl} and A_r – bearing lands area and recess area, respectively; n_r – number of recesses; h_r – recess depth.

The ratio of textured wall shear stress τ to smooth wall shear stress τ_s for Couette flow

$$\frac{\tau}{\tau_s} = \alpha(1-\varphi) + \frac{\varphi k h}{h+h_c}, \quad (2)$$

where α – inter-groove land shear correction factor, $\alpha = \tau_l/\tau_s$; τ_l – shear stress on flat inter-groove lands on a textured surface; φ – texture area ratio, $\varphi = l_c/(l_c + l_b)$; k – normalized vortex transmission factor representing the fraction of main-flow shear transmitted through the cavity vortex to the groove floor,

$$k = \frac{\tau_g}{\tau_l} \cdot \frac{h + h_c}{h},$$

τ_g – shear stress on the groove floor; l_c – groove width; l_b – width of the inter-groove land.

The groove aspect ratio A_g for a textured surface

$$A_g = \frac{l_c}{h_c}.$$

Pressure, velocity, wall shear stress distributions, and mass flow rate were derived using ANSYS Fluent simulation.

3. Results and Discussion

The main parameters of the tested simplified journal hydrostatic bearing model were as follows: p_s=2 MPa; p_r =1 Mpa; lubricant is oil VG5 with ρ=820 kg/m^3 and η =0.007 Pa·s taken at 20°C; U = 17.58 m/s; h = 0.025 mm; recess depth h_r =3 mm; a=5 mm; b×c – 75×65 mm. The geometric sizes of the studied microtexture were taken as $l_c = l_b = h$ = 0.025 mm; l_t =0.2 mm and l_a =4.6 mm.

Figure 3 presents the area-averaged wall shear stress and the total mass flow rate through two bearing axial lands for fluid domain 2 in the streamwise direction for all four cases.

All three textured configurations demonstrate significant friction reduction compared to the smooth reference. In particular, texture 2 yielded the greatest reduction in wall shear stress, approximately 38%; conversely, it exhibited the largest increase in mass flow rate, rising by 29%.

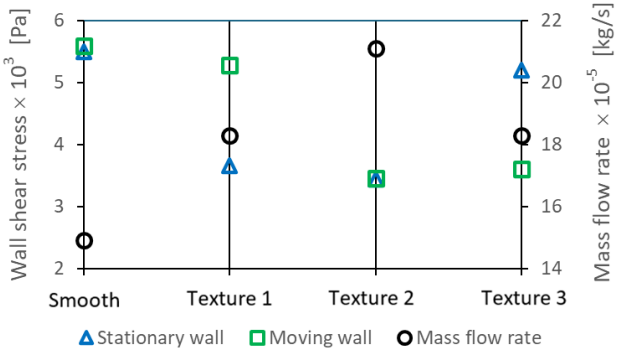

Figure 3. Comparison of wall shear stress and mass flow rate for fluid domain 2 in streamwise direction

Figure 4 shows the area-averaged wall shear stress for fluid domains 1 and 2 in the transverse direction for 3 cases.

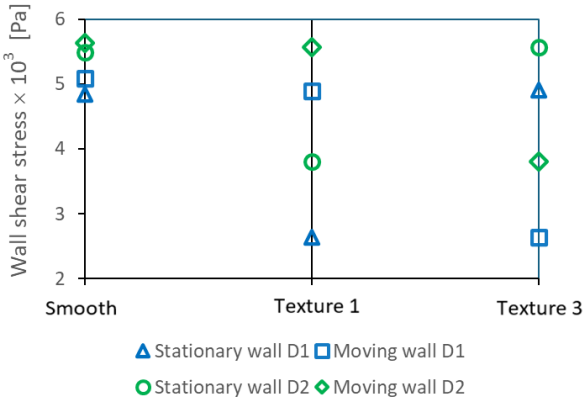

Figure 4. Comparison of wall shear stress for domain 1 (D1) and domain 2 (D2) in transverse direction

Notably, on the circumferential land (domain 1, pure Couette flow), transverse Texture 3 achieves a 48.3% wall shear stress reduction on the moving wall - significantly outperforming its streamwise counterpart (33.1%). This orientation dependence is a key finding discussed in Section 3.3.

3.2. Total Power Losses

Figure 5 illustrates power losses estimation for streamwise direction calculated using Eq. 1. It shows that Textures 2 and 3 achieved the highest reduction in total power losses for the streamwise orientation, lowering them by approximately 30% compared to the smooth case.

Figure 6 indicates total, pumping, and friction power losses, which are shown separately for domain 1 (D1) and domain 2 (D2) for the transverse direction. The transverse alignment of microgrooves on a moving wall (texture 3) achieves a 27.7% total loss reduction. This is because the circumferential lands (domain D1), which benefit most from transverse grooves, contribute significantly to total friction.

Combining transverse grooves on D1 with streamwise grooves on D2 yields the optimal result (Fig. 7): a 32.2% total loss reduction from 509 W to 345 W.

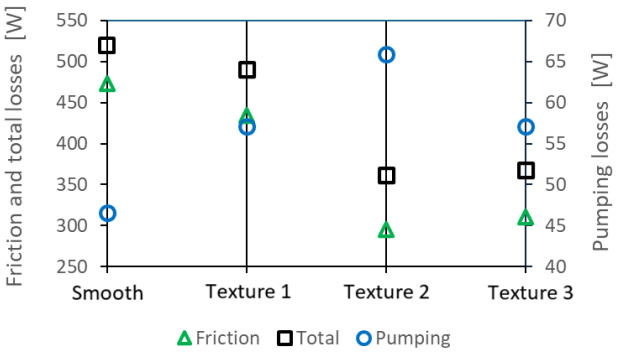

Figure 5. Power losses estimation for streamwise direction of texture

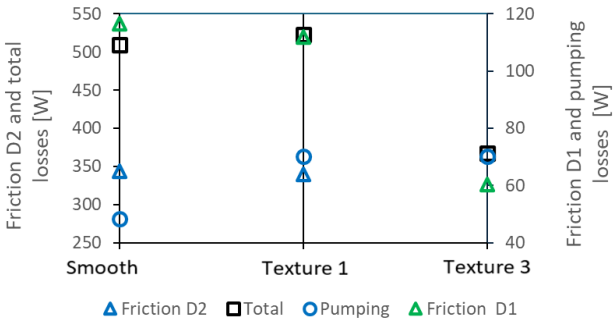

Figure 6. Power losses estimation for transverse direction of texture

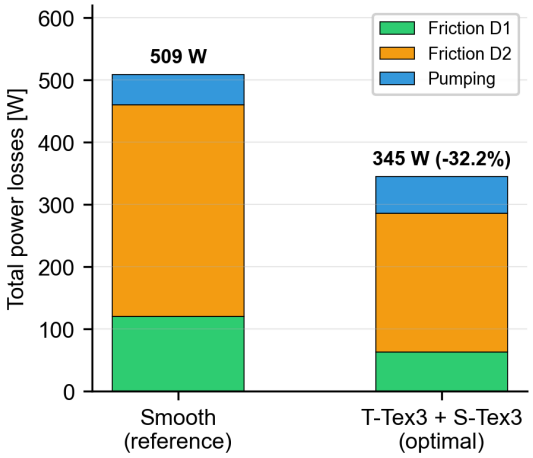

Figure 7. Full-bearing power losses: smooth reference vs optimal configuration (transverse Texture 3 on D1 + streamwise Texture 3 on D2)

3.3. Physical Mechanism of Friction Reduction

The physical mechanism underlying the observed friction reduction is depicted schematically in Fig. 8. When lubricant flows over a surface groove, the moving wall drags fluid into the cavity, generating a recirculating lid-driven vortex. This vortex partially decouples the high-velocity moving wall from the bulk flow in the bearing gap, effectively reducing the shear stress transmitted to the groove floor. Flow separation occurs at the leading edge and reattachment at the trailing edge of each groove, confining the recirculation within the cavity.

It was established that vortex factor k depends strongly on groove orientation, as summarised in Table 2. In the table, τ/τ_s (model) denotes the friction ratio predicted by the analytical formula given in Eq. 2, while τ/τ_s (CFD) is the ratio obtained directly from the CFD simulation results.

On the circumferential land (D1, pure Couette flow), transverse grooves achieve $k = 0.15$ versus $k = 0.33$ for streamwise, explaining the large orientation dependence observed in Section 3.1. The physical origin lies in the vortex topology: in transverse grooves, the main flow crosses the

groove perpendicularly, generating a stable 2D recirculation whose axis is parallel to the groove length. This lid-driven cavity flow effectively seals the groove interior from the high-momentum main stream. In streamwise grooves, the flow enters the groove along its length, producing a weaker helical secondary flow that transmits more shear to the groove floor.

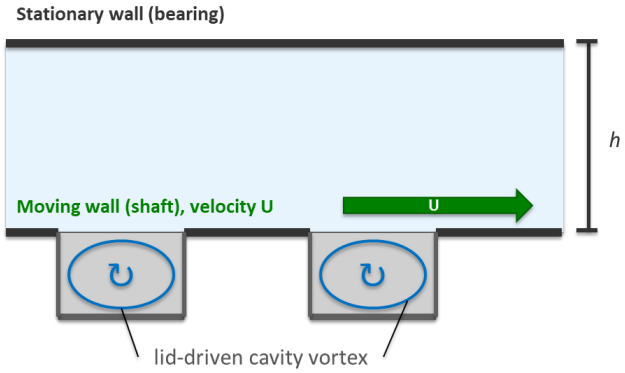

Figure 8. Groove cross-section schematic with lid-driven cavity vortex

Table 2. Vortex transmission factor k and friction reduction by orientation and domain

Orientation	Domain	k	τ/τ_s (model)	τ/τ_s (CFD)
Transverse	D1 (Couette)	0.15	0.52	0.52
Streamwise	D1 (Couette)	0.33	0.71	0.67
Transverse	D2 (Couette+ Poiseuille)	0.35	—	0.68
Streamwise	D2 (Couette+ Poiseuille)	0.33	—	0.64

On the axial land (D2), where Poiseuille flow coexists with Couette flow, the transverse advantage diminishes ($k \approx 0.35$) because the pressure-driven component is largely unaffected by transverse grooves. The groove aspect ratio $A_g = 2.5$ supports a single, well-defined vortex; for $A_g \ll 1$ multiple vortices may appear, while for $A_g \gg 1$ the vortex weakens, and direct shear increases k.

A critical concern is whether friction reduction compromises bearing stiffness or LCC. Surface texturing can increase the effective flow conductance of axial lands, leading to higher leakage flow rates. For a capillary-restricted hydrostatic bearing operating at the optimal restrictor ratio $\beta = 0.5$ [1], the stiffness K is proportional to $4\beta(1-\beta)$. When texturing increases the flow conductance by a factor r_Q, the restrictor ratio shifts to $\beta_{tex} = 1/(1+r_Q)$, affecting both LCC and stiffness. Table 3 summarizes these effects.

Table 3. Impact of texturing on bearing performance

Configuration (D1 + D2)	ΔQ_m [%]	ΔLCC [%]	ΔK [%]	ΔL [%]
Smooth + Smooth	0	0	0	reference
S-Tex3 + S-Tex3	+22.8	-10.2	-1.0	-28.7
T-Tex3 + Smooth	0	0	0	-11.1
T-Tex3 + S-Tex3	+22.8	-10.2	-1.0	-32.2
T-Tex3 + T-Tex3	+45.5	-18.5	-3.4	-27.7

Note: ΔQ_m – change in mass flow rate through D2 axial lands compared to the smooth reference; ΔLCC – change in load-carrying capacity; ΔK – change in bearing film stiffness; ΔL – change in total power losses; T and S – denote transverse and streamwise orientations, respectively.

Furthermore, the leakage increase caused by texturing can be compensated by re-optimizing the capillary restrictor. When texturing increases the bearing land conductance (lowering land resistance), the restrictor resistance must decrease by the same factor to restore $\beta = 0.5$. This requires increasing the capillary diameter. For example, for the optimal configuration (Tranverse-Texture 3 and Streamwise-Texture 3), the flow conductivity increases by $r_Q = 22.8\%$. The required increase in diameter is 5.3%. This simple geometric modification fully recovers the 10.2% LCC loss and restores bearing stiffness to its maximum value, while preserving the entire 32.2% friction reduction.

The cavity vortex dynamics that reduce friction are governed by local groove geometry and are independent of restrictor settings. Consequently, restrictor re-optimization and texture design can be treated as independent, sequential steps.

For precision spindles operating at near-zero eccentricity, uniform texturing across all lands preserves circumferential symmetry. This prevents the introduction of new error motion sources, ensuring that neither static stiffness nor dynamic precision is compromised.

4. Summary

This study evaluated the efficacy of micro-texturing in mitigating viscous friction within the hydrostatic journal bearings of precision grinding spindles using a simplified model. The analysis compares four distinct topologies: a smooth reference surface and three textured patterns varied by their orientation to the flow stream.

The physical mechanism of friction reduction was identified as lid-driven cavity vortex formation in the surface grooves. The vortex partially decouples the moving wall from the bulk lubricant, reducing the effective wall shear stress. The vortex transmission factor $k = 0.15$ for transverse grooves versus $k = 0.33$ for streamwise grooves explains the strong orientation dependence of friction reduction.

Among the tested patterns, transverse Texture 3 on circumferential lands combined with streamwise Texture 3 on axial lands achieves the optimal balance, reducing total power losses by 32.2% with only 1.0% stiffness reduction. After restrictor re-optimization, the LCC and stiffness losses can be fully recovered at zero cost to friction savings.

When balancing performance with manufacturing costs, Texture 3 emerges as the most suitable solution; it necessitates texturing of only the shaft journal surface while resulting in only 1.8% higher power losses than Texture 2.

Future work is planned to experimentally validate these findings and account for cavitation and viscous heating effects.

This research is supported by the Machine Tool Engineering Foundation and the Institute of Fluid Science of Tohoku University.

References

[1] Rowe W.B. 2012 Hydrostatic, aerostatic and hybrid bearing design. (Waltham: Butterworth-Heinemann Press).
[2] Etsion I. 2005 State of the art in laser surface texturing. J. Tribol. **127(1)** 248–253.
[3] Gropper D., Wang L., Harvey T.J. 2016 Hydrodynamic lubrication of textured surfaces: A review of modelling techniques and key findings. Tribol. Int. **94** 509–529.

euspen's 26th International Conference & Exhibition, Krakow, PL, June 2026
www.euspen.eu

A new backlight imaging method for in-machine measurement of flank wear

Lukas Jansen[1], Knut Sørby[1]

[1]*Department of Mechanical and Industrial Engineering, NTNU Norwegian University of Science and Technology, Trondheim, Norway*
lukas.jansen@ntnu.no

Abstract
A new method for in-machine measurement of tool wear in milling machines, based on backlit imaging, is presented. An established approach for measuring flank wear with this type of equipment is to estimate the wear from tool diameter reduction. However, this approach is highly sensitive to small errors in the diameter measurement, making it necessary to measure the diameter within single digit micrometer values.
To address these limitations, we propose a new method for estimating flank wear, based on the assumption that flank wear land is a part of a cylindrical surface coaxial to the tool axis. In the proposed method, images of the tool are taken while incrementally rotating it. When measuring the diameter based on points on the worn area, the diameter value is constant across multiple images. The results show good agreement between the new proposed method and conventional microscope measurements.

Backlight imaging; Flank wear measurement; Optical sensor; Machining

1. Introduction

Tool wear is one of the major, uncertainties in machining making it one of the main limitations for cost minimization in automated machining processes. Hernandez et al.[1] found that the average tool is retired well before it is worn out, making use of only half of the possible lifetime. They also found that some tools are used beyond their useful life, threatening damage to the workpiece. Colantonio et al. [2] look at different imperfect tool replacement strategies. They conclude that cost savings of 8.1% and a reduction in CO_2 equivalent emissions of 8.7% can be achieved with tool monitoring as compared to replacing the tools after a fixed usage time. In their scenario, which includes tool, workpiece and machine, the tool is responsible for 70% of the CO_2 equivalent emissions for parts production, further highlighting the need to use tools to their full potential. This is enabled by monitoring the tool condition.

While measuring tool wear is an established process and described in ISO standard 8688-2 (for milling tools) [3], the method is not intended for in-process measurement of tools for condition monitoring.

Automating tool wear measurements within the machine is of great interest and has successfully been implemented by others in experimental environments. While many different solutions using direct and indirect measurements of tool wear and its effects have been presented, we focus on direct optical approaches. Most often images of the tool are taken, and the captured information is then used to measure the wear on the flank of the tool directly [4-8]. The automated processes that look at the flank of the tool directly face many difficulties in practice due to changing conditions such as illumination and tool coatings with different reflectiveness, making them less reliable.

An alternative approach is the use of backlighting which leads to only the tool silhouette being visible to the camera. This method is more robust because it is independent of the tool's visual appearance. Liang et al. [9] presented a method to use the reduction in the tool diameter and the flank clearance angle to calculate tool wear. A disadvantage of this approach is that the tools' flank clearance angle is typically not published by the tool manufacturer, making a measurement of it necessary. Additionally, the estimation of flank wear from tool diameter reduction gets more complex since the clearance surfaces of the tool rarely have simple geometries but instead are shaped by multiple radii. Lastly the tool diameter must be measured very precisely to get reliable flank wear measurements. One unit length in tool diameter reduction leads to a 5 to 10 units increase of flank wear for common clearance angles of 6 to 12 degrees.

To make use of the benefits of backlit optical tool wear measurements while omitting some of its disadvantages we suggest a new measurement method.

In the method section, the idea of the new measuring process is introduced and the experimental set up is presented. Next, the process as well as the reference measurements are presented and then discussed. Finally, the conclusion of the paper and an outlook on further work is given.

2. Method

Flank wear is the most widely used measurement of tool wear and tends to be the dominant wear type in machining of metals with conventional cutting parameters.

The effect of flank wear on the tool geometry is easily visualized in a turning tool, where it leads to a loss of the cutting edge. Due to the flank's clearance angle, a wear zone that increases in length with progressing wear is formed (*Figure 1*).

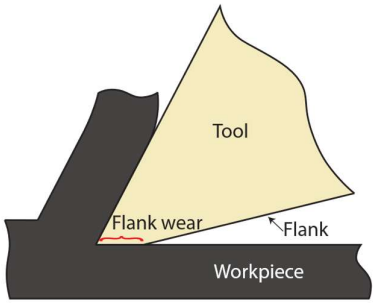

Figure 1. Flank wear in orthogonal cutting.

The increase of cutting force that correlates with flank wear is caused by the increased area on the tool that rubs against the work piece [10]. It is also possible to measure a decrease in electrical resistance between tool and workpiece [11]. This is

caused by an increasingly larger contact zone between tool and workpiece.

Considering the increase in cutting force and decrease in resistance across the tool-workpiece interface we assume that the entire flank wear zone is in contact with the workpiece.

In milling, the tool wear is generated by a rotational movement of the tool. The presented measurement method uses the assumption that the worn area is a part of an imaginary cylinder that is coaxial with the tool axis. Figure *2* shows an illustration of the coaxial wear zone.

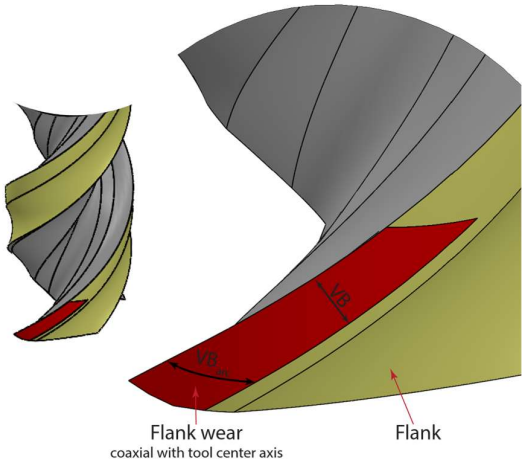

Figure 2. Flank wear on a milling tool (red coloured area). The flank wear land is assumed to be part of a cylindrical surface.

The outcome of the measurement process is the length of the flank wear zone measured from the current cutting-edge up to the end of the flank wear parallel to the cutting direction, called VB_{arc} here after.

To capture VB_{arc} a camera-based sensor (CU2 Tool) manufactured by Conoptica AS is used. The sensor is usually used as a tool setter and is therefore built such that it can permanently remain within the milling machine's work envelope.

A 10 mm end mill with a helix angle of 32 degrees manufactured by UOP is used to test the process. Controlled flank wear is artificially created with the tool in the spindle of the milling machine. A grinder is placed on the machine table and tilted slightly. With the spindle engaged, the tool is then brought into contact with the grinding wheel. This creates tapered flank wear on the tool. As a reference, the artificially created flank wear is measured with an Alicona G4 focus variation microscope.

3. Results

3.1. Measuring VB_{arc}

To measure VB_{arc}, images of one side of the tool are taken. Since backlighting is used, the silhouette of the tool is visible. The edge of the silhouette represents the outermost visible contour of the tool. When spinning the tool, each point on that contour appears to move in and out in the recorded images. By rotating a sharp tool and plotting the edge position, a parabola shaped diagram is created. This shape arises because the cutting edge is the part of the tool that lies farthest from its central axis. As it approaches an orthogonal orientation relative to the camera's line of sight, its apparent radial position increases before decreasing again.

Following our earlier assumption of the coaxiality of the flank wear region to the tool's central axis, plotting a similar diagram for a worn tool will lead to a different shape of the curve. Instead of a clear peak, the diagram will show a plateau, the length of which corresponds to VB_{arc}. A representation of the measurement principle and the resulting plots for a sharp and a worn tool can be seen in *Figure 3*.

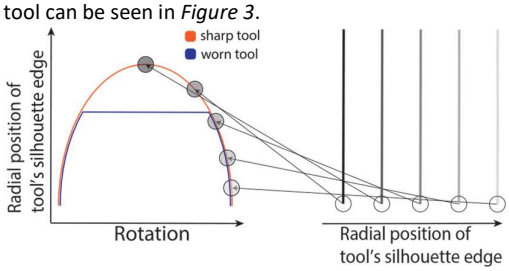

Figure 3. Tool silhouette edge radial position plot based on edge position across multiple images.

The distance the cutting-edge travels along an arc (T_{arc}) between two images depends on the rotational speed of the tool (n) as well as the frame rate at which the camera takes images (f_s).

Since both values can be adjusted within the equipment's limits it is practical to define T_{arc} so, that it is sufficiently small to capture the expected flank wear. This can be done for a maximum allowable flank wear value as defined in ISO 8688-2 or if flank wear is to be tracked over time, by defining a resolvable minimum flank wear value. Since flank wear follows an S-shaped curve, with a high wear rate early on, and since smaller values of VB_{arc} are harder to resolve, it is practical to define T_{arc} such that it can resolve the flank wear after the initial wear phase. After defining T_{arc} the tool rotation between images, θ, can be calculated based on T_{arc} and the tool's cutting diameter, D:

$$\theta = \frac{T_{arc}}{\pi \cdot D} \cdot 360 \tag{1}$$

Since an unpractically high frame rate would be required to capture all images within one revolution of the tool, only one image per revolution is captured. For this the required frame rate (f_s) of the camera can be calculated:

$$f_s = n \cdot \frac{360 - \theta}{360} \tag{2}$$

3.2 Image processing

The developed measuring process is implemented in Python. The steps taken to get from the captured images to VB_{arc} measurements are seen in **Error! Reference source not found.**. The process can be divided into two parts, one which repeats the same step for one image at a time, and a second step that repeats the same process for one axial position along the cutting edge of the tool. The second step is based on the data extracted in the first step.

The rough edge position for each image is found using Canny [12] edge detection. Small gaps between the detected edges are then closed with morphological edge closing. To get a smooth and continuous edge, a spline curve is fitted. Since the tool silhouette extends to the limits of the image, the spline fit is not sufficiently defined at the ends. To prevent erratic spline fits the ends of the spline are defined based on the slope of the spline further into the image. This is acceptable since the edge slope changes only slowly.

With knowledge of the approximate edge location fine edge detection is done. Based on the work of Venkatachalam et al. [13], who compare different sub-pixel edge detection methods, quadratic edge detection is chosen for its high accuracy and relative simplicity.

Lines orthogonal to the rough silhouette edge are used as a guide to obtain the intensity of a set of neighbouring pixels across the edge. To the pixel intensities a cubic function is fitted and differentiated. The cubic function is used to avoid the

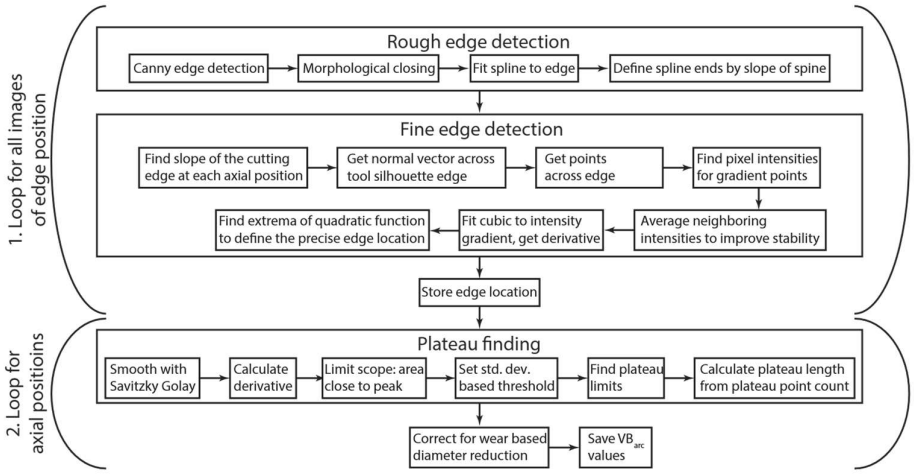

Figure 4. *Measuring process to determine VB_{arc} based on tool silhouette images.*

amplification of noise when directly differentiating the pixel intensities [14]. The quadratic function represents the change in intensity. The cutting-edge is located at the peak of the quadratic function where the intensity change is at its maximum. The process of finding an edge precisely based on a quadratic function is described by Seitz [15].

The fine edge location is determined in the same manner for every image and then stored. In the next step the edge position extracted over all images for one axial position is considered. The same steps are then repeated for all axial positions.

By plotting the edge points of one axial position, a diagram close to a parabola with a flat plateau on top is created (Figure 3). The number of data points that lie within that plateau determine VB_{arc}[1]. Therefore, the size of the plateau must be found. This is done based on the derivative of the data, which is equal to zero for a true plateau. Since the edge locations are collected from real images, there is some noise present in the data, which gets amplified in the derivative. To reduce that noise the edge position data is smoothed using a Savitzky Golay [14] filter. Since this does not fully eliminate noise, a threshold based on the standard deviation of the signal is set to define the data points to be part of the plateau. More noise in edge detection is seen in areas of the tool that are further from their peak radial position. This can be attributed to the measured point being further from the focus plane of the sensor resulting in a more blurred image. To avoid these high noise areas, the scope for defining the standard deviation-based threshold is limited to an area close to the absolute maximum of the cutting-edge position.

As seen in Equation 1, the length of the arc between images depends on the diameter of the tool, which decreases with wear. To compensate for this, we estimate the tool diameter reduction by comparing the maximum radial silhouette edge location in an unworn area to the local maximum radial silhouette edge location. Using the resolution of the optical sensor an approximate reduction of the tool diameter is calculated. It should be noted that this correction will contain some error itself due to the lenses distortion which we do not compensate for here.

Figure 5 shows the measured radial positions of the silhouette edge for all axial positions, as well as the found plateaus.

In *Figure 6*, VB_{arc} as calculated by the described process is plotted over the axial position.

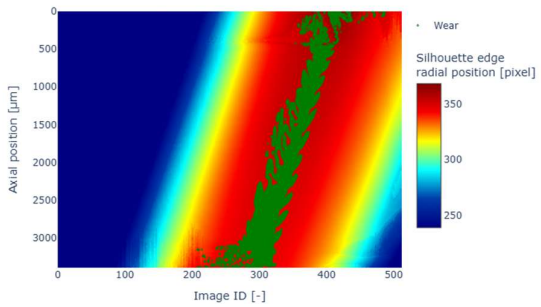

Figure 5. Radial position of silhouette edge development across images for all axial positions and found wear.

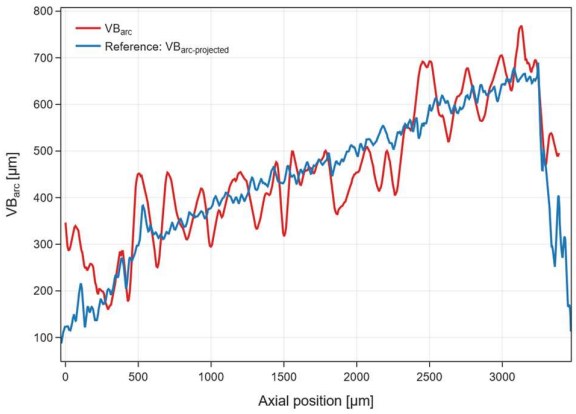

Figure 6. VB_{arc} as determined by the camera-based sensor and the focus variation microscopy-based reference measurement.

To evaluate the VB_{arc} measurements, they are compared to reference measurements taken with the focus variation microscope.

The base data exported from the microscope is a three-dimensional point cloud of the worn flute. This data is first cleaned of outliers and then separated into two dimensional slices along the tool's axis. It is also smoothed using a Savitzky

[1] Other approaches for determining the plateau size can be applied. Calculating the distance between the outermost points of the plateau yields less reliable results, as the plateau size is often overestimated due to outliers.

Golay filter. When plotting this data one slice at a time a diagram with a kink (breakpoint) at which the flank surface transitions into the worn zone is created. By finding and then plotting this point over all axial positions, the limits of the worn zone can be found (Figure 7).

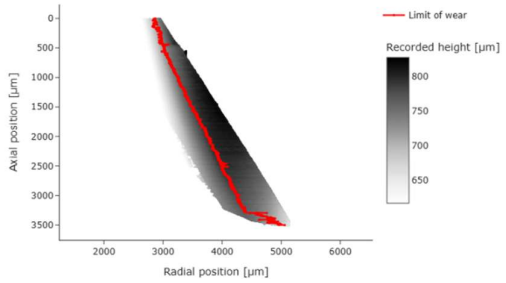

Figure 7. Wear area based on focus variation microscopy data.

For each y position, the distance between the cutting edge and the wear zones limit is calculated. The result is the projected length of VB_{arc}. Trials with fitting a circle section to the found sections of the wear zone, to get the non-projected length of VB_{arc} were prone to a large amount of noise that is larger than the small error from using the projected VB_{arc} length. The resulting plot of VB_{arc}-projected depending on the axial position can be seen in Figure 6.

4. Discussion of results

The resulting wear plots in Figure 6 show good agreement between the camera-based measurement and the reference measurement. This proves that measurement of wear on the flank of the tool is possible with the presented method, given that this wear is concentric to the tool axis. The camera-based results show more variation than the reference measurement, but small deviations in the mean value. This is likely caused by the difficulties in the detection of the plateau of the radial position curve. The camera-based measurement also detects wear in the unworn section (axial position < 450 µm). This is likely caused by the limitation of the plateau detection method when no actual plateau is present. The reference method does also have some limitation in detecting zero wear. This method is based on detection of a break point between the worn area and the unworn flank face.

Towards the bottom of the tool (axial position > 3200 µm) both measurements drop off steeply. This is due to the pointed tool geometry at the bottom, these measurements are not representative.

Considering the section between 450 µm and 3200 µm, the measurements have a relatively small bias of 2.97 µm, but a large average absolute deviation of 49 µm. This again is likely caused by deviations in the plateau or edge detection.

Looking at Figure 5 a repeating pattern can be seen, the cause of that pattern has not yet been determined.

5.Conclusion and outlook

A new method for measuring the length of the worn section along a tool's flank face is presented in this paper. It uses the assumption that the worn area is a cylindrical surface that is coaxial with the tool axis.

The main benefits of the method are its robustness to changes in the tool's optical properties due to use of backlit images and its independence of unavailable tool geometry data. It is also possible to deploy it within the machine tools work envelope. Measurements taken with the described process are compared to measurements from a focus variation microscope.

The measurements show good correlation in the development of wear for different levels of tool wear, showing that a detection of these coaxial flank wear zones is possible with the described process. Based on this, further work in the following areas needs to be undertaken: (1) The process variation is large and should be addressed by improving the algorithms used to find the cutting edge in the base images and the plateau size. (2) It is of interest to calculate VB as defined in ISO 8688-2, based on the proposed backlit method. For this some corrections like compensation of the helix angle and movement of the cutting edge under wear must be made.

References

[1] A. E. B. Hernández, T. Beno, J. Repo, and A. Wretland, 'Analysis of Tool Utilization from Material Removal Rate Perspective', *Procedia CIRP*, vol. **29**, pp. 109–113, 20153.

[2] L. Colantonio, G. Moroncini, O. Sénéchal, P. Dehombreux, F. Ducobu, and L. Equeter, 'Cost and Environmental Assessment of Tool Replacement Strategies Under Imperfect Wear Monitoring in Ti6Al4V Milling', *Int. J. Progn. Health Manag.*, vol. **16**, no. 4, Nov. 2025.

[3] *ISO 8688-2:1989-05 Tool life testing in milling; part 2: end milling*.

[4] S. Mehta, R. A. Singh, Y. Mohata, and M. B. Kiran, 'Measurement and Analysis of Tool Wear Using Vision System', in *2019 IEEE 6th International Conference on Industrial Engineering and Applications (ICIEA)*, Tokyo, Japan: IEEE, Apr. 2019, pp. 45–49.

[5] P. J. Bagga *et al.*, 'Experimental investigation of different NN approaches for tool wear prediction based on vision system in turning of AISI 1045 steel', *Int. J. Interact. Des. Manuf. IJIDeM*, vol. **17**, no. 5, pp. 2565–2582.

[6] C. Zhang and J. Zhang, 'On-line tool wear measurement for ball-end milling cutter based on machine vision', *Comput. Ind.*, vol. **64**, no. 6, pp. 708–719, Aug. 2013.

[7] A. Agarwal, N. Potthoff, A. M. Shah, L. Mears, and P. Wiederkehr, 'Analyzing the evolution of tool wear area in trochoidal milling of Inconel 718 using image processing methodology', *Manuf. Lett.*, vol. **33**, pp. 373–379, Sep. 2022.

[8] L. Fernández-Robles, G. Azzopardi, E. Alegre, and N. Petkov, 'Machine-vision-based identification of broken inserts in edge profile milling heads', *Robot. Comput.-Integr. Manuf.*, vol. **44**, pp. 276–283, Apr. 2017.

[9] R. Liang, Y. Li, L. He, and W. Chen, 'A novel image-based method for wear measurement of circumferential cutting edges of end mills', *Int. J. Adv. Manuf. Technol.*, vol. **120**, no. 11–12, pp. 7595–7608, Jun. 2022.

[10] J. Wang, C. Z. Huang, and W. G. Song, 'The effect of tool flank wear on the orthogonal cutting process and its practical implications', *J. Mater. Process. Technol.*, vol. **142**, no. 2, pp. 338–346, Nov. 200.

[11] M. Murata, S. Kurokawa, O. Ohnishi, M. Uneda, and T. Doi, 'Real-Time Evaluation of Tool Flank Wear by In-Process Contact Resistance Measurement in Face Milling', *J. Adv. Mech. Des. Syst. Manuf.*, vol. **6**, no. 6, pp. 958–970, 2012.

[12] J. Canny, 'A Computational Approach to Edge Detection', *IEEE Trans. Pattern Anal. Mach. Intell.*, **vol. PAMI-8**, no. 6, pp. 679–698, Nov. 1986.

[13] V. Venkatachalam and R. M. Wasserman, 'Comprehensive investigation of subpixel edge detection schemes in metrology', presented at the Electronic Imaging 2003, M. A. Hunt and J. R. Price, Eds, Santa Clara, CA, May 2003, p. 200.

[14] Abraham. Savitzky and M. J. E. Golay, 'Smoothing and Differentiation of Data by Simplified Least Squares Procedures.', *Anal. Chem.*, vol. **36**, no. 8, pp. 1627–1639, Jul. 1964.

[15] P. Seitz, 'Optical superresolution using solid -state cameras and digital signal processing', *Opt. Eng.*, vol. **27**, no. 7, Jul. 1988,

euspen's 26th International Conference & Exhibition, Krakow, PL, June 2026

Measurement and improvement of bit error rate in 16QAM using laser hydrophones

Rin Furuya[1], Norio Tsuda[1], and Daisuke Mizushima[1]

[1]Aichi Institute of Technology

v25723vv@aitech.ac.jp

Abstract

At present, piezoelectric hydrophones are primarily employed in underwater acoustic communications. However, conventional hydrophones require direct contact with the acoustic field to detect the ultrasound. Consequently, they are unsuitable for environments with high bubble concentrations or water flow unless complex optical systems are employed. To address this limitation, a laser hydrophone based on the self-coupling effect of semiconductor lasers was proposed. This study explores the application of laser hydrophones in underwater acoustic communication. To achieve this objective, we previously conducted detection experiments with fundamental digital modulation methods such as Frequency Shift Keying, Amplitude Shift Keying, and Phase Shift Keying.

In this study, we extend the study to 16 Quadrature Amplitude Modulation, which incorporates both phase and amplitude modulation components. We aim to demonstrate the detection of its digital modulation waveforms and the measurement of BER. In addition, the characteristics obtained with visible and infrared lasers are compared to identify the optimal laser conditions for detecting 16QAM signals.

Acoustic, Laser, Measuring instrument, Sensor

1. Introduction

At present, underwater wireless communication in seawater is primarily based on underwater acoustic communication (UWAC), which employs ultrasonic waves rather than radio or optical waves because of their lower attenuation and ability to transmit information over long distances [1,2].

UWAC signals are mainly transmitted and received using piezoelectric hydrophones as transducers. However, piezoelectric hydrophones exhibit frequency response and directivity characteristics arising from the resonance of piezoelectric elements. In addition, because the sensing surface must be in direct contact with the acoustic field, it is highly susceptible to disturbances such as turbulence and bubbles [3,4].

These issues can be solved by an acoustic sensor that applies the self-coupling effect of a semiconductor laser (LD: Laser Diode). By utilizing the self-coupling effect, a compact and low-cost system configuration can be realized [5]. The self-coupling effect has mainly been used to measure the distance and velocity of a target, as well as for acoustic sensing applications. When this principle is applied to underwater acoustic detection, the device is referred to as a laser hydrophone.

This study aims for apply laser hydrophones to underwater acoustic communication. In particular, this paper compares the bit error rate (BER) obtained when digitally modulated waveforms, especially 16QAM, which is practically used in UWAC, are detected using a laser hydrophone at two wavelength bands with different water absorption coefficients.

2. Detection principle

The schematic diagram of an optical system exhibiting self-coupling is shown in Fig. 1. A continuously operating LD and a reflector are positioned facing each other, forming an external cavity between them. In a laser hydrophone, the water in a tank placed between the LD and reflector acts as an external cavity. Part of the reflected light returns to the active layer of the LD and interferes with the emitted light, causing variations in the optical output, which is referred to as the self-coupling effect.

Acoustic waves are density waves in a medium, and the refractive index changes owing to the compression and rarefaction caused by the acoustic wave. A laser hydrophone detects wavelength changes in the laser light induced by refractive index variations in the external cavity as phase changes in the self-coupling interference signal. The relationship between the refractive index of water, the laser wavelength, and the interference phase in the external cavity is shown in Fig. 2.

3. Experimental setup

The experimental setup is shown in Fig. 3. A 3M RP45 RED reflector (reflectivity 60%) was used. For the laser diode (LD), a ROHM RLD84PZJ2 was used for the infrared (IR) laser with a nominal emission wavelength of 840 nm, and a SHARP GH05280E2K was used for the visible (VIS) laser with a nominal emission wavelength of 520 nm. The lens and the semiconductor laser are mounted within a laser mount. The absorption coefficient of water at 840 nm is relatively high at 2.93×10^{-7}, whereas that at 520 nm is much lower at 1.32×10^{-9} [6].

The biconvex lens and LD are contained in a laser mount, and the water tank has a diameter of 300 mm. The laser mount and the tank, as well as the tank and the reflector, are installed in direct contact. The acoustic source (OKI OST2140) is placed 50 mm from the laser beam at a right angle. An ND filter is mounted on the reflector to maintain a reflectivity of 2×10^{-8}.

Five types of digital modulation schemes were used: FSK (Frequency Shift Keying), ASK (Amplitude Shift Keying), BPSK (Binary Phase Shift Keying), QPSK (Quadrature Phase Shift Keying), and 16QAM (16 Quadrature Amplitude Modulation). The fundamental frequency f_0 was set to 200 kHz, and the fundamental amplitude A_0 was 60 $V_{p\text{-}p}$. For FSK, a frequency deviation $\Delta f = 50$kHz was used, with the transmitted bit "0"

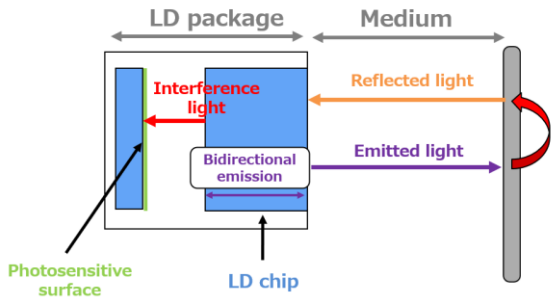

Figure 1. An optical system in which the self-coupling effect occurs.

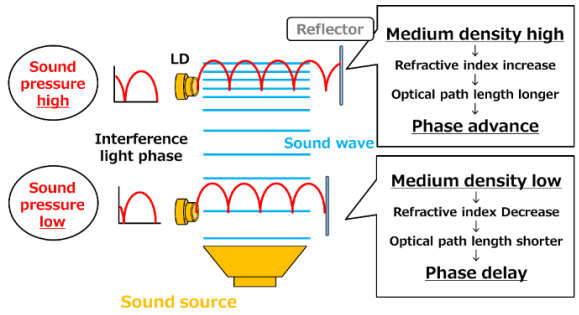

Figure 2. Relationship between refractive index, laser wavelength, and interference phase.

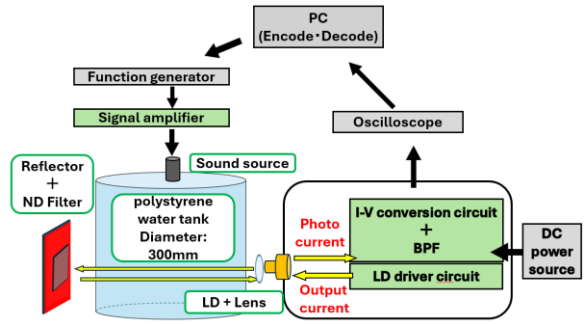

Figure 3. Experimental setup.

corresponding to a frequency of f_0 and the transmitted bit "1" corresponding to $f_0 + \Delta f$. For ASK, a modulation index of $m = 0.8$ was used, with the amplitude of the transmitted bit "1" set to $A_0$and that of bit "0" set to $(1 - m)A_0$. In BPSK, the phase is inverted by 180° depending on whether the transmitted bit is "0" or "1". For QPSK, the phase is shifted by 90° increments corresponding to the transmitted bits "0", "1", "2", and "3". In 16QAM, every four bits are mapped to a single 16QAM symbol, with the upper two bits assigned to the in-phase (I) component and the lower two bits to the quadrature (Q) component. The amplitude levels of both I and Q components were mapped to $\{-3, -1, +1, +3\}$.

4. Results and discussion

The bit error rate (BER) measurement results for IR and VIS lasers at a laser power of 5 mW are shown in Table 1, and those at a laser power of 3 mW are shown in Table 2. From Tables 1 and 2, for all modulation schemes, the BER was lower at smaller laser power when using the VIS laser compared to the IR laser. Furthermore, when comparing the laser powers that yield the minimum BER for each of the IR and VIS lasers, the VIS laser exhibited a lower BER. Previous studies have shown that the noise intensity arising from the self-coupling effect depends on the intensity of the backward-emitted light from the active layer

Table 1. Experimental results (5 mW)

Modulation schemes	BER (IR Laser)	BER (VIS Laser)
ASK ($\boldsymbol{m}$ = 0.8)	11.8	9.8
ASK ($\boldsymbol{m}$ = 0.5)	12.4	12.9
FSK ($\boldsymbol{\Delta f}$ = 50 kHz)	1.5	2.1
FSK ($\boldsymbol{\Delta f}$ = 25 kHz)	5.1	6.8
BPSK	2.4	3.8
QPSK	3.4	4.1
16QAM	5.5	7.5

Table 2. Experimental results (3 mW)

Modulation schemes	BER (IR Laser)	BER (VIS Laser)
ASK ($\boldsymbol{m}$ = 0.8)	15.6	7.1
ASK ($\boldsymbol{m}$ = 0.5)	16.4	9
FSK ($\boldsymbol{\Delta f}$ = 50 kHz)	6.8	1
FSK ($\boldsymbol{\Delta f}$ = 25 kHz)	9.7	5.3
BPSK	3	2.3
QPSK	5.6	3.2
16QAM	8.4	5.1

of the semiconductor laser toward the detection surface, rather than the intensity of the reflected light. The results in Tables 1 and 2 can be attributed to the lower absorption of water at the wavelength of VIS laser, which allows sufficient reflected light intensity to be obtained even at lower laser powers with less noise arising from the backward-emitted light, thereby improving the BER.

5. Conclusion

In this study, to extend the applications of laser hydrophones, we attempted to detect 16QAM signals, which are widely used in underwater acoustic communication (UWAC). Five types of modulation schemes were employed, and the bit error rate (BER) was measured using two different laser powers and two wavelength bands. The results showed that the VIS laser achieved a lower BER than the IR laser, even at lower laser powers, and that overall BER was reduced. This improvement is attributed to the lower water absorption at the VIS laser wavelength, which allows sufficient reflected light intensity to be obtained at lower powers with lower noise, thereby improving BER performance.

Furthermore, in underwater acoustic communication, 64QAM (64-Quadrature Amplitude Modulation) is a practical digital modulation scheme that enables the transmission of more information per symbol. Future work will focus on implementing 64QAM, measuring its BER, and improving its performance. To date, experiments have been conducted under quiescent water conditions with minimal disturbance. To verify the effectiveness of the non-contact laser hydrophone, BER measurements under disturbed conditions will also be carried out in the future.

References

[1] Y. Sato, T. Ebihara, K. Mizutani and N. Wakatsukia 2021 *Japan. J. Appl. Phys.* **60** SDDF01
[2] A. H. Quazi and W. L. Konrad 1987 *IEEE Commun. Mag.* **20** 54
[3] H. Saheban, and Z. Kordrostami, *SENSOR ACTUAT A-PHYS*, **321**(1),1 (2021)
[4] A. Bharath, D. Groulx, and S. Campbell 2014 *Proceedings of the 2014 COMSOL Conference in Boston*
[5] T. Taimre, M. Nikolić, K. Bertling, Y. L. Lim, T. Bosch, and A. D. Rakić 2015 *AOP.* **7**(3) 570
[6] George M. Hale et al., 1973 *Querry* **12**(3) 555-563

euspen's 26th International Conference & Exhibition, Krakow, PL, June 2026
www.euspen.eu

Investigation of a novel motorised milling spindle with thermoelectric temperature control system based on a tubular Peltier module

Eckart Uhlmann[1,2], Mitchel Polte[1,2], Florian Triebel[1],
Alphin Judy[1], Roland Binninger[3], Andreas Moll[4], Jörn Sieberg[4]

[1]*Technische Universität Berlin, Institute for Machine Tools and Factory Management IWF, Pascalstr. 8-9, 10587 Berlin, Germany*
[2]*Fraunhofer Institute for Production Systems and Design Technology IPK, Pascalstr. 8-9, 10587 Berlin, Germany*
[3]*Fraunhofer Institute for Physical Measurement Techniques IPM, Georges-Köhler-Allee 301, 79110 Freiburg, Germany*
[4]*FISCHER Deutschland GmbH, Marie-Curie-Strasse 2, 40764 Langenfeld, Germany*

triebel@iwf.tu-berlin.de

Abstract
Driven by ongoing technological advancements across various industrial sectors such as optics, automotive engineering and information technology, a growing demand for the production of components with geometrical and dimensional accuracies at the submicron scale can be identified. In high-precision machining, the thermomechanical behaviour of machine tools is critical. Motorised spindles represent a significant heat source within machine tools and their thermal behaviour is essential for the achievable working accuracy. Electrical and mechanical power losses in the motor drive and bearings result in the induction of heat into the shaft and housing of the motorised spindle. Despite the implementation of advanced water-cooling systems, these heat flows result in elevated temperatures, which subsequently lead to thermally induced deformation of the components, directly resulting in a displacement of the tool centre point. With the intention to improve the thermoelastic behaviour, a novel thermoelectrically temperature controlled motorised milling spindle was developed. Within this spindle, 40 Peltier stripes are arranged circumferentially around the front bearings, thus forming a tubular Peltier module. This Peltier module enables the adjustment of heat flow between the front bearings and the water-cooling system. Based on this, a precise temperature control at the front bearings is implemented. The present study investigates a prototype of this spindle and demonstrates that the thermoelectric system is capable of controlling temperatures within the range of 30 °C ≤ ϑ ≤ 40 °C. It is shown that temperature control can be achieved with a maximum temperature deviation of $\Delta\vartheta_{max}$ = 1.1 °C under changing rotational speeds. A test procedure is proposed, which involves incrementally rising rotational speeds within the range of 10,000 1/min ≤ n ≤ 50,000 1/min, followed by a temporary spindle stop. Maintaining a constant front bearing temperature results in a 16 % decrease in the change in axial shaft displacement during this test procedure when compared to a reference spindle equipped with a conventional water-cooling system.

Control, Spindle, Temperature, Thermal error

1. Introduction

Amid the continuous evolution of advanced manufacturing technologies across industrial sectors such as optics, automotive engineering, and information technology, the demand for components with geometrical and dimensional accuracies in the submicrometer range constantly increases [1]. However, achieving and maintaining such accuracy is affected by thermally induced errors, which account for up to 75 % of the total error in precision parts [2]. Heat flows $\dot{Q}$ generated by friction and energy conversion within the machine tool lead to non-uniform thermal gradients. These variations in temperature ϑ cause thermal deformation δ_{th} of machine tool components, resulting in tool centre point-displacement d_{TCP} and therefore a reduction in machining accuracy [2]. The motorised spindle is considered to be one of the primary heat sources within machine tools [3]. The integrated motor drive induces heat flows $\dot{Q}_{ind}$ due to electrical losses in addition to bearing and fluid friction losses that occur at high rotational speeds n [4]. To achieve higher machining accuracy, the effects of the thermal loads must be reduced by means of appropriate cooling concepts. DENKENA ET AL. [4] provide a comprehensive overview of cooling strategies for motorised spindles and distinguish between passive and active approaches. A further distinction is made based on the cooling target, differentiating between the cooling of the spindle bearings, the stator, and the shaft.

Passive cooling strategies rely on heat transfer by convection to the ambient air, typically enhanced by heat sinks. Active cooling concepts deploy a flowing cooling medium which is applied in close proximity to the heat sources [4, 5].

A variety of passive cooling concepts use heat pipes of different shapes and configurations, which are integrated inside the spindle housing or in the spindle shaft. In addition, external heat sinks are placed outside the spindle housing to enhance convective heat flow $\dot{Q}_{conv}$ [6-9]. Common approaches of active cooling using water as fluid include differently designed cooling channels [9-10].

Beyond passive and active cooling, approaches to actively control the spindle temperature ϑ_{sp} offer the possibility to maintain a constant spindle temperature ϑ_{sp} and minimize temperature fluctuations during operation. JONATH ET AL. [11] extend the heat pipe-based cooling concept by controlling the rotational fan speed n_F, which affects the convective heat flow $\dot{Q}_{conv}$. The additional integration of a heating foil enables the induction of a heat flow $\dot{Q}_{ind}$. Utilizing the bidirectional heat transport capability of the heat pipes, this setup enables control of the spindle temperature ϑ_{sp}. As a result, a reduction of the

axial shaft displacement d_s by 62 % compared to the uncontrolled configuration is achieved.

WAKIYA ET AL. [12] focus on the cooling unit and controlling the cooling fluid temperature ϑ_{fl} based on the spindle's internal temperature ϑ_{sp}, by mixing two fluid streams at different fluid temperatures ϑ_{fl}. This enables a reduction of changes in spindle temperature ϑ_{sp} caused by changes in rotational speeds n and variations in the ambient temperature ϑ_{amb}. The results show a remaining maximum spindle temperature variation $\Delta\vartheta \leq 0.3$ °C during a change of rotational speed from n_1 = 10,000 1/min to n_2 = 15,000 1/min.

An alternative approach for realizing an active temperature control system is the utilization of Peltier modules. A Peltier module is composed of an alternating pattern of p-doped and n-doped semiconductor legs arranged between two ceramic plates, electrically connected in series and thermally in parallel. Based on the Peltier effect, first discovered by PELTIER [13], a heat flow $\dot{Q}_{pel}$ within the Peltier module can be generated by applying an electric current I_{pel}.

The applicability of this approach is demonstrated by FAN ET AL. [14]. Peltier modules are attached to the outer surface of a spindle housing. This serves to establish a thermal equilibrium between the heat flow $\dot{Q}_{gen}$ generated by the spindle and the heat flow $\dot{Q}_{abs}$ absorbed by the Peltier modules. A reduction of the axial shaft displacement d_s by 58.6 % at a rotational speed n = 10,000 1/min results [15].

UHLMANN ET AL. [16, 17, 18] developed an actively temperature-controlled motorised spindle utilising prismatic Peltier modules. Three groups of Peltier modules, each independently controllable, are integrated between the water cooler and the front and rear bearings, as well as the stator. This configuration enables precise control of the temperature ϑ_{sp} within the spindle. Using this approach, the warm-up time t_w required to reach the thermal steady state of the axial shaft displacement d_s can be reduced by up to 79 %.

With the aim of reducing the expanses of integrating a thermoelectric temperature control system within motorised spindles, the companies FISCHER DEUTSCHLAND GMBH and DR. NEUMANN PELTIER-TECHNIK GMBH, in conjunction with the research institutes FRAUNHOFER INSTITUTE FOR PHYSICAL MEASUREMENT TECHNIQUES IPM and the INSTITUTE FOR MACHINE TOOLS AND FACTORY MANAGEMENT IWF developed a novel thermoelectric temperature control system based on a tubular Peltier module. The integration of a tubular Peltier module between the bearings and the water cooler enables active transfer of heat Q. In comparison with the use of solely conductive elements, as in a state-of-the-art spindles, this offers the advantage that the bearing temperature ϑ_b can be controlled independently of the thermal load. Additionally, due to the bidirectional functionality of the Peltier effect, there is also the possibility of heat transfer from the cooling liquid to the bearings.

The present study investigates the characteristics of the temperature control system within a first prototype spindle, shown in figure 1. Furthermore, the influence of a constant front bearing temperature ϑ_{fb} on the axial shaft displacement d_s is examined.

2. Thermoelectrically temperature-controlled spindle

2.1. Experimental setup

The prototype motorised spindle, shown in figure 1, is based on a high-speed spindle of type MFW-840/50 HSK-E25 by FISCHER DEUTSCHLAND GMBH, Langenfeld, Germany, and equipped with the novel thermoelectric temperature control system. Previous work shows, that an active temperature control at the front bearing seat has the highest impact on the axial shaft displacement d_s. Therefor the rear bearings and the motor drive remain cooled by a conventional water-cooling system. The tubular Peltier module is composed of a number n = 40 Peltier stripes circumferentially arranged around the front bearing seat, shown in figure 2. The water cooler is shrink-fitted to the arrangement of the Peltier stripes, ensuring a mechanical and thermal connection. The assembly of the front bearing seat, the tubular Peltier module and the water cooler is shown in figure 2 b).

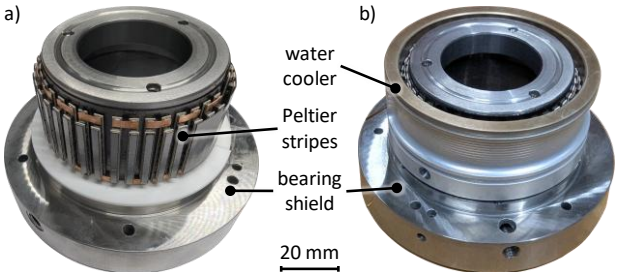

Figure 2. Assembly of the front bearing seat;
a) installed Peltier stripes; b) Peltier stripes and water cooler.

Depending on the direction of the applied Peltier current I_{pel}, the Peltier strips can transfer heat Q from the bearing shield into the water cooler or vice versa. In figure 1, the heat flows $\dot{Q}$ are illustrated in a scenario where the heat flow $\dot{Q}_{ind}$ induced by the bearings is transferred to the cooling liquid. The absorbed heat flow $\dot{Q}_{abs}$ and the emitted heat flow $\dot{Q}_{emi}$ depend on the Seebeck coefficient α, the thermal conductance C and the electrical resistance R of the Peltier strips [19].

$$\dot{Q}_{abs} = \alpha\, I_{pel}\, \vartheta_1 - C\,(\vartheta_2 - \vartheta_1) - (I_{pel}^2\, R)/2 \quad (1)$$

$$\dot{Q}_{emi} = \alpha\, I_{pel}\, \vartheta_2 - C\,(\vartheta_2 - \vartheta_1) + (I_{pel}^2\, R)/2 \quad (2)$$

The absorbed heat flow $\dot{Q}_{abs}$ is determined by the Peltier current I_{pel}, as demonstrated in equation 1. Therefore, it is feasible to control the front bearing temperature ϑ_{fb}, with the Peltier current I_{pel} serving as the controlled variable. For the purpose of measuring the front bearing temperature ϑ_{fb}, a resistance thermometer of type PT1000 by TEMPERATUR

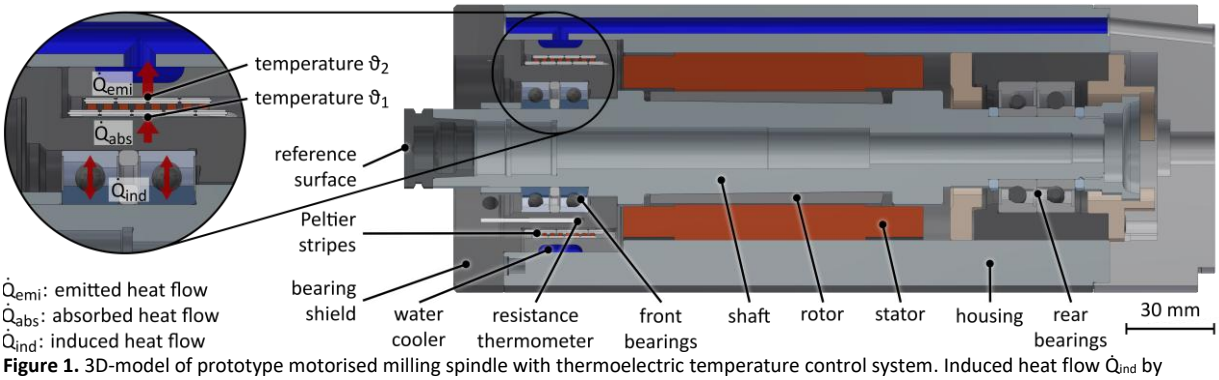

Figure 1. 3D-model of prototype motorised milling spindle with thermoelectric temperature control system. Induced heat flow $\dot{Q}_{ind}$ by the front bearings, absorbed heat flow $\dot{Q}_{abs}$ and emitted heat flow $\dot{Q}_{emi}$ by the Peltier stripes are illustrated, for the scenario of cooling the bearings.

MESSELEMENTE HETTSTEDT GMBH, Maintal, Germany, is integrated between the front bearings and the Peltier stripes.

The Peltier stripes are electrically connected in series and the Peltier current I_{pel} is controlled by a Peltier controller of type PWR-CTRL-M of DR. NEUMANN PELTIER-TECHNIK GMBH, Neuried, Germany. The Peltier controller is able to control the front bearing temperature ϑ_{fb} by means of a PID-controller, whose parameters are identified via an autotune function.

The prototype spindle is operated on a spindle test bench in a laboratory at the FISCHER DEUTSCHLAND GMBH with a maximum rotational speed n_{max} = 50,000 1/min. The spindle is water-cooled at a volumetric flow rate $\dot{V}$ = 3 l/min and a constant fluid temperature ϑ_{fl} = 20 °C with a temperature deviation of $\Delta\vartheta_{fl} \leq 0.1$ °C. The axial shaft displacement d_s of the spindle is measured at a plane reference surface of a tool holder by means of an eddy current sensor of type SGS4701 by MICRO-EPSILON MESSTECHNIK GMBH & CO. KG, Ortenburg, Germany.

2.1. Experimental procedure

In order to examine the capacity of the temperature control system for reference tracking, the front bearing temperature is set to ϑ_{fb} = 30 °C and then changed to ϑ_{fb} = 40 °C before being reset to ϑ_{fb} = 30 °C. The purpose of these tests is to examine the settling time t_s and the maximum overshoot Δh of the closed-loop system. The settling time t_s is specified as the point at which the measured data is first bounded by tolerance band of width w = 0.2 °C, and subsequently remains within these boundaries. This implies that the boundary of the tolerance band is located at ± w/2 = ± 0.1 °C around the setpoint of the front bearing temperature ϑ_{fb}.

Subsequently, the controller's capability for disturbance rejection is evaluated by means of an incremental increase in the rotational speed n. The changes in rotational speed n are accompanied by a change in the heat flow $\dot{Q}_{ind}$ induced at the bearings. The test procedure is specified in table 1. Upon attaining the maximum rotational speed n_{max} = 50,000 1/min, the spindle is brought to an immediate stop. Thereafter, following a downtime of t_d = 2,700 s, the spindle is accelerated to its maximum rotational speed n_{max}. This enables the evaluation of the deviation of the controlled front bearing temperature $\Delta\vartheta_{fb}$ from its setpoint, due to thermal disturbances. The quantification of the maximum change in axial shaft displacement Δd_s is enabled by the deceleration from maximum rotational speed n and subsequent acceleration to maximum speed n.

Table 1. Test procedure with incrementally changes in rotational speed n.

step	duration Δt	rotational speed n
1	900 s	0 1/min
2	900 s	10,000 1/min
3	900 s	20,000 1/min
4	900 s	30,000 1/min
5	900 s	40,000 1/min
6	900 s	50,000 1/min
7	2,700 s	0 1/min
8	1,900 s	50,000 1/min

3. Results

As shown in figure 3, the controlled front bearing temperature ϑ_{fb} is measured while its setpoint is altered from ϑ_{fb} = 30 °C to ϑ_{fb} = 40 °C and vice versa. The measurement is conducted at standstill and rotational speed n = 25,000 1/min. It has been found that a maximum overshoot of Δh = 2.2 °C occurs at a rotational speed n = 0 1/min after the setpoint of the front bearing temperature is altered from ϑ_{fb} = 40 °C to ϑ_{fb} = 30 °C. All setpoint changes regarding the front bearing temperature ϑ_{fb} result in a settling time between 40.4 s ≤ t_s ≤ 50.7 s.

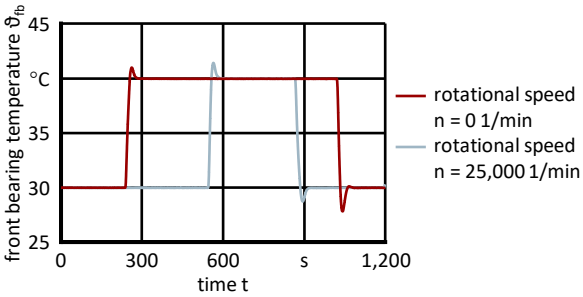

Figure 3. Setpoint alteration of front bearing temperature ϑ_{fb} at rotational speed n = 0 1/min and rotational speed n = 25,000 1/min.

Throughout the entire test procedure, specified in table 1, the setpoint of the front bearing temperature of the prototype spindle remains set to ϑ_{fb} = 30 °C. Figure 4 shows the measured front bearing temperature ϑ_{fb} during this test. It is evident that each alteration of rotational speed n leads to a deviation of the measured front bearing temperature $\Delta\vartheta_{fb}$ regarding the respective setpoint. This phenomenon persists until the measured value again reaches the setpoint. The maximum change in the front bearing temperature $\Delta\vartheta_{fb,max}$ = 1.1 °C is observed when the immediate stop is invoked, see line 6-7 in table 1. For the purpose of comparison, figure 4 shows the front bearing temperature ϑ_{fb} measured during the same test procedure with a reference spindle of type MFW840/50. It is evident that there is a positive correlation between the front bearing temperature ϑ_{fb} and the rotational speed n. When the rotational speed n is increased, the temperature rises abruptly. This is followed by a gradual rise until a steady state is reached. The maximum change in the front bearing temperature of the reference spindle during the test procedure is $\Delta\vartheta_{fb,max}$ = 10.6 °C.

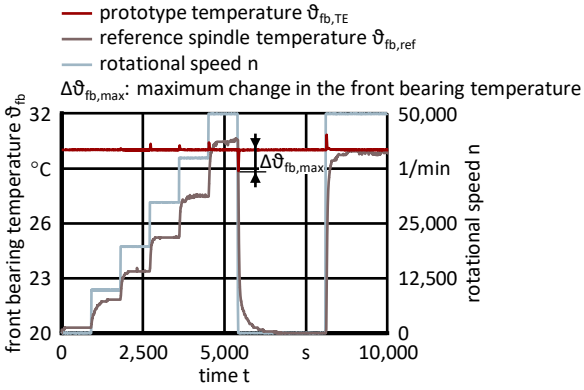

Figure 4. Measured front bearing temperature ϑ_{fb} under the influence of incrementally changing rotational speed n.

Simultaneously, the axial shaft displacement d_s is measured, see figure 5. It is evident that the axial shaft displacement d_s increases with the incremental increase in rotational speed n. The axial shaft displacement d_s initially rises abruptly, evolving into a slower change until a steady state is reached. The abrupt rise in axial shaft displacement d_s can be attributed to the centrifugal forces F_c acting within the angular contact ball bearings and the gyroscopic moment M_g, e.g., described by JEDRZEJEWSKI AND KWASNY [20]. The slower changes in axial shaft displacement d_s can be attributed to the thermal behaviour.

The same test procedure is performed under identical conditions with a reference spindle, see figure 5. The reference spindle is equipped with a conventional water-cooling system and differs from the prototype only in terms of the unmodified front bearing section. The measurements demonstrate a

qualitatively comparable trend, whilst it can be observed that the reference spindle shows a larger change in axial shaft displacement Δd_s subject to the varied rotational speed n. For both spindles, the maximum change in axial shaft displacement Δd_s occurs at the point of change between maximum rotational speed n_{max} and spindle stop. For the reference spindle, the maximum change in axial shaft displacement is $\Delta d_s = 33.7$ µm, and for the prototype, the maximum change in axial shaft displacement is $\Delta d_s = 28.2$ µm. This is equivalent to a 16 % reduction.

A further quantitative difference in the measurements, shown in figure 5, can be observed after the spindle stop. In this instance, the axial shaft displacement d_s of the prototype exhibits a significantly slower decrease in comparison to that of the reference spindle. This can be attributed to the maintenance of the setpoint of the front bearing temperature at $\vartheta_{fb} = 30$ °C, even at standstill. This results in a reduction of the cooling rate of the affected spindle components.

Controlling the front bearing temperature ϑ_{fb} independently of the thermal load enables the spindle components to be prevented from cooling down during downtime t_d due to a tool or workpiece change. This has the potential of reducing the time to reach a steady state with regard to the axial shaft displacement d_s, i.e. the warm- up time t_w after a downtime t_d.

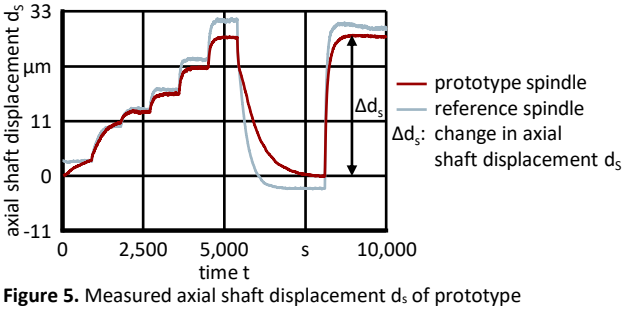

Figure 5. Measured axial shaft displacement d_s of prototype and reference spindle during the test procedure specified in table 1.

4. Conclusion and future work

The present work introduces a novel thermoelectric temperature control system for motorised spindles, based on a tubular Peltier module. A prototype spindle was equipped with such system at the front bearing seat. This prototype could be demonstrated capable of controlling front bearing temperatures within the range of $30\ °C \leq \vartheta_{fb} \leq 40\ °C$. Furthermore, it was demonstrated that thermal disturbances caused by changes in rotational speed n lead to a maximum change in the front bearing temperature of $\Delta\vartheta_{fb,max} = 1.1$ °C, where the maximum change in the front bearing temperature of the reference spindle is $\Delta\vartheta_{fb,max} = 10.6$ °C. It was also demonstrated that controlling the front bearing temperature ϑ_{fb} exerts an influence on the axial shaft displacement d_s. In particular, maintaining a constant front bearing temperature of $\vartheta_{fb} = 30$ °C results in a 16 % decrease in the change in axial shaft displacement Δd_s during changes of the rotational speed n when compared to a reference spindle. Furthermore, the measurement of the axial shaft displacement d_s indicates, that controlling the front bearing temperature ϑ_{fb} independently of the thermal load has an effect on the cooling rate of spindle components.

A future objective is to substantially minimise the warm-up time t_w following a spindle stop, for instance after a workpiece or tool change in the machine tool. As demonstrated in previous research of UHLMANN [18], this objective can be accomplished by increasing the front bearing temperature ϑ_{fb} during downtime t_d of the spindle. Reducing warm-up time t_w decreases non-productive time, contributing to increased productivity.

Acknowledgments

The authors would like to express their sincere gratitude to the DR. NEUMANN PELTIER-TECHNIK GMBH for their invaluable support in conducting this research and for provision of a Peltier controller.

This work was funded within the Fraunhofer-DFG transfer program by Fraunhofer Society and Deutsche Forschungsgemeinschaft (DFG, German Research Foundation) - 529738427.

References

[1] Uhlmann E, Mullany B, Biermann D, Rajurkar K P, Hausotte T and Brinksmeier E 2016 Process chains for high-precision components with micro-scale features *CIRP Ann.* **65** (2) 549-572

[2] Mayr J et al. 2012 Thermal issues in machine tools *CIRP Ann.* **61** (2) 771-791

[3] Brecher C and Wissmann A 2011 Compensation of thermo-dependent machine tool deformations due to spindle load: investigation of the optimal transfer function in consideration of rough machining *Prod. Eng. Res. Devel.* **5** (5) 565-574

[4] Denkena B, Bergmann B and Klemme H 2020 Cooling of motor spindles—a review *Int. J. Adv. Manuf. Technol.* **110** (11–12) 3273-3294

[5] Li S and Wu Y 2010 A study on oil/air lubrication and preload of a high frequency fully ceramic motor spindle *International Conference on E-Product E-Service and E-Entertainment 2010* 1-4

[6] Putra N and Ariantara B 2017 Electric motor thermal management system using L-shaped flat heat pipes *Appl. Therm. Eng.* **126** 1156-1163

[7] Fang G, Yuan W, Yan Z, Sun Y and Tang Y 2019 Thermal management integrated with three-dimensional heat pipes for air-cooled permanent magnet synchronous motor *Appl. Therm. Eng.* **152** 594-604

[8] Kajikawa S, Morita S, and Sugita N 2024 Cooling of spindle shaft for machining center using heat exchangers *J. Adv. Mech. Des. Syst. Manuf.* **18** (3) 1-15

[9] Xia C, Fu J, Lai J, Yao X and Chen Z 2015 Conjugate heat transfer in fractal tree-like channels network heat sink for high-speed motorized spindle cooling *Appl. Therm. Eng.* **90** 1032-1042

[10] Huang Y-H, Huang C-W, Chou Y-D, Ho C-C and Lee M-T 2016 An experimental and numerical study of the thermal issues of a high-speed built-in motor spindle *Smart Sci.* **4** (3) 160-166

[11] Jonath L, Luderich J, Brezina J, Gonzalez Degetau A M and Karaoglu S 2023 Improving the thermal behavior of high-speed spindles through the use of an active controlled heat pipe system *3rd International Conference on Thermal Issues in Machine Tools (ICTIMT2023) Lecture notes in production engineering* 203-218

[12] Wakiya S, Ishida R, Kusuyama J and Nakao Y 2023 Temperature control performance of a built-in motor spindle by developed temperature feedback control system *Int. J. Autom. Technol.* **17** (5) 512-520

[13] Peltier J C A 1834 Nouvelles expériences sur la caloricité des courants électrique *Ann. Chim. Phys.* **2** (56) 371-386

[14] Fan K, Xiao J, Wang R and Gao R 2022 Thermoelectric-based cooling system for high-speed motorized spindle I: design and control mechanism *Int. J. Adv. Manuf. Technol.* **121** (5-6) 3787-3800

[15] Fan K, Xu R, Wang R and Gao R 2022 Thermoelectric-based cooling system for high-speed motorized spindle II: Optimization and validation strategy *Int. J. Adv. Manuf. Technol.* **119** (9-10) 6521-6533

[16] Uhlmann E, Polte J, Salein S, Iden N, Temme P, Hartung D and Perschewski S 2020 Entwicklung einer thermoelektrisch temperierten Motorspindel *wt Werkstattstechnik online* **110** (5) 299-305

[17] Uhlmann E, Polte M, Triebel F, Salein S, Temme P, Hartung D and Perschewski S 2022 Reduction of warm-up period after machine downtime by means of a thermoelectric tempered motorized milling spindle *euspen SIG Meeting: Thermal Issues*

[18] Uhlmann E 2023 Recent advances in precision, sustainability and safety of machine tools *J. Mach. Eng.* **23** (3) 5-25

[19] Goldsmid H J 2016 *Theory of Thermoelectric Refrigeration and Generation* Springer Ser. Mater. Sci. **121**

[20] Jedrzejewski J and Kwasny W 2010 Modelling of angular contact ball bearings and axial displacements for high-speed spindles *CIRP Ann.* **59** (1) 377-382

euspen's 26th International Conference & Exhibition, Krakow, PL, June 2026
www.euspen.eu

Evaluation of the temperature influence in the measurement uncertainty of a telescopic simultaneous ball-bar for manufacturing systems verification

Francisco Javier Brosed [1,2,3], Juan José Aguilar [1,2], Sergio Aguado [1,2], Marcos Pueo [1,2], Ana Cristina Majarena [1,2], Jesús Velázquez [1,2]

[1] *Department of Design and Manufacturing Engineering, University of Zaragoza, María de Luna 3, 50018 Zaragoza, Spain.*
[2] *Instituto de Investigación en Ingeniería de Aragón (I3A), 50018 Zaragoza, Spain*

[3] *fjbrosed@unizar.es*

Abstract
Machine tool and industrial robot verification processes increasingly demand higher accuracy due to the growing presence of high value-added operations in manufacturing. Several commercial solutions are currently available for the verification of manufacturing systems. Among them, telescopic systems are used to track the position of a manufacturing system by measuring three-dimensional coordinates. This verification can be performed using a single telescopic arm and tracking from three different positions, i.e. repeating the process three times, or by using three telescopic arms simultaneously to obtain the three-dimensional coordinates without repeating measurements. The work presented at euspen's ICE 2026 investigates the influence of temperature on the measurement results of an interferometry-based instrument using simultaneous multilateration. The measurement system consists of a telescopic simultaneous ball-bar composed of three telescopic arms that simultaneously measure the distances between three fixed reference spheres and a single moving sphere mounted on the spindle of a machine tool or on the end-effector of an industrial robot, which constitutes the manufacturing system under inspection. This study models the complete measurement process and the influence of temperature from the initial calibration steps—required to adjust each telescopic ball-bar—through to the final determination of the three-dimensional position. Intermediate measurement stages, such as the measurement of distances between the three fixed reference spheres using the telescopic ball-bars, are also included in the model.

Keywords: Interferometry; Measuring instrument;Thermal error;Verification

1. Introduction

Temperature significantly influences dimensional metrology through thermal expansion, causing parts and measurement tools to change size, creating errors relative to the 20°C standard, requiring compensation or controlled environments to maintain accuracy, especially for high-precision work where subtle shifts become critical [1-4].

The geometric tolerances in manufacturing require trazable dimensional metrology to guarantee the production quality [5,6]. The behaviour of the manufacturing systems can be improved through verification and compensation techniques [2]. There are different ways to perform a machine tool (MT) verification: measuring the movement of each axis with an interferometer [7]; measuring circular paths with a ball-bar [8]; measuring the displacement of the head with a laser tracker [9] or triangulating distances that are measured from several points on the MT bed plate to a point fixed to the MT head using laser tracers [10] and laser ball-bars [11, 12], this last method usually requires several cycles modifying the position of the equipment fixed on the bed plate of the MT.

In any of these processes, temperature changes that occur during the use of measuring instruments affect the accuracy and repeatability of the measurement result. Temperature variations occur both during equipment setup and data acquisition during verification, impacting the results of the verification and compensation of the production system.

This paper studies the influence of temperature on the measurement results of an instrument based on interferometry and simultaneous multilateration. The instrument, classified within the group of laser ball-bars, consists of a telescopic simultaneous ball bar (TSB), composed of three telescopic arms, which simultaneously measures the distances between three fixed spheres and a single sphere located on the headstock of a machine tool or robot—the manufacturing system under inspection. This work models the measurement process and the influence of temperature from the initial steps, which allow for the adjustment of each telescopic ball-bar (TB), to obtaining the measurement results, also modeling the intermediate steps, such as measuring the distance between the three fixed spheres with the TSB.

The TSB has been analyzed in previous works: [13] presents an evaluation of the uncertainty with TSB calibration and [14] shows the use of the system and a comparison of its measurement results with an interferometer. This work complements these studies, focusing on evaluating the influence of temperature on the measurement uncertainty of the TSB.

The paper is structured as follows: Section 2 describes the TSB, its measurement procedure, and the errors associated with the effect of temperature. Section 3 details the methodology followed in the analysis and the configuration of each simulated test. Section 4 presents the results obtained from the study that isolate the effect of temperature on TSB measurement results. Finally, Section 5 presents the main conclusions of the study.

2. Hardware model and measurement procedure

This section describes the use of a TSB to measure 3D coordinates of a point in space multilaterating from the distances between the point under measurement and three fixed points located on the bed plate of the system. The main effects due to temperature changes during the set up and the measurement process are also described.

2.1. Telescopic simultaneous ball-bar

The TSB measure 3D coordinates of a point in space. The TSB is composed by three TB. Each TB measures the distance between two steel spheres using an interferometer. The special design of each TB allows three ends pointing to the same steel sphere while the other end of each TB is located in a fixed kinematic support, KS [15]. This configuration allows the simultaneous tracking of a steel spheres with the TSB: three TB simultaneously measuring the distance between three fixed points (the kinematic supports, KS_i, with i from 1 to 3) and the steel sphere, figure 1.

From the three distances between spheres measured simultaneously, $L_{i,p}$ with i from 1 to 3, by each TB of the TSB, the coordinates of the centre of the steel sphere, P (P = {$X\ Y\ Z$}'), can be multilatered as shown in (1) to (3).

$$X = \frac{L_{1,p}{}^2 - L_{2,p}{}^2 + X_{KS2}{}^2}{2 \cdot X_{KS2}} \quad (1)$$

$$Y = \frac{L_{1,p}{}^2 - L_{3,p}{}^2 + X_{KS3}{}^2 + Y_{KS3}{}^2}{2 \cdot Y_{KS2}} - \frac{X_{KS3}}{Y_{KS3}} \cdot X \quad (2)$$

$$Z = \sqrt{L_{1,p}{}^2 - X^2 - Y^2} \quad (3)$$

Where. $X_{KSi}\ Y_{KSi}\ Z_{KSi}$, with i from 1 to 3, are the coordinates of the centre of the sphere located in each kinematic support (KS) expressed in the TSB reference system (RS_{TSB}), (4) to (6).

$$X_{KS} = L_{12} \quad (4)$$

$$X_{KS3} = L_{13} \cdot \cos(\beta_{13}) \quad (5)$$

$$Y_{KS3} = L_{13} \cdot \sin(\beta_{13}) \quad (6)$$

Where β_{13} is the angle between the segment joining KS1 and KS3 with the segment joining KS1 and KS2 (Figure 1) and its cosine can be calculated from the cosine theorem with the three distances between the KSs ($L_{i,j}$,with i≠j and i,j form 1 to 3), (7). The remaining values that do not appear in (4) to (6) are zero.

$$\cos(\beta_{13}) = \frac{L_{2,3}^2 - L_{1,2}^2 - L_{1,3}^2}{-2 \cdot L_{1,2} \cdot L_{1,3}} \quad (7)$$

2.2. Measurement procedure

The first step of the procedure (STEP1) is to set up the reference distance for the interferometer of each TB. A calibrating ball beam artifact (CBBA) is used to materialice the reference distance, L_0, with an uncertainty of 1.3 µm with a coverage factor k=2 in accordance with the Guide to the Expression of Uncertainty in Measurement, GUM [16].

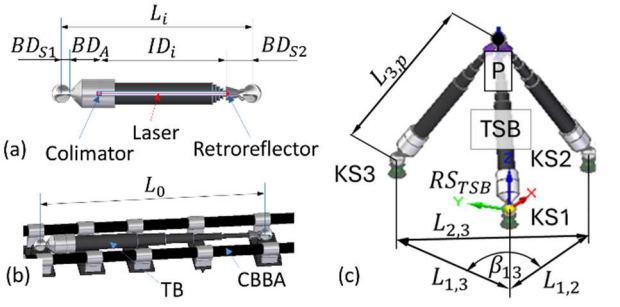

Figure 1. (a) TB: Balance distance, $BD_S = BD_{S1} + BD_{S2}$, and interferometer distance, ID_i. Both distances make up the resulting distance between spheres. (b) Set up of a TB with the CBBA in the reference position, L_0. (c) TSB mode. Reference systems and characteristics of the TSB: RS_{TSB}, KC, $L_{i,j}$ (measured in the second step of the measurement procedure) and $L_{i,p}$ (measured in the third step).

The interferometer measures the distance between spheres with an offset (balance distance, BD) due to its integration into the TB (Interferometer distance, ID), (8).

Once each TB is set up with L_0, the distance obtained from the laser interferometer is the increment from L_0, (9), and the distance between spheres need to be internaly computed. This aply for the following steps (second and third).

$$L_0 = BD + ID_0 \quad (8)$$

$$L_i = BD + ID_0 + \Delta ID_i \quad (9)$$

$$BD = BD_S + BD_A = BD_{S1} + BD_{S2} + BD_A \quad (10)$$

Where BD_S and BD_A are the lengths of the balance distance manufactured with steel (54%) and aluminium alloy (46%) respectively.

The second step (STEP2) is the measurement of the distances between the fixed KS, $L_{i,j}$. Each TB measures simulateously one of the three $L_{i,j}$.

The third step (STEP3) is the measurement of $L_{i,p}$. In this step each TB measures simulateously the distance between a KS and the sphere in the manufacturing system head, P.

At each measurement step environmental temperature, ET, and the temperatures of the machine and the TSB are recorded along with each measurement.

Finally, STEP4, is the reconstruction of the 3D coordinates of P from (1) to (7).

2.3. Effect of the temperature in the measurement procedure

In a temperature-controlled environment where working temperature can be assumed to coincide with reference temperature ($T_R = 20°C$), (9) can be rewritten as equation (11).

$$L_i = L_0 + \Delta ID_i \quad (11)$$

However, temperatures other than T_R modify the dimensions of the materials according to their coefficient of thermal expansion. For the materials analyzed, their coefficient of linear thermal expansion (CLTE) was considered with a constant value within the operating temperature range (Table 1).

Table 1. Coeficients of linear thermal expansion (CLTE) and estimated uncertainty according to ISO 230 [17].

Material	CLTE $/K^{-1}$	$\sigma = u_{CLTE}\ /K^{-1}$
Aluminium Alloy (α_A)	$23.00 \cdot 10^{-6}$	$0.66 \cdot 10^{-6}$
Steel (α_S)	$11.00 \cdot 10^{-6}$	$0.58 \cdot 10^{-6}$
Carbon Fiber (α_{CF})	$-0.74 \cdot 10^{-6}$	$0.58 \cdot 10^{-6}$
Machine Tool (α_M)	$12.00 \cdot 10^{-6}$	$0.58 \cdot 10^{-6}$

In STEP1 the CBBA dimension depends on the artifact temperature (T_a) and the material used for its manufacturing, in this case carbon fiber. The interferometer reading in STEP1 (ID_0) will depend on the CBBA dimension and the BD dimension at the TB temperature during setup (T_{TB}). Since the adjustment must be performed on-site prior to taking measurements, ID_0 will be affected by the temperature, (12).

$$L_0(1 + \alpha_{CF}\theta_a) = BD_S(1 + \alpha_S\theta_{TB}) + BD_A(1 + \alpha_A\theta_{TB}) + ID_0(1 + \alpha_{CF}\theta_a) \quad (12)$$

$$\theta_i = T_i - T_R \quad (13)$$

$$ID_0 = L_0 - \frac{BD_S(1+\alpha_S\theta_{TB}) + BD_A(1+\alpha_A\theta_{TB})}{(1+\alpha_{CF}\theta_a)} \quad (14)$$

$$L_i(1 + \alpha_M\theta_{Mi}) = BD_S(1 + \alpha_S\theta_{TBi}) + BD_A(1 + \alpha_A\theta_{TBi}) + ID_0(1 + \alpha_{CF}\theta_a) + \Delta ID_i(1 + \alpha_M\theta_{Mi}) \quad (15)$$

During setup, STEP1, the CBBA and TSB temperatures are T_a and T_{TB} respectively.

In the next steps, after STEP1, the measurement provided by the interferometer as a function of temperature, T_{Mi}, ($\Delta ID_i(1 + \alpha_M\theta_{Mi})$; where α_M is the CLTE of the machine tool and θ_{Mi} is the diference between, T_{Mi}, the temperature of the machine tool and T_R) is used to calculate the value of the length measured between spheres, L_i, (15),

After STEP2 and STEP3, $L_{i,j}$ and $L_{i,P}$ are calculated, (15), and used to obtain the 3D coordinates of P with (1) to (7).

3. Methodology and simulation test

The thermal effect in the uncertainty of a length measurement can be modelled, according with ISO/TR 16015 [18], from three

main uncertainty components: the effect of the ET variation, the effect of the uncertainty of each CLTE and the effect of the uncertainty in the measurement of the temperature.

The variation of the ET during the measurement process, which lasts approximately 40 minutes, is defined, based on previous experiments, as 1°C from the beginning to the end of the measurement process. To simulate this effect, a temperature curve is defined that follows (16) with k = 0.05 min^{-1}.

$$T_i^{\square} = T_{out}^{\square} + (T_{ini}^{\square} - T_{out}^{\square})e^{-kt} \quad (16)$$

The outside temperature of the workshop, $T_{out}^{\square}$, is randomly selected between 14 and 27 °C in each iteration. The initial temperature, $T_{ini}^{\square}$, is randomly selected with an increment of ±0.5 °C relative to $T_{out}^{\square}$ in each iteration. (16) estimates the ET for each step described: In STEP 1, an ET is established for the adjustment of each TB ($T_{0,1}^{\square} = T_i^{\square}(t=1)$, $T_{0,2}^{\square} = T_i^{\square}(t=2)$, $T_{0,3}^{\square} = T_i^{\square}(t=3)$, with t in minutes). In STEP 2, $T_{i,j}^{\square} = T_i^{\square}(t=4)$, because the three distances are measured simultaneously, $L_{i,j}$,with i≠j and i,j form 1 to 3. In STEP 3, an ET is estimated for each of the 214 points of the VV ($T_{i,P}^{\square}$,= $T_i^{\square}(t)$, with t increasing by 10s for each measured point).

Following the measurement procedure in section 2.2, the model establishes a temperature for each element of the system involved in the process, based on the estimated ET for each step. Temperature influences the dimensions of the materials according to their CLTE and the uncertainty of the CLTE estimate influences the uncertainty of the length measurement. Table 1 shows the CLTE and its estimated uncertainty according to ISO 230 [17]. In the simulation, the CLTE uncertainty is modelled by introducing normally distributed noise to the CLTE value identified for each material.

Environmental compensation unit (ECU) calibration allows for the correction of systematic error in temperature measurement, but the measurement uncertainty, although known, will introduce an error into the compensation model. To simulate the temperature measurement uncertainty the model generates normally distributed noise ($\sigma = U_{ECU}/k_{ECU}$) for each temperature measured in the process. From the ECU calibration $U_{ECU} = 0.01\,°C$ and a coverage factor $k_{ECU} = 2$ are obtained, in accordance with the GUM [16].

The simulation model calculates ΔID_i using nominal values for the temperature (17). ΔID_i is used to recalculate the L_i' values. L_i' values correspond to the L_i values calculated introducing noise into the temperature data to simulate the uncertainty in the measurement of the temperature (18).

$$\Delta ID_i = L_i - \frac{BD_S(1+\alpha_S\theta_{TBi}) + BD_A(1+\alpha_A\theta_{TBi}) + ID_0(1+\alpha_{CF}\theta_a)}{(1+\alpha_M\theta_{Mi})} \quad (17)$$

$$L_i' = \Delta ID_i + \frac{BD_S(1+\alpha_S\theta'_{TBi}) + BD_A(1+\alpha_A\theta'_{TBi}) - ID_0(1+\alpha_{CF}\theta'_0)}{(1+\alpha_S\theta'_{Mi})} \quad (18)$$

From (17) and (18) the simulated values $L'_{i,j}$ and $L'_{i,P}$ are obtained allowing the 3D reconstruction of the coordinates of P'. The coordinates of P' are compared with the nominal value of P obtaining an error value for each point, (19) and (20).

$$XYZ'_{Error} = XYZ'^{\square}_{\square} - XYZ^{\square}_{\square} \quad (19)$$

$$D'_{Error} = \sqrt{\left(X'^{\square}_{\square} - X^{\square}_{\square}\right)^2 + \left(Y'^{\square}_{\square} - Y^{\square}_{\square}\right)^2 + \left(Z'^{\square}_{\square} - Z^{\square}_{\square}\right)^2} \quad (20)$$

With the aim of understanding the thermal effect in the case where the thermal expansion of the materials is not compensated for, a second model is proposed (21) to (23).

$$L_i'' = \Delta ID_i + L_0 \quad (21)$$

$$XYZ''_{Error} = XYZ''^{\square}_{\square} - XYZ^{\square}_{\square} \quad (22)$$

$$D''_{Error} = \sqrt{\left(X''^{\square}_{\square} - X^{\square}_{\square}\right)^2 + \left(Y''^{\square}_{\square} - Y^{\square}_{\square}\right)^2 + \left(Z''^{\square}_{\square} - Z^{\square}_{\square}\right)^2} \quad (23)$$

The verification volume (VV) consists of 214 points, distributed with varying TB lengths from 500 mm in 100 mm increments to a maximum of 1000 mm so that a representative VV of the TSB is covered.

The effect of the temperature in the measurement uncertainty of the TSB is estimated using the Monte Carlo Method [19].

The number of iterations is an important parameter of the Monte Carlo simulation. From previous works, the Monte Carlo simulation converge using 10^6 iterations [13].

The simulation model allows the thermal influence on the measurement uncertainty estimate for the TSB to be isolated. The results are compared with the nominal values and with those obtained without temperature compensation.

4. Simulation results

Following the methodology exposed in the previous section the simulation has been performed. The 10^6 iterations to apply the Monte Carlo Method took 540 s with a 3.0 GHz CPU clock speed.

The effect of length measurement errors on reconstructing the coordinates of measured points depends on the location of the points within the VV. Since the effect of temperature on the measurement result is to introduce errors in the measurement of lengths, the magnitude of its influence varies depending on the area of the VV in which the measured point is located.

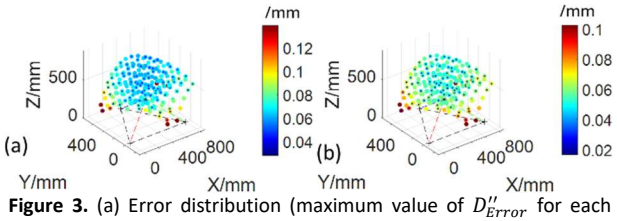

Figure 3. (a) Error distribution (maximum value of D''_{Error} for each point) in the TSB VV. (b) Distribution in the VV of the uncertainty (maximum value of the triple: Uncertainty of X, Y and Z) due to the lack of temperature compensation in the measurement process.

Figure 3 shows the error distribution in the TSB VV and the effect on uncertainty as the calculated uncertainty value when only the effect of temperature is considered. For the proposed variations, between 14 and 27 °C, the error introduced in the reconstruction of the point coordinates reaches 139 µm (XYZ''_{Error} and D''_{Error}), while the effect on the estimated uncertainty in the coordinate reconstruction reaches 102 µm.

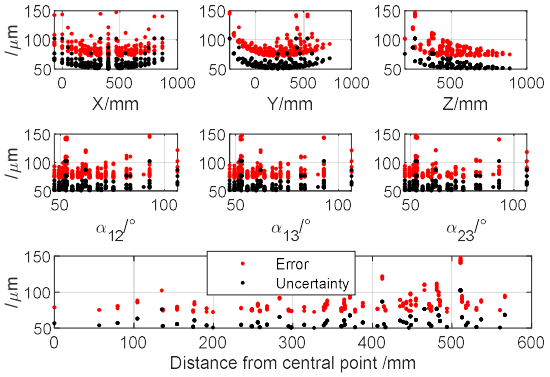

Figure 4. The coordinates of each measured point (X, Y, Z) are plotted in the abscissa in the first row, the angles formed by the TBs in the second row, and the distance from the central point in the third row versus the maximum value of D''_{Error} for each point (red) and the estimated uncertainty (maximum value of the triple: Uncertainty of X, Y and Z) for each point in ordinates (black).

The error and uncertainty trend as a function of the coordinates, as a function of the angles formed by the TBs and as a function of the distance to the central point of the TSB (point where the arms form a trirectangular trihedron, represented by an asterisk in Figure 2 b) is represented in Figure 4.

When temperature is compensated, the error decreases so that the effect on the measurement results is limited. By compensating for temperature, the error in the reconstruction

of the points (XYZ'_{Error} and D'_{Error}) is reduced to 11 µm. The effect on the measurement uncertainty is below 7 µm (Figure 5).

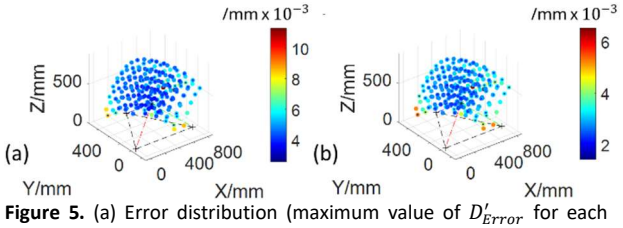

Figure 5. (a) Error distribution (maximum value of D'_{Error} for each point) in the TSB VV. (b) Distribution in the VV of the uncertainty (maximum value of the triple: Uncertainty of X, Y and Z) due to the uncertainty in the measurement of temperature for its compensation in the measurement process.

The error and uncertainty trend for the case where the temperature effect is compensated can be seen in Figure 6.

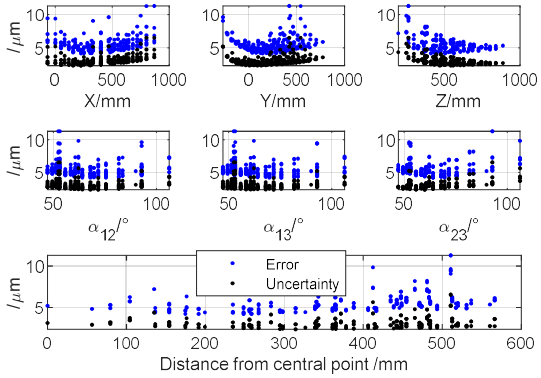

Figure 6. The coordinates of each measured point (X, Y, Z) are plotted in the abscissa in the first row, the angles formed by the TBs in the second row, and the distance from the central point in the third row versus the maximum value of D'_{Error} for each point (blue) and the estimated uncertainty (maximum value of the triple: Uncertainty of X, Y and Z) for each point in ordinates (black).

Table 2 shows the effect of temperature compensation on the uncertainty and the measurement error.

Table 2. Main effects on uncertainty and thermal errors obtained from the simulation. Temperature compensation is obtained from equations (17) to (20), $XYZ'_{\square}$. Values without temperature compensation are obtained from equations (21) to (23), $XYZ''_{\square}$.

/µm	Uncertainty			Thermal erorrs		
	X	Y	Z	X	Y	Z
$XYZ''_{\square}$	36.3	24.4	102.5	52.8	41.2	138.9
$XYZ'_{\square}$	2.8	2.5	6.5	5.0	4.8	11.3

4. Conclusions

When the temperature deviates from the reference value, systematic errors are introduced into the measurement process if their effects are not compensated. Furthermore, uncertainty in temperature measurement propagates into length measurements, increasing overall measurement uncertainty and degrading the accuracy of point coordinate reconstruction.

The proposed model effectively compensates for temperature-induced effects, reducing both measurement uncertainty to 6.5 µm and systematic measurement error to 11.3 µm.

Future work will focus on characterizing temperature effects when additional materials commonly used in production systems are involved, such as aluminum-based structures.

Acknowledgments: This research was funded by the Ministerio de Ciencia e Innovación with project number PID2022-139280OB-I00, by Aragon Government (Department of Industry and Innovation) through the Research Activity Grant for research groups recognized by the Aragon Government (T56_17R Manufacturing Engineering and Advanced Metrology Group). This is co-funded with European Union ERDF funds.

References

[1] Swyt DA. Uncertainties in Dimensional Measurements Made at Nonstandard Temperatures. J Res Natl Inst Stand Technol. 1994 Jan-Feb; **99**(1):31-39. doi: 10.6028/jres.099.004.

[2] Schwenke H, Knapp W, Haitjema H, Weckenmann A, Schmitt R, Delbressine F 2008 Geometric error measurement and compensation of machines – An update *CIRP Ann.* **57** (2) 660-75, https://doi.org/10.1016/j.cirp.2008.09.008.

[3] Ferrucci M, Haitjema H, Leach R 2018 Chapter: Dimensional Metrology in: Basics of Precision Engineering (R. Leach, S. T. Smith, R. Leach, S.T. Smith, Boca Raton), CRC Press, 151-203 978-1-4987-6085-0.

[4] De Groot P, Badami V, Liesener J 2016 Concepts and geometries for the next generation of heterodyne optical encoders *Proc. ASPE* (Portland, Oregon) **65** 146–149.

[5] Moona G,Jewariya M, Sharma R 2019 Relevance of Dimensional Metrology in Manufacturing Industries *MAPAN* **34** (1) 97–104, https://doi.org/10.1007/s12647-018-0291-3.

[6] BIPM, IEC, IFCC, ILAC, ISO, IUPAC, IUPAP, OIML 2008 International vocabulary of metrology—Basic and general concepts and associated terms, JCGM 200 Bureau International des Poids et Mesures (BIPM), 2008.

[7] Jiang X, Meng T, Wang L, Liu C 2020 Rapid calibration method for measuring linear axis optical paths of computer numerical control machine tools with a laser interferometer *Int. J. Adv. Manuf. Technol.* **110** 3347-64, https://doi.org/10.1007/s00170-020-05976-6.

[8] Zhong L, Bi Q, Wang Y 2017 Volumetric accuracy evaluation for five-axis machine tools by modeling spherical deviation based on double ball-bar kinematic test *Int. J. Mach. Tools Manuf.* **122** 106-19, https://doi.org/10.1016/j.ijmachtools.2017.06.005.

[9] Aguado S, Samper D, Santolaria J, Aguilar J J 2012 Identification strategy of error parameter in volumetric error compensation of machine tool based on laser tracker measurements *Int. J. Mach. Tools Manuf.* **53** (1) 160-9, https://doi.org/10.1016/j.ijmachtools.2011.11.004.

[10] Zha J,Wang T,Li L, Chen Y 2020 Volumetric error compensation of machine tool using laser tracer and machining verification *Int. J. Adv. Manuf. Technol.* **108** (7- 8) 2467-81 https://doi.org/10.1007/s00170-020-05556-8.

[11] Fan K C, Wang H, Shiou F J, Ke C W 2004 Design analysis and applications of a 3D laser ball bar for accuracy calibration of multiaxis machines *J. Manuf. Syst.* **23** (3) 194-203 https://doi.org/10.1016/S0278-6125(05)00009-9.

[12] Etalon X-AX LASERBAR, https://www.etalonproducts.com/en/products/x-ax_laserbar/, 2021 (Accessed: January 2024).

[13] Brosed F J, Aguilar J J, Acero R, Santolaria J, Aguado S, Pueo M 2022 Calibration and uncertainty budget analysis of a high precision telescopic instrument for simultaneous laser multilateration *Measurement* **190** 110735. https://doi.org/10.1016/j.measurement.2022.110735.

[14] Acero R, Brosed F J, Pueo M, Aguado S, Aguilar J J, Velazquez J, Evaluation of a telescopic simultaneous ballbar in a 3-axis machine tool using a reference equipment, Precision Engineering, **88**, 2024, 117-124, ISSN 0141-6359, https://doi.org/10.1016/j.precisioneng.2024.02.001.

[15] Acero R, Aguilar J J, Brosed F J, Santolaria J, Aguado S, Pueo M 2021 Design of a Multi-Point Kinematic Coupling for a High Precision Telescopic Simultaneous Measurement System *Sensors* **21** 6365 https://doi.org/10.3390/s21196365.

[16] BIPM, IEC, IFCC, ILAC, ISO, IUPAC, IUPAP, OIML 2008 Evaluation of Measurement Data—Guide to the Expression of Uncertainty in Measurement, JCGM 100 Bureau International des Poids et Mesures (BIPM), 2008.

[17] International Organization for Standardization (ISO) 2012 Machine Tools. Test code for machine tools—ISO 230. ISO.

[18] International Organization for Standardization. (2003). Geometrical product specifications (GPS)—Systematic errors and contributions to measurement uncertainty (ISO/TR 16015:2003). ISO.

[19] BIPM; IEC; IFCC; ILAC; ISO; IUPAC; IUPAP; OIML 2008 Evaluation of Measurement Data—Supplement 1 to the Guide to the Expression of Uncertainty in Measurement—Propagation of Distributions Using a Monte Carlo Method; JCGM 101 Bureau International des Poids et Mesures (BIPM), 2008.

euspen's 26th International Conference & Exhibition, Krakow, PL, June 2026
www.euspen.eu

A compact cube-shaped parallel kinematic machine for dynamic and high-precision positioning in six degrees of freedom

Tillmann Volz [1], Stefan Schulz[1], Stephanie Streit[1]

[1]*Physik Instrumente (PI) SE & Co. KG*

T.Volz@PI.de

Abstract
This paper introduces a compact, direct-driven, cube-shaped parallel kinematic machine (PKM) that employs electromagnetic voice coil motors with linear cross-roller bearings. The motion of the motors is directly transferred to the end effector via passive struts, and adjustable magnetic counterbalances are paired with the motors to compensate for the lack of self-locking. Unlike typical PKM configurations with parallel top and base plates, this cube-shaped PKM uses three pairs of actuators, where these pairs of motors, bearings, and passive struts are aligned along Cartesian axes, forming a cubic structure. Each pair of struts is attached to a planar top plate, which is then interconnected to form a corner-cube-shaped top plate, offering three faces for payload attachment and versatile integration into systems. The design ensures consistent stiffness, resolution, and dynamic capabilities in all Cartesian directions, even when oriented with one surface of the top plate facing downward. Additionally, the absence of ball- or roller-screws, commonly used in standard PKMs for high-precision positioning, enhances the system's lifetime, while also providing significantly higher dynamics (velocity and acceleration).

Hexapod, Positioning, Dynamic

1. Introduction

PKMs with ball- or roller-screws, combined with electromagnetic motors saw a large growth over the last years and are today the go to and turn-key solution in a vast number of applications whenever motion in six degrees of freedom, very high precision down to the nanometre range and high stiffness is demanded. By their nature however, such systems are limited, mainly in two regimes. One being dynamic capabilities, namely velocity and acceleration. The other being lifetime, especially due to dynamic motion with small step sizes or amplitudes that may cause accelerated wear and tear of raceways and rolling elements used in driving components. To expand the application range of PKMs and enable a wide application in an industrial environment where high reliability, high lifetime and high throughput are necessary, an approach with a direct transfer of the electromagnetic motor motion to the PKMs platform is promising. The development of the cube-shaped PKM, that is presented in this paper, is a natural progression from a series of direct-driven PKMs that Physik Instrumente (PI) SE & Co. KG has developed over recent years, such as an air-bearing hexapod presented by Matitschka et al. [1] and the lever-actuated direct-driven PKM presented by Volz et al. [2]. Further advancements in fully flexure-based direct-driven PKMs have been made by Naves et al. [3, 4, 5]. Unlike the aforementioned direct-driven PKM configurations, where the top and base plates are typically arranged in parallel in the initial position and exhibit exceptional stiffness and resolution, especially in the direction normal to the baseplate (usually the Z direction), the cube-shaped hexapod presented in this paper features a unique design. In this, three pairs of actuators and passive struts (see figure 1) are aligned parallel to the Cartesian axes. Each pair of actuators is housed in a separate unit, which is then assembled to form the cube-shaped PKM. The top plate forms the corner of the cube, providing three faces available for payload attachment, and is connected to the actuators via six passive struts with two universal and one rotational joint (URU). In this configuration, there is no preferred orientation but stiffness, resolution and dynamics are the same in all three Cartesian directions. The cube-shaped design allows flexible positioning of the payload on the three surfaces of the top plate without reorienting the PKM. Even in a rotated configuration, where one face of the top plate faces downward, dynamic behavior and stiffness remain largely unchanged, unlike in conventional Stewart platforms.

2. Mechanical Design and Specifications

As mentioned, the PKM is designed to provide isotropic stiffness along the Cartesian axes by using three pairs of passive struts aligned parallel to these axes (see figure 1 on the right). This setup provides mechanical decoupling of the struts, simplifying the control of the PKM. Each passive strut connects the corner-cube-shaped top plate to a linear voice coil motor integrated with linear crossroller guides, enhancing stiffness and ensuring precise positioning.

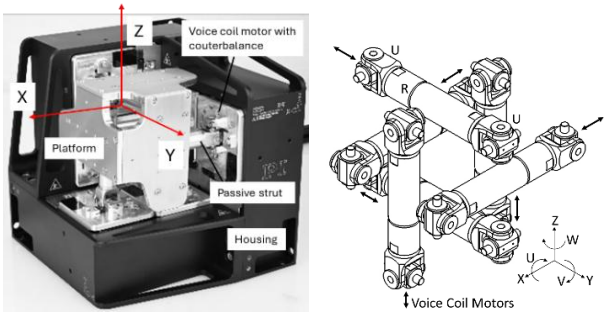

Figure 1. Cube-shaped PKM in an upright orientation (left) and schematic arrangement of passive struts connecting platform and actuators (right)

Additionally, each actuator features an adjustable magnetic counterbalance that compensates for the payload, thereby increasing dynamics and reducing power consumption and with that, thermal drift. The setup allows for a lateral workspace of ±5 mm and a rotational range of ±5 degrees. A summary of the mechanical specifications of the PKM is shown in the following table 1.

Table 1 Mechanical specifications overview

Specification	Value
Cube edge length	195 mm
Translation (X, Y, Z)	± 5 mm
Rotation (U, V, W)	± 5°
Payload	~ 1 kg
Maximum speed	> 200 mm /s
Theoretical resolution	< 2,5 nm

3. Motion Performance

For an evaluation of the motion performance, as well as comparison to high precision spindle-driven PKMs in comparable size, the smallest possible step size or minimal incremental motion (MIM), bidirectional repeatability, crosstalk, linearity and position noise were measured externally using an interferometer that tracks the position of the top plate via an attached mirror. The used setup is shown in figure 2 below.

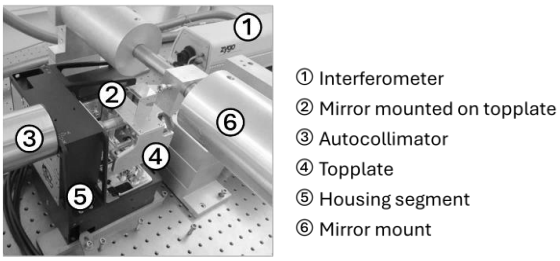

Figure 2. Measurement setup for evaluating the motion performance

The evaluation results are shown in table 2. Compared to compact spindle-driven PKMs, such as the H-811 from PI, the motion performance measurements are comparable and even superior in terms of unidirectional repeatability. Due to the high-resolution sensor and cross-roller bearings, the smallest possible steps, around 20 nm, are very good, even despite the lack of any transmission mechanism. The results also demonstrate that the performance regarding the smallest steps in the X, Y, and Z directions is very consistent, whereas, in classical Stewart platform configurations, the smallest possible steps in the Z direction are usually better than those in the X and Y directions.

Table 2 Mechanical specification overview

Specification	Value
Smallest step size X, Y, Z	20 nm / 20 nm / 20 nm
Position noise 1-sigma X, Y, Z (10s)	4,7 nm / 4,7 nm / 5,8 nm
Crosstalk (X motion, Y error, 8 mm)	314 nm
Linearity X, Y, Z over 8 mm stroke	182 nm / 430 nm / 281 nm
Unidir. repeatability mean X, Y, Z (8 mm)	±22 nm / ±9 nm / ±13 nm

4. Lifetime investigations and alignment tests

One key advantage of the direct-driven and cube-shaped PKMs with cross-roller bearings over spindle-driven PKMs is their extended lifespan, particularly in applications involving dynamic motion trajectories like photonics testing. These applications typically require small, high-frequency movements in the micrometer range, which can accelerate wear in ball screw spindles significantly. To assess the durability of the cross-roller guides used in the cube-shaped PKM, a lifetime test was conducted with a setup featuring a voice coil motor and the cross-roller guides with a short stroke lubricant, but without the magnetic counterbalance or passive strut. The test involved sinusoidal motions with amplitudes decreasing from 10 µm to 1 µm at a constant frequency of 50 Hz, mimicking a planar circular scan for fiber alignment. The starting point was within a 10 µm window, akin to real scan applications where starting points are variable. The condition of the guides was evaluated externally using an interferometer to measure position error and bidirectional repeatability. After over 1.5 billion motions, no significant increase in motion error or deterioration was observed, indicating excellent durability of the cross-roller guides and superiority regarding lifetime compared to spindle-driven PKMs.

Additionally, a single fiber alignment test was conducted using 100 random starting points (see blue dots in Figure 3) within a 10 µm x 10 µm window around the position with maximum signal intensity. The PKM executed a gradient scan to achieve optimal alignment (see orange dots in Figure 3). Results were compared to the H-811 hexapod based on the standard deviation of final positions. The comparison shows a similar performance that demonstrates a significant advantage of the cube-shaped PKM, as its extended lifetime can enable industrial-scale applications.

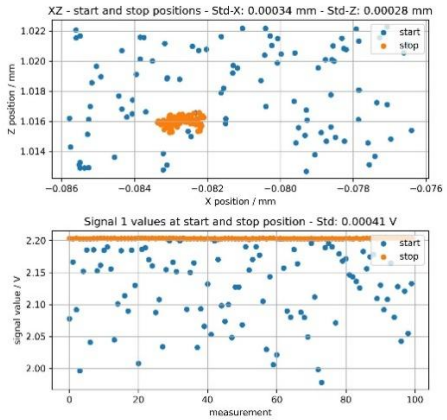

Figure 3. Start- and endpoints of the performed gradient scan

5. Summary and conclusion

A cube-shaped PKM was designed, assembled, and qualified in terms of motion performance and lifetime. Without mechanical transmission, its smallest steps match the precision of spindle-driven PKMs, while achieving significantly higher maximum velocity. Additionally, the cube-shaped PKM demonstrated an impressive lifetime indicating suitability for industrial-scale applications, including those requiring short stroke motions.

References

[1] Volz T et al. 2024 C*ompact lever actuated direct driven 6-dof parallel kinematic positioning system, Proc. of the 24th Int. Conf. of the EUSPEN*

[2] Matitschka J et al. 2023 Air bearing hexapod fr motion and positioning in six degrees of freedom with sub-micrometer precision*, Proc. of the 23th Int. Conf. of the EUSPEN*

[3] M. Naves 2021 Design and optimization of large stroke flexure mechanisms, PhD thesis

[4] M. Naves et al. 2021 T-Flex: A fully flexure-based large range of motion precision hexapod, Precision Engineering 72, pp. 912-928

[5] M. Naves et al. 2020 Flexure-based 60 degrees stroke actuator suspension for a high torque iron core motor, Precision Engineering, Volume 63, pp. 105-114

euspen's 26th International Conference & Exhibition, Krakow, PL, June 2026
www.euspen.eu

Design and calibration of a single-camera near-field photometric stereo head with tiltable illumination

Seunghun Oh[1], Jinsung Son[1], Kihyun Kim[2] , Hyo-Young Kim[2], Moon-Gu Lee[3] and Jaehong Shim[2*]

[1] *Department of IT and Semiconductor Convergence Engineering, Graduate School, Tech University of Korea (TU Korea)*
[2] *Department of Mechatronics Engineering, Tech University of Korea (TU Korea)*
[3] *School of Mechanical Engineering, Ajou University, Korea*

**jhshim@tukorea.ac.kr*

Abstract
Inline inspection on fast-changing lines often involves glossy, rough, or multi-material surfaces; compact, high-speed, non-contact sensing is needed without line stops. Structured-light capture, laser-line sensing, and 3D depth sensors provide absolute depth but typically require multi-frame projection or scanning, leave gaps under occlusion or glare, and require additional image-to-point-cloud registration. A photometric stereo system uses a single RGB camera and four angle-adjustable LED panels to emphasise micro-topography for defect detection. The panels are arranged as opposing pairs along the x- and y-axes and controlled 100° of tilt by a z-axis linear-motor crank–slider. After a brief angle search, one image per direction is acquired; including LED switching and exposure, four views take about 0.5 s. A Convergence Radius (CR) directs near-field sources toward a virtual ring on the measurement plane, and the photometric model compensates for distance- and angle-dependent attenuation, stabilising results under small camera-to-part spacing changes. For 3D recovery and metric scale, CR ring calibration projects panel light through a slitted ring artefact and uses the shadows to centre the setup, set the Z scale, and level the reference plane. Outputs are a shape-enhanced image and per-pixel surface-slope maps in the camera image coordinates, enabling pixel-level decisions and direct use in learning pipelines without extra registration. Qualitative tests reveal micro-relief around Ra ≈ 3.2 µm and indicate that angle selection reduces unnecessary captures and computation while enabling fast inline detection of shallow defects on glossy and mixed-material surfaces. The system can be mounted on a robot end effector for multi-position inspection, with demonstrated use on weld seams, painted panels, and moulded or machined parts, detecting scratches, orange peel, and weld-line marks.

Keywords: photometric stereo; inline inspection; near-field lighting; calibration; specular surfaces.

1. Introduction

In fields where surface shape information is central to decision-making—such as precision manufacturing, cultural heritage documentation, and robot vision—the ability to reliably recover fine surface slopes and micro-relief strongly affects the level of quality, safety, and long-term preservation. In practice, however, surface reflectance varies widely (non-Lambertian and highly specular surfaces). As the light sources move closer to the target, the effective lighting direction and irradiance distribution can vary across pixels, and occlusions, shadows, and highlights may occur at the same time, which can easily increase the error of image-based 3D reconstruction. Photometric Stereo (PS) is a representative approach that estimates surface normal and albedo cues from multiple images captured at a fixed viewpoint (a single camera) under varying illumination [1], and it has the advantage that it allows quantitative comparison on both benchmark datasets and real captured data. Under near-field conditions, however, it is difficult to assume distant directional lighting; the solution becomes more sensitive to lighting geometry (position and direction) calibration, and this can increase instability in the normal estimation and depth integration stages [2, 3].

Illumination layouts used in 2D vision inspection can be broadly divided into bright-field and dark-field configurations. In bright-field mode, components with relatively small incidence angles with respect to the camera optical axis are emphasised, which is useful for observing overall surface reflectance. In dark-field mode, components with relatively large incidence angles are emphasised, so fine defects and micro-scattering features become more visible [6]. To enable efficient surface analysis across a wider range of surface properties, this study builds a single-device PS system that supports bright-field/dark-field switching and LED tilt control, and then defines the Convergence Radius (CR) so that the tilt state of four lights can be set intuitively by directly linking it to the target size. Here, CR is defined as "the diameter of the circle formed by the four points where the illumination axes (virtual lines normal to each LED panel passing through its centre) intersect the measurement plane." With this definition, users can reproduce a lighting state by specifying h (the distance from the light centre to the measurement plane) and a target CR, rather than relying on motor counts. In addition, the procedure includes capturing a half-ring calibration target and using the shadow boundaries formed on the ring to calibrate the lighting direction (or effective lighting vector), so that the height scale is consistent during reconstruction. Finally, to mitigate the known weakness of least-squares (LS) based PS to shadows, highlights, noise, and boundary mixing, we propose a robust regression-based PS method that interprets the swept image stack as a spatio-temporal volume (STV) and combines spatial (patch) weighting, edge-aware weighting, temporal outlier rejection, and the Huber loss.

The remainder of this paper is organised as follows. Section 2 presents the methodology, including the CR definition and the mathematical formulation for device control, the half-ring shadow-based calibration, and the STV-based robust PS regression. Section 3 describes the benchmark (DiLiGenT) and real data configuration and the evaluation protocol. Section 4 reports quantitative results (normal angular error and processing time) obtained by applying the proposed method. Section 5 provides the summary, conclusions, and future research directions.

2. Methodology

2.1. System overview and illumination mode

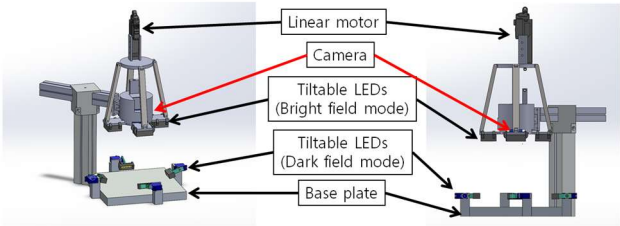

Figure 1. (System composition)

The bright-field illumination module proposed in this study is arranged vertically in four directions (east, west, south, and north) and is mounted to a cylindrical camera module. It performs a tilting motion while remaining fixed to the cylinder, driven by a linear-motor–crank–slider mechanism. The dark-field illumination module is also arranged in four directions (east, west, south, and north) near the measurement plane, and it performs rotational motion driven by a servo motor. Let m_0 denote the motor value at which the illumination axis has a reference direction. For a motor input m, the unit direction vector of the i-th illumination axis is defined as $n_i(m) \in \mathbb{R}^3$(where $\mathbb{R}$ denotes the set of real numbers and $\mathbb{R}^3$ denotes the three-dimensional real vector space). The 3D position of the i-th light centre is denoted by $C_i(m) = [C_{i,x}(m), C_{i,y}(m), C_{i,z}(m)]^{\mathrm{T}}$. The user-defined parameter h is the distance between the light centre and the measurement plane. When the measurement plane is defined as z=0, $\mathrm{h} = C_{i,z}(m)$, and this value can vary depending on the device configuration. Let τ be a scalar parameter along the axis. Then the line of each illumination axis is expressed as Eq. (1):

$$r_i(\tau) = C_i(m) + \tau n_i(m) \quad \cdots (1)$$

Let $P_i(m)$ be the intersection po int of this line with the measurement plane z=0. When z-componet of$n_i(m)$, denoted by $n_{i,z}(m)$, satisfies $n_{i,z}(m) \neq 0$, the intersection is given by Eq.(2):

$$P_i(m) = C_i(m) - \frac{C_{i,z}(m)}{n_{i,z}(m)} n_i(m) \quad \cdots (2)$$

If $P_{i,xy}(m) = [P_{i,x}(m), P_{i,y}(m)]^{\mathrm{T}}$, as the 2D coordinate on the measurement plane, the Convergence Radius (CR) is "the diameter of the circle formed by the four intersection points." Let R(m) be the radius of this circle, where R(m) is the radius of the best-fit circle to the four points $P_{i,xy}(m)$. Then CR is defined by Eq. (3):

$$\mathrm{CR(m)} = 2\mathrm{R(m)} \quad \cdots (3)$$

When the device is ideally symmetric and the four intersection points lie on the same radius, (m) can be simplified as $\mathrm{R(m)} = \|P_{i,xy}(\mathrm{m})\|$. If the symmetry is not perfect, (m) is estimated using a circle fitting procedure on the four points. The practical meaning of this definition is that the tilt state of the lights can be set by directly linking it to the object size (e.g., a target illuminated diameter). In other words, the user can specify a lighting state using the pair (h,) rather than motor counts.

To formulate this as a control problem, given a user-specified target $CR^{\backslash *}$, the motor input m is determined by the following inverse problem:

$$m^{\backslash *} = arg\min_m |CR(m) - CR^{\backslash *}| \quad \cdots (4)$$

2.2. Illumination modes and acquisition protocol

This device provides both bright-field and dark-field modes using tiltable LEDs. In this study, the two modes are selected or combined depending on the surface reflectance characteristics of the object to form an image stack. Let the illumination index be t = 1,…,T, and let the lighting state turned on at each frame be $\mathcal{L}(\mathrm{t})$. The captured observation image is denoted by $I_t(p)$ (where p is the pixel coordinate). The full image stack $\{I_t\}_{t=1}^{T}$, the mask M, and the per-frame lighting metadata (motor input m, BF/DF mode, and the lighting pattern) are then used as inputs to a unified processing pipeline.

2.3. Shadow-based calibration using half-ring target (CR ring calibration)

This study performs lighting calibration using a half-ring calibration target so that the height scale of the reconstruction is physically consistent. Assuming that the half-ring geometry (size and cross-sectional shape) is known, the shadow boundary produced by illumination i constrains both the lighting direction (effective lighting vector) and the object height scale. To this end, we first perform an illumination sweep. By comparing an "all-lights-on" image with each "single-light-on" image, we separate the additional shadow contribution of the i-th illumination and extract the shadow boundary ∂S_i . The extracted ∂S_i is corrected using a homography H so that it is mapped consistently from the camera image coordinates to the measurement plane (world coordinates). This is an essential step for handling lighting direction and depth scale within the same coordinate system. Next, the lighting direction (or effective lighting vector) s_i is initialised using a kinematics-based estimate, and an optimisation problem is formulated to either fine-tune s_i or adjust a depth-scale parameter so that the observed shadow boundary on the ring is consistent with the known ring geometry. In other words, the purpose of this procedure is to use the constraints provided by "ring geometry + shadow boundary" to suppress the propagation of residual lighting-direction errors into the final reconstructed height in near-field conditions.

2.4. STV-based robust photometric stereo

In the basic linear model of photometric stereo, the observation at pixel p is approximated by Eq. (5) using an effective lighting vector $s_t \in \mathbb{R}^3$ and an unknown vector $\mathrm{g}(p) \in \mathbb{R}^3$ Here,. $I_t(p)$ represents an effective lighting term that includes near-field distance- and incidence-angle-dependent attenuation Eq (5):

$$I_t(p) \approx s_t^{\mathrm{T}} \mathrm{g}(p)$$

$$\cdots (5)$$

where $g(p) = \rho(p)n(p)$, $\rho(p)$is the albedo, $n(p)$ is the unit surface normal. Global least-squares (LS) initialisation can estimate $g(p)$ efficiently using all frames, but it is vulnerable to shadows, highlights, noise, and boundary mixing effects. The proposed STV−based method interprets the swept image stack $I(x, y, t)$ as a spatio-temporal volume (STV) and updates $g(p)$ robustly by jointly using neighbouring patch information and temporal information.

Let $N(p)$ denote a neighbourhood patch around pixel , and define a patch weight $w_{patch}(p, q)$ for $(q \in N(p))$ that reflects both a spatial weight and an edge-aware weight. Temporal outlier rejection is implemented as a binary weight $w_{temp}(q, t) \in \{0,1\}$,which excludes frames where the observation $I_t(q)$ is judged to be a shadow/highlight outlier. Finally, for the residual $r(p, q, t) = I_t(q) - s_t^{\mathrm{T}}$we apply the Huber loss $\phi_\delta(\cdot)$to suppress the influence of large residuals [5], where δis the Huber threshold parameter. The vector $g(p)$ is then iteratively updated to minimise the robust objective in Eq. (6):

$$\min_{g(p)} \sum_{q \in N(p)} \sum_{t=1}^{T} w_{patch}(p, q) w_{temp}(q, t)\, \phi_\delta\left(I_t(q) - s_t^{\mathrm{T}} g(p)\right) + \lambda \parallel g(p) - \bar{g}(p) \parallel^2$$

$$\cdots (6)$$

where $\bar{g}(p)$ is the LS initial estimate and λ is a regularisation coefficient that encourages convergence toward the initial estimate. After the iterations, albedo and normal are separated using Eq. (7):

$$\rho(p) = \parallel g(p) \parallel, \quad n(p) = \frac{g(p)}{\parallel g(p) \parallel}$$

$$\cdots (7)$$

3.Experiment evaluation

The experiments are organised in two tracks: benchmark data and real captured data. As the benchmark, we use the DiLiGenT dataset [4], which provides, for each object, an aligned image stack, lighting directions (or lighting vectors), an object mask, and a ground-truth normal map, enabling quantitative evaluation using normal angular error. The real captured data are acquired by performing illumination sweeps with the BF/DF and tilt-control device proposed in this study. The swept multi-illumination images are converted into a benchmark-like structure (image stack, lighting metadata, and mask) and processed using the same algorithm pipeline.

The half-ring target based calibration is included as a preprocessing step in the real-data pipeline to ensure consistency of the lighting direction (effective lighting vectors) and the depth scale. This calibration takes, as input, a ring image stack captured under four directional illuminations, separates the per-illumination shadow components (shadow separation), and refines the lighting-direction parameters using constraints from the ring geometry (known radius, thickness, height, etc.) and the observed shadow boundaries. Using the calibrated lighting parameters, we then compute a normalised relative height distribution within the ring region (ring height normalised). This output is used for (i) a qualitative check that the lighting-direction calibration behaves as intended and (ii) setting a reference for lighting parameters and scale to be used in real object reconstruction. Figure 2 summarises the half-ring calibration outputs: (a) ring images under four directional illuminations, (b) per-illumination shadow separation for shadow-boundary isolation, and (c) a normalised ring-height map for checking lighting-calibration consistency and depth-scale behaviour.

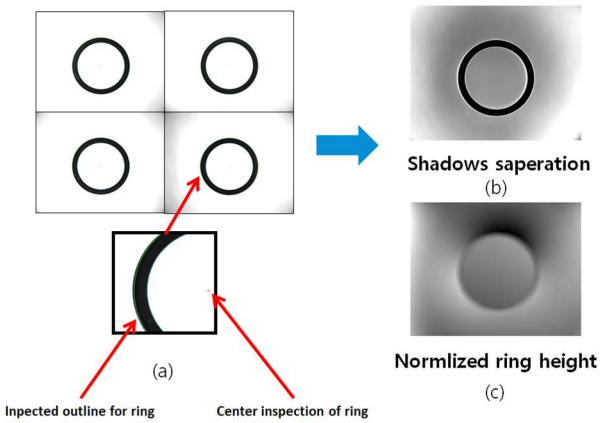

Figure 2. Half-ring target based calibration.

4.Results

Based on the reconstructions on the DiLiGenT dataset, we observed that the proposed STV-based robust regression tends to reduce the normal angular error for many objects compared with global LS initialisation. Over the 10-object average, the mean angular error decreased from 16.150 to 14.412, and the p90 angular error decreased from 31.509 to 28.786. For individual objects, readingPNG showed the largest improvement, with p90 decreasing from 47.031 to 38.373, and p90 reductions were also confirmed for ballPNG and bearPNG. However, for harvestPNG, p90 increased from 60.881 to 63.033, indicating that STV does not consistently reduce upper-quantile errors for all objects (Figure 5 and Table 1).

For real object measurements, a standard surface roughness specimen (12.5 μm R_a) and a laminated-coated copper specimen were captured. In Figure 3, we compare the normal maps produced by the baseline LS method and STVPS, and confirm that distinguishable surface patterns can be represented down to 3.2 μm R_a .We also captured data under both BF and DF conditions and found that DF can provide more effective results for certain surface features. In Figure 4, we present a glossy laminated-coated copper plate (thickness 3 mm) and compare reconstructions before and after applying the ring calibration.

Table 1 . Comparison with DiLigenT benchmark data

object	mean_LS	median_LS	p90_LS	mean_STV	median_STV	p90_STV
ballPNG	4.705	3.108	10.927	**3.451**	**2.629**	**6.536**
catPNG	8.781	6.990	15.159	**8.020**	**6.262**	**13.330**
pot1PNG	10.288	8.419	17.294	**9.401**	**7.113**	**15.691**
bearPNG	9.154	6.894	18.023	**7.571**	**5.517**	**14.389**
pot2PNG	16.708	13.652	33.520	**14.602**	**11.564**	**30.235**
buddhaPNG	15.448	11.202	32.521	**14.466**	**9.762**	**31.896**
gobletPNG	18.868	16.321	36.269	**17.339**	**14.484**	**32.952**
cowPNG	26.794	27.941	43.464	**24.846**	**25.195**	**41.424**
harvestPNG	31.568	26.319	60.882	**29.214**	**22.509**	**63.034**
readingPNG	19.194	11.305	47.032	**15.212**	**8.882**	**38.373**

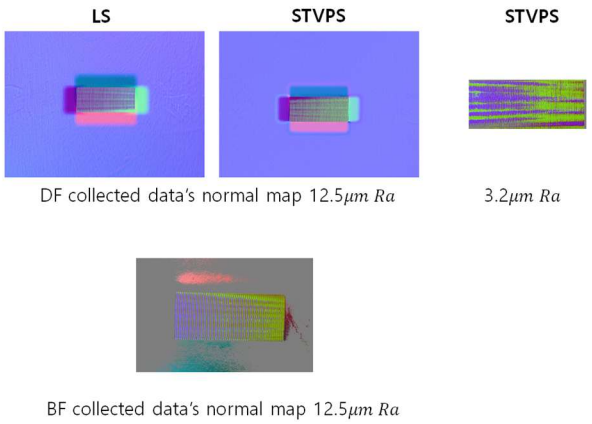

Figure 3. Real object application experiments-standard surface roughness specimen.

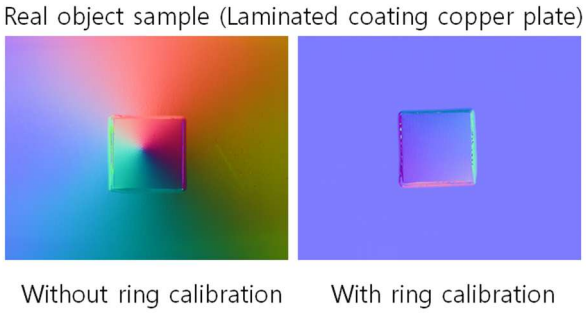

Figure 4. Real object application experiments- Laminated coated copper specimen.

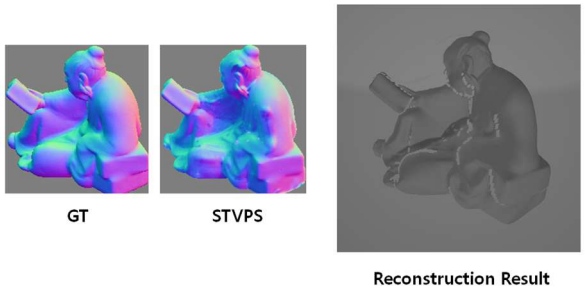

Figure 5. DiligenT benchmark normal map comparison and results

5. Conclution

This study proposed a methodology to address both illumination setting and reconstruction stability in near-field conditions using a single-device photometric stereo system that supports BF/DF switching and LED tilt control. First, the Convergence Radius (CR) was defined as the diameter of the circle formed by the four intersection points on the measurement plane, where the illumination axes of the east–west–south–north lights meet the plane. This definition provides a framework to control the lighting state in an interpretable and reproducible way using (h,CR), rather than motor counts. Second, a procedure was included to calibrate the lighting direction (or effective lighting vector) using shadow boundaries observed on a half-ring target, so that the height scale in reconstruction becomes physically consistent. Third, the instability of least-squares based PS, which is sensitive to shadows, highlights, and noise, was mitigated by introducing an STV-based robust regression that combines patch-based spatial weighting, edge-aware weighting, temporal outlier rejection, and the Huber loss. In the benchmark (DiLiGenT) batch evaluation, an overall tendency for the mean and p90 normal angular errors to decrease was observed.

The conclusions drawn from this work are as follows. In near-field PS, performance degradation is typically not caused by a single factor; instead, it often appears as a combined effect of "sensitivity to lighting-geometry calibration" and "observation outliers (shadows, highlights, and boundary mixing)." Therefore, practical applicability can be improved when device design (illumination mode switching and tilt control), interpretable illumination setting (CR), calibration (half-ring shadows), and robust estimation (STV regression) are integrated into a single, consistent pipeline. In particular, CR allows users to specify a lighting state in an intuitive way that matches the object size, which can support standardised operation and improve reliability for repeated measurements. However, STV introduces higher computational cost, and for some objects the upper-quantile error can increase. For this reason, application conditions and guidelines for parameter selection should be provided together.

Future work can be extended in three directions. First, the processing speed should be improved by reducing the computational cost of the STV iterative regression, for example through GPU acceleration, patch reuse, and multi-resolution strategies. Second, the relationship between CR, motor input, and tilt— i.e., $\mathrm{n}_i(\mathrm{m}), \mathrm{C}_i(\mathrm{m})$ —should be stabilised using measurement–based calibration that accounts for backlash, mechanical play, and elastic deformation, thereby improving control reproducibility for a target CR^{*}. Third, to report the quantitative impact of half-ring calibration on "height-scale alignment" in real device data, the ring dimensions and the rules for shadow-boundary extraction should be fixed, and, if possible, comparison should be performed using external measurements or repeatability-based metrics.

Acknowledgement

This study was supported by Korea Institute for Advancement of Technology(KIAT) grant funded by the Korea Government(MOTIE) [(P0021527), (RS-2025-24536353) and (RS-2024-00409639) HRD Program for Industrial Innovation]

References

[1] Woodham R J 1980 Photometric method for determining surface orientation from multiple images Opt. Eng. 19 139–144
[2] Mecca R, Wetzler A, Bruckstein A M and Kimmel R 2014 Near Field Photometric Stereo with Point Light Sources SIAM J. Imaging Sci. 7 2732–2770
[3] Logothetis F, Mecca R and Cipolla R 2017 Semi-Calibrated Near Field Photometric Stereo Proc. IEEE Conf. Comput. Vis. Pattern Recognit. (CVPR) 941–950
[4] Shi B, Wu Z, Mo Z, Duan D, Yeung S K and Tan P 2016 A Benchmark Dataset and Evaluation for Non-Lambertian and Uncalibrated Photometric Stereo Proc. IEEE Conf. Comput. Vis. Pattern Recognit. (CVPR) 3707–3716
[5] Huber P J 1964 Robust Estimation of a Location Parameter Ann. Math. Statist. 35 73–101
[6] Forte P M F, Felgueiras P E R, Ferreira F P, Sousa M A, Nunes-Pereira E J, Bret B P J and Belsley M S 2017 Exploring combined dark and bright field illumination to improve the detection of defects on specular surfaces Opt. Lasers Eng. 88 120–128

euspen's 26th International Conference & Exhibition, Krakow, PL, June 2026
www.euspen.eu

A novel approach for a coordinate measuring machine probing head with a levitating probe integrating the Kibble-balance principle and a Maxwell-clamp-like mounting concept

Yujie Zhong[1], Tino Hausotte[1], Georg Hein[2], Julien Schinn[1], Norbert Rogge[2] and Thomas Fröhlich[2]

Friedrich-Alexander-Universität Erlangen-Nürnberg (FAU), Faculty of Engineering, Department of Mechanical Engineering,
[1]Chair of Manufacturing Metrology

Technische Universität Ilmenau, Department of Mechanical Engineering
[2]Institute of Process Measurement and Sensor Technology

yujie.zhong@fmt.fau.de

Abstract
In order to enable coordinate measuring machines (CMMs) to achieve measurement accuracy in the nanometre range and a higher dynamic, an innovative probing head has been developed. Conventional CMM probing heads operate either as simple through-trigger head or with elastomechanical deflections of parallel leaf-spring guides as passive system or active system, with additional electromechanical actuators. All of these systems have limitations regarding probing force calibration and metrological traceability.
In this paper, a novel design of traceable, active, force- and torque-measuring CMM probing head with a levitating probe is presented. The probe and carrier plate are levitated by six voice coil actuators (VCA) in hexapod-like arrangement without any leaf-springs. This parallel kinematic is controlled in position and orientation using the measuring signals of three 2D position sensors. The arrangement allows the forces of the actuators to be calibrated according to the Kibble-balance principle. A strict separation of the force/torque and position/orientation measuring loops, as well as the special design of the connection between the two loops using a Maxwell-clamp-like mounting, enables the combination of lightweight and rigid materials for the force and torque measuring loop with materials with low thermal expansion for the position and orientation measuring loops. Subsequently, finite element simulations were performed to determine how temperature changes affect the position of the measuring result.

Keywords: CMM, probing head, Kibble-balance, Maxwell-clamp

1. Introduction

Coordinate measuring machines (CMMs) play an important role in the field of advanced manufacturing and precision engineering. In the last decades, an increasing demand for dynamic probing and measurement with nanometre-level accuracy are observed [1]. A probing result is typically influenced by the force/torque that the probing head applies to the stylus, and the interaction between the stylus and workpiece. Therefore, the achievable dimensional measurement accuracy is strongly influenced by the probing force. In conventional probing head concepts, the applied forces/torques are generated and calibrated indirectly, which leads to limited metrological traceability [2].

This article presents a novel approach for a CMM probing head that applies the Kibble-balance principle for traceable force/torque measurements and simultaneous control of the position and orientation of the probing head. Previous work at the Technische Universität Ilmenau has successfully applied the Kibble-balance principle to traceable mass measurements using voice coil actuators (VCAs) based on gravitational force measurements [3,4]. Although the probing heads of CMMs measure the dimensions or surfaces of workpieces fundamentally by measuring forces and torques, the Kibble-balance principle has not been applied to any probing head yet.

In the following section, the concept of the proposed probing head is introduced. First, a traceability-driven actuation concept using voice coil actuators (VCAs) with a hexpod-like arrangement is described, with consideration of their thermal implications. Subsequently, the separation of the force/torque and position/orientation measuring loops is presented. Finally, a finite element simulation (FEM-simulation) was performed to predict the expected thermal behavior of the probing head constructures.

2. Traceable probing head concept

Conventional CMMs probing heads face complex and indirect force calibration procedures and an increasing demand for improvement in measurement accuracy. After the redefinition of the SI unit of kilogram in 2019, traceable force measurements based on electromagnetic force generation using VCAs have become an established concept in precision metrology. To overcome the challenges, which were mentioned ahead, VCAs were used in this study as both actuators and force sensors. This will make in-situ calibration of probing forces possible by implementing different working modes as in mentioned in [4].

However, a single coil actuator allows multiple degrees of freedom (DOFs), which means, the coil and pot magnet can perform lateral and rotative movements with respect to each other. The arrangement of individual VCAs along the coordinate axes should be avoided. Therefore, a hexapod-like arrangement

is adopted in this concept, so that all actors carry part of the weight of the flotor. As shown in the Figure 1, six VCAs are arranged in three opposing pairs, and symmetrically distributed at angles of 120°. This configuration allows the flotor to move in six DOFs and therefore enables not only the measurement of the probing forces, but also the measurement of torques on the stylus and flotor.

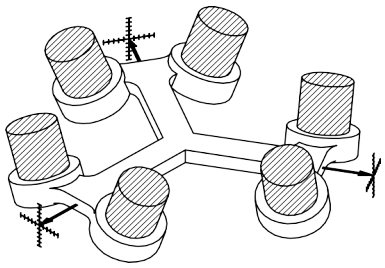

Figure 1. Schematic illustration of hexapod-like arrangement of VCAs

In addition to force sensors, position sensors are required to control the position and orientation of the flotor. Thus, a type of optical 2D-position sensors are assigned to each actuator pair. As the VCAs are in working status, they generate not only heat but also force/torque and vibration to the system. The separation of force/torque loops and position/orientation measuring loops helps to avoid the influence of these factors on the position and orientation measurement with the 2D-position sensor. In this way, better control of position and orientation can be provided. As shown in Figure 2, an extra structural frame was designed to decouple the position sensors from the VCAs. The interface between both loops uses three leaf-spring guides and is distributed similarly to the arrangement of actuator pairs, thereby forming Maxwell-clamp-like mountings. This mounting concept improves the assembly repeatability and positioning accuracy [5].

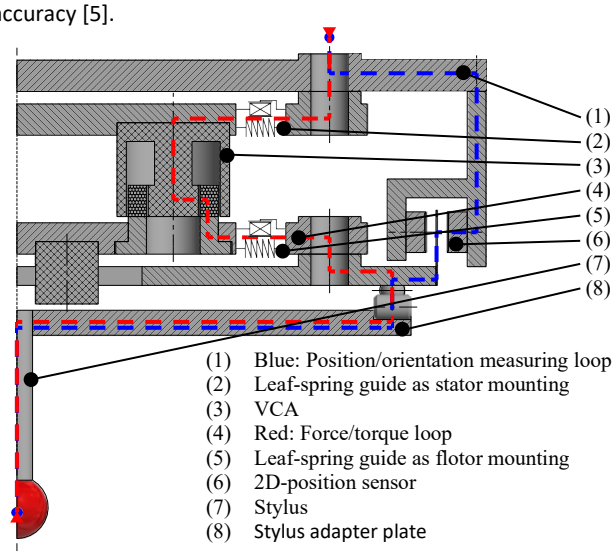

Figure 2. Schematic illustration of the separation of the force/torque loops and position/orientation measuring loops.

3. Expected thermal behaviour

As shown in Figure 2, both the force/torque loops and the position/orientation measuring loops share a common base plate for mounting the probing head to the ram. In practice, they exhibit different thermal behaviors and, therefore, different thermal expansions. Considering the heat generated by the VCAs, a flexible construction for the stator plate and mounting of the pot magnet was designed. During the measurement, the leaf-spring guides act as springs and reduce the stresses at the fastening point resulting from different thermal expansion.

After completing the structural design, FEM simulations were performed to determine the influence of the thermal expansion of the stator plate of the probing head, as shown in Figure 3. The FEM simulation result shows that the thermal expansion of the stator plate is more than 10 µm in the radial direction for a temperature increase of 10 K. However, the center of the stator plate remains at the same position. The same principle was appled for the flotor plate for the mounting of the actor coils. The displacement of the stylus, which is attached at the centre of the flotor, due to the thermal expansion of the stator plate and flotor plate is effectively reduced.

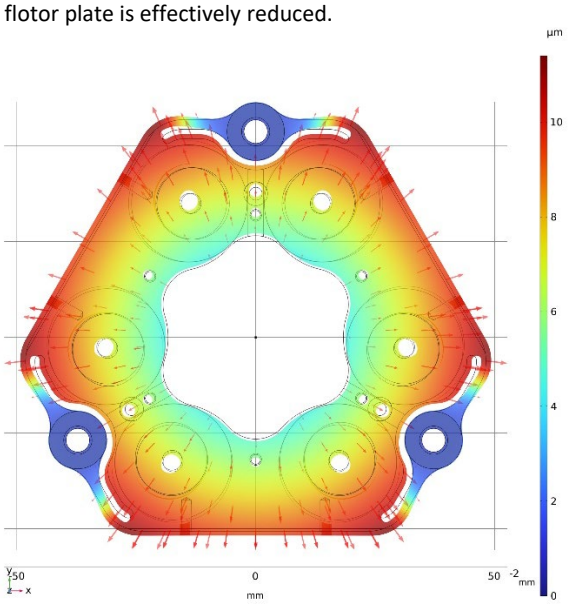

Figure 3. FEM simulation result of stator plate of a temperature increase of 10 K.

4. Conclusion and outlook

In this article, a novel probing head concept for CMMs has been presented with the aim to provide a traceable force and torque measurement with potential of in-situ calibration. By using VCAs as both actuators and force sensors. This concept applies the Kibble-balance principle to CMM probing. Six VCAs are arranged in a hexapod-like geometry, which allow this probing system to move in all six DOFs and therefore enable the measurement of both probing force and torque. This presented design provides a combination of traceability, thermal stability and high measurement accuracy in one probing head.

However, the probing head exists as prototype and has not been operated in probing measurements yet. It will be focus on the implementation of measuring signal processing system and poseture controlling of the probing head in future works, followed by experimental validation of the functionality.

Funded by the Deutsche Forschungsgemeinschaft (DFG, German Research Foundation) – Projektnummer 505063926.

References

[1] Claverley J.D. and Leach R.K. 2015 A review of the existing performance verification infrastructure for micro-CMMs *Precision Engineering* **39**, 1-15
[2] Weckenmann A. et al. 2004 Probing Systems in Dimensional Metrology *CIRP Annals* **53**, 657-684
[3] Fröhlich T. et al. 2020 Neue Wege zur Kalibrierung von E2-Massenormalen und Darstellung von Kräften bis 10,N *tm - Technisches Messen* **87**, 280-293
[4] Vasilyan S. et al. 2021 The progress in development of the Planck-Balance 2 (PB2): A tabletop Kibble balance for the mass calibration of E2 class weights *tm - Technisches Messen* **88**, 731-756
[5] Weigert F. et al. 2021 Experimental Setup for the Investigation of Reproducibility of Novel Tool Changing Systems in Nanofabrication Machines *Nanomanufacturing and Metrology* **4**, 181-189

euspen's 26th International Conference & Exhibition, Krakow, PL, June 2026
www.euspen.eu

A Reduced-Order Modelling Framework for the Receptance Coupling Method

Özgür Taylan Kenanoğlu[1,2], Yiğit Özcan[1,2], Shashwat Kuswaha[1,2], Dominiek Reynaerts[1,2]

[1]Department of Mechanical Engineering, Manufacturing Processes and Systems, KU Leuven, Leuven 3001, Belgium [2]Member Flanders Make, Belgium

oezguertaylan.kenanoglu@kuleuven.be

Abstract

This study presents a reduced-order modelling technique for the Receptance Coupling Substructure Analysis, RCSA. The approach addresses critical aspects of precision manufacturing: accurately estimating tool-spindle dynamics and the practical limitations and trade-offs of carrying out reduced-order analysis.
The first stage involves identifying the coupled dynamics of the tool holder and spindle system using the Receptance Coupling Method. Numerical methods are employed to model the tool and holder assembly under free-free boundary conditions, while experimental frequency response measurements capture spindle characteristics. Mathematical coupling achieved by the Receptance Coupling Method is used to derive the tool center point frequency response function. The second stage focuses on the resultant dynamic characteristics of the reduced order RCSA and discusses the practical limitations and the supposed benefits of reduced experimental processes and lessened computational effort. The results are compared with impact hammer tests, and the margins of error are argued, and complementary methods to decrease the said errors are discussed.
By integrating dynamic modelling with geometric simulation, this methodology may provide a predictive capability for compensating machining errors before production. The combined use of numerical and experimental techniques reduces reliance on trial and error adjustments, improving efficiency and ensuring compliance with tolerance requirements in high-precision manufacturing operations.

Keywords: Receptance Coupling, Frequency Response Function, Substructure Coupling

1. Introduction

The frequency response function (FRF) is an analytical tool for improving machining process stability, estimating surface quality and dimensional tolerance accuracy, and modelling the dynamic behaviour of the tool-center-point (TCP). There exists several factors that affect the resultant workpiece geometry, such as thermo-dynamic factors, workpiece compliance, and structural vibrations. Among these, structural vibrations can be identified using several different methods, such as hammer or shaker tests of the assembled spindle-tool pairs, the Receptance Coupling Method, the Inverse Receptance Coupling Method, Operational Modal Analysis, as well as methods employing neural networks [1].

Often, these methods require extensive experimentation and are often impractical in industrial environments. Limited accessibility, industry standards, and sensor constraints are detrimental to in-situ measurement of assembled spindle and tool-tip pair FRFs. On the other hand, methods that require operational states of the CNC machine tools prove to be ill-suited to industrial settings. Although FEM can be used to represent spindle assemblies, the practical modelling application and resultant characterization are severely limited. Accurate characterization of the spindle through numerical methods for accuracy is not practically useful, as high-load machinery is prone to wear and tear.

Consequently, modelling approaches that combine experimentally identified substructures with numerical methods have gained significant attention. Receptance Coupling Substructure Analysis (RCSA) is proven to be an effective framework for predicting the dynamic behaviour of the assembled spindle and tool-tool holder pairs.

Several studies have investigated different methods for the formulation of RCSA [1], including tool-holder modelling using beam theory or FEM formulations, and demonstrated the importance of including shear deformation and the importance of rotational degrees of freedom. Timoshenko beam representation has been shown to provide improved agreement with experimental validation compared to Euler-Bernoulli assemblies of tool and tool holder pairs [2].

Despite these advances, many studies assume the availability of complete spindle driving point FRFs or neglect the influence of missing rotational outputs and moment inputs on the receptances. The extent of reduced order of spindle characteristics that can be neglected without detrimentally affecting the coupling solution, therefore, remains an open question, particularly when rotational degrees of freedom can be included in the coupling formulation.

In this study, a receptance coupling framework is presented where we incorporate a *4x4* non-axial translational and rotational representation of the tool and tool-holder pair employing Timoshenko beam theory and an experimentally identified spindle assembly, characterized by a semi-reduced *2x4* driving point FRF matrix, incorporating only translational inputs. The proposed approach is validated through impact hammer experiments performed on the physically assembled model and is compared to the mathematical coupling. The results demonstrate that reliable tool-tip dynamics can be estimated through the semi-reduced modelling of the spindle dynamic identification.

2. Methodology

Formulation of the mathematical coupling of receptances is prone to error due to a number of unmodelled dynamics. The lack of modelled dynamics of the rotational degrees of freedom

of the numerically modelled tool and tool holder pairs and experimentally estimated spindle is shown to be detrimental [1].

2.1. Experimental identification of the spindle FRFs

An SK40 ER16 collect chuck holder (HOLEX, A=100 mm) is axially shortened by wire EDM in order to create a well-defined coupling plane for the receptance coupling procedure. Figure 2 shows the resultant components of the wire EDM operation. The shortened tool holder is then installed on the CNC plant—DMU 50 machining center, where all experiments are conducted. The spindle position in the machine coordinate system is saved and ensured to remain consistent through the experimentations.

The base of the tool holder is excited using an instrumented impact hammer (PCB Piezotronics, Model 086C03). The vibration responses are measured utilizing a set of triaxial accelerometers (PCB Piezotronics, Model 356A17). In total, four distinct combinations of sensor placement and axial excitation sets are recorded. The axial excitations consist of *X* and *Y* axes of the DMU 50 machining center, while the accelerometer positions consist of the cut tool holder's outermost edges on the axes, lying on the axis line, aimed to measure the vertical displacements.

Figure 2. Axially shortened tool holder, HOLEX SK40 ER16.

The vertical displacement results of the two sensors are later utilized for the estimation of the rotational frequency response functions. The force and acceleration signals were acquired using a CompactDAQ data acquisition chassis (NI, cDAQ).

$$H_{22} = \begin{bmatrix} H_{xx}(\omega) & H_{xy}(\omega) & H_{xM_x}(\omega) & H_{xM_y}(\omega) \\ H_{yx}(\omega) & H_{yy}(\omega) & H_{yM_x}(\omega) & H_{yM_y}(\omega) \\ H_{R_xx}(\omega) & H_{R_xy}(\omega) & H_{R_xM_x}(\omega) & H_{R_xM_y}(\omega) \\ H_{R_yx}(\omega) & H_{R_yy}(\omega) & H_{R_yM_x}(\omega) & H_{R_yM_y}(\omega) \end{bmatrix} \quad \text{Eq. (1)}$$

From each set of unique impact locations and sensor placements, five impacts are selected. Equation 1 depicts the FRF matrix of the spindle that is aimed to be formed. From the selected data sets, the first two columns of the said FRF matrix are estimated using the H_1 estimator. The coherence function is computed as the normalized squared cross-spectrum, and the results are accepted as valid where the coherence function stays above a value of 0.6 without the interference of the anti-resonance frequencies.

2.2. Numerical Modelling of Tool Holder

The tool holder and tool pair are modelled as a Timoshenko beam to account for the transverse shear and rotary inertia. Introduction of the said parameters is significant for short and thick structures in the mid-to-high range operating frequencies.

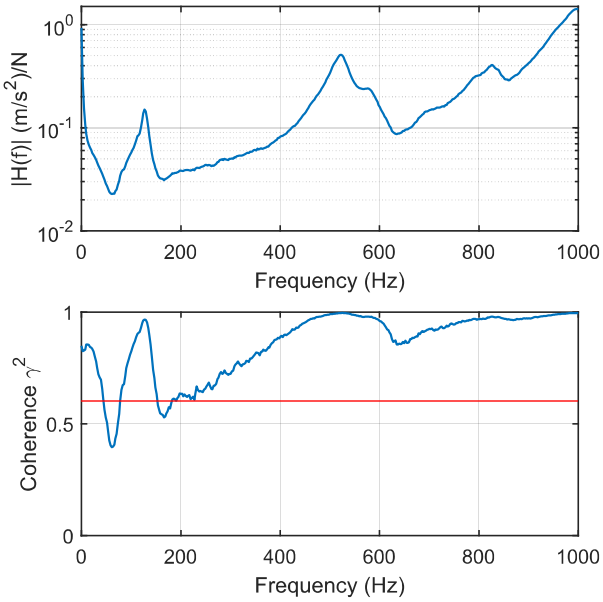

Figure 3. Frequency response function and resulting coherence of the collocated impact hammer experiments of the spindle. First element, $H_{xx}(\omega)$, of the four-by-four FRF matrix given in Equation 1.

Timoshenko beam theory for modelling of tool and tool-holder pairs is particularly beneficial for the purposes of dynamic compliance estimation due to the Euler-Bernoulli formulation's assumption on planer section remaining normal to the perpendicular axis of the tool. Timoshenko beam theory relaxes the said constraint, resulting in estimations that carry higher fidelity [3].

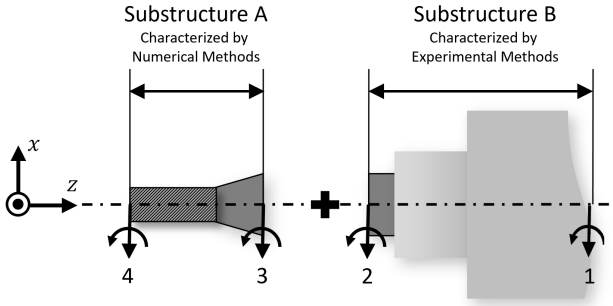

Figure 4. Substructures of the coupling. Substructure (A): the tool and tool holder pair where point 4 lies on the TCP and point 3 lies on the coupling plane. Substructure (B): the spindle of the machinery, where point 2 lies on the coupling plane and point 1 is accepted as grounded with infinite stiffness.

The assembled mass and stiffness matrices are used for the computation of the frequency-domain accelerance and receptances by solving the dynamic equilibrium equation. The driving point translational and rotational sub-matrices are extracted to form *4x4* blocks that are needed for the coupling. The formulation enables compatibility between the sample frequency of the experimental data and the numerical method, resulting in a physically consistent estimation of the coupled TCP.

Figure 4 shows the coupling structure of the tool and tool holder pair and the spindle. Substructure B contains points 1 and 2, where they are defined as the grounding and the coupling plane of the spindle assembly, respectively. $H_{22}(\omega)$ is the FRF of the said coupling plane, only containing translational inputs. Accordingly, four sets of matrices are acquired to formulate Substructure A. The matrices relate to;

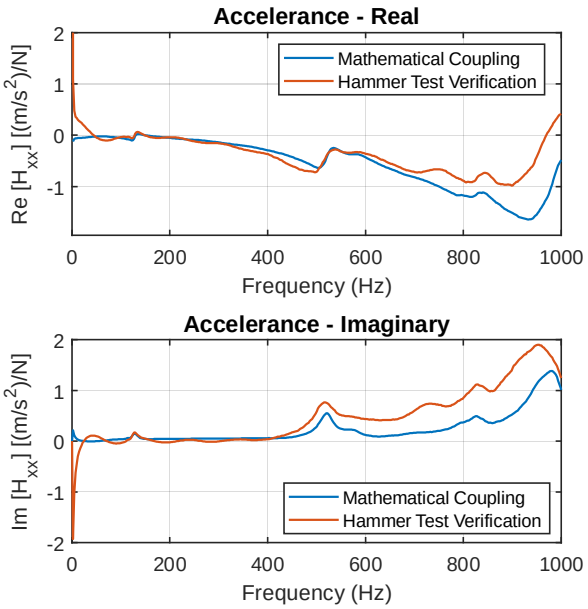

Figure 5. Real and Imaginary parts of the mathematical coupling and the hammer test verification results for the accelerance of the TCP.

(i) Uncoupled TCP FRF, $H_{44}(\omega)$,
(ii) Cross FRF between the TCP and coupling plane, $H_{43}(\omega)$,
(iii) Cross FRF between the coupling plane and TCP, $H_{34}(\omega)$,
(iv) Uncoupled coupling plane FRF, $H_{33}(\omega)$,
where each matrix follows the generalized form that is defined in Eq. 1, formed through translational and rotational degrees of freedom.

2.3. Formulation of the Coupling

The resultant FRFs of the machine tool's spindle and the tool and tool holder pair are used for the mathematical coupling of the physical assembly. The mathematical coupling is estimated as;

$$H^c{}_{44} = H_{44} - H_{43}\, H^{-1}{}_T\, H_{34}, \quad \text{Eq.(2)}$$

where,

$$H_T = H_{22} + H_{33}. \quad \text{Eq.(3)}$$

The elements H_{44}, H_{43}, H_{34} and H_{33} are the resultant FRFs of the numerical formulation explained in Subsection 2.2, while H_{22} is the FRF of the machine tool assembly explained in Subsection 2.1.

The product of Equation 2, the dynamic behaviour of the TCP where the substuctures are formulated to be mathematically coupled, is denoted as, $H^c{}_{44}$.

The element, H_T, computes the compliances of the series spindle assembly and the tool and tool holder coupling planes, and is prone to error for being ill-conditioned near anti-resonances and therefore is inverted with the Moore-Penrose pseudo-inverse.

2.4. Verification of the mathematical coupling

An uncut version of the SK40 ER16 collect chuck holder, arqued in Subsection 2.1, is installed on the DMU 50 machining center. Impact hammer experiments on the uncut tool holder are carried out with the same methodology, and the results are saved. The measured FRFs are subsequently used for the validation of the mathematical coupling approach.

3. Results

This section presents the estimated TCP dynamic response obtained using the Receptance Coupling formulation against the hammer measurements performed on the uncut tool holder. The mathematical coupling is carried out numerically with each corresponding data point frequency pair. Agreement is evaluated in terms of frequency-dependent compliance, providing a quantitative validation.

Figure 5 shows the accelerance comparison between the mathematical coupling and the impact hammer verification test. It is observed that the real part of the accelerance FRF shows good tracking characteristics to the verification tests; however, the Imaginary part shows a divergence. The error is thought to have occurred because of the unmodelled damping and energy dissipation characteristics. Accurate system identification of damping in tool-holder-spindle assemblies remains a challenge due to its high dependence on coupling conditions and preload, and therefore requires experimental frequency response identification rather than numerical modelling [4].

Figure 6 shows the receptance comparison between the mathematical coupling and the impact hammer verification test. It is observed that receptance results show similar characteristics to the accelerance. The peak behaviour near zero frequency is assumed to be an estimation error due to the conversion of accelerance to receptance. This effect is thought to be amplified by the limited low-frequency response prediction characteristics of piezoelectric accelerometers.

Figure 7 compares the magnitude of the tool-tip receptance obtained from the receptance coupling method with the corresponding impact hammer measurements. The coupled model accurately reproduces the compliance level and the dominant characteristics across the investigated frequency range. Above 200 Hz, a good agreement is observed between the measured and estimated response on the basis of amplitude and trend. Discrepancies are still observed at low frequencies, which are thought to be a result of accelerance to receptance conversion and limited near quasi-static capabilities of the sensors, as argued beforehand.

The results are then compared on a quantitative basis. Table 1 depicts the mean absolute error, median absolute error, RMS error, correlation coefficient, and the frequency band of the tool-tip frequency response estimation and the corresponding impact hammer measurements in the 250-1000 Hz frequency range.

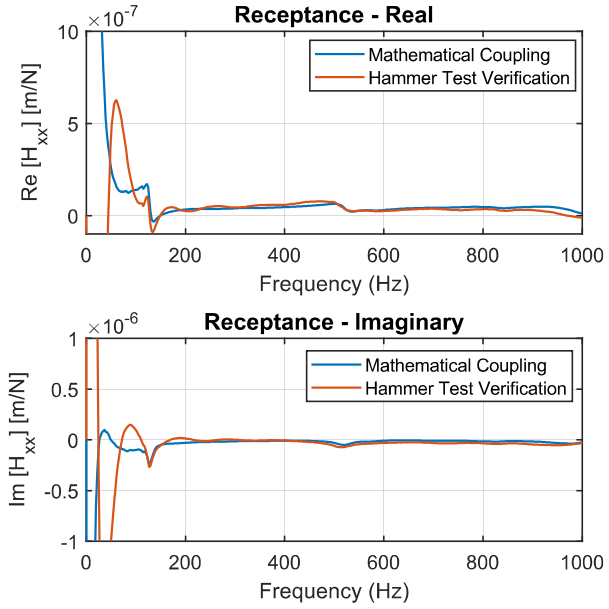

Figure 6. Real and Imaginary parts of the mathematical coupling and the hammer test verification results for the receptance of the TCP.

Within the concerned range, the coupled model shows a mean absolute error of 13.03% while the median error is 8.85%. In addition correlation coefficient of 0.986 depicts a good agreement in the response shape. Therefore, the quantitative results support the agreement observed through the frequency response comparisons and validate the receptance coupling method for the estimation of TCP dynamics.

Table 1 Quantitative error metrics for tool-tip FRF estimation

Metric	Accelerance [(m/s^2)/N]
Mean absolute error	13.03%
Median absolute error	8.85%
RMS error	14.2%
Correlation coefficient	0.986
Frequency band	250-1000 Hz

4. Discussion

The results demonstrate receptance coupling approach, combined with the Timeshenko beam representation of the tool and tool holder dynamics, is capable of predicting the tool-tip frequency response with good accuracy compared to impact hammer tests for each unique tool and tool holder assembly and spindle pairs. In particular, the coupled model captures the response magnitude in the frequency range of 250-1000 Hz, which is the most relevant for milling fidelity estimation.

The agreement observed in both real and imaginary components of the FRFs indicates that the proposed formulation not only reproduces the response magnitude but also captures the phase behaviour of the system. The correlation coefficient of 0.968 also confirms this behaviour, despite the presence of unavoidable experimental and numerical uncertainties.

The discrepancies in the imaginary magnitude are thought to be due to the non-ideal modelling of the damping in the tool and tool holder pair. It is shown in the literature that accurate identification of damping ratios in tooling systems is inherently difficult and detrimental to the accuracy of FRF estimation. In particular, it has been found that identified damping ratios for tool holders show significant variance and cannot be reliably predicted using simplified numerical models, and experimental identification instead shows higher accuracy [5].

It should also be noted that the experimental measurements of the spindle assembly to be employed in the coupling method are carried out with the employment of piezoelectric accelerometers. Those show an incapable characteristic of measuring static, near-DC signals, and as a consequence, low-frequency components of the measurement are affected. When converting accelerance to receptance through uncausal methods, these effects are significantly amplified, leading to an apparent divergence and spurious peaks and zeros.

Alternative sensing technologies, such as capacitive displacement probes or laser-Doppler vibrometers, offer improved low-frequency and quasi-static response estimations and can provide a more reliable receptance measurement near zero frequencies. However, many times those instruments may require careful alignment and calibration, which may also prove unsuitable for industrial settings.

Overall, the proposed methodology provides a practical balance between the modelling fidelity and experimental effort.

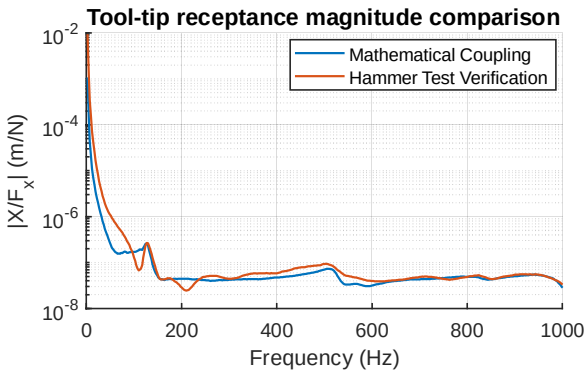

Figure 7. Absolute magnitude of the TCP receptance.

Experimentally measured spindle dynamics, which incorporate three-axis accelerometers to form the rotational responses of the spindle, can be utilized together with Timoshenko beam theory to estimate the coupled response with-in an acceptable margin of error.

5. Conclusion and Future Work

This study presented a receptance coupling framework which incorporates the full DOF of moments and rotations, a *4x4* matrix, of the nonaxial displacement and rotational input and output pairs of the tool and tool holder, with displacement and rotational outputs only, totaling to a *2x4* matrix, of the spindle assembly.

Nevertheless, the results are deemed acceptable for the employment of the methodology and FRF extraction of TCP, and its effect on resultant workpiece geometry.

The future work consists of identifying a common Laplace-domain realization of the coupled dynamics and calculating the full rank spindle FRF matrix through a series of reduced-order modals that preserve the symmetric consistency. The moment inputs are to be obtained from the fitted model by enforcing the generalized modal shapes upon the diagonal elements of the spindle coupling plane.

Another planned development is to incorporate capacitive sensors and Laser-Doppler sensors to measure both the spindle assembly FRF and the tool and tool holder pair FRF, and the extraction of the tool-tool holder pair's damping characteristics. These developments have the potential of further enhancing the predictive capability of the receptance coupling approach for tool-tip dynamics in practical applications.

Overall, the presented framework demonstrates that a reliable tool-tip dynamics estimation can be acquired through reduced representation. The proposed method provides a practical and experimentally feasible mathematical-based modelling framework, while offering a pathway for future studies that require future refinement through model-based methods and more capable sensing techniques.

References

[1] Iglesias A, Tunç L T, Özsahin O, Franco O, Munoa J and Budak E 2022 Alternative experimental methods for machine tool dynamics identification: A review *Mechanical Systems and Signal Processing* 170

[2] Filiz S, Cheng C-H, Powell K B, Schmitz T L and Ozdoganlar O B 2009 *An improved tool–holder model for RCSA tool-point frequency response prediction* Precision Engineering 33(1) 26–36

[3] Chavan P S, Brecher C and Schröder K U 2023 *Substructuring Methods for Efficient Prediction of Spindle-holder-tool Assembly Dynamics*, RWTH Aachen University Library

[4] Schmitz T L and Smith K S 2009 *Machining Dynamics: Frequency Response to Improved Productivity* Springer, New York

[5] Andersson C 2015 *Dynamic Characteristics of a Tool Holder Shank*, Licentiate Thesis, Department of Machine Design, KTH Royal Institute of Technology, Stockholm, Sweden

euspen's 26th International Conference & Exhibition, Krakow, PL, June 2026
www.euspen.eu

Metrological constraints in predicting tool deflection for error compensation

Paweł Majda[1], Paweł Dunaj[1], Bartosz Powałka[1] and Andreas Archenti[2]
[1]West Pomeranian University of Technology, Szczecin, Poland
[2]KTH Royal Institute of Technology, Stockholm, Sweden

pawel.majda@zut.edu.pl

Abstract
Accurate prediction of tool deflection is essential for compensating force-induced machining errors, yet it depends on the metrological quality of cutting force and stiffness measurements. While cutting force measurement benefits from well-established calibration artefacts and traceability, stiffness remains a derived quantity with inconsistent measurands, limited comparability, and largely unquantified uncertainties. This work investigates the feasibility of tool deflection prediction by linking measurement uncertainties of force and stiffness through a simplified elastic model. Representative benchmark values were defined from the literature, and the resulting uncertainty of tool deflection was analysed for different combinations of cutting force and machine tool stiffness. The results show that cutting force uncertainty plays a lesser role than stiffness uncertainty, which dominates particularly in low-stiffness regimes. For high-stiffness machines, current measurement practice is sufficient to support compensation, whereas for medium stiffness improved accuracy is required, and for low stiffness reliable prediction remains impractical. The study highlights stiffness measurement as the key bottleneck, underscoring the need for standardized measurands, procedures, and validated uncertainty budgets.

tool deflection; cutting force; machine tool stiffness; uncertainty machine tool

1. Introduction

The accuracy of manufactured components underpins the performance and competitiveness of modern industries. Aerospace, automotive, medical, and energy sectors demand dimensional tolerances that are increasingly stringent, since even small deviations can compromise functionality, safety, and cost-effectiveness. Despite major advances in machine design, error compensation, and digital control, deviations from the programmed tool path remain unavoidable due to the interaction between machine structure and cutting process physics [1].

Among the multiple error sources – geometric imperfections, thermal drift, and vibration – tool deflection caused by cutting forces acting on a structure of limited stiffness is particularly critical [2]. Elastic displacement of the tool directly alters the form and size of the workpiece. As tolerances tighten and productivity demands increase, reliable prediction and compensation of tool deflection has become a central challenge in precision engineering [3].

Compensation strategies, whether offline or adaptive, require two measurable inputs: the applied cutting forces and the stiffness/compliance of the machine's structural loop [4]. Together, these define the expected elastic displacement of the tool under load. Although conceptually straightforward, prediction accuracy is fundamentally limited by measurement quality, the lack of interlaboratory validation, and the absence of universally accepted standards [5].

Cutting force measurement benefits from a mature metrological foundation. Piezoelectric dynamometers remain the reference, supported by internationally recognized calibration procedures and traceability to national standards. Research trends include structure-integrated sensors [6] and non-invasive estimation from spindle currents [7] or accelerometers [8]. These approaches enhance industrial applicability but introduce calibration challenges and typically lower accuracy [9].

Machine tool stiffness (or compliance) is a derived quantity defined as the ratio of externally applied force to the resulting displacement. Unlike cutting force, it lacks standardized measurands, and accredited calibration procedures, which limits comparability across studies. ISO 230-1 defines external and internal loading methods [10], but both are limited to simplified evaluations. More advanced techniques include six-degree-of-freedom multi-sensor systems [11], stiffness workspace mapping [12], and loaded double ball bar tests combined with multi-body or compliance modelling [13]. Other methods incorporate indirect joint compliance estimation [14] or triaxial excitation mapping [15].

This contrast highlights a critical metrological imbalance: while cutting force measurement is sufficiently mature for many compensation tasks, stiffness measurement lacks standardized measurands, calibration procedures, and validated uncertainty budgets. As a result, predictive models of tool deflection may rest on inputs of widely differing credibility.

Previous studies have largely advanced either measurement techniques for stiffness or cutting force monitoring, or developed compensation algorithms assuming idealized input data [16]. The distinctive contribution of this work is to address explicitly the metrological feasibility of tool deflection prediction. Rather than proposing new hardware or algorithms, the focus here is on assessing whether current measurement accuracies suffice to justify machining error compensation.

A measurement-oriented framework is introduced in which tool deflection is evaluated from a simplified elastic model, linking the uncertainties of cutting force and stiffness measurements. This approach enables identification of conditions in which compensation meets target uncertainty requirements and those where current metrological limitations preclude its application.

The structure of the paper is as follows. Section 2 reviews the state of the art in stiffness and cutting force measurements and establishes representative values for benchmarking. Section 3 introduces the simplified measurement model and the uncertainty evaluation. Section 4 presents and discusses the results of the parametric analysis. Section 5 concludes by highlighting the implications for machining accuracy and the need for validated stiffness measurement methods as a prerequisite for reliable tool deflection compensation in both machine tools and robots.

2. Uncertainties in stiffness and cutting force measurements

Accurate prediction of tool deflection requires dependable information on both machine tool stiffness and cutting forces. Both quantities, however, are affected by metrological limitations that constrain their reliability in practical use. Reviewing these limitations allows identification of representative benchmark values that form the basis for subsequent analysis.

2.1. Cutting force measurements

Cutting force is one of the few quantities in machining that can be confirmed with well-established calibration and traceability. Piezoelectric dynamometers remain the reference, supported by accredited calibration procedures and direct links to national standards. Under controlled conditions, expanded uncertainties as low as 0.1-0.2 % of full scale have been reported [17,18] confirming their suitability as reference instruments.

In machining applications, however, the dominant contributions to uncertainty arise not from the sensors themselves but from process-related effects such as workpiece heterogeneity, fixturing, dynamic excitation, and thermal drift. Consequently, while calibration studies define the achievable metrological performance of dynamometers, cutting experiments consistently reveal higher variability.

Axinte et al. [19] reported an expanded uncertainty of 24 N (3.2 %) for turning forces up to 740 N, with about half of the error attributed to process variations. Ciecieląg et al. [20] observed 9-12 % uncertainty (3.5-5 N) for forces up to 40 N, driven by repeatability, reproducibility, and sensor error. Under analogous tests on aluminium alloys, Zawada-Michałowska et al. [21] reported expanded uncertainties of 7-11 N (9-14 %) for forces up to 80 N.

As an alternative approach, *feeling machines* enable in-process force monitoring and tool deflection prediction through in-situ calibration. This is typically achieved using controlled tool-workpiece collision cycles, which simultaneously calibrate the force response and determine static tool stiffness. Reported accuracy, however, remains limited: Denkena et al. [22] observed mean-square errors of 25 N in X/Y and 100 N in Z, reduced to 25 N after low-pass filtering. Errors closely matched bias relative to dynamometer readings up to 300 N, decreasing at higher loads. Process-based and offline calibration achieved maximum bias of about 10 % for forces up to 500 N, with a resolution of 10 N in X and Y [23].

In summary, although cutting force measurement benefits from established calibration methods, its practical application remains constrained by process-related variability that significantly increases measurement uncertainty.

2.2. Stiffness measurements

Stiffness, in contrast, is a derived quantity defined as the ratio of applied force to measured displacement. Unlike force, it lacks standardized measurands, reference artefacts, and accredited calibration procedures. Reported values vary widely depending on machine configuration, loading method, and measurement setup, which complicates comparison between studies. Consequently, while stiffness data provide essential insight into machine tool behaviour, their metrological credibility remains limited by the absence of traceability and consistent uncertainty evaluation.

Several approaches have been reported in the literature. Archenti [13] introduced an elastically linked system using a loaded double ball bar combined with multi-body and finite element modelling, reporting stiffness in the range of 7-12 N/µm with repeatability of 0.2-0.6 N/µm. Beglarzadeh et al. [14] applied indirect joint compliance estimation with a telescopic double ball bar, obtaining stiffness around 17 N/µm with repeatability of 0.1 N/µm. Majda and Jastrzębska [11] proposed a generalized 6-DoF method, reporting translational stiffness of 2-30 N/µm and rotational stiffness of 0.2-8 Nm/µrad, with axis-dependent standard uncertainties ranging from 0.03 to 0.34 N/µm. Pawełko et al. [24] developed a hydraulic multi-axis loading system to map workspace stiffness, reporting directional values of 8-18 N/µm with expanded uncertainties of about 1.4-1.8 N/µm depending on axis.

In summary, although stiffness measurement provides valuable insight into machine tool behaviour, its practical application remains constrained by the lack of standardized procedures and traceable uncertainty evaluation.

2.3. Benchmark values

For the analysis, simplified benchmark ranges were adopted to represent typical and extreme operating conditions. Two cutting force levels were selected: 50 N, corresponding to finishing operations, and 800 N, representative of roughing or high-performance machining. To capture the extremes of structural rigidity, two stiffness levels were considered: 2 N/µm, typical of low-stiffness systems such as robots or slender machines, and 30 N/µm, characteristic of high-stiffness machine tools. These consolidated benchmark values, summarized in Table 1, form the basis for the uncertainty analysis presented in Section 4.

Table 1. Representative benchmark values of cutting force and stiffness adopted for uncertainty analysis.

Measurand	Reference value	Representative system
machine tool stiffness	2 N/µm	robots, low-stiffness machine tools, machine tools with long overhang tools or workpieces
	30 N/µm	high-stiffness machine tools
cutting force	50 N	finishing operations
	800 N	roughing/high-performance machining

Based on the literature, achievable values of expanded uncertainty were also defined, ranging from 8-40 N for force and 0.5-2.0 N/µm for stiffness. These benchmarks provide a consistent basis for evaluating the metrological feasibility of tool deflection prediction.

3. Uncertainty of Tool Deflection Measurement

The starting point is a measurement model for tool deflection δ consistent with the measurement objective, *i.e.* determining tool deflection with an uncertainty that represents a specified fraction of the tolerance of the relevant feature of size.

In the simplest one-dimensional case, δ is expressed as:

$$\delta = \frac{F}{K} + \sum \Delta_i, \quad (1)$$

where F is the constant component of the cutting force, K the equivalent stiffness of the structural loop, and Δ_i correction reflecting additional effects (tool/workpiece geometry, machine properties, dynamics, modelling corrections).

Since uncertainties of the corrections Δ_i of are practically unattainable, the model is simplified to:

$$\delta = \frac{F}{K}. \quad (2)$$

A justification for this approximation, including the relative order of magnitude of neglected terms, is given in [25], where the simplified model is supported by a theoretical and metrological analysis with a quantitative evaluation of systematic error and uncertainty.

This retains the dominant elastic effect while allowing uncertainty evaluation based only on inputs with quantifiable data. Assuming independent inputs, the combined standard uncertainty is:

$$u_\delta = \sqrt{\sum (c_i \cdot u_i)^2} = \sqrt{\left(\frac{1}{K} \cdot u_F\right)^2 + \left(-\frac{F}{K^2} \cdot u_K\right)^2}, \quad (3)$$

where: u_i – standard uncertainties, c_i – sensitivity coefficient and the expanded uncertainty is:

$$U_\delta = k \cdot u_\delta. \quad (4)$$

where k – coverage factor.

This simplified model provides a consistent basis for assessing the impact of force and stiffness uncertainties on tool deflection.

4. Results and discussion

The results presented in this section follow directly from the benchmark values established in Section 2.3 and the simplified measurement model introduced in Section 3. Tool deflection uncertainties were evaluated as a function of the input uncertainties in cutting force and machine tool stiffness, with representative scenarios defined by two force levels (finishing and roughing) and two stiffness levels (low- and high-rigidity systems).

Figure 1 illustrates the uncertainty of tool deflection as a function of the uncertainties in cutting force and stiffness. The results present the expanded uncertainty corresponding to a coverage factor $k = 2$. Each subplot represents a specific combination of cutting force and stiffness, allowing direct comparison of how input variability propagates into the variability of tool-deflection prediction. In the contour plots, fully transparent regions indicate ranges of measured quantities for which current metrological methods provide sufficiently accurate determination, whereas the opaque regions correspond to values beyond the presently achievable measurement capability and thus lie outside the range of reliable metrological assessment.

The results in Figure 1 reflect how uncertainties in cutting force and stiffness propagate into overall dispersion of tool deflection prediction through the simplified elastic model. The subplots illustrate that both parameters contribute significantly, but their influence depends strongly on the absolute values of force and stiffness.

At low stiffness values (≈2 N/µm), the uncertainty of tool deflection increases rapidly even with modest rises in stiffness uncertainty, particularly under high cutting forces. For example (see Fig. 1), at a cutting force of F = 800 N and stiffness K = 2 N/µm, the resulting tool deflection is approximately 400 µm, while the associated uncertainty ranges from 200 µm to 750 µm, corresponding to a relative uncertainty of about 50% to 190% of the deflection value. This indicates that for low-rigidity systems such as robots or slender machine tools, reliable prediction of tool deflection is strongly constrained by the present state of stiffness metrology. For finishing forces (≈50 N), the predicted uncertainties remain moderate, but at roughing levels (≈800 N) they increase sharply, suggesting that error compensation in this regime is unlikely to be justified. When compared with currently achievable accuracies, expanded uncertainties of 8-40 N for force and 0.5-2.0 N/µm for stiffness, as identified from the literature, it becomes clear that such low-stiffness scenarios lie beyond present metrological feasibility.

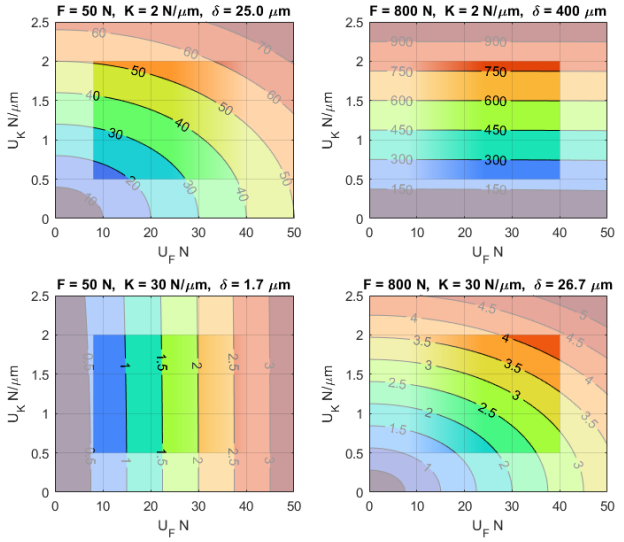

Figure 1. Tool deflection uncertainty as a function of force and stiffness inputs.

At higher stiffness (≈30 N/µm), the effect of stiffness uncertainty is strongly attenuated, as stiffness enters the model in the denominator. Here, force uncertainty becomes the dominant factor, but even with conservative input values the resulting tool deflection uncertainty remains relatively small. Under the same benchmark ranges, these high-stiffness cases fall within practical feasibility, confirming that current metrology already supports reliable compensation strategies.

These results indicate a general trend: the feasibility of tool deflection prediction improves markedly with increasing structural rigidity, whereas low-stiffness systems remain constrained by the absence of stiffness measurement methods capable of achieving the target uncertainty defined in this study. In practical terms, this means that error compensation is realistic for conventional high-stiffness machine tools but remains highly challenging for flexible systems, underscoring the need for standardized stiffness metrology.

From a practical standpoint, the presented results can be used to establish measurement targets for both laboratory and industrial setups. For example, stiffness uncertainty below 0.5 N/µm should be considered a realistic benchmark for validating compensation strategies in high-stiffness machines, whereas values above 1.5-2.0 N/µm make compensation questionable. For robotic or lightweight systems, current stiffness measurement methods do not yet meet this requirement, emphasizing the need for improved calibration standards and in-process identification techniques.

5. Conclusions

This study examined the uncertainty of tool deflection prediction based on cutting force and stiffness measurements. The analysis confirmed that while cutting force measurement is well established and supported by calibration artefacts, stiffness

measurement remains inconsistent, poorly standardized, and without confirmation of interlaboratory comparisons.

The results show that in high-stiffness machines, current levels of measurement accuracy are sufficient to experimentally verify reliable compensation of force-induced errors. In medium-stiffness systems, compensation becomes feasible only if stiffness uncertainty can be reduced, while in low-stiffness configurations, particularly in robotic and lightweight machining systems, it remains impractical with present metrology.

From an application perspective, the proposed framework enables assessing the feasibility of tool deflection compensation under real measurement conditions. It identifies scenarios where compensation is justified (in the context of achieving target uncertainty) or limited by metrological constraints, supporting process planning and measurement system design.

Overall, stiffness measurement emerges as the bottleneck for uncertainty-based tool deflection prediction. Future progress will therefore depend not on new force sensors but on validated stiffness measurement methods, including standardized measurands, procedures, and interlaboratory comparisons.

Future work should extend the present uncertainty-based framework to dynamic conditions, where tool-workpiece interaction and thermal effects amplify compliance variability. Integrating stiffness identification into adaptive control or digital twins could bridge the gap between calibration and in-process compensation, especially in flexible or robotic systems.

Acknowledgements

This research was funded in part/in whole by the National Centre for Research and Development (NCBR), Poland within Project no. INNOGLOBO/I/116/ITWA/2022 (INNOGLOBO programme). The research was founded by Polish National Agency for Academic Exchange within The Bekker NAWA Programme no. BPN/BEK/2023/1/00340. The work has received support from the Centre for Design and Management of Manufacturing Systems (DMMS) and Excellence in Production Research (XPRES) at KTH Royal Institute of Technology.

References

[1] Chanal, H., Duc, E., and Chevalier, A., 2022, "Studying the Influence of the Machining Process on the Geometrical Defects of the Standardized S-Shape Test Part," Precis. Eng., 75, pp. 193–209. https://doi.org/10.1016/j.precisioneng.2022.02.008.

[2] Gao, W., Ibaraki, S., Donmez, M. A., Kono, D., Mayer, J. R. R., Chen, Y.-L., Szipka, K., Archenti, A., Linares, J.-M., and Suzuki, N., 2023, "Machine Tool Calibration: Measurement, Modeling, and Compensation of Machine Tool Errors," Int. J. Mach. Tools Manuf., 187, p. 104017. https://doi.org/10.1016/j.ijmachtools.2023.104017.

[3] Habibi, M., Arezoo, B., and Vahebi Nojedeh, M., 2011, "Tool Deflection and Geometrical Error Compensation by Tool Path Modification," Int. J. Mach. Tools Manuf., 51(6), pp. 439–449. https://doi.org/10.1016/j.ijmachtools.2011.01.009.

[4] Pan, Z., Wang, L., Fang, Q., Sun, Z., and Qu, W., 2022, "Study on Tool Deflection Compensation Method Based on Cutting Force Observer for Orbital Drilling of CFRP/Ti Stacks," J. Manuf. Process., 75, pp. 450–460. https://doi.org/10.1016/j.jmapro.2021.12.058.

[5] Tomczyk, K., and Kowalczyk, M., 2025, "Assessment of Uncertainties When Determining the Upper Bound on the Dynamic Error in the Measurement of Cutting Forces," Measurement, 249, p. 116997. https://doi.org/10.1016/j.measurement.2025.116997.

[6] Denkena, B., Bergmann, B., and Witt, M., 2020, "Feeling Machine for Process Monitoring of Turning Hybrid Solid Components," Metals, 10(7). https://doi.org/10.3390/met10070930.

[7] C. Ni, J. Yang, and H. Ding, 2025, "Unsupervised Domain Adversarial Adaptive Regression Network for Cutting Force Prediction at Varying Spindle Speeds," IEEEASME Trans. Mechatron., 30(1), pp. 252–263. https://doi.org/10.1109/TMECH.2024.3395436.

[8] Postel, M., Aslan, D., Wegener, K., and Altintas, Y., 2019, "Monitoring of Vibrations and Cutting Forces with Spindle Mounted Vibration Sensors," CIRP Ann., 68(1), pp. 413–416. https://doi.org/10.1016/j.cirp.2019.03.019.

[9] Cao, H., Zhang, X., and Chen, X., 2017, "The Concept and Progress of Intelligent Spindles: A Review," Int. J. Mach. Tools Manuf., 112, pp. 21–52. https://doi.org/10.1016/j.ijmachtools.2016.10.005.

[10] 2012, "Test Code for Machine Tools Part 1: Geometric Accuracy of Machines Operating under No-Load or Quasi-Static Conditions."

[11] Majda, P., and Jastrzębska, J., 2021, "Measurement Uncertainty of Generalized Stiffness of Machine Tools," Measurement, 170, p. 108692. https://doi.org/10.1016/j.measurement.2020.108692.

[12] Jastrzębska, J., Parus, A., Jastrzębski, D., and Pawełko, P., 2023, "Measurement and Identification of Translational Static Stiffness in Workspace of a Machine Tool," Int. J. Adv. Manuf. Technol., 125(5), pp. 2601–2608. https://doi.org/10.1007/s00170-023-10904-5.

[13] Archenti, A., 2014, "Prediction of Machined Part Accuracy from Machining System Capability," CIRP Ann., 63(1), pp. 505–508. https://doi.org/10.1016/j.cirp.2014.03.040.

[14] Beglarzadeh, B., Mayer, J. R. R., and Archenti, A., 2021, "Modelling and Indirect Measurement of Machine Tool Equivalent Joint Compliances," CIRP J. Manuf. Sci. Technol., 35, pp. 882–895. https://doi.org/10.1016/j.cirpj.2021.10.001.

[15] Kono, D., Moriya, Y., and Matsubara, A., 2017, "Influence of Rotary Axis on Tool-Workpiece Loop Compliance for Five-Axis Machine Tools," Precis. Eng., 49, pp. 278–286. https://doi.org/10.1016/j.precisioneng.2017.02.016.

[16] Ozoegwu, C., and Eberhard, P., 2024, "A Literature Review on Prediction Methods for Forced Responses and Associated Surface Form/Location Errors in Milling," J. Vib. Eng. Technol., 12(4), pp. 5905–5934. https://doi.org/10.1007/s42417-023-01227-6.

[17] "Certifications and Accreditations | Kistler PL." [Online]. Available: https://www.kistler.com/PL/en/standards-and-certificates/C00000458. [Accessed: 28-Aug-2025].

[18] Uncertainty of Force Measurements. EURAMET e.V., Technical Committee for Mass and Related Quantities, Braunschweig, Germany., Mar. 2011.

[19] Axinte, D. A., Belluco, W., and De Chiffre, L., 2001, "Evaluation of Cutting Force Uncertainty Components in Turning," Int. J. Mach. Tools Manuf., 41(5), pp. 719–730. https://doi.org/10.1016/S0890-6955(00)00095-X.

[20] K. Ciecielag, A. Skoczylas, and J. Matuszak, 2024, "Measurement of Cutting Forces in Conventional and Climb Milling by Recurrence Analysis," 2024 11th International Workshop on Metrology for AeroSpace (MetroAeroSpace), pp. 531–536. https://doi.org/10.1109/MetroAeroSpace61015.2024.10591550.

[21] Zawada-Michałowska, M., Józwik, J., Legutko, S., Mika, D., Pieśko, P., and Pytka, J., 2020, "Cutting Force during Surface Layer Milling of Selected Aluminium Alloys," Materials, 13(24), p. 5725. https://doi.org/10.3390/ma13245725.

[22] Denkena, B., and Boujnah, H., 2018, "Feeling Machines for Online Detection and Compensation of Tool Deflection in Milling," CIRP Ann., 67(1), pp. 423–426. https://doi.org/10.1016/j.cirp.2018.04.110.

[23] Denkena, B., Litwinski, K. M., and Boujnah, H., 2016, "Detection of Tool Deflection in Milling by a Sensory Axis Slide for Machine Tools," Syst.-Integr. Intell. New Chall. Prod. Prod. Eng., 34, pp. 95–99. https://doi.org/10.1016/j.mechatronics.2015.09.008.

[24] Pawełko, P., Jastrzębski, D., Parus, A., and Jastrzębska, J., 2021, "A New Measurement System to Determine Stiffness Distribution in Machine Tool Workspace," Arch. Civ. Mech. Eng., 21(2), p. 49. https://doi.org/10.1007/s43452-021-00206-6.

[25] Majda, P., Dunaj, P., Powałka, B., and Archenti, A., 2026, "Metrological Constraints and Uncertainty of Tool Deflection Measurements in Machine Tools and Articulated Robots," Precis. Eng. https://doi.org/10.1016/j.precisioneng.2026.03.028.

euspen's 26th International Conference & Exhibition, Krakow, PL, June 2026
www.euspen.eu

Capability Modelling of Robotic Machining System based on Digital Twin

Abdullah All Mamun Anik[1]*, Andrew Longstaff[1], Simon Fletcher[1], Xianzhi Zhang[1]

[1] School of Computing and Engineering, University of Huddersfield, Huddersfield, Queensgate, United Kingdom

* Corresponding Author: Abdullah All Mamun Anik (abdullahallmamun.anik@hud.ac.uk)

Abstract

In the era of technological advancements, digitalisation, advanced manufacturing, and industrial revolution, the world is moving forward with intelligent manufacturing processes. Robotic machining is becoming very popular nowadays for their manufacturing capabilities. Manufacturing Engineers are making their production planning through manual check before robotic machining without any organised capability modelling. Traditional capability evaluation method is manual, and human centric. It is non-standardised and time consuming. There is a high risk of human error. Capability modelling of robotic machining system through bridges the gap between theoretical robot specifications and practical machining applications, driving innovation and competitiveness in automated and cloud manufacturing. In cloud manufacturing, Digital Twin are now established technology on the market and are commonly deployed for robotic machining. Capability modelling is a part of digital twin for robotic machining production planning, feasibility analysis, and demand estimation. However, digital twin technology does not have any capability modelling architecture with it for ensuring production plan and forecasting robot's operational capacity. Existing research focus on bi-directional real-time data exchange without much effort on capability modelling. Creating a capability model for Digital Twin of robotic machining will enable autonomous cloud manufacturing. In this research, a capability profile of robotic system has been proposed and implemented. An industrially inspired component was used as a case study. This research work demonstrates data modelling, capability modelling, CAD file geometric data extraction system to build an intricate model for digital twin. The main components incorporate the judgement of the component design on the basis of size, machining envelope, operational details, cutting tools, cutting strategy, machining coordinate position, operational time, and data analysis. This paradigm extends transformative mechanism towards intelligent, data-driven manufacturing ecosystems for robotic machining.

Keywords: Digital Twin, Machining Capability, Robotic Machining, Industrial Robot

1. Introduction

Capability modelling of robotic machining system is playing a pivotal role for enhancing accuracy, efficiency, safety, and Industry 4.0 integration through simulation, robotic machining process optimisation, and verification. Challenges like simulating dynamics and integrating data hinder scalability. This unique framework focuses on robotic machining, using CAD data extraction for the inspection in a cloud-integrated setup. Unlike other digital twins (aerospace, automotive sectors, etc.) this research targets articulated robots for machining feasibility from CAD files, making it a pioneering framework for automated manufacturing. The research specialises in articulated robots like KUKA KR 210. The capability modelling infrastructure linking of traditional digital sectors with this research underscores the potential for advanced, data-driven insights in robotic manufacturing process, showcasing an innovative framework that has not been explored before in robotic machining contexts. Thus, this work paves the way for future advancements in automated and cloud manufacturing. It extends transformative mechanism towards intelligent, data-driven cloud manufacturing ecosystems for robotic machining by utilising the proximity of innovation. The aim of this research is to investigate the machining feasibility of a given CAD model based on capability modelling of robotic system by involving logical judgement of robotic machining for industrial robot. Some objectives to reach the main focus point of this research work are to develop integrated capability modelling of robotic machining framework bridging CAD geometry with robot operational specifications, achieve automated feature detection and operation classification from CAD data by utilising capability assessment platform, ensure strategic recommendations operational quality control, and operational efficiency objectives by ensuring effective and secure robotic machining, and create expandable, scalable methodology for pre-screening, production planning, feasibility analysis, and demand estimation for manufacturing before physical machining.

3. Literature review

The Digital Twin technology is exceedingly scalable innovation for industry ready technological manufacturing process. It extends the capability and competence of conventional robotic machining system. But there is no established integrated digital twin framework for robotic machining capability assessment platform available in traditional robotic machining. Limited academic work on automated CAD-to-capability translation and insufficient integration of geometric analysis with robot operational constraints. Missing automated decision support system and manual check through human judgement for production planning, pre-screening, feasibility analysis, logical assessment, and demand estimation before physical robotic machining can do huge human error. Data security protocol, adequate measuring unit, and manual guide for users will play a pivotal role for advanced machining virtually for Digital Twin based manufacturing system [1]. Utilising Digital Twin driven intelligent manufacturing reality have several challenges to ensure precision and quality control regarding productive

outcome assurance. Unfortunately, virtual technological advancements are shifting rapidly in today's world. To implement Industry 4.0 integrated manufacturing process in the virtual realm, several digital and onsite challenges exist [2]. intelligent manufacturing reality have several challenges to ensure precision and quality control regarding productive outcome assurance. Unfortunately, virtual technological advancements are shifting rapidly in today's world. To implement Industry 4.0 integrated manufacturing process in the virtual realm, several digital and onsite challenges exist [3]. Digital environments may enhance all present manufacturing procedures as well as the development of novel goods. This emerging trend is known as Smart Manufacturing. It is defined as "the use of an incorporated, computerised system that includes simulation, visualization in three dimensions, data analysis, and collaboration capabilities for generating product and manufacturing process definitions concurrently". The simulated method is vital in a production context since it saves time and money when adopting an innovative manufacturing procedure [4]. Vichare et al. emphasise advancements in depicting machine tools and support systems through showcasing their static functionalities. This method outlines the dynamic data linked to a specific machine tool by aiding in the arrangement of different components together. This approach also features improvements to existing STEP-NC standards on defining machine tool capabilities [5]. Utilising Digital Twin driven intelligent manufacturing reality have several challenges to ensure precision and quality control regarding productive outcome assurance. Unfortunately, virtual technological advancements are shifting rapidly in today's world. To implement Industry 4.0 integrated manufacturing process in the virtual realm, several digital and onsite challenges exist [7, 8]. Digital environments may enhance all present manufacturing procedures as well as the development of novel goods. This emerging trend is known as Smart Manufacturing. It is defined as "the use of an incorporated, computerised system that includes simulation, visualization in three dimensions, data analysis, and collaboration capabilities for generating product and manufacturing process definitions concurrently". The simulated method is vital in a production context since it saves time and money when adopting an innovative manufacturing procedure [9-12]. Vichare et al. emphasise advancements in depicting machine tools and support systems through showcasing their static functionalities. This method outlines the dynamic data linked to a specific machine tool by aiding in the arrangement of different components together. This approach also features improvements to existing STEP-NC standards on defining machine tool capabilities [13-16].

4. Methodology

The research develops a Capability Assessment Platform (CAP) system using 3D visualization and JavaScript with Three.js for CAD evaluation with a KUKA robot. Usability issues may occur on older browsers. The system lacks touch support for mobile users and detailed movement options, with security concerns from client-side file checks. It prioritizes speed in analysis functions but struggles with complex CAD geometries due to limited library integration. Suggestions for improvement include server-side CAD operations and feature recognition. This research methodology has been divided by 3 consecutive sections. They are:

a) **CAD Data Processing:** This part starting from the digital twin visualisation and leading to geometric validation, and assessment before processing to the capability assessment phase.

b) **Capability Assessment:** This procedure for capability evaluation in robotic machining detailing a clear step by step capacity reviewing and judgement process that guides the robotic machining assessment process from input data to feasibility determination.

c) **Robot Model Processing:** Robot model processing methodology highlighting the physical articulated robot's same to same virtual model (e.g: KUKA, ABB, FANUC etc) by utilising every robot's capability profile. This process emphasises the steps from support generations to validation and decision making regarding production readiness based on capabilily assessment for robotic machining based on Digital Twin.

5. Implementation with case studies

5.1. Digital Resource Data Model of KUKA KR 210 Robot

The KUKA KR 210, with 6 axes, lifts up to 210 kg, suitable for diverse industrial tasks, fits modern production systems. Resource models are crucial for effective robotic system operation in factories. Figure-1 guides the digital data needs for robotic machining analysis.

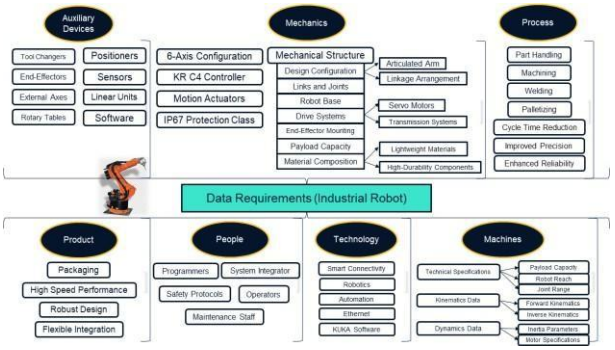

Figure 1. Digital Data Requirements of Industrial Robot for Machining Capability Analysis.

5.2. Physical Robot's Virtual Capability Profile

In this capability modelling research work based on Digital Twin for robotic machining, the established platform is required any physical robot's same to same virtual capability profile by utillising dataset other standard robot's information or specification to do the capability assessment for Computer Aided Production Planning (CAPP) from CAD model information translation against an kind of industrial robot and their specific model for instances KUKA, FANUC, ABB, and other robot. In this research, for examination and experimenta purpose KUKA KR 210 robot has been used for analysing robotic machining capacity based on information integrated Digital Twin of industrial articulated robot. Figure-2 shows the detailed capability profile dataset and information integrated virtual robot of KUKA KR 210 robot's physical working model by using its appropriate robot specification, joint information, reach limit, payload data, repeatability, degrees of freedom, and mounting info, and D-H parameters for robotic machining capability assessment.

Robot Model	Physical Specifications	Value	Joint Motion Specifications	Value (°)	Value (°/s)	Performance Metrics	Value	D-H Parameters			
								θ_i	d_i (m)	a_i (m)	α_i (rad)
KUKA KR 210	Payload	210 kg	J1 Base	±180°	86°/s	Accuracy Class	±0.05mm				
	Reach	2700 mm	J2 Shoulder	±135°	84°/s	Max Cycle Time	< 15 sec	θ_1	0.75	0.35	(-90°)
	Repeatability	±0.12 mm	J3 Elbow	±150°	84°/s	IP Rating	IP54	θ_2	0	1.25	(0°)
	Mass	1267 kg	J4 Wrist Pitch	±120°	100°/s	Controller	KRC4	θ_3	0	-0.054	(-90°)
	DOF	6 Axes	J5 Wrist Yaw	±270°	110°/s	Power	10-20 kW	θ_4	1.5	0	(90°)
	Mounting	Floor/Inverted	J6 Wrist Roll	±360°	184°/s	Duty Cycle	Continuous	θ_5	0	0	(-90°)
								θ_6	0.303	0	(0°)

Figure 2. Robot Capability Profile dataset and information integrated virtual robot of KUKA KR 210 robot's physical working model.

5.3. Digital Twin's Data Modelling and Diverse Working Framework

The program software algorithm describes an 8 step procedure for digital twin's modelling capabilities in a robotic machining

system from loaded CAD component's geometric analysis in figure-3 by using Unified Modeling Language (UML) sequencing flowchart. This technique focusses on the KUKA KR 210 robot which uses Digital Twin software to optimise along with enhance manufacturing phases ranging from computer assisted design conception to testing actual production limitations.

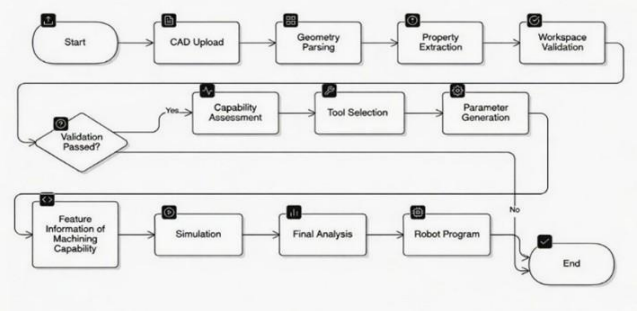

Figure 3. Digital Twin's Capability Modelling Process (Step by Step).

6. Result and discussion

The capability modelling mechanism attempts to accomplish the industrial articulated robot's (KUKA KR 210) data modelling, performance modelling, and machining capacity assessment over the course of numerous programming, experiments, and investigations. It additionally generates initial judgements of robotic machining through reviewing the computerised 3D design geometry. Various items and components are used as loaded CAD model before performing tangible machining in a manufacturing robot interface utilising the digital twin infrastructure. The digital twin model integrates client/ user side and robot side to ensure proper capability analysis output from the new machining capability observation envelope before physical robotic machining in industrial environment.

6.1. Capability Assessment Platform Interface for KR 210

The recent robotic manufacturing capability modelling interface established a capability assessment framework based on Digital Twin interface by adding virtual KUKA KR 210 robot specifications and capability modelling platform. From this architecture, the system can observe, review, and understand the CAD files of machining operations instructions. After that the digital twin framework can make extract all the information from the loaded file, initial judgement of component's mechanical operation, and make proper capability analysis of robotic machining on the basis of KUKA KR 210 robot by using the digital twin. Figure-4 describes the initial Digital Twin interface by accumulating KUKA KR 210 Robot.

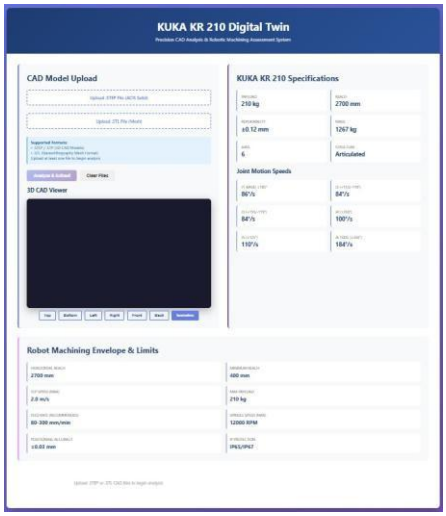

Figure 4. Capability Assessment Platform (CAP) by Integrating KUKA KR 210 Articulated Robot.

6.2. Capability Assessment Platform Case Study (KUKA KR 210)

Capability modelling ensures the proper operational indication by extracting the loaded computer aided design model of machining component through Digital Twin. It assists the users or clients to understand the machining capacity, and other operational information judgement by using industrial robot. In this research work, the capability assessment platform has been utilised to upload different types of 3D CAD components digital model to know the machining capability, operational efficiency analysis, and other judgements by relating with the digital version of KUKA KR 210 robot by utilising digital twin. Serially, figure-5 demonstrates the loaded wheel component in the digital twin platform and its different angle (Top, Bottom, Front, Back, Left, Right, Isometric) 3D viewer to rotate and check the full design for capability analysis, figure-6 illustrates the intelligent analysis of dimensional information (Length, Width, Height, Surface Area, Estimated Mass, Reach Assessment, Payload Assessment) of the loaded wheel's CAD design in Query one (Q1), Figure-7 explains the manufacturing features along with detected manufacturing feature, internal and boundary hole count of the loaded CAD component, surface complexity area analysis, vertices count, edges and faces count, Euler characteristics, and implied features in Query two (Q2), Figure-8 features the suggested machining operations in the machining capability analysis through digital twin in Query three (Q3) by integrating KUKA KR 210 capability assessment outcome.

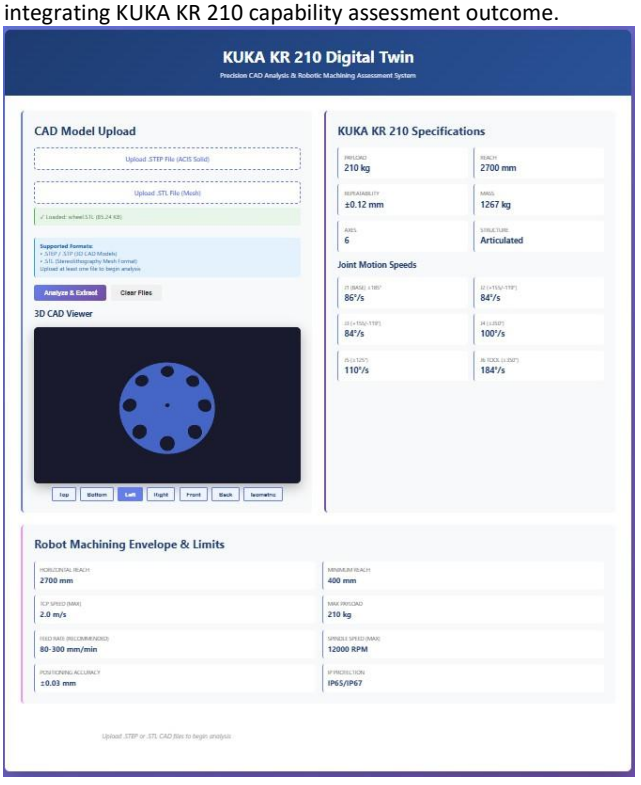

Figure 5. Loaded 3D CAD Model of Wheel in Digital Twin and 3D View from Different Angle.

Figure 6. Intelligent Dimensional Information Analysis of Wheel in Query: 1,

Q1.

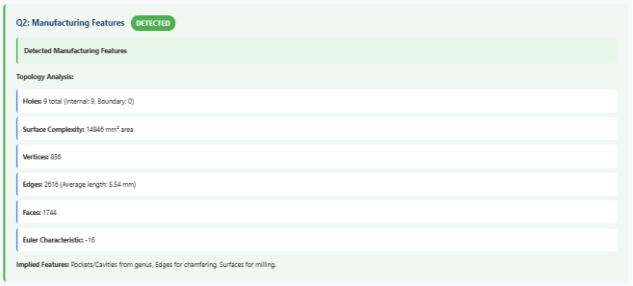

Figure 7. Robotic Machining Feature Analysis of Wheel in Query: 2, Q2.

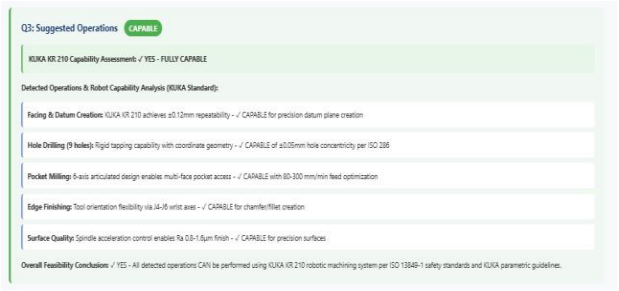

Figure 8. Capability Assessment of Suggested Machining Operations of Wheel by using KUKA KR 210 Robot in Query: 3, Q3.

7. Conclusion

This research ideology and explanation provides the framework for future advances at the nexus of robots and intelligent manufacturing. In the marketplace, there are a lot of Digital Twin for robot and robotic machining systems available but there is no established computerised capability assessment framework for Digital Twin for Computer Aided Production Planning (CAPP), feasibility analysis, logistics and resource analysis and demand estimation for robotic machining. The total mechanism of this research work shows how Digital Twin technology can change manufacturing, making it more flexible, exact, and efficient. The methodology and capability modelling of this inventive research helps to move towards smarter, data-driven intelligent manufacturing. The virtual data processing system focusses upon three essential elements for articulated robots (KUKA KR 210) performing drilling and milling tasks at the robotic machining interface. The capability assessment platform makes it possible to virtually simulate machining envelopes, identify features involving pockets and holes, and assess capacity in relation to robot requirements for instances payload, reach, and repeatability of KUKA KR 210 articulated robot. An interactive online platform employs Three.js for CAD geometry analysis is used to carry it out. By collecting geometric data from STL/STEP files and suggesting cutting tools/strategies, the capability modelling system bridges the virtual and physical realities to enable actual-time decision-making and self- diagnosis mechanism. Capability assessment progression is used for data extraction increases precision in this capability modelling for robotic system. The research work's findings are significant for advancing automated machining in Industry 4.0 through cloud-based robotics systems.

References

[1] Mohd Javaid A, Haleem A and Suman R 2023 Digital twin applications toward Industry 4.0: A review Cognitive Robotics **3** 71-92

[2] Laaki H, Miche Y and Tammi K 2019 Prototyping a digital twin for real-time remote control over mobile networks: Application of remote surgery IEEE Access **7** 20325-20336

[3] Zhang, X., Wu, B., Zhang, X., Duan, J., Wan, C., & Hu, Y. (2023). An effective MBSE approach for constructing industrial robot digital twin system. Robotics and Computer-Integrated Manufacturing, **80**, 102455. https://doi.org/10.1016/j.rcim.2022.102455

[4] Zhang X, Zheng L, Fan W, Ji W, Mao L and Wang L 2024 Knowledge graph and function block based digital twin modeling for robotic machining of large-scale components Robotics and Computer-Integrated Manufacturing **85** 102609

[5] E. Vichare, A. Nassehi, S. Kumar and S. T. Newman, "A unified manufacturing resource model for representing CNC machining systems", Robotics and Computer-Integrated Manufacturing, vol. 25, no. 6, pp. 999–1007, 2009. doi:10.1016/j.rcim.2009.04.014

[6] Mohd Javaid, Abid Haleem, & Rajiv Suman (2023). Digital twin applications toward Industry 4.0: A review. Cognitive Robotics, 3, 71-92. https://doi.org/10.1016/j.cogr.2023.04.003

[7] Lu, Y. (2020). Digital twin-driven smart manufacturing: Connotation, reference model, applications, and research issues. Robotics and Computer-Integrated Manufacturing, 61, 101837. https://doi.org/10.1016/j.rcim.2019.101837

[8] Laaki, H., Miche, Y., & Tammi, K. (2019). Prototyping a digital twin for real time remote control over mobile networks: Application of remote surgery. IEEE Access, 7, 20325-20336. https://doi.org/10.1109/ACCESS.2019.2897018

[9] E. Vichare, A. Nassehi, S. Kumar and S. T. Newman, "A unified manufacturing resource model for representing CNC machining systems", Robotics and Computer-Integrated Manufacturing, vol. 25, no. 6, pp. 999–1007, 2009. doi:10.1016/j.rcim.2009.04.014

[10] Zhang, X., Wu, B., Zhang, X., Duan, J., Wan, C., & Hu, Y. (2023). An effective MBSE approach for constructing industrial robot digital twin system. Robotics and Computer-Integrated Manufacturing, 80, 102455. https://doi.org/10.1016/j.rcim.2022.102455

[11] Zhang X, Zheng L, Fan W, Ji W, Mao L and Wang L 2024 Knowledge graph and function block based digital twin modeling for robotic machining of large-scale components Robotics and Computer-Integrated Manufacturing 85 102609

[12] Peng L, Yang Z, Ye X, Xu W and Li R 2025 A digital twin approach for online reconfiguration of robotic manufacturing systems toward plug-and-produce International Journal of Computer Integrated Manufacturing 1-27.

[13] T. K. Valijonovich, T. K. Qahramonovich and N. Ayubjonovna, "Innovative pedagogical approaches for teaching advanced manufacturing processes in mechanical engineering", Строительство и..., 2025. Available: https://cyberleninka.ru/article/n/innovative-pedagogical-approaches-for-teaching-advanced-manufacturing-processes-in-mechanical-engineering

[14] J. Xiao, N. Anwer, H. Huang, R. Bonnard, B. Eynard, C. Huang and E. Pei, "Information exchange and knowledge discovery for additive manufacturing digital thread: A comprehensive literature review", International Journal of Computer Integrated Manufacturing, vol. 38, no. 8, pp. 1052–1077, 2025. doi:10.1080/0951192X.2024.2387768

[15] Y. Zhao, Q. Liu, W. Xu, H. Yuan and P. Lou, "An ontology self-learning approach for CNC machine capability information integration and representation in cloud manufacturing", Journal of Industrial Information Integration, vol. 25, p. 100300, 2022. doi:10.1016/j.jii.2021.100300

[16] X. Xu, "From cloud computing to cloud manufacturing", Robotics and Computer-Integrated Manufacturing, vol. 28, no. 1, pp. 75–86, 2012. doi:10.1016/j.rcim.2011.07.002

euspen's 25th International Conference & Exhibition, Krakow, PL, June 2026
www.euspen.eu

Axial spindle deformation due to Poisson's effect under centrifugal loading

Byron R. Knapp, Dave Arneson, and Dan Oss

Professional Instruments Company, Hopkins, Minnesota, USA

bknapp@airbearings.com

Abstract
Centrifugal loading in high-speed ultra-precision spindles induces radial expansion of the rotor, which leads to micrometer-level axial shortening of the rotor through Poisson-coupled deformation. This work develops a finite element model to quantify speed-dependent axial displacement of an air-bearing spindle and validates the model experimentally. The spindle exhibits instantaneous micrometer-level axial contraction that increases approximately with the square of rotational speed, in agreement with analytical predictions. Experimental measurements reveal two distinct mechanisms of axial motion: a rapid elastic shortening due to centrifugal loading and a slower thermal drift arising from viscous shear heating of the air films. By applying linear drift removal, the thermal contribution is isolated, enabling direct comparison of the elastic response to model predictions. The corrected measurements and finite element model results agree within 3% at high speeds, demonstrating high fidelity of the modeling approach. The analysis further shows that the magnitude of axial deformation depends strongly on overhung length and attachments to the rotor, underscoring the importance of spindle design for high-speed applications. These validated results provide a foundation for real-time compensation of centrifugal-induced axial error in ultra-precision machining.

Air bearing design

1. Introduction

Increasing demands for deterministic machining of optical surfaces and molds require ultra-precision air bearing spindles capable of operating at higher rotational speeds for improved production efficiency [1]. Increasing spindle speed is a key strategy for enhancing machining productivity, reducing cycle times, and enabling the processing of brittle materials [2]. However, axial spindle motion directly affects tool position, cutting depth, and form errors, making micrometer-scale deviations unacceptable. High-speed spindle operation introduces two distinct axial error sources—axial thermal drift and induced axial deformation due to centrifugal loading—which may be misidentified despite occurring on fundamentally different time scales. In this paper, a model describing axial deformation induced by Poisson's effect under centrifugal loading in an ultra-precision air bearing spindle is developed and experimentally validated. To date, most published work on high-speed spindle error mechanisms has focused on thermal behavior [3,4], while comparatively little attention has been given to elastic deformation driven purely by centrifugal loading. Moreover, this effect becomes increasingly important for axial sensitive direction constant surface speed machining applications. In constant surface speed machining maintaining a fixed cutting velocity requires an increase in spindle speed as the cutting diameter decreases. Understanding and quantifying this deformation is therefore essential for developing accurate compensation strategies for next-generation ultra-precision machining systems.

2. Background

Centrifugal loading of a spindle rotor is a result of inertial forces that increase quadratically with rotational speed. These centrifugal forces cause radial expansion of the spindle as rotational speed increases. Due to the Poisson effect, radial expansion results in axial shortening even though there is no applied axial load. A rotor rotating with constant speed and unconstrained ends has zero axial stress but the axial strain ε_z is caused purely by the Poisson effect from the radial and tangential stresses:

$$\varepsilon_z = -\frac{\nu}{E}(\sigma_r + \sigma_t) \tag{1}$$

where ν is Poisson's ratio, E is Young's modulus, σ_r is the radial stress, and σ_t is the tangential (hoop) stress. This negative value indicates that the rotor contracts axially as it expands radially due to rotation.

Assuming a hollow cylinder of length L with inner radius r_i and outer radius r_o and density ρ the axial deformation δ_z is

$$\delta_z = \varepsilon_z \cdot L = -\frac{\nu\rho\omega^2(r_o^2+r_i^2)}{2E} \cdot L \tag{2}$$

Similarly, as the inner radius approaches zero, we have the following for the axial shortening of a solid cylinder

$$\delta_z = -\frac{\nu\rho\omega^2 r_o^2}{2E} \cdot L \tag{3}$$

Equations 1 and 2 can be used to estimate the axial deformation of a rotating shaft for the simple cases of solid and hollow shafts of constant cross-section. For more complex geometries, including multiple components attached to the spindle shaft, a finite element model must be used [5].

3. Finite element model

A finite element model is developed for the air bearing spindle shown in Figure 1 supported by experimental verification. The spindle features a captured thrust bearing positioned axially between two journal bearings, providing axial stiffness while the widely-spaced journal bearings provide radial and tilt stiffness. During operation at speeds up to 10,000 RPM, centrifugal effects induce instantaneous axial shortening that is directly proportional to the axial distance between the thrust bearing and the free end of the shaft, including any tooling, fixtures, or auxiliary components mounted to the shaft. Consequently, the axial placement of the thrust bearing and the effective overhung length of the shaft play a critical role in determining the magnitude of axial displacement due to centrifugal loading.

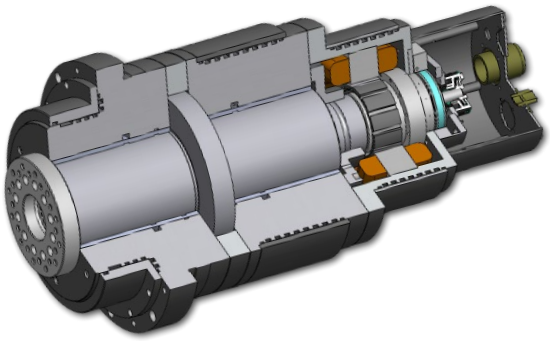

Figure 1. Professional Instruments ISO 5.5 air bearing spindle is the subject of this work.

Solidworks Simulation is used for the linear static analysis with the curvature-base mesher using solid elements and the h-adaptive solver. The model is reduced to a quarter-shaft representation (Figure 2) due to axis symmetry, decreasing computational cost and enabling application of the boundary conditions to prevent rigid-body motion of the model. Constraints are applied along the symmetry planes, resulting in two radial constraints normal to the symmetry planes and a third constraint applied in the axial direction normal to the thrust bearing surface.

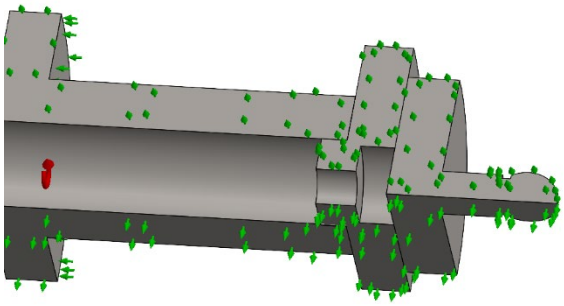

Figure 2. Finite element model of quarter shaft with boundary conditions and centrifugal loading.

To enable evaluation of axial deformation, a dedicated metrology surface is incorporated into the model. Specifically, a spherical testball is attached to the free end of the shaft, providing a well-defined geometric reference for axial displacement measurement. The complex geometry of the measurement hardware introduces some errors in the lumped model (Equations 1 and 2) due to the assumption of uniform axial strain. However, the axial strain is accurately predicted by the finite element analysis as shown in Figure 3.

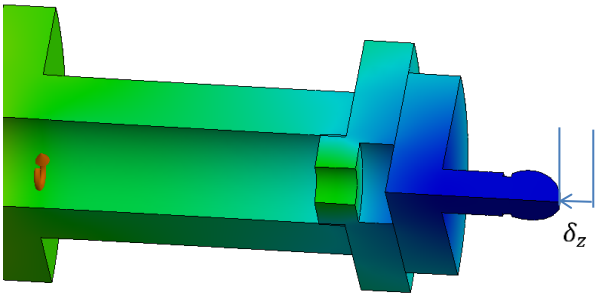

Figure 3. Finite element analysis showing axial displacement.

4. Experimental verification

To validate the finite element model, a series of controlled experiments were conducted to measure the axial displacement of the shaft of an ISO 5.5 air bearing spindle. Axial motion was measured using a non-contact capacitive displacement sensor with nanometer resolution (Lion Precision C23-C). As illustrated in Figure 4, the sensor was aligned with the axis of rotation and targeted a spherical artifact rigidly mounted to the rotor.

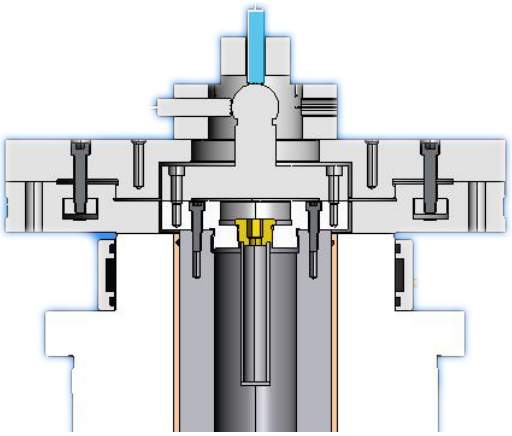

Figure 4. Setup to measure axial motion at speed.

Each experimental run followed a consistent speed profile. Starting from rest, the spindle was accelerated to a prescribed constant rotational speed, maintained at that speed for several seconds to allow transient effects to stabilize, and then decelerated to a complete stop. The resulting axial displacement of the shaft was recorded continuously throughout the entire cycle.

The measured response captures two distinct mechanisms contributing to axial motion as shown in Figure 5. First, the instantaneous axial displacement associated with centrifugal loading is observed during the acceleration and deceleration phases, corresponding to elastic deformation of the shaft and attached components. Second, a slower, time-dependent axial drift is evident during the constant-speed period. This drift is attributed to thermal effects arising from viscous shear of the air bearing films, which generates heat and produces axial expansion of the spindle structure. Over the short duration of the test, the thermal contribution is approximately linear with respect to time, allowing the centrifugal and thermal effects to be separated for comparison with model predictions.

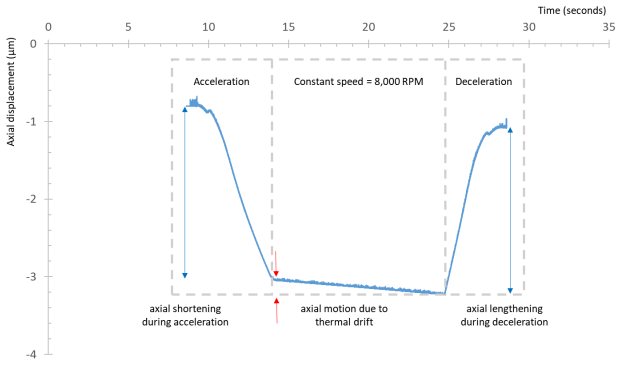

Figure 5. Axial displacement measurement before removal of thermal drift.

Measurement data similar to that presented in Figure 5 were collected over a range of spindle speeds from 500 RPM up to 10,000 RPM. For each test condition, axial displacement was recorded continuously throughout the acceleration, constant-speed, and deceleration phases. The test is conducted without liquid cooling and thermal expansion of the aluminum spindle housing is greater than the expansion of the stainless steel shaft, resulting in thermal displacement in the negative direction. To isolate the elastic response of the shaft, the time-dependent thermal component was removed from each data set by fitting and subtracting a linear trend, as illustrated in Figure 6. This approach is justified by the approximately linear thermal drift observed over the short duration of each test.

Following removal of the thermal contribution, the remaining axial displacement is dominated by the elastic deformation of the shaft under centrifugal loading. The resulting axial shortening increases with spindle speed and exhibits the expected symmetry during acceleration and deceleration, providing a clear experimental signature of the centrifugal loading mechanism. The processed data therefore enable direct comparison with finite element predictions of speed-dependent axial deformation.

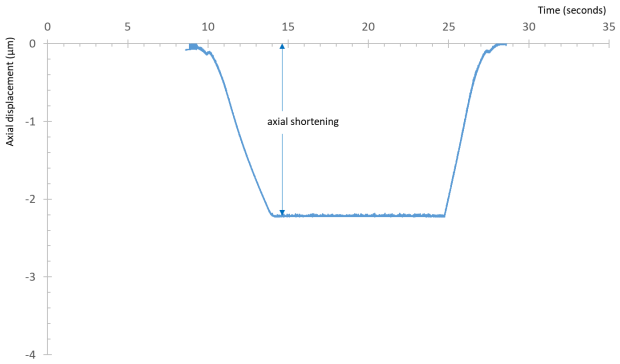

Figure 6. Axial displacement measurement after removal of thermal drift.

5. Results

The finite element model developed for the spindle rotor assembly shows strong predictive capability for the axial deformation induced by centrifugal loading, and these predictions are in close agreement. Figure 7 presents the comparison between modeled and measured axial shortening after removal of the thermally induced drift component. The finite element model results confirm that axial contraction increases approximately with the square of rotational speed, consistent with the analytical trends predicted by Equations 2 and 3. At low rotational speeds (less than 5,000 RPM), both the modeled and measured axial displacements are relatively small, approaching the noise floor of the measurement. As speed increases, however, the deformation becomes clearly measurable, and by 10,000 RPM the spindle exhibits 3.5 µm of instantaneous axial shortening. This behavior reflects the combined influence of radial and tangential stress components in the shaft and attached tooling, which drive the Poisson-induced axial contraction predicted by the model.

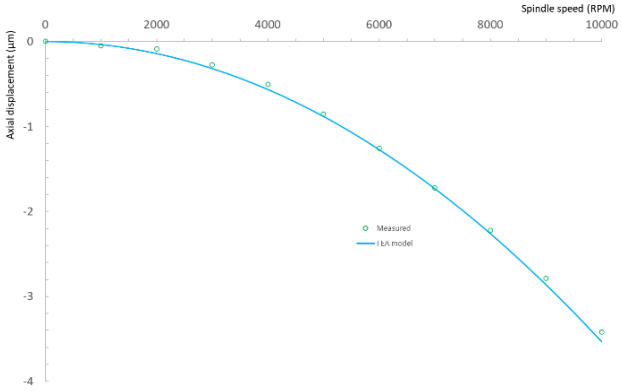

Figure 7. Verification of the modeled axial displacement versus speed.

The experimental measurements clearly reveal two distinct timescales of axial motion:

- Instantaneous deformation occurring during acceleration and deceleration, driven by centrifugal loading of the shaft.
- Time-dependent drift occurring during constant-speed operation, attributed to thermal expansion caused by viscous air-film shear heating.

Following linear removal of thermal drift from the experimental data, the measured elastic response closely tracks the finite element model predictions. Above 5,000 RPM, where the deformation signal is well separated from measurement noise, the difference between the modeled and measured axial shortening remains within 3%, demonstrating excellent quantitative agreement. This level of correlation validates the modeling assumptions and confirms that the dominant mechanism—centrifugal radial expansion coupled through Poisson's effect—is accurately captured by the finite element analysis.

6. Discussion

The agreement between model and experiment demonstrates that centrifugal-induced axial shortening is a predictable and significant contributor to axial motion in high-speed ultra-precision spindles. A key implication of this work is the impact of centrifugal deformation on machining applications with axial sensitive direction that employ constant surface speed cutting. Since the spindle speed must continuously increase as cutting diameter decreases, the dynamic change in spindle speed introduces an accompanying speed-dependent axial shift that directly affects cutting depth and form accuracy.

The results presented here show that axial shortening scales approximately with the square of spindle speed, meaning that deformation increases rapidly when diameters are smallest and

rotational speeds are highest. Without compensation, this can introduce micrometer-level form deviations—an unacceptable outcome for applications requiring sub-100 nm accuracy. This phenomenon is especially relevant for spindles with long overhung lengths and fixtures attached to the rotor that magnify the axial displacement induced by centrifugal loading.

The findings indicate that axial tool-position error during high-speed or constant surface speed machining can be estimated and compensated in real time using spindle speed. Since the elastic response is instantaneous and reversible, integration of a predictive model—such as the finite element framework validated here—into the machine control system would allow direct correction of the axial tool position as speed changes. Such compensation becomes even more critical when combined with thermal drift, which evolves on a slower timescale but can obscure the underlying elastic behavior if uncorrected.

Overall, the validated finite element model provides not only physical insight into Poisson-driven axial shortening but also a practical foundation for implementing real-time compensation strategies. As machining systems continue to pursue higher throughput, smaller feature sizes, and more aggressive machining strategies, accounting for centrifugal deformation will become increasingly essential for achieving deterministic accuracy in ultra-precision manufacturing.

7. Conclusion

This work demonstrates that centrifugal loading in high-speed ultra-precision spindles produces measurable axial shortening through Poisson-coupled radial expansion, and that this elastic deformation is both instantaneous and strongly dependent on rotational speed. A finite element model was developed to quantify this behavior for a practical air-bearing spindle, and experimental measurements confirmed the predicted speed-dependent response. After removal of the slower thermal drift component, the measured axial shortening agreed with the model within 3% at high speeds, validating the accuracy of the modeling approach.

The results show that axial deformation scales approximately with the square of spindle speed, making it increasingly significant in machining strategies—such as constant surface speed cutting—that require continuous acceleration as tool diameter decreases. This speed-induced axial shift can introduce micrometer-level form errors if not properly accounted for. Because the elastic response is instantaneous and reversible, the validated model provides a practical basis for real-time compensation of speed-dependent tool-position error.

Overall, this work establishes both the physical mechanism and quantitative magnitude of centrifugal-induced axial shortening in ultra-precision spindles, and it provides a predictive framework that can be directly integrated into next-generation machining systems to improve accuracy in high-speed and constant-surface-speed applications.

References

[1] E Brinksmeier and L Schönemann (Eds.) Ultra-precision High Performance Cutting. Report of DFG Research Unit FOR 1845. Springer Nature Switzerland AG Cham: 2020.

[2] M Tunesi et al. Effect of cutting speed in single point diamond turning of (100)Ge. Manufacturing Letters. 38: 15-18, 2023.

[3] H Yoshioka et al. Minimizing thermal deformation of aerostatic spindle system by temperature control of supply air. JSME Intl. C. 49: 606-611, 2006.

[4] S Rakuff and P Beaudet. Thermally induced errors in diamond turning of optical structured surfaces. Optical Engineering. 46:10, 2007.

[5] K Yokoyama. Analysis of deformation of air-spindle due to centrifugal force. J of JSPE. 64:1,137-141, 1998.

euspen's 26th International Conference & Exhibition, Krakow, PL, June 2026
www.euspen.eu

Investigation of spindle thermal displacement and cooling unit energy consumption characteristics under various operating conditions

Gyungho Khim[1], Sungchuel Lee[1], and Jeong Seok Oh[1]

[1] *Department of Ultra Precision Machines & Systems, Research Institute of Autonomous Manufacturing, Korea Institute of Machinery and Materials*

gyungho@kimm.re.kr

Abstract
This study investigates the thermal displacement characteristics of a machine tool spindle and the energy consumption of its cooling unit under various spindle operating conditions. To reduce energy consumption during non-machining periods, the cooling unit was placed in standby mode, and the resulting changes in spindle temperature, thermal displacement, and cooling unit energy consumption were experimentally measured and analyzed. The results show that placing the cooling unit in standby mode during non-machining periods can reduce energy consumption, while also causing changes in spindle temperature and thermal displacement. Based on the experimental data, a predictive model for spindle thermal displacement was developed by incorporating the cooling unit operating state, spindle temperature, and spindle speed, and its performance under different operating conditions was examined. The results of this study suggest the potential for improving energy efficiency while maintaining thermal accuracy in machine tool spindle operation.

Machine tool, Spindle cooling unit, Thermal displacement, Energy consumption, Energy efficiency

1. Introduction

With the growing global emphasis on carbon neutrality and environmentally friendly manufacturing, improving energy efficiency has become an important research topic in the machine tool industry [1-3]. In response to this trend, leading machine tool manufacturers have introduced a variety of energy-saving technologies. Despite these efforts, reducing energy consumption during machining remains challenging, as not only servo systems but also auxiliary components must operate continuously to ensure stable machining performance. Consequently, most existing approaches focus on reducing energy consumption during non-machining periods by actively controlling auxiliary devices, for example by turning them off or placing them in standby mode during setup or idle states.

However, such energy-saving strategies may negatively affect machine tool accuracy, particularly due to thermal displacement caused by changes in the operating conditions of auxiliary systems. Therefore, it is necessary to consider both energy consumption and machining accuracy simultaneously and to investigate strategies that can effectively reduce energy consumption while maintaining accuracy. In this study, the thermal displacement behavior of a machine tool spindle and the energy consumption characteristics of its cooling unit are investigated under different operating conditions of the spindle and cooling unit. During non-machining periods, the spindle cooling unit is switched to standby mode, and the spindle temperature, thermal displacement, and cooling unit energy consumption are measured and analyzed to identify their relationships.

Based on the experimental data, a predictive model for spindle thermal displacement is developed by considering the operating state of the cooling unit, spindle temperature, and spindle speed. The applicability of the proposed model under different operating conditions is briefly examined.

2. Experiment

2.1. Experiment setup

Figure 1 shows photographs of the measurement setup for the thermal displacement of the spindle and power consumption of the cooling unit in a three-axis machining center. Temperature sensors were installed on the spindle head and the structural components of the machine tool, and a master pin was mounted on the spindle. Displacements in the X-, Y-, and Z-directions were measured using capacitive displacement sensors. To measure the power consumption of the cooling unit, power meters were installed. The spindle cooling unit employs an inverter-type cooler, and the spindle thermal displacement is effectively controlled using an oil-jet cooling method.

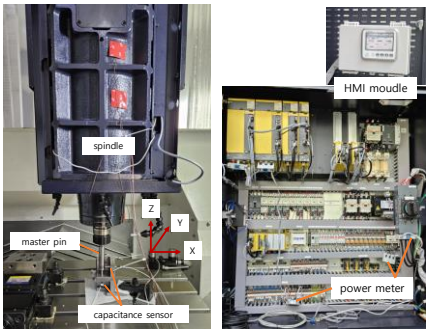

Figure 1. Experimental setup for spindle thermal displacement and cooling unit power consumption

2.2. Measurement of energy consumption and temperature

Two different spindle operating cycles were prepared: one cycle was used for modeling, and the other was used for validation. Figure 2 shows, as an example, the spindle operating condition, Cycle I used for modeling. The spindle was operated under both constant-speed and variable-speed conditions. The

cooling unit was always operated when the spindle was running, however, during periods when the spindle was not in operation, the spindle cooling unit was placed in standby mode to reduce energy consumption. For spindle safety, the cooling unit was switched to standby mode after a sufficient thermal stabilization period of 30 minutes after the spindle stopped, and was reactivated 30 minutes prior to spindle restart.

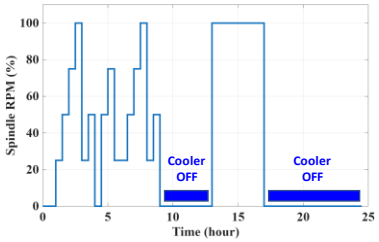

Figure 2. Spindle and cooling unit operating conditions in Cycle I

Figure 3 shows the measured power consumption of the cooling unit. When the cooling unit is operation, it consumes a baseline power of approximately 0.7 kW. After the spindle stops, when the cooling unit is placed in standby mode (the black-shaded region), the power consumption decreases to a very low standby level as the motor is turned off and only the control panel remains powered.

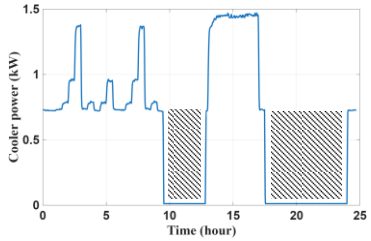

Figure 3. Measured cooling unit power and energy-saving region (black-shaded) in Cycle I

Temperatures were acquired at multiple locations, and the spindle displacement was simultaneously measured to model thermal displacement. Figure 4 shows several representative temperature measurement results for Cycle I. The temperature of the spindle head (T4-head2) increases during periods when the cooling unit is in standby mode. When the cooling unit is reactivated before the spindle starts operating, these temperatures decrease accordingly. It can also be observed that, while the temperature of the spindle head (T4-head2) increases during spindle operation, the temperature at the cooling unit outlet (T6-coolerO) and in the region of the spindle (T2-spindle2), where the cooling oil channel supplied from the cooling unit is located, decreases, indicating effective control of spindle thermal displacement. T8-envirl denotes the ambient temperature.

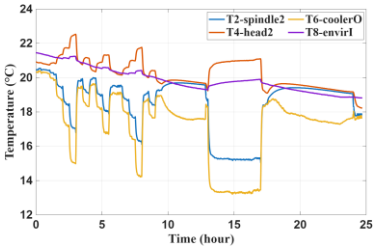

Figure 4. A few representative temperature measurement results

3. Modeling and validation of the thermal displacemenet of the spindle

Figure 5 shows the measured and modeled thermal displacement of the spindle in the Z-axis direction for Cycle I. For the thermal displacement modeling method, a widely used regression model was employed to facilitate practical implementation for compensation purposes, even though AI-based modelling methods generally show better performance. Overall, the predicted model (red line) shows good agreement with the measured thermal displacement (blue line) under various operating conditions.

After 9:30 and after 17:30, when the cooling unit was placed in standby mode, the thermal displacement increased, whereas after 24:00, when the cooling unit was reactivated, it decreased rapidly. As shown in Fig. 5, large spikes in thermal displacement were associated with variations in spindle speed. However, the residual error shows that the proposed model still tracks the experimental data well in these regions.

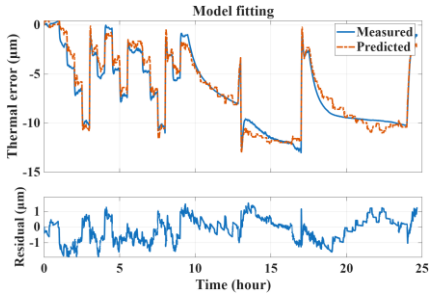

Figure 5. Modeling of thermal error in the Z-direction

To validate the developed model, experiments were conducted under an operating pattern different from Cycle I, denoted as Cycle II, which is omitted here due to limited space. When the prediction model derived from Cycle I was applied to Cycle II, the predicted results showed good agreement with the measured results. As a result, energy consumption can be reduced by placing the cooling unit in standby mode when it is unnecessary during non-operating periods of the spindle. Moreover, by modeling and compensating for the thermal displacement of the spindle that occurs during these periods, it is possible to maintain spindle accuracy while achieving energy savings.

4. Summary and future work

In this paper, a modeling method is proposed to reduce energy consumption by placing the cooling unit in standby mode when it is unnecessary during spindle non-operating periods, while maintaining machining accuracy by compensating for the resulting thermal displacement of the spindle.

Future work will focus on applying the proposed model to an actual machine tool system to compensate for spindle thermal displacement, aiming to reduce energy consumption while maintaining machining accuracy.

Acknowledgement

This work was supported by the research programs 00416035 and 20021902 funded by the Ministry of Trade, Industry & Energy (MOTIE, Korea).

References

[1] Denkena B, Abele E, Brecher C, Dittrich M, Kara S and Mori M 2020 *CIRP Ann.-Manuf. Technol.* **69** 646-667

[2] Sihag N and Sangwan K 2020 *J. Cleaner Prod.* **275** 123125

[3] Mori M, Fujishima M, Inamasu Y and Oda Y 2011 *CIRP Ann.-Manuf. Technol.* **60** 145-148

euspen's 26th International Conference & Exhibition, Krakow, PL, June 2026
www.euspen.eu

Robust Parameter Estimation for Optical Surface Roughness Measurement Using a Physics-Based Model

Sungcheul Lee [1], Hyun-soo Kim [1], Seong-Kook Ro [1]

[1]*Ultra Precision Machines and Systems, Korea Institute of Machinery and Materials, 156, Gajeongbuk-ro, Yuseong-gu, Deajeon, Republic of Korea*

sclee@kimm.re.kr

Abstract

Optical-based surface roughness measurement is widely used in precision manufacturing; however, measured signals are strongly influenced by surface-induced angular scattering and optical system geometry, limiting the generalizability of empirical regression models. To address this issue, this study proposes a physics-based $FR2$ model that represents a machined surface as a statistical ensemble of micro-facets with a Gaussian slope angle distribution. The slope distribution is parameterized as a logarithmic function of the arithmetic mean roughness R_a, and the optical response is defined as the probability that reflected light falls within the finite acceptance angles of the receiving optics. Robust parameter estimation under strong nonlinearity and numerical integration is achieved using a multi-start optimization framework combined with the Nelder–Mead algorithm, resulting in improved fitting accuracy compared to conventional grid-based approaches.

Keywords: Surface Roughness, Optical-based, Flux Ratio, Global Optimization

1. Introduction

Optical-based surface roughness measurement is widely used in precision manufacturing due to its non-contact nature. However, measured signals depend not only on surface height but also strongly on the angular distribution of reflected light, imposing a fundamental limitation on simple empirical regression models. Physics-based modeling approaches that interpret surface roughness as a statistical ensemble of micro-facets and probabilistically describe the collected light within the effective angular range of the optical system are therefore required to overcome these limitations [1,2].

In this study, an $FR2$ model is proposed to describe the relationship between the surface roughness parameter R_a and the optical measurement responses. The standard deviation of the micro-slope angle distribution is parameterized as a function of R_a. Considering the nonlinear characteristics of the model, including numerical integration, this study aims to establish a coefficient estimation framework with low sensitivity to initial values and high reproducibility.

2. Formulation of the Surface Roughness Model

2.1. Concept of the Surface Roughness Model

Figure 1 illustrates the conceptual configuration of an optical-based surface roughness measurement sensor. A diode laser is used as the light source, and the incident light flux is measured after beam splitting and focusing. In the receiving unit for reflected light measurement, scattered light is collimated using an objective lens, and the reflected light flux is measured through an additional beam splitter and collecting lenses with different apertures. The effective receiving angles of the lenses are defined as θ_1=9.46° and θ_2 =3.58°, respectively as shown in Figure 1. Based on the relationship between the incident light flux and the two reflected light fluxes, a light flux ratio is defined. The ratio of Φ_2 to Φ_1 is defined as $FR2$ and is used as the primary measurement indicator because it reduces the number of input variables and is advantageous for optimization [3].

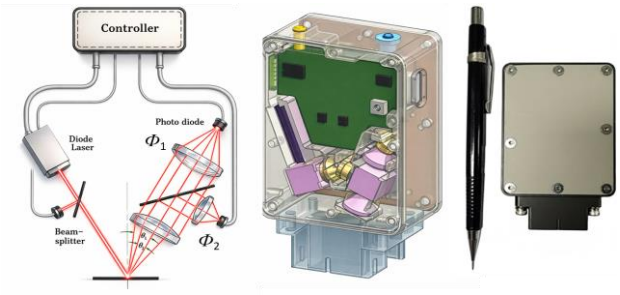

(a) (b) (c)

Figure 1. (a) concept (b) conceptual design (c) product of optical based surface roughness measurement sensor

2.2. Micro-Slope Angle Distribution Model

A machined surface can be microscopically interpreted as a structure composed of numerous micro-facets, and the distribution of their normal directions reflects the statistical characteristics of surface roughness. Previous studies have commonly approximated the micro-slope angle distribution using a Gaussian distribution [3].

In this study, the probability density function of the micro-slope angle θ is assumed to follow a Gaussian distribution with zero mean and standard deviation σ_s.

$$f(\theta) = \left(\frac{1}{\sqrt{(2\pi)}\sigma_s}\right) exp\left\{-\frac{1}{2}\left(\frac{\theta_s}{\sigma_s}\right)^2\right\} \quad (1)$$

The parameter σ_s represents the statistical magnitude of surface roughness; as σ_s increases, reflected light is distributed over a wider angular range.

Since it is difficult to directly measure the relationship between the surface roughness parameter R_a and angular dispersion, σs is modelled as a function of R_a.

$$\sigma_s = a + b\, log_{10}(R_a) \quad (2)$$

A logarithmic linear model is adopted to represent the gradual increase in angular dispersion with increasing roughness, while

ensuring model stability and identifiability with a minimal number of parameters.

2.3. Definition of the Finite-Angle Probability Function

The optical signal detected by the system is determined not by all reflected light but by the portion contained within the effective angular range of the optical system. To reflect this, a probability function Φ_i is defined by integrating the Gaussian probability density function over a finite angular range.

$$\Phi_i = \int_{-0.5\theta_i}^{0.5\theta_i} f(\theta_s)\, d\theta_s \quad (3)$$

Here, θ_i represents the effective angular range of the receiving optics. Φ_i corresponds to the probability that reflected light falls within the specified angular range due to surface roughness and is directly related to the geometric collection efficiency of the optical system.

The $FR2$ indicator is finally defined as the ratio of two probability functions.

$$FR2 = \frac{\Phi_2}{\Phi_1} \quad (4)$$

This definition quantitatively reflects the physical phenomenon in which increasing surface roughness causes the micro-slope angle distribution to broaden, thereby reducing the proportion of light concentrated within a specific angular range. This study models surface roughness as a probabilistic slope distribution, consistent with physics-based modeling requirements in precision engineering.

3. Parameter Optimization

3.1. Initial Value Optimization Strategy

The coefficient estimation problem of the proposed $FR2$-based roughness model constitutes a nonlinear least-squares problem with high sensitivity to initial values. This sensitivity arises from the combination of multiple nonlinear transformations and numerical integration processes linking surface roughness and optical response, rather than from nonlinearity alone.

In regions where the denominator term becomes small, the gradient of the objective function changes rapidly, resulting in a smooth but generally non-convex objective function. Under such conditions, local optimization methods initiated from a single initial value are prone to converge to local minima rather than the global minimum, particularly when analytical gradients are unavailable and numerical integration is involved.

To mitigate initial value dependence and ensure reliable parameter estimation, a multi-start optimization strategy is adopted. This strategy defines a physically meaningful parameter space and performs independent local optimizations from multiple initial points within that space. The solution yielding the minimum objective function value is selected as the final estimate.

In this study, the parameter ranges are restricted to $a \in [0.01, 1.0]$ and $b \in [-1.0, 1.0]$, which satisfy the condition $\sigma_s > 0$ while sufficiently covering roughness–angular dispersion relationships observed in practical machining processes.

3.2. Parameter Optimization Method

For local optimization at each initial point, the Nelder–Mead simplex algorithm is employed. This derivative-free direct search method iteratively transforms a simplex in the parameter space to reduce the objective function value. In the two-dimensional case, the simplex consists of three vertices forming a triangle, which is updated through reflection, expansion, contraction, and shrink operations.

The dataset used for parameter estimation consists of five surfaces with nominal Ra values of 0.2, 0.4, 0.8, 1.6, and 3.2 µm, prepared by surface grinding. Ra was measured using a contact profilometer traceable to national standards (ISO 4287). $FR2$ measurements were repeated 10 times per surface under identical conditions, and the mean values were used for model fitting and are shown as data points in Figure 3. The 2σ repeatability of $FR2$ ranged from 0.011 to 0.024 across the five surfaces, corresponding to a coefficient of variation below 1.8 %.

As a result, the multi-start Nelder–Mead optimization framework adopted in this study enables robust parameter estimation without simplifying the numerical integration-based physical model. Compared to the conventional grid-based parameter search, the proposed approach reduced the sum of squared errors (SSE) from 0.00311 to 0.00216, corresponding to an improvement of approximately 30.5 % (Figure 3).

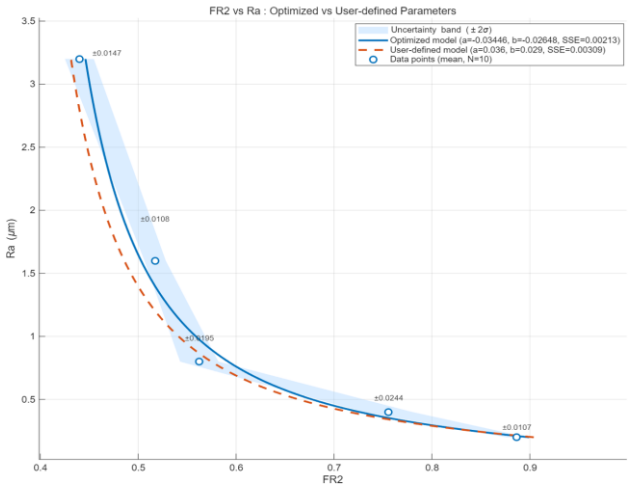

Figure 3. Comparison of optimization results: optimized vs. previously selected variables

4. Conclusion

This study aimed to establish a physics-based $FR2$ model and a robust parameter estimation framework for optical surface roughness measurement, overcoming the generalization limitations of conventional empirical regression approaches. By representing machined surfaces as a statistical ensemble of micro-facets and physically linking surface roughness to optical response through a Gaussian slope distribution, the proposed model maintains full physical interpretability of the model parameters. A multi-start optimization strategy combined with the Nelder–Mead algorithm was employed to mitigate strong initial value sensitivity, reducing the SSE by approximately 30.5 % compared to conventional grid-based parameter search, thereby demonstrating improved fitting accuracy and reproducibility across diverse machining processes and optical configurations.

Acknowledgement

This work was supported by the Ministry of Trade, Industry and Energy (MOTIE) of the Republic of Korea (No. 20026431) and the Korea Institute of Machinery and Materials (No. NK263A).

References

[1] Tian P, Chen X, Jin J, Lu J Q, Liang X and Hu X-H 2018 *Opt. Eng.* 57 094104

[2] Su P, Eri Q T and Wang Q 2014 *Appl. Opt.* 53 2324–30

[3] Hong S W and Kim H S 1995 J. *Korean Soc. Precis. Eng.* 12 46–54

euspen's 26th International Conference & Exhibition, Krakow, PL, June 2026
www.euspen.eu

Design and experimental analysis of a thermoelectrically temperature controlled bearing shield for motorised spindles

Leon Naatz[1,2], Florian Triebel[1], Katrin Schmitt[3,4], Jürgen Wöllenstein[3,4], Roland Binninger[3]

[1]*Technische Universität Berlin, Institute for Machine Tools and Factory Management IWF, Pascalstr. 8-9 10587 Berlin, Germany*
[2]*Technical University of Applied Sciences Wildau, Hochschulring 1, 15745 Wildau, Germany*
[3]*Fraunhofer Institute for Physical Measurement Techniques IPM, Georges-Köhler-Allee 301 79110 Freiburg, Germany*
[4]*University of Freiburg, Department of Microsystems Engineering – IMTEK, Laboratory for Gas Sensors, Georges-Köhler-Allee 102, 79110 Freiburg, Germany*

Corresponding author: Roland Binninger; roland.binninger@ipm.fraunhofer.de

Abstract
With the rapid technological advancements in high-tech industries, the demand for components with sub-micrometre geometric and dimensional accuracy is increasing. The thermal behaviour of machine tools is of crucial importance in the high-precision machining of such components. Considerable efforts are made to dissipate the heat generated by machine components such as actuators and motorised spindles. Despite the use of complex water cooling systems, these heat flows lead to elevated temperatures, which in turn result in thermally induced component deformation and thus reduced machining accuracy. Due to their exposed position with direct contact to the workpiece and their speed-dependent thermal load, motorised spindles and their thermal behaviour are of great importance and the subject of intensive research. Thermal stabilization of the front bearings of motorised spindles, even under varying speeds, can stabilize the shaft's thermal deflection.

This study addresses the design, measurement, and control of a thermoelectrically controlled front bearing for a motorised spindle. Here, 40 thermoelectric strips were assembled into a tubular Peltier module that connects the cylindrical surface of the bearing shield to the surrounding water cooling system. A prototype, consisting of the bearing shield, tubular Peltier module, heating coil, temperature sensors, and water cooling system, was used to investigate the thermal behaviour of the bearing shield under various head loads in detail. Different PID (proportional-integral-derivative) control strategies for a Peltier temperature controller were tested using step response measurements. The measurement results of the investigated IMC (internal model control) PID and CHR (Chien-Hrones-Reswick) PID strategies were compared with those of a commercial controller. Depending on the PID parameters and changes in conditions, a temperature stability within a tolerance range of ±0.1 K can be attained in between 8 second for thermal disturbance rejection and 16 seconds for reference tracking.

Temperature regulation; Peltier module; PID Controller; motorised spindle

1. Introduction

Driven by the increasing demand from the high-tech industry for components and parts with geometrical accuracies in the sub-micrometre range, the requirements for machine tool manufacturing are increasing. Besides increasing accuracy through sophisticated control systems and improved machine quality, the thermal behaviour of machine tools and their components significantly influences the achievable machining accuracy [1, 2]. To achieve higher machining accuracy, it is essential to minimize the effects of thermal stresses through suitable cooling concepts. Denkena et al. [3] provide a comprehensive overview of cooling strategies for motorised spindles, distinguishing between passive and active approaches. Passive cooling strategies are primarily based on convective heat transfer to the ambient air, which is typically enhanced by optimizing the heat sink geometry. In contrast, active cooling systems primarily use a flowing cooling medium, such as oil, water or active air flow which is applied in the immediate vicinity to the heat sources [3, 4].

An alternative approach, which serves as the basis for this work, involves the use of Peltier modules. A Peltier module consists of alternating p- and n-doped semiconductor elements positioned between two ceramic plates, electrically connected in series and thermally in parallel. Based on the Peltier effect, first discovered by Peltier [5], a heat flow can be generated in the Peltier module by applying an electric current. The applicability of this method was demonstrated by Fan et al. [6], who attached Peltier modules, combined with a heat conduction sleeve, to the outer surface of the motorised spindle housing.

Uhlmann et al. [7, 8, 9] developed an actively temperature-controlled motorised spindle that employs prismatic Peltier modules integrated within the motorised spindle housing, situated between the water cooling channels and the primary heat sources. Three groups of independently controllable Peltier modules are arranged circumferentially around the front and rear bearings, as well as the stator. This configuration facilitates precise control of the front bearing temperature $T_{bearing}$, rear bearing temperature, and stator temperature. Using this approach, the warm-up time required to reach the thermal steady state of the axial shaft displacement can be reduced by up to 79 %. To reduce the costs of integrating a thermoelectric temperature control system into motorised spindles, a novel thermoelectric temperature control system based on a tubular Peltier module was developed.

This study presents the thermal characterisation of such a system and the investigation of different proportional-integral-derivative (PID) control strategies for a Peltier temperature controller used in a functional prototype of the front bearing shield of a motorised spindle.

2. Functional prototype

2.1. Design and experimental setup

To investigate the behaviour of a bearing shield and to design a control system for temperature control using thermoelectric modules, a functional prototype was developed based on the bearing shield of a motorised spindle (MFW840/50, FISCHER DEUTSCHLAND GMBH, Langenfeld, Germany). The functional prototype, illustrated in Figure 1, consists of a bearing shield with build-in temperature sensor, a coil tube heating cartridge, a tubular Peltier module, and a water-cooling system. The design is based on the work of Uhlmann [9].

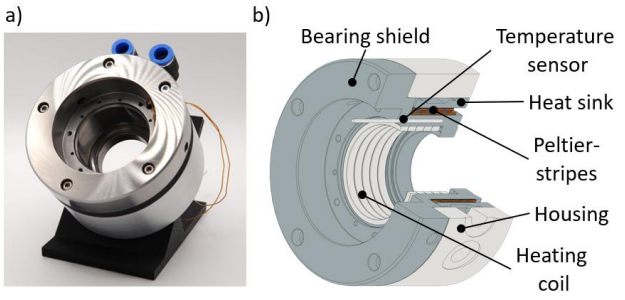

Figure 1: a) Photo of the assembled functional prototype without coil tube heating cartridge. b) Cross-sectional representation of the functional prototype with labelled components.

The tubular Peltier module consists of 40 individual stripes, each containing four pellet pairs made of p- and n-doped thermoelectric material. These Peltier stripes are electrically connected in series through copper bridges. To ensure optimal thermal and mechanical coupling between the bearing shield, the tubular Peltier module, and the heat sink, the thermoelectric stripes were placed to the bearing shield using double-sided adhesive graphite foil, while the heat sink was thermally shrunk onto it. The cooling channel was sealed with two O-rings between the heat sink and the housing, and the housing was subsequently bolted to the bearing shield.

For temperature measurement within the bearing shield, a calibrated PT1000 temperature sensor (TEMPERATUR MESSELEMENTE HETTSTEDT GMBH, Maintal Germany) was utilized. To minimize external influences such as convection and thermal radiation, the functional prototype was insulated both inward and outward. During the experiments, the water cooling was maintained at a constant temperature of 20 °C with a volumetric flow rate of 3.6 l/min.

To demonstrate the performance and temperature stability of the functional prototype, an initial measurement series was conducted to assess the temperature of the bearing shield as a function of the heating power of the heating coil and the Peltier current. The heating power was increased from 30 W to 100 W in increments of 10 W, while the current was raised from 0 A to 6 A. Based on previous measurements, it can be assumed that a heating power of 100 W should cover the heat load of the motorised spindle at a rotation speed of 50.000 1/min. To protect the Peltier module from potential defects during extended measurement campaigns, the current was limited to 6 A and the minimum bearing shield temperature was set to +10 °C. In the motorised spindle, Peltier modules can also be operated at higher currents and lower temperatures for rapid control over short time periods.

2.1. Results

The measurement points shown in Figure 2 represent the temperatures in the bearing shield after reaching thermal steady state. From the measurement at 0 W heating power, it can be inferred that an increase in the heating coil power by 10 W results in a temperature rise of the bearing shield by 4.7 K ± 0.2 K. This increase in temperature can thus be assumed to be linearly dependent on the heating power. Utilising the linear relationship, an extrapolation to 0 W heating power and 0 A Peltier current results in a heating shield temperature of approximately 20 °C, which is equivalent to the cooling water temperature. As the Peltier current increases, the temperature in the bearing shield decreases because heat is pumped from the bearing shield to the coolant via the Peltier effect. Although the heat conduction through the Peltier effect is approximately linear, the decrease in bearing shield temperature is not, as the Joule heat increases quadratically with rising current, which must be additionally dissipated along with the pumped heat. To illustrate this trend, a trend line is drawn at the heating power P_{Heater} = 70 W, see Figure 2.

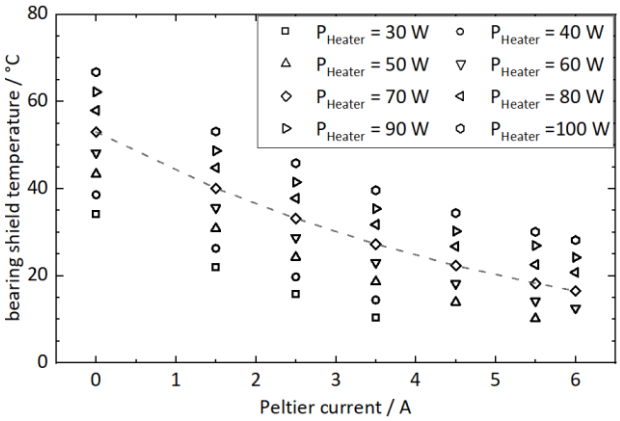

Figure 2: Bearing shield temperatures at different heating powers and Peltier currents.

To quantify the performance of the Peltier module, it can be investigated at which maximum heating power the bearing shield can be cooled to up to a certain temperature. This is a recognized method for determining the maximum current and maximum heat flow for standard Peltier modules [15]. For this purpose, the recorded curves were extrapolated using a second-order polynomial fit.

In the first step, the Peltier currents, required to achieve bearing shield temperatures of 20 °C and 30 °C, can be calculated. These values are summarised in table 1.

Table 1 Required Peltier currents for bearing shield temperatures of 20 °C and 30 °C at different heater powers.

heating power	Peltier current for $T_{bearing}$ = 20 °C	Peltier current for $T_{bearing}$ = 30 °C
30 W	1.81 A	0.48 A
40 W	2.45 A	1.01 A
50 W	3.23 A	1.65 A
60 W	4.08 A	2.32 A
70 W	5.02 A	3.01 A
80 W	6.31 A	3.80 A
90 W	/ n.a. /	4.56 A
100 W	/ n.a. /	5.51 A

As can be seen, the functional prototype cannot achieve a bearing shield temperature of 20 °C with heating powers exceeding 80 W. To determine the maximum cooling power of

the Peltier module, the minimum achievable temperatures at the respective heating powers of the heating coil were derived from the extrapolations. These values approximate the maximum cooling capacity of the functional prototype to 89 W at 8.6 A in thermal steady state.

Based on the complete characterization of the system, it can be demonstrated that the cooling capacities required for the operation of the motorised spindle can be adjusted based on the current. Thus, the current can be used as the direct control variable for regulating the temperature of the system.

3. PID controller evaluation

To define control parameters, several methods described in the literature were investigated. The most promising, namely CHR-based [10, 11] and IMC-based [12], were applied, with step tests conducted as presented by Widagdo et al. [10] and Diwakar et al. [13]. The basis for this were the measurements shown in Figure ***2*** at 30 W heating power and 1.5 A Peltier current.

The resulting PID parameters for the CHR-based approach, featuring fast control in response to setpoint changes and a disturbance with 0 % overshoot, as well as the mathematical IMC-based approach for λ values of 3 and 5, are presented in Table 2. Thereby λ is an adjustable parameter that determines the speed of response, increasing λ raises the closed-loop time constant and slows down the speed of response. Conversely, decreasing λ has the opposite effect. λ can be adjusted to compensate for model mismatch in the design of the control system. The higher the value of λ, the greater the robustness of the control system [14].

Table 2 Examined control strategies with derived PID values

	P	I	D
IMC λ 3	2.5109	0.0362	0.4964
IMC λ 5	1.5978	0.0231	0.4964
CHR	5.2348	1.3987	2.6174

These derived control parameters were compared with the auto-tuning feature of the commercially available Peltier controller type PWR CTRL M (Dr. Neumann Peltier Technik GmbH, Neuried, Germany) as a reference. The parameters, defined in table 2, were implemented in a PID controller, running on a modular real-time system Adwin-Pro II (Jäger Computergesteuerte Messtechnik GmbH, Lorsch, Germany).

To assess the capacity of the different PID controllers for reference tracking, the temperature of the functional prototype was regulated to 30 °C using a cooling water temperature of 20 °C, a flow rate of 3.6 l/min, and a heating power of 50 W. After 300 seconds, the setpoint was raised to the bearing shield temperature of 40 °C, and the settling time to reach the target temperature was measured. The settling time is defined as the point in time at which the measurement data first lie within a tolerance range of ±0.1 K of the target temperature and subsequently remain within these limits.

After additional 300 seconds, the system was set back to 30 °C. In addition to the settling time, the overshoot and undershoot is evaluated for each set of PID parameters. After 600 seconds, the power of the heating coil was set to 0 W to simulate a stop of the motorised spindle, and after 900 seconds, it was returned to 50 W to show the behaviour at a restart of the motorised spindle. Figure 3 shows the controlled temperatures during this procedure for all four PID controllers.

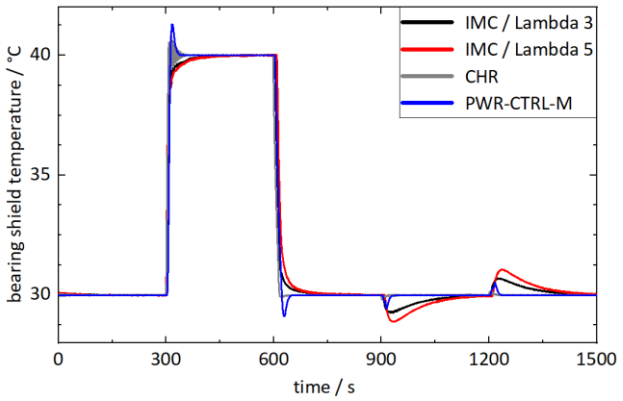

Figure 3: Representation of the complete load cycle of the functional model with changes in the target temperature at 300 and 600 seconds and a simulated engine stop at 900 seconds, followed by restarting at 1200 seconds.

Table 3 presents the settling times of the different PID controllers for individual load changes in the system. 30 °C – 40 °C and 40 °C – 30 °C indicates the rise of in temperature and vice versa, 50 W – 0 W and 0 W – 50 W the change in the heat load of the heating coil.

Table 3: Settling times for different load changes

	30-40°C	40-30°C	50-0 W	0-50 W
IMC λ 3	89 s	100 s	93 s	196 s
IMC λ 5	117 s	123 s	140 s	245 s
CHR	41 s	16 s	8 s	10 s
PWR-CTRL-M	33 s	43 s	24 s	26 s

Figure 4 shows a section of the measurements taken after 300 seconds. It is evident that the auto-tuning feature integrated within the Peltier controller of type PWR-CTRL-M (Dr. Neumann Peltier Technik) provides effective and smooth temperature control, although it exhibits the most significant overshoot in this range. In contrast, the signals derived from the IMC control parameters are noticeably slower during all temperature and load transitions. The CHR parameter set demonstrates a pronounced, nearly critical oscillation but is the fastest controller. With the CHR control parameters and the reference (Dr. Neumann Peltier Technik), temperature stability after changes in head load and target temperature of less than 0.2 K can be achieved within seconds.

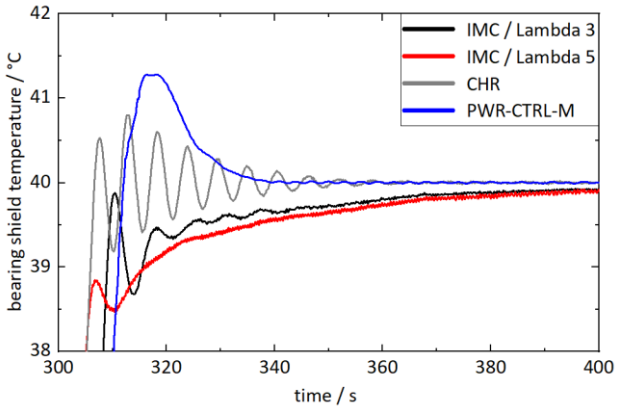

Figure 4: Section of the measurement between 300 and 400 seconds showing the oscillation behaviour of the individual control parameters.

3. Conclusion and future work

This study presents a novel approach to thermoelectric temperature control for the bearing shield of a motorised

spindle, along with potential PID parameters for such temperature control.

Using measurements on a functional prototype consisting of a bearing shield, a heating coil, a tubular Peltier module, and a water cooling system, the system has been fully characterized and the influence of heating power and Peltier current on the bearing shield temperature has been determined. A maximum heat load of 89 W at 8,6 A is achievable at thermally steady state.

Different control parameters were examined and the effectiveness of the temperature control and settling time for changing boundary conditions were demonstrated. The regulated operation can achieve a temperature stability of less than 0.2 K. Depending on the PID parameters and changes in conditions, a temperature stability within a tolerance range of ±0.1 K can be attained in between 8 second for thermal disturbance rejection and 16 seconds for reference tracking.

In the future works, the findings presented in this work will be transferred to the control of a thermoelectric motorised spindle. In addition, the control parameters will be extended and validated in further tests to cover the entire range of possible applications for the motorised spindle. Furthermore, bearing shields with different tubular Peltier module configurations will be prepared and characterized.

Acknowledgments

The authors would like to express their sincere gratitude to Dr. Neumann Peltier-Technik GmbH for their invaluable support in conducting this research and for the providing the Peltier controller.

This work was funded within the Fraunhofer-DFG transfer program by Fraunhofer Society and Deutsche Forschungs-gemeinschaft (DFG, German Research Foundation) - 529738427.

References

[1] Creighton E, Honegger A, Tulsian A and Mukhopadhyay D 2010 Analysis of thermal errors in a high-speed micro-milling spindle, International *Journal of Machine Tools and Manufacture, Volume 50, Issue* **4** 386-393,

[2] Taniguchi N 1983 Current Status in, and Future Trends of, Ultraprecision Machining and Ultrafine Materials Processing *CIRP Ann.* **32** (2) 573-582,

[3] Denkena B, Bergmann B and Klemme H 2020 Cooling of motor spindles—a review *Int. J. Adv. Manuf. Technol.* **110** (11–12) 3273-3294

[4] Li S and Wu Y 2010 A study on oil/air lubrication and preload of a high frequency fully ceramic motor spindle *International Conference on E-Product E-Service and E-Entertainment (ICEEE 2010)* 1-4

[5] Peltier J C A 1834 Nouvelles expériences sur la caloricité des courants électrique *Ann. Chim. Phys.* **2** (56) 371-386

[6] Fan K, Xiao J, Wang R and Gao R 2022 Thermoelectric-based cooling system for high-speed motorized spindle I: design and control mechanism *Int. J. Adv. Manuf. Technol.* **121** (5-6) 3787-3800

[7] Uhlmann E, Polte J, Salein S, Iden N, Temme P, Hartung D and Perschewski S 2020 Entwicklung einer thermoelektrisch temperierten Motorspindel *wt Werkstattstechnik online* **110** (5) 299-305

[8] Uhlmann E, Polte M, Triebel F, Salein S, Temme P, Hartung D and Perschewski S 2022 Reduction of warm-up period after machine downtime by means of a thermoelectric tempered motorized milling spindle *euspen SIG Meeting: Thermal Issues*

[9] Uhlmann E 2023 Recent advances in precision, sustainability and safety of machine tools *J. Mach. Eng.* **23** (3) 5-25

[10] Widagdo R S, Hariadi B, Setyadjit K 2023 Modelling and analysis of Ziegler-Nichols and Chien-Hrones-Reswick tuning PID on DC motor speed control *Jurnal Teknologi Elektro* **14** (1)

[11] Ahamad N, Uniyal S, Sikander A, Singh G 2019 A Comparative Study of PID Controller Tuning Techniques for Time Delay Processes, *UPB Scientific Bulletin, Series C: Electrical Engineering* **81** (3) 129–142

[12] Zhao K L and Wang Z Y 2015 Application of boiler superheated steam pressure control which based on IMC-PID *2015 IEEE Int. Conf. Industrial Technology (ICIT)* 586ff

[13] Diwakar B, Gokul Anandh M, Brindaa R, Jayashree Devi S R and Aravind P 2015 IMC Based Design of PI Controller for Real Time Pressure Process *International Journal of Innovative Research in Electrical, Electronics, Instrumentation and Control Engineering*, **3** (10) 12–15

[14] Rivera D E 1999 Internal Model Control: A Comprehensive View *Arizona State University, Tempe, Arizona* 85287-6006

[15] Binninger R, Unmuessig S, Vergez M, Bartel M, Schaefer-Welsen O Customized measuring station for Peltier modules *Heliyon* **10** (4) e25743

euspen's 26th International Conference & Exhibition, Krakow, PL, June 2026
www.euspen.eu

Automatic Text Analysis for Machine Maintenance in Float-Zone Crystal Growth Production

Eugenia Freggia[1], Marta Barbieri[2], Irene Spada[1], Gualtiero Fantoni[1], Matteo Calaon[2]

[1]*University of Pisa, 56122 Pisa, Italy* [2]*Technical University of Denmark, 2800 Kgs. Lyngby, Denmark*

mabarb@dtu.dk

Abstract

The continuous evolution of electronics and optoelectronics has led to a growing demand for ultra-high-quality silicon wafers. In this context, the Float-Zone crystal growth technique plays a key role, as it enables the production of silicon with very low impurity levels and high electrical resistivity, making it suitable for high-power electronic devices and high-efficiency solar cells. Float-Zone production is characterized by high manufacturing costs, largely driven by the need for extremely pure and expensive raw material. Yield losses may occur in specific industrial contests due to process instabilities, equipment failures, and operational anomalies. In industrial setting, a substantial amount of knowledge related to machine behavior, failures, and corrective actions is recorded during daily operations in the form of unstructured maintenance logs. While this information is potentially valuable for improving yield and reducing costs, it is often difficult to access and exploit due to its fragmented, inconsistent, and multilingual nature. As a result, maintenance knowledge remains largely difficult to access and to exploit. This study addresses this challenge through a case study conducted in a Danish industrial setting involving Float-Zone silicon crystal growth. More than 18 thousand maintenance logs, exhibiting significant variability in structure and terminology, have been analyzed. Building on existing applications of Text Mining and Natural Language Processing in industrial maintenance, this work focuses on their targeted adaptation to a highly specialized and quality-critical production process. We propose tailored preprocessing, text classification and clustering to identify recurring families of problems and corrective actions, thereby structuring previously inaccessible maintenance knowledge. The analysis improves traceability between failures and actions, enhancing the understanding of issues related to process stability. The findings show the potential to support systematic and data-driven maintenance analysis and further predictive maintenance developments.

Keyword: Entities relation discovery, Data processing, Text information, Maintenance records

1. Introduction

The growing demand for electronic devices is driving the increasing production of high-purity silicon wafers. In this context, the Float-Zone (FZ) crystal growth technique is adopted because extremely high material quality is required although its high production cost [1]. Thus, yield improvements are critical objective both in manufacturing and maintenance. Larger volumes of data from industrial records and logs are increasingly leveraged within smart manufacturing and data-driven maintenance [2]. While most existing approaches focus on structured machine and sensor data, textual maintenance records remain largely underexplored despite containing valuable information on machine behavior, failures, and corrective actions.

This work addresses the posed challenge through the application of Text Mining (TM) and Natural Language Processing (NLP) techniques to maintenance logs from an industrial FZ silicon crystal growth case study. The proposed approach normalizes and structures unstructured textual data to identify recurring families of problems and corrective actions and analyze their relationships, thereby supporting improvements in manufacturing processes.

2. Methodology

The methodology consists of an initial text preprocessing phase and five main steps.

Maintenance logs were first segmented into individual sentences by splitting the text at operator identifiers, which typically mark the completion of an action or the description of a problem. Although some sentences contained both elements, this approach proved effective for structuring heterogeneous and inconsistently reported data. The text was then normalized through standard preprocessing operations, including lowercasing, removal of identifiers, and expansion of abbreviations and domain-specific terminology using a custom vocabulary validated by an industry domain expert.

The logs were translated from Danish into English using the open-source *Helsinki-NLP/opus-mt-da-en* model, as most NLP models are primarily trained on English corpora [2]. Translation was performed locally to ensure data confidentiality.

A supervised classifier was then used to categorize sentences as problem or action. The classifier was initially trained on the *Aircraft Historical Maintenance Dataset* (MaintNet), which provides explicitly labeled maintenance records in an industrial context [3]. To address domain differences, it was then finetuned on an annotated subset of 200 company-specific sentences, previously labeled by a domain expert and selected to reflect recurring issues and actions. Misclassified sentences were manually corrected and incorporated into a retraining phase. To limit bias and overfitting, only this annotated subset was combined with the original dataset during retraining, assigning higher weights to company-specific instances to prioritize domain-relevant patterns while preserving general maintenance knowledge.

Subsequently, sentences classified as problems and actions were clustered separately to identify recurring families. HDBSCAN was adopted to capture clusters of varying size and treat non-representative sentences as noise, making it suitable for heterogeneous text data.

Next, representative keywords were extracted using a term-weighting scheme (c-TF-IDF) designed to highlight words that are distinctive of each cluster. These keywords were then used to generate concise semantic labels with the support of a locally deployed large language model, ensuring interpretability while preserving data confidentiality.

Finally, the identified problem and action clusters enabled the organization of maintenance knowledge originally embedded in unstructured textual records, providing a structured basis for subsequent analysis.

3. Results

The proposed approach was applied to a dataset of 18 107 maintenance logs collected from a Float-Zone silicon crystal growth process. In the classification task, domain finetuning improved precision, i.e., the proportion of correctly classified sentences among all sentences assigned to a given class, from 78% to 80% for problem sentences and from 83% to 87% for action sentences. Clustering of the classified data resulted in 19 problem clusters and 21 action clusters, capturing the diversity of recurring issues and corrective interventions.

Figure 1 and Figure 2 depict clustering results in a two-dimensional space, referred as *Problem Map* and *Action Map*.

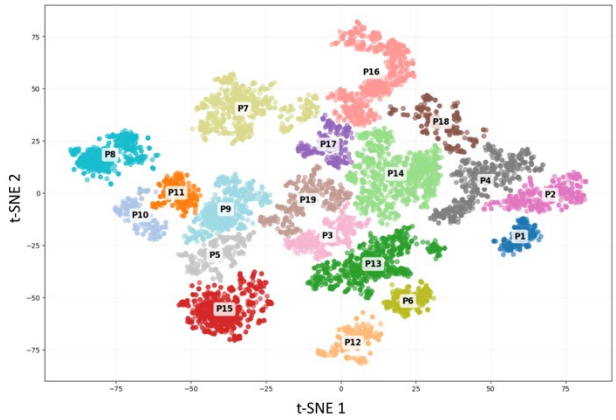

Figure 1. Clusters of problems extracted from logs in the semantic space.

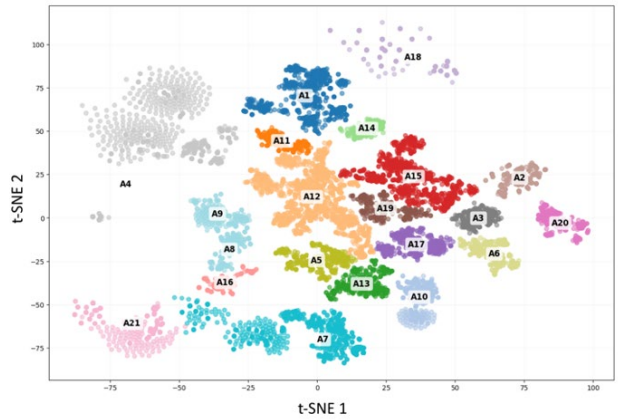

Figure 2. Clusters of actions extracted from logs in the semantic space.

In Figure 1, clusters span horizontally from component-specific to machine-level issues, reflecting fault severity, and vertically from production-related to production-independent problems, indicating production dependence. In Figure 2, clusters range horizontally from generic interventions to highly specific corrective actions, reflecting action specificity, and vertically from software-related activities to hardware-related interventions, indicating the action domain. Cluster quality was assessed through the silhouette score, yielding 0.416 for problem clusters and 0.5066 for action clusters. These values are consistent with moderately separated clusters and reflect a certain degree of overlap, which is expected given the heterogeneous and ambiguous nature of maintenance logs.

Figure 3 presents the correlation between problem and action clusters, illustrating how frequently specific problems are associated with specific corrective actions.

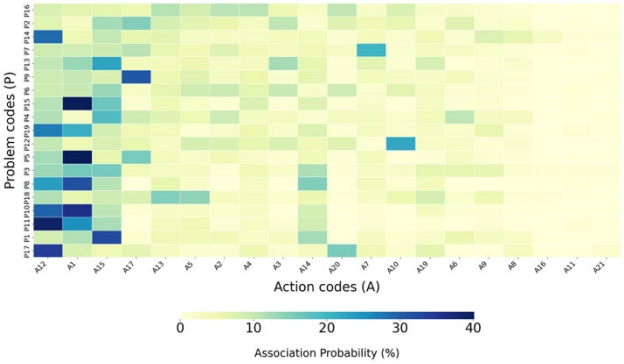

Figure 3. Correlation map linking clusters of problem and action.

The correlation shows that critical problems are often addressed through immediate interventions, suggesting a predominantly reactive maintenance strategy. At the same time, some problem-action pairs exhibit strong one-to-one relationships, suggesting the presence of specialized corrective procedures. In contrast, several problem clusters display weak and dispersed correlations across multiple actions, indicating a lack of standardized corrective responses.

Overall, the findings indicate the effectiveness of TM and NLP techniques in structuring maintenance logs and addressing the identified data-related limitations

4. Conclusion

This work discusses how TM and NLP techniques can be applied to transform unstructured maintenance logs into structured knowledge in an industrial context. The approach enables performance improvements by identifying problem and action instances, assessing their relevance, and providing insights into maintenance practices through the analysis of relationships between problems and corrective actions. We acknowledge several limitations, including the sentence segmentation strategy, the lack of longitudinal analysis of historical data, and the absence of integration between textual maintenance logs and machine-level data. Future work may explore the use of domain-specific large language models to address these limitations and further enhance information extraction in data-driven maintenance applications.

References

[1] W. Von Ammon, 'FZ and CZ crystal growth: Cost driving factors and new perspectives: FZ and CZ crystal growth', *Phys. Status Solidi A*, vol. 211, no. 11, pp. 2461–2470, Nov. 2014, doi: 10.1002/pssa.201400043.

[2] K. Zhong, T. Jackson, A. West, and G. Cosma, 'Natural Language Processing Approaches in Industrial Maintenance: A Systematic Literature Review', *Procedia Computer Science*, vol. 232, pp. 2082–2097, 2024, doi: 10.1016/j.procs.2024.02.029.

[3] P. Wang, J. Karigiannis, and R. X. Gao, 'Ontology-integrated tuning of large language model for intelligent maintenance', *CIRP Annals*, vol. 73, no. 1, pp. 361–364, 2024, doi: 10.1016/j.cirp.2024.04.012.

euspen's 26th International Conference & Exhibition, Krakow, PL, June 2026
www.euspen.eu

A multiphysics finite element model for hydrostatic guideway systems

Markel Alaña[1], Julen Bastardo[1], Gorka Aguirre[1], Harkaitz Urreta[1]
[1]*Design and Precision Engineering, IDEKO, Elgoibar, Gipuzkoa, Spain*

hurreta@ideko.es

Abstract
This paper presents a coupled elasto-hydraulic finite element framework for the multiphysics simulation of hydrostatic guideway systems in large machine tool rotary tables. The model simultaneously solves the linear elasticity equations for structural deformations and the Reynolds lubrication equation for thin fluid films, enforcing bidirectional coupling through a monolithic system of equations. The approach is applied to a five-metre diameter rotary table with a maximum load capacity of 100 tonnes and is benchmarked against an equivalent rigid-body assumption. Results demonstrate that structural flexibility significantly alters oil film thickness distribution, reduces global guideway stiffness, and lowers energy consumption, effects that are not captured by conventional rigid-body design tools.

Hydrostatic bearings; fluid-structure interaction; Reynolds equation; finite element method; machine tools

1. Introduction

Hydrostatic guideways are widely used in precision machine tools because of their high load-carrying capacity, near-zero friction, and excellent damping characteristics [1]. In the specific context of large rotary tables for heavy-duty machining, these advantages become critical: workpiece masses can exceed 100 tonnes and diameter requirements surpass several metres, placing stringent demands on guideway design [2].

The design of such systems traditionally relies on analytical or numerical models that treat structural components as rigid bodies. This assumption simplifies the problem considerably, but increasingly thin oil films mean that the elastic deformation of the table can become comparable in magnitude to the nominal film thickness itself as a consequence of the high loads. Under these conditions, the pressure distribution generated by the fluid directly influences structural deformation, and vice versa, creating a strongly coupled fluid-structure interaction (FSI) problem [3].

Coupled elasto-hydrodynamic models have been applied to journal bearings and thrust pads in rotating machinery, yet their systematic application to large-scale hydrostatic guideways in machine tools remains limited. Michalec et al. [1] provide a comprehensive review of large hydrostatic bearing design but note the lack of tools that incorporate FSI effects. Direct coupling finite element approaches have been demonstrated for simpler guideway geometries [3], and multiphysics models are established in aerostatic bearing design [4], but a validated framework targeting large rotary table architectures is still needed.

This paper presents an in-house finite element framework that couples structural and hydraulic physics in a monolithic formulation. The model is described in Section 2. Its application to a 5 m diameter proof-of-concept table is detailed in Section 3. Key results — oil film distribution, guideway stiffness, and power consumption — are discussed in Section 4, followed by conclusions in Section 5. Summing up, the challenge of the work is the application of FSI simulation in an industrial case where currently the analytical rigid body calculations are the standard.

2. Coupled elasto-hydraulic formulation

2.1. Governing equations

The structural domain is governed by linear elasticity. Assuming quasi-static loading and small displacements, the equilibrium equation is:

$$\nabla \cdot \sigma + \mathrm{F} = 0 \tag{1}$$

where σ is the Cauchy stress tensor and F the body force vector.

The pressure field in the thin lubricant film is described by the Reynolds equation, derived from the Navier-Stokes equations under the assumptions of laminar, incompressible flow and negligible film inertia [5]:

$$\nabla_{xy} \cdot \left(\frac{h^3}{12\mu} \nabla_{xy} \cdot P \right) = \nabla_x \left(\frac{hU}{2} \right) + \frac{\partial h}{\partial t} \tag{2}$$

where h is the local film thickness, μ the dynamic viscosity, P the pressure and U the sliding velocity.

2.2. Monolithic coupling and FEM discretisation

The two physics are coupled bidirectionally: fluid pressure acts as a distributed load on the structural surfaces, while structural displacements modify the local film thickness h entering Eq. (2). This coupling is enforced simultaneously — rather than through sequential staggered iterations — yielding a monolithic system after finite element discretisation:

$$\begin{bmatrix} [K_S] & [K_{SP}] \\ [K_{PS}] & [K_P] \end{bmatrix} \begin{bmatrix} u \\ p \end{bmatrix} = \begin{bmatrix} f \\ q \end{bmatrix} \tag{3}$$

Here Ks is the structural stiffness matrix, Kp the hydraulic stiffness matrix, Ksp and Kps are the off-diagonal coupling matrices, u and p are the nodal displacement and pressure vectors, and f and q are the applied force and flow-rate vectors, respectively.

Because Kps and Kp depend nonlinearly on the film thickness h, which is itself a function of u, the system is solved iteratively. Fluid viscosity is additionally updated as a function of temperature at each iteration, introducing a further source of nonlinearity. Convergence is assessed on both displacement and pressure increments.

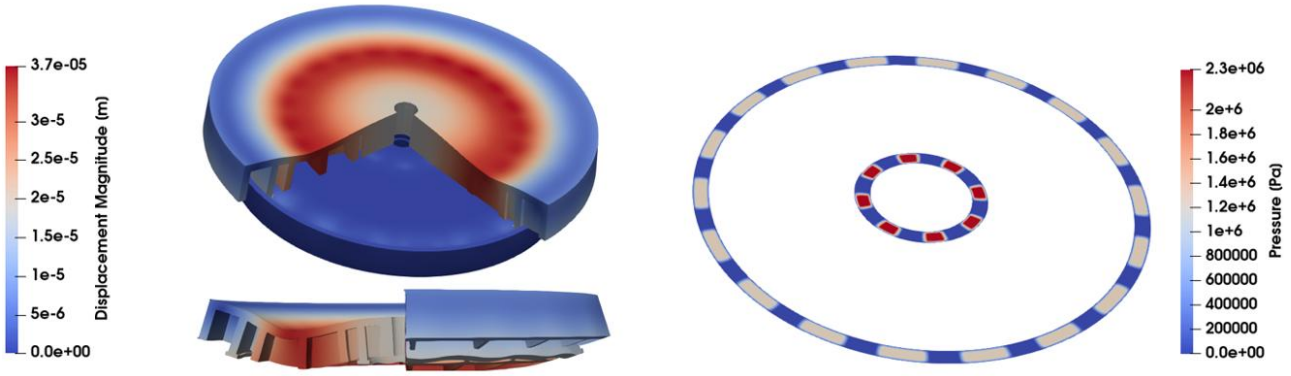

Figure 1. Displacement and pressure fields of the rotary table and fluid film, respectively.

3. Application to a large rotary table

The framework is applied to a 5 m diameter rotary table designed for heavy-duty machine tools, with a nominal load capacity of 100 tonnes and a supply pressure of 30 bar regulated through capillary restrictors. The table architecture consists of radial and circumferential ribs supporting two concentric hydrostatic rings, each equipped with multiple bearing pads. The structural material is FG-30 grey cast iron. This design is selected as representative case of heavy machin tool application.

The base structure is constrained at discrete mounting points, and the radial bearing is modelled by restraining in-plane rigid-body degrees of freedom. Simulations are performed across the full admissible load range (25–125 tonnes). To quantify the importance of structural flexibility, each load case is also run with the solid stiffness artificially increased by a factor of 10^4, producing a quasi-rigid reference solution equivalent to conventional rigid-body design tools.

4. Results and discussion

First at all, mention that the simulation tool and solvers where validated by simplified models and analytical solutions. The final model shown in Figure 1 has 348.072 DoF, it's solved in a i9-12950HX (12ª gen) with 16 cores and 24 threads with an average iteration time of 9,5 minutes.

The coupling mechanism is shown in Figure 1, which depicts the deformation of the solid bodies as a result of the pressure of the oil film. The difference between the inner and outer ring pressures is induced by the deformation of the rotary table, which creates very different film thicknesses.

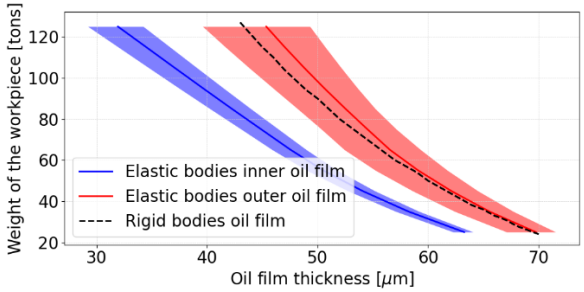

Figure 2. Load-gap curve for elastic body and rigid body rotary tables.

Across the studied load range, the mean oil film thickness decreases monotonically with load for both elastic and rigid models, as depicted in Figure 2. However, the divergence between the two solutions grows with load: the elastic table exhibits a lower mean film height in the inner ring and a higher one in the outer ring compared to the rigid case. This also means that the actual stiffness of the table is lower than in the rigid case. Regarding the energy consumption, Figure 3 shows that the pumping power is also different when coupling mechanism is considered, with lower energy consumption compared to the ideal rigid models.

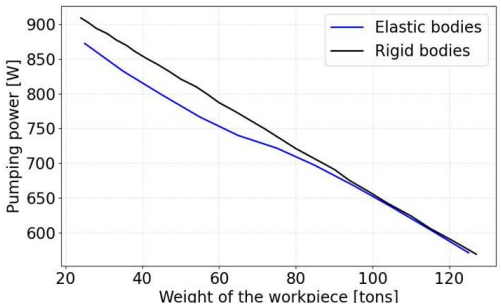

Figure 3. Pumping power as a function of the workpiece load.

5. Conclusions

A monolithically coupled elasto-hydraulic finite element framework has been presented and applied to a large rotary table with hydrostatic guideways. The key findings are:

– Structural deformation produces non-uniform oil film distributions within and between bearing rings.

– Global guideway stiffness is overestimated by rigid-body models because the differential film response of the two bearing rings reduces the effective parallel stiffness.

– Energy consumption may vary in coupled models compared to their rigid counterparts due to the gap variability.

These results demonstrate that structural flexibility must be accounted for in the design of large hydrostatic guideway systems. Future work will extend the model to dynamic (rotating) load cases and will incorporate thermal coupling to capture viscosity gradients across the film.

References

[1] Michalec M, Svoboda P, Křupka I and Hartl M 2021 A review of the design and optimization of large-scale hydrostatic bearing systems Eng. Sci. Technol. Int. J. 24 936–958

[2] Cheng Q, Zhan C, Liu Z, Zhao Y and Gu P 2015 Sensitivity-based multidisciplinary optimal design of a hydrostatic rotary table with particle swarm optimization J. Mech. Eng. 61 issues, pages 7-8, 432-447

[3] Wu Y, Qiao Z, Ge H, Xue J and Wang B 2023 Application of direct coupling method to design problems of hydrostatic guideways accounting for fluid-structure interactions Adv. Eng. Softw. 177 103410 publishing house , ISBN (Taylor&Francis, 9780429215315)

[4] Aguirre G, Al-Bender F and Van Brussel H 2010 A multiphysics model for optimizing the design of active aerostatic thrust bearings Precis. Eng. 34 507–515

[5] Hamrock B J, Schmid S R and Jacobson B O 2004 Fundamentals of Fluid Film Lubrication (CRC Press)

Session 3: Precision Manufacturing Processes

euspen's 26th International Conference & Exhibition, Krakow, PL, June 2026
www.euspen.eu

Monocular Vision for Online Feedback Control in Volumetric 3D Printing

Shuai Peng[1, 2], Boyang Cai[1, 2], Geming Chen[1, 2] & Yu Liu[1, 2,*]

[1]*School of Mechanical Engineering, Jiangnan University*
[2]*Jiangsu Key Laboratory of Advanced Food Manufacturing Equipment &Technology, Jiangnan University*

**Email: yu.liu@vip.163.com*

Abstract
Volume 3D printing, also called volumetric additive manufacturing or computed axial lithography, is a new way to create objects in which the entire 3D shape forms at once inside a liquid resin, rather than being built layer by layer. Currently, this system operates in an open-loop mode, where adjustments can only be made by trial after printing is complete, which limits further improvement in printing accuracy and production. To address this issue, this work proposes a method for monitoring and feedback through multi-angle light scattering image acquisition based on monocular vision: the foreground image of the light scattering image is extracted via background subtraction and threshold calibration, and then the 3D reconstruction of the printed model is achieved by combining filtered back-projection, edge extraction, and volume rendering algorithms. Meanwhile, the projected light dose is adjusted based on the forming status to achieve closed-loop control. Experimental results show that this method effectively addresses excessive curing in large features.

Keywords: volumetric printing; monocular vision; 3D reconstruction; feedback adjustment; closed-loop control

1. Introduction

Volumetric 3D printing (V3DP) borrows from computed tomography (CT) imaging, decomposing the target's three-dimensional light dose field into multi-angle two-dimensional projection patterns using Radon transform, and then sequentially projecting these patterns onto a photosensitive material [1]. When the accumulated light dose in the target area exceeds the curing threshold, the structure solidifies entirely within the material, achieving rapid prototyping. This paradigm avoids layer-by-layer stacking, thus possessing advantages such as speed, no layering, no support required, and high structural freedom, showing potential applications in biomedicine, flexible electronics, ceramics, and optical devices [2, 3].

However, V3DP is still constrained by problems such as insufficient repeatability, light scattering, difficulty in quantitative process monitoring, and limited precision for small features. Existing work has improved forming quality through offline light dose correction or post-printing reconstruction, but these rely on the results of the previous round to correct the next round of the process, making it difficult to suppress error accumulation in a timely manner [4, 5]. To address this, this paper constructs an online monitoring and feedback system. It uses a CCD to acquire formed images and extract the foreground sequence, combining filtered backprojection and geometric reconstruction to achieve three-dimensional reconstruction and quantitative process monitoring. Based on this, it adjusts the projected light dose in a closed loop, thereby improving the forming precision of small features and printing repeatability.

2. Methods and materials

In this study, to achieve online monitoring of the volumetric 3D printing process, we designed a photocuring system that undergoes phase separation during polymerization/gelation, forming a polymer-rich phase and a polymer-poor phase. The microscopic inhomogeneity caused by phase separation significantly enhances light scattering during the gelation stage; therefore, the cured region appears milky white with high scattering, while the uncured region remains clear and transparent.

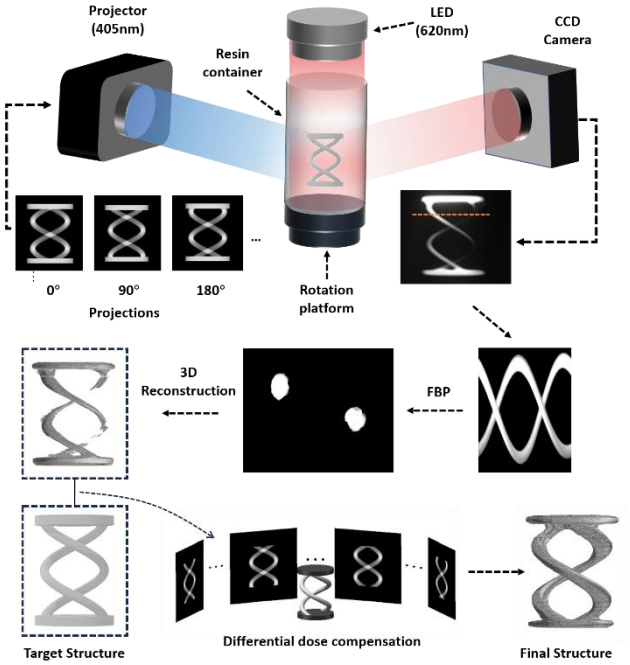

Figure 1. Schematic diagram of an online monitoring and feedback system for volumetric 3D printing

As shown in Figure 1, after extracting the foreground image, the forming process of the forming region can be observed after eliminating background interference. When a new feature is formed in the forming region, the projection is stopped and the rotary table is rotated one revolution to obtain light scattering data of the forming model at different angles. By analyzing the scattering data at different angles within one cycle, the lateral

scattered light of the forming model can be analyzed to construct the projection sine curve of each two-dimensional cross-section of the model. Back-projection of these projection sine curves can construct the two-dimensional cross-sectional image of each layer of the model. However, since the two-dimensional cross-sectional image obtained by direct back-projection is the projection value of each angle back-projected onto the image plane, the reconstructed two-dimensional cross-sectional image will have problems such as blurred edges, radial artifacts in high-contrast areas, and low-frequency information redundancy. To counteract this distortion and correct the frequency characteristics of the projection data, a filtering function is introduced during back-projection to obtain the filtered back-projection (FBP) cross-sectional image. After obtaining the two-dimensional cross-sectional images of each layer of the formed model, the three-dimensional model can be reconstructed by stacking these cross-sections in the Z direction.

After 3D reconstruction of the forming effect, the forming status of the printed model during the printing process can be further analyzed, and this can be used as a basis to determine whether printing is complete. If only some feature areas of the printed model are formed, and printing is not complete, the light dose can be adjusted based on the actual forming status of the printed model, as shown in Figure 1. This feedback method overcomes the problem that volumetric 3D printing systems cannot perform dynamic mode correction, and also solves the problem of over-curing caused by the continued accumulation of light dose in already formed areas during subsequent printing processes. This further improves the forming accuracy of the printed model and establishes a closed-loop control system that adjusts the light dose based on the forming status during the printing process.

3. Results

Figure 2 illustrates the forming evolution of the double-helix structure model during the printing process. The reconstructed 3D model shows that before light dose feedback adjustment, the larger feature (the two flat cylindrical features at the top and bottom) appears first, followed by the smaller feature (the middle helical structure). Upon completion of printing, the larger feature underwent over-curing, with the light-receiving side over-curing to the bottle wall, resulting in significant forming errors.

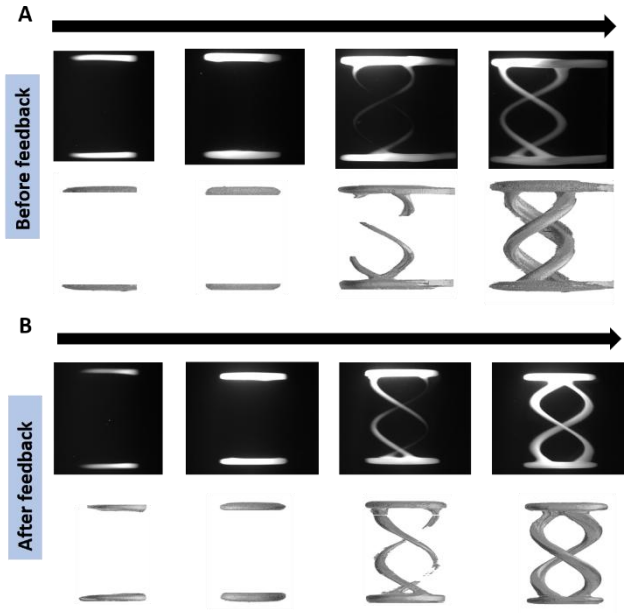

Figure 2. Diagrams of the printing model forming process before and after feedback

After feedback adjustment, when the larger feature (the two flat cylindrical features) was fully formed, the light dose projection of that feature was stopped, while the unformed portion (the middle helical structure) maintained its projection. This reduced the impact of inconsistent curing times for features of different sizes within the target area, improving the forming accuracy of the smaller feature area while preventing over-curing of the larger feature area, effectively enhancing the forming accuracy of the printed model.

Furthermore, Figure 3 shows the molding results of the microchannel structure and boat model printed under the designed volumetric additive manufacturing monitoring and feedback system, and provides the corresponding 3D reconstruction model. The results demonstrate that the system can perform non-contact 3D measurement of the molded body during the printing process, and achieve closed-loop feedback adjustment of the light dose based on the measured shape deviation, thus avoiding the accuracy degradation caused by the difficulty in dose correction based on the actual molding state in traditional printing. Using this method, the shape error of the printed model is controlled within ±200 μm, significantly improving the printing accuracy.

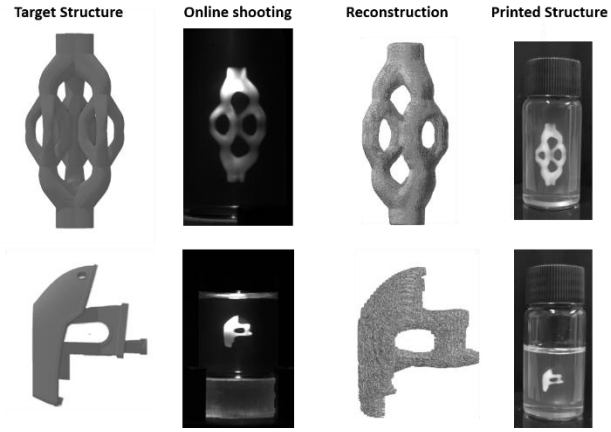

Figure 3. Other structural model printing and 3D reconstruction

4. Conclusion

This paper constructs an integrated monitoring and feedback scheme for volumetric 3D printing and verifies its effect on improving forming accuracy and process stability. First, a 3D reconstruction method is proposed to achieve non-contact 3D measurement of the forming process during printing. Second, a photometric dose feedback strategy is proposed to address the problems of under-curing/distortion of small features and over-curing of large feature areas. This strategy achieves adaptive dose adjustment based on the forming state, effectively improving the forming quality of detailed features and suppressing local over-curing, providing system-level methodological support for high-fidelity, repeatable volumetric 3D printing.

References

[1] Kelly B E, Bhattacharya I, Heidari H, Shusteff M, Spadaccini C M and Taylor H K 2019 *Science* **363** 1075-9
[2] Peng S, Chen G, Luo X, Zhang X, Li D, Xu Y, Sun C, Shang E, Wang X and Liu Y 2024 *Additive Manufacturing* **95** 104536
[3] Peng S, Xu J, Li D, Ren J, Zhang M, Wang X and Liu Y 2023 *International Journal of Extreme Manufacturing* **5** 035007
[4] Loterie D, Delrot P and Moser C 2020 *Nature Communications* **11** 852
[5] Orth A, Sampson K L, Zhang Y, Ting K, van Egmond D A, Laqua K, Lacelle T, Webber D, Fatehi D, Boisvert J and Paquet C 2022 *Additive Manufacturing* **56** 102869

euspen's 26th International Conference & Exhibition, Krakow, PL, June 2026
www.euspen.eu

Microstructuring of cutting punches for tribological optimization of stamping processes

Torsten Schmidt[1], Karsten Richter[1], Jan Edelmann[1], Verena Kräusel[1]

[1]*Fraunhofer Institute for Machine Tools and Forming Technology IWU, Chemnitz, Germany*

jan.edelmann@iwu.fraunhofer.de

Abstract
Efficient, cost-effective production requires stable operations and minimal downtime. One such industrially implemented process is the cutting of sheet metal materials in high-performance stamping presses. Key technological parameters – such as cutting gap, cutting-edge design and tribological conditions – are decisive for tool wear and consequently, the resulting quality of the sheared edge. The investigations presented in this paper aimed to reduce wear mechanisms through microstructuring of the lateral surfaces of cutting punches without compromising cutting-edge stability. Reducing the contact area between the punch and the sheared surface can increase tool life quantity and reduce production costs. The primary objective is to develop innovative solutions for demanding industrial applications, e.g. improving tool life when cutting high-strength steels. In a first step, various suitable microgeometries were developed and necessary manufacturing strategies for applying them to the lateral surfaces of cutting punches was derived using a short-pulse and ultrashort-pulse laser system. To analyse and evaluate their effect, the tribological behaviour of the functionalised punches was subsequently investigated in cutting tests. The functionality and enhanced tool life of microstructured cutting punches was successfully demonstrated.

Keywords Laser micro machining, Punching Quality, Stamping, Tribology

1. Motivation and objectives

Punching is a widely used industrial manufacturing technology for the economical production of cut-outs and trimming of sheet metal components [1]. The stresses on cutting punches vary depending on the materials being cut, the cutting geometry and process parameters, particularly the stroke rate and cutting gap [2, 3]. High mechanical and tribological loads often lead to wear, manifesting as adhesion, abrasion and surface damage.

Tool wear directly affects the quality of cut surfaces. If critical limits are exceeded, this can result in inadequate component quality and costly production interruptions due to punch breakage. Therefore, targeted adjustment of the tribological system is an important approach to reducing tool wear and improving component quality in shear cutting. As well as selecting suitable tool coatings and lubricants which must be tailored for the respective sheet metal material, micro-structuring cutting punches is a relatively unexplored way of increasing tool life quantity.

This article presents the different geometrical variants for microstructures introduced to the lateral surface of cutting punches using short- and ultrashort-pulse laser systems. These punches were then examined in terms of their tool life quantity when punching stainless steel strips of alloy 1.4462 on an automatic punching press. The wear characteristics of the structured punches were analysed in comparison to those of reference punches without microstructures.

2. State of science and technology

Innovative approaches to reducing tool wear during shear cutting include designing the punch geometry for a specific purpose, selecting suitable punch materials and using functional coatings. Recently, microstructuring the lateral surfaces of cutting punches has been investigated to improve tribological properties and reduce wear. Studies on surface hammering show that micro-indentations with depths of up to 2.5 µm can lead to a significant increase in tool life quantity, despite a relatively small reduction in contact area of 15–20% [6, 7]. Other microstructuring approaches use pulsed laser systems. Ultrashort pulse lasers are particularly suitable for highly stressed functional surfaces due to their low thermal influence. Laser-based material removal enables a high degree of geometric flexibility and precise control over surface quality [8, 9]. Kitamura reported on the introduction of micro-dimples up to 3 µm deep in TiCN-coated cutting punches using picosecond lasers. These dimples served as lubricant reservoirs and contributed to friction reduction during fine blanking [10].
It is also known that reducing the cutting gap and increasing the cutting-edge radius increases the friction surface and friction forces between the punch and the hole wall [2]. While reducing the contact surface through undercut can reduce the retraction forces. Reduced damping of punch-induced vibrations simultaneously increases the risk of punch breakage. Overall, the current state of research highlights the potential of targeted geometric and surface optimisations to increase the tool life quantity of cutting punches and ensure economical punching processes.

3. Methodology and Validation

3.1 Structural design of microstructures for cutting punches

The development of a methodology for the structural design of microstructures on the lateral surfaces of cutting punches is based on the objective of reducing the contact area between the punch and the hole wall of the sheet metal. It is well understood

that a reduction in cutting clearance increases the proportion of smooth cut surfaces, while an increase in the cutting-edge radius leads to a reduction in the resulting hole diameter. Both effects enlarge the frictional contact area and increase the friction force between the punch side surface and the hole wall. This accelerates wear on the punch lateral surface.

Based on this background, various microstructural designs were developed for structuring the punch lateral surfaces in the form of supporting contact geometries. These microstructures enable localized contact between the punch and the hole wall, allowing defined regions of the punch to slide along the wall. This design ensures adequate stabilization of the punch during the cutting process while simultaneously reducing the effective contact area. An overview of the investigated structural variants is presented in Figure 1.

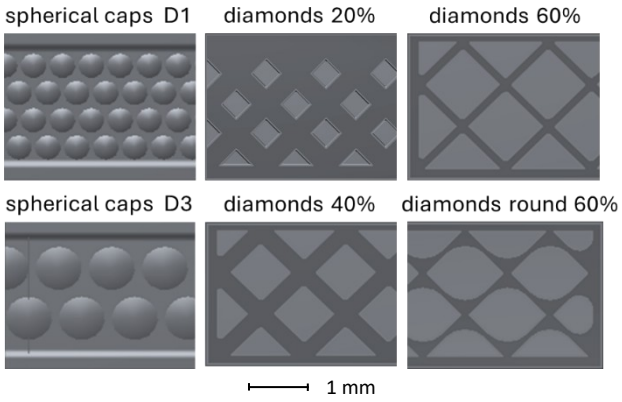

Figure 1: Overview of the developed structural variants

The spherical cap structure was derived with the aim of maintaining the punch guide within the hole wall at specific points with as little surface area as possible. The diamond structure and its variants were developed with the aim of maintaining continuous lateral, flat support through the remaining webs. This is expected to result in less local wear. In the derivation of the round diamond structure, all corners are rounded in the axial punch stroke direction so that potential material removal cannot collect in the structure corner and cause damage. The distance between the microstructure and the cutting edge was set to 0.3 mm for all punches. The percentages shown in Figure 1 indicate the degree of contact surface reduction. The target for the diamonds was a reduction in surface contact of between 20 and 60%. For the spherical caps D1 and D3 this is initially 84%. With increasing wear, the degree of contact area reduction for the smaller spherical caps D1 (four-row) decreases more rapidly than for the spherical caps D3 (two-row). For example, wear of 15 µm for spherical cap D1 resulting in a reduction of the circumference corresponds to a remaining contact area reduction of 58.8%, whereas spherical cap D3 exhibits a value of 62.4%.

The structural design was based on the sheet thickness of 0.8 mm to be cut and the process- and machine-dependent penetration depth of the punch into the sheet material. As illustrated in Figure 2, an unstructured region is located adjacent to the cutting edge, followed by a structured region. Depending on the structure configuration and the punch penetration depth, this structured region has a height of approximately two to three times the sheet thickness. The height of structuring area and the unstructured area constitutes the effective range. Together with the punch circumference, it defines the developed surface area to be structured. The distances between individual structures, web widths, and structure dimensions were calculated using a custom-developed Excel tool and optimized with the Solver add-in integrated in Excel.

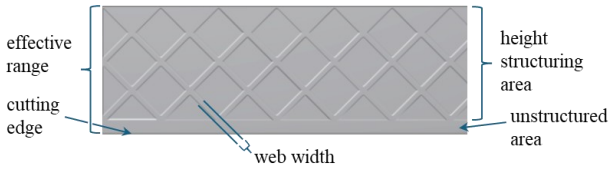

Figure 2: Overview of structural design

The optimization criterion was the maximization of the reduction in the targeted contact area. In addition, the developed surface length of the rhombic, rectangular or round punches served as the basis for calculating the structure distribution.

All shaped and round punches used as test specimens were manufactured from Vanadis 23 (SPM23) powder-metallurgical high-speed steel (material numbers according to EU standard: 1.3395 (1.3394)). This steel grade is widely used in industrial applications for machining stainless steels and spring strips and is characterized by high toughness, good wear resistance, and low hardness distortion. The punch geometries employed in the experiments are shown in Figure 3.

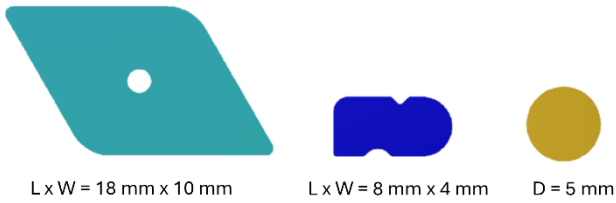

Figure 3: Punch shapes from left to right: rhombus-shaped cutting punch, rectangular cutting punch, round punch

The following analysis of the test results focuses on the wear behaviour and achievable tool life quantity of round punches with a diameter of 5 mm. These punches were manufactured using a short-pulse laser system to investigate possible changes to the boundary layer of the punch material caused by short-pulse laser processing. This issue primarily arises when processing with short-pulse lasers, which are still widely used in industry.

3.2 Microstructuring of cutting punches

The microstructuring of cutting punches comprises three main steps. First, the optimum material removal parameters for the cutting die material are determined to maximize the cost-effectiveness of the additional machining process with respect to the achievable extension of tool life quantity. To this end, the laser power, pulse frequency and duration, feed and line distance were varied, and in ten parameter combinations were examined for ablation characterisation. (Figure 4)

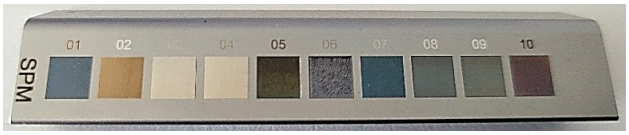

Figure 4: Test fields for ablation characterisation by laser parameter variation

The selection of suitable machining parameters represents a trade-off, as high ablation rates and low surface roughness constitute competing objectives. To evaluate the individual parameter combinations, the initial surfaces of reference punches were measured using a confocal microscope (MarSurf CM mobile). The determined roughness values served as reference and comparative metrics for the assessment of the test fields.

In the second step, a suitable fixture for holding the cutting punches in the laser system's machining unit was designed and manufactured according to the respective die geometry. For round punches, a concentric fixture is sufficient, as the laser focal position remains unchanged during rotation. For non-rotationally symmetric punch geometries, such as rhombic or rectangular shapes, however, eccentric positioning may be required. In these cases, the laser focus must be maintained by repositioning the laser head, which may adversely affect the achievable structural accuracy.

The third step involves adapting the structural specifications to the respective punch geometry and mounting configuration. First, the developed surface length is determined, and the microstructure to be applied is subdivided into defined individual segments. While only a single segment is required for round punches, the developed surface of rhombic punches is divided into multiple segments to ensure reproducible structure transfer.

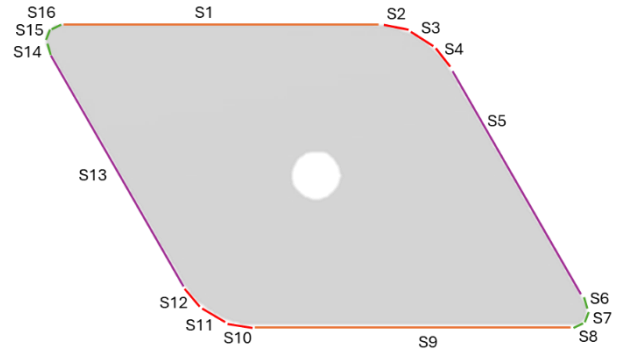

Figure 5: Example for division of the punch shell surface into 16 sub-segments to structure the rhombus punches

The calculation of the segment division is illustrated using the D1 spherical cap structure as an example. For the structuring process, the segment length, the angular position of the indexing device and the Z-position of the laser head are calculated and programmed as positional parameters for each segment. The structure segments are implemented as negative geometries in STL format.

To transfer the structural variants, three-dimensional negative developments were generated for each structure using a CAD program and subsequently applied to round punches with a diameter of 5 mm as well as to shaped punches. Measurements of the fabricated microstructures confirmed that the specified minimum structure depth of 35 µm was achieved. Minor deviations toward greater structure depths do not affect the punching process, as the effective contact area reduction remains unchanged. Although the project successfully demonstrated that microstructures shown in Figure 1 can be applied to complex punch geometries shown in Figure 3 and offer practical advantages when cutting different material classes, the discussion of the results below is limited to round dies. This allows us to illustrate the fundamental mechanisms of action using their simple geometry.

3.3 Experimental validation

The cutting punches manufactured in the described manner were used in experimental investigations. An automatic punching press BRUDERER BSTA 510-150B2 was used for the systematic cutting tests using a set of three punches from each microstructure family. The specific structure used was determined in preliminary tests thus choosing spherical caps D1, diamonds 40% and round diamonds for the experimental validation. Experience-based, the targeted test duration was set at 200,000 strokes. The press operated at a rate of 350 strokes per minute. Additionally, reference tests were carried out with round punches without microstructured outer surfaces. Strips of corrosion-resistant stainless steel 1.4462 (X2CrNiMoN22-5-3) with a tensile strength of 800 MPa and a sheet thickness of 0.8mm were cut.

It was demonstrated that the lifetime of cutting punches can be positively affected by microstructuring. In the reference test, none of the six punches used achieved the target of 200,000 strokes. On statistical average, the reference punches achieved a tool life quantity of 74,800 strokes, with a minimum value of 15,500 strokes and a maximum value of 150,000 strokes. In contrast, all punches of the three structure variants investigated achieved a tool life quantity of 200,000 strokes. The cutting tests were then continued beyond the initial target. Here, it was found that the microstructured cutting punches all exceeded a tool life quantity of 275,000 strokes. The use of microstructured cutting punches thus led to a significant increase in tool life quantity which contributes to fewer production interruptions and thus higher productivity. This enables an economical use of these cutting punches despite the increased manufacturing costs associated with microstructuring. [11]

The cutting forces differ only slightly between the reference punches and those with microstructures. In contrast, a significant reduction in retraction forces was achieved, which can be regarded as an indication of improved tribological conditions, particularly during punch retraction.

Figure 6 shows microscope images of the three structural variants examined, each at 0 stroke and after 200,000 strokes. In addition, the best performing reference punch is shown at 0 stroke and after 150,000 strokes. The latter one shows significant pitting on the cutting edge.

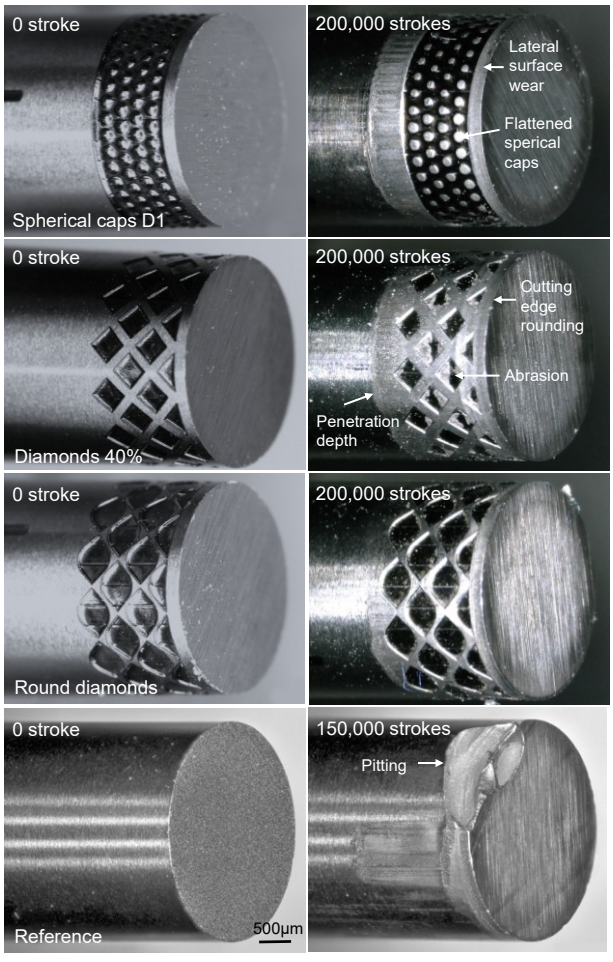

Figure 6: Comparison of cutting punches

All punches show an increase in cutting edge rounding as the number of strokes increases. Punches with the spherical cap structure variant D1 show wear on the front area of the outer surface. The spherical caps are significantly flattened, which means that abrasive wear has occurred. As a result, the contact area between the punch and the hole has increased again over the course of the test. In the diamond structure variant 40%, the microstructure appears sharp-edged and has a metallic sheen in the pockets. As the test progresses, there are hardly any noticeable changes to the microstructure. A certain amount of wear is also evident on the front area of the outer surface. It is noticeable that after 200,000 strokes, a considerable amount of abrasion has accumulated in the pockets of the microstructure. This is probably due to a kind of filing effect caused by the sharp corners of the rhombuses. However, such phenomena cannot be observed with the round diamond structure variant. No changes to the microstructure are visible here. The extent of wear on the cutting edge is like that observed with the other two structure variants. All punches were measured regarding their cutting edges using a 3D-MicroCAD system. This measurement shows a reduction in punch diameters of approximately 15 µm. The microstructures on the dies were partially measured and evaluated using a Mahr Surf Mobile before and after the tests. Due to the extensive measurement data and complex test matrix, the results can only be discussed in general terms.

Technologically, each of the three structural variants examined offers certain advantages and disadvantages, particularly in terms of specific wear behaviour and the specific progression of retraction forces. However, all three structural variants significantly increased tool life quantity compared to the reference, highlighting the great potential of this adaption of the punching process. Taking all the relevant criteria into account, the round diamond structure variant is recommended for the cutting task under review, as it exhibits the least wear after 300,000 strokes. Whether these observed advantages result primarily from the reduced retraction forces is subject of further research. When adapting the cutting task, it is advisable to review the selection of the structural variant (considering the sheet thickness and material properties of the sheet metal to be cut), and to test it in field trials, if necessary, before putting microstructured cutting punches into industrial use.

4. Economical uses of microstructured cutting punches

The cost-effectiveness of surface-adapted punching tools largely depends on their manufacturing costs and the tool life quantity achieved during the punching process. The manufacturing costs of structured cutting punches include the material costs of the punch as well as the set-up and production times of both the punching press and the laser system. Laboratory tests have shown that the manufacturing costs of a microstructured cutting punch are approximately 2.5 times higher than those of a reference punch.

Tests conducted at Fraunhofer IWU demonstrated that using structured punches resulted in an almost quadrupled tool life quantity. Despite the initially higher tooling costs, this results in an overall cost saving of approximately 35% compared to the reference test. [11]

5. Summary

Microstructuring of cutting punches offers the potential to optimise cutting processes tribologically and increase the achievable tool life quantity. As part of the research work presented, various microstructures were developed which were introduced into the outer surfaces of cutting dies by laser ablation. In continuous cutting tests, it was demonstrated that this can significantly extend the achievable tool life quantity while maintaining the same cutting surface quality. It was shown that the economical use of such dies is even possible if the dies are manufactured under laboratory conditions. A significant increase in tool life quantity was achieved compared to non-structured reference punches. The results illustrate the potential for tribological optimisation of punching processes using microstructured cutting punches. Furthermore, it was shown that processing with a short-pulse laser system has no negative impact on the tool life quantity of the structured cutting punches. Various improvements in a prospective industrial and further automated microstructuring process can further reduce the costs of punch production considerably. This includes further optimisation of the ablation parameters of the short-pulse laser with the aim of achieving shorter processing times, i.e. accepting slightly higher roughness levels in exchange for faster ablation. Alternatively, the use of a femtosecond laser also offers the potential for shorter structuring times. The set-up times in the laser system can be significantly reduced by using devices for fast and reliable mounting of the cutting stamps. This enables a further reduction in costs and an increase in the economic advantage resulting from the use of tribologically optimised cutting punches.

Acknowledgements

The work presented was part of the joint project “Wir! – GRAVOmer – TriboCuttingPunch – Microstructuring of cutting punches for the tribological design of punching processes” which was funded by the German Federal Ministry of Research, Technology and Space (reference number: 03WIR2012D) and carried out in collaboration with the companies KMLT GmbH, Werkzeugbau Fischer GmbH, and Cefeg GmbH. We would like to thank BRUDERER GmbH for providing the punching press.

References

[1] Westkämper, E.; Warnecke, H.-J.: Einführung in die Fertigungstechnik. Wiesbaden: Vieweg + Teubner 2010.

[2] Neumayer, F. F.: Ermittlung und Auswirkung der Durchbruchkraft beim Scherschneiden. Dissertation, TU München, München 2020.

[3] Kolbe, M.: Stamping Practice. High Performance Stamping. Wiesbaden: Springer Fachmedien 2022.

[4] Winter, S.; Galiev, E.; Nestler, M.; Psyk, V.: Verschleißerscheinungen an PM- und HM-Stempeln beim Stanzen. Zeitschrift für wirtschaftlichen Fabrikbetrieb 115 (2020) 9, S. 621–624.

[5] Winter, S.; Stein, C.; Richter, K.; Höfer, M.; Sittinger, V.; Psyk, V.; Kräusel, V.: Erprobung anwendungsadaptierter CVD-Diamantschichten beim Stanzen. Zeitschrift für wirtschaftlichen Fabrikbetrieb 116 (2021), 7–8, S. 464–468.

[6] Schumann, P., Arne, V., Groche, P..: Improved Process Efficiency with Microtextured Blanking Punches Using MHP. Defect and Diffusion Forum 441 (2025), 19–27.

[7] Schumann, P.; Groche, P.: Tribologische Optimierung von Schneidstempeln durch Mikrostrukturierung mittels maschinellem Oberflächenhämmern. Hannover: Europäische Forschungsgesellschaft für Blechverarbeitung e.V 2023.

[8] Gärtner, E.; Schell, F.; Nitschke, L.; Okafor, R.C.; Zwahr, C.; Hackl, C.: Replicative Production of Multifunctional Microfluidic Polymer Films for Biomedical Disposables. Procedia CIRP 125 (2024).

[9] Schmidt, T.; Gärtner, E.; Schneider, J.; Edelmann, J.: Microstructure rolling process with laser structured roller tools. In: Proceedings of the 21st Int. Conf. of the EUSPEN 2021, Kopenhagen 2021.

[10] Kitamura, K.; Makino, T.; Nawa, M.; Miyata, S.: Tribological effects of punch with micro-dimples in blanking under high hydrostatic pressure. CIRP Annals 65 (2016) 1, S. 249–252.

[11] Richter, K.; Schmidt, T.; Nestler, M.; Kräusel, V.; Edelmann, J.: Standmengenerhöhung durch die Mikrostrukturierung von Schneidstempeln. Zeitschrift für wirtschaftlichen Fabrikbetrieb 121 (2026) 1–2, 72-77.

euspen's 26th International Conference & Exhibition, Krakow, PL, June 2026
www.euspen.eu

Recycled Walnut Shell Abrasives as a Sustainable Feedstock for Binder Jetting

Luwen Zhang[1], Rezo Aliyev[1] and Henning Zeidler[1]

[1]*Institute for Machine Elements, Engineering Design and Manufacturing, Chair of Additive Manufacturing, TU Bergakademie Freiberg, 09599 Freiberg, Germany*
Luwen.zhang@imkf.tu-freiberg.de

Abstract
Additive manufacturing (AM) opens new possibilities for the valorisation of materials that would otherwise be wasted. Industrially applied walnut shell abrasives, chosen for gentle abrasive cleaning and surface finishing due to their favourable hardness-to-wear ratio, are typically discarded once their sharp edges are worn down. Previous attempts to use walnut shell powder in polymer material extrusion AM (MEX-TRB/P) filaments required high polymer loadings, limiting the effective use of the biogenic fraction and reducing overall sustainability. Binder jetting (BJT) enables walnut shell powders to be used directly without thermoplastic polymer matrices, thereby increasing material usage efficiency.
In this study, walnut shell particles were used as feedstock. After milling and sieving, powders below 180 µm were selected for BJT experiments. Powder flowability, spreadability, packing density, and layer formation were systematically evaluated. Fine (<63 µm) and coarse fractions were blended in varying ratios to assess their effect on printability. Polyvinyl alcohol (PVA) was used as the binder. Particle size distributions were analysed before and after printing to identify optimal blends.
Printability was strongly influenced by particle size distribution. Fractions containing more than 65% of particles below 63 µm exhibited improved spreading behaviour, better layer cohesion, and enabled stable printing without slippage. Optimal performance was achieved with a liquid saturation of 120% and a layer thickness of approximately 90 µm. A balanced mix of fine and coarse fractions facilitated binder penetration and minimised printing defects.
This study demonstrates that recycled walnut shell abrasives can be processed into powders suitable for BJT when appropriate particle size distributions and process parameters are applied. Compared with polymer-based filament processing, BJT utilises walnut shells more efficiently, thereby enhancing the environmental benefits of recycling this by-product for AM.

Binder jetting, recycled walnut shell, particle size distribution, PVA binder, sustainable additive manufacturing

1. Introduction

Additive manufacturing (AM) offers material efficiency, geometric freedom, and compatibility with bio-based or recycled feedstocks. Among AM technologies, Binder Jetting (BJT) is particularly attractive in this regard. As a non-thermal process, BJT deposits a liquid binder onto thin powder layers at room temperature [1,2], enabling processing of temperature-sensitive materials that would degrade under high thermal loads.

Walnut shells, abundant agricultural by-products that are industrially used as blasting abrasives prior to AM, are often discarded after this application. Despite edge erosion, they retain remarkable structural integrity. Their polylobate sclereid cell architecture forms an interlocked 3D network, forcing cracks to propagate through lobes rather than cell boundaries, yielding high tensile strength [4]. This robustness has been exploited in composites such as particle boards and concrete [5,6].

In AM, walnut shell research has mostly focused on Material Extrusion (MEX-TRB/FFF). Mechanical properties are highly sensitive to printing parameters [7], and print consistency remains challenging [8]. MEX-TRB applications face limitations: walnut shell content is typically less than 30 wt% to avoid nozzle clogging; hydrophilic biomass poorly adheres to hydrophobic PLA, requiring surface treatment [9-11]. Achieving balance between tensile strength and dimensional accuracy is difficult [12].

BJT overcomes these issues by eliminating thermoplastics and high temperatures. This study explores repurposing spent walnut shell abrasives as BJT feedstock, optimising particle size distribution (PSD) and powder behaviour to convert this by-product into functional, sustainable AM material.

2. Materials and Methods

2.1. Materials

Recycled walnut shell abrasive (Adsom GmbH, Germany) was used as the primary feedstock. A water-soluble polyvinyl alcohol (PVA) powder (Aurelio, Germany) was selected as the binder for its good compatibility with lignocellulosic powders, low toxicity, and effective water-activated bonding.

2.2. Powder Preparation and Characterization

The spent walnut shell abrasive was milled using an ultra-centrifugal mill (ZM100, Retsch GmbH, Germany) with 250 µm, 500 µm, and 750 µm ring sieves to vary comminution intensity. The milled powders were then classified using a vibratory sieve shaker (AS 450 control, Retsch GmbH, Germany), and only fractions below 180 µm were retained for further study.

Two representative fractions were chosen: a fine fraction (<63 µm) and a coarse fraction (63-180 µm). For BJT trials, the fractions were blended with fine-fraction ratios ranging from 10 to 100 wt%, and a constant 30 wt% of water-soluble PVA was added to prepare the printing feedstock. Previous tests confirmed that PVA addition had negligible influence on powder flowability at room temperature, allowing particle size distribution to remain the dominant factor affecting printability.

Following printing experiments, the particle size distribution (PSD) of the blend yielding the best printability was measured

using dynamic image analysis (Camsizer XT, Retsch GmbH, Germany) to verify the optimal ratio and ensure reproducibility.

2.3. BJT Trials

BJT was performed on a Z310 system (Z Corporation, USA) using a water-based solution to activate the PVA. Printability was evaluated based on powder bed stability, layer cohesion, and green part integrity. While a sufficient fraction of fine particles improved interlayer friction and powder bed stability, excessive fines could become airborne during recoater movement, increasing the risk of printhead clogging. Printing parameters were systematically varied, and stable printing was achieved at 120% liquid saturation and approximately 90 µm layer thickness. Cylindrical specimens (Ø 20 mm × 20 mm) were printed at least three times per blend to validate reproducibility.

3. Results and Discussion

Figure 1 shows the particle size distributions (PSD) of recycled walnut shell powders after milling with 250 µm, 500 µm, and 750 µm ring sieves. Milling with the 500 µm and 750 µm sieves was inefficient, yielding less than 50% of particles below 180 µm. In contrast, the 250 µm sieve produced a finer powder, with approximately 90% of particles below 180 µm and around 65% below 63 µm. Consequently, the 250 µm sieve configuration was selected for preparing feedstock for subsequent trials.

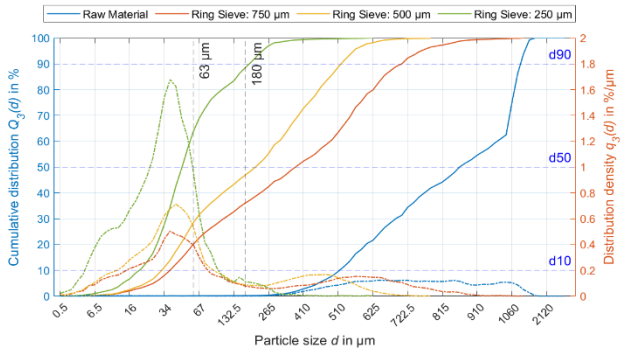

Figure 1. Particle size distributions of recycled walnut shell powders after milling with 250 µm, 500 µm, and 750 µm ring sieves. Dashed lines indicate the particle size thresholds of 63 µm and 180 µm relevant for binder jetting.

Printing trials were then conducted using blends of fine (<63 µm) and coarse (63-180 µm) walnut shell fractions, classified via vibratory sieving (amplitude 1.4 mm, 10 + 10 min). Figure 2 shows the PSD of the optimal blend, formulated with 60 wt% fine fraction. The measured content of particles <63 µm was approximately 65 wt%, slightly higher than expected due to residual fines remaining in the coarse fraction from the high-throughput sieving process.

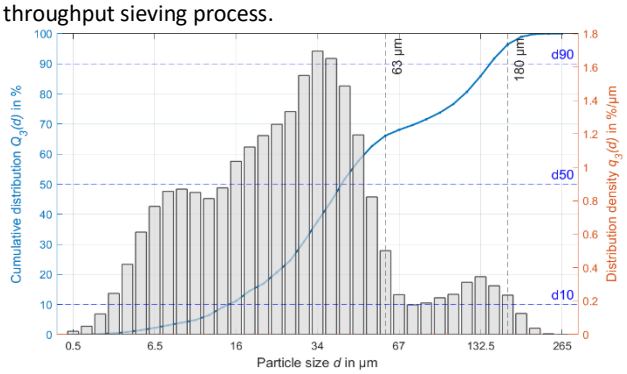

Figure 2. Particle size distribution of the optimised powder blend (60 wt% fine fraction).

Comparison of the PSDs after milling (Figure 1) and after blending and printing trials (Figure 2) highlights the key indicators for optimal printable powders. This suggests that direct milling with a 250 µm sieve could streamline feedstock preparation.

Cylindrical specimens (Ø20 mm × 20 mm) printed under these conditions exhibited excellent shape retention and layer integrity (Figure 3). Reproducibility was confirmed with three repetitions per blend.

Figure 3. Printed cylindrical specimen (Ø 20 mm × 20 mm) from the optimised 60 wt% fine fraction blend.

4. Conclusion and Outlook

This study demonstrated that discarded walnut shell powders can be effectively recycled as a feedstock for BJT, offering a sustainable approach for high-value utilisation in AM. Powders produced with the 250 µm sieve provided the highest usable fraction for printing.

Printing trials confirmed the powders' inherent printability. Blends of fine (<63 µm) and coarse (63-180 µm) fractions achieved stable powder bed spreading and interlayer friction, producing defect-free green parts. The optimal blend contained approximately 65 wt% fine particles, balancing layer stability with minimal risk of printhead clogging. Addition of 30 wt% water-soluble PVA enabled reliable printing without adversely affecting powder flowability, achieving a recycled walnut shell utilisation rate of at least 70 wt%.

The printed parts consist solely of walnut shell powder and water-soluble PVA, making them fully biodegradable and environmentally benign. This demonstrates a practical route to convert biogenic waste into functional materials for AM, highlighting both environmental and process efficiency benefits.

Future work could explore direct milling with a 250 µm sieve, alternative binders, or incorporation of other sustainable biomaterials to further improve printability, material utilisation, and mechanical performance. This study provides a foundation for more circular, resource-efficient AM processes and opens opportunities for expanding sustainable, bio-based feedstocks in industrial 3D printing applications.

References

[1] Ziaee M and Crane N B 2019 *Addit. Manuf.* **28** 781–801

[2] Bose S, Jo Y, Majumdar U and Bandyopadhyay A 2022 *ASM Handbook: Addit. Manuf. Biomed. Appl.* **23A** 77-91

[3] Fordos S, Abid N, Gulzar M, Pasha I, Oz F, Shahid A, Khan M K I, Khaneghah A M and Aadil R M 2023 *Biomass Conv. Bioref.* **13** 14389-411

[4] Antreich S J, Xiao N, Huss J C, Horbelt N, Eder M, Weinkamer R and Gierlinger N 2019 *Adv. Sci.* **6** 1900644

[5] El Hamri A, Mouhib Y, Chkala H, Oulhakem O, Chigr M and El Mansouri N E 2025 *J. Compos. Sci.* **9** 183

[6] Beskopylny A N, Stel'makh S A, Shcherban' E M, Mailyan L R, Meskhi B, El'shaeva D and Varavka V 2023 *Materials* **16** 1752

[7] Mazur J, Sobczak P, Panasiewicz M, Łusiak P, Krajewska M, Findura P, Obidziński S and Żukiewicz-Sobczak W 2025 *Sci. Rep.* **15** 5847

[8] Demir M, Sözen A, Seki Y and Selli F 2022 *8th Int. Tech. Textile Cong. (ITTC)* 59-63

[9] Palaniyappan S, Annamalai G, Sivakumar N K and Muthu P 2023 *J. Build. Eng.* **65** 105746

[10] Song X, He W, Yang S, Huang G and Yang T 2019 *Appl. Sci.* **9** 4892

[11] Palaniyappan, S., Sivakumar, N. K., and Pandiaraj, S., 2024 *Food Packag. Shelf Life* **41** 101226

[12] Palaniyappan S, Veeman D, Sivakumar N K, and Natrayan L 2022 *Structures* **45** 163–78

euspen's 26th International Conference & Exhibition, Krakow, PL, June 2026
www.euspen.eu

Automated algorithm for the evaluating of burr formation in micro milling

Maximilian Vierling[1], Jan C. Aurich[1]

[1]*University of Kaiserslautern-Landau, Institute for Manufacturing Technology and Production Systems*

maximilian.vierling@rptu.de

Abstract

Micro milling is a machining process that enables the fabrication of surfaces with defined structures in the micrometer range. Applications for micro structured surfaces can for example be found in bioprocess engineering. However, burrs are formed on most metal materials during machining. This impairs the precision of the structures produced, leading to the need to minimize the formation of burrs. To achieve the greater goal of minimizing burr formation, a reliable method to describe burrs quantitatively is needed first. This paper presents an automated algorithm that enables a quantitative evaluation of changes in burr formation. Its development was based on slots created by micro milling using tools with diameters of 50 µm. 3D images of these slots were taken by a confocal microscope. The influences of the size of the image section and the brightness of the sample exposure during measurement on the results were investigated.

micro milling, burr evaluation algorithm

1. Introduction

Micro milling can be used to machine micro structured surfaces in a wide range of materials. Applications for micro structured surfaces can e.g. be found in bioprocess engineering. Here, the adhesion of microorganisms to various surface profiles is improved by creating defined structures [1,2]. Such applications require a high surface quality. Burrs impair the quality of the produced microstructures. Their subsequent removal in micro machining is associated with considerable time and costs and carries the risk of damaging the manufactured structures. It is therefore advantageous to take measures during the milling process to minimize burr formation [3]. This results in the necessity to make burrs evaluable quantitatively, so different series of experiments can be compared to each other.

Medeossi et al. [4] addressed this topic by developing an algorithm for burr evaluation based on confocal microscope images. The burrs were created by micro milling slots in cp titanium grade 2. The diameter of the micro mills was 300 µm. The algorithm developed uses a z-height histogram to divide the sample surface and the slot bottom. The dividing line was set by the centre of mass of the histogram. All points higher than two times the standard deviation of the height distribution of the sample surface were considered burr. Three parameters were chosen to characterize the burrs: mean burr width, max burr width and burr ratio. Burr ratio is the ratio between mean width and max width.

Akkoyun et al. [5] micro milled slots with tool diameters of 1,000 µm in Inconel 718 alloy. 2D images of the slots were taken by a scanning electron microscope (SEM). The burrs were evaluated by an automized algorithm. The picture was processed by different filters and converted into grayscale. For every row of pixels parallel to the slot, the color values of the pixels were summed up. The peaks of the resulting profile were used to define the slot borders. This way two regions of interest were defined, which include the burrs on the up milling side (UM side) and on the down milling side (DM side). For each region, the burr was extracted. The burr width was calculated to evaluate the burrs.

Hajiahmadi et al. [6] used a milling tool of 1,000 µm in diameter to machine slots in stainless steel 316L. They used an optical microscope to determine the burr height and a SEM to determine the burr thickness. The values were calculated as the mean values from eight discrete measurements at different points. The measurements were executed by researchers and not automated.

The first attempt involved reproducing and using the Medeossi et al. [4] algorithm on cp-Ti. It was found that in our case, the center of mass of the histogram does not allow a clean division of the surface from the slot bottom. So, using this method to divide the surface from the slot bottom is not reliably applicable in general. Furthermore, even if the surface was already detected correctly, the threshold of two times the standard deviation proposed by Medeossi et al. [4] did not allow a generally reliable distinction between surface and burr.

The work of Akkoyun et al. provides only two-dimensional information and was also preliminary examined. The detection method for the slot borders can lead to parts of the burr areas next to the slot and protruding into it being attributed to the slot. The algorithm had to be adjusted for each burr type investigated to detect the burrs correctly.

Hajiahmadi et al. did not use an automated algorithm but measured the burrs at discrete points by hand. This leads to a strong dependency on the researcher and the chosen measurement points. The results are therefore not reproduceable.

This paper presents an automated algorithm, applicable to different kinds of burrs and image sizes. Parameters are defined to describe the burrs quantitatively. The influence of the brightness of the sample exposure during measurement and the size of the surface area captured next to the slot on the calculated burr parameters was investigated. Furthermore, an investigation was conducted to determine if the measured slot

length of 0.52 mm is sufficient to quantify the burrs or whether the measured length is too short for a global statement.

2. Methodology

The investigated slots were manufactured on a desktop machine tool using micro end mills with effective diameters of 50 µm and a helix angle of 0°. A helix angle of 0° is chosen, because it maximizes the core cross section of the tool and reduces deflection effects. Micro mills have very small diameters and therefore exhibit low stiffness and high susceptibility to tool deflection and breakage. Consequently, tool geometries with increased structural rigidity are preferred [7]. The manufacturing of the tools is described by Aurich et al. [8]. The depth of cut was 5 µm and the feed per tooth 1 µm. The rotational speed of the spindle was at 30,000 rpm, resulting in a cutting speed of 4.71 m/min. The sample surface was face milled before the slots were manufactured.

To enable the development of a new algorithm applicable for a wide range of burr types, slots were created and evaluated for four different Materials: Stainless steel 316L, commercially pure titanium grade 2 (cp titanium), AlCuMgSi and brass. An overview of the resulting burr types is shown in figure 1.

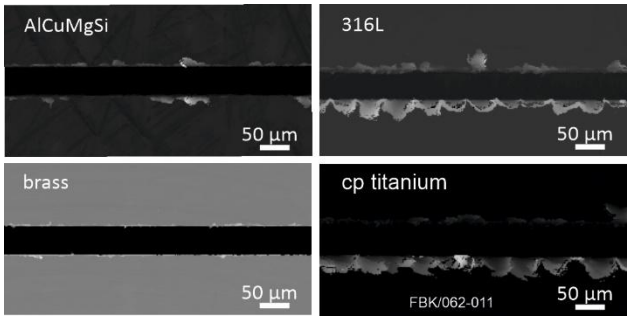

Figure 1. Comparison of the investigated burr types

The created slots were measured using the confocal microscope µsurf OEM from the manufacturer nanofocus[2]. The confocal microscope provides height information for each recorded measuring point, which makes three-dimensional images possible. The used objective is of the type 260S, has a magnification of 60x and a numerical aperture (NA) of 0.9. Its measuring field size is 260 µm x 260 µm. Since larger slot areas were analyzed, multiple individual images were taken and stitched together within one measurement. This was done automatically by the measurement software µsoft metrology by nanofocus[2]. Measurements were carried out consisting of two and nine stitched pictures in the length direction of the slot per measurement. This resulted in evaluated slot length of 0.52 mm and 1.9 mm. Furthermore, some measurements concerning brass were executed with different brightness of the sample exposure during measurement.

The images were post processed using the software MountainsMap by Digital Surf[2]. In this software, the images were aligned so that tilting caused by the camera not being perfectly perpendicular to the surface was corrected. Then, void pixels were filled with the average value of the neighbouring pixels. Void pixels are pixels for which no height value could be measured. If environment of the sample was part of the image, it leads to regions mostly filled with void pixels. These regions cannot be processed by the algorithm and were cut off. The slot had to be horizontally aligned if this was not the case. The up milling side needed to be on the top to later ensure correct assignment of the two edges. Finally, the height values of each pixel of the surface layer were extracted and the data was exported to a .txt file, hereinafter referred to as height map. This height map was then imported into MATLAB[2], the programming and development environment used to develop the algorithm.

3. Burr evaluation algorithm

This section describes the algorithm and the parameters used to quantify the burrs. The influences of the image size and the brightness during measurement on the results of the algorithm are presented.

3.1. Functionality of the algorithm

The detection of the burrs is done by calculating a height threshold and defining the image regions above this threshold as burrs. This corresponds to the approach of Medeossi et al. [4] However, the procedure is different. Based on Akkoyun et al. [5], the height values for every row of pixels parallel to the slot are summed up. A resulting height profile plotted into the corresponding height map shows figure 2.

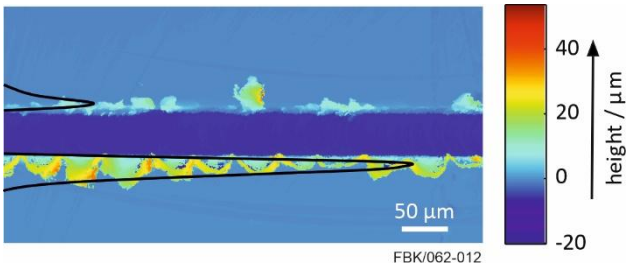

Figure 2. Height map with corresponding height profile

The profile is smoothed by a moving average, so the number of peaks is reduced to the two main peaks. The peaks enclose the slot and parts of the burrs next to it. The vertical positions of the peaks are calculated. The height values of all pixels below the lower peak and above the higher peak are used to calculate an arithmetic mean value of the surface height and a standard deviation. The mean value and the standard deviation are used to calculate a confidence interval. The upper value of the confidence interval defines the threshold between sample surface and burr. The burr areas lie above the threshold and are separated from the surface by converting the height map into a binary matrix.

A resulting problem is that investigating different burr types leads to the need for different confidence intervals to detect the burrs properly. For this reason, the algorithm uses different confidence intervals for detecting the burrs depending on different standard deviations of the surface height.

Contaminants like chips, material accumulations or dirt on the sample surface are detected as burrs, if they exceed the threshold. To exclude such falsifications, a band is defined between the two detected peaks in figure 2. Only image regions detected as burrs that are included in this band or touch it are considered as burrs. All burrs detected outside this band are considered as measurement errors.

The burr areas include holes surrounded by burr that are considered surface by the algorithm. These holes are filled to create a throughout burr area. The result is a binary image used to evaluate the burrs. The binary image is directly used to calculate planar burr parameters and as a mask to extract height information from the height map. The planar and height parameters are calculated for the UM side and the DM side separately. Therefore, the image is split in the middle of the slot. To detect the middle of the slot, the two peaks in figure 2 are used again. The slot middle is defined as the middle line between these two peaks.

3.2. Burr parameters

A system of parameters is developed to describe the burrs quantitatively. The mean burr width w is calculated as mean of the burr widths y in each of the n columns of the height map. When calculating the mean burr width, the edge areas without burr are not taken into consideration. So, the mean burr width only refers to those edge areas where burrs develop. The mean height is calculated in the same way as the width, using the height information z for each of the p pixels that are considered part of the burrs in the final binary matrix. The mean values of burr width and burr height give information about the sizes of the burrs. The deviation ratios dw and dh for the burr width and the burr height are the quotient between the standard deviation and the mean value. The deviation ratios add information about the uniformity of the burrs. The ratios are chosen instead of the standard deviations, because they give information about how large the size of the burrs varies relative to the mean values. On the other hand, the standard deviations are absolute values and therefore not suitable to compare burrs that differ in size to a high degree. The length ratio lr is the ratio between the summed lengths of the machined edge parts with burrs to the length of the machined edge as a whole L in percent. It defines the proportion of a milled edge, that is afflicted with burr. The calculation of the parameters is shown below:

$$w = \frac{\sum_{i=1}^{n} y_i}{n} \quad (1)$$

$$h = \frac{\sum_{i=1}^{p} z_i}{p} \quad (2)$$

$$dw = \frac{\sigma_w}{w} \quad (3)$$

$$dh = \frac{\sigma_h}{h} \quad (4)$$

$$lr = \frac{\sum_{i=1}^{m} l_i}{L} \cdot 100\,\% \quad (5)$$

As an example, for the calculated burr parameters the mean burr widths for the four investigated materials differentiated according to UM side and DM side can be seen in figure 4. Each value but the ones from AlCuMgSi represents the mean of four different slots. Only three different slots are used with AlCuMgSi. The error bars represent the combined standard deviations of the measurements.

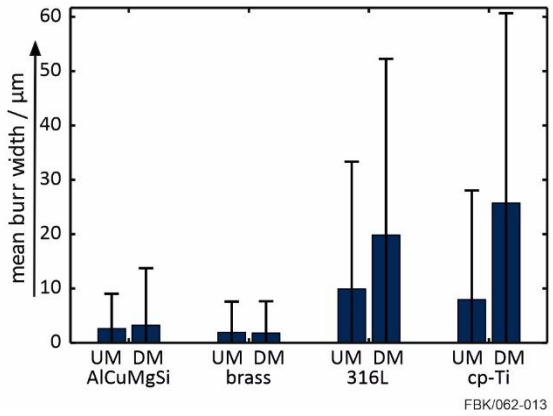

Figure 4. Mean burr widths and combined standard deviations

3.3. Influences on the accuracy of the algorithm

For the sake of clarity only the size of the burrs is discussed based on the mean burr width. This is possible because the mean burr height shows tendencies like the mean burr width. The length ratio and the two deviation ratios are left out in this section since the focus is on identifying relevant influences rather than conducting a comprehensive parameter study. Table 1 shows the change in mean burr width if the image is narrowed by 20 % and 40 %, thereby reducing the proportion of the sample surface to the slot width in the overall image.

Table 1 Change of the mean burr width with changing proportion of the surrounding surface area of the slot by -20 % and -40 %

		Absolut value of the parameter changes / %	
material	**milling strategy**	**-20 % image width**	**-40 % image width**
316L	UM	1.81	0.19
	DM	0.43	1,85
cp Ti	UM	0.04	6.89
	DM	0.1	0.8
AlCuMgSi	UM	0.03	0.68
	DM	0.14	1.2
brass	UM	1.21	3.22
	DM	0.73	0.83

In both cases, the cropped areas are distributed equally across the top and bottom edges of the image. The deviations between original image and narrowed image with less surface area are small in most cases. However, the deviation tends to increase with a further reduction of the surface area surrounding the slot. Furthermore, table 1 includes one single value of up to nearly 7 %. Even if it is an outlier, it means significant deviations are possible and cannot be ruled out. For this reason, the images taken to compare burrs should be roughly the same width to obtain reliable results.

Table 2 provides an overview over the deviations occurring in burr width, if the brightness of the sample exposure during measurement is varied for three different slots manufactured in brass.

Table 2 Change of the mean burr width with varied brightness specified in % of the maximum brightness value during the measurement of bras samples

breightness 1 / % | brightness 2 / %	**milling strategy**	**Absolut value of the parameter changes / %**
32.3 | 38.9	UM	5.4
	DM	0.1
33.1 | 46.7	UM	7.8
	DM	1
36.2 | 56	UM	2.2
	DM	4.4

The deviations can be significant with values up to 7.8 %. For good reliability, a brightness as constant as possible should be chosen during measurement. These results suggest that a quantitative comparison between different burr types are only possible with larger uncertainties. This is because of different ratios between burr width and surrounding surface area and the brightness during measurement must often be adjusted for each measurement.

Table 3 shows the comparison between the calculated mean burr width resulting from the two different slots length 0.52 mm and 1.9 mm. The deviations with a minimal value of 11.6 % suggest that the small slots excerpts include not enough information to allow a reliable calculation of globally valid burr parameters. This does include a statement of whether the long slots are capable of doing so, or not.

Table 3 Change of the parameters from the long slot to the short slot

material	**parameter**	**milling strategy**	**Absolut value of the**

			parameter changes / %
316L	mean burr width	UM	18.3
		DM	22.7
cp Ti	mean burr width	UM	14.6
		DM	11.6
AlCuMgSi	mean burr width	UM	12.7
		DM	47.6
brass	mean burr width	UM	28.7
		DM	26.1

4. Qualitative validation of the algorithm

To validate the algorithm qualitatively, the contour of the detected burrs is determined and plotted into a top few of the original height map. Figure 5 shows an example for such a plot. The plot includes an illustration of the micro mill cross section. Furthermore, the directions of the rotational speed n and the feed rate v_f are presented. The determined contour encloses the structure recognizable as burr. This is the case for all measured slots.

The deviations detected in section 3.3 are not directly striking when comparing the corresponding contour plots. For this reason, the images are not presented here. Only small deviations between plots can be seen in the edge areas of the burrs. So, the quantitative deviations measured in section 3.3 do not result from an incorrect workflow of the algorithm itself. This suggests that a different brightness used during the measurement or different amounts of surface area next to the burrs only change the calculated threshold to cut off the burrs from the surface.

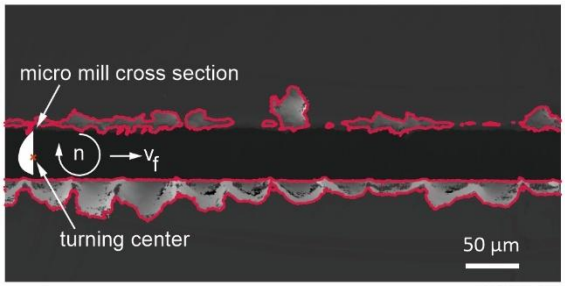

Figure 5. Height map with contour plot of the burrs

5. Conclusion

An automated algorithm was developed that can detect burrs of different magnitudes and with different proportions of sample surface next to the slots to slot width. Five parameters are defined to describe the burrs quantitatively. The parameters are the length ratio, the mean burr width and its deviation ratio and the mean burr height and its deviation ratio.

It has been shown that the proportion of surrounding surface area next to the slot and the brightness of the sample exposure during measurement can have a significant influence on the calculated burr parameters.

Furthermore, it was shown that a measured slot length of 0.52 mm is not enough to describe the burrs globally. However, the necessary measured length to do so is not yet specified.

Through the successful development of a new evaluation algorithm, it is now possible to describe different kinds of burr automatically without major adjustments. The same is achieved for different amounts of sample surface areas next to the slots.

It was shown that the brightness during measurement and the size of the analyzed image section influence the results of the algorithm. They should therefore be kept as constant as possible to acquire comparable, quantitative results. There have been no other studies found concerning burr evaluation addressing these issues.

Larger parts of the slots than 0,52 mm need to be evaluated to make a global statement about the burr size.

The next step will be an evaluation of how long the measured part of a slot must be, to calculate global burr parameters for the experimental setup used. Another investigation will be done into how reliable the results are for different slots machined with parameters as constant as possible. Then, the algorithm is used in studies that aim on minimizing the burr formation when micro milling slots in cp titanium and stainless steel 316L.

Acknowledgement

Funded by the Deutsche Forschungsgemeinschaft (DFG, German Research Foundation) - project number 544559694.

[2] Naming specific manufacturers is done solely for the sake of completeness and does not necessarily imply an endorsement of the named companies nor that the products are necessarily the best for the purpose.

References

[1] Huttenlocher K, Davoudi N, Schlegel C, Bohley M, Müller-Renno C, Aurich J, Ulber R, Ziegler C 2018 Paracoccus seriniphilus adhered on surfaces: Resistance of seawater bacterium against shear forces under the influence of roughness, surface energy, and zeta potential of the surface. Biointerphases **13** 1–13

[2] Kleine D, Chodorski J, Mitra S, Schlegel C, Huttenlocher K, Müller-Renno C, Mukherjee J, Ziegler C, Ulber R 2019 Monitoring of biofilms grown on differentially structured metallic surfaces using confocal laser scanning microscopy. Engineering in Life Science **19** 513-521

[3] Gillespie L 1979 Deburring precision miniature parts. Precision Engineering **1** 189-198

[4] Medeossi F, Sorgato M, Bruschi S, Savio E 2018 Noval method for burrs quantitative evaluation in micro-milling. Precision Engineering **54** 379-387

[5] Akkoyun F, Ercetin A, Aslantas K, Pimenov D, Giasin K, Lakshmikanthan A, Aamir M 2021 Measurement of Micro Burr and Slot Widths through Image Processing: Comparison of Manual and Automated Measurements in Micro-Milling. Sensors **21** 1-16

[6] Hajiahmadi S 2019 Burr size investigation in micro milling of stainless steel 316L International Jounrnal of Lightweight Materials and Manufacture **2** 296-304

[7] Ullah, Najeeb; Rehan, Muhammad; Farooq, Muhammad Umar; Li, Huaizhong; Yip, Wai Sze; To, Sandy Suet (2025): A comprehensive review of micro-milling: fundamental mechanics, challenges, and future prospective. In: *Int J Adv Manuf Technol* 137 (9-10), S. 4309–4351. DOI: 10.1007/s00170-025-15388-z.

[8] Aurich J, Reichenbach I, Schüler G 2012 Manufacture and application of ultra-small micro end mills. CIRP Annals **61** 83-86

euspen's 26th International Conference & Exhibition, Krakow, PL, June 2026
www.euspen.eu

Development of an innovative process chain to enhance the durability of functionalized polymer surfaces for real-world applications.

G. Baruffa[1]; G. Lucchetta[1]; M. Sorgato[1]

[1]Department of Industrial Engineering, University of Padova, via Venezia 1, Padova, 35131, Italy

giacomo.baruffa@studenti.unipd.it

Abstract
Surface engineering enhances injection-molded polymers components via micro- and nanometric features, but the poor durability of these nanostructures limits their real-world application. Two methods can boost robustness: self-protective surfaces, in which micrometric features shield nanopatterns from mechanical stress, and self-recovering surfaces, made from elastic materials that can rebound after deformation. This work demonstrates an IM-based process chain using micro-injection molding (μ-IM) to manufacture touch-resistant functionalized surfaces. Self-protective surfaces result from superimposing micrometric protective grids onto laser-induced periodic surface structures (LIPSS) responsible for structural coloration. Surface replication was studied using a rigid thermoplastic (PP) and a thermoplastic elastomer (SEBS). The effects of molding parameters on replication accuracy and uniformity at micro- and nanoscales were systematically examined. The results reveal markedly different replication mechanisms for the two materials. For PP, replication uniformity is primarily governed by the distribution of packing pressure and the hesitation effect. In contrast, SEBS replication is dominated by shear-induced macromolecular relaxation, which affects both replication accuracy and uniformity. Abrasion tests confirm that both strategies enhance surface durability; the self-recovering approach is more effective but more challenging to apply. Overall, this study provides new insights into the replication behavior of thermoplastic elastomers in μ-IM and establishes practical guidelines for industrial implementation of durable, nanostructured polymer surfaces.

Keywords: Molding (or moulding); Polymer; Wear; Microstructure

1. Introduction

Injection molding (IM) is widely used for the large-scale production of polymer components with micro- and nanoscale surface features [1]. However, nanofeature durability is limited by their small size and low mechanical properties of polymers, making the nanotexture sensitive to minimal stresses, such as the human touch [2]. A common mitigation strategy, known as self-protective surfaces, employs hierarchical architectures in which microscale features absorb most mechanical loads, thereby protecting the functional nanofeatures [3]. In this case, durability depends on the integrity of the microfeatures, which may degrade under repeated loading. The use of elastomers improves surface durability by enabling self-recovery of shape after load removal [2,4]. Thus, thermoplastic elastomers (TPEs) are suitable for combining self-recovering surfaces with IM.

Integrating nano-scale features into IM components requires defining a process chain to produce the nanotextures on the mold surface and accurately replicate them during molding [1].

Accurate replication is crucial for surface functionality, as poor replication can impair performance. Processing parameters significantly affect replication quality [5]. In the case of rigid thermoplastic materials, high mold and melt temperatures, raised injection speeds, and increased packing pressures are commonly reported as effective strategies to enhance replication accuracy [5,6]. Moreover, several studies have demonstrated that the replication quality is also affected by the distance between the gate and the features [6,7]. Conversely, the effect of IM process parameters on the replication accuracy of TPEs has been significantly less explored. TPEs are phase-separated materials, composed of a hard crystalline phase and a soft elastomeric phase, which respond differently to molding conditions. As with rigid thermoplastics, raised packing pressures and higher mold temperatures generally improve replication accuracy; however, these conditions may also lead to surface defects [8]. The influence of injection speed remains poorly understood, with some studies reporting adverse effects on replication accuracy [9]. Moreover, results have differed regarding the impact of melt temperature on replication accuracy [9,10]. To the best of the authors' knowledge, the replication uniformity of TPEs has not yet been fully studied.

This study demonstrates the feasibility of combining self-protective and self-recovering strategies within a single μ-IM process chain to manufacture touch-resistant diffractive gratings for structural coloration. Surfaces were replicated using a rigid thermoplastic (polypropylene, PP) and a thermoplastic elastomer (styrene–ethylene–butylene–styrene, SEBS). By systematically investigating the distinct replication mechanisms of these two materials and evaluating durability through abrasion tests, the effectiveness of the proposed approach was confirmed. Overall, this work provides new insights into TPE replication in μ-IM and establishes a practical framework for integrating robust nanofeatures into injection-molded components, offering comprehensive process and design guidelines for real-world applications.

2. Materials and methods

2.1. Micro injection molding

In this study, three previously developed self-protective surfaces were considered [11]. The surfaces, textured through ps-laser machining, consist of a diffractive grating based on infrared Laser-Induced Periodic Surface Structures (LIPSS), onto

which a square protective grid is superimposed (Fig. 1a). The protective microstructure differs across the surfaces: two mold inserts feature protective grids with pitches of 40 µm and 250 µm, respectively. In contrast, the third insert lacks a protective grid and is therefore referred to as Unprotected (UP). The protective grid exhibits a triangular cross-section, with a width of 10 µm and a height of 2.5 µm (Fig. 1b).

The inserts were mounted in a µ-IM mold, with a part thickness of 2 mm in the textured area, and replicated using a micro-injection molding machine (Micropower 15, Wittmann Battenfeld). The surfaces were replicated in both PP and SEBS, and the processing parameters were optimized for each material using a Design of Experiments (DoE) approach. In particular, the mold temperature (T_{mold}) and melt temperature (T_{melt}) were varied within the ranges recommended by the material supplier (Simax S.p.A.). The injection speed (V_{inj}) was varied between 50 and 200 mm/s, while the packing pressure (p_{hold}) ranged from 100 to 300 bar. For each experimental condition, three repetitions were performed, and ten molding cycles were interposed between the sampling of consecutive DoE points.

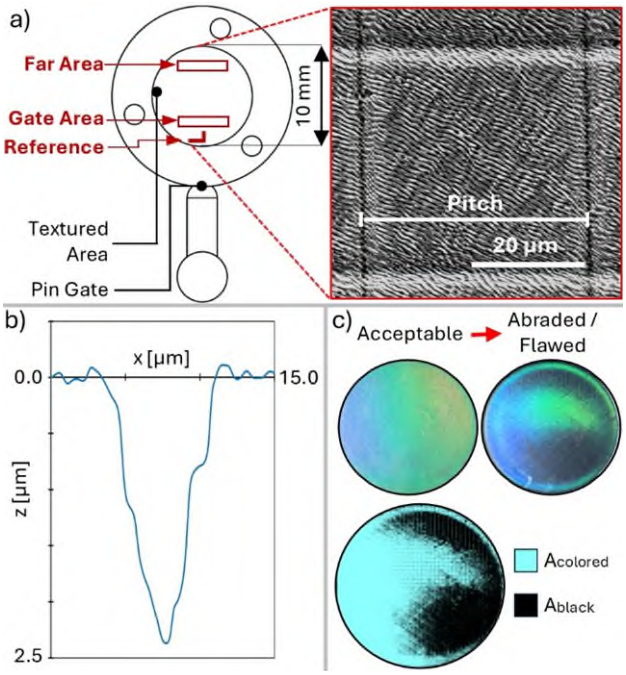

Figure 1. Surface manufacturing and evaluation: (a) schematic of the mold cavity and micrograph of the texture; (b) cross-section of the microfeatures; (c) functionality evaluation.

2.2. Surface geometrical evaluation

Both the mold inserts and the IM samples were geometrically characterized to quantify the degree of feature replication. Quantitative surface characterization was performed using a confocal profilometer equipped with a 100× objective (Plu Neox, Sensofar, SP). Reference features with L-shaped geometry were introduced on the mold surfaces in the gate area to maximize positioning accuracy. Surface scans (1.1 mm × 0.3 mm) were acquired in two different regions of each molded sample: one located 2.5 mm from the reference (*gate area*) and the other at a distance of 7.5 mm from the reference (*far area*) (Fig. 1a). Replication was assessed at micro- and nano-scales due to the hierarchical nature of the surfaces. Replication of the protective microfeatures was quantified by comparing the depth of the microfeatures on the mold inserts (d_{mold}) with the height of the protective mesh on the molded samples (h_{sample}). The micro-scale replication parameter, Q_{micro}, was defined as in eq.1:

$$Q_{micro} = (h_{sample} / d_{mold}) \times 100 \qquad \text{(eq. 1)}$$

Conversely, due to the difficulty of directly measuring LIPSS, sub-micrometric replication was quantified by comparing the roughness parameters Spk and Svk measured on the mold inserts and the molded samples, in accordance with ISO 25178-3. Two replication parameters were therefore defined: one for positive (Q_p, eq.2) and one for negative features (Q_v, eq.3):

$$Q_p = (Spk_{,sample} / Svk_{,mold}) \times 100 \qquad \text{(eq.2)}$$

$$Q_v = (Svk_{,sample} / Spk_{,mold}) \times 100 \qquad \text{(eq.3)}$$

For each acquired scan, the microfeatures were sampled at six locations, while roughness measurements were performed over three distinct areas.

2.3. Abrasion tests

The durability of the µ-IM-fabricated samples was evaluated using a tribometer (MFT-5000, Rtec Instruments), in which a PDMS counterface, consisting of a cylindrical PDMS pad with a diameter of 10 mm and an elastic modulus of 14 MPa, was slid against the textured surfaces. PDMS was selected as the abrasive material as it is considered representative of human touch [11]. A normal load of 5 N was applied, resulting in a nominal contact pressure comparable to that experienced under human finger contact. The abrasive moved sinusoidally over the entire surface at a sliding speed of 25 mm/s. The test was repeated on five different samples for each surface.

Surface functionality (visible structural color) was assessed for all samples that underwent abrasion tests using an optical microscope. The microscope's integrated illumination system ensured consistent lighting during each measurement, enabling the diffraction of white light and structural coloration. Images were captured after each wear test with a 20× objective.

As mechanical loading was applied, areas without structural color gradually appeared on the surface (A_{black}) (Fig. 1c). The size of these regions was quantified through a threshold-based image analysis of the captured pictures. This method allowed monitoring of the surface area that retained functionality under mechanical stress, defined as the colored area ($A_{colored}$) (Fig. 1c).

3. Results and Discussion

3.1. Replication with PP

All process parameters considered were found to be statistically significant in the replication of textures with PP. Process optimization for maximizing the replication accuracy of PP required high values of T_{mold} = 100°C, T_{melt} = 220°C, v_{inj} = 200 mm/s, and p_{hold} = 300 bar. These results are consistent with the literature, where high T_{mold} and T_{melt} reduce the solid skin thickness and material viscosity, respectively, while elevated V_{inj} and p_{hold} promote feature filling [5,6].

Interestingly, the nanoscale replication of LIPSS (Q_p and Q_v) drops sharply on surfaces with microgratings with a pitch of 40 µm (Fig. 2a). This effect is attributed to hesitation and feature-filling dynamics: the injected material initially fills the substrate, then the microcavities, and finally the LIPSS, in an order determined by flow resistance [12]. For surfaces with a 40 µm pitch grid, the high grid density delays LIPSS filling, promoting a thicker solid skin and thus reducing LIPSS replication [11].

Fig. 2b shows the mean replication indices as a function of the distance from the reference position in the gate area, indicating that replication fidelity decreases with increasing distance under identical processing conditions. Q_{micro} is the parameter least affected by distance from the gate, with differences below 5%. In contrast, Q_p and Q_v decrease significantly with increasing distance from the gate, with differences of up to 12.5% and 7.95%, respectively. This behavior is consistent with literature reports attributing it to the distribution of packing pressure in the cavity, highlighting the importance of this parameter for uniform replication of rigid thermoplastics [7].

Results for PP samples are acceptable: Q_{micro} stays above 90%, and variations in Q_p and Q_v don't affect texture functionality.

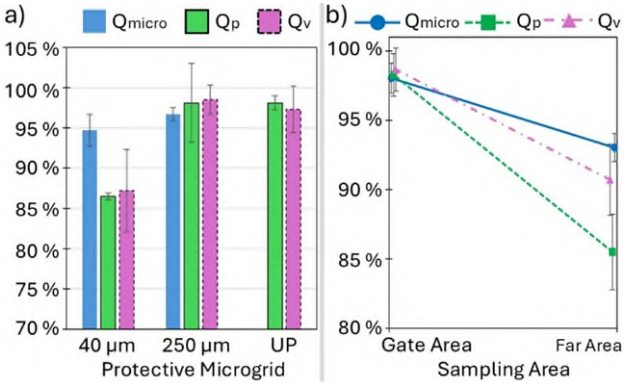

Figure 2. Replication with PP: (a) Surface replication indices; (b) Replication uniformity.

3.2. Replication with SEBS

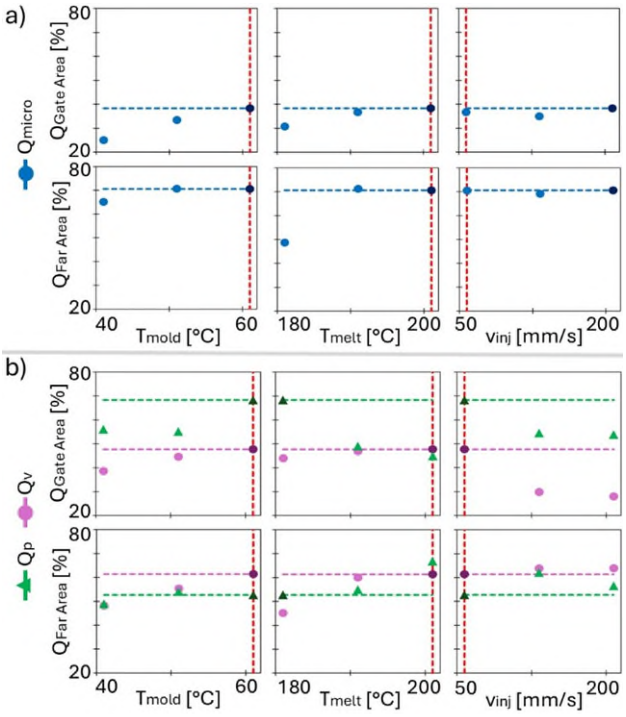

Figure 3. SEBS replication uniformity: a) microfeatures; b) LIPSS.

Process parameter optimization was also performed for SEBS, with the results shown in Fig. 3. Horizontal lines indicate the optimized values, and vertical lines represent the parameters selected for the final replication phase. Analysis of the collected samples revealed that the structural color exhibited a non-uniform distribution across the molded components (Fig. 4a), a phenomenon linked to pronounced heterogeneity in texture replication. Unlike previous reports on rigid thermoplastics and some studies in the literature, ANOVA analysis conducted on the SEBS replication DoE indicates that, although increasing the p_{hold} improves replication, this parameter is statistically negligible compared to the others [5,8].

Fig. 3 also shows that Q_{micro} uniformity is maximized at high injection speeds, whereas the opposite trend is observed for LIPSS replication. In this work, priority was given to replicating sub-micrometric features to preserve surface functionality; therefore, given the minimal effect of injection speed on Q_{micro}, the final samples were molded using v_{inj} = 50mm/s (Fig. 3a). Interestingly, replication near the gate is generally lower than in the region opposite it (Fig. 4a), contrary to observations in µ-IM of rigid thermoplastics [7]. At first glance, and considering the statistically negligible influence of packing pressure, this distribution might be attributed to feature replication during the filling phase. However, this explanation is contradicted by the observed decrease in replication fidelity with increasing injection speed (Fig. 3b). A more plausible explanation is that this behavior arises from greater polymer chain relaxation near the injection point [8,13]. During IM, macromolecules align along the flow direction, with a high degree of alignment at higher shear rates. Upon cooling, macromolecules in the hard phase of SEBS (styrene) become immobilized when their glass-transition temperature (T_g) is reached. In contrast, chains in the soft phase (ethylene-butylene), with a T_g below room temperature, retain some mobility. Consequently, soft-phase macromolecules undergo contraction, the extent of which correlates with their degree of chain alignment [13]. To verify this hypothesis, two injection molding simulations were performed using Moldflow software. In these simulations, the v_{inj} was varied between 50 and 200 mm/s, while the remaining parameters were kept constant at their highest set values to account for the most favorable conditions for replication (T_{mold} = 60°C; T_{melt} = 200°C; p_{hold} = 300 bar) (Fig. 3). The results confirmed the proposed mechanism: in downstream regions, cavity enlargement and the transition from velocity-controlled to pressure-controlled flow reduced shear rates. Higher shear rates in the gate area led to greater macromolecular elongation and relaxation, thereby compromising replication fidelity (Fig. 4a). This region exhibited poor structural color and insufficiently defined nanostructures. Overall, these findings highlight the strong influence of shear rate on macromolecular relaxation and its key role in replication quality, emphasizing the importance of minimizing shear to achieve uniform, high-fidelity surface replication in TPEs (Fig. 4a). The results obtained provide further insight into the complex role of v_{inj} in TPE replication, offering an initial explanation for some findings in the literature [8,9].

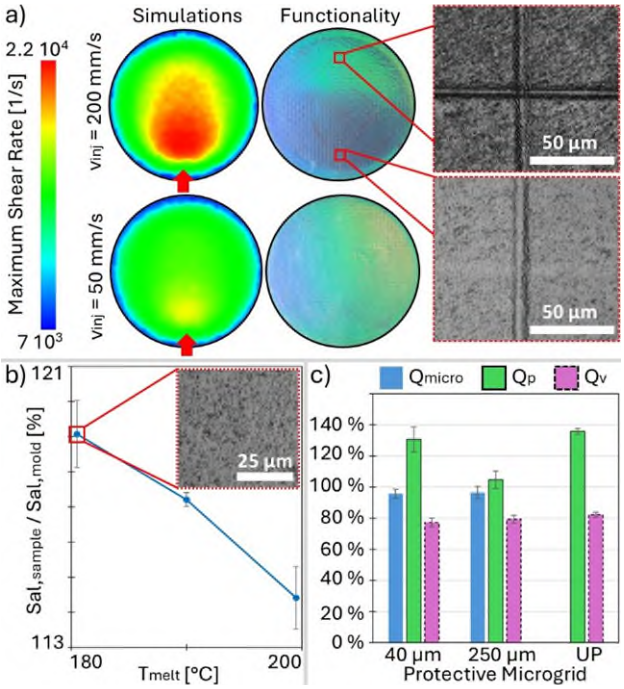

Figure 4. Replication with SEBS: (a) effect of cavity shear rate; (b) nanofeature periodicity in the gate region; (c) final values of the replication metrics.

Except for Q_p, the optimization suggests using high T_{melt} for all processing parameters (Fig. 3). The apparent anomaly in Q_p arises because low T_{melt} promotes surface defects near the gate (Fig. 4b), likely due to relaxation phenomena [8]. Specifically, as T_{melt} decreases, the periodicity of nanostructures increasingly deviates from that of the LIPSS mold inserts. Fig. 4b compares this behavior across different melt temperatures. Analysis using the roughness parameter Sal, sampled according to the

methodology in Section 2.2, shows that lower melt temperatures produce surfaces with nanofeatures significantly exceeding the mold periodicity. Based on this, a higher T_{melt} of 200 °C was chosen for the samples intended for wear testing. These latter observations may partly explain the conflicting results reported in the literature on the effect of T_{melt} [9,10].

Finally, increasing mold temperature consistently improved texture replication; therefore, a high T_{mold} of 90 °C was chosen for subsequent experiments. It is clear that T_{mold} is one of the most critical parameters for the replication of micro- and nanofeatures, even in µ-IM of TPEs [7,8]. The average replication parameter values obtained from the samples are shown in Fig. 4c, highlighting the significant influence of T_{mold}. The replication of the protective grid was excellent in both cases. Interestingly, increasing T_{mold} led to Q_p values exceeding 100%, likely due to adhesion phenomena between the polymer and the mold. In contrast to observations for PP, the variations in replication indices are not correlated with the protective grid pitch. This confirms that, as in TPE replication, the dominant factor is macromolecular relaxation rather than the hesitation effect, and cavity pressure [12,13].

3.3. Abrasion Tests

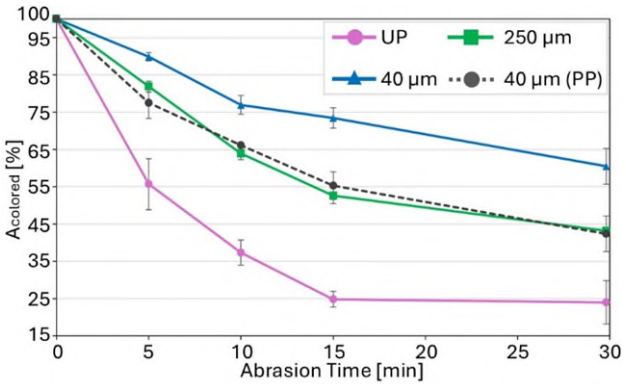

Figure 5. Abrasion test results.

After fabricating all surfaces, abrasion tests were conducted. Results in Figure 5 depict how the residual functional area evolves over abrasion time. The self-protective strategy was tested on SEBS, with similar trends seen in PP [11].

For each time interval, an increase in protective grid density results in a larger residual functional area ($A_{colored}$). The presence of a fine-pitch grid prevents the initial contact between the LIPSS and the PDMS counterface, thereby delaying the onset of abrasion. This behavior is not observed in the 250 µm pitch grid, where the microfeatures primarily reduce the contact pressure between the nanostructures and the abrasive surface [2,11]. The unprotected (UP) surface does not benefit from these mechanisms and consistently exhibits the lowest residual functionalized area among the three configurations.

The self-recovery effect was assessed only for the surface featuring microstructures with a 40 µm pitch. The SEBS surface exhibits enhanced abrasion resistance since it recovers the applied deformations upon removal of the mechanical load [4].

Both strategies enhanced surface durability. The self-recovery approach proved more effective; however, its implementation is technologically more demanding due to TPEs' requirements. Achieving uniform replication in TPEs requires careful control of cavity shear rates and the use of 2K-IM when the final component is a rigid polymer. In contrast, the self-protective strategy does not require material modifications, and the packing pressure mainly governs replication uniformity. This makes the issue readily addressable by adjusting the position of the textured area relative to the injection gate or, when this is not feasible, by employing injection–compression molding [6].

4. Conclusions

The objective of this study was to assess the potential to improve the durability of nanostructured surfaces produced by IM by combining self-protective and self-recovering strategies. To this end, texture replication was first optimized for both rigid thermoplastics and a TPE. In the case of PP, replication accuracy and uniformity were strongly influenced by the packing pressure distribution within the cavity and by hesitation effects during feature filling. Conversely, for TPEs, the replication process was primarily limited by shear-induced macromolecular relaxation in the soft phase, driven by elevated shear rates in the cavity.

Both proposed strategies resulted in enhanced surface durability. The self-protective approach, although less effective, offers greater industrial applicability due to its simplicity and compatibility with conventional injection molding processes. Overall, this work demonstrates different and complementary routes for implementing nanostructured surfaces in real-world applications, where they are expected to withstand repeated human touch and mechanical interaction.

References

[1] Zhang, H., Liu, H., & Zhang, N. (2022). A review of microinjection moulding of polymeric micro devices. *Micromachines*, **13**(9), 1530.

[2] Quan, Y. Y., Chen, Z., Lai, Y., Huang, Z. S., & Li, H. (2021). Recent advances in fabricating durable superhydrophobic surfaces: a review in the aspects of structures and materials. *Materials Chemistry Frontiers*, **5**(4), 1655-1682.

[3] Romano, J. M., Gulcur, M., Garcia-Giron, A., Martinez-Solanas, E., Whiteside, B. R., & Dimov, S. S. (2019). Mechanical durability of hydrophobic surfaces fabricated by injection moulding of laser-induced textures. *Applied Surface Science*, **476**, 850-860.

[4] Mirmohammadi, S. M., Hoshian, S., Jokinen, V. P., & Franssila, S. (2021). Fabrication of elastic, conductive, wear-resistant superhydrophobic composite material. *Scientific reports*, **11**(1), 12646.

[5] Vera, J., Brulez, A. C., Contraires, E., Larochette, M., Trannoy-Orban, N., Pignon, M., ... & Benayoun, S. (2017). Factors influencing microinjection molding replication quality. *Journal of Micromechanics and Microengineering*, **28**(1), 015004.

[6] Calaon, M., Tosello, G., Garnaes, J., & Hansen, H. N. (2017). Injection and injection-compression moulding replication capability for the production of polymer lab-on-a-chip with nano structures. *Journal of Micromechanics and Microengineering*, **27**(10), 105001.

[7] Lucchetta, G., Sorgato, M., Carmignato, S., & Savio, E. (2014). Investigating the technological limits of micro-injection molding in replicating high aspect ratio micro-structured surfaces. *CIRP Annals*, **63**(1), 521-524.

[8] Birkar, S., Mendible, G., Park, J. G., Mead, J. L., Johnston, S. P., & Barry, C. M. (2016). Effect of feature spacing when injection molding parts with microstructured surfaces. *Polymer Engineering & Science*, **56**(12), 1330-1338.

[9] Stormonth-Darling, J. M., Saeed, A., Reynolds, P. M., & Gadegaard, N. (2016). Injection Molding Micro-and Nanostructures in Thermoplastic Elastomers. *Macromolecular materials and engineering*, **301**(8), 964-971.

[10] Vega, M. D. J., Mead, J., & Barry, C. (2016). Injection molding microstructured substrates from rubber-containing polymers. *In AIP Conference Proceedings* (Vol. 1779, No. 1, p. 020012). AIP Publishing LLC.

[11] Sorgato, M., Baruffa, G., Oubellaouch, K., Zaniboni, G., & Lucchetta, G. (2025). A novel method for high-volume manufacturing of self-protective plastic surfaces to ensure durable anti-counterfeiting functionality. *CIRP Annals*.

[12] Yang, C., Huang, H. X., Castro, J. M., & Yi, A. Y. (2011). Replication characterization in injection molding of microfeatures with high aspect ratio: Influence of layout and shape factor. *Polymer Engineering & Science*, **51**(5), 959-968.

[13] Lu, J., Zhang, H., Chen, Y., Ge, Y., & Liu, T. (2022). Effect of chain relaxation on the shrinkage behavior of TPEE foams fabricated with supercritical CO2. *Polymer*, **256**, 125262.

euspen's 26th International Conference & Exhibition, Krakow, PL, June 2026
www.euspen.eu

Ultrafast laser fabrication of transparent superhydrophobic silica glass for optical window applications

Kai Liao[1], Chi Fai Cheung[1,*], Chunjin Wang[1]

[1]*State Key Laboratory of Ultra-precision Machining Technology, Department of Industrial and Systems Engineering, The Hong Kong Polytechnic University, Hung Hom, Kowloon, Hong Kong, China.*

**Corresponding author: benny.cheung@polyu.edu.hk*

Abstract

Transparent and durable superhydrophobic surfaces are critical for optical window applications. Inspired by the water-responsive transparency of Hydrangea hirta leaves, this paper presents a novel femtosecond laser processing method using a temporally shaped dual-pulse approach to fabricate large-area superhydrophobic silica glass surfaces with high optical transparency. By temporally shaping the laser pulses and adjusting the energy distribution, free-electron dynamics were precisely controlled to form uniform hierarchical micro/nanostructures, promoting dense nanowire and nanoparticle growth, enhancing the hierarchical structure, and facilitating superhydrophobicity. These structures stabilize a Cassie–Baxter wetting regime and minimize optical scattering. By using a single-scan, maskless process, a 1.5 × 1.5 cm² sample was fabricated in 75 seconds, demonstrating rapidity and scalability of the method. After fluorocarbon coating, the surface exhibited a water contact angle of 154.5° and optical transmittance above 88% in the 300–800 nm range. Surface analysis revealed a high CF_2/CF_3 ratio correlating with enhanced hydrophobicity. The surfaces also showed excellent mechanical, thermal, and chemical durability. More importantly, they appear translucent in air and become highly transparent underwater, with optical transmittance exceeding 90%. This work provides a rapid, scalable, and versatile method to produce transparent, durable, superhydrophobic silica glass surfaces for optical windows, self-cleaning coatings, anti-fouling surfaces, and smart optical devices.

Keywords: Ultrafast laser processing; Temporal pulse shaping; Silica glass; Superhydrophobic surface; Optical window applications

1. Introduction

Transparent optical components are widely used in optical windows [1], imaging systems [2], and sensing applications [3], where high optical transmittance is maintained under complex environmental conditions. However, conventional glass surfaces are easily contaminated by water droplets, dust, and organic pollutants, leading to optical degradation and reduced reliability.

Superhydrophobic surfaces, characterized by water contact angles exceeding 150°, provide an effective route to address this issue due to their water repellency and self-cleaning capability [4-6]. In such surfaces, droplets remain in a Cassie–Baxter (C-B) state, where trapped air pockets reduce the solid–liquid contact area and facilitate droplet removal [7]. However, achieving superhydrophobicity on transparent substrates remains challenging, as the micro/nanostructures required for water repellency often introduce strong light scattering, thereby reducing optical transparency. In addition, conventional fabrication methods, such as chemical etching and coating-based approaches, typically involve multi-step processes and limited controllability [8-10].

Femtosecond laser processing offers a promising solution for direct structuring of transparent materials, enabling localized energy deposition and flexible patterning without masks [11]. Various micro/nanostructures can be generated to modify surface wettability. Nevertheless, controlling the structural morphology to simultaneously achieve high hydrophobicity and high optical transparency remains a key challenge, particularly when balancing structure depth, feature size, and processing efficiency. To address these challenges, a microgroove-based surface architecture is proposed in this study, aiming to minimize the solid–liquid contact fraction while limiting the modified area to preserve optical clarity. A single-scan femtosecond laser strategy is employed to improve fabrication efficiency, and a temporally shaped dual-pulse approach is further introduced to enhance energy deposition and promote the formation of hierarchical micro/nanostructures.

The resulting surfaces exhibit high water contact angles, low adhesion, and high optical transmittance. This study demonstrates a controllable and scalable approach for fabricating transparent superhydrophobic surfaces, providing potential applications in optical windows, anti-fouling coatings, and advanced photonic devices.

2. Materials and methods

2.1. Materials

Commercial fused silica glass substrates with dimensions of 20 mm × 20 mm × 1 mm were used as the base material. Prior to laser processing, the samples were ultrasonically cleaned sequentially in acetone, ethanol, and deionized water for 10 min each to remove surface contaminants.

2.2. Methods

Surface structuring was performed using a femtosecond laser system with a central wavelength of 1030 nm and a pulse duration in the femtosecond regime. The laser beam was focused onto the silica surface through a galvanometer scanning system. The sample was mounted on a computer-controlled three-axis translation stage. To regulate energy deposition during laser–matter interaction, temporal pulse shaping was employed to tailor the energy distribution.

During processing, the laser beam scanned across the surface in a raster pattern. The scanning parameters, including pulse energy, scanning speed, and scanning interval, were optimized

to produce uniform hierarchical structures. The fabrication process was completed in a single-pass scanning strategy, enabling rapid large-area patterning. After laser structuring, the samples were treated with a fluorocarbon-based coating to reduce the surface energy. The coating was applied via vapor-phase deposition, forming a thin hydrophobic layer on the hierarchical structures.

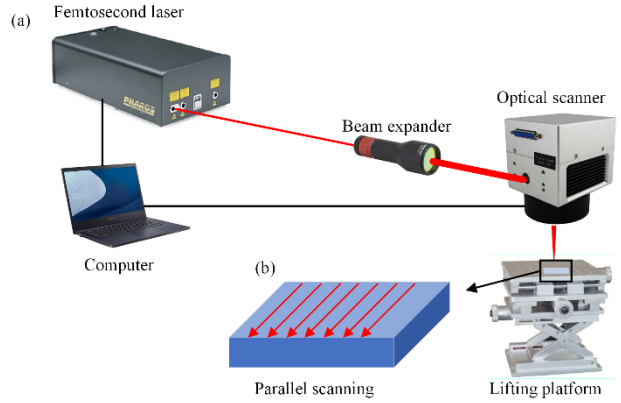

Figure 1. Schematic of the femtosecond laser processing setup: (a) optical configuration; (b) parallel scanning path.

2.3. Characterization

Surface morphology was characterized by scanning electron microscopy (SEM) and laser scanning confocal microscopy (LSCM). Surface wettability was evaluated by measuring the static water contact angle using a contact angle goniometer. The dynamic wetting behavior of water droplets was recorded using a high-speed camera. Optical transmittance was measured using a UV–visible spectrophotometer over the wavelength range of 300–800 nm. The surface chemical composition was analyzed by X-ray photoelectron spectroscopy (XPS), with particular focus on the relative contents of CF_2 and CF_3 groups. Mechanical durability was assessed through repeated abrasion tests, while thermal stability was evaluated by heating the samples at elevated temperatures. Chemical resistance was examined by exposure to acidic and alkaline solutions.

3. Results and Discussion

3.1. Design of superhydrophobic microstructures via single-scan processing

To achieve a balance between superhydrophobicity, optical transparency, and fabrication efficiency, an one-dimensional microgroove-based surface architecture was designed using a single-scan femtosecond laser processing strategy. The designed structure consists of periodically arranged microgrooves with controlled groove width (a), spacing (d), and depth (h), forming a composite solid–air interface that supports a stable C–B wetting state. The apparent contact angle is governed by the solid–liquid contact fraction (f_s), which can be approximated as $f_s = a/d$. As a result, minimizing f_s is essential for enhancing surface hydrophobicity [12].

From a structural design perspective, reducing the groove width or increasing the spacing can effectively decrease f_s. However, excessive spacing may lead to an increase in the effective ridge width due to laser–material interaction effects, thereby increasing the contact fraction. This introduces a trade-off, requiring an optimized spacing to balance contact reduction and structural fidelity. In addition to lateral parameters, the groove depth (h) plays a critical role in maintaining a stable C–B state. insufficient depth may result in liquid penetration and transition to the Wenzel state. As a result, the groove depth must exceed a critical value (hcr) to ensure the stability of the air-trapped interface [13].

Considering the laser spot size (~30 μm), the achievable groove width is constrained to the same order of magnitude. Consequently, the structural design primarily focuses on optimizing the spacing (d) to control groove overlap and fs. a spacing of 30 μm enables well-defined groove formation with sufficient depth while maintaining a reduced contact fraction.

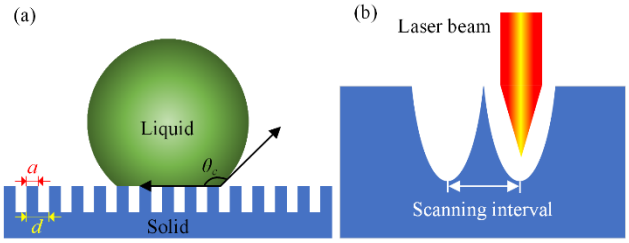

Figure 2. (a) Schematic illustration of droplet behavior in the C–B state. (b) microgroove formation under laser ablation.

3.2 Fabrication of microgroove structures via single- and dual-pulse laser ablation

To realize the designed microgroove structures, femtosecond laser ablation was first performed using a single-pulse scanning strategy to establish a baseline process window. By adjusting scanning speed and pulse energy, uniform microgroove arrays could be obtained under optimized conditions (80 μJ pulse energy, 100mm/s scanning speed,). However, despite achieving well-defined microstructures, the resulting surface exhibited a water contact angle of 145.8° after chemical modification (Fig.6a), which is below the superhydrophobic threshold.

To overcome this limitation, a dual-pulse laser strategy was introduced to enhance energy deposition. The dual-pulse sequences, generated using the burst mode of the laser system, consisted of two sub-pulses separated by ~20 ns. Three energy distribution modes—2:3 (Type 1, low–high), 1:1 (Type 2, equal), and 3:2 (Type 3, high–low)—were investigated at a constant total pulse energy of 80 μJ.

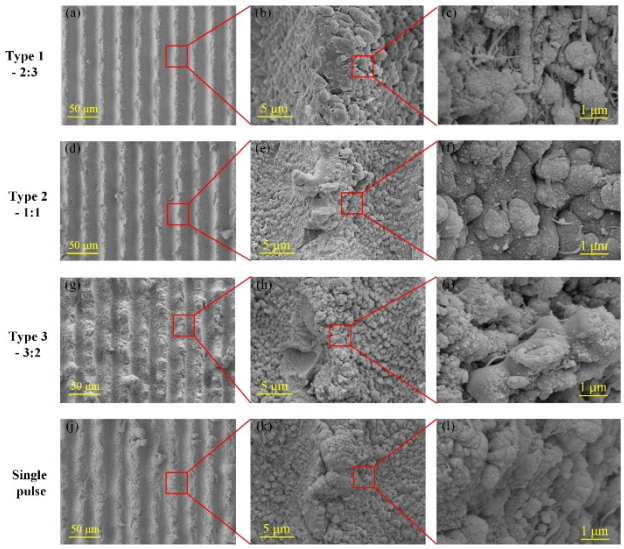

Figure 3. SEM of surface morphologies under different pulse modes. (a–c) Type 1; (d–f) Type 2; (g–i) Type 3; (j–l) single-pulse.

Compared with the single-pulse mode, the dual-pulse strategy significantly modified the resulting surface morphology. As shown in Fig. 3, the low–high sequence (Type 1) produced

uniform microgrooves with well-preserved ridge structures, accompanied by a dense distribution of nanoscale features, including nanoparticles and nanowire-like structures. These hierarchical micro/nanostructures are beneficial for enhancing surface roughness and promoting air entrapment. In contrast, Type 2 generated moderately developed nanostructures, while Type 3 resulted in irregular grooves with sparse nanoscale features. In addition to the improved nanoscale morphology, the dual-pulse strategy also enhanced the ablation depth. As shown in Fig. 4, the groove depth reached 16.8 μm for Type 1, which exceeds the critical depth required to maintain a stable Cassie–Baxter state (Fig.4).

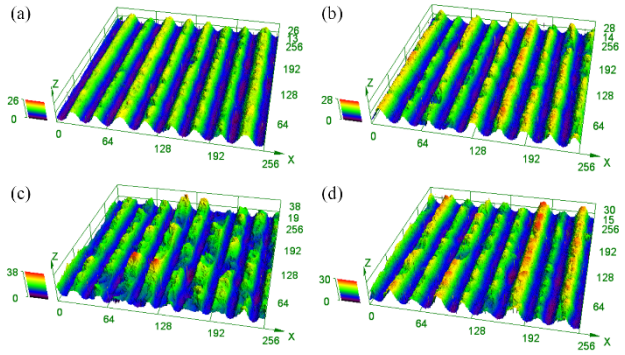

Figure 4. LSCM surface morphologies and under different pulse modes: (a) Type 1; (b) Type 2; (c) Type 3; (d) Single-pulse.

The superior performance of the low–high dual-pulse configuration can be attributed to the temporal modulation of energy deposition. As shown in Fig. 5, the initial low-energy pulse preconditions the surface, reducing reflectivity and plasma shielding, thereby enhancing the absorption of the subsequent high-energy pulse. This staged energy delivery facilitates more efficient material removal and promotes the formation of hierarchical structures.

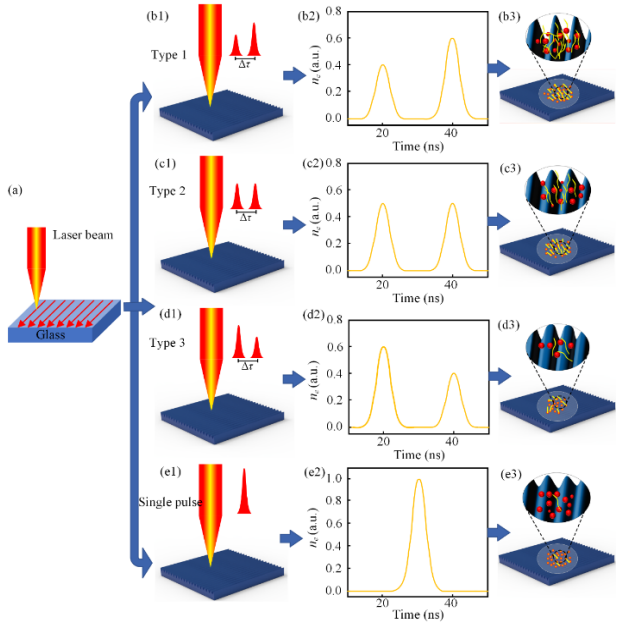

Figure 5. Schematic illustration of surface micro/nanostructure formation under various pulse modes.

On the whole, the low–high configuration (Type 1), enables the simultaneous formation of deeper microgrooves and richer nanoscale features. This synergistic enhancement of structure depth and hierarchical morphology provides a robust foundation for achieving stable superhydrophobicity in subsequent surface functionalization.

3.3. Performance evaluation of laser-fabricated surfaces

The functional performance of the optimized laser-fabricated surface was evaluated in terms of wettability, optical transparency, chemical composition, and stability.

3.3.1 Static wettability

The optimized surface exhibits a water contact angle of 154.5° after fluorination, indicating a stable Cassie–Baxter wetting state and superhydrophobic behavior. A low sliding angle of 2.8° further confirms minimal droplet adhesion (Fig. 6b).

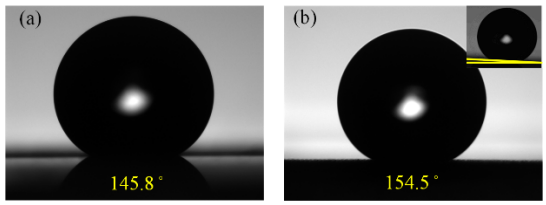

Figure 6. Static WCAs for surfaces under different pulse modes: (a) single-pulse. (b)Type 1 (with water sliding angle).

3.3.2 Dynamic wettability

Dynamic wettability was evaluated using droplet impact tests. The droplets spread upon impact and rapidly recoiled, bouncing off the surface without fragmentation. Multiple rebounds were observed, indicating low adhesion (Fig. 7).

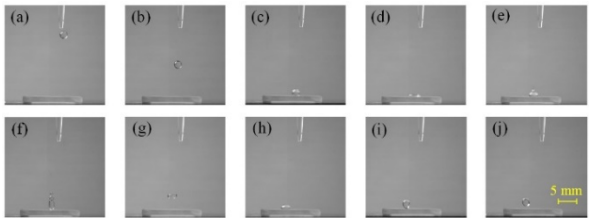

Figure 7. High-speed imaging of droplet impact dynamics on the laser-fabricated superhydrophobic glass surface.

3.3.3 Optical transparency

The optimized surface maintains a high optical transmittance of 88.78% in the visible range, compared to 93.23% for untreated glass. After surface fluorination, the transmittance remains at 87.67%.

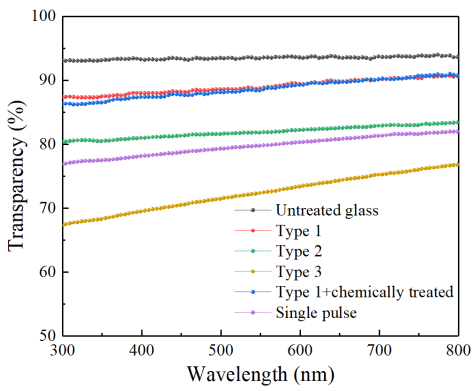

Figure 8. Comparison of optical transmittance in the visible wavelength range for samples processed under different pulse configurations.

3.3.4 Chemical composition

XPS analysis confirms the formation of a fluorinated surface layer with a high content of low-surface-energy functional groups, particularly $–CF_3$ species. This chemical composition contributes to reduced surface energy and plays a key role in achieving superhydrophobicity.

3.3.5 Stability and robustness

The optimized surface demonstrates excellent mechanical and environmental stability. The C-B state remains stable under droplet compression, and repeated tape-peeling tests show negligible degradation in wettability. In addition, the surface maintains its performance under outdoor exposure, water jet impact, thermal treatment, and chemical immersion, confirming its durability for practical applications.

4. Applications

The transparent superhydrophobic surface fabricated via the dual-pulse femtosecond laser single-scan strategy exhibits coupled optical and wetting functionalities, which are particularly relevant for optical window applications. In air, the hierarchical micro/nanostructures induce strong light scattering, resulting in a frosted appearance. Upon exposure to water, refractive index matching between water and glass suppresses scattering, leading to a rapid transition to a transparent state.

As shown in Fig. 9, the Hydrangea hirta leaf shows a similar behavior, appearing opaque in air and becoming transparent after wetting. The laser-fabricated surface mimics this mechanism, switching from a translucent state in air to a highly transparent state underwater. Quantitative measurements indicate a transmittance of ~88% in air and ~90% in water, with only a minor reduction compared to untreated glass.

This environment-responsive optical behavior enables dynamic regulation of light transmission, allowing the surface to maintain high clarity under wet or submerged conditions. Such characteristics make it highly suitable for optical windows operating in humid, rainy, or underwater environments, where both transparency and contamination resistance are critical.

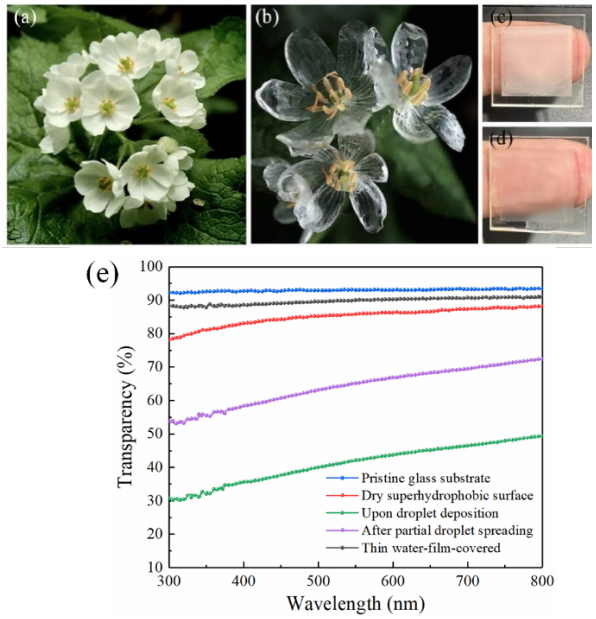

Figure 9. Bioinspired environment-responsive transparency：(a) Paraboea rufescens leaf in air (opaque); (b) after wetting (transparent); (c) laser-fabricated glass in air (frosted); (d) with water film (enhanced transparency); (e) transmittance comparison in air and underwater with untreated glass.

5. Conclusion

A femtosecond laser-based strategy was developed to fabricate transparent superhydrophobic microstructures on silica glass for optical window applications. By employing temporal pulse shaping, hierarchical micro/nanostructures composed of nanowires and nanoparticles were generated, enabling a stable Cassie–Baxter state with a water contact angle of 154.5° after surface modification.

High optical transparency was preserved despite surface structuring, with transmittance exceeding 88% in the visible range. Notably, the structured surface exhibited environment-responsive behavior, appearing translucent in air while achieving high transparency underwater (transmittance >90%) due to refractive index matching.

The process demonstrates high fabrication efficiency, enabling rapid patterning via a single-pass scanning strategy (1.5 × 1.5 cm^2 in 75 s), while maintaining good structural uniformity and durability. These results indicate a practical route for integrating superhydrophobicity and high optical performance in optical windows, with strong potential for self-cleaning and anti-fouling applications.

Acknowledgments

This work was supported by Innovation and Technology Commission (ITC) of the Government of the Hong Kong Special Administrative Region, China (ITS/609/24FP) and the postdoc matching fund of The Hong Kong Polytechnic University (Project Code: 1-W31V).

References

[1] Guan S, Li Y, Xu C, Yin N, Xu C, Wang C, Wang M, Xu Y, Chen Q, Wang D, Zuo L and Chen H 2024 Adv. Mater. **36** e2400342

[2] Zhao Z, Kuzhandaivel D, Zhou X, Zhang W, Yuan Y, Zhang G and Weng Z 2025 Prog. Org. Coat. **204** 109255

[3] Liao K, Wang W, Wang C and Cheung C 2025 ACS Appl. Mater. Interfaces **17** 17530–17542

[4] Liu Y, Moevius L, Xu X, Qian T, Yeomans J M and Wang Z 2014 Nat. Phys. **10** 515–519

[5] Li C, Wang F, Wang Y, Guo M, Li J, Deng C, Song F, Yang W and Wang Y 2025 Nat. Commun. **16** 2729

[6] Luo J and Guo Z 2024 Nanoscale 16 16404

[7] Liu Y, Zhang L, Hu J, Cheng B, Yao J, Huang Y and Yang H 2024 Surf. Coat. Technol. **477** 130352

[8] Zhang M and Li H 2025 Mater. Chem. Phys. **338** 130634

[9] Tong W, Wu Z and Xiong D 2023 Sustain. Mater. Technol. **37** e693

[10] Wang L, Liu M, Wu Y and Zheng H 2022 Nanomaterials **12** 4203

[11] Li K, Myers N, Bishop G, Li Y and Zhao X 2022 J. Manuf. Process. **79** 177–184

[12] Zhu J, Li W, Wang T, Feng H, Cheng J, Lin C, Wang X, Wang W and Chen S 2025 Chem. Eng. J. **505** 159218

[13] Liao K, Wang W, Mei X, Zhao W, Yuan H, Wang M and Wang B 2023 Mater. Des. **225** 111501

euspen's 26th International Conference & Exhibition, Krakow, PL, June 2026
www.euspen.eu

Porous metal aerostatic bearing restrictors manufactured with laser-based powder bed fusion

Onni Leutonen[1], Mikael Miettinen[1], Valtteri Vainio[1], Roy Björkstrand[1], Mika Salmi[1], Raine Viitala[1]

[1]*Aalto University, School of Engineering, Department of Energy and Mechanical Engineering, Espoo, Finland*

onni.leutonen@aalto.fi

Abstract

Aerostatic bearings are commonly used in precision and high-speed applications. Porous aerostatic bearings separate surfaces with a high-pressure gas film. The bearing type has no static friction and negligible dynamic friction at low speeds. Porous graphite is commonly used due to its crash resistance and the availability of the material with suitable permeability. However, the variability in material permeability leads to variation in bearing performance. Laser-based powder bed fusion of metals has been proposed as a method for manufacturing porous aerostatic bearing restrictors, with permeability adjustable by manufacturing parameters such as hatch spacing and laser power. In this study, a batch of four sets of four samples was manufactured, each set manufactured with a different hatch spacing. The permeability of the samples was measured before and after abrasive finishing, and the static load capacity, air consumption, and gap height were measured. The results were compared to a set of commercial porous graphite aerostatic bearings. The permeability and air consumption of the porous metal bearing samples were similar to those of the porous graphite bearings, with three out of the four sets showing similar results. The porous metal bearings had lower gap height than the porous graphite bearings at the same loads. The results indicate that the investigated porous aerostatic bearings, manufactured with laser-based powder bed fusion of metals, exhibit a level of repeatability similar to the tested set of commercial porous graphite aerostatic bearings.

Additive manufacturing, Gas bearing, PBF-LB/M, 3D printing

1. Introduction

Aerostatic bearings are used in precision engineering applications, including coordinate-measuring machines and high-speed spindles, where low friction and the absence of stick-slip are required. Aerostatic bearings are gas bearings that utilise an external pressure supply to form a thin, high-pressure film between the bearing and the opposing surface separating the surfaces [1]. Film thickness commonly ranges from 1-10 µm [1] to 5-20 µm [2], depending on the application. Compressed air is commonly used as it is readily available in industrial settings. The static friction of aerostatic bearings is zero, and the dynamic friction due to gas film shearing is negligible at low speeds [1].

Aerostatic bearings have a restrictor to limit the flow rate and to distribute the supplied pressurised gas to the gap between the bearing and the opposing surface. The permeability of the restrictor influences the stability, stiffness, load capacity, and operating gas consumption of the bearing. The restrictor types include porous median, slot, groove and orifice [2]. Bearings with porous restrictors generally exhibit high stiffness and load capacity while remaining stable [2].

A common material for porous median aerostatic bearing restrictors is synthetic porous graphite, such as graphite made for electrical discharge machining (EDM) electrodes. Graphite has favourable properties for use as a restrictor material due to its porous nature and crash resistance [1,3]. Although porous graphite aerostatic bearings have favourable properties, variation in graphite permeability affects the reproducibility [3]. Additional lacquer impregnation of the restrictor surface can be done to adjust the permeability [4-5]. The variation in performance limits the use of porous graphite aerostatic bearings in precision applications [3, 6].

The manufacturing of porous median restrictors using an additive manufacturing (AM) method, laser-based powder bed fusion of metals (PBF-LB/M), has been proposed where the open porosity of the restrictor is controlled by varying the laser power [7] or hatch spacing [8-9]. A grid pattern of vertical pillar-shaped pores spanning through the restrictor can be achieved with a suitable scan pattern and large enough hatch spacing to prevent full melting of the powder bed. There has been only limited research on this method to produce porous restrictors.

Previously, the authors have presented the manufacturing of porous metal aerostatic bearing restrictors with permeability and static load capacity comparable to porous graphite aerostatic bearings [9-10]. In the present study, the number of samples manufactured with the same hatch spacing is increased to four to evaluate the repeatability of the manufacturing process. The permeability, static load capacity, air consumption, and air gap height of four sets of porous metal aerostatic bearing samples are evaluated and compared with those of a set of four commercial porous graphite aerostatic bearings.

2. Methods

2.1. Bearing samples

The porous metal restrictors were manufactured with PBF-LB/M AM method from PH1 stainless steel powder. The restrictors were 37 mm diameter disks manufactured flat on the build plate. 0.5 mm of the outer edge of the disks was manufactured solid, and the rest was manufactured with varying hatch spacing parameters to achieve open porosity throughout

the sample. The hatch spacing values were selected based on the study by Leutonen et al. [9], which used similar samples with hatch spacings ranging from 110 µm to 220 µm. In the present study, hatch spacings of 165 µm, 170 µm, 180 µm, and 190 µm were used. Four samples for each hatch spacing parameter value were manufactured.

In the AM process of the porous restrictor, a meander pattern with 90° rotation was used with a layer height of 40 µm, a scan speed of 1083 m/s, a laser power of 225 W, and a laser spot diameter of 80 µm. No upskin was used to leave the pores open. The restrictors were cut to a thickness of 4.5 mm with wire EDM as the samples were removed from the build plate. The restrictors were mounted to bearing bodies with epoxy adhesive (Figures 1 and 2) as is commonly done with graphite restrictors.

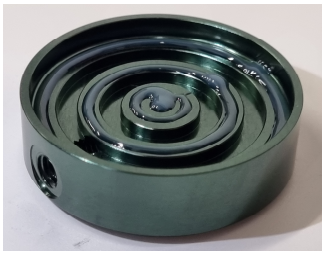

Figure 1. Anodised aluminium bearing body with air supply grooves. Epoxy adhesive applied with a robot [11].

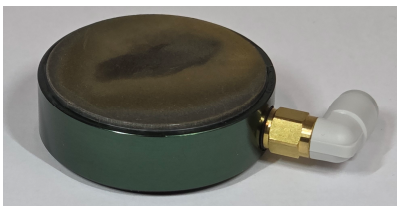

Figure 2. Porous metal restrictor cut with wire EDM joined to the bearing body with adhesive.

Due to the internal stress from the AM process, the restrictor disks had deformed after removal from the build plate to an extent rendering them unsuitable for aerostatic bearings (Figure 3). The restrictors were finished first with 100 µm and then with 30 µm abrasive film until a flat surface was achieved (Figure 4). Light abrasive finishing was used to minimise smearing of the metal surface, which could block the pores. A finished sample is shown in Figure 5, and the porous surface is shown in Figure 6.

A set of four commercial New Way porous graphite aerostatic bearings with the same porous restrictor dimensions was selected as a reference for the performance measurements.

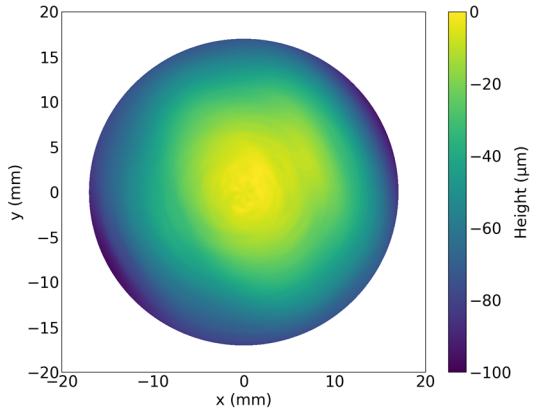

Figure 3. Exemplary restrictor surface flatness, measured with a contacting form measurement machine, after removal from the build plate with wire EDM.

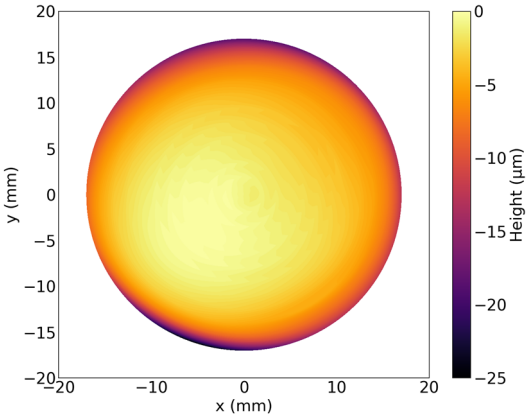

Figure 4. Exemplary restrictor surface flatness, measured with a contacting form measurement machine, of the same sample as in Figure 3 after abrasive finishing. The scale is different to Figure 3.

Figure 5. Sample finished with an abrasive.

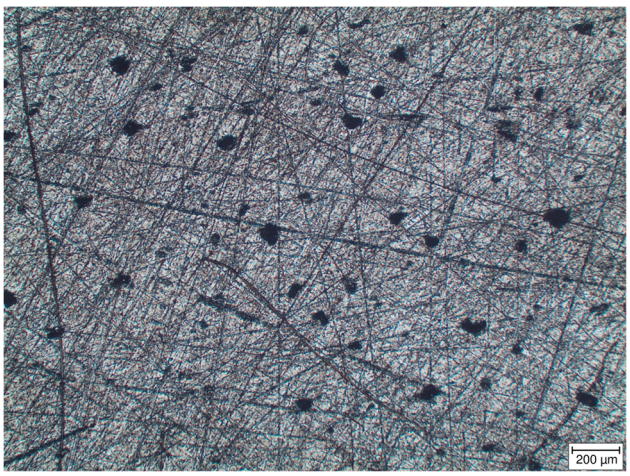

Figure 6. Restrictor surface of sample with 190 µm hatch spacing after abrasive finishing.

2.2. Measurement setup and procedure

The automated measurement setup is presented in Figure 7. The bearing sample was mounted to a four-bar linkage system with a ball joint. The four bar linkage system had flexures to enable free movement only in the vertical direction. A force was applied to the loading bar with a pneumatic cylinder. The applied load was measured with a force transducer mounted between the four-bar linkage system and the ball joint. The gap height between the bearing and the opposing surface was measured with three capacitive displacement sensors. The capacitive displacement sensors were attached around the bearing in a separate holder to disconnect the measurement frame from the loading frame.

The bearings were loaded with the pneumatic cylinder with force ranging from 50 N to 600 N in 20 even steps. In each measurement, the bearing was first loaded without supply pressure to measure the reference values for the capacitive displacement sensors to counteract the effect of the loading frame deflecting. The bearing then was pressurised to 0.6 MPa, and the loading cycle was repeated. The system was let to stabilise after each load change before the measurement.

The short circuit flow rates of the bearing samples were measured without an opposing surface. 0.6 MPa pressure was supplied to the bearing, and the flow rate was allowed to stabilise before measuring the flow rate. The sample permeability κ was calculated with Darcy's equation (Equation 1) where Q_{SC} is the short circuit flow rate, μ is the dynamic viscosity of air, h is the porous restrictor height, A is the surface area of the restrictor porous section, p_s is the supply pressure and p_a is the ambient pressure [5, 12].

$$\kappa = \frac{2Q_{SC}\mu h p_a}{A(p_s^2 - p_a^2)} \quad (1)$$

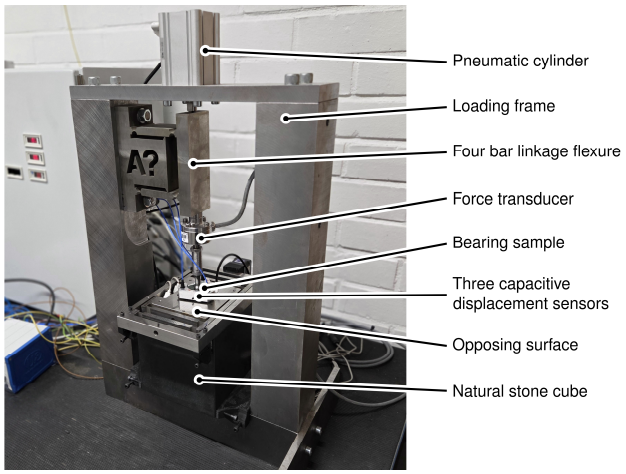

Figure 7. Measurement setup developed by Miettinen et al. [12].

3. Results and discussion

The restrictors manufactured with PBF-LB/M were deformed after the removal from the build plate (Figure 3). The restrictor surfaces were finished with an abrasive to reach a flat surface (Figures 4 and 5). The permeability results before and after abrasive finishing are presented in Figure 8. All but one sample had permeability within the optimal range before abrasive finishing, and all the samples were in the optimal range after abrasive finishing. The samples with hatch spacings of 165 µm, 170 µm, and 180 µm have permeabilities similar to the porous graphite reference samples, while the samples with 190 µm hatch spacing have higher permeability.

Although the permeability of the samples is on a similar level to the porous graphite bearings, the porous metal restrictor does not distribute the supplied pressurised gas uniformly to the surface of the restrictor. The porous graphite restrictor has pores spanning across the material allowing the flow of gas to all directions. Due to the PBF-LB/M AM process used in this study, the pores of the porous metal restrictors are only vertical through the restrictor. Therefore, the supplied gas can flow only straight through the vertical pores of the restrictor, and the gas does not flow through some of the pores. The supplied gas is not distributed to the whole surface of the restrictor when it exits the restrictor, but only on the areas where it was supplied on the opposite side of the restrictor. The permeability was calculated based on the measured flow through the restrictor and the total surface area of the restrictor.

The feed geometry could be adjusted to evenly distribute the supplied pressurised gas across the whole surface area of the restrictor on the supply side, ensuring even distribution of gas to the gap between the bearing and the opposing surface.

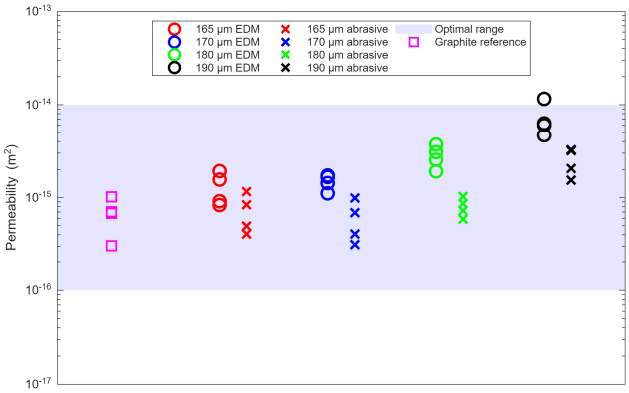

Figure 8. Bearing restrictor permeability after wire EDM cutting and after an additional abrasive finishing. Permeability calculated with Equation 1 with the measured short circuit flow rate at 0.6 MPa supply pressure. The shaded area is the permeability range for optimal static and dynamic performance of porous aerostatic bearings [3].

The load and gap height results for the four sets of samples and an additional set of four commercial New Way porous graphite aerostatic bearings are presented in Figure 9, with the average of each set of four bearings marked with a line and a shaded area that includes all four samples. The measurement results show that the load and air gap height for all samples with hatch spacing of 165 µm, 170, µm and 180 µm overlap while the samples with 190 µm hatch spacing have higher gap height. The reference porous graphite samples maintain a higher gap heights with increased load compared to the other tested samples. The width of the area including all the samples is approximately the same for all the tested sets of samples indicating a similar level of variation in the performance.

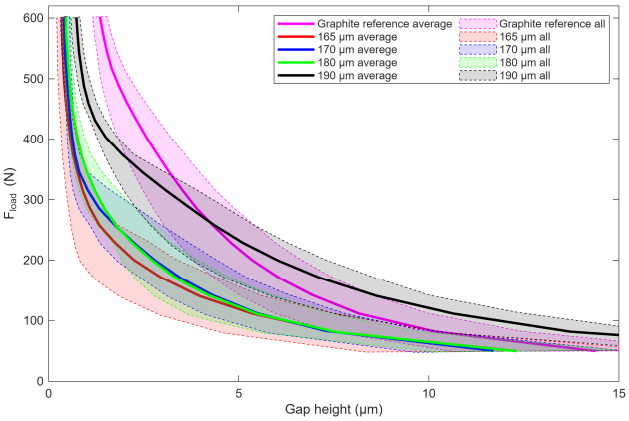

Figure 9. Bearing gap height and load capacity. The average of four samples is shown as a line, and the shaded area includes all four samples. Results include one set of commercial porous graphite aerostatic bearings as a reference and four sets of porous aerostatic bearings with metal restrictors.

In similar manner as in Figure 9, the air consumption and gap height are presented in Figure 10 with a line representing the average of the set of samples and a shaded area including all the samples. The samples with 165 µm, 170 µm, and 180 µm hatch spacing have flow characteristics similar to the porous graphite reference samples. However, at gap heights of below 5 µm, the

flow rates deviate with porous graphite flow rate gradually decreasing with decreasing gap height while the porous metal samples maintain the flow rate better with decreasing gap height. This is presumably due to the slight convex shape of the porous metal restrictor surfaces, which is not ideal for porous aerostatic bearings.

The convex shape (Figure 4) leaves a larger gap on the outer part of the restrictor compared to the centre. As the reference for air gap height is the point of contact between the restrictor and the opposing surface, the effective air gap is larger at the outer section of the restrictor surface. A larger gap height means less flow restriction for the flow out of the gap and therefore increases the measured flow rate. Improved performance could be achieved with a flatter or slightly concave restrictor surface geometry. Heat treatment could help relieve stress and reduce deformation of the restrictor after removal from the build plate. Additionally, improved surface finishing process, such as EDM, could be used to achieve a flatter surface geometry and fewer pores being closed.

The samples with 190 µm hatch spacing have significantly higher flow rate at all gap heights compared to all the other tested samples. The higher flow rate is expected based on the higher permeability than the other samples in Figure 8.

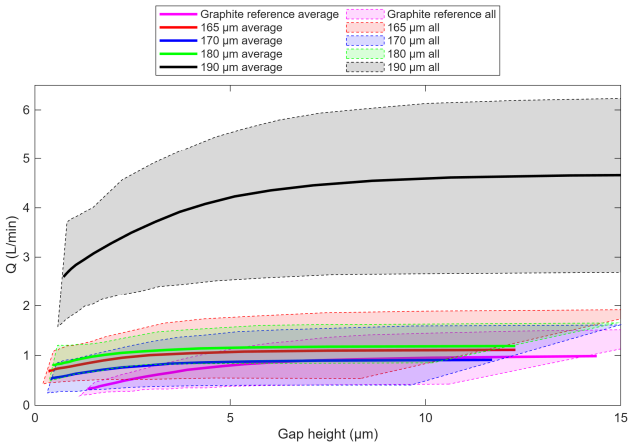

Figure 10. Bearing gap height and air consumption. The average of four samples is shown as a line, and the shaded area includes all four samples. Results include one set of commercial porous graphite aerostatic bearings as a reference and four sets of porous aerostatic bearings with metal restrictors.

4. Conclusions

A batch of porous metal restrictors were manufactured with PBF-LB/M AM method. The permeability of the restrictors was adjusted by varying the hatch spacing. The restrictors were mounted to bearing bodies and the restrictor surfaces were finished with an abrasive. Permeability, static load capacity, air consumption, and gap height were measured. A set of commercial porous graphite aerostatic bearings was also measured for reference.

The permeability of all the samples was within the optimal range found in the literature. The samples with 165 µm, 170 µm, and 180 µm hatch spacing had similar permeability as the porous graphite samples while the samples with 190 µm hatch spacing had slightly higher permeability. The abrasive finishing slightly decreased the permeability of all the samples.

The samples with 165 µm, 170 µm, and 180 µm hatch spacing had similar static load capacity while the samples with 190 µm hatch spacing had higher gap height compared to the other samples. The reference samples had similar gap height when the gap height was above 5 µm and higher gap height than the bearings with metal restrictors when the gap height was below 5 µm. This is presumably due to the convex shape of the porous metal restrictor surfaces. The width of the graphs of the porous metal bearings and the porous graphite bearings were approximately the same, indicating similar level of variation in gap height at each load step.

The samples with 165 µm, 170 µm, and 180 µm hatch spacing had similar air consumption to the porous graphite bearings while maintaining higher flow rate at gap heights of less than 5 µm, presumably due to the convex shape of the restrictors. The variation in the flow rates was also similar to the porous graphite bearings. The samples with 190 µm hatch spacing had significantly higher air consumption.

The results of this study corroborate the feasibility of manufacturing porous metal restrictors with the PBF-LB/M process. The results indicate that AM porous aerostatic bearings exhibit a level of repeatability similar to the tested set of commercial porous graphite aerostatic bearings. However, further research is needed to determine the optimal AM process for the porous region and the optimal postprocessing and finishing methods for the bearing surface.

5. Acknowledgements

The research was funded by Business Finland (Better bearing, seal and vibration technology, grant number 1740/31/2025).

Part of the research was performed at the Aalto Digital Design Laboratory of Aalto University.

References

[1] Slocum A H 1992 Precision Machine Design

[2] Gao Q, Chen W, Lu L, Huo D, Cheng K 2019 Aerostatic bearings design and analysis with the application to precision engineering: State-of-the-art and future perspectives *Tribology International* 135 pp 1-17 doi: 10.1016/j.triboint.2019.02.020

[3] Al-Bender F 2021 *Air Bearings - Theory, Design and Applications*

[4] Rasnick W H 1972 Air-bearing rework and impregnation *United States Atomic Energy Commission*

[5] Rasnick W H, Arehart T A, Littleton D E and Steger P J 1974 Porous graphite air-bearing components as applied to machine tools *Society of manufacturing engineers*

[6] Vainio V 2025 Porous aerostatic bearing manufacturing and static performance, Doctoral thesis, Aalto University

[7] Sadahiro R, Nakayama S, Kawada S, Miyatake M, Sasaki S and Yoshimoto S 2023 Development of aerostatic porous bearings manufactured using metal 3d printing technology *Proc. IMechE, Part J: Journal of Engineering Tribology* 237 pp 1306–15 doi: 10.1177/13506501211070090

[8] Schoar S, Elspaß A, Dohmen H J, Kleszczynski S and Benra F 2021 Design and fabrication of optimised aerostatic dry gas seals using advanced numerical models and next generation production technology, *Polytechnic & design* 9 no 3 pp 156–66 doi: 10.19279/TVZ.PD.2021-9-3-11

[9] Leutonen O, Björkstrand R, Miettinen M, Salmi, M and Viitala R 2025 Additively manufactured porous restrictor for aerostatic bearing *euspen, Conference Proceedings - 25th International Conference and Exhibition*

[10] Leutonen O, Miettinen M, Viitala R 2025 Performance of additively manufactured surface ground porous metal aerostatic bearings *euspen and ASPE, Special Interest Conference: Advancing Precision in Additive Manufacturing*

[11] Leutonen O, Vainio V, Harding L, Haverinen P, Miettinen M, Viitala R 2024 Mechanized adhesive applying for porous aerostatic bearings *euspen, Conference Proceedings - 24th International Conference and Exhibition*

[12] Miettinen M, Vainio V, Theska R and Viitala R 2024 On the static performance of aerostatic elements *Precision Engineering* 89 pp 1-10 doi: 10.1016/j.precisioneng.2024.05.017

euspen's 26th International Conference & Exhibition, Krakow, PL, June 2026
www.euspen.eu

Investigation of the transferability of pulsed electrochemical machining process parameters from simple substitute models to complex manufacturing applications

Falko Böttcher[1], Sepideh Ghorbanalipour[2], Jan Edelmann[1]

[1]*Fraunhofer IWU, Institute for Machine Tools and Forming Technology, Reichenhainer Straße 88, 09126 Chemnitz, Germany*
[2]*Chemnitz University of Technology, Reichenhainer Straße 70, 09126 Chemnitz, Germany*

Jan.Edelmann@iwu.fraunhofer.de

Abstract

Pulsed electrochemical machining (PECM) is an innovative manufacturing technology that is used to produce high-precision components with finishing properties. Before starting to manufacture functional components, it is necessary to develop a tailored removal fixture. This consists of several components, whereby the fabrication of the cathode can be time-consuming and expensive. To prevent defects on the removal fixture during process launch or fine adjustment of the PECM process, typically operating at a front working gaps less than 0.030 mm, the use of a substitution model is advisable. By using a less complex removal fixture, as the one used in electrochemical material characterization DIN SPEC 91399, it is possible to quantify the material-specific dissolution behavior and determine initial process parameters for the desired application.
The investigations focus on the transferability of the PECM process from a simplified substitution model to the complex manufacturing fixture for producing an internal gear wheel. First, the two PECM removal fixtures are compared in terms of fixture design. Using the material characterization method DIN SPEC 91399 with the proposed substitution model, the removal of the difficult-to-machine martensitic stainless steel ASTM F899 is analyzed by varying the voltage, feed rate, and pulse length. By conducting experiments with both PECM fixtures using identical machine parameters, the change of the front working gap and the machine current is analyzed for lowering of the voltage potential.
Based on the comparison, the transferability of the proposed method for appropriately adjusted process parameter can be rated. By optimized machine input parameters for PECM applications, possible short-circuit errors can be prevented that could damage the customized removal fixture. Furthermore, this solution helps to predict the frontal end working gap during the fine adjustment of the dimensional accuracy of the components.

Keywords: Electrochemical machining (ECM), Fixture, Gear, Precision

1. Introduction

1.1. PECM process

Pulsed electrochemical machining (PECM) is a production technology that uses electrical pulses to process and shape electrically conductive materials. It is used in manufacturing and materials research founded on an advanced development of traditional electrochemical machining. The principle is based on the anodic material dissolution, in which a metallic workpiece is dissolved by electrochemical reactions into an electrolyte solution induced by a voltage potential between a tool (cathode) and the workpiece (anode). In PECM the material removal is superimposed with a pulsed direct current and narrow interelectrode gaps of less than 0.1 mm, creating the negative shape of the cathode direct onto the workpiece during a continuous motion of the tool. Besides typical process advantages like a cold, burr-free and contact-free material manufacturing without introducing process-induced residual stress into the workpiece, components manufactured by PECM show a high surface finish and tight tolerances [1].

1.2. Material processing in the interelectrode gap

Due to the contact-free machining, the machining area is basically emphasized as interelectrode gap, considering the area between the cathode and anode. It is commonly divided into a frontal gap and a lateral gap as shown in ***Figure 1***.

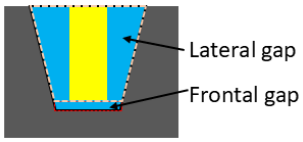

Figure 1. Basic scheme of the frontal gap s_f and a lateral gap s_l for ECM.

The distribution of the interelectrode gap is influenced by various factors. These include the working medium (electrolyte solution), the specific dissolution behavior of the workpiece material, the cathode geometry and the used electrolyte flow design. The applied electrical parameters, such as voltage potential, pulse length, and the pulse repetition frequency, causing a material processing through the electrical field distribution in the interelectrode gap. However, the multiphysical phenomena highlight challenges for achieving high process accuracy quickly. Nethertheless, an high precision PECM process requires knowledge of the exact size of the evolving interelectrode gap [2].

Previous investigations on the production of internal gears have shown that the design and fabrication of the shape cathodes can sometimes be time-consuming and expensive when using PECM as a finishing technology [3]. It was found that

frontal working gap of less than 0.03 mm was necessary to achieve tight shape tolerances and at high surface qualities. The functionally necessary tight working gaps put high demands on the fine adjustment of the process parameter to prevent the tool from being damaged as a result of a undesired short circuit.

This study addresses the question of the potential for utilizing a simplified substitution model to determine the PECM process input variables in advance and, in a second step, apply those for the development of a dedicated gear application process. The transferability is examined based on comparisons of the frontal end working gaps.

2. Material, experimental setup and methods

2.1. Material

In the experiments the stainless steel X30CrMoN15-1/ ASTM F899/ DIN 1.4108 was used. The martensitic phase allows a widely usablility for medical equipment, wear-resistant and corrosion-sensitive drivetrain or maritime applications, to highlight a few. Through the hardened condition of the samples between 40 to 44 HRC, this steel can be classified as difficult-to-cut material. The primary alloying elements of the chemical composition are listed in ***Table 1*** [4].

Table 1. Primary alloying elements of the stainless steel ASTM F899.

	Cr	Mo	N	C	Si	Fe
Min	14.5	0.30	0.35	0.28	0.30	Balance
Max	16.0	0.60	0.44	0.34	0.80	

2.2. PECM machine

The experiments were conducted on an industrial PECM machine, model PEM Center 8000 from PEMTec SNC. The electrical power has a maximum voltage of 20 V at a machine current up to 8000 A. An integrated electrolyte purification with regulation of temperature, electrical conductivity, and pH-value guarantees a reproducible PECM processing. During the experiments, the parameters listed in **Table 2** were constant.

Table 2. Constant parameters during the PECM experiments.

Constant Parameter	Value
Electrolyte solution	Sodium nitrate $NaNO_3$
pH value	7.0
Temperature	20.5°C ± 1.0°C
Electrical conductivity	72.0 mS/cm ± 1 mS/cm
Tool oscillation (Amplitude)	On (0.350 mm)
Pulse frequency	50 Hz
Frontal start working gap	0.050 mm ± 0.005 mm

2.3. Design of PECM removal fixtures

All electrochemical machining tasks can essentially be broken down into the basic elements of an electrolytic cell. These consist of a tool (cathode), the workpiece (anode), the electrolyte solution, and an electrolyte flow system which delivers the fresh working medium to the processing area (inflow) and removes the reaction products from the processing point (outflow). A stable mounting in the machining room is achieved using clamping elements. Figure 2 shows a conceptual design of these fixture components for removal fixture 1 (proposed substitution model) and removal fixture 2 (gear manufacturing). Further core aspects of the removal fixture design are summarized in **Table 3**.

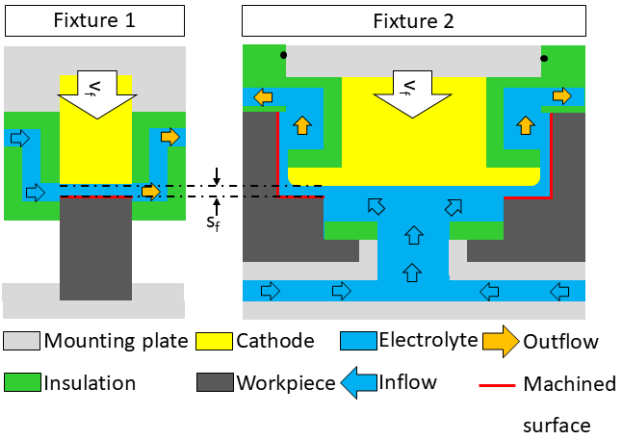

Figure 2. Conception of PECM removal fixtures.

Table 3. Core aspects of the removal fixture design.

	Fixture 1 Substitute model	**Fixture 2** Gear application
Machining orientation	Frontal gap only	Frontal and lateral gap
Cathode shape (projection area)	Circular area	Inverse gear profile
Cathode area	113 mm²	618 mm²
Sample dimension (projection area)	Rod, d = 12 mm	Circular ring with Internal diameter of d_i = 75.75 mm
Flushing direction	Side	Side
Sinking depth	Max. 60 mm	Max. 29 mm

2.4 Analytical aspects towards the adjustement of the interelectrode gap

Pulsed electrochemical machining enables high dimensional accuracy and surface quality using small interelectrode gaps of less than 0.1 mm. To adjust the dimensions of applications, often the variation of the voltage potential is selected [5]. As a result of the voltage potential reduction, the electrical resistance of the electrolyte solution decreases, allowing a stable reduction of the interelectrode gap width s, which can be determined using analytical methods as follows [1]:

$$s = \frac{(U - \Delta U) \cdot V_{sp} \cdot k}{v_f}$$

The value U is voltage potential in V, ΔU the polarization voltage, V_{sp} the specific material removal, k the electrical conductivity of the electrolyte and v_f the applied feed rate. The process input parameter are determined using the method DIN SPEC 91399. The results provide information about the specific material removal depending on the applied machine input parameters [6]. For the determination of the frontal interelectrode gap width, the machine's internal short-circuit detection system was used. The gap width value was accepted, after a constant material removal and machine current of at least 30 seconds had been realized.

3. Experimental validation of the PECM process

3.1 Repeatibilty measurement of the sinking axis

First, the repeatability of the sinking axis was measured using removal fixture 1. Ten contact runs were performed along the sinking path to determine the position of the component surface at the frontal gap, while the resulting axis coordinate being

recorded for each experiment. The following **Figure *3*** shows the deviation of the sinking axis repeatability, normalized to the first measurement R1.

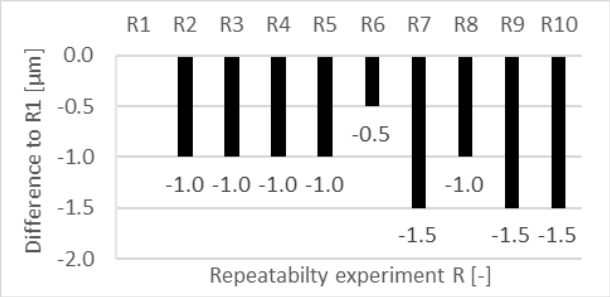

Figure 3. Summary of the 10 experiments for checking the repeatabilty of the PECM sinking axis.

After 10 experiments, the average deviation was within 1 µm. Regardless of the surface roughness of the samples before processing, the initialization shows that the PECM machine has a very high position accuracy of the sinking axis.

3.2 Process input parameter derivation for the material 1.4108

The electrochemical material characterization was conducted using the DIN SPEC 91399 method to derive the process input parameter for the material ASTM F899. During the experiments the machine input parameter voltage, pulse length and feed rate were varied from large to small. The interelectrode gap remained in the range of 0.05 mm ± 0.005 mm during the experiments using fixture 1. **Figure *4*** shows the feed rate v_f as function of the current density J.

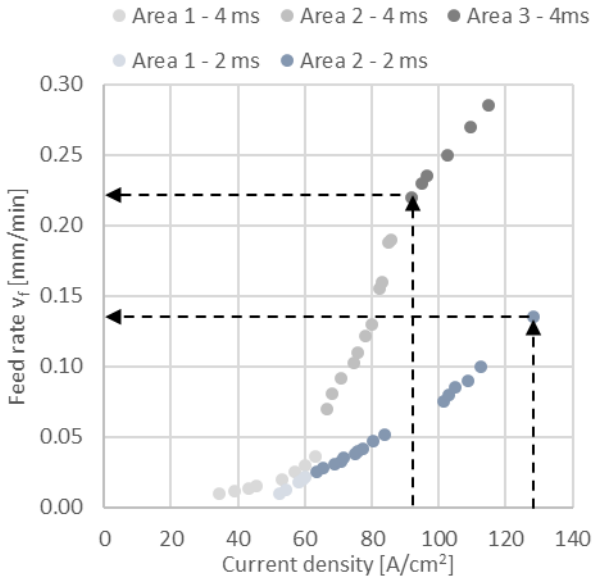

Figure 4. Feed rate v_f as function of the current density J at a frequency f of 50 Hz and two pulse lengths t_p 2 ms vs. 4 ms for ASTM F899.

The graph shows that increasing the current density results in higher feed rates. The curve is not linear due to metal oxidation during processing in sodium nitrate. For 50 Hz pulse frequency and a pulse length of 2 ms (duty cycle 10 %) and 4 ms (duty cycle 20 %) individual dissolution zones were found and classified using the removal efficiency analyses [7]. A metal oxidation occurring at lower current densities is caused by a change of the valence reaction capability, representing a functional electrical resistance. This leads to a more intense gradient of the current density occurring between dissolution zone 2 and zone 3 for 4 ms pulse length [8]. Using linear regression models, for each dissolution zone the removal functions are derived and summarized in **Table *4*** [6].

Table 4. Derived material-specific removal functions depending on the current density.

Dissolution area	Current density range	Anlytical function
Area 1 – 4 ms	35 – 63 A/cm²	$v_f = 0.0009 \cdot J - 0.022$
Area 2 – 4 ms	64 – 90 A/cm²	$v_f = 0.0060 \cdot J - 0.336$
Area 3 – 4 ms	91 – 115 A/cm²	$v_f = 0.0028 \cdot J - 0.034$
Area 1 – 2 ms	52 – 63 A/cm²	$v_f = 0.0015 \cdot J - 0.068$
Area 2 – 2 ms	63 – 145 A/cm²	$v_f = 0.0016 \cdot J - 0.080$

For 4 ms pulse length a process start was chosen at 92 A/cm² and 0.220 mm/min representing the edge between dissolution zone 2 and 3. At 2 ms pulse, the 50 % shorter removal time leads to a lower sinking speed at equal current density [1]. Thus, a sinking speed of 0.135 mm/min was selected at a current density of 128 A/cm².

3.3 Comparison of the frontal end working gaps

Experiments were conducted using the material-specific process input parameter derived in advance. After PECM processing, the stability of the frontal end working gap s_f was tested for both removal fixtures for the reduction of the voltage potential. **Table 5** summarizes the varied parameters, the resulting frontal end working gaps s_f and their deviation Δs_f of both fixtures.

Table 5. Comparison of the frontal end working gap for fixture 1 and 2 using similar machine input parameter.

#	Pulse length [ms]	Voltage potential [V]	Fixture 1 s_{f1} [µm]	Fixture 2 s_{f2} [µm]	Δs_f [µm]
1	4	13.8	53	64	11
2		11.8	39	49	10
3		9.8	27	34	7
4		8.8	26	28	3
5	2	15.0	47	50	3
6		13.0	34	39	4
7		11.0	29	33	4
8		10.0	23	23	0

Basically, a reduction in voltage potential by 5 V resulted in a decrease of the frontal working gap by almost 50 % after PECM processing. Nethertheless, both fixtures show different frontal end working gaps and a strong dependence on the set voltage potential as well as pulse duration. It is noticable that for the same applied voltage potential removal fixture 2 had higher gap widths compared to removal fixture 1. However, the deviation of the frontal end working gaps decrease with lowering the machine voltage. For a pulse length of 4 ms, the deviation was reduced from 11 µm at 13.8 V to 3 µm at 8.8 V. For a pulse length of 2 ms it becomes clear, that the deviation Δs_f is smaller across the tested voltage range. The frontal end working gap decreases from 3 µm at 15.0 V to 0 µm at 10.0 V, representing an ideal transferability. It is assumed that the larger processing

area and machining orientation of fixture 2 produces overall a higher material removal volume at high voltage potentials and 4 ms pulse durations, resulting in larger final working distances. The shorter the current pulse such as for 2 ms pulse length, the smaller is the resulting removal volume and the process precision increase by the smaller interelectrode gap. Thus, for a pulse duration of 2 ms and the lowest set voltage potential of 10.0 V, an identical value was achieved for both removal fixtures at 23 µm frontal end working gap.

3.4 Comparison of the machining current for both fixtures

As shown in Table 3, the removal fixtures differed in terms of machining direction and current-transmitted area. Fixture 1 is designed for complete front gap machining, while the more complex removal fixture 2 produces the desired geometry in the lateral working gap. The different machining direction is also visiable in the machine current that was recorded in the machine log. The machine current values show the last 30 seconds of the removal process. For 4 ms pulse length, the machining current for both fixtures are compared **Figure 5**.

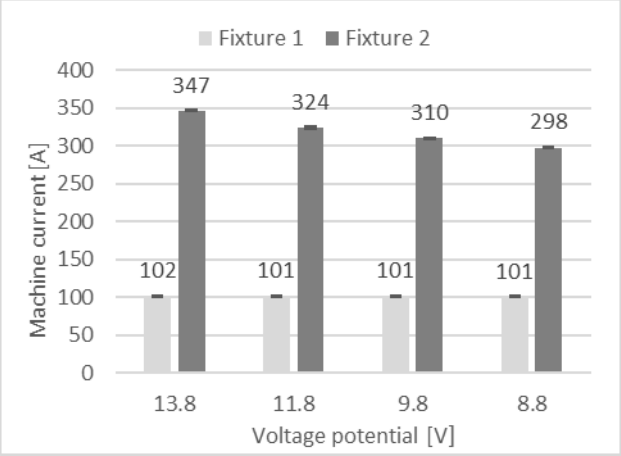

Figure 5. Comparison of the machining current of both removal fixtures for 4 ms pulse length, showing the last 30 seconds of the machining.

The comparison of the machine currents show very different behavior for a reduction voltage potential of 5 V using both removal fixtures. Removal fixture 1 has a negligible reduction of machine current by 1 A. This change of around 1 % is considered to be approximately constant. Removal fixture 2 shows for the same reduction a decrease in machine current of 49 A, representing a machine current drop of approximately 14 %.
It is expected that the constant current-transmitting surface area during only frontal gap machining of fixture 1 results in an almost constant machine current for lowering the machine voltage. The significant decrease of machine current for removal fixture 2 is explained by the fact that the current-transmitting surface area in the lateral gap is reduced by the change of the electrical field distribution [5].

4. Summary and outlook

Electrochemical precision machining offers great potential to produce various shapes in components in favored high-strength or difficult-to-cut materials. In this paper, a comparison of the PECM process using two different removal fixtures was researched for the machining of the martensitic stainless steel ASTM F899. The two fixtures, an simple substitution model for only frontal machining, and an complex fixture for internal spur gear manufacturing using lateral gap machining, were compared regarding their design and their core features. Experiments were conducted, considering the material-specific dissolution zones determined with the electrochemical material characterization in advance. Based on the evaluation of the experiments, the transferability of the frontal end working gap for various machine settings was shown. The main findings are:

1. A very high positioning accuracy of 1 µm was found for the sinking axis of the PECM system
2. Initial machine input parameter were derived for the studied material using DIN SPEC 91399. For the tested current density range, an nonlinear removal behaviour was found for both pulse lengths. This is typical for machining in sodium nitrate, due to the changes of the reaction manner of the valence electrons.
3. It was approved that a reduction of the voltage potential leads the smaller frontal end working gaps.
4. Compared to removal proposed fixture 1, fixture 2 tends to a higher material removal at larger frontal end working gaps. Netherthless, at 4 ms pulse length a minimum deviation of 3 µm at 8.8 V and for 2 ms at 10.0 V even no deviation was achieved.
5. Hightlighting the change of the machine current for 4 ms pulse length, lowering the voltage showed an almost constant machine current for only frontal gap machining using fixture 1, meanwhile for fixture 2 showed an reduction of the machine current by 14 %. It is expected that during lateral gap machining a reduced current-transmitting surface area is the root cause for the machine current decrease.

Summarizing the approach to use a simplified substation fixture for the PECM process initialization, the comparison of the process with a complex gear manufacturing fixture evidenced an sufficient transferability of the frontal end working gap adjustment. Thus the basic process input parameters can be determined using the simplified substitution model. However, a final parameter optimisation is necessary for complex manufacturing tasks to guarantee the dimensional accuracy for the evolving interelectrode gap.

Acknowledgments

The authors gratefully acknowledge the german Federal Ministry for Economic Affairs and Climate Protection (BMWK) program for the financial support of the project ARGONAUT – Innovative Herstellungstechnologien für Zahnräder, Funding No. 20Y2101B.

References

[1] Bergs T and Klocke F 2025 Berlin Springer Verlag 177-221
[2] Wei B, Rajurkar K P, Talpallikar S 1997 *J. Electrochem. Soc.* **144** 11 3913–3919
[3] Böttcher F 2024 Aachen *Apprimus Verlag* 9–13
[4] BGH Edelstahlwerke GmbH 2025 Material data sheet 1.4108
[5] Schaarschmidt I 2025 Auerbach *Verlag Wissenschaftliche Scripten* **17**
[6] Meichsner G, Köppl A, Wengerek . Schulze R, Hackert-Oschätzchen M Berlin *Beuth Verlag* 2018
[7] Meichsner G, Hackert-Oschätzchen M, Krönert M, Edelmann J, Schubert A, Putz M 2016 *Procedia CIRP* **46** 123–126
[8] Böttcher F, Ghorbanalipour S, Edelmann J 2025 *Technische Universität Chemnitz* 25-32

euspen's 26th International Conference & Exhibition, Krakow, PL, June 2026
www.euspen.eu

Study on effect of tool edge geometry on residual stress in metal cutting

Hiroyuki Sasahara [1)] and Tatsuya Tanaka [1)]

[1]*Tokyo University of Agriculture and Technology*

sasahara@cc.tuat.ac.jp

Abstract

The objective of this study is to investigate the effects of tool edge geometry and friction on residual stress through orthogonal cutting experiments and finite element analysis (FEA), and to clarify the mechanism of residual stress formation. The workpiece material used was A6061 aluminium alloy, and the analysis was conducted using the FEA software DEFORM-2D. Instead of a simple circular arc, the tool edge roundness was modelled as an elliptical shape, configured as either horizontally elongated or vertically elongated. This approach represents one of the novel aspects of this study. FEA results revealed that tool edge roundness, edge geometry, and friction significantly influenced material flow and stress distribution within the workpiece. A stagnation zone was observed in front of the tool edge, where the material first moved upward and was then pushed downward beneath the edge. The extent of this upward movement varied depending on the edge geometry: it was smaller for the vertically elongated ellipse and larger for the horizontally elongated ellipse. This deformation history during tool passage manifested as residual stress in the machined surface. According to the FEA results, the vertically elongated elliptical edge promoted compressive residual stress, whereas the horizontally elongated elliptical edge tended to result in a more tensile residual stress state. In addition, friction at the tool–chip interface affected both material flow and the resulting residual stress state.

Cutting, FEM, Tool edge radius, Residual stress, Machined surface

1. Introduction

Cutting processes are widely employed in various industrial fields, including automotive, aerospace, and medical applications. When cutting is used as a finishing operation, it is well known that residual stresses are generated on the machined surface of the workpiece. Because residual stresses affect the durability, fatigue life, and deformation of workpieces [1, 2], a deeper understanding of the underlying mechanisms is essential for preventing or mitigating their occurrence. To date, numerous studies have investigated residual stresses induced by cutting, and it has been reported that their magnitude and distribution vary depending on machining conditions and material properties [3-5]. However, the generation mechanism itself remains insufficiently understood [6].

Therefore, this study investigates the influence of tool edge radius, tool edge geometry, and friction on the tool rake and flank faces on residual stress through a series of two-dimensional cutting experiments. In addition, analytical investigations are conducted using the finite element method (FEM) with the software DEFORM-2D to examine their effects on residual stress under two-dimensional cutting conditions. In this study, the influence of pure mechanical interaction at the tool edge, such as indentation, shear and the material flow, on the residual stress distribution was investigated by selecting cutting speeds that minimize thermal effects. This approach allowed us to suppress variations in flow stress and thermal expansion/contraction caused by temperature and strain rate changes. By comparing and discussing the results obtained from both experiments and simulations, the objective of this work is to clarify the mechanism of residual stress generation in cutting processes depending on the tool edge geometry and the friction between the tool and the workpiece.

2. Influence of Tool Edge Geometry on Residual Stress

2.1. Analytical Modelling

A finite element model was developed using the FEM simulation software DEFORM-2D to predict cutting forces and residual stresses during machining. Using this model, analyses were conducted under extremely low cutting speeds to investigate the effects of tool edge radius, tool edge geometry, and friction conditions.

Figure 1 shows the simulation model employed in this study. The model consists of three components: the workpiece, the tool, and the bottom die. The bottom die is a virtual plate introduced to prevent chip–workpiece contact that would otherwise cause interruption of the computation during analysis.

Figure 2 and Table 1 summarize the tool edge geometries used in the simulations. The tool edge geometry was defined by the combination of the major axis Sa and minor axis Sb of an elliptical arc at the tool edge.

In addition, the cutting simulations incorporated an exponential friction model using a user subroutine in DEFORM, expressed by Eq. (1), where τ_t and σ_t are the frictional stress and normal stress at tool-chip interface, k and λ are the yield shear stress and the frictional characteristic constant respectively [7]. As a larger λ value corresponds to higher friction, a value of λ = 1.0 was used to represent dry cutting, while λ = 0.1 was used to simulate lubricated conditions when cutting oil was applied [8]. Cutting speed was 0.1 m/min, depth of cut was 0.1 mm, rake angle and clearance angle were 6 degrees and 5 degrees respectively.

$$\tau_t = k\left(1 - e^{\frac{\lambda\sigma_t}{\kappa}}\right) \qquad (1)$$

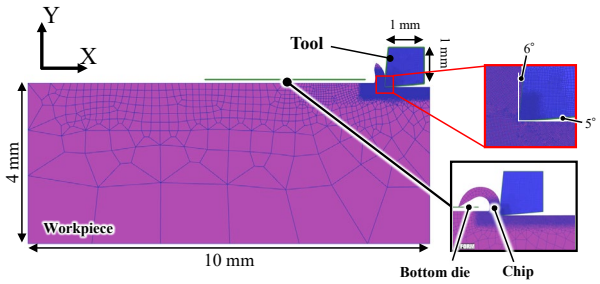

Figure 1. Simulation model.

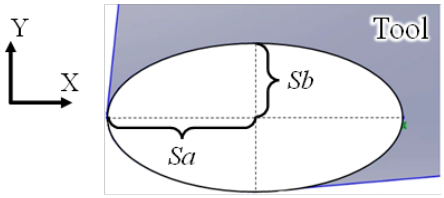

Figure 2. Tool edge profile.

Table 1 Tool edge parameters.

	(*Sa*, *Sb*) [μm]		
Ellipse① ($Sa < Sb$)	(30, 60)	(30, 60)	
Round ($Sa = Sb$)	(15, 15)	(30, 30)	(40, 40)
Ellipse② ($Sa > Sb$)	(60, 30)	(90, 30)	(120, 30)

2.2. Simulation results

Figure 3 shows the velocity distribution inside the workpiece during cutting for tool edge radii of R = 15 μm to R = 40 μm. The material flow is visualized using vector arrows. It can be observed that the material first flows upward toward the tool edge and then descends along the tool profile.

When comparing the material flow for different edge radii, the upward flow height decreases as the tool edge radius decreases from R = 40 μm. Consequently, the area of material that is pushed downward toward the machined surface by the tool edge becomes smaller. In addition, as the edge radius increases, the stagnation zone—shown in dark blue arrow—at the tool tip becomes noticeably larger.

Next, the effect of friction is examined. Regardless of the magnitude of the tool edge radius, the stagnation zone becomes smaller under the low-friction condition (λ = 0.1), and the upward displacement of material increases. Differences also appear in the velocity of the material along the rake face, indicating that chip formation behaviour is influenced by friction.

Figure 4 shows the velocity distribution inside the material when the tool edge geometry is varied. Compared with the case of R = 30 μm shown in Fig. 3(c), the vertically elongated edge geometry in Fig. 4(a) produces a larger stagnation zone at the tool tip. In contrast, the horizontally elongated elliptical geometry exhibits a smaller stagnation zone.

For the vertically elongated elliptical shape, the increased stagnation zone suppresses the upward flow of material in front of the tool. Furthermore, regardless of tool geometry, reducing friction decreases the size of the stagnation zone and increases the height of the upward material flow.

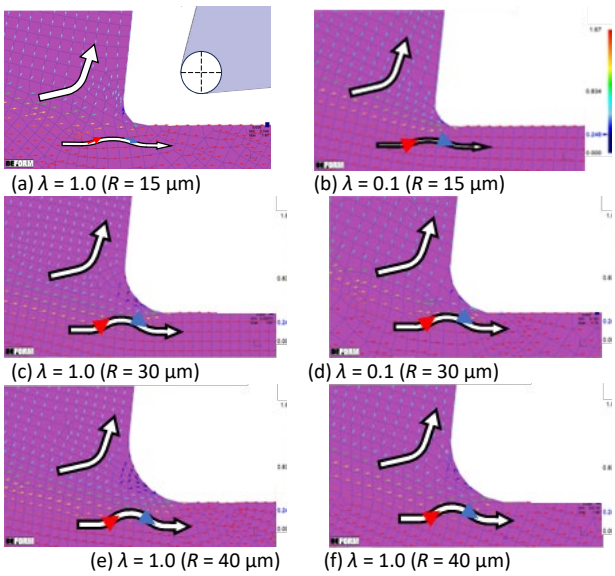

Figure 3. Analysis results of velocity distribution with round tool edge.

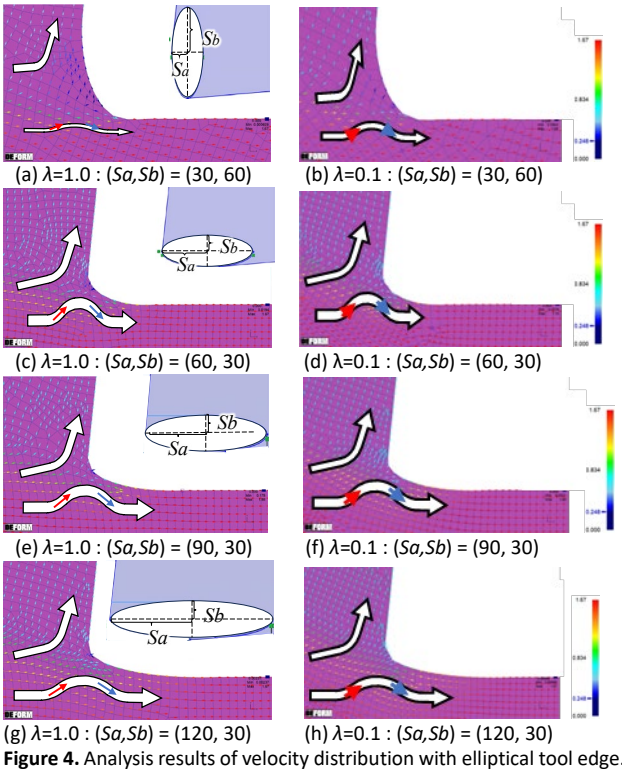

Figure 4. Analysis results of velocity distribution with elliptical tool edge.

Figure 5 shows the distribution of the residual stress σ_x for circular tool edge radii ranging from R = 15 μm to 40 μm. A compressive residual stress is generated along the machined surface after the tool passes. As the edge radius increases, this compressive residual stress extends over a wider region and its magnitude also becomes larger.

Furthermore, when the friction coefficient is reduced, the region of compressive residual stress becomes wider at R = 15 μm.

Figure 6 shows the σ_x distribution after cutting when the tool edge is modelled as vertically or horizontally elongated elliptical shapes. For the vertically elongated elliptical geometry, the residual stress distribution is similar to that of the circular geometry with R = 40 μm, but the compressive residual stress extends to a greater depth compared with the R = 40 μm case.

In contrast, the horizontally elongated elliptical geometry results in a distinctly different residual stress distribution. Immediately after the tool passes, compressive residual stresses below –50 MPa appear near the surface, but the compressive tendency weakens along the machined surface and shifts toward tensile stress. As the major axis in the X-direction (Sa) increases, this trend becomes more pronounced. At *Sa* = 120 µm, a wide region of tensile residual stress exceeding +50 MPa appears near the machined surface.

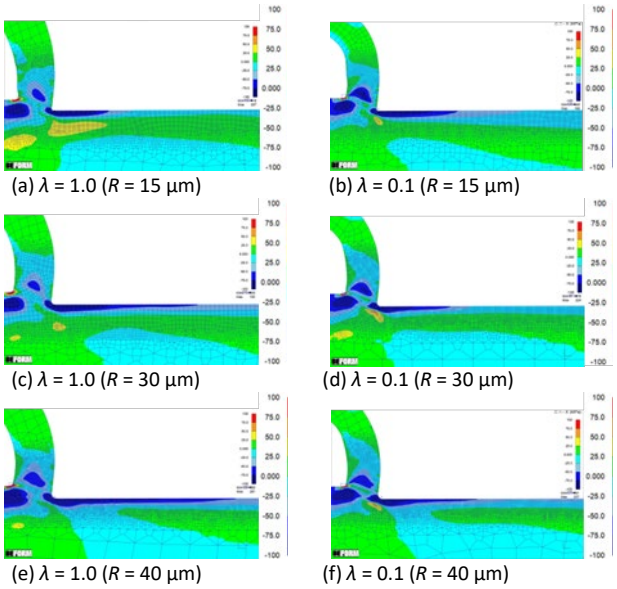

(a) λ = 1.0 (R = 15 µm) (b) λ = 0.1 (R = 15 µm)

(c) λ = 1.0 (R = 30 µm) (d) λ = 0.1 (R = 30 µm)

(e) λ = 1.0 (R = 40 µm) (f) λ = 0.1 (R = 40 µm)

Figure 5. Analysis results of stress distribution in cutting direction (σ_x) with round tool edge.

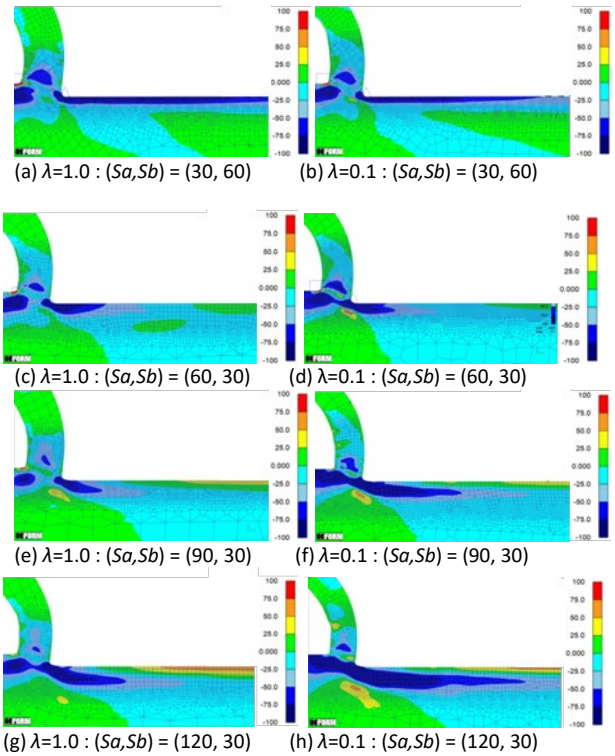

(a) λ=1.0 : (*Sa*,*Sb*) = (30, 60) (b) λ=0.1 : (*Sa*,*Sb*) = (30, 60)

(c) λ=1.0 : (*Sa*,*Sb*) = (60, 30) (d) λ=0.1 : (*Sa*,*Sb*) = (60, 30)

(e) λ=1.0 : (*Sa*,*Sb*) = (90, 30) (f) λ=0.1 : (*Sa*,*Sb*) = (90, 30)

(g) λ=1.0 : (*Sa*,*Sb*) = (120, 30) (h) λ=0.1 : (*Sa*,*Sb*) = (120, 30)

Figure 6. Analysis results of stress distribution in cutting direction (σ_x) with elliptical tool edge.

Figure 7 shows the residual stress distribution in the surface layer for different circular edge radii and for different elliptical tool edge geometries. At the machined surface (horizontal axis = 0), the residual stress transitions from tensile to compressive in the following order: horizontally elongated elliptical edge, circular edge, and vertically elongated elliptical edge. This tendency was observed regardless of the friction coefficient.

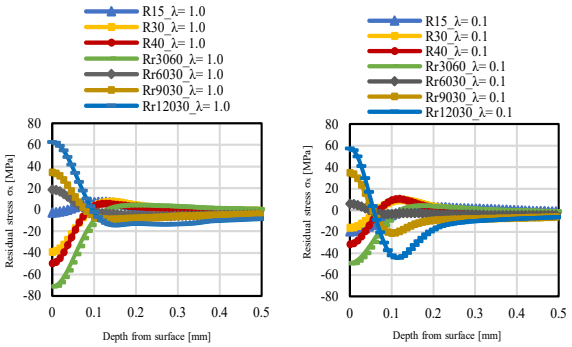

(a) λ=1.0 (b) λ=0.1

Figure 7. Analysis results of residual stress (σ_x) after cutting.

3. Experimental validation

Orthogonal cutting experiments were conducted on the end face of an A6061 aluminium alloy workpiece to investigate the effects of tool edge geometry and friction on the resulting residual stress.

Figure 8 shows the experimental setup. A square tool holder was mounted on the spindle, the spindle rotation was fixed, and extremely low-speed cutting was performed by feeding the table. The experimental conditions and tool edge geometry are summarized in Tables 2 and 3. Residual stress on the machined surface was measured using a portable X-ray residual stress measurement device (PULSTEC µ-360) with the cosα method. The measurement conditions included a collimator diameter of 1.0 mm, an incident angle of 25°, and an irradiation time of 30 seconds. Cr-Kα radiation was used as the characteristic X-ray source. In this experiment, an increase in tool edge radius led to higher cutting forces. Moreover, the vertically elongated elliptical geometry produced larger cutting forces than the horizontally elongated elliptical geometry.

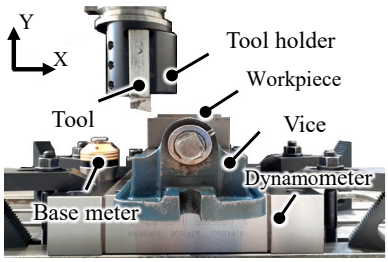

Figure 8. Experimental setup.

Table 2 Experimental conditions.

Workpiece material		A6061
Tool material		Tungsten carbide (K10)
Cutting speed	m/min	0.050
Depth of cut	mm	0.10
Width of cut	mm	4.0
Rake angle	deg.	6
Clearance angle	deg.	5
Lubricant		DH30

Table 3 Tool edge parameters.

	(*Sa*, *Sb*) [µm]		
Ellipse① ($Sa < Sb$)	(32, 52)		
Round ($Sa = Sb$)	(10, 10)	(25, 25)	(40, 40)
Ellipse② ($Sa > Sb$)	(53, 31)		

Figure 9 shows the measured residual stress distributions for circular tool edge radii R. For R = 10 µm and R = 25 µm in Fig. 9 (a), the residual stress exhibits a tensile distribution under the DRY condition, whereas it becomes compressive under the WET condition.

In Fig. 9(b), as the radius increases to R = 40 µm, the residual stress tends to shift further toward compression under both DRY and WET conditions, and under WET cutting, a highly compressive residual stress exceeding −150 MPa is observed.

Figure 10 shows the residual stress distributions for different elliptical tool edge geometries. A comparison between the horizontally elongated ellipse in Fig. 10(a) and the vertically elongated ellipse in Fig. 10(b) indicates that the vertically elongated geometry exhibits a stronger compressive residual stress tendency, particularly under the wet condition. In addition, comparison between dry and wet conditions demonstrates that the wet condition consistently results in more compressive residual stress, irrespective of the tool edge geometry.

The FEM analysis predicts that the vertically elongated elliptical tool edge generates higher compressive residual stress than the horizontally elongated geometry, and this trend is experimentally confirmed under the wet condition. However, under the dry condition, the experiments didn't show a clear difference in the residual stress between the horizontal and vertical ellipse tools. Regarding the residual stress results for the circular tool shown in Fig. 9, the experimental results under the dry condition also did not fully support the FEM analysis.

Under the dry cutting condition, a built-up edge acting as dead metal or severe adhesion was observed to form in front of the tool tip during the orthogonal cutting experiments. The formation of this dead-metal-type built-up edge effectively modified the actual tool edge geometry during cutting and reduced the effective contact area between the tool and the machined surface. As a result, the geometric differences between the horizontally and vertically elongated elliptical edges may have been obscured, leading to no clear difference in the measured residual stress under the dry condition.

It should be noted that this built-up edge formation, which was not accounted for in the FEM model, represents a limitation of the present experimental validation and may partly explain the discrepancy between the numerical and experimental results under dry conditions.

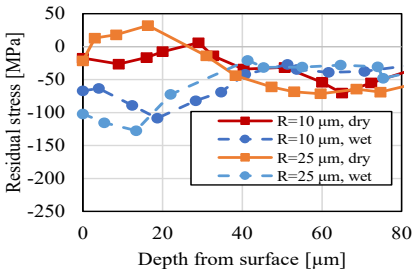

(a) R = 10, 25 µm

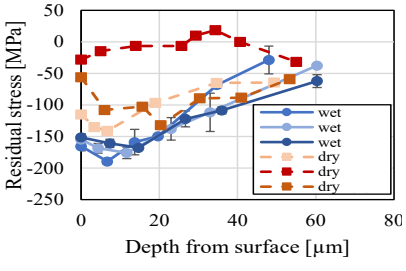

(b) R = 40 µm

Figure 9. Effect of tool edge radius and lubricant on residual stress on machined surface.

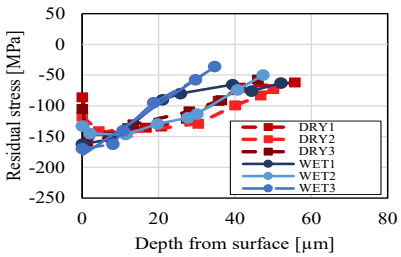

(a)Horizontal ellipse

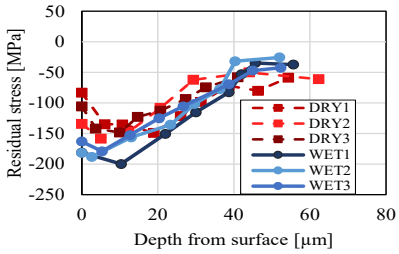

(b) Vertical ellipse

Figure 10. Effect of tool shape and lubricant on residual stress on machined surface.

5. Conclusions

The effects of tool edge geometry and the frictional conditions at the tool–chip interface on residual stress were investigated through finite element analysis and orthogonal cutting experiments.

(1) The depth-wise distribution of residual stress in the surface layer increased in the compressive direction as the tool edge radius became larger. This trend was consistent with that observed in the two-dimensional cutting experiments.

(2) The influence of vertically and horizontally elongated elliptical edge on residual stress was found to differ. Both the FEM analysis and the cutting experiments under the wet condition demonstrated that the vertically elongated elliptical geometry promotes higher compressive residual stress compared with the horizontally elongated geometry.

(3) According to the FEM analysis, higher friction at the tool–chip interface tended to promote compressive residual stress. However, in the cutting experiments under the dry condition, dead-metal-type built-up edge formation altered the effective cutting conditions, and experimental results fully supporting this tendency could not be obtained.

References

[1] James M N, Hughes D J, Chen Z, Lombard H et.al. 2007 *Engineering Failure Analysis*, **14,** 2384-395

[2] Sasahara H 2005 *Int. J. Mach. Tools & Manuf.*, **45**, 2 131-136

[3] Mohamed N A N, Ng E G, Elbestawi MA 2007 *Int. J. Mach. Tools & Manuf.*, **47**, 401-411

[4] Özel T, Zeren E 2007 *Int. J. Adv. Manuf. Technol.*, **35,** 255-267

[5] Yang D, Xiao X and Liang X 2019 *Int. J. Adv. Manuf. Technol.*, **103**, 2965-2976

[6] Zhuang K, Fu C, Weng J et al 2021 *Int. J. Adv. Manuf. Technol.*, **116**, 2045-2092

[7] Usui E, Shirakashi T 1982, *ASME Ped*, **7**, 13-35.

[8] Sasahara H, Obikawa T, Shirakashi T 1997, *Trans. NAMRI/SME*, **XXV**, 213-218

euspen's 26th International Conference & Exhibition, Krakow, PL, June 2026
www.euspen.eu

Dimensional accuracy and IT7 fits in FDM-printed PLA elements: statistical evaluation and correction guidelines

Bartłomiej Byczuk[1], Mirosław Rucki[1], Marcin Wikło[2], Arturas Kilikevicius[1], Patryk Osuch[3]

[1]*Vilnius Gediminas Technical University, Vilnius, Lithuania*
[2]*Casimir Pulaski Radom University, Radom, Poland*
[3]*Precision Machine Parts Poland sp. z o.o., Radom, Poland*

Correspondence: m.rucki@urad.edu.pl

Abstract
Accuracy of Additive Manufacturing (AM) technique is a crucial task when producing components of high precision. The study focused on the possibility of achieving IT7 fits while maintaining the geometry of elements produced by Fused Deposition Modelling (FDM) technology. Test samples made of polylactic acid (PLA) material were manufactured and subsequently measured using a coordinate measuring machine (CMM) with an accuracy of 1.7 µm, supported by PC-DMIS metrology software. The obtained data were analysed statistically to determine dimensional deviations and to evaluate the extent to which corrections should be increased or decreased, expressed as a percentage. In addition, the influence of process parameters on dimensional stability was examined to identify the main factors affecting the fit accuracy. The analysis provided not only numerical corrections but also practical recommendations for improving the repeatability of the precise FDM process. The results contributed to a better understanding of the limitations of AM in precision applications and may serve as a reference for industrial implementation. Moreover, the study enabled the formulation of guidelines that may support the development of quality standards for the geometry of products manufactured by FDM technology.

Keywords: additive manufacturing, FDM, tolerances, dimensional accuracy, correction

1. Introduction

Fused Deposition Modeling (FDM) is a widely adopted additive manufacturing (AM) technology due to its cost-effectiveness and geometric flexibility. However, achieving precision comparable to traditional manufacturing methods remains challenging due to notable dimensional deviations and variability of FDM parts. Typical baseline dimensional accuracy for desktop FDM objects lies in the range of ±0.1–±0.3 mm, corresponding roughly to coarse tolerance classes IT11–IT14 [1]. Accurate fits such as ISO IT7 corresponding with ±0.006–±0.011 mm for small features, are generally considered beyond the native FDM capabilities.

Recent research emphasizes the necessity of systematic calibration and compensation methods to improve FDM dimensional accuracy. A comprehensive review highlights that process parameters, machine characteristics, material properties, and environmental control significantly influence dimensional precision; however, there is no singular standard method for achieving high tolerance grades without iterative refinement [2]. Studies also demonstrate that shrinkage compensation—whether via pre-print scaling, slicer expansion, or software-based corrections—can substantially reduce dimensional errors in AM parts [3,4]. This study investigates whether such calibration methods can be extended systematically to achieve ISO IT7 tolerance compliance on a desktop FDM printer using PLA. The goals were as follows:

- To quantify inherent dimensional biases across a range of feature sizes.
- To apply iterative compensation (offset + scale + feature-specific corrections).
- To validate compliance with ISO 286-1 IT7 tolerance bands using high-precision metrology.

2. Materials and methods

A thin-walled ring was chosen as a part for evaluation, its height was 5 mm and nominal wall thickness 0.8 mm. The analysis covered XY outer dimensions, Z-axis height stacking accuracy, and thin-wall feature fidelity. Five nominal sizes of 5 mm, 10 mm, 15 mm, 20 mm, and 25 mm were tested. Each was printed individually to eliminate inter-part thermal effects that can distort geometry, as it was mentioned in [2].

For each nominal size, a batch of 100 samples was printed (total of 500 initial parts for the coarse test). All parts were printed using the Bambu Lab X1 Carbon FDM printer with PLA Basic filament. A standard 0.4 mm nozzle, 0.2 mm layer height, and moderate print speed were applied to reflect typical production settings. An enclosed chamber reduced environmental variation, which is known to affect dimensional repeatability in material extrusion methods.

Dimensional measurement was conducted in two stages. First, caliper measurements (digital caliper, 0.01 mm resolution) were used for coarse evaluation and iterative correction computation. Its Type A uncertainty was estimated as U_{95}= 0.014 mm with k=2. And then, high-precision CMM/optical CMM with 1–2 µm accuracy was used for final verification, necessary for tight tolerances near the IT7 band. For the specific measurement task relevant for this study, Type A uncertainty was estimated as U_{95}= 0.0017 mm.

Each measurement was repeated 10 times. Dimensions were classified according to ISO 286-1 standard tolerance classes, and parts within the IT7 half-width tolerance were considered successful.

3. Results

Without compensation, all XY dimensions were systematically undersized by approximately −0.12 mm across the nominal size range. The variability was relatively small (std ca. 0.03–0.04 mm), but the consistent undershoot suggested a systematic error likely due to thermal shrinkage and slicer path generation combined with extrusion width effects.

Z-height overshoot (ca. +0.05 mm) was observed, likely driven by slight layer thickness inaccuracies or first-layer calibration bias, a known challenge in layer-based AM systems.

Thin wall thickness was undersized (0.75–0.78 mm), consistent with reported issues in single-perimeter features where actual printed line width differs from nominal.

3.1. Initial IT Classification

With no compensation, the following features were noted:

- All parts failed IT7 in XY dimensions.
- Height deviations were outside IT7 bands.
- Thin walls exhibited substantial deviation beyond IT7 limits.

These results aligned with reports specifying that uncalibrated FDM parts typically reside in coarse tolerance bands IT11–IT14 or worse, if no systematic compensation is applied [1].

3.2. First Iteration: Uniform Offset Compensation and IT7 outcome

Given the relatively constant negative bias, a horizontal expansion offset of +0.064 mm per side was applied. After reprinting and re-measuring it was found, as follows:

- Larger features (25 mm) were near nominal.
- Smaller features exhibited slight overshoot (~+0.016–+0.025 mm).
- Dimensional distributions became centered around target, though variance increased slightly for smaller features.
- Ca. 30% of 25 mm parts met IT7 requirements in XY.
- Less than 5% of smaller sizes met IT7.
- No consistent improvement in thin wall and Z-height were achieved without dedicated corrections.

This outcome demonstrated that a simple uniform offset was able to remove systematic bias but did not fully compensate for size-dependent and feature-dependent errors. Thus, it could be suggested that a hybrid approach of offset combined with proper scale might provide improved dimensional fidelity.

3.3. Second Iteration: Hybrid Calibration

Based on regression of measurement error vs. nominal size, the following features were applied in the second iteration:

- Reduced horizontal expansion (+0.05 mm per side) to avoid overcompensation in small features.
- Global XY scale factor (around +0.09%) applied via firmware steps-per-mm or slicer adjustments.
- Z-axis recalibration (ca. −1%) via layer height tuning.
- Feature-specific extrusion compensation (ca. +2–3%) to improve thin wall thickness.

Such hybrid compensation provided results expected in the light of strategies investigated for shrinkage reduction and dimensional control in the available published papers [3,4].

3.43. Final Results: IT7 Achievement

Final FDM-printed parts after calibration showed following features:

- Mean deviations measured on CMM were close to zero (below ±0.0003 mm) across all sizes.
- IT7 compliance was demonstrated by more than 95% pass rates when measured by caliper, while CMM measurement confirmed all samples within IT7 limits.
- Reduced variation of dimensions was confirmed by the standard deviation of 1–4 µm.
- Thin wall thickness and Z-height also met IT7 and even tighter standards.

These results demonstrate that with targeted iterative calibration, FDM can achieve precision previously considered unattainable without post-processing.

4. Discussion

4.1. Interpretation of Calibration Effects

The initial constant bias likely arises from a combination of thermal shrinkage, extrusion width differences, and slicer path offsets — effects consistently noted in studies on dimensional accuracy in FDM (Equbal et al., 2024; Grgić et al., 2023). A hybrid compensation model (offset + scale + feature corrections) effectively addresses both fixed and proportional error components, consistent with shrinkage compensation strategies documented in AM research (Shan et al., 2025; Koers, 2023).

4.2. Process Control and Variability

Even after systematic calibration, remaining variability is influenced by material cooling behavior, slight machine dynamics, and local feature sensitivity — factors highlighted in the broader literature on AM dimensional control [2]. Rigorous environmental control and consistent process settings were essential to achieve tight dimensional repeatability.

5. Conclusions

This work demonstrates that a modern desktop FDM printer can produce PLA parts that comply with ISO IT7 tolerance grades through structured iterative calibration:

- Baseline prints without compensation resulted in coarse tolerance performance.
- First iteration offset calibration eliminated systematic bias.
- Second iteration hybrid calibration (offset, scale, feature compensation) achieved IT7 compliance in all critical dimensions.

It was found that the iterative calibration was essential. Simple offsets improved bias but they had to be combined with scaling and feature compensation. High-precision metrology was necessary for verification. Calipers could provide useful trends, but CMM/optical metrology was required for final validation. Feature-specific compensation was demonstrated to be crucial, since the thin walls and small features required targeted extrusion tuning.

Also the process stability was found to be critical, such as temperature control, slicer consistency, and frequent calibration. The methodology provided a systematic path toward precision control of FDM parts and supports broader industrial adoption where dimensional fit is critical

References

[1] Grgić I, et al. 2023 Accuracy of FDM PLA Polymer 3D Printing Technology Based on Tolerance Fields *Processes*, **11(10)** 2810

[2] Equbal A, et al. 2024 A recent review on advancements in dimensional accuracy in FDM 3D printing *AIMS Materials Science* **11(5)** 950–90

[3] Shan Y, Wang X and Mao H 2025 Shrinkage compensation of additively manufactured parts with measured dimensions using affine transformations *Manufacturing Letters* **44** 928-935

[4] Koers T and Magyar B 2023 Compensation of the Shrinkage Behavior Occurring in Cylindrical Components in the FDM Process *Macromolecular Symposia* **411(1)** 2200185

euspen's 26th International Conference & Exhibition, Krakow, PL, June 2026
www.euspen.eu

Sustainable manufacturing of metallic wires through solid-state processes with continuous Al6061 chips

Zichen WANG[1,2], Vincent Beng Chye TAN[1], Dennis Wee Keong NEO[2], and Nicholas Yew Jin TAN[2,3]

[1]*Department of Mechanical Engineering, National University of Singapore, 9 Engineering Drive 1, Singapore 117575, Republic of Singapore*
[2]*Singapore Institute of Manufacturing Technology (SIMTech), Agency for Science, Technology and Research (A*STAR), 5 Cleantech Loop, Singapore 636732, Republic of Singapore*
[3]*Advanced Remanufacturing and Technology Centre (ARTC), Agency for Science, Technology and Research (A*STAR), 3 Cleantech Loop, Singapore 637143, Republic of Singapore*

Email: wangzichen@u.nus.edu

Abstract
As environmental challenges intensify and expectations for responsible manufacturing grow, sustainable process development is emerging as a strategic response. Solid-state processes provide a sustainable alternative to heat-based routes, reducing energy consumption and material waste. Prior work has explored the use of solid-state methods in transforming discontinuous machining chips into metallic wire in a melt-free manner. However, the discontinuous nature of the chips often introduces inter-chip interfaces and defects. Thus, this study proposes an alternative solid-state process that uses continuous Al6061 chips to produce wires. In this process, a controlled turning operation is conducted to generate long and continuous chips by varying cutting speed, uncut chip thickness, and tool cutting angles. Subsequently, the usability of the continuous chips was assessed through a tensile test. Variation of the three machining parameters produced either continuous smooth or serrated chips. The serration is a result of strain localization in the adiabatic shear band region, which is influenced by the three machining parameters through thermal softening. Tensile testing and fractography analysis indicated that non-serrated chips retain ductility and exhibit dimple dominated cup-and-cone fracture, whereas serrated chips show reduced load-carrying capacity associated with work hardening, and notch defects inherited from serration. As a result, serrated chips exhibited slant fracture, making them less ideal for subsequent deformation processing. As a preliminary feasibility assessment, this study validates the proposed solid-state process as a viable alternative method for producing thin metallic wires. Future studies will investigate the usability of the continuous wires produced through this method, particularly for wire-based additive manufacturing applications.

Sustainable manufacturing, machining chips, machining, finite element modelling

1. Introduction

As the manufacturing industry steers towards Industry 5.0, sustainable manufacturing processes have become the centre of focus in recent years. Sustainable manufacturing processes, such as the solid-state process, have gained attention as an innovative process to minimise emissions [1]. The solid-state process is often carried out under room temperature and pressure conditions, significantly reducing energy consumption. This is achieved through severe local plastic deformation, without the need for additional heat sources. The manufacturing of metallic wires, which are frequently used in additive manufacturing, automotive, and construction, is also an energy-intensive process. This is due to the repetitive wire drawing process at high temperature conditions to achieve the desired diameter. Subsequently, the wires undergo heat treatments such as annealing and quenching to achieve the desired material properties, which further adds on to the energy consumed [2]. To address this, research has begun to explore the use of the solid-state process to manufacture metallic wires as an alternative to conventional wire drawing. Friction Stir Extrusion (FSE) is a promising solid-state process to simplify and reduce emissions from wire drawing [1]. The FSE process begins with discarded machining chips from turning or milling processes and consolidates the chips to form wires through severe plastic deformation. This simplifies the wire-making process, and it is conducted at room temperature and pressure conditions, significantly reducing the energy consumed. However, this process mainly uses discontinuous chips, which often introduce defects and segmentations in the produced wires, especially when extruding thin wires [3]. Thus, this study proposes an alternative solid-state process that uses continuous chips to produce thin wires.

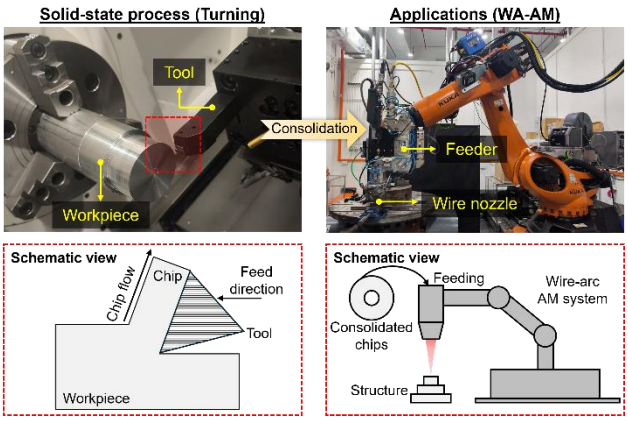

Figure 1. The proposed solid-state process to produce continuous wires and its potential applications.

As shown in Fig. 1, a controlled turning process is used to generate long and continuous chips by varying cutting speed, depth of cut, and tool rake angle. Subsequently, the usability of the chips was assessed through tensile testing. The main focus of this preliminary study is on the turning process, which plays a crucial role in producing defect-free continuous chips suitable for subsequent processing. Continuous chip formation is particularly advantageous, as it minimizes defects associated with inter-chip interfaces when fabricating thin wires. Hence, this work investigates the turning process in detail, with specific attention to chip morphology and the conditions that promote continuous chip formation.

2. Methodology

2.1. Turning process

In this study, all experiments were conducted on a DMG Mori NLX2500 Computer Numerical Control (CNC) lathe machine. The workpiece used was a cylindrical Aluminium 6061-T6 alloy billet with a diameter of 80 mm and a length of 200 mm. The cutting tool consisted of a rhombic carbide insert with a clearance angle of 7° and no chip breaker, referenced as DCMW11T304. Two types of tool holders were used, with a rake angle of 0° and -6°, respectively. The machining parameters used in the experiment are listed in Table 1. The turning experiments were repeated on a fresh workpiece of the same material to ensure reproducibility of the results.

Table 1. Machining parameters for the turning experiments

Machining parameter	Unit	Values
Cutting speed, V_c	m/min	100, 150, 200
Depth of cut, a_p	mm	0.25, 0.50, 0.75, 1.00
Feed, f	mm/rev	0.50
Tool rake angle, γ	°	-6, 0

2.2. Tensile testing, chip characterisation and fracture analysis

Tensile tests were conducted with a universal testing machine, Instron 8501, in reference to ASTM E8/E8M. The chips were aligned with a 40 mm gauge length, and a crosshead speed of 0.6 mm min^{-1} was applied, giving a nominal strain rate of 0.015 min^{-1}. The chip morphology was examined using an Optical Microscope, Keyence VHX-7000. Fractography analysis was performed using Scanning Electron Microscopy (JEOL JSM-IT200) on the fracture surfaces. The surfaces were cleaned with ethanol before imaging. Images were collected from low to high magnification to document the fracture features such as dimples, shear lips, and fracture path.

2.3. Finite element modelling

To enhance the physical comprehension of the formation of machining chips during the cutting of Al6061 alloy, the finite element method (FEM) was implemented. A 2D orthogonal cutting setup, taking reference from Mabrouki et al, was considered to approximate the turning process [4]. The workpiece was modelled using four-node bilinear plain strain elements with reduced integration and enhanced hourglass control (CPE4R), and the tool was modelled as an analytical rigid body. The explicit solver from the Abaqus 2023 software was used to perform the simulation. The workpiece is assumed to behave based on the Johnson-Cook plasticity constitutive material model. This provides a good description of metals undergoing large strains, high strain rates, and thermal softening. The constitutive law is established as follows

$$\bar{\sigma} = (A + B\bar{\varepsilon}^n)\left[1 + C\ln\left(\frac{\dot{\bar{\varepsilon}}}{\dot{\bar{\varepsilon}}_0}\right)\right]\left[1 - \left(\frac{T - T_r}{T_m - T_r}\right)^m\right] \quad (1)$$

Where $\bar{\sigma}$ is the plastic stress, $\bar{\varepsilon}$ is the equivalent plastic strain, A is the initial yield strength, B is the hardening parameter, n is the work hardening exponent, C is the strain rate dependency coefficient, $\dot{\bar{\varepsilon}}$ is the plastic strain rate, $\dot{\bar{\varepsilon}}_0$ is the reference strain rate, T_m is melting temperature, T_r is reference temperature, and m is the thermal softening coefficient. The J-C values and relevant thermal-mechanical properties for Al6061 are listed in the table below.

Table 2. Thermal-mechanical and damage properties of Al6061-T6

Parameter	Values	Parameter	Values	Parameter	Values
Elastic modulus (GPa)	70	A (MPa)	324	D_1	-0.77
Poisson's ratio	0.33	B (MPa)	114	D_2	1.45
Density (kg/m^3)	2700	n	0.42	D_3	-0.47
Melting temp (°C)	660	m	1.34	D_4	0
Specific heat (J/kg °C)	900	C	0.002	D_5	1.6
Thermal conductivity (W/m°C)	237	$\dot{\varepsilon}_0$ (s^{-1})	1	Taylor–Quinney factor	0.9

To model the chip formation process, the Johnson-Cook damage model was used. It is considered that failure will occur when the damage parameter exceeds a critical value, and the element will be deleted. The damage criterion is defined as

$$D = \frac{\bar{\varepsilon}_0^p + \sum\Delta\bar{\varepsilon}^p}{\bar{\varepsilon}_f^p} \quad (2)$$

The increase in equivalent plastic strain, $\Delta\bar{\varepsilon}^p$ is summed at the end of each increment. The equivalent plastic strain for damage initiation, $\bar{\varepsilon}_f^p$ is determined based on

$$\bar{\varepsilon}_f^p = \left[D_1 + D_2\exp\left(D_3\frac{P}{\bar{\sigma}}\right)\right]\left[1 + D_4\ln\left(\frac{\dot{\bar{\varepsilon}}^p}{\dot{\bar{\varepsilon}}_0}\right)\right]\left[1 + D_5\left(\frac{T - T_r}{T_m - T_r}\right)\right] \quad (3)$$

In which D_1 is the initial failure strain, D_2 is the exponential factor, D_3 is the triaxiality factor, D_4 is the strain rate factor, D_5 is the temperature factor, and $P/\bar{\sigma}$ is the stress triaxiality. The corresponding values of the damage constants are also listed in table 2. The friction at the tool-chip interface is also a significant factor in affecting the chip formation process in the simulation. Coulomb's friction law is used in this study, with the coefficient of friction set to 0.3. This value is an acceptable assumption for low- and medium-speed cutting conditions.

3. Results and discussion

3.1. Chip morphology

Machined chips were collected and examined under the optical microscope. The results are summarised in Fig.2. Generally, all the chips formed are long, continuous, and helical. In addition, two main classes of chips were collected: continuous smooth chips and continuous serrated chips. In Fig.2, the red square indicates serrated and the black indicates smooth. It was observed that as the depth of cut increases, serration becomes likely. Moreover, as the cutting speed increases, serration becomes unlikely. Lastly, for a negative rake tool, the appearance of serrated chips becomes more frequent.

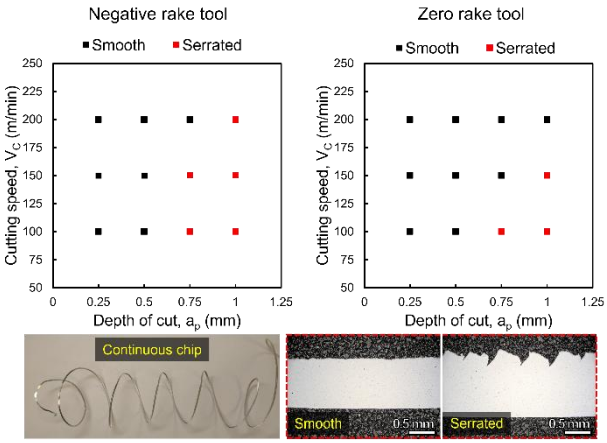

Figure 2. Chip morphology of the machining chips obtained

The fundamental cause of chip serration can be correlated to the adiabatic shear banding (ASB) phenomenon during machining [5]. It is often reported in various literature that cutting speed is the main factor contributing to chip serration and it occurs for high-speed machining, at about 460 m/min for aluminium alloy [6]. However, in this study, serration occurred under moderate cutting speed. This is because in this study, the feed and depth of cut are larger than the usual machining operation to achieve the desired dimensions of the machining chips. Thus, it is more appropriate to evaluate the serration phenomenon based on the collective effects from various machining parameters rather than just focusing on an isolated cutting parameter. Chip serration is governed by the two competing effects: the stabilising influence of work hardening, and the destabilising influence of thermal softening. The Recht criterion can be used to determine the influence of the two effects. The Recht criterion (4) indicates that shear instability occurs when the thermal softening contribution exceeds the strain hardening contribution. Accordingly, the Recht ratio R, when below one, suggests that chip segmentation is likely, and the lower the ratio, the higher the degree of serration [7].

$$\frac{\partial \tau}{\partial \gamma} + \frac{\partial \tau}{\partial T}\frac{dT}{d\gamma} \leq 0 \tag{4}$$

$$R = \frac{\partial \tau / \partial \gamma}{-(\partial \tau / \partial T)(dT/d\gamma)} \tag{5}$$

In equation (4), the first term represents the strain hardening rate, while the second term represents the thermal softening contribution, which consists of material thermal sensitivity and the adiabatic heating rate, respectively. As it is difficult to quantify the terms experimentally for the turning process, these terms are evaluated using FE fields $(\gamma, \dot{\gamma}, T)$ together with the Johnson–Cook constitutive relation. The J-C flow law, when expressed in shear form

$$\bar{\tau} = \frac{1}{\sqrt{3}}\left(A + B\left(\frac{\bar{\gamma}}{\sqrt{3}}\right)^n\right)\left[1 + C\ln\left(\frac{\dot{\bar{\gamma}}}{\sqrt{3}\dot{\varepsilon}_0}\right)\right] \left[1 - \left(\frac{T - T_r}{T_m - T_r}\right)^m\right] \tag{6}$$

Where $\bar{\tau}$ is the plastic shear stress, and $\bar{\gamma}$ is the plastic shear strain. The strain hardening rate and thermal sensitivity can be determined by taking partial derivatives of equation (6). Lastly, in adiabatic conditions, the adiabatic heating term is approximated by as

$$\frac{dT}{d\gamma} = \frac{\beta \tau}{\rho c} \tag{7}$$

In which, β is the Taylor–Quinney factor, ρ is density, and c is the specific heat capacity. By using equation (1), (6), and (7), the respective hardening and softening terms can be computed, and the Recht ratio is computed using (5). The results are summarized in the figure below.

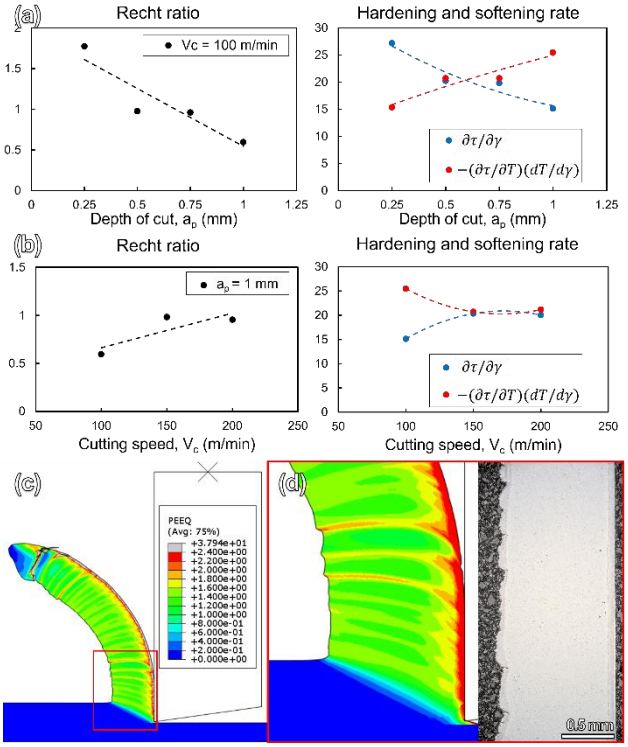

Figure 3. The Recht ratio, strain hardening, and thermal softening rate: (a) Varying ap with Vc = 100 m/min; (b) Varying Vc with ap = 1 mm; (c) FE result showing the PEEQ field; (d) Comparing simulation and experimental results.

It is observed that as the depth of cut increases, the FE simulations predict higher temperatures in the shear zone and along the tool–chip interface, which increases dT/dγ and the magnitude of ∂τ/∂T. Consequently, the thermal softening rate increases with depth of cut, implying that thermal softening becomes increasingly competitive relative to strain hardening and chip serration becomes likely (Fig 3a). When investigating the effect of cutting speed, it was observed that chip serration occurred at moderate cutting speed, whereas the literature reported that chip serration happens at high cutting speed. The results from this study remain consistent with this general trend. As shown in Fig 3b, the Recht ratio peak at 150 m/min and start to decrease at 200 m/min. The decrease in the Recht ratio indicates that thermal softening becomes more dominant at higher cutting speeds, which aligns with prior studies. However, the Recht ratio is well below one for 100 m/min, implying that serration can occur even at moderate cutting speeds when other parameters, particularly depth of cut, promote shear localization. In other words, the influence of depth of cut is sufficiently strong that it shifts the onset of chip serration to lower cutting speeds. Therefore, this result has shown that evaluating the occurrence of chip serration with a single cutting parameter is insufficient, and future studies will conduct more extensive investigations on various cutting conditions and establish a cutting criterion for chip serration under the collective influence of those cutting parameters. In addition, this FE-Recht criterion framework can accurately detect the onset of chip serration. For the case when the Recht ratio is around 0.96, experimental observation also shows slight serration (Fig. 3c,d). The Recht ratio can be used as the critical value in determining the usability of the machining chips. In the following section, this usability is assessed through a tensile test and fractography analysis.

3.2. Fractography analysis

Fractography analysis aids in the establishment of the fracture mechanism by examining the fracture surface. These observations link the material behaviour, such as ductility and toughness, to the machining parameters, and provide empirical evidence to justify the existence of an optimised processing zone for desired chips. By comparing the side profile view along the specimen axis, it can be observed that the smooth chip exhibits cup-and-cone fracture, while the serrated chip shows slant fracture. This can be correlated to the surface defects on the serrated chips. Those sharp edges served as areas of high stress concentrations, promoting the crack to initiate with a lesser load required. The smooth chips showed pronounced necking, indicating substantial plastic deformation and load-carrying capacity prior to fracture. This is further confirmed through examining the chips cross-section. The existence of dimples is concrete evidence of void nucleation and coalescence, commonly observed in ductile materials after exceeding the critical plastic strain. The deep dimples also suggest that smooth chips exhibit better toughness as compared to serrated chips, which show shallower dimples. The equiaxed shape dimples on the smooth chips also suggest that it is a tensile-dominated failure, whereas serrated chips failed dominantly due to shear, leading to the formation of directional elongated dimples.

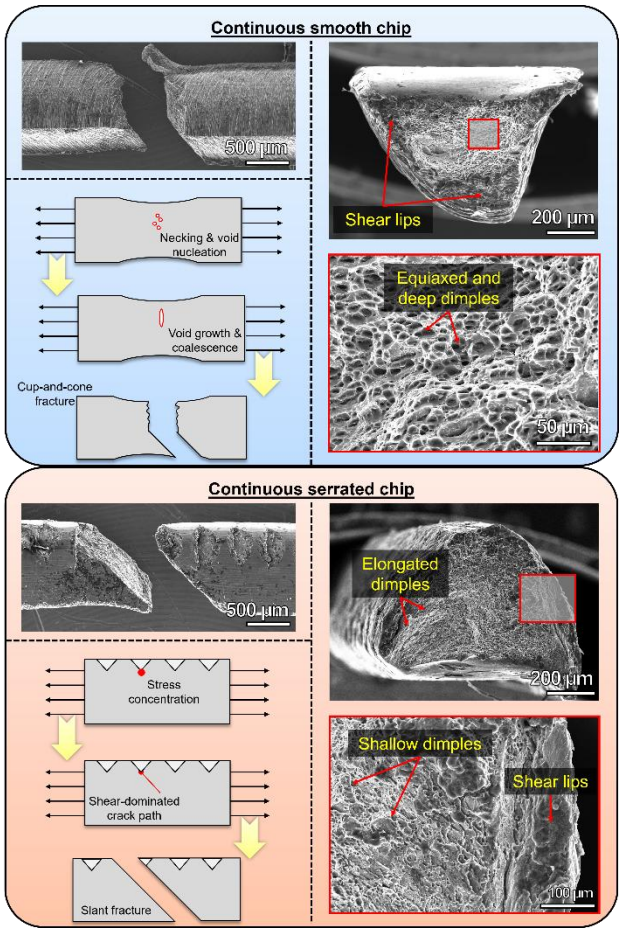

Figure 4. Fractography and fracture mechanism of serrated and smooth machining chips

The fractography analysis suggests that serrated chips will have limited applications and usability due to the reduced ductility and toughness. This part of the study aims to produce machining chips that can be used for further processing and development. In addition, the results also correlate well with the previous findings, in serrated chips, the thermal softening effect localised the strain in a narrow band. As a result, this area is excessively deformed, allowing minimal further plastic deformation, thus showing lowered material toughness and exhibiting shallow dimples on the fracture surface. Therefore, it is clear that chip serration is an undesirable phenomenon, and by careful control of the machining parameters, desired chips can be produced for subsequent processing and forming.

4. Conclusion

In conclusion, this paper presented a feasibility study to produce continuous wires through solid-state processes. As a preliminary assessment, the study identified chip serration as a key factor affecting the quality of wires produced. As shown experimentally, machining parameters affect the type of machining chips produced, as it has an influence on the stabilising and destabilising factors in shear band formation. Whenever the destabilising influence of the thermal softening outweighs the stabilising effect from the work-hardening during plastic deformation, the serration phenomenon occurs. The use of the Recht criterion with FE models to quantify the degree of serration is also presented, showing good agreement between numerical and experimental results. From the fractography analysis, it is evident that chip serration is an undesirable phenomenon, and smooth machining chips with a higher Recht ratio (>0.9) are desirable for subsequent processing and usage. Subsequent studies will first determine the optimum process window for the turning process with the use of the FE-Recht criterion framework. Secondly, to improve the quality of the wires, studies will be conducted to understand if the wires can sustain further deformation and processing to ensure usability. Finally, the usability of the continuous wires produced will be evaluated through their applications in wire-based AM techniques.

Acknowledgement

This work is supported by the Agency for Science, Technology and Research (A*STAR), Singapore, through the RIE2025 MTC IAF-PP grant (Grant No. M24N2a0041) and the A*STAR Graduate Scholarship (Scholarship No. SEAGS24003).

References

[1] B. Wan, W. Chen, T. Lu, F. Liu, Z. Jiang, and M. Mao, "Review of solid state recycling of aluminum chips," *Resources, Conservation and Recycling,* **vol. 125**, pp. 37-47, 2017, doi: 10.1016/j.resconrec.2017.06.004.

[2] L. Chabbi, S. Hasler, H. Roelofs, and H. Haupt-Peter, "Challenges and Innovation in Steel Wire Production," *Materials Science Forum,* **vol. 892**, pp. 3-9, 2017, doi: 10.4028/www.scientific.net/MSF.892.3.

[3] W. Tang and A. P. Reynolds, "Production of wire via friction extrusion of aluminum alloy machining chips," *Journal of Materials Processing Technology,* **vol. 210**, no. 15, pp. 2231-2237, 2010, doi: 10.1016/j.jmatprotec.2010.08.010.

[4] T. Mabrouki, F. Girardin, M. Asad, and J.-F. Rigal, "Numerical and experimental study of dry cutting for an aeronautic aluminium alloy (A2024-T351)," *International Journal of Machine Tools and Manufacture,* **vol. 48**, no. 11, pp. 1187-1197, 2008, doi: 10.1016/j.ijmachtools.2008.03.013.

[5] A. Chakraborty and S. Roy, "Shear localization and shear banding: A review about the complex interplay between material, microstructural and process variables," *Materials Characterization,* **vol. 218**, 2024, doi: 10.1016/j.matchar.2024.114501.

[6] G. G. Ye, Y. Chen, S. F. Xue, and L. H. Dai, "Critical cutting speed for onset of serrated chip flow in high speed machining," *International Journal of Machine Tools and Manufacture,* **vol. 86**, pp. 18-33, 2014, doi: 10.1016/j.ijmachtools.2014.06.006.

[7] R. F. Recht, "Catastrophic thermoplastic shear," *Journal of Applied Mechanics,* **vol. 31**, pp. 189-193, 1964.

euspen's 26th International Conference & Exhibition, Krakow, PL, June 2026
www.euspen.eu

Robust design of diffractive optical elements for anticounterfeiting mould texturing

Marco Sorgato[1,*]; Giacomo Baruffa[1]; Giovanni Lucchetta[1]; Enrico Savio[1]

[1]*Department of Industrial Engineering, University of Padova, via Gradenigo 6/A, 35131 Padova, Italy*

[*]*Marco.sorgato@unipd.it*

Abstract

Counterfeiting significantly affects injection molding, a technology widely used for high-volume, low-cost production. Developing robust, cost-effective anti-counterfeiting features that can be directly integrated into injection-molded polymer components is a relevant industrial challenge. Diffractive optical elements (DOEs) are promising candidates, as they enable the projection of holographic images combining easy visual authentication with complex optical signatures. This work presents a systematic prototyping framework for phase-only DOEs using two-photon polymerization lithography. The framework aims to identify geometries compatible with the spatial resolution and accuracy of industrial mold texturing processes. In the first phase, the influence of pixel pitch and phase discretization levels on holographic image quality was evaluated using contrast transfer function and mean-squared-error metrics. An optimal configuration with a 7 µm pixel pitch and 3 phase levels was identified, balancing image quality and manufacturability. In the second phase, the robustness of this configuration was assessed by introducing controlled defects in pixel height and pitch. Results show that although such defects affect hologram quality, functional performance remains within error ranges compatible with state-of-the-art mold texturing technologies. Overall, the study provides quantitative guidelines for integrating DOE-based holographic anti-counterfeiting features into injection-molded components.

Diffractive optical elements; surface functionalization; two-photon polymerization; prototyping.

1. Introduction

Counterfeiting is a growing global concern, and injection molding (IM) is particularly vulnerable due to its high-volume, low-cost production model [1]. This motivates the development of cost-effective anti-counterfeiting solutions that can be directly integrated into IM components. A promising approach is to replicate diffractive micro- and nanostructures from textured molds to generate structural-color tags [1]. However, effective protection should combine easily recognizable features with elements that are difficult to interpret and replicate, such as diffractive optical elements (DOEs) implemented as computer generated holograms. DOEs exploit micro- or nanoscale features to manipulate light and project holographic images under controlled illumination, with phase-only transmission-mode DOEs generally preferred for their high efficiency [2,3].

Although DOEs are compatible with IM due to the absence of undercuts, their direct integration into molds is limited by the resolution of current texturing technologies [4]. DOEs are usually produced via lithographic processes [2,3], which, despite providing high spatial resolution, are unsuitable for direct mold texturing due to the costs related to mask fabrication and the need to operate in a vacuum. Moreover, such processes cannot be directly applied to standard mold materials [5].

Finally, DOE performance is highly sensitive to dimensional inaccuracies. Errors in pixel height and pitch directly affect phase modulation and diffraction angles [6,7]. Consequently, the precision and accuracy limitations of the texturing processes significantly impact the quality of the projected images [5]. While previous studies have numerically analyzed the influence of fabrication defects on diffraction efficiency, experimental studies linking inaccuracies to holographic image quality remain limited, particularly in the context of the IM process chain [5–7].

Overall, integrating DOEs into injection molds requires a quantitative understanding of the spatial resolution required to preserve holographic image quality and of the effects of process-induced inaccuracies on DOE functionality, to define a viable process chain for direct mold texturing.

Two-photon polymerization lithography (TPL) provides a suitable experimental platform to address these aspects. Based on direct laser writing and two-photon absorption, TPL enables the high-accuracy fabrication of complex three-dimensional optical micro- and nanostructures with ≈100 nm spatial resolution [7,8]. Its flexibility allows systematic variation of key geometrical parameters, making it particularly suitable for controlled parametric investigations and rapid prototyping [6].

In this work, TPL was used to study the effect of key DOE parameters, pixel pitch and phase discretization, on holographic image quality. Fabricated DOEs were first geometrically and functionally characterized to quantify the relationship between feature dimensions and image quality, thereby identifying an optimal trade-off between manufacturability and surface functionality. Subsequently, hologram robustness was evaluated by introducing controlled errors in pixel pitch and height to simulate manufacturing defects, and the results were compared with mold nanotexturing capabilities to define a geometry suitable for IM integration [4]. Overall, the study provides quantitative design guidelines for robust DOE-based anti-counterfeiting features in IM polymer components.

2. Materials and methods

2.1. DOE Design

The DOE design begins with the selection of a target image (Fig. 1a). The NBS 1952 resolution test chart was chosen due to its low sensitivity to the zero-order spot and its extended line features, which facilitate the identification of aberrations in the

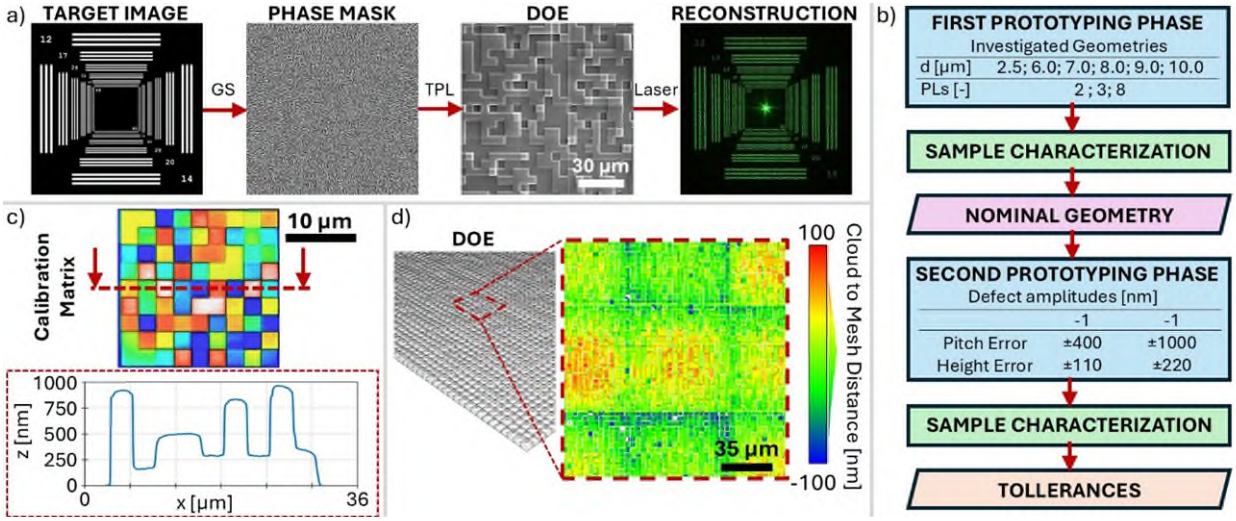

Figure 1. Surface design and validation: (a) DOE design workflow; (b) prototyping process workflow; (c) calibration matrix verification through profile analysis; d) DOE verification using point-cloud–to-mesh distance.

projected image. The target image, initially 2600 × 2600 pixels, was first resized to match the DOE footprint of 2.4 mm × 2.4 mm. A phase mask was then computed from this resized image using the Gerchberg–Saxton (GS) algorithm with 200 iterations and a 50-pixel padding to minimize edge effects. Finally, a height map was calculated by applying eq. 1 to each pixel of the phase mask:

$$h = (\Delta\phi \cdot \lambda) / (2\pi(n-1)) \quad \text{(eq.1)}$$

where $\Delta\phi$ is the phase shift assigned to the pixel, h is the corresponding pixel height, λ is the wavelength of the incident light, and n is the refractive index of the polymerized resin.

The GS algorithm with eq.1 yields continuous phase modulation from −π to +π, which was quantized into finite phase levels (*PLs*) due to the layer-by-layer TPL process. Finally, each pixel was given a nominal lateral dimension (*d*) in the X–Y plane.

2.2. TPL Process

Two-photon polymerization lithography (TPL) uses a focused laser to polymerize a photosensitive resin via two-photon absorption [8]. All DOEs were fabricated using a Photonic Professional GT system (Nanoscribe GmbH) equipped with a 63×/1.4 objective and the negative-tone photoresist IP-Dip2 (n = 1.55), on 25 × 25 × 0.7 mm fused silica substrates. A 0.6 µm base layer was added beneath each printed structure to enhance adhesion and compensate for any interface detection errors or plane tilt [7]. After printing, samples were developed in propylene glycol monomethyl ether acetate (PGMEA) for 12 min and rinsed in isopropyl alcohol (IPA) for 2 min.

All DOEs were printed using the same process parameters: laser power of 21.25 mW, beam scan speed of 20 mm/s, slice distance of 120 nm, and hatch distance of 200 nm. The process parameters used were selected to maximize printing accuracy.

2.3. Prototyping Phases

The DOE prototyping was organised in two phases (Fig.1b): (i) study of the effect of DOE geometry (*d* and *PL*) on functional performance, and (ii) study of the effect of defects on image reconstruction. In both stages, the DOEs' footprint was fixed at 2.4 mm (±50 µm), fully inscribed within the 3.5 mm laser beam.

In the first stage, 14 DOEs were fabricated with characteristic dimensions *d* ranging from 2.5 to 10 µm and phase levels of 8, 3, and 2, corresponding to minimum height steps of 120, 320, and 480 nm, respectively. Three 9x9-pixel matrices (referred to as "calibration matrices") matching each DOE geometry were printed alongside the samples to monitor TPL stability (Fig. 1c).

In the second prototyping stage, a reference DOE (*d* = 7 µm, *PL* = 3) was systematically perturbed following a full-factorial design of experiments (Fig. 1b). To simulate manufacturing defects, constant absolute deviations, evenly split between positive and negative values, were applied to 66% of randomly selected features. Specifically, height errors modified the nominal pixel heights, while pitch errors altered the widths (*d*) of randomly chosen rows and columns. The error magnitudes were based on current mold nanotexturing precision limits.

2.4. Sample Characterization

All printed surfaces (calibration matrices and DOEs) were evaluated using a confocal profilometer (Plu Neox, Sensofar; 100× objective) to quantify printing accuracy.

The calibration matrices were analyzed via a point-cloud-to-CAD comparison conducted with CloudCompare software, which mapped local deviations by comparing profilometer scans against the nominal STL geometries. To ensure measurement reliability, surface profiles were extracted at pixel centers to evaluate the pixel heights (Fig. 1c). Each of the 3 matrices printed for each geometry was geometrically characterized.

Printing accuracy of the DOEs was then assessed using the CAD comparison approach. For each DOE, two 0.5 × 0.5 mm areas relating to the start and end of the printing were scanned. From each scan, a 100 × 100 µm sub-area was extracted and compared with the nominal mesh. Results are reported as the mean and standard deviation of the distances (Fig. 1d).

The optical performance of each fabricated DOE was evaluated by analyzing its reconstructed holographic image. Each sample was mounted on an alignment system, centered in a DPSS laser beam (λ = 532 nm, power = 4.5 mW, beam diameter = 3.5 mm), and projected onto a planar screen located 3.1 m away in a light-controlled environment. Finally, the images were captured under identical exposure settings using a Raspberry Pi 5 system equipped with an HQ camera and a 16 mm lens.

The quality and sharpness of the images were evaluated using contrast (*c*) and mean squared error (MSE). Optical metrics were calculated and averaged over 3 image acquisitions per sample.

Contrast was computed for the line-pair groups (numbered 12, 17, 24, 34, 48, and 68 from the NBS calibration chart in Fig. 1a) located in the upper-right quadrant of the target image using the Michelson contrast definition:

$$c = (I_{max}-I_{min})/(I_{max}+I_{min}) \quad \text{(eq.2)}$$

where I_{max} and I_{min} are the maximum and minimum intensity values sampled along the considered line pair.

Finally, the MSE was computed via a pixel-by-pixel comparison between the reconstructed image and a reference photograph of a physical target matching the holographic image dimensions. This approach yields an MSE value independent of the acquisition system's resolution.

3. Results

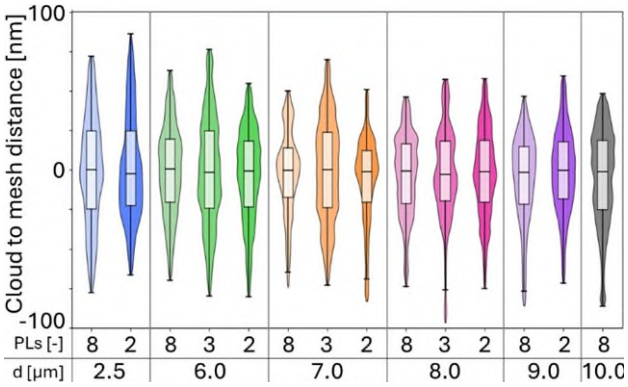

Figure 2. Calibration matrix validation through point cloud.

Comparisons between profile and point-cloud–to–mesh measurements showed no systematic trends, and differences were often within the instrument uncertainty (4–8 nm). This indicates that CAD-based comparison is a reliable method for verifying DOE dimensions. Figure 2 presents violin plots of the geometric deviation distributions measured on the calibration matrices through the CAD-comparison approach. Larger deviations are mainly associated with smaller pixel pitches, primarily due to edge effects at pixel margins, which become less significant as *d* increases. For all samples, the interquartile range lies within ±25 nm, and 95% of the data fall within ±75 nm. These deviation levels are consistent with literature values, although printing accuracy is often assessed only indirectly [6,9].

The geometric verification of the DOEs showed a mean error of approximately 0 nm across all surfaces. Standard deviation ranged from 57 nm for the DOE with *d* = 7 µm and *PL*s = 2 to 67 nm for with *d* = 2.5 µm and *PL*s = 8. No statistically significant trends were observed, and the variation in standard deviations was considered negligible. Compared with the calibration matrices, the standard deviation increases by approximately 35 nm for the DOEs. This increase is attributed to the stitching strategy of the TPL system: because DOE dimensions exceed the objective writing field, fabrication requires stitching multiple adjacent fields (Fig.1d) [8]. The resulting overlaps introduce local imperfections, while minor laser power fluctuations and uncertainties in detecting the FS–resin interface can further cause defects and misalignments between writing fields [7].

Overall, process accuracy remains stable across different geometries and over time (Fig. 2), and variations in process precision and accuracy do not significantly affect the functional performance of the individual DOEs.

The functionality of all DOE printed in the first prototyping stage was evaluated. MSE results are reported in Fig. 3a; a marked increase in MSE is observed for $d \geq 9$ µm, due to reduced phase and image discretization and to the contraction of the high-intensity region, which increases the relative noise contribution at the center of the reconstructed image [5,6]. In contrast, MSE variations are limited for *d* = 6–8 µm, indicating more stable reconstruction quality and the growing influence of the acquisition system's background noise, which becomes comparable to the decreasing background noise in the diffraction pattern. A systematic increase in MSE is also observed with decreasing *PL* number, due to reduced diffractive efficiency [5,10]. Among the tested configurations, the 3-*PL* DOE represents a practical compromise, offering better image quality than 2 *PL*s while holding lower fabrication complexity than 8 *PL*s.

Figure 3b shows the contrast transfer functions (CTFs), obtained by plotting the contrast of line pairs in each group of the target chart versus the line-pair period of the original image. A contrast threshold of 0.3, experimentally determined as the minimum for visual distinguishability, is overlaid on the curves. In all cases, line-pair contrast decreases with increasing lines' spatial frequency. When evaluating the influence of geometric parameters, a progressive reduction in contrast is observed as *d* increases. Consistent with previous results (Fig. 3a), DOEs with a $d \geq 9$ µm produce images with markedly inferior quality. It is also observed that DOEs with 2 *PL*s generally yield lower image sharpness than those with 8 *PL*s. However, DOEs with 3 *PL*s exhibit contrast values for line groups, up to 1.0 line pairs per 100 pixels, comparable to those obtained with 8 *PL*s. These findings indicate that a 3-level phase discretization is sufficient to preserve good image sharpness and visibility of line pairs. Nevertheless, as the phase discretization becomes coarser, noise increases in the central region of the reconstructed image and in the areas between adjacent groups (Fig. 3a).

Based on these results, DOEs with *d* = 6 and 7 µm and 3 *PL*s represent optimal compromises, with *d* = 7 µm preferred due to higher compatibility with industrial manufacturing constraints [4]. This choice is supported by the indefinable lines in the group with 1.0 line pairs per 100 pixels for *d* = 8 µm and 3 *PL*s (Fig. 3b).

The selected surface serves as a reference for the second prototyping phase (Fig. 3a). Because preliminary tests showed a complete loss of the holographic image when ±220 nm height errors affected 66% of the pixels, deviations of ±110 nm and ±220 nm were applied in equal numbers. This specific condition is denoted as '±220 nm' in Fig. 4. ANOVA of the design of experiment indicated that both defect types significantly affect *c* and MSE, while their interaction was not statistically significant. Figure 4a presents the main effects of pixel pitch and height defects on the MSE of reconstructed images. As expected, increasing deviation amplitudes reduces optical performance, with a pronounced decrease in MSE at higher defect levels, which is unacceptable due to increased noise and reduced image contrast (Fig. 4a). In particular, the hologram response strongly depends on the type of defect introduced. Height errors primarily increase background noise, mainly due to incorrect phase modulation [6,11]. While errors in the lateral dimensions induce image asymmetries, leading to the loss of visibility of one half of the line-pair groups along the image diagonal, this effect is ascribed to local changes in phase and diffraction angle [5,11].

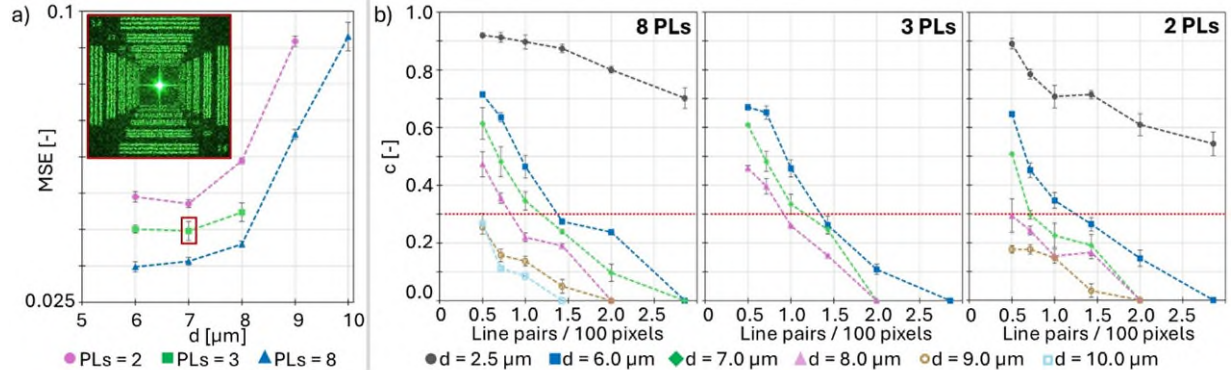

Figure 3. Evaluation of the effect of DOE geometry: (a) effect of feature size on MSE; (b) CTF curves.

Figure 4b presents the mean CTFs for reconstructed images obtained after introducing defects on the diffractive surface, with amplitude equal to the first level investigated (Fig. 1b). The maximum standard deviation for *c* in samples of the second prototyping phase is 0.04 (consistent with Fig. 3b). Notably, the addition of either pitch or height defects alone reduces the mean *c* within individual line groups but does not compromise the visibility of any group. However, the simultaneous introduction of both defect types results in a loss of visibility of the lines in the group with 1.0 line pairs per 100 pixels.

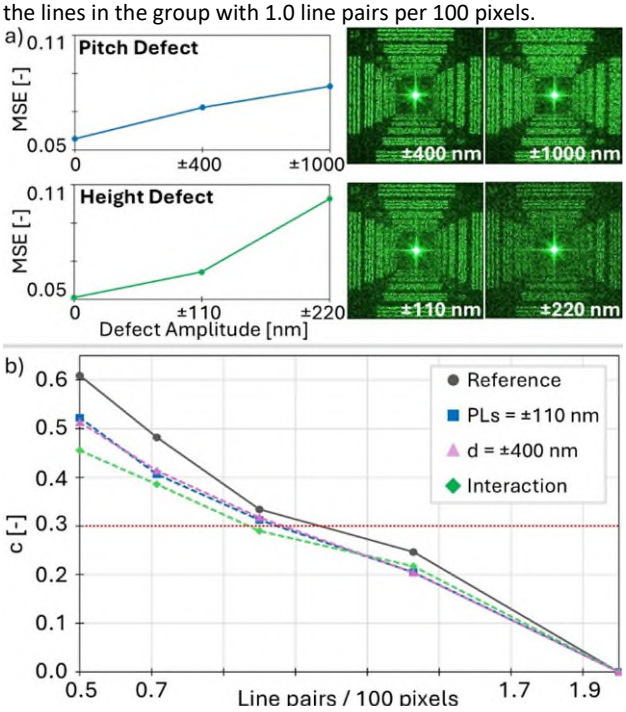

Figure 4. Effect of manufacturing defects: (a) MSE main effects plots; (b) CTF curves of DOEs with defects.

4. Discussion

From both economic and technological perspectives, laser ablation is the most viable process for producing the desired mold surface, with femtosecond (fs) laser machining providing superior control over ablation volume and improved surface quality [4,12]. Few studies have reported DOE fabrication via fs-laser processing of materials such as sapphire or quartz [9,13], typically using UV wavelengths and high numerical aperture (NA) optics to limit ablation depth and achieve tight focusing. While suitable for mold inserts, these materials are costly, and high-NA systems are not widely available industrially. More recent work on UV fs-laser ablation of conventional mold materials using low-NA optics has demonstrated ablation depths (≈320 nm) and lateral feature sizes (≈7 µm) compatible with DOE requirements, with similar spatial resolutions achieved using single-pulse fs-laser processing at longer wavelengths [12,14]. However, low-NA systems may require beam shapers to obtain square, flat-top intensity profiles.

Fs-laser ablation precision is typically ±70 nm [9,13], so the defect amplitudes considered in this study are conservative and representative of industrial conditions, including polymer shrinkage. Lateral pixel-size defect magnitudes were chosen based on the precision and accuracy of positioning systems typically employed in fs-laser platforms [9,14]. To maintain image sharpness, positioning errors should be kept within ±400 nm, requiring the laser system to be equipped with nanoscale positioning and control capabilities.

Analysis of manufacturing accuracy relative to image sharpness highlights the range of images that DOEs can effectively project and the achievable quality of holographic images. These results are particularly relevant for anti-counterfeiting, where reliable reconstruction of patterns with varying visual complexity enables encrypted security codes [2,3].

5. Conclusions

This work presents a systematic prototyping strategy to evaluate the integration of DOEs as anti-counterfeiting features in IM polymer components, considering both optical performance and manufacturing constraints. Quantitative analysis of pixel pitch and phase discretization identified an optimal trade-off between image quality and manufacturability, with DOEs featuring a 7 µm pixel pitch and 3 phase levels delivering robust holographic performance. The robustness of this configuration against realistic manufacturing defects confirms its compatibility with fs-laser mold texturing. Overall, the methodology provides practical design guidelines bridging optical design and industrial fabrication. Future work will investigate surface roughness and polymer shrinkage–induced refractive index variations to further refine DOE integration.

References

[1] Sorgato, M., Baruffa, G., Oubellaouch, K., Zaniboni, G., & Lucchetta, G. (2025). A novel method for high-volume manufacturing of self-protective plastic surfaces to ensure durable anti-counterfeiting functionality. *CIRP Annals*, **74**, 783-787.

[2] Ruffato, G., Rossi, R., Massari, M., Mafakheri, E., Capaldo, P., & Romanato, F. (2017). Design, fabrication and characterization of computer generated holograms for anti-counterfeiting applications using OAM beams as light decoders. *Scientific reports*, **7**(1), 18011.

[3] Mohammad, N., Meem, M., Wan, X., & Menon, R. (2017). Full-color, large area, transmissive holograms enabled by multi-level diffractive optics. *Scientific reports*, **7**(1), 5789.

[4] Masato, D., Piccolo, L., Lucchetta, G., & Sorgato, M. (2022). Texturing technologies for plastics injection molding: a review. *Micromachines*, **13**(8), 1211.

[5] Taghizadeh, M. R., Blair, P., Layet, B., Barton, I. M., Waddie, A. J., & Ross, N. (1997). Design and fabrication of diffractive optical elements. *Microelectronic Engineering*, **34**(3-4), 219-242.

[6] Wang, H., Liu, Y., Ruan, Q., Liu, H., Ng, R. J., Tan, Y. S., ... & Yang, J. K. (2019). Off-Axis holography with uniform illumination via 3D printed diffractive optical elements. *Advanced Optical Materials*, **7**(12), 1900068.

[7] Wang, H., Wang, H., Zhang, W., & Yang, J. K. (2020). Toward near-perfect diffractive optical elements via nanoscale 3D printing. *ACS nano*, **14**(8), 10452-10461.

[8] Wang, H., Zhang, W., Ladika, D., Yu, H., Gailevičius, D., Wang, H., ... & Yang, J. K. (2023). Two-photon polymerization lithography for optics and photonics: fundamentals, materials, technologies, and applications. *Advanced Functional Materials*, **33**(39), 2214211.

[9] Li, Q. K., Chen, Q. D., Niu, L. G., Yu, Y. H., Wang, L., Sun, Y. L., & Sun, H. B. (2016). Sapphire-based Dammann gratings for UV beam splitting. *IEEE Photonics Journal*, **8**(6), 1-8.

[10] Pavelyev, V., Osipov, V., Kachalov, D., & Chichkov, B. (2013). Diffractive optical elements with radial four-level microrelief fabricated by two-photon polymerization. *Optics Communications*, **286**, 368-371.

[11] Roeder, M., Schilling, P., Hera, D., Guenther, T., & Zimmermann, A. (2018). Influences on the fabrication of diffractive optical elements by injection compression molding. *Journal of Manufacturing and Materials Processing*, **2**(1), 5.

[12] Genieys, T., Sentis, M., & Utéza, O. (2020). Measurement of ultrashort laser ablation of four metals (Al, Cu, Ni, W) in the single-pulse regime. *Advanced Optical Technologies*, **9**(3), 131-143.

[13] Stonyte, D., Jukna, V., Lukosiunas, I., Zakarauskas, P., Huang, H. H., Katkus, T., ... & Paipulas, D. (2024). Four-level diffractive photon sieves by deep-UV femtosecond laser ablation. *Optics Express*, **32**(24), 43102-43117.

[14] Buchner, B., Mittelmann, S., von Toussaint, U., & Neu, R. (2025). Investigation of UV-Femtosecond laser ablation on metallic substrates. *Applied Physics A*, **131**(9), 693.

euspen's 26th International Conference & Exhibition, Krakow, PL, June 2026
www.euspen.eu

Influence of Cutting Temperature on Affected Layer in Cutting of Aluminum Alloy Castings with PCD tool

Hiroo Shizuka[1)], Katsuhiko Sakai[1)], Koki Tokai[1)]

[1] *Shizuoka University,3-5-1 Johoku Naka-ku Hamamatsu Shizuoka 432-8561 Japan*

shizuka.hiroo@shizuoka.ac.jp

Abstract
In this study, the influence of cutting temperature on the machining-affected layer and residual stress during the cutting of aluminum alloy castings (Al-Si7Mg) using PCD tools was investigated. The results showed that, although little deformation was observed in the microstructure near the finished surface, changes in the residual stress were confirmed at the outermost surface. Furthermore, it was clarified that the tensile stress on the workpiece surface increased with an increase in the cutting temperature caused by an increase in the cutting speed. In addition, it was found that, in the extremely low-speed range where nearly no heat is generated by cutting, compressive stress due to mechanical factors occurs on the finished surface.

Orthogonal cutting, affected layer, cutting temperature, residual stress, aluminum alloy casting

1. Introduction

Aluminum alloys are metallic materials with superior machinability compared with steel. In recent years, significant advancements in machine tool motion accuracy and cutting tool manufacturing technology have enabled cutting speeds of several thousand millimeters per minute for aluminum alloy machining using diamond tools [1]. However, machining-affected layers occur in aluminum alloy cutting, similar to steel, which can lead to a deterioration in product performance and safety [2]. Most previous studies on machining-affected layers in aluminum cutting have focused on conventional cemented carbide tools, whereas research on diamond tools such as PCD, which have become widely used in recent years, remains scarce [3]. Therefore, this study investigates the effects of cutting speed, tool geometry, and cutting temperature on the machining-affected layer and the residual stress during the cutting of aluminum alloy castings (Al-Si7Mg) using PCD tools.

2. Experimental Method

To accurately measure the machining-affected layer and the residual stress caused by cutting, the surface of the workpiece must be free from damage prior to machining owing to preliminary processing. For this reason, the test specimens were repeatedly machined under the cutting conditions shown in Table 1, gradually reducing the depth of cut from 0.1 mm to 0.003 mm in six steps, to create a surface with minimal machining-affected layer and residual stress. Orthogonal cutting of the aluminum alloy castings (ISO: Al-Si7Mg) was then performed using PCD tools under the conditions listed in Table 2. The workpiece material was removed from the aluminum wheels, and a dedicated orthogonal cutting machine was used. Residual stress on the machined surface was measured using a portable X-ray residual stress measuring device (μ-X360S, Pulstec Industrial Co., Ltd.). Measurements were performed on the machined surface in both the cutting direction (parallel) and cutting width direction (perpendicular). To eliminate measurement errors caused by surface irregularities, X-rays were irradiated from two directions (forward and reverse) at each measurement point and the average value was calculated. Four points were measured on each machined surface, and their average was considered as the residual stress value for the cutting condition. The cutting temperature was measured using the tool–workpiece thermocouple method.

3. Results and discussion

Figure 1 shows the microstructure of the workpiece cross-section. The cutting direction was from right to left, and the upper edge of the figure represents the machined surface. The image on the right shows the same location after cutting to a thickness of 0.1 mm. A comparison of the crystal shapes before

Table 1 Cutting conditions for specimen preparation

Tool	PCD
Rake angle [deg]	10
Relief angle [°]	6
Cutting speed [m/min]	0.05
Depth of cut [mm]	0.1, 0.05, 0.025, 0.01, 0.005, 0.003

Table 2 Cutting conditions for orthogonal cutting

Rake angle [°]	5, -5
Depth of cut [mm]	0.100
Cutting width [mm]	2
Cutting speed [m/min]	0.01, 0.1, 1, 10, 100

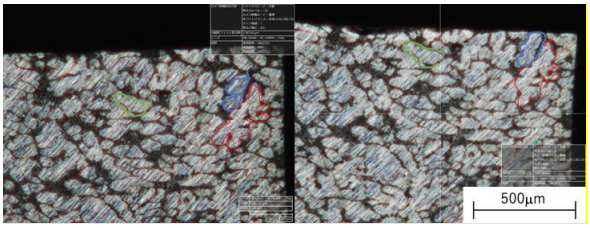

Figure1. Microstructure of the workpiece cross-section (Right: before cutting, Left: after cutting)

and after cutting revealed no significant deformation, as indicated by the area circled in blue. Furthermore, no plastic flow layer is detected on the finished surface. These observations confirm the absence of a machining-affected layer from the microstructural analysis of the finished surface. Figure 2 shows the residual stress measurement results on the finished surface plotted as a semi-logarithmic graph with the cutting speed on the horizontal axis. The results indicate that changes in the rake angle did not affect the residual stress. Regarding the cutting speed, no change in residual stress was observed below 1 m/min; however, above 1 m/min, the tensile stress increased with cutting speed. The occurrence of tensile stress during cutting has also been reported in studies on high-speed cutting of steel, and similar results have been observed for aluminum alloy castings [4]. Figure 3 shows the cutting-temperature measurement results obtained using the tool–workpiece thermocouple method. Although calibration experiments were conducted to derive the calibration coefficient for determining cutting temperature from the thermoelectric voltage between the PCD tool and aluminum alloy casting, accurate coefficients could not be obtained; therefore, the figure shows the thermoelectric voltage. Below 1 m/min, nearly no voltage is generated, indicating negligible heat generation during cutting. Above 1 m/min, the voltage increased with cutting speed. This result is consistent with the residual stress measurements shown in Figure 2, suggesting that the increase in cutting temperature due to the increased cutting speed leads to increased residual stress on the finished surface. Furthermore, regarding the effective measurement depths of residual stress and cutting temperature, X-ray residual stress analysis is sensitive primarily to an extremely shallow region near the specimen surface, whereas the tool–workpiece thermocouple method measures the thermoelectric voltage generated at the tool–workpiece contact interface. Although the exact correspondence between the measurement depths of these two methods cannot be strictly defined, both techniques can be regarded as providing information related mainly to the near-surface region of the workpiece. The mechanism is as follows. During machining, the region near the cutting point tends to expand owing to the temperature increase but is constrained by the surrounding cooler regions, resulting in tensile stress. The greater the cutting speed, the larger the temperature difference and, thus, the greater the tensile stress. Therefore, the tensile stress observed at cutting speeds above 1 m/min can be attributed to thermal effects. Furthermore, Figure 2 shows that compressive stress occurs at cutting speeds below 1 m/min, where nearly no heat is generated. Focusing on the thrust force shown in Figure 4, the thrust force is large at cutting speeds below 1 m/min. When the thrust force is large, the material on the finished surface tends to plastically deform and spread but is constrained by the surrounding regions, resulting in compressive stress. Therefore, the compressive stress at cutting speeds below 1 m/min is considered to be caused by mechanical factors.

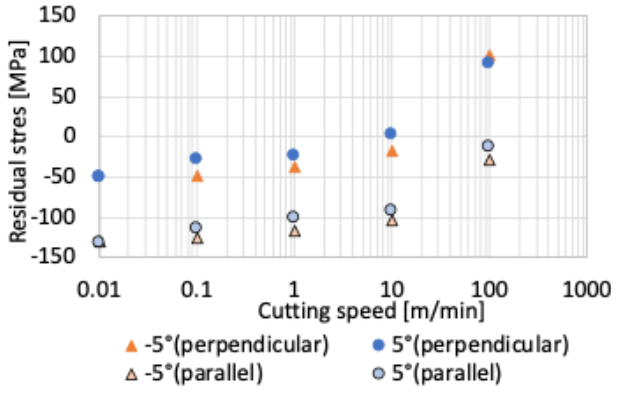

Figure2. Residual stress

4. Conclusion

In this study, the influence of cutting temperature on the machining-affected layer and residual stress during the cutting of aluminum alloy castings (Al-Si7Mg) using PCD tools was investigated. The results showed that, although little deformation was observed in the microstructure near the finished surface, changes in the residual stress were confirmed at the outermost surface. Furthermore, it was clarified that the tensile stress on the workpiece surface increased with an increase in the cutting temperature caused by an increase in the cutting speed. In addition, it was found that, in the extremely low-speed range where nearly no heat was generated by cutting, compressive stress due to mechanical factors occurred on the finished surface. Moreover, differences in the rake angle had only a minimal effect on the residual stress on the machined surface.

References

[1] Sumiya H., Harano K., Sato T. 2012 Practical Development of Binderless Nano-polycrystalline Diamond J. JSPE. **78** 108-111

[2] Sato H., Miura E., Watanabe Y. Formation Behavior of Nanostructural Layer Induced by Sliding Wear 2011 Mater. **50** 331-338

[3] Yamada H., Tanaka T. Effects of Mg, Cu on built-up edge and cutting temperature in turning of Al-7%Si alloy 1985 J. Jpn Inst. Light Met. **35** 415- 418

[4] Kakino Y., Okushima K. Theoretical Analysis of Thermal Effects to Residual Stress 1969 J. JSPE. 35 775-779

Acknowledgement

We are deeply appreciative of the funding provided by Johoku Industrial Co.Ltd,.

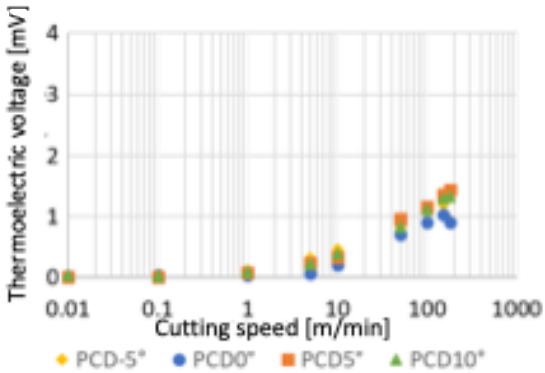

Figure3. Measurement results of thermoelectric voltage by the tool–workpiece thermocouple method

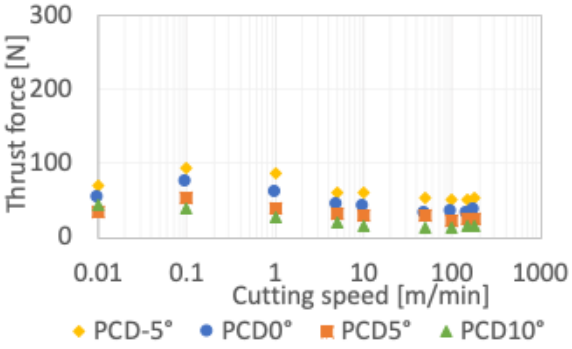

Figure4. Cutting speed and thrust force

euspen's 26th International Conference & Exhibition, Krakow, PL, June 2026
www.euspen.eu

Electrochemical machining of pre-defined kinematic surface roughness on nickel 201 with continuous electrolyte jet

André Martin[1,*], Tehreem Javed[1], Sepideh Ghorbanalipour[1], Andreas Schubert[1]

[1]*Chemnitz University of Technology, Professorship Micromanufacturing Technology, Reichenhainer Str. 70, 09126 Chemnitz, Germany*

andre.martin@mb.tu-chemnitz.de

Abstract
Nickel and its alloys are widely used in microsystems due to their high strength, ductility, and resistance to corrosion and fatigue. As performance demands grow, there is an increasing interest in developing methods for producing high-quality pure-nickel micro-components. However, nickel and its alloys are considered as difficult-to-machine materials due to their mechanical and chemical properties such as high tendency to strong work hardening. Thus, individual surface structures such as micro-fluidic channels or structured surfaces to increase the size of the active area for chemical reactions and to improve performance and efficiency is challenging. Alternative thermal ablation techniques cause microstructural changes of the base material and strong surface oxidation, which should usually be avoided. For these reasons, electrochemical machining (ECM) for surface shaping was investigated. Applying a continuous jet of electrolyte (Jet-ECM) offers the possibility for flexible shaping of metal surfaces with micrometre-scaled grooves that are characterized by a specific, kinematic surface roughness. However, the dissolution characteristics of pure nickel with Jet-ECM was not sufficiently investigated before. Hence, applicable combinations of electrolyte composition and machining strategy were investigated to prepare kinematic surface roughness values. Concentric arrangements of cylindrical groove sections with lateral infeed distance of 150 µm were manufactured on initially plane, mechanically turned surfaces of nickel 201 parts. The most efficient dissolution was realized with a sodium chloride electrolyte. From further experiments, nozzle motion speeds of 900 µm/s, 1800 µm/s and 3000 µm/s were derived to machine whole cylindrical sample surfaces. The measurements prove good accordance with the highest target roughness of *Rz* 27 µm, while the lower roughness values significantly differ from the targeted *Rz* of 20 µm and 15 µm. Hence, Jet-ECM represents a promising technique for structuring of pure nickel to increase surface area, but further optimizations are required to better meet the targeted roughness.

Keywords: electrochemical machining, Jet-ECM, kinematic surface roughness, nickel

1. Introduction

Nickel and nickel alloys exhibit good chemical resistance in many media [1]. Furthermore, they exhibit mechanical and chemical material properties that qualify them for applications in both high- and low-temperature ranges. Numerous applications in macro- and micro-apparatus construction and process engineering, such as fuel cells, are conceivable [2].

Non-alloyed, pure nickel 201, which is optimized for applications at temperatures above 300°C, is often used as electrode material for hydrogen electrolysis or in alkaline fuel cells [3]. To increase efficiency, an increase in the active reaction surface is sometimes sought [4]. This can be achieved by deliberately creating a kinematic roughness. Nickel, however, is difficult to machine with cutting processes, due to its high ductility, strong tendency to work hardening and chemical affinity to various cutting materials [5].

Finish machining processes, which are often used to reduce surface roughness, can be also used for targeted surface modification using micro-tools and sufficiently deep penetration depths. However, these often require very high machining forces, which can lead to excessive loads and initiate surface damage due to excessive compressive residual stresses [6].

Thermal machining processes such as laser beam machining and spark erosion cause surficial oxide formation, since nickel tends to form oxide layers under heat impact [7]. In addition, the heat impact might also cause changes of the microscopic grain structure, which can have negative influences on the material's mechanical properties.

Electrochemical machining (ECM) offers material dissolution without mechanical and thermal impacts on the material's microstructure. Using a continuous electrolyte jet (Jet-ECM) offers confined machining with high flexibility. With kinematics comparable to mechanical milling, micro-grooves can be arranged on the part's surface. While dissolution characteristics of pulsed-electrochemical sinking [8,9,10] and wire-electrochemical machining [11] of pure nickel were recently investigated, Jet-ECM of the same material is hardly reported and mainly known for machining holes and through-slots. Others focus on Jet-ECM of nickel alloys instead of pure nickel [12].

The lateral expansion of single removals machined with Jet-ECM is predefined by the nozzle's diameter and vertical expansions can be adjusted by processing parameters, which can be chosen individually [13]. However, the Jet-ECM technique to create kinematic roughness by overlapping grooves on surfaces of pure nickel workpieces is hardly investigated.

In the present study, initial experiments with three electrolyte compositions were carried out to choose the most efficient one. With the chosen electrolyte, the influence of nozzle motion speed on the surface topography was analysed. From a free non-linear interpolation, adequate values were chosen to realize a targeted *Rz* of 15 µm, 20 µm and 27 µm to increase the surface area.

2. Methodology

The Jet-ECM setup recently reported to machine additively manufactured steel [14] was used in this study. The following table 1 gives an overview of the experimental parameters.

Table 1 Experimental parameters of preliminary investigations

Parameter	Value / symbol	Unit / description
Sample material	Ni 201	pure nickel
Nozzle diameter	100	µm
Nozzle motion speed	500 - 3000	µm/s
Voltage	60	V
Electrolyte type and concentration	NaCl, 15 $NaNO_3$, 30 NaOH, 4	wt.-%
Electrolyte supply rate	10	mL/min
Working distance	200	µm

A nozzle made of stainless steel was used to supply a free jet of electrolyte. The working distance between the nozzle's front surface and the workpiece surface was measured by electrostatic probing and adjusted while machining by a normal vector-based compensation of the surface inclination.

3. Analysis of the most efficient electrolyte

Concentric circles with diameters ranging from 15 mm to 37 mm and a radial distance of 150 µm were arranged as nozzle motions. To reduce machining time, 10° angles were machined as preliminary sectional experiments. Three electrolyte compositions based on previous studies and own experiences from Jet-ECM experiments of metal alloys were chosen to be analysed. The electrolyte solutions were prepared with comparable electric conductivities between 150 mS/cm and 170 mS/cm. The conductivities were chosen as compromise between sufficiently high values for useful dissolution rates and sufficiently low to avoid supersaturation. In addition, the three compositions with a certain variation of the pH with slightly acidic (NaCl, pH 5), neutral (NaNO3, pH 6) and alkaline (NaOH, pH 10) character.

The image in figure 1 c) shows a photograph captured during the Jet-ECM process. The overview image in figure 1 d) shows the arrangement of the experiments. The single electrolyte compositions are indicated by different colours, and the respective nozzle speeds are indicated by numbers, e.g., the blue-coloured "NaCl1000" was machined with NaCl electrolyte at a nozzle speed of 1000 µm/s.

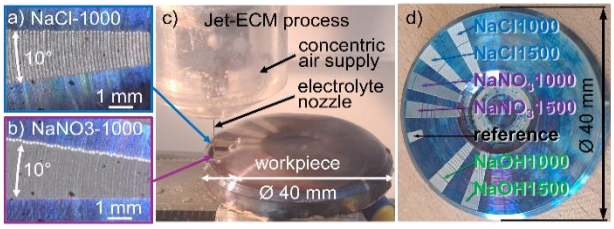

Figure 1. Detailed microscope image of machining results with NaCl (a) and $NaNO_3$ electrolyte (b), photograph of Jet-ECM (c), and arrangement of 10° sectional experiments with electrolyte variation (d)

Before and after carrying out the experiments with each of the different electrolytes, the sample was flushed with deionized water. A blue coloration can be seen on the initial surface, which is expected to be caused by spontaneous oxides. After Jet-ECM, no blue colours are cognizable, hence, the resulting oxide thickness is expected to differ from the initial one. The two exemplary top view microscope images show details of the machining results realized with NaCl (figure 1 a) and $NaNO_3$ (figure 1 b) electrolytes. The single circular grooves are clearly visible. However, certain deviations regarding localization of the electrochemical dissolution that result in differences of the kinematic roughness can be expected.

The point diagrams in figure 2 show the electric current over time of the three electrolytes detected at consistent nozzle motion speed of 1000 µm/s. Each machining operation is cognizable from current values higher than 10 mA, while recurring drops to approx. 0 mA represent infeed movements.

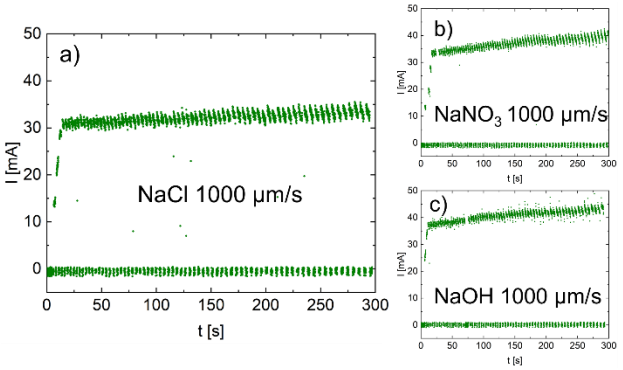

Figure 2. Electric current over time, electrolyte: NaCl (a), $NaNO_3$ (b) and NaOH (c), nozzle motion speed 1000 µm/s

According to the similar electrolyte conductivities, the measured electric currents are comparable, too. However, slightly lower average values of (30…35) mA were measured when machining the planar surface section with the NaCl electrolyte, compared to (32…42) mA with $NaNO_3$ and (36…45) mA with NaOH. In every experiment, the lowest values were detected in the beginning. The slight increase over the 300 s machining time in every experiment indicates a slight conical shape of the initial sample surface that was not compensated with the chosen strategy, which only provides a compensation of the inclination. A cognizable increase in electric current was expected at higher nozzle speed in case of a significantly reduced removal depth. However almost similar characteristics were determined at 1500µm/s, which indicates only a slight change in relation to the initial working distance. Hence, these results are not explicitly presented.

The quantification of realized surface roughness was carried out by tactile measurements with a Mahr LD 120. Three positions named P1, P2 and P3 were analysed, which were arranged in a radial distance of approximately 20 mm, 25 mm and 30 mm from the centre of the cylindrical sample. The average (AV) and standard deviation (SD) were calculated from the three single values. The results charted in Table 2 indicate the highest roughness with NaCl, even if the lowest electric currents were measured in this case. It is expected that this is caused by the highest current efficiency of this electrolyte.

Table 2 Surface roughness *Rz* of 10° sections with electrolyte variation

electro-lyte	*v* in µm/s	*Rz* in µm				
		P1	P2	P3	AV	SD
NaCl	1000	13.1	13.1	13.7	**13.3**	0.3
NaCl	1500	12.1	11.3	10.8	**11.4**	0.5
$NaNO_3$	1000	10.7	10.1	10.1	**10.3**	0.3
$NaNO_3$	1500	10.6	10.8	10.3	**10.6**	0.2
NaOH	1000	8.5	8.3	8.3	**8.4**	0.1
NaOH	1500	6.8	6.9	6.8	**6.8**	0.1

The roughness realized with $NaNO_3$ is slightly lower with approximately 80-90 % of the values realized with NaCl. With NaOH significantly lower values, partially only 50% compared to NaCl, were realized. Even if these electrolytes provided higher

electric charge exchange, a significantly larger amount of it was consumed by side reactions rather than for electrochemical dissolution resulting in lower charge efficiency. Thus, the NaCl solution was chosen as most adequate electrolyte and used for further investigations.

4. Investigation of surface roughness as function of the nozzle motion speed with the selected electrolyte

Further experiments with NaCl electrolyte were carried out to analyse the influence of the nozzle motion speedon the machining results focusing on the surface roughness value *Rz*. Since the nozzle speeddetermines machining time and thus the depth of the single grooves, the kinematic roughness is mainly influenced by the nozzle speed. As a basis for an interpolation, six velocities ranging from 500 µm/s to 3000 µm/s with a step size of 500 µm/s were investigated. The remaining parameters were kept according to the previous investigations explained before and charted in table 1. The image in figure 3 a) shows an overview of all experiments and figure 3 b) gives a detailed view on the section machined with 1500 µm/s.

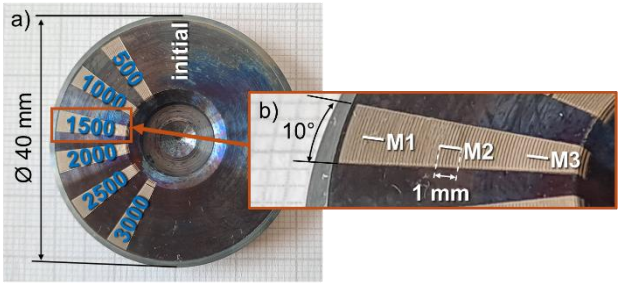

Figure 3. Overview of the 10° sectional experiments with nozzle speedvariation (left), detailed view on the section machined with 1500 µm/s (right), NaCl electrolyte

As indicated in the detailed image, three measurement lines were arranged on each section, which are situated near the sample's outer edge (M1), in the centre of the section (M2) and near the sample's inner edge (M3). Almost constant measuring lengths of approximately 1 mm were arranged perpendicularly to the circular removals after Jet-ECM to detect the kinematic roughness. For comparison, a similar arrangement was measured on the initial sample surface as indicated in the upper part of the left-handed image. In this case, the measuring lines were situated perpendicularly to the turning marks of the mechanically prepared, initial surface.

The measuring lines were captured with a Keyence VK-9700 confocal laser-scanning microscope after Jet-ECM. The VK-Analyzer software provided by the manufacturer of the microscope was used for the evaluation. To exclude strong deviations, e.g. by dust particles, the measured profiles were corrected by smoothing the surface height via the option 'simple average' of '+/-2' values 'over all areas'. The measurement of the initial surface roughness showed a value of *Rz* = 17 µm.

The point diagram in figure 4 shows the comparative results after Jet-ECM along with the initial roughness indicated by the dashed, horizontal line. The points represent the average values of three measurements M1 – M3, and the error bars highlight their standard deviations. The highest roughness of *Rz* = 32 µm was realized at the slowest nozzle speed of 500 µm/s. Here, the deepest grooves were realized by the highest electric charge exchange, which exhibited approximately 20.0 C according to an integration of the measured current over time. The lowest roughness *Rz* = 15 µm was realized at the highest nozzle speed of 3000 µm/s, where the least charge exchange of approximately 2.8 C was measured. When comparing with the initial value, a slight machining effect is also cognizable from the slight roughness reduction by approximately 2 µm.

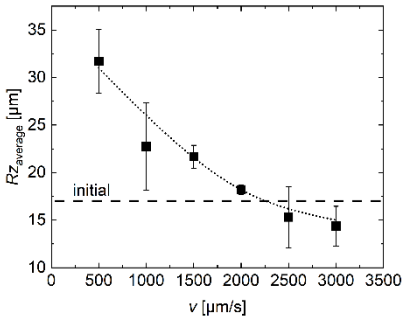

Figure 4. Average surface roughness as function of the applied nozzle motion speed with NaCl electrolyte, the dotted line indicates a non-linear spline interpolation

A declining decrease of *Rz* is cognizable with increasing nozzle speed, which is highlighted by the dotted line from a free spline interpolation. The interpolated trend was used to derive adequate nozzle motion speeds for three target surfaces characterised by surface roughness values. Grinding techniques typically result in *Rz* ≤ 10 µm, which was defined as too low for a significant increase of the surface area. High values that typically result from rough milling are at *Rz* ≥ 30 µm, which would result in an excessive machining time in Jet-ECM. Hence, three values in between were chosen considering the concentric arrangement with a radial groove distance of 150 µm resulting in a similar wavelength. Thus, *Rz* 27 µm, 20 µm and 15 µm, which represent aspect ratios slightly less than 1/5, similar to 1/7.5 and 1/10, respectively, were identified as useful target values. From the interpolated trend in figure 4, nozzle speeds of 900 µm/s, 1800 µm/s and 3000 µm/s were derived applicable.

5. Jet-ECM shaping of full sample surfaces

For prospective applications where the full surface is required as functional area, a circular arrangement with a concentric layout similar to the preliminary investigations was used and expanded to 360° circles. As shown in the top view microscope image of figure 3 a), the complete sample surfaces were machined by Jet-ECM.

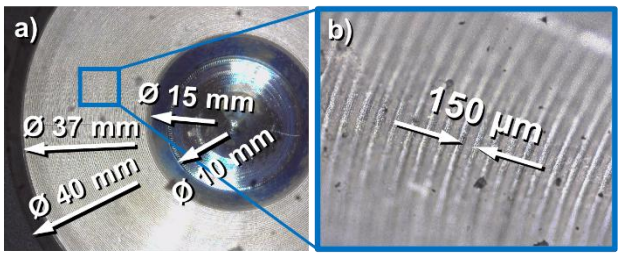

Figure 5. Top view microscope image (a) and inclined detailed view on a section (b) of a surface machined with 1800 µm/s, NaCl electrolyte, 360° circular nozzle movements

The overview image shows the machined sample surface with an outer diameter of 40 mm and an inner diameter of 10 mm. Considering the chamfers on the inner and outer edge, a machining area ranging from an inner diameter of 15 mm to an outer diameter of 37 mm remains as plane surface. The detailed image in figure 3 b) shows an inclined view on 20 out of a total of 74 circular grooves machined with a radial infeed distance of 150 µm.

The point diagram in figure 6 shows the electric current measured over time of the machining experiment with a nozzle speed of 3000 µm/s.

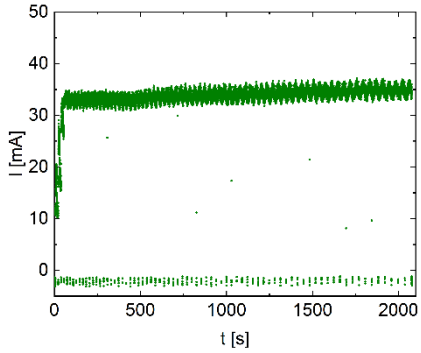

Figure 6. Electric current over time of a 360° full surface machining experiment with a nozzle speedof 3000 µm/s, NaCl electrolyte

Almost similar current values were measured compared to the preliminary experiments with the same electrolyte shown in Figure 2. A certain non-compensated deviation of the sample surface can be retraced from the regular current fluctuations of approximately ± 2 mA within the 74 machining steps that last between 20 s and 40 s according to the size of the single radii. Similar to the preliminary experiments, a slight deviation of plane surface towards a concave shape can be retraced from the current increase over time. Hence, the average current rises from 32 mA in the beginning to 35 mA at the ends of the machining process.

The integral of the electric current calculated over time resulted in an electric charge exchange of 68.7 C at the fastest nozzle speed of 3000 µm/s. The machining time in this case was 35 min. Reducing the nozzle speed to the medium value of 1800 µm/s resulted in an almost linear increase of the electric charge to 118.0 C. Due to the slower nozzle speed, the total machining time was raised to 57 min. The further reduction of the nozzle speed to the minimum value of 900 µm/s also led to an almost linear increase of the charge exchange. Here, the highest value of 226.4 C was calculated after a total machining time of 113 min. The linear correlations indicate that the average electric currents remained almost constant, regardless of the nozzle speed and machining time.

Figure 5 shows top view microscope images with colour-scaled representation of the surface topographies.

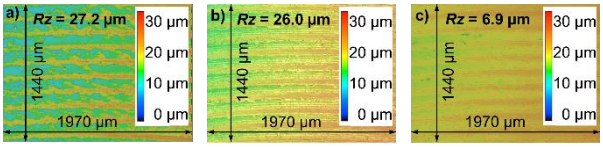

Figure 5. Colour-scaled top view microscope images of the surfaces machined by 360° circular motions with NaCl-electrolyte at a nozzle motion speedof 900 µm/s (a), 1800 µm/s (b) and 3000 µm/s (c)

The measured sections of the machined surfaces contain approximately ten single grooves cognizable from their horizontal developments. Turning marks of the preliminary mechanical preparation process are still cognizable on the original surfaces between the Jet-ECM grooves in figure 5 b) and in figure 5 c), which were machined at medium and highest speed resulting in lower removal depths compared to the result in figure 5 a). For the latter one, the turning marks were almost completely removed by the deeper grooves. The roughness measurement in this case resulted in an *Rz* of 27.2 µm, which represents very good accordance with the targeted *Rz* of 27.0 µm. However, the result shown in the central image with an *Rz* of 26.0 µm differs from the targeted value of 20.0 µm. Most significantly, the result in the right-handed image with an *Rz* of 6.9 µm represents a deviation to less than half of the targeted value of 15.0 µm.

6. Summary and conclusions

Jet-ECM was successfully carried out on sample surfaces made of nickel 201. Concentric circular grooves were machined with three electrolytes. A solution of 15 wt-% NaCl represented the most efficient machining results. Further experiments revealed a non-linear correlation between the roughness *Rz* and the applied nozzle motion speed. Discrete nozzle speeds were derived to machine the complete surfaces of initially plane samples with targeted surface roughness. While the largest target roughness of 27 µm corresponds well with the result, the medium roughness was exceeded by 30 % and the lowest value was underrun by 54 %.

A linear correlation between electric charge exchange and nozzle speed, and hence machining time, was determined. Due to the constant nozzle diameter, a constant current density distribution, and thus, consistent groove width was expected. Hence, a linear influence on the removal depth, and thus on the roughness, was expected. But the deviations indicate non-linear correlations, which indicates significant influence on the groove width that should be analysed in future. In addition, influences of the initial turning marks, which were not completely removed, on the resulting roughness need to be considered.

Obvious blue colorations of the initial surfaces were not cognizable anymore after Jet-ECM. Considering subsequent applications, where surface chemistry might be a crucial property, future analyses should be carried to determine the chemical composition of the surface and to measure changes in oxide thickness before and after Jet-ECM.

References

[1] Schütze M, Rebak R B, Bender R 2014 *Corrosion Resistance of Nickel and Nickel Alloys Against Acids and Lyes*, ISBN: 978-3-527-33849-8
[2] Fortuna S, Gurianov D, Nikonov S, Ivanov K, Mironov Y, Vorontsov A 2022 *Materials* **15**, DOI: 10.3390/ma15248882
[3] Ehlers J C, Larrazábal G O, Egelund S D, Chatzichristodoulou C 2025 *Chemical Engineering Journal* **525**, DOI: 10.1016/j.cej.2025.169990.
[4] Mølmen L, Alexandersson A, Leisner, P 2019 *Transactions of the IMF* **97**, 112–114, DOI: 10.1080/00202967.2019.1596573
[5] Thellaputta G R, Chandra P S, Rao C S P 2017 *Materials Today* **4** 3712-3721, DOI: 10.1016/j.matpr.2017.02.266
[6] Liao Z, Xu D, Luna G G, Axinte D, Augustinavicius G, Sarasua J A, Wretland A 2021 *Journal of Materials Processing Technology* **298** 117313, DOI: 10.1016/j.jmatprotec.2021.117313
[7] Gouton L, Dal M, Aubry P, Maskrot H, Caron N, Pacquentin W, Foucault M, Peyre P, Favier V 2015 *Proc. ICALEO 2015,* 536-543 DOI: 10.2351/1.5063201
[8] Berger T, Martin A, Ghorbanalipour S, Schubert A 2025 *Proc. 21st International Symposium on Electrochemical Machining Technology*, DOI: 10.51382/978-3-96100-259-7-11
[9] Zeiner M, Frank A, Hall T, Baehre D 2024 *Proc. 20th International Symposium on Electrochemical Machining Technology*, DOI: 10.18154/RWTH-2024-10232
[10] Zeiner M, Frank A, Hall T, Baehre D 2025 *Proc. 21st International Symposium on Electrochemical Machining Technology*, DOI: 10.51382/978-3-96100-259-7-04
[11] Bi X, Zeng Y,, Qu N 2020 *J. Precision Eng*. **61** 14-22, DOI: 10.1016/j.precisioneng.2019.09.015
[12] Niu S, Qu N, Fu S, Fang X, Li H 2017 *Int. J. Adv. Manuf. Tech.* **93** 2123-2132, DOI: 10.1007/s00170-017-0680-8
[13] Martin A, Zeidler H, Hackert-Oschätzchen M, Schubert A 2016 *4M/IWMF2016* **712** 95–98, DOI: 10.3850/978-981-11-0749-8_712
[14] Yahyavi Z M, Schubert A 2025 *Proc. 21st International Symposium on Electrochemical Machining Technology*, DOI: 10.51382/978-3-96100-259-7-08

euspen's 26th International Conference & Exhibition, Krakow, PL, June 2026
www.euspen.eu

Surface alloying of stainless steel parts with tungsten during electrical discharge machining for increased hardness

Viet D. Bui[1*], André Martin[1], Andreas Schubert[1,2]

[1]*Chemnitz University of Technology, Professorship Micromanufacturing Technology, Reichenhainer Str. 70, 09126 Chemnitz, Germany*
[2]*Fraunhofer Institute for Machine Tools and Forming Technology, Reichenhainer Str. 88, 09126 Chemnitz, Germany*

** Corresponding author. Email address: duc-viet.bui@mb.tu-chemnitz.de*

Abstract

Surface alloying is a technique used to modify surface properties of a material by creating a new alloy layer on its surface. Various techniques can be employed such as laser surface alloying, plasma treatment, and electron beam treatment. However, they are solely used for producing the alloy layer. Additional processing steps and manufacturing methods are required for shaping and structuring the components, e.g., wear- and corrosion-resistant parts made of stainless steel utilized as cutting blades in food industry or industrial cutting equipment.
In this study, electrical discharge machining (EDM) using hydrocarbon based dielectric fluid will be used for ablating the workpiece surface and concurrently alloying its surface layer. Tool electrodes with diameter of 2.4 mm made from WC6Co material are used for machining stainless steel workpieces by applying a negative tool polarity. Machining parameters are chosen in with the scope to adjust roughness levels based on the VDI 3400 standard with VDI 36 and VDI 18 classes. To increase tungsten content in the modified layer, a re-modification strategy was utilized. The modified layer generated by applying VDI 36 was re-modified using VDI 18 over 30 s and 40 s of machining time. Results show that the modified layer with thicknesses from 4 µm to 25 µm contain tungsten with an amount up to 26.5 wt. %. Considering maximum removal rates higher than 0.05 mm³/min, the EDM process is a potential technique to shape components, and concurrently to alloy their surface layers, e.g., to increase wear and corrosion resistance.

Keywords: EDM, surface alloying, composition, layer thickness

1. Introduction

Surface alloying is a technique used to modify the surface properties of a material by creating an alloyed layer on its surface. This is achieved by introducing alloying elements into the substrate material, typically through melting and diffusion. Various methods can be employed, such as laser surface alloying [1], plasma treatment [2], and electron beam treatment [3]. A laser process was used to generate an alloyed layer on AZ91D magnesium alloy surface by adding Zr powder during the melting process. Results showed that the hardness of alloying layer was 6-7 times higher than that of the substrate, which is due to formation of re-phases of Zr, ZrO_2, and Al_3Zr. Additionally, wear and corrosion resistance of the surface was significantly improved [1]. A Cu-Ni alloyed layer on titanium was obtained by using a plasma surface alloying technique to improve mechanical properties and antibacterial activity. The formation of Cu-containing phases such as $TiNi_{0.8}Cu_{0.2}$, $Cu_{0.81}Ni_{0.19}$, Cu_2Ti_4O and Ti_2Cu resulted in the improvement of wear resistance. The hardness of the alloyed layer was approx. 445 HV, while only 210 HV was measured on the substrate [2]. A high-current pulsed electron beam was studied to create an alloyed layer on Ti6Al4V with Cr powder assistance. A significant improvement was reported for surface hardness, the coefficient of friction, wear and corrosion resistance of the Cr-enriched surface [3].

It is well known that the content of deposited material influences the mechanical properties of the alloyed surface layer [4]. NiCrSiBC-WC powders with varying percentage of WC (40 %, 50 % and 60 %) were laser-cladded on the same medium carbon steel substrates. No visible crack was found in the top surface and cross-section after coating with 40 % WC composite. In contrast, for 50 % WC and 60 % WC composite coatings, obvious cracks occurred on their top surfaces. The high WC content had a positive effect on the hardness, whereas residual stress was negatively effected [6]. However, an increased wear resistance by at least a factor 3 compared to the layer alloyed without WC was reported. In addition, the increase of WC content significantly improved the wear coefficient [7].

An investigation of electrical discharge machining (EDM) for alloying a tool steel surface by tungsten copper tool electrodes, which contain W contents from 5 % to 15 %, was performed. Results showed that the hardness of the workpiece surface increased with increasing W content of the tool electrode [8]. In another study, W powder was mixed into the dielectric fluid when using W-Cu, brass, and graphite electrodes to alloy different tool steel materials. The highest hardness was achieved with the W-Cu tool electrode [9].

From literature, it can be realized that various techniques, such as laser surface alloying and plasma treatment, are applicable to achieve significant improvements of the mechanical properties through alloying of their surfaces. Since most of these techniques are solely used to create alloyed layers, additional techniques are required for shaping and structuring the components.

EDM has shown its potential to deposit material from tool electrodes to the workpiece surface. However, influences of discharge parameters on the deposited tungsten content, which is not yet sufficiently investigated, need to be analyzed. Consequently, within the scope of this study, WC6Co tool

electrodes are used to modify the surface of stainless steel EN 1.4404. Different parameters of the EDM process based on VDI 36 and VDI 18 classes and the re-modification strategy are utilized. It concentrates on the tungsten deposition on the workpiece surface as well as morphology of the modified layer under the effects of the VDI class and the re-modification.

2. Methodology

The experiments were performed on a ZK genius 700 sinking EDM machine from Zimmer & Kreim GmbH (*Brensbach, Germany*) using hydrocarbon-based dielectric fluid of the type Ionoplus IME-MH made by Oelheld GmbH (*Stuttgart, Germany*). In the EDM die sinking experiments, tool electrodes made of WC6Co with diameter of 2.4 mm were used. Workpieces made of stainless steel EN 1.4404 were machined by applying a negative tool polarity. The applied EDM parameters based on the VDI 3400 standard are given in Table 1.

Table 1 EDM processing parameters

VDI class	***U*** [V]	t_{on} [µs]	t_{off} [µs]	***I*** [A]
36	260	125	65	1
18	260	5	10	1.5

In the first step, three experiments were repeated with each VDI class to machine workpiece with a constant depth of 150 µm without tool rotation. After each experiment, an ethanol filled ultrasonic bath was utilized to clean the sample for 10 minutes at room temperature, and then it was dried in air. The modified surfaces were scanned by a Keyence VK9700 3D laser-scanning confocal-microscope. MountainsMap 7.4 software was utilized to analyze their roughness and topography. The elemental composition of the modified surfaces was analysed by energy dispersive X-ray spectroscopy (EDS), whereby a spectrum of approx. (1.5 x 1.5) mm^2 was analysed in the center of each surface. Scanning electron microscopy (SEM) was used to analyse the surface topography. For analyses of the modified layer in the cross section, the samples were cut, then ground and polished by a wet abrasive paper. Afterwards, they were chemically etched by a V2A pickling solution. The cross-sectional layer was analysed by SEM images. To analyse the layer thickness, the cross section was scanned with the Keyence microscope. A Keyence VK Analyser software was used to analyse fifty positions on each sample thus allowing for a calculation of an average thickness and standard deviation. Analyzed results are basic for calculating durations of the re-modification.

Related to an investigation of material removal rate (MRR) and tool wear rate (TWR), a depth of 500 µm was machined by the EDM process with each VDI class. The Keyence microscope was used to scan the machined surfaces, after which the removed material volume (V) was analyzed with the MountainsMap software. MRR, TWR and wear ratio were calculated by Eqs. (1), (2) and (3):

$$\text{MRR} = V / t \quad (1)$$

$$\text{TWR} = \pi r^2 h / t \quad (2)$$

$$\text{Wear ratio} = \text{TWR} / \text{MRR} \quad (3)$$

Here, h is the height of the frontal tool wear, r is the tool diameter, and t is the machining time.

In the second step, a re-modification strategy was investigated. To do that, the EDM process applying VDI 36 in the first step with a machining depth of 150 µm was repeated to create a thick modified layer. Right afterwards, the EDM process using VDI 18 was performed to re-modify the modified layer without changing the tool electrode and without tool rotation. The re-modification processes with a duration of 30 s was named VDI 36-18_{30s}, and with a duration of 40 s VDI 36-18_{40s}, respectively. The durations were determined from the results of the first step and preliminary experiments, whereby the modified layer was re-modified on its whole surface without removing it. The relative position between tool and workpiece was kept, since it remained un-changed as no tool rotation was used. Hence, uniform machining of a thin layer over the whole workpiece surface was assured in the re-modification step. Three repetition experiments were performed for statistical analyses. The cleaning process and analyses were done similarly to the first step.

3. Results and discussions

In this section, the content of deposited tungsten, thickness and roughness of the modified layer, as well as MRR and TWR are presented and discussed.

3.1. Average content of deposited tungsten

Figure 1 shows the content of deposited tungsten depending on the VDI class and strategy of the modification and re-modification process.

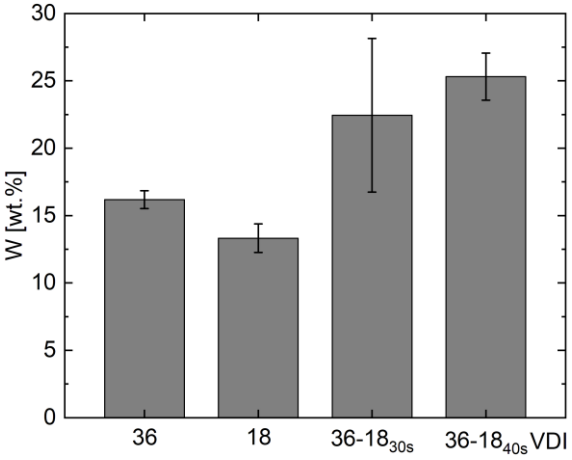

Figure 1. The content of deposited tungsten in the modified layer

Results show that the modified layer contains approx. 17 % W when applying VDI 36 with a high energy, whereas the deposited tungsten content only amounts to approx. 13 % when using VDI 18 with a low energy. A reduction of the applied energy leads to a decrease of the deposition efficiency. A significant reduction of spattered materials, which contains a large amount of material deposited from the tool electrode [10], is the main reason for lower amount of tungsten when applying VDI 18.

The new strategy of re-modification increases the deposited content significantly with both process durations of 30 s and 40 s. Surfaces containing tungsten contents up to approx. 26.5 % were achieved. This is due to a containment of tungsten in the modified layer formed by applying VDI 36, which combines with tungsten deposited from tool electrode during the re-modification with VDI 18. The increased tungsten content can improve the hardness of the surface according to [8,9].

As can be seen from Figure 2, backscattered electron images of the surfaces modified by the EDM process applying VDI 36 and VDI 18 classes are presented. Spattered materials were formed in both cases, however it is much less with VDI 18 compared to VDI 36. The spattered materials need to be avoided due to their low adhesive strength on the substrate surface. Additionally, by applying the VDI 18 class, the formation of micro-cracks is remarkably lower. Very few cracks were observed on the modified surface.

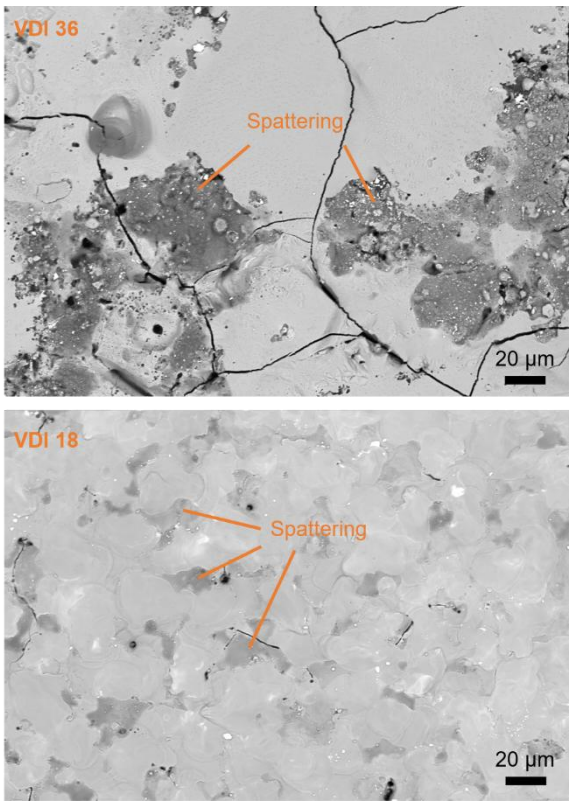

Figure 2. Backscattered electron images of the surfaces modified by the EDM process using VDI 36 and VDI 18 classes.

3.2. Analysis of the modified layers

The modified layers formed by the EDM process with each VDI class and modification strategy are presented in Figure 3. A modified layer with thickness of approx. 25 µm is generated by using VDI 36, whereby it is approx. 4 µm by VDI 18 due to applying a much lower discharge energy. However, with a high energy of the VDI 36 class, micro-cracks with a width up to approx. 1 µm are observed. Additionally, a porosity is formed, especially in case of VDI 36 with a thick layer. With VDI 18, a much faster solidification process occurred due to a much thinner modified layer, which leads to have insufficient time to nucleate and grow of gas bubbles [11]. Therefore, the pore's size is significantly smaller.

With the re-modification strategy, the thicknesses of the modified layer are approx. 15 µm and 10 µm when the re-modification process with VDI 18 is performed in 30 s and 40 s, respectively. A double-layer is cognizable after re-modification, which consist of a lower layer formed at high discharge energy using VDI 36 and an upper layer formed at lower discharge energy applying VDI 18. The lower layer has a thickness of approx. 11 µm after re-modification over 30 s duration, whereas it only amounts to approx. 6 µm after 40 s. The depth of large micro-cracks, which were generated by the step of applying VDI 36, was reduced with an increase of the re-modification duration. However, additionally formed micro-cracks were detected after re-modification, hence, the total amount of micro-cracks is increased, which is the case for both re-modification durations.

Figure 4 represents exemplary profiles of the modified surfaces.

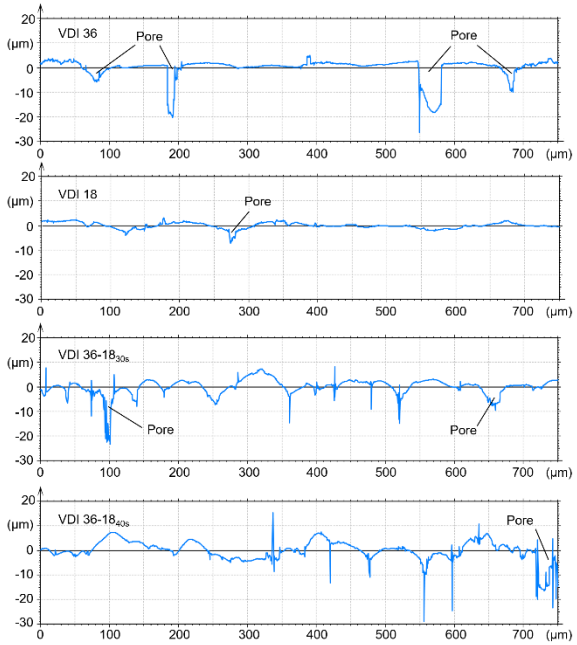

Figure 4. Typical profiles of surfaces modified by different VDI classes and strategies

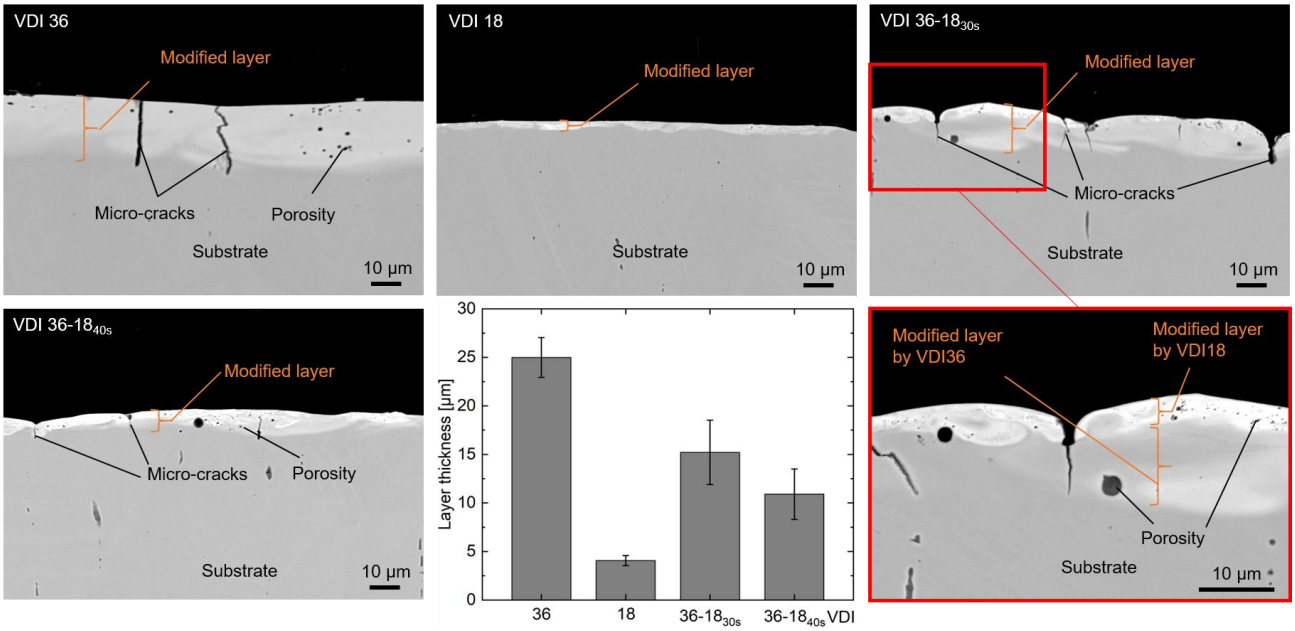

Figure 3. SEM images of the modified layer and effect of the VDI class and strategy of the modification process on the layer thickness

It can be realized that the surface generated by the EDM process applying VDI 36 class is quite flat. However, big and deep pores of the modified layer was formed. When using the VDI 18 class, a quite smooth surface with some small and shallow pores is achieved.

The re-modification process in this investigation forms uneven surfaces. Although VDI 18 was utilized in the re-modification process, the reuse of the tool electrode already worn after the first modification step led to non-uniform machining results after re-modification. However, the depth of big pores is significantly decreased.

Figure 5 shows a point diagram of the roughness values *Ra* and *Rz* of the modified surfaces.

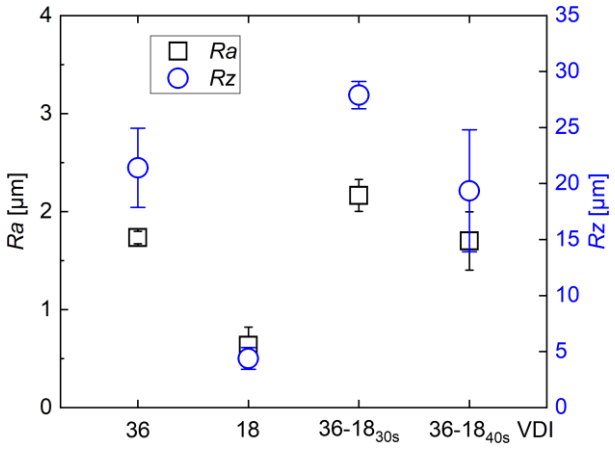

Figure 5. Surface roughness *Ra* and *Rz* depending on the modification process

Roughness values *Ra* achieved by applying VDI 36 and VDI 18 classes are 1.74 µm and 0.64 µm, respectively. They are much lower than *Ra* values of 6.3 µm and 0.8 µm of the VDI 3400 standard of these classes. This is due to the use of a negative tool electrode for the modification with the aim of W deposition.

The re-modification process, due to the uneven surfaces, results in a high value of roughness. In case of re-modifying in 30 s, the final surface is even rougher than the surface formed by VDI 36 with *Ra* = 2.16 µm. With re-modification duration of 40 s, the surface is flatter than after 30 s with a roughness value similar to the surface modified by using VDI 36.

3.3. Analysis of material removal rate and tool wear

MRR and TWR realized in the machining processes utilizing VDI 36 and VDI 18 classes are shown in Figure 6.

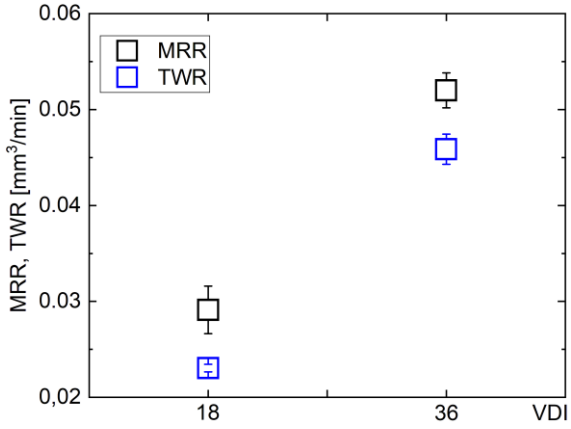

Figure 6. MRR and TWR as function of the VDI classes

In both cases TWR is only slightly lower than MRR. Co, which is the metallic binder material of the WC6Co tool electrode, has a melting and evaporation points of approx. 1320 °C and approx. 2700 °C, respectively, whereas they are approx. 2800 °C and approx. 6000 °C for WC. Therefore, melting and evaporation of the EDM process mainly affects Co rather than WC, and WC grains are expected to be released after melting and evaporation of Co resulting in the deposition of WC on the modified layer. A high discharge energy, such as with the VDI 36 class, results in a higher MRR compared to a lower discharge energy of VDI 18. In addition, when applying VDI 36 the wear ratio with a value of 0.88 is also higher compared to 0.79 of VDI 18. It means that more molten tool material is generated and deposited.

4. Conclusion

In this study, WC6Co tool electrodes were used to machine stainless steel with EDM sinking and concurrently deposit tungsten from the tool electrode to the workpiece surface. From the results, the following conclusions can be drawn:

- The deposited content of tungsten is significantly influenced by the VDI class and modification strategy. The modified surface contains a maximum tungsten content of 26.5 %.
- Re-modification with lower discharge energy significantly increases the tungsten content in the modified layer.
- Modified single layers or double layers with thicknesses from 4 µm to 25 µm can be generated.
- Generation of micro-cracks and porosity is a challenge.
- The EDM process offers a promising potential for shaping the workpieces with concurrent alloying of the surface layer, e.g., to increase wear and corrosion resistance.

Recommendation

Further studies are recommended to characterize the modified layer in cross-section regarding the distribution of deposited material within the layer. Mechanical properties and metallurgical structures of the modified surface should be evaluated.

References

[1] K. Huang, X. Lin, C. Xie, T. M. Yue. Laser cladding of Zr-based coating on AZ91D magnesium alloy for improvement of wear and corrosion resistance. In: *Bull. Mater. Sci.*, 2013, vol. 36, pp. 99-105

[2] X. Zhang *et al.* Microstructure, antibacterial properties and wear resistance of plasma Cu-Ni surface modified titanium. In: *Surf. Coatings Technol.*, 2013, vol. 232, pp. 515-520

[3] L. Zhang, C. T. Peng, X. Yao, Q. Guan, R. Lu. Surface alloying of Cr on Ti6Al4V alloy induced by high-current pulse electron beam. In: *Surf. Coatings Technol.*, 2019, vol. 370, pp. 288-297

[4] H. Yang *et al.* Effects of alloying elements (Sn, Nb, Cr, and Mo) on the microstructure and mechanical properties of zirconium alloys. In: *J. Nucl. Sci. Technol.*, 2015, vol. 52, no. 9, pp. 1162-1173

[5] A. Li *et al.* Effects of Zr Alloying on Microstructure Evolution and Mechanical Properties of CoCrNi Medium Entropy Alloy. In: *Crystals*, 2025, vol. 15, no. 3, p. 258

[6] X. Shen, X. He, L. Gao, G. Su, C. Xu, N. Xu. Study on crack behavior of laser cladding ceramic-metal composite coating with high content of WC. In: *Ceram. Int.*, 2022, vol. 48, no. 12, pp. 17460-17470

[7] J. Verwimp, M. Rombouts, E. Geerinckx, F. Motmans. Applications of laser cladded WC-based wear resistant coatings. In: *Phys. Procedia*, 2011, vol. 12, pp. 330-337

[8] A. S. Gill, S. Kumar. Surface alloying of H11 die steel by tungsten using EDM process. In: *Int. J. Adv. Manuf. Technol.*, 2015, vol. 78, no. 9-12, pp. 1585-1593

[9] A. Bhattacharya, A. Batish, N. Kumar. Surface characterization and material migration during surface modification of die steels with silicon, graphite and tungsten powder in EDM process. In: *J. Mech. Sci. Technol.*, 2013, vol. 27, no. 1, pp. 133-140

[10] V. D. Bui, A. Martin, A. Schubert. Investigation of Magnetic Field assisted Electrical Discharge Sinking of Ti6Al4V. In: *Procedia CIRP*, 2025, vol. 137, pp. 431-435

[11] Y. Zhang, *et al*. Influence of dielectric type on porosity formation on electrical discharge machined surfaces. In: *Metallurgical and Materials Transactions B*, 2012, vol. 43(4), pp. 946-953

euspen's 26th International Conference & Exhibition, Krakow, PL, June 2026
www.euspen.eu

Pore-aware dwell map construction from in-situ pad-glass contact imaging in optical polishing

Nico Zettler[1], Adam Wilczek[1], Prof. Dr. Rainer Börret[1]

[1]*Aalen University, Center for Optical Technologies (ZOT), Beethovenstr. 1, 73430 Aalen, Germany*

nico.zettler@hs-aalen.de

Abstract
Conventional dwell maps in optical polishing assume smooth tool influence functions that ignore the porous structure of real pads. We present an in-situ imaging method that constructs pore-resolved dwell maps directly from measured pad-surface contact, without prior TIF assumptions. Using a telecentric sub-surface imaging setup (5 MP, 12 fps) during force-controlled polishing of N-BK7 substrates (10 N, 830 rpm, ABB IRB 2400 robot), we extract continuous contact intensity maps and accumulate them over time. Radial averaging of each frame's contact intensity captures both the pad's radial contact heterogeneity and velocity variation ($v = \omega \times r$) in a single processing step. Validation against white-light interferometry (nine experiments, two substrates) using leave-one-out cross-validation shows that the pore-aware model ($R^2 = 0.908$) significantly outperforms a uniform topography-free baseline ($R^2 = 0.885, \mathrm{p} = 0.004$). With drift and edge corrections, the full pore-aware model achieves $R^2 = 0.930 \pm 0.033$. The method enables direct observation of pad microstructure effects on material removal and provides a foundation for improved process modelling in deterministic optical fabrication.

optical polishing, dwell map, tool influence function, in-situ monitoring, image processing, material removal prediction

1. Introduction

Computer-controlled optical surfacing (CCOS) is widely used for deterministic fabrication of precision optics and has been a subject of extensive research in optical manufacturing [1,2]. These processes rely on accurate dwell time maps that specify how long the polishing tool must remain at each position to achieve the desired material removal distribution. The relationship between dwell time and removal is governed by the tool influence function (TIF), which describes the spatial distribution of material removal rate beneath the polishing tool [3].

According to the Preston equation, the local material removal rate is proportional to the product of contact pressure and relative velocity [4]. In practice, TIFs are often modeled using smooth, parametric functions such as Gaussian-like profiles, which approximate the spatial distribution of material removal as a function of local contact conditions and tool kinematics [5, 6]. For bonnet polishing, finite element analysis combined with Preston's law has been shown to predict near-Gaussian TIF shapes that agree well with experimental spot tests [7].

However, real polishing pads exhibit porous, heterogeneous microstructures that deviate substantially from these idealized models. Polyurethane pads contain distributed pores that create spatially varying contact conditions at the pad-workpiece interface [8]. While the effect of pad porosity, asperity distribution, and mechanical pad properties on macroscopic material removal rates has been investigated in several experimental studies [9-11], conventional TIF models do not resolve the pad microstructure. The mismatch between assumed smooth contact and actual pore-scale variations may limit the accuracy of deterministic polishing, particularly when pixel-level prediction is required.

Several approaches exist to characterize TIFs experimentally, including spot polishing tests [12] and interferometric removal measurements that provide high-resolution surface topography and removal maps before and after polishing [13]. Recent work has also demonstrated in-situ monitoring approaches for polishing pad surface shape or pad–workpiece interaction during the polishing process [14,2], as well as sensor-based process monitoring combined with machine learning for material removal prediction [15]. However, these methods remain indirect, as they infer the influence function from observed removal rather than measuring the underlying contact distribution directly. To our knowledge, no method has been reported that extracts pore-resolved contact maps from in-situ imaging during the polishing process.

In this work, we present an imaging-based method that constructs pore-resolved dwell maps directly from measured pad-surface contact, without assuming a parametric TIF shape. Using a telecentric camera mounted beneath transparent N-BK7 substrates, we capture the pad-glass interface during polishing and extract continuous contact intensity maps that preserve the pad's porous microstructure. By radially averaging and accumulating these maps over time, we obtain dwell maps that can be validated against interferometrically measured material removal. We demonstrate the method on nine polishing experiments across two optical substrates, achieving $R^2 = 0.930 \pm 0.033$ for the full pore-aware model, significantly outperforming a uniform topography-free baseline at pixel resolution using leave-one-out cross-validation.

2. Experimental setup

The experimental setup consists of a robotic polishing system with integrated sub-surface imaging capability. An ABB IRB 2400 industrial robot (ABB Ltd., Switzerland) guides a rotating polishing head across flat N-BK7 glass substrates (65 mm

diameter). The polishing pad is a porous polyurethane disc (Ø 12 mm) mounted on a pneumatic spindle operating at approximately 830 rpm. The pad follows a meander trajectory with 14 mm path width over five passes per experiment. Each polishing run lasted approximately 90 seconds, yielding peak removal depths of circa 0.8 µm. A constant normal force of 10 N is applied via force control throughout the polishing process. Cerium oxide slurry is supplied continuously to the pad-glass interface.

The key feature of the setup is a telecentric imaging system positioned beneath the transparent substrate. A 5-megapixel monochrome camera (Manta G-504B, Allied Vision) equipped with a telecentric lens captures the pad-glass contact zone from below at approximately 12 frames per second. The imaging system provides a spatial resolution of approximately 43 µm/pixel, sufficient to resolve individual pad pores. Coaxial LED illumination ensures uniform brightness across the field of view. This configuration enables direct observation of the porous pad structure in contact with the glass surface during polishing. Figure 1 illustrates the experimental configuration and exemplary camera images showing the pad microstructure.

Material removal is validated using a Zygo NewView 8300 white-light interferometer (WLI), which measures the surface topography before and after each polishing run with sub-nanometer vertical resolution. The difference map provides the ground-truth material removal distribution for comparison with the image-derived dwell maps.

A total of nine polishing experiments were conducted across two N-BK7 substrates, each comprising a complete polishing trajectory with synchronized image acquisition and subsequent WLI measurement.

3. Methods

Image acquisition and preprocessing. During each polishing run, the telecentric camera captures a continuous image sequence of the pad-glass interface at approximately 12 fps. A background model is computed from the first and last frames of the sequence, when the pad is not actively pressing against the substrate. Each frame is preprocessed by subtracting the background model and applying a circular surface mask that isolates the optical substrate from the surrounding bright ring artifacts.

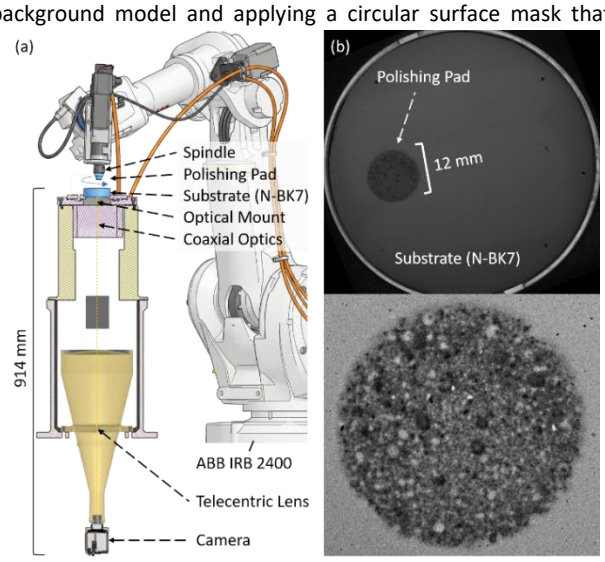

Figure 1. Experimental setup for in-situ pad-glass contact imaging. (a) Schematic showing the ABB robot with polishing head, transparent N-BK7 substrate, and telecentric camera beneath. (b) Top: Raw camera image with polishing pad (ø 12 mm) in contact with the substrate. Bottom: Magnified view revealing the porous pad microstructure, where bright regions indicate pores and dark regions indicate pad-glass contact.

Contact intensity extraction. A calibration step determines the intensity range within detected pad regions across a representative subset of frames. Contact intensity is computed by percentile-based normalization:

$$c(x,y) = \mathrm{clip}\left(\frac{I(x,y) - P_5}{P_{95} - P_5}, 0{,}1\right)$$

where P_5 and P_{95} denote the 5th and 95th percentile of pixel intensities within detected pad regions during calibration. This linear mapping scales the raw intensity to a continuous contact value in [0, 1], where higher values indicate stronger pad-glass contact. The 5th and 95th percentiles provide robust normalization bounds that exclude outliers from specular reflections and sensor noise while preserving the full dynamic range of contact intensities.

Pad detection. For each frame, the pad region is detected using Otsu thresholding on the preprocessed image. The largest connected component is extracted and morphologically filled to obtain a coherent pad mask. The pad center (c_x, c_y) and radius R are determined from the center of mass and equivalent circular area of the detected region.

Pore-aware dwell map construction. The contact maps are accumulated over time to form the pore-aware dwell map D_{pore}. For each pixel location (x, y) on the substrate:

$$D_{pore} = \sum_t c_t(x,y)$$

where the summation runs over all frames in which the pixel falls within the detected pad region. Before accumulation, each frame's contact intensity map is radially averaged with respect to the detected pad center: all pixels at the same radial distance receive the mean intensity of their radial ring. This step captures both the radial contact heterogeneity arising from the pad's porous microstructure and the velocity variation across the pad $(v = \omega \times r)$ in a single representation. Figure 2 illustrates this core processing pipeline. The following refinements are applied during model fitting but not visualized, as their parameters are determined through cross-validation.

Registration and validation. An affine transformation registers the image-derived dwell maps to WLI-measured removal maps. Registration parameters were optimized by maximizing normalized cross-correlation in the overlap region. The coefficient of determination (R^2) quantifies the pixel-wise correspondence between predicted dwell and measured removal. A uniform baseline model D_{uni}, which assigns constant intensity (1.0) within the detected pad region and zero outside, serves as a topography-free reference for quantifying the contribution of pad surface information.

Drift correction. Residual analysis revealed systematic spatial trends along the polishing trajectory: predicted removal underestimated the measured removal at the trajectory start and overestimated it towards the end. This gradient is attributed to progressive changes in pad-glass contact visibility during polishing, likely caused by slurry redistribution, pad conditioning, or surface smoothing effects. These trends are modeled by a second-order polynomial surface:

$$D_{drift}(x,y) = \gamma_1 x + \gamma_2 y + \gamma_3 x^2 + \gamma_4 y^2$$

where x, y are normalized pixel coordinates. Second-order terms capture smooth systematic gradients without overfitting to local variations; higher-order polynomials showed no significant improvement in cross-validation.

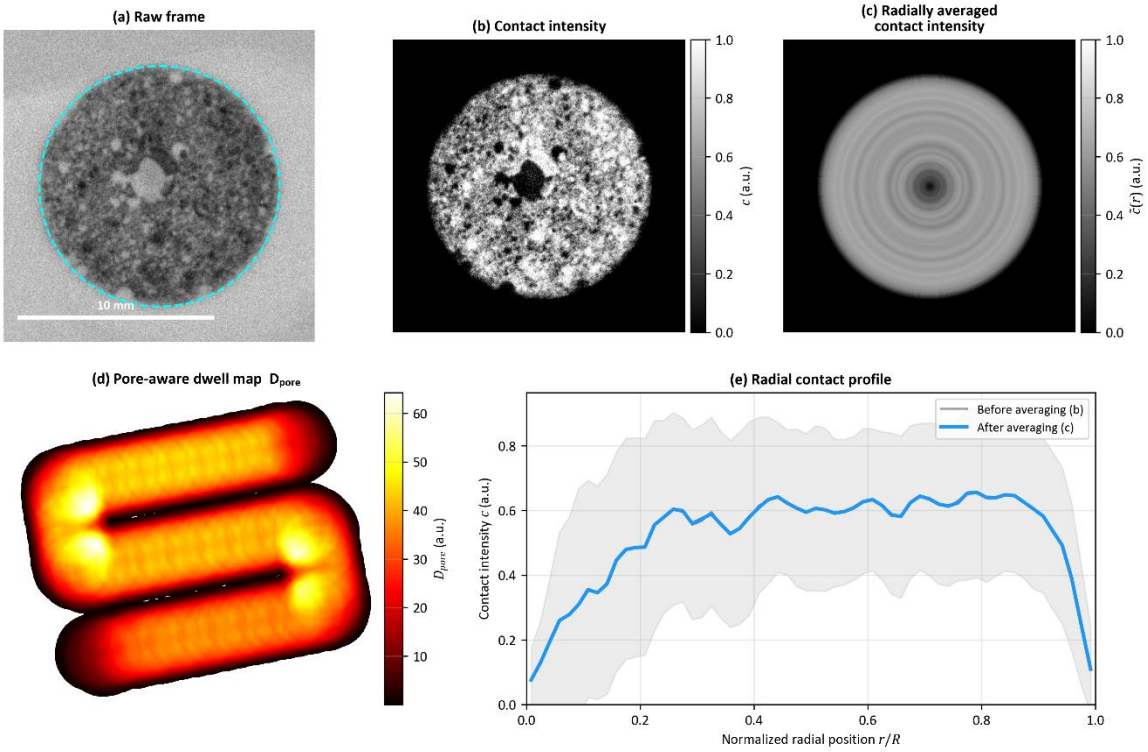

Figure 2. Core processing pipeline for pore-aware dwell map construction. (a) Single video frame with detected pad boundary (dashed circle). (b) Contact intensity after background subtraction and percentile normalization. (c) Radially averaged contact intensity: all pixels at equal radial distance receive the mean intensity of their radial ring. (d) Pore-aware dwell map D_{pore} from temporal accumulation of radially averaged frames. (e) Radial contact profile for a single frame before (gray, showing azimuthal spread) and after (blue). Additional corrections (drift, edge) are applied during model fitting (see Methods). All colorbars in arbitrary units (a.u.).

Edge correction. Contact intensity near the pad boundary is attenuated using a cosine weighting function to account for reduced pressure as the pad transitions on and off the substrate:

$$w\left(\frac{r}{R}\right) = \frac{1}{2}\left(1 + \cos\left(\pi \frac{\left(\frac{r}{R} - r_{cutoff}\right)}{\left(1 - r_{cutoff}\right)}\right)\right) \text{ for } \frac{r}{R} > r_{cutoff}$$

where r_{cutoff} is optimized on training data. The cosine weighting function was selected empirically from candidate functions (linear, cosine, sigmoid) based on cross-validation performance. The full model combines all components:

$$D_{full} = \alpha \cdot \left(D_{pore} \cdot w\right) + D_{drift}$$

The same model structure is applied to the uniform dwell map, yielding $U_{full} = \alpha \cdot (D_{uni} \cdot w) + D_{drift}$, where all parameters are fitted independently.

Cross-validation. Leave-one-out cross-validation (LOOCV) ensures unbiased performance estimates: for each held-out experiment, all parameters (α, γ_1-γ_4, r_{cutoff}) are optimized on the remaining eight experiments and evaluated on the held-out data.

4. Results

Figure 3 shows a representative result from one polishing experiment. The measured removal map (figure 3a) and the predictions from both the pore-aware full model D_{full} (figure 3b) and the uniform full model U_{full} (figure 3c) show close visual agreement. The difference in prediction error (figure 3d) reveals where the pore-aware model improves: it reduces the absolute error in 70% of pixels compared to the uniform model, with the largest improvements concentrated in regions of high cumulative pad contact.

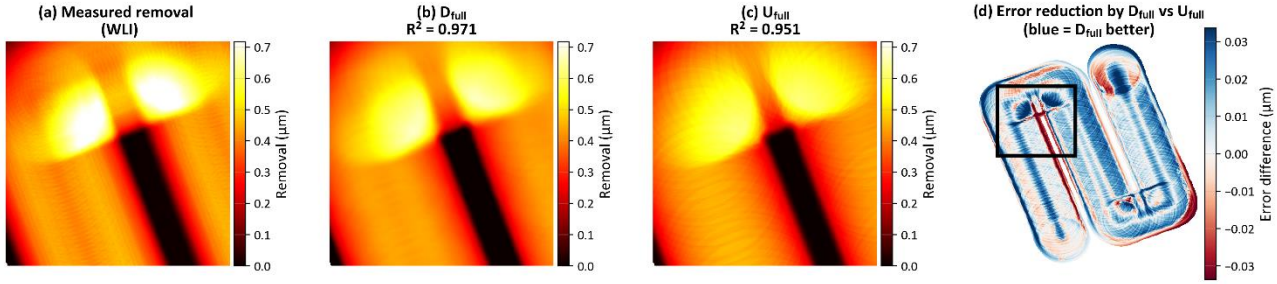

Figure 3. Representative results for one experiment (LOOCV). (a) Measured material removal (WLI), zoomed to region marked in (d). (b) Pore-aware prediction D_{full} ($R^2 = 0.971$). (c) Uniform prediction U_{full} ($R^2 = 0.951$). (d) Prediction error reduction across the full substrate: difference in absolute residuals between U_{full} and D_{full}. Blue indicates regions where the pore-aware model reduces prediction error (70% of pixels). Black rectangle marks the region shown in (a) – (c). Mean performance across all nine experiments is reported in Table 1.

Table 1 summarizes the quantitative results across all nine experiments. Eight model configurations were evaluated using leave-one-out cross-validation, comparing uniform (D_{uni}) and pore-aware (D_{pore}) dwell maps, each with optional drift and edge corrections. The uniform baseline achieves $R^2 = 0.885 \pm 0.038$. The pore-aware model achieves $R^2 = 0.908 \pm 0.039$, a significant improvement ($p = 0.004$, Wilcoxon signed-rank test). This improvement is consistent when corrections are applied: D_{full} ($R^2 = 0.930$) outperforms U_{full} ($R^2 = 0.904$) by $\Delta R^2 = 0.026$ ($p = 0.008$). Notably, the pore-aware model without any corrections ($R^2 = 0.908$) exceeds the uniform baseline with all corrections applied ($R^2 = 0.904$), demonstrating that pad surface information alone provides more predictive value than geometric corrections on a topography-free baseline.

Table 1. Model comparison across nine experiments (LOOCV, mean ± std).

Corrections	D_{uni} (R^2)	D_{pore} (R^2)	ΔR^2
None	0.885 ± 0.038	0.908 ± 0.039	+0.023
Drift	0.893 ± 0.035	0.926 ± 0.033	+0.033
Edge	0.897 ± 0.039	0.915 ± 0.037	+0.018
Drift + Edge	U_{full}: 0.904 ± 0.038	D_{full}: 0.930 ± 0.033	+0.026

5. Discussion and Conclusion

The results demonstrate that pore-resolved dwell maps constructed from in-situ imaging of the pad-glass interface significantly outperform a uniform topography-free baseline. The pore-aware model captures radial contact heterogeneity arising from the pad's porous microstructure, achieving $R^2 = 0.908$ compared to 0.885 for the uniform baseline ($p = 0.004$). With drift and edge corrections, D_{full} achieves $R^2 = 0.930 \pm 0.033$ at pixel resolution using leave-one-out cross-validation.

Radial averaging of each frame's contact intensity captures both the pad's pore-induced contact variation and the velocity gradient ($v = \omega \times r$) in a single predictor, avoiding the need for separate contact and velocity regressors. The improvement over the uniform baseline is consistent across all nine experiments and persists when both models receive identical drift and edge corrections ($\Delta R^2 = +0.026, \mathrm{p} = 0.008$), confirming that the gain originates from pad surface information rather than model complexity. The spatial distribution of the error reduction (figure 3d) supports this interpretation: the largest improvements are concentrated in regions of high cumulative pad contact, where the polishing tool dwells the longest. In these regions, the radial contact profile of the porous pad accumulates over many frames, amplifying the difference between the pore-aware and uniform models. In contrast, regions with short dwell times show smaller differences, as the per-frame contribution of the pore structure is insufficient to produce a measurable effect.

The method offers several advantages over conventional TIF-based approaches. First, it does not require prior calibration through spot polishing tests, as the contact distribution is measured directly during the process. Second, it preserves the spatial heterogeneity of real polishing pads, which smooth TIF models inherently discard. Third, it provides a potential ground-truth reference for validating or refining parametric TIF assumptions. Furthermore, the camera-based approach determines the actual pad position and contact area directly from each frame, avoiding uncertainties inherent in trajectory-based approaches that rely on commanded robot positions. Edge and drift corrections contribute additional improvements for both models, but the pore-aware advantage is maintained across all correction levels (Table 1).

Some limitations remain. The method requires transparent substrates for sub-surface imaging, limiting direct applicability to optical glasses and similar materials. Extension to opaque substrates would require alternative sensing modalities. Process parameters (force, speed, pad type) were held constant across all experiments to isolate model validation from process variability; generalization to other parameter combinations remains for future investigation. Furthermore, the removal rates in this study (0.8 µm in 90 s) represent pre-polishing conditions chosen for measurable signals within practical imaging durations. Validation under finishing conditions with sub-100 nm removal remains for future work. The pore-aware improvement may be more pronounced for larger pad diameters, where radial contact variation spans a wider spatial range, and for variable process conditions, where pad wear and conditioning alter the pore structure over time.

In conclusion, we have presented an imaging-based method for constructing pore-aware dwell maps from in-situ measurements of pad-surface contact during optical polishing. The approach enables direct observation of pad microstructure effects and provides a foundation for improved process modeling in deterministic optical fabrication.

Acknowledgement

This research is part of the "KI-Booster" project (Grant No. P2019-00-043), funded by the Carl Zeiss Foundation, and conducted at Aalen University.

References

[1] Kim D W, Kim S-W and Burge J H 2009 Opt. Express 17 21850–66
[2] Fang F, Zhang X and Weckenmann A 2019 Int. J. Extrem. Manuf. 1 022001
[3] Wang T, Ke X, Huang L, Negi V, Choi H and Kim D W 2024 Light: Adv. Manuf. 5 21
[4] Preston F W 1927 J. Soc. Glass Technol. 11 214–56
[5] Walker D D, Brooks D, King A, Freeman R, Morton R, McCavana G and Kim S-W 2003 Opt. Express 11 958–64
[6] Pan R, Zhang Y, Chen S and Wang Z 2017 Int. J. Mach. Tools Manuf. 118–119 1–11
[7] Li H, Walker D, Yu G and Zhang W 2013 Appl. Opt. 52 5781–87
[8] Prasad A, Fotou G and Li S 2013 J. Mater. Res. 28 2380–93
[9] Thakurta D G, Borst C L, Schwendeman D W, Gutmann R J and Gill W N 2000 Thin Solid Films 366 181–90
[10] Luo J, Dornfeld D and Liang S 2001 IEEE Trans. Semicond. Manuf. 14 112–33
[11] Tseng W-T and Wang Y-L 1999 J. Electrochem. Soc. 146 427–34
[12] Suratwala T, Menapace J, Steele R, Wong L, Tham G, Ray N, Bauman B, Gregory M and Hordin T 2021 Appl. Opt. 60 201–14
[13] de Groot P 2015 Adv. Opt. Technol. 4 301–11
[14] Yin J, Jiao X, Tang W and Zhu J 2018 Opt. Eng. 57 074103
[15] Schneckenburger M, Höfler S, Garcia L, Almeida R and Börret R 2022 SN Appl. Sci. 4 21

euspen's 26th International Conference & Exhibition, Krakow, PL, June 2026
www.euspen.eu

Residual stress modification and surface enhancement of PBF-LB/M components via particle blasting and plasma electrolytic polishing

Neel Kamal Gupta[1]*, Toni Böttger[1], Christian Schimpf[2], Henning Zeidler[1]

[1]*Institute for Machine Elements, Engineering Design and Manufacturing (IMKF), Technische Universität Bergakademie Freiberg, Freiberg, Germany*
[2]*Faculty for Materials Science and Materials Technology, Technische Universität Bergakademie Freiberg, Freiberg, Germany*

[*]*Corresponding Author: neel.gupta@imkf.tu-freiberg.de*

Abstract
Powder Bed Fusion – Laser Beam/Metals (PBF-LB/M) is one of the most versatile additive manufacturing techniques for fabricating complex metal geometries with high design freedom. Despite these advantages, components produced via PBF-LB/M typically exhibit significant tensile residual stresses due to rapid melting and solidification, along with a poor surface finish caused by partially fused particles and surface irregularities. These drawbacks not only limit the fatigue life of the component but also necessitate additional post-processing steps to achieve functional performance. Plasma electrolytic polishing (PEP) has emerged as a promising surface finishing technique for PBF-LB/M parts, providing a substantial reduction in surface roughness while imparting a glossy appearance. However, prior to PEP, particle blasting serves as an essential intermediate treatment. Particle blasting not only reduces the initial roughness and oxide layer on the as-built surface but also effectively relieves tensile residual stresses by converting them into a more desirable compressive state. This transition is critical for enhancing the mechanical reliability and longevity of the manufactured components.
In this study, the influence of particle blasting on PBF-LB/M components is systematically investigated. The results show that residual stresses, which are heterogeneous and tensile in the as-built state, become uniform and compressive after particle blasting. Furthermore, the treatment removes loosely adhered particles and surface asperities, creating a stable foundation for subsequent polishing. When followed by PEP, a substantial improvement in surface finish is achieved, confirming that particle blasting acts as a crucial bridging step between printing and final functional deployment of PBF-LB/M components.

Keywords: Additive Manufacturing, Particle Blasting, Plasma Electrolytic Polishing, Residual Stresses, Surface Finish.

1. Introduction

Additive manufacturing (AM) has evolved from prototyping to direct functional components since its commercialisation in the late 1980s. According to ASTM ISO standards, there are seven classes of AM [1], which can be applied to a wide variety of materials. Directed energy deposition (DED) and powder bed fusion (PBF) are the two most popular classes of AM for metallic components, with each having its benefits and challenges [2]. DED provides a high deposition rate but induces significant residual stress, which affects component usage and requires machining as a necessary step for dimensional accuracy [3-4]. In contrast, powder bed fusion of metals using laser beam (PBF-LB/M) has a lower deposition rate, yet produces high-quality parts suitable for many applications, requiring minimal machining for high-precision features [2]. However, the surface finish of such components is critical and requires post-processing to enhance their properties. Various mechanical and chemical processes exist to enhance surface quality, and in most cases, mechanical-based processes are inferior due to the complexity of the components, making chemical-based processes the preferred option. Electrochemical-based post-processing is one of the available options; however, due to its hazardous operation involving corrosive and toxic acids, which are also non-recyclable [5], plasma electrolytic polishing (PEP) is a more suitable alternative. PEP offers faster processing with environmentally friendly, chemically neutral, non-toxic water-based electrolytes [6-7].

Residual stresses have always been seen to be critical for metal AM due to repeated heating and cooling cycles, and exhibit tensile residual stress on the surface, which also affects the fatigue life of the components. Compressive stress, achieved through various mechanical operations, is thus required to remove the locked-in residual stress from the components. Hammering/peening is commonly used for DED components [8], while particle blasting (PB) is suitable for small to medium-sized components, making it a suitable choice for PBF components [2].

This study focuses on the effect of PB on PBF-LB/M components, with a particular emphasis on the residual stress behaviour of both as-built and particle-blasted components. The effect of PB on surface roughness has also been studied, as the impact of the particle alters both residual stress modification and initial roughness, making PEP a more efficient process and reducing the surface roughness.

2. Materials and methods

The materials used in this study were pure aluminium and stainless steel of grade SS 316L. Aluminium samples were used to fabricate the test samples at different angles, as shown in Figure 1. The parameters used for sample preparation were: laser power, 370 W; layer thickness, 0.04 mm; hatch distance, 0.14 mm; and scanning speed, 1300 mm/s. These samples were treated with particle blasting, which has a planetary motion-based setup and a mixture of spherical and irregular stainless-steel particles. The speed for blasting varied from 9000 (maximum) to 4000 (minimum) RPM, with a maximum time of

30 minutes at maximum speed, followed by 5 minutes at each reducing speed from 8000 to 4000 with an interval of 1000 RPM.

These samples were studied for the residual stresses in both the as-built and post-PB conditions. The residual stress measurement was conducted on an X-ray diffraction-based setup with the following parameters: Wavelength, Cu 1.54056 Å; two-theta angle, 114.5°; and beam optics, 2 mm point focus. Further, another test specimen was fabricated using SS 316 material with the following parameters: laser power, 230 W; layer thickness, 0.04 mm; hatch distance, 0.11 mm; and scanning speed, 900 mm/s. These samples were sufficiently large to conduct surface roughness measurements, as the larger surface area provides minimal chances of error. The residual stress and surface roughness measurements were conducted on the top surface. PEP was performed on a bath-based, 80kVA high-voltage setup; a schematic representation is shown in Figure 2. The surface roughness measurement was conducted using Mahr, Marsurf CM explorer microscope with Mountains version 11 as the user interface.

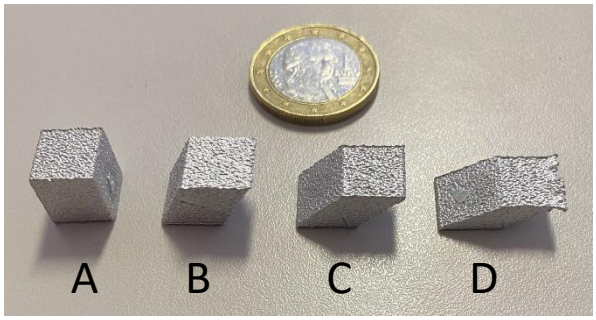

Figure 1. Aluminium samples for residual stress analysis

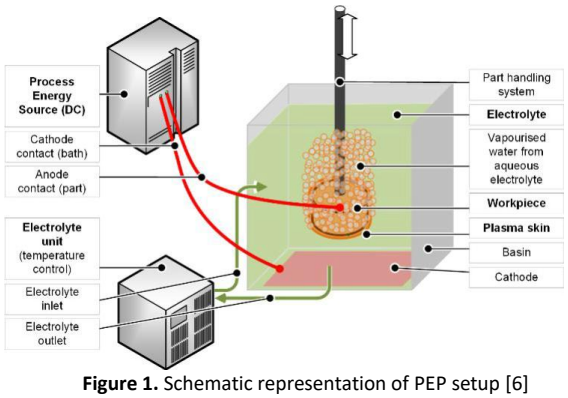

Figure 1. Schematic representation of PEP setup [6]

3. Results and discussion

The residual stress values measured on the top surface are presented in Table 1. It can be observed that in the as-built condition, the residual stress is tensile in nature and after particle blasting, the nature of stress is compressive due to the application of compressive loading during particle blasting.

Table 1: Residual stress values for each sample on the top surface

Samples	Residual Stress (in MPa)			
	As built		After PB	
	σ_{xx}	σ_{yy}	σ_{xx}	σ_{yy}
A	51	48	-34	-39
B	48	42	-42	-52
C	40	39	-45	-45
D	42	41	-35	-35

This was the basis for further experiments, which demonstrated that particle blasting helps reduce tensile residual stress. For further analysis, the samples were treated with particle blasting before undergoing PEP for surface enhancement. PEP parameters were optimised by varying different factors at various levels. Furthermore, the optimised parameters were used to conduct the tests, and three steel samples were tested for their roughness values at three different stages: as-built, after particle blasting, and after PEP. The Surface roughness was considered for measurement as it covers a wide area and is not direction-dependent, unlike the case of line roughness, and presents a better surface morphology. Within surface roughness, S_q (root mean square) values were studied, as Sq is more sensitive to peaks and valleys than Sa (arithmetic mean). The average surface roughness for three samples was reported as 13.7 µm in as-built conditions, 7.5 µm after particle blasting, and 2.7 µm after PEP. A clear indication of particle blasting states that, apart from residual stress relaxation, significant changes in roughness values were observed from 13.7 to 7.5 µm. Furthermore, polishing the particle-blasted sample results in lowering the roughness to 2.7 µm. As PEP is an effective method for reducing surface roughness, its effectiveness is reflected in the results, with the addition of PB leading to further enhancement of efficiency.

4. Conclusions and future scope

PB effectively eliminates tensile residual stresses and promotes the formation of a more uniform compressive residual stress state through the application of compressive loading by bombarding particles. This process further reduces the initial surface roughness by removing partially sintered powder and mitigating surface features associated with the lack of remelting. PEP is recognised as an effective surface enhancement technique, and the results demonstrate that integrating PB further improves the efficiency of the PEP process. Furthermore, additional experiments with varying parameters are planned to further investigate potential improvements in residual stress and surface roughness.

References

[1] DIN EN ISO/ASTM 52900:2022-03, Additive Fertigung-Grundlagen-Terminologie, Berlin.

[2] Lohani, D., Gupta, N. K., Zeidler, H., Böttger, T., Erler, M., & Streek, A. (2025). Plasma Polishing as a Post-Processing Method for Surface Improvement in Macro-PBF-LB/M Components. Procedia CIRP, **137**, 425-430.

[3] Gupta, N. K., S, S., Karade, S. R., G, G., Gote, G. D., Dubey, S., & Karunakaran, K. P. (2025). Enhancing 5-axis deposition with a double slicing method in wire arc additive manufacturing. *Rapid Prototyping Journal*, ***31***(6), 1264-1279.

[4] Karade, S. R., Siddhartha, S., Gupta, N. K., G, G., Karunakaran, K. P., & Zeidler, H. (2025). Hybridization in Metal Wire Additive Manufacturing: A Case Study of an Impeller. *Metals*, **15**(1), 71.

[5] Belkin, P. N., Kusmanov, S. A., & Parfenov, E. V. (2020). Mechanism and technological opportunity of plasma electrolytic polishing of metals and alloys surfaces. *Applied Surface Science Advances*, **1**, 100016.

[6] Nestler, K., Böttger-Hiller, F., Adamitzki, W., Glowa, G., Zeidler, H., & Schubert, A. (2016). Plasma electrolytic polishing–an overview of applied technologies and current challenges to extend the polishable material range. *Procedia Cirp*, **42**, 503-507.

[7] Nevyantseva, R. R., Gorbatkov, S. A., Parfenov, E. V., & Bybin, A. A. (2001). The influence of vapor–gaseous envelope behavior on plasma electrolytic coating removal. *Surface and Coatings Technology*, **148**(1), 30-37.

[8] Gupta, N. K., Ganesan, G. B., Karade, S., Mehta, A. K., & Karunakaran, K. P. (2022, March). Effect of multiple technologies on minimizing the residual stresses in additive manufacturing. In ICRS 11-The 11th International Conference of Residual Stresses.

euspen's 26th International Conference & Exhibition, Krakow, PL, June 2026
www.euspen.eu

Voxel-Scale Misalignment Detection for Orthogonal Metasurface-produced Holograms via Error-Compensated Volumetric Imaging

Gavin Stafford[1], Timothy Yap[2], Michael Cullinan [1]

[1,2]*The University of Texas at Austin, Walker Department of Mechanical Engineering*

ghstaff@utexas.edu

Abstract

Metasurfaces are thin diffractive optical elements composed of subwavelength structures that can alter the amplitude, phase, and/or polarization of incoming light. These structures can be tuned to reconstruct a 3D light intensity pattern composed of voxels, input as a computer-generated hologram (CGH), within a photocurable resin. This metasurface-based additive manufacturing process, much like conventional projection lithography, is limited in its axial resolution by the square of the NA (numerical aperture) of the optical system. However, with the addition of a second, orthogonal metasurface, and careful tuning of light intensity and resin chemistry, photopolymerization can be localized to only those regions enclosed by the voxels of both metasurface projections simultaneously, improving the axial resolution. To make this orthogonal curing possible, the voxels of the two projected holograms must overlap, meaning that alignment at the scale of the voxel is necessary. To achieve this, we introduce an error-compensated volumetric imaging system for misalignment detection and correction. The system uses four-focal-length relays to transport both hologram images from their locations within the sample volume to a CMOS (Complementary metal-oxide-semiconductor) sensor mounted on a precision stage, which determines their relative displacement and orientation. A calibration artifact is used to compensate for systematic error in this process through imaging of its features along both arms. By comparing the CMOS-imaged relative feature locations to the actual relative feature locations of the target, a transformation matrix for each arm can be calculated that incorporates systematic error in the relays. These matrices will allow future closed-loop feedback control of the hologram alignment by mapping the volumetric imaging captured by the CMOS to misalignment values, which can then be plugged into the motorized stage of the moveable metasurface to bring the two holograms into alignment.

Additive Manufacturing, Metasurfaces, Alignment, Lithography

1. Introduction

Traditionally, holographic lithography is done as a variable process, in which holograms are rapidly encoded into an SLM (spatial light modulator) in order to change the projected light intensity pattern. This is done with tomographic 2D projections in the case of computed axial lithography [1], as well as with multi-foci projections [2] in order to produce volumetric prints. While adaptable, these processes are inherently limited in the optical resolution they can achieve due to the large minimum pixel size of SLMs. Metasurfaces, on the contrary, cannot be changed in their design once printed, but are limited in their pixel size only by the feature resolution capabilities of their fabricating device. This allows for much smaller pixels, and thus a much higher achievable optical resolution. Moreover, fabrication methods for metasurfaces are arbitrarily scalable, such as TPA (two-photon absorption) printing, meaning that the size of the metasurface can be increased to permit the desired volumetric throughput of the metasurface lithographic process while maintaining optical resolution, provided the stitching between fabrication regions of the metasurface does not affect the produced hologram.

Metasurfaces, while reaching higher resolution than SLMs, still suffer from low resolution along the optical axis, where the square of the NA limits the spatial confinement of light. To overcome this hurdle, a method of overlapping orthogonal holograms is introduced, for the purpose of only curing within a desired overlapping volume. This requires precise overlap of the target holograms. This paper presents a novel misalignment detection method based off of registering each hologram with a common reference target, and using this common frame to calculate the centroidal displacement of the two holograms. These misalignment values can be used in future work to correctly align and print with orthogonal metasurfaces.

These metasurfaces are made using an optical inverse design algorithm, as shown in Figure 1, which takes a 3D shape, slices it into planes, and optimizes a phase mask such that the intensity of the electromagnetic field it produces best matches those planes. This mask is then fabricated and used for vat photo-polymerization.

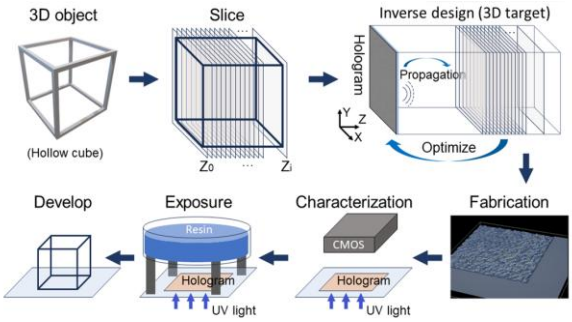

Figure 1. Holographic Metasurface Lithography Process

2. Methodology

2.1. Optical Setup

Alignment of the holograms starts with the illumination of the phase mask by a uniform, coherent light source. The optical system used is built to deliver this coherent source to the mask at normal incidence, and with full coverage. Figure 2 shows the CAD of the optical setup, which was replicated in the lab. The 405 nm coherent laser source is aligned, filtered and magnified, and finally passed through the phase masks.

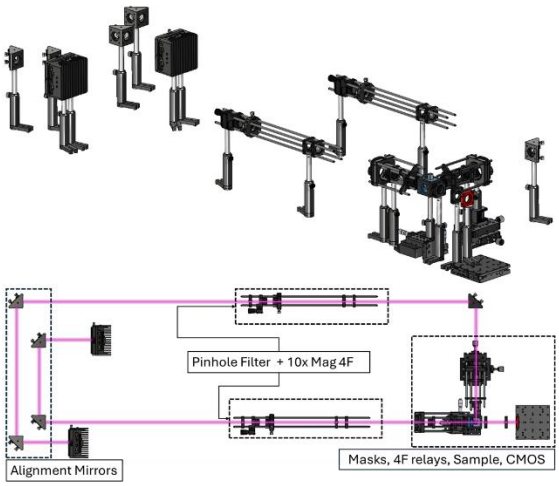

Figure 2. CAD of Illumination Optics

Figure 3 shows a close up view of the phase mask projection assembly, where 4f (4-focal-length) lens relays are used to relay the cube-shaped holograms produced by the masks to the sample/target stage.

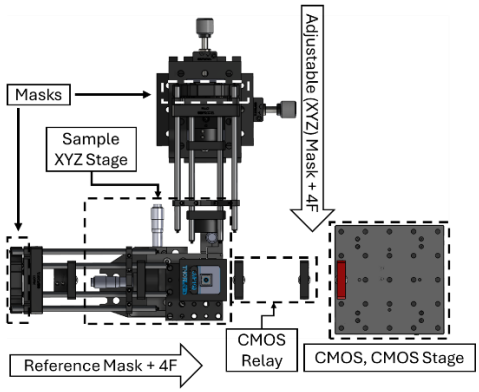

Figure 3. CAD of Sample/Target Stage Area

This is a zero magnification relay done solely to arbitrarily increase the projection distance of the phase masks from their designed 3 mm. These projected holograms are designed as point clouds, or "gaussian dot" approach, with these dots being 2-3 pixels in diameter, effectively acting as 10-15 µm voxels. The sample cuvette holder is shown on the XYZ stage, which is present when doing printing. Figure 4 shows a picture of this sample XYZ stage with a calibration target and diffuser in place, which are used for the focus scanning. The axes labelled in this figure are the "global" axes by which the final hologram misalignments will be defined. This figure also shows the 4f relays that relay the hologram images from the sample or target frame to the CMOS detector. These are composed of two 1 inch diameter, 30 mm focal length achromatic lenses.

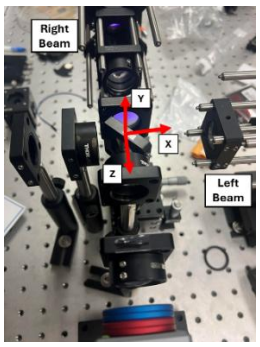

Figure 4. Sample XYZ Stage with Diffuser and Calibration Target

2.2. Checkerboard Scanning, Focus Scoring

Once there is confidence in the illumination optics, the alignment scheme is started. It consists of a mirrored process, where the left hologram is scanned and removed, then the calibration target is placed, and the left focus scanning is done for two sample stage locations. The CMOS is then moved opposite the right beam, and completes the focus scanning for that axis at two sample stage locations. Finally, the right hologram is inserted and scanned. This mirrored process of scanning hologram, target, target, hologram is implemented such that each hologram is tied to its respective focus scan, and the focus scans are tied to one another through the calibration target. Any other order would fail the registration of the holograms with their scans, or the scans with one another, as the target must be removed to scan the holograms. The movement of the sample stage to two different locations for each focus scan is necessary to satisfy the non-coplanarity requirement for a set of points that defined a 3D rigid body transformation.

This focus scanning process moves the image relayed to the CMOS across the angled calibration target and maps which X coordinates (5.5 µm pixels on the CMOS) contain the most in focus corners of the calibration grid, at that Z location. The resulting XYZ point coordinates are recorded, and matched with their pair of coordinates in the target frame, which is easily calculated due to the known width of the target squares (250 µm). These points are shown in Figure 5 for single frames within the each of the 4 scans of the checkerboard.

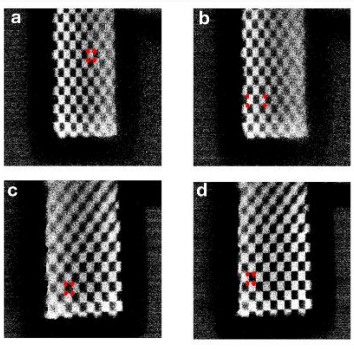

Figure 5. Corners of Interest in: (a) First Left Scan (b) Second Left Scan (c) First Right Scan (d) Second Right Scan

When initially scanning the angled calibration target along the Z axis, there was a large range (5 mm +) where the squares had little aperture diffraction, thus it was difficult to use the minimum of this aperture diffraction as a measurement of focus, as originally planned. The solution to this was placing a diffuser in front of the target, which scatters the illuminating light before it hits the target, drastically increasing the range of illumination

angles. This decreased the range where the checkerboard was in focus enough for the shift in focus along the screen to become obvious as the Z location of the CMOS changed.

The metric used to determine this focus was the Binary Shannon Entropy of the 4 quadrants surrounding each corner of interest, as shown in Figure 6.

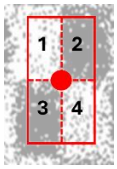

Figure 6. Quadrants for Shannon Entropy Calculation

Shannon entropy, defined in Eq. 1 for the binary images it evaluates, calculates the information density of a region. For a given region, this roughly equates to the number of variables necessary to fully define it. For example, a cup of coffee with cream sitting on top as a single layer would have low Shannon entropy, and as it is mixed, its Shannon entropy would grow larger and larger as more variables would be necessary to define the position of the cream as it mixes into the coffee. In the case of the checkerboard, for a perfectly black pixel or white pixel quadrant, the Shannon entropy would be at a minimum, and for a region of completely intermixed and random black and white pixels, the Shannon entropy would be at a maximum. This score is defined in Eq. 2, where the entropy of the surrounding quadrants is averaged to give an accurate representation of the focus at the corner.

$$H(Q_i) = -[p \log_2 p + (1-p)\log_2(1-p)] \quad (1)$$

Where H is the Shannon entropy, Q is the quadrant, and p is the probability of a black (or white) pixel. This probability is what is scraped from the image.

$$Focus\ Score = 1 - \frac{\sum_{i=1}^{4} H(Q_i)}{4} \quad (2)$$

Each scan consisted of 80 2048×2048 pixel images spaced at intervals of 20um. Videos of these scans were made in order to watch and qualitatively determine which grid corners went from defocus, to focus, and again to defocus within the scan. These corners were then selected for the Shannon entropy algorithm to evaluate. A graph of this focus score along the Z scan is shown in Figure 6, where two points, Peak 3 and Peak 4, were selected due to their superior peak spacing, which closely resembled that expected, based on the tilt angle of the target (measured by comparing the width of the squares in the image to their actual 250 µm width).

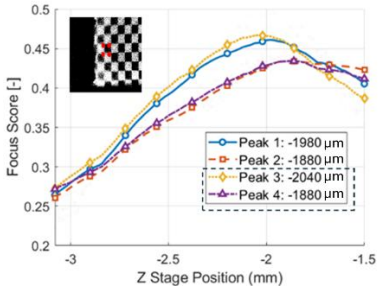

Figure 6. Focus Score Curves for 4 Points Along the Second Right Scan

Even though Peak 1 and Peak 2 have almost the same focus curves, their calculated peaks are not spaced adequately for fitting to the periodicity of the angled target. A 25 scan wide average was applied to these curves to eliminate random noise and deduce the overall focus trend. This is how all of the 4 CMOS – target point pairs were found for each of the 4 scans, yielding the 8 sets of points for each transformation.

The hardware error budget for the scanning procedure is shown in Table 1, where the most contributing factor is the large focus sampling interval of 20 µm, which was chosen for speed. This can, in the future, be decreased down to the repeatability of the CMOS stage, 1 µm. The resulting RMS error value due to the hardware was 23.07 µm.

Table 1. Hardware Error Budget for Focus Scanning

CMOS Pixel Resolution [µm]	5.5
CMOS Stage Bi-Directional Repeatability [µm]	± 1
Target Stage Bi-Directional Repeatability [µm]	±10
Target Grid Resolution [µm]	1
Focus Sampling Interval Resolution [µm]	20

2.3. Frame Transformations

The 4f relays for the CMOS were aligned carefully before use so that the CMOS to target transforms could be defined by rigid transformations instead of affine transformations. This was done with a mind to the large hardware RMS error present, as an affine transform, with its extra degrees of freedom, could overfit to that random error.

The method used to determine the best rigid transform matrix was a Procrustes analysis that optimized the rotation and translation matrices between frames to minimize the RMS error of the transform, which is shown in Eq. 3.

$$E_{rigid} = \sqrt{\frac{1}{n}\sum_{i=1}^{n} \|T_i - (RS_i - t)\|^2} \quad (3)$$

Where E_{rigid} is the RMS error of the rigid transform, T_i is the current point in the CMOS frame, S_i is the point pair in the target frame, R is the rotation matrix, and t is the translation vector.

Once these transformations are calculated, one for the left beam and one for the right beam, the left and right holograms themselves are scanned for transformation. This is done by identifying visually the start and end planes of each hologram, and generating points for their corners, such that a cube can be defined for each. These planes are shown in Figure 7.

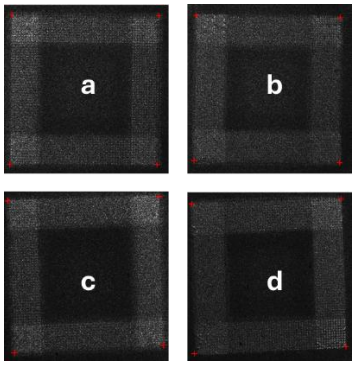

Figure 7. CMOS Images of Start/End Hologram Planes (a) Left Start (b) Left End (c) Right Start (d) Right End

3. Results

The results of the rigid transformation optimization produced transforms with RMS errors shown in Table 2.

Table 2. RMS Error of Left and Right Rigid Transforms

RMS Error, Left Transform [µm]	RMS Error, Right Transform [µm]
45.81	30.43

These values being higher than the hardware RMS indicate that there is also non-trivial error in the Shannon entropy focus finding algorithm. Once performed on the cube representations of the holograms, their misalignment in the global reference frame can be calculated as shown in Table 3 and visualized as shown in Figure 8, where the cubes represent the holograms, and the tails on these cubes represent the direction the light travels from.

Table 3. Misalignment Values in the Global Reference Frame (Note: Values reference the coordinate frame shown in figure 8)

Misalignment X [µm]	Misalignment Y [µm]	Misalignment Z [µm]
-2377.84	207.98	2361.52

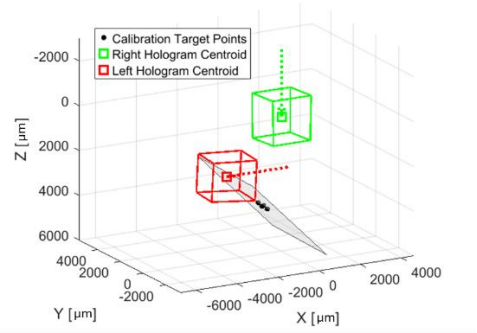

Figure 8. Misalignment of Cubes in 3D with Calibration Target as Reference

4. Discussion

The RMS error inherent to the calculated transforms is partially due to the hardware and scan interval, and partially due to the inability of the Shannon entropy-based focus algorithm to accurately track the focus shift. This was not a narrow band of focus, nor was it sharp. Instead, it was a few squares wide, and dropped off over the course of 1-2 squares. With the width of the tilted squares being 150-200 µm depending on the tilt angle, this meant an effective area of focus almost 1 mm wide, discernable by the human eye, as seen in Figure 5. The Shannon entropy image processing allows a much tighter evaluation of the focus along the checkerboard than this 1mm band, as it quantitatively discerns differences in the entropy of a point as the focus band moves over it, allowing the identification of a peak of focus. This is solely for finding valid points for the geometric transforms, which when applied to each hologram, give their relative displacements in a common reference frame. Therefore, this 1mm focus band has absolutely no bearing on the range of misalignment values that can be detected. It will only influence the RMS errors of the transforms it informs. For a tighter band of focus, a higher NA lens should be used to gather higher incoming angles of light, and a lower grit diffuser should be used to scatter at those higher angles. The addition of a diffuser is what made the focus shift sensitive enough for the Shannon entropy measure to track, so a diffuser with more scatterability could increase that shift sensitivity even more. Additionally, the high scanning interval of 20 µm can be decreased to drastically improve the hardware RMS error. These are the two most effective ways to eventually get single digit micron alignment with this method.

The misalignment values (Table 3) indicate exactly why this method was necessary. The Y misalignment is small because it is possible to visually align the two holograms within a couple hundred µm in this axis by using a fluorescent card. The large X and Z misalignments of 2 mm are the result of an inability to accurately probe the location of the hologram peak planes along its optical axis with a fluorescent card, as the human eye cannot discern the subtle changes in contrast that occur from plane to plane. A qualitative alignment scheme was previously implemented that used the calibration target as a beam combination as half of the squares are reflective. This showed both holograms on a CMOS at the same time, which allowed for them to be aligned along the global Y axis and the CMOS X axis. The trouble is that this CMOS X axis did not correspond to either of the global X or Z axes, because of the reflection transformation on the hologram. They simply couldn't be aligned effectively with the CMOS along their optical axes, because if they weren't sitting at the intersection point of the two beams, then alignment along the optical axes didn't correspond to alignment in the global X-Z plane. This method solves that problem by providing a common register to compare the optical axis of each hologram to.

5. Conclusion

A novel misalignment detection method for orthogonally projected holograms was developed based on the hologram volumes themselves, not on the phase masks that detect them, and the use of a common target to register the hologram centroids to one another. This target was placed at an angle between the two projection directions, and a diffuser was positioned in front of the target to scatter the light from one direction, then the other. A focus scan was then performed to find the Z locations of minimum Shannon entropy for selected X-Y points on the target, indicating that those points were in focus at that Z location. These X-Y-Z points were then paired with their corresponding target frame points, and rigid transformations were calculated with a Procrustes analysis. The final error of these transforms that defined the misalignment was 45.81 µm and 30.43 µm for the left and right transforms, respectively. These values were on the scale of the size of the 10-15 µm diameter point cloud based voxels. The current error ceiling is set by the large area of focus of roughly 1 mm and the large Z sampling interval of 20 µm. Despite these restrictions, both holograms were successfully registered to a common reference frame, and their misalignment values were found. These values will be used in future work to bring the orthogonal holograms into alignment via high resolution stages and print structures.

References

[1] Álvarez-Castaño M I, Madsen A G, Madrid-Wolff J, Sgarminato V, Boniface A, Glückstad J and Moser C 2025 Holographic tomographic volumetric additive manufacturing *Nat. Commun.* **16** 1551

[2] Rietz P, Somers P, Kalt S, Schneider J L G, Kiefer P and Wegener M 2025 Dynamic Multi-Focus 3D Laser Nanoprinting Based on Two-Step Absorption and Computational Holography *Laser Photonics Rev.* **19** 2500187

euspen's 26th International Conference & Exhibition, Krakow, PL, June 2026
www.euspen.eu

Novel niobium carbide cermet and manufacturing techniques for moulds towards improving durability and flowability in ceramic injection moulding

Muhammad Hazak Arshad[1,5], Victor Laermans[2], Mian Monib Ur Rehman[3,5], Tim Evens[2], Shuigen Huang[4], Krishna Kumar Saxena[1,5], Sylvie Castagne[3,5], Albert Van Bael[2], Jozef Vleugels[4], Dominiek Reynaerts[1,5,*]

[1]Department of Mechanical Engineering, *Manufacturing Processes and Systems, Micro- & Precision Engineering Group, KU Leuven, Leuven, Belgium.*
[2]Department of Materials Engineering, *Structural Composites and Alloys, Integrity and Nondestructive Testing, Polymer Processing & Engineering Group, KU Leuven, Diepenbeek, Belgium.*
[3]Department of Mechanical Engineering, *Manufacturing Processes and Systems, Laser Micromanufacturing Group, KU Leuven, Leuven, Belgium.*
[4]*Department of Materials Engineering, Surface and Interface Engineered Materials, KU Leuven, Leuven, Belgium.*
[5]*Member Flanders Make, Leuven, Belgium.*

[*]*dominiek.reynaerts@kuleuven.be*

Abstract
Ceramic injection moulding (CIM) enables net-shape fabrication of complex ceramic components for biomedical, aerospace, energy and luxury sectors but requires high injection pressures (up to 2000 bar) due to the limited flowability of ceramic feedstocks with powder volume fraction up to 60%. Combined with the abrasive nature of the feedstock, this leads to severe mould wear and frequent replacement, increasing process cost and limiting precision. This work investigates the process chain of CIM by exploring a new mould material, machinability investigation, laser surface structuring for flowability and mould surface repair.
Niobium carbide with nickel binder cermet (NbC-Ni) was investigated as the mould material which offers a hardness (1468 HV_{30}) comparable to tungsten carbide while avoiding cobalt binders. Initial CIM tests show that NbC-Ni suffers less dimensional wear in depth (~46% lower) and width (~86% lower) after 10,000 shots in comparison to tool steel (Uddelholm Stavax® ESR) with Al_2O_3 feedstock. This shows NbC-Ni is suitable for moulds but its high hardness, modest thermal conductivity and multi-phase microstructure pose significant challenges for machining and surface texturing. Hybrid laser-electrochemical machining (LECM) is explored as a hardness-independent process for machinability evaluation. Compared to conventional electrochemical machining (ECM), LECM demonstrates improvement in shaping precision by 24% and surface quality (Sa) by 30%. In parallel, laser surface texturing with feature sizes below 50 µm is being investigated to enhance feedstock flowability while avoiding texture replication on products. Preliminary experiments have shown it is possible to fabricate micro-dimples with a diameter of 30 µm and a wide range of aspect ratios, with minimal thermal defects at the perimeter on NbC-Ni using femtosecond laser machining. Additionally, a proof-of-concept process chain was developed for bi-directional ECM and electrochemical additive manufacturing (ECAM) using a single-hybrid tool towards repair of mould surfaces.

Keywords: Injection moulding, Electrochemical Machining, Hybrid laser-ECM, Ultrashort pulsed laser, Electrochemical additive manufacturing, ceramics, cermets

1. Introduction

Ceramic injection moulding (CIM) is a near net-shape manufacturing process for producing geometrically complex ceramic components [1]. It is widely applied in biomedical, aerospace, energy and luxury sectors using alumina and zirconia feedstocks. However, CIM faces challenges in achieving high dimensional accuracy, surface quality and process reliability, particularly for components with sub-mm/µm features. A key limitation in CIM arises from the rheological behaviour of ceramic feedstocks, which typically contain up to 60 vol.% ceramic powder. The resulting high viscosity affects flowability [2] and complicates filling of fine mould features, necessitating injection pressures up to 2000 bar. These high pressures in combination with the abrasive nature of ceramic particles, accelerate mould wear and degrade surface integrity on common mould materials like tool steels, making CIM an expensive process.

Cermets such as tungsten carbide-cobalt offer improved wear resistance but rely on Co binders, which are increasingly restricted due to health and environmental concerns. In this context, niobium carbide-nickel binder cermet (NbC-Ni) is a promising alternative as it exhibits hardness (1468 HV_{30}) similar to WC-Co [3]. However, its high hardness, modest thermal conductivity (14 W/mK) and multi-phase composition make it difficult to machine with both conventional and non-conventional processes. Hybrid laser-electrochemical machining (LECM) [4] represents a possible solution to these challenges. It combines µs-pulsed electrochemical machining (ECM) with coaxial ns-pulsed laser to enhance electrochemical reaction kinetics, weaken passivation and improve removal of less reactive phases. Additionally, the process is independent of material hardness and maintains the athermal nature of electrochemical machining (ECM), making it particularly suitable for machinability (shaping) investigation of NbC-Ni.

Beyond material and machining considerations, mould surface functionality plays a critical role in CIM performance. Surface texturing has been proposed as a method to reduce the friction coefficient and improve feedstock flow behaviour [5]. However, surface features on moulds can replicate onto the products. Therefore, texturing is explored in this study with feature dimensions targeted below 50 µm to minimise texture transfer.

Femtosecond laser micromachining was employed for this, as it is hardness-independent and minimises the influence of modest NbC-Ni thermal conductivity to enable precise surface texturing with minimal thermal defects.

Furthermore, given the high costs and lead times of precision mould manufacturing, repair strategies are being researched for resusing dies and moulds [6]. Hence, this work also presents a proof-of-concept repair process chain combining ECM for surface smoothening and exposing surface/subsurface cracks, with electrochemical additive manufacturing (ECAM) for localised and athermal repair-material deposition.

2. Experimental details

2.1. Ceramic powder injection moulding machine

The CIM tests were conducted on a Wittmann® Smartpower 50 machine (**Fig. 1a**) and mould inserts (**Fig. 1b**) were machinined out of tool steel (Uddelholm Stavax® ESR) and NbC-Ni cermet using die-sinking electrical discharge machining at a mould manufacturer without texturing. The NbC-Ni cermet was synthesized in-house through liquid phase sintering at 1420 °C. The CIM feedstock was K1008 from INMATEC® (Al_2O_3, 96 wt% in polyolefine based binder). Experiments were conducted for 10,000 shots at an injection speed of 40 ccm/s and a barrel temperature of 150 °C. To ensure complete filling of the mould, a backpressure of 600 bar was used. The mould inserts were thoroughly cleaned prior to measurements.

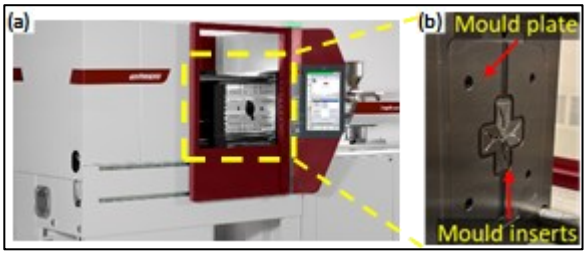

Figure 1: (a) Wittmann® Smartpower 50 machine and (b) mould inserts.

2.2. Mutlifunctional electrochemical machine tool

The in-house developed 3-axis multifunctional electrochemical (EC) machine tool (**Fig. 2**) was used for NbC-Ni ECM/LECM machinability (shaping) investigations and ECM/ECAM experiments for proof-of-concept mould surface repair demonstration. It is equipped with a ns-pulsed green laser source (532 nm, max avg. 30 W) to coaxially and simultaneously supply laser and electrolyte through a tubular steel cathode-tool (1.2 mm O.D., 0.65 mm I.D.) onto the workpiece (anode) surface to realise LECM (**Fig. 2b**). For more details on the process principle and machine tool, the readers are referred to [4]. The tubular tool can be replaced with a hybrid EC-tool (**Fig. 2a**) to enable sequential ECM and ECAM processes by switching the electrolyte and tool/workpiece polarity [6]. It supplies electrolyte through a metal nozzle (0.3 mm I.D.) with an air-column around it to localise machining and deposition.

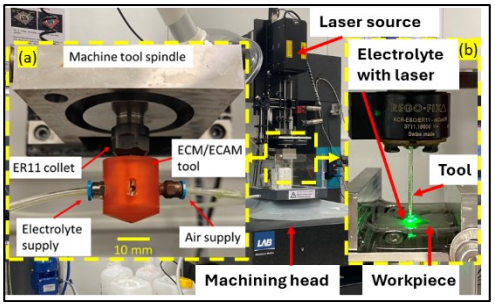

Figure 2: Multifunctional machine tool with (a) hybrid EC-tool for ECM/ECAM and (b) tubular tool for ECM/LECM.

For ECM/LECM experiments, 30 × 10 x 4 (L x W x H) mm bars of NbC-Ni were prepared through wire-EDM on the GF Cut E 600 and the surface was ground to Sa of ~1.2 µm (measured with Senosofar® S Neox, L-filter 25 µm). Preliminary experiments were conducted to find suitable process parameters (**Table 1**) to conduct groove machining experiments using 2.4M $NaNO_3$ electrolyte.

Table 1. Process parameters for ECM and LECM of NbC-Ni.

Parameter	Value
Voltage parameters	30 V, 10 µs pulse on-time, 50% duty cycle
Interelectrode gap	80 µm
Feed rate	80 µm/s
Electrolyte flow rate	0.5 mL/s
Laser parameters	48.5 µJ, 150 kHz, 50 ns pulse on-time

For ECM/ECAM experiments, groove machining of flat stainless steel (SS304) substrates with copper (Cu) deposition on machined grooves with subsequent machining was initially investigated using 1M $CuSO_4.5H_2O$ electrolyte to realise bi-directional process sequencing. Thereafter, nickel (Ni) deposition was conducted using 0.4M $Ni(NH_4)_2(SO_4)_2.6H_2O$ electrolyte in premachined cavities (3 mm width, 1.5 mm depth) on SS304 substrates to check the feasibility on a mould representative feature. The process parameters for these experiments are summarised in **Table 2**, which are based on preliminary experiments on these materials. Afterwards, all samples (ECM, LECM, ECAM) were cleaned in de-ionised water.

Table 2. Process parameters for ECM and ECAM experiments.

Parameter	ECM of SS / Cu	ECAM of Cu	ECAM of Ni
Voltage	20 V / 10 V	5 V	5 V
Interelectrode gap	100 µm	100 µm	100 µm
Electrolyte flow rate	0.45 mL/s	0.1 mL/s	0.1 mL/s
Scan rate	0.8 mm/s	0.8 mm/s	0.8 mm/s
Scan layers	2	40	20
Air pressure	1.1 bar	1.1 bar	1.1 bar
Voltage pulse parameters	20 µs pulse on-time, 50 % dutyc cycle		

2.3. Laser texturing machine

Surface texturing of ground NbC-Ni samples was conducted using a femtosecond laser micromachining system (CARBIDE, Light Conversion Ltd.) [7] (**Fig. 3a**). The system has a laser with an output wavelength of 1030 nm, pulse duration of 250 fs, maximum average power of 20 W, maximum pulse energy of 400 µJ and maximum pulse repetition rate (PRR) of 1 MHz. The laser beam has a Gaussian intensity profile and is focused with a 125 mm focal length lens for a beam waist radius of 17 µm.

A design of experiment approach was employed to produce micro-dimples with base diameters around 30 µm through percussion drilling (**Fig. 3b**).

The experimental matrix involved systematic variation of pulse energy from 2 to 4 µJ in increments of 0.5 µJ and the number of

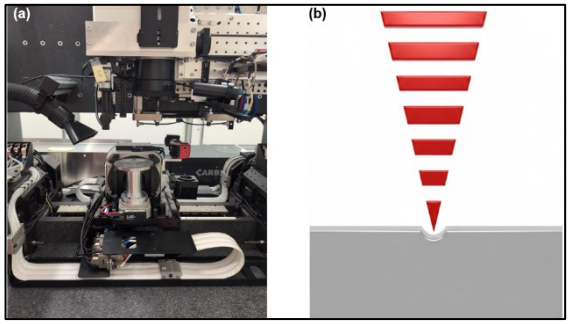

Figure 3: (a) Femtosecond laser micromachining system (b) Schematic of percussion drilling scan strategy.

pulses from 20 to 100 in steps of 10 pulses. Other parameters, such as PRR and pulse duration, were kept constant. The complete set of processing parameters are presented in **Table 3**.

Table 3. Process parameters for micro-dimples laser machining.

Parameter	Values/description
Pulse energy (µJ)	2, 2.5, 3, 3.5, 4
Number of pulses per micro-dimple	20-100 (step size 10)
Pulse repetition rate (KHz)	500
Pulse duration (fs)	250
Scan strategy	Percussion drilling

3. Results and discussion

3.1. Wear assessment of mould insert materials during CIM

The wear behaviour of tool steel and NbC-Ni mould inserts was evaluated after 10,000 CIM shots by analysing the dimensions and surface topography of the uppermost step of the Y-shaped mould cavity (**Fig. 4a**). Dimensional measurements were performed using a Werth VideoCheck® HA coordinate measuring machine equipped with a Renishaw® SP25 tactile probe (MPE 1.5 µm). Surface topography was characterised using a Sensofar S Neox optical microscope operating in confocal mode, with a third-order polynomial F-filter applied to remove form. Three measurements were done before and after experiments to calculate the average and standard deviation for dimensional wear and surface topography metrics (Sa, Sal).

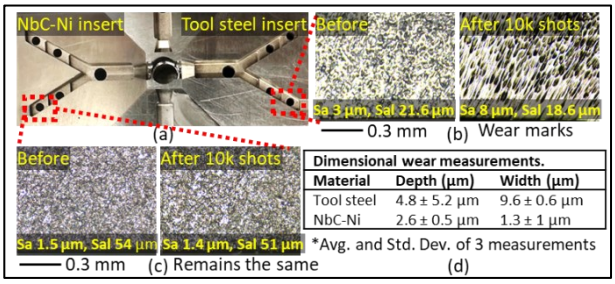

Figure 4. (a) Moulds inserts, surface topographies of (b) tool steel and (c) NbC-Ni cermet, and (d) dimensional wear measurements.

Distinct wear marks were observed on the tool steel mould insert surface after 10,000 shots alongwith a pronounced degradation of the surface integrity. The surface roughness (Sa) increased by approximately 167% compared to the as-manufactured condition (**Fig. 4b**). In contrast, the NbC-Ni mould insert surface exhibited no visually observable wear features and the measured Sa value remained similar (**Fig. 4c**). The autocorrelation length (Sal) of NbC-Ni insert was also higher than for tool steel indicative of less wear marks. The dimensional wear measurements summarised in **Fig. 4d** confirm these observations. The tool steel insert experienced material wear of 4.8 ± 5.2 µm in depth and 9.6 ± 0.6 µm in width. In comparison, the NbC-Ni insert experienced less wear, with an increase in depth of 2.6 ± 0.5 µm and in width of 1.3 ± 1.0 µm.

These results demonstrate the superior wear resistance of NbC-Ni under high-pressure CIM conditions and highlight its potential as a durable mould material. Therefore, its machinability was further investigated with ECM and LECM.

3.2. Machinability evaluation of NbC-Ni cermet with LECM

Apart from the high hardness (1468 HV_{30}) and low thermal conductivity (14 W/mK) of NbC-Ni, which make it challenging to machine (shape) with conventional and non-conventional processes, it also has a high passivation tendency (oxide formation) and different phases with varying reduction potentials that make it difficult to machine by ECM with high precision and surface quality. In LECM, a laser acts as assisting energy source to ECM by locally heating the workpiece surface to focus current density in the center to enhance reaction kinetics, passivation weakening and removal of less reactive phases, leading to improved precision and surface quality [4]. This is demonstrated by the results shown in **Fig. 5**, where the machined grooves and surface topography metrics (Sa, Sdr) were measured (3 measurements) using Sensofar® S Neox. For the surface topography, a F-filter of polynomial order 3 and L-filter of 25 µm were applied. Furthermore, the cross-section was observed by SEM for better visualisation of removal behaviour. The profiles in **Fig. 5a** show improvement in precision by 24% with LECM where the width reduced from 1.95 mm to 1.48 mm along with an increased depth from 0.11 mm to 0.14 mm icompared to ECM. Additionally, due to the current density focusing effect, the residual hill in the groove center with ECM was removed with LECM. The improved dissolution behaviour is further evidenced in **Fig. 5b**, where LECM shows a reduction in inhomogeneous material removal. Preferentially passivating ridges and dissolving crevices observed in ECM were suppressed, indicating a more uniform phase dissolution. This improvement is also reflected in the surface topography measurements as the surface roughness (Sa) and developed interfacial area ratio (Sdr) reduced by ~30% and ~50%, respectively, with LECM (**Fig. 5c**). The passivation weakening capability of LECM on NbC-Ni surface was also verified with energy dispersive X-ray spectroscopy (EDS), which showed reduction in O content by 11 wt.% in comparison to ECM.

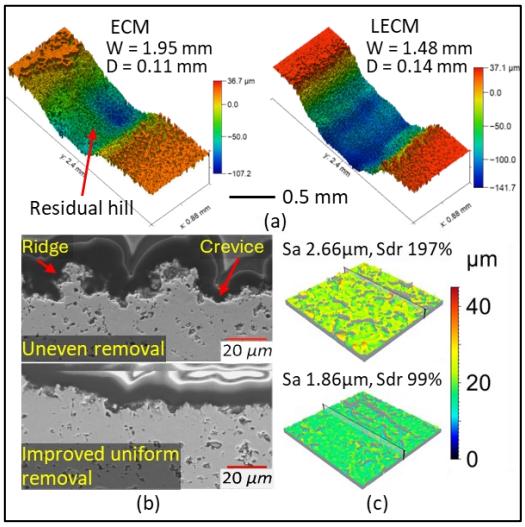

Figure 5. Machining results of ECM and LECM on NbC-Ni. (a) Shape morphology, (b) cross-section views and (c) surface topography.

3.3. Laser surface texturing investigation

The micro-dimples on the NbC-Ni surface were analyzed using a Philips XL 30 FEG SEM microscope and Sensofar® S Neox. Three depth measurements of micro-dimples were taken to calculate the average and standard deviation. The surface topography of the micro-dimples is shown in **Fig. 6**, where **Fig. 6a** shows the SEM image (top view), and **Fig. 6b** shows the 2D profile of the micro-dimples created with 50 pulses of 4 µJ pulse energy.

Minimal thermal defects and recast layer were observed on the periphery of the micro-dimples. The 2D profile shows that the micro-dimples have an inverted conical shape, which is a result of the Gaussian profile of the incident laser beam.

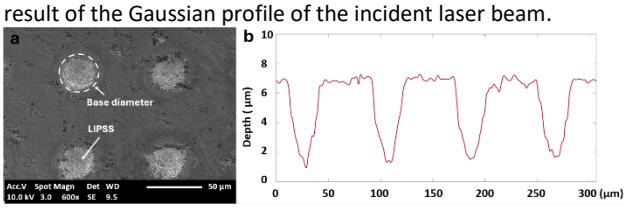

Figure 6. Surface topography of micro-dimples. (a) SEM image showing top view of surface, (b) 2D profile of micro-dimples

The variation of the micro-dimples depth with pulse energy and number of pulses is shown in **Fig. 7**. The dimple depth increased almost linearly with an increase in pulse energy as well as pulse number. However, no significant variation in the base diameter was observed by varying either of the two parameters. Therefore, for a constant base diameter of 30 µm, a wide range of micro-dimple depths (1.5 to 12.5 µm) can be achieved, which corresponds to aspect ratios between 0.05 and 0.45.

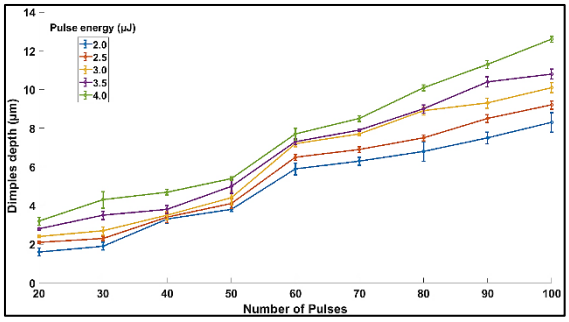

Figure 7. Micro-dimple depth evolution with increasing pulse energy and number of pulses.

3.4. Electrochemical manufacturing method for surface repair

This section presents work in progress results for developing an electrochemical-manufacturing based mould surface repair technique for reusing moulds, thereby improving durability. To assess the feasibility of the repair technique, a sequential processing with ECM and ECAM was evaluated first. The result in **Fig. 8a** shows different process sequences i.e. (i) ECM groove on SS substrate of 14 mm length (red line), (ii) ECAM of Cu in the machined groove up to 10 mm length (green line) and (iii) ECM groove machining of Cu deposit up to 7 mm length (black line). This shows the possibility to achieve bi-directional and sequential material removal and addition in close proximity, which is demonstrated for the first time in mask-free electrochemical manufacturing. The average of 3 measurements indicates that ECAM had a scan layer thickness of ~0.5 µm.

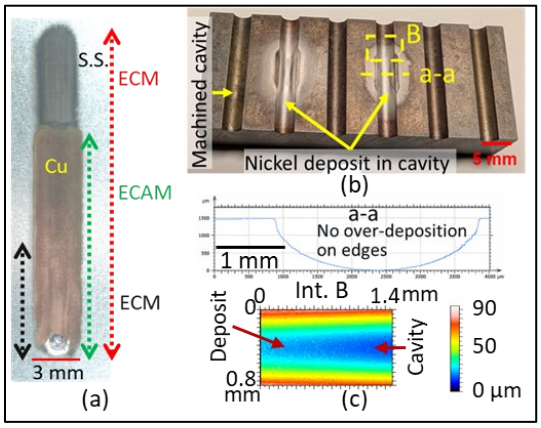

Figure 8. (a) Process sequences of ECM and ECAM. (b) Mould surface repair demo with measurement of (c) 2D profile and 3D interface.

This approach was used to investigate the mould surface repair feasibility using Ni as a repair-material on a SS substrate with premachined cavities representative of mould features (**Fig. 8b**). These initial materials were used to test feasibility to further research nickel-based high performance alloys as repair materials for mould substrates (NbC-Ni, tool steels) in the future. The measurements of the 2D profile and 3D interface in **Fig. 8c** show that with an appropriate ECAM tool scan strategy the shape of the cavity can be maintained while depositing Ni on the SS surface with negligible overdeposition at cavity edges [6] to minimise further post-processing requirements.

4. Conclusion

This work investigated a new cermet and manufacturing techniques to improve mould durability, machinability and surface functionality in ceramic injection moulding (CIM). A work in progress of mould cavity surface repair using simple metals is also presented. A NbC-Ni cermet was evaluated as an alternative mould material to conventional tool steels for CIM. CIM tests with alumina feedstock showed that NbC-Ni exhibits enhanced wear resistance. After 10,000 shots, dimensional wear was reduced by approximately 46% in depth and 86% in width compared to tool steel with negligible changes in surface roughness, demonstrating its suitability for CIM mould inserts.

The machinability (shaping) of NbC-Ni was investigated using hybrid laser-ECM (LECM). Relative to ECM, LECM achieved an improvement in shaping precision by 24% and surface roughness by 30%. This was attributed to laser-assisted current density focusing, enhanced passivation weakening and more uniform dissolution of the multi-phase cermet microstructure.

Femtosecond laser surface texturing on NbC-Ni demonstrated the feasibility of producing 30 µm diameter micro-dimples with controllable aspect ratio and minimal thermal damage. Furthermore, a proof-of-concept mould surface repair strategy combining ECM and ECAM was demonstrated using a single hybrid-EC tool. This approach enables bi-directional process sequences to locally remove and deposit material with a scan layer thickness of ~0.5 µm and minimal postprocessing needs.

Future work will focus on transferring the preliminary findings on laser texturing to a spiral mould for flow length investigations while minimising replication on products, and mould surface repair strategy for depositing advanced repair alloys on mould substrates and assessment of functional properties of the repair layer for adhesion and wear resistance.

Acknowledgment

The authors acknowledge financial support from KU Leuven (C3/23/060, C2E/23/022) and CELSA (CELSA/24/015), VLAIO IM (HBC.2025.0277), FWO Sr Postdoc (1235425N), FWO medium-scale infra FemtoFac (I001120N).

References

[1] R. Gadow and F. Kern, "2.06 - Advanced Manufacturing of Hard Ceramics," in *Comprehensive Hard Materials*, V. K. Sarin, Ed. Oxford: Elsevier, 2014, pp. 207–230.

[2] E. Hnatkova, B. Hausnerova, and P. Filip, "Evaluation of powder loading and flow properties of Al2O3 ceramic injection molding feedstocks treated with stearic acid," *Ceram. Int.*, vol. 45, no. 16, pp. 20084–20090, Nov. 2019.

[3] N. Rajendhran, K. Pondicherry, S. Huang, J. Vleugels, and P. De Baets, "Influence of abrasive characteristics on the wear micro-mechanisms of NbC and WC cermets during three-body abrasion," *Wear*, vol. 530–531, no. December 2022, p. 205007, 2023.

[4] M. H. Arshad, K. K. Saxena, S. Huang, and D. Reynaerts, "Macro and micro-scale material removal mechanisms during ECM / hybrid laser-ECM of a passivating multiphase NbC – Ni cermet," *Int. J. Mach. Tools Manuf.*, vol. 200, p. 104182, 2024.

[5] J. Schneider, D. Braun, and C. Greiner, "Laser textured surfaces for mixed lubrication: Influence of aspect ratio, textured area and dimple arrangement," *Lubricants*, vol. 5, no. 3, 2017.

[6] M. H. Arshad, A. Peeters, X. Chen, D. Reynaerts, and K. K. Saxena, "Process compatibility analysis for hybrid electrochemical removal and accretion towards a multifunctional machine-tool: An application-oriented approach," *Electrochem. commun.*, vol. 178, p. 107997, Sep. 2025.

[7] K. Yildirim, B. Nagarajan, T. Tjahjowidodo, and S. Castagne, "Development of a multi-sensor system for in-situ process monitoring of femtosecond laser micromachining," *Int. J. Adv. Manuf. Technol.*, vol. 135, no. 1, pp. 799–813, 2024.

euspen's 26th International Conference & Exhibition, Krakow, PL, June 2026
www.euspen.eu

Fused Filament Fabrication System for continuous fibre reinforcement

J. Polte[1, 2], E. Uhlmann[1, 2], S. Bode[1], L.-A. Edinger[1]

[1] *Institute for Machine Tools and Factory Management IWF, Technische Universität Berlin, Germany*
[2] *Fraunhofer Institute for Production Systems and Design Technology IPK, Germany*

stefanie.bode@tu-berlin.de

Abstract
Additive manufacturing offers significant potential for industrial applications due to its capacity to produce complex geometries while concurrently processing materials efficiently. In particular, the integration of continuous fibres in fused filament fabrication (FFF) enables the production of prototypes and functional components with significantly improved mechanical properties and customisable structures. However, the current state of the art is limited in terms of flexible fibre positioning, which limits targeted component reinforcement and optimisation of material properties. A modified FFF system, incorporating a double bowden extruder, an integrated cutting unit and automated build field calibration for flexible continuous fibre deposition, can be employed to create an open research platform for investigating and optimising fibre-reinforced additive manufacturing processes. The control of the process is facilitated by means of customisable G-code commands, which permit the definition of deposition parameters such as fibre orientation, layer height and feed rate in a flexible manner. Systematic experimentation of the fibre extrusion has been undertaken to demonstrate the influence of these process parameters on defect formation and fibre-matrix interaction during continuous fibre deposition.

fused filament fabrication, continuous fibre reinforcement, defect analysis

1. Introduction

Additive manufacturing is becoming increasingly important for the production of functional components, but still has limitations in terms of mechanical component properties, particularly in polymer-based processes such as fused filament fabrication (FFF) with which the influence of individual process parameters can be specifically investigated [1,2]. The objective of this study is to develop and conduct experimental research on an open FFF system for continuous fibre integration. One method of enhancing the mechanical properties of a material is to introduce fibres into the plastic matrix. While short fibre-reinforced materials achieve only limited reinforcement effects, continuous fibres aligned with the load enable a significantly higher increase in strength and stiffness [3]. In the FFF process in particular, continuous fibres can be specifically integrated into components due to the linear application of material and free path control [4]. Commercial continuous-fibre FFF systems, such as those provided by MARKFORGED INC., Watertown USA, allow the production of fibre-reinforced components but offer only limited flexibility regarding fibre placement strategies and process parameter modification. For research purposes, there is a need for open, flexibly adaptable systems with which the influence of individual process parameters can be specifically investigated.

2. System concept and modification

The starting point is a commercially available desktop FFF printer that has been extensively modified. A dual Bowden extruder system has been implemented to separately feed the matrix material and continuous fibre, keeping the print head mass low and enabling precise path guidance as shown in Figure 1.

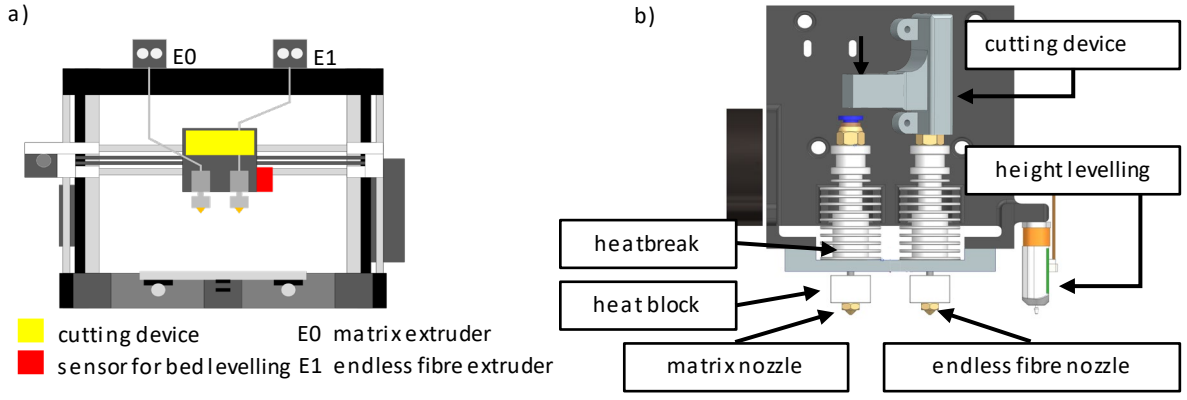

Figure 1. Modified FFF printing system with dual nozzles for matrix material and continuous fibre, including integrated cutting and calibration unit

The coated continuous fibre is fed into the print head via a specially developed cutting and feeding unit and applied to the surface of the matrix material. A multi-part cutting mechanism was developed to cut the continuous fibre while maintaining compatibility with the print head. The linear cutting movement is performed by an electromagnetic solenoid motor from HESCHEN, Foshan, China. A cutter blade is inserted at the front of the adapter. Due to the positioning of the cutting blade, the minimum fibre length is $l_{mF} \leq 105$ mm. This value corresponds to the distance between the fibre cutting device and the deposition point at the nozzle. As a result, fibre segments shorter than this distance cannot currently be produced by the system. This limitation restricts the use of short reinforcement segments and locally defined fibre placements within small component geometries. Consequently, reinforcement strategies must primarily rely on longer continuous fibre paths.

3. Method

The verification of the newly developed printer is carried out in several stages. Once the basic functions of the printer have been tested, the focus is on the production of test specimens from PLA-Basic from BAMBULAB, Shenzhen, China, as the matrix material with integrated continuous glass fibre filament from MARKFORGED INC., Watertown, USA. This initial test series analyse the influence of process and structural parameters on the quality of fibre deposition, such as the fibre deposition angle ϕd in the component plane, as well as the interaction between matrix extrusion and fibre transport. A systematic statistical evaluation with repeated trials will be part of future investigations. A similar study was conducted for the continuous carbon fibre filament from MARKFORGED INC., Watertown, USA. Fibre deposition angles $\phi d_a = 30°$, $\phi d_b = 60°$, $\phi d_c = 90°$, $\phi d_d = 120°$, $\phi d_e = 150°$ and $\phi d_f = 180°$ were investigated [5]. As part of this work, defects are to be detected for the same fibre deposition angles ϕd using microscopy and analogies and deviations from the aforementioned study are to be found. Ultimately, a recommendation is to be derived as to the maximum fibre deposition angle ϕd_{max} at which processing without cutting is feasible.

The samples were evaluated visually and by means of microscopic analysis in order to identify typical defects such as fibre breakage, delamination, insufficient impregnation and positional deviations. A VHX-5000 digital light microscope from KEYENCE, Osaka, Japan, was used for all microscopic examinations.

4. Results

The experimental investigations visbile in Figure 2 show that the fibre deposition angle has a significant influence on process stability and defect formation during continuous fibre integration. At small deposition angles, there is an increase in fibre kinks, local detachments and irregular embedding of the continuous fibre in the matrix. These defects are due to increased deflection of the fibre in the print head and unfavourable relative movements between the nozzle and the fibre. As the fibre deposition angle increases, the stability of the fibre deposition improves significantly. For deposition with as few defects as possible, an optimal range of up to $\phi d_{max} \leq 60°$ has been identified, although initial changes in the cross-section of the fibre have already been observed. If the aim is simply to avoid the formation of fibre folds, deposition up to $\phi A_{max} \leq 90°$ is possible.

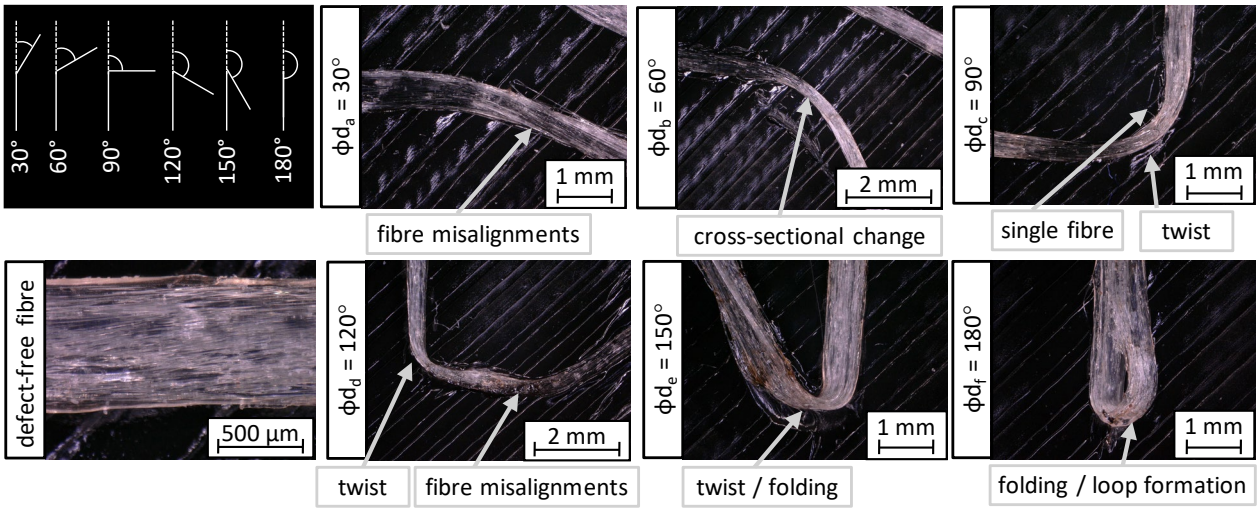

Figure 2. Microscopic images of continuous fibre deposition

5. Conclusion and outlook

The flexible G-code-based control system allows specific process windows to be identified in which reproducible and defect-free continuous fibre integration is possible. The developed system thus enables systematic investigation of the interactions between process parameters and component quality. The experimental results show that the system is particularly suitable for investigating process-related defects and optimising fibre-matrix interaction. Future work will focus on quantitative mechanical testing and the integration of more complex reinforcement strategies and additional fibre-matrix combinations.

References

[1] Gebhardt, A. et al.: Additive Fertigungsverfahren Additive Manufacturing und 3D-Drucken für Prototyping - Tooling - Produktion. München, Hanser (2013).

[2] Gibson, I. et al.: Additive Manufacturing Technologies. Heidelberg, Springer (2020).

[3] Ismail, K. I.; Yap, T. C.; Ahmed, R.: 3D-Printed Fiber-Reinforced Polymer Composites by Fused Deposition Modelling (FDM): Fiber Length and Fiber Implementation Techniques. Polymers 14 (2022) 21, 4659.

[4] Vietor, T.; Prüß, H.: Neue Gestaltungsfreiheiten durch 3D-gedruckte Faser-Kunststoff-Verbunde. In: RTeJournal – Fachforum für Rapid Technologie 2015. Hrsg.:Bremen, Fachhochschule Aachen (2015).

[5] Zhang, H.; Chen, J.; Yang, D.: Fibre misalignment and breakage in 3D printing of continuous carbon fibre reinforced thermoplastic composites. Additive Manufacturing 38 (2021), 101775.

euspen's 26th International Conference & Exhibition, Krakow, PL, June 2026
www.euspen.eu

Electrochemical deposition of active materials towards integrated sensing on mechanical components

Zhaozhi Lyu[1, 2], Muhammad Hazak Arshad[1, 2], Krishna kumar Saxena[1, 2, *], Dominiek Reynaerts[1, 2, *]

[1]KU Leuven, Department of Mechanical Engineering, Manufacturing Processes and Systems, Micro- & Precision Engineering Group, Leuven, Belgium.
[2]Member Flanders Make, Leuven, Belgium.

*dominiek.reynaerts@kuleuven.be, krishna.saxena@kelueven.be

Abstract
The evolution of advanced manufacturing is increasingly defined by the integration of smart functionalities such as sensors and encoders while facilitating active communication on mechanical components; enabling real-time monitoring, control and data-driven decision making in intelligent manufacturing systems. In this context, electrochemical layered micromanufacturing techniques (selective deposition and machining of layers) has the potential to enable integrated active functionalities on mechanical components such as on-machine direct writing of high-bandwidth and high-gauge factor strain gauges on prototype mechanical components.
In the same line, this work investigates electrochemical deposition (ECD) as a low-cost and scalable route for integrating sensing through deposition of active materials (e.g. semiconductors, bimetals) directly onto mechanical components. Zinc oxide (ZnO) layers were electrodeposited on stainless-steel substrates with different electrolyte concentration. The deposited layers exhibit uniform morphology, near-stoichiometric composition and tunable crystal orientation confirmed by SEM/EDS and XRD characterization. UV–Vis analysis indicated a direct bandgap of ~3.34 eV, validating the semiconducting quality. This approach will be extended towards mask-free and low-energy growth directly on metallic substrates, enabling conformal sensing layers on curved and load-bearing components.

Keywords: Electrochemical deposition (ECD), active materials, Integrated sensing.

1. Introduction

Intelligent manufacturing increasingly depends on integrated sensing to enable state monitoring, adaptive control, and predictive maintenance of production equipments[1]. Among various sensing modalities, strain gauges remain widely adopted due to their minimal influence on structural stiffness and dynamic behavior[2].

However, conventional strain gauges rely primarily on adhesive bonding of metallic/semiconductor strain gauges. These approaches suffer from limitations including muti-step processing and restricted compatibility with complex surfaces.

Recent advances in additive and hybrid manufacturing have motivated the exploration of alternative routes for direct integration of sensing functionalities onto mechanical components. In this context, electrochemical deposition (ECD) offers a localized, low-cost, and mask-free fabrication technique capable of depositing functional materials directly on metallic substrates. While ECD has been extensively investigated for metallic coating and bimetallic structures[3], its application to semiconductor sensing layers requires further research.

This work explores the electrochemical deposition of wide bandgap (3.37 eV) semiconductor material zinc oxide (ZnO) as an active piezoresistive materials for integrated strain sensing on mechanical components, with a focus on process feasibility, deposition quality and suitability for sensor integration.

2. Experimental methods and materials

Electrochemical deposition of ZnO was carried out using a conventional and stationary beaker-based two-electrode configuration at 343 K with different precursor concentrations. 0.1 M $NaNO_3$ was added to increase electrolyte conductivity (~11.57 mS/cm). A gold coated steel rod served as the counter electrode and the working electrode was SS304 (5 x 5 mm^2 surface area, i.e. deposition area). These experiments were conducted to investigate the suitable process window and electrolyte concentration to adapted towards more flexible jet-based electrochemical deposition. The experimental parameters employed in this study are summarized in Table 1.

Table 1 Experimental parameters for ECD of ZnO layers

Parameter	Value
$Zn(NO_3)_2{\cdot}6H_2O$	10, 25, 50, 100 mM
Supporting electrolyte	0.1 M $NaNO_3$
Working electrode	SS304 (5 x 5 mm^2)
Counter electrode	Au
Deposition potential	-1.5 V
Current density	~ 1 mA/cm^2
Temperature	343 K
pH	~ 6.5
Deposition time	300 s

During deposition, OH^- is generated at the cathode through the electrochemical reduction of nitrate species, followed by the precipitation and dehydration reactions leading to ZnO formation. The dominant electrochemical reactions on the cathode can be summarized as[4]:

$$NO_3^- + H_2O + 2e^- \rightarrow NO_2^- + 2OH^-$$
$$Zn^{2+} + 2OH^- \rightarrow Zn(OH)_2 \rightarrow ZnO + H_2O - \Delta Q$$

After deposition, the resulting samples were thoroughly rinsed with deionized water.

3. Results and discussion

3.1. Morphology and chemical composition

Prior to the microscopic investigation, the thickness of the deposited layers were determined to be in the range of 10-15 µm by optical microscopy (S neox, Sensofar). This micron-scale thickness ptovides a complete coverage of the SS304 substrate,

which is further supported by the following SEM/EDX analysis. Fig.1 presents the surface morphology of ZnO layers deposited on SS304 substrates at different $Zn(NO_3)_2{\cdot}6H_2O$ concentrations. A clear evolution in microstructure is observed as the concentration decreases. At high concentration (100 mM), the deposited layer consists of densely stacked, plate-like structures, whereas lower concentrations (10 mM) lead to finer features.

EDX analysis reveals a increase in the O:Zn atomic ratio with decreasing precursor concentration (Table 2). The O:Zn ratio increases from 0.327 at 100 mM to 0.817 at 10 mM, suggesting a shift towards less Zn-rich ZnO compositions at lower precursor concentrations. Although the O:Zn values remain below the stoichiometric ratio, this behavior is consistent with the known limitations of EDX for light element (O) quantification. In addition, non-stoichiometric ZnO exhibits enhanced electrical sensitivity, which is beneficial for resistive strain sensing.

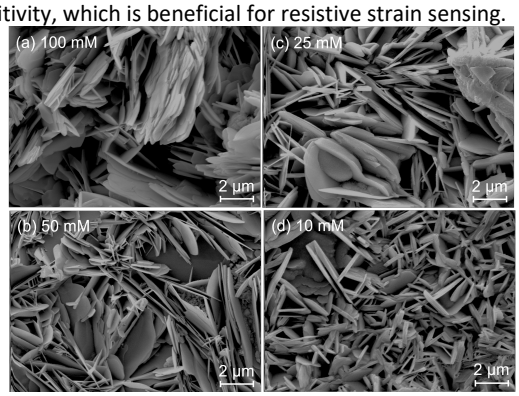

Figure 1. Surface morphology of electrodeposited ZnO layers at different $Zn(NO_3)_2{\cdot}6H_2O$ concentrations. (by XL30 FEG, Philips)

Table 2 Atomic ratio (O:Zn) at different $Zn(NO_3)_2{\cdot}6H_2O$ concentration

Concentration (mM)	Value (O:Zn)
100	0.327
50	0.428
25	0.695
10	0.817

3.2. Structural properties

Fig.2 demonstrates the XRD spectra of various ZnO structures obtained at different precursor concentrations. The major diffraction peaks of ZnO layers can be readily indexed to wurtzite structure (PDF 01-079-5604). A clear dependence of crystal orientation on precursor concentration is observed. For the ZnO layer deposited at 10 mM $Zn(NO_3)_2{\cdot}6H_2O$, the diffraction pattern is dominated by the (002) reflection, indicating a strong preferential orientation along the c-axis. In contrast, ZnO layers deposited at higher concentrations exhibit multiple reflections, suggesting a more randomly oriented polycrystalline structure.

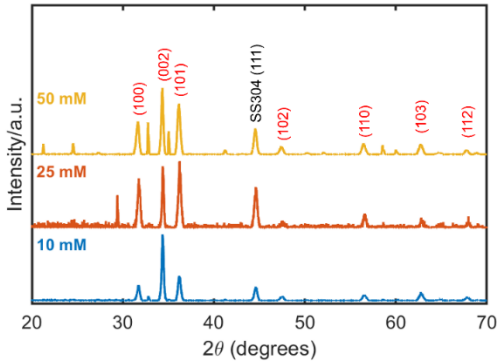

Figure 2. X-ray diffraction patterns of electrodepositied ZnO layers. (by D8 Advance, Bruker)

The enhanced (002) orientation at lower precursor concentration is attributed to a reduced growth rate and improved control of nucleation during ECD[4], which favors polar-axis growth. Such orientation control is particularly relevant for strain sensing applications, as stress applied along the [0001] direction in ZnO is expected to induce enhanced signal change.

2.4. Semiconductor properties

Fig. 3 shows the optical absorption behavior of ZnO layers electrodeposited at different $Zn(NO_3)_2{\cdot}6H_2O$ concentrations, evaluated using UV–Vis diffuse reflectance spectroscopy. The optical bandgap was estimated using the Kubelka–Munk transformation combined with Tauc analysis, assuming a direct allowed transition for ZnO. The extracted bandgap values range from 3.323 eV to 3.356 eV, which are consistent with reported values for intrinsic ZnO. Only minor variations in bandgap are observed as a function of electrolyte concentration, indicating that changes in deposition parameters primarily affect microstructure and crystal orientation rather than the intrinsic semiconducting nature of the deposited layers. The preservation of a stable and well-defined bandgap across different process conditions confirms the suitability of electrochemically deposited ZnO as an active semiconducting layer for integrated sensing applications.

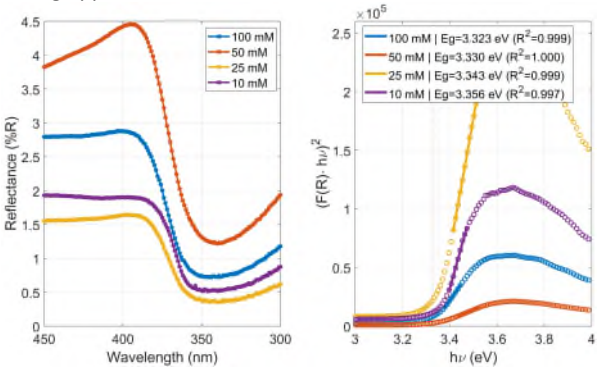

Figure 3. Optical characterization of electrodeposited ZnO layers by UV–Vis diffuse reflectance spectroscopy and Tauc analysis. (by Gary 60 UV-Vis, Agilent Technologies)

4. Summary

This work demonstrates the feasibility of electrochemical deposition as a micromanufacturing route for integrating ZnO-based active sensing layers directly onto mechanical component relevant steel substrates. By systematically varying the $Zn(NO_3)_2{\cdot}6H_2O$ concentration, the morphology, composition and crystal orientation of electrodeposited ZnO layers could be effectively controlled. The results highlight the potential of electrochemical deposition for producing uniform, orientation-controlled semiconductor layers on metallic substrates without post processing. This approach provides a promising foundation for the development of integrated, semiconductor-based strain sensing elements on mechanical components in intelligent manufacturing systems.

References

[1] Bleicher, F., Biermann, D., Drossel, W. G., Moehring, H. C., & Altintas, Y. (2023). Sensor and actuator integrated tooling systems. CIRP Annals, 72(2), 673-696.

[2] Zhang, P., Hong, D., Totis, G., Scalzo, F., Yin, Z., Shu, L., & Sugita, N. (2025). Systematic review of Cutting Force Measuring Systems in machining: Principles, design, filtering techniques and applications. International Journal of Machine Tools and Manufacture, 104308.

[3] Arshad, M. H., Saxena, K. K., Smith, R., Qian, J., & Reynaerts, D. (2022, September). Design of a Low Cost micro-Electrochemical Additive Manufacturing Setup. In Proceedings of the World Congress on Micro and Nano Manufacturing, 2022, 117-121

[4] Zhang, W., He, Y. N., Cui, W. Y., & Zhou, C. B. (2011). Electrochemical Synthesis for Uniform and Large-Scale Zinc Oxide Nano Structure Films. Advanced Materials Research, 194, 429-435.

euspen's 26th International Conference & Exhibition, Krakow, PL, June 2026
www.euspen.eu

Metrological Characterization of Shrinkage in Precision Injection Moulded Polypropylene Plates through Experimental Measurements and Process Simulation

Juan J. Ortiz-Vazquez[1,2], Hallgrimur Kjartansson[1], Renan Melhado Mazza[3], J. Israel Martínez-López[2], Alireza Mollaei Ardestani[1], Yang Zhang[1] and Guido Tosello[1]

[1] *Department of Civil and Mechanical Engineering, Technical University of Denmark, DK-2800 Kgs. Lyngby, Denmark*
[2] *School of Engineering and Science, Tecnologico de Monterrey, MX-64700 Monterrey, México*
[3] *AB Tetra Pak, SE-223 55 Lund, Sweden*

guto@dtu.dk

Abstract

This study assesses the potential of numerical simulations to accurately predict the dimensional shrinkage behaviour of polypropylene (PP) injection-moulded plates. A set of manufacturing experiments was conducted on an ARBURG Allrounder 370 A machine using SABIC PP 579S polypropylene. Mould cavity and moulded part specimens were characterised using a Coordinate Measuring Machine (CMM), an analytical balance and a micrometre. The data was employed as an input for the process simulations in Moldex3D.

The experimental data showed shrinkage of 1.18% and 1.24% in length (along the flow direction) and width (across the flow direction), respectively. Furthermore, numerical simulations predicted values of 1.00% and 1.02%, respectively, within a deviation of 0.22% in each direction. In contrast, the thickness direction exhibited a negative shrinkage (expansion) of −1.47%, whereas simulations predicted a contraction of 2.53%. Short-term experiments showed a clear dependence of thickness on injection volume, indicating that the discrepancy is influenced by pressure-dependent tooling and consequent material behaviour. Factors such as melt compressibility, elastic mould deformation, release of residual compressive stresses, and incomplete mould sealing under high packing pressure are not fully accounted for in conventional simulation boundary conditions, limiting the accuracy of thickness-direction shrinkage predictions.

Overall, results confirm the capability of the injection moulding simulations to accurately predict shrinkage in planar dimensions, while highlighting the sensitivity of thickness behaviour to processing and tooling conditions. This study demonstrates the importance of integrating precise experimental measurements with numerical simulations to improve the reliability of shrinkage prediction in polymer injection moulding.

Keywords: Injection moulding, Shrinkage characterization, Polypropylene (PP), Dimensional metrology, Simulation validation.

1. Introduction

Injection molding is one of the most widely used manufacturing processes for polymer components production, particularly in automotive, medical, and consumer goods applications, due to its ability to produce complex geometries with high repeatability and efficiency [1,2]. However, achieving precise dimensional accuracy remains a significant challenge, primarily due to material shrinkage during cooling and solidification [3-5].

Shrinkage arises from the volumetric contraction of polymers as they transition from the molten to the solid state and can lead to dimensional deviations, residual stresses, and warpage, which negatively affect the part quality and functionality [4,6].

The magnitude and direction of shrinkage depend on both material properties and processing conditions; thus, understanding and predicting shrinkage behaviour is critical for optimizing mold design, processing parameters, and material selection [3,7].

Process simulation tools such as Moldex3D, Autodesk Moldflow or Cadmould, are widely used to predict shrinkage and support mold design and process optimization. Nevertheless, the accuracy of these predictions strongly depends on the quality of the input data, material models, and boundary conditions, making experimental validation essential [5,8].Previous studies have investigated the shrinkage behaviour in polypropylene (PP) under various injection molding conditions; however, the strong dependency on material grade, tooling, and processing parameters limits the generalizability of existing results [9].

In this study, the shrinkage behaviour of precision injection moulded polypropylene plates is experimentally characterized using high accuracy dimensional metrology and systematically compared with numerical process simulations.

Particular attention is given to differences between planar (length and width) and thickness shrinkage, providing insight into the limitations of current simulation approaches and the influence of tooling and process related effects. The resulting dataset serves as a reliable benchmark for validating shrinkage predictions in polymer injection molding.

2. Materials and Methods

A moulding including two flat rectangular PP plates was produced using a two-cavity injection mould (Figure 1). This relatively simple geometry enabled the evaluation of the shrinkage behaviour along the flow (length), transverse to the flow (width), and thickness directions.

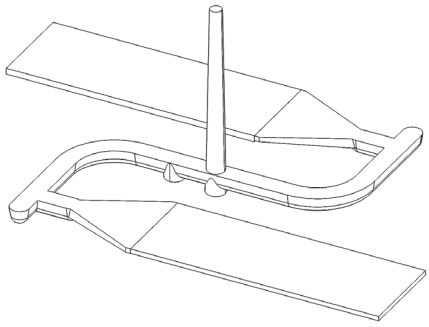

Figure 1. Geometry of the injection-moulded PP plates.

2.1. Measurement Uncertainty and Repeatability

To ensure statistically valid results, a preliminary analysis was conducted to assess the variability in the subsequent measurements and determine the minimum number of measurements per sample needed for reliable shrinkage evaluation. A sequential measurement strategy was followed: multiples measurements were taken incrementally in one single part, and the evolution of the mean and standard deviation for each measurement was tracked. The goal was to identify the point at which the relative standard deviation (RSD) defined as the ratio between the standard deviation (σ) and the mean (μ) stabilized, indicating that further measurements would not significantly change the estimated variability.

$$RSD = \frac{\sigma}{\mu} \quad (1)$$

RSD stabilization was observed after approximately six to eight measurements for all variables (length, width, thickness, and weight). Based on this result, ten measurements per dimension and condition were selected to ensure repeatability while keeping the workload manageable.

2.2. Mold Measurements

Mold cavity dimensions were measured using a ZEISS PRISMO CMM equipped with a tactile probing system [10]. All measurements were conducted under controlled laboratory conditions, with the mould rigidly fixed and aligned prior to measurement. Length (flow direction) and width (transverse direction) were selected as reference dimensions for the evaluation of planar shrinkage.

Each dimension was measured at three locations within the cavity using six probing points per axis to capture local dimensional variations (Figure 2). The resulting mean values and standard deviations were used as reference dimensions for the shrinkage analysis.

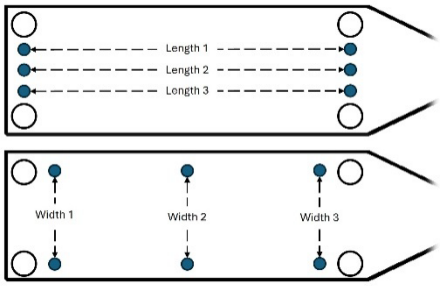

Figure 2. Distribution of probing points used for cavity dimension measurements.

2.3. Part Production

Injection molding trials were carried out using an ARBURG Allrounder 370 A 600–70 All Drive injection molding machine, designed for high-precision applications [11], and SABIC PP 579S [12]. A parametric variation of injection volume was introduced to produce short-shot and fully filled parts with evaluated volumes of 7, 9, 11, 13, 15, 16, and 17 cm^3. All other process parameters- including filling time, melt and mold temperatures, packing time and pressure, cooling time, and total cycle time- were kept constant across all experimental runs. The complete set of processing parameters is summarized in Table 1.

Table 1. Filling, packing and cooling injection parameters.

Parameter	Value	Unit
Filling		
Filling time	0.83	s
Melt temperature	225	°C
Mold temperature	35	°C
Max injection pressure	250	MPa
Packing		
Packing time	9.00	s
Max packing pressure	250	MPa
Cooling and Cycle		
Cooling time	10.00	s
Mold open time	5.00	s
Ejection temperature	90	°C
Ambient air temperature	25	°C
Total cycle time	24.83	s

2.4. Dimensional and Mass Measurement of Parts

After molding, all parts were allowed to stabilize at room temperature under controlled environmental conditions (20±1°C and 35-50% relative humidity). The length and width of fully filled parts were measured using a DeMeet 400 optical CMM [13], whereas short-shot parts were measured using a Mitutoyo digital calliper due to their incomplete geometry.

For complete parts, six reference points were defined along both the length and width edges, following the same coordinate pattern used for mold measurements (Figure 2). Ten parts from each cavity were evaluated. Each dimension was measured ten times per part at the same defined locations.

For short shots, ten samples from each cavity were considered. Each part was measured ten times using the Mitutoyo digital calliper. Due the incomplete condition of the short shots, the measurement strategy was limited to the length dimension, defined as the distance from the gate edge to the most distal point of the part contour, as illustrated in Figure 3.

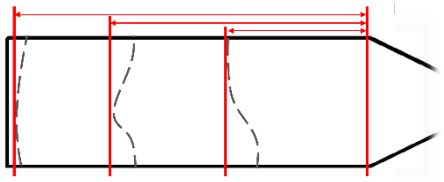

Figure 3. Reference for short shot length measurements.

Thickness measurements were performed using a Mitutoyo digital micrometre with a resolution of 0.001 mm [14]. Ten parts per cavity were evaluated, and each part was measured ten times at nine consistent reference locations, as illustrated in Figure 4.

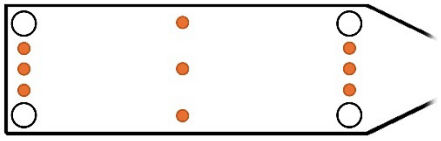

Figure 4. Distribution of reference probing points used for thickness measurements.

Mass was measured using an OHAUS DV215CD precision balance with a resolution of 0.0001 g [15]. A total of ten parts were weighed, with each part measured ten times. Parts were handled using a clean tissue to avoid any contamination. Measurements were recorded only after stabilization of balance reading within the draft shield, to minimize variability due to airflow, handling, and surface contamination.

2.5. Process Simulation

To complement the experimental study, a numerical process simulation was performed in Moldex3D Studio 2025R1OR, including filling, packing, cooling, and warpage analyses.

The CAD geometry based on CMM measurements was imported into Moldex3D in STEP format. A three-dimensional solid mesh was generated. The mesh resolution was set for 1 mm for the hole geometry and locally refined with a minimum element size of 0.23 mm in the gate and connector regions to improve simulation accuracy (Figure 5).

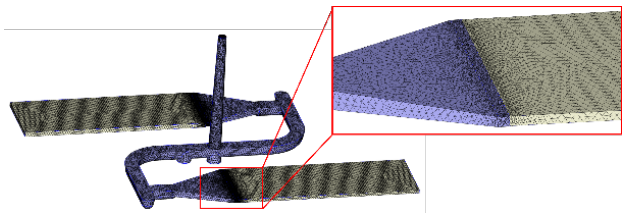

Figure 5. Mesh configuration used Moldex3D. A finer resolution was applied in the connector areas.

The SABIC PP 579S material model and the ARBURG Allrounder 370 A 600–70–18 machine were selected directly from the Moldex3D databases. Process parameters were defined and were matched to the experimental conditions used for the fully filled parts.

2.6. Shrinkage Calculation

Shrinkage was calculated by comparing reference dimensions to the corresponding dimensions of the evaluated part, whether physical or simulated. Shrinkage percentage S was calculated as:

$$\%S = \frac{D_{ref} - D_{evaluated}}{D_{ref}} \times 100 \qquad (2)$$

Where D_{ref} corresponds to the nominal CAD or the mold cavity dimension obtained via CMM measurements, and $D_{evaluated}$ describes either measured part dimensions or simulation output dimensions. Positive values indicate dimensional contraction, while negative values correspond to dimensional expansion.

3. Results

3.1. Dimensional Analysis

Table 2 presents the measured mould cavity dimensions together with the nominal CAD values. Length and width deviations in both cavities were below 0.04 mm, whereas substantial deviations were observed in the thickness direction. Cavity 1 exhibited a thickness reduction of approximately 1.1 mm relative to the nominal geometry, while Cavity 2 showed a larger reduction of nearly 1.6 mm, indicating a significant discrepancy between the nominal and manufactured mould geometries.

Table 2. Comparison of nominal values and measured mould dimensions for both cavities (mean ± standard deviation).

Dimension	Nominal [mm]	Mold Cavity 1 [mm]	Mold Cavity 2 [mm]
Length	78.000	78.039 ± 0.003	78.015 ± 0.001
Width	28.000	28.035 ± 0.001	28.021 ± 0.007
Thickness	(1) 1.900 (2) 1.400	1.914 ± 0.034	1.420 ± 0.013

Based on these findings, the CAD geometry was corrected to reflect the measured cavity dimensions prior to performing the Moldex3D simulations, as illustrated in Figure 6. Based on these findings, the CAD geometry was corrected to reflect the measured cavity dimensions prior to performing the Moldex3D simulations, as illustrated in Figure 6.

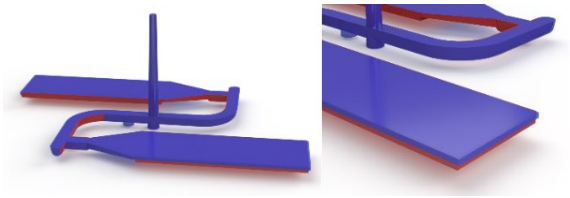

Figure 6. Comparison between the nominal CAD (red) and the corrected CAD model (blue) used for simulation.

Subsequently, fully filled parts were measured to characterize geometry and repeatability across both mould cavities. These measurements form the basis for the shrinkage analysis. Table 3 reports the mean values and standard deviations for length, width, and thickness.

Table 3. Measured dimensions of complete parts (mean ± standard deviation).

Dimension	Cavity 1 [mm]	Cavity 2 [mm]
Length	77.143 ± 0.078	77.067 ± 0.101
Width	27.701 ± 0.114	27.660 ± 0.049
Thickness	1.940 ± 0.022	1.443 ± 0.020

To examine the origin of the negative thickness shrinkage, short-shot parts were measured as a function of injection volume. Table 4 summarizes the thickness results.

Table 4. Measured thickness of short-shot parts as a function of injection volume for both mold cavities (mean ± standard deviation).

Setting [cm³]	Cavity 1 [mm]	Cavity 2 [mm]
7	1.910 ± 0.004	1.431 ± 0.011
9	1.920 ± 0.003	1.436 ± 0.010
11	1.924 ± 0.017	1.437 ± 0.012
13	1.923 ± 0.019	1.439 ± 0.010
15	1.928 ± 0.023	1.438 ± 0.011

In addition, progressive filling behavior was confirmed through short-shot trials over the evaluated injection volume range (7–17 cm³). Measured part length increased steadily with injection volume during short-shot trials, converging to final values of approximately 77.1 mm for both cavities in complete parts, with standard deviation average below 0.24 mm.

Part weight increased monotonically with injection volume, ranging from 8.67 g for the lowest short-shot condition to approximately 12.10 g for complete parts, with a standard deviation below 0.04 g. These results indicate consistent volumetric filling and stable processing conditions, supporting

the use of short-shot experiments as a reliable basis for the subsequent shrinkage analysis.

3.2. Shrinkage Analysis

Dimensional shrinkage was calculated for each cavity using the corrected mold dimensions as reference. Shrinkage was computed following Eq. (2). Table 5 compares the experimentally measured shrinkage of complete parts with the corresponding Moldex3D simulation results for length, width, and thickness.

Table 5. Comparison of experimental and simulated shrinkage for both cavities.

	Cavity 1		Cavity 2	
Dimension	Experimental [%]	Simulation [%]	Experimental [%]	Simulation [%]
Length	1.148	1.012	1.215	0.986
Width	1.191	1.036	1.288	1.000
Thickness	-1.365	3.646	-1.572	1.408

The results show good agreement between experiment and simulation for length and width in both cavities, with comparable shrinkage magnitudes. In contrast, a pronounced discrepancy was observed in the thickness direction. Experimental measurements revealed negative shrinkage (expansion), whereas the simulation predicted significant positive shrinkage.

Thickness shrinkage was evaluated on short-shot parts as a function of injection volume. Figure 7 shows the resulting trends for both cavities, including the transition to fully filled parts. This is due to elevated mould compliance.

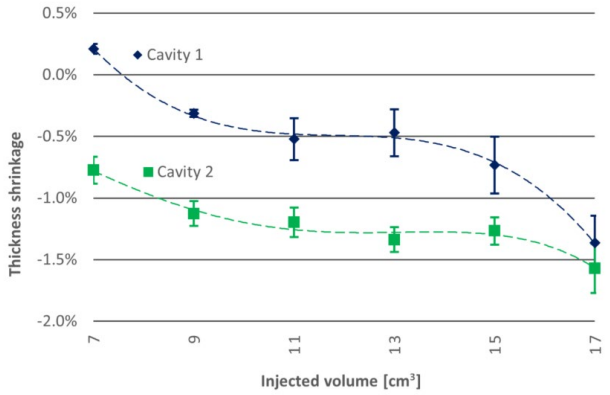

Figure 7. Thickness shrinkage relative to mould cavity dimensions as a function of injected volume for short-shot and fully filled parts in both cavities; negative values indicate expansion.

The results in Figure 7 show meaningful trends. In Cavity 1, thickness expansion increased with injection volume, suggesting that higher cavity pressure may promote slight mold opening, leading to apparent expansion in the thickness direction. In Cavity 2, the trend was less pronounced during short-shot conditions. However, both cavities exhibited a consistent decrease in thickness shrinkage with increasing injection volume. This behaviour supports the hypothesis that process effects, rather than material shrinkage alone, play a significant role in the observed thickness expansion.

In summary, although shrinkage in length and width aligns well with simulation, the behaviour in thickness is not adequately captured by the model and appears to be strongly influenced by experimental limitations.

4. Conclusions

This paper presents an experimental evaluation of shrinkage behaviour in polypropylene (PP) injection-moulded plates and a comparison with numerical simulation results. The conclusions are as follows:

(i) Experimental measurements showed consistent planar shrinkage in both cavities, with average values of approximately 1.2% in length and width. Moldex3D simulations accurately predicted this in-plane shrinkage, with deviations below 0.25% relative to experimental results, confirming the suitability of the simulation framework for planar dimensional prediction.

(ii) In contrast, a pronounced discrepancy was observed in the thickness direction: simulations predicted positive shrinkage, whereas experiments consistently exhibited negative shrinkage (expansion). Short-shot analysis revealed a clear dependence of thickness behaviour on injection volume, indicating that tooling- and process-related effects, such as imperfect mould sealing during filling and packing, significantly influence the measured thickness.

(iii) Overall, the study confirms the capability of Moldex3D simulations to predict planar shrinkage in polypropylene injection-moulded parts, while highlighting the need for careful experimental validation when assessing out-of-plane dimensional behaviour.

References

[1] Rosato D V, Rosato D V, Rosato M G 2000 *Injection Molding Handbook* (Springer)

[2] Strong B 2006 *Plastics: Materials and Processing* (Pearson Prentice Hall)

[3] Menges G, Michaeli W, Mohren P 2001 *How to Make Injection Molds* (Hanser)

[4] Alves P S F F 2008 *Shrinkage and warpage behaviour on injection moulding parts* (Universidade do Minho)

[5] Jain K, Das S R and Kumar D 2016 International *Conference on Production and Industrial Engineering* (Jalandhar, India)

[6] Osswald T 2007 *Choice Reviews Online, American Library Association*

[7] ASTM D955- 2015 *Standard Test Method of Measuring Shrinkage from Mold Dimensions of Thermoplastics*

[8] Kramschuster A, Cavitt R, Ermer D, Chen Z B and Turng L-S 2006 *Rubber and Composites* **35(5)** 198–209

[9] Chopade D, Metkar R and Panchal A T 2021 *Springer*

[10] Carl Zeiss Industrial Metrology 2017 *ZEISS PRISMO: Specifications Manual*

[11] ARBURG GmbH + Co KG 2024 *Arburg 370 A: Technical Data*

[12] SABIC Europe 2024 *SABIC PP 579S: Datasheet*

[13] Schut Geometrical Metrology 2021 *DeMeet 3D CNC CMM Series: Specifications*

[14] Mitutoyo Corporation 2020 *Digital Micrometer QuickMike Series 293: Specifications and Features*

[15] OHAUS Corporation 2021 *Explorer Semi-Micro and Analytical Balances: Models and Specifications*

euspen's 26th International Conference & Exhibition, Krakow, PL, June 2026
www.euspen.eu

Mechanical properties of additive manufactured components with combined short and continuous fiber reinforcement

J. Polte[1, 2], S. Bode[1], S.Yazgan[1]

[1] *Institute for Machine Tools and Factory Management IWF, Technische Universität Berlin, Germany*
[2] *Fraunhofer Institute for Production Systems and Design Technology IPK, Germany*

suemeyra.yazgan@tu-berlin.de

Abstract
Additive manufacturing of fiber-reinforced plastics offers high potential for lightweight applications through combining short fiber-reinforced polymers with continuous fibers. While individual fiber types have been investigated, limited research exists on optimizing double fiber-reinforced components. This study analyses continuous glass fiber reinforcement in tensile strength of additively manufactured components made of short fiber-reinforced polyamide 6 (Onyx). Samples with varying fiber content, layer positioning, and reinforcement strategies are manufactured and tested. Results show that increasing fiber content significant enhances tensile strength, while the exact position of the fiber layers within thin specimens has only a minor influence. Continuous fiber reinforcement also achieves comparable properties with reduced infill.

additive manufacturing, fused filament fabrication (FFF), short fiber-reinforced polymers, continuous fiber, tensile tests

1. Introduction

Additive manufacturing of fiber-reinforced plastics offers great potential for industrial and lightweight applications, combining design freedom with adjustable mechanical properties. Short fiber-reinforced polymers combined with continuous fibers increase strength and stiffness [1, 2]. Few studies examine systematic optimization of double fiber-reinforced components [3]. This work investigates the influence of continuous glass fiber (CGF) reinforcement on mechanical properties of tensile specimens, varying fiber content, layer arrangement, and reinforcement design.

2. Experimental setup

Tensile specimens were produced from the short carbon fiber-reinforced filament Onyx and selectively reinforded with CGF, both supplied by MARKFORGED INC. (Watertown, USA). Onyx consists of polyamide with a short carbon fiber (CF) fraction of 11 % ≤ ϕ_{CF} ≤ 15 % [4]. It offers increased stiffness, good toughness, high chemical and thermal resistance. CGFs were fed from a spool and introduced during printing in specific layers or as outlines.The component design was carried out using NX CAD software from the company SIEMENS AG (München, Germany) while process preparation and fiber placement were performed using Eiger slicer software. The investigated parameters included the continuous fiber content, the number and position of the reinforced layers, the infill density, and the reinforcement layout. The samples were produced using an Onyx Pro FFF system (2nd generation, MARKFORGED INC., Watertown, USA). This desktop 3D printer has a build volume of 320 mm × 132 mm × 154 mm and allows the processing of short fiber-reinforced filaments and the integration of continuous fibers [4]. The Onyx material was processed at θ_{Onyx} = 275 °C and the CGF at θ_{CGF} = 230 °C. Depending on the specimen variant, either ρ_{infill} = 100 % solid infill or ρ_{infill} = 37 % triangular infill was used, while both Onyx and glass fibers (GF) were generally deposited in alternating ±45° orientation, except for the Onyx100_LinesGF configuration.

3. Experimental Procedure and Analysis

3.1. Tensile test specimens

Standardized tensile specimens with different reinforcement strategies were produced and mechanically tested to evaluate the influence of CGF reinforcement. Tensile test specimens were made of short fiber-reinforced polyamide and, depending on the variant, additionally reinforced with CGFs. Unreinforced specimens served as references. To investigate continuous fiber influence, fiber content, positioning, and reinforcement design were varied, resulting in GF fractions of 11.4 % ≤ ϕ_{GF} ≤ 24.8 % (Table 1). In addition to fully reinforced layers, variants were also considered in which the CGFs were applied exclusively as concentric outlines. Samples with reduced polymer infill were also produced in order to evaluate the influence of the material content in conjunction with continuous fiber reinforcement (CFR). All samples were produced lying flat, with the continuous fibers being laid alternately in a ±45 °orientation in all cases.

3.2. Tensile Testing

The mechanical characterization of the samples was carried out using quasi-static tensile tests. These were performed at a test speed of s = 2 mm/min, a preload of p = 3 N, and a clamping length of l = 200 mm. An extensometer with a measuring range of r = 25 mm was used to precisely record the strain. Five samples were tested for each test variant, resulting in a total of 35 tensile samples being examined. Depending on the variant, the CGF content of the reinforced samples ranged from 11.4 % ≤ ϕ_{GF} ≤ 24.8 % (Table 1). The elastic modulus E_t, maximum strain ε_{max}, and tensile stress σ_m were determined from the stress-strain curves (Figure 1).

Sample designation	Onyx-Infill	Endless GF	GF layers	Order of GF layers	Elastic modul (E_t)	Max. strain (ε_{max})	Tensile stress (σ_m)	GF content
Onyx100_0GF	100 %	no	-	-	566.37 MPa ± 61.49	61.77 % ± 12.03	28.08 MPa ± 1.30	0 %
Onyx100_4GF	100 %	yes	4	full surface	1580.32 MPa ± 41.35	3.77 % ± 0.16	46.01 MPa ± 3.51	16.2 %
Onyx100_6GF	100 %	yes	6	full surface	2138.28 MPa ± 186.17	3.76 % ± 0.15	61.50 MPa ± 3.41	24.4 %
Onyx100_6GF3	100 %	yes	6	full surface (each 3. layer)	1956.98 MPa ± 94.25	3.69 % ± 0.09	58.16 MPa ± 2.48	24.8 %
Onyx100_LinesGF	100 %	yes	several	outlines	3273.92 MPa ± 72.47	3.50 % ± 0.16	107.29 MPa ± 3.97	11.4 %
Onyx37_0GF	37 %	no	-	-	464.33 MPa ± 23.08	45.93 % ± 8.01	16.73 MPa ± 0.33	0 %
Onyx37_4GF	37 %	yes	4	full surface	2072.82 MPa ± 57.06	4.10 % ± 0.26	55.37 MPa ± 2.70	16.2 %

Table 1 Overview of the tensile samples examined and results of tensile testing

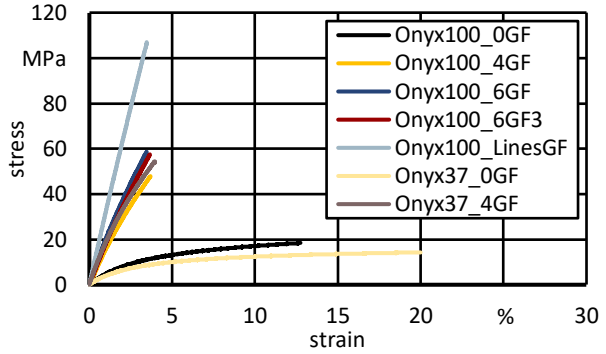

Figure 1. Stress-strain diagram

The diagram shows that increasing CGF content leads to higher tensile strength, while variations in fiber positioning at a constant number of reinforced layers have only a minor influence. Specimens reinforced with CGF outlines achieve the highest tensile strength (σ_m = 107.29 MPa). Although reduced polymer infill generally decreases strength, CFR compensates for this effect, as specimens with 37 % infill and four GF layers exceed the strength of fully filled specimens. These trends are consistent with previous studies reporting increased strength and stiffness with higher continuous fiber content [6]. Based on the elastic modulus, pure Onyx specimens can be classified as semi-rigid plastics, whereas continuous fiber-reinforced specimens exhibit rigid material behavior, which is reflected by a steeper initial slope and more brittle fracture in the stress–strain curves. In addition to the stress–strain curves, the fracture behavior of the tensile specimens was analyzed to identify dominant damage mechanisms. Figure 2 shows representative fracture features observed after tensile testing:

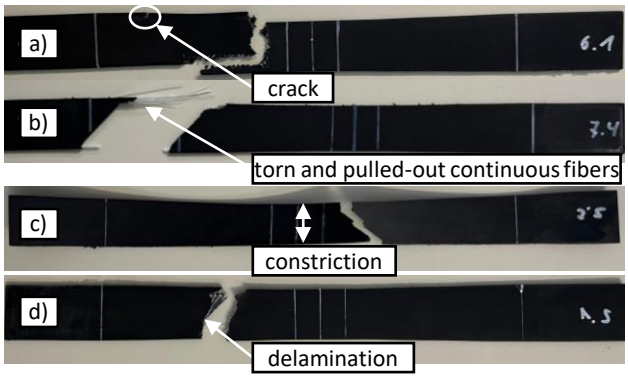

Figure 2. Breaking behavior of the tensile specimens (a: Onyx100_6GF, b: Onyx100_LinesGF, c: Onyx37_0GF, d: Onyx37_4GF)

In specimens reinforced with CGFs, a low and narrowly distributed strain at failure in the range of 3.4 % ≤ ε_{max} ≤ 4.1 % was observed, indicating brittle, fiber-dominated failure. Pronounced crack initiation at the specimen edges is visible in Figure 2a, indicating local stress concentrations. These cracks form first and propagate, leading to failure after multiple cracks. In specimens reinforced only by continuous fiber outlines, such as Onyx100_LinesGF, failure occurs abruptly without prior crack growth (Figure 2b). Pulled-out and exposed CGFs are observed, while the surrounding polymer matrix fails along the Onyx infill pattern, indicating limited bonding, insufficient limited stress transfer, and local interfacial debonding between fiber outlines and infill regions. Specimens without CFR exhibit a different failure mode, with pronounced necking prior to fracture (Figure 2c), reflecting ductile matrix behavior. Local delamination between CGF layers and the surrounding matrix is observed in Figure 2d. These interfacial separations indicate insufficient bonding under tensile loading, reduce the efficiency of load transfer between fiber and matrix, and contribute to reduced elongation and more brittle fracture behavior of continuous fiber-reinforced specimens.

4. Conclusion

This study investigated the influence of combined short fibers and CFR on additively manufactured tensile specimens. CGF reinforcement increases tensile strength and stiffness with higher fiber content further improving mechanical properties, while layers positioning has only minor influence. Fracture mechanisms correlate with the stress-strain response, indicating increased stiffness and strength at the expense of ductility, while enabling high strength at reduced infill.

References

[1] Ding, S., Zou, B., Zhuang, Y., Wang, X., Li, L. u. Liu, J., Hybrid layout and additive manufacturing of continuous carbon/glass fibers reinforced composites, and its effect on mechanical properties. Composite Structures 319 (2023).

[2] Gao, J., Li, B., Bu, H., Li, X. u. Zhan, X., Effect of infill density and reinforced perimeters on tensile properties and fracture mechanism of 3D printing carbon fiber–reinforced composite. The International Journal of Advanced Manufacturing Technology (2023).

[3] Almeida Jr., J. H. S., Christoff, B. G., Tita, V. u. St-Pierre, L., A concurrent fibre orientation and topology optimisation framework for 3D-printed fibre-reinforced composites. Composites Science and Technology 232 (2023).

[4] Markforged Inc. u. Mark3D GmbH, Fertigung neu definiert. Mark3D GmbH (2023).

[5] Soete, Jeroen, Badoux, Brice, Swolfs, Yentl, Gorbatikh, Larissa, Wevers u. Martine (Hrsg.), Defect detection in 3D printed carbon fibre composites using X-ray Computed Tomography, 2019.

[6] Dong, C., Davies, I. J., Mechanical Properties of Continuous Glass Fibre-Reinforced Composites Made by Material Extrusion. Progress in Additive Manufacturing (2024).

euspen's 26th International Conference & Exhibition, Krakow, PL, June 2026
www.euspen.eu

Development of Lattice Structures of pure Tungsten for Applications in Fusion Energy

Miguel Zavala-Arredondo[1], Ahmed Tawfik[2], Liam Blunt[2], Jeong-Ha You[3].

[1] UKAEA, 2A Lanchester Way, Advanced Manufacturing Park, Rotherham, S60 5FX, UK.
[2] The Future Advanced Metrology Hub fr Sustainably Manufacturing, University of Huddersfield, UK
[3] IPP (Max Planck Institute for Plasma Physics), Garching, Germany

l.a.blunt@hud.ac.uk

Keywords. Fusion, additive manufacturing, lattice, tungsten

Abstract

Nuclear fusion is a critical element in moving to non-hydrocarbon energy sources where there are advantages to fusion reactors based on reliable shut down capability and significantly reduced half-life of waste materials. However, fusion requires temperatures in the range of $100x10^6$ °C consequently the energising plasma must be critically maintained within the reactor to allow the fusion reactions to occur. Tungsten has been defined as the optimal material to line the reactor internal walls. Tungsten is characterized unique material properties; the highest melting point metal (3422°C), high hot tensile strength (350 MPa at 1000°C), large heat capacity and maximal vapor shielding [1]. The use of tungsten as a plasma facing components for reactor wall lining, is enhanced if the tungsten is orientated to present a porous lattice structure to the plasma[2].

To date, attempts to use produce complex lattice-based plasma facing components based on thermal modelling of function and produced using LBPF (laser 3D printing) have resulted in substandard lattices, where the microstructures are characterized by numerous defects consisting of micro-cracks, micro-voids and non-designed pores. These observations indicate that the likely cause of the cracking is through thermal shock due to the rapid cooling (~104 K/s) during printing of the lattice[3].

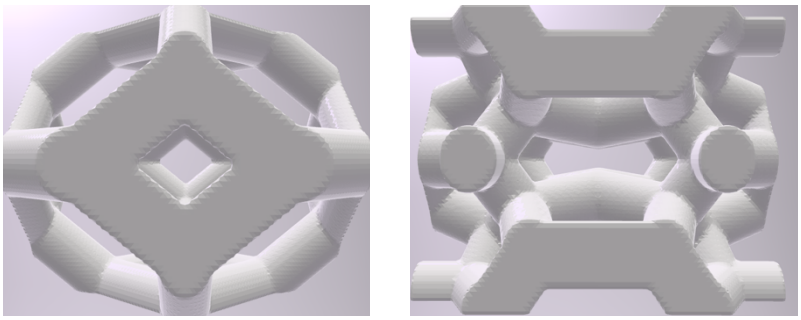

Figure 1 a) base line "C" cell design b) new "W" cell design

In the present study LBPF additive manufacturing (AM) of tungsten lattice structures has been investigated. A new method is proposed to adapt L-PBF process parameters for lattices and alternate lattice unit cell designs are investigated including the baseline C-cell design also known as Kelvin cell – previously developed by the EUROfusion Consortium for higher thermal performance [3]. New lattice designs "W cell" are investigated to reduce manufacturing process induced defects and manage thermal loads during processing in the unit cell structure, figure 1. The unit cell designs were manufactured and mechanically tested to compare with the baseline data, figure 2 &3.

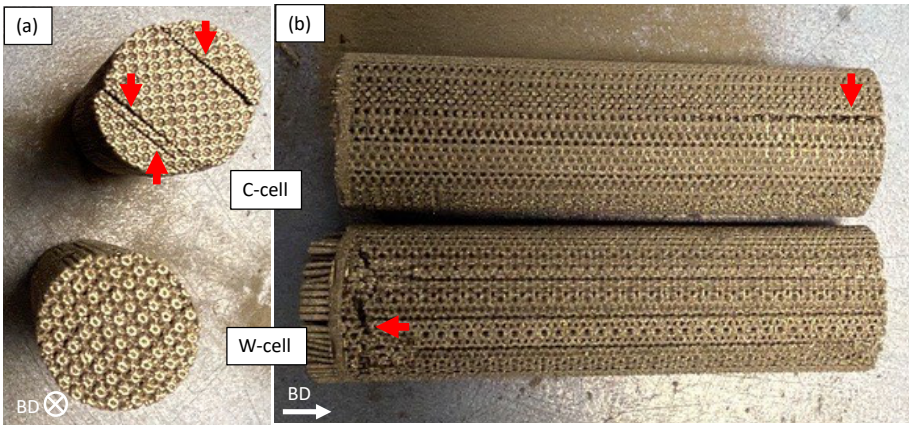

Figure 2 – (a) Top and (b) side views of C-cell (top) and W-cell (bottom) tensile lattice specimens tested without solid caps. Red arrows show location of fractures.

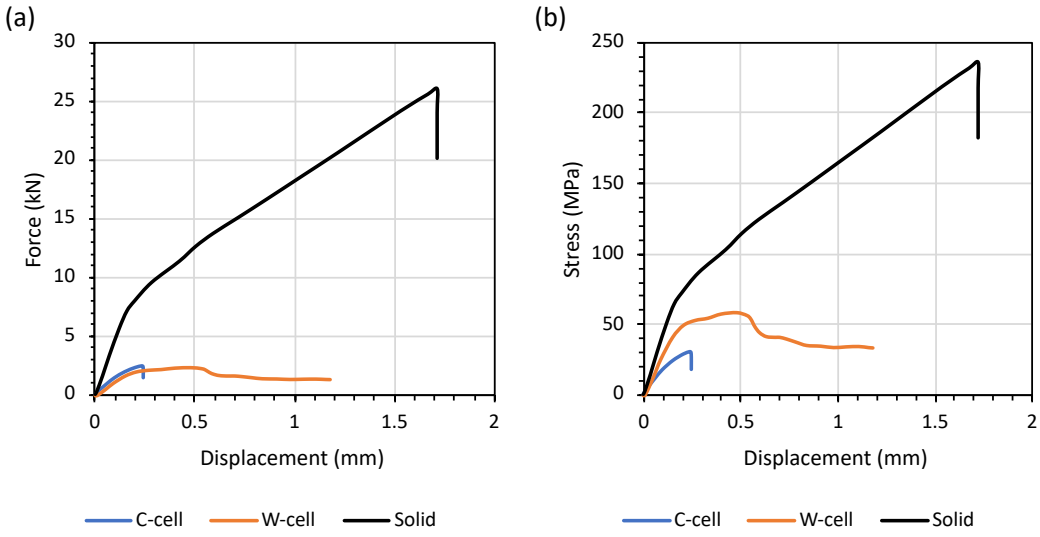

Figure 3 - (a) Force- and (b) stress- displacement curves from tensile testing of C- and W-cell lattice specimens compared to a solid specimen. Cylinder specimens with overall diameter of 11.88 mm was used.

The modified unit cell design denominated the “W-cell” showed improved manufacturability. Crack density, crack length, and crack width in the W-cell were reduced around 67 %, 25 %, and 56 %, respectively, in comparison with the C-cell reference. Preliminary tests indicate that W-cell lattice structures could improve strength and ductility under both compressive and tensile loads, in comparison with C-cell lattice structures with the same mass. Further study is needed to understand the thermal performance of the modified W-cell for limiter plasma facing component application. A compromise between thermal performance and manufacturability is proposed as a critical consideration for new plasma facing component designs.

1 .D Tsuru, M Fukumoto “Design, research and development for plasma facing components” JT-60SA- Physica Scripta N T171
2. J. H. You *et al.*, “Limiters for DEMO wall protection: Initial design concepts & technology options,” *Fusion Engineering and Design*, vol. 174, p. 112988, Jan. 2022,
3. J. H. You ., “Limiters for DEMO wall protection: Initial design concepts & technology options,” *Fusion Engineering and Design*, vol. 174, p. 112988, Jan. 2022,

euspen's 26th International Conference & Exhibition, Krakow, PL, June 2026
www.euspen.eu

Productivity enhancement and burr reduction in Ti6Al4V single lip microdrilling using ultrasonic vibration assistance

Bernie Cheruiyot*, Richard Börner, Andreas Nestler, Andreas Schubert

Professorship Micromanufacturing Technology, Chemnitz University of Technology, Reichenhainer Str. 70 09126 Chemnitz, Germany

*kiplelgo@proton.me

Abstract
Mechanical microdrilling is a critical process in advanced manufacturing of high-precision components, such as in medical and aerospace industries. However, the process is limited by low tool stiffness, poor chip removal and significant burr formation. Ultrasonic assistance is proposed to overcome some of these challenges, converting the continuous cutting process into an intermittent one. Some of these benefits are the support of chip breaking and reduced friction between the tool and the bore wall. This research evaluates the effectiveness of ultrasonic assistance in single flute microdrilling of Ti6Al4V alloy. Experiments were conducted for a diameter of 1 mm at feeds of 2 µm and 4 µm, both with and without ultrasonic assistance. Results demonstrate that while the tool is broken at 4 µm feed in regular drilling, the process is technically feasible with ultrasonic assistance, effectively halving the drilling time per hole. Additionally, the ultrasonically assisted process shows improvements in chip formation, burr reduction and process stability.

Microdrilling, single flute drill, Ti6Al4V, ultrasonic vibration assistance

1. Introduction

Micro-holes (diameter < 1 mm) are a critical feature in high precision applications. These include microscopic nozzles in fuel injectors for combustion engines [1] and aerospace cooling channels for turbine engines [2]. Microdrilling is also useful for orthopaedic implants such as intramedullary nails, as research done on mice in veterinary medicine shows [3]. Mechanical microdrilling is preferred in many applications of medical manufacturing for achieving high hole straightness and surface quality. Additionally, drilling avoids formation of a chemically altered heat-affected zones and microcracks that may arise from thermal ablation methods such as electro-discharge machining (EDM) and laser drilling [4]. This is especially important for medical materials such as Ti6Al4V, which is preferred for medical applications due to its corrosion resistance, high strength, low weight and biocompatibility [5]. At a micro-scale, drilling suffers problems such as low tool stiffness, chip entanglement and high burr formation [4]. The material removal mechanism shifts to forming due to very low undeformed chip thickness in the same order of magnitude as the cutting edge radius, where material is pushed away and formed rather than cut into a chip [6]. This increases the specific energy required for material removal. Ti6Al4V exhibits characteristics that make it difficult to process, such as a high specific strength and resistance to thermal softening [7]. Single flute gun drills are a special drill geometry particularly suitable to microdrilling, with higher stiffness due to a greater cross-sectional area, and internal coolant delivery incorporated into their design. They are typically used at lower feeds than twist drills. High-pressure internal coolant (80 bar – 120 bar) is essential for their application [8]. Pressure values are dependent on drill diameter and hole aspect ratio, with tool manufacturers usually providing a guide to the pressure setting. Ultrasonic (US) assistance has been explored as an enhancement to mechanical microdrilling, transforming the cutting into an intermittent process [9]. This leads to benefits such as better chip formation and minimal burr formation [4]. This research aims to extend the productivity of single flute microdrills by increasing the viable feed as well as reduce burrs at the hole exit by leveraging the benefits of US assistance. These outcomes are to be validated experimentally.

2. Methodology

Conventional mechanical microdrilling has two main motions of the tool: the feed of the tool into the workpiece, as well as the rotation of the tool about its axis. US assistance introduces a third motion, the oscillation of the tool along its axis, occurring at ultrasonic frequencies. The cutting is thus transformed from a continuous chip formation process to an intermittent process, subject to the process parameters falling within a specific operating window and combination with each other. The intermittent contact between the tool and workpiece results in more steady thrust and cutting forces, as well as smaller, more manageable chips. Chip breaking is promoted by the varying undeformed chip thickness and intermittence of cutting. These benefits create the possibility to extend the productivity and enhance the stability of mechanical drilling using this technique.

2.1. Kinematics of ultrasonic-assisted drilling

The kinematics of the drill bit can be modelled mathematically by taking into consideration the linear feed movement and rotation of the tool, as well as the ultrasonic oscillations. The z-, x- and y-axis positions of a point on the circumference of the tool as seen in Figure 1 can be determined as follows:

$$z = -f \times n \times t + A \times sin(2\pi f_{US} t) \quad \text{Eq 2.1}$$

$$x = r \times cos\ \theta \quad \text{Eq 2.2}$$

$$y = r \times sin\ \theta \quad \text{Eq 2.3}$$

A represents the amplitude of oscillations, i.e. half of the peak-to-peak displacement, f_{US} is the frequency of ultrasonic oscillation and *r* is the radius of the tool. The feed is given by *f*,

representing the feed per revolution, which in the case of single flute drills is equivalent to the feed per tooth. The rotational speed is given by n and t represents the time. The tool path can be mathematically plotted in 3D space as shown in Figure 1, showing the path of a single point on the tool circumference.

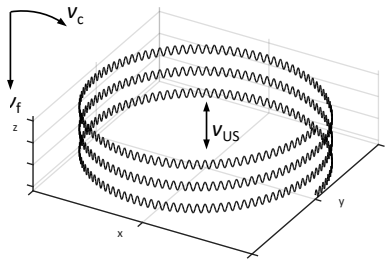

Figure 1. Path of a point on the outer cutting edge. v_f represents the feed velocity, v_{US} represents velocity due to ultrasonic oscillation and v_c represents the cutting speed.

To ensure that the intermittent cutting is attained, the feed velocity must be less than the maximum instantaneous velocity of the oscillating tool (critical velocity). The critical velocity is determined by the ultrasonic parameters amplitude and frequency. Intermittent cutting is only attained if the feed velocity is lower than the critical velocity. Following the previously described model, this relation is specifically constrained to a point on the tool periphery.

2.2. Experimental parameters and instrumentation

Experiments were designed to isolate the effects of feed and ultrasonic amplitude. The first experiment was conducted to establish a baseline of the machining performance and characteristics as recommended by the tool manufacturer. Subsequently, the effectiveness of US assistance and its benefits were evaluated. This was followed by testing the possibility of US assistance extending productivity levels beyond the standard recommended parameters. Table 1 shows the machining and US parameters used for the experiments.

Table 1. Experimental parameters

Test	Feed/ µm	Peak-peak US amplitude / µm	Holes drilled
Ref2	2	0	100
US2	2	3	100
Ref4	4	0	22
US4	4	3	550

The spindle speed was kept constant at 9550 1/min, corresponding to a cutting speed of 30 m/min for the 1 mm drill bit used. An internal coolant pressure was set to 40 bar, the maximum for the KERN Pyramid Nano machining centre applied. Although this pressure is below the minimum recommended pressure due to machine limitations, the setup can be used as a test case for extending the functionality of existing systems with limited capabilities. A botek Type 113 single flute cemented carbide drill with a TiAlN coating was used, with a drill-point angle of 110° and drill body length of 62 mm. US oscillations were induced by a VibroCut Precision Line oscillator, fitted with a 6 mm shrink fit chuck for the drilling tool, which was set to its minimum power level. The resulting peak-to-peak amplitude of 3 µm (A_{pp}) was applied for the experiments. The specimen used in this experiment was a 12 mm thick Ti6Al4V disc with a diameter of 70 mm, onto which a rectangular pattern of holes was drilled. As single flute drills are asymmetrical and not inherently capable of self-centering, the specimen was pre-piloted with holes of 1.01 mm diameter using a botek Type 153 pilot drill with a drill-point angle of 140° to a depth of 2.5 mm, followed by drilling through the whole depth of the specimen. The single flute drill was initially fed into the pilot holes at a lower spindle speed of 50 1/min to aid the location of the hole and then spun up to the operational spindle speed. The experimental setup used is shown in Figure 2.

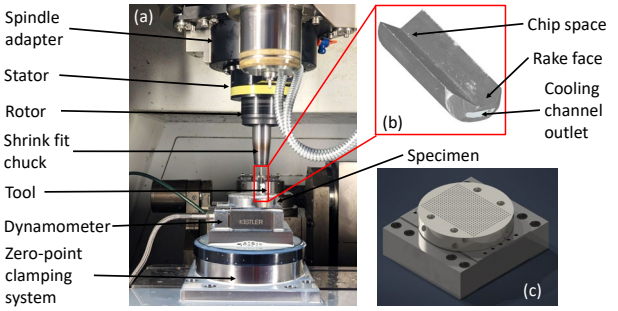

Figure 2. The experimental setup used, showing (a) the setup in the machining centre, (b) 3D scan of the tool and (c) 3D construction of the mounted and pre-piloted specimen.

2.3. Evaluation and process characterisation

Axial and lateral forces were measured using a dynamometer, onto which the test specimens were mounted, at a sampling frequency of 1 kHz. The raw force signal was evaluated using a custom MATLAB script to isolate the data for individual holes, enabling the calculation of mean forces and standard deviations on a per-hole basis. The z-direction signal is a measure of the thrust force, which is of primary interest in this investigation. RMS values were calculated for forces in x-direction in order to capture both positive and negative values generated by the rotating tool during drilling.

Intermediate micrographs of the tool were taken at fixed intervals to monitor the progression of tool wear as well as their operability. Chips collected from each experiment were analysed using both a Keyence digital light microscope as well as a scanning electron microscope (SEM) to characterise their shape and dimensions.

3. Results

3.1. Baseline experiment – Feed of 2 µm

The initial experimentation focused on establishing a process baseline and validating the process feasibility. A target of 100 holes drilled was successfully achieved using the maximum recommended feed of 2 µm. The thrust forces in this experiment were considerably low, with a starting value of 4.8 N and rising to a maximum of 11.2 N. This progression can be seen in Figure 3. Error bars are added to every fifth hole to enhance readability, showing the standard deviation of the thrust forces.

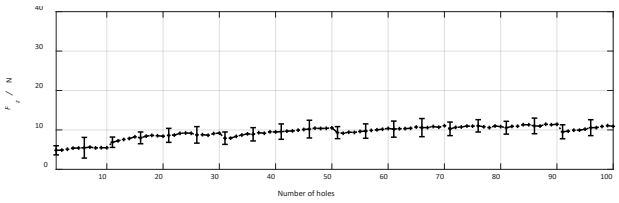

Figure 3. Thrust forces in reference experiment, 2 µm.

Introduction of US oscillations results in both a higher magnitude of forces, as well as greater dispersion. The standard deviation rises from a maximum of 3.0 N to 7.5 N. The average force is only marginally increased, starting at 8.1 N and rising to a maximum of 13.8 N. This is a smaller increase compared to the reference experiment for the same number of holes drilled. The progression of forces in this experiment can be seen in Figure 4.

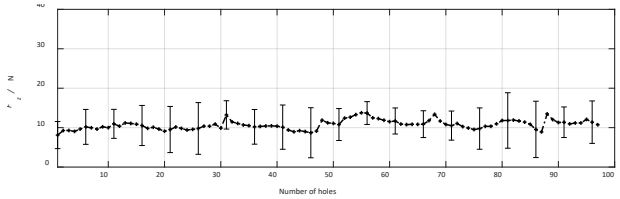

Figure 4. Mean thrust force using US assistance with feed of 2 µm.

The forces in x-direction in the reference experiments were also very low, with a grand mean RMS value of 0.19 N and within a narrow force envelope. This is due to the low chip load caused by the small feed, requiring less energy to form the chip. There is a more noticeable difference in the lateral forces with the additional of US assistance, with an average $F_{x,RMS}$ of 1.15 N, an increase of about 500 %. These forces are considerably low, with no tool chatter that would indicate imminent tool failure.

Tool wear is slightly worse using US assistance, which can be attributed to the repeated hammering of the cutting edge in the workpiece. A side-by-side comparison of the tool rake face is as shown in Figure 5, where the increased wear of the inner cutting edge can be seen in Figure 5 (b).

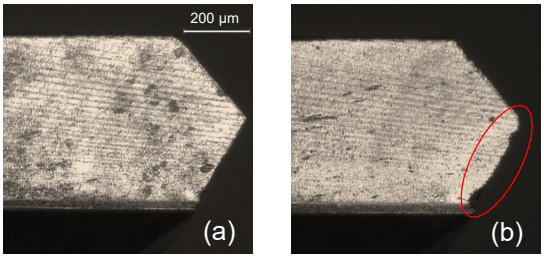

Figure 5. Side-by-side comparison of tool rake face at 2 µm after 60 holes (a) without US assistance and (b) with US assistance.

3.2. Experiments with increased feed of 4 µm

The initial test conducted at 4 µm feed without US assistance yielded only twenty-two holes before the tool irretrievably broke. This was taken as an indicator of technical infeasibility, as 4 µm is double the maximum recommended feed. However, a subsequent test with US assistance was successful. The mean forces in this experiment were considerably higher than at 2 µm feed, reaching a peak mean of 25.8 N with a grand mean of 19.0 N. Dispersion also increased, with an average standard deviation of 8.4 N. The progression of the forces through the 100-hole sequence with US assistance is as shown in Figure 6.

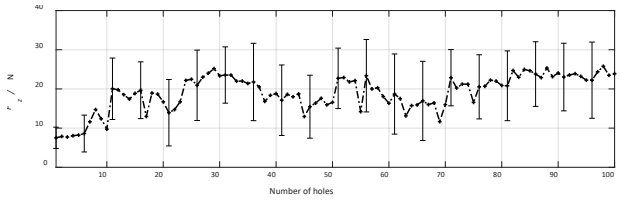

Figure 6. Mean thrust forces using US assistance with feed of 4 µm.

The force signal was observed to show two zones, an initial low and stable zone, followed by a second zone with higher magnitude and greater signal dispersion. This is attributable to the friction inside the hole walls that causes the tool to stick, increasing the thrust force required to maintain the set feed. A representative force signal from a sample hole in this experiment is shown in Figure 7, with the portion of the signal from the tool engagement point to hole exit marked.

The lateral forces in this experiment showed a falling trend that roughly corresponds to the magnitude of thrust force. The magnitude of forces (RMS) was higher than the previous experiments, with a minimum RMS of 1.0 N, maximum RMS of 2.4 N and a grand RMS mean of 1.6 N. This is a modest increase compared to the experiment conducted at 2 µm which does not linearly correspond to feed being doubled. However, the drilling time per hole is halved.

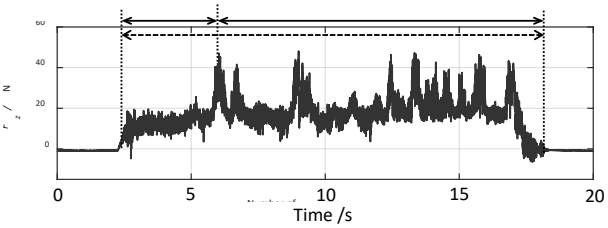

Figure 7. Representative force signal of a hole drilled at 4 µm showing the two-zone progression of thrust force as the hole is drilled

The tool used in this experiment showed the greatest extent of wear both on the cutting edge as well as at the tool tip. This is expected as the tool is subject to the greatest stress, with a higher chip load in addition to the ultrasonic hammering. The process is, however, free from chatter and other indications that the tool may be under excessive stress. Figure 8 shows the damage on the cutting edge of the tool.

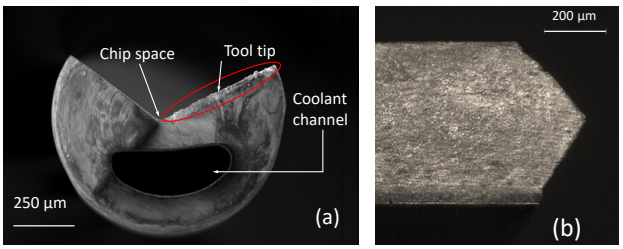

Figure 8. Tool wear after 500 holes represented by (a) SEM image of the tool tip and cutting edge and (b) rake face image.

3.3. Endurance test – 4 µm

The same parameters were used to further test the robustness of the system, and a total of 500 holes were drilled before the experiment was concluded. During this endurance test, the forces remain stable within a narrow window with no significant increasing trend. The thrust forces show a peak value of 25.8 N, with a grand mean value of 19.0 N and a standard deviation of 8.4 N. Thus, the process with US assistance is a viable choice for serial production, particularly considering that the regular test conducted without US assistance resulted in a broken tool. The trend of thrust force is shown in Figure 9.

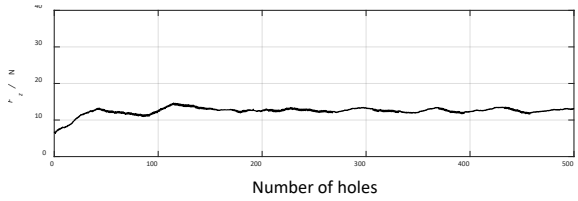

Figure 9. Force progression (rolling mean) in endurance test, 4 µm.

3.4. Formation and reduction of burr

An additional problem with microdrilling is the formation of high exit burrs. At the bottom of the drilled hole, just before the drill exits the workpiece, the thin layer of material left is formed into a burr rather than being removed cleanly by cutting. This problem is exacerbated at high feeds, as the final layer is thicker and results in a larger burr. US assistance may help in reducing the burr, as the high impact of the oscillating tool results in a clean cut. The analysis of burr formation was done by classifying the burrs into three categories: nearly no burr formation (Category 0), various formations of a burr around the hole

circumference (Category 1), and the formation of a drill cap (Category 2). Sample SEM micrographs of the burr types observed, which were taken from the through-hole exit side, are shown in Figure 10.

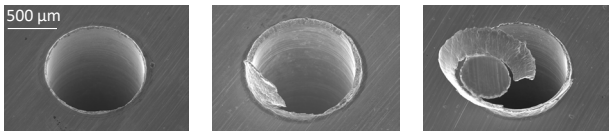

Category 0 Category 1 Category 2

Figure 10. The burr classification categories at the hole exit.

The classification data confirms that occurrence of burr formation is increased at a higher feed. At 4 µm feed, 99 % of holes drilled have a burr. Burr sizes were also higher, with over 50 % of holes drilled exhibiting a drill cap.

As the frequency of burr formation and burr size is reduced at a lower feed, a machining strategy was conceptualised to minimise the formation of burrs. This involved drilling at a compound feed, beginning at 4 µm as had been previously done. The feed was then lowered to 1 µm for the last 500 µm. A test was conducted on a fifty-hole sequence using the same drilling tool as for the ultrasonic test at 4 µm up to 500 holes. Of these, a drill cap was formed in twelve holes, while the remaining thirty-eight were nearly burr-free, representing a 76 % rate of nearly burr-free drilling. This shows that the use of a compound feed can be an effective strategy in reducing burr formation. Crucially, the drilling time is not significantly increased, with the compound feed strategy requiring about 17 s compared to 14.5 s using a constant 4 µm feed. This benefit would be even greater for deep drilling, as a much larger proportion of the hole is drilled faster at the higher feed. The distribution of burrs formed in each category grouped by experiment is shown in Figure 11. The label 'US4*' represents the burr reduction test.

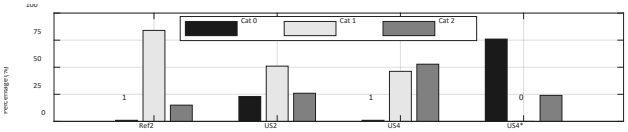

Figure 11. Distribution of burr formation by type.

3.5. Chip formation and morphology

The chips formed in the experiments were also observed by SEM, revealing differences in their size and morphology. The chips formed at 2 µm feed without US assistance were the longest, exhibiting a conical shape with several cracks formed. Addition of ultrasonic vibrations promoted chip breaking through the intermittent cutting and a varied undeformed chip thickness, resulting in considerably smaller and more broken chips. On further raising the feed to 4 µm, the chips are slightly larger in size but are still broken into smaller particles. The chips formed in the three experiments can be seen in representative samples shown in Figure 12. All micrographs were taken with the same magnification.

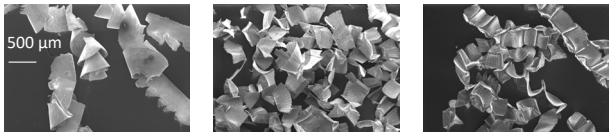

Ref2 US2 US4

Figure 12. Chip micrographs from the microdrilling experiments.

4. Summary and conclusions

The potential of US assistance in microdrilling is confirmed for Ti6Al4V in this study. A higher feed than is feasible under regular drilling conditions is made possible using US assistance. The result is a stable and robust process suitable for continuous operation. Notably, the compound feed machining strategy yields a nearly burr-free result, while chip fragmentation is aided by the US oscillations to improve evacuation and avoid clogging. The maximum feasible feed for these single flute micro drills is doubled from 2 µm to 4 µm, halving the drilling time without causing premature tool failure. This was validated in the 500-hole sequence. US assistance effectively mitigates some of the micro-scale effects such as chip forming due to a very low chip load, transitioning the material removal mechanism towards a more stable intermittent cutting process. This is an important improvement to the mechanical microdrilling process using single flute micro-drills. It enables serial production of parts that are required in high quantities, such as medical implants and orthopaedic fixtures which are required in high quantities and disposable for hygienic reasons.

Further research should establish the operational limits of US assistance in mechanical microdrilling. As the current process parameters already achieve clear tool-workpiece separation, further raising the ultrasonic amplitude may yield diminishing returns while increasing the impact energy on the tool edge, potentially accelerating tool wear by chipping. In addition, critical feeds should be defined, where the intermittent cut is maintained with high process stability. Other difficult-to-machine materials, such as nickel-based superalloys, may also benefit from this technique, allowing broader industrial application.

References

[1] H. Yu, G. Chen, J. Xu, J. Wang, Z. Yu and X. Tang, "An Experimental Study of Ultrasonic Assisted Micro-Holes Drilling," in *2018 IEEE Int. Conf. on Manipulation, Manufacturing and Measurement on the Nanoscale (3M-NANO)*, 2018.

[2] L. Subasi, M. I. Gokler and U. Yaman, "A process modeling approach for micro drilling of aerospace alloys with a waterjet guided laser system," *Optics & Laser Technology,* vol. 148, p. 107682, April 2022.

[3] T. Histing, M. D. Menger, T. Pohlemann, R. Matthys, T. Fritz, P. Garcia and M. Klein, "An Intramedullary Locking Nail for Standardized Fixation of Femur Osteotomies to Analyze Normal and Defective Bone Healing in Mice," *J. of Visualized Experiments : JoVE,* p. 54472, November 2016.

[4] M. Hasan, J. Zhao and Z. Jiang, "A review of modern advancements in micro drilling techniques," *J. of Manuf. Processes,* vol. 29, p. 343–375, October 2017.

[5] E. Marin and A. Lanzutti, "Biomedical Applications of Titanium Alloys: A Comprehensive Review," *Materials,* vol. 17, p. 114, January 2024.

[6] X. Huang, F. Jiang, Z. Wang, X. Wu, S. Huang, Y. Liu, J. Zhang and X. Shi, "A review on the balancing design of micro drills," *Int. J. of Advanced Manuf. Tech.,* vol. 126, p. 4849–4871, June 2023.

[7] G. Gao, Z. Yuan, Z. Xia, Z. Fu, D. Xiang and B. Zhao, "Study on thrust force of ultrasonic-assisted vibration micro-hole drilling of titanium alloy," *The Int. J. of Advanced Manufacturing Tech.,* vol. 112, p. 3399–3413, January 2021.

[8] E. Oezkaya, A. Baumann, S. Michel, D. Schnabel, P. Eberhard and D. Biermann, "Cutting fluid behavior under consideration of chip formation during micro single-lip deep hole drilling of Inconel 718," *Int. J. of Modelling and Simulation,* vol. 43, p. 49–63, March 2023.

[9] S. Ullah, Z. Liang, Y. Ma, Y. Du, Z. Su, Z. Yin, L. Xiong, M. U. Rehman, K. Pattamaporn and T. Zhou, "State-of-the-art review on ultrasonic vibration-assisted micro-drilling," *The Int. J. of Advanced Manufacturing Tech.,* vol. 138, p. 4935–4963, June 2025.

euspen's 26th International Conference & Exhibition, Krakow, PL, June 2026
www.euspen.eu

Elucidating the effect of wobble frequency on the fluid flow and keyhole dynamics in the laser lap welding of electric vehicles battery packs

Akash Meena[1], Guido Tosello[1]

[1] *Department of Civil and Mechanical Engineering, Technical University of Denmark, 2800 Kgs. Lyngby, Denmark*

akmee@dtu.dk

Abstract The integrity of the laser welding joints at the interface between battery tabs and busbars is crucial for ensuring the safety and efficiency of electric vehicles (EVs). Despite advancements in laser welding techniques, the effect of varying interface position on melt pool morphology, fluid flow, and keyhole stability remains unexplored. This study examined how wobble frequency in a lap-joint laser welding affected fluid flow, melt pool depth and keyhole dynamics in AA1050 aluminum sheets. A ring spot beam introduced to minimize spatter in the melt pool. A combined experimental and numerical methodology was adopted, in which the 150 Hz wobble condition was validated experimentally and additional wobble frequencies were analysed using a CFD-based FLOW-3D model. The results reveal that the different wobble frequency alters heat distribution, melt pool convection patterns, and keyhole stability. A 3D multiphysics simulation of laser wobbling with a ring spot beam was implemented. For the 150 Hz case, the predicted melt-pool depth below the interface (~2000 µm) showed close agreement with the experimental value (~1956 µm), while additional simulations indicated a reduction in penetration with increasing wobble frequency.

Keywords: Multiphysics simulation; laser wobble welding; wobbling frequency; laser beam shaping; lap joints; ring beam profile.

1. Introduction

The connection between the busbar and battery tab is critical in electric vehicle (EV) battery packs, directly influencing overall efficiency, safety, thermal stability, and long-term reliability [1,2]. The joint must provide low electrical resistance while maintaining adequate mechanical integrity under vibration, thermal cycling, and service loads [3–5]. In this context, laser welding has emerged as a highly attractive joining technology due to its high precision, localized energy input, automation compatibility, and high productivity [6–8]. Nevertheless, achieving robust and repeatable joints requires careful selection and optimization of process parameters, because small changes in process stability can lead to defects that significantly degrade joint performance.

A large part of the fundamental understanding of laser welding particularly regarding melt-pool fluid flow and keyhole dynamics has been established using single workpiece configurations [9–12]. While such studies are valuable for isolating physical mechanisms, the lap welding configuration introduces additional complexity that remains less explored. The schematic diagram of laser keyhole welding is shown in **Figure 1**.

Kang et al. [10] further linked keyhole instability to bubble generation via three primary mechanisms that contribute to pore formation.

Li et al. [11] used a validated model to quantify porosity reduction in adjustable ring-mode laser welding of aluminium alloys, showing that a ring beam lowers porosity by mitigating keyhole collapse and stabilising melt-pool flow, thereby limiting pore formation at both the gas-liquid and liquid-solid interfaces.

Laser lap welding is particularly sensitive to keyhole instability, which may cause intermittent keyhole collapse, spatter, and pore entrapment near the interface which is the most critical region for mechanical and electrical performance [13–16]. To improve process robustness and widen the effective seam, beam wobbling is frequently applied.

Wobbling can increase weld width (beneficial for mechanical strength and alignment tolerance) and can modify the melt-pool circulation and keyhole response through controlled redistribution of energy in space and time. However, the wobbling strategy involves multiple coupled parameters such as amplitude, frequency, scanning pattern, and often power modulation and their combined influence needs systematic investigation [17].

Among these parameters, wobble frequency is particularly important because it directly sets the timescale of beam motion relative to the characteristic response times of the melt pool and keyhole. In practical terms, frequency strongly affects the degree of overlap between successive oscillation cycles and thereby governs the stability of the keyhole wall, and the development of flow structures in the molten pool.

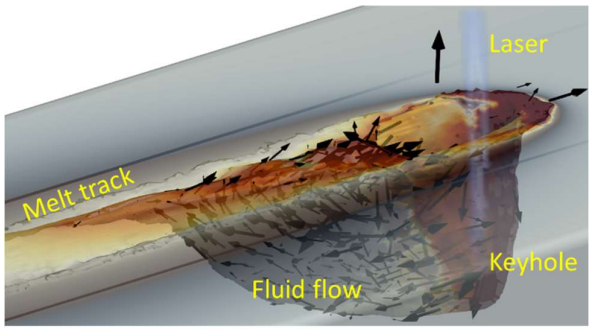

Figure 1. Schematic diagram of laser keyhole welding.

Despite increasing industrial adoption of wobble welding, most laser lap welding studies have emphasized outcomes such

as intermetallic compound formation, part-to-part gap effects, segregation behavior or focused on weld-quality trends [18–22].

In contrast, there remains a clear gap in the analysis of fluid flow and keyhole dynamics in laser lap wobble welding. In addition, ring beam shaping has been introduced to mitigate spatter and stabilize the molten pool, further motivating a deeper understanding of the underlying dynamics.

This work aims to elucidate how wobble frequency governs melt-pool flow behaviour and keyhole dynamics, and how these changes translate into weld morphology. The outcomes provide a clearer physical interpretation and support more robust selection of wobble parameters for high-quality laser lap welds in battery interconnect applications.

2. Methodology

This work investigates how wobble frequency influences melt-pool fluid flow and keyhole dynamics during laser lap welding. A controlled experimental work has been conducted by varying wobble frequency (100 Hz, 125 Hz and 150 Hz) while keeping other key processing conditions constant. In parallel, the commercial finite-volume computational fluid dynamics (CFD) solver FLOW-3D (by Flow Science, Inc., Santa Fe, New Mexico, USA) was employed to compute the coupled mass, momentum and energy transport for laser lap wobble welding under different wobble frequencies. The accommodation coefficient (bounded between 0 and 1) was used to represent interfacial phase change behaviour at the free surface, i.e., the fraction of vapour molecules that lose sufficient energy upon impingement to condense into the liquid phase at the vapour-liquid interface. Direct experimental quantification of the evaporation rate is difficult because it is highly sensitive to process conditions (e.g., laser speed, laser power, resulting linear energy density) as well as temperature-dependent material properties. [23,24].

2.1. Experimental design

The experiments were carried out on AA1050 in a lap-joint configuration, using a wobble frequency of 150 Hz. The lap joint consisted of a 1.5 mm upper sheet and a 2.5 mm lower sheet. The applied laser processing parameters are summarized in **Table 1**. A focusing optic with 255 mm focal length and 150 mm collimation length was used, and the laser beam was inclined by approximately 3° to minimize back reflections. X-ray CT scanning was additionally performed to assess the distribution of porosity. All experiments were conducted using a TRUMPF TruDisk 6001 solid-state disk laser equipped with a PFO 33-2 processing head shown in **Figure 2.** The weld length is 15 mm, made using a circular wobbling technique, and the welds were oriented across the sheet width of 25 mm. This modulation was synchronized with the wobble motion to control the laser energy density along the oscillation path. The welding path followed a wobbling pattern generated by a circular laser beam as shown in **Figure 3**. The wobbling amplitude of 1.2 mm and frequency of 150 Hz were selected based on initial parameter screening and are within the relevant range used in industrial practice. Laser power was modulated from 6 kW (100%) to 4.8 kW (80%), and ring beam shaping are shown in

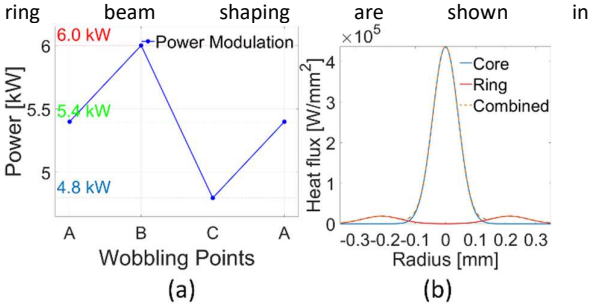

Figure 4.. The core and ring intensities were selected to reproduce the experimental beam-shaping condition and were kept constant in all cases in order to investigate the effect of wobble frequency. All specimens were cleaned with 2-propanol before performing the laser welding experiments. Each experimental condition was repeated twice to ensure reproducibility.

Table 1 Laser welding parameters

Laser parameters	
Power (kW)	6
Power modulation	100-80%
Amplitude (mm)	1.2
Frequency (Hz)	(100, 125, 150) Hz
Feed rate (mm/s)	95, 105, 115, 125
Accomodation coefficient	0.5
Surface tension gradient (N/m/s)	0.00026
Surface tension coefficeint (N/m)	0.871

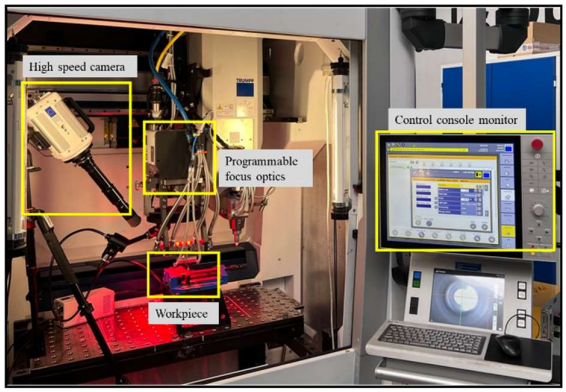

Figure 2. Experimental setup for laser welding experiment.

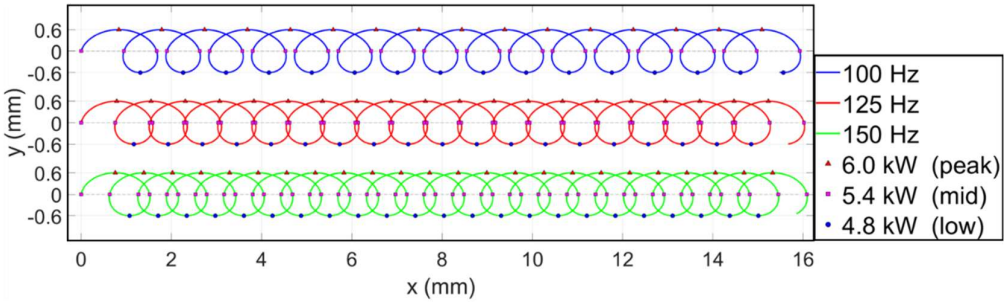

Figure 3. Schematic of laser wobbling path with three different wobble frequency (100 Hz, 120 Hz, 150 Hz).

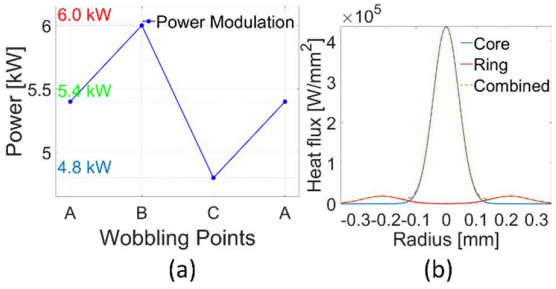

Figure 4. (a) Power modulation during laser wobble welding and (b) Heat flux distribution using the core and ring spot beam used in the laser wobbling process.

2.2. Numerical model

A multi-physics model was implemented in the commercial finite-volume solver FLOW-3D® (v12.0.2.01, release 7 update 3) using the WELD® module, accounting for key mechanisms including recoil pressure, multiple keyhole reflections, a ring-spot beam heat source, and the Marangoni effect.

The main governing equations of mass, linear momentum and energy balance are given by:

$$\nabla \cdot \boldsymbol{u} = \mathbf{0} \tag{1}$$

$$\frac{\partial(\rho \boldsymbol{u})}{\partial t} + \rho(\boldsymbol{u} \cdot \nabla)\boldsymbol{u} = -\nabla p + \mu \nabla^2 \boldsymbol{u} - \frac{K_c(1 - f_{liq})^2}{C_k + f_{liq}^3}\boldsymbol{u} + F_m \tag{2}$$

$$\rho\left[\frac{\partial h}{\partial t} + (\boldsymbol{u} \cdot \nabla)h\right] = \nabla \cdot (\kappa \nabla T) + \dot{Q}_e \tag{3}$$

In equation (1), **u** (m·s^{-1}) represents the velocity vector. In equation (2), ρ (kg·m^{-3}) is the fluid density, p (Pa) is the pressure, μ (Pa·s) is the dynamic viscosity and K_c (-) and C_k (-) are two coefficient in Darcy's law to dampen the fluid velocity belonging to the Carman-Kozeny drag force [25], and F_m is the body force that is acting on the liquid/vapour interface. In equation (3), h is the enthalpy (J), κ (W·(m·K)$^{-1}$) is the thermal conductivity, and Q_e (J) is the energy source term.

3. Results

In this section, the melt pool depth is evaluated for different wobbling conditions and the agreement between experimental measurements and numerical predictions is assessed. Figure 5 **(a)** compares the melt pool depth below the interface obtained from the experimental cross-section and the corresponding simulated melt pool profile. Figure 5 **(b)** summarizes the melt pool depth as a function of welding velocity, showing how the penetration changes with travel speed under the same laser and wobbling settings.

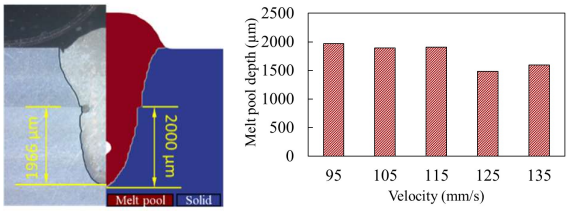

Figure 5. (a) Experimental and numerical comparison at 95 mm/s and (b) and comparison of melt pool height at different feed rate at 150 Hz wobble frequency.

Figure 6 shows that increasing the wobbling frequency reduces the melt pool penetration at the 7.5 mm cross-section. At 100 Hz the melt pool reaches a depth of ~3670 µm, which slightly decreases to ~3600 µm at 125 Hz and drops further to ~3190 µm at 150 Hz.

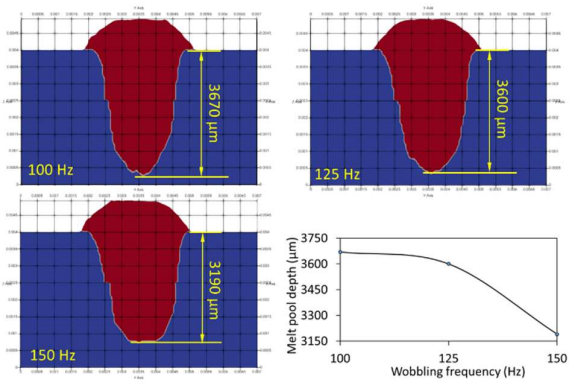

Figure 6. Melt pool depth at 7.5 mm cross-section at 100 Hz, 125 Hz and 150 Hz with 6 kW at 95 mm/s.

This trend indicates that higher wobbling frequencies distribute laser energy over a larger number of oscillation cycles per unit travel length, lowering the local dwell time (and peak heat input) [26]. Hu et al. [27] reported that higher oscillation frequencies required higher laser power to maintain full penetration. This suggests that beam oscillation redistributes the laser energy due to the higher beam velocity along the oscillation path, reducing the local interaction time and effective heat accumulation at a given position. As a result, additional laser power may be required to ensure sufficient penetration.

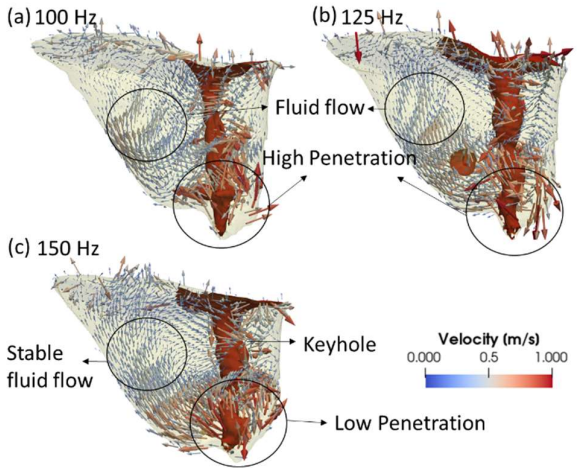

Figure 7. Fluid flow and keyhole depth at (a) 100 Hz, (b) 125 Hz and (c) 150 Hz

Figure 7 illustrates the simulated melt-pool flow field and keyhole morphology at different wobbling frequencies. As the wobbling frequency increases, the keyhole depth gradually decreases, indicating a reduction in penetration. This behaviour can be attributed to the shorter local interaction time of the laser beam at a given position, which reduces the local heat accumulation and limits sustained keyhole development. In addition, the flow field shows a change in the melt-pool dynamics with increasing frequency. At lower frequency, stronger and more irregular recirculating flow patterns with relatively higher local velocities are observed. In contrast, at higher wobbling frequency, the flow appears more uniform and comparatively less intense, suggesting a more stable melt-pool behaviour with reduced fluid velocity. These results indicate that increasing wobbling frequency not only suppresses excessive

keyhole growth but also promotes a more stable fluid-flow pattern within the molten pool.

4. Conclusion and Future work

This paper investigated laser lap wobble welding using three wobble frequencies to clarify how wobbling frequency influences melt-pool depth and the resulting weld morphology for battery interconnect applications. Quantitatively, the simulated melt pool depth at a 7.5 mm cross-section decreased with increasing frequency, from ~3670 µm (100 Hz) to ~3600 µm (125 Hz) and ~3190 µm (150 Hz) under identical power and travel speed conditions. A second comparison between experiment and simulation for penetration below the interface showed close agreement, with ~1966 µm (experiment) versus ~2000 µm (numerical), corresponding to an error of ~2%.

From these results, it is demonstrated that wobble frequency is a primary control parameter for penetration in lap wobble welding: increasing frequency (with other parameters fixed) leads to a systematic reduction in melt pool depth, and therefore shallower penetration. This is important because penetration depth directly governs joint formation and robustness in lap welds, and the observed sensitivity means that frequency selection must be treated as a design variable.

Future work will include: (1) extension of the parameter space by varying wobble amplitude and wobble diameter together with frequency to separate geometric spreading effects from frequency effects; (2) carrying out experimental work with all the simulates frequency.

References

[1] P. Stavropoulos, K. Sabatakakis, H. Bikas, Welding Challenges and Quality Assurance in Electric Vehicle Battery Pack Manufacturing, Batteries 2024, Vol. 10, Page 146 10 (2024) 146. https://doi.org/10.3390/BATTERIES10050146.

[2] M.F.R. Zwicker, M. Moghadam, W. Zhang, C. V. Nielsen, Automotive battery pack manufacturing – a review of battery to tab joining, Journal of Advanced Joining Processes 1 (2020) 100017. https://doi.org/10.1016/J.JAJP.2020.100017.

[3] A. Das, D. Li, D. Williams, D. Greenwood, Joining Technologies for Automotive Battery Systems Manufacturing, World Electric Vehicle Journal 2018, Vol. 9, Page 22 9 (2018) 22. https://doi.org/10.3390/WEVJ9020022.

[4] T.I.C. Buidin, F. Mariasiu, Battery Thermal Management Systems: Current Status and Design Approach of Cooling Technologies, Energies 2021, Vol. 14, Page 4879 14 (2021) 4879. https://doi.org/10.3390/EN14164879.

[5] A. Das, A. Barai, I. Masters, D. Williams, Comparison of Tab-To-Busbar Ultrasonic Joints for Electric Vehicle Li-Ion Battery Applications, World Electric Vehicle Journal 2019, Vol. 10, Page 55 10 (2019) 55. https://doi.org/10.3390/WEVJ10030055.

[6] Z. Zhao, S. Janasekaran, G.T. Fong, W. Tayier, J. Zhao, Laser Applications in Ceramic and Metal Joining: A Review, Metals and Materials International 2024 30:7 30 (2024) 1743–1782. https://doi.org/10.1007/s12540-023-01618-0.

[7] M. Dada, P. Popoola, Recent advances in joining technologies of aluminum alloys: a review, Discover Materials 2024 4:1 4 (2024) 86-. https://doi.org/10.1007/s43939-024-00155-w.

[8] R. Nopriantoko, Advancements in Welding Technology: A Comprehensive Review of Techniques, Materials, and Applications, Journal PEP Bandung 2 (2025) 62–110. https://doi.org/10.1234/JM6E4W53.

[9] S. Pang, K. Hirano, R. Fabbro, T. Jiang, Explanation of penetration depth variation during laser welding under variable ambient pressure, J. Laser Appl. 27 (2015) 022007. https://doi.org/10.2351/1.4913455.

[10] S.G. Kang, J. Shin, Numerical and experimental study on melt-pool heat transfer and weld characteristics in dual-mode fiber laser welding of aluminum alloy, Opt. Laser Technol. 158 (2023) 108805. https://doi.org/10.1016/J.OPTLASTEC.2022.108805.

[11] J. Li, P. Jiang, S. Geng, J. Xiong, Numerical and experimental study on keyhole dynamics and pore formation mechanisms during adjustable-ring-mode laser welding of medium-thick aluminum alloy, Int. J. Heat Mass Transf. 214 (2023) 124443. https://doi.org/10.1016/J.IJHEATMASSTRANSFER.2023.124443.

[12] C. Tan, Y. Liu, B. Xu, H. Wang, F. Liu, X. Gong, Z. Zeng, B. Chen, X. Song, Numerical and experimental study of thermal fluid flow and keyhole dynamic in laser welding of aluminum alloy assisted by electromagnetic field, Opt. Laser Technol. 157 (2023) 108718. https://doi.org/10.1016/j.optlastec.2022.108718.

[13] G. Chianese, Q. Hayat, S. Jabar, P. Franciosa, D. Ceglarek, S. Patalano, A multi-physics CFD study to investigate the impact of laser beam shaping on metal mixing and molten pool dynamics during laser welding of copper to steel for battery terminal-to-casing connections, J. Mater. Process. Technol. 322 (2023) 118202. https://doi.org/10.1016/j.jmatprotec.2023.118202.

[14] L. Chen, C. Wang, G. Mi, X. Zhang, Effects of laser oscillating frequency on energy distribution, molten pool morphology and grain structure of AA6061/AA5182 aluminum alloys lap welding, Journal of Materials Research and Technology 15 (2021) 3133–3148. https://doi.org/10.1016/j.jmrt.2021.09.141.

[15] J. Ma, F. Kong, B. Carlson, R. Kovacevic, J. Ma, F. Kong, B. Carlson, R. Kovacevic, Mitigating Zinc Vapor Induced Weld Defects in Laser Welding of Galvanized High-Strength Steel by Using Different Supplementary Means, Welding Processes (2012). https://doi.org/10.5772/53562.

[16] W. Meng, Z. Li, J. Huang, Y. Wu, J. Chen, S. Katayama, The influence of various factors on the geometric profile of laser lap welded T-joints, The International Journal of Advanced Manufacturing Technology 2014 74:9 74 (2014) 1625–1636. https://doi.org/10.1007/s00170-014-6114-y.

[17] S. Sanati, S.F. Nabavi, R. Esmaili, A. Farshidianfar, H. Dalir, A Comprehensive Review of Laser Wobble Welding Processes in Metal Materials: Processing Parameters and Practical Applications, Lasers in Manufacturing and Materials Processing 2024 11:2 11 (2024) 492–528. https://doi.org/10.1007/s40516-024-00245-w.

[18] E.C. Ozkat, P. Franciosa, D. Ceglarek, Development of decoupled multi-physics simulation for laser lap welding considering part-to-part gap, J. Laser Appl. 29 (2017). https://doi.org/10.2351/1.4983234.

[19] R. Oh, D.Y. Kim, D. Ceglarek, The Effects of Laser Welding Direction on Joint Quality for Non-Uniform Part-to-Part Gaps, Metals 2016, Vol. 6, Page 184 6 (2016) 184. https://doi.org/10.3390/met6080184.

[20] D. Basile, R. Al Botros, M. De Maddis, V. Razza, P. Franciosa, Monitoring part-to-part gap and laser power effects in remote laser welding of 1050 aluminum busbar-to-terminal connections via optical microphone sensing, Opt. Laser Technol. 192 (2025) 113494. https://doi.org/10.1016/j.optlastec.2025.113494.

[21] G. Chianese, S. Jabar, P. Franciosa, D. Ceglarek, S. Patalano, A multi-physics CFD study on the part-to-part gap during remote laser welding of copper-to-steel battery tab connectors with beam wobbling, Procedia CIRP 111 (2022) 484–489. https://doi.org/10.1016/J.PROCIR.2022.08.075.

[22] H.-K. Kim, Effects of part-to-part gap and the direction of welding on laser welding quality, (n.d.). https://scholarworks.unist.ac.kr/bitstream/201301/82863/2/000001696715.pdf

[23] S.C.K. De Schepper, G.J. Heynderickx, G.B. Marin, Modeling the evaporation of a hydrocarbon feedstock in the convection section of a steam cracker, Comput. Chem. Eng. 33 (2009) 122–132. https://doi.org/10.1016/J.COMPCHEMENG.2008.07.013.

[24] F. Municchi, H.R. Moran, I. El Mellas, O.K. Matar, M. Magnini, DIRECT NUMERICAL SIMULATIONS OF FLOW BOILING IN MICROCHANNELS, (2022) 4–6.

[25] V.R. Voller, C. Prakash, A fixed grid numerical modelling methodology for convection-diffusion mushy region phase-change problems, Int. J. Heat Mass Transf. 30 (1987) 1709–1719. https://doi.org/10.1016/0017-9310(87)90317-6.

[26] L. Chen, C. Wang, G. Mi, X. Zhang, Effects of laser oscillating frequency on energy distribution, molten pool morphology and grain structure of AA6061/AA5182 aluminum alloys lap welding, Journal of Materials Research and Technology 15 (2021) 3133–3148. https://doi.org/10.1016/j.jmrt.2021.09.141.

[27] K. Hu, W. Muneer, J. Zhang, X. Zhan, Effect of beam oscillating frequency on the microstructure and mechanical properties of dissimilar laser welding of AA2060 and AA6061 alloy, Materials Science and Engineering: A 832 (2022). https://doi.org/10.1016/j.msea.2021.142431.

euspen's 26th International Conference & Exhibition, Krakow, PL, June 2026
www.euspen.eu

Determination of packing parameters influence on the accuracy of precision moulded components by coordinate metrology

Guido Tosello[1], Giacomo Pietrobon[1,2], Alireza Mollaei Ardestani[1], Klaus Litorp[1], Carsten Lund[3], Lorenzo Didonè[2], Enrico Savio[2]

[1] *Department of Civil and Mechanical Engineering, Technical University of Denmark, 2800 Kgs. Lyngby, Denmark*
[2] *Università degli Studi di Padova, Dipartimento di Ingegneria Industriale, 35131 Padova, Italy*
[3] *Epsilonplus, 4295 Stenlille, Denmark*

guto@dtu.dk

Abstract
High-volume manufacturing of polymer components increasingly demands micrometric dimensional tolerances and stable geometric quality across multi-cavity moulds. We report a metrology-driven experimental study on a six-cavity tool and precision injection moulding process for polypropylene moulded rings, where a tactile coordinate measuring machine (CMM) and analytical weighing were used to quantify the effect of holding pressure (200–600 bar applied for 6 s) and holding time (1–4 s at 400 bar of packing pressure) on product dimensions (inner/outer diameters) and roundness, and part mass. A Design of Experiments (DOE)-based analysis shows that measurement repeatability is negligible compared with process-induced variation; expanded measurement uncertainties for the main dimensional responses are 0.6-0.7 µm, confirming capability for sub-micrometric discrimination. Across 10 cycles per setting (producing 60 parts per cycle), holding pressure/time significantly increases part mass and characteristic dimensions while decreasing roundness error up to an over-packing threshold. Cavity-dependent three-lobed deformation is mitigated as pressure approaches 500 bar, yet material inefficiency emerges beyond this level as sprue weight increases disproportionately versus product weight, consistent with gate-limited feeding. The results establish a practicable framework for advanced product and process control in precision injection moulding using coordinate metrology and provide actionable set-up recommendations balancing quality and sustainability.

Keywords: Precision injection moulding; Coordinate metrology; CMM; Multi-cavity moulds; DOE; Roundness; Process control.

1. Introduction

Precision injection moulding (IM) has evolved to deliver geometries with tolerances down to 10-20 µm over 10–100 mm characteristic lengths (i.e., 0.01-0.20%), driven by stringent functional and assembly requirements in medical, energy, mobility and consumer devices [1,2]. Achieving such performance at scale (i.e. 10^6-10^8 parts/year) hinges on robust product and process control across the full moulding cycle and all cavities within the mould [3].

Coordinate metrology – especially with tactile coordinate measuring machines (CMMs) probing – provides traceable dimensional and form measurements with sub-µm resolution and single-digit micrometric accuracy, enabling discrimination of small process-induced variations that might otherwise be buried by process as well as measurement noise [2]. These measurements provide reliable data for process optimisation and associated economic benefits [4].

Packing pressure and packing time are among the strongest levers for minimizing shrinkage/warpage in conventional parts, often through statistical optimization (e.g., design of experiments) or data-driven techniques (e.g., machine learning) [5–6].

Multi-cavity variation studies have shown that cavity-dependent mechanics and thermal fields produce substantial dimensional scatter. Instrumentation and modelling link these aspects to mould compliance and imbalance [7], as well as to differential shrinkage between external and internal geometrical characteristics, e.g., in micro rings [8].

This work develops and validates a metrology-centric methodology for mapping and controlling relationships between process parameters of the moulding cycle packing phase (holding pressure and holding time) and product characteristics (diameters, height, roundness, mass) for a thermoplastic mechanical part produced in a six-cavity two-plate cold-runner mould. In the study, measurement planning, part fixturing, CMM program design and uncertainty estimation are combined with factorial design of experiments (DOE) and effect screening.

The study uncovers how holding pressure and time drive part dimensions and form, identifies cavity-specific deformation modes, and quantifies an over-packing regime where further pressure and time primarily increase sprue mass rather than part mass. Control levers (parameter set-points, cavity-specific corrective actions, gate/runner improvements) to optimize quality and material efficiency are recommended.

2. Methodology

2.1. Part, material and moulding setup

The target product is a polypropylene (PP) ring-shaped mechanical part with thin sections (see Figure 1, left), manufactured on an Arburg 420C Golden Edition machine (equipped with a Ø25 mm diameter screw) using Total PPC 5660 (PP YA42-006). Production uses a six-cavity two-plate cold-runner mould (see Figure 1, right).

Figure 1. Precision moulded polypropylene ring (left); six-cavity two-plates cold-runner mould (left).

During the experiments, two groups of parameters were varied: (i) holding pressure at 200, 300, 400, 500, 600 bar (holding time fixed at 6 s); (ii) holding time at 1, 2, 3, 4 s (holding pressure fixed at 400 bar). For each setting, 10 cycles were targeted for process monitoring, so 60 parts were produced for each experiment to be measured.

2.2. Dimensional metrology planning and measurands

A tactile CMM (ZEISS PRISMO [9], maximum permissible error for length measurement MPE(E150) = 0.9 + L/400 µm, L in mm [10] and scanning single stylus form probing error P(FTU) = 1.0 µm [11]) measurement procedure was designed to maximize repeatability on irregularly shaped, flexible polymer parts lacking reference planes. The probe diameter was 3 mm, scanning speed was 5 mm/s, and probing force was 50 mN. The principal measurands considered were: inner diameter D1 (at a specific axial height of z6=6 mm from the top surface), outer diameter D2 (at z6), and roundness of D1 and D2 (both measured to z6) (see Figure 2). The coordinate features were built from point clouds acquired with controlled probing strategies on the selected planes. Roundness profile plots (consisting of 400 points collected around its circumference) were recorded for each cavity and setting.

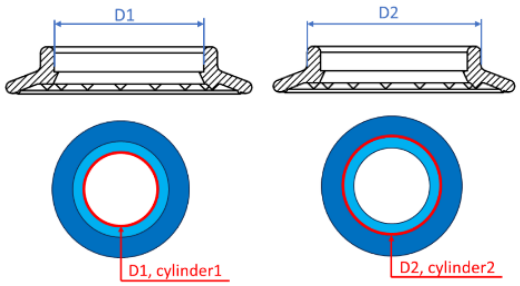

Figure 2. Measurands of the precision moulded polypropylene rings.

2.3. CMM part fixturing

The fixturing adopted a mechanical clamping concept with two spring clips and an optical flat (flatness 0.2 µm) to improve datum stability while avoiding part deformation (see Figure 3). The alignment was performed via a well-defined base alignment sequence and feature referencing at each run. Programmed strategies used a combination of discrete points, arcs and circular scan paths, with careful avoidance of clamp interference on bottom planes.

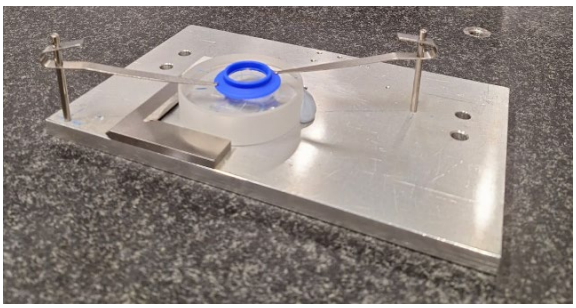

Figure 3. Ring fixturing on the CMM granite plane.

2.4. Mass measurements

The dataset also includes part mass from an analytical balance. Mass was measured on an OHAUS Discovery semi-micro analytical scale (declared repeatability 0.1 mg). The weighing step preceded CMM inspection and employed compressed-air cleaning to eliminate debris.

2.5. DOE design and analysis workflow

Two DOEs were executed in this work:

• DOE-1 (holding pressure 200-300-400-500-600 bar, 6 s holding time) to estimate the main effects of holding pressure along with cavity and cycle factors on D1, D2, roundness plots and mass partition between parts and sprue.

• DOE-2 (holding time 1-2-3-4 s hold at 400 bar holding pressure) to estimate the main effects of holding time along with cavity and cycle factors on D1, D2, roundness plots and mass partition between parts and sprue.

2.6. CMM measurement uncertainty and capability

An expanded uncertainty budget was estimated using the PUMA simplification of GUM [12], aggregating instrument resolution, reference standards, and a combined term for workpiece/fixturing/environment/procedure derived from five repeated measurements with re-clamping and re-alignment after each cycle. The resulting expanded uncertainties (k≈2) were: U(D1) = 0.7 µm and U(D2) = 0.6 µm, confirming that the measurement system is capable of discriminating process effects at the micrometric level, with sub-µm resolution.

3. Results

3.1. DOE-1: main effects of holding pressure

Holding pressure dominates cavity and cycle effects across all dimensional responses and part mass. Cavity differences exceed cycle-to-cycle differences, reflecting robust machine stability yet non-uniform cavity behaviour.

As pressure increases from 200 bar to 500 bar, both mass and characteristic diameters/height increase, while roundness error decreases, indicating enhanced packing that offsets material shrinkage and partially stabilizes shape. The improvement plateaus and can reverse at 600 bar for some features due to material over-packing (see Figure 4).

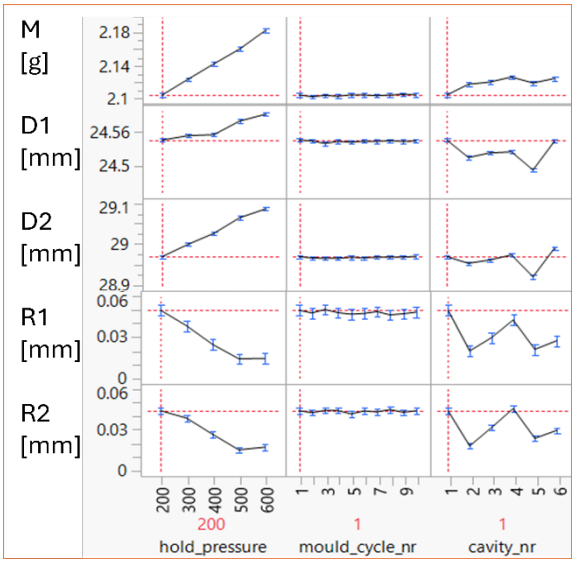

Figure 4. Influence of holding pressure, moulding cycle, cavity number on mass (M), ring internal diameter (D1), ring external diameter (D2), and their respective roundness (R1, R2).

Roundness plots reveal a three-lobed mode predominantly in cavities 1 and 4 for D1 and D2, which diminishes with pressure and is largely resolved near 500 bar (see Figure 5). Since inner and outer sections share the mode and respond similarly to pressure, the cause is attributed to flow-induced deformation rather than geometric errors in individual cavity inserts.

Averaging part mass across six cavities per cycle and pairing with the corresponding sprue mass reveals a nonlinear shift between 500 bar and 600 bar (see Figure 6). Sprue mass increases markedly more than product mass, indicating gate bottlenecking during the holding phase, with material accumulating in the runner system rather than feeding the cavities. This behaviour aligns with increasing thermos-viscous effects in the gate as it cools and solidifies under extended high pressure. The practical consequence is diminishing returns and material inefficiency above 500 bar for this geometry and tooling.

Although the best roundness is achieved near 500 bar, 400 bar is selected as a balanced set-point considering marginal quality gains vs. increased energy use, potential mould fatigue, and higher sprue mass at elevated pressures.

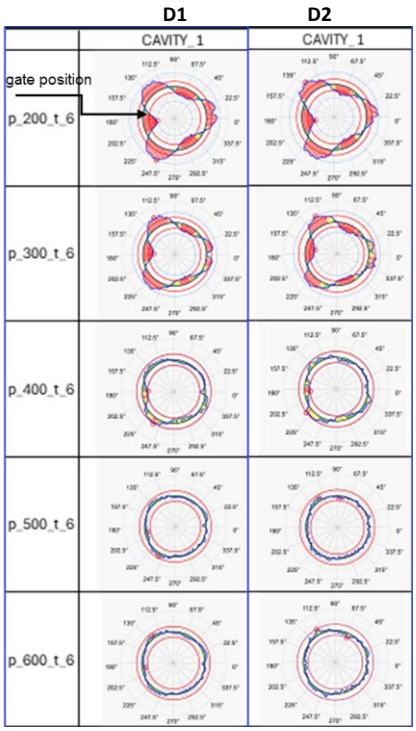

Figure 5. Influence of holding pressure on roundness R1 profile of the internal diameter (D1) and on roundness R2 of the external diameter D2.

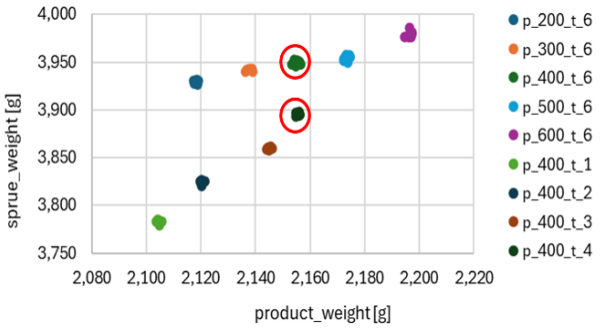

Figure 6. Influence of holding pressure and holding time on the moulded ring mass roundness and the sprue mass. An increase of packing time from 4 s to 6 s with a packing pressure of 400 bar cause an increase of sprue mass while the moulded product mass remains constant (see details in the red circles).

3.2. DOE-2: main effects of holding time

Holding time dominates cavity and cycle effects, echoing DOE-1: process parameters ≫ cavity ≫ cycle.

Mass and characteristic dimensions increase with holding time (from 1 s to 4 s), confirming slight improved shrinkage compensation under extended packing. Roundness decreases modestly but exhibits limited benefit beyond 3 s (see Figure 7).

Three-lobed deformation in cavities 1 and 4 remains the dominant mode and is not fully eliminated by longer holding times, reinforcing a flow/temporal imbalance rather than static cavity geometry error (see Figure 8). A recurring protrusion at 180° (gate location) is observed in roundness plots, compatible with differential local shrinkage because the gate region cools last.

Both sprue and product mass increase with time, but product gains saturate earlier than sprue gains: for some pairs of settings with equal pressure but different times, longer time yields a heavier sprue with negligible product mass benefit (see Figure 6). This suggests a wasteful holding regime and reinforcing the selection of shorter holding times.

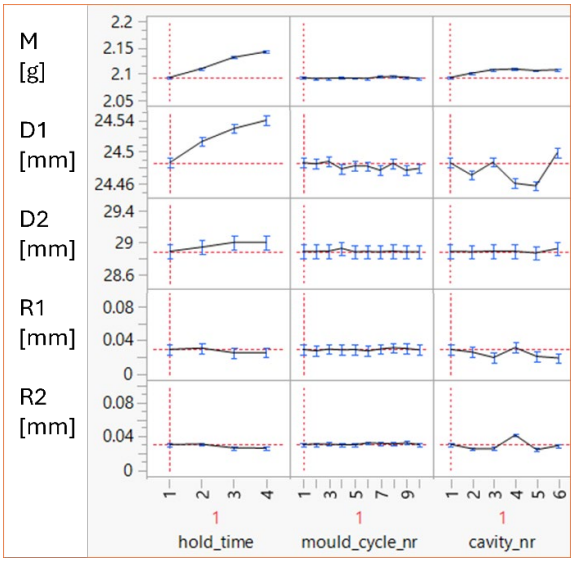

Figure 7. Influence of holding time, moulding cycle, cavity number on mass (M), ring internal diameter (D1), ring external diameter (D2), and the respective roundness (R1, R2).

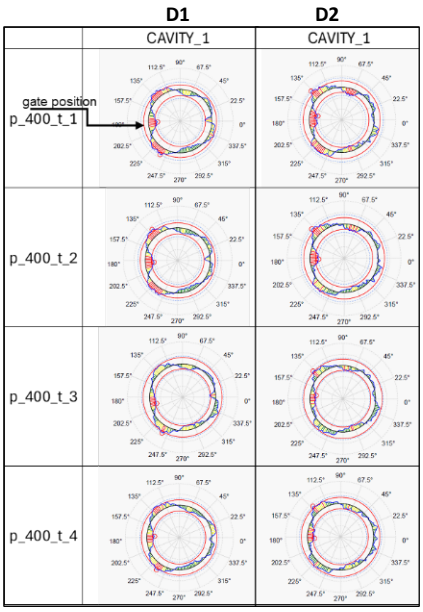

Figure 8. Influence of holding time on roundness R1 profile of the internal diameter (D1) and on roundness R2 of the external diameter D2.

4. Discussion

4.1. Cavity influence on part for error

The consistent three-lobed mode in cavities 1 and 4 across inner and outer sections indicates a global deformation mechanism (e.g., asymmetric flow front, local thermal gradient, or runner balancing) rather than localized cavity machining defects. Its mitigation under higher pressure suggests that improved local packing and more uniform pressure transmission can counteract the deformation, yet long-term elimination should focus on runner/gate balance and, potentially, local temperature control near the problematic cavities.

4.2. Overpacking and material efficiency

Material allocation between parts and sprue provides a sustainability perspective on process parameters setting selection. Beyond ≈500 bar or long holding times, the gate becomes a dominant restriction as viscosity increases during cooling, so additional energy predominantly packs the runner/sprue rather than the parts. In production, this raises scrap (sprue regrind) and energy use without proportional quality gains. The data support moderate pressure levels (e.g., 400 bar) and short holding times (e.g., 1 s) for the studied geometry/material/tooling combination, achieving robust dimensional targets while minimizing waste and energy consumption.

5. Conclusion and Future work

An advanced product and process control framework for precision injection moulding based on high-accuracy coordinate metrology and designed experiments has been demonstrated. Key outcomes are:

1. A CMM-based measurement strategy with robust fixturing and program design can deliver sub-µm expanded uncertainties on critical dimensions, enabling clear discrimination of process, cavity, and moulding reproducibility effects.
2. Holding pressure and holding time are dominant factors during the packing phase. Their increase raises part mass and characteristic dimensions while reducing roundness error up to an over-packing threshold.
3. Cavity-dependent lobing reflects flow-induced deformation and is mitigated near 500 bar. Addressing runner/gate balance is recommended for full elimination.
4. Sprue vs product mass analysis reveals diminishing returns beyond 500 bar or prolonged holding, supporting moderate pressure (~400 bar) and short holding time (~1 s) to balance quality, energy and material efficiency.

The results are specific to the considered PP moulded ring, a particular six-cavity mould and a defined machine. The study intentionally focused on the holding phase (i.e., pressure and time). Future work should integrate melt and mould temperatures, injection velocity, and switchover position to complete the factor space (i.e., including also the filling phase). Finally, only tactile CMMs were used for measurements in this study. Optical CMMs and X-ray computed tomography systems may be considered for speed and full 3D representation capabilities respectively. However, uncertainty of these systems should be carefully considered and verified if they are sufficient for precision moulding applications with multi-cavity moulds.

Acknowledgements

This research work was undertaken in the context of DIGIMAN4.0 project (“DIGItal MANufacturing Technologies for Zero-defect Industry 4.0 Production”, http://www.digiman4-0.mek.dtu.dk/). DIGIMAN4.0 is a European Training Network supported by Horizon 2020, the EU Framework Programme for Research and Innovation (Project ID: 814225). Support from the Department of Civil and Mechanical Engineering (DTU CONSTRUCT, https://construct.dtu.dk/) at the Technical University of Denmark is greatly acknowledged.

References

[1] Greener, J., Wimberger-Friedl, R. (2006). Precision Injection Molding: Process, Materials, and Applications. Hanser. ISBN 1569904006

[2] Tosello, G., Hansen, H.N., Gasparin, S. (2009). Applications of dimensional micro metrology to the product and process quality control in manufacturing of precision polymer micro components, CIRP Annals, Volume 58, Issue 1, Pages 467-472, https://doi.org/10.1016/j.cirp.2009.03.027

[3] Kulkarni, S. (2017). Robust Process Development and Scientific Molding. Hanser.

[4] Savio, E., De Chiffre, L., Carmignato, S., Meinertz., J. (2016). Economic benefits of metrology in manufacturing. CIRP Annals, Volume 65, Issue 1, Pages 495-498, https://doi.org/10.1016/j.cirp.2016.04.020

[5] Guerra, N.B., Reis, T.M., Scopel, T. et al. (2023) Influence of process parameters and post-molding condition on shrinkage and warpage of injection-molded plastic parts with complex geometry. Int J Adv Manuf Technol 128, 479–490, https://doi.org/10.1007/s00170-023-11782-7

[6] Zhao, Ny., Lian, Jy., Wang, Pf. et al. (2022) Recent progress in minimizing the warpage and shrinkage deformations by the optimization of process parameters in plastic injection molding: a review. Int J Adv Manuf Technol 120, 85–101, https://doi.org/10.1007/s00170-022-08859-0

[7] Mahshid, R., Zhang, Y., Hansen, H. N., Slocum, A. H. (2021). Effect of mold compliance on dimensional variations of precision molded components in multi-cavity injection molding, Journal of Manufacturing Processes, Volume 67, 2021, Pages 12-22, https://doi.org/10.1016/j.jmapro.2021.04.048

[8] Baruffi, F., Calaon, M., Tosello, G., (2018) Effects of micro-injection moulding process parameters on accuracy and precision of elastomer micro-rings,” Precision Engineering 51, 353–361, https://doi.org/10.1016/j.precisioneng.2017.09.006

[9] Coordinate Measuring Machine CMM-001-Zeiss-PRISMO, Mechanical Engineering Metrology Laboratory, Department of Civil and Mechanical Engineering, Technical University of Denmark, DOI: 10.57735/6095

[10] ISO 10360-2:2009, Geometrical product specifications (GPS) — Acceptance and reverification tests for coordinate measuring machines (CMM) – CMMs used for measuring linear dimensions

[11] ISO 10360-5:2020, Geometrical product specifications (GPS) — Acceptance and reverification tests for coordinate measuring machines (CMM) – Part 5: Coordinate measuring machines (CMMs) using single and multiple stylus contacting probing systems using discrete point and/or scanning measuring mode

[12] ISO 14253-2:2011, Geometrical product specifications (GPS) — Inspection by measurement of workpieces and measuring equipment – Part 2: Guidance for the estimation of uncertainty in GPS measurement, in calibration of measuring equipment and in product verification

euspen's 26th International Conference & Exhibition, Krakow, PL, June 2026
www.euspen.eu

Electrochemical accretion of high entropy alloy traces from aqueous electrolytes towards modular moulds, tools and integrated sensing applications

Krishna Kumar Saxena[1,2,*], Adnan Al Farisi[1,2], Muhammad Hazak Arshad[1,2], Dominiek Reynaerts[1,2]

[1]*KU Leuven, Department of Mechanical Engineering, Micro -& Precision Engineering Group, Belgium.*
[2]*Member FlandersMake, Belgium*
krishna.saxena@kuleuven.be

Abstract
High-entropy alloys (HEAs) exhibit exceptional combinations of strength, wear resistance, and thermal stability due to their multi-element compositions and high configurational entropy. This work investigates the electrochemical accretion of CoCuFeMoWNi HEA traces from an aqueous electrolyte. The influence of key process parameters, including voltage, pulse characteristics, pH, and electrolyte temperature, on deposit morphology and composition was examined. Results demonstrate the feasibility of producing multi-element HEA deposits via controlled electrochemical accretion, indicating a promising route for integrating HEA features into manufacturing process chains.

Keywords: Electrochemical manufacturing, electrochemical deposition, electrochemical accretion, high entropy alloy.

1. Introduction

High-entropy alloys (HEAs) are a relatively new class of metallic materials composed of multiple principal elements, typically five or more, in near-equiatomic proportions [1]. Unlike conventional alloys that are based on one dominant element, HEAs derive their stability from high configurational entropy, which lowers the Gibbs free energy of the system ($\Delta G = \Delta H - T\Delta S$). This thermodynamic effect promotes the formation of stable solid-solution phases rather than brittle intermetallic compounds. As a result, HEAs often exhibit a unique combination of mechanical strength, hardness, corrosion resistance, and thermal stability, making them attractive for demanding environments where conventional alloys show performance limitations. Because of these characteristics, HEAs are being actively explored for applications in sectors such as aerospace, energy systems, high-value components, and precision manufacturing [2], [3]. In particular, the ability to introduce HEA layers or localised material features through surface engineering provides opportunities for advanced tooling technologies. Tool and mould materials frequently experience severe thermal cycling, oxidation, and abrasive contact while maintaining strict dimensional tolerances. Materials capable of retaining mechanical and chemical stability under such conditions are therefore of high interest. Beyond structural functionality, HEAs are also promising for high-temperature sensing applications (> 1200 degC) due to their compositional stability and resistance to degradation in harsh environments, enabling durable conductive paths or sensing elements integrated directly within structural components.

Electrochemical accretion or layered deposition offers a promising route for fabricating such material systems on metallic substrates [4], [5]. Compared with conventional synthesis routes such as casting, sputtering, or laser-based deposition, electrochemical manufacturing operates at relatively low temperatures and can be implemented with lower energy consumption. In addition, electrochemical parameters including current density, electrolyte composition, and pulse conditions provide significant control over the composition and morphology of deposited layers. However, the electrodeposition of multi-component HEAs remains challenging because the constituent elements often exhibit substantially different reduction potentials and deposition kinetics, complicating controlled co-deposition from aqueous electrolytes [5].

This work presents an initial investigation into the electrochemical deposition of a six-component high-entropy alloy (HEA), CoCuFeMoWNi, on steel substrates representative of mould base materials. The selected alloy system is known for its favorable combination of hardness, wear resistance, and corrosion stability at elevated temperatures, and typically forms a dual-phase microstructure consisting of FCC and BCC phases. Electrodeposition experiments are carried out using aqueous electrolyte systems [6], focusing on how key process parameters including current density, pulse duty cycle, pulse frequency, electrolyte pH, and bath temperature affect the formation of localised HEA deposits. By systematically studying these variables, the work explores the conditions required to achieve stable co-deposition of the multiple alloying elements. The objective of this study is to assess the feasibility of producing localised, multi-element HEA traces through electrochemical accretion, with potential relevance for modular mould and tooling concepts as well as for the fabrication of conductive paths suitable for high-temperature sensing applications.

2. Experimentation

A multi-element aqueous electrolyte was formulated to enable the electrodeposition of CoCuFeMoWNi high-entropy alloy (HEA) system. The electrolyte consisted of $NiSO_4.7H_2O$ (0.15 mol/l), $CoCl_2.6H_2O$ (0.02 mol/l), $Na_2WO_4.2H_2O$ (0.2 mol/l), $FeSO_4.7H_2O$ (0.02 mol/l), $Na_2MoO_4.2H_2O$ (0.007 mol/l), $CuSO_4.5H_2O$ (0.007 mol/l). Hydrated metal salts were selected due to their high solubility and stable ion release in water, ensuring consistent metal ion availability during deposition. The electrolyte composition was designed considering electrochemical first principles i.e. elements with more negative reduction potentials were introduced at higher concentrations to promote incorporation into the deposit. Interactions such as induced co-deposition (e.g., Fe facilitating Mo and W reduction) and competitive deposition (e.g., Ni competing with Mo and W)

were also considered. Citric acid (0.4 mol/l) was used as a complexing agent to stabilise ions and moderate potential differences, while boric acid (0.4 mol/l) acted as a buffer to maintain stable pH conditions. Experiments were conducted in a lab-scale beaker setup using a gold-coated rod as the anode and W-EDM cut steel strips (5 mm width) as cathodes. Process parameters included voltages of 1-2 V, pulse-on times of 50-1000 µs, duty cycle of 50%, electrolyte temperatures of 20-50 °C, and pH values of 3, 6 under constant charge conditions (Q = 12.69 C).

3. Results and discussion

Figure 1 summarises the results of the electrochemically accreted HEA traces where voltage was used as a key parameter instead of current density to achieve better control over the process. The configurational entropy (ΔS_{conf}) of the deposits was estimated from the atomic fractions obtained by EDX analysis (oxygen excluded) using the Boltzmann expression $\Delta S_{conf} = -R\Sigma c \ln c$, where c denotes the atomic fraction of each element.

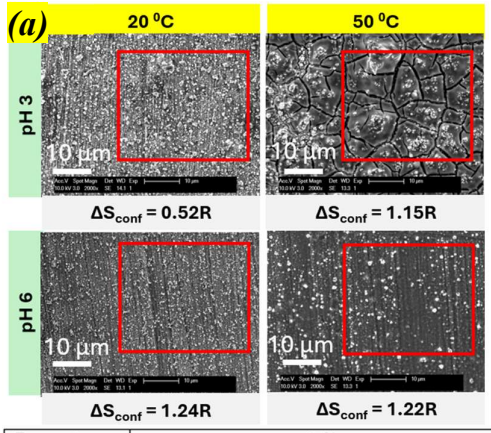

Parameters		wt. %					
pH	T (°C)	W	Mo	Cu	Ni	Co	Fe
3	20	2.85	1.73	85.67	2.85	0.00	6.89
	50	29.05	7.32	49.83	3.63	0.00	10.16
6	20	7.63	3.64	55.33	9.11	5.32	18.96
	50	17.76	10.45	52.98	10.28	0.51	8.02

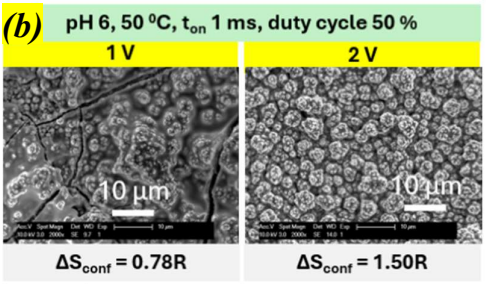

	wt. %					
Voltage	W	Mo	Cu	Ni	Co	Fe
1 V	15.14	7.11	70.37	2.03	0.00	5.34
2 V	27.33	7.35	38.80	12.04	4.64	9.84

Figure 1. (a) HEA traces deposited under varying pH and temperature conditions using a constant direct voltage of 1 V. (b) SEM micrographs and corresponding EDX-derived compositions (excluding oxygen) of the traces deposited under pulsed voltage conditions at 1 V and 2 V.

Figure 1(a) shows the evolution of surface morphology and composition at different pH values and temperatures under a constant potential of 1 V. At pH 3, the deposits were dominated by copper and cobalt was not detected. In contrast, at pH 6 all six intended elements were incorporated into the deposit. The calculated entropy values at pH 6 were comparable for both investigated temperatures (20 °C and 50 °C). The layer formed at 50 °C exhibited a more homogeneous morphology and contained relatively higher amounts of Mo and Ni. Further experiments were performed under pulsed electrochemical accretion conditions at pH 6 using applied voltages of 1 V and 2 V (Figure 1(b)). At 1 V, cobalt was still absent from the deposits despite the presence of citric acid in the electrolyte, whereas nickel was detected. Increasing the voltage to 2 V enabled the incorporation of all six elements, although cobalt remained the least abundant, while tungsten and copper showed preferential deposition. Morphologically, the deposit formed at 1 V displayed cracks and isolated granular features, possibly associated with differences in grain growth. In contrast, the layer deposited at 2 V showed a more uniform granular surface without visible cracking. The maximum configurational entropy reached 1.5R at 2 V (Figure 1(b)), approaching the typical HEA range of 1.61–1.76R expected for equiatomic six-element alloys. Figure 2 presents the elemental distribution map for the deposit obtained at 2 V (Fig. 1(b)), confirming the spatial presence of all six elements across the surface. The granular surface texture together with the measured roughness (Sa = 0.39 µm, Sensofar®) further indicates the formation of a successful deposit.

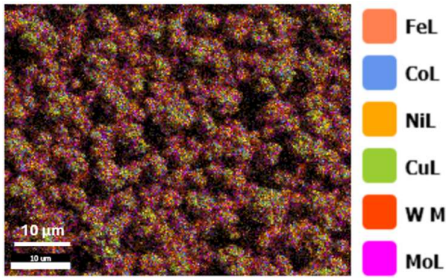

Figure 2. Elemental distribution map (oxygen excluded) of the surface deposited at 2 V (Fig. 1(b)), confirming the presence of all six HEA constituents across the workpiece coupon.

4. Concluding remarks

This study investigated the electrochemical synthesis of a six-component HEA (CoCuFeMoWNi) using an aqueous electrolyte system. The preliminary experiments resulted in a maximum configurational entropy of approximately 1.5R, which approaches the theoretical entropy range of 1.61-1.76R expected for six-element HEAs with atomic fractions between 5–35%. Under suitable conditions pH 6, electrolyte temperature of 50 °C, applied voltage of 2 V, pulse-on time of 1 ms, and a duty cycle of 50%, the deposited layer exhibited a uniform granular morphology without visible surface cracking. Elemental analysis further confirmed the successful incorporation of all six alloying elements. Future work will focus on refining the electrolyte composition and optimising electrochemical process parameters to achieve improved control over elemental distribution and phase formation.

Acknowldegement

The authors would like to acknowledge funding support from FWO senior postdoctoral project #1235425N, KU Leuven IOF C3 funds #C3/23/060 VLAIO IM # HBC.2025.0277.

References

[1] Choi W M, Jo Y H, Sohn SS, Lee S, Lee BJ 2018, *npj Comput. Mater.*, **4**, no. 1, pp. 1-9.

[2] Klink A, Harst S, Olivier M, Tombul U, and Bergs T 2020, *Procedia CIRP*, **95**, pp. 178-182.

[3] Martin A, Pfaffendorf F, and Schubert A 2021, *proc. of. INSECT 2021*, p. 93.

[4] Wittenburg J, et al. 2024, Procedia CIRP, **123**, pp. 197-202.

[5] Shojaei Z, Khayati G R, et. al. 2022, *Int. J. Miner. Metall. Mater.*, **29**, no. 9, pp. 1683-1696.

[6] Ahmadkhaniha D, Kruemmling J, and Zanella C 2022, *J. Electrochem. Soc.*, **169**, no. 8, p. 082515.

Session 4: Advances in Precision Engineering

euspen's 26th International Conference & Exhibition, Krakow, PL, June 2026
www.euspen.eu

Design of Test Setup for Measurement of Microslip in Clamped Interfaces using a Balanced Heterodyne Interferometer with Picometer-Resolution

Walter Knulst[1], Pablo Ruiz Beltri[2], Joris Looman[3], Kees Verbaan[2]

[1] *VSL, National Metrology Institute, Thijsseweg 11, 2629 JA, Delft, The Netherlands*
[2] *Mechanical Engineering (DPE-group), Eindhoven University of Technology, Groene Loper 3, 5612 AE, Eindhoven, The Netherlands*
[3] *ASML B.V., De Run, Veldhoven, The Netherlands*

wknulst@vsl.nl

Abstract

This paper introduces a novel experimental approach for characterizing microslip with picometer-level resolution, utilizing the picodrift interferometer, a balanced twin heterodyne interferometric system developed at VSL, the National Metrology Institute in The Netherlands. The instrument provides traceable displacement measurements with a short-term uncertainty of 10 pm and long-term stability below 0.5 nm, enabling unprecedented sensitivity for studying pre-sliding behavior. In this paper the design of a dedicated insert for integration into the interferometer will be presented for applying controlled clamping forces up to 2 kN and tangential loads up to 15 N (push and pull), representative for industrial bolted connections. The setup minimizes environmental influences and ensures alignment within 100 µrad. Preliminary experiments demonstrate stable operation, high signal quality, and inline force measurements. Microslip measurements captured hysteresis loops consistent with pre-sliding behavior of aluminum parts. Under a medium clamping force of 170 N and a tangential load of 7.5 N, a residual offsets of +15.5 nm was observed after a single push-pull cycle (cycle frequency of 1 Hz), confirming irreversible displacement trends that are reduced after repeating motion references, indicating asperity settling. This study establishes a platform for systematic microslip investigation under controlled conditions and opens investigations into future design strategies for picometer-stable clamped interfaces in high-tech systems.

Keywords: microslip, pre-sliding behavior, clamped surfaces, hysteresis loop, metrology, laser interferometer, displacement

1 Introduction

As position requirements for motion stages become more stringent down to subnanometer levels, and at the same time the forces at the interfaces increase due to higher acceleration levels, shortening cycle times, physical phenomena like microslip between clamped parts on the moving platforms become more relevant. Clamped samples on moving stages are exposed to high tangential forces during acceleration phases which induce pre-sliding behaviour due to surface imperfections and irregularities between the clamped surfaces. Typically, high clamping forces prevent macroslip which refers to overall sliding of the surface beyond the global friction force. However, in the regime below stiffer contact points are less likely to deform and may slide, whereas more compliant (flexible) points remain stationary. After the movement at standstill, the compliant points of contact remain unchanged, but the stiffer ones have sled to a new position, changing the average relative position of the two clamped surfaces, and this effect is called microslip.

The goal of this work is to design and develop an experimental setup to characterize microslip in clamped connections to understand and quantify the sensitivity to relevant parameters that determine this pre-sliding behavior. The scope is to study the microslip under typical conditions of firmly bolted connections between flat, industrial machined surfaces. The results will be compared to theoretical models describing the pre-sliding behavior of multi-asperity contacts [1].

Ideally, the global average shift between the asperities, i.e. the displacement between the point of application of the tangential force and the furthest contact point, has to be detected. In three dimensions, the tangential force vector generates a slip front line within a plane perpendicular to the force vector at the contact height. Therefore, measuring the displacement of this line at the force application point is of particular interest when experimentally studying microslip.

2 Picodrift interferometer as metrology platform

Experimental characterization of microslip in clamped interfaces requires a metrology solution that combines extreme displacement sensitivity, long-term stability, and traceability to the SI unit of length. Microslip occurs in the pre-sliding regime, where tangential displacements are typically in the range of nanometers down to sub-nanometer levels, often superimposed on elastic deformation and thermal drift.

To validate analytical models (e.g., Hertzian contact mechanics, Mindlin's theory) and multi-asperity simulations [1], the measurement system must detect irreversible displacements below 1 nm over repeated loading cycles, maintain thermal stability better than 10 mK/h to avoid drift masking microslip, and provide inline integration with force application mechanisms without compromising alignment. These requirements exceed the capabilities of most tribological test benches [2] and necessitate a non-contact interferometric approach with picometer-level resolution.

The picodrift interferometer developed at VSL (National Metrology Institute in The Netherlands), is a balanced twin heterodyne interferometric instrument designed for dimensional stability studies and calibration of displacement sensors with uncertainties in the 10 pm range [3][4]. Its architecture (see figure 1) employs two heterodyne interferometers with equal optical path lengths, cancelling common-mode disturbances such as thermal expansion of the base plate and optical elements. A

dedicated refractometer arm compensates for air refractive index variations. The laser source is stabilized using the Pound-Drever-Hall technique [5] and referenced to a stabilized HeNe-laser for SI traceability [6]. In the sample arm the object will be placed and the interferometer beam is reflected off both ends so that only the length change will be measured and not the lateral movement. Sensors monitor the environmental conditions and material temperatures. The entire instrument operates inside a thermally insulated enclosure achieving 1 mK/h stability [4].

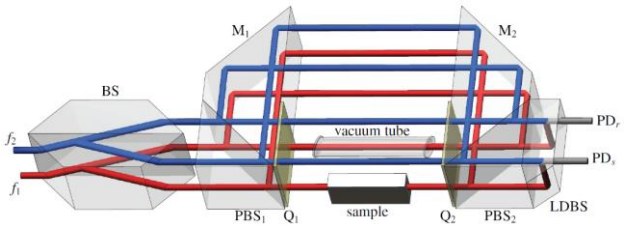

Figure 1: Schematic representation of the balanced double-sided heterodyne interferometer [4], with upper and lower beam at two different modulation frequencies, f_1 and f_2. The beamsplitter BS provides two beams, one into the sample (s) and one into the refractometer (r) interferometer. The polarizing beamsplitters (PBS1 and PBS2), quarter-wave-plates (Q_1 and Q_2) and mirrors (M_1 and M_2) make sure the interferometer beam goes around and touches the sample at both reflective ends. In the refractometer, the interferometer beam passes through the vacuum tube to balance the optical path length. The lower and upper interferometer arms are combined in the final beamsplitter optics (LDBS), and the interference signal is detected by photodiodes (PD_s and PD_r). The system is fibre-coupled for receiving incoming laser beams and outcoupling to the photodiodes.

Key performance after thermal acclimatization is on the short-term 10 pm over seconds to minutes, medium-term 100 pm over an hour and long-term < 0.5 nm over 20 hours [7][8]. These characteristics make picodrift interferometer uniquely suited for detecting microslip displacements, which typically range from tens of nanometers in initial cycles to sub-nanometer offsets after asperity settling [9][10]. Previous applications include calibration of piezo actuators (virtual standards) [11][12] and thermal expansion studies of gauge blocks, confirming robustness under controlled environmental conditions.

The microslip test insert in the sample arm of the picodrift interferometer must comply with strict geometric and optical constraints to preserve its intrinsic stability and enable reliable detection of microslip at picometer resolution. The available space between the two polarizing beam splitters (PBS) is only 95 mm and the insert must avoid obstruction of reference and measurement beams with beam separation of 30 mm vertically and horizontally [3]. Reference surface of the clamped blocks should be mirror polished or have bonded mirrors attached to achieve > 70 % reflectivity. Pre-alignment of the clamped blocks and their rotation (pitch and jaw) during force activation should be limited to ±92 µrad to ensure signal integrity [10]. Heat dissipation from actuators and force sensors must be minimized. The Abbe error should be minimal so that the optical axis of the sample arm is as close as possible to the contacting surfaces of the clamped blocks.

3 Microslip test setup design

The microslip test setup for the picodrift interferometer must generate and measure the microslip behavior between two clamped surfaces, allowing for the parameters studies such as dependence on normal and tangential force, and surface and material properties.

Applying the force in-line with the contact plane is crucial. Any deviation introduces a moment arm, resulting in torque and uneven contact pressure distribution which affects microslip behavior. While sample compliance may cause a delay in the slip-line position as it moves away from the contact plane, the samples in this study are sufficiently stiff. Therefore, this delay is negligible, and the key parameter becomes the shift of the global average position after force relaxation. In this relaxed state, the slip-line position remains constant within the slip plane. Nonetheless, real-time microslip characterization is also desirable. Hence, measuring as close as possible to the contact plane is included as a design guideline.

3.1 Design specifications microslip test setup

After evaluation of the working ranges for the microslip experiments and functional conditions of the picometer interferometer the requirements are formulated for the microslip test setup and summarized in **table 1**.

Table 1: Requirements for the microslip test setup

	REQUIREMENTS
1	Measure with high resolution (sub-nanometer displacements)
2	Generate and measure a normal force up to 2 kN between the samples
3	Generate and measure a tangential (push/pull) force up to 15 N between the samples
4	Generate a contact pressure of at least 50 MPa between the samples
5	Ensure accurate alignment between the samples and the picodrift interferometer beams (± 92 µrad)
6	Obtain enough signal power on the detector of the interference of the sample laser beam (100 – 150 mV)
7	Flexibility in the sample geometry and materials
8	Minimize heat dissipation to avoid disturbing the measurement
9	Fit in the available space (95 mm x 50 mm x 40 mm) avoiding beam blockage (beam clearance radius 2.5 mm)

3.2 Metro plate

The metro plate enables the alignment of the clamped sample to the interferometer beams and maintains alignment during the measurement. Therefore, the metro plate must enable sequential alignment of each sample block in two degrees of freedom (DOF), namely *Ry* and *Rz*, for a total of four DOF with high resolution. However, for clamped samples the *Ry* tilt of the top sample is defined by its contact with the bottom sample and is thus coupled. In the microslip test setup design, manufacturing tolerances are assumed to be sufficient to avoid implementing relative *Ry* alignment between the samples.

Alignment is performed sequentially: first the bottom sample (*Rz*, *Ry*), followed by the top sample (*Rz, Ry*), although final alignment of the clamped sample is possible and desired to optimize the signal power.

3.3 Normal force frame

The normal force frame (NFF) is responsible for accurately generating and measuring the clamping force applied to the sample blocks. This force must be strictly perpendicular to the plane of contact and must not interfere with the alignment of the sample blocks. Therefore, the NFF must either be alignable or compliant with the samples' alignment mechanisms. The NFF design is based on the bolt connection concept to directly clamp the sample blocks and generate the required normal force. A load cell (ALTHEN cylindrical load washer M3 type ALF525) is placed in series with the sample blocks to measure the clamping force.

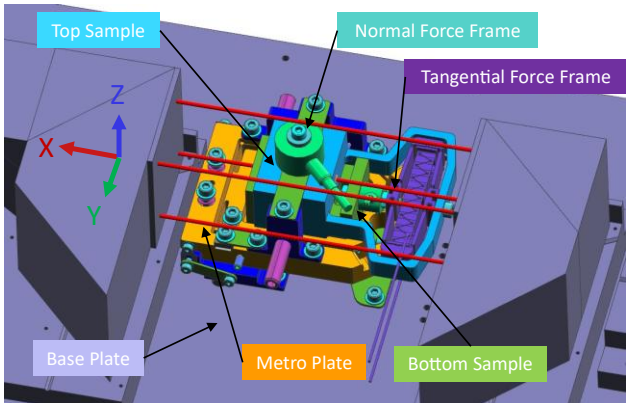

Figure 2: CAD view of the microslip test setup integrated into the picodrift Interferometer with the different functional parts.

To allow sequential alignment of the samples, the clamping force must be applied after alignment. It also serves as a locking mechanism, restraining *Rz* rotation of the top sample. However, torque-based clamping can introduce misalignment during tightening. To mitigate this, a torque release mechanism is implemented. A thin leaf spring is inserted between the top sample and the load cell and fixed in place using bolts at each *Rz* adjustment block. Additionally, a small axial needle bearing is placed between the washer-nut pair and the bottom sample to reduce the impact of the tightening torque in the alignment of the samples.

This setup allows for precise alignment and symmetric stress distribution. Moreover, since microslip is most relevant in bolted connections, this concept closely replicates real-world conditions.

3.4 Tangential force frame

To correctly measure microslip, the relative displacement of the reference surfaces of the clamped samples must be in the direction of the optical axis. This ensures that the true displacement is detected by the interferometer and that the signal remains stable throughout the experiment. While some displacement or tilt in other directions may occur due to the nature of microslip, excessive tilt can lead to signal loss.

Since the actuation surfaces and reference surfaces are not colinear and may differ in orientation due to manufacturing tolerances, applying a force aligned with the optical axis becomes challenging. Only the reference surfaces are aligned precisely using interferometer feedback, so the tangential force frame must accommodate misalignment between the actuation surfaces.

The tangential force frame (TFF) design is based on the car jack concept and utilizes the APF705 amplified piezoelectric actuator from Thorlabs. This actuator features an open frame that preloads the piezoelectric element, which bridges two opposite joints. When voltage is applied, the piezo element expands slightly; this displacement is amplified by the frame, resulting in a noticeable inward movement between the other two joints. Conversely, applying a negative voltage causes the piezo to contract, pushing the actuation faces outward.

Although the APF705 is primarily designed for precise positioning, its force capabilities, amplified range, and compliance in the actuation direction and in *Rz* allows to cope with tolerances in the position of the sample blocks.

To measure the tangential force exerted between the sample blocks, a load cell (ALTHEN load cell type ALF259) is integrated between the actuator frame and the bottom sample. The load cell features threaded studs on both ends, allowing it to measure both compression and tension forces within the force loop.

The actuator is intended to be controlled in closed-loop control using feedback force readings from the load cell. However, during initial experiments it is operated in open-loop mode. A reference voltage signal is applied to the actuator, mimicking the desired force profile. The actual force is measured by the load cell and compared to the displacement recorded by the picodrift interferometer to characterize microslip behavior.

3.5 Sample blocks

The plane of contact is defined by the interface between the top and bottom sample blocks and is characterized by asperity geometry, friction coefficient, shear modulus, surface flatness, and structural stiffness all affecting the microslip behavior. To achieve the required contact pressure while maintaining stability, the nominal area must be carefully dimensioned. The shape should be uniform to ensure the slip front moves directly opposite to the tangential force, avoiding tilt unless caused by asperity distribution. To reach the required contact pressure of 50 MPa with a clamping force of 2 kN, a ring contact area of 27.6 mm^2 is designed, preferred for even pressure distribution, and to minimize the gap between the maximum and minimum contact pressures. The bottom sample includes a compliant extrusion, and the contact area is slightly larger than that of the top sample to maintain consistency during microslip.

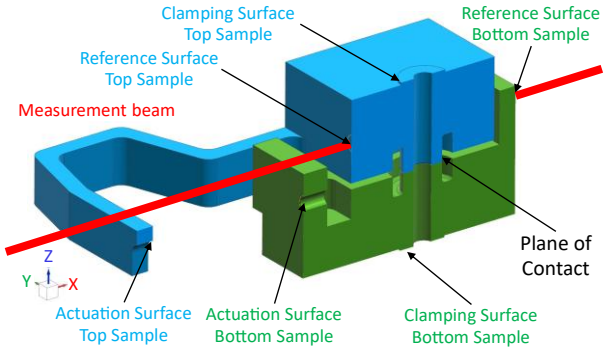

Figure 3: Section view of the sample blocks with detail of the plane of contact and reference surfaces for the interferometer beams.

Each sample block has a reference surface for the interferometer beam. The vertical distance between the plane of contact and the laser beam axis is approximately 10 mm, which is the Abbe offset (see figure 3). Small plane mirrors are glued to the sample block at the reference surfaces.

A number of samples blocks have been manufactured from aluminum 6082 T6. The surface roughness of one bottom sample has been measured using an AFM on 100 x 100 μm^2 measuring areas obtaining an S_q values in the range from 0.05 to 0.09 µm.

4 Experimental results

The microslip test setup is assembled and integrated into the picodrift interferometer. Alignment of the samples to the interferometer is realizable and signal power up to 800 mV is achieved, meaning 61.5 % power of the reference beams. During the microslip measurement, the alignment of the sample blocks is maintained, and the power variation of the signal is negligible. The TFF is able to produce forces up to 15 N for both push and pull between the samples as detected by the load cell. As for the NFF, to evaluate the alignment of this force with the plane of contact wear observation methods could be employed. Nonetheless, the signal of the measurement beam is very stable during the microslip measurements, which means that the clamped samples do not rotate, implying that the alignment of this force is accurate.

Heat sources were minimized in the setup by different design decisions, such as short testing times (≤ 15 min), the use of a

piezo actuator at low frequency, turning off the clamping force load cell during the measurement, the use of heat shields and allow for temperature to settle. The temperature variation recorded during experimentation is kept below 5 mK.

4.1 Microslip experimentation

The tangential actuator is energized to complete one full pull-push cycle (1 Hz). Several cycles are repeated reverting the order of actuation (i.e. pull-push, push-pull, pull-push, pull-push, push-pull, push-pull) and increasing the tangential force applied each series (i.e. 2 N, 5 N, 7.5 N, 10 N, 15 N). The clamping force is maintained during this actuation sequence. Different clamping force levels are studied.

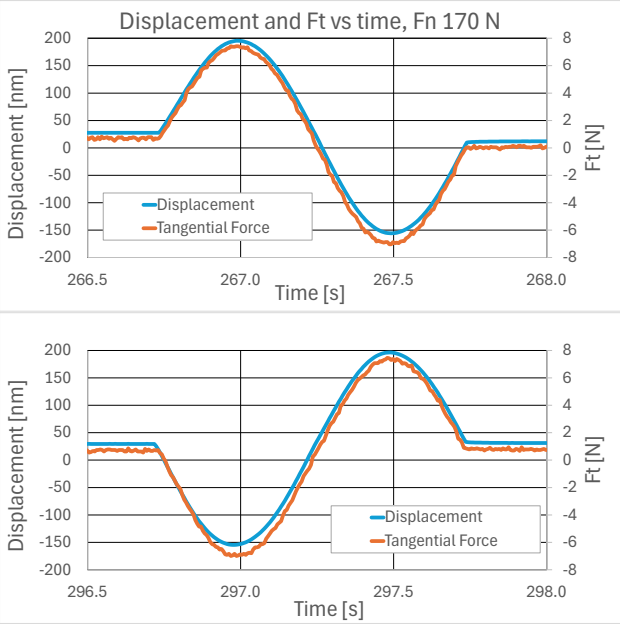

Figure 4: Measured displacement and tangential force versus time during one cycle for 170 N of clamping force: (upper) pull-push reversal resulting in +15.5 nm and +0.63 N, and (lower) push-pull repeated resulting in -1.6 nm and -0.10 N of hysteresis after activation.

After the first cycle (i.e. pull-push), the measured hysteresis displacement between the initial and final position of the reference surfaces of the clamped samples is +15.5 nm (see figure 4 upper graph). This hysteresis captured is consistent in the applied cycles where the order of actuation is reverted, i.e. changing from push-pull to pull-push. For the cycle where the order of actuation is not reverted, the measured microslip displacement is reduced to just -1.6 nm (see figure 4 lower graph). This is consistent with microslip behavior, as asperities find a more stable location.

Because the piezo was operated in open-loop the tangential force reading by the load cell does not drop back to its initial value after activation cycle (see figure 4). Stiffness of the actuator combined with hysteresis in the actuator: when energizing and de-energizing the piezo actuator, it does not return to its initial position. According to spec sheet of the APF705, a 15.4 µm of hysteresis for a full cycle of -30 V to 150 V is expected. This hysteresis combined with the stiffness of the microslip setup could produce a force between the samples. This force can be estimated to 1.03 N. Although it is not fully understood how this effect would show for a constrained displacement of the actuator as it is in this case, the estimated value is very close to that read by the load cell. Therefore, implementation of closed-loop control of the tangential actuator using feedback from the load cell is recommended to improve force accuracy and repeatability.

5 Conclusion and discussion

The realization of the microslip setup meets the majority of the defined requirements: the normal force frame is capable of generating and measuring clamping forces up to 2000 N; The tangential force frame successfully applies bi-directional forces up to 15 N, enabling controlled microslip initiation and measurement; The alignment of the samples to the interferometer was achieved with high precision, maintaining signal power and stability throughout the experiments; The picodrift interferometer provided reliable displacement readings with minimal drift, validating its suitability for microslip characterization; Measurements using the microslip setup captured hysteresis consistent with microslip behavior; The modular design allows flexible adaptation to different materials and geometries of samples, and the use of flexure elements ensures repeatable alignment without mechanical play.

Early testing and final experimentation confirmed the feasibility of the setup and its capability to isolate and measure hysteresis behavior consistent with microslip under controlled conditions.

This result highlights the need for more complete theoretical models and further analysis of the microslip test setup. In summary, this work lays a solid foundation for future microslip research and provides a platform for experimental studies that can inform design strategies in high-precision mechanical systems.

References

[1] Winogrodzka A, *Pre-sliding Behavior of Multi Asperity Ceramic Contacts*, 2015, PhD thesis, University of Twente, Enschede [online]

[2] Fochler D, Schwarz S, Kohlmann L, Krack M, The Black Metal Tribometer: High-resolution measurement of normal load-indentation curves and partial slip hysteresis cycles, 2025, *Tribology International*, **206**, 110560 [DIO]

[3] Ellis J D, *Optical metrology techniques for dimensional stability measurements*, 2010, Delft University of Technology, Delft, ISBN 978-94-91104-06-0 [online]

[4] Voigt D, Ellis J D, Verlaan A L, Bergmans R H, Spronck J W and Munnig Schmidt R H, 2011, Toward interferometry for dimensional drift measurements with nanometer uncertainty *Meas. Sci. Technol.* **22**, 094029 [DIO]

[5] Drever R W P. *et al.*, Laser phase and frequency stabilization using an optical resonator, 1983, *Appl. Phys. B* **31**(2) [DIO]

[6] Schödel R, Yacoot A, Lewis A The new mise en pratique for the metre, 2021, *Metrologia* **58**(5), 052002 [DIO]

[7] Van de Nes A S, Voigt D, Picometer resolution heterodyne interferometry for short to medium term dimensional stability measurments, In R. d. T. Ilmenau (Ed.), *Shaping the Future by Engineering*: Proceedings ; 58th IWK, Ilmenau Scientific Colloquium, Technische Universität Ilmenau, 8 - 12 September 2014 (Vol. **58**, 2014, p. WS. 4.2) [URN]

[8] Spijkers M J J, *Drift investigation of the Picodrift interferometer,* 2024 , MSc Thesis, Eindhoven University of Technology [URN]

[9] Voncken M E J, *Investigation of clamped interface stability*, 2024, MSc Thesis, Eindhoven University of Technology [URN]

[10] Ruiz Beltri P, *Development of an Experimental Microslip Measurement Setup*, 2025, MSc Thesis, Eindhoven University of Technology

[11] Koops R, Van Veghel M, Van de Nes A S, A dedicated calibration standard for nanoscale areal surface texture measurements, 2015, *Microelectron. Eng.* **141** p 250–5 [DIO]

[12] Koops R, Van Veghel M, Van De Nes A S, A virtual lateral standard for AFM calibration, 2016, *Microelectron. Eng.* **153**, 29–36 [DIO]

euspen's 26th International Conference & Exhibition, Krakow, PL, June 2026
www.euspen.eu

Challenges in the design of force sensors based on the structure of high-precision weighing cells

Lennart Frentzel[1], Martin Wittke[1], Matthias Wolf[1], René Theska[1], Hannes Scheibe[1]

Technische Universität Ilmenau, Department of Mechanical Engineering,
[1]Institute for Design and Precision Engineering, Precision Engineering Group

E-Mail: lennart-ramon.frentzel@tu-ilmenau.de

Abstract
As part of the revision of the International System of Units in 2019, it was decided to also redefine the kilogram. Instead of using die International Kilogram Prototype as a physical reference, the unit is now traced back to Planck's constant. The Kibble principle is one of the approaches used to traceably measure masses, forces, and related quantities. Ongoing research into force sensors is based on high-precision weighing cells, as they enable the highest resolution with the lowest uncertainty.
Unlike weighing cells, force sensors do not operate in a static position in the gravitational field, but must fulfill their function properly in arbitrary orientations. The present work investigates the challenges involved in the design of weighing cell-based force sensors. It was found that not only the orientation but also the deflection of the transmission lever from its controlled position influences the force to be measured. The main impact factors are the mass of the links and the mechanical resistance of the flexure hinges, which inhibit the deflection of the system as stiffness. In order to be able to measure forces reproducible, independent of orientation, with a high resolution and low uncertainty, the design of force sensors must integrate features that minimize system stiffness. Approaches to minimize system stiffness include reducing the links masses or the adjustment of trim masses, optimizing the contour, as well as the geometrical parameters and the material of the flexure hinges, as well as using specific sub-mechanisms for compensating the stiffness.

Keywords: force sensor, weighing cell, Kibble principle, Planck balance, stiffness minimization, electromagnetic force compensation, measurement

1. Introduction

The revision of the International System of Units (SI) in November 2019 redefined the traceability of the kilogram to Planck's constant as fundamental natural constant [1]. The Kibble principle is one approach to trace the SI unit of mass, the kilogram, back to Planck's constant [1]. Based on this principle, the Planck balance was developed at the Technische Universität Ilmenau in collaboration with the Physikalisch-Technische Bundesanstalt (PTB) to calibrate weights in accordance with OIML [2,3]. The balance uses a mass comparator weighing cell based on a compliant mechanism, that applies the principle of electromagnetic force compensation to counterbalance the weight of a mass artefact ($\Delta F = mg$) with an electromagnetic counterforce ($\Delta F_A = BL \cdot I$) (Figure 1). The product of B and L is determined by calibrating the actuator in Velocity Mode [10].

Current research focuses on the development of force sensors adapting the concept of the Planck balance for precise and reproducible measurement of forces. Application fields are dimensional measurement and manufacturing technology [4,6] or system calibration [8]. In contrast to balances, force sensors do not have a static orientation and position in the field of gravity. Due to permanent changes in orientation, the design of force sensors faces various challenges that are discussed within this work.

2. Approach

The goal in designing a force sensor based on a compliant mechanism is to measure forces reproducibly with a minimal uncertainty. If the structure of such a sensor is reduced to its essential elements, the basic model can be described as a frame-supported transmission lever (see Figure 1).

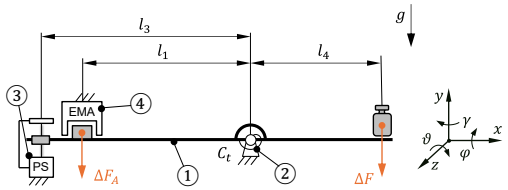

Figure 1. Basic model of a force sensor based on compliant mechanisms and the principle of electromagnetic force compensation.

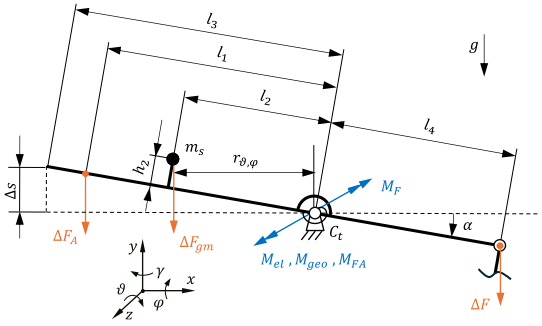

Figure 2. Rigid-body model of the transmission lever of a force sensor using electromagnetic force compensation to visualize acting moments and forces in a loaded state.

A force ΔF acting on one side causes the transmission lever ① to deflect from its controlled position due to the flexure hinge ② (see Figure 2). As a result of the applied force ΔF, the resulting deflection Δs is detected by an optical position sensor ③ and compensated by a counterforce ΔF_A using an

electromagnetic voice coil actuator ④. Since the balanced position is always restored during force measurement (see Figure 1), the moment equilibrium can be established by considering the effective lever arms l_1, l_2, l_3, l_4, h_2 and $r_{\vartheta,\varphi}$. Based on the set electromagnetic force ΔF_A, the acting force ΔF can be directly determined (1).

$$\boldsymbol{M}_{\boldsymbol{F_A}}(\Delta F_A) \;=\; \boldsymbol{M}_{\boldsymbol{F}}(\Delta F) \tag{1}$$

Due to the permanent readjustments of the angle α in the controlled position and its orientation changes in the form of a pitch (ϑ-rotation around the z-Axis) or roll (φ-rotation around the x-Axis) motion (see Figure 2), parasitic forces and moments (2) and (3) are generated that effect the actual force compensation (1). The flexure hinges with the known stiffness c_t additionally generate a moment M_{el} due to elastic deformation that counteracts the deflection motion. Furthermore, the individual masses of the systems links result in a combined centre of mass m_s, which leads to a geometric moment M_{geo} depending on the orientation in the field of gravity.

$$\boldsymbol{M}_{\boldsymbol{F_A}} \;+\; M_{geo} \;+ M_{el} \;=\; \boldsymbol{M}_{\boldsymbol{F}} \tag{2}$$

$$\boldsymbol{\Delta F_A} \cdot l_1 \;+\; \Delta F_{gm} \cdot r_{\vartheta,\varphi} \;+\; M_{el} \;=\; \boldsymbol{\Delta F} \cdot l_4 \tag{3}$$

3. Results

The resistance of a system to deformation can be expressed by the stiffness $C_\alpha = \frac{M}{\alpha}$ or $C = \frac{\Delta F}{\Delta s}$. Equations (1) and (2) can be used to establish stiffness equations (4) and (5) which form the basis for evaluating the force measurements.

$$C_{sys} \;=\; C_{geo} \;+\; C_{el} \tag{4}$$

$$\frac{\boldsymbol{M}_{\boldsymbol{F}}}{\alpha} - \frac{\boldsymbol{M}_{\boldsymbol{F_A}}}{\alpha} = \frac{M_{geo}}{\alpha} + \frac{M_{el}}{\alpha} \tag{5}$$

For the rigid-body model shown in Figure 2, the system stiffness C_{sys} (4) consists of an effective geometric component C_{geo} and an elastic component C_{el}. This relation is illustrated in Figure 3. The sinusoidal curve of geometric stiffness is caused by the size and position of the centre of mass m_S on the transmission lever ①, as well as its orientation in the gravitational field (ϑ and φ). Meanwhile, the constant shift of the graph on the stiffness axis by the amount of elastic stiffness results from the resistance of the hinges to elastic deformation.

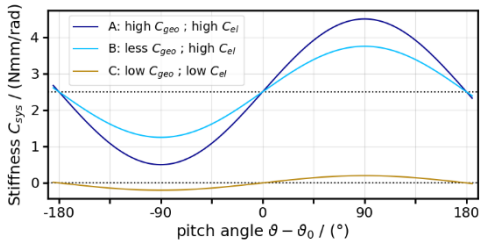

Figure 3. Visualisation of the impact of several methods for the minimization of system stiffness as a function of the pitch angle $\vartheta - \vartheta_0$. (There is no quantitative reference for the stiffness values.)

In order to be able to measure force effects ΔF_A reproducible, independent of orientation and with a high resolution and low uncertainty, the stiffnesses C_{geo} and C_{el} must be minimized when designing balance-based force sensors (6). This indicates that the stiffness characteristic curve needs to be smoothened and then shifted to zero stiffness (see Figure 3, C).

$$\boldsymbol{\Delta F_A} \;= \boldsymbol{\Delta F} \cdot \frac{l_4}{l_1} - \left(C_{geo} + C_{el}\right)\frac{\alpha}{l_1} \tag{6}$$

4. Discussion

Various design and manufacturing methods are available to reduce system stiffness C_{sys} and its components C_{geo} and C_{el}.

4.1. Minimization of elastic stiffness

A reduction in the constant proportion of elastic stiffness C_{el} can be achieved by optimizing the flexure hinges and thus cause a shift of the stiffness curve toward zero (see Figure 3, A and C). Minimizing the elastic stiffness is achieved by optimizing the contour and geometry of the hinges, with a special consideration given to the thickness, as well as by selecting a material with a minimal Young's Modulus.

Although the joints cannot be manufactured any thinner than 50 µm due to manufacturing constraints [9], research results from [7] demonstrate, that optimising the joint contour can reduce stiffness even further.

4.2. Minimization of geometric stiffness

A reduction in the sinusoidal proportion of geometric stiffness C_{geo} can be achieved by adjusting the centres of mass of the frame-beared components or the overall centre of mass m_S. The position of the centre of mass needs to be shifted into the main rotational hinge ② so that there is no geometric moment M_{geo}. On the other hand, a reduction in geometric stiffness C_{geo} can be achieved by minimizing the masses of the links, which cause a reduction in amplitude (see Figure 3, B). [6]

The research results from [6] show that reducing the total mass led to a decrease in rotational dependence and stiffness.

4.3. Stiffness compensation

An additional method to minimize stiffness as a whole, rather than just individual components (C_{geo} and C_{el}), is to implement a compensation mechanism. The principle is based on generating a compensating stiffness that increases proportionally to the deflection of the transmission lever ①. [4]

Theoretical investigations have shown that implementing a compensation mechanism can eliminate geometric and elastic stiffness components [4]. However, in practice, its effectiveness has only been partially demonstrated [5].

5. Summary and Outlook

The current work has shown that the orientation in the gravitational field of force sensors based on compliant mechanisms, has an influence on the measured forces ΔF_A. Since orientation dependence, reproducibility of results and the measured forces are directly related to system stiffness, design features should be incorporated into force sensors to actively minimize stiffness. This can be achieved by reducing and adjusting the individual masses of the mechanism's links, by optimizing the contour, geometry or material of the flexure hinges, and by implementing compensation sub-mechanisms.

Ongoing studies deal with the implementation of these principles for the next generation of SI-traceably measuring force sensors. Initial results have already been presented.

References

[1] Kibble B P 1975 *5th International Conference on Atomic Masses and Fundamental Constants* Paris 545–551
[2] OIML R 111-1 2004 Weights of classes E1, E2, F1, F2, M1, M1–2, M2, M2–3 and M3 - Part 1: Metrological and technical requirements
[3] Rogge N 2023 PhD thesis Technische Universität Ilmenau
[4] Wittke M, Torres Melgarejo M A, Wolf M, Fröhlich T, Theska R 2026 EUSPEN's 25th ICE, Zaragoza
[5] Wittke M, Torres Melgarejo M A, Wolf M, Fröhlich T, Theska R 2026 EUSPEN's 26th ICE, Krakow
[6] Wolf M, Wittke M, Torres Melgarejo M A, Theska R 2024 EUSPEN's 24th ICE, Dublin
[7] Wolf M, Wittke M, Torres Melgarejo M A, Theska R 2024 EUSPEN's 25th ICE, Zaragoza
[8] Dannberg O 2020 PhD thesis Technische Universität Ilmenau
[9] Darnieder M 2024 PhD thesis Technische Universität Ilmenau
[10] Rothleitner C, Schleichert J, Rogge N, Günther L, Vasilyan S, Hilbrunner F, Knopf D, Fröhlich T, Härtig F 2018 Measurement Science Technology **29** 7 074003

euspen's 26th International Conference & Exhibition, Krakow, PL, June 2026
www.euspen.eu

Data-Driven Framework for Machine Learning-Based Uncertainty Evaluation in Coordinate Measuring Machines

Alireza Mollaei Ardestani[1*], Gianfranco Genta[2], Giacomo Maculotti[2], Emanuele Barini[3], Maurizio Galetto[2], Guido Tosello[1]

[1] *Department of Civil and Mechanical Engineering, Technical University of Denmark, 2800 Kgs. Lyngby, Denmark*
[2] *Department of Management and Production Engineering, Politecnico di Torino, 10129 Torino, Italy*
[3] *Hexagon Metrology S.p.A., 10090 Grugliasco, Italy*

Corresponding author: almoa@dtu.dk*

Abstract
The increasing use of Coordinate Measuring Machine (CMM) systems for high-precision dimensional metrology in industrial environments demands not only accurate data but also reliable quantification of measurement uncertainty. Traditional methods, such as ISO 15530-3 and the Guide to the Expression of Uncertainty in Measurement (GUM), require extensive experimental effort and are often directly applicable only to prismatic geometries, limiting their use for novel geometries or conditions. Freeform geometries are increasingly applied in manufacturing for topological and functional optimization, yet conventional CMM uncertainty evaluation methods are tailored to primitive geometries, restricting their applicability.
This work proposes a novel data-driven framework that leverages machine learning (ML) prediction models trained on actual CMM measurement data and integrates an uncertainty analysis to provide predictions with metrological trustworthiness. The approach begins with collecting an extensive dataset, through a factorial design structured by design of experiment (DOE), from tactile CMM measurements on calibrated artefacts with prismatic and freeform geometries. Influential factors such as sampling density, measurement strategy, probe configuration, and alignment are considered as model inputs. A supervised ML algorithm is trained to predict measurement outcomes (e.g., geometric deviations, form errors) as a function of these parameters. Unlike classical statistical models, the ML model captures complex interactions among process parameters and machine behaviour.
Uncertainty is evaluated using a statistical resampling approach based on bootstrap methodology. Multiple bootstrapped samples are generated, and the ML model is retrained for each, producing an ensemble of prediction models. The variability in coefficients and outputs provides estimates of standard and expanded uncertainty in accordance with GUM principles.
The framework bridges conventional DOE-based metrological modelling and modern data-driven methods. It enables quantification of ML prediction uncertainty for CMM processes, supporting virtual validation, metrological digital twins, and bridging towards complex measurement tasks' error compensation strategies.

Keywords: Accuracy, Coordinate measuring machine (CMM), Metrology, Uncertainty

1. Introduction

Coordinate Measuring Machines (CMMs) remain a cornerstone of high-precision dimensional metrology for industrial qualification and conformity decisions, where the credibility of inspection results depends on traceable uncertainty statements rather than nominal deviations alone. In recent work, uncertainty evaluation and optimization for CMM measurement planning have been revisited with stronger emphasis on industrial feasibility and economic impact, highlighting that measurement strategy choices can materially affect both uncertainty and inspection cost. [1]
The challenge becomes more pronounced as inspection tasks shift from mostly prismatic features toward freeform and geometrically complex surfaces, driven by functional design and optimization in modern manufacturing. For such surfaces, the layout of measurement points and sampling strategies can strongly influence achievable accuracy and robustness, motivating dedicated research on measurement point distribution and strategy selection for freeform CMM inspection. [2] In parallel, recent studies on strategy-driven evaluation (e.g., form and orientation assessments) further reinforce that uncertainty is not a fixed "machine constant," but depends on how the measurement is executed (alignment, point selection, probing configuration, and data processing). [3]
Alongside these metrology-specific developments, the broader field is increasingly adopting virtual experiments and digital-twin concepts to support trustworthy prediction and decision-making. Recent frameworks explicitly argue that virtual/DT-based measurement systems must include uncertainty propagation and traceability principles if they are to be used for metrological purposes. [4] Complementary contributions expand on how uncertainty evaluation methods differ when implemented within virtual measurement pipelines and how they should be interpreted for complex measurement tasks. [5]
At the same time, machine learning (ML) has gained traction as a practical way to model highly nonlinear interactions among measurement strategy parameters, probe configuration, alignment choices, and machine behaviour relationships that are difficult to capture with classical linear/statistical models. However, ML predictions are insufficient for metrology unless paired with uncertainty evaluation to communicate the trustworthiness of

predictions. Recent reviews in ML uncertainty quantification provide structured overviews of uncertainty evaluation families and their suitability for safety- and decision-critical deployments. [6]
For data-driven regression models, ensemble and resampling-based approaches remain attractive due to their conceptual simplicity and compatibility with existing pipelines. Also, recent work has shown that bootstrap ensemble spread can be employed to improve uncertainty evaluation accuracy, an insight directly relevant when using bootstrap-based ML ensembles for uncertainty-aware CMM predictions. [7]
Motivated by these needs, the present work proposes a data-driven framework that couples DOE-structured data collection with supervised ML modelling and bootstrap-based uncertainty estimation to deliver uncertainty-aware predictions for CMM measurement outcomes on both prismatic and freeform artefacts.
The approach supports uncertainty-informed inspection planning and provides a pathway toward metrologically trustworthy virtual validation and digital metrology workflows. [8,9]

2. Materials and methods

2.1 Measured artefact and geometry definition

The experimental investigation was conducted using a precision-calibrated spherical artefact (ball bearing sphere, $Ø_{sph}$ = *(107.943±0.003) mm, Sphericity = (4.5±3.0) µm*), selected due to its well-defined geometry, rotational symmetry, and widespread use as a reference feature in coordinate metrology. The sphere can be seen in Figure 1.

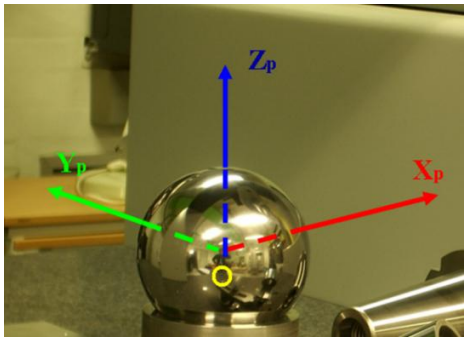

Figure 1: Ball bearing sphere [10]

The sphere provides a controlled yet non-trivial surface for studying the influence of measurement strategy, sampling, and alignment on CMM measurement outcomes while avoiding confounding effects associated with mixed geometries (e.g., cones or cylinders).
The calibrated diameter and sphericity of the artefact were taken as traceable reference values. All measurement deviations were evaluated relative to a nominal CAD model constructed using the calibrated sphere parameters. The sphere centre was used as the primary datum for alignment and evaluation, ensuring repeatability and minimizing datum-related ambiguity.

2.2 Coordinate measuring system and probing configuration

All measurements were performed using a tactile coordinate measuring machine operating in a temperature-controlled environment at (20.0 ± 0.5) °C. A touch-trigger probing system equipped with a ruby stylus of constant ball diameter was employed throughout the experimental campaign to isolate the effects of strategy-related parameters from probe size variability.
Two probe configurations were considered: a single vertical probing direction and a multi-directional probing configuration, allowing assessment of probing orientation effects while maintaining identical tip geometry. Measurement speed (10 mm/s), approach distance (2 mm), and probing force (100 mN) were kept constant across all experiments to reflect an industrially realistic but controlled measurement setup.
All measurements were performed using a ZEISS high-accuracy bridge-type Coordinate Measuring Machine (CMM) installed in a temperature-controlled metrology laboratory at (20.0 ± 0.5) °C. The CMM is designed for high-precision dimensional inspection and offers a maximum permissible error (MPE) of (2.0 + L/500) µm, where L is the measured length expressed in millimetres, ensuring traceable and stable measurement performance. The machine was equipped with a tactile probing system and calibrated according to the manufacturer's specifications prior to the experimental campaign.

2.3 Design of Experiments (DOE)

A full-factorial Design of Experiments was adopted to systematically investigate the influence of key measurement process parameters on spherical CMM measurements. Four factors were selected, each at two levels. Table 1 represents the input variables and their levels. Figures 2 to 4 represent different levels for input variables.

Table 1: DOE factors and levels

Factor	Level 1	Level 2
Sample density (A)	ISO/TS 16610-49	Reduced
Measurement strategy (B)	Transversal	Longitudinal
Probe Configuration (C)	3 mm Star Probe –y, +y, -x, +x	3 mm single probe -z
Alignment (D)	Repeated	Single

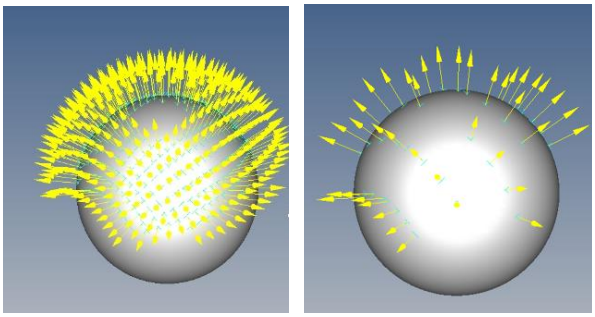

Figure 2: Sampling density, ISO16610-49 (left), and reduced 1/8 (right) [10]

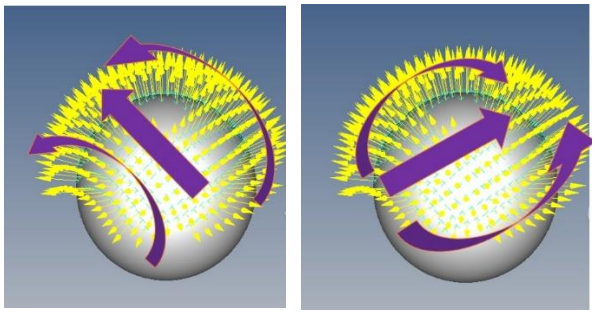

Figure 3: Measurement strategy, Transversal (left), and Longitudinal (right) [10]

The full factorial design resulted in 16 factor combinations. Each experimental condition was repeated three times to

quantify measurement repeatability and enable statistical analysis. The experimental runs were randomized to mitigate systematic temporal effects.

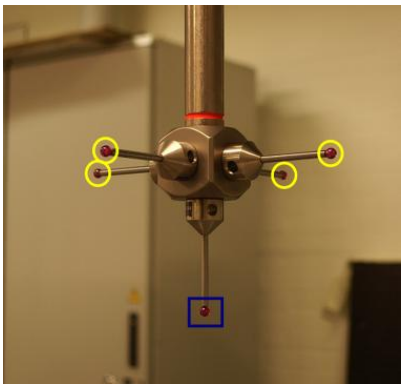

Figure 4: Probe configuration, Star probe (yellow), and a single probe (blue) [10]

2.4 Bootstrap sampling and GUM

Uncertainty associated with the machine learning–based predictions was quantified using a non-parametric bootstrap approach integrated with the Guide to the Expression of Uncertainty in Measurement (GUM). In this study, 1000 bootstrapped datasets were generated based on the original 16-datapoints dataset by resampling the original DOE-based measurement data with replacement. Figure 5 represents a scheme of how bootstrapping with resampling works.

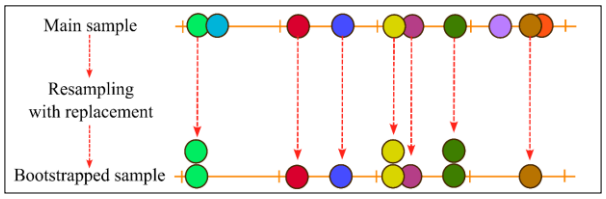

Figure 5: A scheme of bootstrap with resampling

The ML model was retrained for each dataset, producing an ensemble of predictions for sphere diameter deviation and form error. The standard uncertainty was estimated as the standard deviation of the bootstrap prediction distribution, while the expanded uncertainty was obtained using a coverage factor of K=2, in accordance with GUM principles. This approach enables data-driven, GUM-compliant uncertainty estimation without analytical uncertainty propagation.

The proposed framework complements ISO 15530-3, which provides traceable but task-specific uncertainty evaluation requiring dedicated experiments. In contrast, the present approach combines traceable data, interpretable models, and GUM-consistent bootstrap uncertainty to enable scalable estimation across multiple measurement configurations.

The resulting uncertainty should be interpreted as a task-specific uncertainty of model-based predictions, supporting virtual inspection and uncertainty-informed decision-making in digital-twin-based CMM environments.

2.5 Machine learning prediction model

To predict the sphere diameter and form error, regression models were employed as an interpretable white-box machine learning approach to predict CMM measurement outcomes. Polynomial and linear regression models were tried on both the outputs of diameter and form error. Based on the prediction results, due to the overfitting of the polynomial model, the linear regression model is used for the form error. But since the polynomial regression model showed a higher prediction accuracy, without overfitting, for the diameter, it was chosen as the prediction model. The models express the measurand as an explicit analytical function of the input factors, enabling direct interpretation of parameter effects and their coupled influences.

Unlike black-box models, regression models provide a closed-form prediction equation that can be readily integrated with bootstrap resampling and propagated through the GUM framework for uncertainty evaluation. This transparency makes the approach particularly suitable for metrological applications requiring traceable and physically interpretable models.

2.6 Output variables and objectives

The primary output variables are Geometric deviation metrics, including diameter deviation and local form error relative to the calibrated reference.

These outputs served a dual purpose. First, they enabled the identification of the most influential measurement parameters and interactions affecting spherical CMM measurements. Second, they formed the dataset for training supervised machine learning models and for subsequent bootstrap-based uncertainty quantification, supporting uncertainty-aware prediction of CMM measurement outcomes as proposed in the data-driven framework.

3. Results and discussion

As mentioned in the methods section, a machine learning model was trained for each resample, resulting in an ensemble of prediction models. The standard deviations of the regression coefficients obtained from the bootstrap ensemble were propagated through the measurement model using the GUM framework. This procedure enables the transformation of statistical model variability into a metrologically interpretable uncertainty statement for both investigated output quantities.

The adopted approach ensures that the uncertainty associated with model training, parameter estimation, and experimental variability is consistently transferred to the predicted measurand.

3.1 Uncertainty of diameter prediction

A machine learning model was trained on diameter data (assisted with the bootstrapped dataset). The following prediction regression equation was obtained for the diameter prediction:

$$Diameter = 107.94 + 0.0035\times A + 0.0023\times B + 0.0029\times C - 0.0007\times D - 0.0040\times A^2 - 0.0057\times AB - 0.0014\times AC + 0.0016\times AD - 0.0008\times B^2 - 0.0008\times BC + 0.0007\times BD + 0.0005\times C^2 - 0.0001\times CD$$

The GUM-based uncertainty results, including the effective degrees of freedom and expanded uncertainty for diameter prediction, are summarized in Table 2.

Table2: GUM-based uncertainty results for diameter

Description	Symbol	value
Combined variance of y	$u^2(y)$	1.2×10^{-3} mm^2
Standard uncertainty	u(y)	3.4×10^{-2} mm
Effective degree of freedom	v(y)	69
Coverage factor	k	2.0
Expanded uncertainty	U(y)	0.068 mm

For the sample configuration of 1-1-2-2, the predicted diameter value is 107.911. So, the relative expanded uncertainty becomes 0.1%. Among the input variables,

measurement strategy (B) and workpiece alignment (D) have a greater effect on the uncertainty of prediction compared to the other two factors of point density (A) and probe configuration (C).

3.2 Uncertainty of form error prediction

A similar bootstrap-based uncertainty analysis was conducted for the prediction of spherical form error.

For the spherical form error, the regression model obtained from the full dataset is:

$$Form\ error = 47.125 - 21.075 \times A - 3.750 \times B + 0.150 \times C + 2.750 \times D$$

The GUM-based uncertainty results, including the effective degrees of freedom and expanded uncertainty for form error prediction, are summarized in Table 3.

Table 3: GUM-based uncertainty results for form error

Description	Symbol	value
Combined variance of y	$u^2(y)$	4.5 µm^2
Standard uncertainty	u(y)	2.1 µm
Effective degree of freedom	v(y)	69
Coverage factor	k	2.0
Expanded uncertainty	U(y)	4.2 µm

For the sample configuration of 1-1-2-2, the predicted value of the form error is calculated to be 28 µm. So, the corresponding relative expanded uncertainty is calculated to be equal to 15%, significantly higher than for the diameter.

The uncertainty budget reveals that form error prediction is substantially more sensitive to coefficient variability, particularly those associated with sampling density (A) and measurement strategy (B). The larger regression coefficients amplify the propagated uncertainty, resulting in a wider coverage interval.

The ensemble predictions revealed a wider variability compared to diameter estimation, reflecting the higher sensitivity of form measurements to probing strategy and alignment. The framework successfully quantified this variability through the bootstrap-derived uncertainty bands, allowing discrimination between more and less robust measurement configurations. The results highlight that form error uncertainty is particularly influenced by sampling density and probe configuration, underlining the importance of strategy selection when measuring freeform or quasi-freeform surfaces.

3.3 Consistency with GUM principles

For both diameter and form error, the bootstrap-derived prediction distributions enabled GUM-compliant uncertainty reporting, with standard uncertainty obtained from the ensemble spread and expanded uncertainty derived using an appropriate coverage factor. The results confirm that the proposed framework provides stable and repeatable uncertainty estimates without relying on analytical uncertainty propagation or geometry-specific calibrated artefacts. This demonstrates the suitability of the approach for scalable uncertainty evaluation and supports its application within virtual metrology and digital-twin-based CMM workflows.

4. Conclusion

This work presented a data-driven framework for uncertainty-aware prediction in coordinate metrology, combining DOE-based experimental design, supervised machine learning, bootstrap resampling, and GUM-compliant uncertainty propagation.

The results demonstrate that:

- Sphere diameter predictions exhibited low relative expanded uncertainty (0.1%), confirming its robustness as a global geometrical parameter.
- Form error predictions showed significantly higher uncertainty (15%), reflecting their intrinsic sensitivity to sampling density, measurement strategy, alignment configuration, and, in general, a more challenging measuring task.
- The propagated uncertainty values are consistent with known CMM behaviour and physical metrology principles.

The integration of bootstrap resampling with GUM propagation enables the translation of statistical model variability into traceable metrological uncertainty statements. Unlike conventional ISO 15530-3 approaches, the proposed framework does not require geometry-specific calibrated artefacts for each new measurement configuration. Instead, it leverages experimentally acquired datasets to generate scalable uncertainty predictions.

The methodology bridges DOE-based metrology and modern data-driven modelling, providing a structured pathway toward uncertainty-aware virtual CMM validation and digital metrological twins. By quantifying prediction reliability, the framework supports uncertainty-informed measurement planning and adaptive inspection strategies.

Acknowledgement:

The project 23IND12 ADAM 'Application of Digital-Metrological Twins for emerging measurement technology in advanced manufacturing' has received funding from the European Partnership on Metrology, co-financed from the European Union's Horizon Europe Research and Innovation Programme and by the Participating States.

References:

[1] Urban J et al. Optimizing coordinate measuring machine measurement plans. J. Clean. Prod. 2024.

[2] Zeng L et al. Measurement point layout strategy of free-form surface. Int. J. Metrol. Qual. Eng. 2023.

[3] Habibi N et al. Perpendicularity assessment and uncertainty estimation. Int. J. Metrol. Qual. Eng. 2023.

[4] Maculotti G et al. A shared metrological framework for trustworthy virtual metrology. Metrology 2024.

[5] Kok G et al. Measurement uncertainty evaluation: differences between methods. Metrology 2025.

[6] He W et al. A survey on uncertainty quantification methods for deep learning. ACM Comput. Surv. 2023.

[7] Palmer G et al. Calibration after bootstrap for accurate uncertainty quantification in regression models. npj Comput. Mater. 2022.

[8] Schmelter S et al. Metrology for virtual measuring instruments illustrated by applications. Metrology 2025.

[9] Sato O et al. Practical experimental design and uncertainty evaluation method for dimensional and form measurements using coordinate measuring machines. Measurement 2024.

[10] Barini EM, Tosello G, De Chiffre L. Uncertainty analysis of point-by-point sampling complex surfaces using touch probe CMMs: DOE for complex surfaces verification with CMM. Precision Engineering 2010.

euspen's 26th International Conference & Exhibition, Krakow, PL, June 2026
www.euspen.eu

The Satisloh Plasma Polisher: the science, technology development, and commercialisation of atmospheric pressure surface figuring for ultra-precision optics

Dr. Adam Bennett[1,2], Dr. Katherine Gobey[1], Steffen Moos[3], Paul Sauer[3], Hans-Joerg Schlemper[3], Dr. Jürgen Bode[3]

[1]*Cranfield Plasma Solutions Limited, College Road, Wharley End, Cranfield, MK43 0AL, England;*
[2]*Cranfield University, College Road, Wharley End, Cranfield, MK43 0AL, England;*
[3]*Satisloh GmbH, Wilhelm-Loh-Straße 2-4, 35578 Wetzlar, Germany.*

a.d.bennett@cranfield.ac.uk

Abstract
The precision optics technology sector requires rapid surface figuring capability that is aligned with both financial and environmental sustainability. Plasma Figuring, operating at atmospheric pressure, is designed to create the same figure correction capabilities as Magneto Rheological Finishing (MRF) and Ion Beam Figuring (IBF). Plasma Figuring can achieve higher optics manufacturing rates compared to both MRF and IBF; furthermore, it is a technology that uses no harmful chemicals and emits no pollution. The Satisloh Plasma Polisher (SPP) is an atmospheric pressure Plasma Figuring technology that targets mid-spatial frequencies in the 1 mm to 2 mm range. The technology uses a reactive plasma jet to chemically surface figure optics. The plasma jet is powered by a solid-state microwave generator, which operates at less than 50 W average power utilising pulse power mode to reduce the plasma temperature; the ability to discharge a non-thermal plasma at circa 100 ˚C increases the repeatability of the etched Gaussian trenches and maintains the optical surface finish. The SPP is designed to have both lower capital expenditure and lower operational expenditure compared to both MRF and IBF, which is achieved by the relatively low power consumption, the size of the machine, and the system parameters; furthermore, the SPP only consumes 1 L/min of total process gas flow. The presentation will discuss the physics and chemistry that underpins this state-of-the-art technology, the scale-up journey from university to Satisloh, and the successful commercialisation. Results with the SPP are reported that shows the fast figure correction of fused silica on spheres and a-spheres. The presentation concludes with other materials and future directions.

Plasma, Figuring, Optics, Free-Forms, Efficiency, Sustainability.

Introduction

State-of-the-art optics technology applications are driving surface engineering specifications ever closer to the atomic scale [1]. Surface specifications of 10 nm RMS form accuracy and 0.1 nm RMS surface finish are now required in ultra precision applications, which include Acousto-Optic Devices [2], Extreme Ultraviolet (EUV) lithography [3], extremely large telescopes [4], and laser fusion technology [5]. Magneto Rheological Finishing (MRF) and Ion Beam Figuring (IBF) are mature technology solutions used in the final stage of the manufacturing chain of ultra precision optics; however, both technology solutions have very high capital and operational expenditure: the Capital Expenditure of MRF ranges from $500k USD to $1.2M USD and IBF starts at $1M+ USD. Furthermore, MRF is a dirty manufacturing process that uses slurry, with correction limitations set by the size of the contact tool; and, IBF is a very slow process, which is limited to the size of the vacuum chamber. The Plasma Figuring technology described in this paper overcomes all of the aforementioned negatives of the other technologies.

Plasma Figuring technology was developed in Cranfield University (CU) and the Leibniz Institut für Oberflächen Modifizierung (IOM) [6]. Plasma Figuring is a non-contact material removal process that operates at atmospheric pressure and low temperature. MRF and IBF are physical material removal technology; however, Plasma Figuring is a purely plasma chemical etching technology, which avoids the risk of generating sub-surface damage. The low temperature plasma, operating at circa 100 ˚C, yields high thermal control of the substrate and hence high repeatability in the material removal function [7 - 12]. The material removal mechanism is based on a purely chemical reaction between fluorine radicals, which only exist in the plasma, and the surface of the optic. Plasma Figuring of silicon and silicon based optical surfaces has been previously shown [13 - 20].

The Satisloh Plasma Polisher (SPP) is an atmospheric pressure Plasma Figuring technology designed to figure correct optics to the same form accuracy and surface finish as MRF. The SPP targets Mid Spatial Frequency (MSF) errors in the 1 mm to 2 mm range. The SPP is designed to have both lower capital expenditure and lower operational expenditure compared to MRF and IBF, which is achieved by the relatively low power consumption, the size of the machine, the system parameters, and the consumables; furthermore, the SPP only consumes a maximum of 1 L/min of total process gas flow. The Plasma Figuring technology is a clean, environmentally friendly, process that is performed at atmospheric pressure within the SPP chamber. The only byproducts of the process are SiF_4 and CO_2, which are at very low levels, and are none-the-less captured within a bespoke filtration system; measurements of the byproducts are significantly below the Lowest Exposure Limits.

The physics and chemistry that underpins the technology is described in the first SPP paper [21] and the results generated in the Beta Test are shown in the second SPP paper [22].

The paper we now present here describes a summary of the technology, its development, and the latest results.

The Satisloh Plasma Polisher

Technology

The Satisloh Plasma Polisher (SPP) machine has a rapid figuring capability covering a 300 mm by 150 mm area. The five axis precision motion system enables the plasma torch to be moved over the surface of a sphere, asphere or free-form optic to a place in 3D space within ±10 µm. A solid state microwave generator is connected, coaxially, to the plasma torch. A copper tube is inserted into the middle of a brass nozzle. The helium carrier gas, carbon tetrafluoride reactive gas, and oxygen tertiary gas are injected into the copper tube, at flow rates of 400 sccm, 1 sccm, and 1 sccm, respectively. Furthermore, nitrogen shield gas is used to protect the plasma jet from interactions with the air, which would cause instability. The shield gas flow rate matches the carrier gas flow rate.

The microwave generator frequency (the frequency of the photons that are emitted into the gas to generate the plasma) was set to 2.45 GHz. The pulse repetition frequency (the number of microwave pulses per second) was set to 4 kHz. The pulse width (the time period in each ON-OFF cycle that each microwave pulse is ON) was set to 15 µs. The peak power (the maximum amplitude of each microwave pulse, which was the same for each pulse) was set to 250 W. The mean input power, P_m, of the plasma jet was then calculated to be 15 W from

$$P_m = P_p \times f_p \times t_p \quad (1)$$

Where, P_p is the pulse peak power in W; f_p is the pulse repetition frequency in kHz; and, t_p is the pulse width in µs [21].

Figure 1 shows a schematic of the plasma torch processing the surface of an optic.

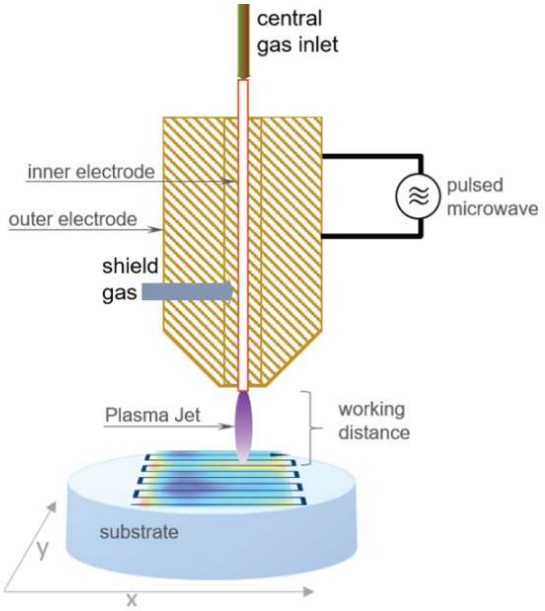

Figure 1. Plasma Torch Process Schematic.

Figure 2 shows the plasma torch during figuring operation over the surface of convex and concave optics. Spheres, a-spheres, and free-forms have been processed. Investigations with customers directed the initial focus, which was on fused silica, followed by ULE, silicon, and finally BK7.

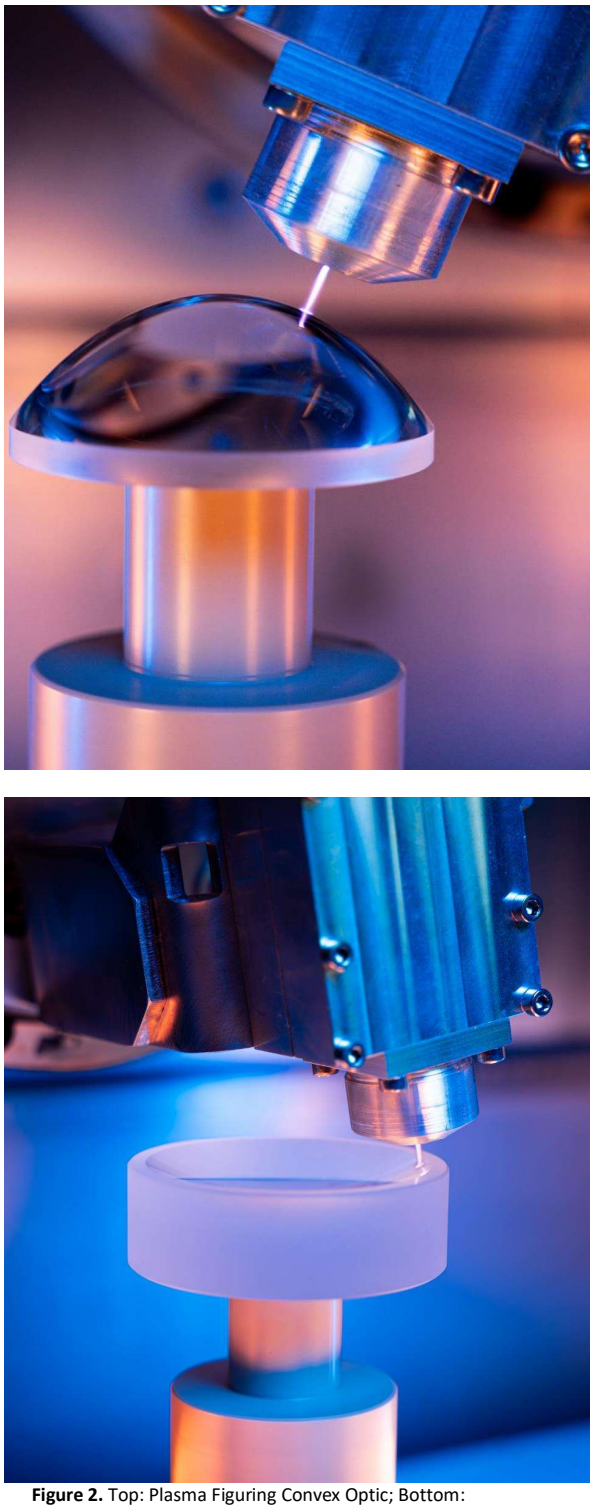

Figure 2. Top: Plasma Figuring Convex Optic; Bottom: Plasma Figuring Concave Optic.

Material Removal Mechanism

The plasma jet discharge is 99 % helium. Helium plasma on its own will only clean the surface of the optic [23]; however, the helium plasma is a stable energy beam, which is used to convert the carbon tetrafluoride inert gas into atomic fluorine and atomic carbon. Fluorine radicals, upon contact with silicon atoms, react and produce SiF_4 gas, which is extracted and stored in a bespoke scrubber unit. The principal chemical reaction, for the case of fused silica, is given by

$$SiO_2 + 4F\bullet \rightarrow SiF_4 \uparrow + O_2 \uparrow \quad (2)$$

Where F• is a fluorine radical. The oxygen tertiary gas was injected to react with the carbon in the plasma and extract it in the form of carbon dioxide gas, which prevents any carbon-based deposition onto the surface of the optic [21].

The material removal reaction rate, R, was dependent on the local surface temperature, which is given by an Arrhenius equation

$$R = C\, j_F exp^{\left\{-\frac{E_A}{k_B T_s}\right\}} \quad (3)$$

Where C is a constant; j_F is the reactive particle flux ($m^{-2}\ s^{-1}$); T_s is the surface temperature (K); k_B is the Boltzmann constant ($m^2\ kg\ s^{-2}\ K^{-1}$); and, E_A is the activation energy (J) [24].

Material Removal Calculations

The stable reactive plasma jet, moving over the surface of an optic, results in a trench with a Gaussian cross section. The Material Removal Rate, $MRR_{Dynamic}$, for a single trench is given by

$$MRR_{Dynamic} = \int_{-\infty}^{\infty} f(y)\, dy\, .L \div t_T = \sqrt{2} D_{Max} \sigma_y \sqrt{\pi}.L \div t_T \quad (4)$$

Where D_{Max} is the maximum depth of the trench (nm); L is the length of the trench (mm); t_T is the time taken to etch the trench (s); and, σ_Y = the Full Width Half Maximum of the trench cross section divided by $2\sqrt{2\ln 2}$ [25].

Satisloh Plasma ADAPT

The interferometric results from the trench material removal experiments were inserted into the Satisloh Plasma ADAPT (Satisloh Plasma Advanced Deterministic Adaptive Polishing Technology) software program. The program is a deterministic process simulator, which is based on Finite Element Modelling that calculates the optimised tool path rates based on the plasma torch, surface geometry, measurement data, and process kinematics. A dwell time algorithm was used to calculate the varying velocity that was required at different points in the raster pattern that was conducted over the surface of the optics.

Results

Reproducibility

Repeatability defines the variance in a process and is the corner stone of precision engineering; however, repeatability only describes the precision in a given system. Reproducibility describes the variance across different systems in different organisations and is an important metric for technology commercialisation. The results in this section show how the SPP systems generate consistent results in Satisloh GmbH and Corning Advanced Optics, Corning Incorporated.

Figure 3 and Figure 4 shows plasma figuring results on a HPFS® ConCave Sphere with a 53 mm Clear Aperture, undertaken on an SPP in Satisloh. The starting surface form was 152 nm PV with 28 nm RMS and the final surface form was 76 nm PV with 10 nm RMS, which was achieved in a single iteration. The surface roughness stayed constant throughout the process.

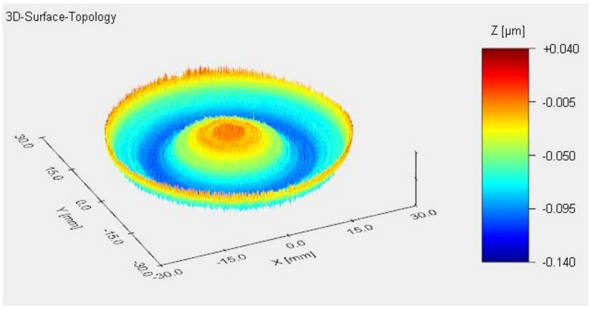

Figure 3. Sphere HPFS 7980 ConCave 53mm CA - Before

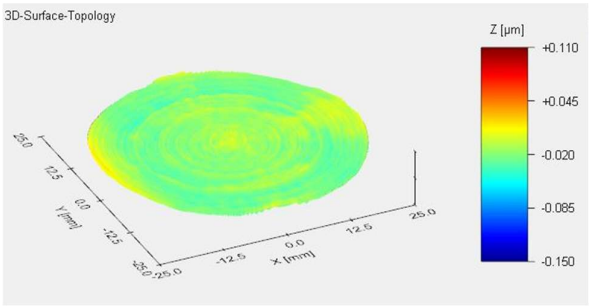

Figure 4. Sphere HPFS 7980 ConCave 53mm CA - After

Figure 5 shows plasma figuring results on a HPFS® ConCave A-Sphere with a 92 mm Clear Aperture and a 250 µm departure from Best Fit Sphere, which was undertaken on an SPP in Corning. The starting surface form was 299 nm PV with 51.5 nm RMS and the final surface form was 51 nm PV with 9.5 nm RMS. The surface form error reduction was achieved in only two steps.

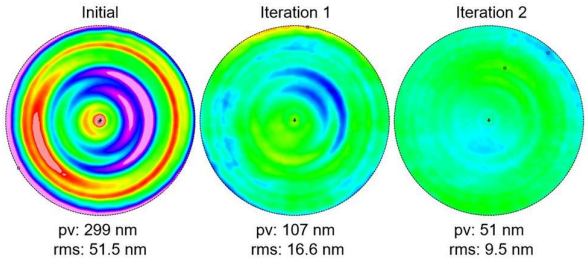

Figure 5. ASphere HPFS 7980 ConCave 92mm CA 250µm BFS

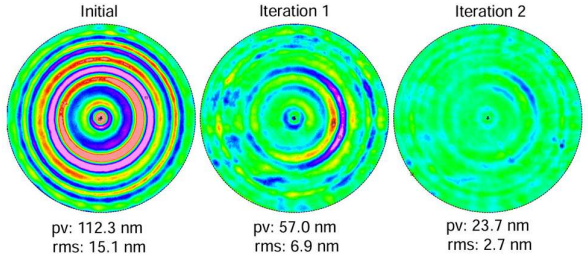

Figure 6. ASphere HPFS 7980 ConCave 92mm CA 250µm BFS Mid Spatial Frequency (MSF) Error Reduction

Figure 6 shows the same data as Figure 5, but with 36 Zernikes removed, which enables a deeper analysis of the Mid Spatial Frequency (MSF) error reduction by subtracting low and mid order wavefront aberrations.

The surface roughness on the HPFS® 7980 stayed constant, throughout the plasma figuring iterations, with a value of circa 2 Å RMS.

Technology Comparison – Optic Processing Times

The cycle time to figure correct optics depends on the starting surface topography and the required surface topography. Different optics will, therefore, have different processing times. Work conducted in Satisloh and during the Beta Test shows that the SPP has processing times that are comparable to MRF. [22]

Future Work

The SPP has demonstrated figuring capability on different materials that are shown in Table 1. Further materials are under development.

Table 1. SPP Figuring Materials Capability

Standard Parameters	Enhanced Parameters
Fused Silica	BK7
Crystalline Quartz	Zerodur
Amorphous Silicon	ULE
Crystalline Silicon	
Germanium	
Silicon Oxide Coatings	

Conclusion

The Satisloh Plasma Polisher (SPP) Plasma Figuring technology corrects Mid Spatial Frequency (MSF) errors at the same speeds as Magneto Rheological Finishing (MRF). The SPP targets MSF errors in the 1 mm to 2 mm range, which are corrected without changing the surface roughness of the optics.

The SPP has both lower capital and operational expenditures compared to both MRF and IBF technology; furthermore, it is an environmentally friendly, clean, low energy process that uses no slurry and has no emissions.

The SPP is a compelling new technology for the sub-aperture figuring toolbox and is an enabler of future strategic capability.

References

[1] Yu, N., Fang, F.Z., Wu, B., Zeng, L., and Cheng, Y., State of the art of intraocular lens manufacturing, The International Journal of Advanced Manufacturing Technology. 98 (5-8), 1103-1130 (2018).

[2] Cai, L., Mahmoud, A., and Piazza, G., Low-loss waveguides on Y-cut thin film lithium niobate: towards acoustooptic applications, Optics express. 27(7), 9794-9802 (2019).

[3] Tallents G, Wagenaars E, Pert G. Optical lithography: Lithography at EUV wavelengths. Nature photonics. 4(12):809 (2010).

[4] Gilmozzi R., Spyromilio J. The European extremely large telescope (E-ELT). The Messenger.127(11): 3 (2007).

[5] Lawrence Livermore National Laboratory. National Ignition Facility & Photon Science. https://lasers.llnl.gov/ (2020).

[6] Fanara, C. *et al.* A new reactive atom plasma technology (RAPT) for precision machining: The etching of ULE® surfaces. *Advanced Engineering Materials*, 8(10), pp. 933–939 (2006)

[7] Yu, N., Yang, Y., Jourdain, R., Gourma, M., Bennett, A., and Fang, F.Z., Design and optimization of plasma jet nozzles based on computational fluid dynamics, The International Journal of Advanced Manufacturing Technology. 108, 2559–2568 (2020).

[8] Sun, R., Yang, X., Ohkubo, Y., Endo, K., Yamamura, K. Optimization of gas composition used in plasma chemical vaporization machining for figuring of reaction-sintered silicon carbide with low surface roughness. Scientific reports, 8(1):1-9 (2018).

[9] Arnold T, Boehm G, Schindler A. Ultrahigh-rate plasma jet chemical etching of silicon. Journal of Vacuum Science & Technology A: Vacuum, Surfaces, and Films. 19(5):2586-9 (2001).

[10] Takino H, Yamamura K, Sano Y, Mori Y. Shape correction of optical surfaces using plasma chemical vaporization machining with a hemispherical tip electrode. Applied optics. 51(3):401-7 (2012).

[11] Jourdain R, Castelli M, Yu N, Gourma M, Shore P. Estimation of the power absorbed by the surface of optical components processed by an inductively coupled plasma torch. Applied Thermal Engineering. 108:1372-82 (2016).

[12] Jin H, Xin Q, Li N, Jin J, et al. The morphology and chemistry evolution of fused silica surface after Ar/CF 4 atmospheric pressure plasma processing. Applied surface science. 286:405-11 (2013).

[13] Engelhardt, M., Pothiraja, R., Kartaschew, K., Bibinov, N., Havenith, M., and Awakowicz, P., Interaction of an argon plasma jet with a silicon wafer, Journal of Physics D: Applied Physics. 49 (14), 145201(2016).

[14] Yu, N., Jourdain, R., Gourma, M., and Shore, P., Analysis of De-Laval nozzle designs employed for plasma figuring of surfaces, The International Journal of Advanced Manufacturing Technology. 87(1-4) ,735-745 (2016).

[15] Castelli, M., Jourdain, R., Morantz, P., and Shore, P., Rapid optical surface figuring using reactive atom plasma, Precision Engineering. 36 (3), 467-476 (2012).

[16] Arnold, T., Böhm, G., Fechner, R., Meister, J., Nickel, A., Frost, F., Hänsel, T., and Schindler, A., Ultra-precision surface finishing by ion beam and plasma jet techniques—status and outlook, Nuclear Instruments and Methods in Physics Research Section A: Accelerators, Spectrometers, Detectors and Associated Equipment. 616 (2-3), 147-156 (2010).

[17] Bennett, A., Yu, N., Castelli, M., Chen, G., Fang, F. Etching characteristics of crystal quartz by surface wave microwave induced plasma. Proc. SPIE 11568, AOPC 2020: Optics Ultra Precision Manufacturing and Testing, 1156807

[18] Guo, J., Wang, C., Yu, N., Cheung, C. Advanced Finishing Technologies for High Performance Manufacturing. Chapter 11: Plasma Ultraprecision Processing. Springer Press: 2025

[19] An, H. *et al.* Process optimization and removal dynamics in atmospheric pressure plasma etching of SiC. *Applied Surface Science*, 724, p. 165682. (2026)

[20] Yamamura, K., Shimada, S. and Mori, Y. Damage-free improvement of thickness uniformity of quartz crystal wafer by plasma chemical vaporization machining. *CIRP Annals*, 57(1), pp. 567–570. (2008)

[21] Bennett, A., Gobey, K., Yu, N., Castelli, M., Moos, S., Schlemper, H., Bode, J. The Satisloh Plasma Polisher: Plasma Surface Figuring Ultra Precision Optics. SPIE Proceedings (OptiFab). 2023; 12778: 127780B. Available at: DOI:10.1117/12.2685860.

[22] Bennett, A., Fess, E., Piché, F., Moos, S., Sauer, P., Schlemper, H., Bode, J. The Satisloh Plasma Polisher: optics surface figuring results. SPIE Proceedings (OptiFab). 2025; 13728: 137281I. Available at: DOI:10.1117/12.3071772.

[23] Williams, D., Kellar, E., Jesson, D., et al. Surface analysis of 316 stainless steel treated with cold atmospheric plasma. Applied Surface Science. 2017; 403: 240–247

[24] Laidler K. The world of physical chemistry. Oxford: Oxford University Press; 1993

[25] Hagen, N, Dereniak, E. Gaussian profile estimation in two dimensions. Applied optics. 47 (36), 6842-6851 2008

euspen's 26th International Conference & Exhibition, Krakow, PL, June 2026
www.euspen.eu

Flexure-based inverted pendulum mechanical inclinometer

Loïc Tissot-Daguette[1], Salah Hasnaoui[1], Florent Cosandier[1], Charles Baur[1] and Simon Henein[1]

[1]*Instant-Lab, EPFL, Switzerland*

loic.tissot-daguette@epfl.ch

Abstract
This article presents a novel fully mechanical flexure-based single axis inclinometer with degressive sensitivity based on an inverted pendulum with visual readout. The mechanism comprises a cantilever beam with a tip mass attached to its free end inducing axial compression load in the beam, thus reducing its bending stiffness. By adjusting the mass, the sensitivity of the mechanism - defined as the ratio between the beam deflection and the inclinometer inclination - can be tailored. In theory, this sensitivity can approach infinity when the load exerted by the tip mass approaches the critical buckling load of the beam. However, increased sensitivity comes at the cost of reduced measurement range, increased nonlinearity and higher impact of manufacturing tolerances. An analytical model based on Euler-Bernoulli beam theory is developed to describe the degressive nonlinear relationship between beam deflection and inclination angle. The analytical model is validated through finite element modeling and experimental testing on a mesoscale titanium alloy prototype fabricated via wire electrical discharge machining. A graduated scale is integrated for direct visual readout of the deflection of the mass, enabling estimation of the inclination angle. Experimental results demonstrate that the designed inclinometer can be used to measure inclinations up to ±35°, with a sensitivity of 1.16 near the nominal position, degressively reducing to 0.425 near ±35°. The adjustable tip mass allows the sensitivity to be tuned for specific application requirements.

Inclinometer, Flexure mechanism, Stiffness reduction, Beam buckling, Degressive sensitivity

1. Introduction

In precision engineering, inclinometers (also called tilt sensors) are used to measure angular deviation relative to the direction of gravity. These devices are essential in a wide range of applications, including mechanical alignment and leveling [1], robotic motion control [2], and structural health monitoring [3].

Flexure-based inclinometers convert tilt angle into strain or displacement without friction and backlash, therefore offering accurate and repeatable measurements. However, their performance is often constrained by the limited deformation range of the compliant elements. Most existing designs consist of a vertical cantilever beam with a tip mass oriented downward in the nominal position [4-6]. In these pendulum-like configurations, the beam is subect to tensile loading, which increases the effective stiffness and consequently reduces both sensitivity and measurement range.

In contrast, the present study investigates an alternative inverted pendulum configuration where the cantilever beam is subjected to compressive loading, which reduces the beam's bending stiffness, thereby enhancing sensitivity to inclination. In Section 2, the mechanism is described, modeled using classical beam theory and simulated via Finite Element Method (FEM). Section 3 presents the experimental setup used to characterize the performances of a mesoscale inclinometer prototype. The results are presented in Section 4, followed by concluding remarks in Section 5.

2. Conceptual Design

2.1. Mechanism description

A schematic of the proposed inclinometer mechanism is shown in Fig. 1. The device consists of a cantilever beam with a weight (mass m) attached to its free end. When the base frame is inclined by angle α relative to the gravity vector, the gravitational force mg generates a moment onto the beam, causing its deflection. This results in a tip rotation angle β, which serves as the output signal corresponding to the applied inclination.

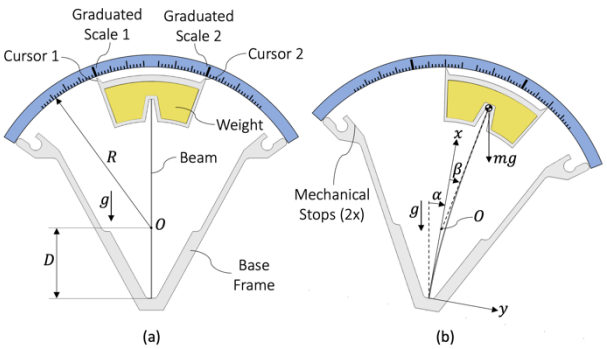

Figure 1. Schematics of the inclinometer (a) in neutral position (i.e., aligned with gravity orientation) and (b) inclined by an angle α

To measure β, one or more graduated scales can be affixed to the base frame. For instance, Fig. 1 illustatres two visual indicators (cursors) with respective graduated scales, that are labeled 1 and 2. This allows the inclination angle to be read from either the left or right side. These edges also act as reference points during the experimental characterization of the inclinometer (Sect. 3). For enhanced measurement accuracy, contactless displacement sensors (e.g., laser triangulation sensors) or strain-based sensing technologies (e.g., fiber Bragg gratings) could be integrated into the design to quantify the rotation angle β with higher precision than visual readout allows.

2.2. Analytical model

This section introduces the theoretical model used to design the inclinometer mechanism. For the calculations, we assume that the cantilever beam is initially straight, slender and aligned with the gravity vector (Fig. 1a). The beam, of length L, is clamped at one end and free at the other extremity. Figure 1b shows the deflection $y(x)$ and the load case of the beam when the base frame of the inclinometer is tilted. The center of mass of the weight is assumed to coincide with the free end of the beam. The gravitational force mg applied to the beam can be divided into a compressive axial force $F_x = mg\cos(\alpha)$ (along x) and a lateral force $F_y = mg\sin(\alpha)$ (along y). Considering small beam deformations, the beam deflection can be computed using Euler-Bernoulli beam theory:

$$M(x) = EIy''(x) \tag{1}$$

where, EI is the flexural rigidity and $M(x)$ is the bending moment. The general defection formula of a compressed beam with a fixed extremity at $x = 0$ is given by [7] as:

$$y(x) = A\sin(kx) + B(\cos(kx) - 1) + Cx \tag{2}$$

where $k = \sqrt{F_x/(EI)}$, and A, B and C are coefficients that are functions of the beam boundary conditions. Since $y'(0) = 0$ and $C = -F_y/F_x$ for small deformations [8], we have:

$$C = -Ak = -\tan(\alpha) \tag{3}$$

The bending moment being null at the beam free extremity (i.e., $M(L) = 0$), the combination of Eqs. (1) and (2) leads to the following relation:

$$B = -A\tan(kL) \tag{4}$$

The deflection angle $\beta = \arctan\big(y'(L)\big)$ can then be expressed as a function of the inclination angle α, as follows:

$$\beta(\alpha) = \arctan\big(\tan(\alpha)\,(\sec(kL) - 1)\big) \tag{5}$$

We define the inclinometer sensitivity at the vicinity of the nominal position as:

$$S_0 = \frac{d\beta}{d\alpha}(\alpha = 0) = \sec(k_0 L) - 1 \tag{6}$$

where $k_0 = \sqrt{mg/(EI)}$. It can be seen that the sensitivity S_0 can be tuned by adjusting the weight mass m. For instance, to obtain a sensitivity of $S_0 = 1$, the mass m must be selected such that $k_0 L = \pi/3$. If $k_0 L = \pi/2$, S_0 tends to infinity because the beam effective stiffness becomes null. Configurations close to this buckled state must be avoided because the measurement range is reduced and the function $\beta(\alpha)$ becomes highly nonlinear. For values of $k_0 L$ above $\pi/2$, the mechanism is bistable, leading to inclinometer reading that would suffer from hysteresis.

The graduated scales are considered to be circular with a radius R and a center O located at a distance D from the fixed extremity of the beam along the x-axis, see Fig. 1. The center O must coincide with the instantaneous rotation center of the beam free extremity in order for the trajectory of the cursors to follow their respective graduated scale. Hence, the relation $y_L = y(L) = (L - D)\tan(\beta)$ must be satisfied. Using Eqs. (2) to (5), the value of D can be expressed as:

$$D = L\left(1 - \frac{1}{kL}\frac{\tan(kL) - kL}{\sec(kL) - 1}\right) \tag{7}$$

2.3. Selected dimensions and materials

Using the analytical model in the previous section, a flexure-based mesoscale embodiment of the inclinometer is designed to demonstrate that the inclinometer works as expected, to provide numerical results for comparison to the analytical model and discuss possible manufacturing limits. The selected dimensions of the beam and the total mass of the weight are summarized in Table 1.

Table 1. Design parameters and corresponding values

	Parameter	Value
Cantilever beam	h	90 µm
	b	3 mm
	L	24.8 mm
Weight	m	4.085 g
Graduation	D	8.61 mm
	R	21 mm

The material of the flexure structure of the inclinometer is chosen to be titanium (Ti-Al6-V4). This material is well suited for its high yield strength ($\sigma_y = 830$ MPa) over Young's modulus ($E = 114$ GPa) ratio [9]. The main material of the weight is selected to be 18 karat gold, chosen for its high density. The total mass $m = 4.085$ g is the sum of the mass of the flexure structure at the free beam extremity and the mass of the gold weight.

The beam has a length $L = 24.8$ mm, a width $b = 3$ mm and a thickness $h = 90$ µm. Using Eq. (6), the nominal sensitivity is $S_0 = 1.16$. Equation (7) shows that D varies slightly with the inclination angle α. The value selected for D is chosen to correspond to the nominal position where $\alpha = 0$. Using the parameter values given in Table 1 and by substituting $kL = k_0 L$ in Eq. (7), this leads to $D \cong 0.347L = 8.61$ mm.

The graduated scales (Fig. 1) are meant to be traced out using the formula $\beta(\alpha)$ given in Eq. (5) and considering a radius $R = 21$ mm. Note that due to the nonlinearity of $\beta(\alpha)$, the distance between two successive graduations is not constant.

Mechanical stops are integrated into the design to limit the rotation of the weight to within $\beta = \pm 30°$. Theoretically, this allows the measurement of inclination angles up to $\alpha = \pm 36°$.

2.4. Finite element modeling

A finite element simulation was conducted using *COMSOL Multiphysics 6.1* to validate the analytical model described in Sect. 2.2. The inclinometer mechanism was modeled using the dimensions and material properties specified in Sect. 2.3. A stationary study was performed using the *Solid Mechanics* module to evaluate the structure's deformation under gravitational loading. Given the planar nature of the mechanism, the analysis was carried out in 2D under the *plane stress* assumption. *Geometric nonlinearity* was enabled, and a *segregated* approach was selected to accurately capture large deformations and potential buckling behavior.

The cantilever beam was discretized using mapped quadrilateral elements, with four elements across the thickness h and 200 along the length L. The remaining structure was meshed with free triangular elements.

A force of constant magnitude mg was applied to the free extremity of the cantilever beam while the base frame was fixed. The direction of the applied force was incrementally varied to simulate inclinations of the mechanism relative to gravity. Specifically, the inclination angle α was swept from -36° to 36° in 2° increments, where $\alpha = 0$ corresponds to the configuration where the force is compressive and aligned with the beam axis.

The tip rotation β, representing the inclinometer output, was extracted as a function of α, yielding the characteristic response $\beta(\alpha)$. The maximum of FEM von Mises stress in the structure

was verified to be below the material yield strength. The FEM results are presented in Sect. 4.

3. Experimental method

The inclinometer structure is monolithically fabricated from titanium alloy using wire-cut electrical discharge machining (EDM). The gold weight is bonded on the moving block at the free beam end of the cantilever beam. The base frame of the flexure mechanism is rigidly mounted between two plexiglass plates.

The assembled inclinometer was installed on a precision rotary stage, with its rotation axis aligned with the center point O and oriented perpendicular to gravity. Inclination angles α were measured using a digital inclinometer (TESA Clinobevel 1-USB), offering a resolution of ±0.01°. A camera (Nikon D800 with AF-S NIKKOR 24-70mm f/2.8E ED lens) was used to measure the deflection angle β as a function of α. The direction of the camera was aligned with point O and its image plane coincided as much as possible with the inclinometer plane to minimize perspective distortion. The camera was placed at a distance of 0.8 m from the inclinometer.

Calibration was performed using a plumb bob, serving as an absolute vertical reference. The reference angle ($\alpha = 0$) was defined when the thread of the plumb bob, suspended between the inclinometer and the camera, was perpendicular to the line connecting two reference points M_1 and M_2 on the base frame.

Discrete inclination angles were applied by rotating the stage, with finer sampling near the nominal position. For each inclination angle, a photograph was captured while the mechanism was at static equilibrium. From each image, the reference frame (x, y) was reconstructed using the positions of M_1 and M_2. The deflection angle β was computed using the coordinates of points P_1 and P_2, based on their positions relative to point O. The final value of β for each inclination angle α was obtained by averaging the measured values from four independent measurement series.

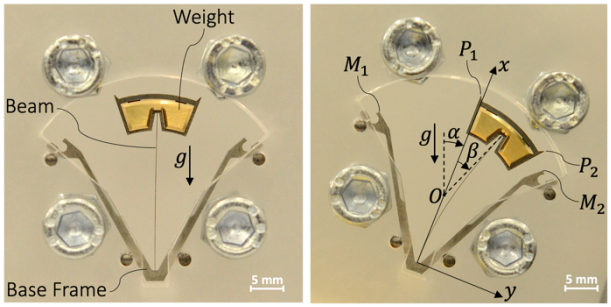

Figure 2. Photographs of the inclinometer prototype (a) in neutral position and (b) inclined by an angle α

4. Results and discussion

Figure 3 shows the deflected angle β as a function of the inclination angle α, comparing the results from the analytical model, FEM simulation, and experimental measurements.

The FEM predicts similar results as compared with the analytical model, the relative error being bounded within 2.8%. In contrast, the experimental data labeled “before calibration” exhibit a noticeable offset from both models. The discrepancy cannot be explained by measurement uncertainty alone, as the maximum standard deviation in β is less than 0.54° (omitted from Fig. 3 for clarity).

When the inclinometer is aligned with gravity (i.e., at $\alpha = 0$), the deflection angle is β_0 = -1.662°. This offset likely originates from manufacturing errors, such as geometric tolerances or residual stress, causing an initial beam deflection even in the absence of external load. Alternatively, it may result from a misalignment between the weight’s center of mass and the x-axis in the nominal position.

To compensate for this systematic error, the inclinometer can be calibrated by rotating the graduated scale by the offset angle β_0 relative to the flexure structure. This ensures that $\beta = 0$ when $\alpha = 0$. The experimental data “after calibration” agree well with the analytical model, with a maximum relative error below 4.2%, confirming the accuracy of the theoretical formulation.

Given that the relationship $\beta(\alpha)$ is well predicted, the inclinometer is suitable for accurately determining inclination angles by reading the deflection β on integrated graduated scales (as shown in Fig. 1).

However, the experiments also revealed that the flexure-based mechanism exhibits a high quality factor (greater than 100) and a low eigenfrequency is (below 5 Hz). As a result, the inclinometer may require several minutes to settle after experiencing external vibrations. To improve damping and reduce stabilization time, it is suggested to immerse the flexure mechanism in a viscous fluid (e.g., water or glycerin), which would attenuate unwanted dynamic responses.

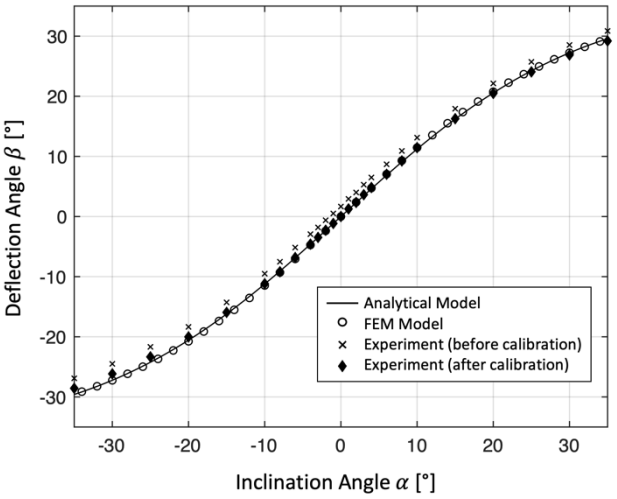

Figure 3. Graph of the deflection angle as a function of the applied inclination angle. The experiment data is plot before and after calibration, and is compared to the analytical and FEM models.

5. Conclusion

This paper presents a novel flexure-based inclinometer composed of a vertical cantilever beam and a tip mass. The mechanism functions as an inverted pendulum in its nominal position, deforming under gravitational load when tilted. The inclinometer exhibits maximum sensitivity of 1.16 near the nominal position (0°) and a minimal sensitivity of 0.425 at ±35°. This sensitivity decreases nonlinearly as the inclination increases. This degressive behavior offers the advantage of a higher measuring resolutions for small angles, while keeping a large measuring range. Analytical and FEM models have been developed to support the design process and predict the behavior of the mechanism. Experimental results agree closely with both models and confirm that the device can reliably measure inclination angles up to ±35°.

The continuation of this work will focus on sealing the mechanism within a viscous fluid (e.g., water or glycerin) to dampen unwanted oscillations and improve dynamic stability. Additionally, we plan to investigate the effect of increased tip

mass to enhance sensitivity for applications requiring finer resolution.

Further prospect may include the extension of the measurement range to ±180° by using multiple cantilever beams oriented at different initial angles to provide continuous sensitivity over a full circle. Another avenue would be the extension of the flexure inverted pendulum principle to the design of a two-axis inclinometer by using a flexible rod (i.e., a beam with circular cross section) and a spherical visual readout grating.

References

[1] Chang H-Y, Chang Y-C and Liu W-F, 2017, A Highly Sensitive Two-Dimensional Inclinometer Based on Two Etched Chirped-Fiber-Grating Arrays, *Sensors*, **17**, 2922

[2] Besnard S and Khalil W, 1999, Calibration of parallel robots using two inclinometers, *Proceedings 1999 IEEE International Conference on Robotics and Automation*, **3**, 1758-1763

[3] Casas J R, Cruz P J, 2003, Fiber optic sensors for bridge monitoring, *Journal of Bridge Engineering*, **8(6)**, 362-373

[4] Pei H-F, Yin J-H and Jin W, 2013, Development of novel optical fiber sensors for measuring tilts and displacements of geotechnical structures, *Measurement Science and Technology*, **24**, 095202

[5] Yang Y, Ma X, Chen K, Wang E, Yu Z and Yu Q, 2018, A high-resolution dynamic fiber-optic inclinometer, *Sensors and Actuators A: Physical*, **283**, 305-312

[6] Zhang C, Zhang S and Cao J, 2023, In-place fiber-optic inclinometer based on a vertical cantilever beam and dual FBGs, *Optics & Laser Technology*, **159**, 108933

[7] Tissot-Daguette L, Smreczak M, Baur C and Henein S, 2021, Load cell with adjustable stiffness based on a preloaded T-shaped flexure pivot, *euspen's 21st International Conference & Exhibition, Copenhagen, DK*

[8] Tissot-Daguette L, Schneegans H, Thalmann E, Henein S 2022 Analytical modeling and experimental validation of rotationally actuated pinned–pinned and fixed–pinned buckled beam bistable mechanisms *Mech. Mach. Theory* **174** 104874

[9] Cosandier F, Henein S, Richard M, Rubbert L 2017 *The art of flexure mechanism design* EPFL Press Lausanne

euspen's 26th International Conference & Exhibition, Krakow, PL, June 2026
www.euspen.eu

Magnetically driven internal finishing of stainless steel tubes by a novel electrostatic flocking and drum-shaped polishing tool

Zhanjie Zhang[1], Chongrui Wang[1] and Jiong Zhang[1*]

1 Department of Mechanical Engineering, City University of Hong Kong, 83 Tat Chee Avenue, Kowloon Tong, Kowloon, Hong Kong SAR

** Corresponding Author / Email: jiong.zhang@cityu.edu.hk, TEL: +852-3442 7345, FAX: +852 3442 0235*

Submitting Author Email: zzhang548-c@my.cityu.edu.hk

Abstract

High-quality internal surface finishing is essential for components used in critical industries such as aerospace and medical devices. Compared to conventional magnetic abrasive finishing (MAF), magnetically driven internal finishing (MDIF) represents a more flexible, controllable, and promising processing technology. However, the MDIF technique is constrained by the utilization of fixed-abrasive tools, which limit the attainable surface roughness to above 100 nm Ra. This study proposes a new MDIF tool that uses electrostatic flocking to coat a specially designed drum magnet with a flocking layer. Compared to manual flocking, this technique can more easily build a more uniform and directional flocking layer, improving material removal efficiency. Experimental results demonstrate that this method can reduce the internal surface roughness Ra of 316L stainless steel tubes from an initial average of 265 nm to 29 nm within 10 minutes, improving surface quality by over 89 %. Furthermore, repeatability experiments have shown tool performance to be highly consistent. Experiments on a larger-diameter tube verified the tool's dimensional versatility. This novel approach markedly advances the MDIF process and attains high efficiency nanofinishing, demonstrating substantial potential for precision internal finishing applications in high-demand industries.

KEYWORDS: Magnetically driven internal finishing, Magnetic polishing tool, Electrostatic flocking, Surface roughness

1. Introduction

The integrity of internal surfaces in tubular components is a critical determinant of the operational efficiency and fatigue lifespan of essential systems in aerospace, semiconductor fabrication, and biomedical engineering. Even minor bumps or damage to the surface or below it can cause flow turbulence, corrosion buildup, or catastrophic material failure [1, 2]. Researchers and practitioners use traditional finishing methods, such as abrasive flow machining (AFM) and magnetic abrasive finishing (MAF), to solve these problems. However, these methods often have issues with process flexibility and the inability to achieve deterministic control over material removal on complex internal geometries [3, 4].

Magnetically driven internal finishing (MDIF) has come up as a promising alternative to traditional methods. Zhang et al. were the first to utilize MDIF, which employs externally rotating magnetic fields to position polishing tools precisely inside the tubular components [5-7]. This is a non-contact, adaptive method for polishing long, thin tubes. Although the existing MDIF process is flexible, it typically utilizes magnetic tools coated with fixed abrasives or bonded magnetic abrasive powders, limiting the final surface roughness above 100 nm Ra [8].

Recently, Zhang et. al. proposed a new approach by using a magnetic tool with flocking fibers [9]. This preliminary investigation indicated that soft nylon fibers, when used for transporting abrasive slurry, could generate a finer workpiece surface compared to fixed abrasive tools. However, this manual fabrication of the tool poses challenges in uncontrollable fiber density, fiber oritentation and uniformity.

To address the above issue, this paper proposed a new process to fabricate the MDIF polishing tool, transitioning from a manually created design to one that utilizes an electrostatic flocking method on a drum-shaped magnet. Using high-voltage electrostatics makes sure that the fibers are lined up perpendicular to the tool substrate, creating a dense, directed, and even polishing layer. Repeatability experiments were conducted to compare two adhesive coating strategies. A larger-diameter 316L stainless steel tube is polished to confirm the versatility. The successful development of this tool is expected to establish a foundation for automated tool fabrication, highlighting its potential as a scalable solution for the ultra-precision finishing of critical components.

2. Experiment

2.1. Workpiece preparation

This study employed 316L stainless steel tubes with two dimensions. The two types of tubes were both 100 mm long and 2 mm thick, but they had different inner diameters (ID): 15 mm and 20 mm. The tubes were cut into the shape shown in Fig. 1(a) using a sawing machine to facilitate the following experiments. A Taylor Hobson Talysurf profilometer (PGI) was used to measure the initial surface roughness. To ensure consistency, three closely spaced measurement lines were taken axially at the geometric center of the polished region, where the tool's dwell time was longest (Cut-off: 0.25 mm, evaluation length: 4.75 mm). The tubes with a 15 mm ID had a roughness range of 250 nm–290 nm Ra (average: 265 nm Ra), and the tubes with a 20 mm ID had a range of 270 nm–290 nm Ra (average: 280 nm Ra). Figures 1(b) and 1(c) display the microscopic profile height graphs corresponding to this.

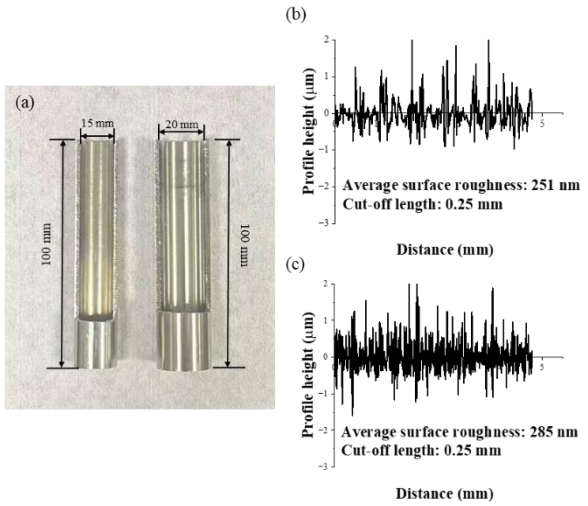

Figure 1. Two 316L stainless steel tubes before polishing (a), microscopic profile height graph (b) of ID15 mm tube, and microscopic profile height graph (c) of ID20 mm tube

2.2. Fabrication process of novel magnetic polishing tools

Figure 2 illustrates the fabrication process of the magnetic tool with flocking fibers. The procedure is meticulously controlled to ensure geometric precision and surface uniformity.

Stage I: Preparing the Substrate. A drum-shaped N35-grade NdFeB magnet is utilized, with a 1.2 mm central hole drilled to facilitate mounting and rotation. To remove all dirt from the surface, the drum magnet is washed with 99.9 % ethanol and then air-dried before the adhesive is put on, which ensures the binding is as strong as possible where it contacts the substrate. Then, a pin is placed through the hole in the middle to keep the magnet in place.

Stage II: Applying the Adhesive. To ensure proper fiber density, achieving a homogeneous adhesive coating is crucial. The pinned magnet is connected to a high-concentricity collet driven by a horizontal motor (Fig. 2(II)) at a constant 30 rpm. A specifically designed flocking glue with high flowability is utilized, which is crucial for maintaining an even film thickness across the curved surface. Following a brief immersion in the adhesive reservoir, the magnet continues rotating for 2–3 minutes to allow for partial curing and leveling before flocking.

Stage III: Flocking with Electricity. Figure 2(III) shows that a high-voltage electrostatic flocking machine (output voltage: 30 kV) is employed to generate the flocking layer. The square metal collecting plate is connected to the positive electrode of the generator, while the flocking barrel is connected to the negative electrode. Nylon fibers with a length of approximately 0.6 mm are used as the flocking medium, pre-dried and passed through a 40-mesh screen to prevent agglomeration. The setup requires precise geometric alignment: both the positive and negative electrodes are positioned 100 mm from the center of the spinning magnet. After the electric field is set up, the flocking barrel is shaken gently and uniformly for approximately 90 seconds. To maintain a constant electric field strength, the distance between the barrel and the magnet remains the same during this phase.

Stage IV: Curing and Post-Processing. The voltage is gently decreased to zero after the flocking phase is over. The magnet continues to spin at 30 rpm for an additional five minutes to facilitate initial air drying. After that, the magnet assembly is removed from the motor and set in an oven for two hours at 55 °C to harden. Finally, it is left at room temperature for 12 hours to fully cross-linked. The diameter of the flocking-treated drum magnet is 8.3 mm ± 0.1 mm, with a magnetic flux density of 0.48 mT ± 0.01 mT.

As illustrated in the schematic diagram in Fig. 2(IV), two distinct fabrication strategies were explored to address edge stability. The first method (full adhesive coated) involves coating the whole surface of the drum, followed by using a blade to cut off the flocking layer from the top and bottom planar faces. This step is critical because it removes irregular fiber clusters on the edges that could render the tool unstable during polishing. The second method (half adhesive coated) utilizes a controlled immersion depth in Stage II to coat only the curved surface, eliminating the need for trimming after treatment. The rationale for evaluating the half-coated strategy is that if it proves to be highly effective, the time-consuming post-trimming step can be completely omitted, which would significantly improve manufacturing efficiency. The original manual coating method [9] was excluded from this specific comparison. While our previous work successfully established the foundational feasibility of fiber-coated magnetic tools, its inherent limitations in fiber uniformity and minimum attainable roughness (>70 nm Ra) are already understood. Consequently, the present study advances this concept by focusing entirely on optimizing the manufacturing strategies within the upgraded electrostatic flocking paradigm to achieve ultra-precision nanofinishing.

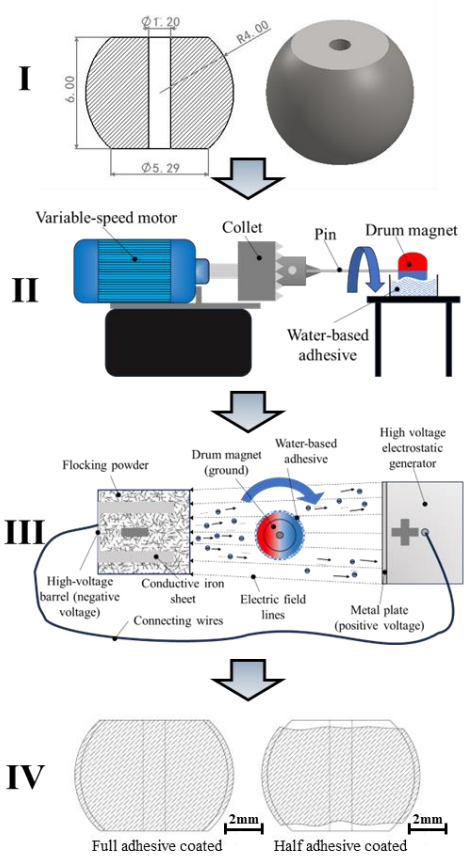

Figure 2. Electrostatic flocking process flowchart

2.3. Polishing setup

The polishing setup of MDIF is shown in Figure 3. The external magnetic field is created by placing four N52-grade cuboid NdFeB magnets on an aluminum prism and arranging their poles in an alternating pattern (N-S-N-S). The spindle of a high-precision CNC machine (Datros-V260) is connected to providing rotation of the external magnetic field. A three-jaw chuck, located on top of a dynamometer, holds the workpiece in place. The dynamometer is fastened to the machine table. A peristaltic pump sends the polishing slurry. And a magnetic stirrer keeps the slurry reservoir mixed up so that it stays uniform and does not settle out.

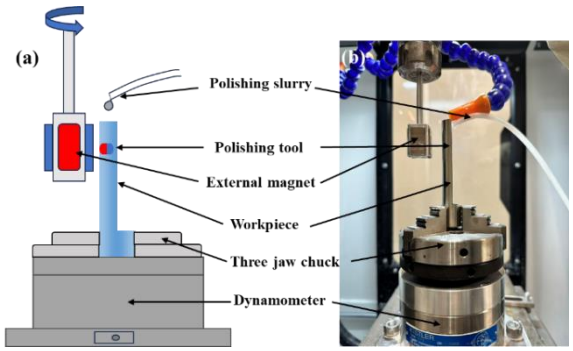

Figure 3. Polishing setup (a) schematic diagram, and (b) actual apparatus

2.4. Experimental procedure

Phase I: The first step was to conduct repeatability tests to compare the two different methods of tool production. Each strategy made three polishing tools. We used these tools to polish the interior of 316L stainless steel tubes (ID: 15 mm, wall thickness: 2 mm) at different locations. The external magnetic field was maintained at 1800 rpm for these tests, with a 10 mm working gap between the external magnet and the outer wall of the tube. Each tool took 10 minutes to process workpiece. The abrasive slurry consisted of 1 µm aluminum oxide (Al_2O_3) particles suspended in deionized water with a mass fraction of 10 %. A peristaltic pump delivered it at a steady flow rate of 5 mL/min.

Phase II: In the second Phase, polishing tools made using the method that worked best and was most stable in Phase I were used to test the tool's versatility. Single-point polishing was performed on larger-bore 316L stainless steel tubes (ID: 20 mm, wall thickness: 2 mm). Three separate tools were used to polish various locations of the same tube. For this test, the rotational speed was set to 2000 rpm, and the working gap was cut to 8 mm. The slurry composition, flow rate, and processing duration (10 minutes) stayed the same as in Phase I. The operational settings were slightly modified from the first group, as using the same parameters on the larger diameter tube made the tool less stable. Fine-tuning was necessary to determine the optimal operating range for the new geometry.

3. Results and discussion

3.1. Repeatability experiment

To determine the most effective method for making tools, we compared the "full adhesive coated" method (which requires edge trimming) with the "half adhesive coated" process (which controls immersion). We measured the surface roughness (Ra) and material removal depth of the workpiece tube for the six polishing tools. Tools 1–3 were used with the full-coating strategy, while Tools 4–6 were used with the half-coating strategy.

Table 1 Summary of repeatable experiments

Polishing tool	Ra / nm	Depth / µm
1	29.3	17.5
2	36.5	16.2
3	41.7	16.5
Average	35.8	16.7
Standard deviation	5.1	0.5
Coefficient of variation	14.2 %	3.3 %
4	59.3	19.5
5	43.8	18.1
6	56.7	17.0
Average	53.3	18.2
Standard deviation	6.8	1.0
Coefficient of variation	12.7 %	5.7 %

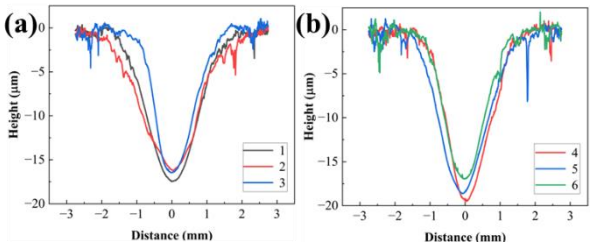

Figure 4. The polished profiles comparison (a) full adhesive coated, and (b) half adhesive coated

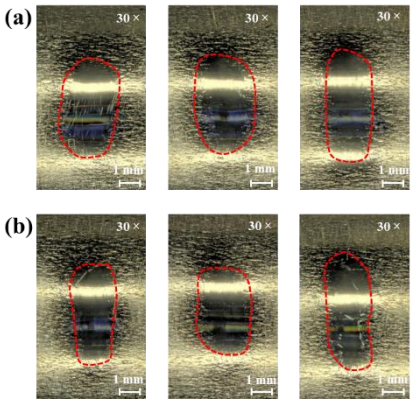

Figure 5. Optical images of polishing marks from three replicate experiments (a) Full adhesive coated, and (b) half adhesive coated

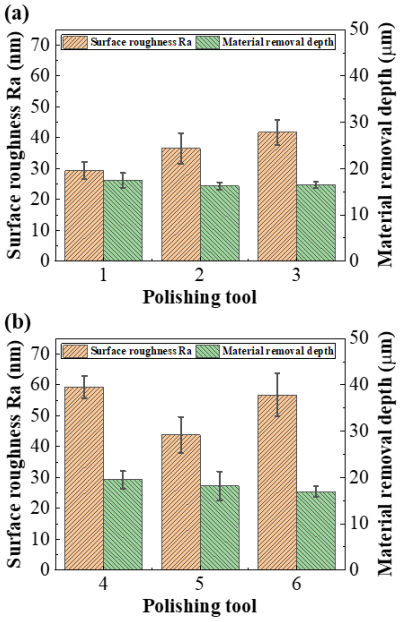

Figure 6. Summary of surface roughness and material removal depth in repeatable experiments (a) full adhesive coated, and (b) half adhesive coated

Table 1 and Figure 6 show that the full adhesive coated strategy (Tools 1-3) demonstrates better finishing capabilities. Figure 6(a) shows that these tools achieved an average surface roughness of Ra 35.8 nm, representing a significant improvement over their original rough state. For this group, the average depth of material removal is 16.7 µm. The optical images in Fig. 5(a) show that the polishing marks are consistent and oriented in a single direction.

On the other hand, the tools made using the half-coating method (Tools 4–6) had an average surface roughness of Ra 53.3 nm and an average material removal depth of 18.2 µm. The half-

coated tools did not produce a surface as good as the former, despite similar material removal rates. Figures 4(b) and 5(b) show that the polishing profiles and marks for this group were not as even as those for the trimmed tools.

For all these tools, the material removal mechanism relies on the dense nylon fibers acting as a flexible brush, retaining the slurry and softly transferring magnetic forces to shear off micro-peaks. While comprehensive lifetime testing is reserved for future work, visual inspections confirmed no noticeable fiber degradation after these 10-minute cycles.

The difference in performance can be traced back to the edge conditions of the flocking layer. As mentioned in the manufacturing process, the full-coating method involves trimming the top and bottom edges of the material. This eliminates the uneven fiber clusters and edge effects that can occur during electrostatic flocking. The half-coating method eliminates steps that need to be performed after the coating. Still, it relies on the adhesive's ability to naturally wet itself during immersion, which is influenced by surface tension. It can be hard to control this wetting all the time, which could cause the fiber density to change at the edges. As a result, the full adhesive coated strategy was chosen for the following versatility experiments because it could create a better surface finish (Ra < 40 nm).

3.2. Large-diameter tubes polishing experiment

To prove that the proposed tool is useful in various situations, the optimized polishing tool (made using a full-coating strategy) was applied to a 316L stainless steel tube with an inner diameter of 20 mm. To make up for the larger aperture size and make sure the tool moved smoothly, the experimental parameters were adjusted to a rotational speed of 2000 rpm and a working gap of 8 mm, as explained in Section 2.4.

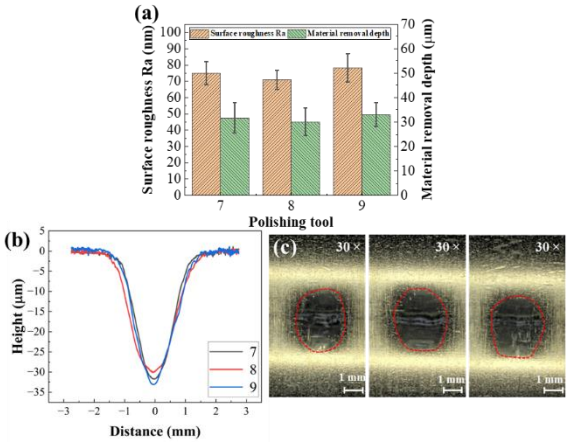

Figure 7. Polishing results of tools manufactured using the full adhesive coated method (a) summary of surface roughness and material removal depth, (b) the polished profiles comparison, and (c) optical images of polishing marks

Table 2 Summary of large-bore tube experiment data

Polishing tool	Ra / nm	Depth / μm
7	74.9	31.7
8	70.8	30.1
9	78.3	33.1
Average	74.7	31.6
Standard deviation	3.1	1.2
Coefficient of variation	4.1 %	3.9 %

The results from the large-diameter tube experiments (Tools 7-9) are shown in Figure 7 and Table 2. The system demonstrated high efficiency in removing material, with an average removal depth of 31.6 μm in just 10 minutes. The significant increase in polishing depth compared to the ID15-mm tube experiments may be attributed to the more stable rotation motion of the tool on the workpiece tube, as evidenced by the small polishing marks in Figure 7(c).

This tool reduced the average internal roughness to 74.7 nm Ra, achieving a ~73.3 % reduction from the initial state. This final Ra is higher than that of the ID 15 mm tube due to two main factors. First, the larger tube had a higher initial surface roughness (280 nm Ra). Second, the reduced working gap generated a stronger magnetic normal force that doubled the material removal depth (31.6 μm), which likely deepened individual abrasive indentations. Nevertheless, the low coefficient of variation (3.9 %) indicates excellent process stability. These results confirm the tool's dimensional adaptability, though further magnetic field optimization is required to match the nanometer-level finish of smaller tubes.

4. Conclusion

This study introduces an innovative Magnetically Driven Internal Finishing (MDIF) tool created using electrostatic flocking to overcome the constraints of conventional fixed-abrasive polishing. Experimental comparisons showed that the full adhesive coating technique with edge trimming gives better performance. This new polishing tool reduces the internal roughness of ID 15 mm 316L stainless steel tubes from 265 nm to 29 nm Ra. Additionally, versatility tests on tubes with a 20 mm inner diameter demonstrated that the tool was capable of removing a substantial amount of material (31.6 μm) with minimal process variation (coefficient of variation 3.9%). These results demonstrate that the tool can achieve high-efficiency nanofinishing, making it a promising and versatile choice for precise internal surface machining in key industries.

Acknowledgements

JZ acknowledges the support of the start-up fund at the City University of Hong Kong with the grant number of 9610646, and National Natural Science Foundation of China with the grant number of 52505524.

Reference

[1] Yamaguchi, H., & Shinmura, T. (2000). Study of an internal magnetic abrasive finishing using a pole rotation system: Discussion of the characteristic abrasive behavior. *Precision Engineering*, **24**(3), 237-244.

[2] Jain, V. K. (2016). Nanofinishing: an introduction. In *Nanofinishing science and technology* (pp. 23-46). CRC Press.

[3] Qian, C., Fan, Z., Tian, Y., Liu, Y., Han, J., & Wang, J. (2021). A review on magnetic abrasive finishing. *The International Journal of Advanced Manufacturing Technology*, **112**(3), 619-634.

[4] Han, S., Salvatore, F., Rech, J., & Bajolet, J. (2020). Abrasive flow machining (AFM) finishing of conformal cooling channels created by selective laser melting (SLM). *Precision Engineering*, **64**, 20-33.

[5] Zhang, J., Hu, J., Wang, H., Kumar, A. S., & Chaudhari, A. (2018). A novel magnetically driven polishing technique for internal surface finishing. *Precision Engineering*, **54**, 222-232.

[6] Zhang, J., Wang, H., Kumar, A. S., & Jin, M. (2020). Experimental and theoretical study of internal finishing by a novel magnetically driven polishing tool. *International Journal of Machine Tools and Manufacture*, **153**, 103552.

[7] Zhang, J., Tian, W., Zhao, F., Mei, X., Chen, G., & Wang, H. (2022). Material removal rate prediction based on broad echo state learning system for magnetically driven internal finishing. *IEEE Transactions on Industrial Informatics*, **19**(5), 6295-6304.

[8] Zhang, J. (2020). *A Study on the Development of Magnetically Driven Internal Finishing Technique* (Doctoral dissertation, National University of Singapore (Singapore)).

[9] Zhang, Z., Wang, C. and Zhang, J., 2024. Surface Quality Enhancement of Metallic Tubes by A Novel Flocking-Fiber Coated Magnetic Tool. *Proceedings of the 9th International Conference of Nanomanufacturing (nanoMan2024)*, pp.117-120.

euspen's 26th International Conference & Exhibition, Krakow, PL, June 2026
www.euspen.eu

Thermal modulation of the water-induced surface ordering effect for tunable machining performance in copper micro-cutting

Zhenyu Liu [1], Jiuxing Tang [2], Wai Sze Yip [2], Jiong Zhang [1, *]

[1]*Department of Mechanical Engineering, College of Engineering, City University of Hong Kong, Hong Kong SAR, China*
[2]*State Key Laboratory of Ultra-precision Machining Technology, Department of Industrial and Systems Engineering, The Hong Kong Polytechnic University, Hong Kong SAR, China*

[*] *Corresponding Author / Email: jiong.zhang@cityu.edu.hk*
Submitting Author / Email: zliu362-c@my.cityu.edu.hk

Abstract
The water-induced surface ordering (WISO) effect, *i.e.*, water molecules ordering the surface atoms of copper, has been shown to dramatically reduce the cutting force in micro-cutting of copper. However, its modulation beyond a simple "on-off" state remains unexplored. In this study, experiments are designed to investigate the regulation of WISO by qualitatively controlling the quantity of surface-bound water molecules via thermal means. Orthogonal micro-cutting was conducted on polycrystalline copper under varying depths of cut (doc) and surface temperatures. The experiments reveal that the cutting force reduction ratio (CFRR), defined as the percentage reduction of cutting force in the region with H_2O compared to that without, demonstrates distinct consistency across doc and thermal sensitivity. Specifically, while cutting forces rise with increasing doc, the CFRR stabilizes at 40%-44% within the range of 15 µm–30 µm doc, which confirms that the effectiveness of WISO remains stable within a specific range of doc. In contrast, as surface temperature increases from 20 °C to 80 °C, the CFRR decreases from 70.72% to 57.67%. Since the increase in actual doc caused by thermal expansion plays a negligible role in the CFRR, this decay is mainly attributed to the thermally induced reduction of effective surface-bound water molecules. This is also demonstrated by the reduced difference in surface roughness Sa between regions with and without H_2O at higher surface temperatures, as the Sa in regions with H_2O remains lower than in regions without H_2O. Furthermore, chip morphology changes from short, thick shapes in regions without H_2O to long, thin ones in regions with H_2O. Ultimately, this study reveals that the quantity of surface-bound water molecules is a crucial factor influencing the WISO effect, and modulating it through thermal means shows potential for controlling the machining performance in copper micro-cutting.

Keywords: Water-induced surface ordering; Micro-cutting; Temperature; Copper; Cutting force

1. Introduction

The micro-cutting of metals presents significant challenges to machining performance, particularly in terms of cutting force, surface roughness, and energy consumption, especially for ductile metals such as copper and aluminum, due to their high ductility [1-5]. To address these issues, recent research has focused on the surface effect, which offers a clean and sustainable approach, such as the Rehbinder effect [6, 7]. The Rehbinder effect is defined as the reduction in strength of solids due to the adsorption of surface-active media (SAM), which is widely utilized in the micro-cutting of metals and has recently become a topic of significant research interest. It has been demonstrated that several types of SAM, including ink, glue, carbon tetrachloride, deep eutectic solvents, and water, can affect certain metals, such as iron, nickel alloys, copper, and aluminum alloys, which can significantly reduce the cutting force, improve the surface roughness and change the chip morphology [5, 6, 8-11]. In particular, the water-induced surface ordering (WISO) effect, *i.e.*, water molecules ordering the surface atoms of Cu, has been shown to dramatically improve machining performance in micro-cutting of copper by reducing both the surface energy and fracture toughness of Cu [6].

However, despite the proven effect of WISO, most existing studies have predominantly treated this phenomenon as a binary "on-off" state, simply comparing SAM-coated conditions against non-SAM-coated conditions. The tunability of this effect and the governing factors that modulate its intensity to meet varying processing requirements remain unexplored. Since the WISO effect is triggered by water bound to the surface of Cu, the quantity of surface-bound water molecules is considered the key factor in the WISO effect. Theoretically, elevated temperatures increase the kinetic energy of the water molecules' thermal motion enough to overcome the intermolecular forces, causing them to escape from the liquid surface [12]. Previous research has indicated that below 100 °C, water interacts with copper mainly through physical adsorption, which is highly reversible. As the temperature increases, the quantity of surface-bound water molecules and molecular coverage on flat Cu surfaces decreases, driven by the thermodynamic tendency for thermal desorption [13-15]. Thus, thermal means could be used to control the quantity of surface-bound water molecules during micro-cutting qualitatively, thereby offering a pathway to regulate the WISO intensity during micro-cutting. However, no studies have been conducted to validate this hypothesis.

Therefore, this paper aims to address the aforementioned research gaps in modulating the WISO effect for tunable machining performance in copper micro-cutting. Experiments were designed to investigate the regulation of WISO by qualitatively controlling the quantity of surface-bound water molecules via thermal means, *i.e.*, changing the surface temperature during cutting. Meanwhile, a series of experiments with varying depth of cut (doc) was conducted to investigate the

consistency across doc of the effect and to exclude the impact of thermal expansion on the actual doc. The cutting forces, the surface roughness of the machined surfaces, and the chip morphology were observed and analyzed. This study presents a new perspective on understanding the WISO effect, offering a viable method to modulate the cutting force in copper micro-cutting.

2. Experimental Setup

Figure 1(a) illustrates the orthogonal cutting (grooving) process on Cu. The workpiece material used in this study was polycrystalline copper, with dimensions of either (10 × 10 × 10) mm or (15 × 15 × 10) mm. The experiment was conducted on a NanoTech 350FG ultraprecision machining center (UPM), and the experiment setup is shown in Figure 1(b). The Cu workpiece was mounted on the spindle of UPM via an aluminum fixture. The Cu workpiece was trimmed by a single-crystal diamond (SCD) cutter with a 0.509 mm nose radius and a 10° rake angle without using flushing coolant, to minimize the influence of initial surface morphology. After trimming, distilled water was applied to the upper half of the Cu workpiece using a cotton swab at room temperature (~22 ℃). When the water was uniformly coated on the target region, the Cu workpiece was placed in air for 10 min, ensuring the macroscopic evaporation of the bulk liquid water. Subsequently, grooving experiments were conducted using an SCD cutter with a 0.828 mm nose radius and a 0° rake angle, which was placed on a Kistler dynamometer for force measurement with a sampling frequency of 2000 Hz. The cutting parameters for trimming and grooving are listed in Table 1.

Table 1. The parameters for the trimming and grooving process.

Parameter	Trimming	Grooving
Spindle speed/ r·min^{-1}	2000	0
Depth of cut / μm	5	1 - 30
Feed rate/ mm·min^{-1}	1.5	50
Surface temperature/ ℃	20	20 - 100

For the experiment of grooving at different surface temperatures, an infrared lamp was integrated into the experimental setup to modulate the workpiece surface temperature. Two K-type thermocouples were attached at different positions on the surface of the Cu workpiece, and a TASI TA611B thermometer was used to monitor the surface temperature in real time to cross-check the accuracy of the Cu surface temperature measurement, as shown in Figure 1(c).

After grooving, the chips were collected and observed via a JEOL JSM-5600 scanning electron microscope (SEM). The surface roughness Sa of the groove was measured using an Olympus OLS 5100 laser confocal microscope with an S-filter of 2.5 μm and an L-filter of 250 μm, in accordance with the ISO 25178 standard. The actual doc of the groove was measured using a Taylor Hobson TalySurf Series 2 phase grating interferometer (PGI).

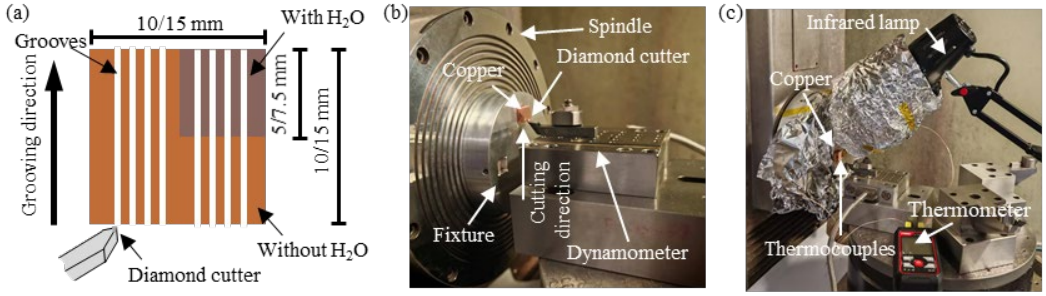

Figure 1. Experimental procedures and equipment. (a) Experimental schematic diagram. (b) Experimental equipment. (c) Infrared heating and temperature measurement device.

3. Results and Discussion

3.1. The influence of depth of cut

The study investigated the influence of different doc, conducted over a range of 2.5 μm, 5 μm, 10 μm, 15 μm, 20 μm, 25 μm, and 30 μm. Figure 2(a) illustrates a typical variation in cutting force with a 15 μm doc, showing that the average maximum cutting force decreases sharply from 9.07 N ± 0.34 N in the region without H_2O to 5.06 N ± 0.18 N in the region with H_2O. To better demonstrate this change in cutting force, the cutting force reduction ratio (CFRR), defined as the percentage reduction in cutting force in the region with H_2O compared to that without it, as shown in Equation (1), was calculated.

$$Cutting\ force\ reduction\ ratio = \left(1 - \frac{Cutting\ force\ in\ the\ region\ with\ H_2O}{Cutting\ force\ in\ the\ region\ without\ H_2O}\right) \times 100\% \quad (1)$$

Figure 2(b) displays the cutting force and CFRR for different doc. For 2.5 μm and 5 μm doc, the cutting force in the region with H_2O was higher than that in the region without H_2O, resulting in a negative CFRR. As the doc increases, the cutting force in both regions increases accordingly, while the CFRR rises and stabilizes at 40%–44% for 15 μm–30 μm doc. It indicates that the effect of WISOs remains consistent within a specific range of doc and demonstrates distinct consistency across doc.

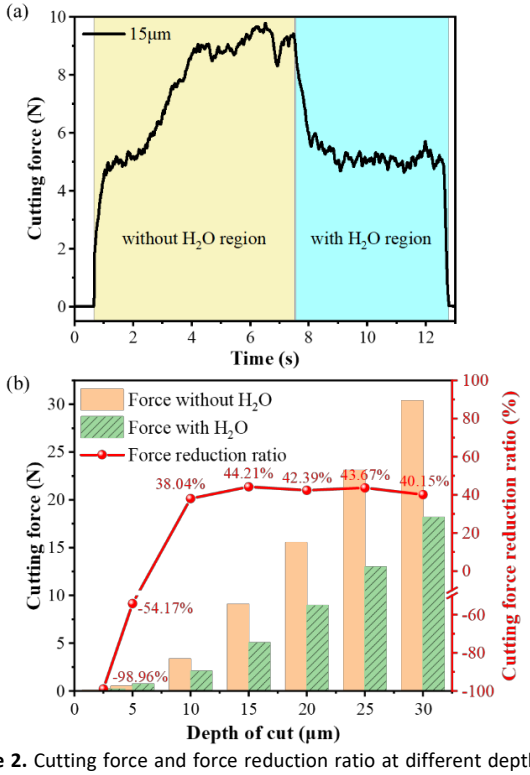

Figure 2. Cutting force and force reduction ratio at different depths of cut. (a) Typical variation of cutting force with a 15 μm depth of cut. (b) Cutting force and force reduction ratio with different depths of cut.

3.2. The influence of surface temperature

The study investigated the influence of surface temperature from 20 °C to 100 °C. Figure 3(a) illustrates a typical variation in cutting force at 20 °C, showing that the average maximum cutting force decreases sharply from 19.62 N ± 0.88 N in the region without H_2O to 5.74 N ± 0.30 N in the region with H_2O, with the CFRR of 70.72% ± 2.01%.

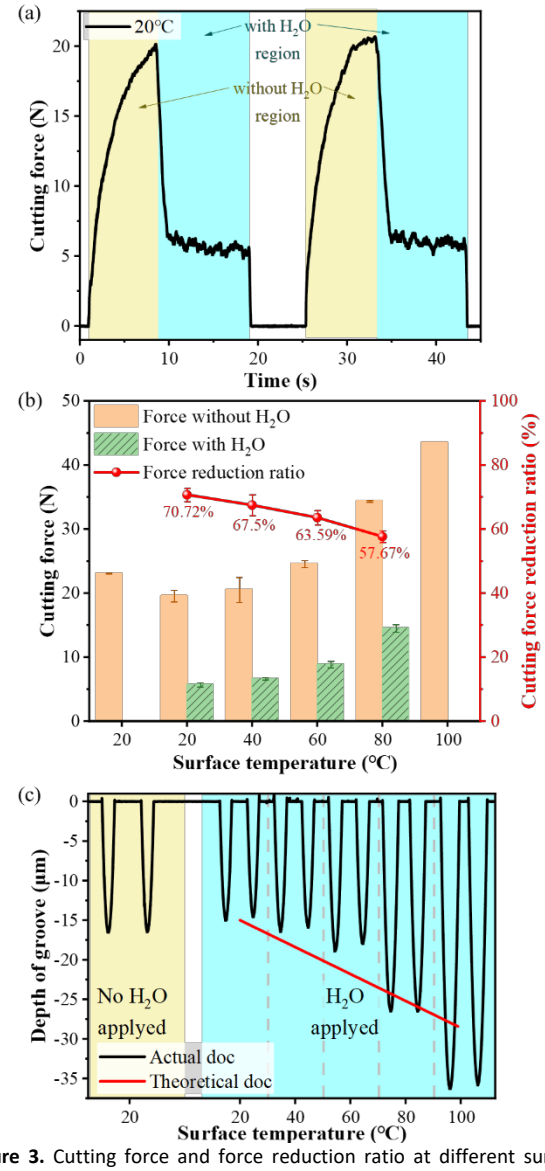

Figure 3. Cutting force and force reduction ratio at different surface temperatures during cutting. (a) Typical variation of cutting force at 20 ℃ during cutting. (b) Cutting force and force reduction ratio at different surface temperatures during cutting. (c) The measured groove profile after cutting and the theoretical groove depth considering thermal expansion at different surface temperatures.

However, as illustrated in Figure 3(b), the cutting force in both regions increases with rising surface temperature during cutting, while the CFRR exhibits a decreasing trend, from 70.72% at 20 °C to 57.67% at 80 °C. Regarding the condition with a surface temperature of 100 °C, the fixture mounted on the spindle exhibited displacement during the cutting process due to the elevated temperature. This resulted in the grooving process failing to traverse the surface of the Cu workpiece as intended fully. Therefore, only the cutting forces in the initial region without H_2O were thoroughly documented and analyzed, whereas those in the H_2O region could not be precisely determined.

The increase in cutting force is due to the thermal expansion of the Cu workpiece as the temperature increases, leading to a larger actual doc. This is evidenced by measuring the depth of the grooves after cutting via the PGI, as shown in Figure 3(c). Figure 3(c) presents that the actual groove depth is similar to the doc, considering thermal expansion at different surface temperatures (red line). However, the experiment of varying doc has demonstrated that the effect of WISO remains consistent within a specific range of doc, which contains the actual doc under different surface temperatures during cutting. Consequently, the change in the actual doc plays a negligible role in the CFRR, and the decay of the CFRR is attributed to the increasing surface temperature during cutting. Research indicates that below 100 °C, water interacts with copper mainly through physical adsorption, forming an oriented water dipole layer. This process is highly reversible, so increasing temperature decreases the quantity of surface-bound water molecules and molecular coverage on flat Cu surfaces, driven by the thermodynamic tendency for thermal desorption [1, 6, 13-15]. The primary reason for the decrease in CFRR may be the reduction in surface-bound water molecules resulting from the increase in surface temperature. Therefore, the quantity of surface-bound water molecules is a crucial factor influencing the WISO effect, and the temperature changes are just one method to influence this parameter.

This is also evident from the surface roughness Sa between water-coated and uncoated regions at various surface temperatures, as shown in Figure 4. The Sa in both regions increases slightly with higher surface temperature during cutting. Notably, although the surface roughness in regions with H_2O remains lower than in those without H_2O, the difference between the two decreases. This confirms the weakening of the WISO effect at higher surface temperatures due to thermal desorption.

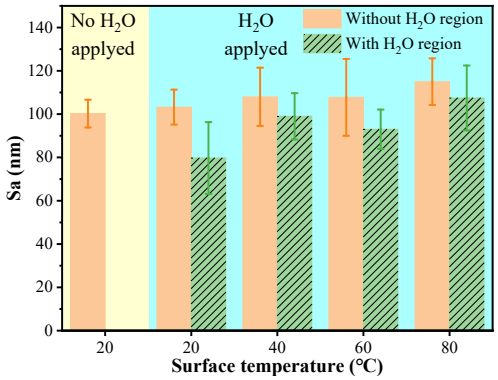

Figure 4. Surface roughness of grooves at different surface temperatures during cutting.

The cutting chips presented in Figure 5 exhibit significant changes in chip morphology with and without H_2O applied before cutting. The chip without H_2O applied is thick, whereas the chip with H_2O is thin, and there are no significant differences in chip morphology at different surface temperatures during cutting, as shown in Figure 5(a)-(c). Magnified views of the chip show that the chip morphology changes from a folded structure in the region without H_2O to a regular layered structure in the region with H_2O, similar to previous studies [1, 6, 13-15]. The reduction in surface energy and strength of solids results in alterations to the surface properties of Cu, which transform the material deformation pattern during micro-cutting, accompanied by an increase in shear angle and a decrease in cutting resistance. Nevertheless, the substantial CFRR, the lower surface roughness in the region with H_2O, and the observed

changes in the chip all indicate that WISO enhances machining performance in copper micro-cutting.

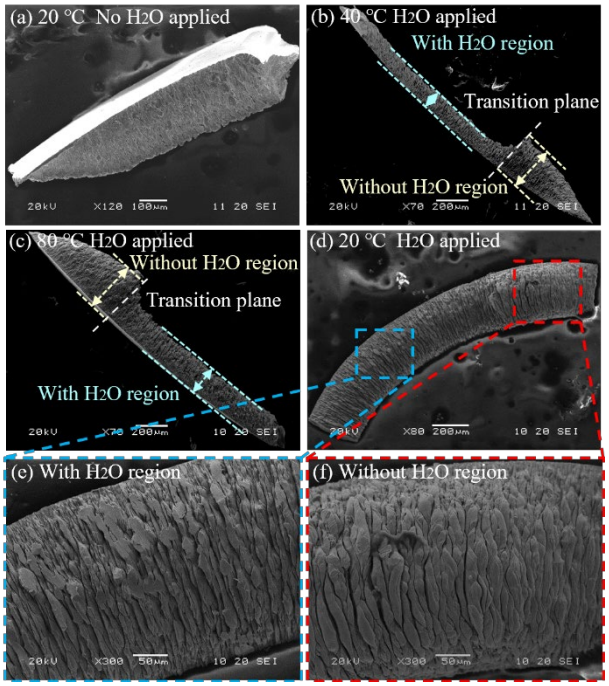

Figure 5. Chip morphology at different surface temperatures during cutting. (a)-(c) Chip morphology of grooves during cutting at 20 °C without H_2O applied, and at 40 °C and 80 °C with H_2O applied, respectively. (d)-(f) Chip morphology and magnified views of a groove during cutting at 20 °C with H_2O applied, respectively.

4. Conclusion

In this study, the regulation of WISO is achieved by qualitatively controlling the quantity of surface-bound water molecules via thermal means. The stable CFRR within the range of 15 µm–30 µm confirms that the effectiveness of WISO remains stable within a specific range of doc. Consequently, the increase in actual doc caused by thermal expansion plays a negligible role in the CFRR of cutting under varying surface temperatures. The CFRR decreases from 70.72% to 57.67% as the surface temperature increases from 20 °C to 80 °C, primarily due to the thermally induced reduction of effective surface-bound water molecules. This is also evident in the surface roughness of grooves at varying surface temperatures during cutting. The difference in surface roughness between regions with and without H_2O decreases, thereby confirming the weakening of the WISO effect at higher surface temperatures. Nevertheless, the surface roughness in regions with H_2O remains lower than in those without H_2O. Furthermore, an analysis of chip morphology reveals a transition from short, thick shapes in regions without H_2O to long, thin shapes in regions with H_2O. The substantial CFRR, the lower surface roughness in the region with H_2O, and the observed changes in the chip all indicate that WISO enhances machining performance in copper micro-cutting. Future work should aim to generalize these findings by investigating the WISO mechanism on a broader range of workpiece materials and exploring alternative modulation strategies beyond thermal control to further advance the capability of surface-active media in precision manufacturing.

Acknowledgements

The authors would like to acknowledge the support of the start-up fund at the City University of Hong Kong with the grant number of 9610646, and Research Grants Council (RGC) through the Early Career Scheme fund with the grant number of 9048323.

References

[[1] Chaudhari, A., et al., *Rehbinder effect in ultraprecision machining of ductile materials.* International Journal of Machine Tools & Manufacture, 2018. **133**: p. 47-60.

[2] Li, W. and S. Kara, *An empirical model for predicting energy consumption of manufacturing processes: a case of turning process.* Proceedings of the Institution of Mechanical Engineers, Part B: Journal of Engineering Manufacture, 2011. **225**(9): p. 1636-1646.

[3] Zhang, Z., J. Yan, and T. Kuriyagawa, *Manufacturing technologies toward extreme precision.* International Journal of Extreme Manufacturing, 2019. **1**(2): p. 022001.

[4] Das, A., et al., *Performance assessment and chip morphology evaluation of austenitic stainless steel under sustainable machining conditions.* Metals, 2021. **11**(12): p. 1931.

[5] Lee, Y.J. and H. Wang, *Current understanding of surface effects in microcutting.* Materials & Design, 2020. **192**: p. 108688.

[6] Zhang, J., et al., *Water-induced surface ordering facilitating the microcutting of ductile metals.* Journal of Cleaner Production, 2024. **481**: p. 143994.

[7] Rehbinder, P., *New physico-chemical phenomena in the deformation and mechanical treatment of solids.* Nature, 1947. **159**(4052): p. 866-867.

[8] Abbá, E., et al., *Deep-eutectic solvents enable tunable control of the micro-mechanical response through electrical actuation.* Materials Today, 2025. **86**: p. 183-201.

[9] Kohn, E., *Role of extreme pressure lubricants in boundary lubrication and in metal cutting.* Nature, 1963. **197**(4870): p. 895-895.

[10] Udupa, A., et al., *Material-independent mechanochemical effect in the deformation of highly-strain-hardening metals.* Physical Review Applied, 2018. **10**(1): p. 014009.

[11] Yeung, H., et al., *Sinuous flow in metals.* Proceedings of the National Academy of Sciences, 2015. **112**(32): p. 9828-9832.

[12] Gerasimov, D.N. and E.I. Yurin, *Kinetics of evaporation*. Vol. 68. 2018: Springer.

[13] Uy, P.S., J. Bardolle, and M. Bujor, *A study of water vapour adsorption on the (110) surface of copper.* Surface Science, 1983. **129**(1): p. 219-231.

[14] Hu, J., et al., *Imaging the condensation and evaporation of molecularly thin films of water with nanometer resolution.* Science, 1995. **268**(5208): p. 267-269.

[15] Lee, S. and R. Staehle, *Adsorption of water on copper, nickel, and iron.* Corrosion, 1997. **53**(1): p. 33-42.

euspen's 26th International Conference & Exhibition, Krakow, PL, June 2026
www.euspen.eu

Design and testing of an advanced honeybee waste heat-powered energy harvester

Petar Gljušćić,[1, 2] Saša Zelenika [1, 2] and Priyesh Pappinisseri Puluckul [3]

[1] *University of Rijeka, Faculty of Engineering, Precision Engineering Laboratory, Vukovarska 58, 51000 Rijeka, Croatia*
[2] *University of Rijeka, Centre for Micro- and Nanosciences and Technologies, Radmile Matejčić 2, 51000 Rijeka, Croatia*
[3] *IDLab, Faculty of Applied Engineering, University of Antwerp - imec, Sint-Pietersvliet 7, 2000 Antwerp, Belgium*

szelenika@uniri.hr

Abstract
An overwintering honeybee colony maintains the hive inner temperature of up to 35 °C, creating a considerable temperature difference Δ*T* with respect to the low ambient temperatures. The resulting temperature gradient, induced by the metabolic waste heat typically lost through hive walls, can be efficiently exploited by using thermoelectric energy harvesting (EH) technologies, providing electrical energy for low power IoT-based autonomous hive monitoring systems. Based on a previously developed proof-of-concept harvester, an advanced setup, comprising six low Δ*T* thermoelectric generators (TEGs), two heatsinks connected by heat pipes, a step-up DC-DC converter, and a supercapacitor for energy storage, is developed and tested in laboratory conditions. A standard 5-frame Langstroth nucleus hive is used, while the temperature difference is controlled to simulate the conditions in actual hives. As the TEG-based transducing device is connected to the DC-DC converter with a pre-set range of input voltages, the interconnection of individual TEG modules needs to be carefully considered in terms of its effect on the capacitor's charging times, which should be minimized. The TEGs are thus tested while connected in series (6S), in parallel (6P), and, by using a combined approach, in a parallel connection of 3 assemblies of 2 serially connected TEGs (3P2S), and a parallel connection of 2 assemblies of 3 serially connected TEGs (2P3S). Based on the obtained results, the chosen configuration of the device is tested in-situ. An initial configuration of an IoT-based sensor node is also proposed. Different harvester device's constituting materials with better thermal properties will be considered next, and additional attention will be placed on the thermal interfaces between the key components.

Honeybee colony, energy harvesting, waste heat, autonomous monitoring system, design configurations

1. Introduction

Effects of climate change, diseases, and human activity have led to issues in managed honeybee colonies, such as increased winter losses, thus reducing the numbers of these pollinators with a very important role in agriculture. Hive monitoring offers here a promising solution by enabling real-time assessment of colony conditions. An upgraded version of a previously proposed innovative energy harvesting (EH) concept [1], intended for battery-less (i.e., environmentally friendly) powering of an autonomous hive monitoring system, which can be aimed at swarm detection [2], measuring temperature [3] or other parameters such as sound, CO_2 percentage and weight [4], is presented in this work. The EH system is designed to collect waste (metabolic) heat generated by a honeybee colony [5] and convert it into usable electrical energy via thermoelectric generators (TEGs). In fact, to maintain the bee cluster temperature at levels of up to 35°C [6], as the colony overwinters, it generates a substantial amount of heat [7]. As shown in Figure 1, the new EH system comprises an assembly of six TEG modules (1), and two heat sinks – respectively for the hot (2) and the cold (3) side, mutually connected via two copper-methanol heat pipes (4). To increase heat conductivity, the heat sinks, as well as the hot (5) and cold side (6) interface blocks, are made of copper, while the methanol heat pipes ensure safe operation at sub-zero ambient temperatures. To minimize heat losses, all the exposed metal surfaces are, in turn, covered by a thermal insulating foam. Due to rather low output voltages typical for TEGs, a DC-DC converter (7) with ultra-low start-up voltage is then used to enable energy storage in a supercapacitor (8).

As multiple TEG modules are used, several connection configurations can be used, i.e., the TEGs can be connected in series (6S) and in parallel (6P), as well as via a parallel connection of 3 assemblies of 2 serially connected TEGs (3P2S), or a parallel connection of 2 assemblies of 3 serially connected TEGs (2P3S). This work presents an experimental study on how the different connections of the TEG modules influence the supercapacitor charging times in laboratory conditions. The new EH device is then tested in-situ using the most suitable TEGs' connection configuration, and the open-circuit voltage values are assessed. An overall autonomous IoT sensor node, comprising sensors and communication units coupled to the EH powering assembly, is also proposed, and the respective duty cycle is calculated.

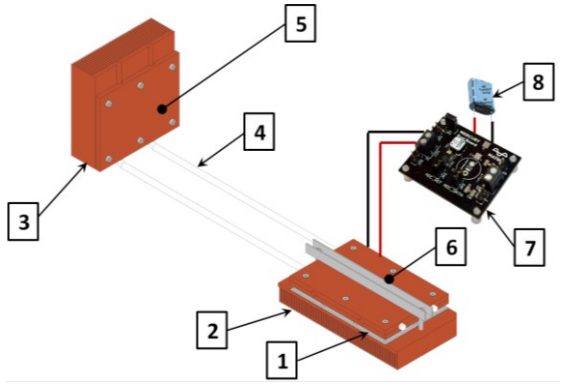

Figure 1. Thermoelectric energy harvester assembly aimed at the utilization of the waste heat of a honeybee colony

2. Connection configurations of multiple TEG modules

The behaviour of the TEG modules connected in series and in parallel, in terms of the respective voltage and current outputs,

is fairly straightforward and well documented [8], while the somewhat more complex cases of combined connections have been experimentally studied only in recent literature [9]. However, due to the typical low output voltages of TEG modules, particularly at relatively low temperature differences in the foreseen operating conditions, as well as the pre-set operating parameters of the considered DC-DC converter, required to charge the supercapacitor, i.e., the minimum start-up voltage and an upper voltage limit, the connection method of the TEGs needs to be carefully considered. The respective study is performed by using an experimental setup comprising two ceramic heaters controlled via a virtual instrument (VI) running on a NI® MyRIO [10] device, thus simulating the heat generated by the honeybee colony. The setup is enclosed in a standard wooden 5-frame Langstroth nucleus hive together with the heaters, while the cold side heat sink is exposed to ambient air, kept at a constant temperature by employing an AC unit. The used TECTEG MFR.® TEG2-126LDT TEG modules [11] are connected to a Matrix® 411-MCRY DC-DC converter [12] with a U_{st} = 24 mV start-up voltage and a U_{lim} = 500 mV input voltage limit, which charges a U_{SC} = 5 V, C_{SC} = 0.5 F supercapacitor. The converter output voltage is U_{out} = 4.2 V, and this value is considered as the indication of a fully charged capacitor, as measured by the VI running on an NI® MyRIO device. A PCE Instruments® PCE-T 420 4-channel temperature data logger [13] is used to measure the temperature values in four different points, i.e., to monitor the ambient temperature and the air temperature within the hive, as well as the temperatures at both the hot and cold side heat sinks. In the used setup, the logger is interfaced to K-type thermocouples, and in the foreseen measurement range it has a measurement resolution of 0.1 °C, and an accuracy of ± 0.2 % of the measured value [13].

As schematically represented in Figure 2, the six used TEG modules are then connected in series (6S), in parallel (6P), in a parallel connection of 3 assemblies of 2 serially connected TEGs (3P2S), and a parallel connection of 2 assemblies of 3 serially connected TEGs (2P3S).

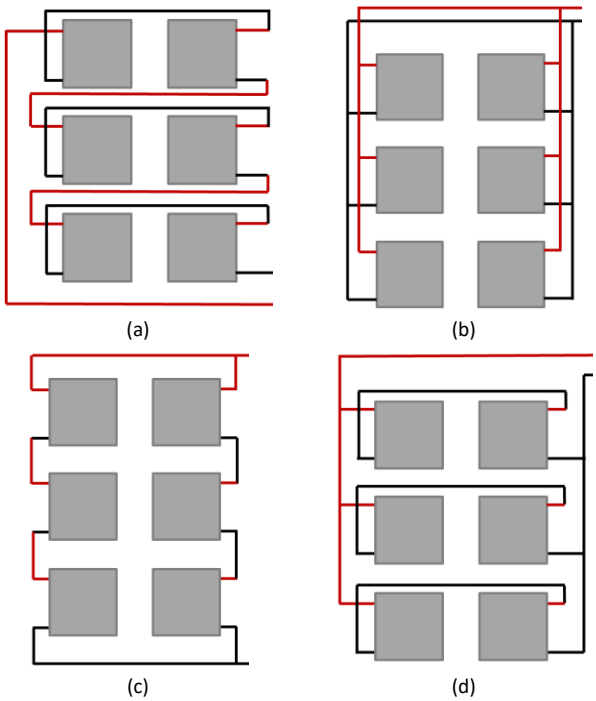

Figure 2. Schematic representation of the considered TEG connection configurations: 6S (a), 6P (b), 3S2P (c) and 2S3P (d)

The times required to achieve the complete charging of the supercapacitor are then measured for the different TEG configurations. The measurements are performed in steady-state conditions at comparable average temperature differences ΔT_{ave}, measured at the heat sinks, ranging from ΔT_{ave} = 16,1 °C for the 3S2P case, up to ΔT_{ave} = 21,8 °C for the 6P case. By maintaining the thermal conditions under control, as well as by keeping the measurements as short as possible, the average temperature differences measured during the experiments were kept within ± 5 % compared to those occurring in a honeybee colony. The significant variation in actual temperature values within an active hive is also taken into account.

The average temperature differences ΔT_{ave} and the respective charging times t_{ch} are listed in Table 1 and graphically displayed in Figure 3. Open circuit (OC) voltage measurements U_{OCave} are also carried out for the considered TEG configurations at average temperature differences $\Delta T_{ave} \approx 10$ °C, and the obtained results are shown in the lower part of Table 1.

Table 1. Charging times and OC voltages for the different TEG connection configurations

Charging times				
	6S	**6P**	**2S3P**	**3S2P**
ΔT_{ave}/°C	21.8	16.9	15.7	16.1
t_{ch}/min	172.7	221.1	54.4	51.4
Average OC voltages				
	6S	**6P**	**2S3P**	**3S2P**
ΔT_{ave}/°C	10.45	11.85	9.5	9.7
U_{OCave}/V	0.503	0.079	0.147	0.144

The results reported in Table 1 and Figure 3 indicate that the 6P configuration implies the longest times to fully charge the supercapacitor, with t_{ch} = 221.1 min, followed by the 6S configuration with t_{ch} = 172.7 min. These long charging times can be attributed to the impedance mismatch and the variation in the overall resistances. Also, in the 6S configuration the output voltages U_{OCave} are so high that they tend to become higher than the converter's upper limit. On the other hand, the combined configurations performed similarly, both requiring around t_{ch} = 50 min to fully charge the C_{SC} = 0.5 F capacitor. Since both configurations, when operating at the considered low temperature differences, nearly coincide in terms of the output voltages (Table 1) and currents, this seems quite reasonable [9]. In any case, the benefits of the combined assemblies can be clearly seen, as both the 2S3P and the 3S2P configuration are significantly better than the fully serial and parallel ones, with the 3S2P configuration resulting in slightly shorter charging times. The benefits are also evident in terms of the OC voltages U_{OCave}, where both the 6S and the 6P configurations induce issues with respect to the voltage input range of the converter, while the combined ones provide similar mid-range voltage values, well suited for the unpredictable temperature differences during real in-situ operation.

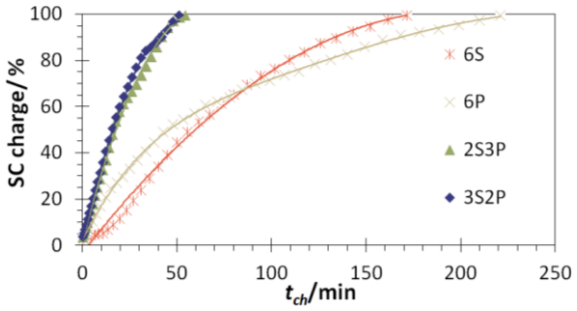

Figure 3. Supercapacitor charging times for the considered TEG connection configurations

3. In-situ testing

To assess the in-situ performances of the proposed EH system in real life conditions, a field test is carried out next. As displayed

in Figure 4a, the six TEG modules are thus connected in a 3S2P configuration and the whole EH system (1) is integrated in a standard Langstroth hive containing an overwintering colony of Carniolan honeybees (lat. *apis mellifera carnica*). The aforementioned 4-channel temperature data logger (2) [13] is employed to keep track of the temperature values within the hive, the surrounding environment, and at both the hot and the cold side heat sinks. The temperature difference between the hive interior and the surrounding air ΔT_{air}, as well as that between the two heat sinks ΔT_{hs}, can hence be assessed. To measure the open circuit (OC) voltage output U_{OC} of the EH device without an attached electrical load, a MadgeTech® Volt101A voltage data logger (3), having a resolution of 0,5 mV and an accuracy of ± 0,016 V [14], is also used.

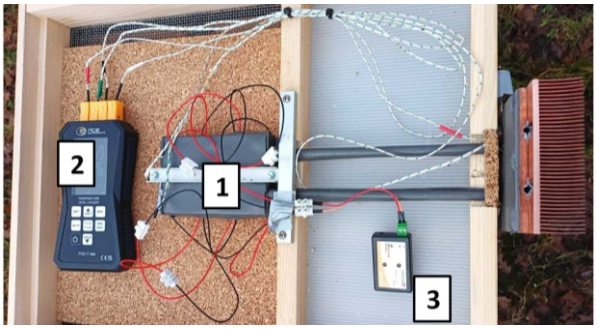

(a)

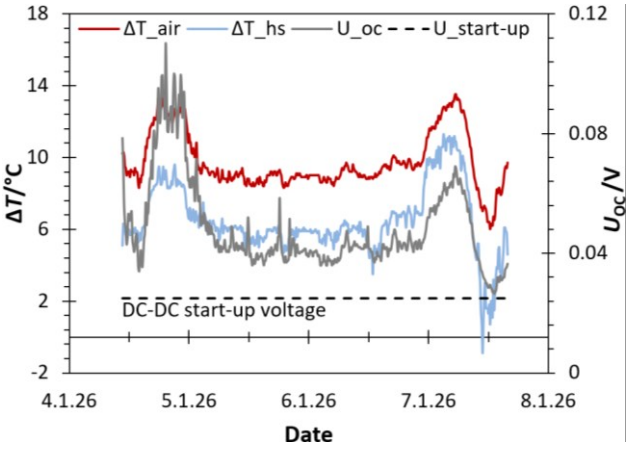

(b)

Figure 4. In-situ setup for testing the EH device in a Langstroth hive (a), and measured U_{OC} values at varying ΔT_{air} and ΔT_{hs} values (b)

The resulting OC voltages, generated by the harvester in real life conditions, are graphically displayed in Figure 4b, along with the aforementioned temperature differences ΔT_{air} and ΔT_{hs}. It can be observed that, due to convection at the heat sinks, there is an expected offset between the values of these temperature differences, ranging from 1.2 up to 7.8 °C. In terms of harvester's performances, the temperature difference between the heat sinks, averaging ΔT_{hs_ave} = 6.5 °C, is considered to be more important, as it is closer to the temperature difference between the hot and cold sides of the TEG modules. The output voltage follows, in turn, the variation in the temperature difference, averaging U_{OCave} = 0.048 V, and displaying maximum values of U_{OCmax} = 0,1 V. The minimum OC voltage values U_{OCmin} are larger than the lowest input voltage required by the considered DC-DC converter U_{st}; in fact, as it can be observed in Figure 4b, U_{OCmin} = 0.027 V, whereas U_{st} = 0.024 V. These results indicate, therefore, that the output OC voltage falls within the input limits of the considered DC-DC converter, thus proving the suitability of the selected TEG configuration 3S2P for the foreseen application.

4. IoT components and duty cycle

Based on previous considerations, i.e., colony waste heat EH viability [15] and colony strength assessment [16], the overall autonomous hive monitoring system should comprise several key ultra-low power IoT components, i.e., a microcontroller unit (MCU), A-D converters, communication modules (LoRa, NB-IoT, Space IoT, or alternatives [8]), as well as the foreseen sensors and the respective data logging and filtering components.

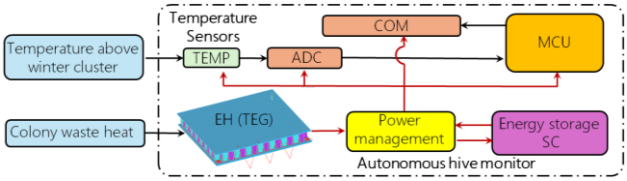

Figure 5. Schematic representation of the considered autonomous IoT sensor node aimed at hive monitoring [15]

The STMicroelectronics® STM32 Nucleo-64 board [17] represents herein the central element of the foreseen system, as it comprises an ultra-low power MCU, a Switched-Mode Power Supply (SMPS), A-D converters, a data storage module, and a communication module using the LoRa protocol. To measure the temperatures within the hive and assess the size and strength of the colony [16], several temperature sensors can then be employed; the Microchip Technology® MCP9700A-E/TO ultra-low power sensors are thus considered [18].

Based on the available data and technical specifications of the mentioned commercially available IoT components, i.e., the Nucleo-64 board manuals [17, 19], MCP9700A temperature sensor [18] and Semtech® LoRa transceiver [21] datasheets, the respective Semtech® LoRa calculator [22], as well as recent literature related to battery-less IoT systems [23], the power requirements of the considered components, their characteristic operational modes, and the corresponding cycles are estimated as listed in Table 2.

Table 2. Power requirements and cycle duration for the considered IoT components

Nucleo-WL55JC2 & MCP9700A-E/TO	
Power requirements	
Mode:	**Current/mA**
Wake MCU @ 48 MHz	3.46
Wake & read temp. sensor (per sensor)	0.015
Wake & read temp. sensor (for 11 sensors)	0.165
Transmit Tx 20 dB	107.1
Total active load (one sensor), I_{active}	110.6
Total active load (for 11 sensors), $I_{active11}$	110,7
Total sleep load, I_{sleep}	0.00107
Cycle duration	
Cycle:	**Time/s**
t_{cycle} = 24 h	86400
MCU wake-up & stabilize	0.02
MCP9700 power & read	0.005
Prepare data package	0.01
LoRaWAN transmission (one sensor)	1.81
LoRaWAN transmission (for 11 sensors)	2.8
Return to sleep	0.005
Total active time, $t_{active11}$	2.84
Total sleep time, $t_{sleep11} = t_{cycle} - t_{active11}$	86397.16

From the listed data, the duty cycle D for 11 sensors is calculated as [24]:

$$D = \frac{t_{active11}}{t_{active11} + t_{sleep11}} \quad (1)$$

while the average load current I_{av} is determined as [24]:

$$I_{av} = I_{active11} \cdot D + I_{sleep} \cdot (1 - D) \quad (2)$$

The useful time of utilisation of the energy stored in the storage system (battery or supercapacitor) SC_{time} can, therefore, finally be assessed as [24]:

$$SC_{\text{time}} = \frac{SC_{\text{capacity}}\ (mAh)}{I_{\text{av}}\ (mA)} \tag{3}$$

For the autonomous sensor node configuration considered in this work, and comprising 11 MCP9700A-E/TO temperature sensors connected to a Nucleo-64 board, and a LoRa transceiver transmitting the collected data, the active current amounts therefore to $I_{\text{active11}} \approx 110.7$ mA. If such a system collects and transmits data once per day, the duty cycle is $D = 3.3\ 10^{-5}$, i.e., 0.0033 %. If the system is powered via the previously considered $C_{SC} = 0.5$ F supercapacitor charged to $U_{out} = 4.2$ V, resulting in $SC_{\text{capacity}} = 0.583$ mAh, the time during which the supercapacitor, even without any additional charging, could provide energy, would be $SC_{\text{time}} = 123.86$ h or 5.16 days. This goes to showing that, by carefully considering the periods of peak power consumption, the limited amount of collected and stored energy can be a trouble-free and very efficient solution for the herein considered autonomous sensor node application.

5. Conclusions and outlook

A new and improved honeybee colony waste heat energy harvester device, based on six TEG modules, is conceived and described in this work. Different TEG connection configurations are considered, i.e., a series (6S), a parallel (6P), and two configurations based on a combination of parallelly assembled sets of serially connected TEGs (3S2P and 2S3P). All the configurations are tested in laboratory conditions on a suitably devised experimental setup. The ability to fully charge a $C_{SC} = 0.5$ F supercapacitor is then assessed by using an apposite control and data acquisition system and a DC-DC converter, whose voltage limitations, when coupled to the different behaviour of the considered TEG configurations, play an important boundary condition. It could thus be shown that, in realistic low ΔT conditions, the combined configurations perform significantly better, fully charging the supercapacitor in around $t_{ch} \approx 50$ min. This can be attributed to the property of such configurations to perform between the two extreme cases of serial and parallel connections, providing thus sufficient voltage at low ΔT to start the converter, while keeping the current high enough to achieve manageable charging times.

To assess the performances of the harvester in real life conditions, the EH device, based on the TEG modules connected in the 3S2P configuration, is subsequently integrated into a standard wooden Langstroth hive occupied by a honeybee colony. The results of the field tests allowed confirming that the proposed approach enables providing voltage values appropriate to initiate and maintain the charging process of the supercapacitor. As the foreseen application is ultimately an autonomous hive monitoring system, essential ultra-low power IoT components, with their respective power requirements, are also considered. The key technical specification and operational cycles of the MCU, data storage, and LoRa communication transceiver modules, combined with temperature sensors, are therefore carefully analysed. The hence determined duty cycle and the resulting useful time of utilisation of the energy stored in the supercapacitor for the considered operating conditions, allowed clearly showing the viability of the proposed solutions.

In the prosecution of the work, the performances of the proposed harvester device will be tested in-situ also in terms of the supercapacitor charging times in various environmental conditions. Various harvester device's constituting materials with better thermal properties will also be considered, and additional attention will be placed on the thermal interfaces between the key components.

The full IoT sensor node will then be assembled and tested in laboratory conditions first, and then during the final field tests. A functional autonomous IoT sensor node aimed at honeybee colony monitoring, powered by the colony's waste heat and able to operate in remote locations during winter conditions, will therefore be obtained. Such a system will provide the beekeeping community with invaluable insights into the state of the overwintering colonies, as well as with an effective tool to prevent and mitigate the respective winter losses.

Acknowledgements

Work enabled by the University of Rijeka research grants uniri-mz-25-38 „Waste-heat powered system for pollinator monitoring (WASP)" and uniri-mzi-25-4 „Environmental monitoring via autonomous sensor networks (EMAS)" financed by the European Union – NextGenerationEU.

References

[1] Gljušćić P and Zelenika S 2025 *Proc. 25th EUSPEN Int. Conf. (Zaragoza, ES)* 208-11

[2] Zacepins A, Kviesis A, Stalidzans E, Liepniece M and Meitalovs J 2016 *Biosyst. Eng.* **148** 76-80

[3] Gil-Lebrero S, Quiles-Latorre F, Ortiz-López M, Sánchez-Ruiz V, Gámiz-López V and Luna-Rodríguez J 2016 *Sensors* **17**/1 55

[4] Cecchi S, Spinsante S, Terenzi A and Orcioni S 2020 *Sensors* **20**/9 2726

[5] Cushman DA www.dave-cushman.net (accessed 24 October 2023)

[6] Oliver R scientificbeekeeping.com/understanding-colony-buildup-and-decline-part-13a (accessed 24 October 2023)

[7] Döke MA, Frazier M and Grozinger ChM 2015 *Curr. Opin. Insect. Sci.* **10** 185-93[8] Mittal M, Tanwar S, Agarwal B and Goyal LM (eds) 2019 *Energy Conservation for IoT Devices* (*Studies in Systems, Decision and Control* ***206***) (Singapore: Springer Nature)

[9] Ruzaimi A, Shafie S, Hassan WZW, Azis N, Effendy Ya'acob M, Elianddy E and Aimrun W 2021 *Energy Rep.* **7** 2379-87

[10] NI MyRIO 1900 www.ni.com/en-rs/shop/model/myrio-1900.html (accessed 18 January 2022)

[11] TEG2-126LDT Body Scavenger tecteg.com/product/teg2-126ldt-body-scavanger (accessed 4 January 2025)

[12] MATRIX Industries www.matrixindustries.com (accessed 3 January 2025)

[13] PCE Instruments PCE-T 394 www.pce-instruments.com/f/t/us/main.htm (accessed 23 May 2025)

[14] MadgeTech Volt101a datalogger www.madgetech.com/products/volt101a (accessed 23 May 2025)

[15] Gljušćić P and Zelenika S 2024 *Proc. 24th EUSPEN Int. Conf. (Dublin, IE)* 335-38

[16] Gljušćić P, Perčić M and S. Zelenika 2024 *Proc 21st IEEE Int. Conf. Mechatronika (Brno, CZ)* 220-5

[17] STM32 Nucleo-WL55Jc board www.st.com/en/evaluation-tools/nucleo-wl55jc.html (accessed 15 October 2025)

[18] MCP9700A-E/TO temperature sensor www.microchip.com/en-us/product/mcp9700a (accessed 17 October 2025)

[19] STM32 Nucleo-WL55Jc manual www.st.com/resource/en/user_manual/um2592-stm32wl-nucleo64-board-mb1389-stmicroelectronics.pdf (accessed 4 January 2026)

[20] Semtech SX1272 LoRa transceiver www.semtech.com/products/wireless-rf/lora-connect/sx1272 (accessed 15 October 2025)

[21] Semtech SX1276/77/78/79 LoRa transceivers cdn-shop.adafruit.com/product-files/3179/sx1276_77_78_79.pdf (accessed 15 October 2025)

[22] Semtech LoRa calculator www.semtech.com/design-support/lora-calculator (accessed 10 January 2026)

[23] Bäumker E, Schüle F and Woias P 2018 *J. Phys.: Conf. Ser.*, **1052** 012005

[24] Rai S (Online) How to Greatly Improve Battery Power Efficiency for IoT Devices www.analog.com/en/resources/technical-articles/greatly-improve-battery-power-efficiency-for-iot-devices.html (accessed 17 October 2025)

euspen's 26th International Conference & Exhibition, Krakow, PL, June 2026
www.euspen.eu

Oxidation Behavior of OVPE-GaN Substrates for Slurry-less Photoelectrochemical Mechanical Polishing

Yuya Ohnishi[1], Sun Rongyan[1], Shigeyoshi Usami[2], Yuji Ohkubo[1], Masayuki Imanishi[2], Yusuke Mori[2], Kazuya Yamamura[1]

[1]*Research Center for Precision Engineering, Graduate School of Engineering, The University of Osaka, Osaka, Japan*
[2]*Division of Electric, Electronic and Information Engineering, Graduate School of Engineering, The University of Osaka, Osaka, Japan*

ohnishi@nms.prec.eng.osaka-u.ac.jp

Abstract
Gallium nitride (GaN), characterized by a wide bandgap, high breakdown field, and excellent electron mobility, is a leading candidate for next-generation power semiconductors. Low-resistivity GaN substrates grown by oxide vapor phase epitaxy (OVPE) are well suited to vertical device architectures, enabling high current density and reduced on-resistance. However, spatial non-uniformity of carrier concentration inherent to OVPE growth alters surface chemical reactivity and impedes attainment of atomically flat, sub-nanometer surfaces. Moreover, it is particularly challenging to process GaN because of its chemical inertness, high hardness, and brittleness. Conventional chemical–mechanical polishing (CMP) exhibits low removal rates, high slurry cost, and post-polish topography correlated with local carrier density; UV- or electrochemical-assisted variants improve removal via surface modification yet still imprint carrier-dependent roughness. In this study, slurry-less photoelectrochemical mechanical polishing (PECMP) was proposed. UV irradiation combined with an electrochemical field induced a controllable modified layer on GaN, which is subsequently removed using fixed-abrasive instead of slurry to achieve high-efficiency, high-quality polishing. This method selectively removes only the oxidized layer, making the oxidation step central to both material removal and final surface quality. Accordingly, the modification mechanism was investigated, and the distinct carrier-concentration dependences of the UV-induced and electrochemical oxidation processes was clarified. By tuning the relative contributions of the two processes, modification is equalized across regions with differing carrier densities, yielding a spatially uniform modified layer.

Keywords: Electro chemical machining (ECM), Nano manufacturing, Oxidation, Photochemical machining

1. Introduction

Gallium nitride (GaN) has attracted widespread attention as a next-generation power device material owing to its superior physical properties. In particular, vertical GaN power devices require substrates with both low electrical resistivity and high crystalline quality, since large currents flow through the substrate thickness. Among the growth techniques for GaN single-crystal substrates that satisfy these requirements, oxide vapor phase epitaxy (OVPE) has recently gained significant interest. OVPE enables the growth of GaN crystals with high carrier concentrations and low threading dislocation densities, making it a promising approach for realizing vertical GaN power devices with low on-resistance [1]. To fully exploit these advantages, OVPE-GaN substrates with highly smooth surfaces are required.

Conventionally, chemical mechanical polishing (CMP) has been employed for the planarization of semiconductor substrates. In CMP, a slurry containing oxidizing agents and abrasive particles is used. Substrates surface is lightly modified with the oxidizing agents and surface planarization is achieved by mechanically removing the oxidized and softened surface layer. However, OVPE-GaN substrates inherently exhibit in-plane non-uniformity in dopant concentration originating from the crystal growth process. When CMP is applied to such substrates, spatial variations in chemical reactivity translate into loval differences in material removal rate (MRR), which degrade surface roughness and can leave characteristic topographic non-uniformities after polishing. In addition, GaN is chemically inert, and the oxidation reaction that initiates CMP proceeds slowly, limiting the MRR to below ~100 nm/h. The resulting long processing times and high slurry consumption increase manufacturing costs and impose an environmental burdens associated with slurry handling and disposal. Consequently, the CMP process has become a bottleneck in the mass production of GaN substrates.

To overcome these challenges, it is necessary to control the oxidation reactivity on OVPE-GaN in a manner that is insensitive to dopant non-uniformity, and selectively remove the modified layer under damage-free mechanical conditions using soft fixed abrasives, without slurry. Since the oxidation reaction of GaN is strongly dependent on hole supply processes and interfacial reaction kinetics, reaction fields with different carrier generation mechanisms and driving forces are expected to exhibit distinct oxidation responses to dopant concentration.

In this study, photochemical and electrochemical reaction fields were considered and the oxidation behavior under individual and combined fields were systematically investigated. By examining the oxidation reactivity as a function of dopant concentration, oxidation conditions capable of mitigating in-plane non-uniformity and enabling the formation of a uniform surface modified layer were discussed.

2. Experimental setup

An n-type OVPE-GaN (0001) substrate provided by Panasonic Holdings Corporation was used in this study. Prior to the oxidation experiments, the substrates were pre-processed by diamond lapping, resulting in a

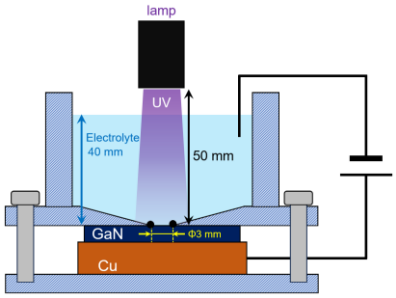

Figure 1. Schematic of the experimental setup.

Table 1. PEC oxidation conditions

Electrolyte	Phosphoric Buffered Solution (pH6.86)
Applied Bias	3.0 / 4.0 / 10.0 V
UV irradiation intensity	250 [mW/cm2] @365 nm
Oxidation Time	60 / 30 / 1 s

surface roughness of *Sa* = 0.8 nm. The GaN substrate was fixed onto a copper plate and used as the anode, while a platinum mesh served as the cathode. Both electrodes were immersed in the electrolyte.

As shown schematically in Fig. 1, the electrolyte was filled into a tank, and only a circular region with a diameter of 3 mm on the GaN substrate was exposed to the electrolyte by sealing the surrounding area with fluororubber. The anode and cathode were connected to a potentiostat (Ivium Technologies, IviumStatXRe) and operated under voltage-controlled conditions. Ultraviolet (UV) irradiation was provided by a UV lamp (USIO Electric Co., SP9-250DB). A neutral phosphate buffer solution (pH 6.86) was used as the electrolyte in order to suppress isotropic etching of gallium oxide. The oxidation conditions are summarized in Table 1. The UV irradiation intensity was 250 mW/cm² at 365 nm, while the applied voltage was systematically varied. The oxidation time was adjusted so that the total reaction charge was maintained at a comparable level among different conditions. After oxidation, the oxide layer was removed by HF cleaning, and the modified interface was exposed and observed using a scanning white light interferometer (SWLI).

3. Results and discussion

Figure 2(a) shows the surface morphology before oxidation under an applied voltage of 3.0 V, while Fig. 2(b) shows the surface after oxidation followed by HF cleaning to remove the oxide layer. As observed in Fig. 2(b), regions where oxidation proceeded more deeply were distributed in a floral-like pattern. This indicated that the local oxidation rate in the floral-like regions was relatively higher than that in the surrounding areas. These floral-shaped regions have been confirmed to correspond to areas with lower carrier concentration [2]. Therefore, in this condition, the oxidation behavior was attributed primarily to UV-assisted oxidation. Under UV irradiation, photogenerated holes were more likely to recombine in regions with higher carrier concentration, resulting in the suppression of the oxidation reaction in those regions [3].

In contrast, Fig. 3(a) shows the surface morphology before oxidation under an applied voltage of 10.0 V, and Fig. 3(b) shows the surface after oxidation followed by HF cleaning. Unlike the results obtained at 3.0 V, the oxidation rate in the floral-shaped low-carrier-concentration regions was relatively lower than that in the surrounding regions. This behavior suggested that anodic oxidation became dominant at 10.0 V. In high-carrier-concentration regions, charge transport was facilitated, which enhanced the oxidation reaction.These results demonstrated that UV-assisted oxidation and anodic oxidation exhibited

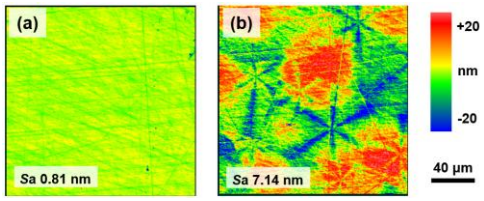

Figure 2. SWLI images of the GaN surface **(a)** before and **(b)** after photoelectrochemical oxidation under UV irradiation with an applied bias of 3.0 V.

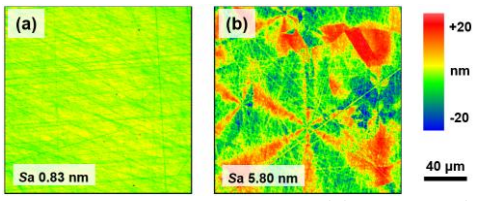

Figure 3. SWLI images of the GaN surface **(a)** before and **(b)** after photoelectrochemical oxidation under UV irradiation with an applied bias of 10.0 V.

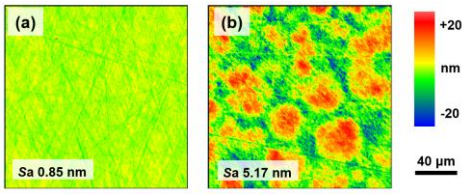

Figure 4. SWLI images of the GaN surface **(a)** before and **(b)** after photoelectrochemical oxidation under UV irradiation with an applied bias of 4.0 V.

opposite responses to in-plane carrier concentration non-uniformity during the oxidation of OVPE-GaN substrates.

Based on this finding, oxidation was carried out at an applied voltage of 4.0 V in order to adjust the relative contributions of the photochemical and electrochemical processes. Figure 4(a) shows the surface morphology before oxidation, and Fig. 4(b) shows the surface after oxidation followed by HF cleaning.

At 4.0 V, oxidation suppression caused by hole recombination during UV-assisted oxidation in high carrier concentration regions was counterbalanced by oxidation enhancement associated with improved charge transport under anodic oxidation. Consequently, in-plane uniform oxidation independent of floral-like pattern carrier concentration non-uniformity was achieved.

4. Conclusions

In this study, it was clarified that anodic oxidation and UV-assisted oxidation exhibit opposite dependencies on carrier concentration under fixed UV irradiation intensity. In high-carrier-concentration regions, oxidation was promoted by the electric field, whereas oxidation tended to be suppressed under UV irradiation. By controlling the applied voltage to adjust the relative contributions of these competing reactions, oxidation rate differences originating from in-plane carrier concentration non-uniformity were effectively compensated, enabling uniform surface modification. In future work, a high-efficiency slurry-less polishing process will be developed by combining the uniform oxidation technique demonstrated in this study with polishing using soft fixed abrasives.

References

[1] Takino et al., *Appl. Phys. Express*, **13**, 071010 (2020).
[2] Takino et al., *Jpn. J. Appl. Phys.*, **60**, 095501 (2021).
[3] D. Toh et al., *AIP Adv.*, **13**, 095113 (2023).

euspen's 26th International Conference & Exhibition, Krakow, PL, June 2026
www.euspen.eu

Experimental characterization of a force sensor for orientation-independent SI-traceable measurements

Martin Wittke[1], Lennart Frentzel[1], Matthias Wolf[1], Hannes Scheibe[1], Thomas Fröhlich[2], René Theska[1]

Technische Universität Ilmenau, Department of Mechanical Engineering,
[1]Institute for Design and Precision Engineering, Precision Engineering Group
[2]Institute of Process Measurement and Sensor Technology, Process Metrology Group

E-Mail: martin.wittke@tu-ilmenau.de

Abstract
Since the revision of the International System of Units (SI) in 2019, the Kibble Principle provides traceability for the measurements of masses, forces, and derived quantities by correlating electrical and mechanical quantities. The application of the principle enables the design of self-contained systems for absolute measurements. In the present work, the initial experimental investigation of a force sensor developed for use in precision technology is described. The sensor operates according to the Kibble principle, utilising spring-based stiffness compensation to realize high-precision measurements irrespective of its orientation within the field of gravity. The measurement data confirm the working principle, including the stiffness compensation by preloading the springs and the measurement window adjustment. However, manufacturing deviations and mounting constraints limit the compensation range.

Keywords: force sensor, load cell, stiffness compensation, Kibble Principle, measurement setup, experimental investigation

1. Introduction

The Kibble Principle [1] ensures traceability in the measurement of masses, forces, and derived quantities according to the revised SI. It is already applied in various fields [2-4] as it enables absolute in-situ measurements. To meet the growing demands for SI-traceable force monitoring in precision technology, a compact force sensor was conceived [5]. The sensor adapts the concept and functions of the Planck balance [6] (see Figure 1).

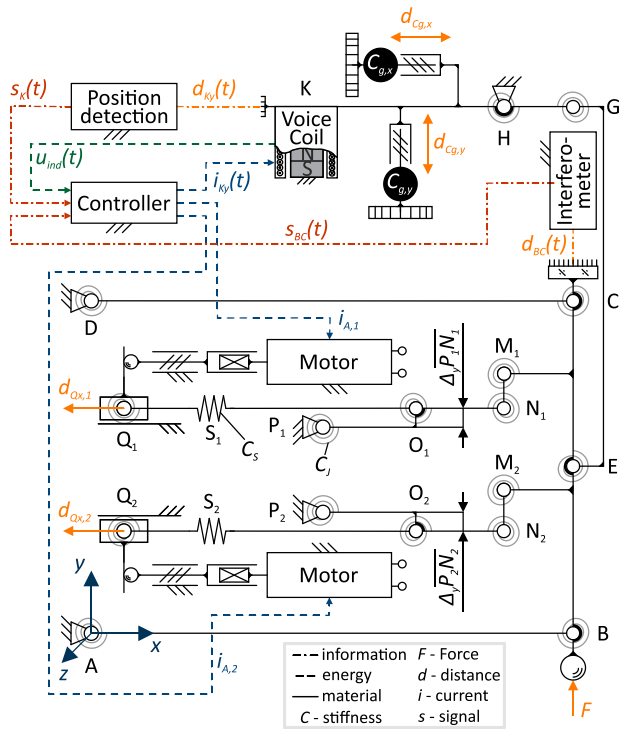

Figure 1. Concept of the developed sensor.

The kinematic structure is designed as a non-monolithic, compliant mechanism with thin, concentrated flexure hinges in order to enable the use of functional materials as well as the interchangeability of components. Spring-based stiffness compensation is applied to increase the resolution and reduce measurement uncertainty regardless of the sensor's orientation in the field of gravity. Two sub-mechanisms are installed to compensate for the stiffness of the mechanism using tunable forces of preloaded springs. The dual configuration also allows for the adjustment of the measuring window. The present work describes the commissioning and experimental investigation of the force sensor. The results are being discussed and deviations to the FE model are identified. [5]

2. Methods

The stiffness of the force sensor is investigated in various orientations using a static experimental measurement method. To identify deviations from the ideal geometry, the etched surface of the flexure hinges in use is measured optically.

2.1. Static-experimental measurement of the stiffness

The stiffness of the force sensor is determined by measuring its force-displacement characteristics. This is achieved with the built-in voice coil actuator and the optical position detection. To be able to align the force sensor in an arbitrary orientation, the measurement setup (see Figure 2) uses two open-beared rotation axes to allow for pitch in γ and roll in α by ±180°.

2.2. Optical measurement of the flexure hinge geometry

The LEXT OLS4100 Olympus 3D laser scanning microscope is used to analyse the etched surface of the flexure hinges. This includes measuring the contour, the length, the width, and the etching depth. The thickness of the hinges is determined using the sheet thickness, which is measured with a micrometer, and the etching depth.

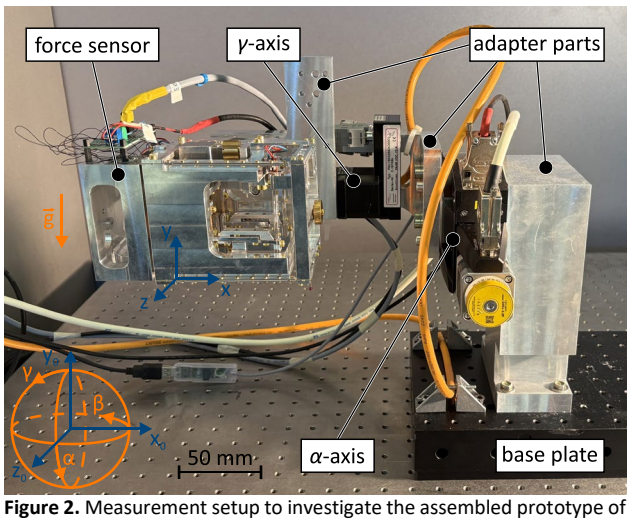

Figure 2. Measurement setup to investigate the assembled prototype of the force sensor. (xyz – local cartesian coordinate system; $x_0y_0z_0$ – global cartesian coordinate system; αβγ – global rotations)

3. Measurement results

For the commissioning, one of the compensation springs had to be preloaded significantly to shift the transmission lever into the measuring window. Subsequently, the curve of the stiffness C was recorded over the roll motion $\alpha = \pm 180°$ for various pitch angles γ (see Figure 3).

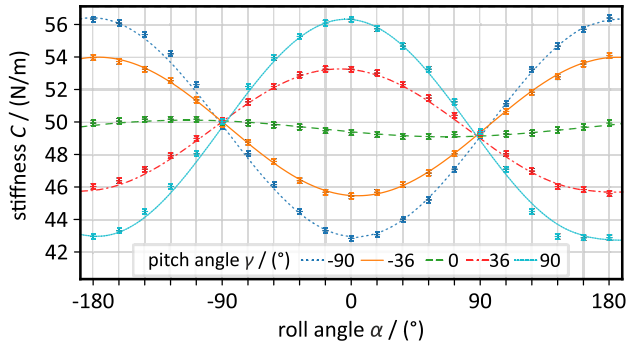

Figure 3. Overall stiffness C for different roll angles α and pitch angles γ.

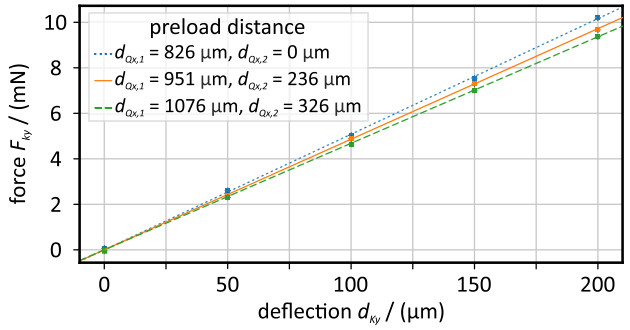

Figure 4. Force F_K across deflection d_K with increasing preload distances $d_{Qx,1}$ and $d_{Qx,2}$ of the stiffness compensation springs.

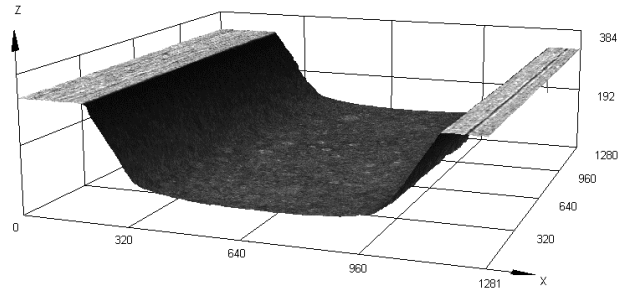

Figure 5. Optically measured topography of the etched surface of a thin copper beryllium flexure hinge.

For the orientation $\alpha = -90°$ and $\gamma = 0°$, the force F_{Ky} was measured across the deflection d_{Ky} for increasing preload distances $d_{Qx,1}$ and $d_{Qx,2}$ of the stiffness compensation springs (see Figure 4). It is evident that the uncertainty of both x-axis quantities is negligible. To detect potential error sources, the geometry of specific flexure hinges was characterized (see Figure 5). An average length of 0.960 mm ± 0.006 mm and an average thickness of 62.612 µm ± 4.233 µm were recorded. It was also determined that the hinges have large etching angles and rounded bending edges.

4. Discussion

The measurement results confirm the anticipated trend in stiffness during roll and pitch motions (see Figure 3). In the unadjusted state, the geometric stiffness accounts for up to 17% of the total stiffness. The absolute value of the total initial stiffness of $C = 50.81$ N/m for $\alpha = 90°$ and $\gamma = 0°$ is higher than the stiffness of $C = 42.58$ N/m of the FE model even though one of the compensation springs is already significantly preloaded. One of the main contributions to this deviation is the substantial discrepancy in the geometry of the built-in flexure hinges. The approximately 4% reduction in bending length and the approximately 25% increase in thickness affect stiffness to the power of three. In combination with large etching angles (see Figure 5), this results in significantly higher elastic stiffness compared to an ideally rectangular hinge contour. During assembly, stresses arose that also increased the elastic stiffness.

The adjustment concept for the stiffness and the measurement window could be validated. The increase in preload leads to a constant reduction in stiffness (see Figure 4). However, significant manufacturing deviations were found in the flexure hinges, as well as residual stresses introduced during assembly. This leads to a substantial disparity in the moment generated by the two compensation mechanisms. One of the preload springs had to be preloaded initially to a significant extent to adjust the force sensor into its measurement window. Consequently, the elastic stiffness could only be compensated by approximately 8%.

5. Summary and Outlook

To meet the growing demand in precision technology, a compact force sensor operating according to the Kibble principle was developed. Spring-based stiffness compensation increases the resolution and minimizes the uncertainty independently of the orientation. Experimental investigations confirmed the adjustment concept for the stiffness and the measurement window. However, manufacturing deviations in the flexure hinges and the frame, as well as assembly-related limitations, prevent the desired minimum stiffness from being achieved.

In future work, the force sensor will be optimized by using a sturdier hinge material, implementing stiffer compensation springs, and compensating for manufacturing deviations in the frame. The experiments will then be repeated.

References

[1] Kibble B P 1975 *5th International Conference on Atomic Masses and Fundamental Constants* Paris 545–551
[2] Mayworm R C, Webster E, Davidson S, Alvarenga A 2022 *Measurement* **203** 111788
[3] Nishino A, Kinoshita M 2022 *Measurement* **194** 111081
[4] Charkasova V 2024 PhD thesis Technische Universität Ilmenau
[5] Wittke M, Torres Melgarejo M A, Wolf M, Fröhlich T, Theska R 2025 *Proceedings of the 25th International Conference EUSPEN Zaragoza* 190-193
[6] Günther L., Rothleitner C, Schleichert J, Rogge N, Vasilyan S, Härtig F, Fröhlich T 2018 *Journal of Physics: Conference Series* **1065** 4 042021

euspen's 26th International Conference & Exhibition, Krakow, PL, June 2026
www.euspen.eu

Design principles for ultimate mechanical stability

Robin Trines[1], Martijn Denissen[1], Niels Bouman[1]

[1]*JPE*

robin.trines@jpe.nl

Abstract

When extreme mechanical stability is required, the well-known design principles of thermal centers and low expansion materials are effective tools to cope with uniform temperature changes. However, they are generally insufficient when local heat sources are involved. The low thermal conductivity of materials such as Invar or Zerodur induces large temperature changes and gradients. Additionally, expansion differences between connected components induce interface stresses which can lead to deformations and/or interface slip. As part of the JPE competence development program, solution strategies to these challenges have been developed and used in multiple high-tech applications.

For certain systems it is beneficial to accept a higher thermal sensitivity in order to reduce temperature changes and/or settling time. In these cases, a more comprehensive system view is required which balances (low) thermal sensitivity with other design aspects such as thermal management, well-defined interfaces, and coping with differences in expansion between components.

This work quantifies the differences between these design approaches by comparing two alternative implementations of an optical cavity. A reference cavity is designed by employing a conventional approach of minimizing thermal sensitivity. The second design applies materials which balance expansion, conductivity, and thermal capacity. Additionally, interfaces are decoupled with flexures and the temperature is actively stabilized using a thermoelectric cooler. These design principles are widely applicable throughout the field of precision engineering.

The relative performance of these two approaches is quantified in a technology demonstrator. In this setup, the two cavities are disturbed by an equal, local heat source. Interferometer measurements show that an order of magnitude improvement in stability and settling time is feasible with the advanced approach. For showcasing the demonstrator, the sensors are replaced by a Fizeau interferometer setup. The real-time deformations of both cavities are visualized by projecting fringe patterns onto a viewing screen.

Design principles, Stability, Precision mechanics, Thermal control, Opto-mechatronics

1. Introduction

In high-end (opto-)mechatronic systems the positioning performance is often affected by mechanical stability of critical components. Examples range from misalignment or deformation of optical components, to drift in the metrology loop of a motion platform. On medium to long time scales (minutes to months), this stability is often dominated by thermal effects. Mechanical stability can be achieved by applying well known design principles such as low expansion materials (Invar), well-defined interfaces, or thermal centers. These are effective measures when dealing with uniform temperature variations, e.g. from ambient temperature fluctuations. However, many precision systems also include local, time-varying heat sources such as dissipating sensors and motors, light absorption by mirrors and lenses, or adiabatic heat loads due to vacuum pump-down. To maintain extreme stability under such conditions JPE has developed advanced solutions as part of its competence development program. This work showcases several design principles for advanced mechanical stability by applying them to a simplified optical system consisting of an aluminum mirror and a glass disk (Fig. 1). The goal is to achieve a stable distance between two optical components and maintain this stability in the presence of local, time-varying heat loads.

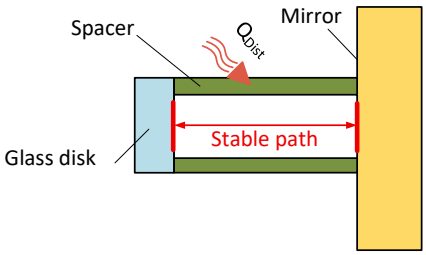

Figure 1. Schematic depiction of a simplified optical system with a glass disk and aluminum mirror. The objective is to stabilize the distance between the backside of the glass disk and the mirror surface.

2. Design approach

The reference design is based on the conventional approach to minimize the thermal sensitivity of the system, i.e. minimize the deformation resulting from a given temperature change. The thermal expansion is described by the following formula:

$$\Delta L = \alpha L \Delta T$$

Hence, to minimize the deformation for a given temperature change, the length L and the Coefficient of Thermal Expansion (CTE) α must be minimized. This is done by connecting the disk directly to the mirror using an Invar spacer (Fig. 2). The spacer is

clamped to the mirror with a statically determined 3-point interface, preloaded with a high bolt force. This creates an interface which has a high stiffness and a low thermal contact resistance. The high preload force reduces the risk of (micro) slip due to expansion differences between the two components.

The glass disk is glued to the front of the spacer. Glass beads are mixed in the adhesive to create a well-defined bond layer thickness. Stability is improved further by applying an adhesive which is geometrically stable due to a low water absorption and low outgassing rate. The disturbance heat is removed via a passive heat sink at the backside of the mirror.

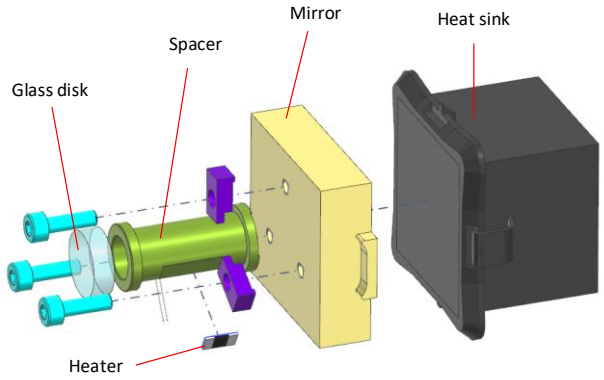

Figure 2. Optical system design which minimizes thermal sensitivity.

On the second system, a more holistic design approach is applied (Fig. 3). This focuses on the thermal management of the system instead of relying on low expansion coefficients.

The spacer connecting the two optical components is manufactured from Tungsten-Copper (WCu). This material has a higher CTE than Invar (~4x higher), but also a higher thermal conductivity (~20x higher). This results in an improved thermal and mechanical stability. An additional benefit of this material is that the CTE is close to that of the N-BK7 glass disk. This leads to smaller expansion differences, and thus lower stresses in the adhesive connection.

The higher thermal conductivity also leads to a significantly smaller thermal time constant. This faster reaction time allows for the active stabilization of the temperature by a PID controller. The temperature of the spacer is measured by a temperature sensor (PT1000) and used to control the heat flux of a Peltier element at the backside of the mirror. The control is implemented by a Meerstetter TEC-1089 temperature controller. A heat sink with fan cools the hot side of the Peltier element.

The mechanical stability in this design is further improved by placing the adhesive in defined glue pockets, instead of between the two components. This way, the glass disk and spacer are in direct contact with each other. Any deformations of the adhesive due to creep or thermal expansion do not directly affect the position of the disk.

Flexures are machined on each end of the spacer. The radial compliance allows for independent thermal expansion of the different components without introducing high interface stresses which may lead to (micro) slip. By placing the flexures symmetrically around the center axis, the thermal center of the system is preserved.

Both systems are mounted to a baseplate via an interface post at the bottom of the mirror. The thermal disturbance is applied by a resistor glued to each spacer.

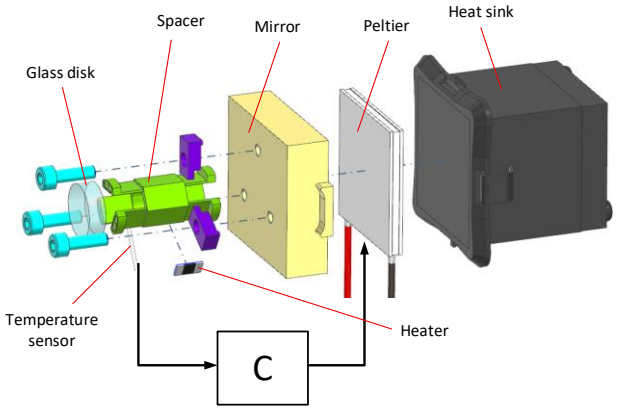

Figure 3. Optical system design which employs advanced stabilization principles.

3. Performance analysis

3.1. Modeling methodology

Each optical system is modelled with a lumped capacity thermal model consisting of 9 nodes (Fig. 4). First, the geometry of each component is approximated by a block, cylinder, or tube of representative dimensions. Nodes are defined within each component. The spacer and mirror have 2 and 3 nodes respectively to model temperature gradients within these components. The simplified geometries are used to derive the thermal capacity of each node, as well as the thermal conduction resistance between nodes. Estimates for thermal contact resistances are included for the bolted interfaces between components. Interface resistance for the adhesive connection between nodes 6 and 7 is neglected, but the conduction resistance of the adhesive bulk is included in the model.

The model contains two fixed temperature nodes. All nodes have a convective heat transfer to the surrounding air (node 8). The system is connected to a fixed temperature base frame (node 9) via the mechanical interface (node 1).

Two heat inputs are defined. The disturbance is injected at the spacer (node 6). Heat is removed at the backside of the mirror (node 2) which represents either the passive heat sink, or the active Peltier element.

The capacity matrix, conduction matrix, boundary condition nodes and heat input nodes are used to rewrite the system in state space description. This allows for simulation of the nodal temperatures due to time-varying heat inputs.

For the ‘advanced stabilization’ case, a PID controller is tuned which controls the heat flux of the Peltier element (node 2) based on the temperature measured by a temperature sensor at node 6.

The nodal temperatures are modelled in the time domain for both systems. Finally, the temperatures of the spacer nodes are used to calculate the length change of the spacer due to thermal expansion.

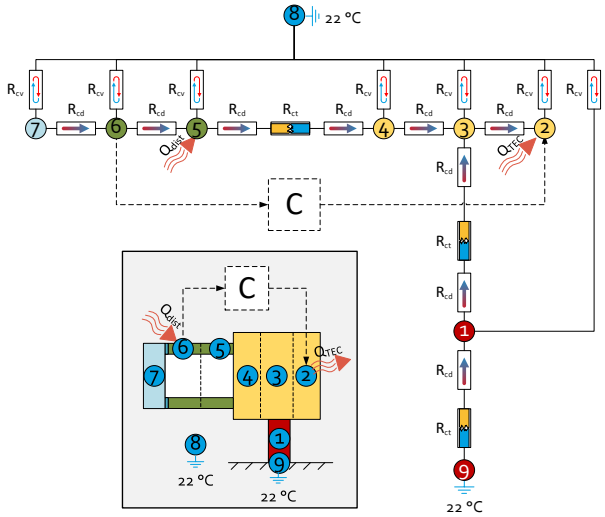

Figure 4. Lumped capacity thermal model with 9 nodes.

3.2. Modeling results

For each design approach, a 2 W constant disturbance is applied for one minute. After this, the disturbance is removed and the systems are allowed to settle. Figure 5 compares the results of the two design approaches. Three distinct differences can be observed in the results.

First, despite the significantly lower thermal expansion coefficient of the 'Minimize Sensitivity' design, the peak deformation is significantly larger than in the 'Advanced Stabilization' case. This is the result of the low thermal conductivity of Invar compared to the WCu. This results in a factor 6 larger ΔT for the Invar spacer, completely negating the gain of the lower CTE.

Second, the 'Advanced Stabilization' approach is able to achieve a steady state situation significantly faster compared to the 'Minimize Sensitivity' approach. This is possible due to the factor 20 higher thermal conductivity.

Finally, both systems do not converge to the same equilibrium state. In the 'Minimize Sensitivity' system, a constant disturbance causes the system to converge to a non-zero equilibrium state. The active system, however, controls the temperature, and resulting deformation, back to the desired setpoint. This way the original cavity length is maintained, despite slow varying disturbances.

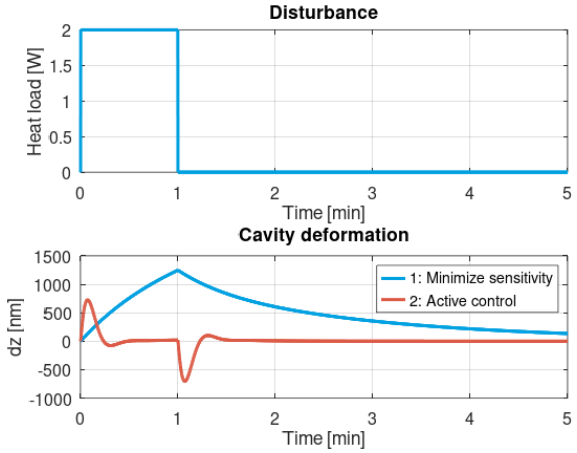

Figure 5. Results of thermal state space model. Input thermal disturbance profile (top) and resulting cavity deformation (bottom) for both design approaches.

4. Realization

Figure 6 shows the realized optical systems. The 'Minimize Sensitivity' design is visible on the left. Note that a fan is mounted to the passive heat sink to shorten the settling time in between experiments.

The 'Advanced Stabilization' design is shown on the right side of Figure 6. Note that this design uses a larger heat sink and fan as not only the disturbance heat, but also the internal power dissipation of the Peltier element has to be extracted.

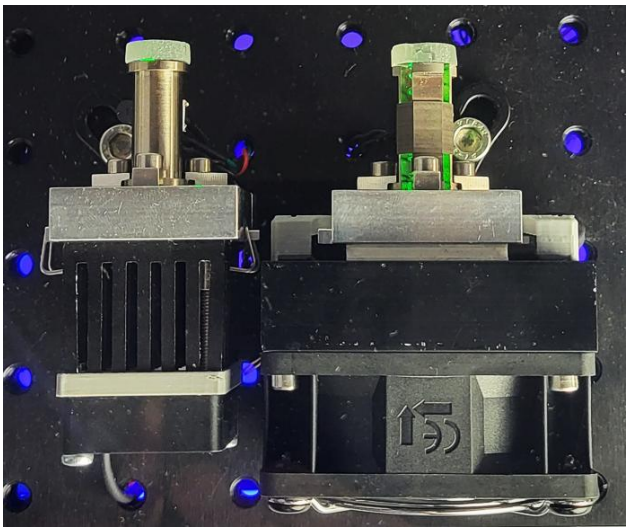

Figure 6. Close-up of the realized setup with the two alternative designs. 'Minimize Sensitivity' (left) and 'Advanced Stabilization' (right)

5. Measurements

5.1. Measurement methodology

After realization of both systems, the performance is quantified using the measurement setup shown in Figure 7. Before the glass disk is glued to the spacer, an interferometer sensor head is clamped to the spacer. By measuring the distance to the aluminum mirror, the mechanical stability of the spacer is quantified under the influence of the thermal disturbance.

The sensor measures not only the thermal expansion of the spacer, but also of a part of the titanium sensor head itself. To reduce this effect, the sensor head is thermally decoupled from the spacer by small ceramic insulators. These have a high thermal resistance, while providing decent mechanical stability due to the high stiffness and low thermal expansion coefficient.

A temperature sensor is mounted on the sensor head (not visible in Figure 3) to measure the temperature change of the sensor head directly and compensate for the remaining thermal expansion in post processing.

The heater is connected to a power supply to provide a 2 W disturbance for 1 minute. Due to limitations of the Peltier controller output power, the disturbance is switched on and off with a 0.4 W/s ramp.

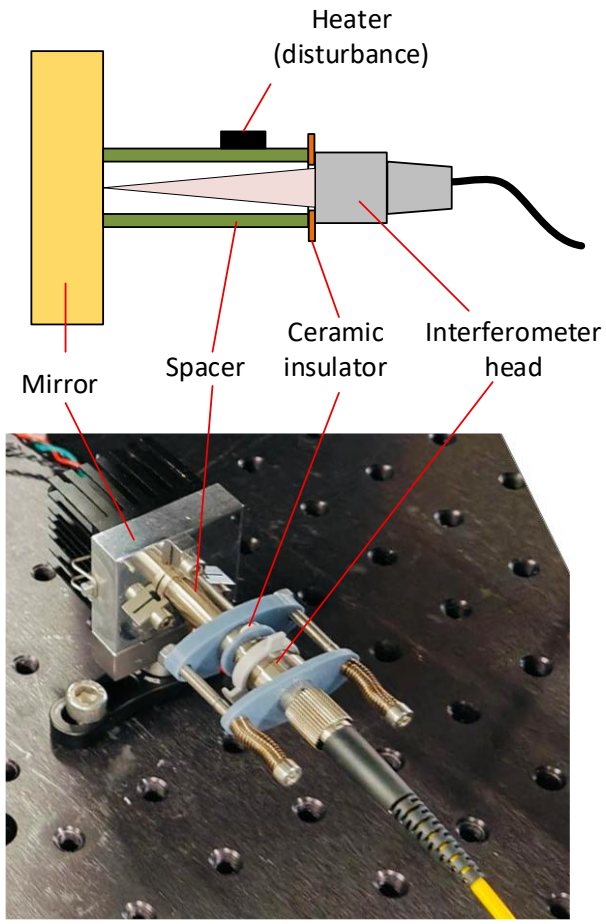

Figure 7. Schematic depiction of cavity length measurement setup (top) and photograph of realized setup (bottom).

5.2. Measurement results

The results of both measurements are plotted in Figure 8. Overall the measured deformations show a similar profile compared to the simulated results of Figure 5. There are, however, several differences.

The total magnitude of the deformation is approximately 3 times lower than in the simulation. The measured disturbance power is electrical power dissipated in the heater element. Due to the limited conductivity of the adhesive used to connect the heater to the setup, a significant fraction of this power is likely lost to convection with the surrounding air. Furthermore, the convective heat transfer from all outer surfaces to the surrounding air is included in the model, but likely underestimated as the large fan of the active heat sink induces forced air flows around both setups.

The additional thermal resistance of the heater adhesive is also observable in the temperature and deformation graphs. The smoother response compared to Figure 5 indicates an additional thermal resistance between the heater element and the spacer.

The temperature response of the active controlled case is slower than in the simulation as the controller has been tuned less aggressively in the realized system. This is done to limit the peak currents drawn by the Peltier element on the flanks of the disturbance.

The stability in the interval from 100 seconds to 200 seconds is 4 nm, while the Minimize Sensitivity setup drifts 230 nm.

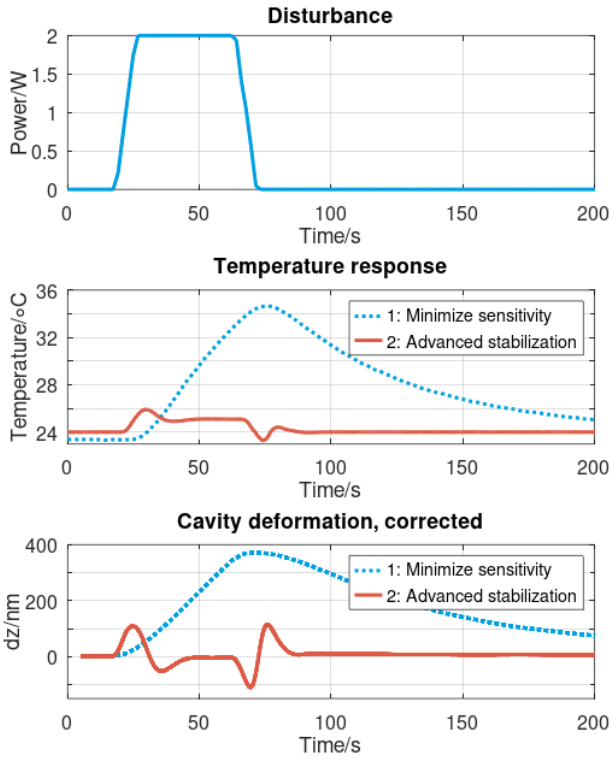

Figure 8. Measurement results with applied disturbance heat flux (top), measured spacer temperatures (middle), and measured cavity deformations (bottom).

6. Conclusion

Minimizing the thermal sensitivity of the critical parts in high-precision applications can be an effective method to achieve high mechanical stability. There are, however, cases where such an approach does not suffice, and a more comprehensive system view is required. This is especially true in situations where local, time-varying disturbances are present in or near the critical components.

This work presents various design solutions that improve thermomechanical stability in high-tech systems. A conventional precision engineering approach that uses low expansion materials is compared to an advanced approach which balances thermal properties and employs active temperature control. The second approach results in an order of magnitude improvement of the settling time and up to an order of magnitude improvement of mechanical stability.

The advanced method actively stabilizes the temperature instead of minimizing the sensitivity to the existing temperature variations. It is therefore a significantly more effective method of decoupling the thermal system behavior from its surroundings. This results in a considerable improvement of the long-term mechanical stability.

The presented design principles are applicable to all precision engineering fields, including semiconductor, defense, space, or metrology.

euspen's 26th International Conference & Exhibition, Krakow, PL, June 2026
www.euspen.eu

Modelling of 3D Surface Topography in Micromilling Process with Material Accumulation Effect

Marcin Gołaszewski[1] Bartosz Powałka[1]

[1]*West Pomeranian University of Technology in Szczecin, Poland*

marcin.golaszewski@zut.edu.pl

Abstract

Modelling of 3D surface topography in micromilling processes remains a key challenge in precision manufacturing. Since not all mechanisms have been fully identified, recent research has increasingly focused on advanced modelling approaches that enable the identification of new factors influencing the machining process. In this context, the present study introduces a hybrid model that combines 2D and 3D modules to predict both the machined surface topography and cutting forces. The model accounts for the phenomenon of material accumulation during micromilling and is applicable for feed per tooth values not exceeding the minimum uncut chip thickness. This accumulation phenomenon results from tool rigidity and the incomplete removal of material in the cross-section of the cut layer. To validate the model, grooves were machined using progressive feed per tooth values of 0.1 µm, 0.2 µm, and 0.3 µm with a flat-end micro tool of diameter D = 0.5 mm. The results confirmed that the marks observed on the machined surface are caused by the accumulation mechanism. The proposed model enables accurate estimation of the size of these accumulation marks. Furthermore, the influence of tool stiffness and minimum uncut chip thickness on the accumulation mechanism was analysed in detail.

micromilling; modelling; 3D surface topography; cutting forces; accumulation mechanism

1. Introduction

Milling is a material removal process in which machining is performed by a rotating multi-edge cutting tool. The cutter features cutting edges uniformly distributed around its axis, and the interaction between its rotational motion and the feed motion of the workpiece enables the generation of the machined surface geometry. Milling is therefore suitable for producing a wide range of surface forms and complex shapes.

The increasing demand for miniaturized components with characteristic dimensions ranging from several tens of micrometers to a few millimeters has stimulated the rapid development of micromachining technologies, with micromilling playing a particularly important role. Micromilling extends the conventional milling process to the microscale, where material removal is governed not only by geometric cutting parameters but also by the uncut chip thickness and microscale-specific material removal mechanisms [1].

According to classical machining theory, the resulting surface topography is primarily determined by the kinematic-geometric projection of the tool tip onto the workpiece, which depends on parameters such as feed per tooth, nominal tool diameter, or corner radius.

However, in micromilling this theoretical description exhibits limited predictive accuracy. The final surface topography is strongly influenced by additional factors. Most often, the literature considers factors such as geometrical errors of machining system, tool wear, vibrations, and other specific phenomena characterizing the micromilling process.

Cutting forces generated during milling have a significant influence on the formation of machined surface topography, as they lead to deflections of the tool tip [2]. These forces induce periodic elastic deformations of the tool and the workpiece, which may result in surface location errors and, in certain cases, contribute directly to surface roughness.

The special case is processing when the frequencies of force variations exceed the frequency corresponding to the feed per revolution [3]. In addition, vibrations and loss of process stability, manifested by the occurrence of chatter, constitute highly undesirable phenomena that affect surface quality. The formation of high-amplitude chatter marks on milled surfaces is influenced by aliasing and pseudo-moiré effects [4]. Furthermore, instantaneous tool tip deflections can induce milling vibrations, which are subsequently transferred onto the machined surface, leading to further deterioration of the surface finish [5].

When the cutting thickness reach level below the minimum chip thickness h_{min}, material removal does not occur through conventional chip formation; instead, the workpiece material undergoes predominantly elastic-plastic deformation, commonly referred to as ploughing. Once the cutting thickness reaches or exceeds h_{min}, the contribution of ploughing is significantly reduced and stable chip formation is established [6,7]. This transition in the material removal mechanism gives rise to the so-called size effect. This behavior is associated with the elevated shear flow stress resulting from the reduced dimensions of the cutting zone [8]. Consequently, the size effect has a substantial influence on both cutting forces and the resulting surface quality of machined components.

This paper presents a micro-machining model for both, the machined surface and the micromilling forces, including the mechanism of chip accumulation. This mechanism plays a key role in machining with low rates of feed per tooth.

2. Micromilling model

In this study, a novel 3D surface topography model dedicated to micromilling and based on a 2D solver is proposed. The developed model describes the trochoidal trajectory of the tool tip as well as the material accumulation mechanism [9]. Furthermore, the modelling framework accounts for instantaneous radial tool tip displacement induced by cutting forces.

The proposed surface topography model integrates a 2D HMT-based approach (Homogenous Matrix Transformation) with a 3D Z-map method within dedicated computational modules. The 2D HMT-based model is employed to determine the instantaneous positions of the cutting edges, which are required to evaluate the instantaneous area of cut and, consequently, to calculate the cutting force components. Additionally, the 2D HMT-based model incorporates both the material accumulation mechanism and radial tool tip displacements. The 3D Z-map model is subsequently used to generate the machined surface topography. It employs the geometrical outlines of successive cutting edges obtained from the 2D HMT-based model by transforming the cutting edges motion into a three-dimensional representation. An overview of the proposed surface topography modelling procedure is presented in Figure 1.

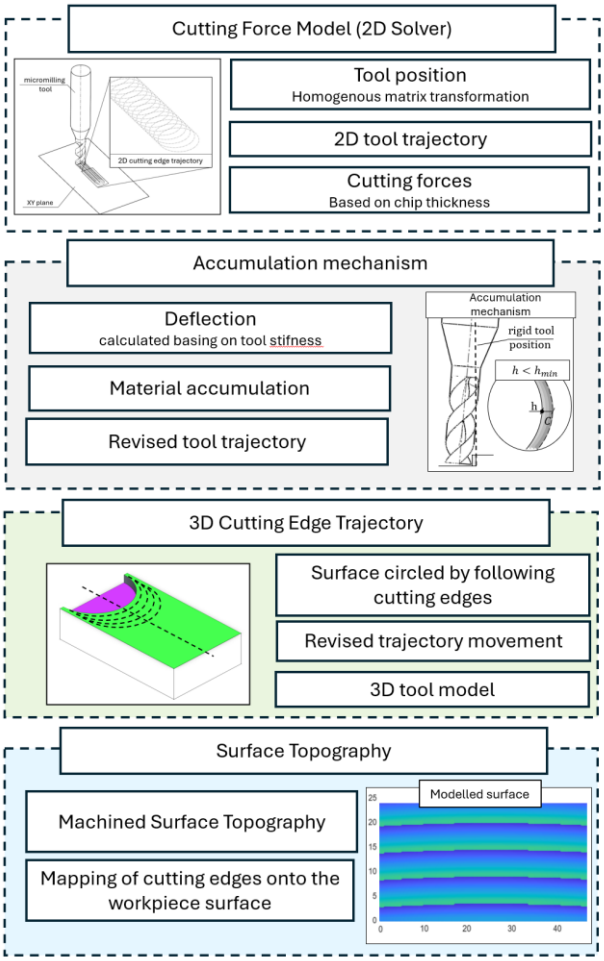

Figure 1. Overview of the proposed modelling procedure

2.1. 2D HMT-based model

In the 2D HMT-based approach, the cutting edge is represented as a point in a two-dimensional plane. This representation enables a reduction in computational time. The employed algorithms require iterative updates of the cutting edge position according to the tool motion as well as accumulation-based tool deflection therefore, reducing the complexity of algorithms is reasonable. The positions of the cutting edges are mutually related and defined with respect to the tool center, which coincides with the rotation axis. Each cutting edge is described by its coordinates in the X and Y axes. The position of cutting edge C is defined as shown in Eq. (1).

The position of a cutting edge at a given time t is determined using a homogeneous matrix transformation that incorporates both translational and rotational components. The angular position of the cutting edge, denoted as φ(t), together with the feed ratio, constitutes the key parameters of this transformation. All changes in tool position resulting from tool deflection and the accumulation mechanism are introduced into the model using homogeneous matrix transformations. The position of the cutting edge at a single time instant t is described by Eq. (2). The motion-related matrices are denoted as $R_z(t)$ for rotation and $T_x(t)$ for feed, while the accumulation-based tool deflection is represented by the matrix $T_r(t)$.

$$C = \begin{bmatrix} x|_{t=0} \\ y|_{t=0} \end{bmatrix} \tag{1}$$

$$C^T = C^T|_{t=0} \cdot T_r(t) \cdot R_z(t) \cdot T_x(t) \tag{2}$$

To determine the trajectory traced by a cutting edge during a single tool revolution, the cutting edge position is evaluated at discrete time intervals. Between two consecutive instants, t and t + Δt, the cutting edge undergoes rotation about the tool axis and a simultaneous displacement of the tool center. This combined motion generates a trochoidal trajectory. During a single tool pass, the rotating cutting edge produces curved trochoidal lines corresponding to the removed material. The material removal region is bounded by the trochoidal lines formed during successive revolutions. Notably, each marked area is associated with an individual cutting edge rather than with the entire tool. Consequently, the model constructs as many surface segments as there are cutting edges. The trochoidal trajectories traced by all cutting edges collectively define the overall material removal process.

2.2. Model of micromilling cutting forces

In order to estimate the instantaneous cutting forces and tool tip displacements, two coordinate systems, XYZ and TRA, are adopted in the modeling framework. In the XYZ coordinate system, the cutting forces measured by the dynamometer are defined. In this system, the Z-axis coincides with the tool axis, the X-axis corresponds to the feed direction, and the Y-axis is defined by the right-hand rule based on the X and Z axes. The TRA coordinate system is a tool-fixed reference frame, with its origin located at the tool tip. In this system, the R-axis represents the radial direction, the A-axis coincides with the tool axis, and the T-axis is defined by the orientation of the A and R axes. The TRA coordinate system rotates together with the tool during spindle rotation.

Assuming perfect rigidity of the system in the axial direction, the force components along the A and Z axes are not considered. The transformation of the cutting force components from the TRA system to the XYZ system is described by Eqs. (3) and (4). The detailed procedure for determining the cutting force components is provided in previous studies [10].

$$F_X = F_T \cdot \cos\varphi(t) + F_R \cdot \sin\varphi(t) \tag{3}$$

$$F_Y = -F_T \cdot \sin\varphi(t) + F_R \cdot \cos\varphi(t) \tag{4}$$

The radial tool deflection Δr is determined using an iterative algorithm. In each iteration, an elementary deflection dr is introduced in the direction that drives the system toward mechanical equilibrium. After applying the elementary deflection, a new tool position is calculated. This positional change results in a reduction of the uncut chip thickness. Based on the updated tool position, new cutting force components in the TRA coordinate system are evaluated. Subsequently, the elastic forces acting on the tool are recalculated. If the equilibrium conditions are not satisfied, the algorithm proceeds to the next iteration.

The elastic force in the j-th iteration, denoted as F_{krj}, is calculated using Eq. (5), where F_{Rm} and F_{krm} represent the force values obtained in the m-th iteration. The iterative procedure continues until an equilibrium state is reached. The tool deflection corresponding to the equilibrium state obtained in the j-th iteration is then determined using Eq. (6).

$$F_{krj} = k_r \cdot \sum_{m=1}^{j-1} \frac{(F_{Rm} - F_{krm})}{|F_{Rm} - F_{krm}|} \cdot dr \tag{5}$$

$$\Delta r = \sum_{m=1}^{j} \frac{(F_{Rm} - F_{krm})}{|F_{Rm} - F_{krm}|} \cdot dr \tag{6}$$

Taking into account the determined radial deflection Δr, the instantaneous position of the cutting edge is updated. Material that would be removed by a perfectly rigid cutting edge during the current pass is transferred to the subsequent pass. Furthermore, it is assumed that when the uncut chip thickness does not exceed a minimum value h_{min}, the material is not removed, despite the presence of non-zero cutting forces. In such a case, the unremoved material is added to the uncut chip thickness in the next cutting edge pass. This phenomenon is referred to as the material accumulation effect. The material continues to accumulate until the cumulative instantaneous uncut chip thickness exceeds the h_{min} value. Once this condition is satisfied, the material is removed and the accumulation cycle restarts. A schematic illustration of the method of uncut chip thickness determination is presented in the figure 2.

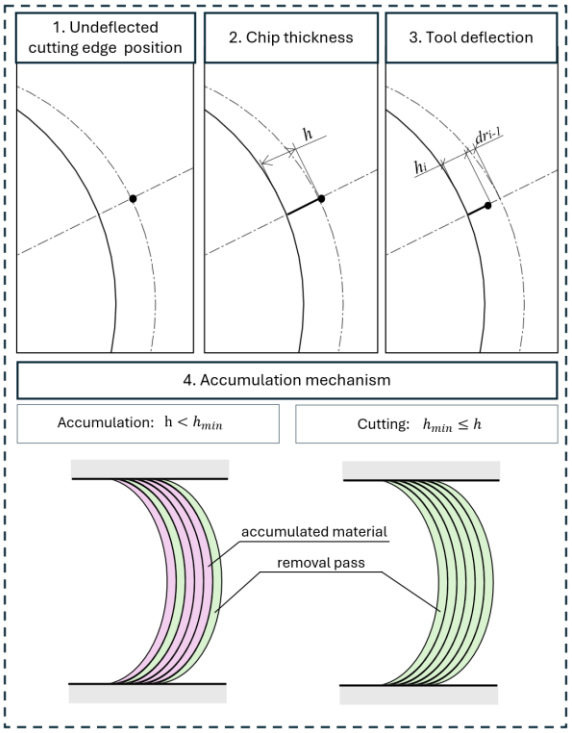

Figure 2. Overview of the proposed modelling procedure

2.3 3D Z-map transformation

The tool trajectory determined in the 2D HMT-based module accounts for both radial tool deflection and the material accumulation mechanism. In this form, the trajectories of the cutting edges can be directly adapted for three-dimensional surface representation.

In the first step, a three-dimensional model of the cutting tool is constructed. The tool is represented as a point cloud, with the cutting edge geometry obtained by determining the intersection of the tool body with a plane inclined by the helix angle λ. The modeled cutting edge is divided into three distinct regions: the face cutting edge, the cylindrical cutting edge, and the corner radius cutting edge. Each region is modeled separately in order to accurately capture the local geometry of the tool body. This segmentation enables a precise representation of the cutting edge geometry and ensures reliable simulation of tool–workpiece interaction.

The workpiece model is limited to the representation of the machined surface only. Similar to the tool model, the workpiece is described using a point cloud format. The grid of workpiece points is based on a rectangular mesh, which is assumed to be the master mesh inherited by the machined surface topography model.

The surface generated by the cutting edge is constructed from its successive positions, forming a radial mesh without predefined nodes. The locations of these nodes are determined dynamically based on the instantaneous position of the cutting edge. Consequently, the mesh of the traced surface differs from the predefined workpiece mesh. To enable accurate surface modeling within the workpiece domain, the nodes of the traced surface mesh are dynamically adjusted. As a result, the cutting edge surface mesh is interpolated to match the predefined workpiece mesh.

Once the surface generated by the cutting edge is described on the same mesh as the workpiece, the Z-map model is applied. The Z-map approach is based on comparing the geometry values at corresponding nodes of two meshes: a modified mesh and a modifying mesh. In the present case, the workpiece material constitutes the modified geometry, while the surface generated by the cutting edge represents the modifying geometry. If the geometry value at a node of the modified mesh is greater than the corresponding value of the modifying mesh, the modified geometry is updated to the value of the modifying geometry. Otherwise, the modified geometry retains its original value.

2.4. Experimental results and discussion

Micromilling experiments were conducted on AISI 1045 carbon steel. Cutting tests were conducted with a radial depth of cut a_e =20 µm and a cutting speed v_c = 47 m/min. The feed per tooth values were set below the minimum uncut chip thickness. For the 2FESM005-010-04 tool with a diameter D = 0.5 mm, the minimum uncut chip thickness was determined as h_{min} = 0.64 µm. This value was estimated based on the cutting edge radius r_n = 3.2 µm. The experiments were carried out for feed per tooth values of f_{z1} = 0.1 µm, f_{z2} = 0.2 µm and f_{z3} = 0.3 µm.

The radial stiffness of the tool was determined experimentally. The displacement was induced using a rigid steel block attached to the moving machine table. The displacement was applied incrementally in steps of 1 µm. The tool tip was supported against a movable block with a cylindrical surface. The resulting radial stiffness was determined as k_r = 0.15 N/µm.

On the machined surface, marks resembling feed marks were observed; however, their spacing did not correspond to the nominal feed per tooth. In order to explain the mechanism responsible for their formation, the algorithm described in the previous section, incorporating the accumulation phenomenon,

was employed. The spacing between consecutive accumulation marks was approximately 5.6 µm, which is significantly greater than the applied feed per tooth.

The accumulation phenomenon, consisting in the gradual build-up of material until the minimum uncut chip thickness is exceeded, is particularly significant for feed values far below h_{min}. This mechanism makes it possible to explain the occurrence of surface marks whose spacing is a multiple of the nominal feed per tooth.

When machining with feed values significantly below h_{min}, material removal does not occur during the first pass of the cutting edge. At this stage, complex plastic deformation processes may take place. In the present study, it is assumed that the material does not undergo any state change: its properties remain constant, no ploughing occurs, and no chip formation takes place. Although cutting forces are observed in the model, material removal does not occur. The retained material is taken into account during the subsequent cutting edge pass, leading to an increase in the effective uncut chip thickness. For very small feed values, chip formation does not occur at this stage either, and the material from both the first and second cutting edge pass remains unremoved. Only when the minimum uncut chip thickness is exceeded in subsequent engagements does chip formation occur and the material is removed.

The described phenomenon explains the multiplication of the observed surface marks, whose spacing does not directly result from the feed per tooth value. **Figure 3** presents the surface marks observed experimentally, together with the modeled surface topography.

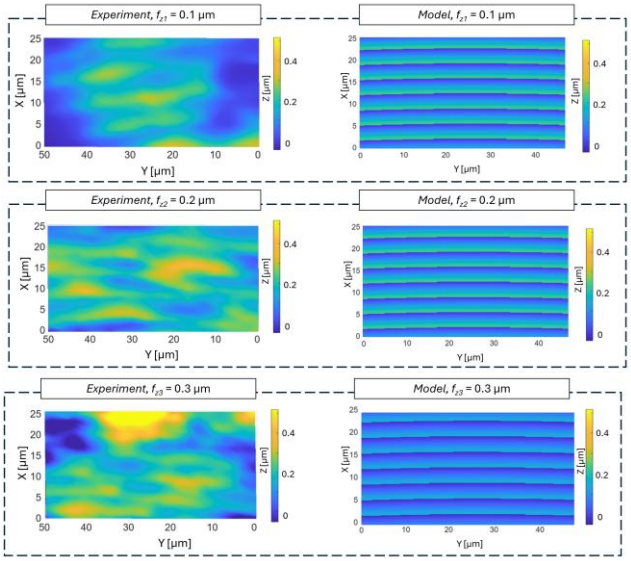

Figure 3. Experimental and modelled surface topographies

Although the accumulation mechanism was incorporated into the model, the size of the accumulation marks does not fully correspond to the size of the marks observed on the machined surface. This discrepancy results from plastic deformation effects that are not included in the model. Figure 4 presents the surface roughness of the experimentally observed surface and the modeled surface. In order to illustrate the influence of the accumulation mechanism, the results obtained using a model without the implemented accumulation mechanism are also included in the comparison. It is clearly visible that the incorporation of the accumulation mechanism leads to a significant improvement in the consistency between the surface roughness values.

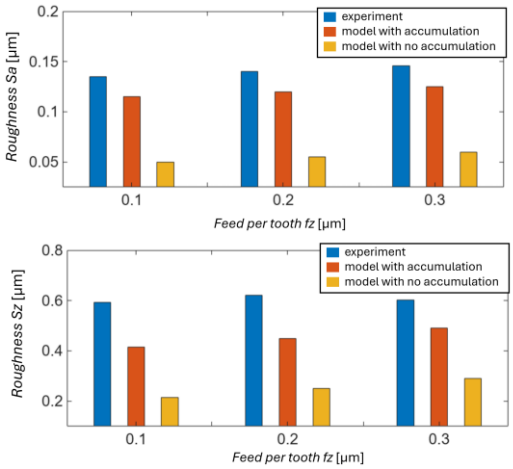

Figure 4. Roughness of experimental and modelled surfaces

3. Conclusion

This paper presents a micromachining model for end milling operations. The model accounts for both cutting forces and the resulting machined surface topography. In addition, the accumulation mechanism of the uncut chip layer is incorporated. The proposed model was validated through machining experiments conducted with feed per tooth values below the minimum uncut chip thickness. Based on the conducted study, the following conclusions can be drawn:

- The accumulation mechanism occurs when the nominal feed per tooth does not exceed the minimum uncut chip thickness.
- Incorporation of the accumulation mechanism makes it possible to obtain surface marks whose dimensions are larger than those resulting directly from the feed per tooth.
- Consideration of the accumulation mechanism improves the consistency between the experimentally obtained surface and the modeled surface.

Despite these improvements, full consistency between the modeled and experimental results was not achieved. The average relative error reached level of 14.5% for the surface roughness parameter Sa and 25.7% for Sz. In order to further improve the consistency, not only in terms of roughness parameters but also in reproducing accumulation marks, the plastic behavior of the machined material should be incorporated into the model.

References

[1] S. Wojciechowski, *Materials* **2021**, *15*, DOI 10.3390/ma15010059.

[2] D. Wang, J. Ren, W. Tian, *Int. J. Adv. Manuf. Technol.* **2020**, *107*, 2023.

[3] S. Wojciechowski, M. Wiackiewicz, G. M. Krolczyk, *Measurement* **2018**, *129*, 686.

[4] N. Grossi, A. Scippa, L. Sallese, F. Montevecchi, G. Campatelli, *Int. J. Mach. Tools Manuf.* **2018**, *133*, 31.

[5] K. J. Kalinski, M. A. Galewski, *Int. J. Mach. Tools Manuf.* **2015**, *92*, 19.

[6] G. Bissacco, H. N. Hansen, L. De Chiffre, *J. Mater. Process. Technol.* **2005**, *167*, 201.

[7] J. Chae, S. S. Park, T. Freiheit, *Int. J. Mach. Tools Manuf.* **2006**, *46*, 313.

[8] A. Simoneau, E. Ng, M. A. Elbestawi, *Int. J. Mach. Tools Manuf.* **2006**, *46*, 467.

[9] S. Wojciechowski, M. Matuszak, B. Powałka, M. Madajewski, R. W. Maruda, G. M. Królczyk, *Int. J. Mach. Tools Manuf.* **2019**, *147*, 103466.

[10] M. Gołaszewski, S. Wojciechowski, B. Powałka, F. Botko, M. Geľatko, *Precis. Eng.* **2026**, *97*, 904.

euspen's 26th International Conference & Exhibition, Krakow, PL, June 2026
www.euspen.eu

Investigation of a positioning mechanism for adjustments with minimal side effects

Mario André Torres Melgarejo, René Theska, Hannes Scheibe

Technische Universität Ilmenau, Department of Mechanical Engineering
Institute for Design and Precision Engineering, Precision Engineering Group

E-mail: mario.torres@tu-ilmenau.de

Abstract
High-precision devices often require the adjustment of highly sensitive units to achieve their intended performance. Deterministic adjustment demands high motion accuracy as well as verification under the intended operating conditions. In applications involving hermetically sealed environments, remote control and automation of the adjustment process are essential. Off-the-shelf positioning stages are commonly employed for this purpose. However, high functional sensitivity of the unit to be adjusted also implies high sensitivity to disturbances. A systematic assessment of the side effects introduced by the adjustment system is often lacking. Previous investigations have identified permanent cable connections as critical sources of mechanical disturbance due to their unstable and unpredictable behavior. Wireless energy transfer or temporary detachment of the cable connection represent possible mitigation strategies. Nevertheless, the in-situ positioning system can introduce non-neglectable side effects and therefore requires similar consideration. This contribution analyzes the disturbances generated by the positioning system, which subsequently serve as the basis for the design of a mechanism enabling low-side-effect adjustments. The positioning performance of the proposed mechanism is investigated experimentally, demonstrating submicrometer resolution and position stability over multiple days.

Keywords: adjustment, side effects, disturbances, positioning mechanism

1. Introduction

High-precision devices, such as those used in mass metrology [1], nanomeasurement technology [2] or semiconductor device manufacturing [3], demand extremely high functional sensitivity while remaining highly insensitivite to disturbances. External influences are often avoided by operating in hermetically sealed environments where conditions are strictly controlled. Residual systematic deviations are addressed for by low-error design, compensation strategies or computational corrections. If these measures prove insufficient, the adjustment of highly sensitive units becomes necessary.

A deterministic adjustment demands not only high accuracy, but also verification under the intended operating conditions. This imposes requirements on remote operability, a high degree of automation as well as environmental compatibility of the adjustment system. Electrically-actuated fine positioning stages are therefore commonly employed, with a broad spectrum of commercially available solutions.

However, electrical energy transfer, its conversion into mechanical energy, and associated energy storage (maintaining of the achieved state) inherently introduce side effects that degrade the adjustment stability. While concepts for low-interference energy transfer concepts have already been proposed in earlier studies [4,5], there is still a lack of a systematic assessment of side effects caused by the positioning system itself.

This contribution analyses disturbance effects of fine positioning systems and presents a mechanism designed for low-side-effect adjustments. The analysis focuses primarly on mechanical, thermal and electromagnetic disturbance effects, while other effects, such as the emission of particles, are not investigated exhaustively. Finally, the positioning performance of the proposed mechanism is investigated experimentally.

2. Side effects in adjustment

In precision devices, adjustment refers to the controlled displacement of a component to achieve the intended device function [6]. The adjustment parameter is measured and compared with a target value, whereupon energy is transferred to the adjustment device, converted into a displacement, and subsequent fixation of the achieved position. This closed-loop sequence is repeated until the target value is reached.

Controlled displacement is typically realized through a combination of an actuator or drive, a transmission and guidance elements. Their side effects are transmitted to both the sensitive unit and the adjustment unit. Heat is mainly generated by losses in the drive and depends strongly on the actuator principle. Actuators may also produce magnetic or electric fields, causing parasitic forces or electromagnetic couplings. Drive operation and its control can induce vibrations or impact loads. Friction at contact interfaces of moving elements under such conditions promotes wear, i.e. particle liberation. Material selection is also associated with particle release and magnetic interactions. Figure 1 shows relevant factors limiting a deterministic adjustment.

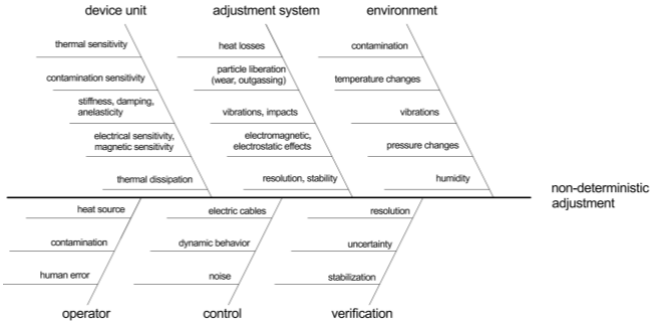

Figure 1. Representation of influences hindering the adjustment.

3. Design of positioning mechanism

Based on the previously discussed side effects, a positioning mechanism for low-side-effect adjustments is proposed (see Figure 2). The intended application is the vertical positioning of trim masses in precision weighing cells [1]. The system combines piezoelectric actuators with a compliant mechanism that fulfills both transmission and guidance functions. Due to the compliant design, friction and wear are largely avoided. However, sliding friction remains at the contact interfaces between moving elements. By operating the actuators in a quasistatic regime, heating becomes negligible and vibrations are minimized. Appropriate material selection further prevents undesired magnetic interactions and minimizes wear and outgassing.

The adjustment motion and its securement are functionally separated, as piezoelectric actuators are not self-locking. The adjustment motion is generated by a first actuator and amplified by a transmission lever. A second actuator, initially decoupled, opens a normally-closed friction locking mechanism prior to the adjustment motion. The locking mechanism consists of a pretensioned spring and a lever that clamps a leaf spring on the output stage.

To reduce the locking force, drive force and its associated friction forces, an initial gap between the output stage and the adjustment lever is introduced. This allows the restoring force of the flexure guide to partially compensate for the weight of the adjustment unit. After the adjustment, the locking actuator is returned, closing the locking mechanism. The adjustment actuator can be then released, thereby securing the adjusted position without need for a continuous power supply. Undesired deformations are avoided by maintaining short force loops and loading structural elements in a mechanically favorable manner.

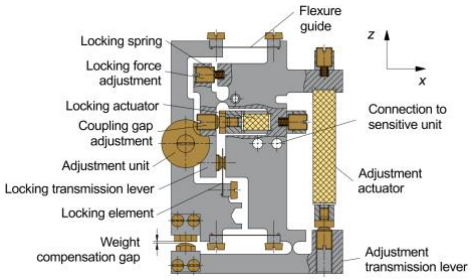

Figure 2. Embodiment design of positioning mechanism.

4. Positioning performance

The positioning performance of the proposed mechanism defines the quality of the adjustment. Figure 3 shows the displacement of the output stage at different input voltages to the adjustment actuator. Due to the hysteresis originating from the piezoceramic material and presence of sliding friction, input voltage and output displacement are not strictly proportional. The theoretical positioning resolution is approximately 25 nm for a voltage resolution of 25 mV at the point of highest sensitivity. However, the locking process induces a backlash motion that displaces the output stage by up to 0.3 µm. This effect can be attributed to misalignments on the leaf spring as well as an initial one-sided contact.

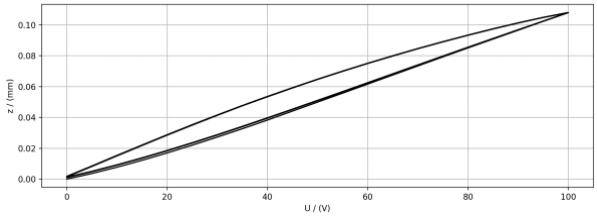

Figure 3. Characteristic curve of proposed mechanism.

Another requirement for the adjustment is a high position stability. Figure 4 shows the change in the position of the output stage over three days inside a temperature-controlled laboratory environment (±1 °C), evaluated at the position of maximum deflection (z = 113.7 µm). A correlation with the temperature drift was observed and a correction was applied. After correction, a stability better than ± 0.5 µm was measured.

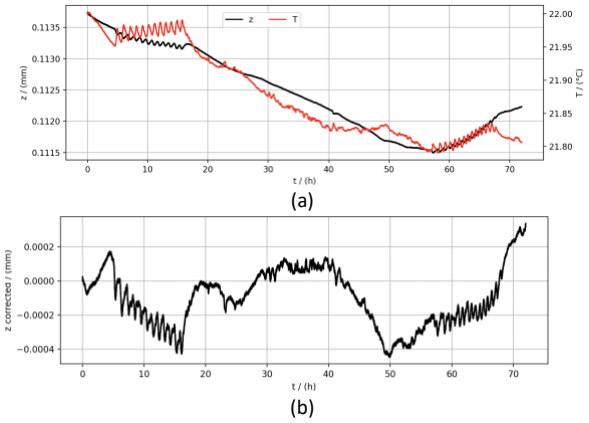

Figure 4. Position stability over three days: (a) without temperature correction, (b) with temperature correction

5. Summary and future work

This papers proposes a positioning mechanism for low-side-effect adjustments based on a systematic assessment of the ocurring disturbances occurring during the adjustment process. Mechanical, thermal and electromagnetic disturbances are considered and minimized through a deliberate selection of the operating principle and materials. The positioning mechanism comprises two piezoelectric actuators and a compliant mechanism. Experimental investigation of the positioning performance demonstrates that submicrometer resolution can be achieved, which is limited by the locking mechanism. In addition, a position stability better than 0.5 µm over a period of three days is demonstrated.

Due to sliding friction between contact interfaces, wear cannot be completely avoided. The use of lubricants compatible with the application environment, e.g. PTFE grease, may reduce friction and trap wear particles. However, in applications where contamination is unacceptable, where static friction is functionally required, e.g. for position securement, or where any loss of mass or volume is impermissible, low-particle adjustment strategies becomes necessary. Future work will therefore focus on investigating novel solution approaches to eliminate particle emissions during the adjustment process.

Acknowledgements

The authors thank the German Research Foundation (DFG) for the financial support of the project with Grant No. TH 845/9-1.

References

[1] Darnieder M 2023 Design and adjustment of weighing cells for vacuum mass comparators

[2] Jäger G, Manske E, Hausotte T, Müller A and Balzer F 2016 *Surf. Topogr.: Metrol. Prop.* **4** 034004

[3] Xu F, Zhang J, Li W, Pan C, and Xia H 2026 *Laser & Photonics Reviews* e01998

[4] Torres Melgarejo M A and Theska R 2024 In-situ fine adjustment system for in-vacuo weighing cells *Proceedings of euspen's 24th International Conference and Exhibition* 249-252

[5] Torres Melgarejo M A and Theska R 2025 Novel in-situ fine adjustment system with contactless energy transfer *Proceedings of euspen's 25th International Conference and Exhibition*

[6] Hansen F 1967 Justierung

Session 5: Large Scale Precision Engineering and Metrology

euspen's 26th International Conference & Exhibition, Krakow, PL, June 2026
www.euspen.eu

Development of high pressure and high temperature injection modules for 4D µCT in synchrotron environment.

Antonio Neto[1], Cassiano Bueno[1], Débora Jesus[1], Everton Oliveira[1], Felipe Varga[1], Gabriel Baldon[1], Gabriel Caron[1], Gabriel Moreno[1], Gabriel Schubert[1], Guilherme Pimentel[1], Gustavo Pozza[1], Jair Neyra[1], João Pereira[1], João Matoso[1], João Silva[1], Ketlen Brito[1],Lucca Campoi[1], Nathaly Archilha[1], Mailson Souza[1], Paloma Zanella[1], Pedro Coutinho[1], Rafael Maluf[1], Stefano Coluccini[1], Talisson Borges[1], Victor Santos[1], Vitor Amaral[1], Arend Aerts[2], Bart Van Dijck[2], Bram Witteman[2], Corne Van Haren[2], Maryn Wijnhoven[2], Martijn Princen[2], Robin Franssen[2], Theo Ruijl[2], Rodrigo Surmas[3]

1 Brazilian Center for Research in Energy and Materials (CNPEM)

2 MI-Partners BV

3 Petróleo Brasileiro S.A. (Petrobras)

cassiano.bueno@lnls.br

Abstract

Mogno Beamline is a high-complexity equipment which performs both Nano and Micro computed tomography (CT) scans in Sirius, the Brazilian Synchrotron at CNPEM (Brazilian Center for Research in Energy and Materials). This Beamline works with a conic X-ray beam, which allows for zoom-in tomography of samples from several areas ranging from geological to biological samples. In the experimental hutch there are two experimental stations, the Nano Station (which allows for image resolution ranging from 130 nm to 12 µm) and the Micro Station (0.5 to 52 µm of image resolution). Currently, the Micro Station is operational with a high throughput setup for dry sample exchanging with a robotic arm and magazine system, but a second experimental setup is under development, which will regard in situ porous media flow imaging under high pressure (up to 1000 bar) and high temperature (90 °C), conditions similar to those found in pre-salt oil reservoirs. With the founding of Petrobras and Equinor, this project aims to advance the study of flow behaviour in porous media by designing equipment with precision engineering techniques to guarantee precise sample positioning and stabilization, together with high-speed data gathering and post processing. This paper aims to display the main considerations needed to perform the before mentioned high complexity experiment, together with the preliminary mechanic and control design results and next steps.

Engineering, Mechatronics, Pressure, Temperature

1. Introduction

The Sirius/LNLS MOGNO (Micro and Nano tomography) beamline is dedicated to performing three-dimensional tomography experiments with synchrotron radiation, ranging from micrometric to nanometric regime. MOGNO beamline [1] is mainly divided into 3 different stations: nano, high-throughput and pre-salt. In 2024, the line incorporated a new experimental infrastructure, the high-throughput micro station, designed for three-dimensional study of representative samples of carbonate rocks from Brazilian pre-salt reservoirs. The third station, called pre-salt, is under development by the LNLS/Sirius engineering team.

The high-throughput station is designed to offer the users a spatial resolution of 500 nm and temporal resolution of seconds for tomographies [2-3], but with a simpler setup for dry samples. The current setup is under technical commissioning to verify the design parameters. Although, with this setup it was already possible to validate gantry motion capabilities (Zoom) and beamline systems operations (detectors and optics) that will be used for pre-salt setup as well.

The development of pre-salt end station aims to expand MOGNO's current experimental capabilities, offering a controlled environment, maintaining high mechanical stability for the execution of CT scans while allowing in-situ tests under controlled pressure and temperature conditions, mimicking pre-salt ones, enabling the direct observation of dynamic processes, such as fluid injection (water, oil or CO_2) and microstructural changes in geological materials. The high-energy radiation spectrum of the MOGNO beamline ensures the penetration needed to image samples with typical thicknesses up to 38.1 mm (1.5 in).

From a constructive point of view, the pre-salt micro station combines structural rigidity, sub-micrometric positioning accuracy and thermal stability, essential for tomography experiments with the fluids of interest mentioned. The mechanical system is designed to ensure fine alignment between the sample and the beam, minimizing vibrational noise and ensuring stability during prolonged acquisitions. The experimental suite includes a sample handling module (section 3.1), a pressurization module (section 3.5), fluid storage modules (section 3.4), and a sample conditioning module (section 3.3), allowing the capture of images (2D projections that, combined, make up 3D CT scans) at rates up to the kilohertz scale (section 4).

2. Main Challenges

A primary challenge of micro station pre-salt is emulating high-pressure and high-temperature flow experiments setups, typically confined to laboratory environments on benchtop CT scanners [4], into the highly constrained and vibration-sensitive setting of a synchrotron beamline. Tomographic imaging requires high mechanical stability, minimal dynamic disturbances during long acquisition times and, in our case, high

acquisition speed to enable 4D imaging. Reconciling these requirements with the presence of pressurized fluids, heating systems, and auxiliary infrastructure near the sample represents a fundamental design constraint.

A second major challenge arises from the intrinsic requirement of tomographic measurements, that is the rotation between X-Ray source and sample. As in a beamline it is not possible to rotate the X-Ray source, so the sample must rotate. This configuration imposes severe constraints on the transfer of pressurized and heated fluids between static infrastructure and the rotating sample environment. Unlike electrical signals, which can be easily handled through slip-ring technologies, fluid transfer under high pressure and temperature demands robust mechanical interfaces capable of maintaining leak-tightness, chemical compatibility, and thermal stability throughout continuous rotation. The limited availability of off-the-shelf solutions suitable for these conditions demands custom approaches and careful integration between mechanical, thermal, and fluidic design domains.

Beyond hardware-related challenges, the micro station pre-salt introduces a highly complex experimental workflow that spans through sample preparation, fluid conditioning, system assembly, transport, and beamline operation. Special fluids, like live oil and carbonated water, must remain pressurized and thermally conditioned throughout the entire process, from laboratory preparation to in-situ tomography, without interruption or need for recombination. This requirement significantly increases the operational complexity, as it demands coordinated procedures, active thermal control during transportation of samples and accumulators, and strict sequencing of experimental steps.

3. Pre-salt Micro Station - Mechanical Overview

The mechanical architecture of the pre-salt micro-station was designed to manage the high complexity associated with the proposed experiment. To address all the requirements in a structured and robust way, the mechanical system adopts modular architecture, in which the overall functionality is distributed across well-defined mechanical modules with clear interfaces.

From development and operational perspective, the modular structure facilitated parallel design, and soon will facilitate independent assembly, testing and incremental commissioning of the station. Moreover, this approach improves maintainability, supports future upgrades and enhances operational flexibility, making modularization a key system-level strategy for the reliable implementation of complex in-situ experiments at the MOGNO beamline.

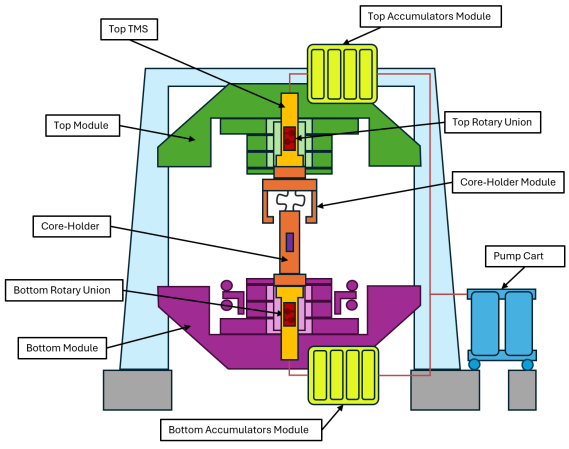

Figure 1. Pre-salt micro-station mechanical modular architecture, with module critical components highlighted.

To address the challenges outlined above, the mechanical structure of the pre-salt micro-station is organized into a set of modules as shown in Figure 1. The modules were splited in such a way to aggregate similar functions, decrease mechanical interfaces and allow a clever workflow of assembly and maintenance. The following sections provide a concise overview of the main mechanical modules and their respective functions, capacities and challenges within the overall system architecture.

3.1. Bottom Module

The Bottom Module is responsible for the precise positioning and dynamic stability of the sample during rotation, as well as for the thermal conditioning of the fluids entering or leaving the core-holder through the lower interface. This module integrates the linear positioning stages (XL and X-Z), the rotational stages (primary and auxiliary), and the thermal management system (TMS), all represented in Figure 2, forming the mechanical and functional foundation of the micro-station.

The main engineering challenge of this module lies in reconciling sub-micrometric stability (≈250 nm) and fast rotation speeds (≈1-4Hz) with the need to accommodate significant rotating masses, high-pressure fluidic interfaces, and additional degrees of freedom for region-of-interest (ROI) selection. To guarantee system target performance, an error budget was constructed with the major sources of errors being floor vibrations propagations to sample, rotary stage runout errors and rotation induced deformations and offsets. As outcome, it was identified that the major contributions to sample position error are rotation induced deformations (≈2µm) and rotary stage runout errors (≈400nm).

To address and mitigate these errors the proposed design has a separation between the primary and auxiliary rotation stages (Ry), together with the implementation of an auto-balancing system, is essential to mitigate dynamic imbalance effects introduced by sample offset during high-resolution tomographic experiments with zoom in ROI. Also, a metrology system was design to measure the primary rotation stage position in relation to the static world, in every DoF apart from the rotation itself using the multiprobe method. Its data will be used to feed the tomography reconstruction algorithm decreasing the uncertainties to levels below the target (≈200nm).

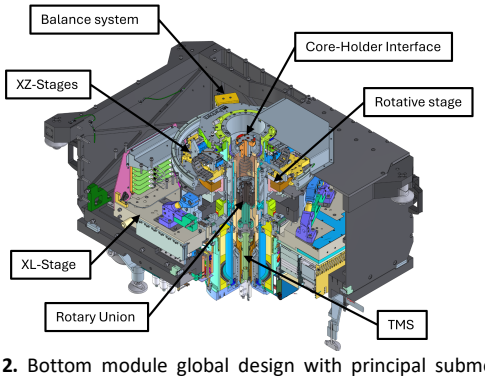

Figure 2. Bottom module global design with principal submodules highlighted.

3.2. Top Module

The Top Module is positioned above the sample and primarily supports and decouples auxiliary systems required for experiment execution, such as upper accumulators, pressure sensors and thermal management components, thereby reducing the effective inertia carried by Bottom Module primary rotation stage. In addition, this module ensures proper heating

and thermal stability of the fluids entering the upper section of the core-holder, the main injection course.

From a mechanical perspective, the main challenge is the compatibility between dynamic decoupling and kinematic tracking, as the Top Module must follow the longitudinal motion of the Bottom Module without introducing parasitic loads on the core-holder. The integration of the thermal core, electrical interfaces between static and rotating domains, and thermal insulation elements makes this module have similar complexities with the bottom one, enabling the use of standard components and assemblies, decreasing design and validation efforts.

3.3. Core-Holder Module

The Core-Holder Module constitutes the experimental core of the micro-station, enabling the controlled reproduction of pressure and temperature conditions representative of pre-salt reservoirs in porous rock samples. This module, shown in Figure 3, comprises the pressure vessel (core-holder), top and bottom interface manifolds, sensor manifold to support absolute and differential pressure transducers, heat exchangers and oven, and the mechanical decoupling system based on helical tubes.

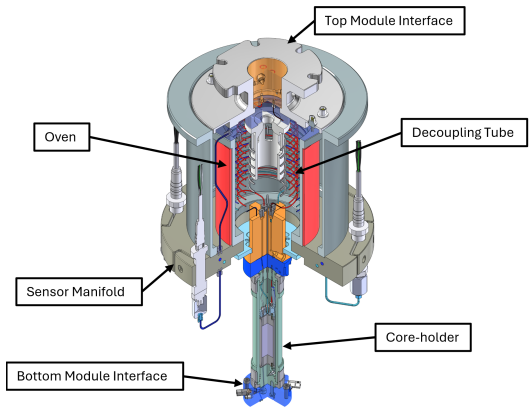

Figure 3. Core-Holder module global design with principal components highlighted.

The primary mechanical challenge is to ensure structural integrity, leak-tightness, and thermal stability under operating conditions (up to 1000 bar and 90 °C), while minimizing the transmission of mechanical loads and dynamic disturbances to the sample and bottom module during rotation. The design ensures high thermal spatial and temporal stability (±0.1 °C) around the sample, to avoid thermal induced flows that could mask the real phenomena. The use of helical pigtails and dedicated heat exchangers provides mechanical compliance and thermal conditioning, effectively decoupling the sensors mass from the sample rotating system and preserving tomographic image quality.

3.4. Accumulators Module

The Accumulators Module is designed to store and supply the fluids used in flow experiments under strictly controlled pressure and temperature conditions. Each accumulator is manufactured from titanium, typically has a volume of 500 ml and can operate independently, allowing different fluids to be used throughout the experimental sequence.

From mechanical and thermal engineering standpoints, the key challenges are individualized thermal control and operational safety. Each accumulator is therefore integrated into a dedicated heating enclosure equipped with thermal blankets, redundant temperature and pressure sensors, relief valves, and methane gas detection devices. The design ensures high thermal stability while maintaining safe-to-touch external surface temperatures, even during operation at 90 °C.

Also, due to the use of fluids with potentially flammable gases dissolved (like live oil with methane gas), the accumulator module requires dedicated exhaust systems. Active exhaust using a sensitive methane gas sensor and a high flow rate fan, ensures the safe removal of leaked or vented gases in confined environment of the oven, mitigating risks related to flammability and explosion.

3.5. Pump Cart

The Pump Cart is the control core of the injection experiment, being responsible for system pressurization, for controlling fluid injections and production during experiments. It integrates high-pressure, pulse-free pumps capable of operating in either pressure- or flow-controlled modes, automated valves, all communicating through a local double controller architecture.

The main challenge of this module lies in the integration of complex fluidic architectures, distributed thermal control and stringent safety requirements, as the Pump Cart also manages thermal control for the other subsystems of the station. A segregated control architecture, combining PLC-based control for pressure and flow with a dedicated FPGA-based system for temperature management, ensures deterministic behavior, data traceability, and operational robustness, which are critical for in-situ experiments under reservoir-representative conditions. More on this architecture will be presented in Section 4.

3.6. Auxiliar Sub-Systems

The auxiliary systems of the pre-salt micro-station include a set of transport carts designed to ensure safe handling, mobility, and operational continuity of the experimental infrastructure between laboratory facilities and the MOGNO beamline. These subsystems comprise the module transport cart and the core-holder transport cart, which together support the logistics, fluid management, and experimental readiness of the station.

A key design requirement common to all carts is the ability to preserve thermodynamic and mechanical integrity during transport. Following saturation, leak testing, and thermal conditioning in the laboratory, cooling and reheating cycles and pressure cycles are avoided to prevent fluid property variations and to reduce the likelihood of leakage during re-pressurization and reheating. For this reason, carts are conceived as active subsystems, incorporating temperature controllers, cooling circuits for thermal shields, and dedicated exhaust systems for safe handling of hazardous fluids.

The module transport cart enables the relocation of the top and bottom modules for maintenance, integration, and replacement activities, while providing adequate structural support and reproducible mechanical interfaces with the beamline and gantry.

The core-holder transport cart allows the complete sample assembly to be moved as a single unit, maintaining pressure and temperature throughout the transport path and eliminating the need for fluid reconditioning at the beamline. Although the integration of active thermal control and safety features increases system complexity, this approach significantly enhances operational robustness and beamtime efficiency once it minimizes the waiting time while X-ray beam is available.

4. Pre-salt Micro Station - Software Overview

To guarantee that all the capabilities designed into the mechanical modules previously described are easily available,

the software for the pre-salt station is re-modularized by experiment functionalities (sample positioning, injection, pressurization, heating) and beamline performance exigencies (Equipment Protection Systems - EPS, Personnel Protection Systems – PPS, data compatibility). These are to be provided through a series of Graphical User Interfaces (GUIs) and monitored by the laboratory interlock systems.

GUIs are hosted in the application layer and made based on views of the injection diagram for the gantry setup, partially presented in Figure 4. To try to guarantee all experiment parameters will be thoroughly set and reviewed by the beamline staff, separate GUIs will be made to control injection pressure, flow limits, heating and tomography configuration and startup. Also, during the injection experiment, all the parameters are displayed in a monitoring GUI, to allow for easy problem identification. All variables monitored through GUIs are to be implemented in the service layer as EPICs process variables (PVs), gathered directly from the controllers allocated into the Pump Cart and hutch. In case of inoffensive behaviors, such as slight temperature or pressure variations (deemed acceptable by the user), a series of pop ups with different alarms guide the user through the equipment control without needing to interrupt the experiment.

While the experiment is ongoing, high-speed data acquisition is performed in the service layer, to be later made available fully compiled and ready for post processing to the user.

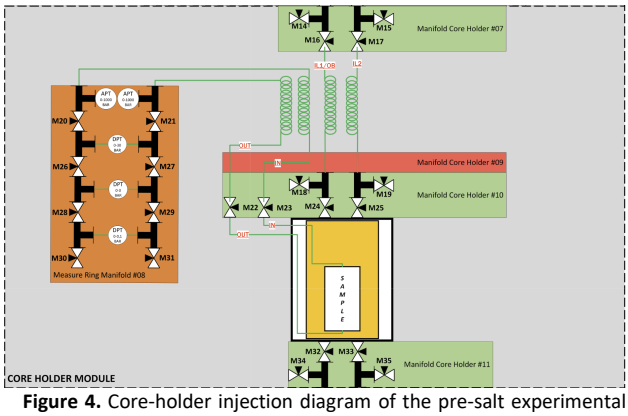

Figure 4. Core-holder injection diagram of the pre-salt experimental setup, with valves, manifolds, absolute pressure transducers (APT), differential pressure transducers (DPT) and sample.

In parallel, there is a complete equivalent system reproduced into the beamline safety interlock system, monitored by a central safety programmable logic controller (PLC). This works with direct signal readings in the device layer to guarantee fast and reliable response independently of network and third parties. The operation parameters and limits are defined to guarantee the wellbeing of humans (PPS) and integrity of the setup (EPS), disregarding experiment configuration. As the Pump Cart is designed to operate both in the beamline and the support laboratory, its internal PLC has a secondary safety monitor loop, which communicates with the main interlock PLC through Process Field Network (PROFINET) Protocol when operating outside the hutch.

All software is designed to work as stand alone, so the scientific users don't need to ponder beamline integrity and maintenance staff can monitor any equipment without needing for experiments to be performed.

5. Next Steps

The next development phase of the pre-salt micro-station focuses on the transition from detailed design to system-level integration, validation, and incremental commissioning. Ongoing activities include the completion of detailed mechanical designs, as shown in Figure 5, procurement of remaining custom components, and the assembly of individual modules, followed by subsystem-level verification and validation testing.

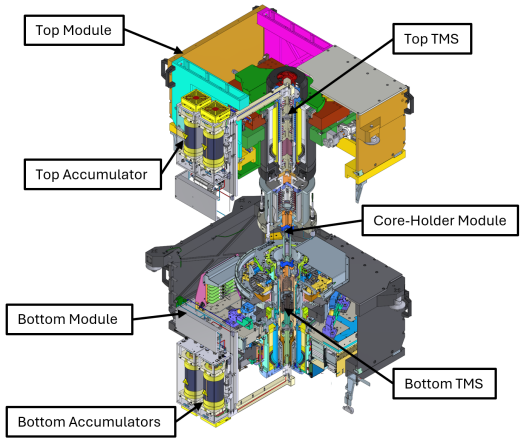

Figure 5. Global design of the beamline setup for micro station pre-salt.

A key priority is the progressive integration of mechanical, thermal, and fluidic subsystems, with particular emphasis on interfaces between static and rotating domains and on the validation of pressurized fluid handling under representative operating conditions. These activities will be supported by staged testing campaigns, initially conducted in laboratory environments and subsequently extended to beamline-compatible configurations.

In parallel, efforts will concentrate on the consolidation of operational workflows, including sample preparation, transport, system assembly, and experimental execution. This includes the refinement of procedures to ensure continuity of pressure and temperature conditions from laboratory preparation through in-situ synchrotron measurements, as well as the validation of safety and interlock strategies.

Finally, the system will undergo incremental commissioning, gradually increasing experimental complexity in terms of pressure, temperature, and fluid composition. This phased approach is intended to mitigate technical risks, validate system performance, and establish a robust experimental framework, ultimately enabling reliable in-situ tomography experiments under reservoir-representative conditions at the MOGNO beamline.

References

[1] Archilha N, Costa G, Ferreira G, Moreno G, Rocha A, Meyer B, Pinto A, Miqueles E, Cardoso B, Westfahl H, 2022 *J. Phys.: Conf. Ser.* **2380** 012123

[2] Archilha *et al.*, Mogno Beamline, the micro and nano tomography beamline at Sirius: early scientific outcomes and future installations 22 B-MRS meeting

[3] Ferreira T, Pires L, Reichardt K, 4D X-Ray Computed Tomography in Soil Science: An Overview and Future Perspectives at Mogno/Sirius. *Braz J Phys* **52**, 33

[4] Aghajanloo M, Jones S, Yan L, Voskov D, Farajzadeh, Evaluation of CO2 Hydrate Saturation in Porous Core Experiments Using Medical CT Images, *Energy & Fuels* ***38*** 12, 11037-11042

euspen's 26th International Conference & Exhibition, Krakow, PL, June 2026
www.euspen.eu

Dense Data Fusion and Uncertainty Quantification in Optical Metrology: The Dust3r++ Framework

Ladji Fofana[1, 2], Katarina Josic[1, 2], Louis-Ferdinand Lafon[1], Charyar Mehdi-Souzani[3], Nabil Anwer[2], Hichem Nouira[1]

[1] *Laboratoire national de métrologie et d'essais/Conservatoire national des arts et métiers, 1 Rue Gaston Boissier, 75015 Paris, France*
[2] *Université Paris-Saclay, ENS Paris-Saclay, LURPA, 91190, Gif-sur-Yvette, France*
[3] *Université Paris-Saclay, ENS Paris-Saclay, LURPA, Université Sorbonne Paris Nord, 91190, Gif-sur-Yvette, France*

ladji.fofana@lne.fr

Abstract

Dense data fusion has become a cornerstone of optical dimensional metrology, but the reliability of reconstructed 3D models is still obstructed by measurement noise, changing acquisition conditions, and the absence of systematic uncertainty evaluation. In this work, we present Dust3r++, a dense fusion framework that couples Optimal Transport (OT) with non-rigid warping to merge multi-view data in a stable and consistent manner. A distinctive feature of Dust3r++ is its uncertainty propagation strategy: uncertainties on fused correspondences are inferred from OT dual variables, warp parameter covariances are obtained from the Hessian of the fitting objective, and both are propagated locally to the reconstructed surface. This leads to dense 3D reconstructions enriched with spatially resolved confidence bounds, bringing the results in line with the principles of the GUM. Tests carried out on several industrial reference parts show that Dust3r++ delivers higher robustness and accuracy than state-of-the-art approaches, while also providing, for the first time, a practical framework for dense uncertainty quantification in image-based 3D inspection. The approach lays the groundwork for traceable and real-time optical metrology within Industry 4.0.

Keywords: Dense data fusion, Optimal Transport (OT), Non-rigid warping, 3D reconstruction, Optical dimensional metrology, Uncertainty propagation, GUM, Spatial confidence bounds, Industrial inspection, Industry 4.0

1. Introduction

Multi-view photogrammetry is increasingly used in dimensional metrology as a non-contact measurement technique for automated inspection in manufacturing [1]. By combining measurements acquired from multiple viewpoints, it allows the estimation of the geometry of complex mechanical parts with a high spatial sampling density [2], beyond what can be achieved from isolated point-cloud measurements. Such systems are well suited to in-line inspection scenarios in the context of Industry 4.0. In this work, we consider an experimental setup developed at LNE (Laboratoire National de Metrology et d'Essais) for stereo-based optical dimensional measurement. The acquisition system consists of an industrial robot ensuring repeatable positioning of a calibrated stereo rig for passive image acquisition, complemented by a structured-light sensor used for reference measurements (Figure 1).

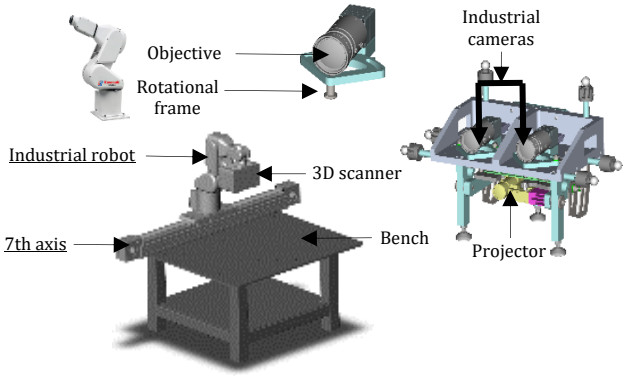

Figure 1. Structured light 3D stereovision scanning system

Despite recent progress, three limitations remain for metrological use [3]: (i) sensitivity to measurement noise and varying acquisition conditions, (ii) susceptibility to outliers and calibration errors in classical correspondence-based fusion [3], and (iii) the lack of uncertainty evaluation and propagation in dense reconstruction pipelines [2][10][11]. To overcome these limitations, this paper introduces Dust3r++, a dense data-fusion framework based on OT and non-rigid warping, providing reconstructed surfaces associated with spatially resolved measurement uncertainties in accordance with the GUM.

2. Dust3r++ dense fusion method

We propose a traceable dense data fusion and 3D reconstruction framework called Dust3r++, which has been developed by the authors and is currently being used by LNE for passive optical imaging. This research framework is not a commercial software product. It is designed to ensure reproducibility, reliability and metrological traceability of the multi-view reconstruction process.

2.1. Measurand definition

The measurand, in the sense of the Vocabulary of Metrology (VIM), is defined as the true surface geometry of the observed object [4], expressed in a common three-dimensional coordinate system. In this work, the geometry of the surface is represented by a dense collection of three-dimensional points,

reconstructed from several acquisitions. Therefore, the measurement process is to estimate this surface geometry from the observations derived from the image. In common photogrammetric frameworks, surface geometry is parametrically defined implicitly by dense point or depth estimates obtained from the corresponding images [5]. These quantities are related to the physical geometry by means of calibrated imaging models and are used for the reconstruction of a three-dimensional surface [6].

2.2. Optical Measurement model and input quantities

An optical measurement model implements a probabilistic estimation process by treating observed geometric values X and corresponding ideal geometric values Y as two random variables that are distributed according to an unknown data distribution [7]. Common state-of-the-art approaches use a pre-trained predictor like a vision transformer (ViT) as measurement model [8]. By considering a measurement model g that is obtained during the learning phase by minimising the empirical risk for a large image pairs dataset, g^* minimises the expected risk for the underlying data distribution. In a regression setting, uncertainty is represented by a Bayesian risk formulation [9]. The total uncertainty associated with the estimate at a given observation x is defined as the conditional expected squared error:

$$U_t(x) = E[(\hat{g}(X) - Y)^2 \mid X = x] \; (1) \; [10]$$

The data (average) uncertainty is related to the internal variability of the measurement process and given by $U_d(x) = E[(g^*(X) - Y)^2 \mid X = x]$. Since the optimal estimator satisfies $g^*(X) = E[Y \mid X]$, the data uncertainty is reduced to the conditional variance $Var[Y \mid X = x]$, which depends only on the measurement conditions. The model uncertainty is then defined as the difference $U_m(x) = U_t(x) - U_d(x)$ and reflects the imperfection of the pretrained measurement model with respect to the ideal estimator [13].

2.3. Estimation of the surface geometry

The estimation process is purely probabilistic [7] and is formulated by modelling the visual observations X and the corresponding geometric ideal Y as two randomly-distributed random variables. The pre-trained estimator $\hat{g}$ is obtained by minimising the empirical risk for the training set, while the ideal g^* minimises the Bayesian risk for the underlying dataset [9]. For dense image fusion, the overall uncertainty evaluation process from image acquisition to surface geometry definition is summarised in the optical measurement chain illustrated in (Figure 2).

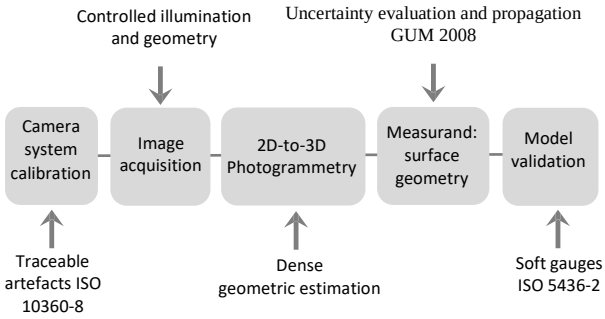

Figure 2. Optical Measurement Chain for Dense 3D Reconstruction with GUM-Based Uncertainty Propagation [11]

The reconstructed surface geometry constitutes the measurement result. In accordance with GUM, this result must be associated with an evaluated measurement uncertainty characterizing the dispersion of values that could reasonably be attributed to the measurand. As illustrated in (Figure 2), uncertainty evaluation and propagation are therefore an integral part of the measurement chain, enabling uncertainty-aware quantification of 3D dense reconstructions for dimensional inspection [10][11].

3. Dust3r++ dense fusion model

Dust3r++ is an extension of the Dust3r (Dense Unconstrained Stereo Reconstruction) [12] measurement model and estimation principles described in (section 2). The goal is to estimate a consistent representation of the geometry measurand from dense, multiple-view geometric observations, explicitly taking into account sources of uncertainty that arise during the fusion process. As shown in (Figure 3), Dust3r++ optimizes the pre-trained state-of-the-art dense image fusion model (Dust3r) with an OT based correspondence formulation that is also refined through non-rigid warping [13].

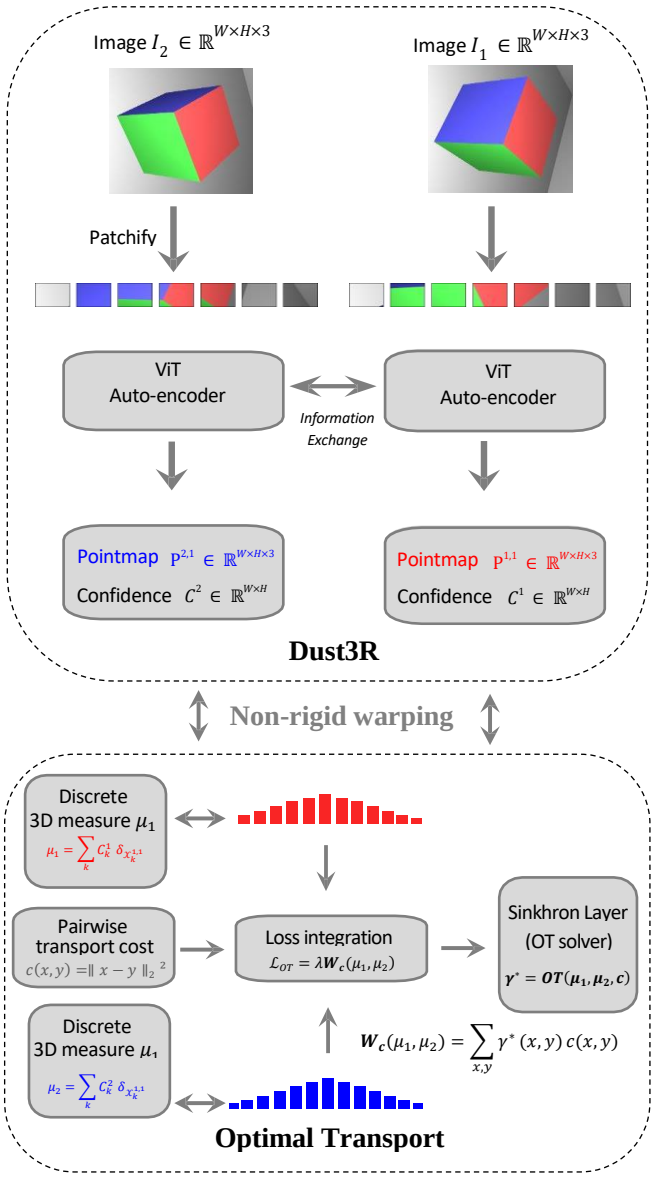

Figure 3. Dust3r++ Overview: Dust3r Features Coupled with Optimal Transport (Sinkhorn) Fusion

3.1. Optimal transport-based correspondences

For each view I, the pretrained dense image fusion model produces a dense point map P^i, and an associated confidence map $C^{i,k}$. Each view is represented by a discrete geometric measure defined by:

$$\mu_{\mathrm{i}} = \sum_k C_k^{\mathrm{i}}\ \delta_{\chi_k^{\mathrm{i,1}}} \quad (2)$$

where δ denotes the Dirac measure located at the estimated point positions. Dense multi-view fusion is formulated as the OT problem between these discrete measures. Given two views i and j, the transport cost between points $P^{i,k}$and $P^{j,k}$ is defined as the squared Euclidean distance $\left\|P^{i,k} - P^{j,k}\right\|^2$. The optimal transport plan γ^* is obtained by minimising the total transport costs under the marginal constraints imposed by μ_i and μ_j. This global formulation provides reliability for outliers and missing correspondences, as geometrically inconsistent points naturally have a low transport cost, without requiring an explicit exclusion of outliers. The OT formulation also gives rise to two variables related to the optimum solution. In Dust3r++, these two variables are interpreted as indicators of correspondence, which reflects the sensitivity of transport costs to changes in input measures. They are therefore the first source of uncertainty information associated with dense correspondences.

3.2. Non-rigid warping

Despite the global enforcement of correspondence by OT, residual geometrical differences remain due to measurement noise, calibration residuals and imperfections in the pre-trained fusion model [3]. We therefore use a non-dynamic warp model as a corrective mechanism in the estimation process. Let p_k denote a fused 3D point obtained after the OT step, and let $W(p_k;\ \theta)$ be a parametric warping function with parameters θ. The parameters θ are estimated by minimizing a least-squares objective of the form $\Sigma_{\mathrm{k}}\|W(p_k;\ \theta) - \bar{p}_k\|^2$, enforcing geometric consistency in a common reference frame. The uncertainty associated with the correction model is quantified by the covariance of the estimated parameters, given by $Cov(\theta) = H^{-1}(\theta^*)$, where H is the Hessian of the objective at the optimum value. This uncertainty is combined with correspondence-related uncertainty inferred from the OT formulation and propagated to the reconstructed surface geometry.

4. Uncertainty propagation to the reconstruction surface

The reconstructed surface geometry is the measurement result and associated with an evaluated measurement uncertainty in accordance with the GUM. We denote by $\hat{y}$ a given reconstructed surface point obtained from the fused correspondences and the non-rigid correction model. The uncertainty associated with $\hat{y}$ results from two contributions: the uncertainty on the dense correspondences obtained through the OT formulation, and the uncertainty on the estimated warp parameters θ. Uncertainty propagation is performed locally by linearizing the surface reconstruction model with respect to these quantities. Therefore, the covariance of the reconstructed surface point is expressed as:

$$Cov(\hat{y}) = J_p Cov(p) J_p^T + J\theta\ Cov(\theta) J\theta^T \quad (3)$$

where p represent the correspondence-related quantities, $Cov(p)$ represents their covariance inferred from the OT formulation, $Cov(\theta)$ is the covariance of the warp parameters obtained from the inverse Hessian of the fitting objective, and J_p and $J\theta$ are the corresponding Jacobians. This formulation yields a spatially resolved uncertainty associated with the surface geometry, corresponding to a model-based (Type A) uncertainty evaluation consistent with the GUM.

5. Experiment and validation

In this work, the experimental validation is conducted on 16 real-world automotive data measured on the LNE optical metrology test bench. These mechanical parts exhibit complex geometries, varying surface orientations, and limited texture. For clarity, a brake caliper is shown here as an example (Figure 4) illustrating the way we represent image pairs for multi-view data fusion.

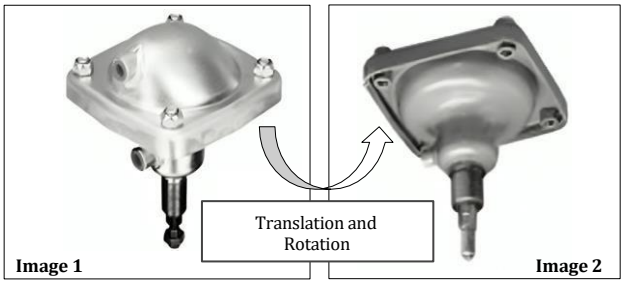

Figure 4. Image Pair Configuration for Dense Fusion of a Brake Caliper

5.1. Dense fusion performances

The robustness of dense fusion models is evaluated by using standard image fusion metrics (reprojection error RE, inlier ratio IR and F1-score). The RE quantifies the geometric consistency of the estimated correspondences, while the IR measures their reliability with respect to outliers and missing data. The two quantities are combined by their harmonic average to give the F1 score, which is a compact indicator of reconstruction accuracy.

Table 1 Dense Fusion Performance Metrics (RE, IR, Chamfer + deviations)

Algorithms	Mean inlier ratio $\bar{\tau}$ (%)	Mean reprojection error $\bar{e}$ (pixel)	Mean Chamfer distance $\bar{d} \pm \Delta\bar{d}$ (µm)
Dust3r++	**91**	**1.45**	$\mathbf{245.63 \pm 1.42}$
Dust3r [12]	88	1.50	287.57 ± 5.05
Mast3r [14]	86	1.50	344.89 ± 6.16
RoMa [15]	74	1.85	352.08 ± 10.68

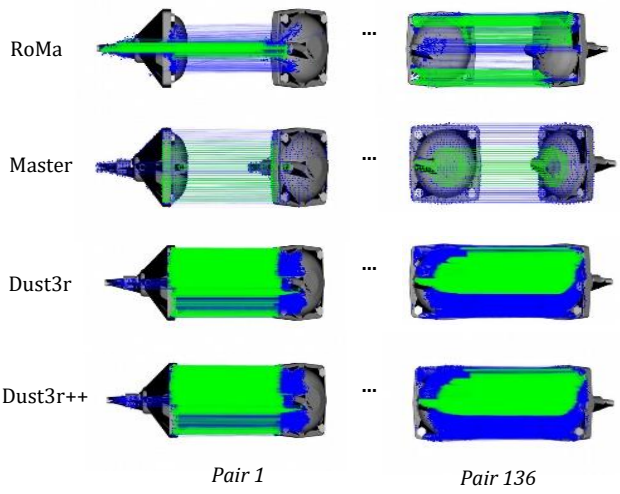

Figure 5. Dust3r++ vs State-of-the-Art Dense Matching on 136 pairs

Compared to state-of-the-art methods, our Dust3r++ method maintains stable reprojection errors and significantly higher inlier ratios across distant viewpoints, demonstrating improved robustness of the dense corfrespondence estimation. This robustness is consistent with the global OT formulation, which naturally downweights inconsistent correspondences instead of relying on hard rejection rules.

5.2. Dust3r++ vs 3D reconstruction benchmarks

Surface reconstruction errors on the brake caliper are evaluated against a traceable CMM reference (ZEISS CONTURA G2 7.10.6; 700 × 1000 × 600 mm³; MPE_E = 1.8 + L/300 µm, MPE_P = 1.8 µm, ISO 10360) [16]. Dust3r++ is compared with COLMAP, AliceVision and OpenMVG/MVS [17] under identical evaluation conditions. Results are reported in Table 2.

Table 2 Comparative reconstruction errors with respect to a CMM

Method	Mean Signed Dist $\bar{d}$(mm)	Mean Std Dev $\bar{\sigma}$(mm)
COLMAP	4,35	0,77
AliceVision	3,30	0,27
OpenMVG/MVS	3,29	0,80
Dust3r++	0,25	0,18
CMM (reference)	0	-

Dust3r++ achieves lower errors and reduced variability, and the reconstructed geometry is closer to the CMM reference, which indicates that it is suitable for dimensional metrology applications below 300 µm using optical systems with a dense image matching algorithm. Figure 6 shows the spatial distribution of signed point-to-surface deviations obtained with Dust3r++.

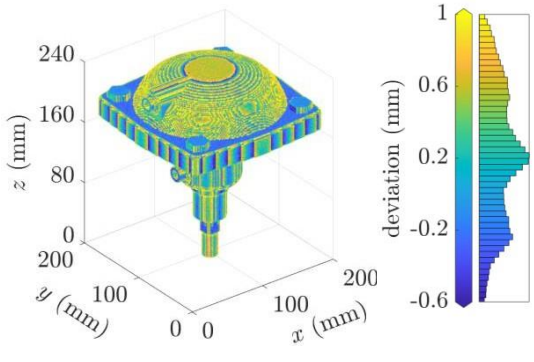

Figure 6. Dust3r++ Reconstruction Error Maps

6. Conclusion and perspectives

In this work, we introduced Dust3r++, a dense multi-view fusion framework with uncertainty-aware surface reconstruction. The proposed approach combines Optimal Transport-based correspondence estimation with a non-rigid warping model to allow a reliable reconstruction of complex industrial geometry, while explicitly propagating uncertainty to the geometry measurand in accordance with the GUM. Experimental validation on a real-world industrial part demonstrates high reconstruction accuracy and lower uncertainty values compared to state-of-the-art matching approaches and 3D reconstruction benchmarks, with a spatial distribution consistent with the observed reconstruction errors. The results contribute to bridging the gap between dense 3D reconstruction and traceable dimensional inspection. Future work will focus on addressing in-line implementation, real-time constraints and extending the dissemination of uncertainty to dimensional properties.

Acknowledgment

This work is part of the project 23IND08 DI-Vision, which has received funding from the European Partnership on Metrology, co-financed from the European Union's Horizon Europe Research and Innovation Programme and by the Participating States.

References

[1] Alberto Mendikute, José Yagüe-Fabra, Mikel Zatarain, Álvaro Bertelsen, and Ibai Leizea. Self-calibrated in-process photogrammetry for large raw part measurement and alignment before machining. Sensors, 17:2066, 09 2017. doi: 10.3390/s17092066.

[2] Shuai Liu, Mengmeng Yang, Tingyan Xing, and Ran Yang. A survey of 3d reconstruction: The evolution from multi-view geometry to nerf and 3dgs. Sensors, 25:5748, 09 2025. doi: 10.3390/s25185748.

[3] Young Kim, Christian Theobalt, James Diebel, J. Kosecka, Branislav Micusik, and Sebastian Thrun. Multi-view image and tof sensor fusion for dense 3d reconstruction. pages 1542 - 1549, 11 2009. doi: 10.1109/ICCVW.2009.5457430.

[4] Philip Potts. Glossary of analytical and metrological terms from the international vocabulary of metrology (2008). Geostandards and Geoanalytical Research, 36, 09 2012. doi: 10.1111/j.1751-908X.2011.00122.x.

[5] Yangming Lee. Three-dimensional dense reconstruction: A review of algorithms and datasets. Sensors, 24:5861, 09 2024. doi: 10.3390/s24185861.

[6] Michael A., Jean-José Orteu, and Hubert Schreier. Volumetric Digital Image Correlation (VDIC), pages 1-16. 02 2009. ISBN 978-0-387-78746-6. doi: 10.1007/978-0-387-78747-38.

[7] Wojciech Toczek and Janusz Smulko. Risk analysis by a probabilistic model of the measurement process. Sensors, 21:2053, 03 2021. doi: 10.3390/s21062053.

[8] Ruiming Jia, Xin Chen, Jiali Cui, and Zhenghui Hu. Mvs-t: A coarse-to-fine multi-view stereo network with transformer for low-resolution images 3d reconstruction. Sensors, 22:7659, 10 2022. doi: 10.3390/s22197659.

[9] Harvey Mitchell. Bayesian Decision Theory, pages 311-331. 11 2025. ISBN 978-3-662-71022-7. doi: 10.1007/978-3-662-71023-414.

[10] Eyke Hüllermeier and Willem Waegeman. Aleatoric and epistemic uncertainty in machine learning: an introduction to concepts and methods. Machine Learning, 110, 03 2021. doi: 10.1007/s10994-021-05946-3

[11] Miroslaw Wojtyla and Wojciech Plowucha. Measurement models - theory and practice of uncertainty evaluation of geometrical deviation measurements. Metrology and Measurement Systems, pages 1-21, 11 2025. doi: 10.24425/mms.2025.154671

[12] Wei Zhang, Yihang Wu, Songhua Li, Wenjie Ma, Xin Ma, Qiang Li, and Qi Wang. Review of feed-forward 3d reconstruction: From dust3r to vggt, 07 2025.

[13] Zhengyu Su, yalin wang, Rui Shi, Wei Zeng, Jian Sun, Feng Luo, and Xianfeng Gu. Optimal mass transport for shape matching and comparison. IEEE Transactions on Pattern Analysis and Machine Intelligence, 37, 11 2015. doi: 10.1109/TPAMI.2015.2408346.

[14] Vincent Leroy, Yohann Cabon, and Jerome Revaud. Grounding image matching in 3d with mast3r, 06 2024.

[15] Johan Edstedt, Qiyu Sun, Georg Bökman, Mårten Wadenbäck, and Michael Felsberg. Roma: Revisiting robust losses for dense feature matching, 05 2023.

[16] R. Koteras, M. Wieczorowski, P. Znaniecki, Acceptance and reverification of cmm in industrial conditions, Advances in Science and Technology Research Journal 12 (2018) 80–88. doi:10.12913/22998624/80987.

[17] E. Stathopoulou, M. Welponer, F. Remondino, Open-source image-based 3d reconstruction pipelines: Review, comparison and evaluation, The International Archives of the Photogrammetry, Remote Sensing and Spatial Information Sciences XLII-2/W17 (2019) 331–338. doi:10.5194/isprs-archives-XLII-2-W17-331-2019.

euspen's 26th International Conference & Exhibition, Krakow, PL, June 2026
www.euspen.eu

Internal Quality Optimisation of Material Extrusion Additive Manufacturing via Computer Vision-Enhanced Layerwise Surface Topography Measurement

Kexin Yin*[1], Yuchu Qin[1], Shan Lou[1], Paul Scott[1], Xiangqian Jiang [1]

[1] *EPSRC Future Advanced Metrology Hub for Sustainable Manufacturing, University of Huddersfield, Huddersfield, United Kingdom, HD1 3DH*

Kexin.yin@hud.ac.uk

Abstract

In-situ quality assurance has become a critical industrial imperative for material extrusion additive manufacturing to guarantee the overall internal quality. However, existing real-time monitoring techniques largely fail to dynamically bridge accessible 2D surface metrology with complex 3D internal structural integrity during the continuous fabrication process. This research proposes a novel closed-loop optimisation framework that integrates a novel ordinal CNN for layerwise Sa and Sdr prediction related to porosity, achieving a Sa prediction RMSE of 2.88(±0.23) and a Sdr prediction RMSE of 4.95(±0.81), and a Gaussian Process Regression controller to dynamically regulate extrusion temperature and velocity against cumulative thermal drift. The framework's overall closed-loop efficacy was verified through physical cross-sectional morphological analyses and an implicit neural network-driven surface simulation, showing autonomous disturbance rejection and self-healing, reducing internal porosity from over 2.0% to below 0.7%.

Keywords

Computer Vision, Artificial Intelligence, In-process Measurement, Optimisation,Additive Manufacturing

1. Background

Despite material extrusion additive manufacturing's widespread application across aerospace, automotive, and biomedical sectors, ensuring overall consistent part quality remains a pressing concern. The fundamental layer-by-layer fabrication of AM leads to defects from heat and conjunctions. Because these defects are often hidden within the structure, the lack of robust, internal quality monitoring remains a major pain point, limiting AM's full adoption in high-stakes manufacturing.

To mitigate these inherent defects, extensive research over the past decade has predominantly focused on the offline optimisation of process parameters. For instance, Rayegani and Onwubolu [1] utilised the group method for data handling to successfully predict and optimise the complex relationship between printing parameters and tensile strength. Addressing surface quality, Abouzaid et al. [2] modelled how temperature variations critically impact the mechanical performance, roughness, and porosity of resulting composite products. While these offline optimisation strategies have laid a solid foundation, they operate under the assumption of static printing conditions and fail to account for dynamic disturbance.

To overcome the limitations of static offline settings, online detection technologies have progressed rapidly in recent years. Kandananond [3] used artificial neural networks and the Box–Behnken method to improve the prediction accuracy of surface roughness in FFF parts based on process parameters. Similarly, Muhammad et al. [4] proposed a deep neural network for predicting Sa roughness in LPBF-built aluminium alloys, achieving high accuracy compared with experimental measurements. In addition, Toorandaz et al. [5] integrated in-situ photodiode sensing with machine learning models such as Random Forest, successfully predicting surface roughness in real time. However, merely identifying defects as they occur is insufficient if the manufacturing system cannot autonomously correct them.

A critical gap persists in effectively bridging the transition from passive online monitoring to active, closed-loop parameter optimisation. To address it, this study proposes a novel closed-loop control framework that integrates real-time surface quality monitoring with a dynamic parameter optimisation algorithm. By establishing a direct correlation between 2D surface morphology and 3D internal defects, this research aims to actively suppress porosity during the printing process.

The primary contributions of this paper are as follows. (1) the development of a rapid, non-destructive online detection method for surface roughness utilizing industrial machine vision; (2) the implementation of a time-varying optimisation GPR model for macroscopic feedforward prediction and a P control strategy for microscopic feedback adjustment; and (3) the proposition of a process-driven digital twin model based on virtual stacking, which effectively maps real-time surface parameters to internal porosity evaluation.

2. Methodology

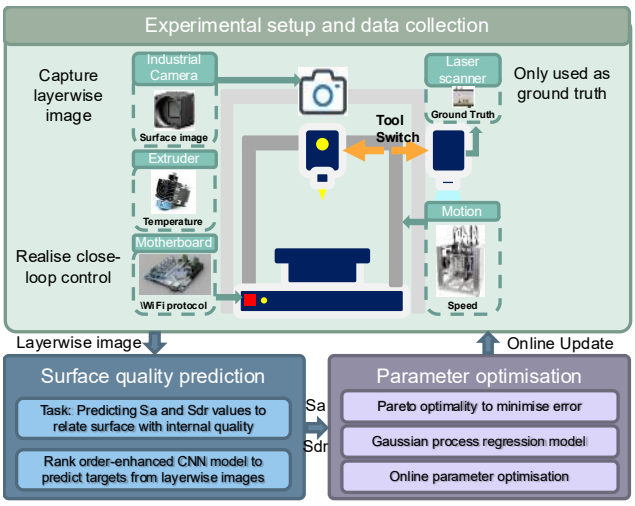

Figure 1. Overview of the workflow

As illustrated in Figure 1, the closed-loop framework is implemented on a Wi-Fi-enabled, 3-axis FDM printer within a stably illuminated chamber. The continuous control cycle initiates immediately post-deposition: a mounted XIMEA camera captures a high-resolution surface image, which is processed by a CNN model to predict surface roughness (Sa) and developed interfacial area ratio (Sdr). Subsequently, a Gaussian Process Regression (GPR) model determines the optimal extrusion temperature (190°C–240°C) and printing speed (40mm/s-150mm/s) for the next layer, actively compensating for cumulative thermal drift while maintaining efficiency. These optimised parameters instantly update the local G-code via Wi-Fi for the subsequent execution. While a scanCONTROL laser scanner was employed exclusively during model development to establish ground-truth point clouds, it was omitted during actual fabrication. Although porosity may be less problematic in large FDM components due to non-solid interiors, it is meaningful to conduct such cheap experiments to prove the feasibility and later transfer the knowledge to metal additive manufacturing. The dataset contains 3130 samples out of 21 30mm height blocks, with 2190 for training and 940 for testing.

2.1. Layerwise surface quality prediction model

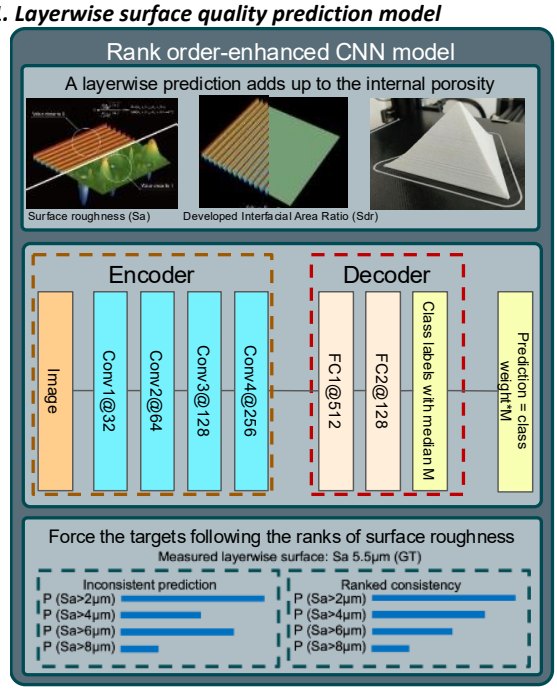

Figure 2. Rank-ordered layerwise prediction model

As shown in Figure 2, Sa and Sdr are selected as the core indicators of layerwise surface quality and are further related to interior porosity. Sa quantifies the average deviation of the surface from a mean plane, providing a measure of surface smoothness. In the context of 3D printing, the smoothness of each layer directly influences the subsequent deposition process. Sdr measures the percentage increase in actual surface area relative to an ideal reference plane and therefore reflects the structural complexity generated by peaks and valleys that form along the extrusion path. In extrusion-based printing, anisotropic surface textures naturally appear due to line-by-line deposition at alternating angles. When Sdr is high, meaning the peaks are tall and the valleys are deep, insufficient material flow or suboptimal filling may leave unfilled gaps within the valleys, forming pores [6]. The accumulation of such voids across multiple layers increases the internal porosity of the component, which directly affects the mechanical and functional performance of the final part.

The proposed layerwise surface quality prediction network adopts a lightweight CNN architecture rather than a deep SOTA model due to limited samples with simple stripe-like textures to avoid overfitting. The classification decoder branch performs coarse classification of each printing layer into six ordered categories [7] defined by K-means clustering of Sa values. The model learns a sequence of binary decisions of the form “Is the surface quality at least Level k?”. Each decision is made by a shared-weight structure that reuses the same feature representation $a_{1...n}$ and applies a series of linear classifiers W1...n to predict the probability y>k. The predicted class is determined by the highest k for which the answer remains true. The final layers of the classification branch are designed as shown in Figure 3. The final numerical result is obtained by the sum of the products of its classification probability and the statistical median of the corresponding category. The loss function CORAL [8] constrains the predicted logits so that class decision boundaries remain monotonic; that is, the logit corresponding to level k+1 must not exceed that of level k, defined as:

$$L_{cls} = -\sum_{i=1}^{N}\sum_{k=1}^{K-1}\left(t_{i,k}\cdot\log\left(\sigma(g_{i,k})\right) + \left(1-t_{i,k}\right)\cdot\log\left(1-\sigma(g_{i,k})\right)\right) \quad (1)$$

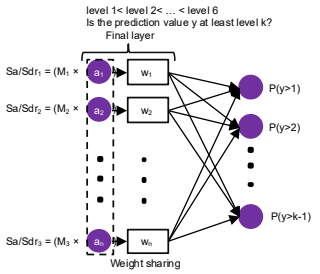

Figure 3. The final layers of the Rank-ordered CNN

2.2. Optimisation Strategy

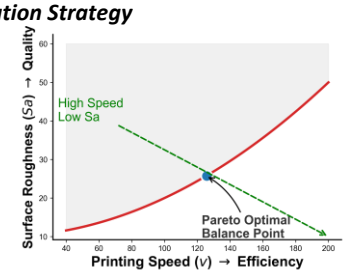

Figure 4. Trade-off explanation between quality and efficiency

The primary objective of the proposed online optimisation model is to accurately control the Sa and developed interfacial area ratio Sdr of the current printing layer by dynamically adjusting the extrusion temperature and printing speed. To achieve this, a comprehensive multi-objective target function, denoted as $J(X_{n+1})$, is formulated for subsequent layers, evaluated by minimising the squared error.

A fundamental challenge addressed by the optimisation is the inherent physical trade-off between manufacturing efficiency and surface quality. As shown in Figure 4, increasing the printing speed v to improve efficiency tends to a higher Sa value. To prevent the algorithm from selecting impractically slow speeds in pursuit of perfect smoothness, an efficiency dependency term, 1/v, is integrated into the target function.

In addition to efficiency, the optimisation model must explicitly compensate for the non-linear thermal accumulation that progressively occurs across successive printed layers. As shown in the thermal drift comparison chart, the actual thermal state of the printed part tends to saturate over time, diverging significantly from a theoretical linear hypothesis. To counteract this phenomenon, a temporally dependent drift compensation function, Φ(n), is embedded.

$$J(X_{n+1}) = \omega_1 \cdot \left(R_{pred} - R_{target}\right)^2 + \omega_2 \cdot \frac{1}{v} + \Phi(n) \quad (2)$$

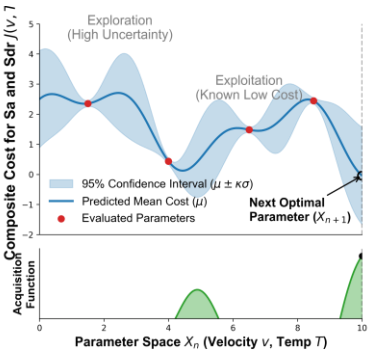

Figure 5. GPR model theorem

To solve the multi-objective target function, a GPR [10] model is employed as the primary optimisation engine. Unlike traditional deterministic algorithms, GPR utilises a non-parametric Bayesian inference approach to output both a predicted mean μ and a 95% confidence interval μ ± σ. This ability to explicitly quantify predictive uncertainty is essential for the FDM process, where layer-wise thermal fluctuations introduce inevitable environmental noise. Guided by these probabilistic outputs, an Upper Confidence Bound (UCB) acquisition function is applied to determine the next optimal parameter, denoted as x_{n+1}. The UCB mathematically drives the search process by strictly balancing 'exploitation' of regions with a known low cost against the 'exploration' of unmapped parameters exhibiting high uncertainty.

$$x_{n+1} = \arg\min_{x} \mu(x) + \kappa \cdot \sigma(x) \quad (3)$$

The underlying smoothness of this GPR model is governed by the Squared Exponential (SE) kernel. This specific kernel is selected because its infinitely differentiable nature aligns perfectly with the gradual, continuous thermal transitions inherent to 3D printing. Modulated by a length scale l and variance σ^2, the SE kernel operates on the physical assumption that operational parameters situated closer together in the input space share maximum correlation, shown as:

$$k(x, x') = \sigma_f^2 \exp\left(-\frac{|x - x'|^2}{2l^2}\right) \quad (4)$$

To actualise dynamic, layer-by-layer execution, a Proportional (P) feedback controller is integrated into the final stage of the online parameter optimisation. While the GPR model already mathematically anticipates temporal thermal drift, the addition of P-control constitutes a complementary necessity rather than a repetition. The GPR function remains inherently vulnerable to unmodelled stochastic disturbances, such as material or ambient temperature shifts. Therefore, the P-control, formulated as $u_{n+1} = f(X_n) + K_p \times$ error, acts as a microscopic corrective mechanism that strictly compensates for immediate, real-time residual errors.

2.3. Process-driven Surface Generator

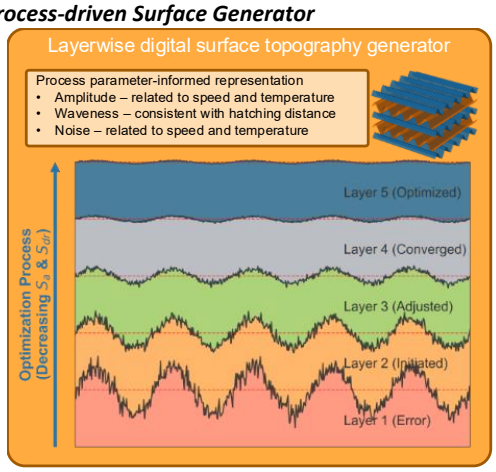

Figure 6. The workflow of the Virtual Metrology

As shown in Figure 6, The digital top surface generation is governed by an MLP designed for implicit morphological prediction. To accurately capture the physical layer-to-layer geometric inheritance the network takes a four-dimensional input vector: the current printing speed v and temperature T, and the preceding layer's quality (Sa_{n-1} and Sdr_{n-1}). The model predicts the topographical amplitude (A) and stochastic noise (σ). Subsequently, these predicted modifiers are injected into the parametric surface generator to digitally reconstruct the 3D point cloud of the current layer. Finally, the simulated Sa_n and Sdr_n are calculated from this generated point cloud for verification. This virtual surface generation is not conducted as a series of isolated, independent single-layer simulations, but rather as a continuously correlated progression with the online optimisation algorithm feedback to improve the v and T. The cross-hatching strategy is used, where each subsequent layer is deposited perpendicularly to the current one.

3. Result

3.1. Layerwise Prediction Performance

From Table 1, the classification-based approach (Base2 + CE) demonstrates a measurable improvement over plain direct regression (Base1). This confirms that initially mapping samples into discrete, ordered quality bands before converting them to numeric values presents an easier learning objective than full-range continuous regression. Furthermore, integrating the CORAL loss function into the classification framework yields the most significant enhancements. Our configuration achieves the highest overall accuracy with the largest std reduction, proving CORAL-enhanced model is not only more accurate but also robust to random initialisation or varying dataset splits.

Table 1 Result comparison of layerwise quality prediction

Model Configuration	Avg RMSE for Sa (Std)	Avg MAE for Sa (Std)	Avg RMSE for Sdr (Std)	Avg MAE for Sdr (Std)
Direct regression [9]	3.71 (0.76)	2.5 (0.23)	6.09 (1.16)	3.84 (0.50)
Classification to value [7] + CE	3.44 (0.65)	2.3 (0.15)	5.90 (1.18)	3.78 (0.41)
Ours	2.88 (0.23)	1.81 (0.05)	4.95 (0.81)	3.05 (0.24)

3.2. Optimisation Model Performance

Table 2 quantitatively evaluates the dynamic performance and stability of the proposed online optimisation strategy. To assess the fundamental accuracy of the surrogate model, Predictive R^2 and Prediction Interval Coverage Probability (PICP) are utilised. The proposed method demonstrates superior prediction accuracy and highly reliable uncertainty quantification compared to the standard GPR model without thermal considerations. Further, the long-term robustness against thermal accumulation is strictly evaluated using the Steady-State Error and the Integral Time Absolute Error (ITAE) score, a metric that heavily penalises uncorrected drifting errors as the printing time increases. While the fixed-parameter baseline completely fails to converge due to severe thermal drift, the proposed method drastically reduces the steady-state error to just 0.21 μm and the ITAE score to 85.3.

Table 2 Result comparison of optimisation modelling

Optimisation Strategy	Predictive R2	Predictive PICP (%)	Steady-State Error (μm)	ITAE Score
Baseline (linear Params) [11]	-	-	3.42 (Drifting)	1450.2
GPR (Without thermal factor) [10]	0.85	82.10%	1.15	420.5
Ours	0.94	94.80%	0.21	85.3

3.3. Internal Quality Verification and Virtual Metrology Results

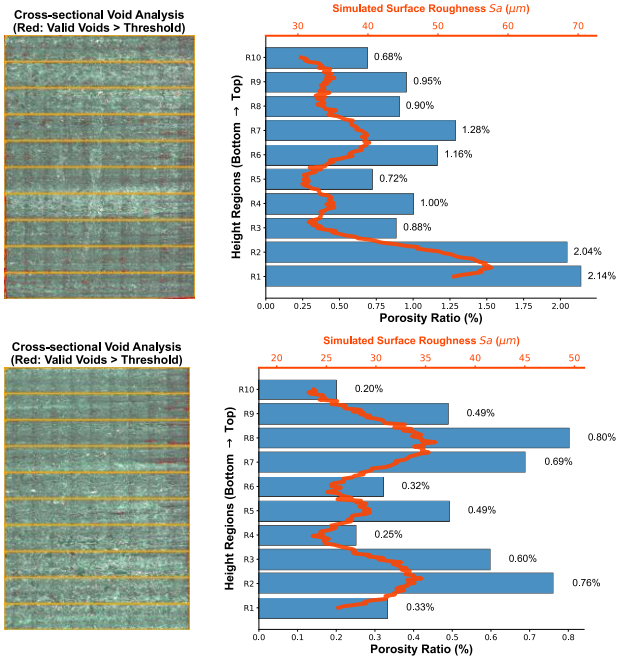

Figure 7. Porosity analysis of the cross-section with dynamically simulated surface quality results – poor start (up) and vibration (down)

To quantitatively evaluate the layer-wise efficacy of the proposed closed-loop framework, two morphological cases were performed on the optical cross-sections of 30 mm height specimens cut along their diagonal [12], which are uniformly segmented into 10 rectangular regions. Following image binarisation and area thresholding to exclusively isolate valid macroscopic voids marked in red, the localised porosity ratio for each region was calculated to track the bottom-to-top evolution of internal structural quality.

As shown in Figure 7, in the first case, a print initiated with severely suboptimal parameters (190°C, 150 mm/s) exhibited significant foundational defects, marked by a 2.14% porosity in R1. However, the surface quality prediction and GPR models iteratively corrected these errors, steadily suppressing defect formation and driving the porosity down to a negligible 0.68% by R10. In the second case, a stable print commencing with optimal parameters (yielding 0.33% initial porosity) was deliberately subjected to sudden temperature and speed disturbances. Although these anomalies caused temporary porosity spikes (peaking at 0.80% around R8), the online system immediately detected the surface degradation and enforced compensatory parameters, rapidly recovering the internal density to a 0.20% porosity by the final layer. Together, these results demonstrate the system's exceptional capability to both autonomously rescue a failing print and dynamically self-heal against unpredictable manufacturing deviations.

The digital top surface generation was governed by empirical mappings from the previous layer quality and current control parameters. As depicted in the simulation results, the digital trajectories closely mirror the physical cross-sections. As shown in orange in Figure 7, in Case 1, the model demonstrates rapid algorithmic convergence, aggressively reducing an initially severe roughness (Sa≈50μm) down to a stable optimum (Sa≈20μm). Conversely, Case 2 clearly illustrates the framework's robust disturbance rejection, where two artificially induced spikes in roughness (Sa≈40μm) are swiftly detected and autonomously suppressed back to the baseline, confirming the optimisation algorithm's stability.

4. *Conclusion and Future Work*

To address the challenge of in-situ quality assurance in FDM 3D printing, this research proposes a closed-loop optimisation framework that bridges 2D surface metrology with 3D internal structural integrity. The system integrates a CORAL-enhanced CNN, achieving a Sa prediction RMSE of 2.88(±0.23) and a Sdr prediction RMSE of 4.95(±0.81), by preserving ordinal data relationships, and a GPR controller optimise extrusion temperature and velocity against cumulative thermal drift dynamically. The framework's efficacy was strictly verified through physical cross-sectional morphological analysis and an implicit neural network-driven virtual stacking simulation. The framework's efficacy was verified through physical cross-sectional morphological analysis and an implicit neural network-driven virtual stacking simulation. Results demonstrated the system's capability in autonomous self-healing and disturbance rejection, suppressing inter-layer defects within 15 layers and reducing internal porosity from over 2.0% to below 0.7%.

Future research will focus on non-destructive X-ray Computed Tomography (XCT) verification and comprehensive inter-layer coupling simulation towards a digital twin.

Acknowledgement

The authors gratefully acknowledge the support of EPSRC funding EP/P006930/1, EP/S000453/1. Thanks for the help from Darragh Broadbent, Weidong Liu, and other colleagues.

References

[1] F. Rayegani and G. C. Onwubolu, The International Journal of Advanced Manufacturing Technology, vol. 73, no. 1–4, pp. 509–519, Apr. 2014, doi: https://doi.org/10.1007/s00170-014-5835-2.

[2] K. Abouzaid, D. Bassir, S. Guessasma, and H. Yue, Mechanics of Composite Materials, vol. 56, no. 6, pp. 805–816, Jan. 2021, doi: https://doi.org/10.1007/s11029-021-09925-6.

[3] K. Kandananond, International Journal of Metrology and Quality Engineering, vol. 12, pp. 17–17, Jan. 2021, doi: https://doi.org/10.1051/ijmqe/2021014.

[4] W. Muhammad, J. Kang, O. Ibragimova, and Kaan Inal, Welding in the World, vol. 67, no. 4, pp. 897–921, Dec. 2022, doi: https://doi.org/10.1007/s40194-022-01445-8.

[5] S. Toorandaz, K. Taherkhani, F. Liravi, and E. Toyserkani, "A novel machine learning-based approach for in-situ surface roughness prediction in laser powder-bed fusion," Additive Manufacturing, vol. 91, p. 104354, Jul. 2024, doi: https://doi.org/10.1016/j.addma.2024.104354.

[6] L. Hu et al., Virtual and Physical Prototyping, Aug. 2025, doi: https://doi.org/10.1080/17452759.2025.2541829.

[7] A. Valikhani, A. Jaberi Jahromi, S. Pouyanfar, I. M. Mantawy, and A. Azizinamini, "Machine learning and image processing approaches for estimating concrete surface roughness using basic cameras," Computer-Aided Civil and Infrastructure Engineering, Aug. 2020, doi: https://doi.org/10.1111/mice.12605.

[8] W. Cao, V. Mirjalili, and S. Raschka, "Rank consistent ordinal regression for neural networks with application to age estimation," Pattern Recognition Letters, vol. 140, pp. 325–331, Dec. 2020, doi: https://doi.org/10.1016/j.patrec.2020.11.008.

[9] F. Jáñez-Martino, E. Fidalgo, S. Martínez-Pellitero, S. Giganto, and E. Alegre, International Journal of Computer Integrated Manufacturing, pp. 1–12, Apr. 2025, doi: https://doi.org/10.1080/0951192x.2025.2498081.

[10] S. H. Lee, Metals, vol. 10, no. 4, p. 461, Apr. 2020, doi: https://doi.org/10.3390/met10040461.

[11] R. Anitha, S. Arunachalam, and P. Radhakrishnan, "Critical parameters influencing the quality of prototypes in fused deposition modelling," Journal of Materials Processing Technology, vol. 118, no. 1–3, pp. 385–388, Dec. 2001, doi: https://doi.org/10.1016/s0924-0136(01)00980-3.

[12] Y. Tao et al., Journal of Materials Research and Technology, vol. 15, pp. 4860–4879, Nov. 2021, doi: https://doi.org/10.1016/j.jmrt.2021.10.108.

euspen's 26th International Conference & Exhibition, Krakow, PL, June 2026
www.euspen.eu

Verification of a Next Generation γ-Ray Spectrometer Mechanical Requirements: Gamma-Ray Energy Tracking Array

Eric S. Buice, Collin Anderson, Heather L. Crawford, and Paul Fallon

Lawrence Berkeley National Laboratory, Berkeley, California 94720 USA

esbuice@lbl.gov

Abstract
The Gamma-Ray Energy Tracking Array (GRETA) is a next-generation γ-ray spectrometer designed to support nuclear structure and nuclear astrophysics research. Initially installed at Lawrence Berkeley National Laboratory (LBNL), GRETA will provide 4π sr angular coverage of the target region with high-purity germanium (HPGe) crystals capable of reconstructing the energy and three-dimensional position of γ-ray interactions. This paper presents the mechanical verification results of GRETA. These results pave the way for the full implementation of GRETA at the Facility for Rare Isotope Beams (FRIB) at Michigan State University.

Keywords: γ-ray spectrometer, requirements verification, integrated testing

1. Introduction

The Gamma-Ray Energy Tracking Array (GRETA) is a next-generation γ-ray spectrometer that builds on the prior arrays Gammasphere [1] and GRETINA [2] to guide its development in support of nuclear-structure and nuclear-astrophysics programs at the Facility for Rare Isotope Beams (FRIB) at Michigan State University. GRETA aims to provide high-efficiency detection with 4π sr coverage in nuclear reactions and to reconstruct the energy and position of γ-ray interactions. To support these programs, GRETA must provide accurate knowledge of the location of each Quad Detector Module (QDM) in 3D space and ensure stable operation of all detector units. Accordingly, the high-level mechanical requirements of GRETA are listed in Table 1. The mechanical design of GRETA was described by Buice et al. [4]. A brief introduction to the mechanical design is provided here. The remainder of this paper focuses on the detailed verification of QDM positions performed at Lawrence Berkeley National Laboratory (LBNL) prior to shipment to FRIB.

Table 1. High-level GRETA system requirements.

Requirement	Value
Number of QDMs support	30 (15 per hemisphere)
Position of QDM	≤ 0.40 mm (x, y, z)
Linear translation	≥ 500 mm
Rotation	±180 degree
LN temperature at QDM dewar	≤ 80 K
Temperature stability of QDM pre-amplifier	± 2 °C
Temperature stability of QDM external electronics (digitizer)	± 2 °C

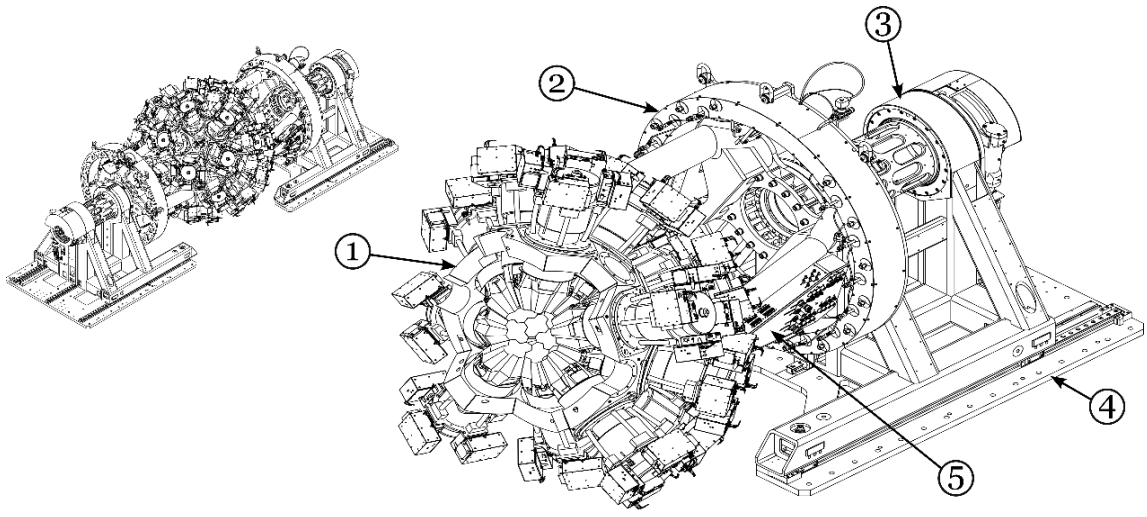

Figure 1. GRETA Assembly. Upper left corner shows the complete assembly with both hemispheres in the closed position. 1. Hemisphere with 15 QDMs installed. 2. Liquid Nitrogen. 3. Support structure with rotary drive. 4. Baseplate with linear drive. 5. Digital IO and glycol cooling enclosure.

2. Mechanical Design Overview

The GRETA mechanical system is illustrated in Figure 1. It is divided into two nearly identical hemispheres that position 30 Quad Detector Modules (QDMs)—15 per hemisphere—to provide 4π sr coverage about a central target position. GRETA comprises four functional elements: (i) a hemispherical mounting structure for the QDMs; (ii) a support frame with ±180° rotation to facilitate QDM insertion and removal; (iii) a base plate with a 500 mm linear translation stage to access the target chamber at the centre of the hemisphere; and (iv) liquid nitrogen and glycol cooling systems to condition the QDMs and associated electronics. Functional elements (i)–(iii) control the final QDM positions and must satisfy the Table 1 requirement of ≤ 0.40 mm in position error. The final QDM positions are critical only in the closed position; consequently, linear and rotational errors are not a primary concern, reducing the apparent complexity of the mechanical design.

2.1 Breakdown of QDM Position Requirement

The QDM position requirement from Table 1 can be further disseminated and can be viewed in Table 2. The first three items pertain to the hemisphere port locations, while the last two pertain to the support frame.

Table 2. Dissemination of the position of the QDM requirement from Table 1.

Requirement	Estimated Error
QDM Port Location (Hemisphere)	± 0.19 mm
QDM Interface Plate Pin	± 0.18 mm
QDM Triplet and Doublet Position Error	± 0.10 mm
Position Error of Support Structure	± 0.10 mm
Support Frame Deformation	± 0.26 mm
Total (Root Sum Square, RSS)	**± 0.40 mm**

2.2 Hemisphere Design – QDM Port

The hemisphere and the QDM are depicted in Figure 2. Each hemisphere comprises three segments, hosting a total of 15 QDM ports. The three segments are referred to as the main body, the doublet, and the triplet sections. To accommodate different experimental configurations, it may be necessary to remove the doublet and triplet sections to provide greater access to the hemisphere centre. The estimated error associated with removing and reinstalling the doublet and triplet is ±0.10 mm.

The QDM position is specified by two items. The first is the hemisphere port location, including the doublet and triplet sections, with an estimated error of ±0.19 mm. Each QDM port is defined on the manufacturing drawing by a surface-profile tolerance of ±0.19 mm, accounting for the QDM port location relative to the hemisphere centre in position (x, y, z), orientation, and flatness. To capture the QDM position during installation, press-fit round and diamond pins are used on each QDM flange. This is defined as a manufacturing tolerance with a positional error of ±0.18 mm. The QDM flange pins interface directly with the QDM interface plate, which has an estimated positioning error of less than ±0.05 mm relative to the QDM end cap. Note that the ±0.05 mm QDM position error is not part of the mechanical estimated errors listed in Table 1 but is assigned to the QDM-system error budget not discussed in this paper.

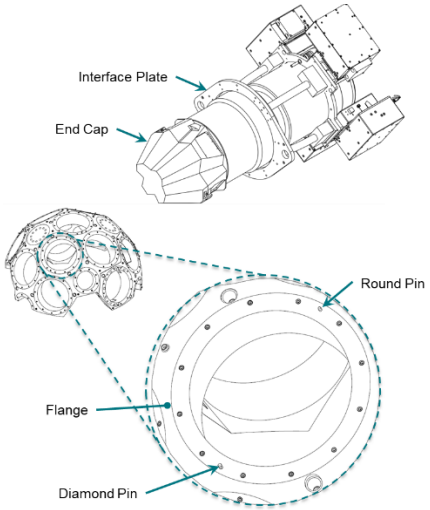

Figure 2. The hemisphere port flange uses of a round and diamond shaped pin to define the location of the QDM (top).

2.3 Support Structure

The support structure is designed to accommodate the installation and removal of the QDMs and to provide access to the centre of the hemisphere where the target chamber would be located. It provides rotation of ±180° to facilitate QDM insertion and removal in a horizontal orientation using a crane and a dedicated lift fixture. A linear drive system provides 500 mm of travel for the entire support structure along the rotation axis, defined perpendicular to the facility beam pipe. The drive-system positional error at the closed position is estimated at ±0.10 mm. To mitigate assembly and alignment errors, three vertical support struts are integrated into the support frame. Each strut provides primary vertical motion of 10 mm and an integrated horizontal motion of 10 mm (perpendicular to the rotation axis), giving a total of five degrees of freedom.

In addition to position errors, the support structure is subjected to different loads depending on the experimental configuration (e.g., removal of the doublet and triplet sections). It is estimated that structural deformation under the corresponding load range of 350 kg to 1,150 kg is ±0.26 mm.

3. Requirements Verification

To verify the different requirements, multiple techniques were implemented and are described below.

3.1 Hemisphere Verification

The hemisphere underwent acceptance verification during manufacture and subsequent post-receipt checks at LBNL using a coordinate measuring machine (CMM). Figure 3 presents the QDM port locations; all ports were within the tolerance specified in Table 2 except for port 10, while port 1 was at the specification limit. Accounting for the CMM measurement uncertainty of ±0.02 mm (2σ), the result could be regarded as within specification. Note that the QDM port

location was defined as a surface profile that includes position, orientation, and flatness. When the surface profile is decomposed into its constituent attributes, the position component is within specification and therefore acceptable.

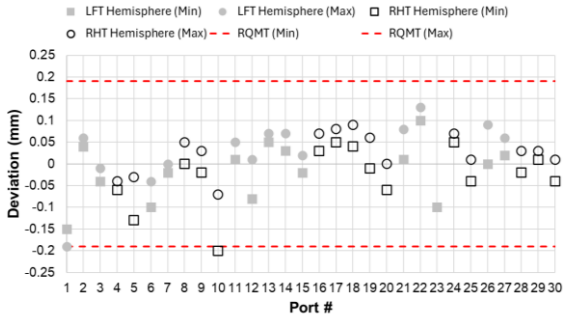

Figure 3. CMM inspection results of QDM port location for all 30 QDM ports.

Part of the hemisphere acceptance tested the locations of the round and diamond pin features on each QDM flange. Measurements with the CMM across all 30 ports yielded a spread from 0.05 mm to 0.15 mm, satisfying the specification in Table 2. The installation and removal of the doublet and triplet sections were performed, with a measured repeatability of ±0.01 mm.

As an additional check, six adjacent QDMs were installed into the hemisphere, and installed gaps were determined with feeler gauges. The nominal design gap between QDM end caps is 1 mm, and measured gaps ranged from 0.9 mm to 1.1 mm (Figure 3). This confirms conformance to the mechanical requirements of the hemisphere.

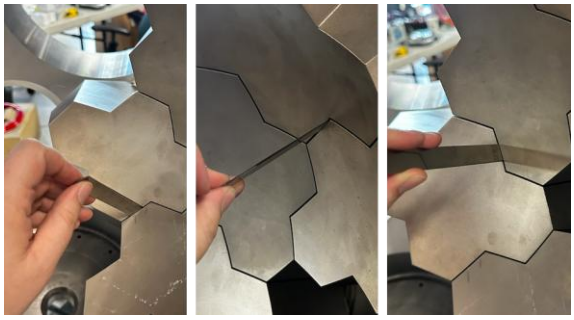

Figure 3. Secondary measurement using feeler gauges to check the gap between QDM end caps.

3.2 Support Structure Verification

The linear and rotational ranges of the support structure were verified using a laser tracker for linear motions and an integrated rotary encoder for rotation about the y-axis. Each hemisphere contains 35 fiducial nests that serve as laser-tracker measurement reference points. Table 3 summarizes the results. The x-axis is defined by gravity, while the z-axis is aligned with the beam direction; these motions are achieved by manual adjustments in combination with the associated rotations. The y-axis motion and the rotation about the y-axis are controlled by a closed-loop controller.

As shown in Table 3, the linear ranges along the x- and z-axes were below the stated requirements due to a design error causing an interference between the structural frame and the linear drive actuator attached to the baseplate. Despite this shortfall, it is deemed acceptable because these adjustments are intended to accommodate alignment errors during installation. Based on experience with similar structures of this size and weight, alignment within approximately 3 mm is typically achievable, so the measured ranges are considered sufficient to align GRETA to the FRIB target chamber.

The rotation about the y-axis also fell short of the ±180° requirement; however, this is not necessary since the largest rotation needed to install or remove a QDM is 170°, making the measured range acceptable.

Table 3. Measured linear and rotational ranges of the support structure.

Direction	Requirement	Linear or Rotation Range
X-axis (manual)	±10 mm	16.5 mm (±8.25 mm)
Y-axis	> 500 mm	> 500 mm
Z-axis (manual)	±10 mm	11.7 mm (±5.85 mm)
Rotation about x-axis (manual)	±0.5 deg	1.46 deg (±0.73 deg)
Rotation about y-axis	±180 deg	+180 deg -172 deg
Rotation about y-axis (manual)	±0.5 deg	1.23 deg (±0.63 deg)
Rotation about z-axis (manual)	±0.5 deg	1.42 deg (±0.71 deg)

During range verification, the relative position error between the two hemispheres was measured with a laser tracker as well. The objective was to demonstrate that the left hemisphere could be aligned to the right hemisphere (taken as the reference position) within ±0.10 mm. The results are presented in Table 4.

Table 4. Alignment error verified by aligning the left hemisphere to the assumed ideal location of the right hemisphere using a laser tracker.

	Left Side	Right Side
X-axis	0.03 mm	0.00 mm
Y-axis	-0.01 mm	0.00 mm
Z-axis	0.07 mm	0.00 mm
Rotation about x-axis	-0.002 deg	0.000 deg
Rotation about y-axis	0.004 deg	0.000 deg
Rotation about z-axis	0.001 deg	0.000 deg

To assess the structural deformation under load, dummy weights were used to emulate QDM mass, and deformation was measured with the laser tracker. Table 5 summarizes the changes between the unpopulated and fully populated hemispheres. The deflection in the x-direction (gravity) is larger than the anticipated ±0.26 mm from the FEA verification. A brief root-cause analysis identified two plausible contributors: (i) the FEA model may have oversimplified or made incorrect assumptions at the angular-contact and radial-bearing interfaces (part of the rotation axis) and other joints (bolted joints, welds); and (ii) angular-contact and radial bearings may not have been preloaded exactly as specified by the manufacturer. Rather than perform additional tests to confirm these potential causes,

the test was repeated to check for permanent deformation. The frame returned from the fully populated state to the unpopulated state and back to less than the laser tracker's measurement uncertainty of ±0.1 mm (2σ). On this basis, the results are deemed acceptable for operation, with the understanding that re-alignment would be required if the load configuration changes or use dummy weights to simulate QDM absence/presence.

Table 5. Support structure deformation changes between unpopulated and fully populated hemispheres.

	Unpopulated	Fully Populated
X-axis	0.00 mm	1.63 mm
Y-axis	0.00 mm	0.16 mm
Z-axis	0.00 mm	-0.19 mm
Rotation about x-axis	0.000 deg	-0.001 deg
Rotation about y-axis	0.000 deg	0.039 deg
Rotation about z-axis	0.000 deg	-0.048 deg

4. Summary and Future Work

GRETA was integrated and tested at Lawrence Berkeley National Laboratory (LBNL) to verify the mechanical system and the performance of the fully integrated GRETA assembly (the latter not presented here). Figure 4 shows the installed GRETA system. While the verification demonstrated general compliance with the mechanical requirements, some deviations were observed, notably deformation of the support structure under full QDM loading. Despite these deviations, the results indicate that GRETA is capable of supporting nuclear-structure and nuclear-astrophysics programs at FRIB within the intended operating envelope.

Future work is to repeat the mechanical verifications with GRETA installed at FRIB, using all 30 QDMs, under realistic FRIB operating conditions.

Acknowledgements

The authors gratefully acknowledge the entire GRETA team for their contributions to the development and verification of GRETA's mechanical system. This work was supported by the U.S. Department of Energy under Contract No. DE-AC02-05CHI1231.

References

[1] Lee I-Y, 1990, The Gammasphere, *Nuclear Physics A*, **520**, c641 – c655.

[2] Paschalis S, et al., 2013, The performance of the Gamma-Ray Energy Tracking In-beam Nuclear Array GRETINA, *Nuclear Instruments and Methods in Physics Research Section A: Accelerators, Spectrometers, Detectors and Associated Equipment*, **709** (1), 44-55, ISSN 0168-9002.

[3] Facility for Rare Isotope Beams (FRIB) at Michigan State University, www.frib.msu.edu

[4] Buice E.S., et al., 2023, Mechanical design of a next generation γ-ray spectrometer: Gamma-Ray Energy Tracking Array (GRETA), eu**spen**'s 23rd International Conference & Exhibition, Copenhagen, DK.

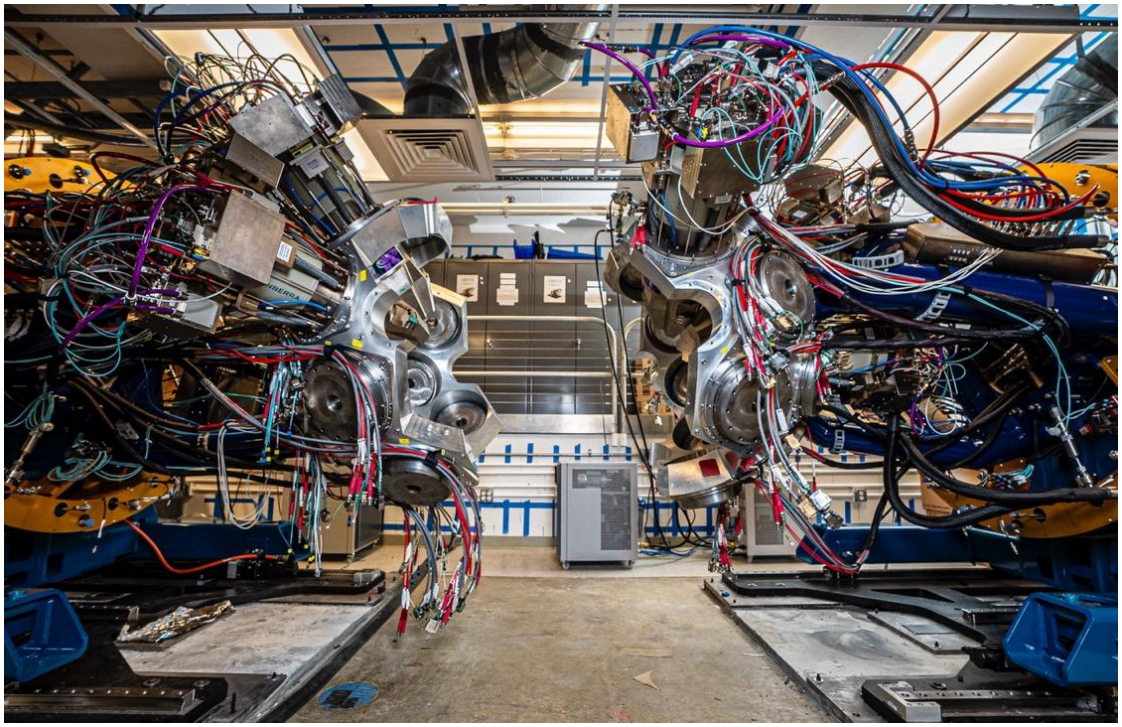

Figure 4. GRETA fully integrated with six QDMs and 24 dummy masses installed into the GRETA mechanical system at LBNL.

euspen's 26th International Conference & Exhibition, Krakow, PL, June 2026
www.euspen.eu

Nanomotion for ALBA II: laboratory, metrology and control for precision engineering

Juan Luis Frieiro,[1] Nilson Bernardo Pereira,[1] Nahikari González,[1] Carles Colldelram,[1] Josep Nicolás[1]
[1]ALBA synchrotron, Cerdanyola del Vallés, Barcelona, Spain

jfrieiro@cells.es

Abstract
The ALBA synchrotron facility, located near Barcelona, is undergoing an upgrade to ALBA II, a fourth-generation machine that will deliver lower emittance and higher brilliance beams. These improvements introduce stringent requirements for motion control, metrology, and synchronization across beamline instrumentation. To address these challenges, ALBA has established the Nanomotion Laboratory, a dedicated space for precision engineering research and development. The laboratory combines ultra-stable infrastructure with cleanroom environments and advanced metrology capabilities to support both beamline services and exploratory projects. Current activities include interferometer-based feedback for optical components, FPGA-driven synchronization for high-speed experiments, runout metrology and correction, and the development of ptychography scanning systems. This paper presents the laboratory's facilities, ongoing projects, and performance targets, aiming to foster collaboration with the broader precision engineering community.

Precision motion control, nanometrology, synchrotron instrumentation

1. Introduction

ALBA is the 3rd generation syncrothron facility located near Barcelona, Spain; currently working on the design of its upgrade to a 4th generation machine, ALBA II.[1] This upgrade will deliver a lower emittance and a higher-brilliance beam, enhancing the resolution and coherence available at the beamlines. These exceptional properties introduce new challenges in precise motion control and equipment synchronization to fully exploit their potential. To address these challenges, alongside the first designs, prototypes, and tests, ALBA has built and recently inaugurated a new Nanomotion Laboratory.

The Nanomotion Laboratory will tackle the aforementioned challenges. Over the coming years, until ALBA II delivers its first beam (currently expected in 2032), the laboratory will test different precision components and designs to support developments carried out by the engineering, electronics, and controls teams. In general terms, the work will focus on applying mechatronics to the current workflow.

This paper introduces the laboratory to the broader precision engineering community, aiming to establish new collaborations with a wider network beyond the synchrotron environment.

2. Laboratory spaces

The laboratory is located in the nominal position of beamline BL17 at ALBA, which would otherwise remain unused due to its short length. This location allows the laboratory to be built on top of ALBA's main slab, which is isolated from the ground. As a result, the laboratory shares similar conditions to those present at the beamlines, with overall improved stability.

See Figure 1 for an overview of the different parts of the laboratory, detailed next.

The main space of the laboratory is constructed as a cleanroom (ISO 2–3 without personnel, ISO 6–7 with personnel). It includes three PC workstations, two optical tables, and a floor plate embedded in the ground. The environment inside is constantly monitored to provide reproducible conditions between tests. The established work procedures use feedthroughs and patch panels connected to racks outside the lab, avoiding the introduction of electronic equipment inside whenever possible to maintain room stability.

If large equipment needs to be introduced into the cleanroom, a set of large double doors provides direct access to ALBA's Experimental Hall. In addition, the ceiling above the floor-embedded plate is removable, allowing the use of the Hall's main cranes.

A smaller room inside the clean room is reserved for the most demanding work. Its main characteristic is the absence of lighting and air conditioning. This passive room is located adjacent to the concrete accelerator tunnel on two walls, with air gaps to the main clean room on the other two walls and the ceiling. The result is an extra level of stability compared to the main room. This space contains an optical bench as a workspace, a patch panel connected to the outside, and a feedthrough on one wall to keep heat-generating electronic equipment outside in the clean room when short cabling is to be used.

The last room of the laboratory is a control room, which includes the dressing area for the cleanroom as well as workstations to control operations inside.

In Figure 2, the monitoring panel displayed in the control room is shown. It presents data from the environmental sensors installed in the laboratory and allows historical review for all of them. Altogether, over two weeks of normal working conditions, the main room maintained a controlled relative humidity of 44 ± 2 %, an overpressure relative to the Experimental Hall of 0.24 ± 0.01 mbar, and a temperature of 22.89 ± 0.03 °C. The super-quiet room maintained a temperature of 23.02 ± 0.01 °C.

3. Ongoing projects

The laboratory operates on two fronts for ALBA. On one side, it provides services to the beamlines. This includes external metrology—performing measurements of motion components before installation to ensure that requested specifications are met—as well as collaborating with other ALBA teams on designs

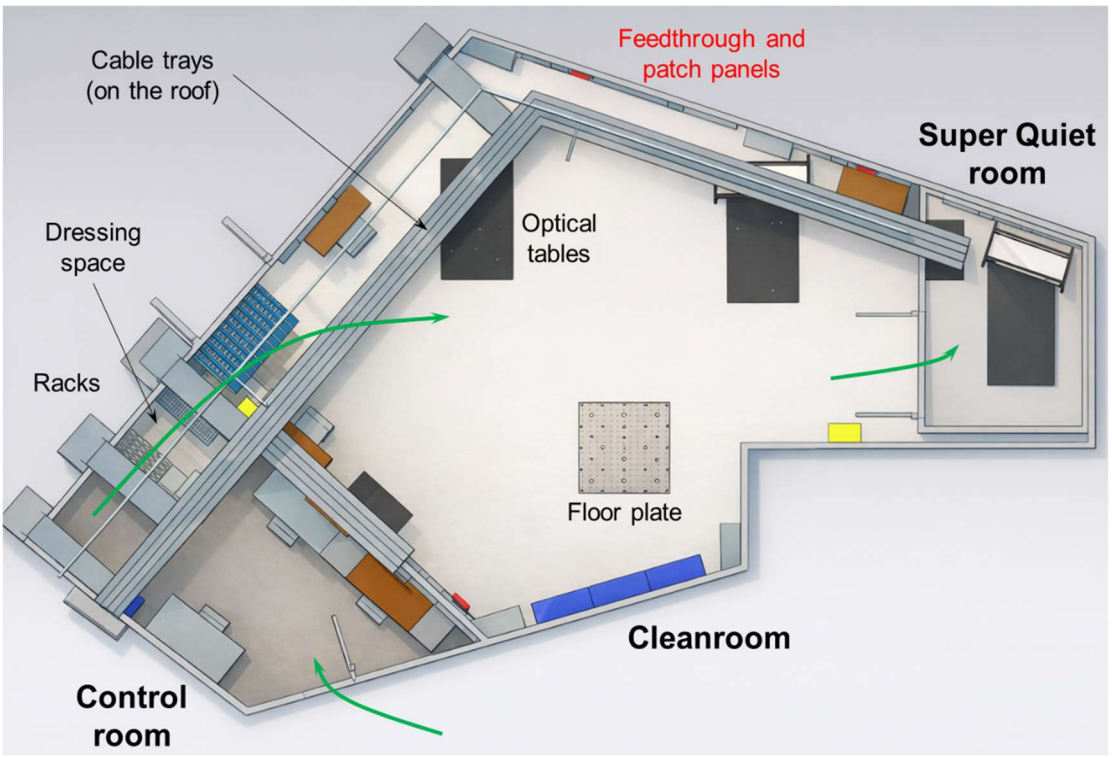

Figure 1. Nanomotion laboratory layout showing the cleanroom, super quiet room, and control room; and some of the infraestructure used.

for improved feedback loops, more stable systems, or dynamically responsive components. On the other side, the laboratory focuses on research tasks. For this, it explores new commercially available products that might be relevant (controllers, actuators, displacement sensors), develops new algorithms for improved feedback or metrology, and evaluates other relevant equipment.

Across these activities, our laboratory targets sub-nanometre measurement resolution (interferometry and capacitive sensors), <50 nm runout after correction (video-based LUT), low trigger jitter at 1 kHz (FPGA), and closed-loop bandwidths up to the low-kHz range for optical elements. These targets guide hardware selection, error budgeting, and control design.

The following sections describe some of the projects in hich the laboratory is currently involved at ALBA.

3.1. Interferometer feedback

After years of using interferometers mainly for metrology applications, ALBA is now introducing interferometer-based feedback on beamline components.

The first test was carried out at BL06-XAIRA, using three sensor heads pointing through viewports at the horizontal focusing mirror upstream of the sample position. While the setup is still temporary, it has demonstrated the ability to provide precise simultaneous measurements of the mirror's displacement, pitch, and curvature. The operation of the interferometer in the kHz range of frequency will allow its incorporation to the feedback loop for mirror stabilization in the future.

In the case of BL15-3SBAR—the first beamline designed with ALBA II specifications in mind—interferometers have been incorporated into the feedback loops of the focusing mirrors and monochromator. This beamline is under construction at the time of writing, and interferometers will be added as components arrive, starting with the monochromator expected in the first half of 2026.

3.2. Fast periodic shutter feedback and trigger

Recently opened to users, BL31-FAXTOR is dedicated to fast X-ray tomography and radiography. For time-resolved tomography experiments, a fast periodic shutter will chop the X-ray beam at high frequency (up to 1000 Hz). The controlled speed of the shutter is expected to fluctuate slightly, so we are actively developing a detection and trigger system to synchronize the experiment.

Figure 2. Environment sensor monitoring and history panel. Two weeks of data are shown. Top: temperature sensors; middle: particle counts and relative humidity; bottom: lab door stauts and control room temperature.

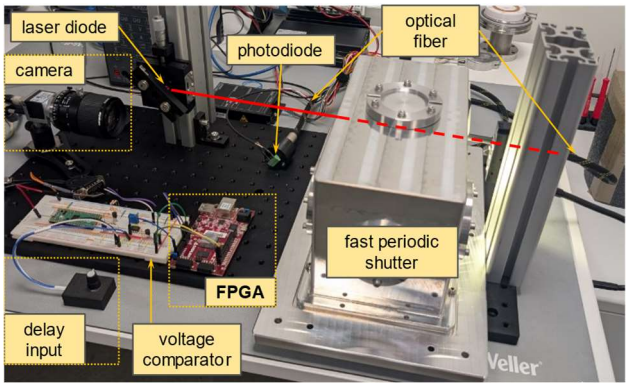

Figure 3. Prototype FPGA-based trigger system for fast periodic shutter synchronization. The setup includes a photodiode signal amplified via a voltage comparator and processed by the FPGA to generate phase-locked triggers for image acquisition.

Symmetrical to the beam path through the shutter, a laser and photodiode can be mounted. The signal captured by the photodiode can be analyzed: its frequency provides an external measurement of the beam chopping and, consequently, the shutter's rotation speed.

Moreover, the group is actively working on FPGA programming to further process the photodiode signal. An FPGA offers the speed and stability needed to generate a phase-locked trigger for the detector to capture an image when the shutter is fully open. This approach ensures deterministic timing and minimizes jitter, critical for high-frequency tomography.

The prototype is shown in Figure 3, and initial tests with a 3D-printed shutter and a camera instead of a detector have yielded very positive results. The photodidode signal is sent to a voltage comparator to condition it for the FPGA input , improving signal integrity and noise immunity. A second input to the FPGA allows the user to delay the trigger to adjust the image acquisition. With these inputs, the FPGA generates the trigger for the camera to acquire the images. In terms of the beamline, this trigger can also be used by other equipment, such as synchronized sample position capture, which is essential for improved tomography reconstruction.

3.3. Runout metrology and online feedback

A key application in synchrotron instrumentation involves rotating samples to acquire data at different angles for reconstruction or increased signal. However, small unwanted motions—such as radial runout, axial displacement, or wobble—can severely compromise the rotation's purpose.

The group has addressed this issue for the sample stage at BL06-XAIRA. A new method for runout measurement was developed, based solely on video acquisition normal to the rotation axis. The video is analyzed frame by frame to calculate rotation and runout. Using this information, a calibrated lookup table for correction can be created. Further details can be found in [2]. Figure 4 shows the measured runout of the stage using this new method: the first measurement was used to calculate the correction lookup table, and the second verifies the result after applying the correction.

The next milestone is to develop an online feedback system for runout correction, based on a multiprobe error separation method. Error separation follows a three-probe, non-symetric arrangement to decouple spindle error harmonics and target shape, as demonstrated in [3] and multiple other works. Correction will be deployed as an open-loop lookup table with planned upgrade to closed-loop overlay. A prototype is currently under assembly. Additionally, the video-based measurement will be employed to corroborate the results obtained.

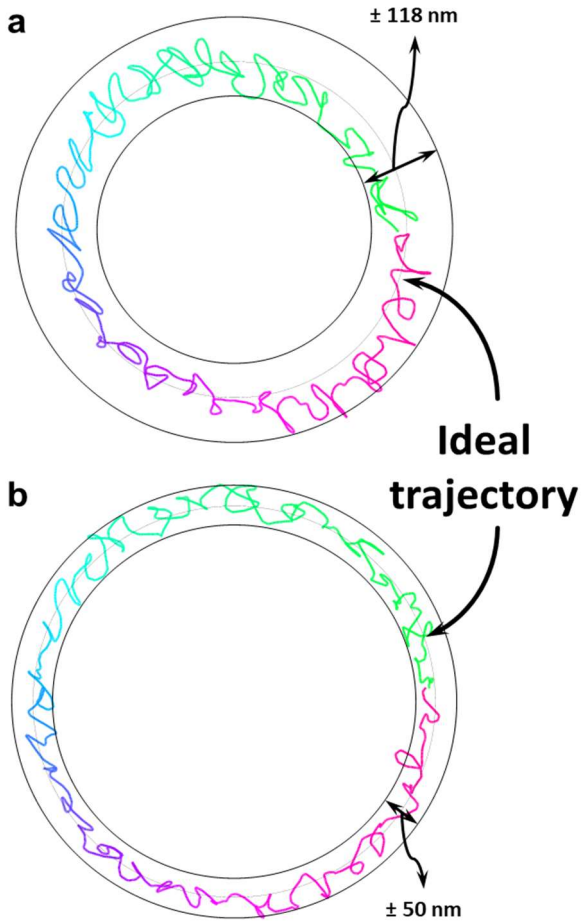

Figure 4. Runout measurement results for the BL06-XAIRA sample stage using video-based analysis. The first dataset (a) was used to compute the correction lookup table; the second (b) verifies the improvement after applying the correction.

3.4. Ptychography scanners

Alongside the ALBA II upgrade, a coherence program is being launched at ALBA. Initial proof-of-concept experiments will be developed in the coming years to gain knowledge about requirements and working procedures. The first of these tests is underway and scheduled to produce results by the end of 2026. The main goal for now is to learn how to run the experiment and process the data.

For the Nanomotion group, these tests are an excellent opportunity to gain experience in mechanics and control. The group will focus on the rapid development of a set of stages with motion controlled via relative displacement measurements from an interferometer between the optics and the sample. The design will follow what is described in [4]. Initial scans will use snake trajectories with overlapping and stability yet to be defined. Once the initial set is ready, improvements to the mechanical assembly will follow using the dynamic error budgeting method, and control will be designed using a mechatronics approach. These concepts are expected to significantly enhance the performance of complex mechatronic systems, as demonstrated by other synchrotron facilities.

3.5. FPGAs

The last major objective of the group is to develop proof-of-concept applications using Field Programmable Gate Array (FPGA) chips. While programming these systems is more complex than regular scripting, the potential gains in speed and deterministic operations justify the effort.

Currently, small applications for device synchronization via triggering are being developed, such as the fast periodic shutter at BL31-FAXTOR mentioned earlier. There is also a list of potential systems that could benefit from FPGA-based control, either by replacing existing components or by modifying their control architecture, which would be tackled in 2026 and 2027.

4. Conclusions

The Nanomotion Laboratory at ALBA has been established to address the demanding requirements of next-generation synchrotron instrumentation, driven by the ALBA II upgrade. Its infrastructure—featuring an isolated slab, cleanroom environments, and a passive ultra-stable space—provides a controlled setting for precision metrology and motion control development.

Current projects span interferometer-based feedback for optical components, FPGA-driven synchronization for high-speed experiments, advanced runout metrology and correction, and the design of ptychography scanning systems. These efforts aim to integrate high-resolution sensing, deterministic control, and dynamic error budgeting into the workflow of the beamlines of ALBA and ALBA II.

Beyond supporting ALBA's internal developments, the laboratory seeks to engage with the broader precision engineering community. Opportunities for collaboration include nanometrology, mechatronic design, FPGA-based control, vibration-decoupling optomechanics, and advanced scanning strategies. By sharing expertise and fostering joint developments, we aim to accelerate innovation in precision engineering for large-scale scientific facilities.

5. Acknowledgements

The authors would like to thank all the ALBA groups in-volved in constructing and equipping the laboratory, espe-cially the Infrastructure, Workshop, Electronics, and IT Systems groups. This project received funding from the European Union under program NextGenerationEU.

References

[1] Biscari C. et al., "ALBA II White Paper", ALBA synchrotron, Barcelona, Spain, May 2023

[2] Frieiro J. L., Pereira N., Nicolas J., Sics I., González N. and Juanhuix J. 2025 *J. Phys.: Conf. Ser.* **3010** 012114

[3] Stankevic T., Engblom C., Langlois F., Alves F., Lestrade A., Jobert N., Cauchon G., Vogt U. and Kubsky S. 2017 *Rev. Sci. Instrum.* **88** 053703

[4] Holler M., Raabe J., Diaz A., Guizar-Sicairos M., Quitmann C., Menzel A. and Bunk O. 2012 *Rev. Sci. Instrum.* **83** 073703

euspen's 26th International Conference & Exhibition, Krakow, PL, June 2026
www.euspen.eu

Basics of preparing a digital twin for a cooperative robot (cobot) with an attached rigid-contact head

Przemysław Jędrzejak [1], Sebastian Kąkol [2], Karol Stroński [3], Łukasz Giza [4], Konrad Kobiela [5], Ksenia Ostrowska [6]

Cracow University of Technology [1,2,3,4,5,6]

Ksenia.ostrowska@pk.edu.pl

Abstract
The article describes the preparation of a collaborative robot for a contact measurement task. Technical and software solutions enabling the performance of such a task were proposed, and then a preliminary, simplified, and initial digital twin model was developed. An analysis of the impact of the robot's operating speed during the collection of measurement points was carried out, and it was shown that the speed of the cobot calibration robot does not affect the accuracy of the read data. Further steps were discussed that would allow for the introduction of corrections to the operation of such a system.

Type the keywords here: digital twin, cobot, metrology, kinematics, measurement systems

1. Introduction

The digital twin (DT) is currently one of the key tools supporting intelligent manufacturing, maintenance, and quality assurance in the Industry 4.0 paradigm. In terms of the ISO 23247 standard, a digital twin is defined as "a purpose-built digital representation of an observable manufacturing element with guaranteed synchronization" between the physical object and its digital representation, whereby data exchange can be unidirectional or bidirectional [1]. The literature review emphasizes that the essence of DT is not the model itself (e.g., CAD), but the continuous coupling of data, the ability to perform what-if analyses, and integration with technologies such as IoT, simulation, and AI [2,3].
In manufacturing applications, DT is being developed, among other things, towards managing geometric and quality variability in near real time. The work of Söderberg and co-authors indicates that "geometric assurance" may become an area where the digital twin combines production and inspection data with tolerance/variability models, enabling a shift from a reactive to a predictive approach.[4] Wärmefjord's research, on the other hand, emphasizes the role of DT in "variation management" – from variability simulation, through setting and tolerance planning, to the use of measurement data for process control [4].
A special case of DT in the area of quality is the digital metrological twin, in which the metrological model of the measuring device and uncertainty simulation play a key role. In coordinate metrology, concepts of virtual measuring machines (VMM) are being developed which, thanks to the kinematic description of the device and error models, enable the generation of measurement results together with uncertainty assessment by simulating multiple measurements (e.g., using the Monte Carlo method).[5] In this approach, DT becomes not only a visualization tool, but also an element of the quality data infrastructure: results (actual and simulated) can be stored in a database and used by metrology, quality, and maintenance, as well as feedback for manufacturing processes [5].
Parallel to the development of digital metrological twins, the importance of collaborative robots (cobots) as carriers of measurement tasks is growing. Cobots are attractive due to their easy system integration, safety when working near the operator and relatively low implementation threshold. At the same time, the limited rigidity of the system, susceptibility to contact loads, and control characteristics (including safety mechanisms/torque limits) mean that the implementation of contact measurements requires a conscious analysis of repeatability and identification of factors affecting the accuracy of TCP determination. From the point of view of a digital twin, this means that it is necessary to adopt a formal description of kinematics (e.g., Denavit–Hartenberg) and prepare the basis for subsequent geometric and functional error models [5].
This article is the first stage of a series of publications aimed at developing a digital twin of the UR3 cobot for measurement applications, as well as developing robot corrections. This stage focused on a preliminary analysis of the repeatability of movement and stability of the robot's position, adapting it to contact measurements, and developing the mathematical basis for the digital twin, without yet taking corrections into account.
The main objectives of the research were: to determine the repeatability of the UR3 cobot's positioning at different speeds, to analyze the effect of speed on the behavior of the robot's axes and the TCP point, and to collect reference data to serve as a basis for further stages of digital twin development.

2. Hardware basics

Before starting the work, the accuracy of the robot (cobot) was checked in accordance with the PN-EN ISO 9283:2003 Industrial robots – Methods for testing functional characteristics [8] standard. Instead of a gripper, a Leica LTD 840 Laser Tracker retroreflector was mounted on the last link (Fig. 1a). The tests were performed in the "oblique" plane (Fig. 1b) recommended in the standard for a six-axis robot with an open kinematic chain. The test of a linear track should be performed along the diagonal of a cube, with a path length equal to 80% of the distance between opposite corners of the selected plane.

The accuracy of the segment mapping expresses the deviation of linear positioning between the set distance and the average value of the actual segment. The accuracy of the segment mapping, which expresses the linear positioning deviation between the specified distance and the average value of the actual segment, was ±0.078 mm for the tested robot, while the repeatability of the segment mapping, which is the value of the dispersion of the actual lengths of the n-times mapped segment, specified in the same direction, was ±0.102 mm.

Figure 1a) Testing the robot in accordance with PN-EN ISO 9283:2003, using the Lieca LTD 840 tracking system, Figure

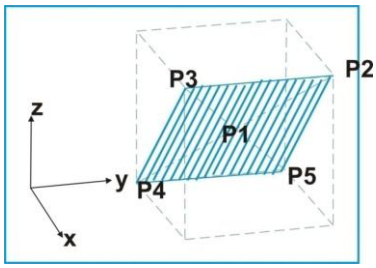

1b) Location of the track where the robot was tested

The tests are of a verification and preparatory nature. Their purpose is not yet to calibrate the robot metrologically, but to check the stability and repeatability of movement under controlled laboratory conditions. At the preliminary stage, a dedicated measuring head was not used, which will be used in further work to perform precise measurements. This decision was based on several important considerations: the high cost of the measuring equipment, the risk of damage during testing, the trajectory and movement parameters, and the need for prior validation of the robot itself as a carrier of the measuring system.

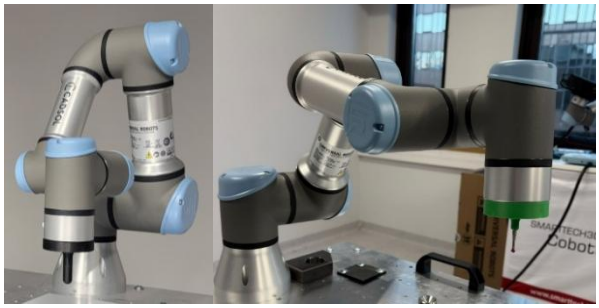

Figure 2a) Gripper equipped with a pin acting as a contact element, 2b) Modeled rigid contact head

Instead of a measuring head, a standard gripper equipped with a pin acting as a contact element was used (Fig. 2a). This solution allows for safe repeatability testing without exposing expensive equipment to overload or collision. It was then decided to use a type of rigid contact head (Fig. 2b), where a measuring pin with a 3 mm diameter ball was rigidly attached to the designed gripper.

The test object is a six-axis industrial robot used for measurement tasks. The kinematic structure of the robot includes the following axes (joints): J1 – Base, J2 – Shoulder, J3 – Arm, J4 – Wrist 1, J5 – Wrist 2, J6 – Wrist 3. The robot operates in Cartesian space, and its position and tool orientation are described by the TCP (Tool Center Point) vector in the form: $TCP=[X,Y,Z,Rx,Ry,Rz]$ (1) where X,Y,Z denote the coordinates of the tool position, while Rx,Ry,Rz denote the angles of orientation of the tool relative to the axes of the coordinate system.

The TCP in the UR 3 robot was determined using the robot's internal software by setting the tool tip four times in the internal cone at different angles.

Figure 2a) View of the tool center point determination from the TCP robot program,
Figure 2b) Photo of an example setting of the measuring tip in the internal cone

The measurements were performed according to a repeatable procedure: the robot approached the measurement point from above, then from the y-axis and then the x-axis (10 points were collected each time), moving in a straight line in Cartesian space. The movement took place at various TCP linear speeds, ranging from 1 mm/s to 10 mm/s. When the pin came into contact with the reference surface, the overload protection was activated. The overload threshold was set to 30-40 (robot system units). When an overload was detected, the robot's movement was immediately stopped. This was followed by a reading of the robot's data, including: the position of all axes (joints), the position and orientation of the TCP. This method allows the moment of contact to be determined unambiguously and ensures the repeatability of the robot's stopping conditions.

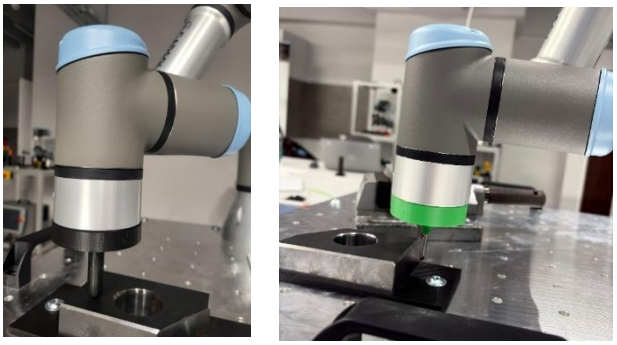

Figure 3a) Contact readings of a gripper equipped with a pin acting as a contact element, Figure 3b) Contact readings of a modeled rigid contact head

Measurements taken at different speeds did not show significant changes in the readings [Table 2], which allows us to conclude that the change in speed did not affect the readings of the contact between the measuring element and the pin. This may be due to the fact that collaborative robots do not reach speeds as high as conventional industrial robots.

3. Mathematical and kinematic foundations of a cobot digital twin

In order to develop a digital model of a robot, it is necessary to determine the kinematic equations describing a robot with an open kinematic chain structure. Its individual links are treated as given solids in space, where only the relationships between them need to be determined. The relationship between two adjacent pairs can be represented by four variables. ai - distance from axis zi to axis zi+1 measured along axis xi , αi - angle between axes zi and zi+1 measured around axis xi , di - distance between the axes xi-1 and xi measured around zi , θi - angle between the axes xi-1 and xi measured around zi .
Every manipulator or robot with the same design can be described using the four variables presented above. The description of kinematics using this convention is referred to in the literature as Denavita-Hartenberg notation [my articles]. The first two parameters describe the link, while the next two describe the connection between them. If there is a rotational pair in the design, then the variable is the configuration angle of the moving link θi, while the rest of the parameters are constant. If there is a translational pair, then the variable is the displacement parameter of the link di, while the rest are constant [Table 1].

Table 1. UR3 Parameters

Parametry D-H dla UR 3				
i	a_{i-1} [m]	d_i [m]	α_{i-1} [rad]	θ_i
1	0	0,1519	$\pi/2$	θ1 (podstawa)
2	-0,24365	0	0	θ2 (bark)
3	-0,21325	0	0	θ3 (ramię)
4		0,11235	$\pi/2$	θ4 (nadgarstek1)
5		0,08535	$-\pi/2$	θ5 (nadgarstek2)
6		0,0819	0	θ6 (nadgarstek3)

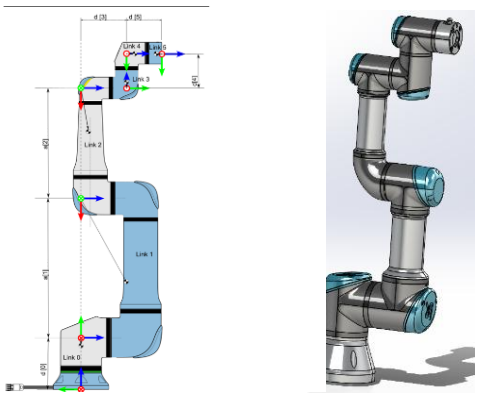

Figure 4a. Description of the UR3 collaborative robot (according to the manufacturer's data), 4b View of the model for digital twin visualization

Homogeneous coordinates were used to describe the transformations between the systems, which allow points to be represented in i-dimensional projective space (a modified geometric space by adding the points of all its directions to the set) using an i+1
coordinate system. The basic task in working with redundant devices with an open kinematic chain is the so-called simple kinematic task. It is a static-geometric task that involves calculating the position and orientation of a working member of a device, e.g., a robot gripper or a measuring head, especially when a set of configuration angles is given. The simple kinematics task maps the description of the manipulator's position in the configuration coordinate space (e.g., readings from angle measurement systems) to a description in Cartesian coordinate space (Cartesian coordinate space is understood here as a space in which the position of a point is determined by three numbers x,y, z, and the orientation of the member is determined by three other numbers). To calculate a simple task, you can use the transformation matrix from the "i" system to the base system. It is obtained by multiplying the homogeneous transformation matrices Ai, corresponding to the parameters describing the relationships between two adjacent pairs [5, 9, 10, 11].

Table 2. Results of averages from 10 readings of a given point at different speeds

1 mm/s			
Średnie z 10 pomiarów:	**Średnia po przeliczeniu przez cyfrowego bliźniaka, mm:**	**Średnie z odczytów z UR, mm:**	**Różnica średnich, mm**
x	7,595	7,494	0,101
y	-349,94	-350,212	0,272
z	82,212	81,956	0,256
2 mm/s			
x	8,293	8,169	0,124
y	-349,925	-350,209	0,284
z	82,212	81,944	0,268
3 mm/s			
x	7,744	7,581	0,163
y	-349,736	-350,153	0,417
z	81,982	81,877	0,105
4 mm/s			
x	7,744	7,61	0,134
y	-349,736	-350,130	0,394
z	81,982	81,883	0,099
5 mm/s			
x	7,595	7,542	0,053
y	-349,94	-350,210	0,270
z	82,212	81,944	0,268
6 mm/s			
x	8,364	8,29	0,074
y	-349,696	-350,141	0,445
z	81,984	81,85	0,134
7 mm/s			
x	8,293	8,223	0,07
y	-349,925	-350,211	0,286
z	82,212	81,93	0,282
8 mm/s			
x	7,944	7,678	0,266
y	-349,932	-350,224	0,292
z	82,212	81,953	0,259
9 mm/s			
x	7,595	7,65	-0,055
y	-349,94	-350,213	0,273
z	82,212	81,957	0,255
10 mm/s			
x	7,666	7,624	0,042
y	-349,711	-350,128	0,417
z	81,984	81,844	0,14

Thanks to this solution, a computational basis for a digital twin of the tested device was developed. The program was written using the Python language. The input data are always actual readings from the device's encoders, and the mathematical model is based on a simple kinematics task. On the rigid contact head, the differences between the digital twin and the actual reading oscillate within 0.5 mm (the maximum reading is 0.596 mm). However, this is a result without robot correction and without head correction, which will ultimately be performed using an artificial neural network (ANN), which in this case will allow learning from the robot's input data. Fast Artificial Neural Network (FANN) is a library implementing ANN, which will be programmed in Python. The principle of operation of ANN is based on approximating a given function. In other words, they learn the given function by observing examples of its operation. According to previous work carried out at the Coordinate Metrology Laboratory, the assumed mathematical model made the measuring head error dependent on the vector of approach to the measuring point. In the case of industrial robots, we are dealing with a situation similar to that of coordinate machines equipped with a rotary tilt head, where it is possible to control the orientation of the measuring head. Therefore, it will be important that the approaches are presented in the head system and not in the main robot system. The model itself will be adopted as a function R3→R1, where the input parameters will be the coordinates of the approach vector, and the result will be the deviation. For this task, programs will be written that will construct spheres, then calculate their parameters along with deviations and determine the approach vector during measurement. Measuring a sphere of known diameter will allow for an average head correction of 50%, which has already been proven[9] by one of the authors of this paper.

4. Conclusions

This article is the first stage of a series of publications aimed at developing a digital twin of the UR3 cobot for measurement applications, followed by modeling its correction. Further work will determine the kinematic errors of the device. A CAA correction matrix will be developed, and both the head and the entire system will be adjusted. The points will be sent to a database where they will be sorted and sent to metrology software for the application of validated algorithms for the construction of geometric elements, i.e., PC Dmis or PolyWorks. In this work, preliminary tests were carried out and assumptions were made by the authors regarding the operation of such a system. Tests were performed on the influence of speed on the repeatability of readings, and indirectly, the accuracy of the digital twin was also determined. The data show only constant spreads, which did not increase or decrease with changes in speed (Table 2).

The collected data is of a kinematic nature (axis positions), spatial (TCP position), and dynamic indirect (the effect of speed and overload on stopping). , it constitutes the first reference data set for: verification of the UR3 kinematic model, analysis of contact point repeatability, identification of axes sensitive to speed changes. At this stage, the digital twin represents the robot in a simplified form, but already allows for comparison of the virtual model's behavior with the real object.

This article is a starting point for the next stages of work, which will include: the use of a dedicated measuring head, detailed analysis of measurement errors, dynamic modeling of the robot, coupling the digital twin with online data, and validation of the digital twin in real measurement tasks.

Literature

[1] Guodong Shao Deogratias Kibira, Simon Frechette. DIGITAL TWINS FOR ADVANCED MANUFACTURING: THE STANDARDIZED. Washington, DC, USA : Springer Nature, 26 Październik 2024.

[2] Qinglin Qi Fei Tao, Tianliang Hu, Nabil Anwer, Ang Liu, Yongli Wei, Lihui Wang, A.Y.C. Nee. Enabling technologies and tools for digital twin. Journal of Manufacturing Systems. 58, 2021, 3-21.

[3] Aidan Fuller Zhong Fan, Charles Day, Chris Barlow. Digital Twin: Enabling Technologies, Challenges and Open Research. IEEE Access. 8, 2020.

[4] Rikard Söderberg Kristina Wärmefjord, Johan S. Carlson, Lars Lindkvist. Toward a Digital Twin for real-time geometry assurance in individualized production. CIRP Annals. 66, 2017, Tom 1, 137-140.

[5] Ksenia Ostrowska Danuta Owczarek, Adam Gąska, Marcin Krawczyk, Robert Kupiec, Jerzy Sładek. Assumptions of the digital twin in coordinate metrology. Measurement: Sensors. 38, 2025.

[6] Kristina Wärmefjord Rikard Söderberg, Benjamin Schleich, Hua Wang. Digital Twin for Variation Management: A General Framework and Identification of Industrial Challenges Related to the Implementation. Applied Sciences. Digital Twins in Industry , 2020.

[7] Qinglin Qi Fei Tao, Tianliang Hu, Nabil Anwer, Ang Liu, Yongli Wei, Lihui Wang, A.Y.C. Nee. Enabling technologies and tools for digital twin. Journal of Manufacturing Systems. 58, 2021.

[8] PN-EN ISO 9283:2003. Roboty i urządzenia dla robotyki. Metody badania charakterystyk funkcjonalnych. Warszawa : Polski Komitet Normalizacyjny, 2003.

[9] Ksenia Ostrowska, Grzegorz Sokal, Marcin Krawczyk, Robert Kupiec, Wiktor Harmatys, Adam Gąska, Małgorzata Kowalczyk, Krzysztof Tomczyk. Correction of the measuring system composed of the contact probe head mounted on the industrial robot, Measurement Journal of the International Measurement Confederation, 203, 111957, 2022

[10] Kang Zeng, Wang Ling, Zhu Chunxiang, Chen Xiai, Xu Suan, A novel calibration method of 6-DOF industrial robots based on a multi-constraint model by grouping parameters, International Journal of Advanced Manufacturing Technology, 141(7-8), pp. 3663–3680, 2025

[11] Jiang Xiaogeng, Li Mingxu, Wang Hao, Wang Yan, An improved kinematic calibration method of industrial robots based on double ball bar measurements, Proceedings of the Institution of Mechanical Engineers Part B Journal of Engineering Manufacture, 240 (1-2), pp. 19–30, 2026

euspen's 26th International Conference & Exhibition, Krakow, PL, June 2026
www.euspen.eu

Preload and alignment mechanism for large scale aerostatic bearing

Jesper Riihola[1], Onni Leutonen[1], Mikael Miettinen[1], Raine Viitala[1]

[1]*Aalto University*

jesper.riihola@aalto.fi

Abstract
Deflection compensated nip rolls are used in the paper industry to press and calender paper. Currently, hydrostatic oil bearings are used to load the roll shell internally to counterbalance the external load and reduce roll from deflection. Recent studies aim to replace hydrostatic oil bearings with aerostatic bearings. An experimental deflection compensated roll with aerostatic bearings has been developed in previous work. The present work further develops the preload mechanism for the bearings to provide better alignment with the guide surface. The existing loading element consists of an air bladder that keep the bearings pressed against the inner surface of the roll. A new bearing design and loading mechanism was developed. The friction and load capacity of the bearing system was measured. The results show an improved performance of the modified preload system at an industrially feasible load.

Gas bearing, paper industry, deflection compensated nip roll

1. Introduction

The pulp and paper industry is a significant part of the overall energy consumption in Finland [1]. Of the industrial energy consumption, it represents more than half and of the total energy consumption about 25 percent [1]. This is not only limited to Finland as other countries also spend a major part of their energy consumption on the pulp and paper industry. Sweden spends almost 50 percent of their yearly industrial energy consumption on the pulp and paper industry [2]. In Germany the pulp and paper industry is in the top five of the highest energy consumers of the total industrial energy consumption [3].

Calendering is one of the manufacturing steps in paper production. In calendaring, the paper web is run through a nip, two rolls pressed against each other. This pressing ensures that the paper web has a consistent thickness across the length and improves the surface finish. The lower roll is equipped with deflection-compensation components. The deflection compensation is commonly achieved with hydrostatic bearings which press against the inside of the hollow nip roll.

Currently, the bearings use oil in the lubrication between the loading shoe and the nip roll. By lowering the viscosity of the oil from 100 to 68 cSt a decrease in the waste energy of around 70 kW was made [4]. If a lubricant with an even lower viscosity were used the savings in waste energy could be even greater. The replacement of hydrostatic bearings with porous aerostatic bearings in deflection compensated rolls has been proposed [5,6].

Aerostatic bearings utilize externally supplied pressurised gas which is fed through a restrictor that distributes the pressure. The distributed pressure creates a thin air film between the bearing and counter surface that is usually between 5 µm to 20 µm [7].

This study aims to further develop the aerostatic loading element developed by Harding [5] by replacing the preload bladder mechanism with a pneumatic cylinders, increasing the surface area of the two bearings, and removing the loading chamber in the middle of the bearings. The setup is validated by measuring the loading force and friction between the bearing and a hollow roll.

2. Methods

2.1. Bearing unit and preload mechanism

Bearings consisted of aluminium bodies with integrated air supply channels. The graphite restrictors for both bearings were machined from a single piece of electrical discharge machining electrode graphite to avoid variation in the permeability between the two restrictors. The machined porous graphite restrictors were bonded to the bearing bodies with an epoxy adhesive. After the adhesive had cured, the remaining of the graphite was machined to match the inner radius of the nip roll. The bearings were then ground against the inner surface of the roll lined with abrasive film in steps of decreasing particles size of 100 µm, 30 µm, 15 µm, and 9 µm. A finished bearing is presented in Figure 1.

Figure 1. A bearing finished with abrasive film installed in the measurement setup.

The preload mechanism utilised two 200 mm pneumatic cylinders, one for each bearing, to simultaneously load the bearings against the inside of the hollow roll on the opposite sides. The measurement setup is presented in Figure 2. Each of the pneumatic cylinders were mounted to the measurement

setup with a flexure system. The flexures enable the vertical and horizontal loads to be measured separately.

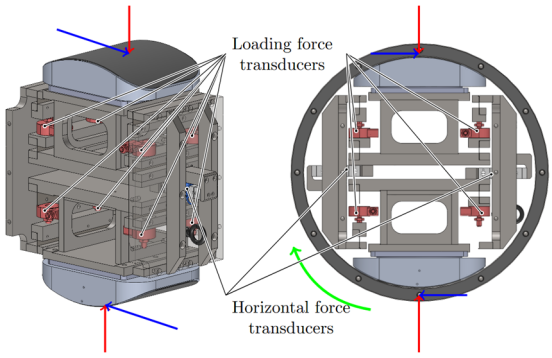

Figure 2. The measurement setup developed by Harding [5]. Figure modified from [5]. The red arrows represent the vertical loading reaction force and the blue arrows the horizontal reaction force. The green arrow indicates the roll rotation.

2.3. Measurement procedure

The setup was tested with loads ranging from 1000 N to 25 000 N with 1000 N increments by adjusting the pressure in the pneumatic cylinders. For the graphite restrictor a supply pressure of 0.8 MPa was used for all the measurements. For each measurement point the data was recorded for 10 s.

The coupling between horizontal and vertical loading force was measured on a stationary roll at each of the load steps. Then the roll was rotated at 756 rpm, and the measurements were repeated. The mean value of the measurement was then used for the given increment. For each measurement the preload force, for both the top and bottom bearing, as well as the horizontal force was measured.

3. Results and discussion

3.1. Static coupling between vertical preload and horizontal force on a stationary roll

The preload force caused some horizontal force which can be seen in the horizontal load measurements at each load increment in Figure 3. This coupling could be caused by the bearings not being in the vertical centre line of the roll which causes a horizontal component when the load is applied. Additionally, the roll was not perfectly round which could cause some alignment error in the bearings.

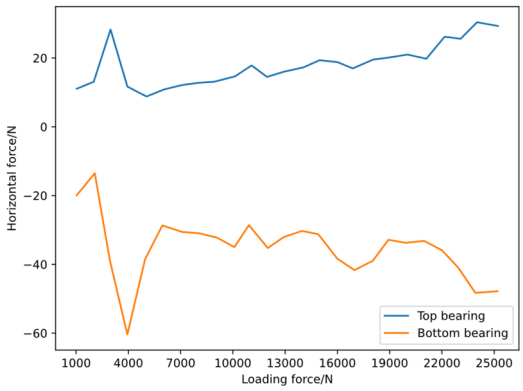

Figure 3. Coupling between the vertical preload force and the measured horizontal force for each force increment from 1 000 N to 25 000 N.

3.2. Horizontal force with rotating nip roll

The measurement result of the horizontal force with varying vertical loading force is presented in Figure 4. The horizontal force was relatively steady up to a loading force of 15 000 N for the top bearing and 19 000 N for the bottom bearing was reached. Further increasing the load, the horizontal force increases for both bearings. Maximum load of 20 000 N was reached when the bearings made contact with the roll. This was presumably caused by the overloading of the bearings due to the imperfect opposing surface of the roll. The inside of the roll was not ground after previous destructive testing where the load on the bearing was increased until a bearing failure. This could have a negative impact on the load carrying capacity of the bearings as the gap between the bearing and the opposing roll surface is not consistent across the bearing surface.

The measured horizontal force indicates low level of friction. The negative horizontal load values are presumably caused by the coupling of the vertical load to the horizontal force measurement.

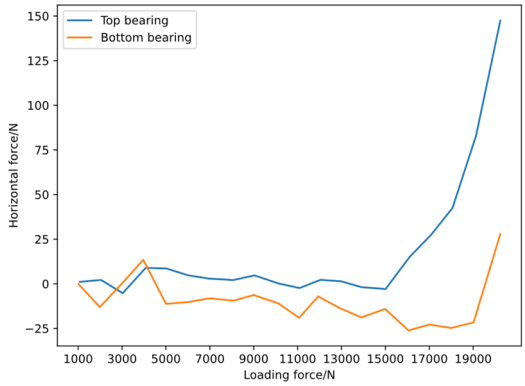

Figure 4. The horizontal force as a function of the loading force for both the top and bottom bearing.

4. Conclusions

The developed preload mechanism improved the maximum force by eliminating leakage. The loading mechanism was able to produce a larger loading force while maintaining alignment with the inner surface of the roll. The horizontal load measurement results indicate low level of friction. However, the coupling of applied vertical load to the horizontal load measurements suggest further research is required.

The premature failure of the bearings was likely caused by the damaged surface of the roll. By resurfacing the inside of the roll, the bearings could be able to withstand even greater loads without contact.

5. Acknowledgements

The research was funded by Business Finland (Better bearing, seal and vibration technology, grant number 1740/31/2025).

References

[1] Enerdata 2024 Finland energy report. URL: https://www.enerdata.net/estore/country-profiles/finland.html.
[2] C. Stenqvist, J. Nilsson, K. Ericsson. G. Modig 2011 Energy management in Swedish pulp and paper industry-the daily grind that matters
[3] L. Vogel, M. Neumann, S. Linz 2023 Calculation and development of the new production index for energy-intensive industrial branches
[4] Valmet 2019 Significant energy savings with oil viscosity upgrade
[5] L. Harding 2025 Porous aerostatic bearings for paper machine roll deflection compensation, Master's thesis, Aalto University
[6] J. Majuri 2023 Robust aerostatic bearing for large rotor, Master's thesis, Aalto University
[7] Gao Q, Chen W, Lu L, Huo D, Cheng K 2019 Aerostatic bearings design and analysis with the application to precision engineering: State-of-the-art and future perspectives *Tribology International* 135 pp 1-17

euspen's 26th International Conference & Exhibition, Krakow, PL, June 2026
www.euspen.eu

Control system modeling for a micro machining spindle with an active magnetic bearing actuator

Felix Zell[1], Maximilian Vierling[1], Jan C. Aurich[1]

[1]*University of Kaiserslautern-Landau, Institute for Manufacturing Technology and Production Systems*

felix.zell@rptu.de

Abstract

In micro machining, achieving high surface quality and extending tool life requires minimizing spindle vibrations across a wide speed range. Air bearing spindles, commonly used for their high precision, lack active control capabilities and are therefore unable to compensate speed-dependent excitations, such as unbalance or cutting forces, and ambient disturbances. Active magnetic bearing spindles provide active vibration control but are rarely used in micro machining due to their complexity and cost. Combining an air bearing spindle with a single active magnetic bearing offers a practical solution to achieve vibration suppression with reduced system complexity.

This paper presents a model of a closed-loop control system for such a hybrid spindle concept that combines an air bearing with one active magnetic bearing. The air bearing stiffness and damping coefficients and the electromagnetic bearing forces are calculated via finite element simulations prior to use in the control loop. They are implemented in the control system via lookup tables to enable realistic system behavior with low computational costs. The system dynamics (e.g. the rotor movement) are computed as functions of the air bearing forces, the electromagnetic force, the motor torque and the unbalance forces.

The vibration response of the spindle is analyzed for operating speeds between 25 000 min^{-1} and 125 000 min^{-1}. The results show that the closed-loop control system can significantly suppress vibrations up to 60 000 min^{-1}, while at higher speeds the system remains stable without notable damping.

These findings demonstrate the potential of hybrid spindle systems to improve vibration performance in micro machining applications and provide a modeling framework for further development of advanced control strategies.

Micro machining, Control, Magnetic bearing, Mechatronic

1. Introduction

Achieving high surface quality in micro milling requires precision spindles, as even minor vibrations can compromise dimensional accuracy and tool life [1, 2]. Due to the small tool diameters, very high spindle speeds are needed to ensure sufficient cutting speeds. At the same time, the undeformed chip thickness is extremely small, which makes the process highly sensitive to dynamic effects. Spindle vibrations, tool run-out, and dynamic compliance are among the dominant limiting factors for surface quality, dimensional accuracy, and tool life in micro milling [1].

For micro machining applications, air bearing spindles are widely used due to their low friction, high rotational accuracy, and suitability for compact machine tools [3]. However, air bearing spindles are inherently passive systems and therefore highly sensitive to disturbances such as rotor unbalance, air supply pressure fluctuations, and electromagnetic motor forces. Sun et al. [4] demonstrated that such disturbances cause periodic spindle vibrations that transfer to the machined surface, resulting in waviness and lower surface quality.

Active magnetic bearings enable the active compensation of disturbing forces by controlling rotor position, stiffness, and damping in real time. Their potential for vibration suppression and stability enhancement in high-speed spindles for micro machining has been demonstrated by Kimman et al. [5].

A less complex and cheaper alternative is the combination of air bearings with a single active magnetic bearing in a hybrid spindle concept. Jang et al. [6] showed that such a hybrid aerostatic bearing–rotor system allows a significant increase in the maximum stable rotational speed up to 35 000 min^{-1} by actively suppressing self-excited whirl and pneumatic-hammer instabilities.

These studies highlight the potential of active magnetic bearing spindles for micro machining and research efforts towards hybrid spindle systems for high speed applications. However, a comprehensive model of hybrid spindles for micro machining, that accounts for nonlinearities and small geometric dimensions, is not yet available. Such a model must incorporate realistic air bearing characteristics, magnetic bearing forces, rotor unbalance, motor torque, and speed-dependent system dynamics to achieve high simulation accuracy.

This paper presents a closed-loop control system model for a hybrid micro machining spindle combining an air bearing spindle with a single active magnetic bearing actuator. The air bearing stiffness and damping as well as the electromagnetic bearing forces are obtained from finite element simulations and implemented using lookup tables for computational efficiency. The rotor dynamics are simulated as a function of air bearing forces, electromagnetic control forces, motor torque, and unbalance excitation. The vibration behavior is analyzed for rotational speeds between 25 000 min^{-1} and 125 000 min^{-1}, demonstrating the vibration suppression capability and stability of the hybrid concept over a wide operating range.

2. Methods

The model of the closed-loop control system of the hybrid spindle is set up as a time-dependent model with three degrees of freedom (positions x and y and angle about the z-axis φ) in MATLAB[1] Simulink R2024b – see figure 1. Two radial aerostatic bearings in addition of one radial magnetic bearing make up the hybrid spindle. The three corresponding equations of motions for the rotordynamics define the plant of the closed-loop system with the rotor mass m , the rotor eccentricity ε the rotor's moment of inertia about the z-axis J, the rotor positions, velocities and accelerations $x, y, \dot{x}, \dot{y}, \ddot{x}, \ddot{y}$, the rotational angle, velocity and acceleration $\varphi, \dot{\varphi}, \ddot{\varphi}$, the magnetic bearing forces $F_{MB,x}$ and $F_{MB,y}$, the air bearing forces $F_{AB,x}$ and $F_{AB,y}$ and the motor torque M:

$$m\ddot{x} = F_{MB,x} - F_{AB,x} + m \cdot \varepsilon \cdot \dot{\varphi}^2 \cdot \cos\varphi \quad (1)$$

$$m\ddot{y} = F_{MB,y} - F_{AB,y} + m \cdot \varepsilon \cdot \dot{\varphi}^2 \cdot \sin\varphi \quad (2)$$

$$J\ddot{\varphi} = M + (y + \varepsilon \cdot \sin\varphi) \cdot \left(F_{MB,x} - F_{AB,x}\right) + (x + \varepsilon \cdot \cos\varphi) \cdot \left(-F_{MB,y} + F_{AB,y}\right) \quad (3)$$

The air bearing forces and the magnetic bearing forces are computed numerically before implementing them into the control loop model via lookup tables. This ensures realistic system behavior with low computational cost.

2.1. Calculation of air bearing forces

The air bearing forces of the investigated aerostatic air bearing spindle can be calculated based on their damping and stiffness coefficients c_{ij} and k_{ij} and the instantaneous positions and velocities $(x, \dot{x}, y, \dot{y})$:

$$F_{AB,x} = c_{xx} \cdot \dot{x} + c_{xy} \cdot \dot{y} + k_{xx} \cdot x + k_{xy} \cdot y \quad (4)$$

$$F_{AB,y} = -c_{xy} \cdot \dot{x} + c_{xx} \cdot \dot{y} - k_{xy} \cdot x + k_{xx} \cdot y \quad (5)$$

The damping and stiffness coefficients are a function of the spindle speed and are calculated numerically. We used the precision air bearing simulator PABS, which is a 2D fluid dynamics simulation tool developed at our institute [7] based on the thin-film theory to simulate the two radial air bearings separatly. The resulting damping and stiffness coefficients are added for implementation in the control model. The inputs for the simulation and the resultant air bearing coefficients are given in table 1 and 2 respectively:

Table 1. Inputs for air bearing coefficient calculation

Parameter	Bearing 1	Bearing 2	Unit
air bearing gap in	18.5	16	10^{-6} m
number of nozzles	8	8	-
nozzle diameter in	0.035	0.035	10^{-3} m
supply air pressure in	6	6	10^5 N/m²
bearing length in	34.4	28.2	10^{-3} m
bearing diameter in	20.7	20.7	10^{-3} m
discharge coefficient c_d	1	1	-
relative eccentricity	0.1	0.1	-

Table 2. Resultant damping and stiffness coefficients

Spindle speed	Direct stiffness	Cross-coupled stiffness	Direct damping	Cross-coupled damping
n in min^{-1}	k_{xx} in $\frac{MN}{m}$	k_{xy} in $\frac{MN}{m}$	c_{xx} in $\frac{kNs}{m}$	c_{xy} in $\frac{kNs}{m}$
1 500	4.540	0.194	0.769	-0.169
25 000	7.246	1.273	1.633	-0.738
50 000	9.919	0.088	0.922	0.052
75 000	11.582	-0.739	0.595	0.212
100 000	12.725	-1.151	0.412	0.162
125 000	13.542	-1.335	0.300	0.069

These damping and stiffness coefficients are implemented in the control loop via 1D lookup tables.

2.2. Calculation of magnetic bearing forces

The magnetic bearing forces are calculated in a three dimensional magnetostatic finite element (FE) simulation using ANSYS[1] Mechanical 2021R2. The parameters of the simulated heteropolar 4 pole-pair active magnetic bearing with differential driving scheme are given in table 3. For detailed information on the FE-model setup we refer to [8].

Table 3. Simulation input data

Parameter	Value	Unit
magnetic bearing gap s_0	0.3	10^{-3} m
bias current i_0	3	A
maximum control current i_c	±2.5	A
coil height	3	10^{-3} m
coil length	10.6	10^{-3} m
coil width	6.1	10^{-3} m
number of coil windings	50	-
inner stator diameter	16	10^{-3} m
outer stator diameter	30.2	10^{-3} m
saturation flux density stator	1.55*	T

* magnetic properties implemented as non-linear BH-curve

Each simulation run calculates the magnetic bearing forces for a given rotor position in x and y for 121 combinations of control currents i_{cx}, i_{cy} in the range of -2.5 A to +2.5 A with a step size of 0.5 A. The results for the magnetic bearing forces $F_{MB,x}$ and

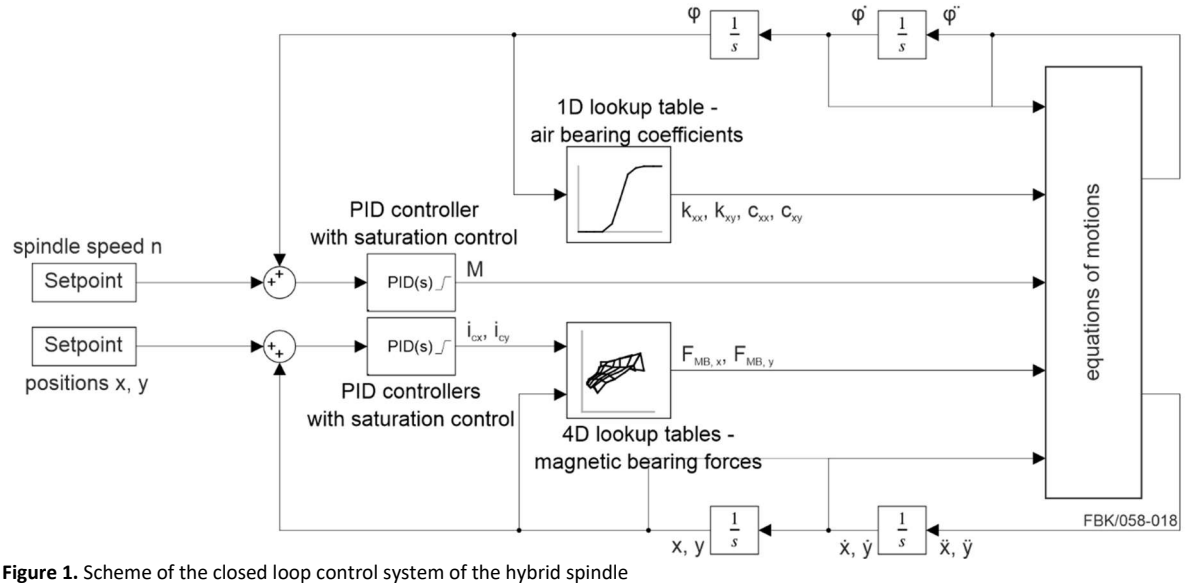

Figure 1. Scheme of the closed loop control system of the hybrid spindle

$F_{MB,y}$ are gathered in 4D lookup tables for implementation in the control loop. There the current rotor position in x and y combined with the currents i_x and i_y are used to extract the corresponding magnetic bearing force from the lookup table.

2.3. Control system simulation

The control system is set up to enable setpoint tracking of the rotor position x, y and the rotational velocity $\dot{\varphi}$ – see figure 1. For the position control the instantaneos difference of the rotor position from the setpoint is fed into single input, single output proportional-integral-derivative (PID) controllers to determine the necessary control currents i_c. Together with the current rotor position these four signals are used to evaluate the corresponding magnetic bearing forces from the 4D lookup tables. For the air bearing forces the damping and stiffness coeffecients are evaluated from the 1D lookup tables based on the current rotational velocity. The magnetic bearing forces, the air bearing coeffecients and the current positions and velocities $x, y, \dot{x}, \dot{y}$ are used to solve equations of motion for the updated accelerations $\ddot{x}, \ddot{y}$. Integrating these twice provide the system with the updated velocities and positions $\dot{x}, \dot{y}$ and x, y, respectively. For control of the rotational velocity, the instantaneous difference from the setpoint value is fed into a single input, single output PID-controller with saturation control to determine the necessary motor torque. This motor torque together with the current bearing forces, rotor positons and velocities is used to solve the equation of motion (3) for the updated rotational acceleration $\ddot{\varphi}$ and in turn the rotational velocity $\dot{\varphi}$. The controller parameters for the rotor position controllers are optimized using the automated MATLAB Simulink 'PID Tuner App' based on the step response of the linearized plant. An overview of input parameters is given in table 4.

Table 4. Control system input data

Parameter	Value	Unit
step size - fixed	$1{\cdot}10^{-6}$	s
solver	ode3	-
simulation time	0.2	s
rotor mass m	0.315	kg
rotor's moment of inertia about z-axis J	$2.1{\cdot}10^{-5}$	kgm²
rotor eccentricity ε	$1.5{\cdot}10^{-6}$	m
maximum motor torque M	1.5	Nm

3. Results

To evaluate the potential of the hybrid spindle concept, two different load scenarios are investigated for the operating range of the air bearing spindle (spindle speeds from 25 000 min^{-1} to 125 000 min^{-1}).

I. Actuator inactive and position setpoints set to 0 at constant spindle speeds. These results are used to validate the system dynamics by comparing them to measured vibration amplitudes of the uncontrolled air bearing spindle [9].
II. Actuator active and position setpoints set to 0 at constant spindle speeds. This scenario corresponds to a free spinning rotor with active vibration control.

The analysis of the hybrid spindle performance is based on a comparison of the simulated responses of the uncontrolled (I) and controlled (II) systems.

The combined results of scenarios I and II are shown as peak-to-peak values of the rotor amplitudes as a function of spindle speeds in figure 2. Since the rotor dynamics, as well as the air and magnetic bearing forces used as input variables, show equivalent results in the x- and y-directions, the results are discussed using the x-direction only. The peak-to-peak values for the experimental data rise from 2.7 µm to 4.4 µm at 30 000 min^{-1} and 125 000 min^{-1}, respectively. A local maximum was found at 80 000 min^{-1} and 3.9 µm. However, the simulated vibration amplitudes without vibration control reach a maximum of 13.3 µm at 35 000 min^{-1}, most likely due to matching a natural frequency. Subsequently the vibration amplitudes drop to 4 µm at 65 000 min^{-1} and keep decreasing to 3.2 µm at 125 000 min^{-1}. Overall the simulated rotor dynamics closely match the real rotor dynamics in the range of 65 000 min^{-1} to 110 000 min^{-1} and overestimate the vibration amplitudes at lower spindle speeds.

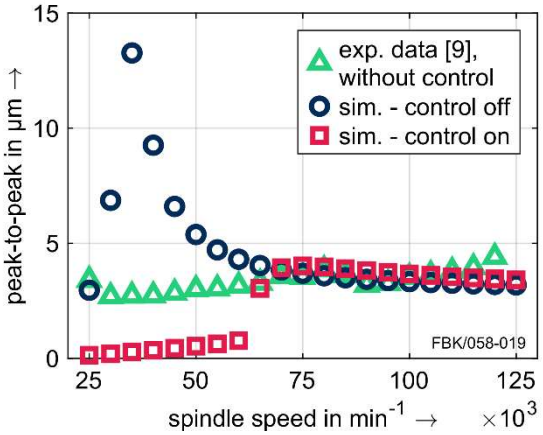

Figure 2. Comparison of peak-to-peak values of rotor vibration amplitudes as a function of the spindle speed for different scenarios

The simulated vibration amplitudes with active control exhibit two-part behavior with a transition range at approximately 65 000 min^{-1}. At low speeds, the peak-to-peak values range from 0.13 µm to 0.60 µm; at higher speeds, they closely match the vibration amplitudes of the uncontrolled spindle. In the transition range, the vibration amplitudes increase sharply, from 0.60 µm to 4 µm with a 10 000 min^{-1} speed increase.

A detailed analysis of the vibration amplitudes with and without enabled control system is shown in figure 3.

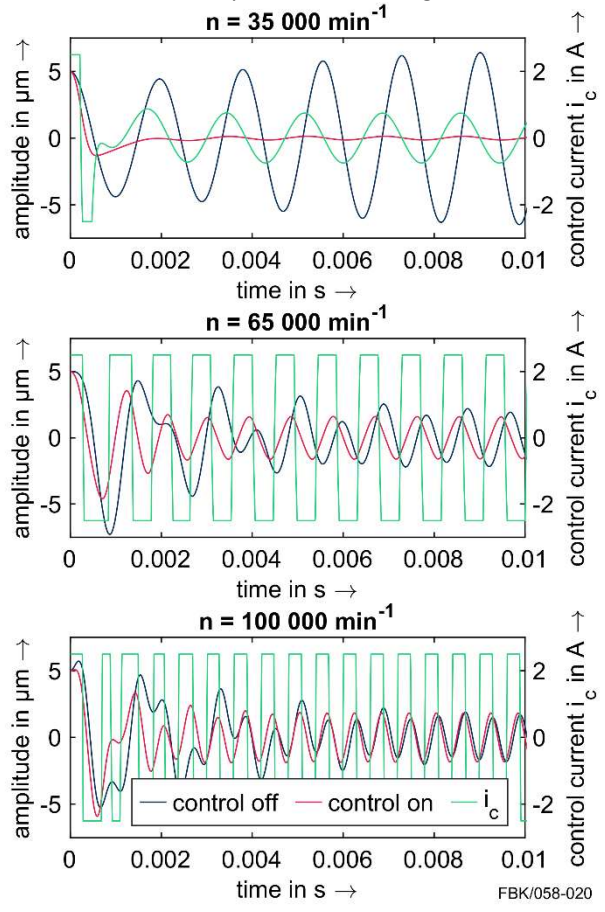

Figure 3. Comparison of the simulated vibration amplitudes for three spindle speeds

For the low spindle speed range – illustrated for n = 35 000 min^{-1} – the vibration control is able to compensate the rotor vibrations within the first revolution effectively by 98 %. The control current amplitude required for this compensation is approximately 0.75 A. For the high spindle speed range – illustrated for n = 100 000 min^{-1} – almost no vibration compensation is registered. After a brief settling phase that takes place over a few revolutions, the vibration amplitudes demonstrate almost identical curves. The control currents i_c fluctuate between the saturation limits of ± 2.5 A with the spindle speed. In case of the transition range – n = 65 000 min^{-1} – the vibration amplitudes are only slightly compensated. The corresponding control currents i_c already reach the compensation limit of ± 2.5 A. A notable difference compared to the high-speed behavior is the greater phase shift between unregulated and regulated vibration amplitudes.

4. Discussion

The results for the peak-to-peak values of the rotor vibrations for the whole operational spindle speed range confirmed that the chosen approach is capable of modeling the rotordynamics. Calculating the magnetic bearing forces and the air bearing forces numerically with finite element simulations enables accurate representation of the real system behavior. The low computational costs necessary for real-time control are ensured by implementing these results via lookup tables in the closed-loop control model. The experimental rotor vibration data is in close agreement with the simulated values. The larger deviation at lower spindle speeds, where the spindle speeds match a natural frequency in the simulation, overestimate the actual system response. Therefore, any conclusions drawn from this system model will lead to a conservative system design.

The detailed analysis of the system behavior in the three distinct speed ranges (figure 3) emphasizes the possibilities and limitations of the current control setup. Up until 60 000 min^{-1} the rotor vibrations can be supressed effectively by at least 75 %. In the following transition range the control currents reach their saturation limit. The induced magnetic forces are not high enough to compensate the rising unbalance forces and force the rotor into the setpoint position with just the feedback control. However, the imposed phase shift between the free and controlled rotor movement suggest that the control forces, i.e. magnetic forces, can significantly influence the rotor movement. Due to the nature of the feedback control environment the control system constantly trails the system response and imposes the phase shift. With advanced control schemes, e.g. feedforward approaches, the achievable control forces could be sufficient to also achieve substantial vibration suppression. Above 70 000 min^{-1} there is basically no change detectable in the system response despite the magnetic actuator forces.

5. Conclusion and Outlook

In this paper, we introduced a control system model for a micro machining spindle with an active magnetic bearing actuator. The simulation of the rotor dynamics is represented through the equations of motion for a lumped mass approach in three dimensions (positions x and y, angle about the z-axis φ). The magnetic bearing forces and the constant for the calculation of the air bearing forces (stiffness and damping coefficients) are determined numerically through three dimensional magnetostatic and two dimensional fluid dynamics finite element simulations. The results of these computationally intensive simulations is implemented via lookup tables in the closed-loop control system model setup in MATLAB Simulink.

A comparison of the control system response without active control and experimental rotor vibration data proved the validity of the model. The subsequent comparison with the closed-loop response (magnetic bearing actuator activated) proved the damping capabilities of the hybrid spindle setup: With the current setup, the system was capable of significantly suppressing rotor vibrations up to 60 000 min^{-1}. At higher spindle speeds the damping capabilities are limited by the feedback control approach and the maximum magnetic forces. While the rotor vibrations can not be suppressed at higher spindle speeds, the system remains stable.

In future work two limitations will be addressed:

- The lumped mass approach does not represent the geometric design and positioning of bearing forces, imbalances and external loads. The model will be extended to five degrees of freedom. With the additional equations of motion for the angles about the x- and y-axis the model can account for tilting of the rotor.
- Instead of strict feedback control, more advanced control strategies (e.g. feedforward control schemes) will be employed to enhance the damping capabilities at higher spindle speeds and decrease the necessary control interventions as much as possible.

Acknowledgment

This research was funded by the Deutsche Forschungsgemeinschaft (DFG, German Research Foundation) – 491400446.

[1]Naming of specific manufacturers is done solely for the sake of completeness and does not necessarily imply an endorsement of the named companies nor that the products are necessarily the best for the purpose.

References

[1] Balázs B Z, Geier N, Takács M and Davim J P 2021 A review on micro-milling: recent advances and future trends *Int J Adv Manuf Technol* **112** 655–684

[2] O'Toole L, Kang C-W and Fang F-Z 2021 Precision micro-milling process: state of the art *Advances in manufacturing* **9** 173–205

[3] Harris P, Wintterer M, Jasper D, Linke B, Brecher C and Spence S 2020 Design and Development of a High Efficiency Air Turbine Spindle for Small-Part Machining *Int. J. of Precis. Eng. and Manuf.-Green Tech.* **7** 915–928

[4] Sun Y, Wu Q, Chen W, Luo X and Chen G 2021 Influence of Unbalanced Electromagnetic Force and Air Supply Pressure Fluctuation in Air Bearing Spindles on Machining Surface Topography *Int. J. Precis. Eng. Manuf.* **22** 1–12

[5] Kimman M H, Langen H H and Munnig Schmidt R H 2010 A miniature milling spindle with Active Magnetic Bearings *Mechatronics* **20** 224–235

[6] Jang H-D, Kim J, Han D-C, Jang D-Y and Ahn H-J 2014 Improvement of high-speed stability of an aerostatic bearing-rotor system using an active magnetic bearing *Int. J. Precis. Eng. Manuf.* **15** 2565–2572

[7] Müller C, Greco S, Kirsch B and Aurich J C 2017 A Finite Element Analysis of Air Bearings Applied in Compact Air Bearing Spindles *Procedia CIRP* **58** 607–612

[8] Lange A, Müller D, Kirsch B and Aurich J C 2021 Numerical analysis of magnetic bearings for micro machining applications *Proc. euspen's 21st International Conference & Exhibition* (Bedford, UK: euspen) **21** 247–250

[9] Zell F, Lange A, Kirsch B and Aurich J C 2024 Analysis of the vibration characteristics of an air bearing spindle to identify and control the magnitude of the radial run-out with an active magnetic bearing *Proc. euspen's 24th International Conference & Exhibition* (Bedford, UK: euspen) **24** 449–452

euspen's 26th International Conference & Exhibition, Krakow, PL, June 2026

www.euspen.eu

Parametric influence of gear surface and geometric features on dynamic performance

Himanshu Singh Maurya[1,*], Robert Tomkowski[1], Andreas Archenti[1]

[1]*Department of Production Engineering, KTH Royal Institute of Technology, Brinellvägen 68, 114 28 Stockholm, Sweden*

[*]*Corresponding author: hsmaurya@kth.se*

Abstract

Gears are the heart of mechanical powertrain systems used in diverse power transmission applications. Traditionally, gear design and validation have focused on static geometric measurements. However, a gear's dynamic performance is significantly impacted by its surface integrity and micro-geometric features introduced during manufacturing. These parameters, including surface roughness, waviness, profile deviations, and tolerances, influence transmission error, vibration noise, and load distribution, ultimately affecting the gear's fatigue life. This study presents a focused and concise overview, linking gear geometric parameters to dynamic performance. This shift aims to advance gear design beyond traditional static evaluation towards performance-driven strategies. This concise review synthesises findings from experimental studies, analytical models, and industrial practices to assess dynamic behaviour like noise, vibration, and harshness monitoring (NVH), as well as dynamic load-dependent testing. It also outlines future directions, including data-driven predictive models, real-time condition monitoring, and smart gear system integration.

Keywords: Gear; Surface integrity; Dynamic performance, Industrial applications.

1. Introduction

The gear systems operate under complex dynamic conditions such as variable loads, fluctuating speeds, and transient operating states. Their functional performance is not only governed by macro-geometry but also by the condition and quality of the tooth surface, where power transfer physically occurs. Vibration and noise measurement are known to contain valuable information about gear behaviour, allowing engineers to detect gross defects, misalignment, and certain irregularities [1,2]. Most research and industrial practices focus on defect detection rather than systematically linking specific gear parameters such as profile, lead, pitch, micro-geometry, surface roughness, and waviness to quantitative functional performance outcomes like vibration noise and load distribution [1,3].

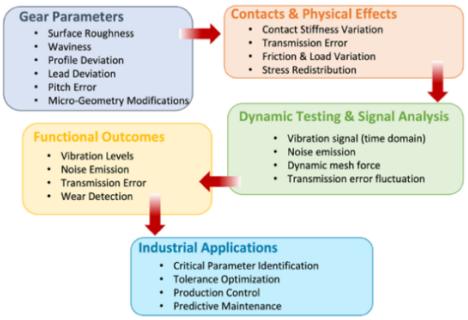

Figure 1. Integrated Framework Linking Gear Surface and Geometric Parameters to Dynamic Functional Performance and Industrial Decision-Making (own study).

However, there is still limited understanding of which parameters are more critical to dynamic behaviour, and the industry lacks a standardized method to use dynamic test data for design optimisation, production control, and tolerances refinement beyond simple pass/fail inspection. Addressing these gaps, this concise review aims to synthesise current knowledge on how surface and geometric features influence dynamic performance, highlight functional validation methods including Fast Fourier Transform (FFT)-based signal analysis, and provide insight to identify critical parameters, improve vibration and noise characteristics, optimise load distribution, and enable performance-driven design and production strategies. Fig. 1 presents an integrated framework that maps gear surface and geometric parameters to dynamic performance indicators, highlighting its potential to support performance-driven industrial design, tolerance optimization, and production control.

2. Surface and geometric features

Surface characteristics of a gear, such as roughness, waviness, and micro topography, play a significant role in the dynamic response of gear systems. Surface roughness contributes to local frictional excitation during tooth engagement, while waviness can induce local stiffness variations that can amplify vibration at specific frequencies [4]. Cheng et al. investigated the intimate connection between the contact surface properties and gear performance, demonstrating that both contact stiffness and damping decrease as surface roughness increases [5]. Gear NVH is highly sensitive to surface waviness, where even extremely small periodic deviations (0.1-1 μm) on the flanks can produce ghost frequencies [6]. Micro geometry modifications, including profile relief, lead crowning, and pitch adjustment, may control load distribution and minimise peak contact stresses. Variations in these parameters can directly influence the transmission error, modulate dynamic mesh stiffness, and excite vibration modes, which in turn affect noise generation and operational efficiency [4]. A conceptual mapping of gear surface and geometric parameters to functional outcomes reveals clear relationships between specific features and dynamic behaviour. Understanding these relationships allows engineers to prioritize design and manufacturing efforts on the most influential parameters, implement targeted quality control, and optimise operational performance. This functional perspective provides a

framework for production-driven decisions, ensuring that industrial gear systems meet performance criteria effectively and reliably.

3. Functional performance and dynamic response

Functional performance metrics, including vibrations, noise, and load distribution, provide critical insights into gear behaviour under operational conditions [2]. Condition monitoring of gear, specifically through vibration signal analysis, has emerged as an effective strategy for early fault detection and for reducing unexpected downtime. Transmission error represents the instantaneous deviation between the theoretical and actual angular displacement, a key indicator linking geometry and surface characteristics to dynamic response [6]. FFT-based signal analysis is widely used to identify dominant excitation frequencies and sidebands generated by deviations in microgeometry and surface quality. Functional validation may enable identification of which parameters influence the dynamic performances, and each tolerance may be relaxed without compromising NVH.

By prioritising functional performance over purely geometric compliance, industries can transition towards performance-driven design and production strategies. Furthermore, data-driven approaches such as machine learning models have demonstrated potential in predicting noise test outcomes based on measured manufacturing data. These models facilitate proactive management of gear NVH through predictive quality control [6].

4. Dynamic testing

Dynamic testing has proven to be a powerful approach for evaluating gear dynamic response beyond traditional static geometric measurements. Dynamic testing methods include accelerometers for high-speed vibration measurement, torque transducers, and strain gauges combined with FFT-based spectral analysis to quantify transmission error, vibration amplitude, and noise levels [7]. Furthermore, dynamic testing is commonly employed to detect gear wear as progressive surface degradation alters contact conditions and modulated mesh stiffness.

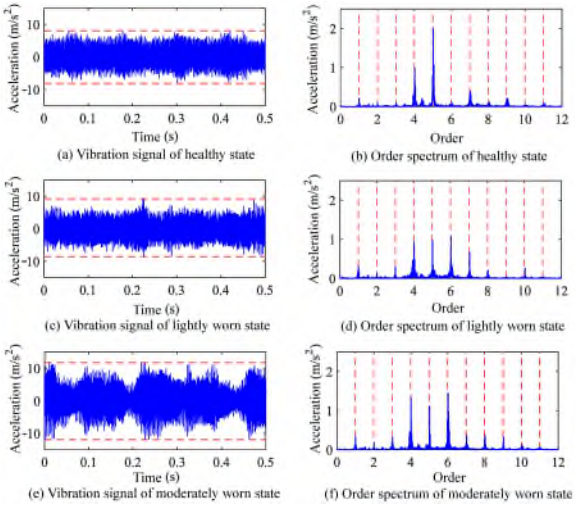

Figure 2. Gear vibration signals and corresponding order spectra at an operating condition for healthy, lightly worn, and moderately worn gear conditions [7].

This enables the identification of early wear patterns, the prediction of maintenance requirements, and the validation of design and micro-geometry modifications (Figure 2). Despite these benefits, such functional testing approaches remain primarily research-focused and are not yet standardized in industrial production, representing a significant opportunity for integrating performance-driven evaluation into manufacturing workflow.

5. Industrial implications and production control

Mapping surface and geometric parameters to functional performance has direct industrial relevance. Identifying parameters that most significantly affect vibration, and noise may enable targeted improvements in micro-geometry, surface finishing, and manufacturing processes, optimising production efficiency while minimising cost. Functional validation will allow selective relaxation of certain geometric tolerances without compromising operational performance, provide greater design freedom, and reduce the need for over-precision. Integration of dynamic test data into production and quality control protocols supports predictive maintenance, enhances consistency of gear behaviour, and reduces unplanned downtime. By linking parametric knowledge to functional outcomes, industries can achieve better gear dynamic performance and, overall, more reliable and efficient gear systems. Mitigating gear NVH demands excellence in both design and manufacturing, as literature consistently shows that achieving optimal performance requires the integration of both rather than relying on them in isolation.

6. Conclusion

Surface and geometric features, including roughness, waviness, and microgeometry, significantly affect gear dynamic performance, influencing vibration, noise, and load distribution. Function performance evaluation through dynamic testing and FFT-based analysis enables systematic identification of critical parameters, offering opportunities for tolerance optimisation, wear monitoring, and design improvement. Incorporating functional validation into industrial practice supports performance-driven design, production control, predictive maintenance, and enhanced quality assurance. By moving beyond traditional static measurements, engineers and researchers can develop the most robust, efficient, and sustainable gear systems, ensuring operational reliability and optimising manufacturing efficiency.

References

[1] Zhang R, Gu F, Mansaf H, Wang T and Ball A D 2017 Gear wear monitoring by modulation signal bispectrum based on motor current signal analysis *Mech. Syst. Signal Process.* **94** 202–13

[2] Feng K, Ji J C, Ni Q and Beer M 2023 A review of vibration-based gear wear monitoring and prediction techniques *Mech. Syst. Signal Process.* **182**

[3] Li Z, Xiao H, Tang Y, Liang G, Wang L and Yang J 2025 A deterministic model of surface profile degradation for evaluating time-varying mesh stiffness and dynamic responses of spur gear considering tooth surface wear evolution *Mech. Syst. Signal Process.* **225**

[4] Chung W J, Park Y J, Choi C and Kim S C 2023 Effects of manufacturing errors of gear macro-geometry on gear performance *Sci. Rep.* **13**

[5] Cheng G, Ma J, Li J, Sun K, Wang K and Wang Y 2024 Study on the Dynamic Characteristics of Gears Considering Surface Topography in a Mixed Lubrication State *Lubricants* **12**

[6] Horvath K and Feszty D 2025 Surface Waviness of EV Gears and NVH Effects—A Comprehensive Review *World Electric Vehicle Journal* **16**

[7] Zhao Z, Zhang T, Xu K, Tang J and Yang Y 2025 Integrated Explainable Diagnosis of Gear Wear Faults Based on Dynamic Modeling and Data-Driven Representation *Sensors* **25**

euspen's 26th International Conference & Exhibition, Krakow, PL, June 2026
www.euspen.eu

FEA-Informed Compensation of Thermal Volumetric Effects on Machine Structure

Daniel Divíšek [1], Martin Mareš [1], Otakar Horejš [1], Matěj Sulitka [1]

[1] *Czech Technical University in Prague, Faculty of Mechanical Engineering, Department of Production Machines and Equipment, RCMT, Horská 3, 128 00 Prague, Czech Republic*

martin.mares@rcmt.cvut.cz

Abstract

Thermally induced errors are a dominant source of machine tool (MT) inaccuracy and are often among the most difficult to mitigate. Software compensation of thermally induced displacements at the tool contact point (TCP) is therefore widely used; however, an extensive set of measured data is typically required to calibrate such models. When a compensation model is intended to be valid across the entire workspace of a large machine tool (such as horizontal milling centre; the target machine in this research), a dense grid of measurement configurations is often needed, making experimental analysis costly and time-consuming. This paper builds on previous research in which a whole-machine finite element analysis (FEA) model was used to identify the spatial dependence of thermal volumetric errors on machine-axis configuration and to select a small set of critical axis positions for targeted experiments. The main contribution of the present paper is the development of a continuously re-tunable, spatially dependent thermal error compensation model trained only on data from these FEA-informed sparse experimental setups. The proposed concept reduces the number of required experiments, thereby minimising machine downtime for thermal characterisation, reducing energy consumption, and lowering the overall cost of developing robust thermal error compensation models. The effectiveness of the approach is demonstrated on experimental data obtained in an additional, generally selected axis configuration used for validation.

Machine tool, Finite element analysis (FEA), Volumetric error, Thermal error compensation

1. Introduction

Machine tools (MT) are loaded during operation by several physical phenomena that cause structural deformations, such as vibrations, chatter, gravitational effects, and thermal loads. Geometric errors resulting from non-stationary thermal phenomena manifest as deviations between the desired and the actual relative motion of the tool and the workpiece. Thermal errors are reported to account for 40–70% of the total MT inaccuracy [1]. Consequently, reducing thermally induced errors has long been a key objective for MT designers and control engineers.

Mitigation approaches can be broadly divided into three groups [2]:

- design measures that reduce sensitivity to heat flux (e.g., thermally symmetric structures, thermal insulation),
- control of the machine and environmental temperatures (e.g., cooling systems and environmental control), and
- thermal error compensation in the control system.

This paper presents an FEA-informed compensation strategy (Figure 1) that combines: 1\ analysis of the thermal behaviour of a horizontal milling centre (target machine) using a spatially reconfigurable finite element model (FEM) to identify the most influential machine-axis configurations, 2\ targeted experiments performed only in these critical configurations, and 3\ development of a continuously tunable volumetric compensation model based on thermal transfer functions (TTF) formulated in a state-space representation.

The proposed concept reduces the number of measurement configurations required during the experimental phase, thereby shortening machine occupancy time and lowering the overall cost of thermomechanical characterisation, while enabling robust compensation of spatially dependent thermal errors particularly relevant for heavy-duty machine tools. The effectiveness of the concept is demonstrated by compensating thermally induced displacements in the *Y* direction of the target machine.

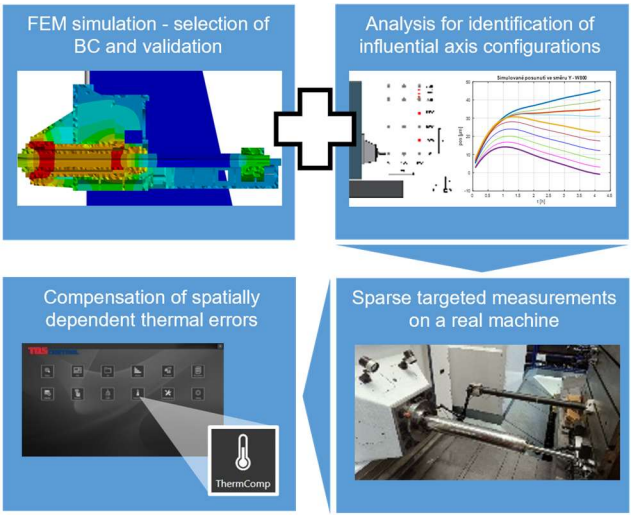

Figure 1. Value chain of the FEA-informed compensation concept

2. Simulation, analysis and measurement

In the preceding study [3], the thermal behaviour of the target machine (Figure 2) was analysed using a whole-machine FEA model with the aim of predicting thermally induced volumetric displacements at the TCP across the workspace without extensive experimental campaigns. The FEA model included the main structural components; drives were represented by lumped masses and/or equivalent springs. Spindle bearings

were modelled using equivalent stiffness and thermal boundary conditions (BC) derived from bearing losses. Forced and free convection, as well as radiation, were applied to external surfaces.

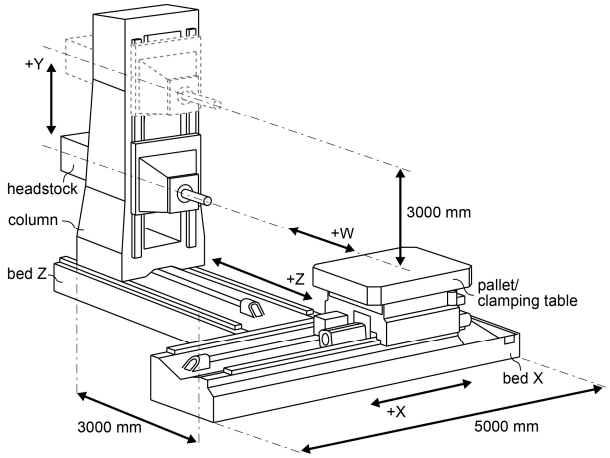

Figure 2. Kinematic description of target machine - horizontal milling centre with a moving table

Simulations were performed for a grid of 18 positions in the *YZ* plane under a constant thermal load corresponding to spindle rotation at 4000 rpm. Displacement at TCP was evaluated after four hours of loading, i.e., after approximate thermal stabilisation. The results showed that the largest absolute thermal error occurs in the *Z* direction, but with only minor variation across the *Y*-axis travel. In contrast, displacements in the *Y* direction showed a strong dependence on *Y*-axis position and exhibited different time trends in different parts of the *Y*-axis stroke. The influence of the *W*-axis (spindle extension) was found to be linear.

Based on the simulated displacement fields, five representative measurement configurations were selected to capture the most critical thermal trends, reducing the number of experimental configurations from 18 to 5 (Figure 3). Subsequent measurements at these configurations — under the same spindle load conditions and in a stable ambient environment (the target machine was located in the manufacturer's prototype & testing hall) — confirmed that, although the absolute deformation magnitudes differ between the FEA model and the experiments, the FEA model reproduces the qualitative trends sufficiently well for the purpose of experiment design.

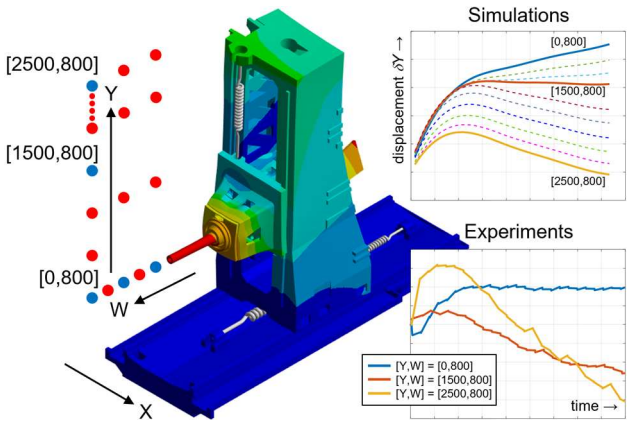

Figure 3. Identified measurement configurations (blue dots), FEA results (upper chart), and experimental verification of *Y*-direction displacements for three configurations along the *Y*-axis: [Y,W] = [0,800], [1500,800], and [2500,800] (lower chart)

The study [3] further indicated that a single global compensation function is inadequate; instead, the workspace should be partitioned into zones, each described by its own sub-model. The present paper builds on these findings by developing and evaluating a spatially dependent compensation model and an interpolation strategy that enables continuous compensation across the workspace.

3. Compensation strategy

The compensation strategy proposed in this paper focuses on thermally induced displacements in the *Y* direction (δY) caused by spindle rotation (only heating phases; left part of Figure 4). As shown in Figure 3, δY depends strongly on *Y*-axis position and exhibits varying time responses along the *Y*-axis stroke. In contrast, the selected model input — measured temperature difference at the rear spindle bearings — shows a similar time evolution in all calibration experiments (right part of Figure 4). This supports the use of a common thermal excitation signal combined with spatially dependent sub-models.

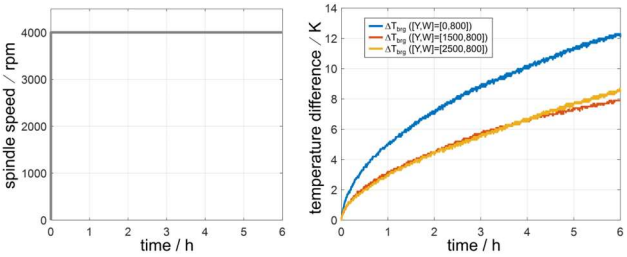

Figure 4. Spindle speed profile (left) and measured temperature difference at spindle rear bearings (right) during FEA-informed calibration experiments

As suggested by [3], the workspace is divided into zones described by locally calibrated sub-models. A continuous compensation function over the full stroke is then obtained by interpolating between these sub-models.

3.1. Sub-model identification in critical axis configurations

System identification theory is used to construct dynamic thermal error compensation sub-models for the FEA-identified critical axis configurations. The thermal transfer function (TTF) approach reflects basic heat transfer principles, which makes calibration of empirical parameters straightforward. The applicability of TTF-based compensation has been verified on various MT structures, equipment, and technologies in [4] and [5]. In discrete form, a TTF describes the relationship between excitation (temperature) and response (displacement):

$$y(t) = \varepsilon.u(t) + e(t) = \frac{a_n z^{-n} + \cdots + a_1 z^{-1} + a_0 z^0}{b_m z^{-m} + \cdots + b_1 z^{-1} + b_0 z^0} u(t) + e(t), \quad (1)$$

where *u(t)* is the input and *y(t)* is the output vector, ε represents the TTF in the time domain, *e(t)* is a disturbance term (further neglected), *z* is the complex variable, *n* is the numerator order, *m* is the denominator order ($m > n$), and $a_{0:n}$ and $b_{0:m}$ are calibration coefficients. The difference equation form in the time domain is given in:

$$y(k) = \frac{u(k-n)a_n + \cdots + u(k-1)a_1 + u(k)a_0 - y(k-m)b_m - \cdots - y(k-1)b_1}{b_0}, \quad (2)$$

where *k–n* (*k–m*) represents an *n*-step (*m*-step) delay at the sampling frequency. Linear parametric ARX (autoregressive with exogenous input) structures are identified in MATLAB® [6].

The basis of the compensation model is formed by three TTFs calibrated in the critical configurations [Y,W] = [0,800], [1500,800], and [2500,800]. The sub-models are expressed as:

$$\begin{aligned}\delta Y_{[0,800]} &= \Delta T_{brg} . \varepsilon_{[0,800]} \\ \delta Y_{[1500,800]} &= \Delta T_{brg} . \varepsilon_{[1500,800]} \\ \delta Y_{[2500,800]} &= \Delta T_{brg} . \varepsilon_{[2500,800]},\end{aligned} \tag{3}$$

where $\delta Y_{[0,800]:[2500,800]}$ are the model-predicted TCP displacements, ΔT_{brg} is the measured rear spindle bearing temperature difference, and $\varepsilon_{[0,800]:[2500,800]}$ are the TTFs representing the spindle thermal influence in the three calibration configurations. Figure 5 compares measured displacements (solid lines) and TTF predictions (dashed lines) for the calibration experiments; the residuals are shown in the right plot.

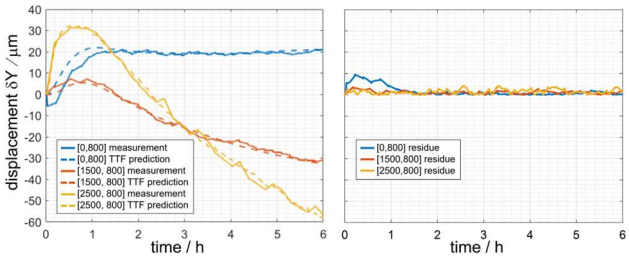

Figure 5. Measured and predicted (left) and residual (right) thermally induced *Y*-direction displacements during FEA-informed calibration experiments

Using the RMSE criterion, the sub-models reduce thermally induced displacement by 51%, 89%, and 93% for [Y,W] = [0,800], [1500,800], and [2500,800] configurations respectively, during the calibration experiments.

3.2. Spatially dependent compensation model (state-space interpolation)

To enable continuous compensation during motion along the Y-axis, the locally identified sub-models must be smoothly interpolated. A direct LPV (linear parameter-varying) formulation, where model parameters depend on the current *Y* position, may suffer from stability issues when parameters vary, even if each local model is stable [7]. To address this, interpolation is performed in state space [8], which preserves the internal dynamics and supports stable transitions between sub-models.

Therefore, each TTF sub-model in equation (3) is converted into the following state-space form:

$$\begin{aligned}\dot{x}(t) &= Ax(t) + Bu(t) \\ y(t) &= Cx(t) + Du(t),\end{aligned} \tag{4}$$

where $x(t)$ is the state vector, $\dot{x}(t)$ is the state derivative, $y(t)$ is the output, $u(t)$ is the input (control), and *A*, *B*, *C*, *D* are the system matrices. A detailed conversion procedure is given in [9].

Extension of the compensation model over the full *Y*-axis stroke is achieved using position-dependent weights. First, an inverse-distance value $v_{[Y,W]}$ from each calibration position is computed:

$$\begin{aligned}v_{[0,800]} &= |0 - Y_{actual}|^{-1} \\ v_{[1500,800]} &= |1500 - Y_{actual}|^{-1} \\ v_{[2500,800]} &= |2500 - Y_{actual}|^{-1},\end{aligned} \tag{5}$$

where Y_{actual} is the current *Y*-axis coordinate. Second, normalisation yields the weights $w_{[Y,W]}$ for each sub-model:

$$\begin{aligned}w_{[0,800]} &= \frac{v_{[0,800]}}{v_{[0,800]}+v_{[1500,800]}+v_{[2500,800]}} \\ w_{[1500,800]} &= \frac{v_{[1500,800]}}{v_{[0,800]}+v_{[1500,800]}+v_{[2500,800]}} \\ w_{[2500,800]} &= \frac{v_{[2500,800]}}{v_{[0,800]}+v_{[1500,800]}+v_{[2500,800]}},\end{aligned} \tag{6}$$

where the following applies:

$$w_{[0,800]} + w_{[1500,800]} + w_{[2500,800]} = 1. \tag{7}$$

The resulting volumetric compensation model in state-space form for an arbitrary *Y* position at full *W*-axis extension (W = 800 mm) is defined as a weighted combination of the sub-models:

$$\begin{aligned}\dot{x}(t) &= A_{[Y,800]}x(t) + B_{[Y,800]}u(t) \\ y(t) &= C_{[Y,800]}x(t) + D_{[Y,800]}u(t),\end{aligned} \tag{8}$$

where:

$$\begin{aligned}A_{[Y,800]} &= A_{[0,800]} \cdot w_{[0,800]} + A_{[1500,800]} \cdot w_{[1500,800]} + \\ &\quad + A_{[2500,800} \cdot w_{[2500,800]} \\ B_{[Y,800]} &= B_{[0,800]} \cdot w_{[0,800]} + B_{[1500,800]} \cdot w_{[1500,800]} + \\ &\quad + B_{[2500,800} \cdot w_{[2500,800]} \\ C_{[Y,800]} &= C_{[0,800]} \cdot w_{[0,800]} + C_{[1500,800]} \cdot w_{[1500,800]} + \\ &\quad + C_{[2500,800} \cdot w_{[2500,800]} \\ D_{[Y,800]} &= D_{[0,800]} \cdot w_{[0,800]} + D_{[1500,800]} \cdot w_{[1500,800]} + \\ &\quad + D_{[2500,800} \cdot w_{[2500,800]}\end{aligned} \tag{9}$$

and

$Y \in \langle 0{,}2500 \rangle$.

4. Concept verification

To verify the concept defined by equations (8) and (9), a validation point was selected in the *YW* plane corresponding to the axis configuration [Y,W] = [2100,200]. The location of this point within the workspace is schematically indicated by the purple dot in the left part of Figure 6.

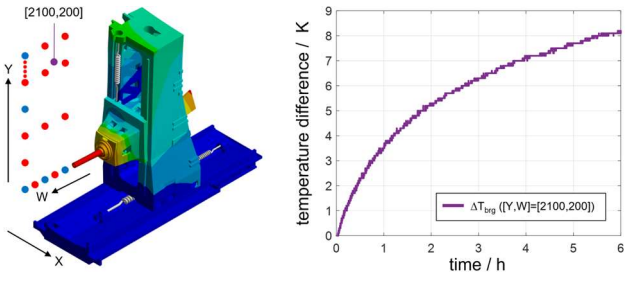

Figure 6. Visualisation of verification configuration [Y,W]=[2100,200] (left) and measured rear spindle bearing temperature difference during the verification experiment (right)

The TTF-based compensation model (equations (8) and (9)) is calibrated for *W* = 800 mm and reliably approximates thermally induced displacements along the *Y*-axis stroke at this full *W*-axis extension. The FEA results in [3] further indicate a linear dependence of the thermomechanical response along the *W*-axis stroke. Based on this assumption, an FEA-derived scaling factor was determined to account for the changed *W* position (*W* = 200 mm). The factor equals 0.7 and is applied to the model

output to approximate measured displacements in the validation configuration [Y,W] = [2100,200], without additional calibration experiments.

The validation experiment was performed under conditions comparable to the calibration tests: the spindle speed followed the profile shown in Figure 4 (left), and the measured variation of the model input temperature during the validation test is shown in Figure 6 (right).

Figure 7 shows the measured displacements (solid line) and the model predictions (dashed line) for the validation experiment; residuals are shown in the right plot. The residual corresponds to the remaining thermal error after compensation by the spatial model (equations (8) and (9)) with the additional *W*-axis scaling factor of 0.7.for the extension of the *W*-axis corresponding to 200 mm.

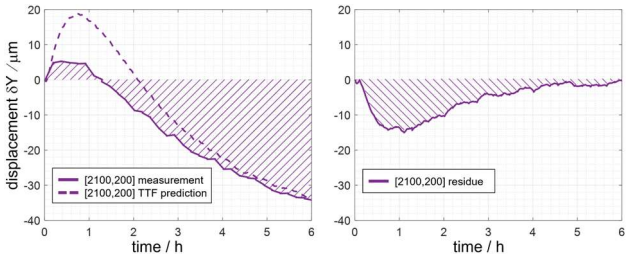

Figure 7. Measured and predicted (left) and residual (right) thermally induced *Y*-direction displacements during the verification experiment

Using the RMSE criterion, the proposed compensation model achieves a 52% reduction of thermally induced *Y*-direction displacement in the general verification configuration [Y,W] = [2100,200].

5. Conclusions

This paper presented an FEA-informed workflow for efficient identification and compensation of spatially dependent thermal volumetric effects in a horizontal milling centre. Building on earlier whole-machine FEA results used to reveal the dependence of thermal errors on machine-axis configuration, the approach uses FEA to select a small number of critical measurement configurations and performs targeted experiments only in these configurations. Local dynamic sub-models were identified using thermal transfer functions (TTF), and a continuous compensation model across the *Y*-axis stroke was obtained by interpolating the sub-models in a state-space representation.

The main findings can be summarised as follows. (i) Whole-machine FEA is effective for identifying axis configurations that exhibit significantly different thermal responses, enabling an experiment plan that captures the dominant spatial trends with a reduced number of measurements. (ii) The locally calibrated TTF sub-models achieved substantial reduction of thermally induced *Y*-direction displacement in the calibration configurations. (iii) State-space interpolation provides a practical way to achieve smooth, continuous compensation across the workspace while mitigating stability issues associated with direct parameter interpolation. The concept was validated in an additional axis configuration not used for calibration. By combining the spatial model with an FEA-derived *W*-axis scaling factor, the model reduced the validation displacement by 52% without additional calibration experiments.

Future work will focus on refining the *W*-axis dependency to quantify potential non-linearities, evaluating robustness under varying spindle speed profiles, ambient conditions, cooling etc. and verify the concept on different types of machines.

Acknowledgement

This research has received funding from the Technology Agency of the Czech Republic (Project TN02000018 - National Centre of Competence ENGINEERING). The work was also supported by the Grant Agency of the Czech Technical University in Prague, grant no. SGS25/135/OHK2/3T/12.

References

[1] Mayr J. et al. 2012 Thermal issues in machine tools. CIRP Annals **61**: 771–791.

[2] Weck M. et al. 1995 Reduction and Compensation of Thermal Errors in Machine Tools. *Annals of the CIRP* **44** (2) 589-598

[3] Divíšek D. et al. 2025 Analysis of Thermal Volumetric Effect on Machine Structure Using FEA Model. *In: euspen's Special Interest Conference: Precision & Performance, Cranfield, United Kingdom,* 53-56, ISBN: 978-0-9957751-6-9

[4] Horejš O. et al. 2022 Compensation of thermally induced errors in five-axis computer numerical control machining centers equipped with different spindles, J. Manuf. Sci. Eng., **144** (10)

[5] Mareš M. et al. 2019 Thermal Error Minimization of a Turning-Milling Center with Respect to its Multi-Functionality, *International Journal of Automation Technology* **14** (3), 475-483

[6] Ljung L L. 2015 System Identification Toolbox™ User's Guide, *The MathWorks*

[7] Toth, R. et al. 2007 Discrete time LPV I/O and state-space represent-tations, differences of behavior and pitfalls of interpolation, *In: Proceedings of the European Control Conference, Kos, Greece,* 5418-5425, ISBN: 978-960-89028-5-5

[8] Chen X. 2021 Lecture on State-Space Representations, *available: https://faculty.washington.edu/chx/teaching/me547/1-6_ss_realization.pdf*

[9] https://www.mathworks.com/help/releases/R2024b/control/ref/ss.html?browser=F1help

Session 6: Applications of Precision Engineering in Bio-Tech Devices

euspen's 26th International Conference & Exhibition, Krakow, PL, June 2026
www.euspen.eu

Ultra-precision machining of superhydrophobic surfaces with re-entrant microstructures

Douwei Liu, Wenbin Zhong*, Wenhan Zeng, Xiangqian Jiang

EPSRC Future Metrology Hub, Centre for Precision Technologies, School of Computing and Engineering, University of Huddersfield, Huddersfield, HD1 3DH, UK

w.zhong@hud.ac.uk

Abstract

Superhydrophobic surfaces have attracted extensive attention due to their outstanding water-repellent properties and promising applications in self-cleaning, corrosion resistance, anti-icing, drag reduction, and microfluidics. Conventionally, superhydrophobicity is achieved through the synergistic effect of surface micro/nanostructures and low-surface-energy chemical modifications. However, chemical surface treatments often suffer from limited durability, poor environmental stability, and complex fabrication processes, which restrict their long-term engineering applications. In this study, a superhydrophobic surface fabrication strategy based on ultra-precision machining is proposed, enabling the direct machining of re-entrant microstructures on a brass substrate. Benefiting from the high precision, material versatility, and geometric flexibility of ultra-precision machining, well-defined re-entrant microstructures were successfully fabricated. Wetting characterization reveals that the fabricated surface can stably maintain the Cassie–Baxter state without any chemical surface modification, exhibiting an apparent water contact angle of approximately 133°, a sliding angle of about 28°, and remarkably low droplet adhesion. These results demonstrate that ultra-precision machining provides a feasible and scalable approach for the fabrication of chemically unmodified superhydrophobic surfaces, offering new opportunities for the engineering application of durable functional surfaces.

Re-entrant; Ultra-precision machining; Superhydrophobic surfaces

1. Introduction

Inspired by natural surfaces such as lotus leaves and insect cuticles, superhydrophobic surfaces have attracted extensive attention due to their outstanding water-repellent properties and broad application potential in self-cleaning, corrosion resistance, anti-icing, drag reduction, and microfluidics. Superhydrophobicity is generally attributed to the combined effect of surface micro/nanostructures and low-surface-energy chemical modifications. Conventional strategies typically rely on constructing hierarchical structures followed by chemical modification with agents such as fluoroalkyl silanes to reduce surface energy [1]. However, these chemical treatments often suffer from poor durability, environmental instability, and complex processing, limiting their long-term practical applications. Consequently, achieving superhydrophobicity without chemical surface modification has become an important research direction.

Re-entrant microstructures, inspired by the cuticular morphology of springtails, have been demonstrated to enable stable superhydrophobicity by sustaining a Cassie–Baxter wetting state without chemical modification. In such structures, trapped air pockets support liquid droplets and reduce the solid–liquid contact fraction, thereby enhancing water repellence [2],[3]. Nevertheless, the fabrication of re-entrant structures generally depends on complex manufacturing techniques, such as photolithography, etching, or two-photon polymerization, which are constrained by material compatibility, feature size, fabrication efficiency, and process complexity [4].

Ultra-precision machining offers notable advantages for microstructure fabrication, including material versatility, high efficiency, and excellent geometric flexibility through tool path control [5]. However, the fabrication of re-entrant structures via ultra-precision machining remains challenging due to unavoidable tool interference arising from geometric constraints, which has limited its application to non–re-entrant microstructures. As a result, studies on machining-based fabrication of chemically unmodified superhydrophobic re-entrant structures are still scarce.

In this work, a novel superhydrophobic surface fabrication method based on ultra-precision machining is proposed. Re-entrant microstructures are designed using classical wetting theory and mechanical equilibrium analysis and then fabricated on an ultra-precision turning platform with on-machine measurement and optimized tool path planning. The wetting performance is evaluated experimentally and through multiphase flow modelling.

2. Method

2.1. Wetting theory and design of re-entrant structures

To stabilize the Cassie–Baxter state on intrinsically hydrophilic surfaces without altering surface chemistry, the introduction of re-entrant microstructures with overhanging features is considered an effective strategy. Re-entrant structures significantly increase the energy barrier that must be overcome for the transition from the Cassie–Baxter state to the Wenzel state, thereby mechanically suppressing liquid penetration into the microstructures.

From a mechanical equilibrium perspective, the stability of a droplet in the Cassie–Baxter state on re-entrant structures depends on whether the capillary pressure generated by the gas–liquid interface can counterbalance the hydrostatic pressure of the droplet, as shown in Figure 1. For a curved gas–liquid interface formed within a re-entrant cavity, the pressure

balance across the interface can be expressed as Eq 1, where $P_g = \rho g h$ represents the hydrostatic pressure of the droplet, with ρ being the liquid density, g the gravitational acceleration, and h the droplet height.

$$P_{l2} = P_{l1} + P_g \quad (1)$$

P_{l1} and P_{l2} denote the Laplace pressures at the external droplet contour interface and at the gas–liquid interface inside the re-entrant structure, respectively, which can be expressed as Eq.2, where γ is the liquid–gas interfacial tension, b_1 is the radius of curvature at the apex of the droplet's external contour, and b_2 is the radius of curvature of the curved gas–liquid interface formed between adjacent microstructures.

$$P_{l1} = \frac{2\gamma}{b_1}, P_{l2} = \frac{2\gamma}{b_2} \quad (2)$$

For simplicity, the droplet shape is approximated as a spherical cap, which facilitates the estimation of the curvature radii and droplet height.

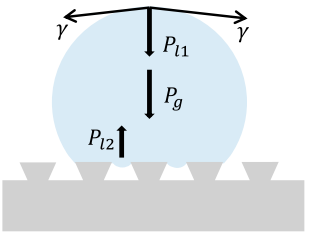

Figure 1. The force balance model of the re-entrant structured surface.

2.2. Ultra-precision machining of re-entrant structured surface

The ultra-precision machining tool, Moore Nanotech 650 FGV2 is used here, and the machining setup is illustrated in Figure 2 (a). The sharp edge single-point diamond cutting tool with the included angle θ_t is used here, as shown in Figure 2 (b). Unlike conventional machining configurations in which the tool tip axis is perpendicular to the workpiece surface, the tool tip is intentionally tilted in this study to enable the machining of re-entrant structures, as shown in Figure 3(a).

After the cutting tool is tilted by angle $\alpha_{r,l}$, its position relative to the initial workpiece coordinate system undergoes corresponding translational displacements $\Delta x_{r,l}$ and $\Delta z_{r,l}$. These displacements are determined by the installation position of the tool tip relative to the machine tool rotational center, characterized by the parameters γ and r. Here, γ denotes the angle between the line connecting the tool tip and the B-axis rotational centre of the machine and the machine z-axis, while r represents the distance from the tool tip to the rotational center.

It can be inferred that the positional offsets are uniquely determined by the rotation angle and the installation parameters. Therefore, accurate calibration of the tool tip installation position is critical for the fabrication of re-entrant structures. In this study, a trial-cutting method is employed to determine the actual installation position of the tool tip point relative to the machine tool. According to the geometric relationship, when the tool tip is rotated by an angle α, the corresponding displacements of the tool tip point are Δx and Δz, which satisfy the following relationships, Eq 3.

$$\begin{cases} \Delta x = 2 * r * \sin\left(\frac{\alpha}{2}\right) * \sin\left(\gamma + \frac{\pi-\alpha}{2}\right) \\ \Delta z = 2 * r * \sin\left(\frac{\alpha}{2}\right) * \cos\left(\gamma + \frac{\pi-\alpha}{2}\right) \end{cases} \quad (3)$$

Scratches are generated on the workpiece surface using the cutting tool, and the displacement Δx and Δz of the scratches is measured by a chromatic confocal probe [6]. Based on these measured values, the actual installation offsets γ, r of the tool tip relative to the machine tool can be calculated according to Eq 3.

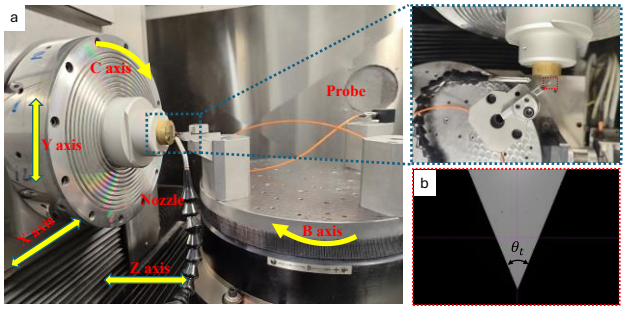

Figure 2. Ultra-precision machining of re-entrant structured surface. (a) machining set-up for the diamond tool and (b) the sharp edge single-point diamond cutting tool used in the machining under tool-setter.

As shown in Figure 3, after tilting, the angle between the tool axis and the Z-axis of the workpiece coordinate system is denoted as α. Accordingly, the re-entrant angle of the machined structure, θ, satisfies the following relationship, Eq 4.

$$\theta = 90^\circ - \alpha + \frac{\theta_t}{2} \quad (4)$$

It can be inferred from this equation that the re-entrant angle θ of the machined structure is jointly determined by the tool included angle θ_t and the tilting angle α. In this study, to fabricate microgrooves with a re-entrant angle of 60°, a diamond tool with an included angle of 45° was employed, corresponding to a tool tilting angle of 52.5°.

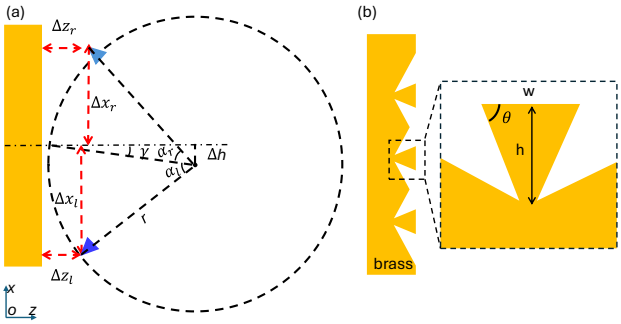

Figure 3. The schematic diagram shows the ultraprecision machining of re-entrant structures with (a) the moving of cutting tool under view of xoz plane of machine tool and (b) the re-entrant structures generated by ultra-precision machining.

After the generation of a single re-entrant structure, the cutting tool is translated along the z-direction to generate an array of re-entrant structures. According to the Eq 1 and Eq 2, the width $w = 25\mu m$ height $h = 15\mu m$ and space with 35 μm of the re-entrant structures showing in Figure 3 are controlled by the tool translation distance. In addition, because the intersection between adjacent tool paths cannot completely remove the substrate material, residual structures are formed between adjacent re-entrant features, as illustrated in Figure 3. In the present study, the spacing between adjacent re-entrant structures is insufficient to allow the liquid droplet to penetrate the microstructure gaps [7]. Moreover, the sagging height of the droplet between adjacent re-entrant structures is not large enough to contact the residual structures [7]. Therefore, the residual height does not affect the wetting behaviour of the droplet and can be neglected in this study.

2.3 Simulation of droplet wetting on re-entrant structured surface

To investigate the wetting behaviour of droplets on re-entrant structured surfaces and the dynamic evolution of the gas–liquid interface, a multiphase flow numerical model based on the phase-field method was established. The wetting process of a

droplet on microstructure surfaces was systematically analysed. The fluid motion of both the gas and liquid phases was governed by the Navier–Stokes equations under laminar flow conditions, while the Cahn–Hilliard equation was employed to solve the phase-field variable, enabling continuous tracking and evolution of the gas–liquid interface.

Since the initial velocity of the droplet during the wetting process can be regarded as zero, and both the gas and liquid phases can be approximated as Newtonian fluids, the characteristic Reynolds number of the system is relatively low. Therefore, a laminar flow model was adopted. The continuity equation is given by Eq 5.

$$\rho \nabla \cdot \mathbf{u} = 0 \tag{5}$$

To accurately capture the evolution of the gas–liquid interface within the phase-field framework, the Cahn–Hilliard model was employed. The governing equations of the phase-field model are expressed as Eq 6, where ψ is the chemical potential, γ is the phase-field mobility parameter, ε represents the characteristic thickness of the gas–liquid interface, and λ is the mixing energy density parameter, which is closely related to the interfacial tension.

$$\begin{cases} \frac{\partial \phi}{\partial t} + \nabla \cdot (\mathbf{u}\phi) = \nabla \cdot \left(\gamma \frac{\lambda}{\varepsilon^2} \nabla \psi\right) \\ \psi = -\nabla \cdot (\varepsilon^2 \nabla \phi) + (\phi^2 - 1)\phi + \frac{\varepsilon^2}{\lambda} \frac{\partial f}{\partial \phi} \end{cases} \tag{6}$$

To ensure numerical stability while accurately representing interfacial tension effects and avoiding nonphysical interface diffusion, the interface thickness and mobility parameters were selected following the parameterization method proposed by Bellussi *et al*[8].

The mixing energy density parameter λ can be expressed as Eq.7, where σ denotes the gas–liquid interfacial tension.

$$\lambda = \frac{3\varepsilon\sigma}{2\sqrt{2}} \tag{7}$$

The boundary conditions of the numerical model were defined as follows: the left and right boundaries as well as the top boundary of the computational domain were set as flow outlets with an outlet pressure of 0 Pa; the re-entrant structured surface was defined as a wetted wall with a no-slip boundary condition applied. The intrinsic contact angle of the wall was set to 71°, which was obtained from experimental contact angle measurements on the brass substrate and was used to define the wetting boundary condition in the phase-field model.

With the above model configuration, the wetting behavior of droplets on re-entrant microstructured surfaces and the stability of the gas–liquid interface can be quantitatively analyzed. All numerical simulations of the wetting model were performed using the commercial finite element software COMSOL Multiphysics 6.3.

The simulation results were shown in Figure 4. During the spreading process, the droplet remains suspended above the structured surface without penetrating the microcavities. Owing to the symmetric configuration adopted in the numerical simulations, the contact angles on the left and right sides of the droplet are identical.

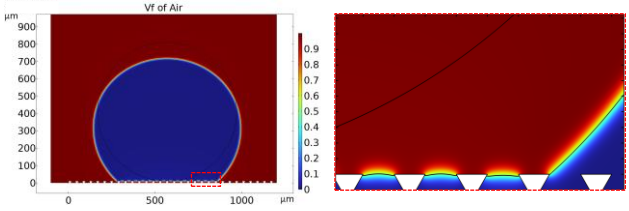

Figure 4. The simulation of droplet on the re-entrant surface.

3. Results and discussion

3.1 Calibration of tool position

Single-sided scratching experiments were conducted with tool tilting angles of $30^\circ$and 45°, respectively. Figure 5 presents the on-machine measurement results of the scratches, from which the corresponding displacement values were calculated, as summarized in Table 1.

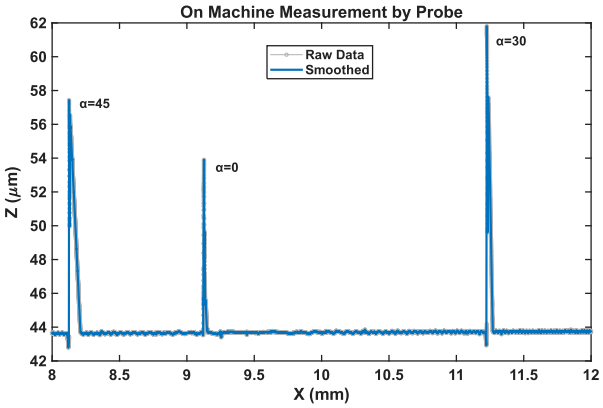

Figure 5. On machine measurement of cutting scratches under different tilting angles.

The results obtained with a tool tilting angle of 30°were used for the calculation. According to the derived equations, the corresponding values of $\gamma = 2.887^\circ$and $\mathrm{r} = 180.402$ mm were obtained. Under the same installation parameters, the differences between the theoretical and experimentally measured displacements in the x and z directions for the 45° tilting case were calculated with $\mathrm{Error_z} = 2$ μm and $\mathrm{Error_x} = 8$ μm, respectively.

These errors may originate from inaccuracies in probe-based measurements of the tool tip position relative to the spindle centre in the untitled configuration. In addition, plastic recovery of the material and wear of the tool tip make it difficult to obtain a perfectly symmetric groove profile, which further affects the measurement of the tool tip position relative to the initial cutting depth. To compensate for the tool tip positioning errors, an additional trial-cutting compensation method was employed during the actual machining process.

Table 1 On machine measurement of cutting tool installation

α(deg)	Δz(mm)	Δx(mm)
30	19.595	91.304
45	46.346	130.063

3.2 The surface characteristics

The machined re-entrant structures were characterized using an Alicona G5 optical measurement system. The surface morphology of the microstructures is shown in the Figure 6. Under the tilted-tool machining strategy, groove structures with a width of 25.1 μm and a space of 35.7 μm were successfully generated. Consistent with the machining principle, material residues formed by the intersection of adjacent tool paths were observed between neighbouring microstructures. Due to the occlusion caused by the re-entrant geometry, it is difficult to directly measure the re-entrant angle. In addition, SEM characterization can reveal the re-entrant angle by measuring the cross-sectional profile. However, the preparation of cross-sectional samples inevitably causes damage to the re-entrant structures, which are particularly fragile at their root regions. Therefore, in this research, the residual material was used as an

indirect indicator for estimating the inclination angle of the re-entrant structures. As shown in Figure 6, the average inclination angle θ of the residual region is calculated to be $15.7°$. As the included angle of diamond tool θ_t is 45°, the re-entrant angle of the fabricated structures is determined to be 60.7°, demonstrating that the fabricated structure is in excellent agreement with the designed re-entrant angle of 60°.

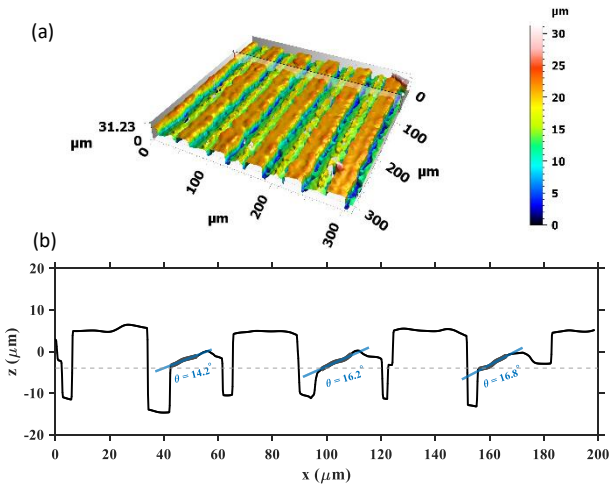

Figure 6. The measurement of generated surfaces with re-entrant structures with (a) showing the 3D of the re-entrant structured surfaces and (b) showing the profile of the re-entrant structures, here θ is the inclination angle of the residual region.

3.3 The wetting result on re-entrant structured surfaces

The wetting behaviour of the fabricated re-entrant structures was characterized using a self-built contact angle measurement system. Deionized water was used as the test liquid, and droplets were dispensed through a needle with an inner diameter of 0.25 mm. The droplet volume was controlled at 4 μL and gently deposited onto the surface. Each droplet was measured four times to reduce experimental uncertainty, and the average value was reported.

As shown in Figure 7, The measured contact angle on the left side of the droplet was $135.7°$, while that on the right side was $130.2°$, resulting in an average contact angle of $132.9°$. The discrepancy between the left and right contact angles arises from tool tilting and machining errors, which lead to slight asymmetry between the two sides of the grooves rather than a perfectly symmetric structure.

Based on the measured structural dimensions, the apparent contact angle of the droplet was calculated using the Cassie–Baxter model and the Wenzel model, respectively. Comparison with the experimentally measured contact angle indicates that the droplet resides in the Cassie–Baxter state rather than the Wenzel state.

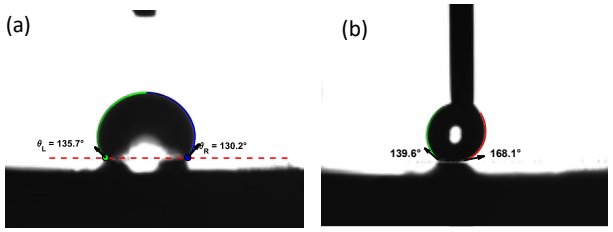

Figure 7. The wetting experiment of droplet on the re-entrant surface with (a) the contact angle and (b) the contact angle hysteresis.

To further verify the wetting state of the droplet on the fabricated re-entrant structured surface, contact angle hysteresis measurements were performed. The results show that the advancing and receding contact angles are $139.6°$and $168.1°$, respectively, yielding a contact angle hysteresis of $28.5°$. The relatively low contact angle hysteresis further indicates the low adhesion of the droplet on the machined re-entrant structures, confirming that the droplet resides in the Cassie–Baxter state. In addition, during droplet rolling experiments, trapped air beneath the droplet within the re-entrant structures can be directly observed, providing further evidence of the Cassie–Baxter wetting state.

4. Conclusion

This study investigated an ultra-precision machining approach for fabricating re-entrant structured surfaces and proposed a tilted-tool-axis machining strategy that enables high-precision fabrication of re-entrant microstructures on a brass substrate. This method effectively circumvents the geometric interference limitations inherent in conventional tool path planning and demonstrates the feasibility and machining flexibility of ultra-precision subtractive manufacturing for complex re-entrant structures.

By wetting experiments the results demonstrate that without any surface chemical modification, the fabricated re-entrant structures can stably maintain the Cassie–Baxter wetting state, exhibiting an apparent contact angle of 132°, a sliding angle of about 28°, and low droplet adhesion. The experiment shows good agreement with the simulation, further elucidating the role of trapped air cavities within the re-entrant structures in supporting the droplet and stabilizing the wetting state.

This work provides a new technological pathway for the design and fabrication of chemically-free superhydrophobic structures and expands the application scope of ultra-precision machining in functional surface engineering. Future studies may focus on optimizing microstructural geometric parameters, extending material applicability, and evaluating the durability of the structures under complex service conditions to further enhance their wetting performance and engineering application potential.

References

[1] Lian, Z., Zhou, J., Ren, W., Chen, F., Xu, J., Tian, Y., Yu, H., 2024. Recent progress in bio-inspired macrostructure array materials with special wettability—from surface engineering to functional applications. *Int. J. Extrem. Manuf.* **6**, 2631-8644.

[2] Cao, L., Hu, H.-H., Gao, D., 2007. Design and Fabrication of Micro-textures for Inducing a Superhydrophobic Behavior on Hydrophilic Materials. *Langmuir.* **23**, 4310–4314.

[3] Wang, B., Chen, J., Kowall, C., Li, L., 2020. 3D-Printed Repeating Re-Entrant Topography to Achieve On-Demand Wettability and Separation. *ACS Appl. Mater. Interfaces* **12**, 35725–35730.

[4] Liu, T. "Leo", Kim, C.-J. "CJ," 2014. Turning a surface superrepellent even to completely wetting liquids. *Science* **346**, 1096–1100.

[5] Lv, B., Lin, B., Sui, T., Zhang, J., Wang, L., Zhou, J., Zhao, P., Li, J., 2024. A 3-DOF spreading precision positional stage for ductile end-face fly-cutting of quartz glass. *Precision Engineering* **91**, 660–677.

[6] Wang, M., Zhong, W., Zeng, W., Gao, F., Yu, Y., Scott, P., Jiang, X., 2025. Towards high-speed on-machine measurement of freeform surfaces: a dynamic error calibration method. *Light: Advanced Manufacturing* **6**, 831–842.

[7] Vu, H.H., Nguyen, N.-T., Kashaninejad, N., 2023. Re-Entrant Microstructures for Robust Liquid Repellent Surfaces. *Advanced Materials Technologies* **8**. 2201-836.

[8] M., Bellussi, F.M., Morciano, M., Asinari, P., Fasano, M., 2023. Method for predicting the wettability of micro-structured surfaces by continuum phase-field modelling. *Methods*X **11**, 2215-0161.

euspen's 26th International Conference & Exhibition, Krakow, PL, June 2026
www.euspen.eu

Automated Multi-Balloon Drug-Coating System with Configurable Process Parameters

Yixue Wang[1], Michal Szczepanski[1], Nicolas Kayser[1], Gregor Dürre[2], Robby Simon[3], Frank Wasmuth[3], André Hutsky[3], Annika Brehmer[1], Julian Polte[1,4]

[1] *Fraunhofer Institute for Production Systems and Design Technology IPK, Germany*
[2] *InnoRa GmbH, Germany*
[3] *Organical CAD/CAM GmbH, Germany*
[4] *Institute for Machine Tools and Factory Management IWF, Technische Universität Berlin, Germany*

yixue.wang@ipk.fraunhofer.de

Abstract
Drug-coated balloon catheters are widely used in minimally invasive cardiovascular interventions, where coating quality and process consistency are critical for clinical performance. Despite their importance, drug-coating processes for balloon catheters are still largely performed manually, leading to limited throughput, variability in coating quality, and potential safety risks due to operator exposure to hazardous chemicals.
This paper presents the Coater Mk2, an automated drug-coating platform for balloon catheters. The nine-axis system processes up to five balloons per cycle, with overlapping coating and drying phases to increase throughput. Each balloon position has individually configurable process parameters, enabling accurate, repeatable coating across heterogeneous balloon designs. A confocal displacement sensor is integrated for automatic detection of balloon geometry and for future spatially resolved coating-thickness measurement. In addition, the use of an open-source control platform allows the delivery of fully accessible source code alongside the machine, enabling end users to adapt and customize the process control software to specific production requirements.
Experimental results demonstrate stable and repeatable automated coating for a representative range of commonly used balloon catheter types, while certain less common balloon geometries remain challenging and are subject to ongoing development.

balloon catheter, drug-coating, automation, multi-workpiece processing, configurable process

1. Introduction

Percutaneous coronary intervention (PCI) is the most widely used treatment for coronary artery diseases (CAD) [1]. Two of the most common long-term complications of PCI are in-stent restenosis (ISR) and stent thrombosis (ST). Although the rates of ST have been nearly abolished and ISR rates have declined with the current gold-standard second-generation drug-eluting stents (DES), late ISR of DES remains a valid concern in the field of interventional cardiology [2]. Drug-coated balloons (DCBs) provide a stent-free alternative to DES, reducing risks like ST and ISR and the need for prolonged dual antiplatelet therapy [3].

Coating balloons with an active substance such as paclitaxel or sirolimus is commonly carried out by spraying, dipping, or micro-pipetting onto the balloon surface [4]. Spraying is straightforward to automate and can provide good coverage, but only part of the sprayed drug solution necessarily reaches and adheres to the balloon, which limits control over the effective drug load. Dipping is simple and robust to perform manually, yet the amount of drug actually taken up by the surface depends on fluid properties, withdrawal conditions, and geometry, and therefore remains difficult to quantify precisely. Micro-pipetting, in contrast, enables accurate volumetric dosing of the drug solution onto the balloon, but achieving a continuous, homogeneous coating layer along the entire balloon length is challenging [5]. These method-specific limitations underline the need for an automated coating system that combines precise dosing, controlled motion, and integrated sensing to ensure reproducible drug loading and coating uniformity across different balloon designs.

Based on an existing prototype [6], the Coater Mk2 project addresses these limitations by developing an automated coating platform suitable for industrial application. The mechanical system was designed and built by ORGANICAL CAD/CAM GMBH, Berlin, Germany while FRAUNHOFER IPK, Berlin, Germany was responsible for the control system, sensor integration, and process development. INNORA GMBH, Berlin, Germany contributed application-specific expertise, supported process definition, and participated in the experimental validation of the coating results. This paper presents the resulting multi-balloon coating system, with a focus on the integration of the hardware platform with real-time control, sensing, and configurable process parameters to enable reliable and scalable drug-coating processes.

In the coating approach adopted here, originally explored in [6], a droplet of drug solution is formed on the balloon surface near one end, dragged along the surface to generate a continuous coating layer, and continuously replenished by the coating needle to maintain an approximately constant droplet volume.

2. Mechanical system

The Coater Mk2 was designed to enable parallel processing of up to five balloon catheters while providing fast, precise, and

responsive motion behaviour for accurate process control, ease of use for operators, and compatibility with cleanroom operation.

As shown in Figure 1, the machine comprises nine CNC-controlled axes. Three linear axes position the needle and confocal sensor relative to the balloons. Five rotational axes drive the catheter positions: for each balloon, both catheter ends are driven synchronously by two coupled motors, avoiding torsion within the balloon during rotation. An additional axis agitates the coating fluid during long coating cycles to maintain a homogeneous drug solution. Typical coating cycles per balloon are in the range of several minutes and are primarily limited by solvent evaporation rather than axis motion.

Catheters are clamped on one side using a chuck and on the other side via a luer lock interface, which also serves for balloon inflation and deflation. Magnetic locking elements between the two ends stabilize the catheter during rotation. The integrated air-pressure system can be connected to a centralized compressed-air supply, with adjustable pressure control to accommodate different balloon types and inflation requirements.

All connectors and fluid paths that contact the coating solution or the catheter use standardized medical interfaces and materials compatible with medical applications. The machine structure is predominantly stainless steel and is designed for installation inside a clean bench within a cleanroom, providing additional containment of solvents and enhanced operator safety, while ensuring that possible spills do not compromise the mechanical integrity of the system.

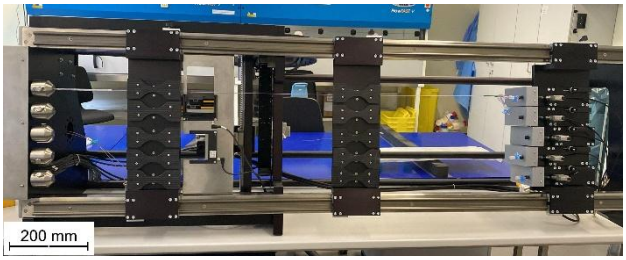

Figure 1. Overall view of the 9-axis Coater Mk2, with one balloon catheter mounted

ORGANICAL CAD/CAM GMBH designed and built the mechanical hardware and implemented the foundational integration of the EtherCAT-based drive system with the LinuxCNC control environment [7], providing the real-time motion platform on which the control and process logic described in the following sections are implemented.

3. Component integration

Several key components were integrated to support automated operation and to prepare the system for future, metrology-based quality assurance.

3.1. Syringe pump

The syringe pump SPM P100-O from the company ADVANCED MICROFLUIDICS, Ecublens, Switzerland controls the delivery of the drug solution during coating and is mounted on the side of the machine, attached to the agitation axis. The pump is driven by its own microcontroller and firmware and exposes a serial communication interface. Integration into the control system was implemented in Rust instead of relying on the manufacturer's closed-source Python library, improving long-term maintainability and portability across different Linux environments. The pump interface supports deterministic triggering and logging of dosing events, enabling synchronization with axis motion and traceable documentation of the applied coating volume.

3.2. Confocal sensor

A high-precision confocal displacement sensor IFD2411-3 from the company MICRO-EPSILON MESSTECHNIK GMBH & CO. KG, Ortenburg, Germany is used for automatic and precise detection of the balloon geometry. Unlike camera- or standard laser-based approaches, confocal sensing is well suited for the highly transparent balloon material, which is difficult to detect optically with conventional methods. The sensor's limited measurement range requires careful positioning to accommodate balloon curvature, but in return it offers repeatable measurements with a typical repeatability $R \leq 10\ \mu m$.

Three main measurement modes are implemented:

- **Radius detection:** The sensor is gradually moved towards the balloon until valid measurement data is obtained. This allows the actual radius r under coating pressure p to be determined, which is typically lower than the nominal operating radius r_n specified by the manufacturer.
- **Roundness measurement:** The balloon is rotated by $\alpha = 360°$ while the sensor measures the radius r, generating a cross-sectional profile with mean radius $\bar{r}$ and standard deviation σ. This enables the user to detect out-of-round balloons or insufficient inflation before coating and to reject unsuitable workpieces.
- **Position detection:** The sensor is moved along the balloon's rotational axis, and an edge-detection algorithm is applied to the measured profile to automatically identify the start and end positions of the balloon. The detected edges can be visually confirmed by the operator.

The roundness measurement mode and position detection mode can be combined to measure the balloon before and after coating, enabling estimation of coating thickness and surface smoothness along the balloon in the future.

3.3. Optical sensors

The light barriers AO903 from the company AUTOSEN GMBH, Essen, Germany are used to reference the needle position. During referencing, the needle is moved through the beam in a staircase pattern to pinpoint the exact position of the needle tip. The measured position is compared to stored reference data to compute an offset, improving repeatability and reducing setup variability.

Together, the integrated pump and sensors provide the necessary feedback and actuation for reliable process execution and establish the basis for future metrology-driven process qualification and automated workpiece screening.

4. Control software

The Coater Mk2 control software is built on top of LinuxCNC and uses the real-time motion and I/O infrastructure described in the previous sections. The software is structured in modular components responsible for axis control, pump control, sensor handling, process sequencing, and the graphical user interface (GUI) (see Figure 2). This modularity facilitates extension and long-term maintainability.

The coating process is implemented as an automated sequence with clearly defined states, including system referencing, balloon detection, coating, and drying. A typical cycle comprises:

1. Referencing of all axes and sensors,
2. Loading of the syringe pump with the drug solution,
3. Automatic detection of balloon position and geometry using the confocal sensor,
4. Configuration or selection of process parameters,
5. Execution of the automated coating and drying cycle.

Coating is executed balloon by balloon, while drying phases overlap with the coating of subsequent balloons. This coordinated sequencing increases throughput compared to single-balloon processing without compromising coating quality.

All process-relevant parameters, including axis speeds, drying time, coating paths and coating volume, are configurable through the GUI. Each of the up to five balloon positions can store an individual parameter set, enabling heterogeneous balloons to be processed within the same batch. This reduces setup effort and allows recipes for frequently used balloon types to be reused.

The GUI provides access to parameter configuration, live status information (axis positions, sensor states, pump status), and basic diagnostics. It is implemented as a thin layer on top of the control logic, with LinuxCNC ensuring deterministic execution of motion and I/O commands in the background. The use of an open-source control platform allows delivery of fully accessible source code with the machine, enabling end users to adapt and customize both process logic and operator interface to specific production requirements.

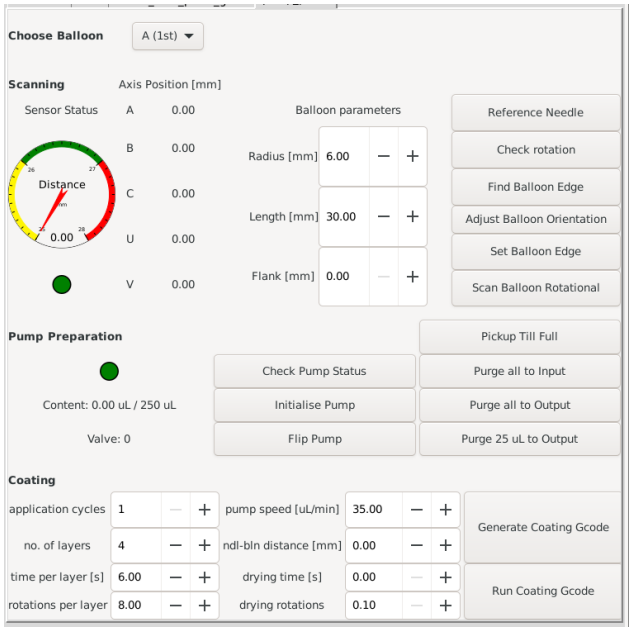

Figure 2. GUI of the Coater Mk2 with configurable process parameters and status monitoring

5. Results

The automated process was validated using three representative balloon catheter types covering a range of geometries and use cases. The automated coating results were evaluated using three acceptance criteria:

- visual control, requiring that the drug coating is distributed over the entire balloon surface including the flank areas;
- average active pharmaceutical ingredient (API) load per surface area, in this case caffeine, determined via wash-off testing followed by high-performance liquid chromatography (HPLC), with a target of m_{API} = 3 µg/mm² ±0.1 µg/mm²;
- coating thickness, measured with a Keyence 065T sensor, requiring a local coating thickness 50 µm ≤ Δr ≤ 200 µm at all measured positions.

5.1. Configuration A

This balloon type had a diameter 10 mm ≤d ≤12 mm and a length l = 30 mm, designed for use with a d_g = 0.035" guidewire. A balloon of configuration A in the drying process is depicted in Figure 3.

For these balloons, an acceptance rate of η_{acc} = 95 % was achieved. The system demonstrated stable and repeatable coating performance, including controlled coating of the balloon flanks. Automated alignment using the confocal sensor, combined with the torsion-free dual-end drive, ensured reliable positioning and rotation. No visible defects such as runs or dripping were observed under the tested conditions. Overlapping of coating and drying phases between different balloon positions was successfully executed, confirming that the multi-balloon architecture can increase throughput for this balloon class without compromising coating quality.

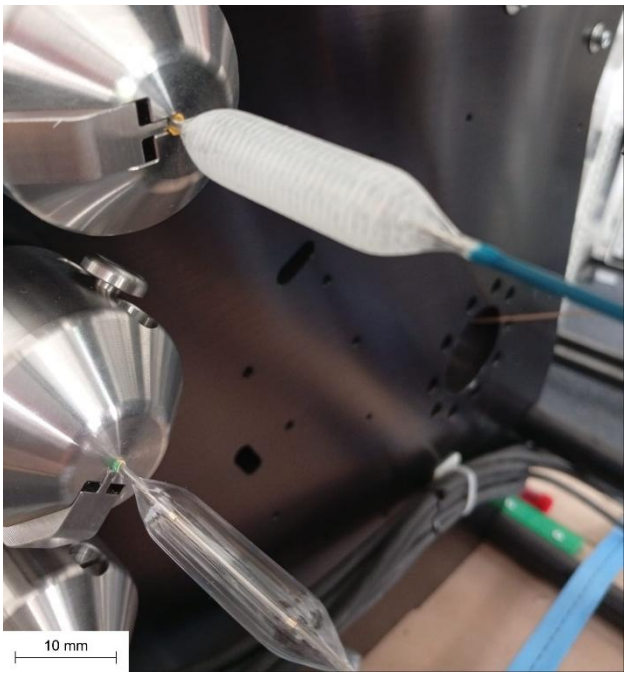

Figure 3. Balloon of configuration A, before coating (bottom) and after coating (top)

5.2. Configuration B

This balloon type had a diameter d = 3 mm and a length l = 40 mm, designed for use with a d_g = 0.035" guidewire.

For this configuration, an acceptance rate of η_{acc} = 85 % was achieved. While geometrically regular balloons were selected, the system was able to perform the full automated sequence including referencing, balloon detection, coating, and drying. However, the small diameter d resulted in a higher sensitivity to geometric tolerances and alignment errors. Minor deviations in clamping or needle positioning had a stronger impact on detection success rate and coating uniformity than for larger balloons. Some balloons had to be rejected before coating while some required repeated manual alignment, indicating a need for better fixtures and alignment strategies optimized for small-diameter balloons.

5.3. Configuration C

This balloon type had a balloon diameter $d \geq 4$ mm and a balloon length $l = 80$ mm on a catheter of length $l_c = 165$ mm, designed for use with a $d_g = 0.018"$ guidewire.

For this geometry, the available mechanical tensioning range and current fixation concept proved to be limiting. The longer balloon and catheter length led to residual sagging and reduced stiffness, which decreased positional stability during rotation and made the coating process more sensitive to disturbances. As a result, process stability did not yet reach the level achieved for the balloons of Configuration A, at a low acceptance rate of $\eta_{acc} = 60$ %. These results point to the need for improvements in the clamping and tensioning mechanism as well as potential adaptations of the process parameters for long balloons.

Overall, the experiments confirm that the Coater Mk2 can reliably automate coating for balloon types within a certain geometric and stiffness envelope, while also revealing the current mechanical limitations for more challenging geometries. The integrated sensing and configurable process parameters proved effective for systematic parameter adjustment and for identifying the key design aspects that require refinement in future iterations.

6. Conclusion

6.1. Summary

This paper presented the development and initial validation of the Coater Mk2, an automated drug-coating platform for balloon catheters. The system is based on a nine-axis mechanical architecture capable of processing up to five balloons in a single process cycle, with overlapping coating and drying phases to increase throughput. It combines LinuxCNC and EtherCAT for deterministic multi-axis motion control, a syringe pump integrated via a dedicated Rust-based interface, a confocal displacement sensor for balloon geometry and position measurement, and optical sensors for needle referencing.

The control software implements an automated sequence comprising axis referencing, balloon detection, parameter configuration, coating, and drying. Three balloon configurations were tested, covering diameters $3 \text{ mm} \leq d \leq 12$ mm and balloon lengths $30 \text{ mm} \leq l \leq 80$ mm. For the balloons with $10 \text{ mm} \leq d \leq 12$ mm and $l = 30$ mm, stable and repeatable coating was achieved, including controlled coating of the balloon flanks. For small-diameter balloons and longer, more flexible balloons, the tests revealed increased sensitivity to clamping, alignment and tensioning, indicating the current boundaries of the mechanical design.

6.2. Conclusions

The results demonstrate that the Coater Mk2 provides a viable platform for automating the coating of balloon catheters within a defined geometric and stiffness envelope. Compared to established manual coating processes such as in [4], the system reduces operator-dependent variability and operator exposure to hazardous solvents, while still supporting operation in a cleanroom environment. In comparison to potentially automated spray-coating (similar to [8]) or dip-coating workflows, the Coater Mk2 achieves superior dosing control, while also creating more evenly coated surfaces than automated micropipette system described in [5]. Compared to the earlier prototype in [6], the Coater Mk2 also advances the state of the art by combining multi-axis motion, integrated syringe pump control, and configurable process parameters, enabling reproducible execution of complex coating sequences and supporting processing of up to five workpieces.

6.3. Future work

Future work will focus on extending the mechanically stable range of balloon geometries, with particular emphasis on longer balloons with lengths up to $l = 200$ mm on $d_g = 0.018"$ guidewires. Achieving this will require revised clamping and tensioning concepts and improved guidance to maintain sufficient stiffness and positional stability over the full balloon during rotation.

On the metrology side, the confocal sensor functionality will be extended from geometric alignment towards quantitative evaluation of coating thickness Δr and surface quality by comparing pre- and post-coating measurements. Additional work will include expanded testing with further balloon variants, refinement of process recipes, and enhanced software functions for recipe management, diagnostics, and data logging. Finally, user documentation covering setup, operation, maintenance and fault diagnosis will be completed to support transfer of the system into routine use and further industrialization.

References

[1] Lee H-I, et al. 2021 A multilayer functionalized drug-eluting balloon for treatment of coronary artery disease *Pharmaceutics* **13** 614.

[2] Bhogal S, Hill A P, Merdler I, Wermers J P, Ben-Dor I and Waksman R 2024 Drug-coated balloons for coronary artery disease: An updated review with future perspectives *Cardiovasc. Revasc. Med.* **69** 79-89.

[3] Her A, Ahmad W, Bang L, et al. 2025 Drug-coated balloons-based intervention for coronary artery disease: The second report of Asia-Pacific Consensus Group *JACC: Asia* **5** 701-17.

[4] Petersen S, Kaule S, Stein F, et al. 2013 Novel paclitaxel-coated angioplasty balloon catheter based on cetylpyridinium salicylate: Preparation, characterization and simulated use in an in vitro vessel model *Materials Science and Engineering C* **33** 10 4244-50.

[5] Fuglsby K, Anderson J A, Engebretson D and Lamichhane S 2020 Development of an automated micropipette coating method for drug-coated balloons *J. Biomed. Mater. Res. B Appl. Biomater.* **108** 2258-75.

[6] Uhlmann E, Hein C, Schlüter M, Wang Y and Dürre G 2023 Automated manufacturing of drug-coated balloons for coronary artery disease *Proc. 23rd Int. Conf. of the European Society for Precision Engineering and Nanotechnology* ICE23244.

[7] LinuxCNC Project 2025 *LinuxCNC* available at https://linuxcnc.org

[8] Jelonek K, et al. 2025 Evaluation of Ultrasonic Spray Method for Application of Sirolimus-Eluting Coating on Bioresorbable Vascular Scaffolds *Int. J. Mol. Sci.* 26(15).

euspen's 26th International Conference & Exhibition, Krakow, PL, June 2026
www.euspen.eu

Modular child lower limb phantom with seven degrees of freedom simulating micrometric bone growth

Krzysztof Popielski[1,2], J.R.R. Mayer [1], Adam Woźniak[2]

[1]*Department of Mechanical Engineering, École Polytechnique de Montréal, 2500, chemin de Polytechnique, Montréal (Québec), H3T 1J4, Canada*
[2]*Warsaw University of Technology, Department of Mechatronics, sw. Andrzeja Boboli 8, 02-525 Warsaw, Poland*

Krzysztof.popielski.dokt@pw.edu.pl

Abstract
Children's growth is a fundamental parameter in paediatrics for assessing physical development. The growth measurement at short time intervals, of typically four weeks, is based on the length of a long bone, mostly the tibia. All measurement methods are contact methods, and they are unsuitable for uncooperative children or younger than 3.5 years old and are significantly affected by soft tissue deflection (STA). A solution could be to use non-contact optical methods. The main challenges in applying such solutions and achieve growth measurement uncertainties below 0.5 mm, are STA, establishing models between the target measurement and the bone growth, and measurement system errors. To enable the validation of various solutions, initially without the influence of STA, a modular phantom of a child's lower limb is proposed that simulates growth in the range 0-12.7 mm for the femur and tibia. The phantom enables movements imitating the motion of the lower limbs, for the hip joint in three degrees of freedom, and in two degrees of freedom for the knee and ankle joints in ranges based on literature data. A ball joint and two universal joints are used. In their current form, all joints have a fixed center of rotation which will allow to test the assumption that growth can be studied using optical systems. Thanks to the modular design of the phantom, in the future, the original knee joint could be replaced with a polycentric mechanism based on a four-bar mechanism with an additional rotational joint, which will correspond to the kinematics of the knee joint. The growth is produced using three manual actuators, and measured with an integrated micrometer located on the central axis tubes, aligned with the joints, to avoid Abbe errors.

Lower limb phantom; growth measurement; anatomical joint simulation;

1. Introduction

The measurement of children's growth is a basic parameter used in pediatrics to assess a child's physical development. To verify the impact of illnesses, medication or diet on a child's development and respond promptly to any undesirable changes the measurement must be done at short time intervals [1] based on the long bone measurement, specifically, the tibia, which growths less than 0.5 mm per day for infants [2] and ~0.4 to 0.5 mm per week for older children [3].

Among the known methods of measuring growth, the most popular is the knemometric method [2–4]. Results obtained using this method are subject to significant errors due to the deflection of soft tissues (STA). Another method [5] is the contact method, also referred to as non-contact measurement conditions, which involves the simultaneous measurement of force and length. However, this method does not allow newborns and toddlers to be measured. The solution to this problem may be the use of optical methods. The main challenges in applying such solutions are STA, determining the centers of rotation of joints (CoR), and measurement system errors [6].

For the lower limb growth values, the determination of the CoR of the joint should be to an uncertainty of the order of one tenth or 0.05 mm for daily growth or 0.35 mm for weekly growth. For this reason, it is essential to develop a phantom that mimics the hip, knee, and ankle joints and simulates bone growth but is independent of STA in order to evaluate the performance of the growth measurement method.

The lower limb contains three joints of varying complexity in terms of anatomical structure and kinematic relationships. The movement of the lower limb is described in three main planes: Sagittal, Frontal/Coronal, and Transverse [7] (Figure 1).

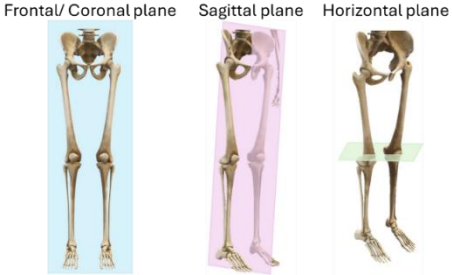

Figure 1. Anatomical planes

The average values, along with their corresponding axes, are presented in Table 1. The values are based on literature [8–11].

Table 1. Anatomical ranges of motion (RoM) of the joints (S – Sagittal, F/C - Frontal/Coronal, T – Transverse)

Joint	Movement	Plane	RoM [°]
Hip	Extension/ Flexion	S	-30/125
	Abduction/ Adduction	F/C	-50/30
	Internal/External Rotation	T	-45/45
Knee	Extension/Flexion	S	-15/135
	Abduction/ Adduction	F/C	-15/15
	Internal/External Rotation	T	-40/30
Ankle	Extension /Flexion	S	-45/20
	Pronation/Supination	F/C	-30/20

The hip joint allows for combined rotation in all three planes of motion. The knee joint is one of the most complex joints in the

human body. It has one dominant axis of movement in the sagittal plane (-15° /135°) and two with a more limited range in the transverse (-40° /30°) and frontal/coronal (-15° /15°) planes [11]. The abduction and rotation must occur only when the joint is bent in the sagittal plane. Due to the anatomy of the knee joint, it provides six degrees of freedom. Thus, during flexion, there is a conjugation of translational and rotational motion, which in turn results in the displacement of the center of rotation of the knee as the joint flexes [12]. Additionally, knee joint movement varies depending on whether it is loaded or unloaded [13]. This is due to the ligaments in the joint, which can change the presumed movement of the joint when significant dynamic forces are applied (e.g., during running or squatting). The ankle joint has two axes of rotation in the sagittal and frontal/coronal planes [14].

The phantoms described in the literature depend heavily on the characteristic being tested. One of the phantom groups focuses on tissue properties and limb appearance, but does not consider joint structure and movement. These phantoms are used in electromyography [15], where they simulate muscles and their chemical and electrical properties, or in radiology [16], where bone marrow, compact bone, and soft tissue are reproduced to study the effects of irradiation. The second group of phantoms focuses on movement reproduction, which also includes prosthetic and orthotic elements. In orthotics, exoskeletons are one of the most advanced lower limb reproductions [17]. Focusing on movement assistance, they are required to reproduce movement well, but usually with a limited number of degrees of freedom compared to human anatomy. In the case of functional lower limb prostheses [18], the primary goal is to replicate movement by replacing anatomical joints with mechanical joints, without focusing on replicating appearance. For the knee joint, a hinge or polycentric joint is most commonly used. In this group, in addition to replicating kinematics, the key factors are the dynamic properties and durability of the construction. There is a gap, then, with the phantom that simulates bone growth, which could be used to validate methods of bone growth measurement without STA.

2. Materials and methods

The methodology describes the process of constructing and validating the phantom, including the assumptions and simplifications made in comparison with the anatomy of the lower limb.

2.1. Construction of the phantom

The most important requirement for a lower limb phantom is the capability to simulate and measure bone growth while maintaining the best possible representation of real lower limb kinematics. Additionally, the phantom should be designed to limit the impact of thermal phenomena and ensure the modularity of the entire mechanism, allowing for future modification and expansion.

Bone growth is the most critical assumption and requirement for the phantom to function. Therefore, the phantom is designed to ensure measurement accuracy of no less than 0.05 mm, and a growth of 12.7 mm for the elements of the tibia and femur, which corresponds to the growth of a newborn, toddler, and older children in the time interval of up to 4 weeks.

The extension element is based on two center-axis round tubes (base tube and carbon tube). The length is adjusted using a microadjuster located outside the tubes, connected by rods. The movement is triggered and locked by turning the nuts on the rods, which allows for precise adjustment and locking of the desired length. The nuts are marked on one side to ensure that each one has the same rotation. The change of length is measured with a micrometer nominally located on the axis between the two consecutive joints (hip-knee and knee–ankle) to avoid Abbe errors. A schematic representation of the growth element is shown in Figure 2.

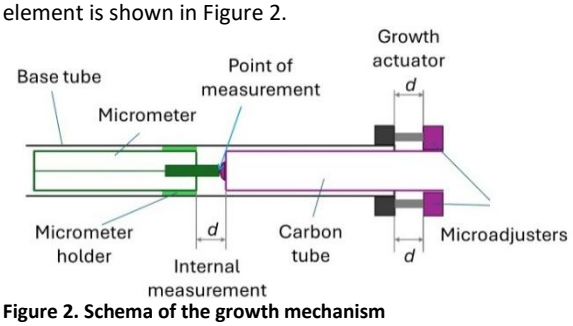

Figure 2. Schema of the growth mechanism

Two extension elements simulating growth areas were used in the phantom at the parts corresponding to the femur and tibia. Due to the slow growth of the foot, which is not proportional to overall growth, and the lack of influence of foot growth on the displacement of other joints, it was designed as a fixed-length element in the phantom. To ensure thermal stability, the parts simulating bones are made of carbon fiber. A schematic representation of a connection of growing parts with joints forming a phantom is shown in the figure below (Figure 3).

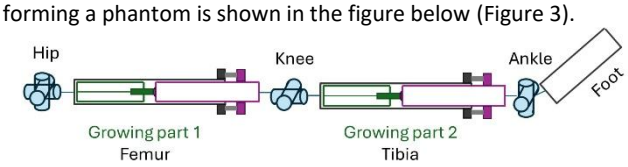

Figure 3. Kinematic schema of the phantom

Anatomical joints have a complex structure that is not fully reflected by familiar mechanical joints. However, since the main element of the phantom is the growth of the link between joints, standard mechanical elements were selected to best approach anatomical movement.

The hip joint is a spherical joint. It therefore allows for combined rotation in all three planes of motion: Sagittal, Frontal/Coronal, and Transverse. To replicate this behavior, a ball joint was selected as the mechanical representation.

The primary movements of the knee and foot that must be considered in the phantom are flexion and extension. Additionally, both joints allow for movement in the frontal/ coronal planes. On this basis, a universal joint was selected as the best mechanical representation. It simplifies the movement of the knee by neglecting the movement in the transverse plane and assuming a fixed center of rotation.

SolidWorks 2025 was used in the design process. Where possible, standard components were used, and the remaining components were manufactured using the Mazak Quick Turn Nexus 200 CNC Turning Center.

2.2. Validation of the phantom

The validation was conducted in two stages. The first stage involved verifying the representation of anatomical angular ranges of motion for the joints based on data from Table 1. The measurement was performed using the Beall Tool Tilt Box, a digital inclinometer with an accuracy of 0.1 degrees and a resolution of 0.05 degrees.

The second part of the validation concerns the increments obtained, their stability, and the accuracy of measurement using the built-in micrometer. The aim is to determine how connections, imperfections in joint construction, and mechanical slack, which may not influence the measurement with the mounted micrometer, affect the elongation of the phantom part. The tests were performed on each part of the phantom. A caliper with an uncertainty of 15 micrometers (calibrated on gauge blocks) was used to measure the lengths. The measurement of the “growing part” was taken at six length

values. The next value is obtained by changing the length using the adjuster. The measurements were taken in three conditions: no external force, tensile force, and compressive force (Figure 4). The force is applied by the operator to simulate the possible displacements that could occur during the phantom movement.

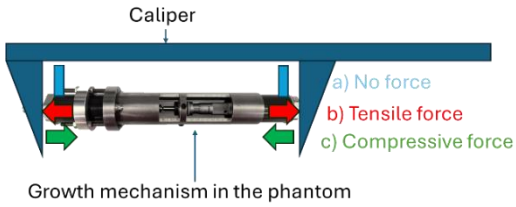

Figure 4. Validation of the growth mechanism under different conditions

Verification of the influence of imperfections in each joint, universal (Figure 5A) and spherical (Figure 5B), on construction was performed. The measurements were taken in three conditions as before.

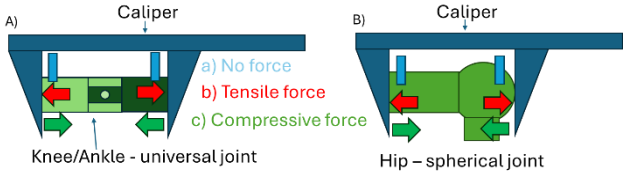

Figure 5. A) Validation of the universal joint under different conditions; B)Validation of the spherical joint under different conditions

3. Results

3.1. Phantom construction

A CAD model of the growing mechanism and the entire phantom were developed.

To simulate growth, a mechanism based on two central axis round tubes was designed as shown in Figure 7. Aligning with machining capabilities, the base element was made of low-carbon steel. Centrally mounted in this element is a Mitutoyo 148-502 micrometer with a ±0.0051 millimeter uncertainty, and the base element itself was cut out on both sides to allow access to the micrometer knob and to read the measured value. The moving "bone" element was made of carbon fiber to reduce thermal influence. A spherical measuring surface was attached to one of its ends, in contact with the micrometer spindle, to ensure the point measurement.

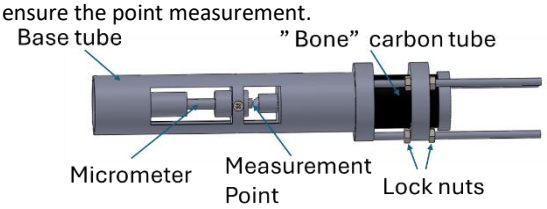

Figure 7. Growth mechanism in the phantom

Two rings, one on each tube, are permanently fixed to the tube and connected with M4 × 0.7 mm rods that act as guide rails. The length is adjusted by moving one of the tubes with the ring attached, and it is locked in position with six nuts. Height measurement using a micrometer is performed manually after a change in height.

The final model, with selected joints, is presented in Figure 8.

The entire structure is based on screw connections to ensure modularity. The connection was blocked using the threadlocker to prevent undesirable unscrewing of the model during movement. The completed and assembled phantom is shown in Figure 9.

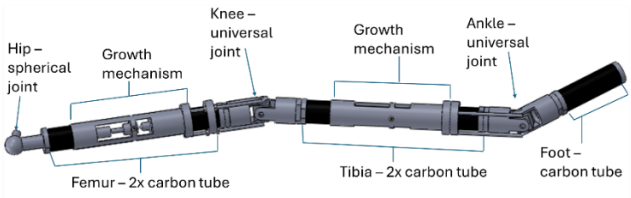

Figure 8. CAD model of the phantom of the lower limb

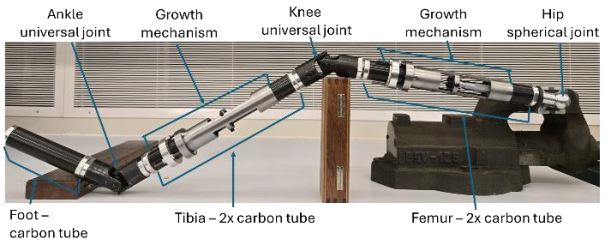

Figure 9. Phantom of the lower limb

3.2. Phantom angular movement validation

Table 2 shows the angular ranges of the Phantom joints.

Table 2. Phantom ranges of motion (RoM) of the joints (S – Sagittal, F/C - Frontal/Coronal, T – Transverse)

Joint	Movement	Plane	RoM [°]
Hip	Extension/ Flexion	S	-180/180
	Abduction/ Adduction	F/C	-28,7/28,6
	Internal/External Rotation	T	-33,21/32,53
Knee	Extension/Flexion	S	-90/90
	Abduction/ Adduction	F/C	-20,25/20,2
Ankle	Extension /Flexion	S	-90/90
	Pronation/Supination	F/C	-25,51/25,48

The use of standard spherical and universal joints means that, unlike the anatomical limb, the angular ranges are symmetrical and the values differ from the anatomical values. For the hip joint, the spherical joint in the sagittal plane has a 150-degree greater range of extension and a 55-degree greater range of flexion. In the other planes, the ball joint has a smaller range by 31.3 degrees for abduction and 12-13 degrees for internal and external rotation. In the case of universal joints, for extension and flexion, they have a range of -90 to 90 degrees, thus allowing for less flexion movement in the knee and greater motion in other directions. For a phantom in a fully extended position, the universal joint in the second rotation also allows rotation in the range of -90 to 90 degrees. However, in other positions, the range of motion is limited by the joint's design, which depends on the pose. For a condition similar to the anatomical occurrence of this movement, i.e., for a knee flexion angle of 83.25 degrees and a foot extension of -28.45 degrees, it ranges from -20.25 to 20.2 degrees for the knee and -25.51 to 25.48 degrees for the ankle.

In the case of movements with a range greater than the anatomical range, operator control is necessary when using the phantom, or it is possible to use specially designed joint limiters that will prevent non-anatomical movements. In the case of abduction and rotation in the hip and flexion in the knee, the use of ready-made joints results in the model losing approximately 30% of its range of motion in these areas. Despite this, the phantom allows for the reproduction of a significant part of the mobility and kinematics of the joints. Anatomical joint movement is not typical in standard mechanical joints. To ensure completely anatomical movement of the phantom joints, it would be necessary to design and manufacture custom joints that replicate the natural movement of the human joints.

3.3. Phantom elements validation

The results obtained from measuring the phantom's growth are presented in the chart below (Figure 10).

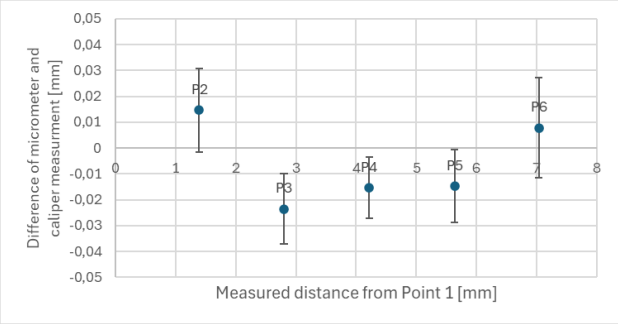

Figure 10. The difference between micrometer and caliper measurements depends on the distance (growth)

The observed differences are within the measurement accuracy of the caliper (±15 µm). No correlation was observed between the differences in measurements taken with the caliper and micrometer, regardless of the distance measured. This allows us to assume that the observed differences do not depend on the measured value, and therefore, the entire mechanism remains rigid over the entire measurement range.

For each of the six lengths, measurements were taken under unloaded conditions with tensile or compressive forces applied. An analysis of variance (ANOVA) was performed to determine whether there are statistically significant differences between the means under these conditions. For all groups, the Shapiro-Wilk test was used to verify that the data are normally distributed, and Levene's test was used to verify that the variances in the individual groups are similar. ANOVA revealed no statistically significant differences between the mean values for the length measurements performed in accordance with Figure 3 for the unloaded, compression, and tension conditions at each point (p-values = 0.85, 0.57, 0.53, 0.41, 0.85, 0.27). This means that there is no play in the growing part, so the growth of this part can be fully measured with the micrometer.

In order to validate the joints, measurements were taken under unloaded conditions and with tensile and compressive forces applied, as shown in Figure 4 and Figure 5. For all groups, the Shapiro-Wilk test showed that the data do not follow a normal distribution, so the Kruskal-Wallis test was performed to check whether the median values in the groups are equal. For the ball joint, the test showed that there is no statistically significant difference among the medians at the 95.0% confidence level (p-value = 0.679). In comparison, for the universal joint at the 95.0% confidence level, there is a statistically significant difference among the medians (p-value < 0.05). This means that during the movement of the phantom, the ball joint maintains its position, while the movement of the universal joint will depend on the force applied during the movement. The average difference between the measurements in the universal joint with compressive force and tensile force applied is 0.213 mm. The force applied was similar to that occurring when using the phantom.

4. 4. Conclusion

The phantom simulates the growth of two long bones of the lower limb. The growing part was validated, and there is no play; the uncertainty of the measurement is ±5,1 µm. However, the universal joint used to replicate the knee and ankle joints has a play of 0.213 mm. That means that the overall error of the phantom is bigger than the required 0.05 mm. The selected joints allow most anatomical movements to be preserved. However, for the universal joint used to replicate the knee and ankle joints, the differences in anatomical ranges of motion are greater than for the hip joint. As a result, the phantom is functional in its current form; however, to maintain anatomical limitations, the presence and control of the operator are necessary.

5. Future work

The phantom could be improved. In particular, a cap could be designed for the universal joint corresponding to the ankle to limit joint movement in accordance with anatomical movement. In the case of the knee, a joint could be created covering policentric center of rotation and full anatomical ranges.

5. Acknowledgment

The authors would like to thank technician Vincent Mayer for their help with machining the phantom's parts.

References

1. Rępalska M, Woźniak A, Kulus M (2018) Application of Coordinate Measuring Arm for Accurate Measurement of Child Growth. *Meas Sci Rev* 18: 201–206.
2. Gibson AT, Pearse RG, Wales JKH (1993) Knemometry and the assessment of growth in premature babies. *Arch Dis Child* 69: 498–504.
3. Bisgaard H (1993) Systemic activity of inhaled topical steroid in toddlers studied by knemometry. *Acta Paediatr Oslo Nor 1992* 82: 1066–1071.
4. Urlacher SS, Snodgrass JJ, Liebert MA, et al. (2016) The application of knemometry to measure childhood short-term growth among the indigenous Shuar of Ecuador. *Am J Phys Anthropol* 160: 353–357.
5. Rępalska M, Wozniak A, Kulus M (2019) Measurement of the growth of children at weekly intervals. *Rev Sci Instrum* 90.
6. Popielski K, Rępalska M, Woźniak A, et al. (2023) Identyfikacja Głównych Źródeł Błędów Pomiaru Wzrastania Dzieci Markerową Metodą Bezstykową, Ryn, Polska.
7. Popovic MB (2019) Biomechatronics, Massachusetts, Elsevier Inc. Academic Press.
8. Kurz T (2003) Stretching Scientifically: A Guide to Flexibility Training, Stadion.
9. Surgeons AA of O (1965) Joint Motion: Method of Measuring and Recording, Churchill Livingstone.
10. Robertson JA (1984) F. P. Kendall and E. K. McCreary "Muscles, Testing and Function" (Third Edition). *Br J Sports Med* 18: 25.
11. Marieswaran M, Sikidar A, Goel A, et al. (2018) An extended OpenSim knee model for analysis of strains of connective tissues. *Biomed Eng OnLine* 17: 42.
12. Choi B, Lee Y, Kim J, et al. (2016) A self-aligning knee joint for walking assistance devices. *Proc Annu Int Conf IEEE Eng Med Biol Soc EMBS* 2016-Octob: 2222–2227.
13. Sinclair J, Hebron J, Taylor PJ (2015) The test-retest reliability of knee joint center location techniques. *J Appl Biomech* 31: 117–121.
14. Graydon R, Fewtrell D, Atkins S, et al. (2015) The test-retest reliability of different ankle joint center location techniques. *Foot Ankle Online J* 8.
15. Schlink BR, Ferris DP (2019) A Lower Limb Phantom for Simulation and Assessment of Electromyography Technology. *IEEE Trans Neural Syst Rehabil Eng* 27: 2378–2385.
16. Wegner M, Azbari NA, Krause D, et al. (2025) Development of an anthropomorphic phantom of the lower extremities for feasibility studies and verification of total-body irradiation. *Phys Med* 136: 105045.
17. Hasan S, Dhingra AK (2020) 8 Degrees of freedom human lower extremity kinematic and dynamic model development and control for exoskeleton robot based physical therapy. *Int J Dyn Control* 8: 867–886.
18. Phoengsongkhro S, Tangpornprasert P, Yotnuengnit P, et al. (2023) Development of four-bar polycentric knee joint with stance-phase knee flexion. *Sci Rep* 13: 22809.

euspen's 26th International Conference & Exhibition, Krakow, PL, June 2026
www.euspen.eu

Functional tools micro-texturing for controlled chip formation in precision dry machining of PEEK

Anna Bottin, Rachele Bertolini, Enrico Savio, Stefania Bruschi

University of Padua, Department of Industrial Engineering (DII), Italy

anna.bottin.1@phd.unipd.it

Abstract

Precision machining of high-performance polymers, such as polyetheretherketone (PEEK), is increasingly required for biomedical and high-value engineering applications. However, dry turning of polymers is often limited by poor chip control, as conventional cutting insert geometries are primarily designed for metals and produce long, continuous chips that degrade process stability, productivity, and the quality of machined parts. This work investigates a functional modification of the tool rake face via laser-generated micro-grooves to influence chip flow without changing the overall tool geometry. Dry turning tests were carried out on PEEK using untextured and textured inserts. Chip morphology and tool-chip contact area were analyzed. Although complete chip breakage was not achieved during dry machining, the modified tools showed clear changes in chip flow, contact length, and chip geometry. The results highlight the limitations of conventional inserts for dry polymer machining and indicate that functional modifications of the rake face represent a promising direction for tool design to improve chip control and process stability in sustainable precision machining of polymers.

PEEK turning; chip control; textured tools; tool-chip contact

1. Introduction

Polyetheretherketone (PEEK) is increasingly used in biomedical and high-performance engineering applications due to its mechanical properties, biocompatibility, and chemical stability [1]. Machining remains a key manufacturing process for producing accurate and customized components. However, dry turning of PEEK is characterized by poor chip control. The material's ductile behavior promotes the formation of long, continuous chips that can wrap around the tool and workpiece, reducing process reliability [2].

The use of cutting fluids is often restricted in biomedical manufacturing due to contamination risks, while alternative cooling strategies, such as cryogenic cooling, introduce additional complexity at the process level [3]. In contrast, tool design solutions for chip control in polymer machining are still limited. Conventional turning inserts are typically optimized for metallic materials and rely on macroscopic chip breakers, which are generally ineffective when machining PEEK.

Surface modification of the tool rake face represents a possible way to influence chip flow without altering the overall tool geometry. Previous studies from the authors have shown that surface textures can affect tool-chip interaction by modifying contact conditions [4]. In this context, the present work aims to assess whether a local modification of the tool rake face can partially compensate for the limitations of standard insert designs by altering chip flow and contact behaviour under dry cutting conditions.

2. Materials and methods

Turning tests were performed on biomedical-grade PEEK (TECAPEEK™, supplied by Ensinger Plastics) using uncoated carbide turning inserts (Tungaloy™ VNMA 160402–330.5 TH10) with a nominally flat rake face (0° rake angle). A set of inserts was modified by laser texturing the rake face with linear micro-grooves oriented perpendicular to the cutting edge (see Figure 1). The texture was designed to introduce a local functional modification near the cutting edge, while keeping the global insert geometry unchanged. Two main design parameters were considered in this study: groove depth (G_d) and distance from the cutting edge (D), as seen in Figure 1. The groove depth, which controls the intensity of the tool-chip interaction, was set to 40 and 10 µm. The distance of the textured zone from the cutting edge was varied to 70, 100, or 130 µm, controlling when the chip engages the functional surface during its formation. While all textures shared the same pitch (P) and groove orientation with respect to the cutting edge.

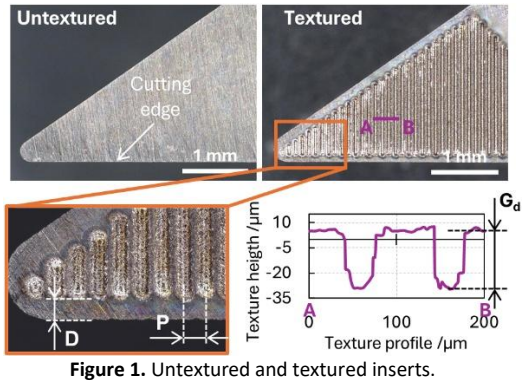

Figure 1. Untextured and textured inserts.

Turning tests were conducted on a lathe (Mori Seiki™ NL 1500 CNC) under dry conditions to isolate the effect of the tool surface modification. Consistent cutting parameters were maintained throughout all trials: cutting speed of 200 m/min, depth of cut of 0.5 mm, and feed of 0.1 mm/rev. After machining, chips were collected and analysed using optical

microscopy (Keyence™ VHX-S770E/S750E) and scanning electron microscopy (FEI™ QUANTA 450 SEM) to evaluate their overall morphology, width, and surface features. Additional short-cutting tests were carried out to assess the tool-chip contact area by analysing the contact imprint left on the rake face.

The analysis focused on identifying changes in chip morphology and contact characteristics induced by the textured surface, rather than on achieving full chip segmentation.

3. Results and discussion

3.1. Chip morphology

In machining with the untextured insert, long, continuous chips were consistently produced. These chips showed limited curvature and a smooth back surface, indicating extended contact with the rake face (see Figure 2 a).

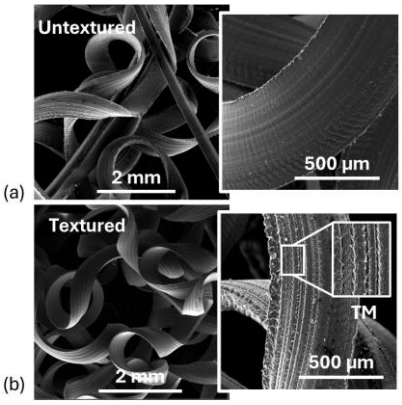

Figure 2. SEM images of the chip obtained with untextured (a) and textured (b) inserts. In the magnification, the texture marks left by the grooves are visible.

The introduction of micro-grooves on the rake face did not lead to chip breakage. However, chips produced with textured tools showed measurable differences compared to those obtained with the standard insert (see Figure 2 b). In particular, a reduction in chip width and an increase in chip curvature were observed. Texture marks (TM) corresponding to the groove pattern were visible on the back surface of the chips, confirming direct interaction between the chip and the modified rake face.

These observations indicate that the textured surface influenced chip flow, even though the deformation was insufficient to fracture the chip under dry cutting conditions.

3.2. Tool-chip contact behaviour

As visible in Figure 3, measurements of the tool-chip contact area showed a shorter tool-chip contact length (λ) and contact width (c) for textured inserts compared to the untextured geometry. This reduction suggests that the micro-grooves locally interrupted continuous contact between the chip and the rake face, promoting earlier chip detachment.

From a tool design perspective, this result is relevant because it shows that the standard insert geometry promotes extended contact, leading to less curved chips, which are therefore unfavourable for chip control in dry polymer machining. On the contrary, the textured insert, while still unable to break the chip, altered the functional behaviour of the tool by modifying how the chip interacts with the rake face.

3.3. Chip formation

The analysis of tool-chip contact shows that both the position and depth of tool textures influence chip formation. For deeper textures, grooves located closer to the cutting edge engaged the chip earlier, promoting greater curling. In contrast, deeper textures positioned farther from the cutting edge interacted with the chip later, producing wider chips with less pronounced curling. Shallower textures exhibited the same trend but with reduced effects: chip detachment from the rake face occurred later, regardless of the groove's distance from the cutting edge.

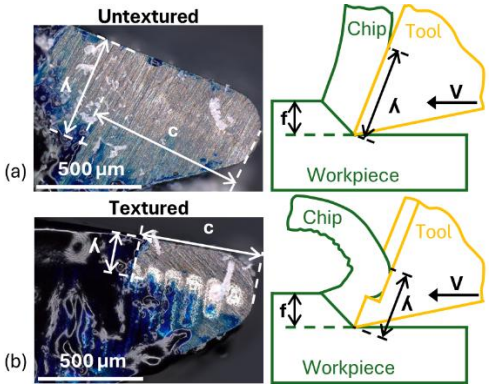

Figure 3. Chip-tool contact area and chip formation for untextured (a) and textured (b) inserts.

These results indicate that effective chip flow control is achieved when deeper textures are located near the cutting edge, as they reduce the tool-chip contact area, guide the material along the grooves, and enhance curling, facilitating chip detachment even under continuous chip formation through the functional role of the textured tool rake face.

4. Conclusion and future work

This work investigated the effect of a local modification to the insert rake face on chip formation during dry turning of PEEK. Although complete chip breakage was not achieved, textured tools clearly influenced chip morphology and tool-chip contact behaviour relative to untextured inserts.

From a precision engineering viewpoint, the results indicate that chip control in polymer machining should be addressed through micro-scale functional design of tool surfaces rather than through conventional insert geometries developed for metals. Local surface modifications of the rake face can influence chip flow and contact behaviour and represent a promising direction for further tool development.

Future work will focus on optimising texture geometry and position to enhance chip curvature and move towards reliable chip segmentation under dry cutting conditions.

Acknowledgements

The authors would like to thank Haizea Gonzalez and Eneko Ukar (Department of Mechanical Engineering, CFAA, University of the Basque Country) for their assistance with the laser texturing of the cutting tools.

References

[1] Panayotov I V, Orti V, Cuisinier F and Yachouh J 2016 Polyetheretherketone (PEEK) for medical applications J. Mater. Sci.: Mater. Med. **27** 1–11

[2] Bertolini R, Bottin A, Zanella C, Bruschi S, Ghiotti A and Savio E 2025 The role of PEEK viscoelasticity in chip formation, surface finish and geometrical accuracy CIRP Ann. **74** 765–769

[3] Jawahir I, Puleo D A and Schoop J 2016 Cryogenic machining of biomedical implant materials for improved functional performance, life and sustainability Procedia CIRP **46** 7–14

[4] Bottin A, Bertolini R, Gonzalez H, Ukar E and Bruschi S 2025 Promoting chip breakage in biomedical-grade PEEK machining through tool texturing and cryogenic cooling Int. J. Adv. Manuf. Technol.

euspen's 26th International Conference & Exhibition, Krakow, PL, June 2026
www.euspen.eu

Functionalization of tantalum oxide coatings on commercially pure titanium by PEO

Pedro Paulo da Graça de Morais[1], Mizael Rodrigues[2], Eduardo Guy Perpétuo Bock[3], Natallie Zillio de Souza Teixeira[1], Nilson da Cruz[2]

[1]*Instituto Federal de São Paulo (IFSP), Campus Boituva, Brazil*
[2]*Universidade Estadual Paulista (UNESP), Campus Sorocaba, Brazil*
[3] *Instituto Federal de São Paulo (IFSP), Campus São Paulo, Brazil*

morais.paulo@aluno.ifsp.edu.br

Abstract

The key point in biomaterials and implant research is biocompatibility. Metals and their alloys, such as titanium and tantalum, present favorable mechanical and physicochemical properties for both bulk applications and functionalized surfaces. Titanium is widely recognized for its use in the field of biomaterials, but tantalum has gained prominence in recent years. Titanium surfaces can be functionalized by depositing a tantalum layer, taking advantage of the positive properties of the bulk material combined with the benefits of a distinct coating, aiming for enhanced biological performance. This deposition is enabled by the technique of plasma electrolytic oxidation (PEO), and the analysis of this new surface is carried out using techniques such as profilometry and goniometry. Surface roughness was assessed as a physical parameter by profilometry, while surface wettability was assessed through the contact angle measured by goniometry. EDS analysis confirmed the incorporation of tantalum onto the surface, validating the proposed functionalization. This modification aims to replace titanium alloys that release cytotoxic ions, such as vanadium, with a biocompatible tantalum surface, representing a potential future option for biomedical applications.

Biocompatibility; surface functionalization; tantalum; biomaterials; implants; plasma oxidation

1. Introduction

Biocompatibility is fundamental to achieving success in biomedical implants [1]. The way a material creates its surface can favor cellular adhesion, improving integration with living tissues [2]. The interior of the material, or bulk, influences physicochemical properties that affect the human body's biological response [3].

Titanium, widely present in medical applications, is known for its good mechanical strength, biocompatibility, and its ability to form a stable passive layer that aids in osseointegration [4,5]. On the other hand, tantalum possesses a structure like trabecular bone [6] and promotes protein adsorption, optimizing the biological response. Applying a tantalum oxide coating over titanium can enhance properties such as surface energy, biocompatibility, and cellular adhesion. Despite the recognized biological potential of tantalum, there is still a scarcity of simple and reproducible deposition routes for incorporating Ta into titanium surfaces using PEO, with metrological control of roughness and wettability.

The Plasma Electrolytic Oxidation (PEO) technique offers the possibility of functionalizing titanium surfaces, promoting improvements in roughness and wettability [7,8]. Wettability, analyzed through goniometry, influences the cell-surface interaction and depends on topography and chemical composition [9]. Additionally, profilometry allows for the evaluation of morphological changes with high precision [10].

2. Methodology

Commercially pure titanium samples with dimensions of (25 x 40 x 1) mm were cleaned in an ultrasonic bath (L100 Ultrasonic Cleaner, Schuster, Santa Maria, Brazil) for 4 minutes using distilled water and neutral detergent (Extran MA 02, Merck KGaA, Darmstadt, Germany) for 15 minutes using a 2% (v/v). Subsequently, they were cleaned for the same duration in the same machine using only distilled water. This process was repeated a third time using isopropyl alcohol, followed by drying on filter paper.

For the deposition of the new tantalum layer via PEO, an electrolyte was prepared in which the samples were submerged inside the plasma reactor. The solution consisted of 0.5 L distilled water, tantalum oxide (Ta2OH5) at a concentration of 15 g/L, and potassium hydroxide (KOH) at 3 g/L. The mixture was prepared using a magnetic stirrer (Fusion Magnetic Stirrer, FUS-100, Corning Inc., New York, USA) under controlled conditions. A power supply (MKO Power Supply, Plasma Technics Ltd., Racine, USA) was used with the following pre-defined parameters: a voltage of 450 V, a frequency of 1000 Hz, duty cycle of 60%. The duty cycle corresponds to the fraction of time the voltage is applied relative to the total pulse cycle time, remaining active for 60% of the duration and inactive for the remaining 40%.

The exposure time across all samples varied from 10 to 30 minutes, aiming to visually achieve a uniform and standardized deposited layer for subsequent testing. The process resulted in the formation of a tantalum-containing oxide layer on the titanium surface, characterized by a rough appearance and a whitish color.

2.1 Profilometry Analysis

Surface roughness analysis was performed by profilometer (Dektak 150, Veeco Instruments Inc., Plainview, USA). A 'Standard Scan' type was employed, with a scan length of 2,000 µm and a duration of 60 seconds, totaling 20,000 data points per measurement. The scanning speed was set at 33.33 µm/s, moving from left to right. A stylus with a 12.5 µm radius was used, applied with a constant force of 3.0 mg. The vertical measurement range was 65.5 µm.

The following parameters were analyzed: arithmetic average roughness (Ra), root mean square roughness (Rq), and the surface asymmetry parameter (ASP). These analyses allowed for the precise observation of topographical variations resulting from the surface treatment applied to the samples.

2.2 Goniometry Analysis

The surface wettability of the samples was verified using a goniometer (Model 500 Advanced Goniometer, Ramé-hart Instrument Co., Succasunna, USA), equipped with fiber optic lighting and a manual microsyringe for droplet control. The analyses were performed using 2 µL droplets of distilled water and diiodomethane, deposited onto both the pure titanium surfaces and the tantalum-coated surfaces. Droplet images were captured by the goniometer's integrated system and analyzed via software to determine the contact angle between the droplets and the surfaces.

3. Results

In this section, the results obtained from the tests performed on commercially pure titanium samples and those functionalized with tantalum are presented. Initially, the wettability was analyzed using the goniometer.

Figure 1 illustrates how water interacts with different commercially pure titanium samples. With a contact angle of 102°, the first sample demonstrates a well-rounded droplet, indicating minimal water spreading and highlighting the characteristics of a highly hydrophobic surface [11]. Conversely, the other two samples show droplets with greater adsorption to the surface.

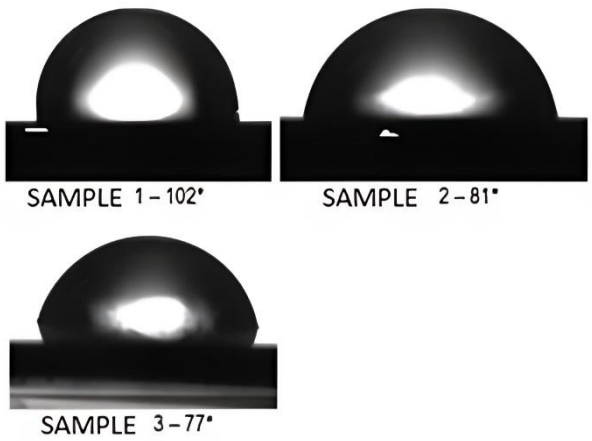

Figure 1. Goniometry assay of commercially pure titanium samples.

These variations in behavior between the liquid and the surface may be linked to subtle differences in the texture or treatment of the pure titanium surfaces, such as their polishing. In practical terms, surfaces that are rougher or possess lower surface energy in the outer layer tend to 'repel' water, causing the droplet to remain rounded as if resisting adhesion to the material.

These preliminary results underscore the importance of wettability in the success of implants. In subsequent tests involving tantalum oxide deposition, it will be possible to compare changes in wettability, which consequently affect the bioactivity and biocompatibility of the samples. A review of hydroxyapatite-doped coatings shows that typically more hydrophilic and rough/porous surfaces enhance interaction with biological fluids, cell adhesion, and proliferation, thereby improving biointegration [12].

Figure 2 shows the adsorption of the diiodomethane droplet by the functionalized surface sample. The way the droplet spreads demonstrates a certain degree of hydrophilicity in the material.

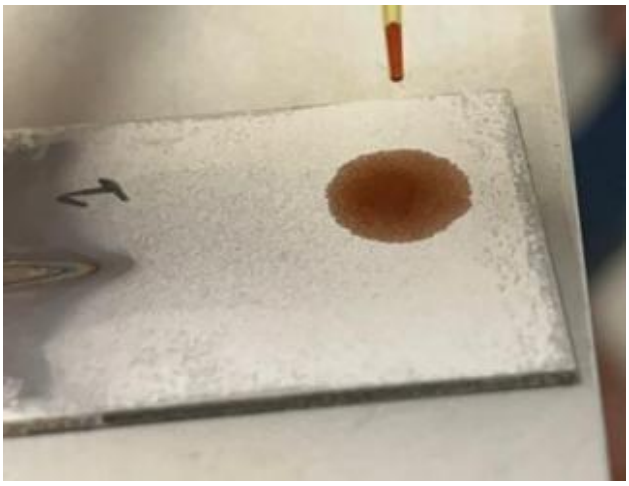

Figure 2. Goniometry assay with diiodomethane on tantalum oxide functionalized titanium samples.

Due to the rapid adsorption of the liquids onto the surface, analysis via contact angle becomes unfeasible. These results indicate that the deposition altered not only the surface characteristics but also the chemical composition of the material, optimizing its affinity for different types of fluids, which may impact cellular adhesion.

As shown in Figure 3, surface roughness (Ra) analysis was performed on twelve commercially pure titanium (cp-Ti) samples and twelve tantalum oxide-functionalized (Ti/Ta) samples using profilometry. The data demonstrate a substantial difference between the roughness values of the two surfaces. The Ti/Ta samples exhibit higher average roughness values, ranging between 10,225.7 nm and 16,239.1 nm, with the highest peak observed in sample 6. In contrast, the commercially pure titanium samples show significantly lower roughness, approximately three times less than the functionalized ones.

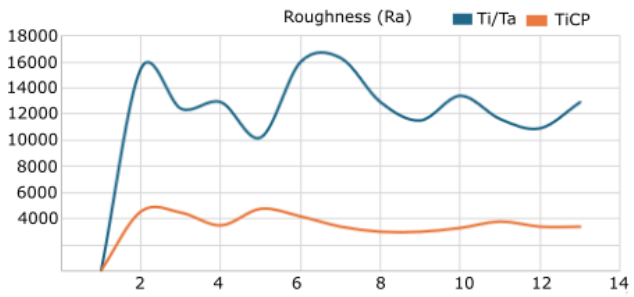

Figure 3. Surface roughness by profilometry of CP-Ti (commercially pure titanium) and Ti/Ta (titanium with deposition).

The increase in the roughness of the Ti/Ta samples indicates that the functionalization by tantalum oxide deposition via PEO contributed to the surface modification in a favorable manner. This increase in roughness is related to a larger contact area with the liquid, which potentially enables cell adhesion and osseointegration in biomedical applications. As shown in Figure 4, EDS reveal the predominant presence of Tantalum on the sample surface at two different points. Furthermore, the porous aspect of the surface morphology is verified. The micrograph of the deposited layer shown in Figure 5 reveals a heterogeneous and irregular surface, which is a common characteristic of coatings obtained by Plasma Electrolytic Oxidation (PEO). The points labeled as 'Spectrum' indicate regions selected for EDS chemical analysis, chosen to represent different morphological features of the same surface. Selecting different points allows for the evaluation of deposition uniformity and the identification of possible local variations in chemical composition. Surface cavities can host cells from body fluids that would come into contact with the surface, favoring cell adhesion and biocompatibility. Nano/micro topography directly influences cell adhesion [13]. As the increase in roughness was confirmed by profilometry, it can be stated that the functionalized layer possesses biological potential.

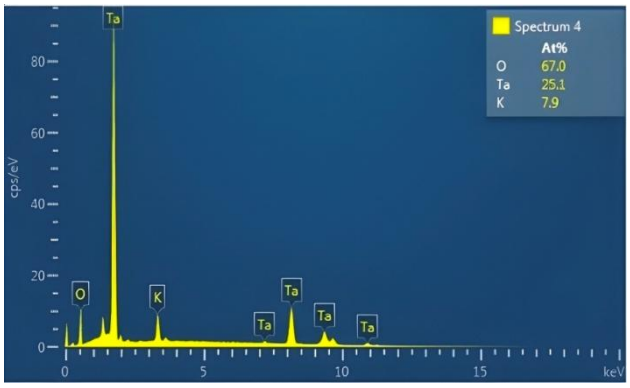

Figure 4. Chemical composition obtained by EDS of the titanium surface functionalized with tantalum oxide, at point 4. Source: The author.

4. Discussion

In this work, an increase in the wettability and surface roughness of the Ti/Ta alloy is demonstrated; these factors are associated in the literature with a better biological response, although they have not yet been directly evaluated by biological assays in this study [1].

Several studies demonstrate that the wettability and roughness of metallic or polymeric surfaces directly modulate protein adsorption, cell adhesion, immune response, and, ultimately, biocompatibility [1,14,15,16,17,18].

The results achieved in this research prove that the functionalization of the titanium surface with tantalum oxide via PEO promotes significant changes in surface properties. The goniometry test demonstrates an increase in wettability, highlighted by the decrease in the contact angle with water and diiodomethane. Profilometry revealed an increase in the average roughness of the functionalized samples, emphasizing a topography favorable to cell adhesion. SEM and EDS analysis confirmed the presence of Tantalum in the functionalized layer.

These alterations contribute to biocompatibility and osseointegration, reinforcing the efficacy of the PEO technique with tantalum oxide deposition for biomedical applications. Future studies may further the investigation with wear resistance and corrosion analysis.

The PEO process in a Ta-containing electrolyte produced a Ta oxide layer with a porous morphology and high roughness, confirmed by EDS and profilometry. Results demonstrated a significant increase in roughness and a drastic shift in wettability. The surface exhibited rapid droplet adsorption, rendering traditional contact angle measurements unfeasible. This behavior indicates a strong affinity for biological fluids, characteristic of superhydrophilic surfaces.

5. Conclusions and future work

Since both variables (roughness and chemical composition) change simultaneously, it is not possible with the current data, to quantitatively separate the individual contribution of each to the increase in wettability. Nonetheless, the presence of Ta is confirmed by EDS and the increase in roughness by profilometry, indicating a combined effect.

These findings suggest that the proposed PEO treatment is an effective and relatively simple method for Ti/Ta surface functionalization. Furthermore, the ability to incorporate tantalum while controlling surface topography presents a promising alternative to conventional Ti-alloys that release cytotoxic ions, such as vanadium, thereby enhancing the biocompatibility of orthopedic implants.

This study validates PEO-based Ti/Ta functionalization as a robust method to enhance biocompatibility through improved wettability. The results provide a clear proof of concept, with tantalum incorporation and topography control strictly verified by EDS, SEM, profilometry, and goniometry.

The research is ongoing. Future corrosion assays and in vivo tests will be conducted to verify and confirm the biocompatibility capacity of the functionalized topology.

References

[1] Fialho L I S G 2021 Design of new biocompatible osseointegrated and antimicrobial dental implant PhD Thesis University of Minho

[2] Bock E, Pfleging W, Tada D et al 2022 Laser-treated surfaces for VADs: from inert titanium to potential biofunctional materials *BME Frontiers* 2022 9782562

[3] Temenoff J S and Mikos A G 2008 Biomaterials: the intersection of biology and materials science (Upper Saddle River: Pearson Prentice Hall)

[4] Pandey L M 2023 Design of biocompatible and self-antibacterial titanium surfaces for biomedical applications *Current Opinion in Biomedical Engineering* **25** 100423

[5] Yang S, Jiang W, Ma X, Wang Z, Sah R L, Wang J and Sun Y 2023 Nanoscale morphologies on the surface of 3D-printed titanium implants for improved osseointegration: a systematic review *International Journal of Nanomedicine* **18** 4171–4191

[6] Levine B R et al 2006 Experimental and clinical performance of porous tantalum in orthopedic surgery *Biomaterials* **27** 4671–4681

[7] António C A 2018 Deposição de revestimento bioativo em titânio por oxidação eletrolítica com plasma MSc Thesis

[8] Mashtalyar D V, Nadaraia K V, Gnedenkov A S et al 2020 Bioactive coatings formed on titanium by plasma electrolytic oxidation:
composition and properties *Materials* **13** 4121

[9] Sun L et al 2021 Tailoring materials with specific wettability in biomedical engineering *Advanced Science* **8** 2100126

[10] Lucas R R et al Análise da espessura e rugosidade de revestimento óxido crescido por oxidação eletrolítica a plasma sobre a liga AA2024-T3

[11] Rodrigues M S et al 2019 Surface roughness of biomaterials and process parameters of titanium dioxide gritblasting for productivity enhancement *TAS Journal* **3** 169–176

[12] Gul I et al 2025 Surface Wettability Response of Hydroxyapatite-Doped Coatings on Metallic Biomaterials: A Concise Review Solid State Phenomena 370 61–72

[13] Hou Y et al 2020 Surface roughness gradients reveal topographyspecific mechanosensitive responses in human mesenchymal stem cells *Small* **16** 1905422

[14] Rupp F, Liang L, Geis-Gerstorfer J, Scheideler L and Hüttig F 2017 Surface characteristics of dental implants: A review Dental Materials 34 40–57

[15] Simon A et al 2024 Influence of micro and nanoporous TiO2 surface modifications on physical-chemical and biological interactions Applied Surface Science 668 160336

[16] Spriano S et al 2017 How do wettability, zeta potential and hydroxylation degree affect the biological response of biomaterials? Materials Science and Engineering: C 74 542–555

[17] Visalakshan R M et al 2019 Biomaterial Surface Hydrophobicity Mediated Serum Protein Adsorption and Immune Responses ACS Applied Materials & Interfaces 11 27915–27923

[18] Arima Y and Iwata H 2007 Effect of wettability and surface functional groups on protein adsorption and cell adhesion using well-defined mixed self-assembled monolayers Biomaterials 28 3074–3082

euspen's 26th International Conference & Exhibition, Krakow, PL, June 2026
www.euspen.eu

Fundamental Investigation of Cutting Mechanisms in Ultra-Precision Machining of KTP Crystals for Quantum Communication

E. Uhlmann[1,2], M. Polte[1,2], T. Hocke[1,2], T. D. Le[1]

[1]*Institute for Machine Tools and Factory Management IWF, Technische Universität Berlin, Germany*
[2]*Fraunhofer Institute for Production Systems and Design Technology IPK, Germany*

le@tu-berlin.de

Abstract
Quantum communication is a key technology for encryption and secure transfer of information, especially in times of highly sensitive data and digital security. Therefore, the use of entangled photons opens new possibilities in information transmission, as they are a fundamental resource of quantum mechanical methods and enable innovative approaches in quantum communication. Potassium titanyl phosphate (KTP) in its periodically poled form (ppKTP) is used as a source for entangled photons due to its nonlinear optical properties. Its inherent brittleness represents a significant limitation for crack-free ultra-precision machining of complex optics for quantum repeaters. Therefore, fundamental investigations of cutting mechansims in ultra-precision machining have been carried out. The ultra-precision planing tests have been carried out on a machine tool of type 650 FG v3 manufactured by MOORE NANOTECHNOLOGY SYSTEMS, USA, equipped with nanopolycrystalline diamond (NPD) cutting tools from A.L.M.T. CORP., Japan. The lowest arithmetic mean height Sa = 0.89 nm and arithmetical mean deviation Ra = 0.76 nm were achieved at a depth of cut a_p = 2.5 µm, a cutting speed of v_c = 50 mm/min and a width of cut a_e = 1.5 µm, using a tool with a corner radius r_ε = 400 µm and a cutting edge radius r_β < 1 µm. With decreasing width of cut, both the number of micro-cracks and the fracture width decreased. In conclusion, the influence of the width of cut and the corresponding undeformed chip thickness on the micro-crack and fracture characteristics of KTP was clarified.

Keywords: hard-brittle materials, nanopolycrystalline diamond tool, ultra-precision machining

1. Introduction

Quantum computers are increasingly important for social and technological development, whereby the optimization of information transmission is also becoming a growing priority. In particular, the use of quantum mechanical interactions offers new application possibilities with far-reaching societal significance. Thus, the field of quantum communication emerged with the approach of transmitting information using entangled photons, representing an important milestone in information security.

Potassium titanyl phosphate (KTP) crystals are used for photonic applications, as periodic poling potassium titanyl phosphate (ppKTP) enables efficient nonlinear optical processes [1]. In addition to suitable optical properties, precise mechanical machining of the crystal is also essential. In this context, this work investigates machining with geometrically defined cutting edges for the machining of the brittle material ppKTP in order to achieve ultra-precision surface qualities and shape accuracy a_s. According to the state of the art, crystals such as ppKTP are primarily machined using tools with undefined cutting edges, such as grinding and polishing [2]. However, these approaches are limited by a curvature radius of r_f < 10 mm. In addition, process-related grooves occur that alter the optical properties of the component and would therefore impair the functionality of the crystals [3]. Consequently, machining with geometrically defined cutting edges, in particular UP-planing and -turning, represent a novel approach for machining of ppKTP materials. For this reason, the overall objective is the realization of UP-planing and -turning of ppKTP for the use of quantum optics. Due to the brittle properties of the ppKTP crystal, machining strategies are required that enable material removal with ultra-precision surface roughness and shape accuracy a_s.

According to the state of the art, this is achieved for brittle materials when a hydrostatic compressive stress state is present [4] as well as the critical undeformed chip thickness h_{crit}, which defines the brittle-to-ductile transition, is not exceeded [5]. Recent investigations showed that ultra-precision machining of ppKTP crystals with sufficient surface roughness and shape accuracy a_s, including their periodically poled form, was achieved using a nanopolycrystalline diamond (NPD) tool, as its applicability was previously demonstrated for brittle materials such as cemented carbide [6]. In the present study, the employed NPD tools have a cutting edge radius of r_β < 1 µm and a corner radius of r_ε = 0.4 mm [7]. Under these conditions, crack-free material removal without the occurrence of brittle fractures was observed for depths of cut of a_p < 4 µm. For this purpose, scratching experiments with increasing depths of cut a_p were conducted to analyse the influence of the depth of cut a_p on surface formation and to identify the respective cutting regimes [7]. While these investigations clarified the influence of the depth of cut a_p, the scratch-based methodology involves continuously varying process conditions, preventing an isolated evaluation of the local undeformed chip thickness h and its direct correlation with surface quality. To address this research gap, the present study proposes partial-cut planing experiments as an analogous approach to enable the isolated investigation of the influence of the undeformed chip thickness h on surface formation. This allows for a systematic variation of the undeformed chip thickness h, while maintaining constant cutting conditions in terms of depth of cut a_p, width of cut a_e and cutting speed v_c,

thus enabling a clear correlation between the undeformed chip thickness h, material removal mechanisms and the resulting surface roughness.

2. Experimental setup and methodology

In this study, a KTP-crystal from the company EKSMA OPTICS, UAB, Vilnius, Lithuania, was used in its original form without periodic poling, due to the high availability and lower cost compared to ppKTP-crystals. While the crystal structure remains unchanged, the optical properties are modified by the poling process [8], as periodic poling is regarded as a functional post-processing step for nonlinear crystals such as KTP. Therefore, the same material-specific machining behaviour applies.

To identify ranges of the undeformed chip thickness h associated with reduced brittle damage, ten grooves were machined. For each groove, a constant width of cut a_e was applied, while varying values were assigned between grooves, ranging from $a_e = 0.5$ µm to $a_e = 5$ µm in increments of $a_e = 0.5$ µm. The depth of cut was kept constant at $a_p = 2.5$ µm, since ductile machining was demonstrated for the employed tool at this value [7]. Likewise, the cutting speed was kept constant at $v_c = 50$ mm/min according to UHLMANN ET AL. [7] to achieve an isolated investigation of the influence of the width of cut a_e and the resulting maximum undeformed chip thickness h_{max}, which can be determined due to the formation of the comma-shaped chip according to Equation (1) [9]:

$$h_{max} = r_\varepsilon - \sqrt{r_\varepsilon^2 + a_e^2 - 2\,a_e\sqrt{2\,r_\varepsilon\,a_p - a_p^2}} \qquad (1)$$

As a result, widths of cut of 0.5 µm ≤ a_e ≤ 5.0 µm corresponds to a range of maximum undeformed chip thicknesses of 55.01 nm ≤ h_{max} ≤ 527.24 nm. The grooves were machined completely over the entire length of cut l = 4 mm under dry conditions, resulting in a groove width of w = 0.1 mm. Table 1 summarises the applied planing parameters.

Table 1 Process parameters for the planing process

Parameter	Symbol	Value
depth of cut	a_p	2.0 µm
cutting speed	v_c	50.0 mm/min
width of cut	a_e	0.5 µm - 5.0 µm
cooling lubricant	-	dry machining

2.1 Machine technology

The experiments were conducted using a 5-axis ultra-precision machine tool type 650 FG v3 manufactured by the company MOORE NANOTECHNOLOGY SYSTEMS, Swanzey, USA. Due to its climate-controlled working environment and the granite machine bed, stable thermal conditions and low vibration levels are ensured. In particular, the aerostatic and hydrostatic bearings of the spindle and linear axes enable slip-stick-free motions, allowing surface qualities in the sub-nanometer range to be achieved.

2.2 Tool geometry and measurement methods

For the experiments, NPD-tools from the company A.L.M.T. CORP., Tokyo, Japan, were used, featuring a corner radius of $r_\varepsilon = 0.4$ mm, a cutting edge radius of $r_\beta < 1$ µm. The grooves were machined with a rake angle of $\gamma_0 = 0°$.

The same type of tool with comparable specifications was employed in the scratching tests conducted by UHLMANN ET AL. [7] to determine the critical depth of cut $a_{p,crit}$.

To quantify the data, the planed surfaces were measured using a white light interferometer (WLI) type ZYGO NEWVIEW 5010 from the company AMETEK GERMANY GMBH, Weiterstadt, Germany, in which the surface roughness Sa was determined. Furthermore, the topographical examination of the grooves and the characterisation of the initial tool condition were performed using a ZEISS LEO 1455 VP scanning electron microscope (SEM) from the company LEICA ELECTRON OPTICS, Wetzlar, Germany. The initial tool condition is shown in Figure 1.

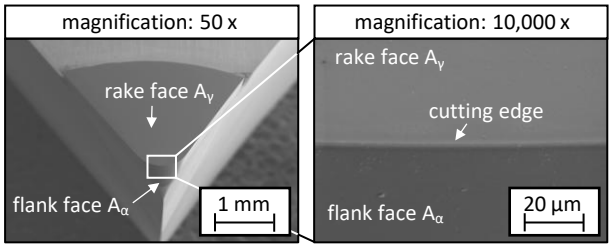

Figure 1. SEM image of the initial condition of the NPD-tool

The tool was geometrically characterised using a focus variation microscope type INFINITEFOCUS manufactured by ALICONA IMAGING GMBH, Graz, Austria, to determine the cutting edge radius r_β. To examine the occurring process forces F_P during the planing process, a 3-component dynamometer of the type KISTLER 9256C2 from KISTLER INSTRUMENT AG, Winterthur, Switzerland, was used.

3. Cutting results

Since the grooves were machined on the free surface of the material, three distinct regions can be identified: full-cut region, partial-cut region and the region of comma-shaped chip formation, as exemplarily illustrated for a single groove with a width of cut of $a_e = 3$ µm in Figure 2.

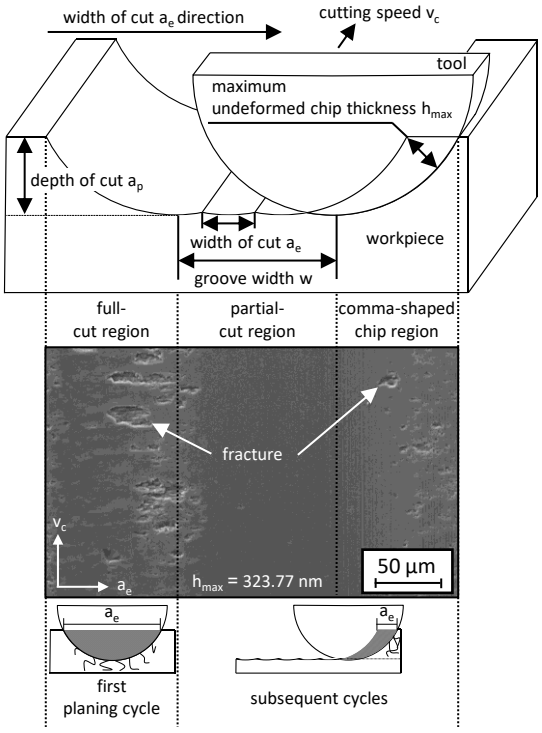

Figure 2. Schematic illustration of the planing process and resulting surface regions shown in a SEM image

The full-cut region corresponds to the first planing cycle and is characterised by continuous fractures that are observed in all grooves. This is expected, as the full-cut condition is solely defined by the cutting speed v_c and depth of cut a_p, which are identical for all grooves. The largest fractures originate at the groove bottom and decrease towards the edge, as the brittle regime is first reached at the groove bottom in the full-cut region. In contrast, the partial-cut region begins from the second planing cycle. Due to the reduced chip cross-section A in the partial-cut region, the material removal mechanism changes, resulting in a distinctly different surface formation compared to the full-cut region and leading to altered cutting forces F_c.. Figure 3 exemplarily shows a cutting force F_c profile of a planing process in which a width of cut of a_e = 0.005 µm was selected.

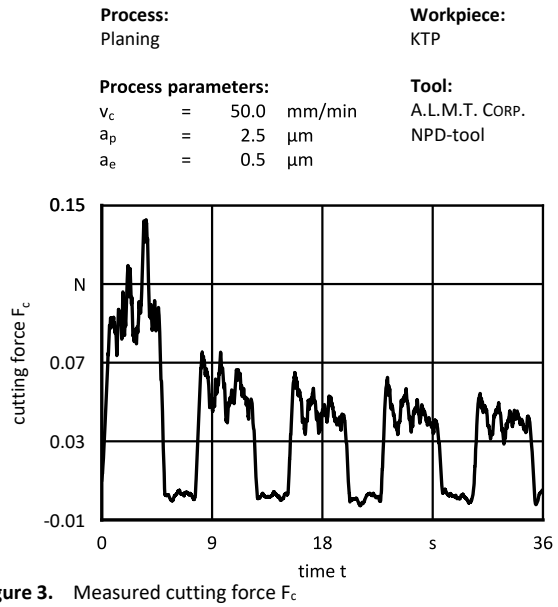

Figure 3. Measured cutting force F_c during full cut and partial cut conditions

In the first planing cycle, maximum cutting forces of $F_{c,max}$ = 0.122 N were identified. In the subsequent planing cycles, the cutting force decreases to an average value of F_c = 0.044 N. This behaviour is attributed to the larger chip cross-section A present during full-cut conditions compared to the subsequent partial-cut cycles. Finally, the comma-shaped chip formation region represents the area generated during the last planing cycle. It can be observed that fractures become more pronounced towards the groove edge in the direction of the width of cut a_e, which was consistently observed for all grooves. Therefore, this region can be considered the origin of fracture formation. This is consistent with the model proposed by BLAKE AND SCATTERGOOD [5], as the critical undeformed chip thickness h_{crit} is consistently exceeded in the upper region of the comma-shaped chip thickness distribution.

In general, ductile machining refers to a plastic material removal process with plastic chip formation, in which crack formation is prevented, thereby suppressing brittle fractures. Accordingly, the topographical analysis shown in Figure 4 reveals a significant decrease in the number of fractures n_f within the partial-cut region with decreasing width of cut a_e, indicating an increasing dominance of ductile-like machining mechanisms. However, it is noticeable that the fracture width w_f does not decrease linearly. Exemplarily, for a width of cut of a_e = 5 µm, fracture widths of w_f < 12 µm were identified, whereas for reduced widths of cut of a_e = 2 µm and a_e = 0.5 µm, fracture widths of $w_f \leq$ 8.5 µm and $w_f \leq$ 5.3 µm were observed within the partial-cut region, respectively. However, even at the smallest width of cut a_e = 0.5 µm within the selected process range, fractures could still be observed. Due to the statistical nature of brittle fractures, it cannot be excluded that neighbouring micro-cracks accumulate, causing the initial crack depth y_c to exceed the critical crack depth $y_{c,crit}$ and propagate to the surface. Consequently, individual fractures and micro-cracks remain in the following planing cycle with. This implies that the width of cut a_e influences the extent and probability of fractures, as evidenced by reductions in fracture width w_f and the number of fractures n_f. This indicates that more than a single planing pass is required to completely prevent fractures of this type.

Figure 5 shows the arithmetic mean height Sa and the arithmetic mean deviation Ra in relation to the width of cut a_e. A range of arithmetic mean heights of 0.89 nm ≤ Sa ≤ 11.97 nm and arithmetic mean deviations of 0.76 nm ≤ Ra ≤ 2.73 nm can be determined. It becomes evident that, initially starting from a width of cut of a_e = 0.5 µm, the arithmetic mean height decreases to Sa = 0.89 nm at a width of cut of a_e = 1.5 µm and subsequently increases to Sa = 11.97 nm up to a width of cut of a_e = 5 µm. A comparable trend is observed for the arithmetic mean deviation Ra.

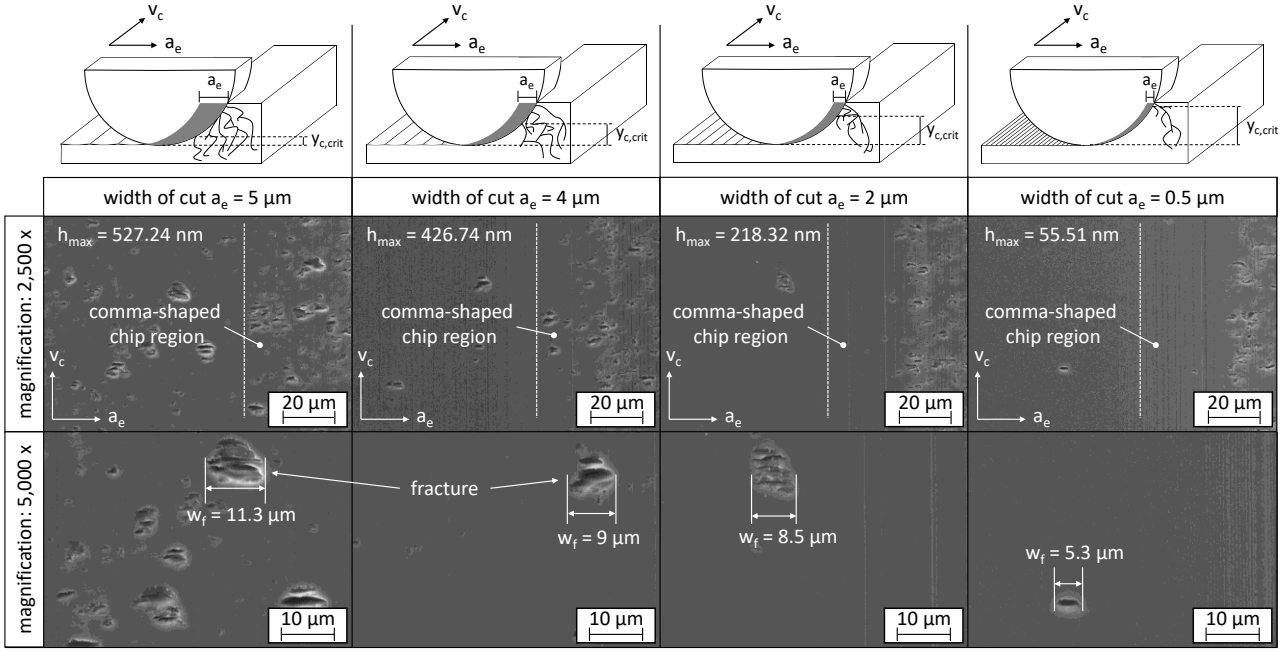

Figure 4. SEM images of crack formation at different widths of cut a_e and magnifications in the partial-cut region

The first reduction can be explained by the fact that, with a decreasing width of cut a_e, the maximum undeformed chip thickness h_{max} is reduced and the region of minimum chip thickness h_{min} shifts towards the main cutting edge S. This means that the achieved maximum chip thickness h_{max} approaches the value of the minimum chip thickness h_{min}, resulting in a higher theoretical roughness depth R_{th} and thus a higher arithmetic mean height Sa and arithmetic mean deviation Ra respectively [10]. This effect is further intensified by the higher cutting edge radius of a NPD-tool with $r_\beta < 1$ µm compared to a single-crystalline diamond tool with a cutting edge radius in the range of 20 nm ≤ r_β ≤ 50 nm [11]. The subsequent increase in the arithmetic mean height Sa and arithmetic mean deviation Ra is attributed to the more pronounced width-of-cut-related marks. Thus, the best surface quality in terms of arithmetic mean height within the selected process range can be identified at a width of cut of a_e = 1.5 µm with an arithmetic mean height of Sa = 0.89 nm and an arithmetic mean deviation of Ra = 0.76 nm.

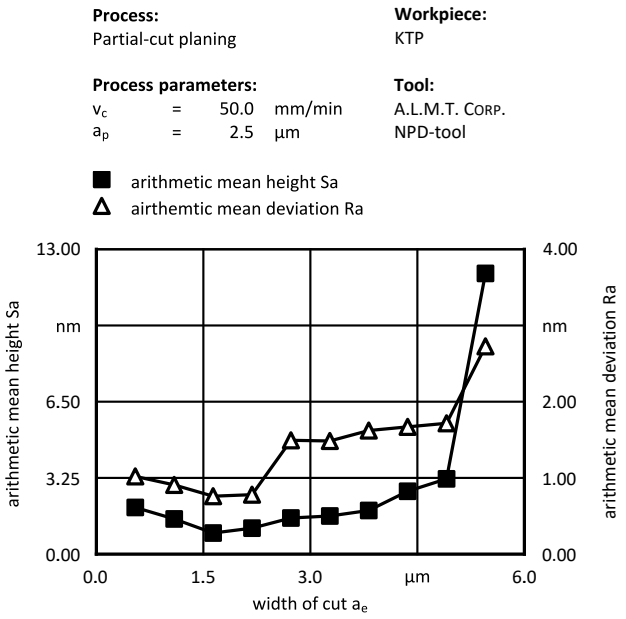

Figure 5. Influence of the width of cut a_e on the arithmetic mean height Sa

However, if fracture widths w_f are included in the surface evaluation, a reduction in fracture width with decreasing width of cut a_e can be observed. This trend is shown in Figure 6 by a linear regression of fracture width w_f versus width of cut a_e.

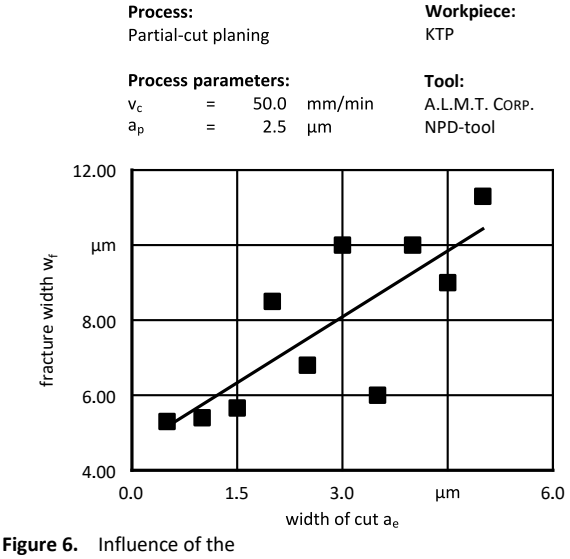

Figure 6. Influence of the width of cut a_e on the fracture width w_f

4. Conclusion

In this study, the influence of the width of cut a_e on surface generation during the machining of KTP was investigated. The results showed that the number of fractures n_b can be significantly reduced with a decreasing width of cut a_e. Within the width of cut range of 0.5 µm ≤ a_e ≤ 4.5 µm, arithmetic mean heights of Sa ≤ 3.21 nm and arithmetic mean deviations of Ra ≤ 1.72 nm could be achieved despite the presence of isolated fractures. However, the best surface qualities in terms of arithmetic mean height within the selected process range, characterized by 0.89 nm ≤ Sa ≤ 1.107 nm, were obtained within the width of cut range 1.5 µm ≤ a_e ≤ 2.0 µm. Consequently, for the planing process, the maximum undeformed chip thickness is within the range of 164.66 nm ≤ h_{max} ≤ 218.31 nm, in which ductile-like machining with an improved optical surface quality in terms of arithmetic mean height Sa can be achieved. If the undeformed chip thickness h is below the optimal range due to a reduced width of cut a_e, the surface quality deteriorates as a result of the increasing influence of the minimum chip thickness h_{min}. Conversely, if the maximum undeformed chip thickness h_{max} exceeds the optimal range due to a larger width of cut a_e, widths of cut marks are formed, which likewise impair the surface quality. Considering the fractures, it can be observed that decreasing the width of cut a_e leads to a consistent reduction in both the number of fractures n_f and the fracture width w_f.

Despite the reduced occurrence and extent of fractures, they were still present in every groove, indicating that fully ductile machining without fractures was not yet achieved.Therefore, these results provide the basis for further investigations into the influence of the rake angle γ_0 on ductile machining, as it represents an additional influencing parameter for the ductile machining of brittle materials.

References

[1] Lee S M, Kim H, Cha M and Moon H S: Polarization-entangled photon-pair source obtained via type-II non-collinear SPDC process with PPKTP crystal Optics Express 24, 2016, pp. 2,940 – 2,952.

[2] Guo J, Shi H and Pan B: Research on chemical mechanical polishing of KTiOPO4 crystal Proc. 8th Int. Conf. Nanomanufacturing and 4th AET Symp. ACSM and Digital Manufacturing 2022, (Nanoman-AETS), pp. 1 – 4.

[3] Rowe W B: Principles of Modern Grinding Technology Oxford. 2nd ed. Elsevier, 2014.

[4] Yan J, Yoshino M, Kuriagawa T, Shirakashi T, Syoji K and Komanduri R: On the ductile machining of silicon for micro electro-mechanical systems (MEMS), opto-electronic and optical applications Mater. Sci. Eng. A297, 2001, pp. 230 – 234.

[5] Blake P N, Scattergood R O: Ductile-Regime Machining of Germanium and Silicon J. Am. Ceram. Soc. 73, 1990, pp. 949 – 957.

[6] Uhlmann E, Polte M, Hocke T, Polte C, Polte J: Precise cutting of cemented carbide with nanopolycrystalline diamond in ductile regime euspen 23th Int. Con. and Exhib, 2023, pp. 1 – 2.

[7] Uhlmann E, Polte M, Hocke T, Wendt M, Polte C and Tschöpel J: Investigation of nanopolycrystalline diamond tools for ultra-precision machining of ppKTP-crystals for quantum communication applications euspen 25th Int. Con. and Exhib, 2025, pp. 1 – 2.

[8] Karlsson H and Laurell F: Electric field poling of flux grown KTiO4 Appl. Phys. Lett. 71, 1997, pp. 3,474 – 3,476.

[9] Bulla B: Ultrapräzisionszerspanung von Nanokorn-Hartmetall mit monokristallinen Diamantwerkzeugen Dissertation, RWTH Aachen, Aachen, 2013.

[11] Uhlmann E: Paris. 5th Meeting of the Collaborative Working Group on Micro Production Engineering CIRP Winter Meeting, 2014.

[10] Brammertz P H: Die Entstehung der Oberflächenrauheit beim Feindrehen Industrie-Anzeiger, 1961, pp. 25 – 32.

euspen's 26th International Conference & Exhibition, Krakow, PL, June 2026
www.euspen.eu

Green-EDM approaches for biocompatible processing of rolled and 3D printed titanium alloys

Agnieszka Żyra[1], Sebastian Skoczypiec[1]

[1]Cracow University of Technology, Faculty of Mechanical Engineering, al. Jana Pawła II 37, 31-864, Krakow, Poland

agnieszka.zyra@pk.edu.pl

Abstract
The present study constitutes a research on the feasibility of employing dry electrical discharge machining (dry-EDM) for medical applications. The investigations aim to evaluate the surface integrity of titanium Grade 2 (rolled semi-finished product) and Ti6Al4V ELI alloy fabricated by direct metal laser sintering (DMLS), subjected to dry-EDM under different gaseous atmospheres. The findings are expected to identify the influence of material preparation method and individual gases on the technological surface layer condition, which is critical for ensuring biocompatibility and promoting osseointegration in biomedical applications. From an environmental perspective, the proposed approach aligns with the principles of *green-EDM*, a sustainable variant of EDM characterized by negligible ecological impact

dry-EDM, titanium, DMLS, medical applications

1. Introduction

Electrical discharge machining (EDM) is a non-conventional manufacturing process in which material is removed as a result of a series of controlled electrical discharges occurring in a narrow interelectrode gap filled with a dielectric medium. Conventional EDM employs liquid dielectrics, such as hydrocarbon-based fluids or deionized water, which present technological and environmental limitations. Hydrocarbon media may deteriorate surface layer integrity, while deionized water can induce oxidation and pose challenges in maintaining stable dielectric properties. For ecological and occupational health reasons, gas-based EDM is considered a promising alternative, as it eliminates harmful decomposition products associated with liquid dielectrics. However, the type of gaseous dielectric significantly influences machining stability, efficiency, electrode wear, and surface integrity [1]. Components such as implants, surgical instruments, and medical robotic elements intended for contact with blood and saliva require controlled surface morphology, chemical stability, and high surface integrity. The development of green-EDM and dry-EDM technologies may therefore constitute a crucial step toward environmentally responsible and clinically safe manufacturing solutions for advanced medical devices [2].

2. Methodology

Dry electrical discharge machining (dry-EDM), was conducted on a dedicated experimental test stand in milling kinematics The test stand was equipped with an electro-discharge generator MATRIX MPS–7163 (160 V / 3 A and gaseous supply system, enabling machining in a gaseous dielectric. In this configuration, carbon dioxide (CO_2) and argon (Ar) were delivered under controlled pressure directly into the interelectrode gap through a thin-walled tubular electrode, thereby ensuring dielectric circulation within the discharge zone (Fig. 1 a)). A single dry-EDM milling experiment involved the removal of ten successive material layers, executed in both tool feed directions, in each pass, the working electrode was lowered by 25 µm**,** which was established in the preliminary investigations The workpieces comprised two specimens fabricated by direct metal laser sintering (DMLS Ti6Al4V) and commercially pure Titanium Grade 2 rolled (semi-finished product), each with nominal dimensions of 40.6 × 15.0 × 12.1 mm. Each trial was repeated three times.

Table 1 Input parameters of the experimental plan

Symbol	Parameter	Values
t	Pulse on time	300 µs
U	Voltage	100 V
I	Current intensity	2.7 A
p	Gas pressure	6 bar

Table 2 Constant machining conditions during tests

Parameter	Values
Working Electrode (WE)	Thin-walled tungsten pipe
WE outer diameter	Ø1 mm
Rotational speed of the WE	250 rpm
Gas medium	Carbon dioxide/argon
Pulse duty factor (Ƞ)	0.5
Removed material layers per trial	10
Kinematics of WE movement	Milling

The material removal rate (MRR) was calculated according to the formula:

$$MRR = \frac{Vm}{t},$$

Where *Vm* is the volume of removed workpiece material and t is the total machining time per trial. 3D surface roughness measureents were conducted using an optical confocal profilometry technique with the Al/Surf 520 measurement system (Al/met). Measurement series were performed over areas of 8 × 2 mm. The following surface roughness parameters wereinvestigated: Ssk, Sku, Sz, Sa. Microstructural observations

were performed using a JSM-IT200 scanning electron microscope.

3. Results

When comparing machining efficiency (Fig. 1 b)), the highest performance was observed for the DMLS-manufactured sample processed in a carbon dioxide atmosphere. In this case, the efficiency was more than three times higher than that obtained under argon. For Titanium Grade 2, machining in carbon dioxide also resulted in higher efficiency compared to argon; however, the difference was considerably less pronounced than that observed for the DMLS-manufactured sample.

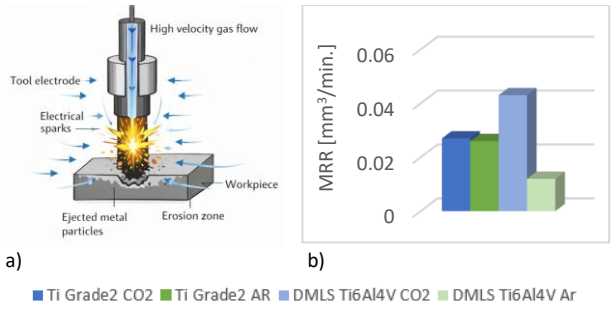

Figure 1. a) Scheme of dry-EDM process, **b)** Material removal rate

EDM is inherently nonlinear and stochastic, with process behavior governed by the workpiece material, dielectric medium, and machining kinematics. Sz represents the total height range and is sensitive to extreme features such as deep craters or resolidified droplets. The highest value was reported for sample fabricated by direct metal laser sintering (DLMS) in argon environment, which was almost two times higher comparing to EDM in CO_2. Lower Sz values were observed for Titanium Grade 2, for which machining in a CO_2 atmosphere also resulted in reduced surface roughness (Fig. 2a)). Sa reflects the overall roughness amplitude and increases with discharge energy, as larger and deeper craters are formed. It can be noticed (Fig. 2a)) that the highest value of Sa was observed for sample fabricated by direct metal laser sintering (DLMS) in argon environment. What is more Sa parameter was also higher for titanium Grade2 machined in Ar compared to CO_2.

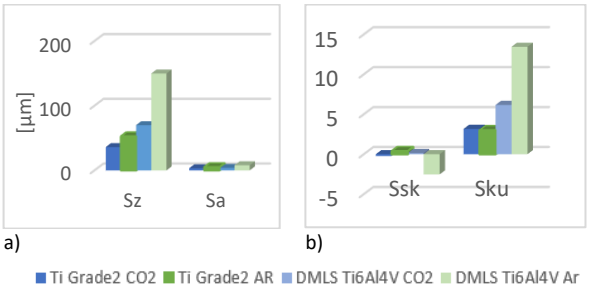

Figure 2. Areal surface texture parameters **a)** Sz, Sa, **b)** Ssk, Sku

The combined selection of Rsk and Rz (Fig. 2b)) is justified by the inherently stochastic character of EDM, where surface topography results from the random superposition of discharge craters formed during machining. Ssk indicates surface asymmetry; EDM surfaces are often valley-dominated (negative Ssk due to crater formation). The lowest Ssk value was recorded for the DMLS-manufactured sample machined in an argon atmosphere. Sku characterizes the sharpness of the height distribution, with high values indicating pronounced peaks or deep valleys typical of stochastic discharge events. The highest Sku value was recorded for the DMLS-manufactured sample machined in an argon atmosphere.

Pronounced differences in the density of microcracks and oxide inclusions were observed in the SEM micrographs of the analyzed surfaces (Tab. 3). In the case of Titanium Grade 2 machined in an argon atmosphere, no microcracks were detected, which may indicate sufficiently effective cooling of the machining zone under these conditions. In contrast, distinct microcracks were identified after machining Titanium Grade 2 in a carbon dioxide atmosphere, as well as in additively manufactured (DLMS) titanium processed in both argon and carbon dioxide environments. The most extensive and pronounced microcracking was observed for Titanium Grade 2 machined in carbon dioxide.

Table 3 SEM micrographs of Titanium Grade 2 and DLMS titanium surfaces after dry EDM in CO_2 and Ar, x500

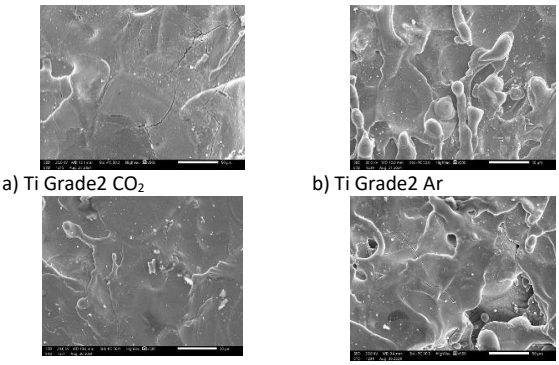

a) Ti Grade2 CO_2 b) Ti Grade2 Ar

c) DMLS Ti6Al4V CO_2 d) DMLS Ti6Al4V Ar

3. Conclusions

In dry-EDM, electrical breakdown occurs only at very small interelectrode gap widths (<50 µm), which may result in the coexistence of short-circuit discharges and prolonged ignition delay times. The breakdown mechanism under gaseous conditions differs fundamentally from that observed in conventional EDM using liquid dielectrics. Based on the conducted experiments, machining efficiency under identical process parameters was higher in a carbon dioxide atmosphere than in argon. A particularly pronounced increase in efficiency was observed for the DMLS-manufactured sample processed in CO_2, where the performance was markedly greater compared to machining in argon. Analysis of the surface roughness parameters indicates that, for both materials, machining in argon resulted in higher surface roughness. The most significant differences were recorded for the DMLS-produced specimen. SEM observations revealed the presence of microcracks and oxide precipitates on several of the analyzed surfaces. However, no microcracks were detected in Titanium Grade 2 machined in an argon atmosphere. This may suggest that, under these conditions, the process proceeded in a stable manner, with appropriately selected parameters and effective heat dissipation from the machining zone.

References

[1] Tao J, Shih AJ, Ni J. Experimental study of the dry and near-dry electrical discharge milling processes. J Manuf Sci Eng Trans ASME 2008;**130**

[2] Şentürk E, Alparslan C, Bayraktar Ş, Korkmaz ME, Günay M. A comprehensive review on sustainability in EDM process of additive manufactured materials. Measurement 2025;**245**

Session 7: Mechatronics and Control

euspen's 26th International Conference & Exhibition, Krakow, PL, June 2026
www.euspen.eu

A dynamics toolbox for modelling and prediction of interconnected systems

Wouter Jutte[1], Nard Strijbosch[1], Max Bolderman[1], Teunis van Dam[1], Arjan van der Wel[1], Ruben Merks[1], Theresa Spaan-Burke[1], Henny Spaan[1]

[1]*IBS Precision Engineering BV*

jutte@ibspe.com

Abstract
Developing new and innovative industrial machines requires delicate balancing of cutting-edge requirements, tight deadlines and limited resources in an environment with many uncertainties. Early identification of issues and quickly adapting is the recipe for success. This requires flexible and efficient analysis tools for continuous monitoring of the expected system performance as the design progresses. In high-performance mechatronic systems the dynamic behaviour is often of critical importance. IBS Precision Engineering BV developed a dynamics toolbox for dynamic system analysis, which changes the analysis from a complex coding exercise to a simple bookkeeping one. This enables quick design iteration cycles with continuous model refinements, a continuous overview of system performance, and allows the analysis to be performed by employees with limited background in the mathematics of dynamics. The dynamics toolbox uses a modular approach often used in systems engineering. This paper describes the concepts and workflow of the dynamics toolbox. The dynamics toolbox is applied to a use-case of an adjustable mirror and the model is verified with experimental measurements.

V-model, FEA, dynamics, toolbox, rigid body modelling, FEA, system identification

1. Introduction

IBS Precision Engineering BV is a leading supplier in the precision industry for new, innovative and custom industrial machines and applications. In these applications the dynamic performance is often of critical importance. One example is a project for laser satellite communication, where optical systems have to aim laser beams over very long distances. The mirrors in these systems have to be stable in the presence of vibrations or else the beam will miss the target as illustrated in Figure 1.

At IBS, the product creation process of new systems follows the V-model illustrated in Figure 2, where user requirements are converted into detailed designs using a top-down approach on the left side of the V-model and performance is verified on the right side using a bottom-up approach. To identify issues early, the system performance is modelled in parallel with the design process, where the models progress in detail as the project does.

The modelling approach from a dynamic perspective is shown on the left side of the V-model in Figure 2. Early concepts and specifications are determined with the use of first order approximations and 1D rigid body models with estimated masses, stiffnesses and forces based on practical experience. As the concepts are worked out, system design is refined and the models are updated with more realistic values. Once the geometry and interface locations become clear the rigid body models are upgraded with inertial and stiffness parameters in 3D. As the design matures, the complex and critical components are analysed with Finite Element Analysis (FEA) software and rigid bodies can be replaced with exported Finite Element Method (FEM) models with many degrees of freedom (DoF).

The process of creating and updating models can be very time consuming. Large mass, damping and stiffness matrices have to be assembled for complex 3D systems with many components. Doing so in a programming environment like MATLAB is a cumbersome task and requires a significant amount of knowledge about the mathematics of dynamics. FEA software is a very powerful tool for detailed analysis of structural dynamics. However, it doesn't lend itself well for first order estimations in the early phases of the product creation process. Also, analysing large complex systems with many components in FEA software is very computationally expensive, which is not effective for frequent design iterations.

Because the available tools did not accommodate our needs well enough, a dynamics toolbox is developed with the goal of making dynamic modelling easy and efficient throughout the whole product creation process.

The remainder of this work is organized as follows: Section 2 describes the concepts of the dynamics toolbox, section 3 applies the modelling approach to a mirror adjustment module, in section 4 the model is experimentally verified, section 5 discusses the results and section 6 concludes the work.

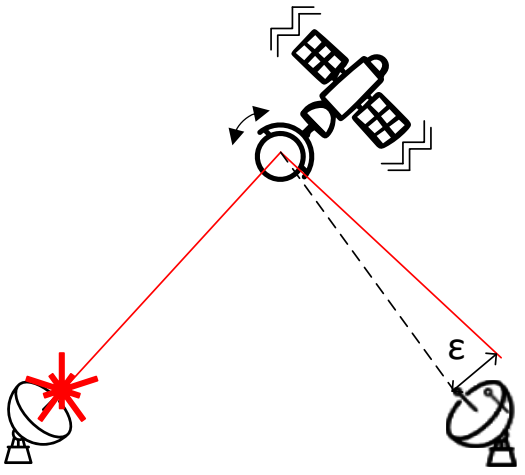

Figure 1. Schematic of beam deflection as a result of a vibrating mirror in Laser satellite communication

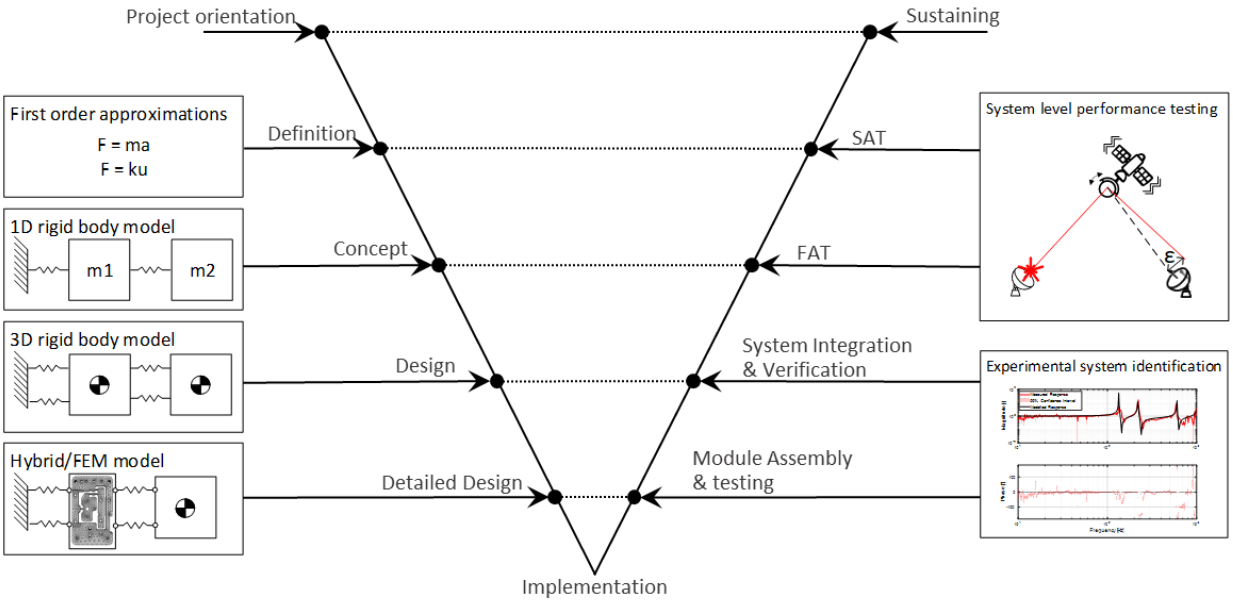

Figure 2. The V-model from the dynamic's perspective. On the left side of the V-model system performance estimations are done based on models, which progress in parallel with designs from first order approximations to assembled FEM models. In the early phases of system integration on the right side of the V-model dynamics are tested by making frequency response functions. In the last phases, system level performance is tested as a whole.

2. Dynamics toolbox concepts

The core functionality of the dynamics toolbox is to reduce the modelling process to the specification of components and their parameters. The different components and parameters used in the toolbox are shown in Table 1. With the specification, the dynamic toolbox automatically interconnects the components and constructs the system matrices of the standard matrix equation (1) which forms the basis for dynamic analysis:

$$\boldsymbol{M}\ddot{x} + \boldsymbol{C}\dot{x} + \boldsymbol{K}x = F, \quad (1)$$

where $\boldsymbol{M}$ is the inertial matrix, $\boldsymbol{C}$ the damping matrix, $\boldsymbol{K}$ the stiffness matrix, F the force vector, x the displacement vector, $\dot{x}$ the velocity vector and $\ddot{x}$ the acceleration vector.

2.1. System Matrix Assembly

The usefulness of the automation concept is illustrated with the 1D rigid body system in shown Figure 3 (a). The first step in the manual system matrix assembly procedure is to draw a free-body-diagram. The generic free-body-diagram for each body in 1D is shown in Figure 3 (b). Using this generic free-body-diagram, the equations of motion for the bodies can be written down:

$$m_1\ddot{x}_1 = f_1 - k_1x_1 - c_1\dot{x}_1 + k_2(x_2 - x_1) + c_2(\dot{x}_2 - \dot{x}_1), (2)$$

$$m_2\ddot{x}_1 = -k_2(x_2 - x_1) - c_2(\dot{x}_2 - \dot{x}_1), \quad (3)$$

where (2) is the equation of motion for the first rigid body and (3) is the equation of motion for the second rigid body. The system of equations can be rewritten in the standard matrix form (1) with:

$$\boldsymbol{M} = \begin{bmatrix} m_1 & 0 \\ 0 & m_2 \end{bmatrix}, \quad F = \begin{bmatrix} f_1 \\ f_2 \end{bmatrix}$$
$$\boldsymbol{K} = \begin{bmatrix} k_1 + k_2 & -k_2 \\ -k_2 & k_2 \end{bmatrix}, \quad \boldsymbol{C} = \begin{bmatrix} c_1 + c_2 & -c_2 \\ -c_2 & c_2 \end{bmatrix}$$
$$\ddot{x} = \begin{bmatrix} \ddot{x}_1 \\ \ddot{x}_2 \end{bmatrix}, \dot{x} = \begin{bmatrix} \dot{x}_1 \\ \dot{x}_2 \end{bmatrix}, \quad x = \begin{bmatrix} x_1 \\ x_2 \end{bmatrix}$$

The complexity of this modelling process increases significantly when adding more bodies and extending the model to 3D. In 3D, 6 equations of motion have to be created for each rigid body (3 translations and 3 rotations). Forces and torques also have a direction and no longer necessarily act in the centre of gravity (CoG), which complicates modelling further.

To reduce the effort, the process of the system assembly procedure is automated. The dynamics toolbox uses an approach similar to the generic free-body-diagram in Figure 3 (b), but then in 3D with the component parameters of Table 1.

Table 1 The components and parameters for 3D system specification in the dynamics toolbox.

Component	Parameters
Fixation	3D position of centre of rotation (x, y, z)
Rigid body	3D CoG position (x, y, z) Inertial parameters (m, I_{xx}, I_{yy}, I_{zz}, I_{xy}, I_{xz}, I_{yz})
Flexible body	Mass, damping and stiffness matrix (exported from FEA software)
Spring/ damper connection	3D position of interface on body 1 (x, y, z) 3D position of interface on body 2 (x, y, z) Stiffness parameters (k_x, k_y, k_z, k_{xx}, k_{yy}, k_{zz}) Relative damping ratio (ζ)

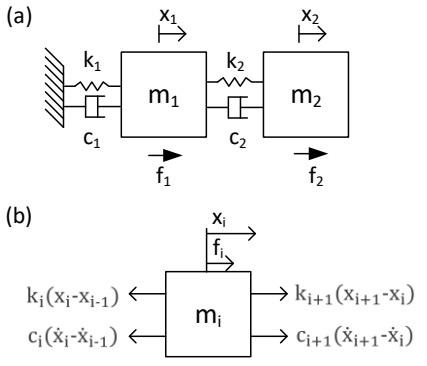

Figure 3. (a) A 1D model with 2 rigid bodies. (b) The generic free-body-diagram for a rigid body in 1D.

2.2. Interfacing with FEM models

In addition to automated system matrix assembly of rigid body models, the dynamics toolbox accommodates interfacing with flexible bodies, which are models exported from FEA software. FEA software is used to create discretized models with many DoF. In the dynamics toolbox, spring/damper connections can be specified between rigid bodies and interfaces of the exported models. It is also possible to connect multiple exported models.

To reduce the computational cost, model-order-reduction (MOR) is applied to the exported FEM models. MOR reduces the DoFs from about 10^5 - 10^6 to 10 - 100 for a typical industrial component. However, some level of accuracy is lost with MOR, which is heavily influenced by the method used. Component mode synthesis [2] is most commonly used in structural dynamics.

3. Modelling of a mirror adjustment module

To showcase how the dynamics toolbox is used in practice, the next section applies the dynamics toolbox to the development process of a mirror adjustment module.

As already described in the introduction, the orientation and stability of mirrors in optical systems is of critical importance. Installation on mechanical tolerances is not always sufficient to align the optical components. Therefore, adjustable mirror mounts are commonly used for fine alignment.

The flexible connection introduced to adjust the mirror can cause problems in the presence of vibrations. The stiffness of the fine adjustment mechanism should be flexible enough to make the adjustment possible, but stiff enough so that it doesn't oscillate too much with respect to the frame it is fixated on.

3.1. Module requirements

The maximum allowable mirror deflection δ (rad) is determined in the initial stages of the V-model, which follows from the application's maximum allowed beam deflection ε, as illustrated in Figure 1. To start the modelling and design process, these specifications have to be converted to specifications for stiffness and inertia.

To get an initial approximation for stiffness and inertia, the module is considered as a 1D single body rigid body model. For rotation around the Z-axis we can use the following equations:

$$T = I_{zz}\ddot{\varphi}_z, \qquad (4)$$

$$T = k_{zz}\delta, \qquad (5)$$

where T (Nm) is the Torque, I_{zz} (kg·m^2) the moment of inertia, k_{zz} (Nm/rad) the rotational stiffness and $\ddot{\varphi}_z$ (rad/s^2) the rotational acceleration. Substitution of (4) in (5) and reordering gives a stiffness requirement [1]:

$$k_{zz} \geq I_{zz}\sqrt{\frac{\ddot{\varphi}_z}{\delta}}. \qquad (6)$$

Given the maximum allowed mirror deflection δ, the expected accelerations $\ddot{\varphi}_z$ exerted on the module and an approximation of I_{zz} based on the material and an estimation of the geometry, the stiffness requirement follows.

Instead of considering the adjustable mirror as a single module, it can be decomposed in two well-defined sub-modules: the adjustment flexure and the mirror. Such a decomposition is useful, because it allows the sub-modules to be independently designed, modelled and iterated on. The approximated stiffness and moment of inertia are distributed over the two sub-modules.

3.2. Concept phase: 1D rigid body model

After an initial specification of the moments of inertia and stiffnesses, 1D rigid body models are typically used for modelling of concept designs. Modelling of the adjustable mirror with 2 sub-modules gives the 1D rigid body model illustrated in top left of the V-model in Figure 2, where the flexure is connected to the fixation and the mirror is connected to the flexure.

Five components have to be defined to model this 1D rigid body system in the dynamics toolbox: The fixation, 2 rigid bodies and 2 spring/damper connections.

For 1D less parameters are required than in Table 1 for 3D. The location of the bodies and the location of the connection interfaces don't matter in 1D. 1D also requires only one stiffness parameter per connection and one inertial term per body. The relative damping is optional. The system can therefore be specified with:

- The inertial parameters for the bodies $I_{zz,mirror}$ and $I_{zz,flexure}$.
- The stiffness parameters $k_{zz,flexure}$ and $k_{zz,mirror}$ for the connections fixation-flexure and flexure-mirror respectively.

These parameters are enough to assemble the system matrices and start 1D system analysis.

3.3. Design phase: 3D rigid body models.

As the project advances in the V-model from the concept phase to the design phase, the geometry and the locations of the interfaces become clearer. In this phase the rigid body models can be upgraded to 3D as illustrated in Figure 2. For 3D analysis all parameters in Table 1 have to be specified.

The inertial parameters, interface locations and stiffnesses can be extracted from commonly used CAD software.

3.4. Detailed design phase: Hybrid/FEM models.

As the designs mature into detailed designs, the final geometry of components becomes clear. The designs of the sub-modules for the adjustable mirror are shown in Figure 4.

The flexure dynamics are complex and a simple rigid body approximation is not good enough to represent the real flexure dynamics. In such a case, the rigid body can be replaced by an exported FEM model. The CAD model is imported in FEA software, where the meshing functionality is used to discretize the model and the created system matrices are then exported.

In the dynamics toolbox connections are defined between the fixation and interfaces of the flexure's FEM model, and between interfaces of the FEM model and the rigid body of the mirror. This hybrid model is illustrated in the bottom left of the V-model in Figure 2.

(a) (b)

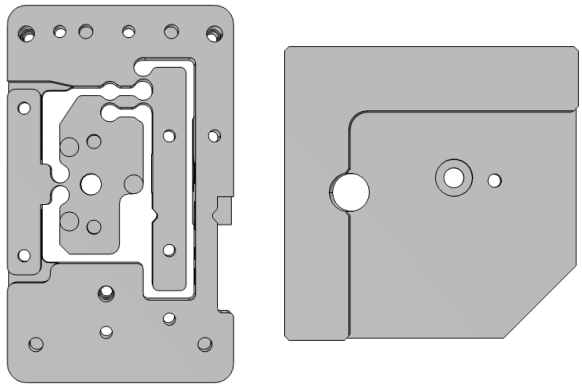

Figure 4. The mechanical designs of (a) the adjustment flexure (b) the mirror.

4. Experimental verification of a mirror adjustment module

After the designs are finished the parts are ordered, manufactured and delivered and the right side of the V-model is started. On the right side of the V-model the system is integrated and verified using a bottom-up approach. The dynamic verification of (sub-)modules is done experimentally by means of system identification, as shown on the right side of the V-model in Figure 2.

4.1. Background

The goal of dynamic system identification is to find the Frequency Response Function (FRF) that maps movement at the input to movement at the output as a function of frequency.

Figure 5 illustrates how the FRF is experimentally obtained for a 1D system. The system is excited at the input with sinusoidal signals of different frequencies. While doing the excitation, the displacement profile at both the input and the output are measured. For each excitation frequency the measured signal at the input and output have the same frequency, but the input and output have a different amplitude and phase. The FRF contains this magnitude and phase relationship between input and output for all the tested frequencies.

The system identification process is very similar in 3D, but the inputs and outputs are measured in 6-DoF and 6 linearly independent excitations have to be applied, 1 excitation for each DoF.

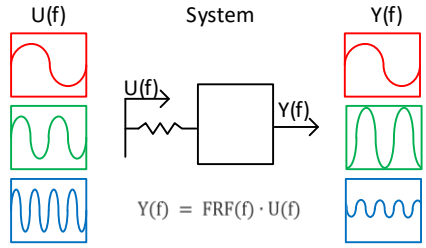

Figure 5. A schematic of system identification in 1D. Input U is excited while measuring input U and output Y to determine FRF(f).

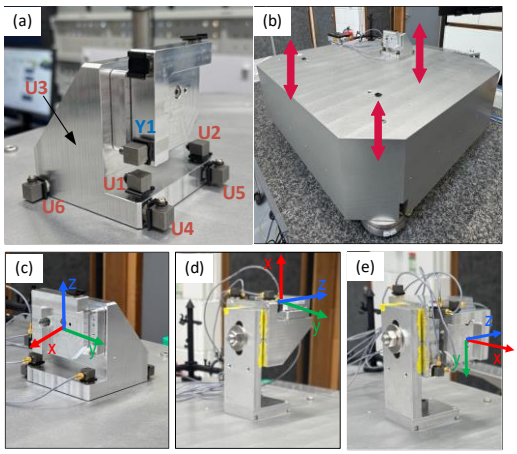

Figure 6. The experimental setup. (a) Shows the location of the 6 input accelerometers U1-U6 and the output accelerometer Y1. (b) The excitation platform has 3 piezos, which can excite in Z/Rx/Ry. (c, d, e) The module is rotated into 3 different orientations, so that all 6 degrees of freedom can be excited.

4.2. Experiment

The experimental setup for the verification of the mirror adjustment module is shown in Figure 6. Figure 6 (a) shows the placement of the accelerometers. To measure all 6-DoF at the input, six accelerometers are placed on a bracket, which is connected to the input of the flexure. Only one accelerometer is placed on the mirror. It is not necessary to measure all 6-DoF of the output at the same time, but it would be more time efficient. To get the full 6-DoF system identification with only one accelerometer, the experiments have to be repeated 6 times while moving the output accelerometer to different positions.

The module is connected to an excitation platform with 3 piezo actuators, shown in Figure 6 (b). With three actuators, the system can only be excited in 3-DoF, i.e., in z, Rx and Ry, see Figure 6 (b). To excite the system in all 6-DoF, the experiment is repeated for different orientations, see Figure 6 (c, d, e). In all orientations a multi-sine excitation is applied to the platform across a range of frequencies while logging all accelerometers.

An FRF is obtained that maps the movement of each measured input to the movement of each measured output. The spectral analysis method [3] is used to get FRFs from the experiments, including a confidence interval of the experimental result.

5. Results

Figure 7 shows the comparison between the experimental results and the model for one of the obtained frequency responses: from input U6 to output Y1 in Figure 6 (a). The modelled response is shown as the dashed black line and the experimental result as a solid red line. The experimental result includes a 99% confidence interval, which shows some uncertainty in the lower frequencies of the measured FRF. This aligns with our expectations, since the used accelerometers are noisier for low frequencies. Apart from that, the modelled and experimental response are very similar.

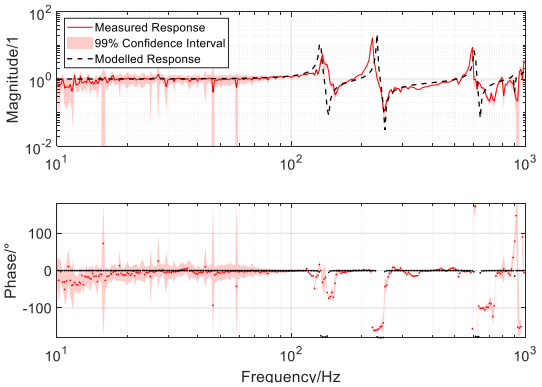

Figure 7. A comparison of the modelled and the experimentally obtained FRF for Y1/U6. Confidence intervals are plotted for the experimental FRF, which show the bounds of the real FRF with 99% confidence.

6. Conclusion

A dynamics toolbox is developed that can automated the assembly procedure of system matrices for dynamic system analysis and it also accommodates interfacing with FEM models. To get the system matrices, parameters of dynamic objects are specified instead of manually doing the assembly procedure. This makes modelling easier and faster. The toolbox allows for incremental upgrades, which accommodate the product creations process of the V-model. The dynamics toolbox is applied to model a mirror adjustment module and the theoretical response is verified experimentally.

References

[1] Munnig Schmidt R, Schitter G, Rankers A and van Eijk J 2020, *The Design of High Performance Mechatronics* (Amsterdam: IOS Press) p128

[2] Hurty W C 1960 *Vibrations of structural systems by component mode synthesis*. J. of the Eng. Mech. Division, 86(4):51–69

[3] Pintelon R and Schoukens J 2012, *System Identification* (Hoboken New Jersey: John Wiley & Sons, Inc.) pp 233-236

euspen's 26th International Conference & Exhibition, Krakow, PL, June 2026
www.euspen.eu

Investigation of Motor Characteristic Analysis under Low Magnetic Field Conditions in Planar Maglev Stages

Takanori Kato[1] and Motohiro Takahashi[1]

[1]*Research and Development Group, Hitachi, Ltd.*

takanori.kato.fv@hitachi.com

Abstract

This study investigates a low-leakage magnetic field planar maglev stage with the movable magnet array for applications requiring both nanometre-scale positioning and leakage magnetic field reduction, such as semiconductor inspection equipment. In this study, we employ a coil array in a single-layer pattern with staggered coils and a Halbach magnet array, which concentrates magnetic flux density beneath the motor to reduce leakage magnetic fields. The planar maglev stages with the movable magnet array currently under development require complex coil-switching control during operation due to changing thrust application points. To efficiently analyze and design the control system, including coil-switching, a novel modeling method based on grid partitioning is proposed. Unlike simplified models with fixed thrust application points (e.g., grid = 1), the proposed grid-partitioning-based model enables control-oriented positioning performance simulation with sufficient accuracy while maintaining practical computational efficiency.

Keywords Ultra-precision, Positioning, Magnetic guide, Mechatronics, Stage system

1. Introduction

In recent years, the miniaturization of semiconductor devices has necessitated nanometer-scale positioning accuracy in manufacturing and inspection equipment [1]. Moreover, the global expansion of semiconductor demand has driven the adoption of magnetic levitation guides to enhance equipment throughput. Planar maglev stages substantially reduce the moving mass, enabling high-speed operation while maintaining high-precision positioning. From a thermal management perspective, positioning the magnets on the levitated side and the coil on the non-levitated side is advantageous. However, in planar motor systems, the proximity between the motor and the electron beam irradiation point allows leakage magnetic fields from the motor to interfere with the electron beam in inspection systems, thereby deteriorating inspection accuracy [2]. The planar maglev stage with the magnet array currently under development requires complex coil-switching control during operation due to changing thrust application points [3]. To efficiently analyze and design the control system, including coil switching, this study proposes a novel modeling method based on grid partitioning.

2. Stage mechanism

The configuration of the planar maglev stage with the movable magnet array is shown in Figure 1. This structure shortens the distance between the magnets and coils by arranging the non-levitation side coil array with single-layer coils in three-phase sets in an alternating configuration. Furthermore, the Halbach magnet array and back yoke concentrate the magnetic flux density toward the lower side (coils). In addition, coil currents are turned off at coordinates not covered by the movable table. These configurations reduce leakage magnetic fields above the motor. Lightweight magnetic shielding is under consideration to further reduce the leakage magnetic field. The magnetic flux density distribution of the planar motor is shown in Figure 2.

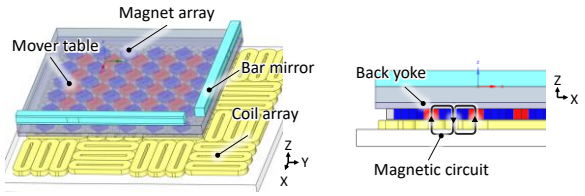

(a) Overview (b) Side section

Figure 1. Overview of the planar maglev stage with movable magnet array.

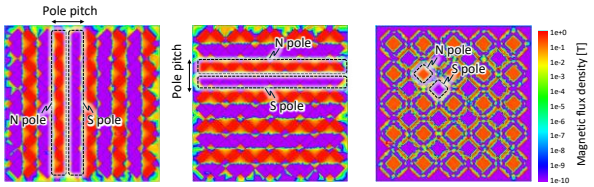

(a) X-axis (b) Y-axis (c) Z-axis

Figure 2. Magnetic flux density distribution on the planar maglev stage.

The magnetic flux density varies along the pattern for each magnetic pole pitch on the X and Y axes, enabling the generation of levitation thrust along the Z axis throughout the entire movable range. Furthermore, the thrust along the X and Y axes is generated by the magnetic flux density along the Z axis of the lattice pattern. A simplified model simulating this characteristic is employed as a magnetic field model for calculating motor thrust [4].

3. Analysis approach of planar motor control characteristics

The analysis model for planar maglev stage control characteristics is shown in Figure 3. This stage control system employs a model-based commutation algorithm [5]. This commutation algorithm calculates the phase coil currents to achieve the desired thrust and torque with decoupling across the 6-degree-of-freedom displacement. Furthermore, the 6-axis feedback controller consists of a PID controller, notch filters, and

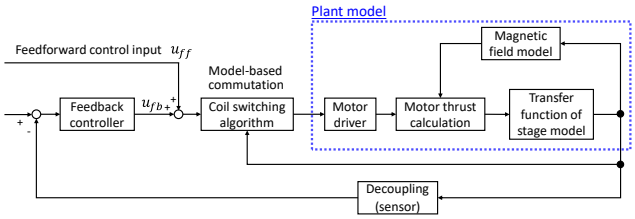

Figure 3. Analysis model for planar stage control characteristics.

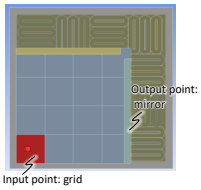

Figure 4. Grid partitioning for the motor thrust application point.

a low-pass filter. These parameters were designed to ensure a sufficient stability margin, while setting the control bandwidth for the X-axis and Y-axis to 100 Hz.

The planar maglev stage with movable magnet array requires complex coil-switching control due to the changing thrust application points during motion. Therefore, in the proposed method, the mechanism characteristics from thrust to position are efficiently calculated for control-oriented simulation by dividing the spatially varying thrust application points into a grid.

The grid partitioning for the motor thrust application point is shown in Figure 4. The mechanism model is defined as a state-space model of a multi-input multi-output system, and its parameters are calculated using the modal analysis results from Ansys Mechanical. The input points in modal analysis are each grid point, and the output points are the bar mirrors.

The driving reaction force by the Lorentz force of each phase coil is distributed to the grid on the movable table, enabling calculation of the thrust along the X, Y, and Z axes. An example of motor thrust calculation on the grid is shown in Figure 5. These calculated thrust on the grid are input into the mechanism model, and the position of the planar stage is calculated.

Figure 6 shows the errors in thrust in the translational direction and torque in the rotational direction when the grid partitioning number is changed. The errors in thrust in the translational direction are zero regardless of the grid partition number. While a coarse baseline model (grid = 1) is computationally inexpensive, it introduces non-negligible torque errors due to insufficient representation of spatially varying thrust application points. As shown in Figure 6, increasing the grid number reduces the torque error asymptotically. In this study, grid = 16 was selected as an efficient compromise that provides sufficient accuracy for control-oriented positioning performance evaluation with practical simulation time.

4. Positioning performance evaluation

Positioning simulation was performed by implementing the planar maglev stage control system shown in Figure 3 in MATLAB/Simulink. In this simulation model, the magnetic flux density distribution of the planar motor varies according to the X-, Y-, and Z-axis coordinates, and motor drive current is calculated using the model-based commutation algorithm. Figure 7 shows the waveforms of the position and tracking error when positioning 60 mm in the X-axis direction using a trapezoidal acceleration profile of 3 m/s^2. Position tracking error during stage movement was within ±2 µm. The simulation time was evaluated using the Simulink sim execution time (tic/toc). The proposed model with grid = 16 required approximately 7.55 s, which is almost identical to that of the baseline model with

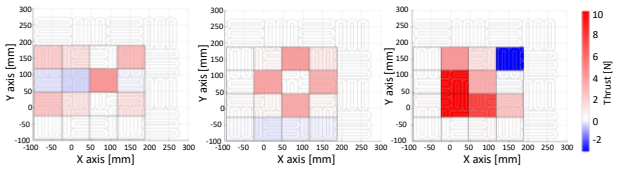

(a) X-axis (b) Y-axis (c) Z-axis

Figure 5. Motor thrust calculation on the grid.

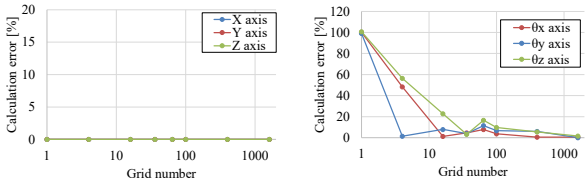

Figure 6. Errors in thrust in the translational direction and torque in the rotational direction when the grid partitioning number is changed.

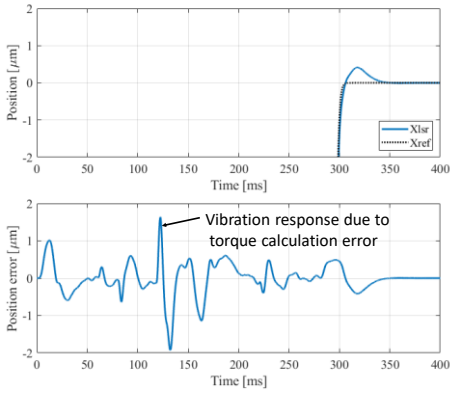

Figure 7. Waveforms of position and position error in the positioning simulation.

grid = 1 (7.4 s), while providing significantly improved torque calculation accuracy. This result indicates that the proposed grid-partitioning approach enhances modeling accuracy without sacrificing computational efficiency.

5. Conclusion

This study proposes an efficient analysis method for the low-leakage magnetic field planar maglev stage with the movable magnet array utilizing grid partitioning for the input points of the mechanism model. Analysis time can be reduced by optimizing the number of grid partitions. The effectiveness of this analysis method was confirmed through performing positioning simulations.

Detailed results on leakage magnetic fields for different planar maglev stage structures and additional leakage magnetic field reduction structures will be presented in the poster session.

References

[1] Butler H 2011 Position Control in Lithographic Equipment *IEEE Control Systems Magazine* **31** 28-47

[2] Bang B H, Yoon K T, Kim D, Kim M and Choi Y M 2025 Design and Evaluation of a Practical Magnetic Shield for XY Linear Motor Stage in SEM Applications Control *ASPE Annual Meeting* **85** 512-516

[3] Takahashi M 2025 Development of Planar Stage with Movable Magnet Array and Coil Switching Control *Int. J. of Auto. Tech.* **19** 397-404

[4] Jansen J W, Lierop C M M, Lomonova E A, and Vandenput A J A 2007 Modeling of Magnetically Levitated Planar Actuators with Moving Magnets *IEEE Trans. on Magnetics* **43** 15-25

[5] Lierop C M M, Jansen J, Damen A A H, Lomonova E A, Bosch P P J and Vandenput A J A 2009 *IEEE Trans. on Industry App.* **45** 1982-1990

euspen's 26th International Conference & Exhibition, Krakow, PL, June 2026
www.euspen.eu

Performance of an X-Y-Theta actuator using piezoelectric elements and electropermanent magnets

Akihiro Torii[1], Yuto Takayama[1], Takato Sakai[1], Suguru Mototani[1], Kae Doki[1]

[1]*Aichi Institute of Technology, Japan*

torii@aitech.ac.jp

Abstract
Microactuators with multiple degrees of freedom offer significant advantages in precision engineering, and are essential in various industrial applications. We proposed an X, Y, and theta (θ) microactuator which consists of three multilayer piezoelectric elements (piezos) and three electropermanent magnets (EPMs). The piezos are arranged to form an equilateral triangle, allowing extension and contraction along its sides, while the EPMs are positioned at the triangle's vertices. Each EPM can switch an electromagnetic force via a short current pulse. The principle of the X-Y-Theta actuator is based on an inchworm mechanism. While two EPMs remain activated, the third—temporarily deactivated—allows minute displacement through deformation of the piezos. Sequential deactivation of the EPMs results and cyclic deformation of the piezos enables long-range motion through repeated incremental steps. This paper presents a preliminary performance of the X-Y-Theta actuator utilizing EPMs and piezos. The principle of the actuator is described followd by experimental results, which demonstrate a linear step displacement of 15 µm and a rotational displacement of 1.3 mrad. These performance metrics can be further improved by applying smaller deformation steps to the piezos.

Piezoelectric element, electropermanent magnet, EPM, inchworm, actuator

1. Introduction

The downsizing of production equipment has gained attention as products become compact. Miniaturization offers advantages such as improved space efficiency and reduced energy consumption. Piezoelectric elements (piezos), which can generate minute displacements, are widely used in compact systems, and various piezo-based actuators have been developed [1]. Examples include mechanisms driven by controlling piezo extension and contraction combined with frictional forces [2]. An inchworm mechanism incorporating piezos and electromagnets has been introduced [3]. However, electromagnets consume substantial energy.

This study shows the preliminary performance of the linear and rotational motion of an X-Y-Theta actuator that uses three electropermanent magnets (EPMs) [4] as a position-holding mechanism in conjunction with three piezos. The use of EPMs, which require short current pulses to switch the electromagnetic force, has the potential to reduce the power consumption of the X-Y-Theta actuator.

2. Electropermanent magnet and X-Y-Theta actuator

Figure 1 shows the schematic diagram of an EPM and an X-Y-Theta actuator. The EPM composed of a neodymium magnet and an alnico magnet arranged in parallel as shown in Figure 1(a). The neodymium magnet is a high-coercivity material, while the alnico magnet exhibits low coercivity. A coil is wound around the alnico magnet. The external magnetic field generated by the EPM can be switched on and off by reversing the magnetization of the alnico magnet using short current pulses. When the magnetizations of the neodymium and alnico magnets are aligned, a magnetic attractive force is produced. Reversing the magnetization of the alnico magnet eliminates the external magnetic field, resulting in no attractive force. This mechanism enables the EPM to switch between on- and of-f states using short current pulses. Figure 1(b) shows the schematic diagram of a delta-type X-Y-Theta actuator. At any moment, two out of three EPMs are on-state, and the other is off-state. The off-state EPM is displaced by the extension and contraction of the piezos connetected.

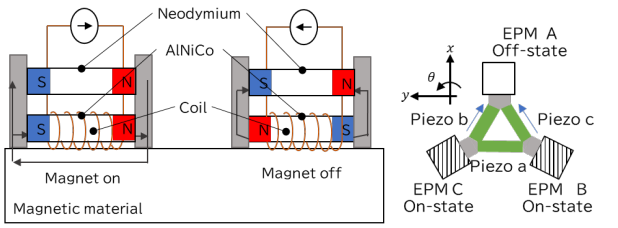

(a) Electropermanent magnet (b) X-Y-Theta actuator

Figure 1. Schematic diagram of electropermanent magnet and X-Y-Theta actuator

Linear displacement in the x-direction is achieved by table 1. First, the on/off states of the EPMs are set by current pulses. Then, the off-state EPM is displaced by the extension and contraction of the piezos. This two-state sequence is repeated. Counter clockwise rotational displacement in the θ-direction is achieved by table 2. In all states, the on/off states of the EPMs are set by current pulses prior to the extension and contraction of the piezos, causing the EPM in the off-state to be displaced. This three-state sequence is three-state sequence is repeated.

Table 1. sequence of linear displacement in x direction

State	EPM			piezo		
	A	B	C	a	b	C
1	off	on	on	contract	extend	Extend
2	on	off	off	contract	contract	Contract

Table 2. Sequence of counter clockwise rotational displacement

state	EPM			piezo		
	A	B	C	A	b	C
1	off	on	on	contract	contract	Extend
2	on	on	off	contract	extend	Contract
3	on	off	on	extend	contract	Contract

3. Experimental setup

Figure 2 shows the photographs of a side view of an EPM and a top view of an X–Y–Theta actuator incorporating three piezos and three EPMs. In Figure 2(a), the EPM consists of a 15 mm long and 8 mm diameter alnico magnet and neodymium magnet, with the alnico magnet wound by a 300-turn coil. The residual magnetic flux density of the alnico magnet and the neodymium magnet is 1.20 T and 1.17 T – 1.23 T, respectively. The friction force generated by the on-state EPM is 50 N, while the friction force of the off-state EPM is 0 N. In Figure 2(b), the piezos are 20 mm long and exhibit a deformation of 17 µm under an applied voltage of 150 V DC. Flexure hingies are used at both ends of the piezos.

The EPM state is updated prior to extension or contraction of the piezos. A positive pulse switches the EPM to the on-state, while a negative pulse switches it to the off-state. A current pulse of 6 A and 5 ms is applied to reverse the magnetization of the alnico magnet. An off-state EPM is displaced by the deformation of the piezos.

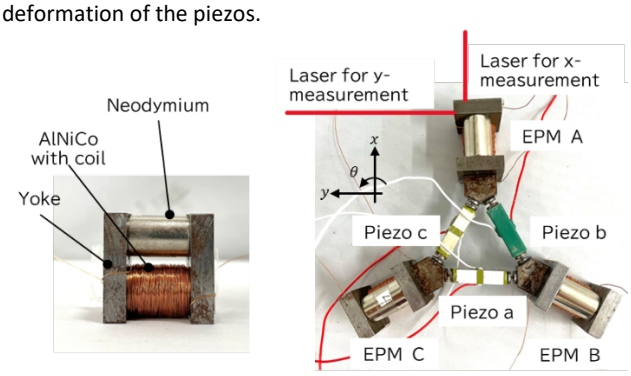

(a) electropermanent magnet (b) X-Y-Theta actuator

Figure 2. photographs of EPM and X-Y-Theta actuator

The control signals are applied to each component of the X–Y–Theta actuator to achieve both linear and rotational displacement. The input voltage to the piezo is 150 V or 0 V, and the resulting linear and rotational displacements are measured. The displacement is measured as shown in Figure 2(b). The linear displacement in the x-direction is defined as the position change of EPM A, which is measured using a commercially available displacement sensor. The rotational displacement in the theta-direction is calculated from the ratio of the tangential (y) displacement of EPM A, which is also measured by the displacement sensor, to the radius of the actuator, which is 50 mm. One full control cycle corresponds to a duration of 1 s.

4. Results and discussion

Figure 3 shows the results of the linear operation. The linear displacement, the voltage applied to piezo b and piezo c, and the current pulse applied to EPM B are shown. The linear displacement is synchronized with the extension of the piezo b and piezo c, and the displacement of the off-state EPM A reaches approximately 20 µm. However, a reverse displacement of approximately 5 µm is observed when the state of EPM B switches from the off-state to the on-state, reducing the net displacement per cycle. Consequently, the resulting displacement per control cycle is approximately 15 µm.

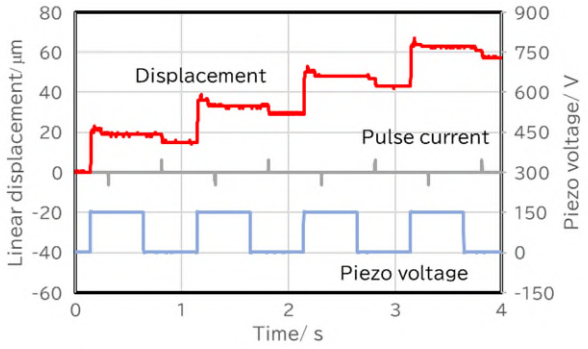

Figure 3. Linear displacement, pulse current, and piezo voltage

Figure 4 shows the results of the rotational operation. The rotational displacement, the voltage applied to piezo C, and the current pulse applied to EPM A are shown. The rotational displacement is synchronized with the extension of the piezo c, and the rotational displacement per cycle of the off-state EPM A reaches 1.3 mrad. In contrast to the linear operation, a reverse rotational displacement does not occur.

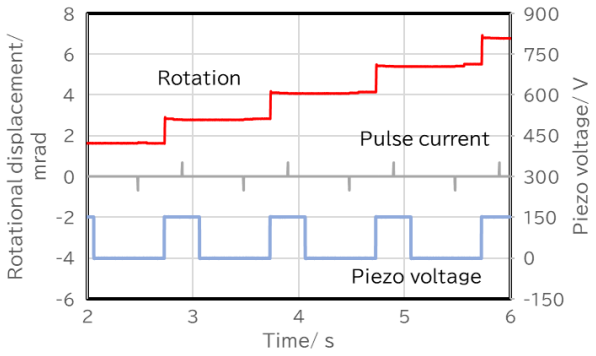

Figure 4. Rotational displacement, pulse current, and piezo voltage

5. Conclusion

This study presented an X–Y–Theta actuator using piezoelectric elements and electropermanent magnets, which serve as the position-holding mechanism and enable switching between the on-state and off-states using short current pulses. Experimental results demonstrated a linear displacement of 15 µm per cycle and a rotational displacement of 1.3 mrad per cycle. These performance metrics can be further improved by applying closed-loop control of the X-Y-Theta actuator. By incorporating high-precision feedback sensors, it will be possible to compensate for environmental disturbances. This approach is expected to improve positioning accuracy, enabling the actuator to support applications requiring nanometer-level control.

References

[1] Chang, Q., Chen, W., Zhang, S., Deng, J. and Liu, Y., 2024 Review on multiple-degree-of-freedom cross-scale piezoelectric actuation technology. *Advanced Intelligent Systems*, **6**(6), p.2300780.

[2] Katsushi Furutani, Toshiro Higuchi, Yutaka Yamagata, Naotake Mohri 1998 Effect of lubrication on impact drive mechanism, Precision Engineering **22**,(2), 78-86

[3] A. Torii, M. Banno, A. Ueda, K. Doki, 2012 A Small-Size Self-Propelled Stewart Platform *Electr. Eng. Jpn.* 2012, **181**, 37-46

[4] Moran, A.M., Vo, V.T., McDonald, K.J., Sultania, P., Langenbrunner, E., Chong, J.H.V., Naik, A., Kinnicutt, L., Li, J. and Ranzani, T., 2024 An electropermanent magnet valve for the onboard control of multi-degree of freedom pneumatic soft robots. *Communications Engineering*, **3**(1), p.117

euspen's 26th International Conference & Exhibition, Krakow, PL, June 2026
www.euspen.eu

Measuring the future - Nanometrology for advanced manufacturing of miniaturized devices

Agnieszka Maria Jastrzębska[1], Madhurya Chandel[1], Andreas Rosenkranz[2], Daniel Moraru[3], Adam Woźniak[1]

[1] *Warsaw University of Technology, Faculty of Mechatronics, św. Andrzeja Boboli 8, 02-525 Warsaw, Poland.*
[2] *Department of Chemical Engineering, Biotechnology and Materials, University of Chile, Avenida Beauchef 851, Santiago, Chile*
[3] *Research Institute of Electronics, Shizuoka University, 3-5-1 Johoku, Chūō-ku, Hamamatsu, 432-8011 Japan*

Abstract
Nanometrology is a cornerstone of modern manufacturing, pivotal in enabling precise measurements and materials characterization at the micro- and nano-scales. Therefore, we provide a short perspective based on [1] that explores the crucial contributions of nanometrology to advancing the frontiers of high-tech manufacturing, with a particular focus on quality control of diverse material assemblies and hybridization. The cutting-edge contribution of nanometrology to the Internet of Things (IoT) is closely tied to the meticulous development of miniaturized devices. The assessment of novel scanning, sensor, and probing techniques generates valuable insights into measuring nanoscale device dimensions, architectures, composition, and properties, while reducing the influence of measurement distortions, noise, and high-aspect ratios. Furthermore, we guide interested readers through methods applicable for field-effect transistors (FET), n-type or p-type metal oxide semiconductor field effect (n/p-MOSFET), metal-insulator semiconductor field effect (MISFET), novel complementary metal oxide semiconductor field effect transistors (CMOSFET), as well as magnetoelectric (ME) micro and nanoelectromechanical systems (ME M/NEMS). In this regard, nanometrology will revolutionize advanced manufacturing of miniaturized devices by ensuring their quality, thus propelling industries towards unprecedented levels of precision, repeatability, and efficiency to meet the ultimate goal of far-field very low frequency (VLF) communication in IoT with minimal energy consumption, low power loss, and outstanding multifunctionality/versatility.

nanometrology, miniaturized devices, fabrication quality, resolution, uncertainty

1. Introduction

As technology advances, precise measurements at smaller scales become increasingly essential for scientific and technological innovation, driven by the downsizing of components and structures to nano-scale dimensions. Therefore, nano-metrology, a specialized branch of metrology, has emerged as a vital tool in the manufacturing of modern devices, enabling the precise measurement and characterization of their features at the nanoscale. Here, we provide a short perspective based on the full paper.[1] Hybrid metrology approaches have the potential to achieve critical sub-nanometer dimensions and can become key to successful nanoscale research and specialised manufacturing designed for the Internet of Things (IoT).[2]

Nanometrology offers suitable tools and methodologies tailored to overcome the limitations of conventional approaches, thereby ensuring the reliability and performance of multimaterial-based miniaturized devices, such as field-effect transistors (FETs), including junction FETs (JFETs) and insulated-gate FETs (IGFETs). Miniaturized IoT-grade devices that require novel nanometrology approaches include CMOS, which has recently moved from bulk optics to detecting optical beams with angular momentum, as well as metal-oxide-semiconductor FET (MOSFET), and novel complementary metal-oxide-semiconductor field-effect transistors (CMOSFET).[3]

Therefore, in [1] we looked beyond the horizon of nanometrology. Its future lies in the continued synergy of innovative measurement technologies and methodologies, setting the stage for more accurate, reliable, and efficient measurement solutions that will drive the next wave of technological breakthroughs.

2. Metrology at the nanoscale

While scaling of miniaturized IoT-grade devices continues to push boundaries deep into the nanoscale, it faces significant metrological limitations as it approaches atomic-scale dimensionality. Therefore, nanometrology tools are required to characterize the nanoscale doping gradients, electrostatic potentials, and material interfaces that govern the operation of MEMS or NEMS devices.

Both MEMS and NEMS combine electrical and mechanical components. However, controlling the quality of nano-component assembly in MEMS is challenging as these are microscopic devices with a characteristic length of less than 1 mm (but greater than 1 µm), while NEMS are nanoscopic devices with a characteristic length of less than 1 µm.[4]

In another example, polaritons generated and propagated in CMOS-compatible plasmonic ultrathin topological insulators can exhibit plasmonic figures of merit comparable to those of noble metals. However, developing reliable methods to track the spatial displacement of plasmonic angular momentum modes in a 100-nm-thick Sb_2Te_3 thin film is challenging.[5]

Alternative transistor architectures, such as Junction-less Transistors (JLTs) and Tunnel FETs (TFETs), are particularly attractive for ultra-low-power electronics. The critical challenge in TFET development lies in optimizing the tunneling efficiency, which is heavily influenced by the material selection, doping profiles, and junction geometry. This requires controlling the uniform doping of high-concentration channels to eliminate the need for source-drain junctions.[6]

Furthermore, integrating TFETs with silicon technology poses a unique metrology challenge, particularly overcoming silicon's indirect bandgap, which requires sub-nanometer resolution and traceability to ensure device reliability.

3. Hybridized nanometrology for miniaturized devices

An ideal reference metrology (RM) system provides International System of Units (SI)-traceable measurements with known and sufficiently low uncertainty. A nanometer-level measurement uncertainty (MU) in critical dimensions (CD) metrology tools is essential for controlling the manufacturing of products with CDs below 100 nm. Two key factors emerged as particularly significant: sample-to-sample measurement bias variation and sampling uncertainty.[7]

Recently, hybridized metrology tools have emerged, aiming at enhancing the accuracy of high-throughput inline or reference metrology tools by integrating measurements from another technology. In this regard, the possibility of hybridizing metrologies was thoroughly reviewed in Ref. [1], and here we present a shortened key discussion. These techniques leverages the strengths of multiple measurement techniques to minimize the uncertainty of a particular measurement.[1]

Figure 1 illustrates the fundamental relationship between analytical resolution, detection limits, analytical spot size, and metrology footprint, highlighting why hybridized metrology approaches are increasingly important for advanced nanoscale characterization. Such integration is particularly important for advanced semiconductor devices, MEMS/NEMS technologies, and IoT-oriented miniaturized systems, where accurate dimensional and functional characterization is essential for ensuring device performance, energy efficiency, and manufacturing reliability [1]. Effective control of CD is essential for successful nanoscale operations. Through extensive research and daily application in the semiconductor industry, it became evident that additional MU components need to be considered.[8]

According to **Figure 1A,** techniques with extremely high spatial resolution often operate over limited sampling areas and may suffer from reduced throughput or sensitivity to measurement noise and surface distortions. Conversely, methods capable of rapid large-area inspection may lack the spatial precision required for sub-nanometer characterization. This trade-off motivates the integration of complementary metrology techniques that combine high-resolution local measurements with statistically relevant large-area analyses.

Figure 1B further demonstrates how the metrology footprint varies as a function of spatial resolution. The footprint defines the effective interaction area between the measurement system and the analyzed structure, directly influencing measurement uncertainty, feature detectability, and reproducibility.

For instance, Scanning electron microscopy (SEM) can achieve resolutions of several nanometers. The total measurement uncertainty (TMU) of CD at SEM is influenced by variations in feature shape caused by changes in the lithography scanner's focus.[9] However, SEM can be hybridized with Atomic Force Microscopy (AFM). In atomic force microscopy, critical dimensions (CD AFM) are often required to evaluate the TMU of the system under test.[9]

In general, CD AFM is a strong candidate for linewidth reference metrology due to its low sample-to-sample bias variation and high sampling efficiency. Sampling efficiency is the degree of sample averaging inherent in a single measurement.[9]

SEM hybridised with Transmission Electron Microscopy (TEM) to enable lower sample-to-sample bias. Although TEM can serve as a reference tool, it is a costly and time-consuming option.[1]

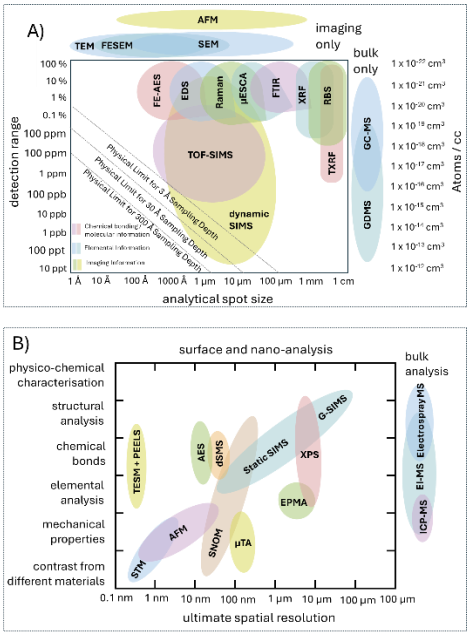

Figure 1. A) Analytical resolution of various measurement techniques versus their detection limits related to analytical spot size and number of features in the detection area. B) Metrology footprint as a function of special resolution, adopted from Ref. [1].

4. Summary

Advances in metrology have been pivotal in driving groundbreaking development in nanoscale materials and device fabrication over several decades. As device dimensions continue to shrink and architectures become more complex, no single measurement technique can simultaneously provide high spatial resolution, large-area coverage, low uncertainty, and sufficient sensitivity to detect critical nanoscale features. In hybridized metrology frameworks, combining techniques with different footprints and sensing principles enables more reliable multidimensional characterization of complex nanoarchitectures, high-aspect-ratio structures, and heterogeneous material assemblies.

References

[1] Chandel M, Rosenkranz A, Moraru D, Woźniak A, Jastrzębska A 2025 Measuring the Future–Nanometrology for Advanced Manufacturing of Miniaturized Devices *Adv. Funct. Mater.* **2501663** 1-28

[2] Wozniak A, Mayer JRR 2007 Recent Advances in Mechatronics, Springer, Berlin, Heidelberg, 621–626

[3] Tripathi PN, Ojha SK, Jha RK, Nazarov A 2021 Investigation of BiFeO3/HfO2 gate stack for ferroelectric field effect transistors in IOT applications *J. Mater. Sci: Mater. Electron.* **32** 22517

[4] Klein O, de Loubens G, Naletov VV, Boust F, Guillet T, Hurdequint H, Leksikov A, Slavin AN, Tiberkevich VS, and Vukadinovic N 2008 Ferromagnetic resonance force spectroscopy of individual magnetic nanoparticles *Phys. Rev. B* **78** 144410

[5] Yue Z, Ren H, Wei S, Lin J, Gu M 2018 Angular-momentum nanometrology in an ultrathin plasmonic topological insulator film *Nat. Commun.* **9** 4413

[6] Colinge J-P, Lee C-W, Afzalian A, Akhavan ND, Yan R, Ferain I, Razavi P, O'Neill B, Blake A, White M, Kelleher A-M, McCarthy B, Murphy R 2010 Nanowire transistors without junctions *Nat. Nanotech.* **5** 225-229

[7] Ukraintsev V, Banke B 2010 Reference metrology for nanotechnology: significance, challenges and solutions, Instrumentation, Metrology, and Standards for Nanomanufacturing IV, SPIE 37–51

[8] Hsu T-R, 2002 MEMS and Microsystems: Design and Manufacture, McGraw-Hill

[9] Sendelbach M, Archie CN 2003 Metrology, Scatterometry measurement precision and accuracy below 70 nm, Inspection, and Process Control for Microlithography XVII, SPIE 224–238

euspen's 26th International Conference & Exhibition, Krakow, PL, June 2026
www.euspen.eu

Levitation characteristics and vibration behavior in ultrasonic levitation actuators

Shota Aoki [1], Akihiro Torii [1], Suguru Mototani [1], Kae Doki [1]

[1]*Aichi Institute of Technology, Aichi, Japan*

v25701vv@aitech.ac.jp

Abstract

This study introduces a non-contact ultrasonic levitation actuator aimed at reducing friction-induced surface damage and positioning errors in precision motion systems. The actuator consists of a stainless-steel inertial mass, a multilayer piezoelectric element, and an aluminum plate. When driven by a high-frequency voltage, the plate generates a squeeze film of air that enables micrometer-scale levitation. To avoid audible noise observed in previous levitation actuators operating in the 10 kHz range, the proposed actuator is driven at ultrasonic frequencies above 20 kHz. Experiments were conducted by varying plate thickness from 1.0 mm to 2.0 mm in 0.2 mm increments under a sinusoidal voltage of 5 Vpp and drive frequencies between 20 kHz and 40 kHz. The maximum levitation height of approximately 44 µm was achieved at 25.5 kHz using a 1.0 mm thick plate with a vibration amplitude of 5.7 µm. These results clarify how plate thickness influences drive frequency and levitation performance, demonstrating the potential of ultrasonic levitation actuators for compact, high-precision positioning applications.

Levitation actuator, Piezoelectric actuator, Levitation characteristics

1. Introduction

In recent years, space constraints have become an issue in factories due to the increasing size of manufacturing equipment. Robots capable of micro-scale motion are receiving increasing attention in various research fields. Among various positioning mechanisms, inchworm-type robots are utilized[1]. Current research efforts are focused on the development of a freely movable inchworm-type robotic system that integrates electromagnetic actuators with piezoelectric elements (piezos) [2]. The locomotion of the robot is achieved through a combined mechanism involving the attraction and release of an electromagnetic coil and the extension and contraction of a piezo. However, this method presents issues, including surface damage caused by friction during the dragging operation of electromagnetic components, as well as a reduction in positioning accuracy. Therefore, we are investigating a levitation actuator as a non-contact mechanism. Previous studies on levitation actuators have employed drive frequencies in the 10 kHz range, resulting in undesirable acoustic noise[3]. In this paper, we aim to develop and characterize an ultrasonic levitation actuator operating beyond the audible frequency range, thereby eliminating noise during levitation.

2. Levitation actuator

Figure 1 shows the structure and operating principle of the proposed levitation actuator. The levitation actuator is composed of a stainless-steel inertial mass, a piezo, and an aluminum plate, which are bonded using a cyanoacrylate adhesive. The inertial mass used in the actuator has a height of 8 mm, a diameter of 20 mm, and a mass of 20 g. The piezo (Tokin, AE0505D16DF) exhibits a maximum displacement of 17.4 µm, when a DC voltage of 150 V is applied. It has a length of 20 mm, a crosssection of 5 mm by 5 mm, and a mass of 5 g. The aluminum plate shown in Figure 1 has a thickness of 1 mm, a diameter of 30 mm, and a mass of 2 g. In our previous study, a plate with the same diameter but a thickness of 3 mm was used, and levitation was achieved at driving frequencies between 4 kHz and 15 kHz.

When a high-frequency voltage is applied to the piezo, it vibrates rapidly in the vertical direction. This vibration generates a repulsive force between the plate and the ground surface, forming an air film known as the squeeze film. This phenomenon, referred to as the squeeze film effect, enables the actuator to levitate several micrometers above the ground. The levitation height is defined as the average value of the instantaneous vertical displacement of the plate, while the vibration amplitude is defined as the difference between the maximum and minimum vertical displacement of the plate.

The levitation is measuted by a laser displacement sensor. The laser beam is directed onto the top surface of the plate at a position within 1 mm from the plate edge to obtain the instantaneous vertical displacement, levitation height, and amplitude of the plate accurately.

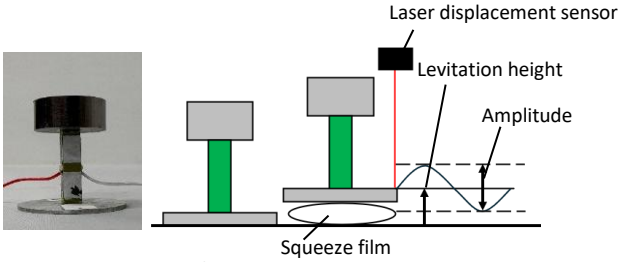

Figure 1. Levitation actuator

3. Experimental setup

The voltage from an oscillator is passed through an amplifier and applied to the piezo. A sinusoidal voltage of 5.0 Vpp, with a frequency ranging from 20 kHz to 40 kHz in 0.5 kHz increments, is applied to the piezo. The instantaneous vertical displacement of the plate is measured by a laser displacement sensor (Keyence, LK-H053). Both the vertical displacement and the applied voltage are recorded on an oscilloscope and a data recorder.

The levitation height defined as the average vertical displacement is obtained over a one-second interval. The vibration amplitude defined as the difference between the maximum and minimum vertical displacement is calculated, which is the peak-to-peak value corresponds to the vertical displacement of the plate.

4. Results and discussion

Figure 2 shows the experimental results of the characteristics of the levitation height for plates with different thicknesses. The horizontal axis and vertical axis denote the drive frequency and the levitation height, respectively. For the levitation actuator equipped with a 1.0 mm thick plate, levitation begins at approximately 25 kHz, and the maximum levitation height of 44.0 µm is achieved at 25.5 kHz. Beyond this frequency, the levitation height gradually decreased.

The levitation height using other plates with different thickness is smaller than that obtained by the 1.0-mm-thick plate. The frequency obtained by an individual plate thickness depends on the thickness of the plate. The second highest levitation height of 25.3 µm is achieved with the 2.0-mm-thick plate at 30.0 kHz.

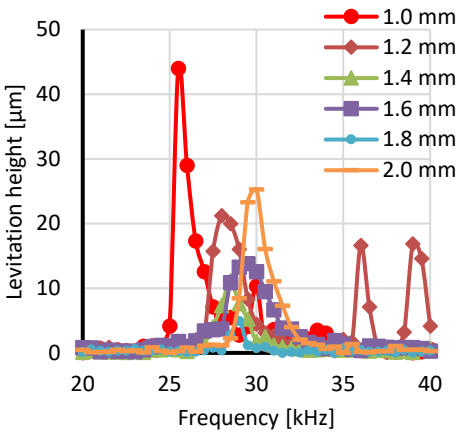

Figure 2. Levitation characteristics

Figure 3 summarizes the relationship between plate thickness, maximum levitation height, and the corresponding drive frequency. For each thickness condition, the levitation height is measured across a range of drive frequencies, and the maximum levitation height together with its corresponding frequency is identified. As the plate thickness increases, the maximum levitation height tends to decrease. The drive frequency at which the maximum amplitude occurs lies within the range of approximately 25 kHz to 30 kHz for all tested thicknesses.

To examine variations in vibration behavior due to plate thickness, the vertical displacements of the 1.0-mm and 2.0-mm plates are measured. Figure 4 shows the vertical displacement of the 1.0-mm and 2.0-mm plates. The 1.0-mm-thick plate exhibits an amplitude of 5.7 µm with a period of 0.039 ms, while the 2.0-mm-thick plate shows an amplitude of 3.1 µm with a period of 0.033 ms. The phase relationship between the applied voltage and the vertical displacement exhibits different phenomena. The 1.0-mm-thick plate lags the voltage by approximately 142.3 degrees, whereas the 2.0-mm-thick plate leads it by 58.3 degrees. These results indicate that plate thickness significantly affects the capacitive and inductive characteristics of the levitation actuator, thereby altering both the resonance frequency and phase response.

At the resonance frequency, the plate oscillates with its maximum amplitude under sinusoidal excitation, resulting in the maximum levitation height. When the plate vibrates with an applied voltage of 5 Vpp, the DC component of the applied voltage does not affect the vibration of the plate. This DC component originates from the capacitive characteristics of the piezo and the output impedance of the amplifier. Consequently, the phase difference between the applied voltage and the vertical displacement is caused by the characteristics of the squeeze air film.

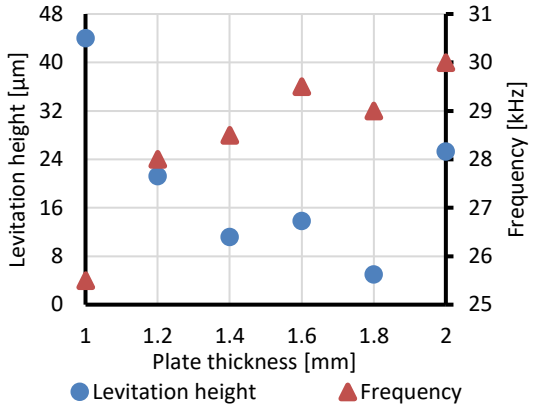

Figure 3. Relationship between plate thickness, Levitation height, and frequency

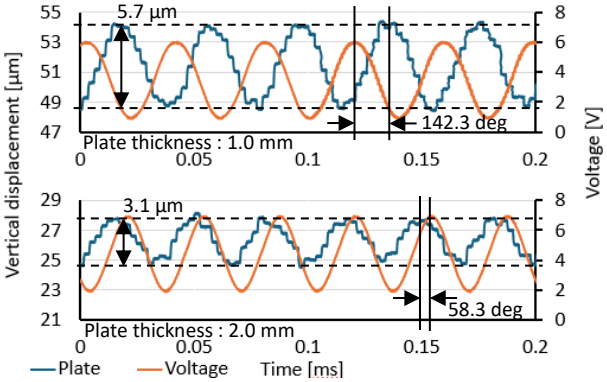

Figure 4. Drive voltage and vertical diaplacement of plates.

5. Conclusion

This study demonstrated the performance of an ultrasonic levitation actuator driven at frequencies above 20 kHz to avoid audible noise. Experiments using plates of varying thickness revealed that thinner plates produce larger vibration amplitudes and greater levitation heights, with the 1.0-mm plate achieving a maximum height of 44 µm at 25.5 kHz. As the plate thickness increases, both the amplitude and levitation height decrease, confirming the strong influence of structural stiffness on squeeze-film dynamics. These results provide practical design guidance for the development of compact, high-precision ultrasonic levitation actuators.

References

[1] S Ishibashi, Y Mitsuyoshi, A Torii, K Doki, S Mototani “THE MOTION OF A 6-DOF INCHWORM ON ROUGH SURFACE” AMERICAN SOCIETY FOR PRECISION ENGINEERING, 2015 ANNUAL MEETING VOL 62, pp. 241 - 244

[2] H Kato, K Hayakawa, A Torii, A Ueda, “XYθ actuators using piezoelectric and electromagnetic actuators” Electrical Engineering in Japan, Vol. 131, No. 4, 2000 pp. 44 -51

[3] R Kawai, H Takashima, A Torii, S Mototani, K Doki, “Characteristics of acoustic levitation system using piezoelectric actuator” euspen’s 23rd Int. con. & Exhibition, Copenhagen, DK, 2023 pp. 319-320

List of authors

Surname	Initial	Page
A		
Abe	M.	76
Acko	B.	68
Aerts	A.	362
Aguado	S.	180
Aguilar	J.J.	180
Aguirre	G.	218
Al Farisi	A.	312
Alaña	M.	218
Albajez	J.A.	82
Aliyev	R.	228
Alves de Jesus	D.	362
Amaral	V.	362
Anderson	C.	370
Anik	A.A.M.	200
Anwer	N.	76,96,124, 366
Aoki	S.	436
Archenti	A.	144,196, 392
Archilha	N.	362
Arneson	D.	204
Arshad	M.H.	284,290,312
Aurich	J.	230,388
B		
Baldon	G.	362
Ballach	F.	126
Balsamo	A.	116
Barbieri	M.	216
Barini	E.	322
Barros Zanoni Lopes Moreno	G.	362
Bartkowiak	T.	72,88
Baruffa	G.	234,260
Bastardo	J.	218
Baur	C.	330
Bennett	A.	326
Bennoune	R.	124
Bergstrand	S.	76
Bertolini	R.	412
Binninger	R.	176,212
Bissacco	G.	158
Bitou	Y.	100
Björkstrand	R.	242
Blateyron	F.	44,80
Blunt	L.	48,298
Bock	E.	414
Boarino	L.	136
Bode	J.	326
Bode	S.	288,296
Bodenbenner	M.	76
Bolderman	M.	426
Borges	T.	362
Börner	R.	300
Börret	R.	146,274
Bosse	H.	136
Böttcher	F.	246
Böttger	T.	278
Bottin	A.	412
Bouman	N.	350
Brault	R.	96
Brehmer	A.	404
Brito	K.	362
Brosed Dueso	F.J.	180
Brown	C.A	88
Bruneau	O.	96
Bruschi	S.	412
Bueno	C.	362
Bui	V.	270
Buice	E.	374
Byczuk	B.	254
C		
Cai	B.	222
Calaon	M.	216
Campoi	L.	362
Caron	G.	362
Cas	L.	68
Castagne	S.	284
Castro	F.A.	136
Catalucci	S.	76,114,120,122
Chandel	M.	434
Chen	G.	222
Chen	X.	134
Cheruiyot	B.K.	300
Cheung	B.C.F.	238
Cho	M.S.	62
Christoph	R.	126
Christoph	R.	126
Colldelram	C.	376
Coluccini	S.	362
Cosandier	F.	330
Coutinho	P.	362

Crawford H.L. 374
Cullinan M. 280
Czulek D. 76

D

Dadbakhsh S. 110
Damak M. 124
Dang Y. 76
Denissen M. 350
Díaz-Pérez L. 82
Didonè L. 76,120,308
Divíšek D. 394
Dobrzyński M. 110
Doki K. 432,436
Dunaj P. 196
Dürre G. 404
Dusek M. 150

E

Edelmann J. 224,246
Edinger L-A. 288
Evangelista Matoso J.V. 362
Evans A. 136
Evens T. 284

F

Faivre A. 44
Fallon P. 374
Fantoni G. 216
Fedorynenko D. 166
Fletcher S. 200
Fofana L. 96,366
Franssen R. 362
Freggia E. 216
Frentzel L. 320
Frieiro Castro J.L. 376
Fröhlich T. 190,348
Frömel L-J. 56,76
Furuya R. 174
Faivre A. 44

G

Galetto M. 76,322
Gallardo Artal D. 82
Gapinski B. 72
Garcia-Berdote A. 76
Gąska A. 56,76,102
Gąska P. 54,102
Gayde J-C. 150
Geiselhart M. 158
Genta G. 76,322
Genzwürker M. 158
Ghim Y-S. 86
Ghorbanalipour S. 246,266
Giza L. 382
Gljušćić P. 342
Gobey K. 326
Gołaszewski M. 354
Gomez-Acedo E. 76
González N. 376
Grochalski K. 72
Gruza M. 54,102
Gupta N.K 278

H

Hageney H. 76
Haikonen S. 128
Hammer M. 126
Hanquist C-H. 76
Harmatys W. 54,56,76,102
Hasnaoui S. 330
Hausotte T. 190
Haverinen P. 140
Heikkinen V. 76
Hein G. 190
Heißelmann D. 56,76
Hemming B. 76
Henein S. 330
Henning A. 52,132
Henriel Pozza G. 362
Hocke T. 418
Horejs O. 394
Huang S. 284
Hung S-H. 154
Hura I. 116
Hutsky A. 404

I

Imanishi M. 346
Imkamp D. 76

J

Jakubowicz M. 72,88
Jang S. 60
Jansen L. 170
Janzen K. 56,76
Jastrzębska A. 434
Javed T. 266

Jedynak M. 54
Jedrzejak P. 382
Jiang X. 48,52,132, 370,400
Joo K-N. 60,62,66
Josić K. 96,366
Judy A. 176
Jutte W. 426

K

Kachelrieß M. 126
Kajima M. 100
Kakol S. 382
Kang C. 162
Kato T. 430
Kato Y. 40
Kayser N. 404
Ke C. 162
Kenanoğlu Ö.T. 192
Khim G. 208
Kilikevičius A. 254
Kim H-Y. 186
Kim H-S. 210
Kim K. 186
Kjartansson H. 292
Klobucar R. 68
Knapp B. 204
Knulst W. 76,136,316
Kobiela K. 54,382
Kok G. 76
Kondo Y. 40
Konnanath Puthanveetil V.R. 132
Korpelainen V. 136
Kortaberria G. 76
Kräusel V. 224
Kumar P. 48
Kushwaha S. 192

L

Laermans V. 284
Lafon L-F. 96,366
Laine E. 128
Lassila A. 76,136
Le T.D. 418
Lee M-G. 186
Lee S. 66
Lee S. 208,210
Leutonen O. 242,386
Li H. 52
Liao K. 238
Linkeová I. 76
Litorp K. 308
Liu D. 400
Liu Y. 222
Liu Z. 338
Longstaff A. 200
Looman J. 316
Lou S. 134,370
Lucchetta G. 234,260
Lund C. 308
Lyu Z. 290

M

Maculotti G. 76,322
Magdziak M. 106
Majarena A.C. 180
Majda P. 196
Maluf R. 362
Mareš M. 394
Maresch T. 76
Markiewicz M. 54
Martin A. 266,270
Martin H. 52,132
Martínez López J.I. 292
Marxer M. 35
Matsuzaki K. 40
Maurya H.S. 392
Mayer J.R.R. 408
Meena A. 304
Mehdi-Souzani C. 96,366
Melhado Mazza R. 292
Merks R. 426
Michihata M. 100
Mietinski P. 88
Miettinen M. 140,242,386
Milecki A. 88
Mirowska A. 110
Miyakawa Y. 40
Mizushima D. 174
Moll A. 176
Mollaei Ardestani A. 292,308,322
Moos S. 326
Morais P. 414
Moraru D. 434
Mori Y. 346
Mototani S. 432,436
Muhamedsalih H. 48
Müller T. 126

Mustafa A.M. 48
Mutilba U. 76

N

Naatz L. 212
Nakao Y. 166
Nalbantoglu D. 76
Neo D.W.K. 256
Nestler A. 300
Neto A. 362
Neuschaefer-Rube U. 56,76
Neyra J. 362
Nguyen M.T. 86
Nguyen N.H. 128
Nicolás J. 376
Nouira H. 76,96,124,366

O

O'Connor D. 136
Oh J.S. 208
Oh S. 186
Ohkubo Y. 346
Ohnishi Y. 166,346
Oliveira E. 362
Ortiz-Vazquez J.J. 292
Oss D. 204
Ostrowska K. 382
Osuch P. 254
Ou J-Y. 52
Owczarek D. 54
Owen R. 132
Ozcan Y. 192

P

Pappinisseri Puluckul P. 342
Pasin D. 122
Paul F. 76
Peng S. 222
Pereira N.B. 376
Pereira J. 362
Phillips D. 136
Pierro A. 76
Pietrobon G. 308
Pimentel G. 362
Plowucha W. 116
Polak K. 150
Polte M. 176,418
Polte J. 36,288,296, 404
Popielski K. 408
Powałka B. 196,354
Princen M. 362
Przyklenk A. 136
Pueo M. 180
Puerto P. 76

Q

Qin Y. 370

R

Rashid A. 110
Rehman M.M.U. 284
Reynaerts D. 192,284,290,312
Rhee H-G. 86
Richter K. 224
Riihola J. 386
Ro S-K. 210
Rodrigues M. 414
Rogge N. 190
Rongyan S. 346
Rosenkranz A. 434
Rucki M. 254
Ruijl T. 362
Ruiz Beltri P. 316

S

Sakai K. 264
Sakai T. 432
Salmi M. 242
Sanetra I. 54
Santos V. 362
Sasahara H. 250
Sato O. 40,76,100
Sauer P. 326
Savio E. 76,114,120,122, 260,308,412
Saxena K.K. 284,290,312
Scheibe H. 320,348,358
Schimpf C. 278
Schinn J. 190
Schlemper H-J. 326
Schmidt T. 224
Schmitt K. 212
Schmitt R.H. 76
Schubert A. 266,270,300
Schubert G. 362
Schulz S. 184
Scott P. 370

Shan	S.	134
Shim	J.	186
Shizuka	H.	264
Sieberg	J.	176
Silva	J.	362
Simon	R.	404
Składanowska	K.	54
Skoczypiec	S.	422
Son	J.	186
Song	L.	162
Sørby	K.	170
Sorgato	M.	234,260
Sosin	M.	150
Soukal	J.	76
Sousa	A.	92
Souza	M.	362
Spaan	H.	426
Spaan-Burke	T.	426
Spada	I.	216
Stafford	G.	280
Streit	S.	184
Strijbosch	N.	426
Stroński	K.	54,382
Sulc	M.	150
Sulitka	M.	394
Sun	P.	144
Sun	W.	134
Szczepanski	M.	404
Szczepański	A.	106
Sze Yip	W.	338

T

Takahashi	M	430
Takahashi	S.	100
Takayama	Y.	432
Tan	N.Y.J.	256
Tan	V.B.C.	256
Tanaka	T.	250
Tang	D.	52,132
Tang	J.	338
Tawfik	A.	298
Theska	R.	320,348,358
Thore	A.	76
Tissot-Daguette	L.	330
Tokai	K.	264
Tomkowski	R.	110,392
Torii	A.	432,436
Torres Melgarejo	M.A.	358
Tosello	G.	76,292,304,308, 322
Townend	D.	52,132
Trapp	P.	126
Triebel	F.	176,212
Trines	R.	350
Tsao	L.	154
Tsuda	N.	174

U

Uhlmann	E.	176,288,418
Urreta	H.	218
Usami	S.	346

V

Vainio	V.	242
Van Bael	A.	284
van Dam	T.	426
Van der Wel	A.	426
Van Dijck	B.	362
van Dijk	M.	76
Van Haren	C.	362
Varga	F.	362
Velázquez	J.	180
Verbaan	K.	316
Verna	E.	76
Vierling	M.	230,388
Viitala	R.	128,140,242,386
Vleugels	J.	284
Volz	T.	184

W

Wang	C.	238
Wang	C.	334
Wang	Y.	404
Wang	Z.	256
Wasmuth	F.	404
Watanabe	M.	100
Watrelot	L.	150
Wendel	T.	144
Wieczorowski	M.	72,88
Wijnhoven	M.	362
Wikło	M.	254
Wilczek	A.	146,274
Wilk	Ł.	54
Williamson	J.	52,132
Witteman	B.	362
Wittke	M.	320,348

Wojtowicz	A.	76
Wojtyła	M.	116
Wolf	M.	320,348
Wöllenstein	J.	212
Woźniak	A.	34,408,434

X

Xhafa	E.	76

Y

Yague-Fabra	J.	82
Yamamura	K.	346
Yap	T.	280
Yazgan	S.	296
Yin	K.	370
You	J-H.	298
Yague-Fabra	J.	82
Yamamura	K.	346
Yap	T.	280
Yazgan	S.	296
Yin	K.	370
You	J-H.	298

Z

Zanella	P.	362
Zavala-Arredondo	M.	298
Zeidler	H.	228,278
Zekalmi Richa	Y.	82
Zelenika	S.	342
Zell	F.	388
Zeng	W.	400
Zettler	N.	146,274
Zha	J.	162
Zhang	J.	334,338
Zhang	L.	228
Zhang	Y.	292
Zhang	X.	200
Zhang	Z.	334
Zhong	W.	132,400
Zhong	Y.	190
Zilio	N.	414
Żyra	A.	422